Wiley Series in Acoustics, Noise and Vibration

ULTRASOUND ELASTOGRAPHY FOR BIOMEDICAL APPLICATIONS AND MEDICINE

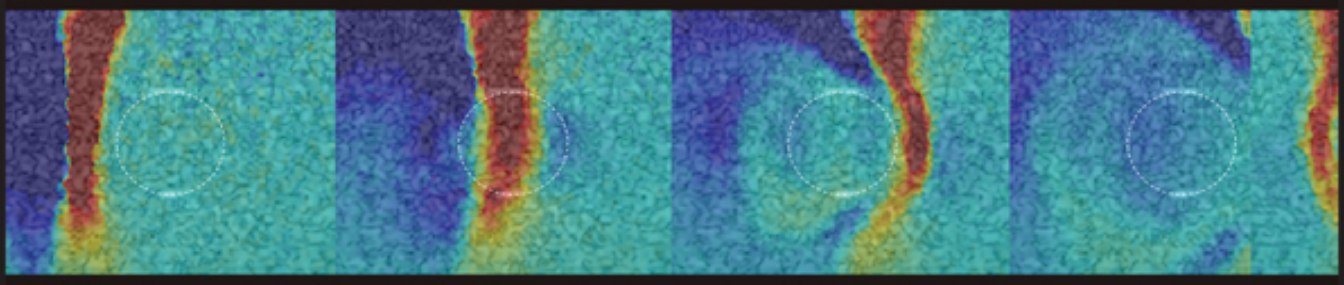

Edited by
Ivan Nenadic
Matthew Urban
James Greenleaf
Jean-Luc Gennisson
Miguel Bernal
Mickael Tanter

WILEY

Ultrasound Elastography for Biomedical Applications and Medicine

Ultrasound Elastography for Biomedical Applications and Medicine

Edited by
Ivan Nenadic
Mayo Clinic
USA

Matthew Urban
Mayo Clinic
USA

James Greenleaf
Mayo Clinic
USA

Jean-Luc Gennisson
Imagerie par Résonance
Magnétique Médicale et
Multi-Modalités
France

Miguel Bernal
Universidad Pontificia
Bolivariana
Colombia

Mickael Tanter
Institut Langevin - Ondes et Images
ESPCI ParisTech CNRS
France

WILEY

This edition first published 2019

Registered Offices
John Wiley & Sons, Inc., 111 River Street, Hoboken, NJ 07030, USA
John Wiley & Sons Ltd, The Atrium, Southern Gate, Chichester, West Sussex, PO19 8SQ, UK

Editorial Office
The Atrium, Southern Gate, Chichester, West Sussex, PO19 8SQ, UK

For details of our global editorial offices, customer services, and more information about Wiley products visit us at www.wiley.com.

Wiley also publishes its books in a variety of electronic formats and by print-on-demand. Some content that appears in standard print versions of this book may not be available in other formats.

Library of Congress Cataloging-in-Publication Data

Names: Nenadic, Ivan Z. (Ivan Zdenko), 1983- editor.
Title: Ultrasound Elastography for Biomedical Applications
and Medicine / [edited by] Ivan Z. Nenadic, Matthew W. Urban, James F.
Greenleaf, Miguel Bernal, Mickael Tanter, Jean-Luc Gennisson.
Description: Hoboken, NJ :Wiley, 2019. | Includes bibliographical references
and index. |
Identifiers: LCCN 2018017424 (print) | LCCN 2018017679 (ebook) | ISBN
9781119021551 (Adobe PDF) | ISBN 9781119021544 (ePub) | ISBN 9781119021513
(hardcover)
Subjects: | MESH: Elasticity Imaging Techniques–methods
Classification: LCC RC78.7.U4 (ebook) | LCC RC78.7.U4 (print) | NLMWN 208 |
DDC 616.07/543–dc23
LC record available at https://lccn.loc.gov/2018017424

Cover Design: Wiley
Cover Image: Image courtesy of Ivan Nenadic, Matthew Urban, James Greenleaf, Jean-Luc Gennisson, Miguel Bernal and Mickael Tanter

Set in 10/12pt WarnockPro by SPi Global, Chennai, India

10 9 8 7 6 5 4 3 2 1

Contents

List of Contributors

Azra Alizad
Department of Radiology
Mayo Clinic
Rochester, Minnesota
USA

Carolina Amador Carrascal
Department of Physiology and Biomedical Engineering
Mayo Clinic
Rochester, Minnesota
USA

Sara Aristizabal
Well Living Lab
Rochester, Minnesota
USA

Stéphane Audière
Echosens
Paris
France

Paul E. Barbone
Department of Mechanical Engineering
Boston University
Boston, Massachusetts
USA

Cécile Bastard
Echosens
Paris
France

Miguel Bernal
Universidad Pontificia Bolivariana
Medellín
Colombia

David Bradway
Department of Biomedical Engineering
Duke University
Durham, North Carolina
USA

Javier Brum
Laboratorio deAcustica Ultrasonora
Instituto de Fisica, Facultad de Ciencias
Universidad de la Republica
Montevideo
Uruguay

Stefan Catheline
LabTAU
INSERM-University of Lyon
Lyon
France

Shigao Chen
Department of Radiology
Mayo Clinic
Rochester, Minnesota
USA

Tomasz J. Czernuszewicz
The Joint Department of Biomedical Engineering
The University of North Carolina at Chapel Hill and North Carolina State University
Chapel Hill and Raleigh, North Carolina
USA

Jan D'hooge
KU Leuven
Leuven
Belgium

Jean Francois Dord
Department of Mechanical Aerospace and Nuclear Engineering
Rensselaer Polytechnic Institute
Troy, New York
USA

Marvin M. Doyley
Department of Electrical and Computer Engineering
Hajim School of Engineering and Applied Sciences
University of Rochester
Rochester, New York
USA

Daniel Escobar
Department of Physiology and Biomedical Engineering
Mayo Clinic
Rochester, Minnesota
USA

Stephanie A. Eyerly-Webb
Department of Biomedical Engineering
Duke University
Durham, North Carolina
USA

Mostafa Fatemi
Department of Physiology and Biomedical Engineering
Mayo Clinic
Rochester, Minnesota
USA

Céline Fournier
Echosens
Paris
France

Caterina M. Gallippi
The Joint Department of Biomedical Engineering
The University of North Carolina at Chapel Hill and North Carolina State University
Chapel Hill and Raleigh, North Carolina
USA

Jean-Luc Gennisson
Imagerie par Résonance Magnétique Médicale et Multi-Modalités
Université Paris-Saclay
Orsay
France

Sevan Goenezen
Department of Mechanical Aerospace and Nuclear Engineering
Rensselaer Polytechnic Institute
Troy, New York
USA

James Greenleaf
Department of Physiology and Biomedical Engineering
Mayo Clinic
Rochester, Minnesota
USA

Timothy J. Hall
Medical Physics Department
University of Wisconsin
Madison, Wisconsin
USA

Brecht Heyde
KU Leuven
Leuven
Belgium

Peter Hollender
Department of Biomedical Engineering
Duke University
Durham, North Carolina
USA

Michael F. Insana
Departments of Bioengineering and Electrical and Computer Engineering
Beckman Institute for Advanced Science and Technology
University of Illinois at Urbana-Champaign
Champaign, Illinois
USA

Jingfeng Jiang
Department of Biomedical Engineering
Michigan Technological University
Houghton, Michigan
USA

Vaibhav Kakkad
Department of Biomedical Engineering
Duke University
Durham, North Carolina
USA

Elisa Konofagou
Department of Biomedical Engineering
Columbia University
New York, New York
USA

Roberto Lavarello
Laboratorio de Imágenes Médicas
Departamento de Ingeniería
Pontificia Universidad Católica del Perú
Lima
Peru

Stephen A. McAleavey
Biomedical Engineering Department
University of Rochester
Rochester, New York
USA

Véronique Miette
Echosens
Paris
France

Oana Mirea
KU Leuven
Leuven
Belgium

Ivan Nenadic
Department of Physiology and Biomedical Engineering
Mayo Clinic
Rochester, Minnesota
USA

Assad A. Oberai
Department of Mechanical Aerospace and Nuclear Engineering
Rensselaer Polytechnic Institute
Troy, New York
USA

Michael L. Oelze
Bioacoustics Research Laboratory
Department of Electrical and Computer Engineering
University of Illinois at Urbana-Champaign
Champaign, Illinois
USA

Jennifer Oudry
Echosens
Paris
France

Kevin J. Parker
Department of Electrical and Computer Engineering
University of Rochester
Rochester, New York
USA

Theo Pavan
Departmento de Física
University of São Paulo
São Paulo
Brazil

Bo Peng
Department of Biomedical Engineering
Michigan Technological University
Houghton, Michigan
USA

Laurent Sandrin
Echosens
Paris
France

Armen Sarvazyan
Artann Laboratories
West Trenton, New Jersey
USA

Magali Sasso
Echosens
Paris
France

Pengfei Song
Department of Radiology
Mayo Clinic
Rochester, Minnesota
USA

Mickael Tanter
Institut Langevin–Waves and Images
Ecole Superieure de Physique et de Chimie Industrielle (ESPCI)
Paris
France

Gregg Trahey
Department of Biomedical Engineering
Duke University
Durham, North Carolina
USA
and
Department of Radiology
Duke University Medical Center
Durham, North Carolina
USA

Matthew Urban
Department of Radiology
Mayo Clinic
Rochester, Minnesota
USA

Luiz Vasconcelos
Department of Physiology and Biomedical Engineering
Mayo Clinic
Rochester, Minnesota
USA

Maryam Vejdani-Jahromi
Department of Biomedical Engineering
Duke University
Durham, North Carolina
USA

Yue Wang
Department of Bioengineering
Beckman Institute for Advanced Science and Technology
University of Illinois at Urbana-Champaign
Champaign, Illinois
USA

Benjamin Wood
Department of Physiology and Biomedical Engineering
Mayo Clinic
Rochester, Minnesota
USA

Heng Zhao
Department of Physiology and Biomedical Engineering
Mayo Clinic
Rochester, Minnesota
USA

Section I

Introduction

1

Editors' Introduction

Ivan Nenadic[1], Matthew Urban[2], James Greenleaf[1], Jean-Luc Gennisson[3], Miguel Bernal[4], and Mickael Tanter[5]

[1] *Department of Physiology and Biomedical Engineering, Mayo Clinic, Rochester, MN, USA*
[2] *Department of Radiology, Mayo Clinic, Rochester, MN, USA*
[3] *Imagerie par Résonance Magnétique Médicale et Multi-Modalités, Université Paris-Saclay, Orsay, France*
[4] *Universidad Pontificia Bolivariana, Medellín, Colombia*
[5] *Institut Langevin–Waves and Images, Ecole Superieure de Physique et de Chimie, Industrielle (ESPCI) Paris, France*

Medical imaging has become an integrated part of modern medicine. Images are made on the basis of exploiting physical processes as contrast mechanisms. For example, X-Ray imaging takes advantage of the differences in mass density of different tissues. Magnetic resonance imaging uses proton densities and magnetic relaxation times to create exquisite images of different soft tissues. Ultrasound imaging takes advantage of acoustic impedance differences related to the compressibility of tissue.

Palpation has been practiced by physicians for centuries because pathological tissue "feels" harder or stiffer than normal tissues, as in the examples of breast tumors. Palpation has some disadvantages – such as being subjective, dependent on the proficiency of the examiner, insensitive to deep or small lesions, and difficult to compare assessments at different time points. For the last 25 years scientists have been working on methods to create images based on the material stiffness differences of tissues in the body. This imaging modality has come to be known as elasticity imaging or elastography. The advantages of such a modality are that it would be objective, quantitative, independent of the examiner, and have high spatial and temporal resolution.

Within the field of elasticity there is a very large parameter space of different material properties – such as the Young's modulus, shear modulus, Poisson's ratio, viscoelasticity, anisotropy, nonlinearity, and density [1]. These different properties vary in different tissue types, some over narrow ranges and some over large ranges – such as the shear modulus which can range over six orders of magnitude [2, 3].

There is a wide range of pathological processes that change the material properties of tissue such as the liver, breast, thyroid, skeletal muscle, pancreas, spleen, kidney, myocardium, vasculature, brain, bladder, prostate, etc. Different conditions, such as inflammation, fibrosis, edema, and cancer, all contribute to changing the material properties of organs because the constituents of the organs are altered on the microscopic scale and that translates into changes observed at the macroscopic scale (micrometers to centimeters).

Elastographic measurements require some form of mechanical stimulation or excitation to cause deformation. Then a measurement system is needed to measure the resulting deformation. The deformation can be caused by an external applied source, such as mechanical vibration, an internal source, such as acoustic radiation force, or an endogenous process, such as the pumping of the heart. Based on the particular form of excitation and its temporal and spatial

Ultrasound Elastography for Biomedical Applications and Medicine, First Edition.
Edited by Ivan Nenadic, Matthew Urban, James Greenleaf, Jean-Luc Gennisson, Miguel Bernal, and Mickael Tanter.

characteristics, different material properties can be evaluated. The measurement system could be magnetic resonance imaging, ultrasound, optical, or acoustic (hydrophone or accelerometer). For the purposes of this book, we focus only on ultrasound-based measurement of deformations.

This book is comprised of chapters written by pioneers and innovators in the field of ultrasound-based elastography. The book is broken up into eight primary sections.

The first section provides an overview of ultrasound physics and imaging theory, a primer on mechanical stimulation of tissue and its response, and ultrasound-based methods for motion estimation. In Chapter 2, Drs. Roberto Lavarello and Michael Oelze provide a systematic review of ultrasound physics and imaging formation relevant for the field of ultrasound-based elastography. Dr. Kevin Parker gives an overview of the continuum of excitation used in this field in Chapter 3. Chapter 4, by Drs. Jingfeng Jiang and Bo Peng, provides a thorough treatment of the ultrasonic and signal-processing methods to measure tissue motion, which is one of the main components of any elastographic measurement.

The second section provides an in-depth theoretical background on continuum mechanics and wave propagation. Wave propagation in anisotropic, bounded, and viscoelastic media is covered in detail. Chapter 5 provides the basis for continuum mechanics and solutions to wave equations as a foundation for elastography. In Chapter 6, Dr. Jean-Luc Gennisson presents theory for shear wave (or transverse wave) propagation in anisotropic media. Chapter 7, by Dr. Javier Brum, describes wave propagation in bounded media, which has applications to thin structures such as vessels, myocardium, cornea, and tendons. Chapters 8 and 9 cover measurements of tissue viscoelasticity.

The third section is devoted to methods that have been developed based on quasi-static compression and endogenous excitations. Compression elastography, particularly as applied in nonlinear materials, is covered in Chapter 10. Dynamic strain and strain rate in cardiac applications are addressed in Chapter 11 by Dr. Jan D'hooge and colleagues. Dr. Marvin Doyley describes vascular and intravascular elastography methods in Chapter 12. Dr. Carolina Amador presents different approaches for measurement of viscoelasticity with creep-based methods in Chapter 13. Lastly, Dr. Elisa Konofagou writes about wave and strain imaging based on the intrinsic motion present in the cardiovascular system in Chapter 14.

The fourth section describes methods based on external vibration for generating propagating waves in the tissue. Two different approaches for performing dynamic elastography measurements with harmonic excitations are presented in Chapters 15 and 16. Methods that produce harmonic acoustic radiation forces including vibro-acoustography, harmonic motion imaging, and shearwave dispersion ultrasound vibrometry are presented by leaders in these methods in Chapters 17–19, respectively.

The fifth section details methods that use mechanical and acoustic radiation force to perturb the tissue within the organ itself with transient excitations. Transient elastography, described by Dr. Laurent Sandrin and colleagues in Chapter 20, is a mechanically based system used primarily for investigation of liver diseases. Dr. Stefan Catheline presents methods to use time reversal techniques for measuring wave propagation in the body in Chapter 21. Chapter 22, by Drs. Tomasz Czernuszewicz and Caterina Gallippi, describes the acoustic radiation force impulse (ARFI) imaging method and its applications. The supersonic shear imaging method is presented by Drs. Jean-Luc Gennisson and Mickael Tanter in Chapter 23. Dr. Stephen McAleavey presents the benefits of applying single tracking location shear wave elastography in Chapter 24. Lastly, Chapter 25 describes the comb-push ultrasound shear elastography method developed by Drs. Pengfei Song and Shigao Chen, which uses multiple simultaneous acoustic radiation force push beams to generate shear waves for measurement of local shear wave velocity.

The sixth section provides insights into emerging areas that are being explored in the elastography field. Chapter 26, by Dr. Sara Aristizabal, provides an overview of different shear wave elastography approaches applied to characterizing elastic properties in anisotropic tissues. The use of guided waves for shear wave elastography and quantitative measurement of mechanical properties in thin tissues is addressed in Chapter 27 by Drs. Miguel Bernal and Ivan Nenadic and colleagues. Rheological model-free approaches for measuring viscoelasticity are described in Chapter 28. Lastly, methods that combine quasi-static compression elastography and dynamic shear wave elastography are presented to measure nonlinear elastic parameters in Chapter 29.

The seventh section reviews clinical application areas, including measurements made in abdominal organs, cardiovascular tissues, the musculoskeletal system, and breast and thyroid tissues. Chapter 30, by Dr. Matthew Urban, provides an overview of these clinical applications. Chapter 31 describes abdominal applications with shear wave elastography in liver, kidney, spleen, pancreas, intestines, bladder, prostate, and uterus. The group at Duke University led by Dr. Gregg Trahey describe the use of ARFI for cardiac applications in Chapter 32. Additional description of other cardiovascular applications of shear wave elastography are provided in Chapter 33. Dr. Jean-Luc Gennisson details the use of supersonic shear imaging for musculoskeletal applications using different levels of contraction of skeletal muscle and measurements in tendons in Chapter 34. Dr. Azra Alizad writes about the use of shear wave elastography in breast and thyroid applications in Chapters 35 and 36, respectively.

The final section provides a reflection on the growth of elastography from a literature-based perspective by Drs. Armen Sarvazyan and Matthew Urban. Different transitions in the field are described from a literature citation approach.

We believe that this book provides a review of the field after two decades of development, a snapshot of current clinical applications, and look to future areas of investigation. Elastographic methods are now installed on a plethora of clinical scanners and the inclusion of these methods is still being introduced in many clinical practices in hepatology, oncology, cardiology, obstetrics, nephrology, and radiology, among others. This past 25 years has been devoted to development of many efficacious methods and we believe that development will continue to evolve such that elastographic methods are available on all types of ultrasound scanners. This will enable another 25 years of clinical application to provide clinicians noninvasive tools for improving diagnosis and monitoring of treatment and other interventions, providing benefit to a multitude of patients worldwide.

References

1 Sarvazyan, A.P., Urban, M.W., and Greenleaf, J.F. (2013). Acoustic waves in medical imaging and diagnostics. *Ultrasound Med. Biol.* 39: 1133–1146.

2 Sarvazyan, A.P., Rudenko, O.V., Swanson, S.D. et al. (1998), Shear wave elasticity imaging: a new ultrasonic technology of medical diagnostics. *Ultrasound Med. Biol.* 24: 1419–1435.

3 Mariappan, Y.K., Glaser, K.J., and Ehman, R.L. (2010). Magnetic resonance elastography: A review. *Clin. Anat.* 23: 497–511.

Section II

Fundamentals of Ultrasound Elastography

2

Theory of Ultrasound Physics and Imaging

Roberto Lavarello[1] *and Michael L. Oelze*[2]

[1] *Laboratorio de Imágenes Médicas, Departamento de Ingeniería, Pontificia Universidad Católica del Perú, Lima, Peru*
[2] *Bioacoustics Research Laboratory, Department of Electrical and Computer Engineering, University of Illinois at Urbana-Champaign, Champaign, IL, USA*

2.1 Introduction

An image is a representation of specific properties of a physical object. The properties of the object that are utilized to form an image depend upon the manner in which the object is perceived. The final representation of the object depends on how the perception of the object's properties is translated into the image space.

In ultrasonic imaging, the properties that are imaged are related to the mechanical structure of the underlying tissue. The manner in which these mechanical properties are perceived is through the transmission and reception of ultrasound waves through the tissue. Signals corresponding to these ultrasound waves are collected by an ultrasonic transducer, converted to a voltage, and processed to convert the perceived properties into an image.

Mathematically, such a process can be described through a processing operation that is a function of the perceived signal

$$I(\mathbf{x}) = \Omega\{r(t)\} \tag{2.1}$$

where I is the image, $r(t)$ represents the perceived signal, and Ω represents the operation on the perceived signal that maps the signal to the image space. The perceived signal in ultrasonic imaging depends on several factors, including the shape and properties of the signal generator and the signal detector, the bulk properties of the propagating medium (sound speed and attenuation), and the reflectivity of the medium. Figure 2.1 depicts an ultrasonic transmitter/detector with the field that emanates from the detector in a medium highlighting an object to be imaged. In a simplified model, assuming the source is excited with an impulse, the perceived signal can be described by a series of convolutions of the different factors

$$r_{\text{tx}}(t) = h_{\text{tx}}(t) * p_{\text{tx}}(t, \mathbf{x}) * s(t, \mathbf{x}) * a(t, \mathbf{x}) * p_{\text{rx}}(t, \mathbf{x}) * h_{\text{rx}}(t) \tag{2.2}$$

In Eq. (2.2), $h(t)$ represents the impulse response of the source (tx) or the receiver (rx), $p(t, \mathbf{x})$ represents the field characteristics of the source (tx) or the receiver (rx), $s(t, \mathbf{x})$ represents the reflectivity of the medium giving rise to scattered and reflected signals, and $a(t, \mathbf{x})$ represents the frequency-dependent attenuation of the medium, which may be spatially dependent. The contrast in the image space and the properties that are being imaged are contained in $s(t, \mathbf{x})$. The other factors in Eq. (2.2) limit how well the object can be perceived.

To understand the physics of ultrasonic imaging is to understand the different factors making up the convolutions in Eq. (2.2), which create the signal perceived from the object. Once these

Ultrasound Elastography for Biomedical Applications and Medicine, First Edition.
Edited by Ivan Nenadic, Matthew Urban, James Greenleaf, Jean-Luc Gennisson, Miguel Bernal, and Mickael Tanter.

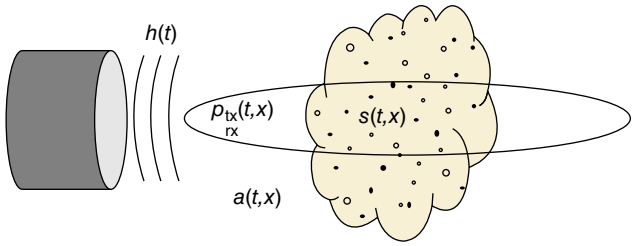

Figure 2.1 Depiction of the field from an ultrasonic sensor interacting with an object to be imaged.

factors are understood, the signal can be processed to create an image of the underlying properties. Different processing schemes can emphasize different aspects of the underlying medium properties, e.g. one can estimate Doppler shifts to provide flow parameters, one can process the brightness of echoes to create B-mode images, one can estimate particle displacements to provide strain or shear wave speed values. Therefore, the rest of the chapter is devoted to breaking down each of the factors in the convolution of Eq. (2.2) that are combined together to create the perceived signal, to model these different factors, and to combine them back together to better understand different approaches that can be taken to process the signals and create ultrasound-based images.

2.2 Modeling the Response of the Source to Stimuli [$h(t)$]

Medical transducer technology has advanced over the last few decades with the development of novel materials, fabrication techniques, and approaches to transducer design. For diagnostic ultrasound, piezoelectrics comprise the majority of transducers in use today [1]. In the future, other types of transducers may play a more prominent role in biomedical ultrasound imaging, e.g. capacitive micromachined ultrasound transducers (CMUTs).

The quality of an ultrasound image is directly related to the quality of the transducer element. In terms of imaging performance, the transducer acts as a bandpass filter to signals both received and transmitted. The transducer also controls the pressure output and the transducer controls the sensitivity to pressure on receive. Therefore, to fully understand the physics of diagnostic ultrasonic imaging, it is important to model the effects of the response of the source or transducer to stimuli.

The piezoelectric effect was first discovered by the Curie brothers [2] in 1880, when they observed that the application of a pressure on certain classes of crystals resulted in a potential difference generated between the two surfaces of the crystal. Subsequently, the inverse piezoelectric effect was discovered by Lippman [3] who observed that an applied electric field resulted in a deflection of the crystal surfaces.

In the piezoelectric effect, a stress is applied to the piezoelectric crystal resulting in a deflection of the surfaces of the crystal [4]. The deflection causes the ions in the crystal to reorient resulting in a net polarization of the crystal surface, which can be poled to produce a voltage reading. In the inverse piezoelectric effect, the application of an electric field causes a reorientation of the constituent ions resulting in the deflection of the surface of the crystal. The deflection of the surface of the crystal produces particle displacements of the fluid surrounding the crystal, which then results in the propagation of an ultrasonic wave outward from the crystal.

A complete description of the relationship between the mechanical response of a piezoelectric crystal and application of an electric field is beyond the scope of this chapter. However, the interested reader can refer to a more complete work on this topic, including the following references [4, 5]. For the purposes of this discussion, a simplified model of the transducer output

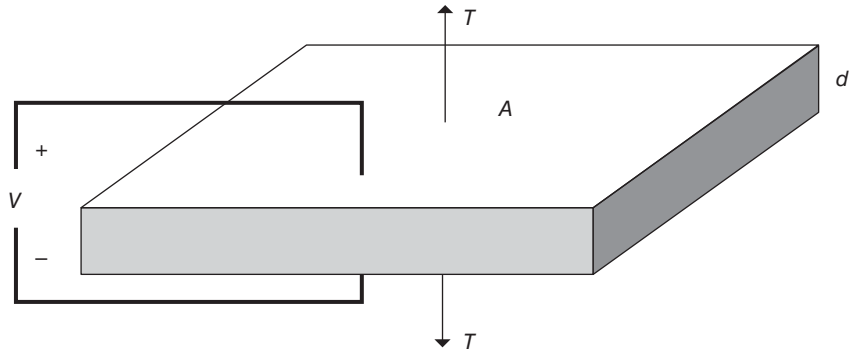

Figure 2.2 Diagram illustrating the thickness mode of a piezoelectric transducer with cross-sectional area *A*, thickness *d*, voltage poling *V*, and stress response *T*.

when provided a given stimulus, i.e. an electric field or a pressure, will suffice. Specifically, we will extend a 1D model of the crystal performance with the assumption of linearity, negligible loss, and lateral dimensions much larger than the crystal thickness.

In most cases, a piezoelectric crystal acting as a transducer will produce sound through the thickness mode. In a simplified model, assume that the transducer is a simple rectangular slab of material with thickness d and width much larger than the thickness (see Figure 2.2). In this case, the capacitance of the slab can be approximated [6]

$$C_0 = {}^{\varepsilon A}/_{d} \tag{2.3}$$

where ε is the dielectric constant of the crystal material. The stress resulting from the voltage applied across the transducer is given through a form of Hooke's law [7]

$$T = \kappa S - hD \tag{2.4}$$

where κ is the elastic stiffness of the material, S is the strain, D is the dielectric displacement, and h is the piezoelectric constant. The first term is a mechanical term, typical of Hooke's law, and the second term incorporates the piezoelectric effect. The dielectric displacement is related to the electric field through

$$D = \varepsilon E = \varepsilon \frac{V}{d} = \frac{C_0 V}{A} \tag{2.5}$$

By applying a voltage impulse across the electrodes, the inverse piezoelectric effect creates an impulse force and deflection of the top and bottom surfaces given [7] by

$$F(t) = TA = \frac{hC_0 V}{2}\left[-\delta(t) + \delta\left(t - \frac{d}{c_{\mathrm{L}}}\right)\right] \tag{2.6}$$

where no reflections from the surfaces are assumed and c_{L} is the longitudinal speed of sound in the crystal. The Fourier transform of these two impulse function results in

$$F(f) \propto \sin[\pi(2n+1)f/2f_0] \tag{2.7}$$

with $f_0 = {}^{c_{\mathrm{L}}}/_{2d}$. This result suggests that the output of the transducer operating in thickness mode will have maximum output at odd harmonics of the fundamental frequency, f_0. Typically, the output of the harmonics decrease with increasing frequency.

The transducer, as described, is a resonant structure with resonant frequency related to the thickness of the transducer. The thinner the transducer, the higher the frequency of the output.

However, piezoelectric crystals can only be sliced to a certain thickness before the crystal integrity is compromised.

Furthermore, because the transducer is a resonant structure, the transducer will ring at a particular frequency when excited by an impulse. A long ring down results in a longer duration pulse, which is not beneficial to ultrasonic imaging. The axial resolution depends on the duration of the excitation pulse and a shorter pulse will result in improved axial resolution for imaging. Because the transducer also acts as a bandpass filter, a shorter pulse is associated with a higher bandwidth transducer. In biomedical imaging, a high bandwidth transducer has a bandwidth of 80% or higher.

In order to improve the output characteristics of the transducer, an acoustic matching layer and an acoustic backing layer can be applied. The purpose of the backing layer is to reduce the ring down of the transducer and improve the bandwidth. As a consequence, the backing layer also results in power loss both in reception and transmission of ultrasound. To obtain a short pulse by reducing ring down while maintaining good transducer efficiency, the backing medium will typically have a high impedance of between 3 and 7 MRayl [1, 8].

An acoustic matching layer is used on the front surface of the transducer to provide more efficient radiation of sound from the transducer into the medium. In its simplest form, a single matching layer could be created that has a thickness of $\lambda/4$ and has an impedance given by $Z_{\mathrm{ML}} = \sqrt{Z_{\mathrm{Tr}} Z_{\mathrm{Me}}}$ where Z_{Tr} is the impedance of the piezoelectric crystal and Z_{Me} is the impedance of the medium. This is a quarter wave matching layer. The matching layer itself acts like a bandpass filter. To improve the performance and extend the tradeoff between gain and bandwidth, multiple matching layers can be employed [9–11].

The output of the transducer is in the form of a pulse. The bandwidth of the transducer, i.e. the impulse response $h(t)$, can be estimated by exciting the transducer with a voltage impulse and recording the signal. The bandwidth is typically characterized by the width at half maximum (−6 dB pulse echo).

2.3 Modeling the Fields from Sources [$p(t, \mathbf{x})$]

Once the transducer is excited, an ultrasonic waveform emerges from the transducer and must propagate through a medium. Consider the general problem of ultrasonic wave propagation in solid media. The interested reader may refer to Beyer and Letcher [12] for a more in-depth discussion of this topic. Interactions between neighboring particles at the boundaries of differential volumes within a continuous medium give rise to stress (in units of $\mathrm{N/m^2}$) tensors, i.e.

$$\overline{\overline{T}} = \begin{bmatrix} T_{11} & T_{12} & T_{13} \\ T_{21} & T_{22} & T_{23} \\ T_{31} & T_{32} & T_{33} \end{bmatrix} \tag{2.8}$$

where T_{ij} represents the stress in the j-th direction on the plane normal to the i-th axis. As a result of the forces, the material suffers rigid transformations (i.e. translations and rotations) and deformations (i.e. changes in dimensions and shape). This latter effect is quantified by the symmetric strain (in units of m) tensor, which is related to the particle displacement vector $\boldsymbol{\xi}$ as

$$S_{ij} = \frac{1}{2}\left\{ \frac{\partial}{\partial x_j}\xi_i + \frac{\partial}{\partial x_i}\xi_j \right\} \tag{2.9}$$

In order to derive the wave equation in solids, the relationships among stress, strain, and particle displacements are required. First, the equation of motion relates the stress tensor and

particle displacement vector as

$$\sum_i \frac{\partial}{\partial x_i} T_{ij} = \rho \frac{\partial^2}{\partial t^2} \xi_j \tag{2.10}$$

where ρ is the mass density in the medium. Next, the constitutive equation in an isotropic medium relates the stress and strain tensors as

$$T_{ij} = \lambda \delta_{ij} \sum_i S_{ii} + 2\mu S_{ij} \tag{2.11}$$

where λ and μ are the first and second Lame's parameters, respectively. The wave equation that governs the particle displacement can be derived by combining the equation of motion and the constitutive equation, combined with the fact that $\sum_i S_{ii} = \nabla \cdot \overline{\xi}$, which results in

$$\rho \frac{\partial^2}{\partial t^2} \xi_j = (\lambda + \mu) \frac{\partial}{\partial x_j} \nabla \cdot \overline{\xi} + \mu \nabla^2 \xi_j \tag{2.12}$$

The solution to the wave equation can be obtained if the particle displacement is expressed in terms of scalar and vector potentials, i.e.

$$\overline{\xi} = \overline{\xi}_{\mathrm{L}} + \overline{\xi}_{\mathrm{S}} = \nabla \varphi + \nabla \times \overline{A} \tag{2.13}$$

By construction, the scalar potential results in an irrotational (or longitudinal) wave whereas the vector potential results in a rotational (or shear) wave. The contributions of each potential are then made to satisfy the wave equation independently. The solution due to the scalar potential can be readily derived if the wave equation is written as

$$\rho \frac{\partial^2}{\partial t^2} \overline{\xi} = (\lambda + \mu) \nabla (\nabla \cdot \overline{\xi}) + \mu \nabla^2 \overline{\xi} \tag{2.14}$$

which results in the familiar scalar Helmholtz equation

$$\rho \frac{\partial^2}{\partial t^2} \varphi = (\lambda + 2\mu) \nabla^2 \varphi \tag{2.15}$$

The solution due to the vector potential can be readily derived if the wave equation is written as

$$\rho \frac{\partial^2}{\partial t^2} \overline{\xi} = (\lambda + 2\mu) \nabla (\nabla \cdot \overline{\xi}) - \mu \nabla \times \nabla \times \overline{\xi} \tag{2.16}$$

which in turn leads to the vector Helmholtz equation

$$\rho \frac{\partial^2}{\partial t^2} \overline{A} = \mu \nabla^2 \overline{A} \tag{2.17}$$

The solutions of the wave equation can be derived in the case of harmonic waves, i.e. waves for which the time dependency is separable and corresponds to a harmonic oscillation at an angular frequency ω. This solution is of particular interest because any arbitrary time dependency can be derived from the simpler harmonic case using Fourier synthesis. The two solutions to the scalar Helmholtz equation can be written as

$$\varphi(\vec{r}, t) = A \exp\{j(\omega t \pm (k_x x + k_y y + k_z z))\} \tag{2.18}$$

and are referred to as plane waves. In order to satisfy the wave equation, the wave numbers k_x, k_y, and k_z should be related as

$$k_x^2 + k_y^2 + k_z^2 = k^2 = \left(\frac{\omega}{c}\right)^2 \tag{2.19}$$

where c is the speed of sound in the medium. The expressions above lead to definitions of the sound speed of the longitudinal and shear components of the particle displacement given by

$$c_{\mathrm{L}} = \sqrt{\frac{\lambda + 2\mu}{\rho}} \tag{2.20}$$

and

$$c_{\mathrm{S}} = \sqrt{\frac{\mu}{\rho}} \tag{2.21}$$

respectively. In most soft tissues, the value of the λ parameter (in the order of a few GPa) is typically much larger than the value of the μ parameter (in the order of a few KPa). Therefore, longitudinal waves typically propagate at a much faster speed than shear waves in soft tissues.

At ultrasonic frequencies, the shear wave attenuates very rapidly in tissues and does not play a substantial role in conventional B-mode imaging. At ultrasonic frequencies, the longitudinal wave is primarily used to image tissues. However, shear waves propagating at lower frequency due to compressions of tissues will result in displacements that can be interrogated using longitudinal waves.

The solutions to the wave equation can be written in terms of other functions when analyzed in other coordinate systems, such as the cylindrical and spherical ones. However, all solutions can ultimately be expressed as a combination of (potentially infinite) plane waves. For example, the well-known monopole source in spherical coordinates can be expressed as a combination of plane waves using Weyl's representation, i.e.

$$\frac{\exp(jkr)}{r} = \frac{i}{2\pi}\iint \frac{\exp\{j(k_x x + k_y y + k_z z)\}}{k_z}\,\mathrm{d}k_x \mathrm{d}k_y \tag{2.22}$$

The field from a monopole source can also represent the field from a simple source. A simple source can take on any shape with the constraint that the dimensions of the simple source are much smaller than the wavelength of sound. Based on the principle of superposition, the field from a larger aperture can be constructed by breaking the larger aperture into small simple sources and summing the field contributions from each simple source at some observation point, r', from the source. The simple source can be described by

$$\mathrm{d}p_{\mathrm{ss}}(r', t) = \frac{C}{r'} e^{j(\omega t - kr')}\mathrm{d}A \tag{2.23}$$

where $\mathrm{d}A$ is the differential area of the simple source and C is a constant. The field from a larger aperture is just the summation of all of these simple sources at the observation point

$$p(r, t) = \int_{-\infty}^{\infty}\int_{-\infty}^{\infty} A_p(x_0, y_0) U(x_0, y_0) \frac{C}{r'} e^{j(\omega t - kr')}\mathrm{d}A_0 \tag{2.24}$$

The integration is over a plane (x_0, y_0) where the aperture resides, $A_p(x_0, y_0)$ is the aperture function and $U(x_0, y_0)$ is called the apodization function. The apodization function weights the contribution of each simple source to the field. In the far field from the aperture ($r \gg (x_0, y_0)$), approximations can be made resulting in

$$p(t, \mathbf{x}) \approx \frac{C'}{r} e^{j(\omega t - kr)} \int_{-\infty}^{\infty}\int_{-\infty}^{\infty} A_p(x_0, y_0) U(x_0, y_0) e^{-j(k_x x_0 + k_y y_0)}\mathrm{d}A_0 \tag{2.25}$$

The equation above indicates that the far field from an aperture is proportional to the Fourier transform of the product of the aperture function and apodization function, where $k_x = k\cos\theta_x$ and $k_y = k\cos\theta_y$. For example, if the aperture function was a rectangular function and the apodization was unity, the resulting field pattern would look like a sinc function versus angle.

Direct integration, angular spectrum approaches, and approximate approaches using the spatial impulse response [13, 14] can provide predictions of field characteristics from a variety of source configurations. Typically, fields from sources result in a beam at broadside or perpendicular to the plane of the transducer surface that narrows as the aperture size increases. Beam side lobes can be controlled by the apodization function and tapering the weight of the source contributions at the edges of the aperture. While axial resolution of an ultrasonic imaging system is dictated by the pulse duration, the lateral resolution in a 2D B-mode image is controlled by the width of the beam coming from the source.

2.4 Modeling an Ultrasonic Scattered Field [$s(t, \mathbf{x})$]

Ultrasonic propagation at its basic level is described by the classical wave equation for longitudinal waves (a generalization of Eq. 2.15)

$$\nabla^2 p + \frac{1}{c_{\mathrm{L}}^2} \frac{\mathrm{d}^2 p}{\mathrm{d}t^2} = 0 \tag{2.26}$$

where p represents the propagating pressure wave and c_{L} represents the longitudinal sound speed of the wave propagation. In a homogeneous fluid medium without loss, an ultrasonic plane wave can propagate out to infinity without any alteration in the wave properties. Of course, in practice there is no such thing as a lossless medium or a medium extending to infinity without inhomogeneities or an infinite plane wave.

Furthermore, while tissue is often considered to act like a fluid, the recent focus on imaging shear properties of tissue indicates that tissue should be considered as an elastic solid with weak shear properties. At frequencies used for clinical ultrasonic imaging (1 to 15 MHz), the contributions of shear to wave propagation and scattering are negligible. At the ultrasonic frequencies, shear modes attenuate very rapidly. However, at lower frequencies, shear modes can propagate much further distances with lower attenuation. The displacements associated with shear wave propagation can be estimated by tracking sub-resolution scatterers that are displaced by the shear wave propagating past the scatterers. Therefore, the modeling of the signals from a scattering medium is important to understanding and predicting how estimates of shear wave propagation can be found from displacements of scattering objects. In addition, the strain imaging technique makes use of the idea that sub-resolution scatterers will move when compressed. Therefore, tracking the motion of these scatterers allows the estimation of strain when a compression is applied to tissue.

Modeling of ultrasonic scattering falls under two distinct approaches. In the first approach, the medium is assumed to be homogeneous with a scattering object embedded in the medium. In the first approach the homogeneous classical wave equation is utilized. In the second approach, the medium is assumed to be inhomogeneous and an inhomogeneous wave equation is applied. In either case, the scatterer is first modeled by assuming an incident wave field and a scattered field direction, as shown in Figure 2.3. For most ultrasonic imaging applications, the observation of the scattered field is nearly 180° out of phase with the incident field direction resulting in the measurement of backscatter.

In the first approach, the linear acoustic wave equation is utilized to derive the Helmholtz equation (Eq. 2.15). The Laplacian in the Helmholtz equation is expanded in a coordinate system that is appropriate based on the geometry of the scattering object, e.g. the Laplacian is expanded in spherical coordinates for a spherical scatterer. The Helmholtz equation provides an expansion of the pressure field in the coordinate system. Next, the boundary conditions at the scattering object surface are used to solve for the scattered field in terms of the incident field

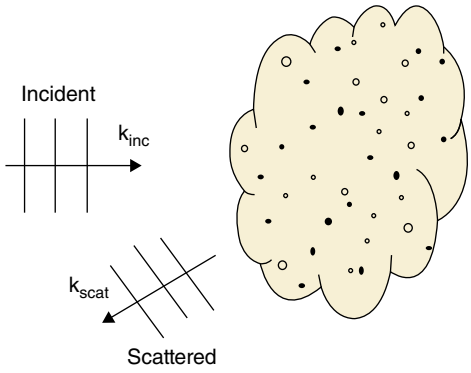

Figure 2.3 Illustration of incident ($\mathbf{k}_{inc}$) versus scattered ($\mathbf{k}_{scat}$) field directions.

pressure. In a fluid, the boundary conditions are the continuity of pressure and the continuity of the normal component of the particle velocity at the surface

$$p_{inc} + p_{sc} = p_{int} \quad \text{and} \quad [u_{inc} + u_{sc} = u_{int}]_{\perp} \tag{2.27}$$

where the subscripts "inc" refers to the incident field, "sc" refers to the scattered field, and "int" refers to the field internal to the scatterer.

The first approach is highly useful in predicting the scattered field from an object embedded in a homogeneous medium if the object has a simple geometric shape, i.e. a sphere or a cylinder. However, if the scattering object is highly irregular in shape, solving for the scattered field can become intractable. Solutions using the homogeneous medium approach for fluid spheres and cylinders have been reported [15]. The expansion of these solutions to include shear in the object function for spheres and cylinders have also been reported [16]. These models have been utilized to describe scattering from cells and collections of cells.

In modeling tissue, the homogeneous approach results in a discrete scattering model. Scattering from multiple objects can be represented by a convolution of the received field with a scattering function corresponding to the location of each scatterer

$$r_{tx}(t) = f(t, \mathbf{x}) * s(t, \mathbf{x}) \tag{2.28}$$

where $f(t, x)$ is the field and $s(t, x)$ is the scattering function incorporating the location of the scattering objects and a transfer function which modifies the field. The scattering function can be expanded further as a summation of scattering functions for multiple objects

$$s(t, \mathbf{x}) = s_1(t - t_1, \mathbf{x}) + s_2(t - t_2, \mathbf{x}) + \ldots + s_N(t - t_N, \mathbf{x}) \tag{2.29}$$

for a collection of N scatterers. The scatterers do not have to be identical. For example, $s_n(t - t_n, \mathbf{x})$ could represent scattering from an interface (a specular reflection)

$$s_n(t - t_n, \mathbf{x}) = R_n f(t - t_n, \mathbf{x}) \tag{2.30}$$

where R_n is the reflection coefficient from the interface. Similarly, the $s_n(t - t_n, \mathbf{x})$ function could represent scattering from a simple object with the scattering function derived from the homogeneous modeling approach, e.g. scattering function for a collection of fluid spheres. This approach has been used to model tissue and tissue mimicking phantoms and can be used to model compression of tissues by adjusting the locations, i.e. t_n, or displacements of the discrete scatterers for a given strain.

In the second approach to scattering, an inhomogeneous medium is modeled using an inhomogeneous wave equation [17, 18]. In this case, the medium is composed of spatially varying density and compressibility

$$\rho(\mathbf{x}) = \rho_0 + \rho_e \quad \text{and} \quad \kappa(\mathbf{x}) = \kappa_0 + \kappa_e \tag{2.31}$$

where ρ_0, κ_0 represent the background density and compressibility and ρ_e, κ_e are the spatially dependent changes in density and compressibility from the background. Variations in density and compressibility result in different kinds of particle motion when presented with a harmonic pressure wave. Given a particle exposed to a pressure gradient, Euler's equation gives

$$\rho(\mathbf{x})\frac{\partial \mathbf{u}}{\partial t} = -\nabla p \tag{2.32}$$

where $\mathbf{u}$ is the particle velocity and its direction is the gradient of pressure. If we consider a harmonic wave and a pressure gradient across a region of background density and a region of variable density, we get the following Euler equations

$$j\omega\rho(\mathbf{x})\mathbf{u}_e = -\nabla p \quad \text{and} \quad j\omega\rho_0\mathbf{u}_0 = -\nabla p \tag{2.33}$$

Relating the equations together gives

$$\rho(\mathbf{x})\mathbf{u}_e = \rho(\mathbf{x})(\mathbf{u}_0 + \Delta\mathbf{u}) = \rho_0\mathbf{u}_0 \tag{2.34}$$

After rearranging,

$$\Delta\mathbf{u} = -\frac{\rho(\mathbf{x}) - \rho_0}{\rho(\mathbf{x})}\mathbf{u}_0 \tag{2.35}$$

which suggests that a fluid particle with different density from background exposed to a pressure gradient will undergo different particle velocity from background density. The variation in density from background causes the particle to move back and forth in the direction of the pressure gradient (direction of pressure wave propagation) resulting in a dipole radiation. In a similar fashion, the variations in compressibility lead to monopole radiation.

Variations in density and compressibility are incorporated in the inhomogeneous wave equation

$$\nabla^2 p + \frac{1}{c_L^2}\frac{\mathrm{d}^2 p}{\mathrm{d}t^2} = \nabla \bullet (\gamma_\rho(\mathbf{x})\nabla p) + \gamma_\kappa(\mathbf{x})\frac{1}{c_L^2}\frac{\mathrm{d}^2 p}{\mathrm{d}t^2} \tag{2.36}$$

where the density scattering source $\gamma_\rho(\mathbf{x})$ incorporates the spatially dependent density variations and the compressibility scattering source $\gamma_\kappa(\mathbf{x})$ incorporates the spatially dependent compressibility variations. The scattering sources are defined in terms of compressibilities and densities as

$$\gamma_\rho(\mathbf{x}) = \frac{\rho(\mathbf{x}) - \rho_0}{\rho(\mathbf{x})} \quad \text{and} \quad \gamma_\kappa(\mathbf{x}) = \frac{\kappa_e - \kappa_0}{\kappa_0} \tag{2.37}$$

Assuming a harmonic wave, i.e. $p(\mathbf{x}, t) = p(\mathbf{x})e^{j\omega t}$, then the inhomogeneous wave equation reduces to

$$\nabla^2 p + k^2 p = \nabla \bullet (\gamma_\rho(\mathbf{x})\nabla p) - k^2\gamma_\kappa(\mathbf{x})p = -f(\mathbf{r}_0) \tag{2.38}$$

A Green's function approach can be used to solve the inhomogeneous wave equation by rewriting the differential equation as an integral. The Green's function $G(\mathbf{r}|\mathbf{r}_0)$ describes the observed pressure field at the detector's location $\mathbf{r}$ resulting from a point source of scattering at $\mathbf{r}_0$. The Green's function is a solution to

$$\nabla^2 G + k^2 G = -\delta(\mathbf{x} - \mathbf{x}_0) \tag{2.39}$$

which is satisfied by the free space Green's function $G(\mathbf{x}|\mathbf{x}_0) = \frac{1}{4\pi|\mathbf{x}-\mathbf{x}_0|}e^{jk|\mathbf{x}-\mathbf{x}_0|}$. Combining with the Helmholtz equation provides

$$[\nabla^2 p + k^2 p = -f(\mathbf{x}_0)]xG - p[\nabla^2 G + k^2 G = -\delta(\mathbf{x} - \mathbf{x}_0)] \tag{2.40}$$

Integrating over a volume V containing the scattering sources gives

$$\int_V (G\nabla^2 p - p\nabla^2 G)\mathrm{d}V_0 = \int_V p\delta(\mathbf{x}-\mathbf{x}_0)\mathrm{d}V_0 - \int_V f(\mathbf{x}_0)G\mathrm{d}V_0 \tag{2.41}$$

where the first integral on the right-hand side reduces to the pressure field at the detector location (i.e. the total field). Recognizing that

$$G\nabla^2 p - p\nabla^2 G = \nabla \bullet (G\nabla p - p\nabla G) = \nabla \bullet \mathbf{A} \tag{2.42}$$

and using the divergence theorem yields

$$p(\mathbf{x}) = \oint_S (G\nabla p - p\nabla G) \bullet \mathrm{d}\mathbf{S} + \int_V f(\mathbf{x}_0)G\mathrm{d}V_0 \tag{2.43}$$

The first term is the total field, the second term represents fields reflected by a boundary surface, S, and the final term represents the sum of the fields from scattering sources. Assuming an unbounded medium (or a medium where we can gate out the signals from boundaries), all that is left of the second term is the incident field giving

$$p(\mathbf{x}) = p_{\mathrm{inc}}(\mathbf{x}) + \int_V f(\mathbf{x}_0)G\mathrm{d}V_0 = p_{\mathrm{inc}}(\mathbf{x}) + p_{\mathrm{sc}}(\mathbf{x}) \tag{2.44}$$

which helps identify the last term as the scattered field.

The scattered pressure is then given by

$$p_{\mathrm{sc}}(\mathbf{x}) = \int_V (\nabla \bullet (\gamma_\rho \nabla p) - k^2 \gamma_\kappa p)G(\mathbf{x}|\mathbf{x}_0)\mathrm{d}V_0 \tag{2.45}$$

Using the divergence theorem on the first term and noting no contribution from scattering sources on the bounded surface of V gives

$$p_{\mathrm{sc}}(\mathbf{x}) = \int_V [k^2 \gamma_\kappa(\mathbf{x}_0)p(\mathbf{x}_0)G(\mathbf{x}|\mathbf{x}_0) + \gamma_\rho(\mathbf{x})\nabla p(\mathbf{x}_0) \bullet G(\mathbf{x}|\mathbf{x}_0)]\mathrm{d}V_0 \tag{2.46}$$

Using a simplifying assumption that the scattered field is observed in the far field of the scattering sources, then the Green's function reduces to

$$G \approx \frac{1}{4\pi\mathbf{x}} e^{jk|\mathbf{x}|} e^{-j\mathbf{K}_{\mathrm{sc}} \bullet \mathbf{x}_0} \quad \text{and} \quad \nabla G \approx -jk^2 \frac{\mathbf{x}}{k} G \tag{2.47}$$

The result of these approximations gives

$$p_{\mathrm{sc}}(\mathbf{x}) = \frac{k^2}{4\pi\mathbf{x}} e^{jk|\mathbf{x}|} \int_V \left[\gamma_\kappa(\mathbf{x}_0)p(\mathbf{x}_0) - j\gamma_\rho(\mathbf{x})\left(\nabla p(\mathbf{x}_0) \bullet \frac{\mathbf{r}}{k}\right)\right] e^{-j\mathbf{K}_{\mathrm{sc}} \bullet \mathbf{x}_0}\mathrm{d}V_0 \tag{2.48}$$

$$p_{\mathrm{sc}}(\mathbf{x}) = \frac{k^2}{4\pi\mathbf{x}} e^{jk|\mathbf{x}|} \int_V F(\mathbf{x}_0) e^{-j\mathbf{K}_{\mathrm{sc}} \bullet \mathbf{x}_0}\mathrm{d}V_0 \tag{2.49}$$

The integral can be interpreted as the Fourier transform of an object function, $F(\mathbf{x}_0)$, which is a function of the scattering sources and total pressure field. The Fourier transform is multiplied by the field of a spherical wave from a point source. The pressure field in the integral is the total field at the location of the scatterer. Assuming a plane wave incidence and invoking the Born approximation, i.e. $p(\mathbf{x}_0) = p_{\mathrm{inc}}(\mathbf{x}_0)$, reduces the scattered field to

$$p_{\mathrm{sc}}(\mathbf{x}) = P_0 \frac{k^2}{4\pi\mathbf{x}} e^{jk|\mathbf{x}|} \int_V (\gamma_\kappa(\mathbf{x}_0) + \gamma_\rho(\mathbf{x})(\mathbf{i} \bullet \mathbf{r})) e^{-j\mathbf{K} \bullet \mathbf{x}_0}\mathrm{d}V_0 \tag{2.50}$$

where P_0 is the pressure amplitude of the incident plane wave, $\mathbf{i} \bullet \mathbf{r} = \cos\theta$ with θ the angle between the incident direction and the observer (i.e. $\theta = 180°$ is the backscatter direction) and

$\mathbf{K} = \mathbf{k}_s - \mathbf{k}_i$ is called the scattering vector. In the backscatter direction $\mathbf{i} \bullet \mathbf{r} = 1$ and the density and compressibility fluctuations contribute equally to the scattered field.

The second approach allows a simple estimate of the scattered field based on taking the spatial Fourier transform of the distribution of variations of density and compressibility of a medium. This allows the medium to be modeled as a discrete scattering medium ($s_n(t - t_n, \mathbf{x}) = p_{sc,n}(t - t_n, \mathbf{x})$) or as a scattering continuum, i.e. a continuously varying density and compressibility. The inhomogeneous medium approach requires that the scattering is weak so that the Born approximation holds. However, the scattered field can be predicted for more complex geometries.

In terms of ultrasonic imaging, scattering modifies the frequency content of the signals returning to the receiver. In most cases of sub-resolution scatterers, the result of scattering is to high pass filter the signal. To some degree, this balances the effects of frequency-dependent attenuation, which low pass filters the signal versus depth.

2.5 Modeling the Bulk Properties of the Medium [$a(t, \mathbf{x})$]

As ultrasound propagates through tissues, changes in compressibility and density at microscale and along surfaces result in reflection and scattering of ultrasound. However, individual tissues and organs may have their respective background sound speed and attenuation properties. These values can affect the response of the imaging system and how different structures are perceived.

Changes in sound speed can cause the refraction of ultrasonic rays away from a straight ray path. Differences in sound speed can also affect the ability to focus ultrasound using arrays based on the time delays, i.e. phase aberration. Therefore, it is important to account for sound speed changes in optimizing image performance. Accounting for sound speed changes from tissue layers results in improved focusing by reducing phase aberration. Figure 2.4 depicts the range of longitudinal sound speed values typical for different tissues at clinical ultrasonic frequencies. Furthermore, sound speed is weakly dispersive in soft tissues at clinical ultrasonic frequencies.

Another bulk tissue property that affects image performance is the frequency-dependent attenuation. Like sound speed, different tissues and organs are associated with a range of frequency-dependent attenuation values. For soft tissues, the frequency-dependent attenuation coefficient is often described by a power law

$$\alpha(f) \approx \beta f^{n} \tag{2.51}$$

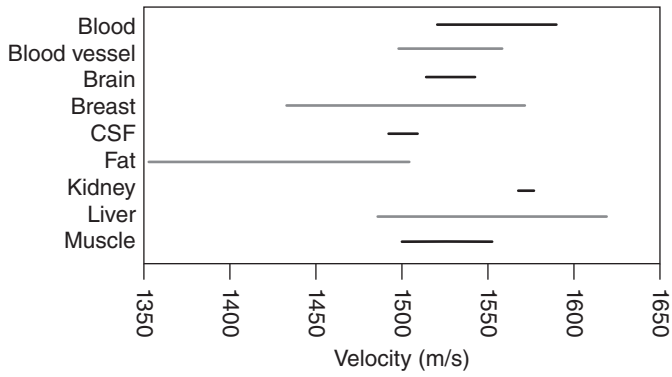

Figure 2.4 List of ultrasonic sound speed estimates from different tissues and organs in humans [19–24].

Table 2.1 List of attenuation estimates from different tissues and organs in humans assuming a power law with exponent, *n* [7, 19–24].

Tissue	α (dB/cm) @ 1 MHz	*n*
Blood	0.12–0.30	1.21
Brain	0.2–0.6	1.14–1.30
Breast	0.75–1.9	1.50
Fat	0.4–0.8	
Kidney	0.8–1.0	1.09
Liver	0.5–1.2	1.00–1.13
Muscle (along fibers)	0.95–1.25	1.0–1.2
Muscle (parallel)	2.7–3.1	1.0–1.2
Spleen	0.4	1.3
Testis	0.17–0.30	1.11

where n is between 1.0 and 2 for soft tissues [22]. Because the attenuation increases with frequency, as the ultrasonic wave propagates through tissue, the center frequency of the ultrasonic pulse downshifts to a lower frequency. This results in beam spreading, i.e. the beam gets wider resulting in a loss of lateral resolution. Furthermore, as the ultrasound propagates through tissue, the bandwidth can also decrease resulting in decreased axial resolution, i.e. a lengthening of the pulse duration. Speckle is modified versus depth due to frequency-dependent attenuation, with speckle becoming larger versus depth of propagation. Furthermore, because the attenuation reduces the amplitude of the ultrasonic wave, attenuation results in a loss of signal-to-noise ratio. Table 2.1 depicts the range of frequency-dependent attenuation values associated with different soft tissues. In ultrasonic B-mode imaging, the depth-dependent effects of attenuation are often compensated by implementing a time-gain compensation (TGC), which seeks to equalize the image intensity versus depth of the image. At a point of observation in a tissue, the total attenuation to the point is the sum of the spatially dependent attenuation along the propagation path, i.e. through intervening tissues, up to the observation point

$$a(t, \mathbf{x}) = \int_{\mathbf{x}_0}^{\mathbf{x}} \alpha(t, \mathbf{x}) \mathrm{d}\mathbf{x} \tag{2.52}$$

Attenuation in soft tissues is due to a combination of absorption and scattering

$$\alpha \approx \alpha_{\mathrm{abs}} + \alpha_{\mathrm{scat}} \tag{2.53}$$

In most soft tissues, attenuation is dominated by absorption [25]. The absorption of ultrasonic energy by the tissue can result in heating of the tissue and a radiation force on the tissue. The radiation force is described by

$$\mathbf{F} = \frac{2\alpha_{\mathrm{abs}}\mathbf{I}}{c_{\mathrm{L}}} \tag{2.54}$$

where $\mathbf{I}$ is the intensity of ultrasound. The radiation force can be used to push or compress tissue at the focus of an ultrasound source. By pushing or compressing the tissue, a low frequency shear wave can be produced that propagates outward from the location of the ultrasonic push. The low frequency shear wave produces displacements that can be estimated through ultrasonic imaging methods, enabling the tracking of the shear wave propagation and estimation of shear moduli [26].

2.6 Processing Approaches Derived from the Physics of Ultrasound [Ω]

Most scanners operate with array transducers, i.e. a group of sensors with specific geometric arrangements which (to a large extent) can be individually operated in transmission and reception. The simplest model for an array is the 1D point source array, which is depicted in Figure 2.5 and consists of N point-like sources arranged along the x-axis.

Several array configurations are provided by manufacturers. Among 1D arrays, three common types are the linear, phased, and curved arrays. Linear arrays conform to the diagram in Figure 2.5, and are typically operated with sub-aperture translation, i.e. several transmit beams are obtained by firing sub-sets of the array elements in a sliding fashion. Typical applications involve visualization of structures with limited field of view and high resolution, such as breast, thyroid, musculoskeletal, and vascular and superficial imaging. Phased arrays also conform to the diagram in Figure 2.5, but have fewer elements and smaller footprints and operate with beam steering (i.e. the electronic deflection of the beam direction over different steering angles) to obtain different beams. Their most common application is cardiac imaging, but are also used for transcranial and abdominal imaging. The curved arrays differ from linear and phased arrays in that the elements are arranged over a curved rather than a straight line. Even though the array is operated with sub-aperture translation as with linear arrays, due to the array curvature the resulting beams describe a polar grid as with phased arrays. Typical applications involve visualization of structures with a wide field of view, such as abdominal imaging.

Unlike the case of single element transducers, the ultrasonic beam characteristics produced by arrays are dynamically modifiable using electronic beamforming. In short, different beams can be produced by exciting the different elements of the array with properly designed electrical signals. The simplest case to analyze corresponds to the simultaneous excitation of all array elements with the same pressure amplitude A [27]. The total pressure field produced by the array under this condition is given by

$$p(r,\theta) = \sum_{i=0}^{N-1} \frac{A}{R_i} \exp(-jkR_i) \tag{2.55}$$

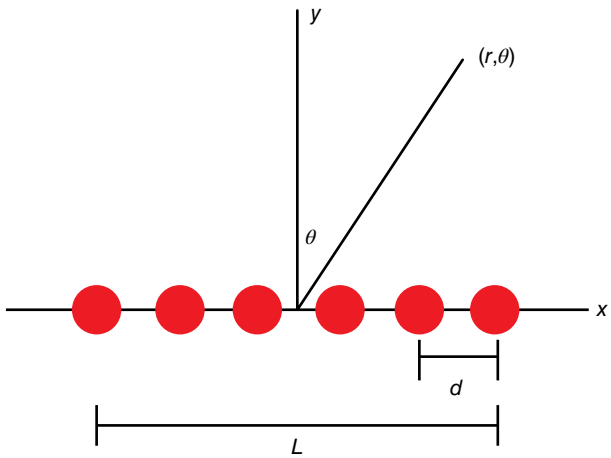

Figure 2.5 Geometry of a 1D point source array.

where R_i is the distance between the observation point and the i-th element in the array, with the latter locations corresponding to points with x coordinates

$$r_i = \left[i - \frac{(N-1)}{2} \right] d; \qquad i = 0,1,\ldots,N-1 \tag{2.56}$$

where d is the transducer pitch (i.e. the spacing between adjacent element centers). If the observation point is far away from the array, the approximations $R_i \approx r - r_i \sin\theta$ and $R_i \approx r$ can be used in the exponential function and the denominator of the summands, respectively, which results in

$$p(r,\theta) = \frac{A}{r} \sum_{i=1}^{N} \exp(-jk(r - r_i \sin\theta)) \tag{2.57}$$

Direct algebraic manipulation of the expression above yields the far field pressure produced by the 1D array

$$p(r,\theta) = NA \frac{\exp(-jkr)}{r} \left[\frac{1}{N} \frac{\sin\left(\frac{1}{2}Nkd\sin\theta\right)}{\sin\left(\frac{1}{2}kd\sin\theta\right)} \right] \tag{2.58}$$

in which the term in brackets is known as the radiation pattern of the array and corresponds to the sampled sinc function. For imaging, it is desirable that the radiation pattern only exhibits one peak at broadside (i.e. the array main lobe). Examples of the far field radiation patterns of 1D linear arrays are presented in Figure 2.6 for arrays with $N = 10$ and $d = \lambda/2$ and $d = 2\lambda$. It can be observed that in the former case, in addition to the main lobe there are lobes with peaks of maximum amplitude at directions different than broadside. These unwanted lobes are termed grating lobes, and are a consequence of sub-optimal spatial sampling of the array aperture. In order to avoid grating lobes, the element separation should satisfy

$$\frac{d}{\lambda} \leq \frac{N-1}{N} \tag{2.59}$$

The 1D array can also be fired at directions different than broadside. This can be easily accomplished if linear time delays are applied to the array elements, i.e. if the i-th element of the array is fired at time

$$\tau_i = \left(i - \frac{N-1}{2} \right) \tau \tag{2.60}$$

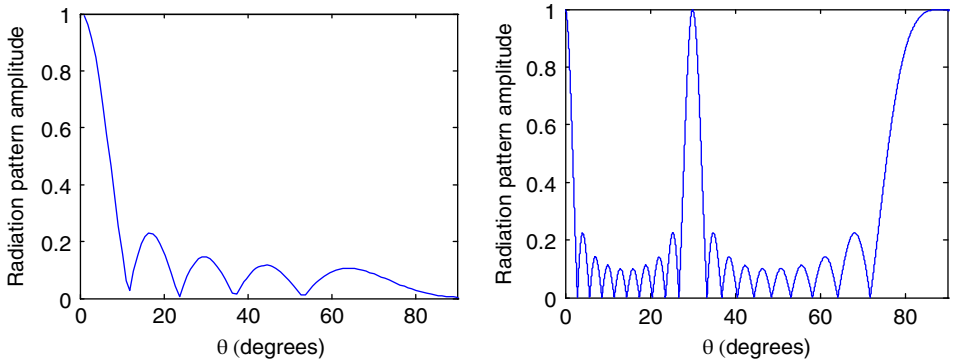

Figure 2.6 Far field radiation patterns corresponding to 10-element arrays with element pitch equal to $\lambda/2$ (left) and 2λ (right).

The corresponding far field pressure is given by

$$p(r,\theta) = NA\frac{\exp(-jkr)}{r}\left[\frac{1}{N}\frac{\sin\left(\frac{1}{2}Nkd(\sin\theta-\sin\theta_0)\right)}{\sin\left(\frac{1}{2}kd(\sin\theta-\sin\theta_0)\right)}\right]; \qquad \sin\theta_0 = \frac{c_L\tau}{d} \tag{2.61}$$

which means the direction of the main lobe can be changed simply by changing the rate at which the transducer elements are fired. Just as in the case of a broadside 1D array, grating lobes will occur for sufficiently large transducer pitch values. In particular, grating lobes can be avoided if

$$\frac{d}{\lambda} \leq \frac{N-1}{N(1+|\sin\theta|)} \tag{2.62}$$

However, the expressions provided for the pressure field are valid only in the far field, which approximately occurs at depths beyond

$$z_{\mathrm{FF}} = \frac{(L/2)^2}{\lambda} \tag{2.63}$$

where L is the length of the array. For the case of ultrasonic waves operating in the MHz range and typical array dimensions, this distance is in the range of tens of centimeters. Therefore, far field conditions can typically not be met for clinical applications. Instead, the transducer is focused in order to bring the far field of the array within the near field range.

Focusing is an operation that spatially converges the energy of an acoustic radiator at an observation point termed the transducer focus. This is achieved by having the waves contributed by every point within the radiating surface to arrive simultaneously at the transducer focus. For the linear array, and assuming the focus is located at coordinates $(0, y_f)$, this correspond to using the time delays

$$\tau_i = \frac{-\sqrt{y_{\mathrm{f}}^2 + r_i^2}}{c} \tag{2.64}$$

The expression above indicates that elements farther away from the focal point need to be fired earlier, as expected. In practice, this expression is not directly applicable because all firing times are negative – a common time offset needs to be considered for all elements. Further, only discretized values of the time delays can be applied due to the increasing use of digital transmit timing at a fixed transmit clock cycle. These considerations also apply to the case of beam steering.

True focusing is only obtained at the focal point, and therefore the quality of focusing degrades away from this location. The focusing quality is mainly dictated by a parameter called the focal number ($f/\#$), which is defined as y_f/L. In the lateral direction, the extent of the focal region can be derived explicitly from the beam pattern expression and is proportional to $\lambda^* f/\#$. In the axial direction, the extent of the focal region is proportional to $\lambda^*(f/\#)^2$. For imaging, it is desired to produce a focal zone with the shortest lateral extent (i.e. short lateral resolution) and the largest axial extent (i.e. large field of view). Unfortunately, both goals are incompatible because of the relationship between the focal number and the dimensions of the focal region.

Unlike single element transducers, the transmit beam pattern $p_{tx}(t,x)$ does not have to be identical to the receive pattern $p_{rx}(t,x)$. In particular, focusing in transmit and in receive are performed differently in practice. In transmit, an electrical signal is sent to each transducer element and the resulting beam pattern is focused by the natural propagation of the induced mechanical waves. In receive, the focusing is achieved by combining the received signals received by each

array element $d_i(t)$ after the appropriate delays have been applied, i.e.

$$r_{\text{tx}}(t) = \sum_{i=0}^{N_a} r^{(i)} d_i(t - \Delta t_i) \tag{2.65}$$

$$\Delta t_i = \frac{x_{\text{f}} + \sqrt{{x_{\text{f}}}^2 + r_i^2}}{c} \tag{2.66}$$

Given that such operations can be performed digitally on the recorded channel data after each transmission, focusing on receive can be implemented continuously for all points in the imaging domain provided the scanner has sufficient computing power. Therefore, dynamic beamforming allows having the whole field of view in focus on receive without the need for multiple transmissions [28].

Other approaches to beamforming allow dynamic focusing on receive as well as on transmit, such as synthetic aperture focusing techniques [29–31]. Recently, plane wave imaging methods have received attention due to the possibility of providing comparable imaging quality to multi-focus beamforming with an improved frame rate [32]. Single plane wave imaging is obtained by transmitting simultaneously with all transducer elements. Such an approach allows the acquisition of echoes from the whole imaging field, but at the expense of decreased image quality due to the lack of focusing on transmit. Compounded plane wave imaging fixes these issues by coherently combining the radiofrequency data obtained from several plane waves illuminating the imaging target at different incidence angles, i.e.

$$\text{CPW}(x, y) = \sum_{i,j} r^{(i,\theta_j)} \left(\frac{y \cos\theta_j + x \sin\theta_j + \sqrt{(x - r_i)^2 + y^2}}{c} \right) \tag{2.67}$$

where θ_j is the incident angle of the j-th transmitted plane wave [33].

The differences in the quality of single focus in transmit and receive, single focus in transmit and dynamic focusing in reception, and compounded plane wave imaging are illustrated in Figure 2.7 when imaging a two-layer phantom. From Figure 2.7, it can be observed that the sharpness of the edge between both layers using the single focus approach degrades quickly away from the focal depth (set in this example at 20 mm), whereas the use of dynamic focusing in reception significantly improves the edge definition throughout the field of view. Moreover,

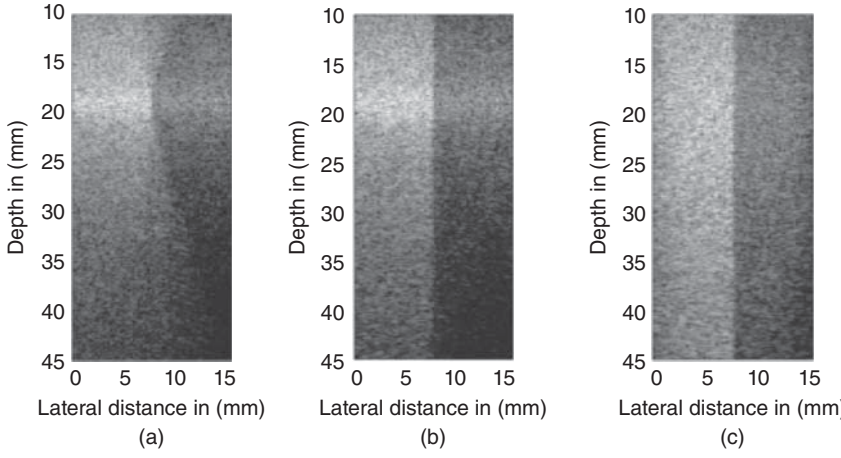

Figure 2.7 Echographic images of a two-layer phantom obtained using (a) single focus in transmit and receive, (b) single focus in transmit and dynamic focusing in reception, and (c) compounded plane wave imaging. Source: © 2014 IEEE, reprinted, with permission, from Salles [35].

plane wave compounding also results in a more uniform signal-to-noise ratio and edge definition throughout the field of view.

The beamforming techniques result in a localizing of the ultrasonic energy or ultrasonic fields transmitted to and recorded from tissue ($p_{\text{tx}}(t, \mathbf{x})$ and $p_{\text{rx}}(t, \mathbf{x})$, respectively). These fields are modified by the frequency-dependent attenuation of the tissue medium, $a(t, \mathbf{x})$, the scattering properties of tissue medium, $s(t, \mathbf{x})$, and the bandpass filtering of the transducer, $h_{\text{tx,rx}}(t)$. This allows the received signal, $r(t)$, for a particular scan line to be represented by Eq. (2.2). A set of lines produced from a scan of tissue produce the beamformed radiofrequency data. This set of radio frequency data can then be processed, $\Omega\{r(t)\}$, to create different types of images.

Echographic images, also known as B-mode images, are the most common image mode in biomedical ultrasound imaging and are produced from the beamformed radiofrequency data. The basic signal processing pipeline involves calculating the envelope of the ultrasonic echoes and applying logarithmic compression in order to improve the dynamic range of the resulting image. In addition, TGC (time gain compression) is performed in order to compensate the effects of depth-dependent attenuation in the amplitude of the received echoes. However, obtaining clinical grade ultrasonic images requires additional processing steps such as nonlinear grayscale mapping, gamma correction, and edge preserving image filtering. The actual algorithms used for the image post-processing and display are typically proprietary knowledge from scanner manufacturers and are not described in detail in the literature.

From Figure 2.7 it can also be observed that the B-mode images exhibit a grainy texture in otherwise homogeneous regions. This phenomenon, known as speckle, is due to the coherent interaction of the echoes produced by several sub-wavelength scatterers within the resolution cell of the transducer. Several models exist for characterizing the statistics of the envelope of the radiofrequency data. If the medium is assumed to have diffusely distributed scatterers that produce echoes with uniformly distributed phase, the probability distribution function of the speckle magnitude follows a Rayleigh distribution which results in a speckle signal-to-noise ratio of 1.91 [34]. This condition is widely accepted to be reached when the medium contains a minimum of 10 scatterers per resolution cell with random spatial locations. For sparser scatterer distributions, or if the scatterers are not diffusely distributed, other probability distribution functions (i.e. Rician, Nakagami, homodyned K) may better model the ultrasonic envelope magnitude.

The speckle can be used to create maps of envelope parameters by fitting the probability distribution to the envelope data. Several researchers have examined the utility of envelope statistics for imaging and medical diagnostics [36, 37]. However, such approaches have not been widely adopted clinically. The contrast mechanism of such envelope statistics images are parameterizations of the envelope statistics.

The presence of the speckle can also provide a means of producing additional types of images taking advantage of different contrast mechanisms. Because the speckle comes from the arrangement of the sub-resolution scatterers, any perturbation of this arrangement will result in either a change of the speckle features or a displacement of the speckle features. By tracking the changing speckle arrangement versus perturbation of the tissue medium and mapping these changes in speckle arrangement, images of displacements can be produced.

Strain imaging utilizes the beamformed radiofrequency data by comparing the displacements of speckle features as a medium is deformed or compressed. Different tissues have different mechanical properties, i.e. the Young's modulus. The contrast inherent in mechanical properties of tissues, such as the Young's modulus, is much higher in tissue than contrast in acoustic impedance, which is the contrast mechanism for B-mode imaging. By imaging the displacements of speckle for given compressions of the tissues, the relative changes in the Young's modulus can be visualized. Such imaging has found applications in detecting cancer and estimating heart muscle strain profiles [38–41].

In a similar manner, certain shear wave imaging techniques exploit the displacements of scatterers and rearrangement of speckle features to estimate and map the shear modulus. Specifically, a compression using an acoustic radiation force mechanism or other mechanism is used to generate a lower frequency shear wave. Ultrasonic imaging is used to capture multiple scan lines and image frames as the shear wave propagates through the tissue. The progression of the shear wave is detected through the tracking of the speckle displacements or rearrangements. By tracking the shear wave and estimating and mapping its speed through a tissue, images of the shear moduli can be constructed [26, 42, 43].

One way to estimate the displacements induced by shear waves propagating through tissue is to utilize Doppler imaging techniques. Doppler imaging techniques in ultrasound have primarily been used to map the flow of blood in tissue and organs. The principle behind Doppler imaging is that objects, e.g. blood cells, flowing away from or towards the transducer will cause a Doppler shift in the sound wave. The flow direction and rate can be estimated through a number of mechanisms including estimating the Doppler frequency shift or tracking the phase of signals from one frame to the next [44]. Pulsed wave Doppler imaging requires short pulses to be transmitted into the tissues at higher pulse repetition rates than typically used for conventional B-mode imaging. The maximum velocity that can be estimated is limited by the rate at which pulses can be transmitted.

2.7 Conclusions

An image is a representation of a physical object. The representation depends fundamentally on the contrast mechanisms within the object that give rise to signals that can be sampled and processed to create the image. In biomedical ultrasound, the basic contrast mechanism is the acoustic impedance differences between different structures. These differences in acoustic impedances give rise to scattering of the ultrasonic fields propagating across different structures. The signal that is received by a transducer is a function of this scattered field, the attenuation of the field as it propagates through the medium, the bandwidth associated with the ultrasonic transducer, and the field characteristics of the transducer. Each of these factors plays a role in the final image that can be produced and the image quality, i.e. spatial resolution, contrast resolution, and signal-to-noise ratio.

The fundamental imaging mode for biomedical ultrasound is B-mode imaging which relates greyscale intensity to structure shapes. B-mode is produced by detecting the envelope of the backscattered signal. B-mode is a qualitative imaging mode whose contrast is simply the differences in scattering from different structures and locations. The scattered intensity depends on the size of the objects, their shape, and their acoustic impedance mismatches.

Other imaging approaches using ultrasound can produce images whose contrast depicts other properties of the tissues, e.g. shear moduli, Young's moduli, flow velocity, etc. Fundamentally, these techniques use the same signals that are generated for B-mode imaging, signals which have their generation from acoustic impedance mismatches. However, by implementing different processing approaches, different contrast mechanisms can be extracted from the signals. For example, a shear wave can be tracked and parameterized by tracking displacements of scatterers as the wave propagates through a medium. The signals coming from the scatterers are still based on the acoustic impedance mismatch between the scatterers and some background. However, by tracking the displacements of the scatterers, the shear wave motion can be estimated generating new images that represent new image contrast. By understanding the underlying physics of signal generation and reception in ultrasound, a variety of imaging modes can be produced through processing of the signals, which can provide distinct images with information that complement each other.

References

1 Cobbold, R.S.C. (2007). *Foundations of Biomedical Ultrasound*. New York: Oxford University Press.
2 Curie, P. and Curie, J. (1880). Developpement par pression de l'electrcite polaire dans les cristaux hemiedres a faces enclines. *Compt. Rendus* 91: 38.
3 Mason, W.P. (1981). Piezoelectricity, its history and applications, *J. Acoust. Soc. Am.* 70: 1561–1566.
4 Neubert, H.K.P. (1963). *Instrument Transducers*. New York: Oxford University Press.
5 Jaffe, B., Cook, W.R., and Jaffe, H. (1971). *Piezoelectric Ceramics*. New York: Academic Press.
6 Halliday, D. and Resnick, R. (1986). *Fundamentals of Physics*. New York: Wiley.
7 Szabo, T.L. (2004). *Diagnsotic Imaging: Inside Out*. Burlington: Elsevier Academic Press.
8 McKeighen, R.E. (1998). Design guidelines for medical ultrasonic arrays. *Proc. SPIE Med. Imaging* 3341: 2–18.
9 Desilets, C.S., Fraser, J.D., and Kino, G.S. (1978). The design of efficient broadband piezoelectric transducers. *IEEE Trans. Sonics Ultrason.* SU-25: 115–125.
10 Goll, J.H. (1979). The design of broadband fluid-loaded ultrasonic transducers. *IEEE Trans. Sonics Ultrason.* SU-26: 385–393.
11 Inoue, T., Ohta, M., and Takahasi S. (1987). Design of ultrasonic transducers with multiple acoustic matching layers for medical applications. *IEEE Trans. Ultrason., Ferroelect., Freq. Control* 34: 8–16.
12 Beyer, R.T. and Letcher, S.V. (1969). *Physical Ultrasonics*. New York: Academic Press.
13 Jensen, J.A. and Svendsen, N.B. (1992). Calculation of pressure fields from arbitrarily shaped, apodized, and excited ultrasound transducers. *IEEE Trans. Ultrason., Ferroelect., Freq. Control* 39: 262–267.
14 Jensen, J.A. (1999). A new calculation procedure for spatial impulse responses in ultrasound. *J. Acoust. Soc. Am.* 105: 3266–3274.
15 Anderson, V.C. (1950). Sound scattering from a fluid sphere, *J. Acoust. Soc. Am.* 22: 426–431.
16 Faran, Jr., J.J. (1951). Sound scattering by solid cylinders and spheres. *J. Acoust. Soc. Am.* 23: 405–418.
17 Morse, P.M. and Ingard, K.U. (1968). *Theoretical Acoustics*. New York: McGraw-Hill.
18 Shung, K.K. and Thieme, G.A. (1993). *Ultrasonic Scattering in Biological Tissues*. Boca Raton: CRC Press.
19 Goss, S.A., Johnston, R.L., and Dunn, F. (1978). Comprehensive compilation of empirical ultrasonic properties of mammalian tissues. *J. Acoust. Soc. Am.* 64: 423–457.
20 Goss, S.A., Frizzell, L.A., and Dunn, F. (1980). Dependence of the ultrasonic properties of biological tissue on constituent proteins. *J. Acoust. Soc. Am.* 67: 1041–1044.
21 Goss, S.A., Johnston, R.L., and Dunn, F. (1980). Compilation of empirical ultrasonic properties of mammalian tissues II. *J. Acoust. Soc. Am.* 68: 93–108.
22 Goss, S.A. and Dunn, F. (1980). Ultrasonic propagation properties of collagen. *Phys. Med. Biol.* 25: 827–837.
23 Duck, F.A. (1990). *Physical Properties of Tissue: A Comprehensive Reference Book*. London: Academic Press.
24 Mast, T.D. (2000). Empirical relationships between acoustic parameters in human soft tissues. *Acoust. Res. Lett. Online* 1: 37–42.
25 Goss, S.A., Frizzell, L.A., and Dunn, F. (1979). Ultrasonic absorption and attenuation in mammalian tissues. *Ultrasound Med. Biol.* 5: 181–186.
26 Sarvazyan, A.P., Rudenko, O.V., Swanson, S.D., et al. (1998). Shear wave elasticity imaging: a new ultrasonic technology of medical diagnostics. *Ultrasound Med. Biol.* 24: 1419–1436.

27 Kinsler, L.E., Frey, A.R., Coppens, A.B., and Sanders, J.V. (1999). *Fundamentals of Acoustics*. New York: Wiley.

28 Schuck, O.H. (1963). Variable focus transducer. US Patent 3,090,030.

29 Flaherty, J.J., Erikson, K.R., and Lund V. (1967). Synthetic aperture ultrasound imaging systems. US Patent, 3,548,642.

30 Burckhardt, C.B., Grandchamp, P.A., and Hoffman H. (1974). An experimental 2 MHz synthetic aperture sonar system intended for medical use. *IEEE Trans. Sonics Ultrason.* 21: 1–6.

31 Jensen, J.A., Nikolov, S.I., Gammelmark, K.L., and Pedesen, M.H. (2006). Synthetic aperture ultrasound imaging. *Ultrasonics*, 55: e5–e15.

32 Cheng, J. and Lu, J.Y. (2006). Extended high-frame rate imaging method with limited-diffraction beams. *IEEE Trans. Ultrason., Ferroelect., Freq. Control* 53: 880–898.

33 Montaldo, G., Tanter, M., Bercoff, J., et al. (2009) Coherent plane-wave compounding for very high frame rate ultrasonography and transient elastography. *IEEE Trans. Ultrason., Ferroelect., Freq. Control* 56: 489–506.

34 Wagner, R.F., Smith, S.W., Sandrik, J.M., and Lopez, H. (1983). Statistics of speckle in ultrasound B-scans. *IEEE Trans. Sonics Ultrason.* 30: 156–163.

35 Salles, S., Liebgott, H., Basset, O., et al. (2014). Experimental evaluation of spectral-based quantitative ultrasound imaging using plane wave compounding. *IEEE Trans. Ultrason., Ferroelect., Freq. Control* 61: 1824–1834.

36 Tsui, P.H. and Chang, C.C. (2007). Imaging local scatterer concnetrations by the Nakagami statistical model. *Ultrasound Med. Biol.* 33: 608–619.

37 Hruska, D.P. and Oelze, M.L. (2009). Improved parameter estimates based on the homodyned K distribution. *IEEE Trans. Ultrason., Ferroelect., Freq. Control* 56: 2471–2481.

38 Cespedes, I., Ophir, J., Ponnekanti, H., and Maklad, N. (1993). Elastography: Elasticity imaging using ultrasound with application to muscle and breast in vivo. *Ultrason. Imaging* 15: 73–88.

39 Heimdal, A., Stoylen A., Torp, H., and Skjaerpe, T. (1998). Real-time strain rate imaging of the left ventricle by ultrasound. *J. Am. Soc. Echocardiogr.* 11: 1013–1019.

40 D'Hooge J., Heimdal, A., Jamal, F., et al. (2000). Regional strain and strain rate measurements by cardiac ultrasound: principles, implementation and limitions. *Eur. J. Echocardiogr.* 1: 154–170.

41 Zaleska-Dorobisz, U., Kaczorowski, K., Pawlus, A., et al. (2014). Ultrasound elastography – review of techniques and its clinical applications. *Adv. Clin. Exp. Med.* 23: 645–655.

42 Bercoff, J., Tanter, M., and Fink, M. (2004). Supersonic shear imaging: a new technique for soft tissue elasticity mapping. *IEEE Trans. Ultrason., Ferroelect., Freq. Control* 51: 396–409.

43 Chen, S., Urban, M.W., Pislaru, C., et al. (2009). Shearwave dispersion ultrasound vibrometry (SDUV) for measuring tissue elasticity and viscosity. *IEEE Trans. Ultrason., Ferroelect., Freq. Control* 56: 55–62.

44 Jensen, J.A. (1996). *Estimation of Blood Velocities Using Ultrasound*. Cambridge, UK: Cambridge University Press.

3

Elastography and the Continuum of Tissue Response

Kevin J. Parker

Department of Electrical and Computer Engineering, University of Rochester, Rochester, NY, USA

3.1 Introduction

From the earliest days of medicine, the palpable "feel" of tissues and organs has been used in diagnostic evaluations. Even today, screening exams include palpation of the liver, breast, prostate, thyroids, skin lesions, and other tissues to characterize their condition. However, manual palpation is limited to accessible surfaces and is not quantitative. By the 1980s, there existed a wide gap between the impressive imaging abilities within radiology and the important but limited information that was obtained from palpation. How could these two disparate domains be bridged to add hidden biomechanical properties into modern radiological imaging systems? As the later chapters in this book will show, some early work took advantage of the availability of Doppler ultrasound devices to study tissue motion and abnormalities in the 1970s and 1980s. Out of this background came a remarkable series of imaging approaches to map out the elastic properties of tissues. Initially, images were produced by vibration sonoelastography, where vibrational shear waves (typically between 50 and 1000 Hz continuous wave) are excited within tissue and the resulting vibrations are imaged and displayed using Doppler-displacement or phase estimators [1, 2]. Other innovative approaches applied step compressions, transient forces, and a variety of additional imaging modalities, such as magnetic resonance elastography (MRE) and optical imaging, to uncover the biomechanical properties of tissue that were previously unobservable with conventional radiology. These major approaches will be covered in subsequent chapters in this book.

While there are an impressive variety of approaches to imaging the elastic properties of tissue, it can be shown that all techniques lie on a continuum of biomechanical responses. In fact, the time-dependent terms can be seen as important drivers of the particular response of tissues, and this leads naturally to a continuum, or spectrum, of approaches ranging from very slow motion, through sinusoidal steady-state motion, to impulsive motion, as depicted in Figure 3.1. An overview of the continuum analysis was given by Parker et al. [3].

Consider a block of tissue-mimicking elastic material as shown in Figure 3.2, constrained on the right side, free on top and bottom, but capable of being displaced from the left side, while being imaged so that internal displacements can be accurately estimated. The equation of motion that governs the displacements u is given by

$$(\lambda+\mu)\frac{\partial^2 u_j}{\partial x_j \partial x_i}+\mu\frac{\partial^2 u_i}{\partial x_j \partial x_j}+\rho f_i=\rho\frac{\partial^2 u}{\partial t^2} \quad \text{or}$$

$$(\lambda+\mu)\nabla(\nabla\cdot\mathbf{u})+\mu\nabla^2\mathbf{u}+\rho\mathbf{f}=\rho\ddot{\mathbf{u}} \tag{3.1}$$

Ultrasound Elastography for Biomedical Applications and Medicine, First Edition.
Edited by Ivan Nenadic, Matthew Urban, James Greenleaf, Jean-Luc Gennisson, Miguel Bernal, and Mickael Tanter.

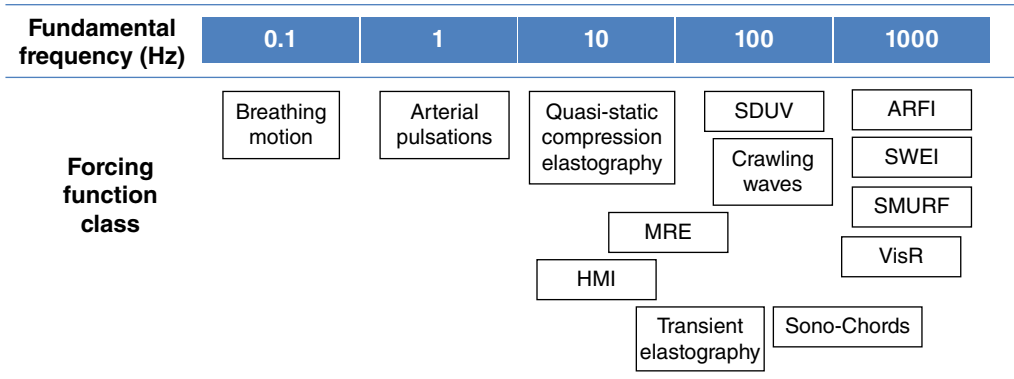

Figure 3.1 Spectrum of natural and applied forces – all positions are approximate as a relative guide. The dominant frequency, or bandwidth, varies from left (slowest frequencies) to right (highest frequencies). Acronyms refer to some major approaches described in other chapters in this book, for example MRE is magnetic resonance elastography, typically applied to the liver with 50 Hz shear waves.

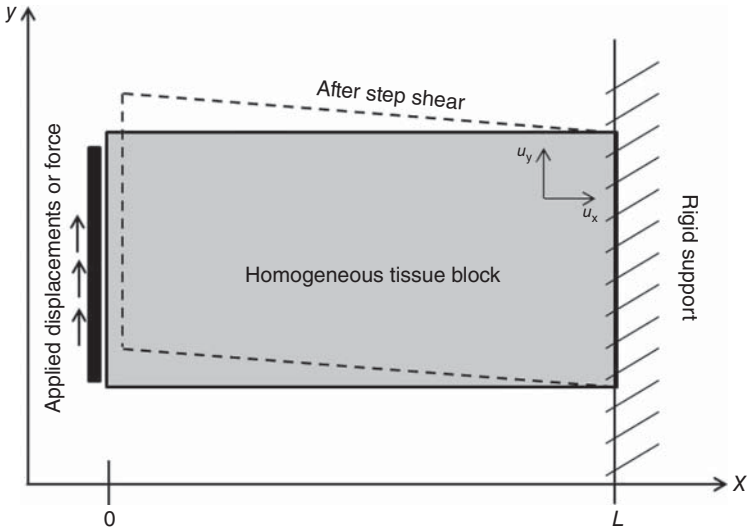

Figure 3.2 A homogeneous block of biomaterial is constrained on the right and is displaced on the left. As the applied displacements move from very slow shear or compression, to higher frequency harmonic shear in the *y*-direction, to broadband (impulsive) excitation, the form of the solution within the interior moves from linear with *x*, to sinusoidal in *x*, to a propagating pulse in *x*. However, all are solutions to the basic equation of motion. In this way, all the major elastographic imaging approaches can be seen as points along a common biomechanical spectrum.

where γ and μ are the Lamé constants, capturing the mechanical properties of the material, and where the body forces $\mathbf{f}$, such as gravity, are assumed negligible except in the important cases where radiation force "pushes" are applied. This equation, with given boundary and initial conditions, governs the general dynamic response of a homogeneous, isotropic, linearly elastic material to a force or displacement excitation.

3.2 Some Classical Solutions

Most textbook solutions to Eq. (3.1) consider particular conditions depending on the type of tractions or body forces applied: static, sinusoidal steady state, or transient. We examine a few of these important cases and then in the next section show how these lie on the continuum.

In classical treatments it is convenient to represent the sinusoidal steady state response in terms of waves propagating within the tissue. Two types of plane wave, shear waves and pressure waves, propagate independently in the bulk material, interacting only at boundaries [4]. The shear wave equation can easily be obtained from Eq. (3.1) by noting that there is no volume change as layers of material move in shear, transverse to the direction of propagation, so the dilatation $\nabla \cdot \mathbf{u} = 0$. The shear wave equation is then

$$\nabla^2 \mathbf{u} = \frac{1}{c_s^2} \ddot{\mathbf{u}} \tag{3.2}$$

where the shear wave speed is

$$c_s = \sqrt{\frac{\mu}{\rho}} \tag{3.3}$$

This equation can either be solved in terms of standing waves or propagating waves, depending on the particular conditions.

Propagating plane pressure waves are irrotational, that is, $\nabla \times \mathbf{u} = \mathbf{0}$ so $\mathbf{u}$ can be written in terms of a potential as $\mathbf{u} = \nabla \psi$. Using the vector identity $\nabla^2 \mathbf{u} = \nabla \nabla \cdot \mathbf{u} - \nabla \times \nabla \times \mathbf{u}$, we can obtain the wave equation for $\nabla \psi$ as

$$\nabla^2 (\nabla \psi) = \frac{1}{c_p^2} (\dot{\nabla} \dot{\psi}) \tag{3.4}$$

and the pressure wave speed is

$$c_p = \sqrt{\frac{\lambda + 2\mu}{\rho}} \tag{3.5}$$

For typical biomaterials, the pressure wave speed is orders of magnitude faster than the shear wave speed. Consistent with this statement, biological tissues are nearly incompressible with $0.49 < \nu < 0.5$. In the limit as ν approaches 0.5, the shear modulus becomes

$$\mu = \frac{E}{2(1+\nu)} \rightarrow E/3 \tag{3.6}$$

Therefore, for a nearly incompressible material, a measurement of the shear wave speed $c_s \approx \sqrt{E/3\rho}$ can be used to obtain information about the stiffness of the material. So in continuous wave elastographic imaging experiments, the focus of attention is typically on the shear wave properties and not on compressional pressure wave properties, which have already been investigated extensively in ultrasonic tissue characterization studies.

Equation (3.1) can also be a starting point for the consideration of step-compression elastography experiments. For static displacement or very low frequency cyclic motion, the inertial terms are negligibly small. And for nearly incompressible biomaterials, the divergence (or dilatation) $\nabla \cdot \mathbf{u}$ is nearly zero, so Eq. (3.1) reduces to Laplace's equation

$$\nabla^2 \mathbf{u} = 0 \tag{3.7}$$

Solutions to Laplace's equation depend on and reach their extrema on the boundary values of **u**. For simple one-dimensional geometry the solution for displacement $u_x(x)$ is linear with x, and therefore the strain (the derivative of displacement) is uniform, a fact that is assumed to be true in most step-compression elastographic imaging experiments for homogeneous materials. Deviations from constant strain are indications of local structures that are harder or softer, forming the basis of imaging in compression elastographic methods.

3.3 The Continuum Approach

Rather than viewing different solutions to Eq. (3.1) (and different elastographic techniques) as isolated special cases, it can be shown that there is a continuum of responses that depend on the degree of the time-varying terms in Eq. (3.1).

If we very slowly compress then hold the block of Figure 3.2, or slowly shear it in the y-direction, the time-varying terms are negligible and the solution to the displacement is simply linear with x (going to zero on the right side where the block is constrained). In the compression-then-hold case, the solution to Eq. (3.1) with negligible time derivatives, no body forces, and near incompressibility comes from Eq. (3.7) and the specific conditions. Assume the compression is a small displacement Δu_x applied at the left surface, so that within the tissue

$$u_x(x) = \frac{\Delta u_x(L-x)}{L} \quad \text{for} \quad \Delta u_x < x \le L \quad \text{and the strain} \quad \frac{\Delta u_x}{L} \ll 1 \tag{3.8}$$

The displacement $u(x)$ is linear and the one-dimensional strain $\partial u/\partial x$ is constant within the block of tissue. Thus, a strain image produced by compression elastography techniques would be uniform in this case, consistent with a homogeneous block of material.

Alternatively, if a shear-and-hold displacement in the y-direction, Δu_y, is applied, the solution is

$$u_y(x) = \frac{\Delta u_y(L-x)}{L} \tag{3.9}$$

within the block. This is illustrated in Figure 3.3. Thus, a shear strain image produced in this case would also be uniform, consistent with a homogeneous block of material.

If we next apply a shear motion in the y-direction in a slow, repeated, sinusoidal motion, the "quasi-static" solution is appropriate, where the displacement is still linear in x but now has a $\cos(\omega_L t)$ term as the temporal dependence

$$u_y(x) = \frac{\Delta u_y(L-x)}{L}\cos(\omega_L t) \tag{3.10}$$

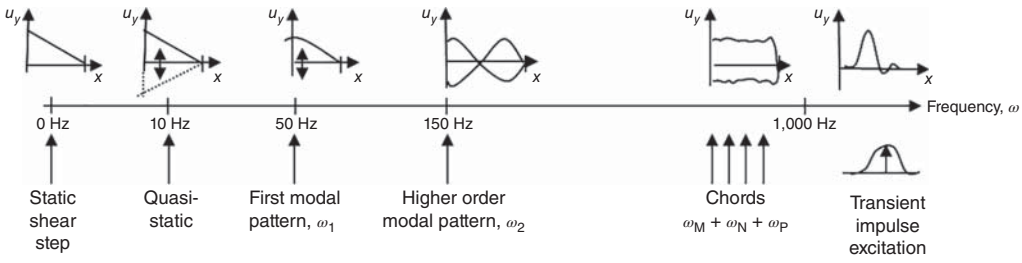

Figure 3.3 Summary image showing the continuum from step displacement through dynamic vibration, multiple tones, and transients. The displacement field u_y is given in each case for the homogeneous block of tissue. The solution for the displacement in the homogeneous object is linear for the static case, sinusoidal for modal patterns at Eigen-frequencies, and approaches a constant for multiple, simultaneous "chord" excitation. Transient or impulsive waves may be broadband or more narrowband from tone burst excitations.

Here the frequency ω_L is so low that the second (temporal) derivative term ω_L^2 is insignificant. Next, as the frequency increases, the time-varying terms of Eq. (3.1) become non-negligible and at some minimum frequency a modal pattern can be established [5–7]. The displacement within the material is now a shear wave of a sinusoidal form, both in time and space. This phenomenon can be present in vibration elastography and MRE depending on the size of the organs being imaged and the frequencies applied. Next, if we displace the left side with multiple frequencies (sono-chords) [8], or short tone bursts, then the displacements are comprised of multiple frequency components and multiple eigenmodes.

Finally, if we displace the left side with a sharp impulsive excitation, then a shear wave is produced that will propagate as a disturbance through the biomaterial, like a ripple on a taut string. In the one-dimensional case, a sharp force f_i in Eq. (3.1) applied interiorly will launch a pair of waves analogous to the classical D'Alembert's solution [9, 10]. When a long, cylindrical beam is used to generate radiation force, the solution in cylindrical coordinates is analogous [11–13], but more intricate due to cylindrical spreading. This is the basis for impulsive shear-wave imaging. Thus, as the frequency content of the applied displacement moves from very low frequencies, to sinusoidal harmonic frequencies above 40 Hz, to higher frequencies and wider bandwidths, finally to an impulsive (broadband) excitation, the particular form of the solution varies, but all are solutions to Eq. (3.1). In this way, the many approaches to imaging the elastic properties of tissue can be related, as depicted in Figure 3.3. The lowest frequencies correspond naturally to breathing, heart rate, and low voice frequencies [14, 15]. Low frequency techniques are covered in detail in Section IV of this book. Radiation force techniques can be broadband (impulsive) or narrowband, as will be discussed in Sections V and VI of this book. The highest frequencies are limited by the high attenuation of shear waves in viscoelastic tissue [16]. This results in a frequency range of useful applications from approximately 1 to 1000 cycles per second.

One important distinction emerges in the context of inverse solutions, however. In order to arrive at a unique, well-conditioned inverse solution, there can be major differences in requirements for data, boundary conditions, and assumptions for different approaches across the continuum [17].

3.4 Conclusion

On the surface, the field of "imaging the elastic properties of tissues" appears to be comprised of a large number of disparate approaches, each one a special case exploiting a unique tissue perturbation. Reinforcing this appearance, the approaches to solving the inverse problem are also widely disparate, depending on the particular excitation being applied. However, at a deeper level, a unifying framework links the different techniques within a continuum. One governing differential equation captures the response of elastic materials to applied forces and tractions. The changing nature of tissue responses can be followed from static or very low frequency behavior, through higher frequency, and then impulsive excitations. Gradual transitions are seen as the time-varying term of the governing equation becomes more significant with higher frequencies. From this perspective, each of the major approaches to elastographic imaging occupy a specific position on a continuum, where the key continuous variable is the frequency range of the excitation and tissue displacements that are imaged and analyzed.

Acknowledgments

This work was supported by the Hajim School of Engineering and Applied Sciences at the University of Rochester, and by National Institutes of Health grants R01 AG016317 and R01 AG029804.

References

1 Lerner, R.M. and Parker, K.J. (1987). Sonoelasticity images derived from ultrasound signals in mechanically vibrated targets. In: *Seventh European Communities Workshop* (ed. J. Tjissen), Nijmegen, The Netherlands.

2 Lerner, R.M., Parker, K.J., Holen, J., et al. (1988). Sonoelasticity: medical elasticity images derived from ultrasound signals in mechanically vibrated targets. *Acoust. Imaging* 16: 317–327.

3 Parker, K.J., Taylor, L.S., Gracewski, S., and Rubens, D.J. (2005). A unified view of imaging the elastic properties of tissue. *J. Acoust. Soc. Am.* 117: 2705–2712.

4 Graff, K.F. (1975). Wave motion in elastic solids. In: *Oxford Engineering Science Series*, 273–310. Oxford: Clarendon Press.

5 Alam, S.K., Richards, D.W., and Parker, K.J. (1994). Detection of intraocular pressure change in the eye using sonoelastic Doppler ultrasound. *Ultrasound Med. Biol*. 20: 751–758.

6 Gao, L., Parker, K.J. Alam, S.K., and Lernel, R.M. (1995). Sonoelasticity imaging: theory and experimental verification. *J. Acoust. Soc. Am.* 97: 3875–3886.

7 Parker, K.J. and Lerner, R.M. (1992). Sonoelasticity of organs: shear waves ring a bell. *J. Ultrasound Med.* 11: 387–392.

8 Taylor, L.S., Porter, B.C. Rubens, D.J., and Parker, K.J. (2000). Three-dimensional sonoelastography: principles and practices. *Phys. Med. Biol.* 45: 1477–1494.

9 Blackstock, D.T. (2000). *Fundamentals of Physical Acoustics*, 1–64. New York: Wiley.

10 Graff, K.F. (1975). Wave motion in elastic solids. In: *Oxford Engineering Science Series*, 9–74. Oxford: Clarendon Press.

11 Baddour, N. (2011). Multidimensional wave field signal theory: mathematical foundations. *AIP Adv.* 1: 022120.

12 Parker, K.J. and Baddour, N. (2014). The Gaussian shear wave in a dispersive medium. *Ultrasound Med. Biol* 40: 675–684.

13 Sarvazyan, A.P., Rudenko, O.V., Swanson, S.D., et al. (1998). Shear wave elasticity imaging: a new ultrasonic technology of medical diagnostics. *Ultrasound Med. Biol.* 24: 1419–1435.

14 de Korte, C.L. and van der Steen, A.F.W. (2002). Intravascular ultrasound elastography: an overview. *Ultrasonics* 40: 859–865.

15 Sohn, C. and Baudendistel, A. (1995). Differential diagnosis of mammary tumors with vocal fremitus in sonography: preliminary report. *Ultrasound Obstet. Gynecol.* 6: 205–207.

16 Ormachea, J., Lavarello, R.J., McAleavey, S.A., et al. (2016). Shear wave speed measurements using crawling waves sonoelastography and single tracking location shear wave elasticity imaging for tissue characterization. *IEEE Trans. Ultrason., Ferroelect., Freq. Control* 63: 1351–1360.

17 Doyley, M.M. (2012). Model-based elastography: a survey of approaches to the inverse elasticity problem. *Phys. Med. Biol.* 57: R35–R73.

4

Ultrasonic Methods for Assessment of Tissue Motion in Elastography

Jingfeng Jiang and Bo Peng

Department of Biomedical Engineering, Michigan Technological University, Houghton, MI, USA

4.1 Introduction

Tracking tissue motion using ultrasound data has been an active field since the 1980s. In the early work [1, 2], researchers attempted to monitor tissue displacements resulting from physiological stimuli, in order to infer tissue mechanical properties or compensate for undesirable physiological motion among multiple images by tracking those unwanted physiological motions [3]. In 1991, Prof. Ophir's group first proposed strain elastography [4], demonstrating its ability to quantify very small internal strains in tissue phantoms and soft tissue samples. Progress in tissue motion assessment made within the framework of ultrasound elastography (including strain elastography, shear wave elastography, and acoustic radiation force imaging) built on those early attempts and were facilitated by improvements in hardware over that used by the earlier investigations.

A number of motion-tracking techniques have been proposed and may be classified into the following categories, according to the signal-processing method used, as follows:

- Frequency-domain techniques: A phase-based method is applied to find zero-phase contour between the pre- and post-deformation ultrasound signals.
- Maximum likelihood (ML) time-domain correlation-based techniques: A time-domain (magnitude) correlation function is used to identify the peak of the correlation function and subsequently find the tissue motion vector.
- Time- and frequency-domain hybrid methods: Both the magnitude correlation function and the phase information are employed to estimate the motion vector.
- Time-domain maximum a posterior (MAP) motion-tracking techniques: Motion tracking is being cast as an optimization problem that requires restoring both the echo signal coherence (between the pre- and motion-compensated post-deformation signals) and physical constraints of tissue motion (e.g. motion continuity and tissue incompressibility).
- Optical flow-based techniques: The classical optical flow technique borrowed from computer vision is applied to estimate tissue motion.
- Mesh-based techniques: in which the region of interest (ROI) is divided into finite elements [5].

Consequently, the solution of the tissue motion has to satisfy two conditions: (1) finding the maximum of the signal correlation (between the pre- and motion-compensated post-deformation signals) and (2) governing equations in theory of elasticity [6].

This chapter provides an overview of above-mentioned methods used for ultrasound elastography, which utilizes tissue displacements as fundamental information to infer mechanical

Ultrasound Elastography for Biomedical Applications and Medicine, First Edition.
Edited by Ivan Nenadic, Matthew Urban, James Greenleaf, Jean-Luc Gennisson, Miguel Bernal, and Mickael Tanter.

properties of biological soft tissues. Results available in the literature have demonstrated that, to some extent, better tracking methods often lead to more accurate elastographic results. Unfortunately, many challenges still remain open, largely due to the complexity of in vivo tissue motion, and the existence of significant echo signal de-correlation.

4.2 Basic Concepts and their Relevance in Tissue Motion Tracking

Some basic concepts are included in this section for the sake of completeness.

4.2.1 Ultrasound Signal Processing

In signal processing, cross-correlation is a basic concept and has been commonly used for pattern recognition in various applications, including time-delay estimation in elastography. Mathematically, for continuous functions f and g, the correlation function is defined as

$$(f * g)(\tau) = \int_{-\infty}^{\infty} [f(t)g^*(t+\tau)]\, \mathrm{d}t \tag{4.1}$$

where g^* denotes a complex conjugate of g and τ is a dummy variable for time lag.

The correlation function can be rewritten for discretely sampled signals f and g as follows

$$(f * g)[n] = \sum_{m=-\infty}^{\infty} \{f[m]g^*[m+n]\} \tag{4.2}$$

Practically, ultrasound signals used for motion tracking have a finite length and are often real signals. Some correlation metrics that have been commonly used to track tissue motion in the ultrasound elastography literature are briefly summarized below. Hereafter, all ultrasound signals in this chapter are discretely sampled real signals with finite lengths.

The normalized correlation coefficient (NCC) between two signals f and g can be written as follows

$$\rho(\tau) = \frac{\sum_{m=0}^{m=N} \{f[m] - \bar{f}\} \times \{g[m+\tau] - \bar{g}\}}{\sqrt{\sum_{m=0}^{m=N} \{f[m] - \bar{f}\}^2} \times \sqrt{\sum_{m=0}^{m=N} \{g[m+\tau] - \bar{g}\}^2}} \tag{4.3}$$

When we substitute the actual time delay δ into Eq. (4.3), the calculated NCC becomes an indicator of motion-tracking accuracy [7, 8]. Hereafter, the calculated NCC value at the actual time delay δ is referred to as the motion-compensated NCC value.

The cross correlation can also be estimated as follows

$$R(\tau) = \sum_{m=0}^{N} \{f[m]\} * \{g[m+\tau]\} \tag{4.4}$$

Calculation of NCC is more computationally intensive but yields a coefficient between 0 and 1, while Eq. (4.3) produces a correlation value in an arbitrary scale. Equation (4.4) can be implemented with the fast-Fourier transform (FFT) to improve its computational efficiency.

The sum-squared error (SSE) and sum-absolute error (SAE) between two signals f and g are defined as functions of the lag τ below, respectively

$$\varepsilon(\tau) = \sum_{m=0}^{N} (f[m] - g[m+\tau])^2 \tag{4.5a}$$

$$\varepsilon(\tau) = \sum_{m=0}^{N} |f[m] - g[m+\tau]| \tag{4.5b}$$

4.2.2 Constitutive Modeling of Soft Tissues

Constitutive equations of materials based on continuum mechanics describe the macroscopic stress response to external mechanical stimuli (e.g. forces). In general, biological soft tissues are nonlinear and inhomogeneous, poro-elastic, and anisotropic [9]. However, for the purpose of ultrasound-based motion assessment, a linearly elastic model is often (implicitly or explicitly) assumed [6]:

$$\theta_{ij} = C_{ijkl} e_{kl} \tag{4.6}$$

where the second-order symmetric stress tensor, θ_{ij}, is linearly related to the second-order symmetric tensor strain tensor e_{kl}. In Eq. (4.6), C_{ijkl} is known as constitutive constants. Equation (4.6) is a simplified expression of Hooke's law and assumes strain linearity for a range of deformation. If those constitutive constants are assumed to be independent of the direction of the applied mechanical stimuli, Eq. (4.6) becomes isotropic. In this case, the constitutive constants are reduced to two Lamé constants. The governing equations for such a situation can be described as follows

$$\theta_{ij} = 2\mu e_{ij} + \lambda \delta_{if} e_{nn} \tag{4.7}$$

$$\frac{\partial \theta_{ji}}{\partial x_i} + f_i = 0 \tag{4.8}$$

$$e_{ij} = \frac{1}{2}\left(\frac{\partial u_i}{\partial x_j} + \frac{\partial u_j}{\partial x_i}\right) \tag{4.9}$$

where $\mu = (E/2(1+\upsilon))$and $\lambda = (E\nu/(1+\nu)(1-2\nu))$ are the Lamé constants in which E is the Young's modulus and ν is the Poisson's ratio. f_i is the body force in the x_i direction and u_i is the displacement vector in the x_i direction.

Numerically, Eqns. (4.7)–(4.9) can be solved in the framework of finite element method (FEM) under given boundary conditions. The numerical solution results in a linear system

$$\mathrm{KU} = \mathrm{F} \tag{4.10}$$

where K is the system stiffness matrix, U is the displacement vector and F is the external force vector. The derivation of Eq. (4.10) is beyond the scope of this chapter and can be found in many FEM textbooks (e.g. [5]). Given the frame rate from a modern clinical ultrasound scanner (typically > 60 frames/second), linear elasticity is a good first approximation when the tissue motion is tracked from frame to frame. That is why a linearly elastic tissue model can be used explicitly or implicitly for tracking tissue motion.

4.3 Tracking Tissue Motion through Frequency-domain Methods

We start our initial discussion of motion-tracking approaches that track one-dimensional (1D) tissue motion. By neglecting the small deformation between two segments of 1D echo (real) signals $s_1(y)$ and $s_2(y)$

$$s_1(y) = s_2(y - \delta y) \tag{4.11}$$

where one signal $s_1(y)$ is shifted along the axial direction with respect to the other $s_2(y)$ by the amount δy, and y is the axial direction. In the terminology of elastography, the subscripts 1 and 2 in Eq. (4.11) denote the pre- and post-deformation RF echo signals, respectively. The cross-correlation between $s_1(y)$ and $s_2(y)$ is given by

$$R(\tau) = \int_{-\infty}^{\infty} [s_1(y+\tau)s_2^*(y)]\, \mathrm{d}y \tag{4.12}$$

Of note, analytic signals can be calculated from real radiofrequency (RF) data by adding an imaginary part to the signal. This imaginary part is equal to the signal's Hilbert transform. It is straightforward to show that this cross-correlation function (see Eq. 4.12) reaches its maximum when $\tau = \delta y$. The relation between the phase function φ and the cross-correlation function $R(\tau)$can be written as follows

$$\Gamma_{1,2}(\omega) = \left\{ \int_{-\infty}^{\infty} [R(\tau)e^{-i\omega\varphi(\tau)}]\, \mathrm{d}\tau \right\} \tag{4.13}$$

where Γ is the cross-spectrum function and ω is the angular frequency. When $\tau = \delta y$, the phase function $\varphi(\tau) = 0$. This phase function $\varphi(\tau)$, with respect to the transducer's centroid frequency ω_0, is a nearly linear function, as shown in Figure 4.1.

Therefore, the root-seeking method can be used to iteratively estimate the time delay corresponding to the zero phase angle as follows

$$\tau_{n+1} = \tau_n - \frac{\varphi(\tau_n)}{\varphi'(\tau_n)} \tag{4.14}$$

where the subscripts n and $n + 1$ represent the n-th and $(n + 1)$-th iterations, respectively, and the superscript $'$ denotes the first-order derivative. Equation (4.14) is, in fact, a Newton–Raphson method [11].

This method was first proposed by Pesavento et al. [10] and has led to a class of efficient and robust methods for estimating the axial shift through the phase of the 1D complex cross correlation without the need for interpolation. The solution is quite robust as the magnitude of the cross correlation is smooth with Gaussian-like characteristics, thus allowing for reliable estimation of the (sampled) peak of the cross-correlation. The true peak of the cross-correlation can be estimated with sub-sample accuracy in a computationally efficient manner by finding the zero-crossing of the phase of the 1D cross-correlation near the maximum magnitude point.

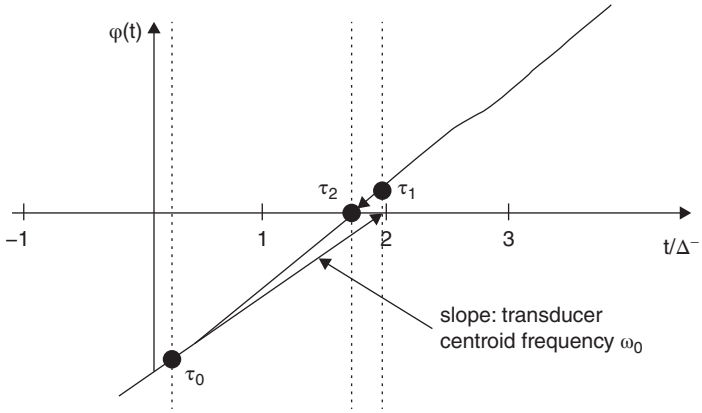

Figure 4.1 An illustration of the process of root-seeking using a Newton–Raphson method in the zero-crossing algorithm proposed by Pesavento et al. Source: © 1999 IEEE, reprinted, with permission, from [10].

Early work has demonstrated that 1D motion tracking may fail to correctly track tissue motion with deformations as small as 0.6% axial strain [12]. This is because soft tissues are often nearly incompressible [9], and the tissues typically move in all three dimensions when they are being deformed primarily in one direction. This motivates the need to develop 2D tracking. However, the 1D phase-tracking method described above cannot be easily translated to two-dimensional (2D) phase-tracking for conventional ultrasound echo data. Mainly, this is because there is no carrier frequency available for the lateral component of the ultrasound echo and therefore there is no lateral phase information. A practical approach suggested by Lubinski et al. [13] is to perform a two-step motion tracking. In the first step, the lateral displacement component can be found using a time-domain method, as described in Section 4.4 below. Then, the above-mentioned zero-crossing method [10] can be applied to obtain the axial displacement component after two signals are aligned using the known lateral displacement component.

We define x and y as the lateral and axial directions, respectively, for 2D motion tracking. We also assume that there is a translation vector (u, v) between two RF signals $s_1(x, y)$ and $s_2(x, y)$. Without losing generality, we assume that $s_1(x + u, y + v) = s_2(x, y)$. In the frequency domain (through Fourier transform)

$$S_2(k_x, k_y) = S_1(k_x, k_y)e^{j(k_x u + k_y v)} \tag{4.15}$$

where S_1 and S_2 are the forward Fourier transforms of the original signals s_1 and s_2, respectively, and k_x and k_y are spatial frequency variables in the x (lateral) and y (axial) directions, respectively. The cross-spectrum function Γcan be written as follows

$$\Gamma_{1,2}(k_x, k_y) = S_1(k_x, k_y)S_2^*(k_x, k_y) = |S_1(k_x, k_y)|^2 e^{j(k_x u + k_y v)} \tag{4.16a}$$

$$\Gamma_{1,2}(k_x, k_y) = |\Gamma_{1,2}(k_x, k_y)|e^{-j\varphi} \tag{4.16b}$$

where the superscript * denotes a conjugate complex, φ is the phase angle of the cross-spectrum function Γ, and | | stands for the magnitude of a complex variable. As inspired by this, Sumi proposed an iterative tracking method [14] based on minimization of the following cost function

$$\text{Cost}(u, v) = \sum_{k_x=1}^{N} \sum_{k_y=1}^{M} |\Gamma_{1,2}(k_x, k_y)| \{\Theta - k_x u - k_y v\}^2 \tag{4.17}$$

It is easy to see that Eq. (4.17) can be solved in a least squares fashion for a small region where the displacement vector (u, v) is a constant. Once the first displacement vector (u^0, v^0) is obtained, the signal s_1 can be warped (also known as motion-compensation) by the displacement vector to create a motion compensation signal s_1^1. Then, a new displacement vector (u^1, v^1) can be calculated again. Superscripts over the displacement vector (u, v) and the signal $s_1$denote the iteration numbers. Iterations continue until certain criteria (e.g. (u^i, v^i) and the difference between s_1^1 and s_2 are small enough) are satisfied.

4.4 Maximum Likelihood (ML) Time-domain Correlation-based Methods

As shown in Figure 4.2, procedures of typical ML time-domain correlation-based methods involve multiple steps. These are briefly presented in this section.

As shown in Figure 4.2, some echo signal decorrelation errors due to gross motion/deformation could be reduced by some optional steps for signal processing prior to the correlation calculations. For instance, companding [15], stretching [16], and applying window functions [13, 17] have been successfully applied. As illustrated in Figure 4.3a, in practice, the

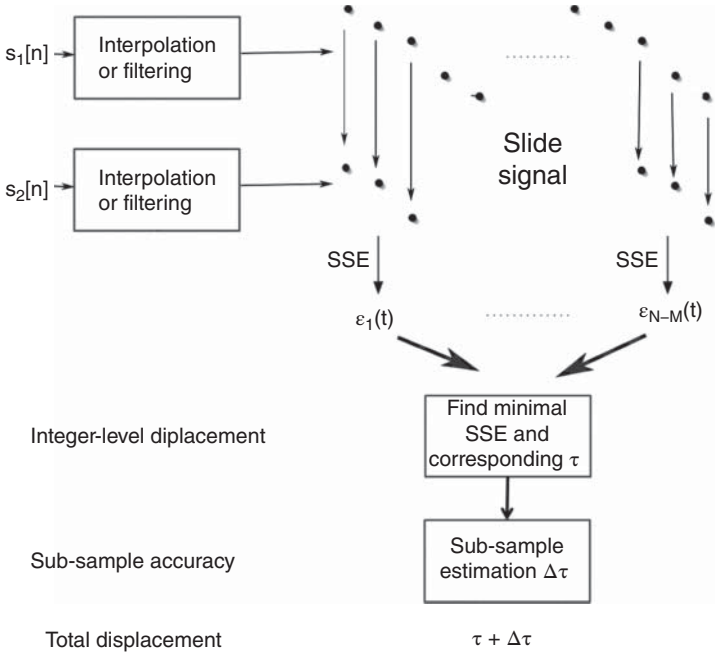

Figure 4.2 A graphic diagram illustrating procedures involving in ML correlation-based time-domain methods. Dots near the top of the plot represent discretely sample signals. $s_2[n]$ slides over the reference signal $s_1[m]$ to calculate SSE.

magnitude of the 1D cross-correlation function $R(\tau)$ (Eq. 4.12) can be evaluated by using the SSE, SAE, NCC, or un-normalized cross-correlation between two echo signals. Alternatively, the calculation of 1D cross-correlation can be implemented using FFT as follows

$$R(\tau) = F^{-1}\{F\{s_1(y+\tau)\}F\{s_2^*(y)\}\} \tag{4.18}$$

where the forward and inverse Fourier transforms are denoted by $F()$ and $F^{-1}()$, respectively. It is worth noting that, prior to the estimation of the cross-correlation, interpolation and/or filtering may be applied to reduce the noise (references) in the original echo signals. The former (SSE, SAE, NCC etc.) falls into the framework of block-matching algorithm (BMA), while the latter is often referred to as FFT-based correlation algorithm. In this section, discreetly sampled data $s_1(y)$ and $s_2(y)$ are written out as $s_1[n]$ and $s_2[n]$, respectively, to emphasize the fact that they are discretely sampled data.

Nevertheless, the magnitude of the cross-correlation function can only be estimated at the integer sample level (Figure 4.3b). To achieve sub-sample accuracy, a number of methods have been proposed in the literature. The basic idea behind those methods is to fit the (discretely estimated) magnitude of cross-correlation function into an underlying analytical function. Consequently, the location of the true correlation peak can be analytical solved. For example, as shown in Figure 4.3c, three points are first selected around the peak of the discretely sampled (magnitude) cross-correlation function (see three red circles in Figure 4.3c), those three points are fitted into a quadratic function (i.e. the solid curve in Figure 4.3c), $y = ax^2 + bx + c$, and then, the x location corresponding to the analytical correlation function can be obtained by solving $\frac{\partial y}{\partial x} = 0$, i.e. the location depicted by * in Figure 4.3c. Other analytical prototype functions such as cosine [18, 19], grid slope [20], and spline [21] functions, and reconstructive interpolation method [19] have also been considered. The reconstructive interpolation method is intended to find two points that have the same correlation value but locate at the two opposite sides of the

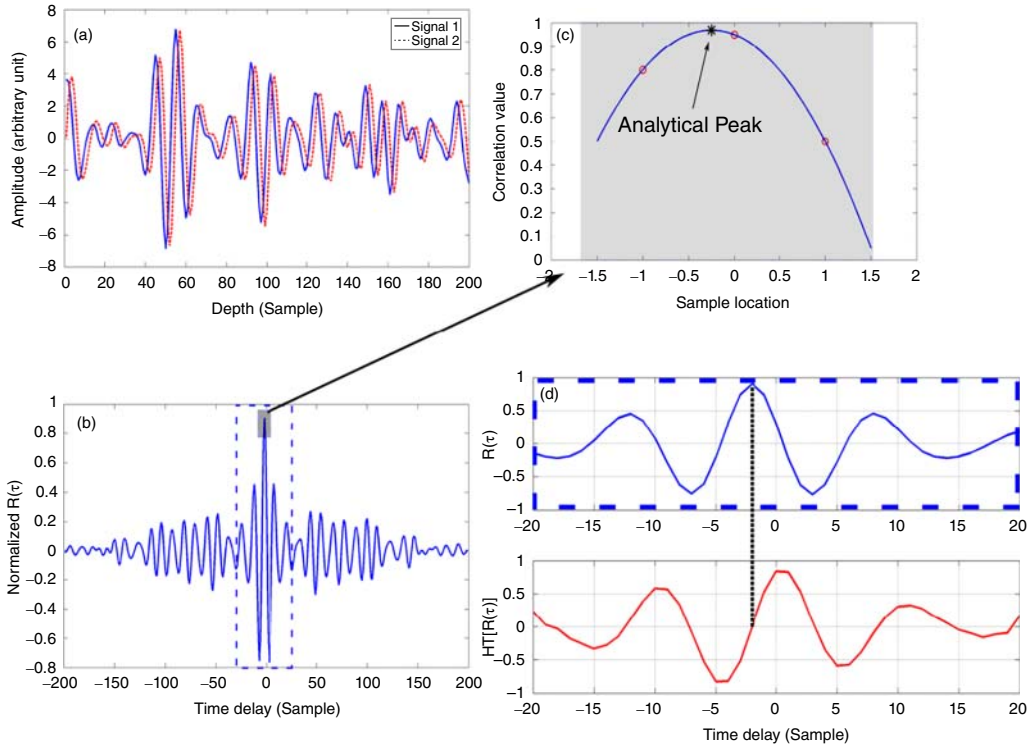

Figure 4.3 An illustration of the steps in ML time-domain correlation methods. Given two discretely sampled signals (a), a normalized correlation metric can be calculated [i.e. the solid line in (b)]. Three points (circles in (c)) equally spaced around the proximity of the (integer level) correlation peak are first selected and, then, fitted into a quadratic curve (illustrated using a solid line in (c)). Finally, the analytical correlation peak can be obtained (see the black star in (c)). In (d), it is shown that the Hilbert Transform (HT) of the magnitude correlation function (i.e. the solid curve in the bottom plot of (d)) can be used to estimate the correlation peak at the sub-sample level.

integer-level correlation peak. Therefore, the middle point of those two points is the estimated displacement [19], assuming the cross-correlation function is symmetric.

As suggested by Cabot [22], displacements at the sub-sample level can also be estimated by evaluating the Hilbert Transform (HT) of the (magnitude) cross–correlation function $R(\tau)$ (Figure 4.3d). In this case, the HT$\{R(\tau)\}$ will not have a maximum value when $\tau = \delta y$. Instead, HT$\{R(\tau)\}$ crosses zero at the time delay $\tau = \delta y$. It can be argued that it is easier to find a zero crossing than a correlation peak when the signal to noise (SNR) of the RF echo signals is not very high. Toward this end, a zero-crossing algorithm similar to that proposed by Pesavento et al. [10] can be used to estimate the sub-sample displacement estimate based on Figure 4.3d.

Most correlation-based methods handle discretely sampled RF echo directly. Viola and Walker [23] proposed an alternate solution by creating a continuous function using a spline interpolation so that a sub-sample estimation is no longer restrained by a pre-determined sample interval. More specifically, in their method, the signal $s_1[n]$ is first processed to determine an analytical representation $\hat{s}_1(y)$. Now, the motion-tracking problem is equivalent to finding a time delay τ that minimizes the difference between $\hat{s}_1(y)$ and the discretely sampled $s_2[y + \delta y]$, as follows

$$\varepsilon(\tau) = \sum_{i=1}^{N} (\hat{s}_1(ik + \tau) - s_2[i])^2 \tag{4.19}$$

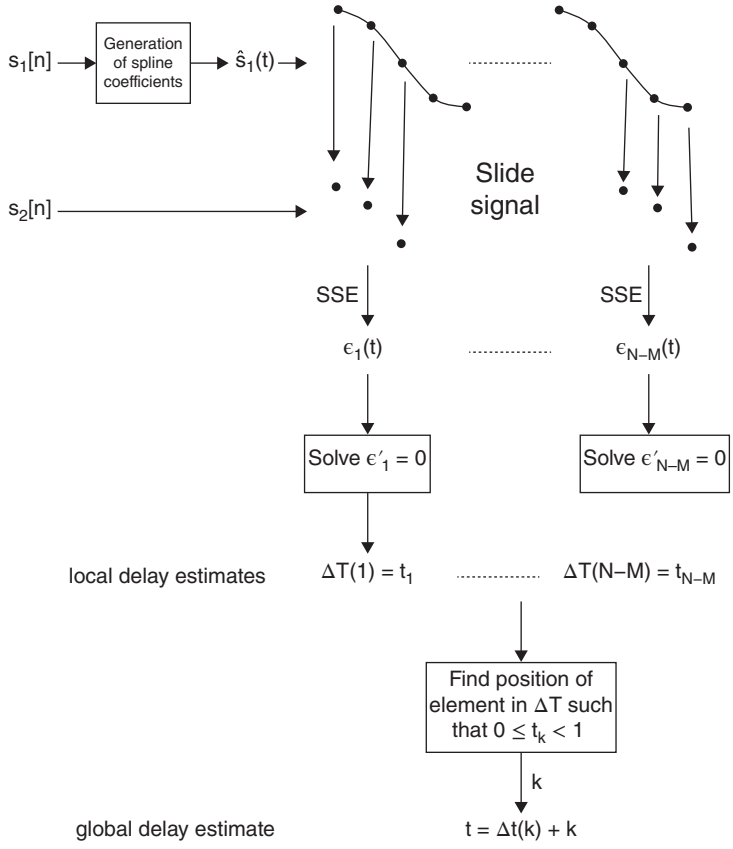

Figure 4.4 A graphic illustration of 1D spline-based motion-tracking algorithm by Viola and Walker [23]. The plot was modified from the original plot in [23]. The two sets of dot-connected lines near the top represent an analytical representation of $s_1[n]$. The dots just below those dot-connected lines denote a discretely sampled signal $s_2[n]$. $s_2[n]$ slides over the reference signal $s_1[m]$ to calculate analytical functions of SSE.

where k is the sample interval that will be used by the continuous analytical function $\hat{s}_1(y)$ to estimate the SSE. The solution to Eq. (4.19) can be obtained by setting $\frac{\partial \epsilon}{\partial \tau} = 0$. The graphic representation of this spline-based algorithm [23] is displayed above in Figure 4.4. In this algorithm, the length of reference signal $s_1(y)$ is longer than the target signal $s_2(y)$ and therefore, the target signal $s_2(y)$ can slide on the reference signal $s_1(y)$ to obtain a set of SSE values.

The need for tracking tissue motion in 2D motivates the development of 2D time-domain motion tracking. In an example using a tissue-mimicking phantom [24], shown in Figure 4.5, it is easy to see that 1D tracking fails to correctly track motion in a tissue-mimicking phantom undergoing axial deformation of 1.5% strain, whereas the 2D tracking performs very well with only occasional mistakes.

We still assume that a simple translation (u, v) exists between two RF signals $s_1(x, y)$ and $s_2(x, y)$. The subscripts 1 and 2 denote the pre- and post-deformation RF echo fields, respectively, and x and y represent the lateral and axial directions, respectively. The cross-correlation between those two signals is given by

$$R(\tau_x, \tau_y) = \int\int_{-\infty}^{\infty} s_1(x - \tau_x, y - \tau_y) s_2(x + u, y + v)\, \mathrm{d}x\mathrm{d}y \tag{4.20}$$

where τ_x and τ_y represent a uniform grid (i.e. dummy variables for time lags) from which a magnitude correlation map can be obtained.

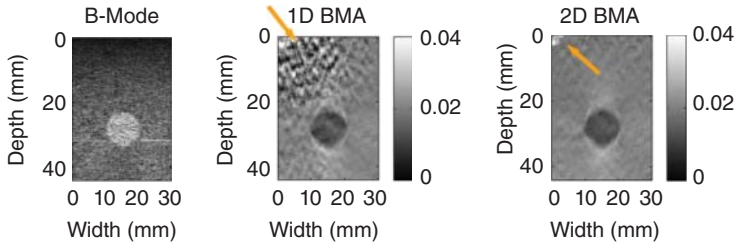

Figure 4.5 Images of B-mode and axial strain from a tissue-mimicking phantom with one spherical inclusion that is approximately two times stiffer than the background. 1D BMA and 2D BMA denote 1D and 2D motion tracking using a classic BMA, respectively. Then, two axial strain images were estimated from resultant axial displacements from 1D and 2D tracking, respectively. Arrows point to motion-tracking errors manifested on the corresponding strain images.

Using the linear system theory of medical ultrasound systems [25–27], it is easy to demonstrate that the log-compressed cross-correlation function (between $s_1$and $s_2$described above in Eq. 4.20) within the proximity of the integer-level correlation peak can be written as follows

$$\log(R[\tau_x, \tau_y]) \approx \frac{(\tau_x - u)^2}{C_1} + \frac{(\tau_y - v)^2}{C_2} \tag{4.21}$$

where C_1 and C_2 are related to the ultrasound system parameters. A log-compressed magnitude correlation map can be calculated by varying τ_x and τ_y. Equation (4.21) indicates that, in the vicinity of the (integer-level) correlation peak, the (log-compressed) correlation function can be approximated as a second-order polynomial surface.

Once a 2D correlation function is obtained and the integer-level time-delay is obtained based on Eq. (4.20), procedures of 2D sub-sample estimation using an analytical function are nearly identical to that described for 1D tracking. The quadratic surface function [28] $z = ax^2 + bxy + cy^2 + dx + fy + h$ and Gaussian function $z = a \times \exp\left\{-\left(\frac{(x-x_0)^2}{2\sigma_x^2} + \frac{(y-y_0)^2}{2\sigma_y^2}\right)\right\}$ are frequently used for estimating the sub-sample displacements. Equation (4.21) explains why the quadratic surface function and the Gaussian function are good choices for the sub-sample displacement estimation.

The 1D spline-based time-delay estimation method [23] has been extended into 2D [29] by Viola and Walker. Consequently, the 2D spline-based time-delay method may be used as a sub-sample tracking algorithm here. Such a combination takes advantage of the low bias and error variance offered by the spline-based algorithm, while maintaining computational efficacy.

A recent method [30] developed from our group took a different approach for the sub-sample displacement estimation. We set the right-hand side of Eq. (4.21) equal to a constant K. Consequently, as seen from Eq. (4.22) below, an iso-contour of the log-compressed correlation function $R[\tau_x, \tau_y]$ is an ellipse.

$$\frac{(\tau_x - u)^2}{C_1} + \frac{(\tau_y - v)^2}{C_2} = K \tag{4.22}$$

Locating the center of this ellipse (u, v) is equivalent to finding the theoretical peak of the correlation function $R[\tau_x, \tau_y]$. As shown in Figure 4.6, this sub-sample method first determines a contour at a correlation value K. Then, coordinates of the contour will be fitted to an ellipse function [31] to obtain the center of the ellipse.

If we now make the assumption that the recorded ultrasound echo signal $s(x, y)$ comprises a deterministic speckle signal $d(x, y)$ plus noise, the digitized echo signal can be modeled as

$$s(x, y) = d(x, y) + n(x, y) \tag{4.23}$$

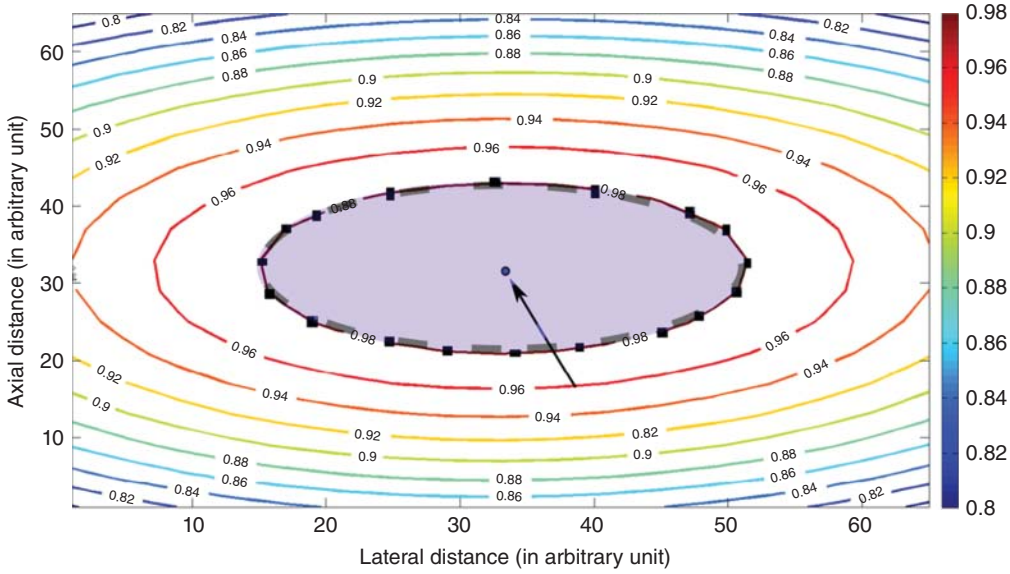

Figure 4.6 A graphic representation of the contour-based sub-sample estimation method by Jiang and Hall [30]. The color bar in the right side denotes the NCC. A fitted correlation contour at the NCC value of 0.98 is depicted by points labelled using rectangles. Coordinates of those points are fitted to an ellipse represented by the dashed curve. The small circle (see the arrow) represents the center of the fitted ellipse and its coordinates are the sub-sample displacements.

where n is a zero-mean noise term. If we calculate the SSE between the pre- and post-deformation signals $s_1(x, y)$ and $s_2(x, y)$, we get

$$\varepsilon(u, v) = \sum [(d_1(x, y) - d_2(x + u, y + v) + n_1(x, y) - n_2(x + u, y + v))]^2 \tag{4.24}$$

We assume that echo data have a constant mean and the noise is described by a statistically independent Gaussian variable with zero mean and constant variance.

As a result, the noise probability density function (PDF) can be written as

$$\Pr(n) = C \times \exp\left\{-\frac{1}{2\sigma^2_{\text{noise}}} \sum_{i=1}^{N} \sum_{j=1}^{M} [d_1(i, j) - d_2(i + u, j + v)]^2\right\} \tag{4.25}$$

where C is a constant. Equation (4.25) is commonly referred to as the ML function [32]. It is obvious that minimizing the SSE is equivalent to the maximization of the ML function (i.e. Eq. 4.25).

$$\widehat{\tau_{\text{MLE}}} = \text{argmax}_{\tau}[\log(P(x|\tau))] \tag{4.26}$$

Toward this end, it is worth noting that the previously discussed time-domain correlation-based speckle-tracking techniques are commonly regarded as unbiased estimators because they try to maximize the ML function (Eq. 4.25) and do not rely on any a priori knowledge of the experiment or tissue properties.

4.5 Tracking Tissue Motion through Combining Time-domain and Frequency-domain Information

Ebbini [33] has provided significant insight for developments along this direction. Now, let us consider the (magnitude) cross-correlation function in the vicinity of true correlation peak (see

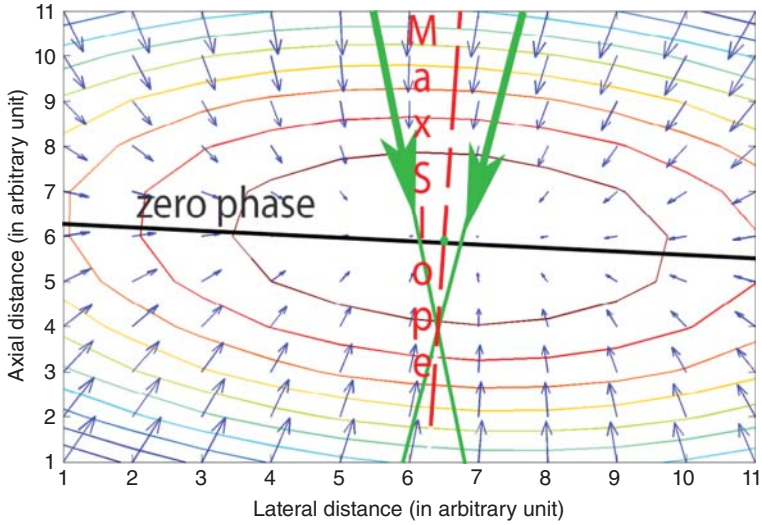

Figure 4.7 A graphic illustration of the phase-coupled tracking algorithm.

Figure 4.7). The zero-phase-contour behaves like a line within the proximity of the magnitude correlation peak (see the black solid line in Figure 4.7). The maximum slope of the (magnitude) correlation function (see the red dashed line) should be perpendicular to the zero-phase line.

Unfortunately, in the discretely sampled RF data, (numerical) estimation of maximum slope is not reliable. Therefore, Ebbini proposed an approximation. Assuming the (magnitude) correlation function retains symmetry around the magnitude correlation peak, we can find two closely spaced "maximum" gradients on the correlation map (see the green arrows in Figure 4.7) which have opposite directions. It is easy to imagine that the maximum slope line (see dashed line in Figure 4.7) passes through the intersection point between the two "maximum" gradients. Finally, the shortest distance from the zero-phase line to the intersection point between above-mentioned two "maximum" gradients can be used to find the actual correlation peak (see the circle in Figure 4.7).

Interested readers are referred to Ebbini's paper [33] for elegant mathematical derivations. In Ebbini's work, the zero-phase line is often estimated through one of the frequency-domain methods, while the maximum slope line can be solved using one of the time-domain correlation methods. Consequently, his method, to our knowledge, is the first and only work to couple time-domain correlation (magnitude) functions with the phase information together to solve the ultrasound motion-tracking problem.

4.6 Time-domain Maximum A Posterior (MAP) Speckle Tracking Methods

4.6.1 Tracking Large Tissue Motion

In Section 4.4, 2D ML time-domain correlation-based methods generally work well for small tissue motion. In this chapter, small tissue motion means tissue motion is smaller than a quarter of the wavelength of the ultrasound echo data. With the increase of tissue deformation/motion, the probability of identifying false correlation peaks will increase. False correlation peaks result in large tracking errors that are known as "peak hopping" errors [34] in the elastography literature. One example showing the generation of false correlation peaks is shown in Figure 4.8.

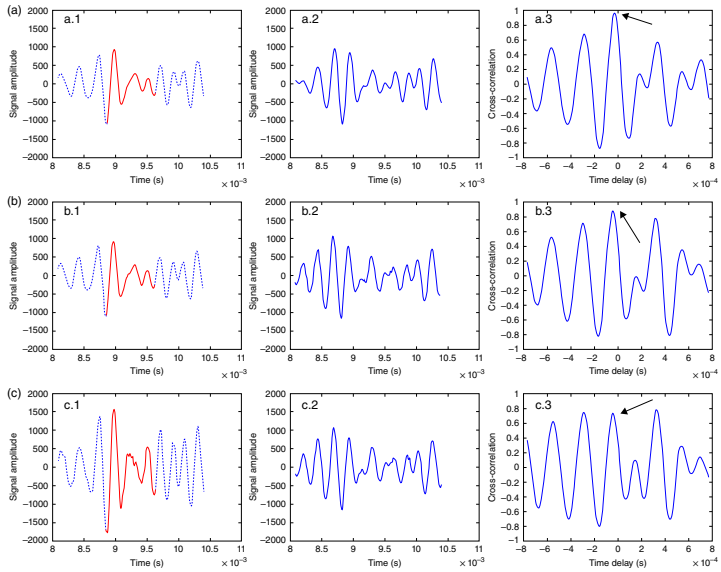

Figure 4.8 Simulated 5 MHz RF echo waveforms and their cross-correlation functions under various cases: (a) highly similar waveforms (first row; SNR = 80 dB, fractional bandwidth = 80%); (b) weakly similar waveforms (second row; SNR = 30 dB, fraction bandwidth = 40%); and (c) narrow band waveforms (third row; SNR = 10 dB; fraction bandwidth = 10%). In each row, the first plot (solid line) is the target signal, while the second plot is the reference signal (solid line). The third plot in each row is the resultant cross-correlation function and the arrow in the third plot points to the primary correlation peak.

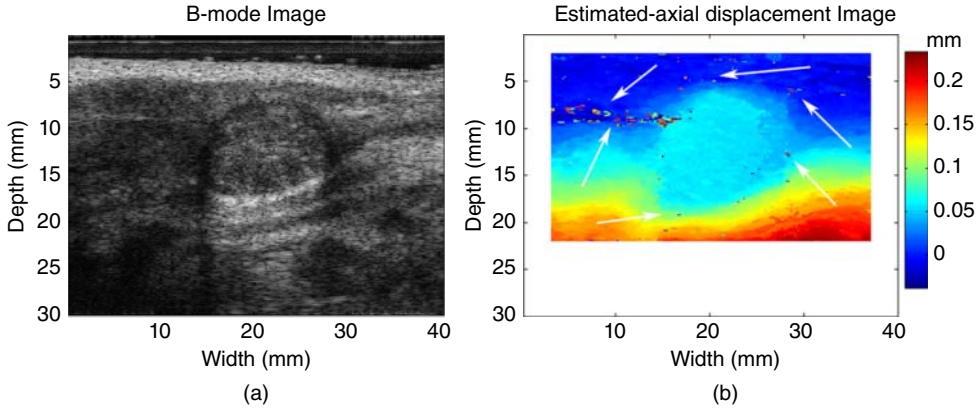

Figure 4.9 Displacement estimation results from an in vivo breast lesion under a nominal 1% of compression: (a) B-mode image and (b) estimated axial displacement in mm. Arrows in (b) point to the large tracking errors due to the presence of elevated secondary correlation peaks. A 2D BMA without any regularization was applied to obtain axial displacements displayed in (b).

Figure 4.8 shows NCC values with respect to different time lags for very similar signals (Figure 4.8a), weakly similar signals (Figure 4.8b), and narrow-band signals (Figure 4.8c). In each case, cross-correlation functions are similar. When the signal-to-noise ratio (SNR) is high and bandwidth is large (Figure 4.8a), the estimated correlation function has a well-defined peak with a correlation value close to 1. When the SNR is low, extrema decrease and are slightly widened. Secondary peaks also are elevated. When both the SNR and signal bandwidth are reduced, secondary peaks rise to a level that is even higher than the primary correlation peak (see Figure 4.8c). In a circumstance like this, a pure correlation-based method selects the secondary peak as the integer-level displacement estimate, thereby resulting in large "peak-hopping" errors during tissue motion tracking. In time-delay estimation, peak-hopping errors modeled by Barankin bounds [35, 36], arise from cycle jumps due to secondary peaks in the cross-correlation function. The theoretically predicted large tracking errors frequently occur in in vivo ultrasound data. An example is shown in Figure 4.9.

4.6.2 Strategies for Accurately Tracking Large Tissue Motion

Most contemporary motion-tracking techniques are based on two important ingredients, a coarse-to-fine search scheme (also known as multi-scale tracking) and injection of biases, to overcome large tracking errors.

The coarse-to-fine search scheme [37–40] starts initial estimates that are computed at a coarser resolution level. Then, those initial estimates representing large-scale structures are successively refined by taking into account the evidence of smaller structures. Tracking tissue motion within the framework of elastography, this coarse-to-fine search scheme could work well because the object being imaged moves as a continuum where the small structures move more or less the same way as larger scale structures. However, this approach may fail as soon as the relative motion of a small-scale object is distinct as compared to the dominant motion of the object being imaged.

Compared with single-level tracking, the multi-scale tracking is intrinsically more robust to decorrelation and error propagation. Particularly, if the envelope data (i.e. the B-mode image) are used, multi-scale tracking is relatively noise tolerant. The similarity metric based on the B-mode data depends on the data's macro-structure, which does not deteriorate so rapidly in the presence of noise and fine-scale RF signal decorrelation [39].

Injection of biases has also been used in order to reduce the large motion-tracking errors. Loosely speaking, we divided methods that fell into this category into the following three sub-categories: maximize the prior information, regularized tracking using smoothness constraint(s), and forming a formal Bayesian tracking scheme.

4.6.2.1 Maximize Prior Information

Basically, the central scheme of methods in this category is that an initial explorative search can first be applied at selected/pre-determined locations and then certain prediction strategies will be employed to advance the estimation process from one point to its neighbors. In fact, this scheme performs a "guided/predictive search" based on the availability of prior information. The first algorithm in this category was developed by Zhu and Hall [41] to achieve computational efficiency for real-time strain image formation while maintaining acceptable image quality. Zhu and Hall's original algorithm used a simple row-to-row prediction [41]. An initial large (e.g. 10 samples × 10 samples) explorative search is first performed for the first row. Those resultant displacements from the first row have to be corrected to eliminate unwanted spikes. Then, the displacement estimation for the second row will be limited to as few as one RF sample in each direction. Of note, the reduced search range will be dependent on the tolerable strain and, in Zhu and Hall's paper, the one-sample search range corresponds to approximately 8% of strain. This process proceeds until displacements in the last row are finished. Variants of this strategy include a column-by-column search [42] and a diagonal search [43].

A new predictive search strategy named "quality-guided" tracking by Chen and colleagues [7] quickly captured our attention. Chen and colleagues have introduced a remarkably simple but very effective predictive strategy. As shown in Figure 4.10, in the preparation step, a (large) initial brutal-force search (for integer level displacements) will be performed for approximately 5% of total number of estimation locations. Let's say the initial search is performed for $M \times N$ locations. For each location, the initial search yields an initial displacement vector and a corresponding motion-compensated NCC value. It is worth noting that the local motion-compensated NCC value was defined as quality by Chen et al. [7] and can be evaluated by Eq. (4.3).

This initial search will be followed by a recursive search until all estimation locations are completed. In the first recursive step, among all MN motion-compensated NCC values, the algorithm will select the maximum NCC value as the initial seed Pt_1 with the location coordinates of l_{x1} and l_{y1}. Other MN-1 displacement estimates, locations, and related motion-compensated NCC values will be stored in a candidate pool (CP). Sub-sample estimation will be used to obtain the full displacement vector for Pt_1. A predictive search will then be performed for four intermediate neighbors of the initial seed (i.e. $(l_{x1} - 1, l_{y1})$, $(l_{x1}, l_{y1} - 1)$, $(l_{x1} + 1, l_{y1})$ and $(l_{x1}, l_{y1} + 1)$) in a reduced search range (e.g. 3 samples × 3 samples) using the displacement estimates at Pt_1 as the guidance. For each neighbor, one motion-compensated NCC value will be obtained. All four displacement vectors, locations, and calculated motion-compensated NCC values will be stored in the CP while removing the current seed Pt_1 and its related parameters will be removed from the CP.

This recursive process will continue. Consequently, the CP contains the following at the k-th recursive step

$$\mathrm{CP}_k = \mathrm{CP}_{k-1} + \mathrm{Neighbor}(\mathrm{Pt}_{k-1}) - \mathrm{Pt}_{k-1} \tag{4.27}$$

$$\mathrm{Pt}_k = \arg\max \{Q(p) | p \in \mathrm{CP}_k\} \tag{4.28}$$

The search continues until CP is empty.

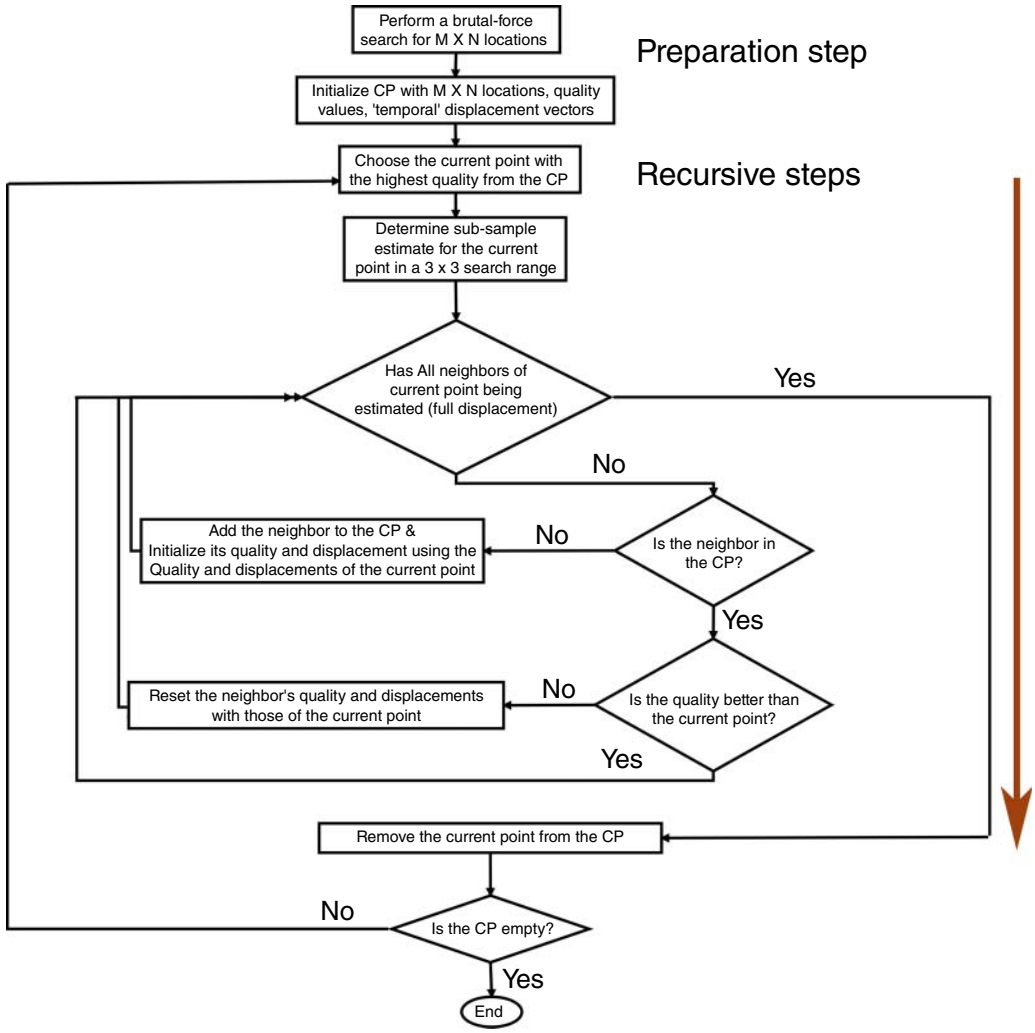

Figure 4.10 A flowchart describing the procedures of speckle tracking in the quality-guided algorithm proposed by Chen et al. [7].

Another advantage of this quality-guided tracking method [7] is its flexibility in tracking tissue motion among several disjoint regions, as long as at least one initial seed can be set up for each disjoint region. The other three predictive search strategies [41–43] mentioned above require global continuity.

However, there is one concern about this quality-guided tracking method. As pointed by Chen and colleagues [7], because there is no guarantee that tracking locations are processed in order of quality, it has been suggested a re-initialization approach is needed if there are localized errors remaining. In other words, the outcome of the quality-guided search (see Figure 4.10) may rely on the selection of those initial candidates in the CP (Figure 4.10). A follow-up paper [8] by our group proposed a hybrid approach where initial candidates were selected by passing tests with the combination of correlation and local continuity. Our preliminary testing results of this hybrid tracking approach [8] showed that it was more stable, as compared to the original quality-guided tracking, in 100+ frame pairs of in vivo breast lesion data investigated [7].

4.6.2.2 Regularized Motion Tracking Using Smoothness Constraint(s)

To use the motion regularization, speckle tracking can be modeled as an optimization problem using an energy function combining the correlation coefficient with speckle motion continuity. This is motivated by the fact that speckle motion corresponding to primary correlation peaks preserve local motion continuity, whereas secondary correlation peaks often lead to false displacement estimates (peak hopping errors) that do not maintain motion continuity. Regularized speckle tracking can effectively eliminate the majority of peak hopping errors [34] (see Figure 4.9).

Given a search region, the cost associated with each possible solution in the solution space can be calculated as follows

$$\text{cost} = \iint_{\Omega} [E_c + \alpha(E_s)]\mathrm{d}\Omega \tag{4.29}$$

where α is an adaptively chosen scale factor, E_c is a measure of speckle similarity/correlation, and E_s is a measure of motion smoothness that is minimized with high motion continuity. Usually, E_c is a form of correlation between two signals, e.g. Eq. (4.5a) or Eq. (4.5b), and, E_s is usually is a smoothness constraint and can be calculated using finite difference scheme from a small neighborhood Ω.

Variants of this methodology have proposed by several groups [40, 44–47]. Pellot-Barakat et al. [44] proposed to solve the generic cost function in Eq. (4.29) using an iterative conditional mode (ICM) algorithm [48], while our groups [40, 45–47] have adopted the dynamic programming approach to solve Eq. (4.29) so that the computational efficiency is sufficient for real-time image formation of strain elastography. Mathematically, all of those optimization algorithms were based on either the theory of random Markov field or Hidden Markov Chain (HMC) models.

4.6.2.3 Bayesian Speckle Tracking

McCormick, Rubert, and Varghese [49] first proposed to use the concept of Bayes theorem [50] to regularize speckle tracking. Their motion-tracking algorithm is a multiple step process for a ROI consisting of $M \times N$ displacement vector estimates, as shown in Figure 4.11.

Their idea was to construct an iterative process where displacement estimation at one location can be gradually improved by taking information from its neighbors.

In the first step, for each displacement estimation location, the correlation map will be calculated given a research region. For instance, for an arbitrary displacement estimation location (i, j), the search region is $-l$ to $+l$ in both directions. By searching through all $(2l + 1) \times (2l + 1)$ possible integer displacement vectors, we will obtain a $(2l + 1) \times (2l + 1)$ correlation matrix; each value in this correlation matrix represents a NCC value corresponding to one possible displacement vector. This correlation matrix can be converted to a PDF if the following two conditions are true for a function: 1) all values of the function are between 0 and 1, and 2) summation of all values of the function is a unity. This (discretely sampled) PDF function will be used as the prior PDF in the framework of Bayes theorem [50]. Of note, for each displacement estimation location, the current displacement estimate is the displacement vector corresponding to the maximum local correlation value in its correlation map.

In the second step, ML function given the current displacement estimate U_x will be calculated based on existing data which are the neighborhood displacements U_N, as follows[49]

$$\Pr(U_N U_x) = \prod_{x' \in N} \max_{V_{x'}} \left[\Pr(V_{x'}) \exp\left(\frac{\| V_{x'} - U_x \|^2}{2\sigma_u^2} \right) \right] \tag{4.30}$$

where x' is one neighbor in the entire neighborhood, $V_{x'}$ is the current displacement estimate for the neighbor, $\Pr(V_{x'})$ is the prior PDF for the current displacement estimate, and σ_u is a parameter used to normalized the above Gaussian-like function in Eq. (4.30) based on the local tissue deformation. It is easy to see, from Eq. (4.30), that displacement estimates resulting in an

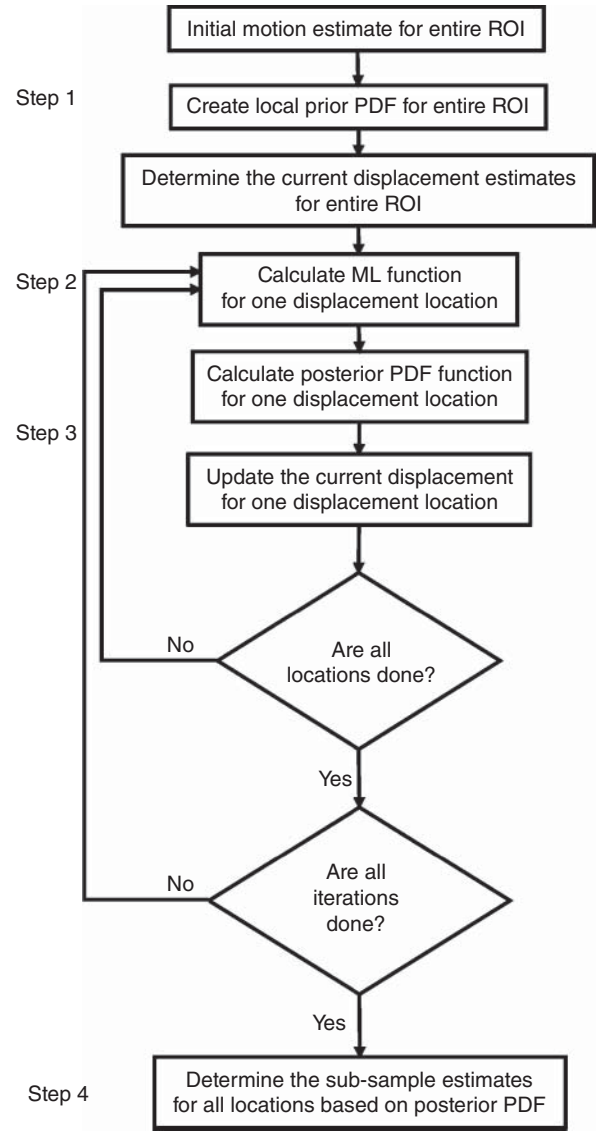

Figure 4.11 A flowchart illustrating procedures involving Bayesian regularization.

excessively large deformation will be penalized. Consequently, Eq. (4.30) is a form of smoothness constraints.

In the third step, once the ML function for each displacement estimation location is determined, the posterior PDF will be calculated based on Bayes theorem [50]

$$\Pr(U_x|U_N) = \frac{\Pr(U_N|U_x)\Pr(U_x)}{\Pr(U_N)} \tag{4.31}$$

Based on the updated posterior PDF $\Pr(U_x|U_N)$, the current displacement estimate for that location will be updated by selecting the displacement vector corresponding to the maximum $\Pr(U_x|U_N)$. There are two iteration loops between the second and third steps, as shown in Figure 4.11. The inner loop is to make sure all locations within the ROI will be covered. Therefore, the local displacement estimation can be recursively improved by updating the displacement estimates following an order. The outer loop is to ensure there is no starting point dependence.

In the fourth step, the sub-sample estimation will be done based on the final local posterior PDF function (see Eq. 4.31) of each location.

Recently, Byram, Trahey, and Palmeri [51, 52] have developed a more general Bayesian framework for speckle tracking following the similar approach by McCormick, Rubert, and Varghese [49]. One of their major contributions was to investigate the construction of the ML function. Their suggested ML function is the following

$$\Pr(U_N|U_x) \propto \exp\left[\frac{\mathrm{SNR}}{\alpha}\rho\right] \tag{4.32}$$

where α is a scaling factor that can be empirically chosen and ρ is the NCC (see Eq. 4.3). It is worth noting that the terminology used by McComick et al. [49] was different than that used in work [51, 52] by Byram et al. The work by Byram et al. demonstrated that the ML function should be appropriately scaled in order to make the ML function have an improved discriminant ability (i.e. a narrower ML function with a sharp peak). In other words, after scaling, the probability corresponding to the true displacement is higher, as compared to the unscaled ML probability density function.

4.6.3 Discussions

There is one thing in common among three strategies described in Section 4.6.2 – they attempt to combine signal correlation assessments with local smoothness as the prior information to improve the displacement estimation. By making use of prior information about the conditions of the measurement, we can eliminate possible outcomes that are non-physical.

Now our discussion will be steered toward Bayes' theorem [50]

$$\Pr(\tau|d) = \frac{\Pr(d|\tau)\Pr(\tau)}{\Pr(d)} \tag{4.33}$$

where d is the data and τ is a possible displacement vector from the solution space. The term $\Pr(d|\tau)$ denotes the ML function, $\Pr(\tau)$ is the prior PDF, and $\Pr(\tau|d)$ is the posterior PDF. In the ultrasound-based motion-tracking literature, researchers often use the correlation function as the ML function and tissue motion continuity as the prior information. If no prior information is injected into the motion-tracking process, i.e. $\Pr(\tau) = \text{constant}$, the posterior PDF is equivalent to the likelihood function. That is why a pure correlation-based motion-tracking method is a ML estimator.

Now referring to those predictive search methods, they rely entirely on prior information. Consequently, if a tracking error inherited from a previous step was not corrected immediately, prior information would no longer be valid, and the error would likely propagate and cause a cascade effect. That is why research efforts have been devoted to more intelligent predictions (e.g. row-by-row [41], column-by-column [42], and diagonal search [43]). It is easy to see that Chen's quality-guided approach [53] can use the prior information more reliably because the quality-guided scheme ensures that the highest quality initial displacement vector gains priority in guiding subsequent speckle tracking. Consequently, errors occurred in early steps should likely be isolated and the algorithm is able to process a region with one or more (geometrical) tissue interfaces, given sufficient ultrasound data quality.

Those approaches using smoothness constraint(s) and Bayesian tracking approaches are mathematically equivalent. This is because a MAP motion-tracking method can be formally written as a method that maximizes the logarithm of the posterior PDF, as follows [32]

$$\begin{aligned}\widehat{\tau_{\mathrm{MAP}}} &= \mathrm{argmax}_\tau[\log(\Pr(\tau|x))] = \mathrm{argmax}_\tau[\log(\Pr(x|\tau)) + \log(\Pr(\tau)) - \log(\Pr(x))] \\ &= \mathrm{argmax}_\tau[\log(\Pr(x|\tau)) + \log(\Pr(\tau))]\end{aligned} \tag{4.34}$$

We have dropped the $\log(\Pr(d))$ term in Eq. (4.34) because there is no direct dependence between the time delay τ and the existing data d in Eq. (4.33). It is straightforward to argue that the generic cost function for smoothness regularized tracking (Eq. 4.29) is mathematically equivalent to maximizing a posterior PDF that combines both the cross-correlation and the smoothness/continuity.

4.7 Optical Flow-based Tissue Motion Tracking

We still assume that a displacement (u, v) exists between two radiofrequency (RF) signals $s_1(x, y)$ and $s_2(x, y)$. The following condition holds under the assumption that the intensity of ultrasound echo data remains constant [54]

$$s_1(x + u, y + v) = s_2(x, y) \tag{4.35}$$

Expanding the left-hand side of Eq. (4.35) in a Taylor series yields

$$\frac{\partial s_1(x,y)}{\partial x}u + \frac{\partial s_1(x,y)}{\partial y}v + s_1(x,y) - s_2(x,y) + \text{H.O.T.} = 0 \tag{4.36a}$$

$$\frac{\partial s_1(x,y)}{\partial x}u + \frac{\partial s_1(x,y)}{\partial y}v + s_1(x,y) - s_2(x,y) \approx 0 \tag{4.36b}$$

where H.O.T. denotes high-order terms truncation by the Taylor expansion above. If the displacement vector (u, v) is sufficiently small (e.g. at the sub-sample level), those high-order terms can be removed without losing the accuracy of Eq. (4.36b). Equation (4.36b) is known as the optical flow constraint equation in Computer Vision. However, Eq. (4.36b) has two unknowns and therefore is not solvable without additional equations. Those methods can be largely divided into two categories: region-based and smoothness constraint-based. In ultrasound elastography literature, there are only few optical flow-based methods [55–57]. Since Eq. 4.36b) is derived based on the Taylor expansion, the optical flow-based methods in the ultrasound elastography are often used for a sub-sample tracking.

4.7.1 Region-based Optical Flow Methods

The displacement vector (u, v) in Eq. (4.36b) can be estimated from the ultrasound echo intensities in the neighborhood Ω consisting of N locations $[\{x_1, y_1\}, \{x_2, y_2\}, \{x_3, y_3\}, \cdots, \{x_N, y_N\}]$ using a least-squares formulation as follows

$$A\begin{Bmatrix} u \\ v \end{Bmatrix} = b \tag{4.37a}$$

$$A = \begin{bmatrix} \dfrac{\partial s_1(x_1,y_1)}{\partial x} & \dfrac{\partial s_1(x_1,y_1)}{\partial y} \\ \dfrac{\partial s_1(x_2,y_2)}{\partial x} & \dfrac{\partial s_1(x_2,y_2)}{\partial y} \\ \cdots & \cdots \\ \dfrac{\partial s_1(x_N,y_N)}{\partial x} & \dfrac{\partial s_1(x_N,y_N)}{\partial y} \end{bmatrix} \tag{4.37b}$$

$$b = \begin{Bmatrix} s_1(x_1,y_1) - s_2(x_1,y_1) \\ s_1(x_2,y_2) - s_2(x_2,y_2) \\ \cdots \\ s_1(x_N,y_N) - s_2(x_N,y_N) \end{Bmatrix} \tag{4.37c}$$

So far, we have explicitly assumed that there is a rigid-body motion within the neighborhood Ω, which is typically a rectangular region in 2D.

Eqns. (4.37a)–(4.37c) can be solved in the least squared sense. Therefore, the rigid-body motion represented by two translations u and v can be written as follows

$$\begin{Bmatrix} u \\ v \end{Bmatrix} = M^{-1}B \tag{4.38a}$$

$$M = \begin{bmatrix} \sum_{i=1}^{N}\left(\frac{\partial s_1(x_i,y_i)}{\partial x}\right)^2 & \sum_{i=1}^{N}\left(\frac{\partial s_1(x_i,y_i)}{\partial x}\right)\left(\frac{\partial s_1(x_i,y_i)}{\partial y}\right) \\ \sum_{i=1}^{N}\left(\frac{\partial s_1(x_i,y_i)}{\partial x}\right)\left(\frac{\partial s_1(x_i,y_i)}{\partial y}\right) & \sum_{i=1}^{N}\left(\frac{\partial s_1(x_i,y_i)}{\partial y}\right)^2 \end{bmatrix} \tag{4.38b}$$

$$B = \begin{Bmatrix} \sum_{i=1}^{N}\left(\frac{\partial s_1(x_i,y_i)}{\partial x}\right)(s_1(x_i,y_i)-s_2(x_i,y_i)) \\ \sum_{i=1}^{N}\left(\frac{\partial s_1(x_i,y_i)}{\partial y}\right)(s_1(x_i,y_i)-s_2(x_i,y_i)) \end{Bmatrix} \tag{4.38c}$$

If the tissue motion within the 2D rectangular neighborhood Ω follows an affine transformation model, the lateral and axial displacements u and v are no longer two constants. They can be expressed by translations, elongations, and shearing as follows

$$\begin{Bmatrix} u(x,y) \\ v(x,y) \end{Bmatrix} = \begin{Bmatrix} T_1 \\ T_2 \end{Bmatrix} + \begin{bmatrix} \frac{\partial u}{\partial x} & \frac{\partial u}{\partial y} \\ \frac{\partial v}{\partial x} & \frac{\partial v}{\partial y} \end{bmatrix} \begin{Bmatrix} x \\ y \end{Bmatrix} \tag{4.39}$$

where T_1 and T_2 are lateral and axial translations, respectively, $\frac{\partial u}{\partial x}$ is the lateral strain, $\frac{\partial v}{\partial y}$ is the axial strain, $\frac{\partial u}{\partial y}$ is the lateral shear, and $\frac{\partial v}{\partial x}$ is the axial shear.

Substituting Eq. (4.39) into Eq. (4.36b), we obtain

$$\frac{\partial s_1(x,y)}{\partial x}\left(\frac{\partial u}{\partial x}x + \frac{\partial u}{\partial y}y + T_1\right) + \frac{\partial s_1(x,y)}{\partial y}\left(\frac{\partial v}{\partial x}x + \frac{\partial v}{\partial y}y + T_2\right) + s_1(x,y) - s_2(x,y) \approx 0 \tag{4.40}$$

Similarly, Eq. (4.40) can also be solved in a least-squares fashion for Ω consisting of N locations $[\{x_1, y_1\}, \{x_2, y_2\}, \{x_3, y_3\}, \cdots, \{x_N, y_N\}]$. The linear system can be written as follows

$$A\begin{bmatrix} T_1 & T_2 & \frac{\partial u}{\partial x} & \frac{\partial u}{\partial y} & \frac{\partial v}{\partial x} & \frac{\partial v}{\partial y} \end{bmatrix}^T = b \tag{4.41a}$$

$$A = \left[\begin{array}{c|c|c|c|c|c} \frac{\partial s_1(x_1,y_1)}{\partial x} & \frac{\partial s_1(x_1,y_1)}{\partial y} & \frac{\partial s_1(x_1,y_1)}{\partial x}x_1 & \frac{\partial s_1(x_1,y_1)}{\partial x}y_1 & \frac{\partial s_1(x_1,y_1)}{\partial y}x_1 & \frac{\partial s_1(x_1,y_1)}{\partial y}y_1 \\ \frac{\partial s_1(x_2,y_2)}{\partial x} & \frac{\partial s_1(x_2,y_2)}{\partial y} & \frac{\partial s_1(x_2,y_2)}{\partial x}x_2 & \frac{\partial s_1(x_2,y_2)}{\partial x}y_2 & \frac{\partial s_1(x_2,y_2)}{\partial y}x_2 & \frac{\partial s_1(x_2,y_2)}{\partial y}y_2 \\ \cdots & \cdots & \cdots & \cdots & \cdots & \cdots \\ \frac{\partial s_1(x_N,y_N)}{\partial x} & \frac{\partial s_1(x_N,y_N)}{\partial y} & \frac{\partial s_1(x_N,y_N)}{\partial x}x_N & \frac{\partial s_1(x_N,y_N)}{\partial x}y_N & \frac{\partial s_1(x_N,y_N)}{\partial y}x_N & \frac{\partial s_1(x_N,y_N)}{\partial y}y_N \end{array}\right] \tag{4.41b}$$

$$b = \begin{Bmatrix} s_1(x_1, y_1) - s_2(x_1, y_1) \\ s_1(x_2, y_2) - s_2(x_2, y_2) \\ \cdots \\ s_1(x_N, y_N) - s_2(x_N, y_N) \end{Bmatrix} \tag{4.41c}$$

The linear system in Eq. (4.41b) can be solved by typical linear equation solvers. Therefore, all affine parameters (see Eqns. 4.41a–4.41c) are the following

$$\begin{bmatrix} T_1 & T_2 & \frac{\partial u}{\partial x} & \frac{\partial u}{\partial y} & \frac{\partial v}{\partial x} & \frac{\partial v}{\partial y} \end{bmatrix}^T = (A^T A)^{-1} A^T b \tag{4.42}$$

Eq. (4.42) indicates that displacements can be obtained along with normal, lateral shear, and axial strains all together [56, 57].

4.7.2 Optical Flow Methods with Smoothness Constraints

While region-based methods are commonly used, optical flow estimation can also be done by assuming certain forms of motion smoothness through nonparametric motion models, rather than an explicit parametric model (e.g. rigid-body or an affine transformation. One such energy functional $E(u, v)$ was proposed by Horn and Schunck [58]

$$E(u, v) = \int \left(\frac{\partial s_1(x, y)}{\partial x} u + \frac{\partial s_1(x, y)}{\partial y} v + s_1(x, y) - s_2(x, y) \right)^2 + \lambda(\|\nabla u\|^2 + \|\nabla v\|^2) \mathrm{d}\Omega \tag{4.43}$$

where ∇ is a gradient operator, $\|\blacksquare\|$ is a L_2 norm, and λ is a positive regularization parameter that balances the fidelity of the echo data (i.e. the first term at the right-hand side of Eq. 4.43) and the contribution needed from the smoothness constraint (i.e. the second term at the right-hand side of Eq. 4.43). Typically, Eq. (4.43) can be solved by Euler–Lagrange equations using the calculus of variation. However, this approach is fairly computationally expensive. To our best knowledge, little research work in ultrasound elastography has been performed to fully incorporate the smoothness constraint to solve the above-mentioned optical flow problem (i.e. Eq. 4.43).

4.8 Deformable Mesh-based Motion-tracking Methods

Similar to techniques developed for finite element-based image registration, deformable mesh-based motion-tracking methods are intended to ensure admissible solutions that satisfy with the theory of elasticity [6]. In this section, heuristic explanations are provided below. Interested readers are referred to the original publications [59, 60] for details.

As illustrated in Figure 4.12a, in deformable mesh-based methods, ultrasound data (either RF echo data or B-mode images) can first be divided into a computer mesh (e.g. consisting of triangles, rectangles, or other polygons). Those meshed elements are interconnected and therefore can ensure the continuity of motion. Recall that, in the theory of FEM [5], the displacement at any point within the domain of interest can be interpolated from corresponding nodal displacements and therefore, at least, the first-order displacement continuity (C^0) can be guaranteed.

Once the computer mesh is generated, the motion-tracking problem can be reformulated as an optimization problem to minimize the following energy function

$$E = E_{\text{mis-match}} + \lambda E_{\text{elasticity}} \tag{4.44}$$

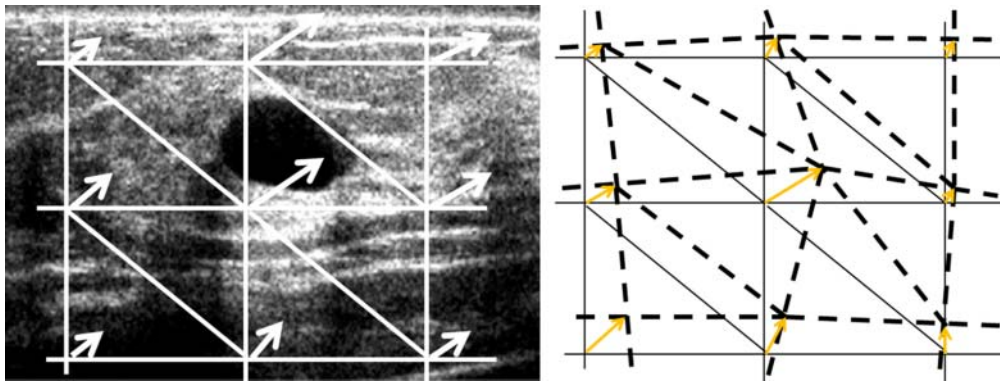

Figure 4.12 An generic illustration of deformable mesh-based motion-tracking algorithm: (a) generation of a finite element mesh with the calculated image nodal forces and (b) the resultant deformed finite element induced by image nodal forces. In (a), arrows represent the calculated nodal forces, while, in (b) arrow represents the calculated nodal displacements.

where λ is a constant balancing the relative contributions between the first and second energy terms in Eq. (4.44). The first energy function relates to a similarity measure representing the mis-match between the pre-deformation signal s_1 and the post-deformation signal s_2. The second term is related to tissue elasticity constraints.

In the work by Zhu et al. [60], the second term in Eq. (4.44) was a smoothness constraint. A "pseudo-steepest descending method" was used to minimize Eq. (4.44). Their method exhaustively searches the entire solution space at the integer-level until an optimal solution of Eq. (4.44) is reached, thereby resulting in a global optimal solution. Unfortunately, this brute-force method may not be computationally efficient.

In the work by Yeung et al. [59], the second term in Eq. (4.44) was the Lamé-Navier's equation. In the framework of FEM, Yeung et al. demonstrated that minimization of Eq. (4.44) is equivalent to solve the following linear system to enforce admissible tissue motion to satisfy the Lamé-Navier's equation [6].

$$(K + I)U = F \tag{4.45a}$$

$$F = \hat{U} \tag{4.45b}$$

where K is the "scaled" system stiffness matrix that is assembled to solve the Lame-Navier's equation in FEM, I is an identity matrix, F is the nodal image force vector, $\hat{U}$ is the displacement vector obtained by a conventional correlation-based motion-tracking algorithm, and U is the unknown displacement. Equation (4.45a) can be solved by a linear equation solver, given certain (displacement) boundary conditions. Using Eq. (4.45a) suggests that the system stiffness matrix K acts like a physics-based "filter" to regularize the initially estimated displacement vector $\hat{U}$. However, the drawback is also apparent because the final estimated displacement vector U will be largely dependent on the selection of the stiffness distribution of the object being imaged. Unfortunately, knowing the stiffness distribution (particularly before the motion tracking) is not feasible in practice, thereby limiting the use of this method in heterogeneous tissues.

A method has been developed by two groups [61, 62] to improve the original approach by Yeung et al. In the new method, the energy function was revised as follows

$$\begin{aligned}&\min_{u,\mu} F(u,\mu)\, F(u,\mu)\\ &= \int_\Omega E_{\text{mis-match}}(u)\mathrm{d}\Omega + \lambda_1 \int_\Omega E_{\text{elasticity}}(u,\mu)\mathrm{d}\Omega + \lambda_2 \int_\Omega E_{\text{incompressible}}(u)\mathrm{d}\Omega\end{aligned} \tag{4.46a}$$

$$E_{\text{mis-match}} = (s_1(x) - s_2(x+u))^2 \tag{4.46b}$$

$$E_{\text{elasticity}} = \int_{\Omega} [-\nabla p + \nabla \cdot (\mu \nabla u + \mu (\nabla u)^T)]^2 \mathrm{d}\Omega \tag{4.46c}$$

$$E_{\text{imcompressibility}} = \int_{\Omega} [\nabla \cdot u]^2 \mathrm{d}\Omega \tag{4.46d}$$

where u is the displacement field, μ is the shear modulus distribution, and p is the pressure. In Eqns. (4.46a)–(4.46b), the soft tissue being imaged was assumed to be linearly elastic and incompressible as a first approximation [9]. Based on Eq. (4.46a)–(4.46d), a FEM formulation can be derived so that both displacement and shear modulus distributions can be simultaneously solved. Consequently, no assumptions regarding the underlying tissue elasticity information are needed in order to estimate tissue motion that is admissible to elasticity equations (i.e. Eqns. 4.46c and 4.46d).

4.9 Future Outlook

It is anticipated that no individual motion-tracking technique will dominate future development of this field, and that motion-tracking techniques will evolve according to their suitability for particular applications. However, we do want to attest that motion-tracking accuracy closely ties to the tracking algorithm used. In order to improve the design of motion-tracking algorithms, there are at least two criteria to consider. The first one, of course, is the sensitivity, i.e. the ability to estimate very small tissue motion. The second criterion is the robustness. This is the ability of a motion-tracking algorithm to cope with other than ideal data. Robustness also means the ability to reliably estimate both large and small tissue motion. In elastography applications, motion-tracking techniques for shear wave elastography [63] likely focus on sub-sample level tracking; whereas, the nonlinear modulus inversion application [64, 65] may have to first solve the problem of tracking tissue deformation without gross errors over a range of deformation. To satisfy the above-mentioned two criteria, our experience is that a good tracking algorithm has to reduce both large "peak-hopping" errors and small jitter errors.

To demonstrate how the reductions of both large "peak-hopping" and small jitter errors can collectively improve the motion-tracking accuracy, we show an in vivo invasive ductal carcinoma (IDC) acquired under free-hand scanning. The IDC was compressed by approximately 1%. Details of the scanning protocol and equipment can be found in the previous work by Hall et al. [66]. Figures 4.13b–4.13g show the axial and lateral displacement estimates by three different algorithms: (1) a classic BMA [i.e. no predictive search and no regularization], (2) a regularized BMA [40] using smoothness constraints and, (3) the coupled sub-sample estimation method [30] was applied to obtained high quality displacement data after the regularized BMA [40] was used to obtain integer displacement estimates. It is easy to see, from Figures 4.13b and 4.13c [see arrows], that the classic block matching algorithm makes large "peak-hopping" errors, while the regularized BMA is able to avoid them. The general appearance of the axial and lateral displacement images (Figures 4.13f and 4.13g) by the new sub-sample estimation method [30] is smoother as compared to results from the regularized BMA (Figures 4.13d and 4.13e). It is interesting to note that the lateral displacement image in Figure 4.13g seems more consistent with the tissue landmarks visible in the B-mode image (Figure 4.13a), i.e. the gross appearance of the lesion and tissue interfaces around it.

4.9.1 Tracking Lateral Tissue Motion

In previous sections, lateral tissue motion was tracked mostly for the purpose of obtaining the "correct" integer-level correlation peaks so that we can better track the axial component of the

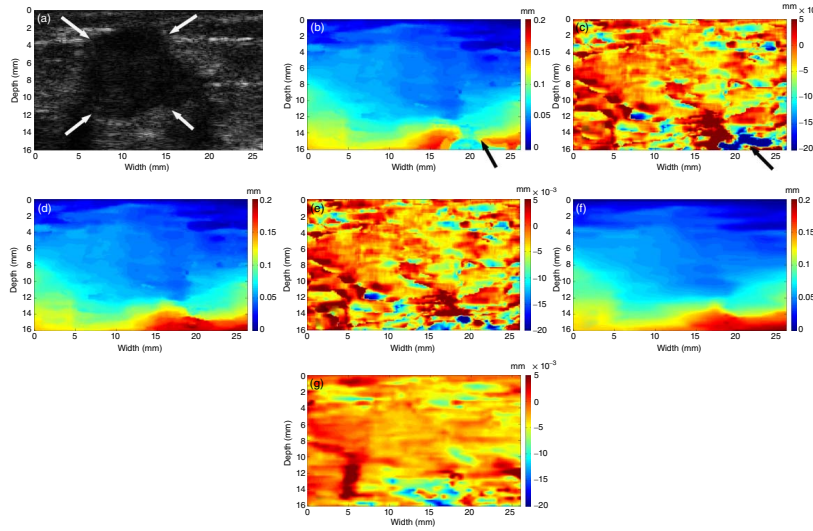

Figure 4.13 (a) B-mode of an in vivo invasive ductal carcinoma (IDC); (b) and (c) axial and lateral displacement images tracked using a classic block-matching algorithm, respectively; (d) and (e) axial and lateral displacement images tracked using a regularized BMA [40], respectively; and (f) and (g) axial and lateral displacement images where the new sub-sample estimation algorithm has been applied, respectively. The arrows on (a) point to the IDC and, arrows on (b) and (c) point to the location where the classical BMA makes large "peak-hopping errors".

tissue motion. Currently, the quality of lateral displacements is still poorer than that of those axial displacement estimates (e.g. see Figure 4.13). There are a couple of reasons for that. First, lack of a lateral phase component in ultrasound echo signals places a fundamental limit on the accuracy of lateral displacement estimates. Second, the speckle cell size is typically too coarsely sampled in the lateral direction, requiring interpolation by large factors. Now, interpolation itself may become a source of error.

In order to improve lateral tracking accuracy, methods in the literature can be divided into two categories. Methods in the first category require significant modifications of the ultrasound imaging hardware (e.g. special beamforming or rapid beam steering). A method independently proposed by Jensen [67] and Anderson [68] attempted to introduce non-axial oscillations/modulations in their respective imaging point spread functions. Techavipoo et al. used "angular compounding" to improve lateral displacements [69].

Methods in the second category are improved (software) tracking algorithms where imaging/mathematical processing techniques were used to enhance lateral displacement estimation. One common scene was to improve the ability to location the true correlation peak. The work by Ebbini [70] and by Jiang and Hall [30], described earlier, falls into this scene. Tissue incompressibility (also known as divergence-free) has been also used to explicitly tie relevant axial and lateral displacements together. Since soft tissues can in general be considered to be incompressible [9], then no volumetric change occurs during the deformation. Further, assuming that the out-of-plane deformation is zero or minimal from frame to frame data (i.e. the plane strain approximation), we can write the following equation for a 2D tracking problem

$$\frac{\partial u}{\partial x} + \frac{\partial v}{\partial y} = 0 \tag{4.47}$$

where u and v are axial and lateral components of the displacement vector.

Konofagou and Ophir [71] proposed a sub-sample estimation approach where axial and lateral displacements can be iteratively improved by re-correlating ultrasound echo signals through instantaneous motion compensations. The incompressibility (Eq. 4.47) was incorporated into their motion compensation scheme.

Another common strategy is to rely on rigorous mathematical optimization. The work by Brusseau et al. [72] formulated motion tracking between two echo frames as an optimization process to find local 2D affine transformations. Therefore, both axial and lateral translations can be jointly solved using constrained nonlinear programming. Viola and Walker [29] proposed multi-dimensional tracking using spline functions. Their solution was based on a gradient-based optimization technique. Rivaz et al. have also applied physical constraints to simultaneously regularize axial and lateral speckle tracking using multiple (time) frames of RF echo data to improve displacement estimations [73] through optimization. Their method also yielded good results.

Although progress has been made, the quality lateral displacement estimates is still relatively poor as compared to its axial counterpart (e.g. see the comparison between Figure 4.13c and Figure 4.13g). Since many ultrasound applications such as temperature mapping [74], modulus inversion [75, 76], and shear strain estimation [71] may need or prefer to have accurate lateral displacements, it is expected that more continued research efforts will be devoted to this important topic.

4.9.2 Tracking Large Tissue Motion

In order to deal with large tissue motion, the consensus is probably that algorithms that are purely based on signal correlation (i.e. the likelihood function) are not sufficient. Therefore, prior information (e.g. smoothness) has to be injected to estimate the posterior PDF. The purpose of construction of the posterior PDF is to balance the information obtained from the

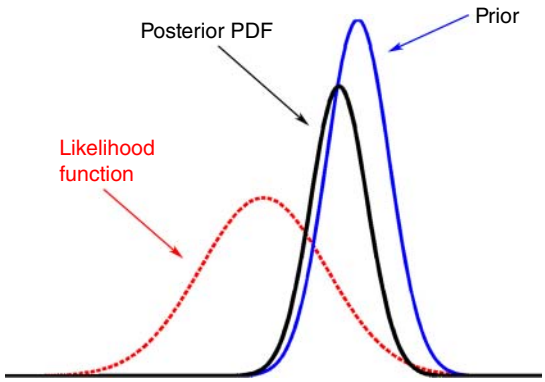

Figure 4.14 A graphical illustration of construction of the posterior PDF.

likelihood function and prior information function, as shown in Figure 4.14. Consequently, it is straightforward to argue that, in the general framework of Bayesian speckle tracking, the estimate could be biased toward non-physical solutions if either the prior function or the likelihood function was not appropriately selected.

In the literature, evidence showed that the design of the posterior PDF could be a major factor. For instance, in the original work by McCormick et al. [49], they found that their posterior PDF was only effective for relative large deformations. Once Byram et al. [51, 52] scaled the ML PDF in their work, their results showed that the sensitivity of the posterior PDF was actually enhanced, thereby improving the motion tracking for fairly small displacements (e.g. shear wave elastography).

Furthermore, Byram et al. [51, 52] discussed their desire of having a prior PDF function that can change its shape. Early work from our group [40] has also explored how to adjust the relative contributions to the generic cost function (i.e. Eq. 4.29) between the signal correlation and the smoothness constraint by using different forms of the smoothness function to apply various levels of the motion continuity constraint. Methodologically, our thoughts are consistent with the idea of Byram et al. [51, 52]. It is possible that a new direction for motion tracking may be "organ-specific" or "application-specific" motion-tracking design. For instance, for motion tracking around breast lesions, motion continuity is expected and therefore should be enforced. However, in situations where irregular motion can be expected, such as when large vessels are present, when there is an inter-organ boundary (e.g. liver, kidney, and prostate), or when there is an intra-organ cavity (e.g. uterine cavity and common carotid artery), only minimal constraints are needed. That can be done through adjusting the shapes of the likelihood function and the prior PDF.

It is worth noting that in several MAP motion-tracking algorithms the addition of smoothness constraints was merely to obtain correct displacement estimates at the integer level. The sub-sample estimation of displacement was still based on the (magnitude) correlation values. More recently, several algorithms have started to use values directly from either the cost function or the posterior PDF to estimate the sub-sample displacements. The work shown by Rivaz et al. [77] has demonstrated that the estimated tissue deformation was influenced by the choice of the smoothness constraints. If the posterior PDF function will be used to obtain the sub-sample estimates, the concern is whether or not those ad hoc posterior PDFs will yield physically correct solution.

Despite the importance of designing appropriate posterior PDF, there is probably no consensus on how to design such a function. Hopefully, more research work will shed light on this topic very soon.

4.9.3 Testing of Motion-tracking Algorithms

Assuming we can design better motion-tracking algorithms, the overarching question now is: "How can we evaluate the outcome of motion tracking so that it will meet the clinical elastography needs?" Regarding algorithm testing, there are generally two aspects: evaluation metrics and benchmark data for performance assessment, as expanded below.

4.9.3.1 Evaluation of Performance

In early work [78–85], attention was focused on estimating lower bounds on error variance for (time-delay and) displacement estimation, That work collectively demonstrated that errors in axial displacement estimates are predictable, once the processing and ultrasound system parameters (i.e. bandwidth, center frequency, tracking window length Z, and window separation distance ΔZ) are known. These theoretical efforts collectively led to better designs for motion-tracking algorithms in general but are inadequate for comparing a group of specific motion-tracking algorithms for two important reasons. First, the derivation of the minimum error variance bounds assumes that all residual motion-tracking errors are sub-sample jitter. This is a good assumption for applications such as radiation-force experiments [86, 87] where deformations are small compared to the acoustic wavelength. But tissue deformations in other applications include maximum displacements of several wavelengths and potentially involve "peak-hopping" errors. Second, the methods used to derive these error bounds assume 1D correlation techniques, but many tracking methods are not purely correlation-based.

Recall that the goal of speckle tracking between two radio frequency (RF) echo fields s_1 and s_2 is to obtain a transformation T that maximizes the similarity between s_1 and $T(s_2)$. Therefore, we can register the two RF echo fields by first applying the displacement estimates (i.e. transformation T) to the deformed echo data and then remapping to the coordinates of the pre-deformation echo data field. $T(s_2)$ is the motion-compensated post-deformation echo field. A higher NCC value between two registered regions (i.e. s_1 and $T(s_2)$) implies that two regions with apparent deformations are better registered. Hence, it may be surmised that displacement estimates between the two RF fields are more accurate. An example of this approach is the trashogram [88] that displays the local motion-compensated NCC values between the pre- and post-deformation RF echo fields as a grayscale image. Another example is the displacement quality metric method (DQM; [89]) developed by our group, though DQM was specifically for strain elastography. One metric of the DQM is the NCC value between the entire pre-deformation and motion-compensated post-deformation RF echo fields. The difference is that a global NCC value was used in the DQM method while the trashogram method used a map of local NCC values.

A comprehensive framework is based on signal coherence between the pre- and motion-compensated post-deformation RF echo signals [90–92]. By comparing the cross-power spectrum between the pre- and motion-compensated post-deformation RF echo signals, Insana and Cook [90] and Cook et al. [91] derived the Fourier cross-talk matrix to assess ultrasonic strain imaging systems. Basically, motion tracking can be evaluated in terms of spatial sampling characteristics. The Fourier cross-talk matrix, to some extent, can be regarded as a graphical representation of signal coherence. The diagonal elements of the cross-talk matrix represent the generalized transfer function, describing the strength of every Fourier coefficient representing the signals. The off-diagonal components of the cross-talk matrix represent the degree of aliasing between any two Fourier coefficients. If the pre- and motion-compensated post-deformation RF fields are aligned perfectly, no off-diagonal elements will be observed. When motion-tracking errors result in signal misalignment, off-diagonal elements in the cross-talk matrix increase. This graphical representation of signal coherence makes this method appealing. Furthermore, the trace of the cross-talk matrix was

offered as a summary performance measure. It would be interesting to see how this method can be used for comparing motion-tracking algorithms, particularly, in conjunction with clinical data.

In short, research efforts are still under way to research a consensus on performance assessment of motion-tracking methods, though several candidates are available for immediate use.

4.9.3.2 Testing Data

Like many new diagnostic imaging systems, phantom development [24, 93, 94], in particular the development of anthropomorphic phantoms [94], has aided in testing prototype elastography systems and potentially uncovering weaknesses in these systems. However, we found that many motion-tracking algorithms perform well and show great promise in phantom experiments (with regular geometry and simple boundary conditions) but fail to live up to expectations in in vivo clinical trials because the underlying motion in phantom experiments is too simple and uniform whereas that found in in vivo tissue motion during clinical trials has significantly heterogeneous mechanical properties and complex boundary conditions.

Toward this end, it is important to create a common repository of clinical ultrasound data for benchmarking tests. Using the same data, it would pave the way of discovering what is the best motion-tracking performance being achieved – whether by a particular motion-tracking algorithm, by a particular ultrasound scanning protocol, or by a combination of multiple tracking strategies. Even with the availability of clinical benchmark data, rigorous assessment of motion-tracking performance is still an open question as described earlier in the previous section. What we need is complex but known tissue motion that is similar to what occurs in vivo.

A virtual strain elastography simulation platform [95] has been recently developed in our group by leveraging existing open source software packages including Field II (ultrasound simulator [26]), VTK (geometrical visualization and processing [96]), FEBio (FEM [97]), and Tetgen (mesh generator [98]). This virtual simulation platform can generate complex ultrasound fields containing complex tissue deformation. One example with simulated breast ductal structures is shown in Figure 4.15.

This software platform may allow comparisons and validations of motion-tracking algorithms with a known but (arbitrarily) complex phantom, and show the correlation between an elastographic image and its underlying soft tissue properties. This software platform is currently expanded into simulation of shear wave elastography. It is our vision that rigorous imaging tests can be transparently done using simulated complex heterogeneous but known media, as a supplement to clinical data. Collectively, this kind of information can then be used to identify gaps so that clinical needs of motion-tracking development can be met at an accelerated rate.

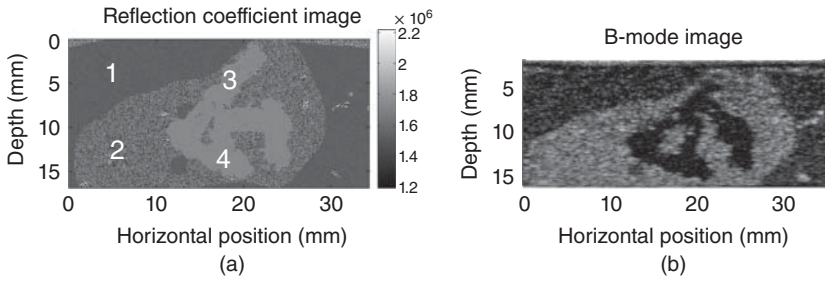

Figure 4.15 A simulated milk-duct structure embedded into the fibro-glandular region: (a) acoustic reflection coefficient image and (b) a simulated B-mode image by Field II. In (a), 1 to 4 denote breast fat, fibro-glandular tissue, milk ducts, and lobe, respectively. Source: reprinted with permission from [95].

4.9.4 Future with Volumetric Ultrasound Data

Most motion-tracking algorithms discussed above were designed and tested only with 2D ultrasound echo data. Furthermore, testing was mainly done with ultrasound data acquired from linear array ultrasound transducers. Now volumetric ultrasound data acquisition became available from clinical or prototype clinical systems. For instance, sweeping a 1D array in the elevational direction thorough mechanical steering provides data points in a curvilinear grid with non-uniform spacing is available in clinical scanners [99–101]. The advent of capacitive micro-machined ultrasound transducers (CMUTs) may also become an opportunity to manufacture 2D array systems with relatively low cost [102, 103]. Work available in the literature [104–106] has demonstrated that full 3D tracking can provide higher quality of displacement data derived from 3D ultrasound echo data, as compared to displacement data obtained from tracking 2D ultrasound data. Consequently, it is logical to anticipate that the availability of these volumetric data and subsequent full 3D motion tracking using the state-of-art techniques will very likely further augment the ability to track complex in vivo tissue motion, though it remains to be seen.

4.10 Conclusions

This chapter represents the current state of the field of ultrasound-based 2D tracking methods for assessing tissue motion. Motion tracking is defined as the determination of a geometrical transformation that aligns points in one 2D view of an object being imaged by ultrasound with corresponding points in another 2D view of that object under ultrasound. Therefore, unique challenges exist to improve motion tracking in 2D while the tissue moves in all three dimensions. Methods of motion tracking exist beyond correlation-based methods. However, the emphasis in this chapter is on correlation-based methods because, as of the time of writing, most of the work and most of the progressing registration has been made in this area.

Ultrasound-based motion tracking is important because it is a core component of many ultrasound elastography applications. Thanks to research listed in the bibliography of this chapter, much is now known about this area, and many effective algorithms have been developed, some of the best of which are described above. Of course, there is a good possibility of unintended omission of other good work because it is nearly impossible to include two decades of excellent work in this short book chapter.

Acknowledgments

Some work described in this book chapter was supported by research grants from National Institutes of Health (R01CA140271 and R15-CA179409). The authors are grateful for the financial support. We also want to thank Mr. Kevin Sunderland and Mr. Yu Wang from Michigan Technological University for proofreading. The first author wants to thank Prof. Timothy Hall from University of Wisconsin-Madison for stimulating discussions related to ultrasound speckle tracking.

Acronyms

ARFI	acoustic radiation force impulse
BMA	block-matching algorithm

CMUT	capacitive micro-machined ultrasound transducer
CP	candidate pool
FEM	finite element method
FFT	fast Fourier transform
HMC	hidden Markov chain
HT	Hilbert transform
IDC	invasive ductal carcinoma
MAP	maximum a posterior
ML	maximum likelihood
NCC	normalized correlation coefficient
PDE	partial differential equation
PDF	probability density function
RF	radio frequency
ROI	region of interest
SAE	sum-absolute error
SNR	signal to noise ratio
SSE	sum-squared error
1D	one-dimensional
2D	two-dimensional

Additional Nomenclature of Definitions and Acronyms

τ	a dummy variable for time lag
δ	actual time delay
$\rho(\tau)$	normalized cross-correlation coefficient
$R(\tau)$	cross-correlation function
θ_{ij}	stress tensor
C_{ijkl}	constitutive constants
e_{kl}	strain tensor
E	Young's modulus
ν	Poisson's ratio
μ, λ	Lamé constants
K	global/system stiffness matrix
I	identity matrix
U	displacement vector
$\widehat{U}$	estimated displacement vector
F	external force vector
$s(y)$	1D radio-frequency signals
$\varphi(\tau)$	phase function
Γ	cross-spectrum function
ω	angular frequency
ω_0	transducer's centroid frequency
$s(x, y)$	2D radio-frequency signals
$S(k_x, k_y)$	forward Fourier transforms of 2D RF signals
k_x, k_y	spatial frequency variables
$F()$	forward Fourier transforms
$F^{-1}()$	inverse Fourier transforms
$\varepsilon(\tau)$	SSE for 1D
$\varepsilon(u, v)$	SSE for 2D

$R(\tau_x, \tau_y)$	2D cross-correlation function
Pr( )	probability density function
Ω	neighborhood for an 2D integration
E_c	a measure of speckle similarity/correlation
E_s	a measure of motion smoothness
∇	gradient operator
$\|\blacksquare\|$	L_2 norm
$T()$	a geometrical transformation

References

1 Dickinson, R.J. and Hill, C.R. (1982). Measurement of soft tissue motion using correlation between A-scans. *Ultrasound Med. Biol.* 8: 263–271.

2 Wilson, L.S. and Robinson, D.E. (1982) Ultrasonic measurement of small displacements and deformations of tissue. *Ultrason. Imaging* 4: 71–82.

3 Morrison, D.C., McDicken, W.N., and Smith, D.S. (1983). A motion artefact in real-time ultrasound scanners. *Ultrasound Med. Biol.* 9, 201–203.

4 Ophir, J., Cespedes, I., Ponnekanti, H., et al. (1991) Elastography: a quantitative method for imaging the elasticity of biological tissues. *Ultrason. Imaging* 13: 111–134.

5 Cook, R.D. (1981). *Concepts and Applications of Finite Element Analysis*, 2nd edn. New York: Wiley.

6 Timoshenko, S. and Goodier, J.N. (1969). *Theory of Elasticity*, 3rd edn. New York: McGraw-Hill.

7 Chen, L., Treece, G.M., Lindop, J.E., et al. (2009). A quality-guided displacement tracking algorithm for ultrasonic elasticity imaging. *Med. Image Anal.* 13: 286–296.

8 Jiang, J. and Hall, T.J. (2011). A fast hybrid algorithm combining regularized motion tracking and predictive search for reducing the occurrence of large displacement errors. *IEEE Trans. Ultrason., Ferroelect., Freq. Control* 58: 730–736.

9 Fung, Y.C. (1993) *Biomechanics: Mechanical Properties of Living Tissues*, 2nd edn. New York: Springer-Verlag.

10 Pesavento, A., Perrey, C., Krueger, M., and Ermert, H. (1999). A time-efficient and accurate strain estimation concept for ultrasonic elastography using iterative phase zero estimation. *IEEE Trans. Ultrason., Ferroelect., Freq. Control* 46: 1057–1067.

11 Ryaben'kii, V.S. and Tsynkov, S.V. (2006). *A Theoretical Introduction to Numerical Analysis*. Boca Raton: CRC Press.

12 Chaturvedi, P., Insana, M.F., and Hall, T.J. (1998). Testing the limitations of 2-D companding for strain imaging using phantoms. *IEEE Trans. Ultrason., Ferroelect., Freq. Control* 45: 1022–1031.

13 Lubinski, M.A., Emelianov, S.Y., and O'Donnell, M. (1999). Speckle tracking methods for ultrasonic elasticity imaging using short-time correlation. *IEEE Trans. Ultrason., Ferroelect., Freq. Control* 46: 82–96.

14 Sumi, C. (1999). Fine elasticity imaging utilizing the iterative RF-echo phase matching method. *IEEE Trans. Ultrason., Ferroelect., Freq. Control* 46: 158–166.

15 Chaturvedi, P., Insana, M.F., and Hall, T.J. (1998). 2-D companding for noise reduction in strain imaging. *IEEE Trans. Ultrason., Ferroelect., Freq. Control* 45: 179–191.

16 Varghese, T., Ophir, J., and Cespedes, I. (1996). Noise reduction in elastograms using temporal stretching with multicompression averaging. *Ultrasound Med. Biol.* 22: 1043–1052.

17 Huang, L., Petrank, Y., Huang, S.W., et al. (2009). Phase rotation methods in filtering correlation coefficients for ultrasound speckle tracking. *IEEE Trans. Ultrason., Ferroelect., Freq. Control* 56: 1368–1382.

18 DeJong, P.G.M., Arts, T., Hoeks, A.P.G., and Reneman, R.S. (1991). Experimental evaluation of the correlation interpolation technique to measure regional tissue velocity. *Ultrason. Imaging* 13: 145–161.

19 Cespedes, I., Huang, Y., Ophir, J., and Spratt, S. (1995). Methods for estimation of subsample time delays of digitized echo signals. *Ultrason. Imaging* 17: 142–171.

20 Friemel, B.H., Bohs, L.N., Nightingale, K.R., and Trahey, G.E. (1998) Speckle decorrelation due to two-dimensional flow gradients. *IEEE Trans. Ultrason., Ferroelect., Freq. Control* 45: 317–127.

21 Geiman, B., Bohs, L., Anderson, M., et al. (1997). A comparison of algorithms for tracking sub-pixel speckle motion. *Proc. Ultrason. Symp. IEEE* 2: 1239–1242.

22 Cabot, R.C. (1981). A note on the application of the Hilbert transform to time delay estimation. *IEEE Trans. Acoust., Speech, Signal Process*. 29: 607–609.

23 Viola, F. and Walker, W.F. (2005). A spline-based algorithm for continuous time-delay estimation using sampled data. *IEEE Trans. Ultrason., Ferroelect., Freq. Control* 52: 80–93.

24 Pavan, T.Z., Madsen, E.L., Frank, G.R., et al. (2010). Nonlinear elastic behavior of phantom materials for elastography. *Phys.Med. Biol*. 55: 2679.

25 Meunier, J. and Bertrand, M. (1995). Ultrasonic texture motion analysis: theory and simulation. *IEEE Trans. Med. Imaging* 14: 293–300.

26 Jensen, J.A. (1991). A model for the propagation and scattering of ultrasound in tissue. *J. Acoust. Soc. Am.* 89: 182–190.

27 Li, Y. and Zagzebski, J.A. (1999). Frequency domain model for generating B-mode images with array transducers. *IEEE Trans. Ultrason., Ferroelect., Freq. Control* 46: 690–699.

28 Zahiri Azar, R., Goksel, O., and Salcudean, S.E. (2010). Sub-sample displacement estimation from digitized ultrasound RF signals using multi-dimensional polynomial fitting of the cross-correlation function. *IEEE Trans. Ultrason., Ferroelect., Freq. Control* 57: 2403–2420.

29 Viola, F., Coe, R.L., Owen, K., et al. (2008). Multi-dimensional spline-based estimator (MUSE) for motion estimation: algorithm development and initial results. *Ann. Biomed. Eng.* 36: 1942–1960.

30 Jiang, J. and Hall, T.J. (2015). A coupled subsample displacement estimation method for ultrasound-based strain elastography. *Phys. Med. Biol.* 60: 8347–8364.

31 Fitzgibbon, A.W., Pilu, M., and Fisher, R. B. (1996). Direct least squares fitting of ellipses. *Presented at the* Proceedings of the 1996 International Conference on Pattern Recognition (ICPR '96) vol. 1, 7270.

32 Kay, S. M. (1993). *Fundamentals of Statistical Signal Processing*. Englewood Cliffs, NJ: Prentice-Hall.

33 Ebbini, E.S. (2006). Phase-coupled two-dimensional speckle tracking algorithm. *IEEE Trans. Ultrason., Ferroelect., Freq. Control* 53: 972–990.

34 Walker, W.F. and Trahey, G.E. (1995). Fundamental limit on delay estimation using partially correlated speckle signals. *IEEE Trans. Ultrason., Ferroelect., Freq. Control* 42: 301–308.

35 Weiss, A.J. and Weinstein, E. (1983). Fundamental limitations in passive time delay estimation – part 1: narrow-band systems. *IEEE Trans. Acoust., Speech, Signal Process* 31: 472–486.

36 Weinstein, E. and Weiss, A.J. (1984). Fundamental limitations in passive time delay estimation – part 2: wide-band systems. *IEEE Trans. Acoust., Speech, Signal Process* 32: 1064–1078.

37 Yeung, F., Levinson, S.F., and Parker, K.J. (1998). Multilevel and motion model-based ultrasonic speckle tracking algorithms. *Ultrasound Med. Biol.* 24: 427–441.

38 Li, P.C. and Lee, W.N. (2002). An efficient speckle tracking algorithm for ultrasonic imaging. *Ultrason. Imaging* 24: 215–228.

39 Shi, H. and Varghese, T. (2007). Two-dimensional multi-level strain estimation for discontinuous tissue. *Phys. Med. Biol.* 52: 389–401.

40 Jiang, J. and Hall, T. (2009). A generalized speckle tracking algorithm for ultrasonic strain imaging using dynamic programming. *Ultrasound Med. Biol.* 35: 1863–1879.

41 Zhu, Y. and Hall, T.J. (2002). A modified block matching method for real-time freehand strain imaging. *Ultrason Imaging* 24: 161–176.

42 Jiang, J. and Hall, T.J. (2007). A parallelizable real-time motion tracking algorithm with applications to ultrasonic strain imaging. *Phys. Med. Biol.* 52: 3773–3790.

43 Zahiri-Azar, R. and Salcudean, S. E. (2006). Motion estimation in ultrasound images using time domain cross correlation with prior estimates. *IEEE Trans. Biomed. Eng.* 53: 1990–2000.

44 Pellot-Barakat, C., Frouin, F., Insana, M.F., and Herment, A. (2004). Ultrasound elastography based on multiscale estimations of regularized displacement fields. *IEEE Trans. Med. Imaging* 23: 153–163.

45 Jiang, J. and Hall, T.J. (2006). A regularized real-time motion tracking algorithm using dynamic programming for ultrasonic strain imaging, in *IEEE Ultrason. Symp*. Vancouver, Canada.

46 Rivaz, H., Boctor, E., Foroughi, P., et al., (2008). Ultrasound elastography: a dynamic programming approach. *IEEE Trans. Med. Imaging* 27: 1373–1377.

47 Petrank, Y., Huang, L., and O'Donnell, M. (2009). Reduced peak-hopping artifacts in ultrasonic strain estimation using the Viterbi algorithm. *IEEE Trans. Ultrason., Ferroelect., Freq. Control* 56; 1359–1367.

48 Besag, J. (1986). On the statistical analysis of dirty pictures. *J. Roy. Stat. Soc. Ser. B* 48: 259–302.

49 McCormick, M., Rubert, N., and Varghese, T. (2011). Bayesian regularization applied to ultrasound strain imaging. *IEEE Trans. Biomed. Eng.* 58: 1612–1620.

50 Lee, P.M. (1992). *Bayesian Statistics: An Introduction*. London, New York: E. Arnold, Halstead Press.

51 Byram, B., Trahey, G.E., and Palmeri, M. (2013). Bayesian speckle tracking. Part I: an implementable perturbation to the likelihood function for ultrasound displacement estimation. *IEEE Trans. Ultrason., Ferroelect., Freq. Control* 60: 132–143.

52 Byram, B., Trahey, G.E., and Palmeri, M. (2013). Bayesian speckle tracking. Part II: biased ultrasound displacement estimation. *IEEE Trans. Ultrason., Ferroelect., Freq. Control* 60: 144–157.

53 Chen, L., Treece, G.M., Lindop, J.E., et al. (2009). A quality-guided displacement tracking algorithm for ultrasonic elasticity imaging. *Med. Image Anal.* 13: 286–296.

54 Barron, J.L., Fleet, D.J., and Beauchemin, S.S. (1994). Performance of optical flow techniques. *Int. J. Comput. Vision* 12: 43–77.

55 Yongjin, Z. and Yong-Ping, Z. (2010) A motion estimation refinement framework for real-time tissue axial strain estimation with freehand ultrasound. *IEEE Trans. Ultrason., Ferroelect., Freq. Control* 57: 1943–1951.

56 Zakaria, T., Qin, Z., and Maurice, R.L. (2010). Optical-flow-based B-mode elastography: application in the hypertensive rat carotid. *IEEE Trans. Med. Imaging* 29: 570–578.

57 Pan, X., Gao, J., Tao, S., et al. (2014). A two-step optical flow method for strain estimation in elastography: Simulation and phantom study. *Ultrasonics* 54: 990–996.

58 Horn, B.K.P. and Schunck, B.G. (1981). Determining optical flow. *Artif. Intell.* 17: 185–203.

59 Yeung, F., Levinson, S.F., Fu, D., and Parker, K.J. (1998). Feature-adaptive motion tracking of ultrasound image sequences using a deformable mesh. *IEEE Trans. Med. Imaging* 17: 945–956.

60 Zhu, Y., Chaturvedi, P., and Insana, M.F. (1999). Strain imaging with a deformable mesh. *Ultrason. Imaging* 21: 127–146.

61 Gokhale, N., Richards, M., Oberai, A., et al. (2004). Simultaneous elastic image registration and elastic modulus reconstruction. In: *Biomedical Imaging: Nano to Macro, 2004. IEEE Int. Symp*. 543–546.

62 Kybic, J. and Smutek, D. (2005). Computational elastography from standard ultrasound image sequences by global trust region optimization. *Inf. Process Med. Imaging* 19: 299–310.

63 Palmeri, M.L. and Nightingale, K.R. (2011). Acoustic radiation force-based elasticity imaging methods. *Interface Focus* 1: 553–564.

64 Oberai, A., Gokhale, N.H., Goenezen, S., et al. (2009). Linear and nonlinear elasticity imaging of soft tissue in vivo: demonstration of feasibility. *Phys. Med. Biol.* 54: 1191–1207.

65 Goenezen, S., Dord, J.F., Sink, Z., et al. (2012). Linear and nonlinear elastic modulus imaging: an application to breast cancer diagnosis. *IEEE Trans. Med. Imaging* 31: 1628–1637.

66 Hall, T.J., Zhu, Y., and Spalding, C. S.(2003). In vivo real-time freehand palpation imaging. *Ultrasound Med. Biol.* 29: 427–435.

67 Jensen, J.A. and Munk, P. (1998). A new method for estimation of velocity vectors. *IEEE Trans. Ultrason., Ferroelect., Freq. Control* 45: 837–851.

68 Anderson, M.E. (1998). Multi-dimensional velocity estimation with ultrasound using spatial quadrature. *IEEE Trans. Ultrason., Ferroelect., Freq. Control* 45: 852–861.

69 Techavipoo, U., Chen, Q., Varghese, T., and Zagzebski, J.A. (2004). Estimation of displacement vectors and strain tensors in elastography using angular insonifications. *IEEE Trans. Med. Imaging* 23: 1479–1489.

70 Ebbini, E.S. (2006). Phase-coupled two-dimensional speckle tracking algorithm. *IEEE Trans. Ultrason., Ferroelect., Freq. Control* 53: 972–990.

71 Konofagou, E. and Ophir, J. (1998). A new elastographic method for estimation and imaging of lateral displacements, lateral strains, corrected axial strains and Poisson's ratios in tissues. *Ultrasound Med. Biol.* 24: 1183–1199.

72 Brusseau, E., Kybic, J., Deprez, J.F., and Basset, O. (2008). 2-D locally regularized tissue strain estimation from radio-frequency ultrasound images: theoretical developments and results on experimental data. *IEEE Trans. Med. Imaging* 27: 145–160.

73 Rivaz, H., Boctor, E.M., Choti, M.A., and Hager, G.D. (2014). Ultrasound elastography using multiple images. *Med. Image Anal.* 18: 314–329.

74 Liu, D. and Ebbini, E.S. (2010). Real-time 2-D temperature imaging using ultrasound. *IEEE Trans. Biomed. Eng.* 57: 12–16.

75 Zhu, Y., Hall, T.J., and Jiang, J. (2003). A finite-element approach for Young's modulus reconstruction. *IEEE Trans. Med. Imaging* 22: 890–901.

76 Kallel, F. and Bertrand, M. (1996). Tissue elasticity reconstruction using linear perturbation method. *IEEE Trans. Med. Imaging* 15: 299–313.

77 Rivaz, H., Boctor, E.M., Choti, M.A., and Hager, G.D. (2011). Real-time regularized ultrasound elastography. *IEEE Trans. Med. Imaging* 30: 928–945.

78 Walker, W.F. and Trahey, G.E. (1995). A fundamental limit on delay estimation using partially correlated speckle signals. *IEEE Trans. Ultrason., Ferroelect., Freq. Control* 42: 301–308.

79 Weinstein, E. and Weiss, A.J. (1984). Fundamental limitations in passive time-delay estimation – Part II: Wide-band systems. *IEEE Trans. Acoust., Speech, Signal Process* 32: 1064–1078.

80 Weiss, A.J. and Weinstein, E. (1983). Fundamental limitations in passive time delay estimation – Part I: Narrow-band systems. *IEEE Trans. Acoust., Speech, Signal Process* 31: 472–486.

81 G. C. Carter (1993). *Coherence and Time Delay Estimation: An Applied Tutorial for Research, Development, Test, and Evaluation Engineers*: IEEE.

82 Cespedes, I., Insana, M., and Ophir, J. (1995). Theoretical bounds on strain estimation in elastography. *IEEE Trans. Ultrason., Ferroelect., Freq. Control* 42: 969–972.

83 Bilgen, M. and Insana, M.F. (1997). Error analysis in acoustic elastography. I. Displacement estimation. *J. Acoust. Soc. Am.* 101: 1139–1146.

84 Bilgen, M. and Insana, M.F. (1997). Error analysis in acoustic elastography. II. Strain estimation and SNR analysis. *J. Acoust. Soc. Am.* 101: 1147–1154.

85 Varghese, T. and Ophir, J. (1997). A theoretical framework for performance characterization of elastography: the strain filter. *IEEE Trans. Ultrason., Ferroelect., Freq. Control* 44: 164–172.

86 Fatemi, M. and Greenleaf, J.F. (1998). Ultrasound-stimulated vibro-acoustic spectrography. *Science* 280: 82–85.

87 Nightingale, K. Soo, M.S., Nightingale, R., and Trahey, G. (2002). Acoustic radiation force impulse imaging: in vivo demonstration of clinical feasibility. *Ultrasound Med. Biol.* 28: 227–235.

88 Pellot-Barakat, C., Frouin, F., Insana, M.F., and Herment, A. (2004). Ultrasound elastography based on multiscale estimations of regularized displacement fields. *IEEE Trans. Med. Imaging* 23: 153–163.

89 Jiang, J., Hall, T.J., and Sommer, A.M. (2006). A novel performance descriptor for ultrasonic strain imaging: a preliminary study. *IEEE Trans. Ultrason., Ferroelect., Freq. Control* 53: 1088–1102.

90 Insana, M.F. and Cook, L.T. (1999). Bioelasticity imaging: System design. *Med. Imaging* 224–235.

91 Cook, L.T., Zhu, Y., Hall, T.J., and Insana, M.F. (2000). Bioelasticity imaging: II. Spatial resolution. *Med. Imaging* 315–324.

92 Insana, M., Cook, L., Bilgen, M., et al. (2000). Maximum-likelihood approach to strain imaging using ultrasound. *J. Acoust. Soc. Am.* 107: 1421–1434.

93 Hall, T.J., Bilgen, M., Insana, M.F., and Krouskop, T. (1997). Phantom materials for elastography. *IEEE Trans. Ultrason., Ferroelect., Freq. Control* 44: 1355–1365.

94 Madsen, E.L., Hobson, M.A., Frank, G.R., et al. (2006). Anthropomorphic breast phantoms for testing elastography systems. *Ultrasound Med. Biol.* 32: 857–874.

95 Wang, Y., Helminen, E., and Jiang, J. (2015). Building a virtual simulation platform for quasistatic breast ultrasound elastography using open source software: A preliminary investigation. *Med. Phys.* 42: 5453–5466.

96 Schroeder, W., Martin, K., and Lorensen, B. (1998). *The Visualization Toolkit*, 2nd edn. Upper Saddle River, NJ: Prentice Hall.

97 Maas, S.A., Ellis, B.J., Ateshian, G.A., and Weiss, J.A. (2012). FEBio: Finite elements for biomechanics. *J. Biomechan. Eng.* 134: 011005–011010.

98 Si, H. and Gartner, K. (2011). 3D boundary recovery by constrained Delaunay tetrahedralization. *Int. J. Numer. Methods Eng.* 85: 1341–1364.

99 Fisher, T.G., Hall, T.J., and Jiang, J. (2007). Volumetric strain imaging, presented at the IEEE Ultrasonics Symposium 2007.

100 Bharat, S. Fisher, T.G., Varghese, T., et al. (2008). Three-dimensional electrode displacement elastography using the Siemens C7F2 fourSight four-dimensional ultrasound transducer. *Ultrasound Med. Biol.* 34: 1307–1316.

101 Treece, G.M., Lindop, J.E., Gee, A.H., and Prager, R.W. (2008). Freehand ultrasound elastography with a 3-D probe. *Ultrasound Med. Biol.* 34: 463–474.

102 Oralkan, A.S., Cheng, C.-H., Johnson, J.A., et al. (2003). Volumetric ultrasound imaging using 2-D CMUT arrays. *IEEE Trans. Ultrason., Ferroelect., Freq. Control* 50, 1581–1594.

103 Daft, C., Wagner, P., Bymaster, B., et al. (2005). cMUTs and electronics for 2D and 3D imaging: monolithic integration, in-handle chip sets and system implications. *IEEE Ultrason. Symp.* 463–474.

104 Deprez, J.F., Brusseau, E., Schmitt, C., et al. (2009). 3D estimation of soft biological tissue deformation from radio-frequency ultrasound volume acquisitions. *Med. Image Anal.* 13: 116–127.

105 Fisher, T.G., Hall, T.J., Panda, S., et al. (2010). Volumetric elasticity imaging with a 2-D CMUT array. *Ultrasound Med. Biol.* 36: 978–990.

106 Seo, Y., Ishizu, T., and Aonuma, K. (2014). Current status of 3-dimensional speckle tracking echocardiography: a review from our experiences. *J. Cardiovasc. Ultrasound* 22: 49–57.

Section III

Theory of Mechanical Properties of Tissue

5

Continuum Mechanics Tensor Calculus and Solutions to Wave Equations

Luiz Vasconcelos[1], *Jean-Luc Gennisson*[2], *and Ivan Nenadic*[1]

[1] *Department of Physiology and Biomedical Engineering, Mayo Clinic, Rochester, MN, USA*
[2] *Imagerie par Résonance Magnétique Médicale et Multi-Modalités, Université Paris-Saclay, Orsay, France*

5.1 Introduction

The phenomenon of wave propagation is well known and extremely common to our lives. One's speech is propagated through sound using the air as medium, for example. Words originate from a forced motion on a portion of a deformable medium; from this point forward the movement is propagated from particle to particle, creating a wave. This process may also be understood as an energy transmission that can be done within small bodies, like medical ultrasound, or large structures, like earthquakes. By analyzing how those waves are transmitted through the medium and the interfaces, a series of properties can be determined and so too can its viscoelastic properties [1].

Many ultrasound elastography methods rely on these transmission characteristics to rheologically define biological tissues, and therefore analyze how they are behaving in comparison to healthy tissue parameters. This process is supported by a very strong mathematical basis – a toolkit of equations that describe the laws of mechanical wave propagation. Once those equations are established all conditions and space configurations can be evaluated and new, and more specific, equations can be derived. The objective of this chapter is set the foundation of those equations, the continuum mechanics [2].

5.2 Mathematical Basis and Notation

The equations that describe physical quantities and laws are called tensor equations. They combine quantities, measured with a number and represented by scalars, with any special direction. Most systems have tensors of order one, or vectors, which represent quantities characterized by direction and magnitude [3].

5.2.1 Tensor Notation

For the theory presented in this chapter, the Cartesian coordinate system is sufficient. The three dimensions are usually specified by the numbers 1, 2, and 3, set as subscripts to a letter. The coordinate is denoted by u_j and base vectors by i_j, where j specifies the dimension. In this manner we will have

$$u = u_1 i_1 + u_2 i_2 + u_3 i_3 \tag{5.1}$$

Ultrasound Elastography for Biomedical Applications and Medicine, First Edition.
Edited by Ivan Nenadic, Matthew Urban, James Greenleaf, Jean-Luc Gennisson, Miguel Bernal, and Mickael Tanter.

Since summations like Eq. (5.1) are very frequent, a summation convention is used to summarize equations, where a repeated subscript implies a sum. In this case we can express

$$u = u_j i_j \tag{5.2}$$

A scalar product of two vectors would be

$$u \cdot v = u_j v_j = u_1 v_1 + u_2 v_2 + u_3 v_3 \tag{5.3}$$

Tensors of second rank, like σ_{ij}, have two free indices. In other words, the number of free indices will specify the tensor rank. An important special tensor is the Kronecker-Delta, defined by

$$\begin{aligned} \delta_{ij} &= 1 \qquad \text{if } i = j \\ \delta_{ij} &= 0 \qquad \text{if } i \neq j \end{aligned} \tag{5.4}$$

The components of a cross product such as $h = u \wedge v$ may be expressed by alternating tensor and summation conventions like

$$h_i = e_{ijk} u_j v_k \tag{5.5}$$

So the components of h are

$$\begin{aligned} h_1 &= u_2 v_3 - u_3 v_2 \\ h_2 &= u_3 v_1 - u_1 v_3 \\ h_3 &= u_1 v_2 - u_2 v_1 \end{aligned}$$

5.2.2 Vector Operators

One of the most important vector calculus operators is ∇, or nabla. When applied to a scalar field it yields a gradient of the original scalar field

$$\text{grad} f = \nabla f = i_1 \frac{\partial}{\partial x_1} + i_2 \frac{\partial}{\partial x_2} + i_3 \frac{\partial}{\partial x_3} \tag{5.6}$$

Partial differentiations are denoted by a comma, like

$$\text{grad} f = \nabla f = i_p f_{,p} \tag{5.7}$$

When there is just a single subscript in $f_{,p}$ it means these are components of a rank one tensor, i.e. a vector.

In a vector field written as $u_i(x_1, x_2, x_3)$, assuming that it is differentiable, all nine partial derivatives written as $\partial u_i(x_1, x_2, x_3)/\partial x_j$, can be rewritten as $u_{i,j}$.

The divergence operator is defined by the vector operator ∇ "multiplied" by a vector

$$\text{div}\, u = \nabla \cdot u = u_{i,i} \tag{5.8}$$

The curl of u is done by taking the cross product of ∇ and u, denoted by $\nabla \wedge u$. If $q = \nabla \wedge u$, the components of q are

$$q_i = e_{ijk} u_{k,i} \tag{5.9}$$

If we take the divergence of a gradient, $\nabla \cdot \nabla$, we'll have a Laplacian operator ∇^2. In this manner we can write

$$\nabla^2 u = \nabla \cdot \nabla u = u_{p,jj} i_p \tag{5.10}$$

In tensor analysis there is one integral theorem that is frequently used. This expression relates a volume integral to a surface integral over the bounded surface of the volume, and it is called

Gauss' theorem. If we consider a convex region B of volume V, with a surface S which possesses a piecewise continuously turning tangent plane. Then, consider a tensor field $\tau_{jkl\ldots p}$ where every component of it is continuously differentiable in B. Then Gauss' theorem states

$$\int_V \tau_{jkl\ldots p,i}\,\mathrm{d}V = \int_S n_i\,\tau_{jkl\ldots p}\,\mathrm{d}A \tag{5.11}$$

where n_i are the components of the unit vector along the outer normal to the surface S. Now we can write Eq. (5.10) with the three components of a vector u successively substituted for $\tau_{jkl\ldots p}$, and if the three resulting equations are added, we have

$$\int_V u_{i,i}\,\mathrm{d}V = \int_S n_i\,u_i\,\mathrm{d}A \tag{5.12}$$

This equation is known as the divergence theorem of vector calculus.

5.2.3 Important Tensors and Notations

The main tensors used in the theoretical elastography are position vector (x_i), displacement vector (u_i), and strain (ε_{ij}) and stress (σ_{ij}) tensors.

5.3 Solutions to Wave Equations

5.3.1 Displacement and Deformation

At first it is important to define how to mathematically describe the particle motion in space, and this is done by the vector called displacement [2, 4]. It indicates both the final and the initial position of the particle, and is denoted by $u(x, t)$. Extrapolating to a notion of continuum, the gradients of the displacement vector describe the deformation of the medium and is denoted by ε, the small-strain tensor, and thus

$$\varepsilon_{ij} = \frac{1}{2}(u_{i,j} + u_{j,i}) \tag{5.13}$$

It is also important to define another tensor of rank two, the rotation tensor φ whose components are defined as

$$\varphi_{ij} = \frac{1}{2}(u_{i,j} - u_{j,i}) \tag{5.14}$$

5.3.2 The Stress Tensor

The continuous media postulate that the mechanical action on particles on one side of a material upon those on another side of the same material can be considered as a surface traction on another surface. So if this surface has a normal n pointing outward we can also define the traction T [4].

Let us consider an object with a body V and a surface S that is subjected to a traction $T(x, t)$. Each element, or particle, may be subjected by a force $f(x, t)$. Following the principles of balance of linear momentum, the resultant of all forces acting on a body at an instant is equal to the instantaneous rate that the linear momentum is changed, and thus

$$\int_S T\,\mathrm{d}A + \int_V \rho f\,\mathrm{d}V = \int_V \rho\ddot{u}\,\mathrm{d}V \tag{5.15}$$

where $\ddot{u}$ is the second time derivative of the displacement. Following the Cauchy's stress theorem which states that a second-order tensor field $\sigma(x, t)$ is defined by the combination

of all traction vectors associated with all planes, that can be simplified in three mutually perpendicular planes with normal n. So we can define the Cauchy stress formula

$$T^{(n)} = \sigma_{kl} n_k \tag{5.16}$$

In other words, σ_{kl} is the component of traction on the surface with a normal i_k in the x_l-direction. Substituting Eq. (5.16) in Eq. (5.15) we have

$$\int_S \sigma_{kl} n_k \, \mathrm{d}A + \int_V \rho f \, \mathrm{d}V = \int_V \rho \ddot{u} \, \mathrm{d}V \tag{5.17}$$

Using the Gauss' theorem to transform the surface integral into a volume integral

$$\int_S (\sigma_{kl,k} + \rho f_l - \rho \ddot{u}_l) \, \mathrm{d}V = 0 \tag{5.18}$$

If the integrand is continuous we have Cauchy's first law of motion

$$\sigma_{kl,k} + \rho f_l = \rho \ddot{u}_l \tag{5.19}$$

5.3.3 Stress–Strain Relation

In basic terms, the relation between the stress tensor and strain tensor components is

$$\sigma_{ij} = C_{ijkl} \varepsilon_{kl} \tag{5.20}$$

where

$$C_{ijkl} = C_{jikl} = C_{klij} = C_{ijlk}$$

This means that only 21 of 81 components of the tensor C_{ijkl} are independent and if these coefficients are constants, then the material is elastically homogeneous. Also, if there is no preferred direction and the elastic constants are the same at any orientation of the Cartesian coordinate system, then we can say the material is isotropic. In isotropic conditions the constants C_{ijkl} can be expressed as

$$C_{ijkl} = \lambda \delta_{ij} \delta_{kl} + \mu(\delta_{lk} \delta_{ji} + \delta_{il} \delta_{jk}) \tag{5.21}$$

so Hooke's law then states

$$\sigma_{ij} = \lambda \varepsilon_{kk} \delta_{ij} + 2\mu \varepsilon_{ij} \tag{5.22}$$

Both equations contain the Lame's elastic constants λ and μ. Setting $j = i$ to Eq. (5.22) we get

$$\sigma_{ii} = (3\lambda + 2\mu)\varepsilon_{ii} \tag{5.23}$$

By rewriting Eq. (5.23) in function of ε_{ii} and applying it to Eq. (5.22) and solving it for ε_{ij}, we obtain the following relation

$$\varepsilon_{ij} = -\frac{\lambda \delta_{ij}}{2\mu(3\lambda + 2\mu)} \sigma_{kk} + \frac{1}{2\mu} \sigma_{ij} \tag{5.24}$$

The small-strain tensor ε_{ij} can only be solved for a given σ_{ij} only if

$$\mu \neq 0 \text{ and } 3\lambda + 2\mu \neq 0$$

For a condition of simple shear where $\sigma_{12} \neq 0$ and other stresses are 0, we have $\sigma_{12} = 2\mu\varepsilon_{12}$. With this we can identify μ as the shear modulus, and since small deformations in σ_{12} and ε_{12} have the same directions it is fair to say $\mu > 0$.

Another important constant implied in certain conditions is the bulk modulus (K). In cases of hydrostatic pressure where $\varepsilon_{ij} = -p\delta_{ij}$ we can use Eq. (5.23) to find $p = -K\varepsilon_{kk}$ and therefore $K = \lambda + \frac{2}{3}\mu$. It is clear that a hydrostatic pressure will cause a reduction of volume and so $K > 0$.

Table 5.1 Isotropic elastic constants relationships [1].

	λ, μ	E, μ	E, ν
λ	λ	$\frac{\mu(E-2\mu)}{3\mu-E}$	$\frac{E\nu}{(1+\nu)(1-2\nu)}$
μ	μ	μ	$\frac{E}{2(1+\nu)}$
K	$\lambda+\frac{2}{3}\mu$	$\frac{\mu E}{3(3\mu-E)}$	$\frac{E}{3(1-2\nu)}$
E	$\frac{\mu(3\lambda+2\mu)}{\lambda+\mu}$	E	E
ν	$\frac{\lambda}{2(\lambda+\mu)}$	$\frac{E-2\mu}{2\mu}$	ν

There are other important constants useful for homogeneous, isotropic, linearly elastic media such as Young's modulus (E) and Poisson's ratio (ν). All these constants are intrinsic characteristics of each media and are related to each other through a set of equations, summarized in Table 5.1.

5.3.4 Displacement Equation of Motion

Now, inserting the stress–strain relation, or Hooke's law (Eq. 5.22), into Cauchy's first law of motion (Eq. 5.19) and we get

$$(\lambda\varepsilon_{kk}\delta_{ij} + 2\mu\varepsilon_{ij})_{,j} + \rho f_i = \rho\ddot{u}_i \tag{5.25}$$

Using Eq. (5.13) to make it a function of displacement (u) gives us

$$\begin{aligned}
&\left(\lambda\delta_{ij}u_{k,k} + 2\mu\frac{1}{2}[u_{i,j}+u_{j,i}]\right)_{,j} + \rho f_i = \rho\ddot{u}_i \qquad (5.26)\\
&\lambda\delta_{ij}u_{k,kj} + \mu[u_{i,jj}+u_{j,ij}] + \rho f_i = \rho\ddot{u}_i\\
&\lambda u_{k,ki} + \mu[u_{i,jj}+u_{j,ij}] + \rho f_i = \rho\ddot{u}_i
\end{aligned}$$

Finally we can rearrange the terms and get the dynamic Navier's equation of equilibrium

$$(\lambda+\mu)u_{j,ji} + \mu u_{i,jj} + \rho f_i = \rho\ddot{u}_i \tag{5.27}$$

or, in its vector equivalent

$$(\lambda+\mu)\nabla\nabla\cdot u + \mu\nabla^2 u + \rho\mathrm{f} = \rho\ddot{u} \tag{5.28}$$

5.3.5 Helmholtz Decomposition

Navier's equation of equilibrium is a very powerful tool to understand the propagation of waves. It can be rewritten in several ways [1]. Using the scalar notation one can decompose it in three equations

$$\begin{aligned}
&(\lambda+\mu)\left(\frac{\partial^2 u}{\partial x^2} + \frac{\partial^2 v}{\partial x\,\partial y} + \frac{\partial^2 w}{\partial x\,\partial z}\right) + \mu\nabla^2 u + \rho f_x = \rho\frac{\partial^2 u}{\partial t^2}\\
&(\lambda+\mu)\left(\frac{\partial^2 u}{\partial y\,\partial x} + \frac{\partial^2 v}{\partial y^2} + \frac{\partial^2 w}{\partial y\,\partial z}\right) + \mu\nabla^2 u + \rho f_y = \rho\frac{\partial^2 u}{\partial t^2} \qquad (5.29)\\
&(\lambda+\mu)\left(\frac{\partial^2 u}{\partial z\,\partial x} + \frac{\partial^2 v}{\partial z\,\partial y} + \frac{\partial^2 w}{\partial z^2}\right) + \mu\nabla^2 u + \rho f_z = \rho\frac{\partial^2 u}{\partial t^2}
\end{aligned}$$

where the particle displacements are u, v, w in the x, y, z directions, respectively. The dilatation of a material is defined, in vector notation, by

$$\Delta = \nabla \cdot u = \varepsilon_x + \varepsilon_y + \varepsilon_z = \varepsilon_{kk} \tag{5.30}$$

Substituting Eq. (5.30) in Eq. (5.28)

$$(\lambda + \mu)\Delta\nabla \cdot u + \mu\nabla^2 u + \rho f_i = \rho\ddot{u} \tag{5.31}$$

Another vector identity can be applied to Navier's equation

$$\nabla^2 u = \nabla\nabla \cdot u = \nabla \times \nabla\times \tag{5.32}$$

so that Eq. (5.30) may also be written as

$$(\lambda + 2\mu)\nabla\nabla \cdot u - \mu\nabla \times \nabla \times u + \rho f = \rho\ddot{u} \tag{5.33}$$

Recalling Eq. (5.14), the rotation vector is defined as

$$\omega = \frac{1}{2}\nabla \times u \tag{5.34}$$

Returning with the dilatation Δ, one can express the equation as

$$(\lambda + 2\mu)\nabla\Delta \cdot u - 2\mu\nabla \times \omega + \rho f = \rho\ddot{u} \tag{5.35}$$

This last form explicitly displays the rotation and dilatation components of displacement. Another characteristic of this variation is that its result is valid for rectangular and curvilinear coordinate systems.

An easier way to define and use the displacement equations is done by applying the scalar and vector potentials Φ and H

$$u = \nabla\Phi + \nabla \times \mathrm{H}, \nabla \cdot \mathrm{H} = 0 \tag{5.36}$$

The Helmholtz theorem, also known as Helmholtz decomposition, states that a vector field in three dimensions is a sum of an irrotational (curl-free) vector and a solenoidal (divergence-free) vector field. To determine the three components of u from the four components of Φ, H the condition $\nabla \cdot \mathrm{H} = 0$ is needed. So one can also express

$$\mathrm{f} = \nabla f + \nabla \times \mathrm{B}, \nabla \cdot \mathrm{B} = 0 \tag{5.37}$$

Substituting Eqs. (5.36) and (5.37) in Eq. (5.28)

$$(\lambda + \mu)\nabla\nabla \cdot (\nabla\Phi + \nabla \times \mathrm{H}) + \mu\nabla^2(\nabla\Phi + \nabla \times \mathrm{H}) + \rho(\nabla f + \nabla \times \mathrm{B}) = \rho(\nabla\ddot{\Phi} + \nabla \times \ddot{\mathrm{H}}) \tag{5.38}$$

Regrouping

$$\nabla\{(\lambda + 2\mu)\nabla^2\Phi + \rho f - \rho\ddot{\Phi}\} + \nabla \times (\mu\nabla^2\mathrm{H} + \rho\mathrm{B} - \rho\ddot{\mathrm{H}}) = 0 \tag{5.39}$$

To satisfy this equation both bracket terms need to vanish and so

$$(\lambda + 2\mu)\nabla^2\Phi + \rho f = \rho\ddot{\Phi} \tag{5.40}$$

$$\mu\nabla^2\mathrm{H} + \rho\mathrm{B} = \rho\ddot{\mathrm{H}} \tag{5.41}$$

This is the complete solution of the displacement equation in terms of irrotational and solenoidal vector fields.

5.3.6 Compressional and Shear Waves

Considering the governing displacement equation without body forces

$$(\lambda + \mu)\nabla\nabla \cdot u + \mu\nabla^2 u = \rho\ddot{u} \tag{5.42}$$

Applying the vector operation of divergence on the above

$$(\lambda + \mu)\nabla \cdot (\nabla\nabla \cdot u) + \mu\nabla \cdot (\nabla^2 u) = \rho\nabla \cdot \ddot{u} \tag{5.43}$$

Since

$$\nabla \cdot \nabla = \nabla^2$$
$$\nabla \cdot (\nabla^2 u) = \nabla^2(\nabla \cdot u) \text{ and}$$
$$\nabla \cdot u = \Delta$$

The dilatation reduces to

$$(\lambda + 2\mu)\nabla^2\Delta = \rho\frac{\partial^2\Delta}{\partial t^2} \tag{5.44}$$

This equation can be rewritten as the compressional wave equation

$$\nabla^2\Delta = \frac{1}{c_\mathrm{p}^2}\frac{\partial^2\Delta}{\partial t^2} \tag{5.45}$$

where the compressional wave propagation velocity is given by

$$c_\mathrm{p} = \sqrt{\frac{\lambda + 2\mu}{\rho}} \tag{5.46}$$

This motion is parallel to the direction of propagation and it is called a longitudinal wave. This type of wave may also be called a compressional wave or P-wave (primary wave).

In the other hand, if the curl operation is applied to the governing equation considering that the gradient of a scalar is zero

$$\mu\nabla^2\omega = \rho\frac{\partial^2\omega}{\partial t^2} \tag{5.47}$$

where $\varphi = \nabla \times u/2$, seen as the rotation vector in Eq. (5.14). This equation can be rewritten as the shear wave equation

$$\nabla^2\omega = \frac{1}{c_\mathrm{s}^2}\frac{\partial^2\omega}{\partial t^2} \tag{5.48}$$

where the shear wave propagation velocity is given by

$$c_\mathrm{S} = \sqrt{\frac{\mu}{\rho}} \tag{5.49}$$

In this case the motion is normal to the propagation direction, and the wave is called a transverse wave. This type of wave is also often called shear wave or S-wave (secondary wave).

Referring to Eqs. (5.40) and (5.41), which resulted from the scalar and vector potentials Φ and H, if the body forces are zero then $\mathrm{f} = \mathrm{B} = 0$, and both equations give the scalar and vector wave equations and contain the velocities c_p and c_S. We can conclude that the vector potential is directly associated to the longitudinal part of the disturbance, while the scalar portion is related to the transverse part.

From Eqs. (5.30) and (5.31) along with Table 5.1, one can derive

$$\frac{c_\mathrm{P}}{c_\mathrm{S}} = \sqrt{\frac{\lambda + 2\mu}{\mu}} = \sqrt{\frac{2(1-\nu)}{1-2\nu}} \tag{5.50}$$

where ν is the Poisson's ratio. In most of materials $0 \leq \nu \leq 0.5$, and it follows that $c_\mathrm{p} > c_\mathrm{S}$. Metals, for example, have very high pressure and shear wave phase velocities. For instance, aluminum

Table 5.2 Approximate values for common materials [1].

Material	ρ (kg/m^3)	c_p(m/s)	c_s(m/s)	κ
Air	1.2	340	–	–
Water	1000	1480	–	–
Steel	7800	5900	3200	1.845
Copper	8900	4600	2300	2
Glass	2500	5800	3400	1.707
Rubber	930	1040	27	38.5

Table 5.3 Approximate values for different tissues [5].

Material	c_p(m/s)	c_s(m/s)
Breast	1450–1570	1.10–3.46
Breast cancer	1437–1584	3.25–9.64
Liver	1522–1623	0.85–3.01
Fibrotic/cirrhotic liver	1535–1581	0.84–5.00
Skeletal muscle	1500–1610	1.56–7.60
Kidney	1558–1562	1.20–3.50
Heart	1528–1602	0.83–7.00
Arteries	1559–1660	2.83–6.09
Brain	1460–1580	1.02–4.63
Skin	1498–1540	2.66–5.99
Lung	577–1472	0.90–3.54
Spleen	1515–1635	1.10–2.36
Cornea	1542–1639	1.43–6.80
Cervix/uterus	1625–1633	2.01–2.58
Thrombus	1586–1597	0.33–1.27
Tendons	1631–3530	79.4
Cartilage	1520–1665	39.71–87.83
Bone	1630–4170	1420–3541

has $c_P = 6300\,\text{m/s}$ and $c_S = 3100\,\text{m/s}$. Tables 5.2 and 5.3 illustrate the differences between some common materials and human tissues. Note from Table 5.3 that the compressional wave velocities occupy a fairly narrow range as a percentage while shear wave velocities change over several orders of magnitude even for soft tissues.

The continuum mechanics presented here has set the basic pillars of modern elastography. Studies have shown that rheological properties have a large dynamic range through different media, which is ideal to characterize different types of tissue, whether normal or pathological [5]. In the past, this was only partially possible by palpation tests done by physicians, therefore relying only on the practitioner's experience and sensibility. Many studies have also demonstrated that biological tissues are viscoelastic materials, that is, their deformation will depend on the time course of the stress applied, and to properly characterize them it is necessary to use complex moduli [5]. The equations derived in this chapter are necessary for a good

understanding of the chapters to come and for ultrasound elastography as a whole. It is very important to comprehend the relations between displacement, strain, and stress, along with all viscoelastic parameters and how they affect wave propagation on materials and tissues.

References

1 Achenbach, J.D. (1973). *Wave Propagation in Elastic Solids*. North-Holland Series in Applied Mathematics and Mechanics, volume 16. Amsterdam, New York: North-Holland Pub. Co.; American Elsevier Pub. Co.

2 Graff, K.F. (1975). *Wave Motion in Elastic Solids*. Oxford Engineering Science Series. Oxford: Clarendon Press.

3 Fetter, A.L. and Walecka, J.D. (2006). *Nonlinear Mechanics: A Supplement to Theoretical Mechanics of Particles and Continua*. Mineola, NY: Dover Publications.

4 Kundu, T. (2004). *Ultrasonic Nondestructive Evaluation : Engineering and Biological Material Characterization*. Boca Raton, FL: CRC Press.

5 Sarvazyan, A.P., Urban, M.W., and Greenleaf, J.F. (2013). Acoustic waves in medical imaging and diagnostics. *Ultrasound Med. Biol.* 39 (7): 1133–1146.

6

Transverse Wave Propagation in Anisotropic Media

Jean-Luc Gennisson

Imagerie par Résonance Magnétique Médicale et Multi-Modalités, Université Paris-Saclay, Orsay, France

6.1 Introduction

In science and technology elastic properties of solids have considerable significance. This information is of fundamental importance in interpreting and understanding the nature of bonding in the solid state, because the elastic properties describe the mechanical behavior of materials. When a material is subjected to a stress it will experience strain. Within the elastic limit, strain varies linearly with the applied stress and leads to the definition of the common elastic material properties, which are the Young's modulus (E), bulk modulus (κ), shear modulus (μ), and Poisson's ratio (υ). Additional to these elastic constants there is the longitudinal modulus and transverse modulus that can be determined from the velocity of propagation of longitudinal waves and transverse waves through a solid. The number of elastic constants for anisotropic solids such as crystals that have been discussed previously [1–5]. Anisotropy has also long been studied in geophysics [6, 7] or in nondestructive testing with ultrasound [8, 9]. In biological media ex vivo, Hoffmeister [10] and Kuo [11] on tendon, Yoon [12] on bone, or Levinson [13] and Andersen [14] on muscle quantify the anisotropic longitudinal elastic moduli. The first technique that tried to quantify shear elastic anisotropy was the sonoelasticity technique by using an external steady state vibrator [15, 16]. Now transient elastography techniques, using the propagation of a low frequency shear wave in vivo [17–19], can measure the Young's modulus of soft tissues.

In this chapter, we describe how these methods can be adapted to study the anisotropic shear moduli of simple muscles in vitro and in vivo. In Section 6.2, theoretical considerations from general to hexagonal anisotropic medium, also called a transverse isotropic medium, are presented and predict the existence of a slow and a fast shear wave in biological tissue such as muscle. In Section 6.3, different techniques are presented to show how shear wave elastography can estimate anisotropy.

6.2 Theoretical Considerations from General to Transverse Isotropic Models for Soft Tissues

Determining the elastic constant by measuring the velocity of sound in crystals is a standard method. The use of high frequency acoustic waves leads to precise results compared to the static methods. The elastic constants are tensors, which measure the crystal property. The mathematical theory of elasticity relates stress and strain in solids [20]. The state of strain (ε_{ij}) in

Ultrasound Elastography for Biomedical Applications and Medicine, First Edition.
Edited by Ivan Nenadic, Matthew Urban, James Greenleaf, Jean-Luc Gennisson, Miguel Bernal, and Mickael Tanter.

the solid at any given point can be expressed by resolving the displacement of an elementary volume originally located at some point along three perpendicular directions and by differentiating these components, one can obtain the nine components of strain tensor. Likewise the state of stress (σ_{ij}), which the volume element is subjected to, could be resolved into interactive forces acting along each of the three coordinate axes. Thus there are three types of stresses, one longitudinal and two shear, perpendicular to each other. There are nine components of a stress–strain proportionality relationship and would involve (9×9) or 81 elastic constants.

By using Einstein's convention, this tensor can be expressed in the general form as

$$\sigma_{ij} = C_{ijkl}\epsilon_{kl} \tag{6.1}$$

The stress tensor and strain tensor are second rank tensors. Hence the constant of proportionality is a fourth rank tensor. This tensor is referred to as the elastic stiffness tensor C_{ijkl}. The stiffness constants and elastic compliances are determined by elastic wave propagation measurements in solids [2, 21–23]. Further, these constants determine the velocity of elastic waves in any direction in an anisotropic solid. C_{ijkl} has 81 elements relating 9 strain components and 9 stress components. In the absence of rotation in the material the stress and strain tensors obey the symmetry $ij = ji$.

The law of reciprocity enables one to interchange the direction of force and displacement without change in the constant of proportionality. Thus the number 81 is reduced to 45 constants. These 45 constants are required to describe the elastic behavior of a triclinic crystal. On the basis of Cauchy's assumption and by the application of the reciprocity relationship, the number of constants reduces to 21 for a triclinic crystal. The reduction in the strain component from 9 to 6 may be summarized by the statement that the elastic strain can be separated into pure strains and rotations and the latter can be ignored. A correct and complete theory of elasticity has necessarily to take all the nine components of the stress and strain tensors into consideration.

Then by introducing a more compact notation (Voigt notation) with two suffixes, C_{ijkl} is replaced by the matrix (C_{IJ}, [IJ = 1, 2, 3, 4, 5, 6]) leading for locally homogeneous medium to the following relationship

$$\begin{bmatrix} \sigma_{11} \\ \sigma_{22} \\ \sigma_{33} \\ \sigma_{44} \\ \sigma_{55} \\ \sigma_{66} \end{bmatrix} = \begin{bmatrix} C_{11} & C_{12} & C_{13} & C_{14} & C_{15} & C_{16} \\ C_{12} & C_{22} & C_{23} & C_{24} & C_{25} & C_{26} \\ C_{13} & C_{23} & C_{33} & C_{34} & C_{35} & C_{36} \\ C_{14} & C_{24} & C_{34} & C_{44} & C_{45} & C_{46} \\ C_{15} & C_{25} & C_{35} & C_{45} & C_{55} & C_{56} \\ C_{16} & C_{26} & C_{36} & C_{46} & C_{56} & C_{66} \end{bmatrix} \begin{bmatrix} \epsilon_{11} \\ \epsilon_{22} \\ \epsilon_{33} \\ 2\epsilon_{44} \\ 2\epsilon_{55} \\ 2\epsilon_{66} \end{bmatrix} \tag{6.2}$$

This introduces another 15 equalities in the elastic constants and reduces the maximum number of independent constants to 21. Further reduction of the number of independent elastic constants is possible when the symmetry of the crystal is considered, and this number is different for the different crystal classes. When suitable directions are chosen as axes, the crystal may be grouped on the basis of its macroscopic morphology into one of 32 crystal classes (point group symmetry) which forms a sub-group among 7 crystal systems [24]. The crystal classes comprise of the combination of the point symmetry operations such as inversion, n-fold rotation, reflection, etc. The basic crystal systems in the order of decreasing symmetry are the following: cubic, hexagonal, tetragonal, trigonal, orthorhombic, monoclinic and triclinic. by applying all symmetry operation, one after another to each tensor component, one can solve the whole set of equations and determine those components which must vanish and also find any relation between the non-vanishing tensors [25]. Then one can obtain the number of non-zero elastic constants for various crystal systems as follow: 21 triclinic, 13 monoclinic,

9 orthorhombic, 7 tetragonal i, 6 tetragonal ii, 7 trigonal i, 6 trigonal ii, 5 hexagonal, 3 cubic, 2 isotropic. For the isotropic solid, two independent constants appear, C_{12} and C_{44}, and are defined as the Lamé constants λ and μ, respectively.

From these considerations the propagation of elastic waves are governed within an anisotropic medium by three linear equations known as "Christoffel equations" which relate velocity, direction of the waves, and elastic constant. Consider an anisotropic medium, which obeys the ideal Hooke's law, and in which body forces, body torques, dissipative processes, and nonlinear or dissipative phenomena can be neglected. A disturbance in such a medium is represented by a set of position and time-dependent particle displacements $u(x,t)$ which are related by the equations

$$\rho \frac{\partial^2 u_i}{\partial t^2} = \frac{\partial \sigma_{ij}}{\partial x_j} \tag{6.3}$$

where ρ is the density of the medium. To obtain the wave equation the right-hand side of this equation is written in terms of the deformation components of u_i. For this the relation between stress and strain is used. This gives the wave equation in the form

$$\rho \frac{\partial^2 u_i}{\partial t^2} = C_{ijkl} \frac{\partial^2 u_k}{\partial x_j \partial x_l} \tag{6.4}$$

The C_{ijkl} is the second-order elastic constant. A plane monochromatic wave $u_i = u_0 \exp[i(kr - \omega t)]$ is a solution of the above equation, where u_0 is the amplitude, k is the wave vector, and ω the frequency, satisfying the condition

$$|C_{ijkl} k_j k_l - \rho \omega^2 \delta_{ik}| = 0 \tag{6.5}$$

The three homogenous equations for u_i have a solution only if the secular equation of their coefficients is satisfied. This requirement leads to the familiar form of a determinantal equation for the propagation velocity $v = \omega/k$. If one writes the propagation velocity in terms of cosines as $k = k\,[n_1, n_2, n_3]$ the secular determinant becomes

$$|\Gamma_{ik} - \rho v^2 \delta_{ik}| = 0 \tag{6.6}$$

where the coefficient Γ_{ik} is called the Christoffel matrix and its elements depend on the direction of wave propagation and elastic constant. Equation (6.4) is a cubic equation for ρv^2, which has three roots with respect to interchange of k and i. The requirement for crystal stability ensures that Γ_{ik} is a positive definite matrix and hence the three eigenvalues are positive. At last by using the Voigt notation for the elastic constants, the Christoffel coefficients are in the most general case given in the Table 6.1.

Table 6.1 Christoffel coefficients.

Γ_{ij}	n_1^2	n_2^2	n_3^2	$2n_1n_3$	$2n_3n_1$	$2n_1n_2$
Γ_{11}	C_{11}	C_{66}	C_{55}	C_{56}	C_{15}	C_{16}
Γ_{22}	C_{66}	C_{22}	C_{44}	C_{24}	C_{46}	C_{26}
Γ_{33}	C_{55}	C_{44}	C_{33}	C_{34}	C_{35}	C_{45}
$\Gamma_{32} = \Gamma_{23}$	C_{56}	C_{24}	C_{34}	$[C_{23} + C_{44}]/2$	$[C_{36} + C_{45}]/2$	$[C_{25} + C_{46}]/2$
$\Gamma_{31} = \Gamma_{13}$	C_{15}	C_{46}	C_{35}	$[C_{36} + C_{45}]/2$	$[C_{13} + C_{55}]/2$	$[C_{14} + C_{56}]/2$
$\Gamma_{21} = \Gamma_{12}$	C_{16}	C_{26}	C_{45}	$[C_{25} + C_{46}]/2$	$[C_{14} + C_{56}]/2$	$[C_{12} + C_{66}]/2$

On evaluating the determinant and equating it to zero, one obtains the secular equation. This is a cubic equation in v^2 and hence it has three solutions and three different velocities are associated with it. Thus for a given direction there are three waves propagating with different velocities. The fastest of the three is the longitudinal wave or quasi-longitudinal wave. The other two are fast and slow transverse waves or quasi-transverse waves. The waves are purely longitudinal or purely transverse only in the pure mode directions in the crystal and the directions are usually the symmetry axes or symmetry planes in the crystal [26, 27]. The three values of ρv^2 are the eigenvalues of the matrix Γ_{ik} and corresponding solutions for the displacement vector u_k are the eigenvectors. While the eigenvalues give the three velocities, the corresponding eigenvectors give the direction of particle motion or the polarization direction of the wave.

From the general expression for elastic waves propagation presented in the above section, one can deduce equations for higher symmetry crystals. This is due to the fact that several elastic constants are zero for the higher symmetries, as shown above. Further simplification occurs when symmetry direction or planes are chosen as the propagation direction so that one or two of the direction cosines n_1, n_2, n_3 are equal to zero.

In the following part, one defines the waves characteristics for an hexagonal system which is the most common system found in the human body and used in elastography experiments. Thus for a hexagonal medium, the nonzero elastic constants are $C_{11} = C_{22}$, C_{33}, $C_{44} = C_{55}$, C_{12}, $C_{13} = C_{23}$ and $C_{66} = [C_{11} - C_{12}]/2$. All other constants in the Christoffel matrix are zero. The coefficients of the Christoffel matrix Γ_{ik} can be written as

$$\Gamma_{11} = C_{11}n_1^2 + C_{66}n_2^2 + C_{44}n_3^2 \tag{6.7}$$

$$\Gamma_{22} = C_{66}n_1^2 + C_{11}n_2^2 + C_{44}n_3^2$$

$$\Gamma_{33} = C_{44}n_1^2 + C_{44}n_2^2 + C_{33}n_3^2$$

$$\Gamma_{23} = (C_{44} + C_{13})n_2n_3$$

$$\Gamma_{13} = (C_{44} + C_{13})n_1n_3$$

$$\Gamma_{12} = (C_{11} + C_{66})n_2n_1$$

Now consider the wave propagation in the xy-plane, which means $n_3 = 0$; the Γ_{ik} coefficients now become

$$\Gamma_{11} = C_{11}n_1^2 + C_{66}n_2^2 \tag{6.8}$$

$$\Gamma_{22} = C_{66}n_1^2 + C_{11}n_2^2$$

$$\Gamma_{33} = C_{44}n_1^2 + C_{44}n_2^2$$

$$\Gamma_{23} = 0$$

$$\Gamma_{13} = 0$$

$$\Gamma_{12} = (C_{11} + C_{66})n_1n_2$$

The determinant equation can be written as

$$\begin{vmatrix} \Gamma_{11} - \rho v^2 & \Gamma_{12} & 0 \\ \Gamma_{12} & \Gamma_{22} - \rho v^2 & 0 \\ 0 & 0 & \Gamma_{33} - \rho v^2 \end{vmatrix} = 0 \tag{6.9}$$

On substitution of the Γ_{ik} values for the xy-plane, considerable algebraic simplification occurs and very simple solutions are obtained, as

$$\begin{aligned}\rho v_0^2 &= c_{44}\\ \rho v_1^2 &= c_{11}\\ \rho v_2^2 &= c_{66}\end{aligned} \tag{6.10}$$

The above results show that the velocity is independent of the direction in this plane and that all modes are pure. v_0 is a shear mode polarized parallel to the z-axis, v_1 is a longitudinal mode, and v_2 is a shear mode polarized normal to the z-axis. The above relations are valid for the directions x,y or any direction in the plane.

Consider propagation in the xz-plane, which means $n_2 = 0$. The coefficients are then obtained as

$$\begin{aligned}\Gamma_{11} &= C_{11}n_1^2 + C_{66}n_2^2\\ \Gamma_{22} &= C_{66}n_1^2 + C_{11}n_3^2\\ \Gamma_{33} &= C_{44}n_1^2 + C_{33}n_3^2\\ \Gamma_{23} &= 0\\ \Gamma_{13} &= (C_{13} + C_{44})n_1n_3\\ \Gamma_{12} &= 0\end{aligned} \tag{6.11}$$

This leads to the characteristic equation

$$(\Gamma_{22} - \rho v^2)[\rho^2 v^4 - \rho v^2(\Gamma_{11} + \Gamma_{33}) + \left(\Gamma_{11}\Gamma_{33} - {\Gamma_{13}}^2\right)] = 0 \tag{6.12}$$

Then the linear part gives one root and the quadratic part gives two roots and

$$\begin{aligned}\rho v_0^2 &= \Gamma_{22}\\ 2\rho v_1^2 &= (\Gamma_{11} + \Gamma_{33}) + \sqrt{(\Gamma_{11} + \Gamma_{33})^2 - 4(\Gamma_{11}\Gamma_{33} + \Gamma_{13}^2)}\\ 2\rho v_2^2 &= (\Gamma_{11} + \Gamma_{33}) - \sqrt{(\Gamma_{11} + \Gamma_{33})^2 - 4(\Gamma_{11}\Gamma_{33} + \Gamma_{13}^2)}\end{aligned} \tag{6.13}$$

v_0 is a pure shear mode polarized normal to the plane, v_1 is a quasi-longitudinal wave, and v_2 is a quasi-shear wave. It can be seen that these expressions are rotationally invariant for rotations about the z-axis. Hence, the same expressions are valid for the yz-plane also.

For propagation in the x-direction, the corresponding direction cosines are $n_1 = 1$, $n_2 = 0$, $n_3 = 0$. In this case the solutions are

$$\begin{aligned}\rho v_0^2 &= C_{44}\\ \rho v_1^2 &= C_{11}\\ \rho v_2^2 &= C_{66}\end{aligned} \tag{6.14}$$

Then the pure mode waves are v_0 transverse mode polarized parallel to the z-axis, v_1 is a longitudinal and v_2 is a transverse mode polarized normal to z.

For symmetry direction along the z-axis the above expressions (Eq. 6.13) can be simplified by putting $n_1 = 0$ and $n_3 = 1$. This gives

$$\begin{aligned}\rho v_0^2 &= C_{44}\\ \rho v_1^2 &= C_{11}\\ \rho v_2^2 &= C_{44}\end{aligned} \tag{6.15}$$

v_1 is a longitudinal mode, v_0 and v_2 are shear modes polarized normal to the z-axis and are degenerate since the two transverse velocities are identical in the z-direction of the hexagonal crystal. Then the z-axis is an acoustic axis of the crystal.

6.3 Experimental Assessment of Anisotropic Ratio by Shear Wave Elastography

The most common organ in the body is muscle. The muscle model considered presents a random distribution of fibers oriented in the same direction. This consideration entails the existence of a symmetry axis along the fibers. It is proven [8] that this kind of symmetry corresponds to a hexagonal system, transverse isotropy. In this part, two main shear elastography techniques are presented to assess anisotropy in biological tissues: transient elastography technique (TE) and supersonic shear imaging technique (SSI).

6.3.1 Transient Elastography

In the transient elastography technique an external vibrator is used to give a low-frequency pulse at the surface of the body in order to generate shear waves from the surface of the skin (see Chapter 20 in this book). In that specific case the generated shear wave is spherical. By changing the shape of the piston source, for example with a rod, the resulting generated shear waves are polarized perpendicularly to the piston rod (Figure 6.1) [17].

The shear elastic constants C_{44} and C_{66} can be obtained with the TE technique from the velocities of shear waves propagating in a direction perpendicular to the fiber axis with a polarization oriented either parallel to the fibers (V_{S3}), or perpendicular to the fibers (V_{S1}). Experimentally by just rotating the rod at the surface of the body both velocities can be measured (Figure 6.1).

6.3.2 Supersonic Shear Imaging

In the supersonic shear imaging technique, the external vibrator is replaced by the acoustic radiation force (see Chapter 23 in this book). Then shear wave are directly generated within tissues and propagate perpendicularly to the ultrasound axis. Then by rotating the probe at the surface of muscles, regarding the orientation of the fibers, it is possible to estimate shear wave velocities and recover C_{44} and C_{66} (Figure 6.2).

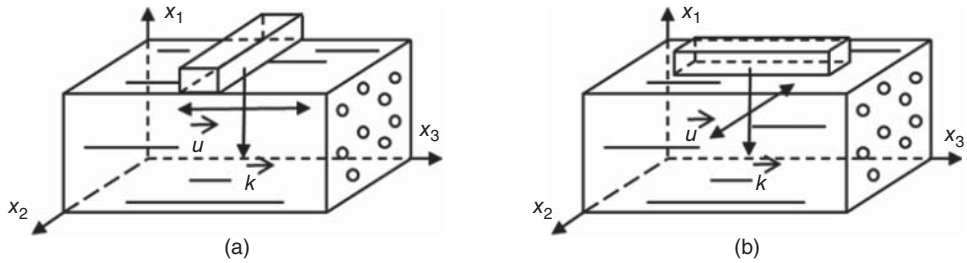

Figure 6.1 Schematics of the TE technique where a rod mounted on a vibrator gives a low-frequency pulse at the surface of the medium generating shear waves. (a) When the rod is perpendicular to the fibers' axis, a shear wave propagates (k, x_1 axis) perpendicularly to the fibers' axis with a polarization (u, x_3 axis) parallel to the fibers' axis. (b) When the rod is parallel to the fibers' axis, a shear wave propagates (k, x_1 axis) perpendicularly to the fibers' axis with a polarization (u, x_2 axis) perpendicular to the fibers' axis. Such configurations give, respectively, access to the elastic constants C_{44} and C_{66}. Source: reprinted with permission from Royer et al. [28], copyright 2011, Acoustical Society of America.

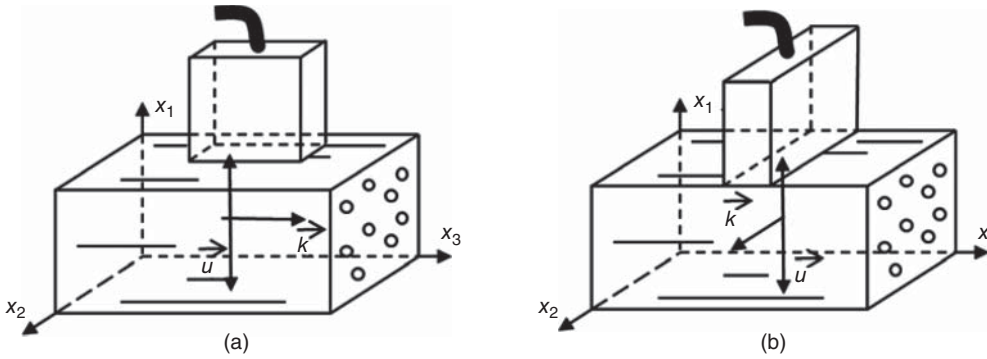

Figure 6.2 Schematics of the SSI technique where a radiation force perpendicular to the fibers' axis generates shear waves. (a) When the ultrasonic probe is parallel to the fibers' axis, a shear wave propagates (k, x_3 axis) parallel to the fibers' axis with a polarization (u, x_1 axis) perpendicular to the fibers' axis. (b) When the ultrasonic probe is perpendicular to the fibers' axis, a shear wave propagates (k, x_2 axis) perpendicularly to the fibers' axis with a polarization (u, x_1 axis) perpendicular to the fibers' axis. Such configurations give, respectively, access to the elastic constants C_{44} and C_{66}. Source: adapted from Royer et al., [28], copyright 2011, Acoustical Society of America.

Finally, soft tissues (muscles, tendons) exhibit a mechanical behavior very different from hexagonal crystals since the bulk modulus is quite large compared to the shear moduli. This unusual behavior of transverse isotropic tissues is the difference of anisotropy according to the type of elastic waves. Regarding the speed of ultrasound waves, the ratio of anisotropy is quite close to unity for longitudinal waves. The anisotropy of soft tissues is mainly related to the shear parameters governing the speed of slow transverse waves. This explains why the anisotropy was not very widely studied in recent decades in ultrasonography.

6.4 Conclusion

Due to the current technology, the full characterization of the anisotropy of a biological tissue is quite challenging. Estimation of the shear wave velocity in ultrasound elastography can only be done in one direction at the time. Thus multiple measurements with different probe placement must be done. Moreover, only a simple model is often assumed when estimating the anisotropic ratio, as for example the transverse isotropic model, but only few organs have this type of symmetry. To solve the full anisotropic tensor, technological improvement must be realized, and having access to volumetric measurement of shear wave propagation could help with this challenge [29].

References

1 Huntington, H.B. (1958). *Elastic Constants of Crystals*. New York: Academic Press.
2 Nye, J.F. (1985). *Physical Properties of Crystals*. New York: Oxford University Press.
3 Federov, F. (1968). *Theory of Elastic Waves in Crystals*. New York: Plenum Press.
4 Musgrave, M.J.P. (1970). *Crystal Acoustics*. San Francisco: Holden Day.
5 Mason W.P. and McSkimin J. (1947). Attenuation and scattering of high frequency sound waves in metals and glasses. *J. Acoust. Soc. Am.* 19: 464.
6 Crampin, S. and Kirkwood, S.C. (1981). Shear-wave singularities of wave propagation in anisotropic media. *J. Geophys.* 49: 43–46.

7 Mensch, T. and Rasolofosaon, P. (1997). Elastic-wave velocities in anisotropic media of arbitrary symmetry – generalization of Thomsen's parameters ϵ, δ and γ. *Geophys. J. Int.* 128: 43–64.

8 Zimmer, E. and Cost, J.R. (1970). Determination of the elastic constants of an unidirectional fiber composite using ultrasonic velocity measurements. *J. Acoust. Soc. Am.* 47: 795–803.

9 Lhermitte, T. and Perrin, B. (1991). Anisotropy of elastic properties of cross-ply fiber-reinforced composite materials. *IEEE Ultrason. Symp. Proc.* 2: 825–830.

10 Hoffmeister, B.K., Handley, S.M., Wickline, S.A., and Miller, J.G. (1996). Ultrasonic determination of the anisotropy of Young's modulus of fixed tendon and fixed myocardium. *J. Acoust. Soc. Am.* 100: 3933–3940.

11 Kuo, P.L., Li, P.C., and Li, M.L. (2001). Elastic properties of tendon measured by two different approaches. *Ultrasound Med. Biol.* 27: 1275–1284.

12 Yoon, H.S. and Katz, J.L. (1976). Ultrasonic wave propagation in human cortical bone – I. Theoretical considerations for hexagonal symmetry. *J. Biomech.* 9: 407–412.

13 Levinson, S.F. (1987). Ultrasound propagation in anisotropic soft tissues: The application of linear elastic theory. *J. Biomech.* 20: 251–260.

14 Anderson, J. (2000) Elasticité musculaire longitudinale et transversale: influence de l'abscence de desmine – Longitudinal and transversal elasticity of muscles: influence of desmin lack. Thesis (in French), Compiègne University of Technology, France.

15 Lee, F., Bronson, J.P., Lerner, R.M., et al. (1991). Sonoelasticity imaging: Results in in vitro tissue specimens. *Radiology* 181: 237.

16 Levinson, S.F., Shinagawa, M., and Sato, T. (1995). Sonoelastic determination of human skeletal muscle elasticity. *J. Biomech.* 28: 1145–1154.

17 Gennisson, J.L., Catheline, S., Chaffaï, S., and Fink, M. (2003). Transient elastography in anisotropic medium: Application to the measurement of slow and fast shear waves velocities in muscles. *J. Acoust. Soc. Am.* 114 (1): 536–541.

18 Gennisson, J.L., Deffieux, T., Macé E., et al. (2010). Viscoelastic and anisotropic mechanical properties of in vivo muscle tissue assessed by supersonic shear imaging. *Ultrasound Med. Biol.* 36 (5): 789–801.

19 Lee, W., Larrat, B., Pernot, M., and Tanter, M. (2012). Ultrasound elastic tensor imaging: comparison with MR diffusion tensor imaging in the myocardium. *Phys. Med. Biol.* 57: 5075–5095.

20 Kittel, C. (1971). *Introduction to Solid State Physics*, 4th edn. New York: Wiley.

21 Every, A.G. (1980). General closed form expression for acoustic waves in elastically anisotropic solids. *Phys. Rev. B* 22: 1746–1760.

22 Brugger, K (1965). Pure modes for elastic waves in crystals. *J. Appl. Phys.* 38: 5366–5374.

23 Neighbours, J.R. (1967). Determination of elastic constant from sound velocity measurements in crystals of general symmetry. *J. Appl. Phys.* 38: 5366–5374.

24 Muller, K.A. and Thomas, H. (1981). *Topics in Current Physics, Structural Phase Transitions*. Heidelberg: Springer-Verlag.

25 Juretschke, H.J. (1974). *Crystal Physics*. Massachusetts: W.A. Benjamin Inc,

26 Chang, P. (1968), Pure transverse waves for elastic waves in crystals. *J. Appl. Phys.* 39 (12): 5669–5680.

27 Borgnis, F.E. (1965). Specific direction of longitudinal wave propagation in anisotropic media. *Phys. Rev.* 98 (4): 1000–1005.

28 Royer, D., Gennisson, J.L., Deffieux, T., and Tanter, M. (2011). On the elasticity of transverse isotropic soft tissues (L). *J. Acoust. Soc. Am.* 129 (5): 2757–2760.

29 Gennisson, J.L., Provost, J., Deffieux, T., et al. (2015). 4D Ultrafast shear wave imaging. *IEEE Trans. Ultrason., Ferroelect., Freq. Control* 62 (6): 1059–1065.

7

Transverse Wave Propagation in Bounded Media

Javier Brum

Laboratorio deAcustica Ultrasonora, Instituto de Fisica, Facultad de Ciencias, Universidad de la Republica, Montevideo, Uruguay

7.1 Introduction

Wave propagation in bounded media has been widely used in several fields (e.g. non-destructive evaluation, seismology, underwater acoustics) to determine different material properties. Recently, ultrasound elastography, motivated by several medical applications, has used guided waves to determine, non-invasively, the mechanical properties of plate-like tissue, such as cornea, skin, myocardium, bladder, arteries, and tendons [1–10]. In these applications, the shear wavelength ($\lambda \sim 1$–10 cm) is comparable to the tissue's thickness (e.g. ∼0.1 cm for arteries and skin, ∼1 cm for myocardium). As a consequence, the shear wave is guided within the tissue due to the successive reflections on the tissue boundaries. In this scenario, the relation between wave speed and elasticity is more complex than in the case of an infinite tissue, where the shear waves propagate in the bulk of the sample (i.e. away from the boundaries). To retrieve the bulk shear wave speed c_T and therefore the shear elasticity of the plate-like tissue, the typical sequence is the following:

- first waves are generated inside the plate
- then the transverse component of the displacement field is acquired by using an ultrafast ultrasound scanner and the wave velocity dispersion curve is extracted from the displacement field through a Fourier analysis
- finally, a given plate model is assumed (e.g. plate in water, plate in vacuum, etc.) and c_T is retrieved by fitting the theoretical dispersion curve to the experimental data.

In this context, the main goal of this chapter is to review the main features of transverse wave propagation in plate structures with application to ultrasound elastography. To this end, the theory of guided wave propagation developed for an elastic solid will be presented and revised for soft tissues in the experimental configurations encountered in ultrasound elastography. Several types of wave guides and boundary conditions adapted to different applications will be studied.

7.2 Transverse Wave Propagation in Isotropic Elastic Plates

The exact solution to the problem of wave propagation in an elastic isotropic plate has been obtained through different approaches. The two most popular approaches are the displacement potentials method and the partial wave technique (see [11] for further reading). In this chapter the partial wave technique will be used since it is more suitable to study wave propagation in anisotropic plates. Furthermore, the partial wave technique leads to more direct wave solutions and provides a deeper insight into the physical nature of the waves.

Ultrasound Elastography for Biomedical Applications and Medicine, First Edition.
Edited by Ivan Nenadic, Matthew Urban, James Greenleaf, Jean-Luc Gennisson, Miguel Bernal, and Mickael Tanter.

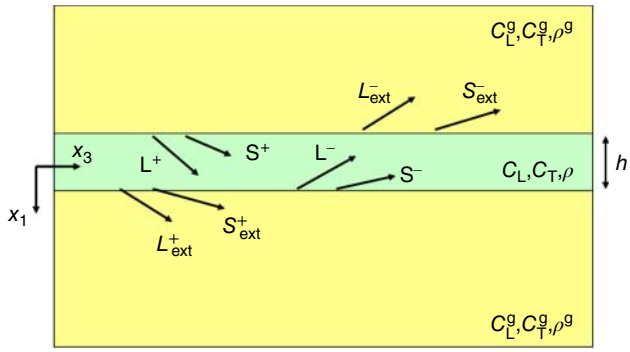

Figure 7.1 Example of sample geometry used in the partial wave technique. In each layer the partial waves ($L^{\pm}$, $S^{\pm}$) that combine to generate the guided wave are presented. Source: © 2012 IEEE, reprinted, with permission, from Brum et al. [13] .

The partial wave technique [12] is based on the fact that the field equations for the displacements and stresses in a flat plate can be written as the superposition of the fields corresponding to four bulk waves within the plate. In Figure 7.1 the case for a single plate embedded in an elastic medium is presented. Inside the plate there are four waves, two shear waves ($S^{\pm}$) and two longitudinal waves ($L^{\pm}$), propagating with positive (S^+, L^+) and negative (S^-, L^-) x_1 components. Due to refraction and mode conversion, these four waves create two kinds of waves in the surrounding medium: one shear wave and one compressional wave.

The first step of the method consists in deriving the field equations for bulk waves, which are solutions to the wave equation in an infinite medium. As a result the stresses and displacements within the plate can be expressed in terms of the amplitudes of all the bulk waves that can exist within that plate. Then by introducing the proper boundary conditions at each interface the rules for coupling between plate and surrounding medium are defined. Finally, the different boundary conditions can be combined into one global matrix which describes the entire system by relating the bulk wave amplitudes to the physical constraints.

7.2.1 Field Equations for Plane Waves in Two Dimensions

In what follows it will be assumed that the wavelengths involved are smaller than the width of the plate and therefore a plane strain analysis is valid. The plane strain hypothesis restricts the model to waves whose particle motion is entirely in the (x_1, x_3) plane, thus excluding for example shear horizontal (SH) modes. SH modes are usually not observed in ultrasound elastography since the ultrasound probe is placed parallel to the plate; however, they may be observed with other imaging modalities, such as MRI. (Please refer to references 11, 14, and 15 for further reading on SH modes and its inclusion into the general theory.)

Under a plane strain hypothesis, where there is no variation of any quantity in the x_2 direction, the coordinate system may be reduced to the plane defined by the wave propagation direction and the normal to the plate (see Figure 7.1). A convenient way of presenting the solutions for bulk waves inside the plate is by introducing Helmholtz potentials. The longitudinal waves (L) are described by a scalar potential ϕ while the shear waves (S) are described a vector potential $\vec{\psi}$ whose direction is normal to the wave propagation direction and the particle motion direction.

$$\phi = -iA_L e^{i(\vec{k}\cdot\vec{x}-\omega t)} \tag{7.1}$$

$$\vec{\psi} = -iA_S e^{i(\vec{k}\cdot\vec{x}-\omega t)}\hat{x}_2 \tag{7.2}$$

Here A_L and A_S are the longitudinal and shear wave amplitudes, $\vec{k}$ is the wavenumber vector, and ω is the angular frequency. From the potentials, the displacements of the longitudinal and shear waves can be calculated as

$$\vec{u}_L = \nabla\phi = \begin{pmatrix} k_1 \\ 0 \\ k_3 \end{pmatrix} A_L e^{i(\vec{k}\cdot\vec{x}-\omega t)} \tag{7.3}$$

$$\vec{u}_S = \nabla \times \vec{\psi} = \begin{pmatrix} -k_3 \\ 0 \\ k_1 \end{pmatrix} A_S e^{i(\vec{k}\cdot\vec{x}-\omega t)} \tag{7.4}$$

7.2.2 The Partial Wave Technique in Isotropic Plates

As stated above, the development of a model for wave motion in plates is achieved by the superposition of longitudinal and shear bulk waves and the imposition of boundary conditions at the different interfaces. For modeling the guided wave propagating along the plate it is sufficient to assume the presence of four bulk waves inside the plate: two shear waves ($S^{\pm}$) and two longitudinal waves ($L^{\pm}$). Each of these bulk waves is termed a partial wave.

Let k_3 be denoted by k, which corresponds to the wavenumber of the guided wave. Then, the k_1 component of the wave vector of each partial wave can be expressed in terms of k and the bulk wave velocities of the plate as

$$k_i = \pm\sqrt{\frac{\omega^2}{c_i^2} - k^2} \tag{7.5}$$

where the subscript $i = \mathrm{L}, \mathrm{T}$ stands for the longitudinal or shear partial wave, c_i denotes the bulk phase velocity of each type of wave in the plate and the + and − signs correspond to a wave moving with positive ("downward") and negative ("upward") x_1 component. The displacements and stresses at any location inside the plate may be found from the amplitudes of the bulk waves using the field equations. In particular, the expressions for the two displacement components u_1 and u_3, the normal stress σ_{11}, and the shear stress σ_{13} will be derived since in a plate system these quantities must be continuous over the different interfaces. From Hooke's law and the strain definition, the stresses can be calculated as

$$\sigma_{11} = \lambda\left(\frac{\partial u_1}{\partial x_1} + \frac{\partial u_3}{\partial x_3}\right) + 2\mu\frac{\partial u_1}{\partial x_1} \tag{7.6}$$

$$\sigma_{13} = \mu\left(\frac{\partial u_1}{\partial x_3} + \frac{\partial u_3}{\partial x_1}\right) \tag{7.7}$$

Thus for the longitudinal partial bulk waves it can be found

$$u_1 = \pm k_L A_{L\pm} e^{\pm i k_L x_1} \cdot e^{i(kx_3-\omega t)} \tag{7.8a}$$

$$u_3 = k A_{L\pm} e^{\pm i k_L x_1} \cdot e^{i(kx_3-\omega t)} \tag{7.8b}$$

$$\sigma_{11} = i\alpha \cdot A_{L\pm} e^{\pm i k_L x_1} \cdot e^{i(kx_3-\omega t)} \tag{7.8c}$$

$$\sigma_{13} = \pm i\beta \cdot k_L \cdot A_{L\pm} e^{\pm i k_L x_1} \cdot e^{i(kx_3-\omega t)} \tag{7.8d}$$

For the partial shear bulk waves

$$u_1 = -k \cdot A_{S\pm} e^{\pm i k_T x_1} \cdot e^{i(k x_3 - \omega t)} \tag{7.9a}$$

$$u_3 = \pm k_T A_{S\pm} e^{\pm i k_T x_1} \cdot e^{i(k x_3 - \omega t)} \tag{7.9b}$$

$$\sigma_{11} = \mp i\beta \cdot k_T \cdot A_{S\pm} e^{\pm i k_T x_1} \cdot e^{i(k x_3 - \omega t)} \tag{7.9c}$$

$$\sigma_{13} = i\alpha \cdot A_{S\pm} e^{\pm i k_T x_1} \cdot e^{i(k x_3 - \omega t)} \tag{7.9d}$$

where $\alpha = \rho(\omega^2 - 2c_T^2 k^2) = \rho c_T^2 (k_T^2 - k^2)$, $\beta = 2\rho k c_T^2$, and ρ corresponds to the medium's density. The displacements and stresses at any location in the plate may be found by summing the contributions due to the four partial wave components.

$$\begin{pmatrix} u_1 \\ u_3 \\ \sigma_{11} \\ \sigma_{13} \end{pmatrix} = \begin{pmatrix} k_L e^{i k_L x_1} & -k_L e^{-i k_L x_1} & -k e^{i k_T x_1} & -k e^{-i k_T x_1} \\ k e^{i k_L x_1} & k e^{-i k_L x_1} & k_T e^{i k_T x_1} & -k_T e^{-i k_T x_1} \\ i\alpha \cdot e^{i k_L x_1} & i\alpha \cdot e^{-i k_L x_1} & -i\beta \cdot k_T \cdot e^{i k_T x_1} & i\beta \cdot k_T \cdot e^{-i k_T x_1} \\ i\beta \cdot k_L \cdot e^{i k_L x_1} & -i\beta \cdot k_L \cdot e^{-i k_L x_1} & i\alpha \cdot e^{i k_T x_1} & i\alpha \cdot e^{-i k_T x_1} \end{pmatrix} \begin{pmatrix} A_{L+} \\ A_{L-} \\ A_{S+} \\ A_{S-} \end{pmatrix} \tag{7.10}$$

The matrix in Eq. (7.10) describes the relation between the wave amplitudes and the displacements and stresses at any position inside the plate. Its coefficients depend on the through-thickness position inside the plate, i.e. x_1; the material properties of the layer, i.e. ρ, c_T, c_L; and the frequency and wavenumber of the guided wave.

By using Eq. (7.10) it is possible to combine all the different boundary conditions at each interface into a single global matrix $[G]$ which represents the entire system [12]. The columns of the global matrix correspond to the amplitudes of the partial wave at each interface, while the rows correspond to each boundary condition. Thus, by multiplying the global matrix $[G]$ by a vector $\{A\}$ containing the partial wave amplitudes, all boundary conditions will be satisfied simultaneously. The resulting equation will always be zero providing the characteristic equation of the system

$$[G] \cdot \{A\} = 0 \tag{7.11}$$

To obtain non-trivial solutions for the vector of partial wave amplitudes $\{A\}$, the determinant of the global matrix in Eq. (7.11) must be zero. This constraint will allow only particular wave numbers k for a given frequency. By changing the frequency it is possible to find the relation $c(\omega) = \omega/k(\omega)$, where c is the phase velocity of the guided wave, i.e. the phase velocity dispersion curve. The phase velocity dispersion curve is the quantity that is usually measured in ultrasound elastography. Consequently, to retrieve the bulk shear wave speed c_T and therefore the shear elasticity of the plate, it is necessary to fit the experimental dispersion curve to a given plate model. In what follows several plate models will be presented along with their different applications and consequences in ultrasound elastography.

7.3 Plate in Vacuum: Lamb Waves

Let us now apply Eq. (7.10) to study transverse wave propagation in an elastic plate in vacuum (i.e. Lamb waves). Although this situation is difficult to meet in practice it will be helpful to establish some basic concepts of guided wave propagation. These concepts will be used later in more complex situations. Let h be the thickness of the plate. For a plate in a vacuum, the

normal stresses should vanish at each interface (i.e. traction-free condition): $\sigma_{11} = \sigma_{13} = 0$ at $x_1 = \pm h/2$. Under this condition Eq. (7.10) results in

$$0 = \begin{pmatrix} \sigma_{11}|_{-\frac{h}{2}} \\ \sigma_{13}|_{-\frac{h}{2}} \\ \sigma_{11}|_{\frac{h}{2}} \\ \sigma_{13}|_{\frac{h}{2}} \end{pmatrix} = \begin{pmatrix} \alpha \cdot e^{-ik_L h/2} & \alpha \cdot e^{ik_L h/2} & -\beta \cdot k_T \cdot e^{-ik_T h/2} & \beta \cdot k_T \cdot e^{ik_T h/2} \\ \beta \cdot k_L \cdot e^{-ik_L h/2} & -\beta \cdot k_L \cdot e^{ik_L h/2} & \alpha \cdot e^{-ik_T h/2} & \alpha \cdot e^{ik_T h/2} \\ \alpha \cdot e^{ik_L h/2} & \alpha \cdot e^{-ik_L h/2} & -\beta \cdot k_T \cdot e^{ik_T h/2} & \beta \cdot k_T \cdot e^{-ik_T h/2} \\ \beta \cdot k_L \cdot e^{ik_L h/2} & -\beta \cdot k_L \cdot e^{-ik_L h/2} & \alpha \cdot e^{ik_T h/2} & \alpha \cdot e^{-ik_T h/2} \end{pmatrix} \begin{pmatrix} A_{L+} \\ A_{L-} \\ A_{S+} \\ A_{S-} \end{pmatrix} \tag{7.12}$$

By combining rows and columns, the determinant of Eq. (7.12), which determines the phase velocity dispersion curve, gives

$$\det(G) = \begin{vmatrix} \alpha \cdot \cos(k_L h/2) & -\beta k_T \sin(k_T h/2) \\ -i\beta k_L \cdot \sin(k_L h/2) & -i\alpha \sin(k_T h/2) \end{vmatrix} \begin{vmatrix} \beta k_L \cos(k_L h/2) & \alpha \cos(k_T h/2) \\ -i\alpha \sin(k_L h/2) & i\beta k_T \sin(k_T h/2) \end{vmatrix} = 0 \tag{7.13}$$

As described by Eq. (7.13), the determinant of the global matrix is calculated as a product of two determinants. Each determinant corresponds to one particular mode of propagation: the one on the left corresponds to the symmetric modes while the one on the right to corresponds to the anti-symmetric modes. For the symmetric modes the longitudinal component of the displacement field (u_3) is an even function of x_1 while the transverse component (u_1) is an odd function of x_1. On the contrary, for the anti-symmetric modes, while u_3 is an even function, u_1 is an odd function of x_1. Consequently, for each mode, the plate movement is either symmetric or anti-symmetric with respect to the median plane of the plate. In Figure 7.2 the phase velocity dispersion curve along with a schematic of the plate movement is presented for the different modes. The anti-symmetric and symmetric modes are denoted with letters A_n and S_n respectively, where the subscript $n = 0, 1, 2, ..$ indicates the order of the mode.

By expanding each determinant in Eq. (7.13) the following characteristic equation is found for the symmetric (Eq. 7.14) and anti-symmetric modes (Eq. 7.15) respectively

$$(k_T^2 - k^2)^2 \cos(k_L h/2) \sin(k_T h/2) + 4k^2 k_L k_T \sin(k_L h/2) \cos(k_T h/2) = 0 \tag{7.14}$$

$$(k_T^2 - k^2)^2 \sin(k_L h/2) \cos(k_T h/2) + 4k^2 k_L k_T \cos(k_L h/2) \sin(k_T h/2) = 0 \tag{7.15}$$

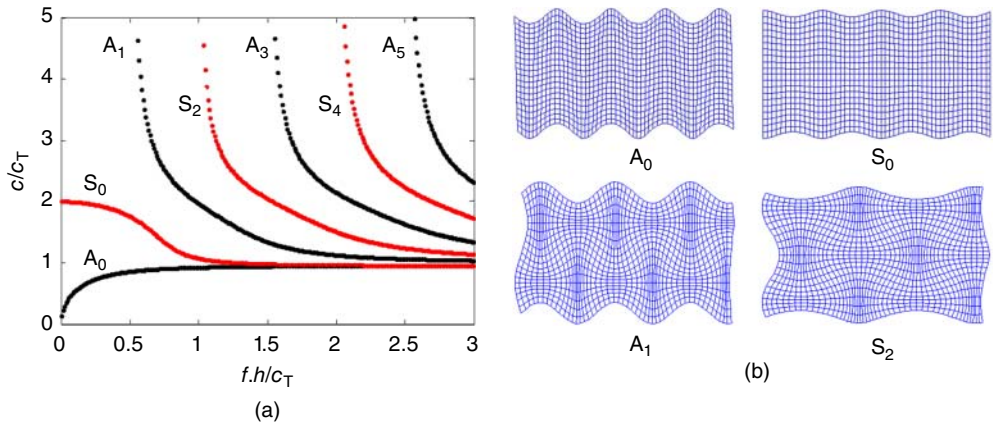

Figure 7.2 (a) Wave velocity dispersion curves for an isotropic plate in vacuum presented in dimensionless variables c/c_T and $f{\cdot}h/c_T$. The longitudinal wave speed was set to 1500 m/s. (b) Schematic of the plate displacement field for the first four modes for $f{\cdot}h/c_T = 1.5$.

7.3.1 Low Frequency Approximation for Modes with Cut-off Frequency

It may be observed in Figure 7.2 that several modes ($n > 0$) present a cut-off frequency. Near the cut-off frequency $c \to \infty$ therefore $k \to 0$, $k_T \to \omega/c_T$ and $k_L \to \omega/c_L$. Consequently, from Eq. (7.10), the displacement field and stresses near the cut-off frequency may be expressed as

$$u_1 = k_L(A_{L+} - A_{L-})\cos(k_L x_1) + ik_L(A_{L+} + A_{L-})\sin(k_L x_1) \tag{7.16}$$

$$u_3 = ik_T(A_{S+} + A_{S-})\sin(k_T x_1) + k_T(A_{S+} - A_{S-})\cos(k_T x_1) \tag{7.17}$$

$$\sigma_{11} = i\rho\omega^2[i(A_{L+} - A_{L-})\sin(k_L x_1) + (A_{L+} + A_{L-})\cos(k_L x_1)] \tag{7.18}$$

$$\sigma_{13} = i\rho\omega^2[(A_{S+} + A_{S-})\cos(k_T x_1) + (A_{S+} - A_{S-})\sin(k_T x_1)] \tag{7.19}$$

where the first term of each equation corresponds to the anti-symmetric modes and the second to the symmetric modes. For the symmetric modes, the even solutions S_{2n} ($n = 1, 2, ..$) correspond to an even displacement field, therefore $(A_{L+} + A_{L-}) = 0$. Consequently, the corresponding boundary condition gives

$$\sin\left(\frac{k_T h}{2}\right) = 0 \to \frac{\omega_c h}{c_T} = n\pi \to f_c = \frac{nc_T}{h} \tag{7.20}$$

This corresponds to a pure longitudinal symmetric mode. On the contrary, the odd solutions S_{2m+1} with $m = 0, 1, 2, ..$, correspond to $(A_{S+} - A_{S-}) = 0$, giving

$$\cos\left(\frac{k_L h}{2}\right) = 0 \to \frac{\omega_c h}{c_L} = \frac{(2m+1)\pi}{2} \to f_c = \frac{\left(m + \frac{1}{2}\right)c_L}{h} \tag{7.21}$$

which corresponds to a pure transverse mode. For the anti-symmetric modes the same reasoning yields the following cut-off frequencies

$$f_c = nc_L/h \tag{7.22}$$

$$f_c = \left(m + \frac{1}{2}\right)c_T/h \tag{7.23}$$

for the even (A_2, A_4, ..) and odd ($A_1, A_3, ..$) anti-symmetric modes respectively.

At this point, it is important to notice the consequences of Eqs. (7.20–7.22) for Lamb wave propagation in soft tissues. In ultrasound elastography $c_L \sim 1500$ m/s, $c_T \sim 1$–20 m/s, $h \sim 1$–20 mm, and the frequency is usually below 2 kHz. Therefore, the even anti-symmetric and the odd symmetric modes will not be generated in an ultrasound elastography experiment since the lowest f_c for these modes is ~ 7.5 kHz (Eq. 7.21). On the contrary, the presence of the even symmetric modes and the odd anti-symmetric modes will depend on frequency and on the ratio c_T/h (Eqs. 7.20 and 7.23). For tissues such as skin, arteries, bladder, or cornea where $h \sim 1$–3 mm, the f_c for these modes will lie in the kHz range and they will not be generated. Consequently, for these kind of tissues the only modes that may be expected are the zero-order symmetric (S_0) and anti-symmetric (A_0) modes, which have no cut-off frequency. For other types of tissue, e.g. the myocardium, where $h \sim 1$ cm and $c_T \sim 5$ m/s, the cut-off frequencies for A_1 is ~250 Hz, for S_2 is ~500 Hz, etc. Therefore, these modes may eventually coexist with the S_0 and A_0 modes, depending on the type of source, frequency, plate thickness, and shear elasticity involved in the experiments. It is important to point out, that although these modes may theoretically be present, to our knowledge they have not been detected yet in a plate of soft tissue. This may be explained by the fact that, as seen above, the odd anti-symmetric and symmetric modes are mainly longitudinal near the cut-off frequencies, which, combined with

a strong attenuation for frequencies above ~400 Hz (i.e. tissue is by nature viscoelastic), makes it very difficult to detect them in the experiments. Consequently, the most common situation in an elastography experiment is the presence of the S_0 and A_0 modes. Let us briefly present the main features of these modes.

7.3.2 Modes Without Cut-off Frequencies

In the low-frequency approximation, i.e. as k and ω approach to zero, Eq. (7.14) and Eq. (7.15) may be reduced to

$$\frac{\omega^4}{c_T^4} = 4k^2\omega^2\left(\frac{1}{c_T^2} - \frac{1}{c_L^2}\right) \tag{7.24}$$

$$\frac{\omega^4}{c_T^4} = \frac{4}{3}h^2k^2\frac{\omega^2}{c_T^2}\left(\frac{1}{c_L^2} - \frac{1}{c_T^2}\right) \tag{7.25}$$

From Eq. (7.24), the phase velocity for S_0 tends to a finite limit given by $2c_T\sqrt{1 - c_T^2/c_L^2}$, which for a soft tissue ($c_L \gg c_T$) may be approximated as $2c_T$. Additionally, it may demonstrated that when $kh \ll 1$, the S_0 mode is essentially longitudinal, i.e. $u_1/u_3 \ll 1$ [15]. Since soft tissue is incompressible, a longitudinal displacement will generate a small but non-negligible transverse displacement (see Figure 7.2b), therefore, this mode may be eventually detected by using ultrasound elastography. Additionally, the velocity of the mode is close to c_T and may be followed by an ultrafast scanner. For A_0, by using Eq. (7.25), it may be demonstrated that its phase velocity may be approximated as

$$c = \sqrt{c_T\omega h/\sqrt{3}} \tag{7.26}$$

Therefore, by fitting this expression to the experimental dispersion curve the value of c_T may be retrieved without cumbersome determinant calculations. In the high-frequency region, i.e. $h \gg 1$, the velocities of the S_0 and A_0 approach to Rayleigh wave velocity which is $\sim 0.95c_T$. Therefore the phase velocity for the S_0 and A_0 modes will always lie between zero and $2c_T$.

Finally, it is important to point out that the generation of each mode will not only depend on the frequency, but also on the type of source used in the experiments [11]. A type of source which is common in ultrasound elastography is the radiation force of ultrasound. This type of source acts all along the thickness of the plate in a direction perpendicular to the plate, generating mainly the A_0 mode, which is a flexural mode (Figure 7.2b).

7.4 Viscoelastic Plate in Liquid: Leaky Lamb Waves

Let us study a more realistic situation than a plate in vacuum. The model of a viscoelastic plate surrounded by non-viscous fluid has widely been used to determine in vivo and ex vivo the shear elasticity and viscosity of several types of tissues, e.g. arteries [6, 7], cornea [1, 16, 17], bladder [5], and myocardium [3, 18]. In these works the Lamb waves were generated by using the acoustic radiation force of focused ultrasound, generating only A_0 mode. Therefore, in what follows, special attention will be devoted to this specific mode of propagation.

7.4.1 Elastic Plate in Liquid

Let us derive the dispersion equation for an elastic plate in liquid by using the partial wave technique introduced in Section 7.2.2. For a plate embedded in a non-viscous fluid of density ρ_{liq} and longitudinal wave velocity c_{liq}, six partial waves should be taken into account. The four

waves inside the plate create two longitudinal waves (L^+_{ext}, L^-_{ext}) in the surrounding fluid. By applying the continuity at each interface of u_1, σ_{11}, and σ_{13} the global matrix governing the system can be written as

$$[G] = \begin{pmatrix} -k_{liq}F_{liq} & -k_L F_L^* & k_L F_L & kF_T^* & kF_T & 0 \\ i\alpha_{liq}F_{liq} & -i\alpha F_L^* & -i\alpha F_L & i\beta k_T F_T^* & -i\beta k_T F_T & 0 \\ 0 & -i\beta k_L F_L^* & i\beta k_L F_L & -i\alpha F_T^* & -i\alpha F_T & 0 \\ 0 & k_L F_L & -k_L F_L^* & -kF_T & -kF_T^* & -k_{liq}F_{liq} \\ 0 & i\alpha F_L & i\alpha F_L^* & -i\beta k_T F_T & i\beta k_T F_T^* & -i\alpha_{liq}F_{liq} \\ 0 & i\beta k_L F_L & -i\beta k_L F_L^* & i\alpha F_T & i\alpha F_T^* & 0 \end{pmatrix} \tag{7.27}$$

where * denotes complex conjugate, $F_{L,T} = e^{ik_{L,T}h/2}$, and F_{liq}, α_{liq}, k_{liq} correspond to the surrounding liquid. By combining rows and columns the determinant of $[G]$ may be calculated as a product of two sub-determinants which give the following characteristic equations

$$(k_T^2 - k^2)^2 \cos\left(\frac{k_L h}{2}\right) \sin\left(\frac{k_T h}{2}\right) + 4k^2 k_L k_T \sin\left(\frac{k_L h}{2}\right) \cos\left(\frac{k_T h}{2}\right) + i\frac{\rho_{liq} k_L \omega^4}{\rho k_{liq} c_T^4} \sin\left(\frac{k_L h}{2}\right) \sin\left(\frac{k_T h}{2}\right) = 0 \tag{7.28}$$

$$(k_T^2 - k^2)^2 \sin\left(\frac{k_L h}{2}\right) \cos\left(\frac{k_T h}{2}\right) + 4k^2 k_L k_T \cos\left(\frac{k_L h}{2}\right) \sin\left(\frac{k_T h}{2}\right) + i\frac{\rho_{liq} k_L \omega^4}{\rho k_{liq} c_T^4} \cos\left(\frac{k_L h}{2}\right) \cos\left(\frac{k_T h}{2}\right) = 0 \tag{7.29}$$

Equations (7.28) and (7.29) correspond to the symmetric and anti-symmetric modes respectively. It is important to notice that these equations differ from the equations for a plate in vacuum (Eqs. 7.14 and 7.15) by one term which takes into account the contribution of the fluid. In Figure 7.3 the phase velocity dispersion curves for the different modes for a plate in water (circles) are compared to the dispersion curves for a plate in vacuum (black dots).

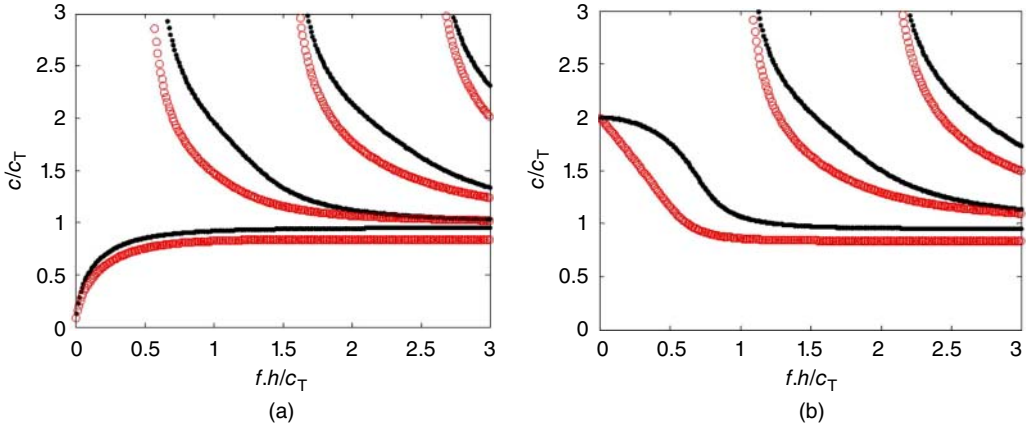

Figure 7.3 Wave velocity dispersion curves for an isotropic plate in a non-viscous fluid (i.e. leaky Lamb mode) shown in circles and a plate in vacuum shown in black dots. For both figures, (a) anti-symmetric and (b) symmetric modes, $\rho = \rho_{liq} = 1000$ kg/m^3 and $c_L = c_{liq} = 1500$ m/s.

7.4.1.1 Leakage into the Fluid

Contrary to what happens for a plate in a vacuum, where the acoustic energy is trapped inside the plate, for a plate surrounded by fluid the energy may leak into the surrounding medium. Leakage may be described by an amplitude exponential reduction with distance along the plate, which can be expressed by a complex wavenumber $k = k_r + ik_i$. The real part of the wavenumber is related to the phase velocity and describes the harmonic wave propagation while the imaginary part describes the wave attenuation in space.

Leakage will depend on the ratio between the phase velocity of each mode and the bulk velocities of the plate. Snell's law requires that all the partial waves share the same frequency and spatial properties in the x_3 direction at each interface. This constrains the angles of incidence, transmission, and reflection of the partial waves inside the plate by

$$\frac{k}{\omega} = \frac{1}{c} = \frac{\sin(\theta_L)}{c_L} = \frac{\sin(\theta_T)}{c_T} = \frac{\sin(\theta_{liq})}{c_{liq}} \tag{7.30}$$

where θ_i are the angles at which longitudinal and shear partial waves propagate with respect to the x_1 direction. Therefore, a leakage angle, θ_{leak}, may be determined as $\sin^{-1}(c_{liq}/c)$. Therefore, if $c < c_{liq}$, the leakage angle would be imaginary, which means that instead of creating a wave that propagates away from the plate, the displacements will decay exponentially and energy will be trapped in the fluid region close to the plate. [The same conclusion is obtained from Eq. (7.5): if ω^2/c_{liq}^2 is smaller than k^2 then k_{liq} is imaginary and the wave is evanescent in the x_1 direction.] Consequently, a mode will not leak if its phase velocity is less than the bulk velocity of any waves that can exist in the surrounding medium. In elastography, since $c_L \cong c_{liq}$ and $c_T \ll c_{liq}$, the phase velocities of the different measurable modes will be lower than c_{liq} (see Figure 7.3) and no leakage should be considered. Therefore, when solving Eqs. (7.28) and (7.29) real values of k should be searched.

7.4.2 Viscoelastic Plate

Another source of wave attenuation is viscosity, which is inherent to any type of tissue. In many applications viscosity had to be taken into account to properly model the guided wave propagation. To introduce viscosity, the elastic constant μ will no longer be considered as a real number but as a complex number instead. For example, if the frequency dependence is assumed to obey a Voigt model, as it was assumed in previous works [3, 9, 18], then μ may be written as

$$\mu = \mu_1 + i\omega\eta \tag{7.31}$$

where μ_1 is the elastic component and η is the viscous component or viscosity. [Other rheological models, such as Maxwell or Zener, will introduce different relations than the one presented in Eq. (7.31); please refer to Fung [19] for further details.] It is important to note that the partial wave technique still remains valid in the presence of viscosity [12]; however, to solve Eqs. (7.28) and (7.29) complex wavenumbers k should be searched: the real part is related to the phase velocity and the imaginary part is related to wave attenuation. In Figure 7.4 the phase velocity and attenuation dispersion curves for different values of viscosity are presented. In this figure $c_T = \sqrt{\mathrm{Re}[\mu]/\rho}$, with Re[ ] being the real part.

From Figure 7.4, it is important to point out, that while the phase velocity dispersion curve differs from the pure elastic case (the solid line) for values of $f \cdot h/c_T > 0.15$, for $f \cdot h/c_T < 0.1$ they practically remain unchanged when viscosity is added. On the other hand, the attenuation dispersion curve is clearly sensitive to viscosity. This effect has already been observed by Nguyen et al. [2] for Lamb waves in viscoelastic isotropic plates and by Brum et al. [9] for guided wave propagation in the Achilles tendon. Consequently, for low values of $f \cdot h/c_T$, the elasticity constant associated with the guided wave can be retrieved directly from the phase

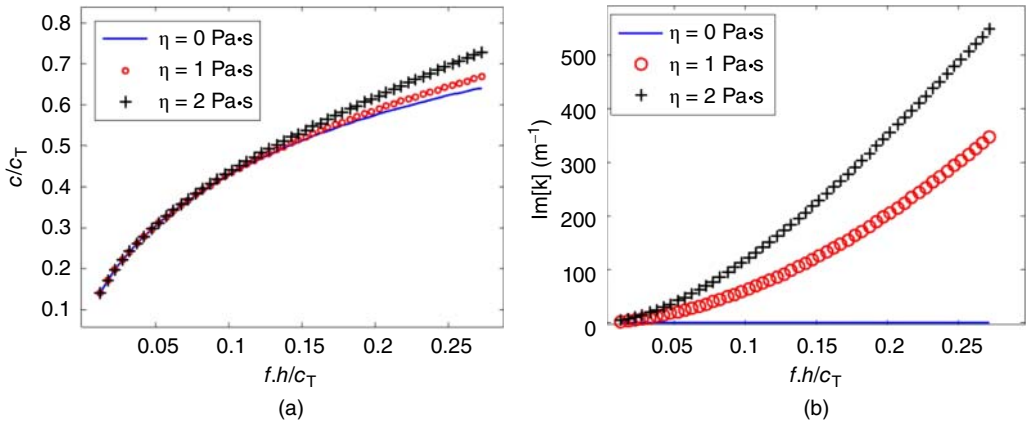

Figure 7.4 (a) Phase velocity and (b) attenuation dispersion curves for the A_0 mode in a viscoelastic plate in water for different values of viscosity η.

velocity dispersion curve independently of the viscosity effects, i.e. elasticity and viscosity are uncoupled.

7.4.3 Empirical Formula

An empirical formula (Eq. 7.32) was first proposed by Couade et al. [6] to retrieve the shear modulus of the arterial wall from the A_0 dispersion curve by assuming the artery to behave as an elastic plate in water.

$$c = \sqrt{\frac{\omega h c_T}{2\sqrt{3}}} \tag{7.32}$$

This formula introduces a correction factor of $1/\sqrt{2}$ when compared to the low-frequency approximation of the A_0 mode for a plate in vacuum (Eq. 7.26).

The validity of this empirical formula was discussed in the work of Nguyen et al. [2] in the case of thin elastic plates submerged in water. In this work, Eq. (7.32) was tested for plate thicknesses and shear wave speeds ranging between 0.5 and 1.5 mm and 5 and 10 m/s respectively, showing that the relative deviation of the empirical formula from simulated dispersion curves is as much as 15% for the thickest and softest plates. However, its deviation was less than 5% for plates of 1 mm thickness whose shear wave speeds were greater than 10 m/s. Therefore, this empirical formula is suitable for some particular applications, e.g. elasticity estimation of cornea, skin, or the arterial wall.

7.5 Isotropic Plate Embedded Between Two Semi-infinite Elastic Solids

The model of an isotropic plate surrounded by two semi-infinite elastic solids of bulk waves speed $c_{L,T}^{g1}$ and $c_{L,T}^{g2}$ has been used in vitro by Brum et al. [13] to measure the elasticity of thin plates embedded in an elastic solid and numerically by Couade et al. [6] to establish the bias of the Leaky lamb model used in their work with respect to other plate models with more realistic boundaries conditions.

For a plate embedded in an elastic medium eight partial waves should be taken into account (see Figure 7.1). The four waves inside the plate create two kinds of waves in the surrounding medium: one shear and one longitudinal wave propagating with positive (L^+_{ext}, S^+_{ext}) and negative (L^-_{ext}, S^-_{ext}) x_1 component. As a consequence at each interface six partial waves should be taken into account. By applying the continuity at each of the interfaces of u_1, u_3, σ_{11}, and σ_{13} the global matrix governing the system can be written as

$$[G] = \begin{pmatrix} -k_L^{g_1}\cdot F_L^{g_1} & -k\cdot F_T^{g_1} & -k_L\cdot F_L^* & k_L\cdot F_L & k\cdot F_T^* & k\cdot F_T & 0 & 0 \\ k\cdot F_L^{g_1} & -k_T^{g_1}\cdot F_T^{g_1} & -k\cdot F_L^* & -k\cdot F_L & -k_T\cdot F_T^* & k_T\cdot F_T & 0 & 0 \\ i\alpha^{g_1}\cdot F_L^{g_1} & i\beta^{g_1}\cdot k_T^{g_1}\cdot F_T^{g_1} & -i\alpha\cdot F_L^* & -i\alpha\cdot F_L & i\beta\cdot k_T\cdot F_T^* & -i\beta\cdot k_T\cdot F_T & 0 & 0 \\ -i\beta^{g_1}\cdot k_L^{g_1}\cdot F_L^{g_1} & i\alpha^{g_1}\cdot F_T^{g_1} & -i\beta\cdot k_L\cdot F_L^* & i\beta\cdot k_L\cdot F_L & -i\alpha\cdot F_T^* & -i\alpha\cdot F_T & 0 & 0 \\ 0 & 0 & k_L\cdot F_L & -k_L\cdot F_L^* & -k\cdot F_T & -k\cdot F_T^* & -k_L^{g_2}\cdot F_L^{g_2} & k\cdot F_T^{g_2} \\ 0 & 0 & k\cdot F_L & k\cdot F_L^* & +k_T\cdot F_T & -k_T\cdot F_T^* & -k\cdot F_L^{g_2} & -k_T^{g_2}\cdot F_T^{g_2} \\ 0 & 0 & i\alpha\cdot F_L & i\alpha\cdot F_L^* & -i\beta\cdot k_T\cdot F_T & i\beta\cdot k_T\cdot F_T^* & -i\alpha^{g_2}\cdot F_L^{g_2} & \beta^{g_2}\cdot k_T^{g_2}\cdot F_T^{g_2} \\ 0 & 0 & i\beta\cdot k_L\cdot F_L & -i\beta\cdot k_L\cdot F_L^* & i\alpha\cdot F_T & i\alpha\cdot F_T^* & -i\beta^{g_2}\cdot k_L^{g_2}\cdot F_L^{g_2} & -i\alpha^{g_2}\cdot F_T^{g_2} \end{pmatrix} \begin{matrix} \to u_1(-h/2) \\ \to u_3(-h/2) \\ \to \sigma_{11}(-h/2) \\ \to \sigma_{13}(-h/2) \\ \to u_1(h/2) \\ \to u_3(h/2) \\ \to \sigma_{11}(h/2) \\ \to \sigma_{13}(h/2) \end{matrix}$$

$$\begin{matrix} L^-_{ext} & S^-_{ext} & L^+ & L^- & S^+ & S^- & L^+_{ext} & S^+_{ext} \end{matrix} \quad (7.33)$$

For the equation of F, α, and β with a superscript g_i with $i = 1,2$, the bulk wave speeds and density of each semi-infinite solid should be used. For the particular case of $c^{g1}_{L,T} = c^{g2}_{L,T} = c^{g}_{L,T}$, Brum et al. [13] demonstrated that the determinant of $[G]$ may be reduced to a product of two determinants

$$\det(G) = \begin{vmatrix} -k_L^g & -k & k_L\cdot\cos\left(\frac{k_L h}{2}\right) & k\cdot\cos\left(\frac{k_T h}{2}\right) \\ k & -k_T^g & -i\cdot k\cdot\sin\left(\frac{k_L h}{2}\right) & i\cdot k_T\cdot\sin\left(\frac{k_T h}{2}\right) \\ i\alpha^g & i\beta^g\cdot k_T^g & \alpha\cdot\sin\left(\frac{k_L h}{2}\right) & \beta\cdot k_T\cdot\sin\left(\frac{k_T h}{2}\right) \\ -i\beta^g\cdot k_L^g & i\alpha^g & i\cdot\beta\cdot k_L\cdot\cos\left(\frac{k_L h}{2}\right) & -i\alpha\cdot\cos\left(\frac{k_T h}{2}\right) \end{vmatrix} \cdot \begin{vmatrix} i\cdot k_L\cdot\sin\left(\frac{k_L h}{2}\right) & i\cdot k\cdot\sin\left(\frac{k_T h}{2}\right) & -k_L^g & k \\ k\cdot\cos\left(\frac{k_L h}{2}\right) & -k_T\cdot\cos\left(\frac{k_T h}{2}\right) & -k & -k_T^g \\ i\cdot\alpha\cdot\cos\left(\frac{k_L h}{2}\right) & i\cdot\beta\cdot k_T\cdot\cos\left(\frac{k_T h}{2}\right) & -i\alpha^g & i\cdot\beta^g\cdot k_T^g \\ -\beta\cdot k_L\cdot\sin\left(\frac{k_L h}{2}\right) & \alpha\cdot\sin\left(\frac{k_T h}{2}\right) & -i\beta^g\cdot k_L^g & -i\alpha^g \end{vmatrix} = 0 \quad (7.34)$$

The determinant on the left corresponds to the anti-symmetric modes and the one on the right to the symmetric modes. Since the plate is embedded in an elastic medium, leakage will occur whenever the phase velocity of the guided wave c exceeds one of the bulk wave velocities of the surrounding medium. Since in elastography $c \ll c_L$, leakage will mainly depend whether c is greater or less than the shear wave speed of the surrounding medium. Therefore, complex wavenumbers should be searched when solving Eq. (7.34).

7.6 Transverse Wave Propagation in Anisotropic Viscoelastic Plates Surrounded by Non-viscous Fluid

Transverse isotropic tissue like tendons and muscles are commonly present in ultrasound elastography. Recently, guided wave propagation along a transverse isotropic plate has been used to model shear wave propagation in vivo in the human Achilles tendon [9, 10]. Another example lies in the cornea [17]. Let us briefly describe the main features of guided wave propagation along transverse isotropic plates.

For an isotropic solid only two constants (i.e. Lamé constants) are needed to characterize it. On the contrary, for a transverse isotropic solid the Christoffel's tensor C_{ij} describing the system is composed of five independent elastic constants: C_{11}, C_{33}, C_{13}, C_{55}, and C_{66}. In an infinite

transverse isotropic medium the elastic constants C_{11}, C_{33}, and C_{13} can be determined from the measurement of longitudinal ultrasound phase velocities along the perpendicular and parallel directions, respectively. Moreover, the elastic constants C_{55} and C_{66} can be deduced from the phase velocity measurement of shear waves propagating either parallel or perpendicular to the fibre direction with a polarization perpendicular to the fibers [20]. However, in a transverse isotropic plate the relation between phase velocity and elasticity is more complex. Let us use the partial wave technique to derive the secular equation for a transverse isotropic plate. Two situations will be considered: k parallel and perpendicular to the fiber orientation.

7.6.1 Guided Wave Propagation Parallel to the Fibers

Let us first consider the case where the wave propagation direction is parallel to the fibers. A plane wave traveling in an arbitrary direction x may be written as

$$\vec{u} = \vec{A} \cdot e^{i(\vec{\mathbf{k}} \cdot \vec{\mathbf{x}} - \omega t)} \tag{7.35}$$

where $\vec{\mathbf{U}}$ is the displacement vector and $\vec{\mathbf{A}}$ is its amplitude. Under a plane strain condition, the nature of the bulk plane waves which can exist within a transverse isotropic plate are determined by Christoffel's equation

$$\rho\omega^2 A_i = \sum_{j,k,l} C_{ijkl} k_k k_j A_l \tag{7.36}$$

Thus, by combining Eq. (7.35) and Eq. (7.36), the following equations relating the plane wave amplitudes A_1 and A_3 are deduced

$$\rho\omega^2 A_1 = C_{11}k_1^2 A_1 + (C_{55} + C_{13})k_1 k_3 A_3 + C_{55}k_3^2 A_1 \tag{7.37}$$

$$\rho\omega^2 A_3 = C_{33}k_3^2 A_3 + (C_{55} + C_{13})k_1 k_3 A_1 + C_{55}k_1^2 A_3 \tag{7.38}$$

From Eq. (7.37) it is possible to express the ratio R between the wave amplitudes A_1 and A_3 as

$$R \equiv \frac{A_3}{A_1} = \frac{\rho\omega^2 - C_{11}k_1^2 - k_3^2 C_{55}}{(C_{55} + C_{13})k_1 k_3} \tag{7.39}$$

By eliminating A_1 and A_3 from Eq. (7.38) by using Eq. (7.39), the following quadratic equation for k_1 in terms of k and the elastic constants is deduced

$$k_1^2 = \frac{k_3^2}{2}(-B \pm \sqrt{B^2 - 4D}) \tag{7.40}$$

where B and D are given by

$$B = \frac{-(C_{55} + C_{13})^2 - (\rho\omega^2/k^2)(C_{55} + C_{11})}{C_{11}C_{55}} + \frac{C_{11}C_{33} + C_{55}^2}{C_{11}C_{55}} \tag{7.41}$$

$$D = \frac{\rho\omega^2}{k^2}\frac{\rho\omega^2/k^2 - C_{33}}{C_{11}C_{55}} - \frac{\rho\omega^2}{k^2}\frac{1}{C_{11}} + \frac{C_{33}}{C_{11}} \tag{7.42}$$

Let us define k_p and k_m as the two values of k_1 obtained from Eq. (7.40) with + and – signs respectively. Also, R_p and R_m will denote the value of R when k_p and k_m are respectively substituted in Eq. (7.39).

The equations above, derived for bulk plane waves propagating in an unbounded transverse isotropic medium, predict the presence of four partial waves. These partial waves are the equivalent of the two shear and the two longitudinal partial waves described in the case of an isotropic

plate described in Section 7.2. Consequently, the displacements inside the plate may be written as a superposition of partial waves

$$u_1 = e^{i(kx_3-\omega t)}\left[A_{p+}e^{ik_p x_1} + A_{p-}e^{-ik_p x_1} + A_{m+}e^{ik_m x_1} + A_{m-}e^{-ik_m x_1}\right] \tag{7.43}$$

$$u_3 = e^{i(kx_3-\omega t)}\left[R_p A_{p+}e^{ik_p x_1} - R_p A_{p-}e^{-ik_p x_1} + R_m A_{m+}e^{ik_m x_1} - R_m A_{m-}e^{-ik_m x_1}\right] \tag{7.44}$$

where the subscript i = p,m stands for the partial wave propagating with wave number component k_p and k_m respectively. By coupling these displacements along with the stresses ($\sigma_{11} = C_{11}(\partial u_1/\partial x_1) + C_{13}(\partial u_3/\partial x_3)$ and $\sigma_{13} = C_{13}(\partial u_1/\partial x_3 + \partial u_3/\partial x_1)$ to the ones of the surrounding fluid, the global matrix gives

$$[G] = \begin{pmatrix} X & X^{-1} & Y & Y^{-1} & k_{liq}e^{ik_{liq}h/2} & 0 \\ X^{-1} & X & Y^{-1} & Y & 0 & k_{liq}e^{ik_{liq}h/2} \\ G_p X & -G_p X^{-1} & G_m Y & -G_m Y^{-1} & \rho_{liq}\omega^2 e^{ik_{liq}h/2} & 0 \\ G_p X^{-1} & -G_p X & G_m Y^{-1} & -G_m Y & 0 & -\rho_{liq}\omega^2 e^{ik_{liq}h/2} \\ H_p X & H_p X^{-1} & H_m Y & H_m Y^{-1} & 0 & 0 \\ H_p X^{-1} & H_p X & H_m Y^{-1} & H_m Y & 0 & 0 \end{pmatrix} \begin{matrix} \rightarrow u_1(h/2) \\ \rightarrow u_1(-h/2) \\ \rightarrow \sigma_{11}(h/2) \\ \rightarrow \sigma_{11}(-h/2) \\ \rightarrow \sigma_{33}(h/2) \\ \rightarrow \sigma_{33}(-h/2) \end{matrix}$$

$$\begin{matrix} A_{p+} & A_{p-} & A_{m+} & A_{m-} & A_+^F & A_-^F \end{matrix} \tag{7.45}$$

where $X = e^{ik\text{p.h}/2}$, $Y = e^{ik\text{m.h}/2}$, $G_{p,m} = C_{11}k_{p,m} + C_{13}R_{p,m}.k$, $H_{p,m} = R_{p,m}k_{p,m} + k$. By combining columns and rows, the determinant of the global matrix can be calculated as follows

$$|G| = \begin{vmatrix} \cos(k_p h/2) & \cos(k_m h/2) & k_{liq}e^{ik_{liq}h/2} \\ iG_p \sin(k_p h/2) & iG_m \sin(k_m h/2) & \rho_{liq}\omega^2 e^{ik_{liq}h/2} \\ H_p \cos(k_p h/2) & H_m \cos(k_m h/2) & 0 \end{vmatrix} \begin{vmatrix} i\sin(k_p h/2) & i\sin(k_m h/2) & k_{liq}e^{ik_{liq}h/2} \\ G_p \cos(k_m h/2) & G_p \cos(k_m h/2) & \rho_{liq}\omega^2 e^{ik_{liq}h/2} \\ iH_p \sin(k_p h/2) & iH_m \sin(k_m h/2) & 0 \end{vmatrix} \tag{7.46}$$

The determinant on the left corresponds to the anti-symmetric modes while the one on the right corresponds to the symmetric modes. This determines the dispersion relation for the different modes of a wave propagating along a transverse isotropic elastic plate in a direction parallel to the fibers. In this case the velocity dispersion curve will depend on following elastic constants: C_{11}, C_{33}, C_{13}, and C_{55}. To introduce viscosity, the elastic constant C_{55} should be considered as complex number.

7.6.2 Guided Wave Propagation Perpendicular to the Fibers

To solve the problem of guided wave propagation in the direction perpendicular to the fibers it is important to note that this is the same problem of wave propagation along the parallel direction but in a different reference frame. Thus, it suffices to change the subscript 3 to 2 and replace C_{55} by C_{66} in Eqs. (7.39) to (7.42) to re-obtain Eq. (7.46). However, since the plate is transverse isotropic: $C_{11} = C_{22}$ and $C_{12} = C_{11} - 2C_{66}$. Under these conditions $H_{p,m}$, $G_{p,m}$, and $k_{p,m}$ are reduced to the following expressions

$$k_p = k \cdot [(\rho\omega^2)/(k^2 C_{66}) - 1]^{1/2}$$

$$k_m = k \cdot [(\rho\omega^2)/(k^2 C_{11}) - 1]^{1/2}$$

$$H_p = (k^2 - k_p{}^2)/k$$

$$H_m = 2k$$

$$G_p = 2C_{66}k_p$$

$$G_m = C_{66}(k_p{}^2 - k^2)/k_m$$

Consequently Eq. (7.46) may be reduced to Eqs. (7.28) and (7.29), which corresponds to the Leaky Lamb wave equation for an isotropic plate of shear wave speed of $(C_{66}/\rho)^{1/2}$ and longitudinal wave speed of $(C_{11}/\rho)^{1/2}$. Again, to introduce viscosity C_{66} may be considered to obey a Voigt model, thus, $C_{66} = c_{66} + i\eta_{66}$.

7.7 Conclusions

Throughout this chapter the main features of transverse wave propagation in plate structures with application to ultrasound elastography have been reviewed. Wave propagation in such a configuration may be described as a superposition of different modes of propagation (e.g. symmetric/anti-symmetric modes) which depend on the geometry, isotropy, mechanical properties, and boundary conditions of the wave guide. Moreover, the generation of each mode will depend on the frequency and type of source used in the experiments. In this scenario, it is mandatory to take the dispersive nature of each mode into account in order to retrieve the shear wave speed of the plate, otherwise bias in the shear wave speed estimation will be introduced. For a given application, once a plate model is assumed (e.g. plate in water, plate in vacuum, etc.) the shear wave speed of the plate may be retrieved by identifying the corresponding mode and fitting the theoretical dispersion curve to the experimental data. At the moment, the only mode that was consistently detected using ultrasound elastography is the zero -order anti-symmetric mode. However, new applications will shortly lead to the detection of other types of modes as well as to the development of the theory for different types of geometries, sources, wave guides, etc.

Acknowledgments

The author would like to thank Dr. Nicolás Benech, Dr. Carlos Negreira, and Dr. Xiaoping Jia for the interesting discussions on guided wave generation and propagation. Javier Brum is supported by PEDECIBA-Física, Uruguay and Agencia Nacional de Investigación e Innovación (ANII), Uruguay.

References

1 Tanter, M., Touboul, D., Gennisson, J.L., et al. (2009). High-resolution quantitative imaging of cornea elasticity using supersonic shear imaging. *IEEE Trans. Med. Imaging* 28: 1881–1893.

2 Nguyen, T.M., Couade, M., Bercoff, J., and Tanter, M. (2011). Assessment of viscous and elastic properties of sub-wavelength layered soft tissues using shear wave spectroscopy: theoretical framework and experimental in vitro experimental validation. *IEEE Trans. Ultrason., Ferroelectr., Freq. Control* 58: 2305–2315.

3 Nenadic, I.Z., Urban, M.W., Aristizabal, S., et al. (2011). Lamb wave dispersion ultrasound vibrometry (LDUV) method for quantifying mechanical properties of viscoelastic solids. *Phys. Med. Biol.* 56: 2245–2264.

4 Urban, M.W., Pislaru, C., Nenadic, I., et al. (2013). Measurement of viscoelastic properties of in vivo swine myocardium using Lamb wave dispersion ultrasound vibrometry (LDUV). *IEEE Trans. Med. Imaging* 32: 247–261.

5 Nenadic, I.Z., Qiang, B., Urban, M.W., et al. (2013). Ultrasound bladder vibrometry method for measuring viscoelasticity of the bladder wall. *Phys. Med. Biol.* 58: 2675–2695.

6 Couade, M., Pernot, M., Prada, C., et al. (2010). Quantitative assessment of arterial wall biomechanical properties using shear wave imaging. *Ultrasound Med. Biol.* 36: 1662–1676.

7 Bernal, M., Nenadic, I., Urban, M.W., and Greenleaf, J.F. (2011). Material property estimation for tubes and arteries using ultrasound radiation force and analysis of propagating modes. *J. Acoust. Soc. Am.* 129: 1344–1354.

8 Dutta, P., Urban, M., Le Maitre, O., et al. (2015). Simultaneous identification of elastic properties, thickness, and diameter of arteries excited with ultrasound radiation force. *Phys. Med. Biol.* 60: 5279–5296.

9 Brum, J., Bernal, M., Gennisson, J.L., and Tanter, M. (2014). In vivo evaluation of the elastic anisotropy of the human Achilles tendon using shear wave dispersion analysis. *Phys. Med. Biol.* 59: 505–523.

10 Helfenstein-Didier, C., Andrade, R.J., Brum, J., et al. (2016). In vivo quantification of the shear modulus of the human Achilles tendon during passive loading using shear wave dispersion analysis. *Phys. Med. Biol.* 61: 2485–2496.

11 Auld, B.A. (1973). *Acoustics Fields and Waves in Solids*, Vol. 2. New York: Wiley.

12 Lowe, M. (1995). Matrix techniques for modelling ultrasonic waves in multi-layered media. *IEEE Trans.Ultrason., Ferroelectr., Freq. Control* 42: 525–542.

13 Brum, J., Gennisson, J.L., Nguyen, T.M., et al. (2012). Application of 1D transient elastography for the shear modulus assessment of thin layered soft tissue: comparison with supersonic shear imaging technique. *IEEE Trans. Ultrason., Ferroelectr., Freq. Control* 59: 703–714.

14 Graff, K.F. (1975). *Wave Motion in Elastic Solids*. New York: Dover Publications.

15 Royer, D. and Dieulesaint, E. (1996). *Elastic Waves in Solids I: Free and Guided Propagation*. Berlin: Springer.

16 Nguyen, T.M., Aubry, J.F., Toubul, D., et al. (2012). Monitoring of cornea elastic properties chnages during UV-A/riboflavin-induced corneal collagen cross-linking using supersonic shear wave imaging: a pilot study. *Invest. Ophthalmol. Vis. Sci.* 53: 5948–5954.

17 Nguyen, T.M., Aubry, J.F., Fink, M., (2013). In vivo evidence of porcine cornea anisotropy using supersonic shear wave imaging. *Invest. Ophthalmol. Vis. Sci.* 55: 7545–7552.

18 Nenadic, I.Z., Urban, M.W., Mitchell, S.A., and Greenleaf, J.F. (2011). On Lamb and Rayleigh wave convergence in viscoelastic tissues. *Phys. Med. Biol.* 56: 6723–6738.

19 Fung, Y.C. (1993). *Biomechanics: Mechanical Properties of Living Tissues*. New York: Springer.

20 Royer, D., Gennisson, J.L., Deffieux, T. and Tanter, T. (2011). On the elasticity of transverse isotropic soft tissues. *J. Acoust. Soc. Am.* 129: 2757–2760.

8

Rheological Model-based Methods for Estimating Tissue Viscoelasticity

Jean-Luc Gennisson

Imagerie par Résonance Magnétique Médicale et Multi-Modalités, Université Paris-Saclay, Orsay, France

8.1 Introduction

As was shown in Chapter 5 in this book, the wave equation can be expressed in terms of the different pair parameters of elastic properties of tissue. It was shown that two types of waves propagate in the solid: compressional waves and shear waves. Each of these waves will be intuitively linked to the speed propagation (c_P, c_S), but they can also be connected to the pair of bulk and shear moduli (κ, μ). Thus the equations for the compression and shear waves can be reformulated as

$$\rho \partial^2_{t^2} u_p = \kappa \Delta u_p \tag{8.1}$$

$$\rho \partial^2_{t^2} u_s = \mu \Delta u_s \tag{8.2}$$

where ρ, u_p, u_s are respectively the density, the longitudinal displacement, and the shear displacement.

It is then possible to make an analogy with the oscillations of a spring or even the behavior of any unamortized oscillator. The left-hand side is the product of the mass of the object and its acceleration, whereas the right-hand side corresponds to the restoring force which allows the oscillations of the object considered. As stated, the formalism of this equation is the equation of motion for an undamped oscillator (i.e. oscillations exist indefinitely). In other words, this equation assumes that the waves will propagate in the environment remaining unchanged and can be propagated indefinitely if it is considered that the solid has no limit.

But biological tissues are known to be characterized by a greater attenuation of the shear waves (i.e. the amplitude of the shear wave decreases during propagation). The nature of this attenuation can be described by many models [1–4]. For this attenuation to be considered in the wave equation, it is necessary to consider that the shear modulus is not a real number but a complex number. To be convinced, it may be interesting to determine the equation of shear wave solution when the shear modulus μ^* is a complex number of the form: $\mu^* = \mu_d + i \cdot \mu_l$. The general solution of the wave equation in one dimension is of the form

$$u_t(x, t) = u_0 e^{i(\omega \cdot t - k \cdot x)} \tag{8.3}$$

with ω the wave pulsation and k the wave vector. When the displacement is replaced by this expression in the equation of the shear waves previously established, it is then possible to express the wave number as follows

$$k^2 = \frac{\rho \cdot \omega^2}{\mu^*} \tag{8.4}$$

Ultrasound Elastography for Biomedical Applications and Medicine, First Edition.
Edited by Ivan Nenadic, Matthew Urban, James Greenleaf, Jean-Luc Gennisson, Miguel Bernal, and Mickael Tanter.

In this case, if the shear modulus is complex, then the wave vector is complex since the pulsation and the density are positive real numbers. The wave vector can be written $k = k_d + i \cdot k_l$, leading to

$$u_t(x,t) = u_0 e^{k_l \cdot x} e^{i(\omega \cdot t - k_d \cdot x)} \tag{8.5}$$

The imaginary part of the shear modulus allows to show a wave attenuation term. Also, it is possible to take into account the attenuation of shear waves in the equation describing their propagation in biological tissues whereas shear modulus is a complex number. Whatever is the attenuation model considered, it is then necessary to adapt the expression of the shear modulus.

8.2 Shear Modulus and Rheological Models

In this section, solid mechanical properties are limited to single shear. It is possible to see the problem only in shear terms by considering only the complex shear modulus, where the wave equation becomes

$$\rho \partial_{t^2}^2 u = \mu^* \Delta u \tag{8.6}$$

The behavior of the solid is then described by the expression of the complex shear modulus. The complex shear modulus can simplify the notation and its expression will allow us to describe some solid behaviors. The different patterns of behavior actually correspond to rheological models whose complexity varies greatly according to the desired use [5].

8.2.1 Rheological Models and Mechanical Response of the Solid

The study of the characteristics of the deformable body (elasticity, viscosity (η), plasticity, fluidity) is better known under the name of rheology. This word was created in 1929 by E.C. Bingham from the Greek words λογος (meaning "speech" and, by extension, "science"), and ρεος (meaning "the current" or "the fluid"). Thus the objective is to study the rheology of fluid flow and, by extension for deformable solids, viscoelastic properties. The rheology is mainly based on a phenomenological modeling of elastic behavior. These models are shown with the same formalism: the elementary bricks connect deformations ε to stresses σ. Elementary units are associated in series or in parallel as schematic representations of electrical circuits. The two basic components used in rheology are the spring ($\sigma = k \cdot \varepsilon$) and the damper ($\sigma = \eta \cdot \partial_t \cdot \varepsilon$).

The rheological models can be characterized according to their static or dynamic behavior. The static characterization is carried out by means of two types of experiments: creep and relaxation. Creep is to subject the system to a constant stress and to observe the distortion of the system. Relaxation comes to free the system from its restraint and observe its return to balance. The dynamic characterization amounts to expressing the shear modulus according to the characteristics of the considered model and observe its behavior as a function of the frequency.

8.2.2 Voigt's Model

The Voigt model, also called the Kelvin–Voigt model, describes the behavior of viscoelastic materials that are characterized by both elasticity k^{Vo} and viscosity η^{Vo}. This model takes its name from two physicists: the British William Thomson, first Baron Kelvin, and the German Woldemar Voigt. This model consists of a spring and a damper which are connected in parallel. As the spring and the damper are in parallel, it is possible to express the stress versus strain as follows

$$\sigma = k^{Vo}\varepsilon + \eta^{Vo} d_t \varepsilon \tag{8.7}$$

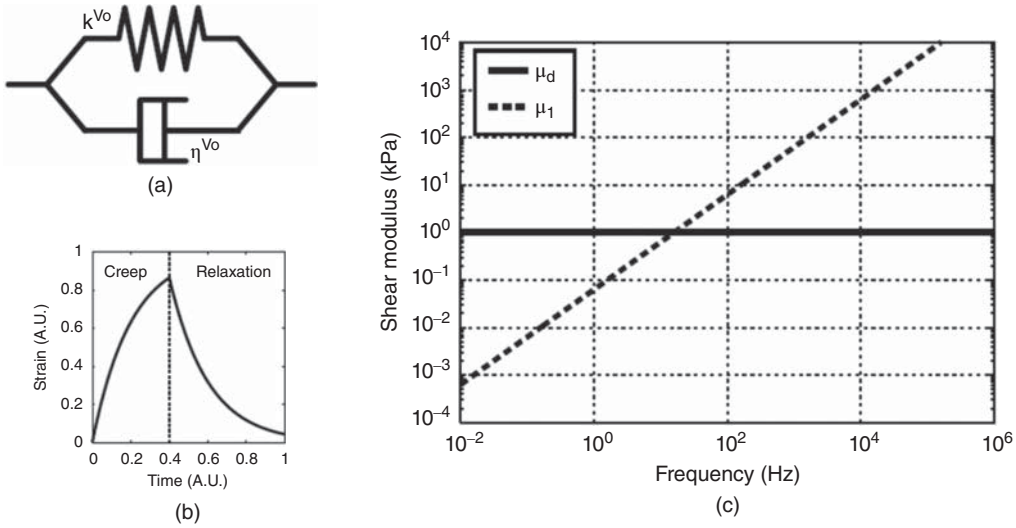

Figure 8.1 Voigt's model ($k^{Vo} = 1$ kPa, $\eta^{Vo} = 10$ Pa·s). (a) This model consists of a spring and a damper in parallel. (b) The typical response of a Voigt-like material is characterized by a progressive deformation followed by a decrease related to damping properties. (c) The dynamic behavior of Voigt's model is relatively simple since the dynamic part of the shear modulus is constant while the attenuation part is proportional to the frequency of elastic waves propagating in the medium.

Figure 8.1a shows the Kelvin–Voigt model. Examples of the strain response from an applied step force (Figure 8.1b) and the dynamic behavior (Figure 8.1c) are shown for $k^{Vo} = 1$ kPa and $\eta^{Vo} = 10$ Pa·s.

From Eq. (8.7), it is also possible to determine the wave propagation equation in terms of the elasticity of the spring and the viscosity of the shock absorber for an object whose viscoelastic properties are described by a Voigt's model. Note that this dynamic study consists in studying the behavior of complex shear modulus as a function of frequency. In this case, the wave equation is considered in the case of monochromatic waves characterized by pulsation ω. So that

$$-\rho\omega^2 u = k^{Vo}\Delta u + i\eta^{Vo}\omega\,\Delta u \tag{8.8}$$

From this expression, it is possible to express the real and imaginary parts of the shear modulus

$$\mu_d = k^{Vo} \tag{8.9}$$

$$\mu_l = \eta^{Vo}\omega \tag{8.10}$$

The real part of the complex shear modulus is constant as a function of the frequency, which means that the elasticity remains unchanged irrespective of the frequency of the propagating waves. The imaginary part of the complex shear modulus is proportional to the frequency. By using such a viscoelastic model, it is evident that the elastic wave propagation does not depend on the frequency, but the attenuation of such waves depends on the frequency.

8.2.3 Maxwell's Model

The Maxwell model describes the behavior of viscoelastic materials that are characterized by both k^{Ma} and viscosity η^{Ma}. This model takes its name from the physicist James C. Maxwell, who proposed it in 1867. The Maxwell model consists of a spring placed in series with

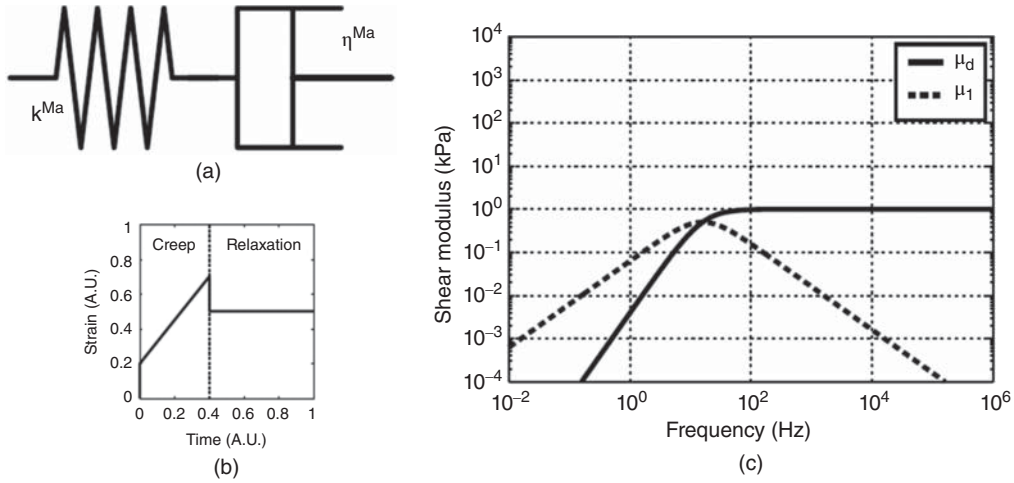

Figure 8.2 Maxwell's model ($k^{Ma} = 1$ kPa, $\eta^{Ma} = 10$ Pa·s). (a) This model consists of a spring and a damper in series. (b) The typical response of a Maxwell-like material is characterized by a progressive deformation followed by a decrease related to damping properties. (c) The real part of the shear modulus is proportional in a first time to the square of the frequency then remains constant for the elastic waves of high frequency. The attenuating part on the contrary increases with frequency to decrease thereafter.

damper. Due to the structure of this model, it is possible to express the stress versus the strain as follows

$$\sigma + \frac{\eta^{Ma}}{k^{Ma}} d_t\sigma = \eta^{Ma} d_t\varepsilon \tag{8.11}$$

Figure 8.2a shows the Maxwell model. Examples of the strain response from an applied step force (Figure 8.2b) and the dynamic behavior (Figure 8.2c) are shown for $k^{Ma} = 1$ kPa and $\eta^{Ma} = 10$ Pa·s.

From Eq. (8.11), it is also possible to determine the propagation equation of the waves depending on the elasticity of the spring and viscosity of the damper for an object whose viscoelastic properties are described by a Maxwell's model. The wave equation is considered in the case of monochromatic waves characterized by pulsation ω. So that

$$-\rho\omega^2 u + i\frac{\eta^{Ma}}{k^{Ma}}\rho\omega^3 \cdot u = -i\omega\eta^{Ma}\,\Delta u \tag{8.12}$$

From this expression, it is possible to express the real and imaginary parts of the shear modulus

$$\mu_d = \frac{A^2}{1+A^2}k^{Ma} \tag{8.13}$$

$$\mu_l = \frac{A}{1+A^2}k^{Ma} \tag{8.14}$$

where A is the ratio between viscosity and elasticity: $A = \eta^{Ma}\,\omega/k^{Ma}$.

The dynamic modulus is proportional to the square of the frequency for low frequencies and then reaches a plateau corresponding to the spring for the high frequencies. The attenuation modulus also increases for low frequencies, but there is just proportional to the frequency. The dynamic modulus thus increases significantly faster than the attenuation modulus on the same range of low frequencies. However, the attenuation modulus then decreases for high frequencies in contrast to the dynamic modulus. This decrease is due to the fact that the imaginary part of the shear modulus is proportional to the inverse of the frequency for the high frequencies.

8.2.4 Standard Linear Model

The standard linear model, also called Zener's model, was introduced to describe an instantaneous response to a mechanical solid described by a Voigt's model. The structure of this model is therefore based on a spring #1 and a damper placed in parallel and to which a spring #2 is added in series to create this instantaneous mechanical response. Due to the structure of this model, it is possible to express the stress versus the strain as follows

$$\sigma + \frac{\eta^{\mathrm{Ze}}}{k_2^{\mathrm{Ze}}} d_t \sigma = k_1^{\mathrm{Ze}} \varepsilon + \eta^{\mathrm{Ze}} d_t \varepsilon \tag{8.15}$$

Figure 8.3a shows the standard linear model. Examples of the strain response from an applied step force (Figure 8.3b) and the dynamic behavior (Figure 8.3c) are shown for $k_1^{\mathrm{Ze}} = 10\,\mathrm{Pa}$, $k_2^{\mathrm{Ze}} = 1\,\mathrm{kPa}$, $\eta^{\mathrm{Ma}} = 10\,\mathrm{Pa{\cdot}s}$.

From Eq. (8.15) it is possible to establish the propagation equation of the waves depending on two elasticities and the viscosity. The wave equation is considered in the case of monochromatic waves by pulsation ω. So that

$$-\rho\omega^2 u + i\frac{\eta^{\mathrm{Ze}}}{k_2^{\mathrm{Ze}}}\rho\omega^3 u = k_1^{\mathrm{Ze}}\Delta u - i\omega\eta^{\mathrm{Ze}}\Delta u \tag{8.16}$$

From this expression, it is possible to express the real and imaginary parts of the shear modulus

$$\mu_{\mathrm{d}} = \frac{1}{1+A^2}k_{\mathrm{mean}} + \frac{A^2}{1+A^2}k_2^{\mathrm{Ze}} \tag{8.17}$$

$$\mu_{\mathrm{l}} = \frac{A}{1+A^2}k_2' \tag{8.18}$$

where k_{mean} is the average of the two resulting elasticities of the model, k_2' is the elasticity of the second spring weighted by both elasticities, and A is the ratio between the viscosity and the two elasticities. The expressions of these three characteristic quantities of the model are then

$$k_{\mathrm{mean}} = \frac{k_1^{\mathrm{Ze}}k_2^{\mathrm{Ze}}}{k_1^{\mathrm{Ze}}+k_2^{\mathrm{Ze}}},\ k_2' = \frac{(k_2^{\mathrm{Ze}})^2}{k_1^{\mathrm{Ze}}+k_2^{\mathrm{Ze}}},\ k_{\mathrm{mean}} = \frac{k_1^{\mathrm{Ze}}k_2^{\mathrm{Ze}}}{k_1^{\mathrm{Ze}}+k_2^{\mathrm{Ze}}} \tag{8.19}$$

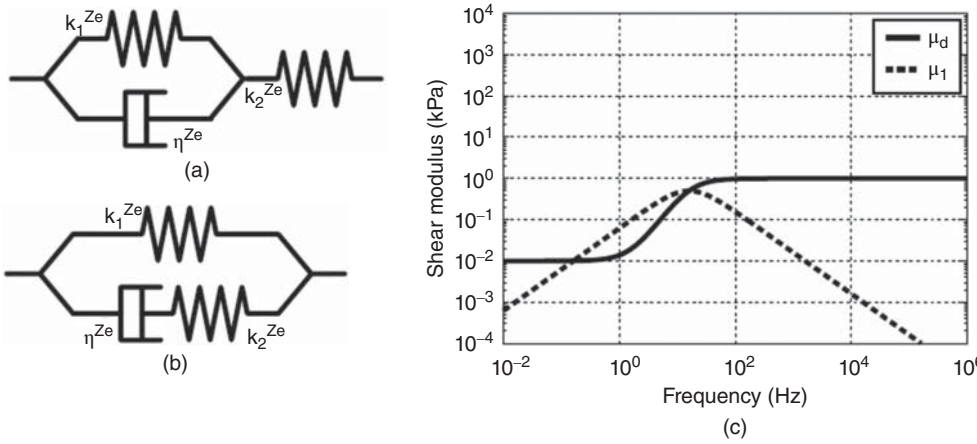

Figure 8.3 Standard linear model ($k_1^{\mathrm{Ze}} = 10\,\mathrm{Pa}$, $k_2^{\mathrm{Ze}} = 1\,\mathrm{kPa}$, $\eta^{\mathrm{Ma}} = 10\,\mathrm{Pa{\cdot}s}$). (a) This model consists of a spring and a damper in parallel where a second spring is associated in series. (b) The second representation of the Zener model is equivalent in terms of the relationship between stress and strain. (c) The dynamic modulus of this model provides constant values to low and high frequencies. The attenuation modulus is comparable to that of Maxwell's model: it is growing at low frequency and decreasing at high frequency.

From the expressions of real and imaginary parts of the complex shear modulus in the case of standard linear model, there are three important variables: k_{mean}, k_2^{Ze} and k_2'. The first two variables are involved in the expression of the dynamic modulus μ_d. The average elasticity k_{mean} is the value taken by the low dynamic modulus frequency. This non-zero elasticity allows the material to behave like a solid on this frequency range. Similarly, the elasticity k_2^{Ze} allows the material to be characterized by a dynamic modulus or a constant elasticity for high frequencies. More particularly, this constant elasticity allows the system to have an instantaneous response during a sudden mechanical stress at high frequencies. Finally, the elasticity k_2' will be responsible for the position of the maximum of the attenuation modulus. Indeed, the attenuation modulus is an increasing function for low frequencies, and is a decreasing function for high frequencies. Also at low frequency as well as at high frequency, Zener's type materials will exhibit almost a zero attenuation for low and high frequencies while at the same frequency range the dynamic modulus is constant.

The study of this third rheological model has shown that it was possible to model instantaneous mechanical response for a solid described by the Voigt model adding a spring. It is thus possible to model each of the mechanical properties of a solid by adding base components. More generally, it is difficult to model the behavior of any solid from a single pair of values (elasticity, viscosity) and this results in difficulty in that the viscoelastic behavior is generally different according to the scale at which they are observed. To be able to model the dynamics of the material over a wide spectral range, it is then necessary to generalize this approach by concatenating several basic models to describe material dynamics at different scales.

8.2.5 Fractional Rheological Models and Biological Tissues

8.2.5.1 Spring-pot

By establishing a network of rheological building blocks, it is possible to describe the behavior of a solid. However, this method quickly becomes complex, particularly if the aim is to estimate the viscoelastic properties of biological tissues. To prevent this escalation in the number of rheological parameters, a generalization of Newton's law was introduced to stop considering the stress as proportional to the first derivative of the deformation, but rather as a fractional derivative [4, 6–8]. This generalization was behind the introduction of a new elementary rheological building block: the spring-pot, a mixture of a spring (spring) and a damper (dashpot). This new element is characterized by an elasticity E_α parameter and a fractional derivative $D_{t^\alpha}^{\alpha}\varepsilon$. This new element particularly allows us to adopt a type of model while having an adjustable α parameter to describe the best dynamic behavior of the studied material. Such an approach has shown convincing results for measurements made with both rheometers [9] and with optical tweezers [10] over wide frequency ranges.

The viscoelastic behavior of biological tissue can be modeled by means of the different models previously introduced. Indeed, these materials have together a liquid structure (Maxwell's model) because they are mostly water, and a solid structure (Voigt's model) as they do not flow and they have a certain stiffness. Instead of using models with multiple parameters, the introduction of the spring-pot eliminates a number of parameters through the fractional derivative which can be expressed through the integral of Riemann-Liouville [11]

$$D_{t^\alpha}^{\alpha} f(t) = \frac{1}{\Gamma(-\alpha)} \int_0^t \frac{f(\tau)}{(t-\tau)^{\alpha+1}} \mathrm{d}\tau \tag{8.20}$$

where Γ is the Bessel integral. As the fractional order derivative α is found midway between the order 0 of Hooke's law and the order 1 of Newton's law, this new approach seems to better describe biological tissues that are halfway way between a solid and a liquid behavior [12].

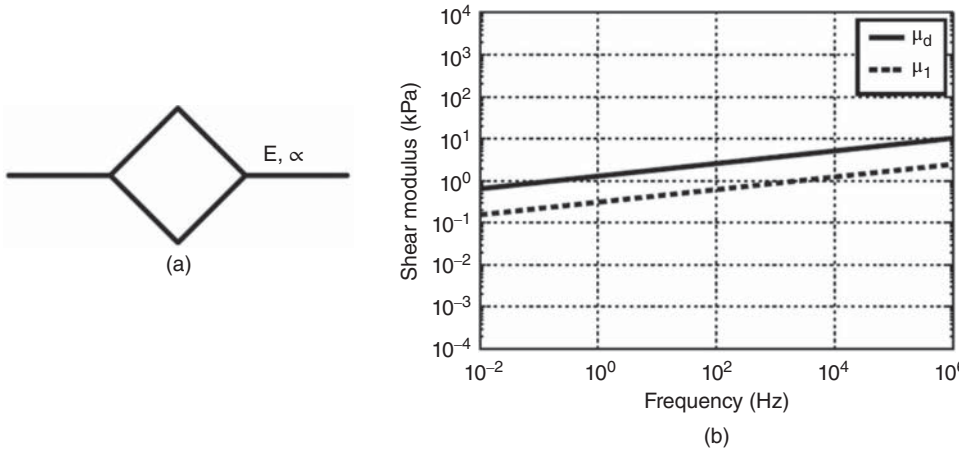

Figure 8.4 Frequency of a spring-pot (a) behavior ($E = 1$ kPa·s$^{-\alpha}$, $\alpha = 0.15$): (b) dynamic and attenuation moduli satisfy the same non-integer power law of the frequency.

The wave propagation equation can be determined in the same manner as above from the relationship between stress and strain for elastic waves of a monochromatic pulsation ω

$$-\rho\omega^2 u = E(i\omega)^{\alpha}\,\Delta u \tag{8.21}$$

From the wave equation in an environment described by a unique spring-pot, it is then possible to express the real and imaginary parts of the complex shear modulus based on the actual number α and the pseudo-elasticity E

$$\mu_{\mathrm{d}} = E\omega^{\alpha}\cos\left(\alpha\frac{\pi}{2}\right) \tag{8.22}$$

$$\mu_{\mathrm{l}} = E\omega^{\alpha}\sin\left(\alpha\frac{\pi}{2}\right) \tag{8.23}$$

In order to keep the real and imaginary parts of the complex shear modulus positive, it is necessary that the power α takes values between 0 and 1. This need shows that the spring-pot is an intermediate building block between the spring and the shock absorber in terms of rheological function. While $\alpha = 0$, the spring-pot acts as a spring and thus shows pure elasticity, while if the spring-pot $\alpha = 1$ it behaves as a pure damper.

Figure 8.4a shows the spring-pot model. An example of the dynamic behavior (Figure 8.4b) is shown for $E = 1$ kPa·s$^{-\alpha}$, $\alpha = 0.15$.

From this expression, it appears that both the real and imaginary parts of the complex shear modulus have a neighboring term since their ratio is constant regardless of the frequency of the monochromatic elastic wave. In addition, the dynamic and attenuation moduli are proportional to a non-integer frequency power α. Such behavior can be interesting and at midway between the solid and liquid behavior. Also, it may be interesting to consider generalized models of Voigt and Maxwell for which the damper was replaced by a spring-pot.

8.2.6 Generalized Maxwell and Voigt Models

In the case of the generalized Voigt model [4], the relationship between stress and strain can be established and the equation governing the propagation of elastic waves in such a medium is

$$-\rho\omega^2 u = k\Delta u + E(i\omega)^{\alpha}\Delta u \tag{8.24}$$

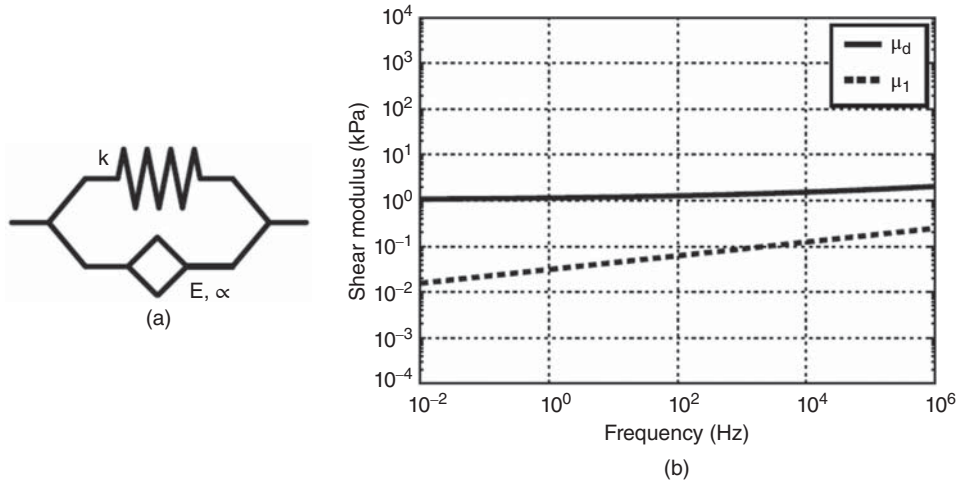

Figure 8.5 The generalized Voigt model ($E = 1$ kPa·s$^{-\alpha}$, $\alpha = 0.15$, $k = 1$ kPa). (a) The spring-pot replaces the damper in the classical Voigt model. (b) The dynamic modulus is close to the value of the elasticity k at low frequency before following an increase in ω^{α}, and the attenuation term is growing as for the spring-pot alone.

It is then possible by identification to recover the complex shear modulus as follows

$$\mu_{\mathrm{d}} = k + E\omega^{\alpha} \cos\left(\alpha\frac{\pi}{2}\right) \tag{8.25}$$

$$\mu_{\mathrm{l}} = E\omega^{\alpha} \sin\left(\alpha\frac{\pi}{2}\right) \tag{8.26}$$

Figure 8.5a shows the generalized Voigt model. An example of the dynamic behavior (Figure 8.5b) is shown for $E = 1$ kPa·s$^{-\alpha}$, $\alpha = 0.15$, $k = 1$ kPa.

The frequency behavior of the complex shear modulus is comparable to that obtained when only a spring-pot is considered. It should be noted, however, that the dynamic modulus is close to the value of the elasticity k for the propagation of a wave of low frequency. This is related to the fact that the term ω^{α} is small compared to the constant elasticity k for low frequencies. However, at high frequencies the elasticity of the spring is no longer involved since the end of the spring-pot in the expression of the dynamic modulus becomes predominant.

As was done for the classical Voigt model, it is possible to build a generalized Maxwell model by replacing the damper with a spring-pot. Such a model has been used in several works bearing both on polymers [12–14] or soft tissue [15, 16]. As before, it is possible to easily establish the equation of the constraint in terms of design and of deformation and the equation governing the propagation of elastic waves of monochromatic pulsation ω.

$$-\rho\omega^2\left(1 + \frac{E}{k}(i\omega)^{\alpha}\right)u = E(i\omega)^{\alpha}\Delta u \tag{8.27}$$

It is then possible to recover the complex shear modulus by identification of terms, as follows

$$\mu_{\mathrm{d}} = \frac{A^2 + A\cos\left(\alpha\frac{\pi}{2}\right)}{1 + 2A\cos\left(\alpha\frac{\pi}{2}\right) + A^2}k \tag{8.28}$$

$$\mu_{l} = \frac{A + A\sin\left(\alpha\frac{\pi}{2}\right)}{1 + 2A\cos\left(\alpha\frac{\pi}{2}\right) + A^2}k \tag{8.29}$$

with A the ratio between the viscosity term $E\omega^{\alpha}$ and the elasticity term k.

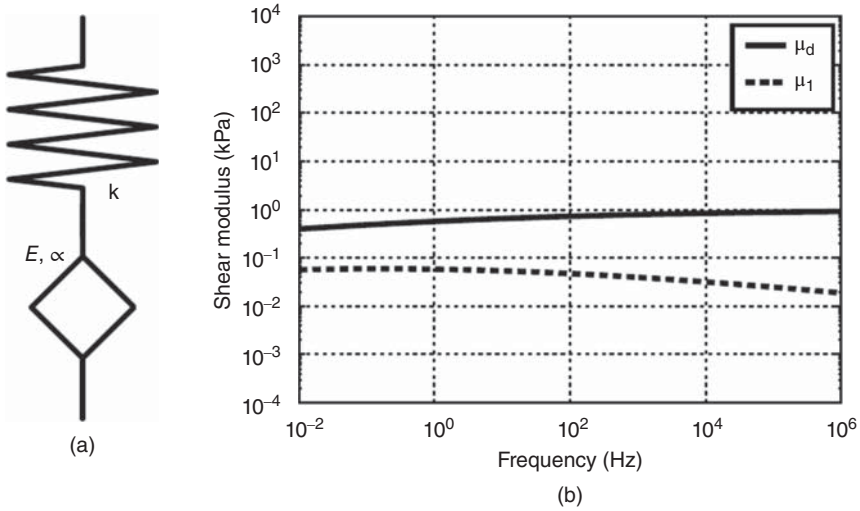

Figure 8.6 The generalized Maxwell model ($E = 1$ kPa·s$^{-\alpha}$, $\alpha = 0.15$, $k = 1$ kPa). (a) The spring-pot replaces the damper in the classical Maxwell model. (b) The dynamic modulus follows an increase in ω^{α} for low frequencies before reaching a horizontal asymptote corresponding to the spring placed in series with the spring-pot. As for the classic model, the attenuation modulus increases in ω^{α} for low frequencies before decreasing for high frequencies.

Figure 8.6a shows the generalized Maxwell model. An example of the dynamic behavior (Figure 8.6b) is shown for $E = 1$ kPa·s$^{-\alpha}$, $\alpha = 0.15$, $k = 1$ kPa.

The frequency behavior of the complex shear modulus is comparable to that observed in the classical Maxwell model. The dynamic modulus increases for low frequencies according to a non-integer power-law ω^{α}. Then for high frequencies the curve admits a horizontal asymptote corresponding to the spring placed in series with the spring-pot. This particular behavior is due to the presence of the spring which enables it to provide an instant response to the mechanical system. In the case of the attenuation modulus, the analysis of the function as well as the graph allows us to identify two behaviors at low and high frequency. Initially, the attenuation modulus increases at low frequency with a non-integer power-law ω^{α} and decreases at high frequency according to a reverse non-integer power-law $\omega^{-\alpha}$.

The use of the spring-pot adds more freedom in modeling viscoelastic materials. This result is even more enhanced by the fact that it is possible to describe a spring-pot from rheological networks simply composed of springs and shock absorbers [12, 17]. The advantage of using spring-pots is the need to determine only the two parameters α and E instead of having to determine all the parameters of the springs and shock absorbers constituting the equivalent network. Finally, it should be noted that from this base, it is also possible to refine the rheological model in order to describe the different characteristics of viscoelastic materials experimentally observed.

8.3 Applications of Rheological Models

Understanding the use of such models and their basics elements, allows a user to build any rheological model that describes experimental data well in order to better understand material behavior. In this way it is possible to link shear wave measurements to rheological models; however, to completely understand the rheological behavior of the investigated medium, it is necessary to acquire measurements over multiple decades of frequencies. In the following

sub-sections, two examples show how to recover the rheological behavior of blood during coagulation or hydrogels by combining shear wave measurements and other rheological approaches with rheometers.

8.3.1 Blood Coagulation

In one of our studies, blood from healthy pigs was used for experimentation [18]. In order to completely characterize blood during coagulation, multiple measurements with different set ups were used.

At low frequency, rheological experiments were performed using a Haake Mars II rheometer (Thermo Fisher Scientific Inc, Waltham, MA, USA) between 0.25 and 25 Hz. From rheological results, G' (dynamic modulus) and G'' (loss modulus), the shear wave phase velocity (v) was calculated in order to get the shear wave dispersion curve at low frequency by using the following formulae

$$v(\omega) = \sqrt{\frac{2(G'^2 + G''^2)}{\rho G' \left(1 + \sqrt{1 + \frac{G'}{G''}^2}\right)}} \tag{8.30}$$

At high frequency, shear wave experiments were performed using the supersonic shear imaging technique described in Chapter 23 in this book by using an ultrafast ultrasound device ($V1^2$ prototype, Supersonic Imagine, Aix-en-Provence, France). Results were recovered between 50 and 300 Hz by using the shear wave spectroscopy method [19].

All measurements with both techniques were performed on two different blood samples from the same blood sample at different times during coagulation initiated at the same time (the entire experiments lasts 2 hours with one measurement every minute). By combining both sets of results, the dispersion of the shear wave phase velocity was recovered over multiple decades and plotted on Figure 8.7 over coagulation time. Then by using the expression of the shear wave phase velocity for different models it is possible to fit all the results and to define what is the best rheological model for describing the material.

$$\text{Maxwell's model } v(\omega) = \sqrt{\frac{2\mu}{\rho\left(1 + \sqrt{1 + \frac{\mu^2}{\omega^2\eta^2}}\right)}} \tag{8.31}$$

$$\text{Voigt's model } v(\omega) = \sqrt{\frac{2(\mu^2 + \omega^2\eta^2)}{\rho(\mu + \sqrt{\mu^2 + \omega^2\eta^2})}} \tag{8.32}$$

$$\text{Zener's model } v(\omega) = \frac{\omega}{\sqrt{\frac{\sqrt{A^2+B^2}-A}{2}}} \tag{8.33}$$

where $A = \dfrac{-\omega^2\rho(\omega^2\eta^2(\mu_1 + \mu_2) + {\mu_1}^2\mu_2}{\mu_1^2\mu_2^2 + \omega^2\eta^2(\mu_1 + \mu_2)}$ and $B = \dfrac{\omega^3\rho\mu_1^2\eta}{\mu_1^2\mu_2^2 + \omega^2\eta^2(\mu_1 + \mu_2)^2}$

Results shows that the choice of a rheological model to describe biological tissue can be complicated. By taking only shear wave elastography measurements at high frequency, the three models can fit the data well, but by adding the low frequency measurements it reveals that the Zener model is the simplest model that best fits blood during coagulation.

8.3.2 Hydrogel Characterization

In the same way, this sub-section presents a study on hydrogels by using multiple techniques over five orders of frequency [20]. The technique used were strain-controlled rheometry,

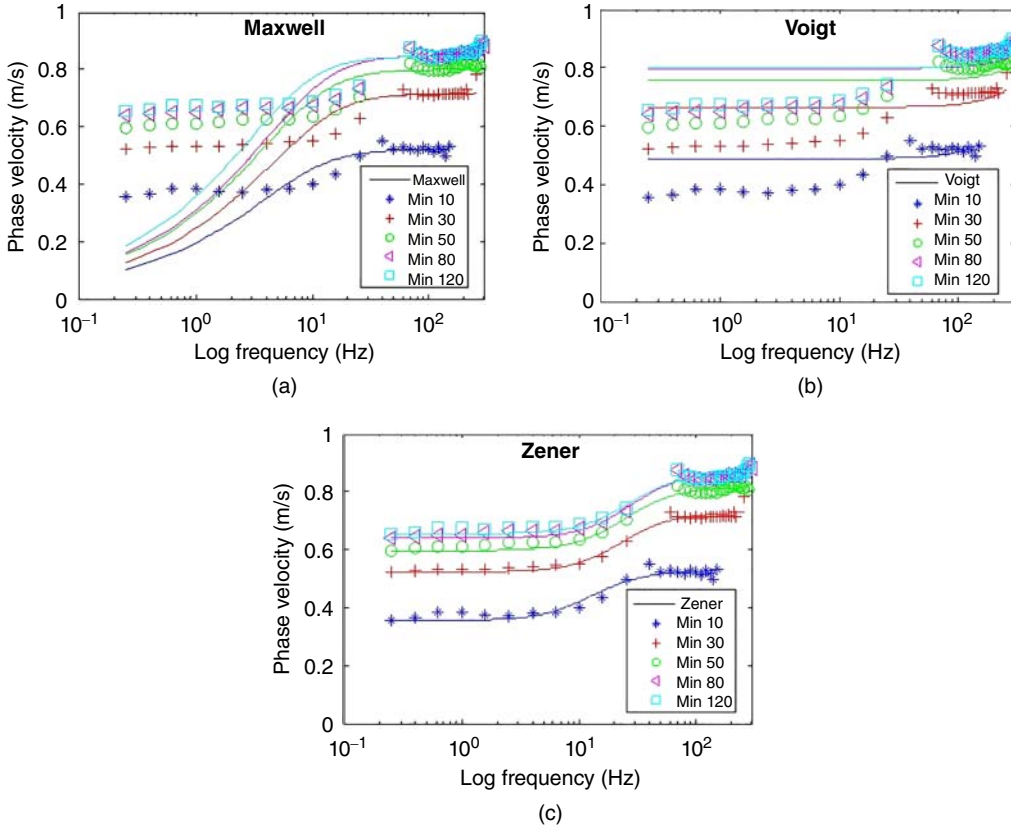

Figure 8.7 Fitting of Maxwell, Voigt, and Zener models to the experimental dispersion curves at selected times of coagulation (10, 30, 50, 80, and 120 min) in a blood sample. The solid lines in each panel represent best fit (least mean square error minimization) of each model at the given time point. Source: reprinted from Bernal et al. [18] with permission from Elsevier.

transient elastography (Chapter 20 in this book), and supersonic shear wave imaging (Chapter 23 in this book). Such a combination of techniques allows one to characterize materials over a huge frequency range between 10^{-2} Hz and 1200 Hz. With results obtained in strain-controlled rheometry giving access to G' and G'', and by using Eq. (8.30), shear wave phase velocity was recovered between 10^{-2} Hz and 15 Hz. By using transient elastography technique and supersonic shear imaging technique, shear wave phase velocity was recovered between 25 Hz and 800 Hz, and between 200 Hz and 1200 Hz respectively. In Figure 8.8, the shear wave phase velocity is presented for all techniques over five decades of frequency for two different hydrogels.

A delicate point in this work is the assumption of the rheological model of the hybrid hydrogels at the frequency range of rheology. Here the model that can best describe the frequency behavior is a power law, as was previously reported in the literature concerning hydrogels [21–23]. Such characterization at relatively low frequencies does not signify that the viscoelastic behavior of the gels follows the same model at high frequency. The choice of the power law was only used to extrapolate conservation and loss moduli at high frequency. All elastography measurements are well distributed within the standard deviation of the extrapolated power law (not shown here, refer to Gennisson et al. [20]).

These two examples show that dynamic ultrasound elastography techniques can characterize tissues, biomaterials, and polymers in an unusual range of frequencies compared to classical

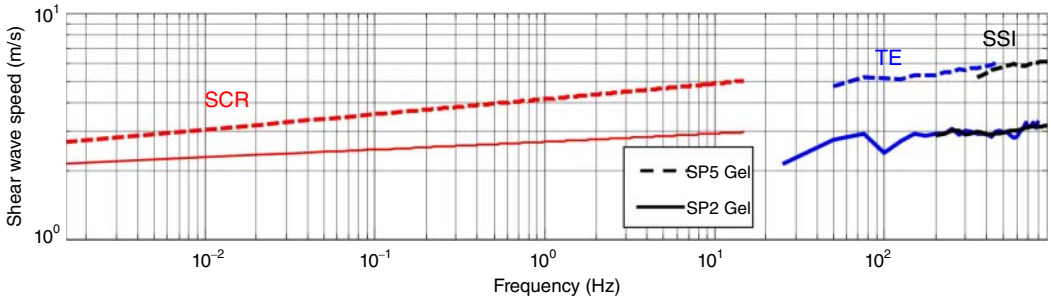

Figure 8.8 Logarithmic representation of shear wave velocity calculated from strain-controlled rheometry (SCR) measurements and shear wave phase velocity measured by transient elastography (TE) and supersonic shear imaging (SSI) for two different hydrogels (solid and dashed lines, respectively) Source: © 2014 IEEE, reprinted, with permission, from Gennisson et al. [20].

rheology, giving direct access to conservation and loss moduli. This shows also that the choice of a rheological model to characterize a material or a biological tissue is very complicated without knowing large decades of frequencies. By using only shear wave elastography techniques the characterization of the rheological model can be easily missed by the small range of frequency assessed, but the choice of a simple model could be relevant over the frequency range investigated.

8.3.3 Some Conclusions

As a conclusion, future work should focus on the shear wave attenuation measurements to give direct access to conservation and loss moduli directly. As shear wave phase velocity and shear wave attenuation are directly linked to dynamic and loss moduli, this allows to choice of the rheological model to be made without any assumption on it [24]. Such measurements will permit clinical in vivo characterization over a high frequency bandwidth, compared to classical rheology, and opens interesting perspectives for material characterization.

References

1 Kinsler, L.E. (1982). *Fundamental of Acoustics*. Wiley.
2 Sushilov, N. and Cobbold, R. (2004). Frequency-domain wave equation and its time-domain solutions in attenuating media. *J. Acoust. Soc. Am.* 115 (4): 1431–1436.
3 Manduca, A., Oliphant, T., Dresner, M., et al. (2001). Magnetic resonance elastography : non-invasive mapping of tissue elasticity. *Med. Image Anal.* 5 (4): 237–254.
4 Bagley, R. and Torvik, P. (1983). A theoretical basis for the application of fractional calculus to viscoelasticity. *J. Rheol.* 27 (3): 201–10.
5 Lemaitre, J. (2001). *Handbook of Materials Behavior Models*. Academic Press.
6 Hildebrandt, J. (1969). Comparison of mathematical models for a cat lung and viscoelastic balloon derived by Laplace transform methods from pressure-volume data. *Bull. Math. Biophys.* 31: 651–667.
7 Glöckle, W. and Nonnenmacher, T. (1991). Fractional integral operators and Fox functions in the theory of viscoelasticity. *Macromolecules* 24 (24): 6426–6434.
8 Szabo, T. and Wu, J. (2000). A model for longitudinal and shear wave propagation in viscoelastic media. *J. Acoust. Soc. Am.* 107 (5 Pt 1): 2437–2446.

9 Kiss, M., Varghese, T., and Hall, T. (2004). Viscoelastic characterization of in vitro canine tissue. *Phys. Med. Biol.* 49 (18): 4207–4218.

10 Desprat, N., Richert, A., Simeon, J., and Asnacios, A. (2005). Creep function of a single living cell. *Biophys J.* 88 (3): 2224–2233.

11 Oldham, K.B. and Spanier, J. (1974). *The Fractional Calculus*. New York: Academic Press.

12 Schiessel, H., Metzler, R., Blumen, A., and Nonnenmacher, T.F. (1995). Generalized viscoelastic models : their fractional equations with solutions. *J. Phys. A: Math. Gen.* 28 (23): 6567–6584.

13 Lion, A. (1997). On the thermodynamics of fractional damping elements. *Continuum Mech. Thermodyn.* 9 (2): 83–96.

14 Pritz, T. (1999). Verification of local Kramers-Kronig relations for complex modulus by means of fractional derivative model. *J. Sound Vib.* 228 (5): 1145–1165.

15 Djordjevic, V., Jaric, J., Fabry, B., et al. (2003). Fractional derivatives embody essential features of cell rheological behavior. *Ann. Biomed. Eng.* 31 (6): 692–699.

16 Kohandel, M., Sivaloganathan, S., Tenti, G., and Darvish, K. (2005). Frequency dependence of complex moduli of brain tissue using a fractional Zener model. *Phys. Med. Biol.* 50 (12): 2799–2805.

17 Schiessel, H. and Blumen, A. (1993). Hierarchical analogues to fractional relaxation equations. *J. Phys. A: Math. Gen.* 26 (19): 5057–5069.

18 Bernal, M., Gennisson, J.L., Flaud, P., and Tanter, M. (2013). Correlation between classical rheometry and supersonic shear wave imaging in blood clots. *Ultrasound Med. Bio.* 39 (11): 2123–2136.

19 Deffieux, T., Montaldo, G., Tanter, M., and Fink, M. (2009). Shear wave spectroscopy for in vivo quantification of human soft tissues viscoelasticity. *IEEE Trans. Med. Imag.* 28: 313–322.

20 Gennisson, J.L., Marcelan, A., Dizeux, A., and Tanter, M. (2014). Rheology over five orders of magnitude in model hydrogels: agreement between strain-controlled rheometry, transient elastography, and supersonic shear wave imaging. *IEEE Trans. Ultrason., Ferroelect., Freq. Contr.* 61 (6): 946–954.

21 Kong, H.J., Wong, E., and Mooney, D.J. (2003). Independent control of rigidity and toughness of polymeric hydrogels, *Macromolecules* 36 (12): 4582–4588.

22 Abdurrahmanoglu, S., and Okay, O. (2010). Rheological behavior of polymer-clay nanocomposite hydrogels: Effect of nanoscale interactions. *J. Appl. Polym. Sci.* 116 (4): 2328–2335.

23 Carlsson, L., Rose, S., Hourdet, D., and Marcellan, A. (2010). Nano-hybrid self-crosslinked PDMA/silica hydrogels. *Soft Matter* 6 (15): 3619–3631.

24 Budelli, E., Brum, J., Bernal, M., et al. (2017). A diffraction correction for storage and loss moduli imaging using radiation force based elastography, *Phys. Med. Biol.* 62 (1): 91–106.

9

Wave Propagation in Viscoelastic Materials

Yue Wang[1] *and Michael F. Insana*[2]

[1] *Department of Bioengineering, Beckman Institute for Advanced Science and Technology, University of Illinois at Urbana-Champaign, Champaign, IL, USA*
[2] *Departments of Bioengineering and Electrical and Computer Engineering, Beckman Institute for Advanced Science and Technology, University of Illinois at Urbana-Champaign, Champaign, IL, USA*

9.1 Introduction

Utilizing dynamic-wave elastographic techniques for estimating mechanical properties of tissue offers several advantages. Firstly, among the many methods now available for visualizing tissue viscoelastic properties, wave-based techniques are valued for their ability to quantitatively map shear modulus G. The shear moduli of human tissue can span six orders of magnitude, from a few hundred Pa for brain tissue to several GPa for bone and cartilage. Also, the shear moduli of diseased tissues can increase 2–10-fold when compared to healthy baseline values [1–3]. High elasticity contrast for disease states is beneficial in clinical diagnosis but can pose challenges when estimating properties. Secondly, unlike static compression elastography, dynamic methods apply stress or strain locally with adjustable frequency in wave-based techniques, thus estimation bias concerns from stress distributions and boundary conditions outside of the region of interest are reduced. Ultrasound and other phase-sensitive imaging modalities (MRI, optical coherence tomography (OCT)) have been available for capturing the complex wave motion thanks to their high sensitivity to sub-millimeter-scale movements. Therefore, wave-based elastography techniques have much potential to offer accurate mechanical property information with high diagnostic value.

Mechanical-wave stimulation/excitation is usually the key aspect that determines the quality of elasticity imaging. Except for passive elastography, which utilizes waves generated by physiological motion such as breathing and cardiac activities [4], most wave-based elastography techniques introduce exogenous waves, often with a controllable geometry, amplitude, and frequency bandwidth. Bulk and surfaces waves may be generated when pulsed or harmonic sources are applied. An impulse stimulus or a single-cycle sinusoid induces a broadband force-wave pulse with a group velocity that is predictive of tissue elasticity [2, 5, 6]. Harmonic-force stimulus, on the other hand, generates a narrowband force-wave burst that improves the signal-to-noise ratio (SNR) for estimating wave speed and attenuation at each excitation frequency [7–9]. The scope of this chapter is restricted to the discussion of exogenous harmonic-wave stimulation and its applications in estimating mechanical properties of elastic and viscoelastic media.

Ultrasound Elastography for Biomedical Applications and Medicine, First Edition.
Edited by Ivan Nenadic, Matthew Urban, James Greenleaf, Jean-Luc Gennisson, Miguel Bernal, and Mickael Tanter.

9.2 Estimating the Complex Shear Modulus from Propagating Waves

The theory of shear-wave propagation in viscoelastic media is well established [10–12]. This section briefly summarizes the equations that describe local displacements associated with shear waves as a function of the spatially varying complex shear modulus.

The relationship between strain ε and stress σ tensors can be expressed when displacements in the medium are small by the expression

$$\sigma_{ij} = C_{ijkl}\varepsilon_{kl}, \text{ where } i,j,k,l = 1,2,3 \tag{9.1}$$

where C is a fourth-rank tensor. For isotropic materials, C reduces to just two independent variables, the Lamé constants λ and μ, where μ is the shear modulus

$$\sigma_{ij} = 2\mu\varepsilon_{ij} + \lambda\varepsilon_{nn}\delta_{ij} \tag{9.2}$$

For source (applied force) f, the equation of wave motion is

$$\rho\frac{\partial^2 u_i}{\partial t^2} = \nabla_j \cdot \sigma_{ij} + f_i \tag{9.3}$$

which describes how stress influences the displacement-field vector $\mathbf{u}$. Usually stress is difficult to measure experimentally. Therefore, we eliminate it by substituting Eq. (9.2) into Eq. (9.3), using the definition $\varepsilon_{ij} = (\mathbf{u}_{i,j} + \mathbf{u}_{j,i})/2$ as well as the assumption that the analysis wave field does not include an active source. (We use the partial derivative notation $\mathbf{u}_{i,j} = \partial u_i/\partial x_j$.) The result is

$$\rho\frac{\partial^2 \mathbf{u}}{\partial t^2} = \mu\nabla^2\mathbf{u} + (\lambda+\mu)\nabla(\nabla\cdot\mathbf{u}) \tag{9.4}$$

If we further assume that the contribution from longitudinal waves can be ignored, Eq. (9.4) simplifies to

$$\rho\frac{\partial^2 \mathbf{u}}{\partial t^2} = \mu\nabla^2\mathbf{u} \tag{9.5}$$

because the divergence of the shear-wave component and the curl of the longitudinal-wave component are both zero. If longitudinal-wave energy is significant, Eq. (9.5) can remain valid by applying the curl operation to the displacement vector ($\nabla\times\mathbf{u}$) to remove its effects.

Knowing the density of the medium ρ and estimating field $\mathbf{u}$, we can directly compute shear modulus μ as a function of position from Eq. (9.5). This is the Helmholtz inversion technique. Normally, Helmholtz inversion is performed in the frequency domain, combined with heavy filtering of the displacement vector to avoid amplifying errors from the Laplacian in Eq. (9.5). Finite element-based techniques have been developed to iteratively solve for μ in a way that minimizes the error between simulated and experimentally acquired wave fields [13, 14]. The drawback of such techniques is a long computational time.

Alternatively μ may be estimated using a phase-gradient technique [12]. For harmonic-wave motion, and assuming local homogeneity, Eq. (9.5) reduces to

$$\rho\omega^2 = \mu k_s^2 \tag{9.6}$$

In linear-elastic media, both μ and k_s are real numbers representing, respectively, the shear modulus and the wave number at each location. In viscoelastic media, like most biological tissues, $k_s = k_r - i\alpha$ is complex with real part $k_r = \omega/c_s$ and imaginary part $\alpha(\omega)$, the frequency-dependent attenuation coefficient for shear waves. Consequently, the shear modulus $\mu(\omega) = \mu_r(\omega) + i\mu_i(\omega)$ is complex for viscoelastic media.

To measure μ_r and μ_i independently, both wave speed and attenuation must be estimated. It is very challenging to estimate shear-wave attenuation unless the wave-front geometry is well known. However, attenuation estimation is not necessary if a mathematical model is adopted to describe the behavior of μ_r and μ_i as a function of frequency. With the model, shear-wave speeds dispersion curve is a function of those model parameters (Eq. 9.7). One can determine the best model parameters through least-square fitting of Eq. (9.7) to the dispersion curve.

$$c_s(\omega) = \sqrt{\frac{2(\mu_r^2 + \mu_i^2)}{\rho(\mu_r + \sqrt{\mu_r^2 + \mu_i^2})}} \tag{9.7}$$

Speed c_s is estimated from the shear-wave phase gradient along the direction of shear-wave propagation where rheological model parameters are obtained as a function of position. The range over which phase gradients yield accurate wave-speed estimates depends on the homogeneity of the medium. There is an inherent tradeoff between spatial resolution and phase-estimation accuracy with this approach.

9.3 Wave Generation and Propagation

Most readily accessible ultrasound machines support only two-dimensional echo acquisition. This restricts the direction of shear-wave propagation to be along the lateral direction of a 1D array. Cylindrical waves and surface waves are widely used to mechanically excite tissues [15–21]. Other wave geometries, such as plane and Lamb waves, are used in some circumstances; for example, when imaging a vessel wall [19]. However, they are difficult to apply in media with amorphous structure, such as biological tissues. There are several advantages to using cylindrical or surface waves. Both wave geometries are easy to generate experimentally by, for example, vibrating a needle inserted into the medium [16], acoustic radiation force (ARF) [18], dual-focus ultrasound transducer [21], or through a sequence of ARF pulses over a range of depths that generate a shock wave [20].

Cylindrical waves provide radially symmetric excitation fields about the vibrating needle, making it possible to image tissues at any depth. Figure 9.1 gives an example of a cylindrical wave propagating in homogeneous gelatin gels (an elastic medium at these frequencies). More detail about the setup is presented in ref. [16]. A biopsy needle vibrating at 200 Hz along the z axis generates harmonic shear waves that are imaged by a Doppler probe (7 MHz, PRF 12.5 kHz). In the direction of shear-wave propagation, the phase of the wave shifts linearly while its amplitude decreases exponentially. Even if $\theta \neq 0$, the phase remains linear near the source at depths as much as 40 mm in gelatin gel. Ultrasonically guided breast needle biopsy is an opportunity to excite tissues with harmonic cylindrical waves for shear-wave imaging without adding to patient risk.

There are several noninvasive techniques for generating approximately cylindrical waves in tissues, e.g. ARF impulses are commonly applied. Fink et al. [20] transmitted a sequence of ARF push pulses that excite a Mach-cone-shaped shear wave, which is approximately cylindrical for large Mach numbers. The method takes advantage of the fact that the speed of the compressional-wave ARF pulses in tissues is about 1000 times faster than that of the shear waves they generate.

Rayleigh-type surface waves are generated when a forcing source is applied at or near a free surface of a solid sample [22], e.g. see Figure 9.2. Rayleigh waves are a mixture of shear and longitudinal particle motions, and yet its phase velocity can be directly related to shear-wave velocity by a constant between 0.92 and 0.96 depending on Poisson's ratio for the medium [23].

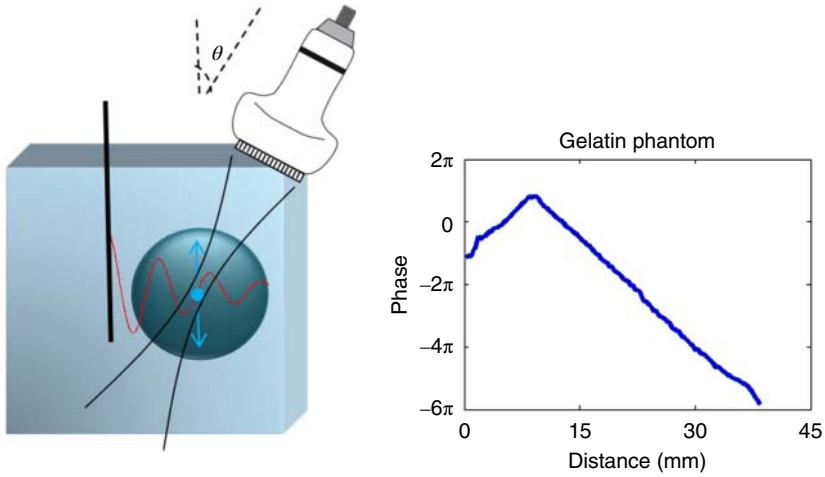

Figure 9.1 A vibrating needle generates patterns of 200 Hz cylindrical shear waves inside a gelatin block that are imaged using standard ultrasonic Doppler techniques at angle θ. Measurements of a linear phase shift with lateral position about the needle are shown (right).

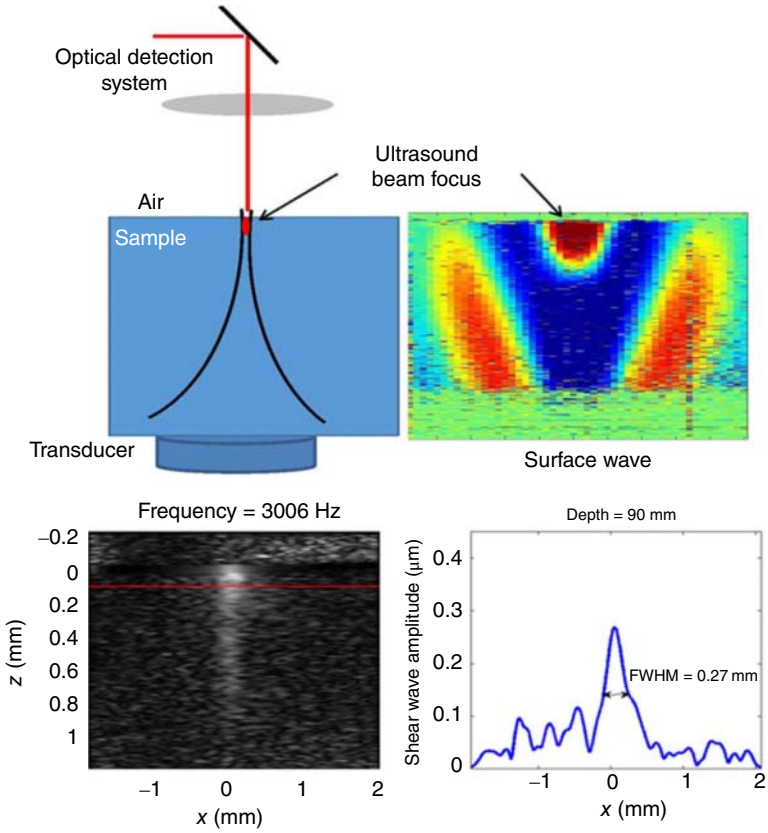

Figure 9.2 Acoustic radiation force geometry (upper left) generates surface waves inside a gelatin block (upper right) over a region approximately 1 mm × 4 mm. Lower left grayscale image shows optical coherence tomographic (OCT)-detected displacement amplitude for a 3 kHz ARF excitation. A plot of displacement amplitude at the depth indicated by the horizontal line is shown on the lower right. Source: republished with permission from CRC Press from [27]; permission conveyed through Copyright Clearance Center, Inc.

Although the speeds of surface and bulk waves are about 5% different, the amplitudes of both waves decay according to the geometric factor $1/\sqrt{r}$ with distance r from a point source in elastic media. In more viscous media, the frequency-dependent shear-wave attenuation reduces the amplitude more rapidly. Thus, we are able to apply similar estimation algorithms for imaging surface and bulk transverse waves.

Surface waves are easier to excite using noninvasive sources than are cylindrical shear waves, because the impedance discontinuity at the surface acts to strongly couple the transfer of pulse momentum to the medium surface. Surface waves travel with some depth in the medium. They propagate about one to two wavelengths in depth so both optical and ultrasonic Doppler techniques can image this motion. Ultrasound is sensitive to transverse-wave particle motion over many centimeters of depth, while optical coherence tomography (OCT) is more sensitive to the small displacement amplitudes of high-frequency transverse waves but only 1–2 mm deep [24]. High-frequency surface waves enable measurement of mechanical properties at higher spatial frequencies and with higher spatial resolution, which is particularly beneficial for imaging heterogeneous tissues.

One characteristic of surface waves is depth-related velocity dispersion. The velocity of surface waves is a function of material property at each depth location that the wave penetrates. The wavelength of a surface wave and its penetration depth each decrease inversely in proportion to frequency. If the mechanical property of the material varies with depth, it will be reflected in the surface wave velocity-dispersion curve. This curve can be used to resolve spatially varying mechanical information in layered media if the material is not too strongly dispersive [25, 26].

Figure 9.2 illustrates images of surface waves in a homogeneous 8%-concentration gelatin gel using an ARF source applied from below. A compressional wave pulse traveling upward is totally reflected at the sample–air surface, thus generating a transverse surface wave. That surface wave travels horizontally with a cone-shaped geometry in the image plane near the source. In this example, 800 Hz waves are imaged using OCT to measure particle motion along the top surface of the sample [27]. The wave amplitude map for a 3 kHz source is also shown on the bottom left of Figure 9.2. The top of the sample is located at depth $z = 0$, and the brightest spot at the center is the excitation source.

Cylindrical shear waves and radial surface waves have each been successfully applied in elasticity imaging. The choice of wave excitation method depends on specific experimental conditions, as well as sample size, shape, and degree of inhomogeneity. In practice, transverse wave propagation is distorted by sample heterogeneities and boundaries that can bias shear modulus estimates. For example, distortion of the phase front will bias low the shear-wave speed estimated using phase-gradient methods [28]. Most of these effects are minimized when the sample size is larger than two shear wavelengths. In some cases, directional filters can help reduce the influence of reflected shear waves [29]. Internal wave reflections pose a significant challenge for 2D ultrasonic phase measurements near tissue interfaces. In highly attenuating media, reflections are less of a factor; instead displacement SNR is the limiting factor for modulus estimation.

9.4 Rheological Models

The complex shear modulus $\mu = \mu_r + i\mu_i$ as a function of frequency provides a model-independent metric that characterizes the viscoelastic behavior of a material under dynamic loading. Rheological constitutive models are proposed as a way to connect physical and experimental parameters to the real and imaginary parts of the property μ; for example, the Kelvin–Voigt (KV) model implies μ_r is the elastic shear modulus E and μ_i is the viscous coefficient times the radial frequency, $-\eta\omega$. That is, for $\sigma = \mu\varepsilon$ the KV model gives

Table 9.1 Comparison between the Kelvin–Voigt model and the Maxwell model.

	Kelvin–Voigt	**Maxwell**
description	$\sigma = E\varepsilon + \eta\frac{\mathrm{d}\varepsilon}{\mathrm{d}t}$	$\frac{1}{E}\frac{\mathrm{d}\sigma}{\mathrm{d}t} + \frac{\sigma}{\eta} = \frac{\mathrm{d}\varepsilon}{\mathrm{d}t}$
μ	$A\cos\varphi + iA\sin\varphi = E - i\omega\eta$	$\frac{i\omega\eta E}{E - i\omega\eta} = \frac{\omega^2\eta^2 E}{E^2 + \omega^{2\eta^2}} - i\frac{\omega\eta E^2}{E^2 + \omega^{2\eta^2}}$

$\mu = E - i\omega\eta$. Other models have been proposed in attempts to summarize in just one or two imaging parameters values representing μ for very complicated materials. The basic problem with these simple models is that tissues are not the material continua assumed. Tissues are better described as multiphasic composites and sometimes structures, depending on the measurement scale. No model fully captures the constitutive complexity of soft tissues, which prompts some investigators to avoid them altogether by adopting methods that estimate μ directly.

When models are assumed, the simplest and most-often applied are the Kelvin–Voigt (KV) and Maxwell models, summarized in Table 9.1. The KV model describes solid materials while the Maxwell model describes viscoelastic fluids, and both offer two parameters that are frequently mapped into elasticity images. Since soft tissue is neither solid nor fluid, a combination – the Zener model – is somewhat more realistic. Others models proposed include the Jeffrey model, the generalized Maxwell model, and the generalized KV model, most of which are higher order combinations of KV and Maxwell elements [30]. Recently, fractional derivative (FD) models are proving to be efficient in summarizing the dynamic behavior of viscoelastic materials over a wide frequency range with just 2 or 3 parameters [31, 32]. Figure 9.3 shows the dispersion behaviors predicted by the different models.

Given that all models are limited in their ability to predict behavior, we settle for those that yield physically meaningful imaging parameters that are sensitive to the presence of disease. The best models offer parameters that are correlated with inflammation, hyper cellularity, fibrosis, and other classic pathological biomarkers. At this point in elasticity imaging development, we are still correlating model parameters with tissue states characteristic of disease.

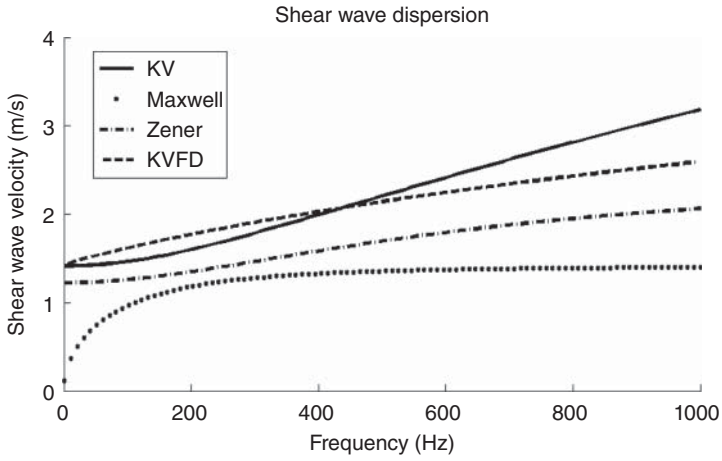

Figure 9.3 Dispersion curves as predicted by four rheological models over the same frequency range.

9.5 Experimental Results and Applications

9.5.1 Validation of Shear Wave and Surface Wave Elasticity Imaging on Phantoms

Pure gelatin gels (<15% concentration) do NOT model soft tissue behavior accurately. However, gelatin samples are well suited for directly comparing elastic imaging results with materials characterization techniques such as mechanical indentation, which provides methodological validation for different measurement approaches. We and others have shown that the elastic modulus remains approximately constant over a large force-frequency bandwidth, as predicted by the KV model, so results can be directly compared [16, 33].

Shear-wave and surface-wave measurements were compared for 4% gelatin-concentration samples in Figure 9.4. Although each measurement is most sensitive in different frequency ranges, there is overlap showing similar estimates below 300 Hz. The Young's modulus values (calculated from the average of c_s estimates over all frequencies) were 1.95 ± 0.08 kPa for a shear-wave method and 2.38 ± 0.14 kPa for a surface-wave method. Young's modulus measured using quasi-static Hertzian indentation estimated was 1.75 ± 0.06 kPa for the same sample [34]. Since the viscosity of gelatin is ignored during estimation, modulus values can be expected to bias measurements at high frequency, contributing to the observed differences. These similarities provide confidence that wave-based elasticity imaging can reliably yield moduli that compare well among standard materials measurements.

9.5.2 3D Modulus Reconstruction of Sample with Inclusion

Resolution is essential in any imaging system due to the heterogeneous nature of human tissue. Wave-based elasticity imaging may never provide micrometer-level resolution but it can clearly distinguish a lesion with mechanical contrast relative to the background. In this study, a soft cylindrical inclusion (4%) was embedded in a stiff gelatin gel block (8%), which was imaged using ultrasonic shear-wave methods and a vibrating needle source. 3D ultrasonic data were obtained from stacking multiple 2D images in the elevation direction. The measured shear-wave patterns near a cylindrical inclusion are in good agreement with predictions. The wavelength shortens as the shear wave enters the soft inclusion. A 3D Helmholtz inversion technique was used to reconstruct the shear modulus of the object (corresponding results are shown in Figure 6 in ref [35]). The modulus estimation accuracy near the edge of the inclusion is compromised more when only 2D wave data are available.

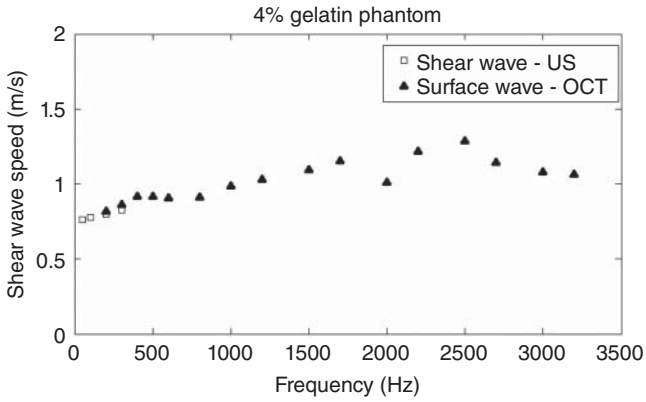

Figure 9.4 Comparison of wave dispersion curves measured on 4% gelatin sample using shear-wave imaging technique and surface-wave imaging technique. Shear waves and surface waves were tracked by ultrasound and optical coherence tomography, respectively.

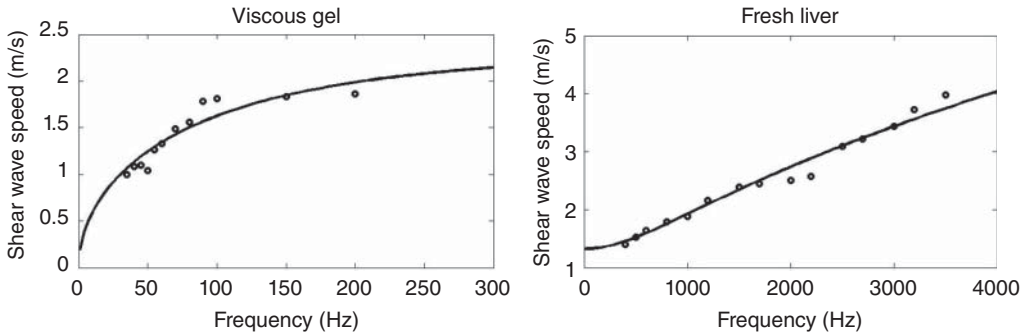

Figure 9.5 (left) Dispersion curve of viscous gel measured by ultrasonic shear wave imaging technique, with Maxwell model fit. (Right) Dispersion curve of an ex vivo fresh porcine liver measured by optical surface wave imaging, with Kelvin–Voigt mode fit.

9.5.3 Modeling of Viscoelastic Material

Wave speed in an elastic material is constant with frequency. In contrast, viscoelastic materials are dispersive; i.e. the wave speed changes substantially with frequency. Dispersive behavior is determined by the components of the materials and their mechanical couplings. In standard rheological models, these components are represented by springs and dash-pots. The combination patterns of springs and dash-pots usually represent certain components or their interactions, and inappropriate models could produce non-physical and perhaps non-diagnostic parametric images. Generally, materials that share similar compositions will be similarly dispersive, thus the same model can be adopted to fit their dispersion curves.

Figure 9.5 shows different dispersive behaviors. On the left is a dispersion curve of a viscous gel that is fitted to a Maxwell model, implying this gel has fluid-like properties. The model parameters are $E = 5.58$ kPa, $\eta = 2.9$ Pa·s. On the right is the dispersion curve of ex vivo porcine liver fitted to a KV model, implying solid material behavior. The model parameters are $E = 1.75$ kPa, $\eta = 0.4$ Pa·s. It is difficult to directly compare these modeling results of the materials because neither are a continuum. The viscous gel is an oil-based cream emulsified in gelatin (a composite material) and liver is a collagen polymer embedded in open- and closed-cell fluid compartments. We need new ways of representing complex mechanical structures.

The solution is not to increase the number of parameters by adding coupled components to existing models. It is unlikely that more complicated models will enhance the diagnostic performance of elastography. There is new hope in recent efforts to model tissue mechanics using fractional derivative models [36]. These models may help resolve the solid–fluid duality of soft biological tissues [37] by offering a compact feature space that is sensitive to disease states.

9.6 Summary

Shear-wave and surface-wave imaging offer quantitative estimates of intrinsic viscoelastic properties of dispersive tissues. Coupling dispersion behavior with rheological models parameterizes measurements as needed for imaging. The appropriate model depends on how well it represents the data and how well it separates healthy and pathological tissues based on histological features. The future for this type of diagnostic imaging continues to brighten as we learn to summarize mechanical properties of tissues from measurements of transverse waves in the body.

References

1 Samani, A., Zubovits, J., and Plewes, D. (2007). Elastic moduli of normal and pathological human breast tissues: an inversion-technique-based investigation of 169 samples. *Phys. Med. Biol.* 52 (6): 1565–1576.

2 Sandrin, L., Fourquet, B., Hasquenoph, J.M., et al. (2003). Transient elastography: a new noninvasive method for assessment of hepatic fibrosis. *Ultrasound Med. Biol.* 29 (12): 1705–1713.

3 Huwart, L., Peeters, F., Sinkus, R., et al. (2006). Liver fibrosis: non-invasive assessment with MR elastography. *NMR Biomed.* 19 (2): 173–179.

4 Gallot, T., Catheline, S., Roux, P., et al. (2011). Passive elastography: shear-wave tomography from physiological-noise correlation in soft tissues. *IEEE Trans. Ultrason., Ferroelect., Freq. Control* 58 (6): 1122–1126.

5 Nightingale, K.R., Palmeri, M.L., Nightingale, R.W., and Trahey, G.E. (2001). On the feasibility of remote palpation using acoustic radiation force. *J. Acoust. Soc. Am.* 110 (1): 625–634.

6 Sato, T., Fukushima, A., Ichida, N., et al. (1984). Nonlinear parameter tomography system using counter-propagating probe and pump waves. *Ultrason. Imaging* 6 (2): 237–237.

7 Oldenburg, A.L. and Boppart, S.A. (2010). Resonant acoustic spectroscopy of soft tissues using embedded magnetomotive nanotransducers and optical coherence tomography. *Phys. Med. Biol.* 55 (4): 1189–1201.

8 Orescanin, M. and Insana, M.F. (2010). Shear modulus estimation with vibrating needle stimulation. *IEEE Trans. Ultrason., Ferroelect., Freq. Control* 57 (6): 1358–1367.

9 Tse, Z.T.H., Chan, Y.J., Janssen, H., et al. (2011). Piezoelectric actuator design for MR elastography: implementation and vibration issues. *Int. J. Med. Rob. Comput. Assisted Surg.* 7 (3): 353–360.

10 Sinkus, R., Tanter, M., Catheline, S., et al. (2005). Imaging anisotropic and viscous properties of breast tissue by magnetic resonance elastography. *Magn. Reson. Med.* 53 (2): 372–387.

11 Zhang, J. and Muthupillai, R. (2014). Magnetic resonance elastography. In: *Handbook of Imaging in Biological Mechanics* (ed. C. Neu and G. Genin), Boca Raton: CRC Press.

12 Greenleaf, J.F., Fatemi, M. and Insana, M. (2003). Selected methods for imaging elastic properties of biological tissues. *Annu. Rev. Biomed. Eng.* 5: 57–78.

13 Van, E.E., Paulsen, K.D., Miga, M.I., et al. (1999). An overlapping subzone technique for MR-based elastic property reconstruction. *Magn. Reson. Med.* 42 (4): 779–786.

14 Van, E.E., Weaver, J.B., Miga, M.I., et al. (2000). Elasticity reconstruction from experimental MR displacement data: initial experience with an overlapping subzone finite element inversion process. *Med. Phys.* 27 (1): 101–107.

15 DeWall, R.J., Varghese, T., and Madsen, E.L. (2011). Shear wave velocity imaging using transient electrode perturbation: phantom and ex vivo validation. *IEEE Trans. Med. Imaging* 30 (3): 666–678.

16 Orescanin, M. and Insana, M.F. (2010). Shear modulus estimation with vibrating needle stimulation. *IEEE Trans. Ultrason., Ferroelect., Freq. Control* 57 (6): 1358–1367.

17 Li, C., Guan, C., Cheng, X., et al. (2012). Quantitative elastography provided by surface acoustic waves measured by phase-sensitive optical coherence tomography. *Opt. Lett.* 37 (4): 722–724.

18 Nightingale, K.R., Palmeri, M.L., Nightingale, R.W., and Trahey, G.E. (2001). On the feasibility of remote palpation using acoustic radiation force. *J. Acoust. Soc. Am.* 110 (1): 625–634.

19 Bernal, M., Nenadic, I., Urban, M.W., and Greenleaf, J.F. (2011) Material property estimation for tubes and arteries using ultrasound radiation force and analysis of propagating modes. *J. Acoust. Soc. Am.* 129 (3): 1344–1354.

20 Bercoff, J., Tanter, M., and Fink, M. (2004). Supersonic shear imaging: a new technique for soft tissue elasticity mapping. *IEEE Trans. Ultrason., Ferroelect., Freq. Control* 51 (4): 396–409.

21 Odagiri, Y., Hasegawa, H., and Kanai, H. (2008) Ultrasonic measurement of strain distribution inside object cyclically compressed by dual acoustic radiation force. *Jpn. J. Appl. Phys.* 47: 4193.

22 Telford, W.M., Geldart, L.P., and Sheriff, R.E. (1990). *Applied Geophysics*, p. 149. Cambridge: Cambridge University Press.

23 Zhang, X. and Greenleaf, J.F. (2007). Estimation of tissue's elasticity with surface wave speed. *J. Acoust. Soc. Am.* 122 (5): 2522–2525.

24 Kirkpatrick, S.J., Wang, R., and Duncan, D.D. (2006). OCT-based elastography for large and small deformations. *Opt. Express* 14 (24): 11585–11597.

25 Bourse, G., Myotte, P., Xu, W.J., and Lanceleur, P. (1999). Evaluation of elastic properties of surface layer from Rayleigh wave dispersion, *Rev. Prog. Quant. Nondestr. Eval.* 18: 1439–1445.

26 Li, C., Guan, G., Reif, R., et al. (2012). Determining elastic properties of skin by measuring surface waves from an impulse mechanical stimulus using phase-sensitive optical coherence tomography. *J. R. Soc. Interface* 9 (70): 831–841.

27 Wang, Y., Adie, S.G., Boppart, S.A., and Insana, M.F. (2014). Ultrasound and optical methods for dynamic viscoelastic imaging. In: *Handbook of Imaging in Biological Mechanics* (ed. C. Neu and G. Genin), 81–94. Boca Raton: CRC Press.

28 Wang, Y. and Insana, M.F. (2013). Viscoelastic properties of rodent mammary tumors using ultrasonic shear-wave imaging. *Ultrason. Imaging* 35 (2):126–145.

29 Manduca, A., Lake, D.S., Kruse, S.A., and Ehman, R.L. (2003). Spatio-temporal directional filtering for improved inversion of MR elastography images. *Med. Image Anal.* 7 (4): 465–473.

30 Schmitt, C., Hadj Henni, A., and Cloutier, G. (2011). Characterization of blood clot viscoelasticity by dynamic ultrasound elastography and modeling of the rheological behavior. *J. Biomech.* 44 (4): 622–629.

31 Sloninsky, G.L. (1967). Laws of mechanical relaxation processes in polymers. *J. Polym. Sci. Part C* 16: 1667–1672.

32 Pritz, T. (2003). Five-parameter fractional derivative model for polymeric damping materials. *J. Sound Vibr.* 265 (5): 935–952.

33 Ahmad, A., Kim, J., Sobh, N.A., et al. (2014). Magnetomotive optical coherence elastography using magnetic particles to induce mechanical waves. *Biomed. Opt. Express* 5 (7): 2349–2361.

34 Altahhan, K.N., Wang, Y., Sobh, N., and Insana, M.F. (2016). Indentation measurements to validate dynamic elasticity imaging methods, *Ultrason. Imaging* 38 (5): 332–345.

35 Orescanin, M., Wang, Y., and Insana, M.F. (2011). 3-D FDTD simulation of shear waves for evaluation of complex modulus imaging. *IEEE Trans. Ultrason., Ferroelect., Freq. Control* 58 (2): 389–398.

36 Magin, R.L. (2006). *Fractional Calculus in Bioengineering*. Begell House, CT.

37 Sinkus, R., Siegmann, K., Xydeas, T., et al. (2007). MR elastography of breast lesions: understanding the solid/liquid duality can improve the specificity of contrast-enhanced MR mammography. *Mag. Reson. Med.* 58: 1135–1144.

Section IV

Static and Low Frequency Elastography

10

Validation of Quantitative Linear and Nonlinear Compression Elastography

Jean Francois Dord[1], Sevan Goenezen[1], Assad A. Oberai[1], Paul E. Barbone[2], Jingfeng Jiang[3], Timothy J. Hall[4], and Theo Pavan[5]

[1] *Department of Mechanical Aerospace and Nuclear Engineering, Rensselaer Polytechnic Institute, Troy, NY, USA*
[2] *Department of Mechanical Engineering, Boston University, Boston, MA, USA*
[3] *Department of Biomedical Engineering, Michigan Technological University, Houghton, MI, USA*
[4] *Medical Physics Department, University of Wisconsin, Madison, WI, USA*
[5] *Departmento de Física, University of São Paulo, São Paulo, Brazil*

10.1 Introduction

Over the last few decades elastography, or elasticity imaging, has emerged as a novel imaging modality that may be used to detect and diagnose malignant tumors [1–3]. The premise behind this role for elastography is that disease often alters tissue microstructure, which in turns leads to altered macroscopic tissue properties. Most efforts in elastography have focused on recovering the linear properties of tissues [4–6] while ignoring their nonlinear behavior which becomes evident at large strains. Recent ex vivo data suggests that the nonlinear elastic behavior may play an important role in differentiating benign and malignant tissue, with the concensus being that malignant tissue tends to stiffen to a larger extent with increasing strain [7–9]. This leads to the intriguing possibility of using the nonlinear behavior of tissue to discern whether a tumor is cancerous. Over the last two-to-three years several studies have demonstrated the feasibility of this idea [10–14].

Motivated by these applications we have developed and implemented an iterative, nonlinear algorithm to determine the nonlinear elastic properties of a tissue from the knowledge of its internal displacement field. We have tested this algorithm in two dimensions in the context of plane-stress and plane-strain approximations [15, 16]. We have benchmarked its performance using synthetic (computer-generated) displacement data. We have also applied it to a small set of patient data [27]. In this chapter we benchmark the performance of this algorithm on experimentally acquired tissue-phantom data. This allows us to work with a realistic set of measured displacements, in terms of the noise and bias introduced by the ultrasound equipment and displacement estimation algorithms, and at the same time provides a ground truth with which to compare our reconstructed material properties. We challenged our reconstruction techniques by performing a "blind" test, in that the reconstruction team was provided no information (shape, number, or contrast of inclusions) about the phantom while the modulus images are reconstructed. Once the reconstruction team delivers its "final" answer, it is compared to the experimental measurements. This answer is not modified in light of what is now known to be the correct answer. We also utilize this study as an opportunity to analyze the effect of various algorithmic choices made in our computational strategy. In particular, we examine the effect of assumed boundary conditions and the values of regularization parameters used in the inverse problem.

Ultrasound Elastography for Biomedical Applications and Medicine, First Edition.
Edited by Ivan Nenadic, Matthew Urban, James Greenleaf, Jean-Luc Gennisson, Miguel Bernal, and Mickael Tanter.

The layout of the remainder of this chapter is as follows. In Section 10.2 we briefly describe the solution of the inverse nonlinear elasticity problem, the ultrasound data acquisition, and the displacement estimation algorithm. Section 10.3 presents the reconstructions for the linear and nonlinear elastic parameters for the tissue-phantom. The following section discusses several algorithmic choices for our reconstruction algorithms. Finally in Section 10.5 we discuss these results and end with conclusions.

10.2 Methods

10.2.1 The Inverse Algorithm

The inversion strategy uses a quasi-Newton optimization algorithm (L-BFGS-B [28, 29]) coupled with a nonlinear finite element code. The objective function is given by the sum of a data matching term and total variation (TV) regularization terms [11, 15]:

$$\pi = \frac{1}{2}\int_\Omega \sum_n^{N_{\text{meas}}} w_n |T(U^n) - T(U^n_{\text{meas}})|^2 + \alpha_\mu \int_\Omega \sqrt{\beta_\mu^2 + |\nabla \mu|^2} + \alpha_\gamma \int_\Omega \sqrt{\beta_\gamma^2 + |\nabla \gamma|^2} \tag{10.1}$$

In the equation above U^n_{meas} is the n-th measured displacement field, U^n is the corresponding predicted displacement field which satisfies the equations of equilibrium for a hyperelastic material, T is a diagonal matrix whose values are selected to emphasize the displacement components that are measured accurately, and w_n is a weight related to the amplitude of U^n. It is selected so that measurements made at disparate levels of strain contribute in equal measure to the data-matching terms. The material parameters are denoted by μ and γ, which denote the shear modulus at zero strain and nonlinear parameter distributions, respectively. Finally, β_μ and β_γ are small constants that ensure the differentiability of the regularization terms at the origin; α_μ and α_γ are the regularization parameters associated with μ and γ, respectively. These parameters determine the relative importance of the data matching and the regularization terms. We note that a change in the material parameters leads to a change in the predicted displacements U^n which in turn leads to a chance in the functional π. The goal is to find the distribution of the material parameters that minimizes π.

We model the material (gel) as an incompressible hyperelastic material. The stress-strain behavior is thus completely determined by the strain energy density function given by

$$W = \mu\left(\frac{1}{\gamma}(e^{\gamma(I_1+1/I_2-3)} - 1) - \frac{1}{2}(I_1 + I_1/I_2 - 3)\right) \tag{10.2}$$

In the equation above μ is the shear modulus at small strains and γ represents the rate of increase of stiffness with strain. In addition I_1 and I_2 are the invariants of the two-dimensional Cauchy-Green strain tensor C. We note that the expression for the strain energy density we have used is the restriction of a simplified Veronda-Westmann model [15, 30] to plane stress.

At every iteration the quasi-Newton algorithm requires the gradient vector which represents the change in π corresponding to a change in μ or γ at a spatial location. This vector is computed efficiently by utilizing the adjoint elasticity equations and a continuation strategy in material parameters [15, 16].

10.2.2 Phantom Description and RF Data Acquisition

A phantom containing four spherical inclusions was manufactured using previously reported ultrasound phantom materials with nonlinear elastic properties [17]. The methods for

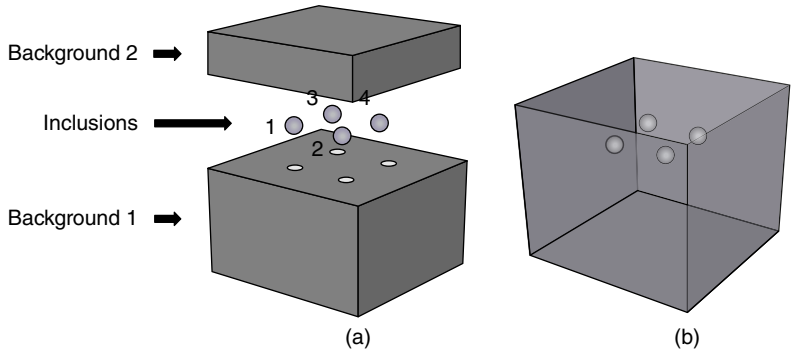

Figure 10.1 Three dimensional depiction of the phantom. (a) Parts that composed the phantom; (b) the phantom in its final form.

manufacturing phantoms with coplanar spherical inclusions were also previously reported [18, 19]. Sketches of the phantom identifying the background layers and individual targets are provided in Figure 10.1. The assembled phantom is a 100 mm cube. Each spherical target is 10 mm diameter. They are separated by 30 mm (center-to-center) and are placed 35 mm (center to phantom edge) from the top and each lateral side of the phantom.

When the phantom components were manufactured, a test cylinder of the same material was also cast to provide identical material with simple geometry to independently test the stress–strain behavior of the material. Mechanical tests were performed with an EnduraTEC ELF 3200 (Bose-EnduraTEC Systems Corporation, Minnetonka, MN, USA) using a 1 kg load cell and Teflon® platens larger than the sample surface. Each test cylinder was stored in oil to prevent desiccation, and that oil was used to lubricate the platens for the mechanical testing. During the mechanical testing, the upper platen was first lowered to make contact with the test cylinder. Then, the platen was lowered further (at 0.04 mm/s) to the center of the cyclic deformation range used for material characterization and the platen remained at that deformation for 5 s. A 1 Hz oscillatory compressive load (ranging from 1% to 25% strain) was applied for 5 s before starting data acquisition to precondition the sample [20, 21]. Following the preconditioning step, force and displacement data were acquired for the randomized range of displacement magnitudes for each phantom material. Thus, the stress–strain curve of each tissue-mimicking material (2 backgrounds and 4 inclusions) was obtained and subsequently fitted to the modified Veronda-Westmann model to estimate the small strain shear modulus μ and the nonlinear parameter γ (see Eq. 10.2).

During phantom experiments, radiofrequency (RF) data were acquired using a Siemens SONOLINE Antares (Siemens Medical Solutions USA, Inc, Malvern, PA) clinical ultrasound system with a linear array ultrasound transducer (Siemens VFX9-4) pulsed at 8.89 MHz. Details of the URI and bandwidth of the Siemens system are given by Brunke et al. [22]. A large (approximately 15 cm by 15 cm) compression plate was attached to the ultrasound transducer to ensure nearly uniaxial deformations of the phantom. More specifically, ultrasound RF data were acquired for every 1.5% increment deformation (after the first few frames of 0.5% strain) up to approximately 20% (with respect to its height). Further details regarding this phantom are reported by Pavan et al. [23].

10.2.3 Displacement Estimation

To obtain large deformations (approximately 20%) required for nonlinear elasticity imaging, we first tracked motion sequentially through multiple frames similar to the multi-compression technique [24]. In the first step, offline motion tracking using RF echo data acquired from the

nonlinear tissue-mimicking phantom was performed between each pair of two adjacent RF echo frames [e.g. from the i-th frame to the $(i + 1)$-th frame] using a modified block-matching algorithm [25]. This modified block-matching algorithm combines smoothness-constrained motion tracking with predictive search [26]. Specifically, this modified block-matching algorithm first estimated reliable motion within a small neigborbood to obtain high quality displacement estimates in a sparse grid (e.g. every 5 mm). Then, these reliable high quality displacements were used as seeds to perform predictions for its immediate neighbors. During this process, a small (approximately 0.5 mm [height] by 1 mm [width]) tracking kernel was first used to obtain integer displacements. Then, sub-sample displacement estimates (necessary for modulus inversion) were obtained with quadratic interpolations. Collectively, this algorithm significantly reduces the occurance of large motion tracking errors between two adjacent RF frames. Once all displacement fields between adjacent RF echo frames were obtained, we mapped all displacement estimates in this sequence (from the first frame to the n-th frame) to the coordinate system of the first echo frame by using B-spline interpolations.

10.3 Results

The displacement data was measured on a 300×231 grid with a resolution of 0.1545×0.1217 mm. It was found that the data close to the boundaries contained more noise than inside the domain. As a result 39 lines were removed from the axial edge close to the ultrasound probe and 8 lines were removed from the opposite axial edge. In addition 9 lines were removed from each of the lateral edges. We define the axial direction to be the direction along the axis of the ultrasound transducer. The lateral direction is the direction in the imaging plane that is perpendicular to the axial direction. In order to keep the problem small the displacement field was downsampled by a factor of four in each direction. The shear modulus and nonlinear parameter images were generated on a 63×54 mesh with a resolution of 0.618×0.487 mm. The displacement measurements were sampled on the same grid. It was recognized that the measured data in the axial direction (y) was much more accurate than in the lateral direction (x). As a result the latter was dropped from the displacement matching term by selecting $T_{xx} = 0$ and $T_{yy} = 1$. The reconstructions were performed by a team comprising of the first four authors of this chapter *without* any a priori knowledge of the phantom and its properties. Further, once the comparison with experimental data was made, these reconstructions were not revisited or polished.

10.3.1 Description of the Forward Problem

As part of our iterative strategy a forward elasticity problem is solved at every iteration of the optimization algorithm. For the boundary conditions in the forward problem, on every edge, the axial component of the displacement was set equal to the measured displacement while in the lateral direction a traction-free state was assumed. This implied perfect slip on the axial (the top and the bottom) edges and zero normal traction on the lateral (left and right) edges. This choice was motivated by the experimental set-up and the fact that the measured lateral displacements were too noisy to be imposed strongly. The effect of other choices for boundary conditions was also explored and is described in Section 10.4.4. The phantom was assumed to be in a state of plane stress, which is appropriate since the phantom was not confined in the elevational direction.

10.3.2 Options for the Optimization Strategy

The material parameters μ and γ were determined sequentially. That is, first μ was reconstructed using measurements at small deformation while keeping γ fixed at 0.1. Thereafter γ

was reconstructed using two displacement fields at large strains while μ was held fixed at the previously computed value.

Several tests (not reported here) demonstrated that the choice of the initial value for μ and γ did not impact the final reconstructions provided that the initial field(s) were in a reasonable range. In this chapter, the initial fields were chosen to be uniform with a value of $\mu = 1.05$ and $\gamma = 0.5$. We would like to emphasize that even though the final results are not influenced by the initial field, the rate of convergence is: not surprisingly, the closer the initial choice is to the final solution, the faster the convergence.

The TV regularization used in Eq. (10.1) is a linear function of the magnitude of the gradient of the fields and consequently for a given contrast in material properties it will tend to reduce the mean value of the field. Additionally, the shear modulus is recovered only to a multiplicative constant as we use only displacement data in our inverse problem. Therefore it is necessary to specify a lower bound for the optimization algorithm. In this chapter, the shear modulus and nonlinear parameter are constrained as follows: $1 \leq \mu \leq 10$ and $0.01 \leq \gamma \leq 10$. Note that we ensured that the upper bound was never obtained for both μ and γ.

The convergence criterion plays an important role in determining the final answer. The L-BFGS-B algorithm implements two stopping criteria: stop when

(i) the relative change in the objective function value is less than a prescribed value, or
(ii) when value of the L_2-norm of the projected gradient is smaller than a prescribed value.

In our experience the iterations terminated due to the first criterion and we set the tolerance to be 0.1ϵ, where ϵ is the machine precision. Choosing such a small value for the tolerance leads to results that are convincingly converged. A slightly higher value could have been chosen to reduce the number of iterations.

10.3.3 Shear Modulus Images

The shear modulus was reconstructed using the displacement measured with an overall strain of approximately 1.5%. The results are shown in Figure 10.2 and the values of the regularization parameters appear in Table 10.1. The robustness of this strategy was verified by using one or more displacement fields with overall strain in the range of 0.5% to 3.5% in order to recover the shear modulus. It was found that this choice did not significantly change the results.

10.3.4 Nonlinear Parameter Images

The nonlinear mechanical behavior can only be observed for rather large deformations and therefore it is appropriate to use deformation states where the strain is around 20%. Figure 10.3 shows the non linear parameter fields obtained when frames 30 (with 18% overall strain) and

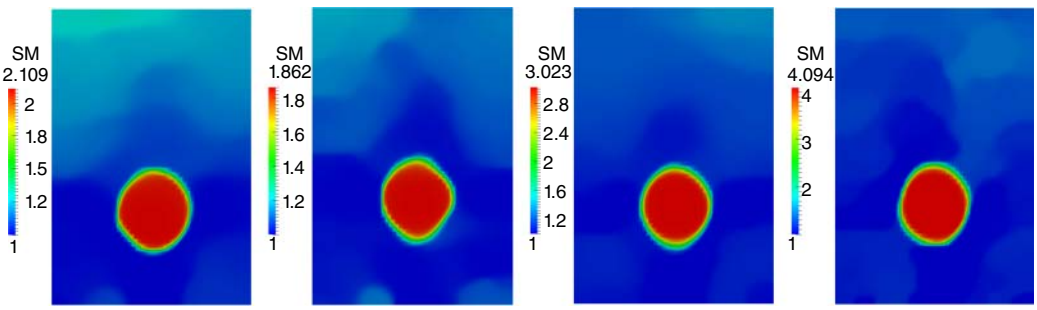

Figure 10.2 Shear modulus μ reconstructions for sections 1 through 4 (left to right).

Table 10.1 Values of the parameters for the reconstructions (Eq. 10.1).

Parameter	set 1	set 2	set 3	set 4
α_μ	7e-5	4e-5	4e-5	1e-5
β_μ	6e-3	6e-3	6e-3	3e-3
α_γ	4e-4	4e-4	7e-5	1e-4
β_γ	7e-3	7e-3	7e-3	7e-3

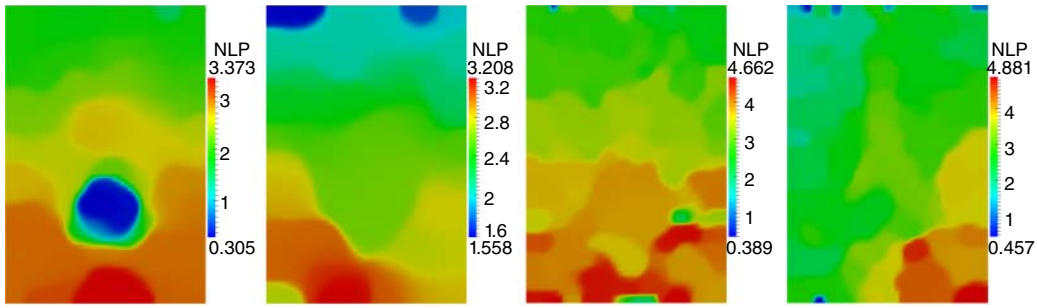

Figure 10.3 Non linear parameter γ reconstructions for sections 1 through 4 (left to right).

36 (with 20.5% overall strain) are used. Note that, since these strains are close to each other, the weights w_n in Eq. (10.1) are identical and equal to unity. As for the shear modulus, the values of the regularization parameters are given in Table 10.1.

10.3.5 Axial Strain Images

The displacement data used in generating the shear modulus and nonlinear parameter images was also used to generate axial strain images. This lead to two strain images for each section of the phantom, at approximately 1.5% and 20.5% overall strain which were evaluated using the gradient filter within Paraview [31]. These images are shown in Figures 10.4 and 10.5. We observe that at small strain the strain contrast changes somewhat from one section of the phantom to another. Also, for a given section it changes rather dramatically from small to large strains.

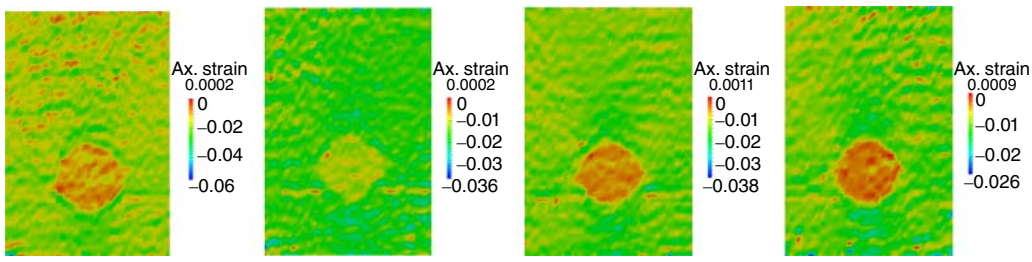

Figure 10.4 Axial strain images at 1.5% overall strain for sections 1 through 4 (left to right).

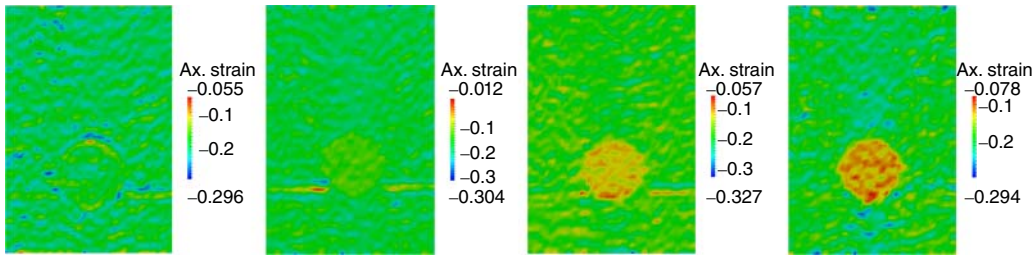

Figure 10.5 Axial strain images at 20.5% overall strain for sections 1 through 4 (left to right).

10.4 Discussion

10.4.1 Analysis of the Shear Modulus Distributions

The shear modulus reconstructions show that every data set contains a circular inclusion in the lower part of the image. We observe that the shape and the sharp boundary of these inclusions have been recovered very accurately. The diameter of these inclusions, measured along the axial and lateral directions, is listed in Table 10.2, where we have also listed the manufactured diameter of these inclusions. We observe very good agreement too, with the maximum error of about 1 mm.

With only measured displacement data, the shear modulus can be determined up to a multiplicative constant and therefore it is interesting to focus on the contrast between the inclusion and the background. The predicted and measured values are compared in Table 10.3. The measured values are obtained as described in Section 10.2.2. That is, a cylinder of each material type was compressed to obtain the uniaxial stress–strain curve, and that curve was matched to the analytical curve for the Veronda-Westmann strain energy density function in order to determine μ and γ.

Table 10.2 Dimensions of the inclusions after segmentation (thresholding at 30% of the maximum contrast).

	incl. 1	**incl. 2**	**incl. 3**	**incl. 4**	**Manufactured**
Lateral diameter (mm)	9.60	9.38	9.28	9.21	10.0
Axial diameter (mm)	10.87	10.94	10.74	10.61	10.0
Area (mm^2)	81.7	76.8	75.8	76.5	78.5

Table 10.3 Reconstructed and measured values of material properties.

Source	**incl. 1**	**incl. 2**	**incl. 3**	**incl. 4**	**backg. 1/ backg. 2**
Recontructed μ	2.11	1.86	3.02	4.09	1 / 1.2
Measured μ	2.83	2.27	3.54	5.26	1 / 1.16
Reconstructed γ	0.35	2.6	3.8	2.9	3.4 / 2.7
Measured γ	2.2	6.5	4.9	4.5	4.7 / 4.3

We observe that in all cases we have underestimated the contrast by about 20%. It is well known that the TV regularization results in diminishing contrast as is apparent here. Further, based on our previous experience with noisy data, a factor of 20 % appears reasonable.

We note that there is a small gradient in the shear modulus reconstruction in the axial direction. In particular the top portion of the phantom appears to be stiffer than the lower portion. We have observed the same effect in all sections and in axial strain images. This is consistent with how the phantom was manufactured in that the top portion of the background was slightly stiffer than the bottom portion (see Section 10.2.2). It is remarkable that the reconstructions are able to pick up this small effect.

10.4.2 Analysis of the Nonlinear Parameter Images

The images for the nonlinear parameter for the sections of the phantoms are shown in Figure 10.3. Here we can clearly see an inclusion only in the first section. For the other sections the inclusion is not clearly seen. This observation is consistent with the actual tissue phantom, where the background material and the inclusion material for inclusions 2, 3, and 4 was constructed to have the same nonlinear behavior. It is remarkable that our reconstructions recover this fact. Additionally, the independent mechanical measurements suggest that top background is slightly more nonlinear than bottom portion; this trend is properly captured in our reconstructions.

The measured and predicted values of the nonlinear parameter are presented in Table 10.1. We observe that, unlike with the values for the shear modulus, there is greater discrepancy between the measured and predicted values. This may be attributed to the following causes:

(i) In order to quantitatively recover γ and to compare the reconstructed and the measured values, as well as to compare the reconstructed values of γ across different, phantom sections, it is necessary to utilize displacement measurement at two, significantly different, levels of finite strain. In our reconstructions we have utilized displacements at 18% and 20.5% overall strain. These may not be sufficiently different so as to measure γ quantitatively.

(ii) Using the formula derived in Gokhale et al. [15], see Equation (56) therein, we conclude that we require a strain of about 24% in the inclusion in order to measure γ accurately. At 20.5% overall strain we are close to, but still less than, this number. Thus the amount of total strain may not be sufficient to accurately estimate γ for the given problem.

We also note that the images for γ display more artifacts than the corresponding images for μ. This may be explained by recognizing that in general the measured displacements are less sensitive to changes in γ than in μ [16], which makes recovering γ from displacement measurements more sensitive to noise. In addition we note that γ is recovered sequentially, that is it is based on utilizing a reconstructed (and hence noisy) μ distribution. Therefore, in addition to the noise in the measured displacements, it is also influenced by errors in the recovered μ distribution.

Finally, we note that strain images can be misleading when interpreting nonlinear elastic effects. A quick glance at Figures 10.4 and 10.5 might convince the reader, that relative to the background, the first two inclusions soften with strain. However, a look at the measured and reconstructed values of γ reveals that this not the case for the second inclusion. Only the first inclusion behaves this way, a fact that is correctly captured in the reconstruction for γ.

10.4.3 Effect of Varying Regularization Parameters

The total variation regularization terms are the last two terms in Eq. (10.1). In these terms α_μ and α_γ are parameters that determine the importance of the regularization term relative to

the data matching term while β_μ and β_γ are parameters that ensure that the integrand of the regularization terms is twice-differentiable when $\nabla\mu = 0$ or $\nabla\gamma = 0$. The idea is to select β to be small enough so that they do not influence the final result, and at the same time provide the problem with enough smoothness so that quasi-Newton methods can be used to solve it.

We have thoroughly investigated the effect of varying β_μ and β_γ on the corresponding reconstructions. In Figure 10.6 we present one such study for reconstructing the nonlinear parameter of the first specimen. We select three different values of β_γ (that differ from each other by a factor of ≈ 7) while keeping all other parameters fixed. We observe that changes in the reconstructions, especially between the two images corresponding to the smaller values of β_γ, are minimal, indicating that we have reached an asymptotically small value for β_γ. We also observe that reducing β_γ adversely effects the smoothness of the problem which translates to an increase in the total number of iterations to convergence.

The effect of varying the regularization parameter α_γ is shown in Figure 10.7, where we plot the reconstructed images for γ for section 1 at three different values of α_γ. We note that the image on the right (Figure 10.7c) is clearly under-regularized and displays strong variations even within the homogeneous background region. The center image (Figure 10.7b) gets rid of this

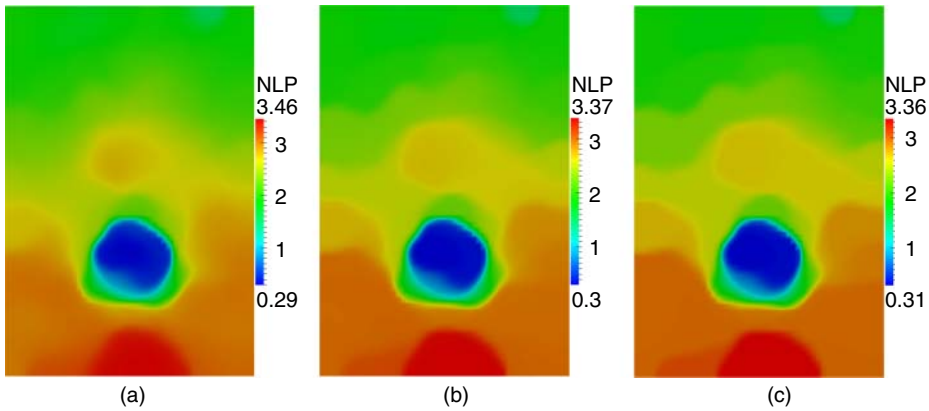

Figure 10.6 Influence of the regularization parameter β_γ on the nonlinear parameter reconstruction for section 1. (a) $\beta = 4e\text{-}2$ (914 iterations to convergence); (b) $\beta = 7e\text{-}3$ (2214 iterations to convergence); (c) $\beta = 1e\text{-}3$ (5977 iterations to convergence)).

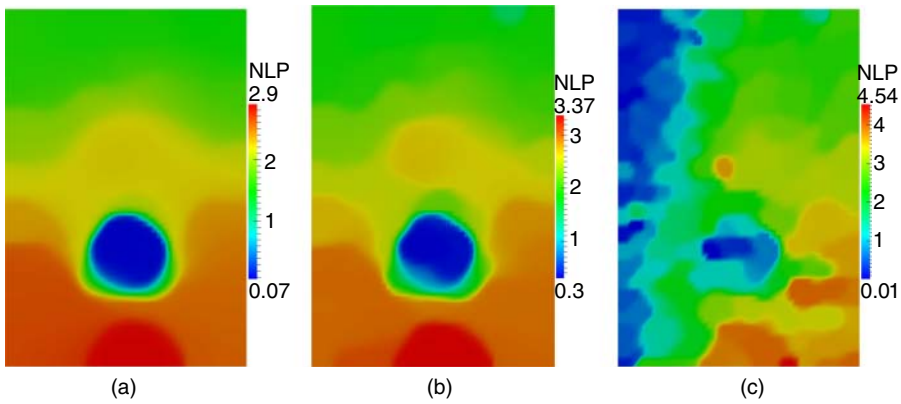

Figure 10.7 Influence of the regularization parameter α_γ on the nonlinear parameter reconstruction for section 1. (a) $\alpha = 1e\text{-}3$ (1852 iterations to convergence); (b) $\alpha = 4e\text{-}4$ (2214 iterations to convergence); (c) $\alpha = 7e\text{-}5$ (1660 iterations to convergence)).

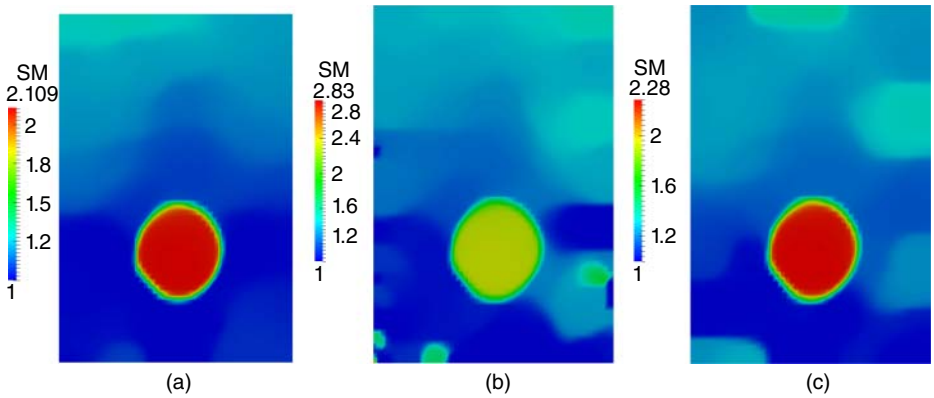

Figure 10.8 Effect of the boundary condition in the lateral direction on lateral faces for section 1. (a) zero traction; (b) measured lateral displacement; (c) smoothed lateral displacement.

artifact while preserving the boundary of the inclusion. The image on the left (Figure 10.7a) has a still higher regularization parameter (around 2.5 times that for the center image). We observe that this image is similar to the center image, although the distribution for γ appears to have shifted to a lower overall value. This is to be expected as this change corresponds to lowering the total variation of γ.

10.4.4 Effect of Boundary Conditions on Lateral Edges

While solving the forward problem we are required to specify a boundary condition in each direction on every edge. In the axial direction the measured displacements are used as boundary conditions on every edge. If we also use the measured displacement in the lateral direction as boundary data we obtain the shear modulus image for section 1 shown in Figure 10.8b. In this image we can clearly see artifacts along the edges due to the noisy lateral displacement estimates that are imposed strongly through the boundary conditions. These artifacts are somewhat mitigated by using a smoothed version of the lateral displacements, as seen in the image in Figure 10.8c. The smoothed displacement field on the boundary is obtained by linearly interpolating between 24 carefully selected points on the boundary. A point is included in this set if its lateral displacement is close to the average lateral displacement on the edge (so as to preclude outliers) and if it is sufficiently far from other points that have already been included in the selected set. Perhaps the best (in terms of a homogeneous background) reconstruction is obtained when homogeneous lateral traction is imposed (see Figure 10.8c). We note that this latter boundary condition is appropriate for our data since the phantom was not constrained along the lateral direction as they were compressed. This is the boundary condition we have used in the reconstructions shown in Figures 10.2 and 10.3.

10.5 Conclusions

We have tested the ability of ultrasound based quasi-static elasticity imaging in creating images of the linear and nonlinear elastic properties of soft materials in two dimensions. For this purpose we have utilized tissue-mimicking phantoms with tunable linear and nonlinear elastic response as our models. We conclude that we are able to accurately reconstruct the spatial variation of the shear modulus and are able to resolve sharp interfacial changes. We are also able to recover the contrast in the shear modulus with an accuracy of about 20%. For the nonlinear

response, we conclude that we are able to distinguish differences in the nonlinear behavior of the constituents of the gelatin phantoms. However, we observe more artifacts and the values of the recovered parameters differ from estimates based on the phantom recipe and independent mechanical tests. We attribute these discrepancies to insufficient overall strain in the phantoms and the lack of displacement measurements at two distinct values of finite strain.

Acknowledgement

The authors would like to acknowledge the support of NIH Grants R21CA133488 and R01CA140271.

References

1 Garra, B.S., Cespedes, E.I., Ophir, J., et al. (1997). Elastography of breast lesions: initial clinical results. *Radiology* 202: 79–86.
2 Itoh, A., Ueno, E., Tohno, E., et al. (2006). Breast disease: clinical application of US elastography for diagnosis. *Radiology* 239: 341–350.
3 Regner, D., Hesley, G.K., Hangiandreou, N.J., et al. (2006). Breast lesions: evaluation with US strain imaging – clinical experience of multiple observers. *Radiology* 238: 425–437.
4 Gao, L., Parker, K.J., Lerner, R.M., and Levinson, S.F. (1996). Imaging of the elastic properties of tissue – a review. *Ultrasound Med. Biol.* 22 (8): 959–977.
5 Mariappan, Y.K., Glaser, K.J., and Ehman, R.L. (2010). Magnetic resonance elastography: a review. *Clin. Anat.* 23: 497–511.
6 Khaled, W.A.W. (2007). Displacement Estimation Analyses for Reconstructive Ultrasound Elastography using Finite-Amplitude Deformations, dissertation. Fakultat fur Elektrotechnik und Informationstechnik an der Ruhr-Universitat Bochum.
7 Krouskop, T.A., Wheeler, T.M., Kallel, F., et al. (1998). Elastic moduli of breast and prostate tissues under compression. *Ultrason. Imaging* 20: 260–274.
8 Wellman, P.S., Howe, R.D., Dalton, E., and Kern, K.A. (1999). Breast tissue stiffness in compression is correlated to histological diagnosis. Technical Report (Harvard BioRobotics Laboratory, Division of Engineering and Applied Sciences, Harvard University).
9 O'Hagan, J.J. and Samani, A. (2009). Measurement of the hyperelastic properties of 44 pathological ex vivo breast tissue samples. *Phys. Med. Biol.* 54: 2557–2569.
10 Karimi, R., Zhu, T., Bouma, B.E., and Kaazempu Mofrad, M.R. (2008). Estimation of nonlinear mechanical properties of vascular tissues via elastography. *Cardiovasc. Eng.* 8 (4): 191–202.
11 Oberai, A.A., Gokhale, N.H., Goenezen, S., et al. (2009). Linear and nonlinear elasticity imaging of soft tissue in vivo: demonstration of feasibility. *Phys. Med. Biol.* 54 (5): 1191–1207.
12 Mehrabian, H. and Samani, A. (2008). An iterative hyperelastic parameters reconstruction for breast cancer assessment. In: *Medical Imaging: Physiology, Function, and Structure from Medical Images*. Proceedings of SPIE, vol. 6916 (SPIE, Bellingham, WA) 69161C.
13 Wang, Z.G., Liu, Y., Wang, G., and Sun, L.Z. (2009). Elastography method for reconstruction of nonlinear breast tissue properties. *Int. J. Biomed. Imaging 06854*, Epub 2009, July 9th, article #6.
14 Amooshahi, A. and Samani, A. (2010). A fast breast nonlinear elastography reconstruction technique using the Veronda-Westmann model. In: *5th Canadian Student Conference on Biomedical Computing and Engineering*.

15 Gokhale, N.H., Barbone, P.E., and Oberai, A.A. (2008). Solution to the nonlinear elasticity imaging inverse problem: the compressible case. *Inverse Problems* 24 (4): 045010.
16 Goenezen, S., Barbone, P.E., and Oberai, A.A. (2011). Solution of the nonlinear elasticity imaging inverse problem: The incompressible case. *Comput. Meth. Appl. Mech. Eng.* 200 (13–16): 1406–1420.
17 Pavan, T.Z., Madsen, E.L., Frank, G.R., et al. (2010). Nonlinear elastic behavior of phantom materials for elastography. *Phys. Med. Biol.* 55: 2679–2692.
18 Koer, J.M., et al. (2001). Improved method for determining resolution zones in ultrasound phantoms with spherical simulated lesions. *Ultrasound Med. Biol.* 27 (12): 1667–1676.
19 Madsen, E.L., Frank, G.R., Hobson, M.A., et al. (2005). Spherical lesion phantoms for testing the performance of elastography systems. *Phys. Med. Biol.* 50: 5983.
20 Fung, Y.C. (1993). *Biomechanics: Mechanical Properties of Living Tissues*. New York: Springer-Verlag.
21 Hall, T.J., Bilgen, M., Insana, M.F., and Krouskop, T.A. (1997). Phantom materials for elastography. *IEEE Trans. Ultrason., Ferroelect., Freq. Control* 44 (6): 1355–1365.
22 Brunke, S.S., Insana, M.F., Dahl, J.J., et al. (2007). An ultrasound research interface for a clinical system. *IEEE Trans. Ultrason., Ferroelect., Freq. Control* 54 (1): 198–210.
23 Pavan, T.Z., Madsen, E.L., Frank, G.R. et al. (2012). A nonlinear elasticity phantom containing spherical inclusions. *Phys. Med. Biol.* 57 (15): 4787–4804.
24 Varghese, T. and Ophir, J. (1996). Performance optimization in elastography: Multicompression with temporal stretching. *Ultrason. Imaging* 18 (3): 193–214.
25 Jiang, J. and Hall, T.J. (2011). A fast hybrid algorithm combining regularized motion tracking and predictive search for reducing the occurrence of large displacement errors. *IEEE Trans. Ultrason., Ferroelect., Freq. Control* 58 (4): 730–736.
26 Zhu, Y. and Hall, T.J. (2002). A modified block matching method for real-time freehand strain imaging, *Ultrason. Imaging* 24 (3): 161–176.
27 Goenezen, S., Sink, Z., Oberai, A.A., et al. (2010). Breast cancer diagnosis using nonlinear elasticity imaging: some initial results. In: *Proceedings of the 9th International Conference on the Ultrasonic Measurement and Imaging of Tissue Elasticity*, Snowbird, Utah.
28 Byrd, R.H., Lu, P., and Nocedal J. (1995). A Limited Memory Algorithm for Bound Constrained Optimization, *SIAM J. Sci. Statist. Comput.* 16 (5): 1190–1208.
29 Zhu, C., Byrd, R.H., and Nocedal, J. (1997). Algorithm 778: L-BFGS-B, FORTRAN routines for large scale bound constrained optimization, *ACM Trans. Math. Softw.* 23 (4): 550–560.
30 Veronda, D. and Westmann, R. (1970). Mechanical characterization of skin finite deformations. *J. Biomech.* 3 (1): 111–122.
31 http://www.paraview.org/

11

Cardiac Strain and Strain Rate Imaging

Brecht Heyde, Oana Mirea, and Jan D'hooge

KU Leuven, Leuven, Belgium

11.1 Introduction

Although some pioneering work had been done in the 1980s, it was not until the 1990s that cardiac strain imaging by ultrasound drew significant clinical interest in the quest for a quantitative measure of regional myocardial (contractile) function. The original methodology relied on Doppler techniques, but later on other techniques – commonly referred to as speckle tracking – entered the scene, avoiding some of the pitfalls of the original methodology. At present, cardiac strain imaging has become an established diagnostic tool in echocardiography that has been demonstrated to be more prognostic than traditional functional indices, e.g. ejection fraction. Moreover, it has now reached a level of maturity to be included in the guidelines for monitoring the progression of certain diseases and/or their treatment.

This chapter starts with a recapitulation of the nomenclature of strain in the cardiac setting. Next, a brief review is given of the different technical approaches taken towards cardiac motion and deformation estimation using ultrasound as well as the available methodologies for validating these measurements. Subsequently, a glimpse on the typical clinical workflow is given and two important clinical applications are presented. Finally, a look into potential future developments concludes this chapter.

11.2 Strain Definitions in Cardiology

In cardiology, "strain" is typically defined as the *total* deformation of the cardiac muscle during the cardiac cycle. Most often, the R-wave on the ECG (i.e. onset of the ejection period) is defined as the reference state (i.e. zero strain) although more recently it has been suggested to use diastasis (i.e. onset P-wave) as an alternative instead [1]. Importantly, this definition of "strain" is thus different from what is typically used in elastography where "strain" refers to the instantaneous change in the dimensions of an object between two subsequent recordings. In the cardiac context, this (instantaneous) strain value would, however, be dependent on the data acquisition rate (i.e. frame rate) as well as on the heart rate and thus be of little meaning in itself. Therefore, the (instantaneous) strain in cardiology is normalized for the acquisition rate thereby resulting in a quantitative estimate of deformation rate, i.e. "strain rate" (SR). Integration of strain rate over the cardiac cycle then results in the effective "strain". In elastography, the latter is typically referred to as "cumulative strain". To summarize, "strain rate" and "strain" in cardiac literature thus correspond to "(instantaneous) strain" and "cumulative strain" in the context of elastography.

Ultrasound Elastography for Biomedical Applications and Medicine, First Edition.
Edited by Ivan Nenadic, Matthew Urban, James Greenleaf, Jean-Luc Gennisson, Miguel Bernal, and Mickael Tanter.

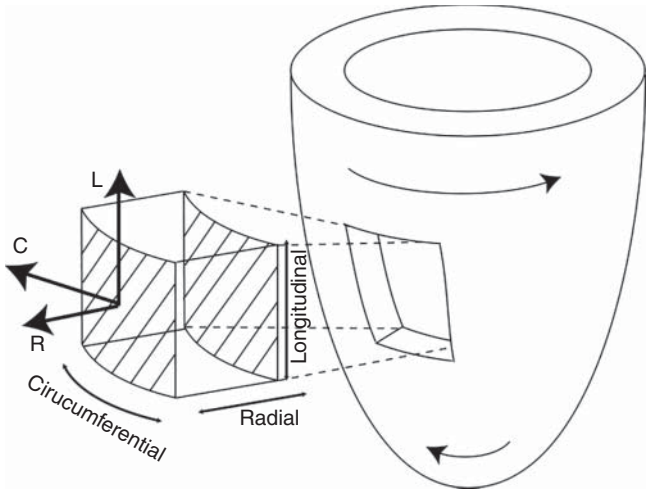

Figure 11.1 Illustration of the local cardiac coordinate system in combination with a schematic of how the left ventricle experiences torsion during the cardiac cycle. Source: modified from D'hooge [2] by permission of Oxford University Press.

In order to interpret cardiac strain, it needs to be related to the cardiac physiology. As such, it is important to describe the measured strains in a cardiac coordinate system. This system has been defined locally to exist of three orthogonal axes (Figure 11.1):

(i) the radial (R) axis which is orthogonal to the epicardial surface and pointing from the left ventricular cavity outwards
(ii) the longitudinal (L) axis which is tangential to the epicardium and points from apex to base and
(iii) the circumferential axis which is tangential to the epicardium and defined in such a way that the RLC-coordinate system is right handed. The three normal strain values (ε_{RR}, ε_{LL}, ε_{CC}) thus refer to local wall thickening, longitudinal, and circumferential shortening respectively while, for example, the CL-shear (ε_{CL}) component represents the local shearing as a result of ventricular torsion (i.e. differential rotation around the ventricular long axis of the basal with respect to the apical segments).

In order to characterize the cardiac strain curves that are – by definition – time dependent, the following parameters are typically reported:

(i) *end-systolic strain*, which is the strain measured at the end of systole, i.e. at the moment of aortic valve closure
(ii) *peak systolic strain*, which is the maximal strain magnitude occurring during the ejection period and
(iii) *post-systolic strain*, which is the continued thickening/shortening of the segment after aortic valve closure.

Similarly, *peak systolic strain rate* – the maximal magnitude of the strain rate during systole – is most often reported to characterize the strain rate curve. These parameters are illustrated in Figure 11.2.

Please note that strain was originally defined as a measure of local wall deformation, and is typically reported as an average per cardiac segment [3] . However, later on, the term "global strain" was defined as a quantity to characterize overall pump function of the ventricle. It can been defined as the average of all locally measured (segmental) strain values or – as currently

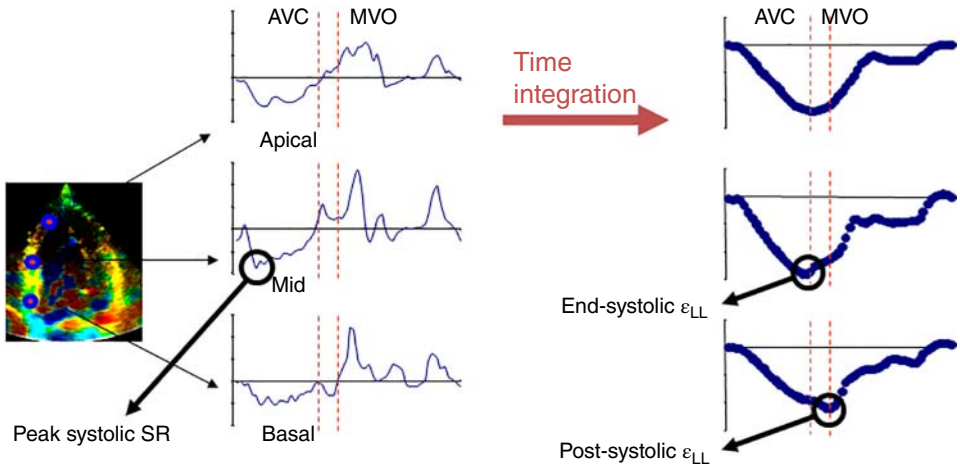

Figure 11.2 Parameters used to characterize the temporal strain (right) and strain rate (middle) curves. In this particular example, longitudinal strain (rate) curves as obtained from an apical transducer position are shown at three locations along the interventricular septum. The left panel shows the instantaneous systolic strain rates color-coded on top of the B-mode image. (MVO: mitral valve opening; AVC: aortic valve closure.)

recommended – as the relative change in length of the entire myocardial border over the cardiac cycle [4].

11.3 Methodologies Towards Cardiac Strain (Rate) Estimation

Although cardiac strain (rate) estimation was originally Doppler-based, over the years a vast number of different techniques have been developed. In this section, a brief overview of this wide range of techniques is given. A schematic overview of the different methodologies is shown in Figure 11.3.

11.3.1 Doppler-based Methods

The original cardiac strain (rate) imaging methodology was based on color tissue Doppler imaging (TDI) which measures local myocardial movement using the exact same measurement principles as the ones used for color flow mapping of blood flow in a conventional Doppler system but with adapted filter settings such that the weakly scattering, relatively fast blood velocities are filtered and only the more strongly scattering, relatively slow velocities originating from myocardial tissue are retained [5]. Cardiac strain rate can subsequently be calculated from this color TDI data set using the spatial velocity gradient, either by sampling velocities over a fixed offset along the beam [6] or as the slope of a regression line through multiple velocities estimated within a certain distance [7]. Strain is then obtained by temporally integrating the strain rate curves.

The strength of TDI-based strain estimation is its sensitivity as well as its temporal resolution that is typically about 200–300 Hz when using a narrow field of view (i.e. sector angle) [8]. Very recently, a novel beamforming approach was proposed to enable wide-field-of-view, high frame rate TDI imaging (i.e. 200 Hz for a 90-degree sector image) [9] but its clinical application remains to be explored.

The major pitfall of the TDI approach is that a Doppler system can only measure the velocity component along the ultrasound image line (i.e. motion towards or away from the transducer).

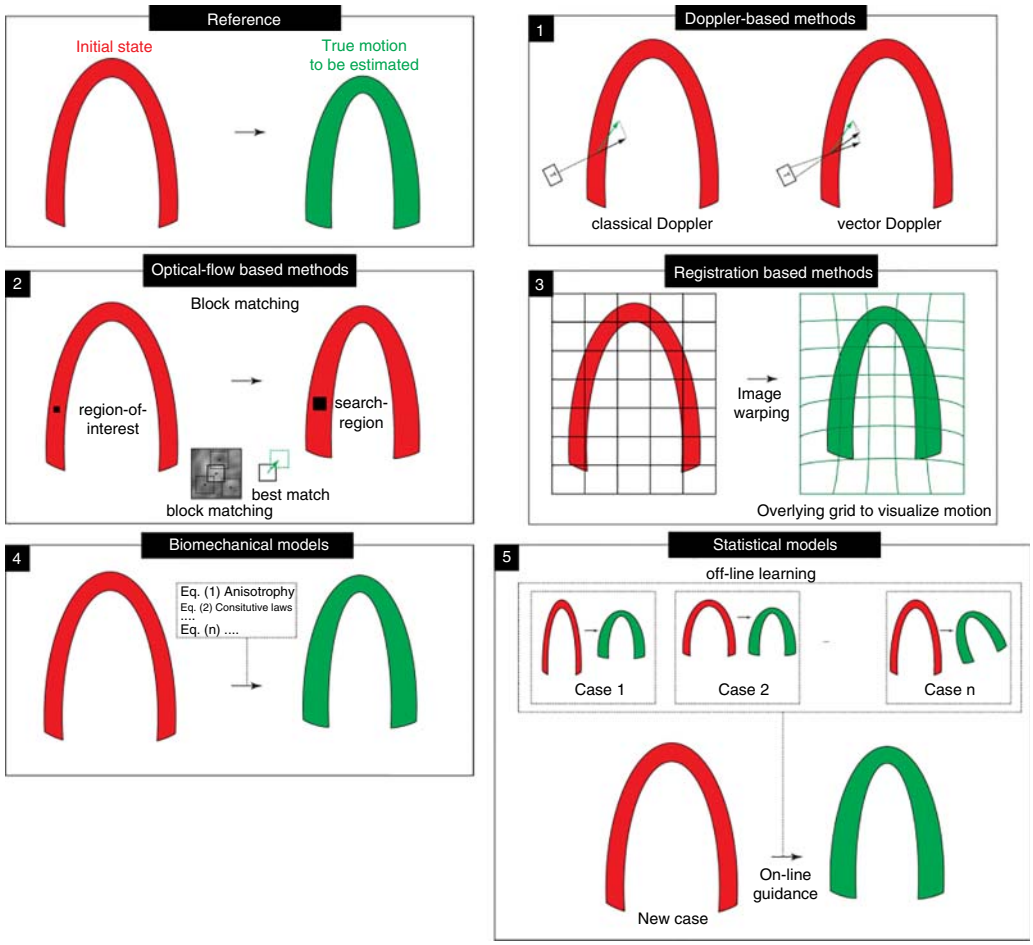

Figure 11.3 Classification of ultrasound-based cardiac deformation techniques.

As the TDI-based strain estimate is derived from this angle-dependent 1D velocity field, it inherits this 1D property and only deformation along the ultrasound line can be assessed. As the number of acoustic windows to the heart is limited, this implies that not all strain components can be measured in all myocardial segments [2].

In order to overcome this angle dependency, vector Doppler (also known as multi-beam or cross-beam Doppler) approaches have been proposed. Vector Doppler combines multiple conventional 1D Doppler measurements from multiple independent directions allowing to reconstruct the 2D (or even 3D) velocity vector. This principle can be implemented in several ways either by using multiple transducers; by moving a single transducer around the region of interest; or by using different apertures within the same transducer [10]. From a practical point of view, the latter approach is preferable and it has been a popular approach in the field of blood velocity estimation. However, its extension to cardiac strain estimation has remained limited, e.g. [11], likely due to relatively small transducer footprints used in cardiac imaging making the angulation (and therefore the accuracy of the resulting velocity vector) between both Doppler acquisitions limited.

For a more elaborate coverage concerning the history of TDI, the underlying technical principles and its clinical applications, the reader is referred to Sutherland et al. [12] or several review papers on this topic [13, 14].

11.3.2 Optical Flow Methods

Optical flow (OF) is the apparent motion of brightness patterns within an (ultrasound) image sequence resulting from underlying tissue motion. Techniques computing OF can be divided into the following categories: differential methods, region-based methods, and phase-based methods [15, 16].

11.3.2.1 Differential Methods

Differential or gradient-based OF methods rely on the assumption that the intensity of a particular point in a moving pattern does not change with time. This is mathematically expressed through the well-known optical flow equation [16]. Nevertheless, without additional constraints, this is an underdetermined problem (also known as the aperture problem), given that at least two velocity components are unknown (for a 2D image sequence) while only one equation is available. Two popular approaches exist to add more boundary conditions. The Horn-Schunck technique regularizes motion globally by imposing smoothness across the whole image [17] while the Lucas-Kanade method estimates the motion locally assuming that the velocity field is constant within a small image region [18]. Both techniques were shown to be reliable in estimating cardiac motion on synthetic US images [19]. The Lucas-Kanade OF has been tested in a clinical setting (e.g. [20, 21]) and was further refined by Suhling et al. to also capture rotation and shearing motion [22]. Finally, the Horn-Schunck OF approach was extended to 3D [23].

The OF equation also acts as the driving force behind the motion-estimation process in a large family of "demons" algorithms which regard image boundaries as diffusive membranes [24]. It was first adopted in the context of cardiac strain estimation by Somphone et al. [25], later followed by a series of further modifications, e.g. [26].

11.3.2.2 Region-based Methods

Region-based methods, also termed block matching (BM) or speckle tracking, assume that a local speckle pattern remains stable between two subsequent frames. Motion of a certain point is found by first defining a local neighborhood and iteratively (often exhaustively) searching for the best match – according to some similarity metric – in its neighborhood in the next frame. Different similarity measures can be used and have been compared, e.g. [27–31]. Moreover, in order to obtain sub-pixel displacement estimates, the similarity metric is typically interpolated [32]. Interesting to note is that such interpolation is not required for the differential OF techniques as they obtain an analytic solution. On the other hand, BM does not make assumptions on the magnitude of the displacement whereas differential OF assumes that they are small.

Block-matching techniques can be applied on either the B-mode (i.e. after envelope detection and scan conversion) or directly on the radio-frequency (RF) data.

B-mode based BM has seen most popularity likely due to its conceptual simplicity and high computational speed. Trahey et al. were the first to successfully apply block matching to track blood motion [33], and were later followed by Bohs et al. who applied the technique to track 2D tissue motion [27]. Cardiac strain estimation based on the BM concept has been extensively validated experimentally, e.g. [34–39] and several implementations have become commercially available. As such, it has been applied in many clinical studies [40], and several commercial implementations are now available [41–46]. As 3D ultrasound systems have become more readily available, it was only natural that the BM concept was also extended for 3D tissue motion estimation [47, 48].

As an alternative, 2D block matching can be performed directly on the RF data by defining a 1D or 2D kernel over the RF signal and finding the optimal shift within a certain 2D search region in the next frame [29, 49–51]. Several studies have shown that due to the higher frequency content of the RF signals, more accurate motion estimates can be obtained in the axial

direction. However, due to faster decorrelation of RF signals compared to B-mode data, frame rate has to be higher [52, 53]. An extension to 3D is therefore challenging given the currently relatively low volumetric acquisition rate [54]. The major difficulty with these RF-based methods is their computational load, which is significantly higher than that for B-mode image processing.

Importantly, the results of the BM process are typically noisy. Therefore, an a posteriori regularization step is typically required, e.g. by median filtering [55] or wavelet denoising of the initial displacement estimates [56], by averaging the strain images [57], or by using least-square strain estimators in 1D (linear curve fitting through the displacement estimates [58]) or in 2D (plane fitting [59]). Several authors have also derived strategies to incorporate confidence measures and only retain those estimates with a high tracking quality, e.g. [48, 49, 60].

Finally, please note that BM-based motion estimates are intrinsically different from Doppler-based motion estimates. Indeed, Doppler measures the instantaneous velocity that is assumed to be constant between subsequent estimates (i.e. no acceleration) while BM measures the average velocity of a region from one frame to the next (i.e. irrespective of acceleration).

11.3.2.3 Phase-based methods

Some authors have proposed to solve the OF equation using image phase rather than image intensity [61, 62]. They argued that using phase information should be less sensitive to brightness fluctuations and more strictly correlated with the image structure. Tautz et al. applied a set of quadrature filters in several directions to extract phase information from volumetric US datasets [63] while Alessandrini et al. applied the OF equation directly on the phase of the monogenic signal [64]. These methods have recently been validated using simulated US datasets, first in 2D [64] and later in 3D [61, 63].

11.3.3 Registration-based Techniques

Registration techniques model cardiac deformation using a weighted set of basis functions. By adjusting the coefficients of the basis functions, different dense deformation fields can be represented in an efficient way. The optimal deformation field is typically found in an iterative fashion by minimizing a cost function describing (dis)similarity between subsequent frames in combination with physical penalties to constrain the possible configurations (e.g. imposing a smooth deformation field). A wide range of basis functions has been employed in medical imaging (e.g. see [65]), but for the analysis of cardiac US images, B-splines, and radial basis functions (RBF) have seen most popularity. The fundamental difference of these approaches over the BM approach is that regularization of the motion estimates is done during the motion estimation process rather than a posteriori.

In free-form deformation (FFD) models, (typically cubic) B-spline functions are placed on a rectangular control point grid [66, 67]. Given the local support of a B-spline, the displacement of any point within the myocardium is therefore governed only by a limited number of control points, allowing a localized description of cardiac deformation. These models were first applied by Ledesma et al. on 2D US images [68]; its feasibility for 3D motion estimation was later demonstrated by Elen et al. in simulated datasets [69], and was followed by in vitro and in vivo validation studies [70, 71]. Several flavors of the algorithm have been proposed over recent years, all designed to add extra layers of regularization. An alternative control point topology adapted to the cardiac morphology and motion was described in [72]. The heart moves in a cyclic fashion throughout the cardiac cycle, which was taken into account by either formulating the transformation as a diffeomorphism [73–75], or by explicitly adding a regularization term imposing smoothness in time [76]. In work by Myronenko et al. [77] and [78], motion estimation was combined with myocardial segmentation by incorporating a segmentation-based energy

in the cost function. Finally, in order to increase the temporal resolution of the resulting strain curves, 3D motion fields were reconstructed within an FFD framework from tri-plane B-mode acquisitions combined with input from TDI [79]. As an alternative, RBFs express the displacement of a given point as a function of its distance to the center of every basis function [80]. The advantage of RBFs is that the center points can be placed anywhere within the image, as opposed to the regular placement on a grid for the FFD models. Their main disadvantage is that they have a global support, which may be undesirable when seeking local transformations. A popular choice for these RBFs are thin-plate splines. They have been used in 3D echocardiography to interpolate motion estimates originating from several inputs. For example, Compas et al. used RBFs to combine motion estimates from speckle tracking and shape tracking [81]. Duan et al. used a block-matching approach to estimate motion on the endocardial and epicardial surfaces only, and obtained a dense motion field by applying RBF interpolation [82].

11.3.4 Biomechanical Models

These techniques exploit knowledge about the deformation properties of tissues and construct biomechanical deformation models to mimic their properties and behavior. The main advantage of these models is their use of informed priors about biomechanical properties that allow estimating a complex deformation with few degrees of freedom.

Papademetris et al. adopted a transversely isotropic linear elastic model for the myocardium, taking into account fiber directions, to generate a dense motion field within the myocardium from the motion estimates obtained at the endocardial and epicardial surfaces. The motion estimates on these surfaces were obtained from a shape-tracking approach [83, 84]. Sermesant et al. presented an electromechanical model of the heart, able to simulate the electrical propagation and the mechanical contraction. By deforming the model to fit the myocardial boundaries it could be used to estimate cardiac deformation [85, 86].

11.3.5 Statistical Models

This class of methods introduces a priori knowledge in the motion estimation process by off-line training a statistical model describing cardiac deformations obtained through a large annotated database in which this deformation is known. Myocardial motion in a new dataset can then be estimated on-line, guided by the statistical model. The advantage of these models is their ability to reduce the computational cost while achieving a robust performance. It is important to note that the set of images used during the learning stage should be representative for the expected range of deformations in the population that it aims to analyze later.

Wang et al. proposed a learning-based framework where information from multiple cues was fused, such as speckle patterns, image boundaries, and motion statistics [87, 88]. Leung et al. used a statistical model of cardiac motion trained from endocardial segmentations to regularize optical flow results [89].

11.4 Experimental Validation of the Proposed Methodologies

The technical validation of a novel cardiac strain estimation methodology is critically important before applying it clinically. Unfortunately, a single, ideal validation setting does not exist as each approach offers its own strengths and weaknesses. In this section, a brief overview is therefore given of the different available validation setups with their respective pro's and con's (Figure 11.4).

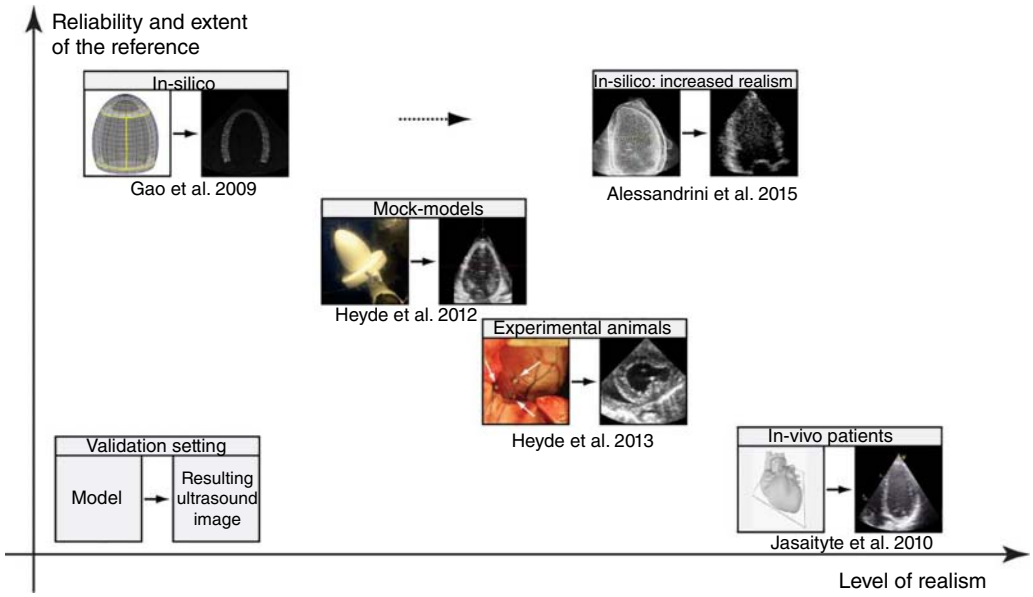

Figure 11.4 Overview of the different validation methodologies schematically showing the trade-off to be made between the level of realism of the images and the corresponding reliability and extent of the reference.

11.4.1 Synthetic Data Testing

By combining kinematic or (electro)mechanical models of the heart with ultrasound simulation tools, the image formation process can be mimicked and synthetic data can be generated. These data can subsequently be processed as if it were real data so that the measured (local) myocardial strain can be contrasted against the ground truth available from the cardiac models. Although these synthetic data sets originally looked rather basic [90], continued efforts have evolved them in such a way that non-expert readers can no longer distinguish them from a real recording [91].

Synthetic data sets have been used to develop a multitude of algorithms and have recently been used to contrast all commercially available speckle tracking solutions [92]. The strength of this validation approach is that the ground truth is precisely known at every location of the myocardium but – despite significant improvements being made in terms of overall realistic appearance – it remains hard to include realistic artifacts and clutter.

11.4.2 Mock Model Testing

Mock models try to mimic the heart both acoustically and mechanically. Often, a tissue-mimicking material (e.g. polyvinyl alcohol) is used that can be shaped into a proper geometry by pouring it in its liquid form into a suited mold. It can then be attached to a hydraulic setup containing blood-mimicking fluids, in which pumps change intra-cavity pressures over time thereby mimicking the cardiac cycle [93]. This "beating heart" is then imaged using a real ultrasound system and the resulting images can be processed. To obtain reference local deformation values, a finite element model of the setup can be built although it is more common to implant sonomicrometry crystals in the model. Different models with differing complexity have been proposed (e.g. [71]), with the most realistic (and complex) ones being passively beating [94, 95] as well as explanted heart setups [96].

The advantage of this mock model approach is that it does not require modeling of the ultrasound acquisition process. However, the reference values have intrinsic measurement error,

are only available in 1 or a finite number of positions on the model, and sonomicrometry might bias the motion estimation process as the crystals show in the resulting ultrasound recordings. Finally, despite the fact that the image acquisition is real, image quality might not be realistic for clinical imaging (e.g. due to artifacts originating from the walls of the imaging tank or the phantom holder), thus potentially biasing the outcome of the measurements.

11.4.3 Experimental Animal Testing

In order to bring the mock model setups closer to the clinical setting, validation can also be done in large animals. Hereto, an open-chest animal preparation is required in order to implant sonomicrometers as reference methodology (cf. mock models, e.g. [97]). Next to having a real ultrasound recording, this setup has the advantage of also providing very realistic physiologic deformation characteristics and competitive image quality. However, the true deformation can only be measured at a limited set of points and image quality is still not identical to that obtained in clinical scanning (e.g. due to the offset of the chest wall and the presence of ribs).

11.4.4 In Vivo Human Testing

The ultimate validation stage is in patients in a clinical setting. The most common approach is to compare strain values extracted via echocardiographic methodologies with those obtained with magnetic resonance imaging approaches, e.g. [34]. Unfortunately, all methods contain error resulting in relatively uncertain reference values for benchmarking. In fact, in this setting, it is most likely better to compare values between different modalities then truly validating one technology against another because of the measurement errors in all approaches.

11.5 Clinical Applications

The availability of speckle tracking echocardiography (STE) and its potential to provide immediate quantitative evaluation of (regional) myocardial deformation led to an extensive use of strain measurements in both clinical and research domains, as shown by the steep increase of publications which addressed the method, thus surpassing its predecessor, tissue Doppler imaging (TDI).

Currently, multiple commercial packages for speckle tracking analysis are accessible both on-board of the ultrasound machines and as stand-alone software for image post-processing. Although each tool has its particularities, the typical workflow includes manual or automated detection of the endocardial border, which generates a myocardial region of interest, followed by the tracking of speckle motion within the cardiac cycle. The timing of cardiac mechanical events is very important for both global and regional strain measurements. The definition of two reference points is pivotal in the analysis of myocardial deformation: the beginning and the end of the systolic period. Hereto, in practice, vendors commonly use the electrocardiographic QRS complex as indicator of end-diastole, although M-mode tracings or mitral spectral Doppler could also be a more reliable surrogate. Similarly, there are several options to select end-systole, e.g. by visually assessing the timing of aortic valve closure in the apical 3-chamber view, by finding the point in time with either the peak strain or the minimal left ventricular volume, or by identifying the end of the LV outflow through a pulsed wave Doppler recording. Irrespective of the chosen method to define the timings, consistency between repeated measurements is extremely important.

Left ventricle longitudinal strain is the most extensively studied parameter and the currently available data indicates that global ε_{LL} (often referred to as GLS) has the most potential for

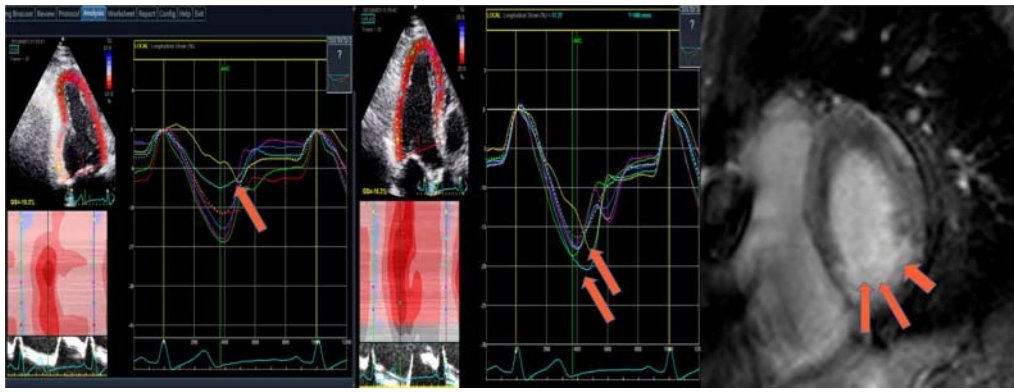

(a) (b) (c)

Figure 11.5 Segmental longitudinal strain in apical four- and three-chamber views in a patient with inferior myocardial infarction. Note the post-systolic shortening (orange arrows) in (a) the basal inferior wall and (b) the basal posterior wall. (c) MRI sequence of the same patient in which the presence of late gadolinium enhancement in the inferoposterior region confirms ischemia at the same areas identified by echocardiography.

clinical use at this moment. In a normal population the values of GLS range between −16% to −22% [98] and in conditions of optimal B-mode images, feasibility was reported to be good to excellent and similar to that of EF measurements [99].

The prognostic and diagnostic efficiency of GLS has been investigated in a number of known or suspected cardiovascular diseases. GLS has demonstrated to be a superior predictor of all-cause mortality when compared to conventional echo measurements such as LV ejection fraction and myocardial wall motion [100]. Moreover, GLS was found to hold independent prognostic value for adverse outcomes in patients with heart failure [101], cardiomyopathies [102], coronary artery disease (CAD) [103], and valvular heart disease [104]. The clinical applicability of circumferential, radial, and rotational strain components is still being explored.

One of the most valuable clinical applications of strain measurements is in the context of ischemic regional myocardial dysfunction. Early experimental studies validated against sonomicrometry showed that both Doppler-derived [105] and STE-derived [106] longitudinal strain can accurately detect the presence and extent of ischemia where post-systolic shortening was shown to be a hallmark of ischemia. Indeed, this post-systolic deformation can easily be assessed by quantifying myocardial deformation, while its visual recognition remains difficult even for experienced echocardiographers (Figure 11.5). As such, strain parameters proved to identify ischemic regions with higher precision than conventional echocardiographic parameters [107].

Studies also reported strain measurements to be sensitive indicators for subclinical cardiac impairment associated with chemotherapy treatment or various pathologies such as chronic kidney disease, diabetes mellitus, and arterial hypertension [108, 109]. Furthermore, in conditions of hypertrophied LV, strain measurements demonstrated to accurately differentiate between primary myocardial disease and disorders of myocardial deposition [110] (Figure 11.6).

The only factor limiting a full integration of strain measurements in clinical practice is their reliability in daily routine. Although several studies demonstrated good to excellent intra- and inter-operator reproducibility of GLS measurements [99, 111], the variability between vendors still raises concern. Indeed, the reported inter-vendor variability of the measurement makes it difficult to apply this technology for long-term monitoring of patients. As such, current recommendations endorse GLS as a robust parameter for clinical use as long as repeated

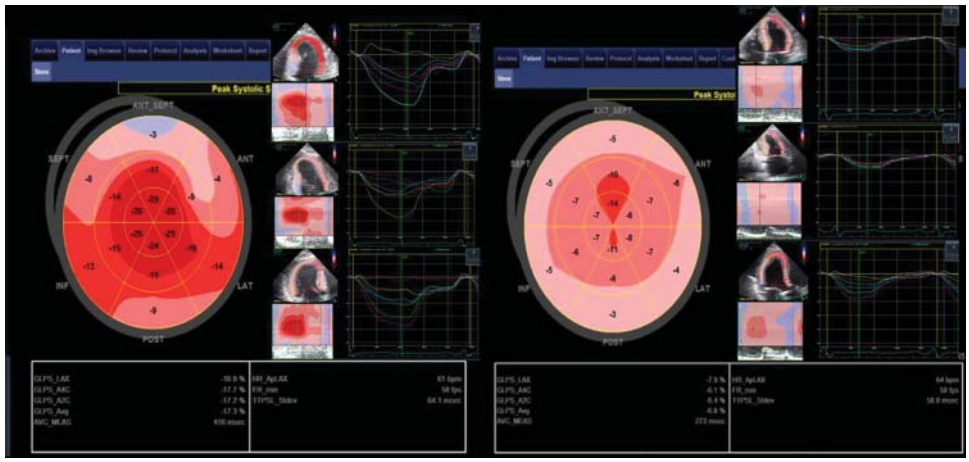

Figure 11.6 Longitudinal strain in two subjects with hypertrophied LV. The subjects are matched for LV wall thickness (19 mm). (a) Patient with hypertrophic cardiomyopathy. Note the reduced longitudinal strain in the basal segments while the apical segments show a preserved function. (b) Patient with amyloidosis. Note the diffuse and severe reduction of longitudinal deformation.

measurements are performed with the same vendor-specific software [112]. Fortunately, standardization of cardiac strain imaging is on-going [113] which – hopefully – will overcome this problem.

11.6 Future Developments

Since its introduction, cardiac strain (rate) imaging has matured into a clinically used modality with proven benefit over traditional approaches. Further developments can be expected to even further strengthen this technology.

- *Automatic definition of the region of interest (ROI)*: at present, most commercial solutions provide an automated solution towards endocardial contouring and subsequently assume the wall thickness to be uniform in order to define the ROI for further deformation analysis. It can be anticipated that novel segmentation approaches will allow making this contouring process fully automatic, thereby making the analysis even less time consuming and observer dependent [114].
- *Strain at high time resolution*: with the continuing developments in fast ultrasound image formation [115], cardiac deformation imaging will become possible at high temporal resolution. While currently most commercial solutions have a time resolution of about 50–60 Hz, which is sufficient to temporally resolve the strain curves, it is anticipated that future image acquisition schemes will operate at a much higher time resolution which will allow more reliable and accurate estimation of local strain rate (as is the case for the original TDI-based approach).
- *True volumetric strain approaches*: although speckle tracking can be done in 3D, in practice, only the longitudinal strain component is being used as it can be measured most reliably. Further developments will enhance the accuracy and reproducibility of the deformation orthogonal to the image line thereby facilitating the measurement of the circumferential and radial strain components [116].

- *Computer-assisted interpretation of strain (rate) data*: at present, the interpretation of strain (rate) data is fully left to the operator and is therefore subject to the amount of experience of the reader. Recently, statistical methodologies have been proposed to help the reader correctly interpret the measured strain (rate) data [117]. Without doubt, this trend will continue whereby ultimately the reader gets a computer-generated suggestion towards the interpretation of the strain (rate) information to be (dis)approved by the treating physician.

References

1 Jasaityte, R., Claus, P., Teske, A.J., et al. (2013). The slope of the segmental stretch-strain relationship as a noninvasive index of LV inotropy. *JACC Cardiovasc Imaging* 6 (4): 419–428.

2 D'hooge, J., Heimdal, A., Jamal, F., et al. (2000). Regional strain and strain rate measurements by cardiac ultrasound: principles, implementation and limitations. *Eur. J. Echocardiogr.* 1 (3): 154–170.

3 Cerqueira, M.D., Weissman, N.J., Dilsizian, V., et al. (2002) American Heart Association Writing Group on Myocardial Segmentation and Registration for Cardiac Imaging: Standardized myocardial segmentation and nomenclature for tomographic imaging of the heart. A statement for healthcare professionals from the Cardiac Imaging Committee of the Council on Clinical Cardiology of the American Heart Association. *Circulation* 105 (4): 539–542.

4 Voigt, J.U., Pedrizzetti, G., and Lysyansky, P. (2015) Definitions for a common standard for 2D speckle tracking echocardiography: consensus document of the EACVI/ASE/Industry Task Force to standardize deformation imaging. *Eur. Heart J. Cardiovasc. Imaging* 16 (1): 1–11.

5 McDicken, W., Sutherland, G., Moran, C., and Gordon, L. (1992) Colour Doppler velocity imaging of the myocardium. *Ultrasound Med. Biol.* 18 (6–7): 651–654.

6 Heimdal, A., Stoylen, A., Torp, H., and Skjaerpe, T. (1998) Real-time strain rate imaging of the left ventricle by ultrasound. *J. Am. Soc. Echocardiogr.* 11 (11): 1013–1019.

7 Fleming, D., Xia, X., McDicken, W., et al. (1994) Myocardial velocity gradients detected by Doppler imaging. *Br. J. Radiol.* 67 (799): 679–688.

8 Bjaerum, S., Torp, H., and Kristoffersen, K. (2001) High frame rate tissue Doppler imaging. *IEEE Int. Ultrason. Symp.* 1417–1421.

9 Tong, L., Ramalli, A., Tortoli, P., et al. (2015) Wide-angle tissue Doppler imaging at high frame rate using multi-line transmit beamforming: an experimental validation in-vivo. *IEEE Trans. Med. Imaging* 35 (2): 521–528.

10 Dunmire, B., Beach, K., Labs, K., et al. (2000). Cross-beam vector Doppler ultrasound for angle-independent velocity measurements. *Ultrasound Med. Biol.* 26 (8): 1213–1235.

11 Arigovindan, M., Sühling, M., Jansen, C., et al. (2007). Full motion and flow field recovery from echo Doppler data. *IEEE Trans. Med. Imaging* 26 (1): 31–45.

12 Sutherland, G., Hatle, L., Claus, P., et al. (2006). *Doppler Myocardial Imaging: A Textbook*, 23–48. SWK bvba, Scientific Consulting and Publishing.

13 Jasaityte, R., and D'hooge, J. (2010). Strain rate imaging: fundamental principles and progress so far. *Imaging Med.* 2 (5): 547–563.

14 Sutherland, G.R., Di Salvo, G., Claus, P., et al. (2004). Strain and strain rate imaging: a new clinical approach to quantifying regional myocardial function, *J. Am. Soc. Echocardiogr.* 17 (7): 788–802.

15 Angelini, E. and Gerard, O. (2006). Review of myocardial motion estimation methods from optical flow tracking on ultrasound data. *IEEE EMBS Annu. Int. Conf.* 1537–1540.

16 Barron, J., Fleet, D. and Beauchemin, S. (1994). Performance of optical flow techniques. *Int. J. Comput. Vision* 12 (1): 43–77.

17 Horn, B. and Schunck, B. (1981). Determining optical flow. *Artif. Intell.* 17 (1–3): 185–203.

18 Lucas, B. and Kanade, T. (1981) An iterative image registration technique with an application to stereo vision. *DARPA Image Understanding Workshop* 121–130.

19 Baraldi, P., Sarti, A., Lamberti, C., et al. (1996). Evaluation of differential optical flow techniques on synthesized echo images. *IEEE Trans. Biomed. Eng.* 43 (3): 259–272.

20 Chunke, Y., Terada, K., and Oe, S. (1996). Motion analysis of echocardiograph using optical flow method. *IEEE Int. Conf. Systems, Man. and Cybernetics* 1: 672–677.

21 Lamberti, C., Sarti, A., and Bertucci, F. (1997). Topology of optical flow in 3D echocardiography. *Comput. Cardiol.* 227–230.

22 Suhling, M., Arigovindan, M., Jansen, C., et al. (2005). Myocardial motion analysis from B-mode echocardiograms. *IEEE Trans. Image Process.* 14 (4): 525–536.

23 Mukherjee, R., Sprouse, C., Pinheiro, A., et al. (2012). Computing myocardial motion in 4-dimensional echocardiography. *Ultrasound Med. Biol.* 38 (7): 1284–1297.

24 Thirion, J. (1998). Image matching as a diffusion process: an analogy with Maxwell's demons. *Med. Image Anal.* 2 (3): 243–260.

25 Somphone, O., De Craene, M., Ardon, R. et al. (2013). Fast myocardial motion and strain estimation in 3D cardiac ultrasound with sparse demons. *Proc. IEEE Int. Soc. Biomed. Imaging* 1182–1185.

26 Curiale, A., Vegas-Sánchez-Ferrero, G., Bosch, J., and Aja-Fernández, S. (2015). A maximum likelihood approach to diffeomorphic speckle tracking for 3D strain estimation in echocardiography. *Med. Image Anal.* 24 (1): 90–105. [Epub, doi: 10.1016/j.media.2015.05.001]

27 Bohs, L., and Trahey, G. (1991). A novel method for angle independent ultrasonic imaging of blood flow and tissue motion. *IEEE Trans. Biomed. Eng.* 38 (3): 280–286.

28 Friemel, B., Bohs, L., and Trahey, G. (1995). Relative performance of two-dimensional speckle tracking techniques: normalized correlation, non-normalized correlation and sum-absolute-difference. *IEEE Int. Ultrason. Symp.* 1481–1484.

29 Langeland, S., D'hooge, J., Torp, H., et al. (2003). Comparison of time-domain displacement estimators for two-dimensional RF tracking. *Ultrasound Med. Biol.* 29 (8): 1177–1186.

30 Viola, F. and Walker, W. (2003). A comparison of the performance of time-delay estimators in medical ultrasound. *IEEE Trans. Ultrason., Ferroelectr., Freq. Control* 50 (4): 392–401.

31 Cohen, B. and Dinstein, I. (2002). New maximum likelihood motion estimation schemes for noisy ultrasound images. *Pattern Recogn.* 35 (2): 455–463.

32 Céspedes, I., Huang, Y., Ophir, J., and Spratt, S. (1995). Methods for estimation of subsample time delays of digitized echo signals. *Ultrason. Imaging* 17 (2): 142–171.

33 Trahey, G., Allison, J., and Von Ramm, O. (1987). Angle independent ultrasonic detection of blood flow. *IEEE Trans. Biomed. Eng.* 34 (12): 965–967.

34 Amundsen, B., Helle-Valle, T., Edvardsen, T., et al. (2006). Noninvasive myocardial strain measurement by speckle tracking echocardiography: validation against sonomicrometry and tagged magnetic resonance imaging. *J. Am. Coll. Cardiol.* 47 (4): 789–793.

35 Behar, V. Adam, D., Lysyansky, P., and Friedman, Z. (2004). Improving motion estimation by accounting for local image distortion. *Ultrasonics* 43 (1): 57–65.

36 Korinek, J., Wang, J., Sengupta, P., et al. (2005). Two-dimensional strain – a Doppler-independent ultrasound method for quantitation of regional deformation: validation in vitro and in vivo. *J. Am. Soc. Echocardiogr.* 18 (12): 1247–1253.

37 Langeland, S., Wouters, P., Claus, P., et al. (2006). Experimental assessment of a new research tool for the estimation of two-dimensional myocardial strain. *Ultrasound Med. Biol.* 32 (10): 1509–1513.

38 Pirat, B., Khoury, D., Hartley, C., (2008). A novel feature-tracking echocardiographic method for the quantitation of regional myocardial function – validation in an animal model of ischemia-reperfusion. *J. Am. Coll. Cardiol.* 51 (6): 651–659.

39 Reant, P., Labrousse, L., Lafitte, S., et al. (2008). Experimental validation of circumferential, longitudinal, and radial 2- dimensional strain during dobutamine stress echocardiography in ischemic conditions. *J. Am. Coll. Cardiol.* 51 (2): 149–157.

40 Marwick, T., Leano, R., Brown, J., et al. (2009). Myocardial strain measurement with 2-dimensional speckle-tracking echocardiography: definition of normal range. *J. Am. Coll. Cardiol: Cardiovasc. Imaging* 2 (1): 80–84.

41 Kleijn, S., Aly, M., Terwee, C., et al. (2012). Reliability of left ventricular volumes and function measurements using three-dimensional speckle tracking echocardiography. *Eur. Heart J. Cardiovasc. Imaging* 13 (2): 159–168.

42 Pérez de Isla, L., Balcones, D., Fernández-Golfín, C., et al. (2009). Three-dimensional wall motion tracking: A new and faster tool for myocardial strain assessment: Comparison with two-dimensional-wall motion tracking. *J. Am. Soc. Echocardiogr.* 22 (4): 325–330.

43 Reant, P., Barbot, L., Touche, C., et al. (2012). Evaluation of global left ventricular systolic function using three-dimensional echocardiography speckle tracking strain parameters. *J. Am. Soc. Echocardiogr.* 25 (1): 68–79.

44 Sahn, D., Ashraf, M., Balbach, T., DesRochers, K. (2011). A new 3D strain method for processing of 4D echo images can delineate regional myocardial dysfunction: validation against sonomicrometry. *J. Am. Coll. Cardiol.* 57 (suppl.): E707.

45 Saito, K., Okura, H., Watanabe, N., et al. (2009). Comprehensive evaluation of left ventricular strain using speckle tracking echocardiography in normal adults: Comparison of three-dimensional and two-dimensional approaches. *J. Am. Soc. Echocardiogr.* 22 (9): 1025–1030.

46 Zhang, L., Gao, J., Xiz, M., et al. (2011). Three-dimensional global longitudinal strain analysis of left ventricle by real-time 3-D speckle tracking imaging in pediatric population: feasibility, reproducibility, maturational changes, and normal ranges. *Circulation* I24 (suppl): A10777.

47 Morsy, A. and von Ramm, O. (1999). Flash correlation: A new method for 3-D ultrasound tissue motion tracking and blood velocity estimation. *IEEE Trans. Ultrason., Ferroelectr., Freq. Control* 46 (3): 728–736.

48 Crosby, J., Amundsen, B., Hergum, T., et al. (2009). 3-D speckle tracking for assessment of regional left ventricular function. *Ultrasound Med. Biol.* 35 (3): 458–471.

49 Kaluzynski, K., Chen, X., Emelianov, S., et al. (2001). Strain rate imaging using two-dimensional speckle tracking. *IEEE Trans. Ultrason., Ferroelectr., Freq. Control* 48 (4): 1111–1123.

50 Lopata, R., Nillesen, M., Gerrits, I., et al. (2009). Performance evaluation of methods for two-dimensional displacement and strain estimation using ultrasound radio frequency data. *Ultrasound Med. Biol.* 35 (5): 796–812.

51 Lubinski, M., Emelianov, S., and O'Donnell, M. (1999). Speckle tracking methods for ultrasonic elasticity imaging using short-time correlation. *IEEE Trans. Ultrason., Ferroelectr., Freq. Control* 46 (1): 82–96.

52 Ramamurthy, B. and Trahey, G. (1991). Potential and limitations of angle-independent flow detection algorithms using radio-frequency and detected echo signals. *Ultrason. Imaging* 13 (3): 252–268.

53 Yu, W., Yan, P., Sinusas, A., et al. (2006). Towards pointwise motion tracking in echocardiographic image sequences – comparing the reliability of different features for speckle tracking. *Med. Image Anal.* 10 (4): 495–508.

54 Lopata, R., Nillesen, M., Thijssen, J. et al. (2011). Three-dimensional cardiac strain imaging in healthy children using RF-data, *Ultrasound Med. Biol.* 37 (9): 1399–1408.

55 Srinivasan, S., Krouskop, T., and Ophir, J. (2004). Comparing elastographic strain images with modulus images obtained using nanoidentation: preliminary results using phantoms and tissue samples. *Ultrasound Med. Biol.* 30 (4): 329–343.

56 Bachner-Hinenzon, N., Ertracht, O., Lysiansky, M., et al. (2011). Layer-specific assessment of left ventricular function by utilizing wavelet denoising: a validation study. *Med. Biol. Eng. Comput.* 49 (1): 3–13.

57 Varghese, T., Ophir, J., and Céspedes, I. (1996). Noise reduction in elastograms using temporal stretching with multicompression averaging. *Ultrasound Med. Biol.* 22 (8): 1043–1052.

58 Kallel, F. and Ophir, J. (1997). A least-squares strain estimator for elastography. *Ultrason. Imaging* 19 (3): 195–208.

59 Lopata, R., Hansen, H., Nillesen, M. et al. (2009). Comparison of one-dimensional and two-dimensional least-squares strain estimators for phased array displacement data. *Ultrason. Imaging* 31 (1): 1–16.

60 Larsson, M., Kremer, F., Claus, P., et al. (2010). A novel measure to express tracking quality in ultrasound block matching. *IEEE Int. Ultrason. Symp.* 1636–1639.

61 Alessandrini, M., Liebgott, H., Barbosa, D., and Bernard, O. (2012). Monogenic phase based optical flow computation for myocardial motion analysis in 3D echocardiography. *Stat. Atlases Comput. Models Heart* 7746: 159–168.

62 Boukerroui, D., Noble, A., and Brady, M. (2003). Velocity estimation in ultrasound images: a block matching approach, *Info. Process. Med. Imaging* 18: 586–598.

63 Tautz, L., Hennemuth, A., and Peitgan, H. (2012). Quadrature filter based motion analysis for 3D ultrasound sequences. *Stat. Atlases Comput. Models Heart* 7746: 169–177.

64 Alessandrini, M., Basarab, A., Liebgott, H., and Bernard, O. (2013). Myocardial motion estimation from medical images using the monogenic signal. *IEEE Trans. Image Process.* 22 (3): 1084–1095.

65 Holden, M. (2008). A review of geometric transformations for nonrigid body registration. *IEEE Trans. Med. Imaging* 27 (1): 111–128.

66 Kybic, J. and Unser, M. (2003). Fast parametric elastic image registration. *IEEE Trans. Image Process.* 12 (11): 1427–1442.

67 Rueckert, D., Sonoda, L., Hill, D., et al. (1999). Nonrigid registration using free-form deformations: application to breast MR images. *IEEE Trans. Med. Imaging* 18 (8): 712–721.

68 Ledesma-Carbayo, M., Kybic, J., Desco, M., et al. (2005). Spatio-temporal nonrigid registration for ultrasound cardiac motion estimation. *IEEE Trans. Med. Imaging* 24 (9): 1113–1126.

69 Elen, A., Choi, H., Loeckx, D., et al. (2008). 3D cardiac strain estimation using spatio-temporal elastic registration of ultrasound images: a feasibility study. *IEEE Trans. Med. Imaging* 27 (11): 1580–1591.

70 Heyde, B., Bouchez, S., and Thieren, S., et al. (2013). Elastic image registration to quantify 3D regional myocardial deformation from volumetric ultrasound: Experimental validation in an animal model. *Ultrasound Med. Biol.* 39 (9): 1688–1697.

71 Heyde, B., Cygan, S., Choi, H., et al. (2012). Regional cardiac motion and strain estimation in three-dimensional echocardiography: A validation study in thick-walled univentricular phantoms. *IEEE Trans. Ultrason., Ferroelectr., Freq. Control* 59 (4): 668–682.

72 Heyde, B., Alessandrini, M., Hermans, J., et al. (2015). Anatomical image registration using volume conservation to assess cardiac deformation from 3D ultrasound recordings. *IEEE Trans. Med. Imaging* 35 (2): 501–511.

73 De Craene, M., Allain, P., Gao, H., et al. (2012). Computational and physical phantom setups for the second cardiac motion analysis challenge (cMAC2). *Stat. Atlases Comput. Models Heart* 7746: 125–133.

74 Piella, G., Porras, A., De Craene, M., and Duchateau, N. (2012). Temporal diffeomorphic free form deformation to quantify changes induced by left and right bundle branch block and pacing. *Stat. Atlases Comput. Models Heart* 7746: 134–141.

75 Zhang, Z., Ashraf, M., Sahn, D., and Song, X. (2014). Temporally diffeomorphic cardiac motion estimation from three-dimensional echocardiography by minimization of intensity consistency error. *Med. Phys.* 41 (5): 052902.

76 Zhang, Z., Song, X., and Sahn, D. (2011). Cardiac motion estimation from 3D echocardiography with spatiotemporal regularization. *Funct. Imaging Model Heart* 6666: 350–358.

77 Myronenko, A. Song, X., and Sahn, D. (2007). LV motion tracking from 3D echocardiography using textural and structural information. *Med. Image Comput. Comput. Assist. Interv.* 4792: 428–435.

78 Myronenko, A., Song, X., and Sahn, D. (2009). Maximum likelihood motion estimation in 3D echocardiography through non-rigid registration in spherical coordinates. *Funct. Imaging Model. Heart* 5528: 427–436.

79 Porras, A., Alessandrini, M., Mirea, O., et al. (2015). Integration of multi-plane tissue Doppler and B-mode echocardiographic images for left ventricular motion estimation. *IEEE Trans. Med. Imaging* 35 (1): 89–97.

80 Buhmann, M. (2009). Radial basis functions. *Acta Numerica* 9: 1–38.

81 Compas, C., Wong, E., Huang, X., et al., (2012). A combined shape tracking and speckle tracking approach for 4D deformation analysis in echocardiography. *International Symposium on Biomedical Imaging* 458–461.

82 Duan, Q., Angelini, E., Herz, S., et al. (2005). Dynamic cardiac information from optical flow using four dimensional ultrasound. *Eng. Med. Biol. Soc.* 4465–4468.

83 Papademetris, X., Sinusas, A., Dione, D., and Duncan, J. (2001). Estimation of 3D left ventricular deformation from echocardiography. *Med. Image Anal.* 5 (1): 17–28.

84 Papademetris, X., Sinusas, A., Dione, D., et al. (2002). Estimation of 3-D left ventricular deformation from medical images using biomechanical models. *IEEE Trans. Med. Imaging* 21 (7): 786–800.

85 Sermesant, M., Delingette, H., and Ayache, N. (2006). An electromechanical model of the heart for image analysis and simulation. *Med. Image Anal.* 25 (5): 612–625.

86 Sermesant, M., Chabiniok, R., Chinchapatnam, P., et al. (2012). Patient-specific electromechanical models of the heart for the prediction of pacing acute effects in CRT: A preliminary clinical validation. *Med. Image Anal.* 16 (1): 201–215.

87 Wang, Y., Georgescu, B., Comaniciu, D., and Houle, H. (2010). Learning-based 3D myocardial motion flow estimation using high frame rate volumetric ultrasound data. *International Symposium on Biomedical Imaging* 1097–1100.

88 Wang, Y., Georgescu, B., Houle, H., and Comaniciu, D. (2010). Volumetric myocardial mechanics from 3D+t ultrasound data with multi-modal tracking. *Stat. Atlases Comput. Models Heart* 6364: 184–193.

89 Leung, E., Danilouchkine, M., van Stralen, M., et al. (2011). Left ventricular border tracking using cardiac motion models and optical flow. *Ultrasound Med. Biol.* 37 (4): 605–616.

90 Gao, H., Choi, H., Claus, P., et al. (2009). A fast convolution-based methodology to simulate 2-D/3-D cardiac ultrasound images. *IEEE Trans. Ultrason., Ferroelectr., Freq. Control* 56 (2): 404–409.

91 Alessandrini, M., De Craene, M.D., M., Bernard, O., et al. (2015). A pipeline for the generation of realistic 3D synthetic echocardiographic sequences: methodology and open-access database. *IEEE Trans. Med. Imaging* 34: 1436–1451.

92 D'hooge, J., Barbosa, D., Gao, H., et al. (2015). Two-dimensional speckle tracking echocardiography: standardization efforts based on synthetic ultrasound data; EACVI/ASE/Industry Task Force to Standardize Deformation Imaging. *Eur. Heart J. Cardiovasc. Imaging* 17 (6): 693–701.

93 Lesniak-Plewinska, B., Cygan, S., Kaluzynski, K., et al. (2010). A dual-chamber, thick-walled cardiac phantom for use in cardiac motion and deformation imaging by ultrasound. *Ultrasound Med. Biol.* 36 (7): 1145–1156.

94 Leopaldi, A.M., Vismara, R., Lemma, M., et al. (2012). In vitro hemodynamics and valve imaging in passive beating hearts. *J. Biomech.* 45 (7): 1133–1139.

95 Leopaldi, A.M., Vismara, R., van Tuijl, S., et al. (2015). A novel passive left heart platform for device testing and research. *Med. Eng. Phys.* 37 (4): 361–366.

96 de Hart, J., de Weger, A., van Tuijl, S., et al. (2011). An ex vivo platform to simulate cardiac physiology: a new dimension for therapy development and assessment. *Int. J. Artif. Organs* 34: 495–505.

97 Langeland, S., D'hooge, J., Wouters, P.F., et al. (2005). Experimental validation of a new ultrasound method for the simultaneous assessment of radial and longitudinal myocardial deformation independent of insonation angle *Circulation* 112 (14): 2157–2162.

98 Yingchoncharoen, T., Agarwal, S., Popović, Z.B., and Marwick, T.H. (2013). Normal ranges of left ventricular strain: a meta-analysis. *J. Am. Soc. Echocardiogr.* 26 (2): 185–191.

99 Barbier, P., Mirea, O., Cefalù, C., et al. (2015). Reliability and feasibility of longitudinal AFI global and segmental strain compared with 2D left ventricular volumes and ejection fraction: intra- and inter-operator, test-retest, and inter-cycle reproducibility. *Eur. Heart J. Cardiovasc. Imaging* 16 (6): 642–652.

100 Stanton, T., Leano, R., and Marwick, T.H. (2009). Prediction of all-cause mortality from global longitudinal speckle strain: comparison with ejection fraction and wall motion scoring. *Circ. Cardiovasc. Imaging* 2 (5): 356–364.

101 Motoki, H., Borowski, A.G., Shrestha, K., et al. (2012). Incremental prognostic value of assessing left ventricular myocardial mechanics in patients with chronic systolic heart failure. *J. Am. Coll. Cardiol.* 60 (20): 2074–2081.

102 Buss, S.J., Emami, M., Mereles, D., et al. (2012). Longitudinal left ventricular function for prediction of survival in systemic light-chain amyloidosis: incremental value compared with clinical and biochemical markers. *J. Am. Coll. Cardiol.* 60 (12): 1067–1076.

103 Ersbøll, M., Valeur, N., Mogensen, U.M., et al. (2013). Prediction of all-cause mortality and heart failure admissions from global left ventricular longitudinal strain in patients with acute myocardial infarction and preserved left ventricular ejection fraction. *J. Am. Coll. Cardiol.* 61 (23): 2365–2373.

104 Lancellotti, P., Cosyns, B., Zacharakis, D., et al. (2008). Importance of left ventricular longitudinal function and functional reserve in patients with degenerative mitral regurgitation: assessment by two-dimensional speckle tracking. *J. Am. Soc. Echocardiogr.* 21 (12): 1331–1336.

105 Urheim, S., Edvardsen, T., Torp, H., et al. (2000). Myocardial strain by Doppler echocardiography: validation of a new method to quantify regional myocardial function. *Circulation* 102 (20): 1158–1164.

106 Aarsaether, E., Rösner, A., Straumbotn, E., and Busund, R. (2012). Peak longitudinal strain most accurately reflects myocardial segmental viability following acute myocardial infarction – an experimental study in open-chest pigs. *Cardiovasc. Ultrasound* 10: 23.

107 Aggeli, C., Lagoudakou, S., Felekos, I., et al. (2015). Two-dimensional speckle tracking for the assessment of coronary artery disease during dobutamine stress echo: clinical tool or merely research method. *Cardiovasc. Ultrasound* 13, 43.

108 Stoodley, P.W., Richards, D.A., Hui, R., et al. (2011). Two-dimensional myocardial strain imaging detects changes in left ventricular systolic function immediately after anthracycline chemotherapy. *Eur. J. Echocardiogr.* 12 (12): 945–952.

109 Panoulas, V.F., Sulemane, S., Konstantinou, K., et al. (2014). Early detection of subclinical left ventricular myocardial dysfunction in patients with chronic kidney disease. *Eur. Heart J. Cardiovasc. Imaging* 16 (5): 539–548.

110 Hensel, K.O., Jenke, A., and Leischik, R. (2014) Speckle-tracking and tissue-Doppler stress echocardiography in arterial hypertension: a sensitive tool for detection of subclinical LV impairment. *Biomed. Res. Int.* 472562.

111 Oxborough, D., George, K., and Birch, K.M. (2012). Intraobserver reliability of two-dimensional ultrasound derived strain imaging in the assessment of the left ventricle, right ventricle, and left atrium of healthy human hearts. *Echocardiography* 29 (7): 793–802.

112 Farsalinos, K.E., Daraban, A.M., Ünlü, S., et al. (2015). Head-to-head comparison of global longitudinal strain measurements among nine different vendors: The EACVI/ASE Inter-Vendor Comparison Study. *J. Am. Soc. Echocardiogr.* 28 (10): 1171–1181.

113 Thomas, J.D. and Badano, L.P. (2013). EACVI-ASE-industry initiative to standardize deformation imaging: a brief update from the co-chairs. *Eur. Heart J. Cardiovasc. Imaging* 14 (11): 1039–1040.

114 Leung, K.Y. and Bosch, J.G. (2010). Automated border detection in three-dimensional echocardiography: principles and promises. *Eur. J. Echocardiogr.* 11 (2): 97–108.

115 Cikes, M., Tong, L., Sutherland, G.R., and D'hooge, J. (2014). Ultrafast cardiac ultrasound imaging: technical principles, applications, and clinical benefits. *JACC Cardiovasc. Imaging* 7 (8): 812–823.

116 Liebgott, H., Basarab, A., Gueth, P., et al. (2010). Transverse oscillations for tissue motion estimation. *Ultrasonics* 50 (6): 548–555.

117 Tabassian, M., Alessandrini, M., De Marchi, L., et al. (2015). Principal component analysis for the classification of cardiac motion abnormalities based on echocardiographic strain and strain rate imaging. *Funct. Imaging Model. Heart* 83–90.

12

Vascular and Intravascular Elastography

Marvin M. Doyley

Department of Electrical and Computer Engineering, Hajim School of Engineering and Applied Sciences, University of Rochester, Rochester, NY, USA

12.1 Introduction

Strokes and heart attacks, which cause more deaths than all cancers combined [1], can occur when a life-threatening plaque ruptures in either the carotid or coronary arteries [2–4]. Conventional imaging techniques can visualize the carotid artery [5], but they cannot detect life-threatening plaques. For example, vascular angiography can assess the extent of stenosis, but the extent of stenosis is a poor indicator of a cerebrovascular event: composition – not stenosis – is the key determinant as to whether plaque will rupture [6]. Multi-slice computed tomography (CT) can visualize the carotid atherosclerosis [7], but like angiography, it cannot characterize plaque composition. High-resolution magnetic resonance imaging (MRI) can characterize plaque composition [8], but MRI is expensive and inflexible, traits that make it an inappropriate screening tool. Ultrasound (US) is relatively inexpensive and more flexible than MRI. Furthermore, ultrasound can assess the extent of stenosis and characterize plaque burden [9, 10], but it cannot characterize plaque composition [11]. Vascular elastography is an emerging ultrasound imaging technique that visualizes the mechanical properties of vascular tissues. In this chapter, we will discuss the general principles of intravascular and endovascular elastography – techniques that have been developed to detect rupture-prone plaques in the coronary and carotid arteries, respectively.

12.2 General Principles

Techniques that have been proposed for visualizing the mechanical properties within vascular tissues are classified as being either strain- or model-based techniques. Strain-based vascular imaging approaches visualize the strain distribution within vascular tissues, which are used as a surrogate for shear modulus by assuming stress uniformity. Model-based inversion techniques use a theoretical model that describes soft tissue mechanics, knowledge of the external boundary conditions, and the measured strains or displacements to compute the spatial variation of relative or absolute values of Young's modulus within vascular tissues [12]. In the following sub-sections, we will discuss both approaches, and illustrate how they are used to characterize the mechanical properties of coronary and carotid arteries.

Ultrasound Elastography for Biomedical Applications and Medicine, First Edition.
Edited by Ivan Nenadic, Matthew Urban, James Greenleaf, Jean-Luc Gennisson, Miguel Bernal, and Mickael Tanter.

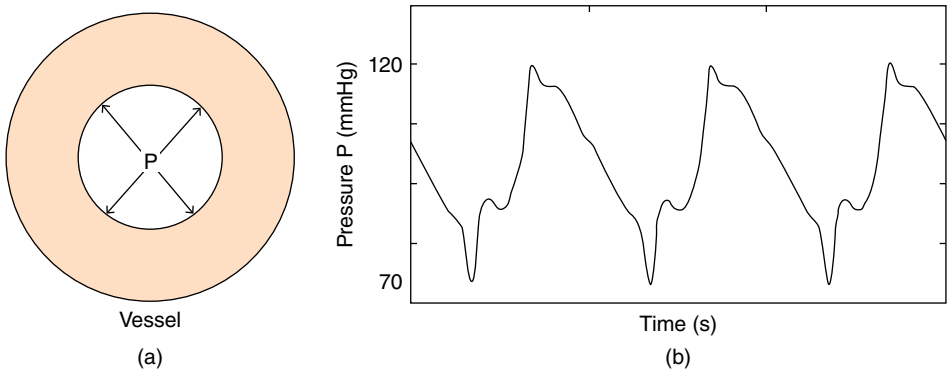

Figure 12.1 Mechanical stimulus employed in vascular elastography. (a) Pressure distribution within vessel. (b) Pulsatile intraluminal pressure.

12.2.1 Strain-based Vascular Imaging Methods

Vascular elastography uses the intraluminal blood pressure as the source of mechanical stimulation (Figure 12.1). Cross-correlation echo is typically used to measure the resulting internal tissue displacements. To do this a pair of radiofrequency (RF) echo-frames are acquired from the vessel at different intraluminal pressure (differential pressure on the order of 2–4 mmHg [13, 14], which are spatially differentiated to produce strain images. Figure 12.2 provides a flowchart that describes the general workflow used to estimate strain and displacements in vascular elastography.

For coronary imaging, a phased array or a rotating element intravascular ultrasound imaging system is used to acquire RF echo at high spatial resolution (~100–200 μm) from within the artery. Since the acquired ultrasound images are in the vessel coordinate system (polar coordinates), axial strain represents the radial strains within the vessel. A limitation of intravascular ultrasound elastography is that it not suitable for real-time application. To address this

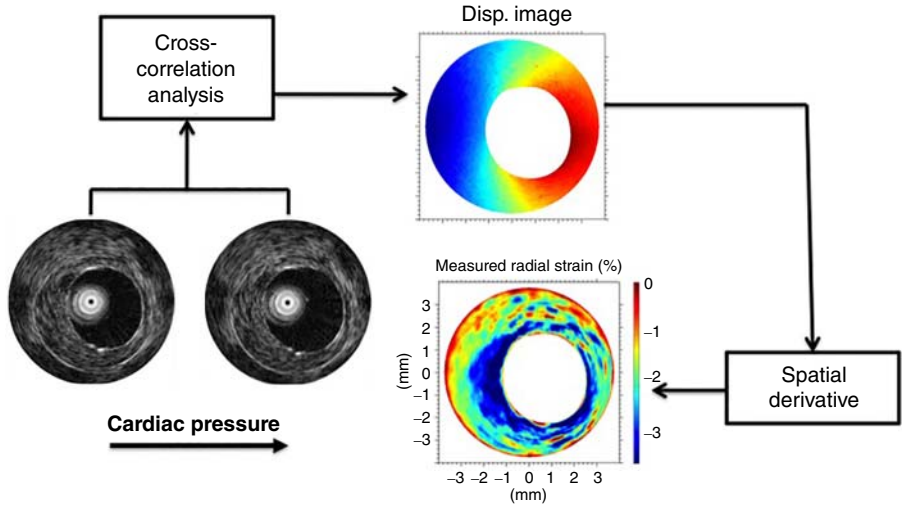

Figure 12.2 Flow chart showing the general principles of vascular elastography. Acquiring a pair of radiofrequency echo frames at two different intraluminal pressures, applying a cross correlation-based echo tracking algorithm to acquired echo frames, and then spatially differentiating the measured displacement to produce radial strain images.

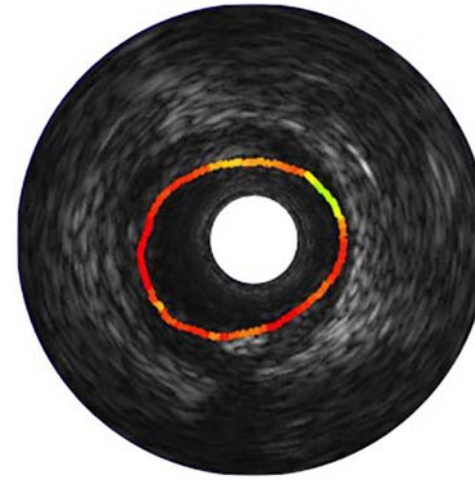

Figure 12.3 Intravascular palpogram. A composite image that contains both echogenic and elastographic information. Source: reprinted from *Ultrasound in Medicine and Biology* [18], with permission from Elsevier.

limitation, an offshoot of intravascular ultrasound elastography known as palpography was developed at Thorax center in the Netherlands [15–17], which is implemented as a selectable option on a commercially available intravascular ultrasound imaging (Volcano Corporation, San Diego, CA, USA). Intravascular palpography measures strain within the inner layer of the arterial wall, which is superimposed on a sonogram to produce a composite image that contains both elastographic and echogenic information (Figure 12.3). The advantage of palpography is that it is fast and robust, which makes it ideally suited for clinical imaging.

Endovascular ultrasound elastography uses a hand-held transducer to measure the mechanical properties of the common carotid artery in either the transverse or sagittal plane. In the sagittal plane, axial and lateral strains are equivalent to radial and circumferential displacements in the vessel.

Figure 12.4 shows a representative example of radial displacement elastograms obtained from the sagittal plane of the carotid artery. Strains measured in the transverse plane are not equivalent to those in the vessel coordinate system [19]. Consequently, strains are transformed from

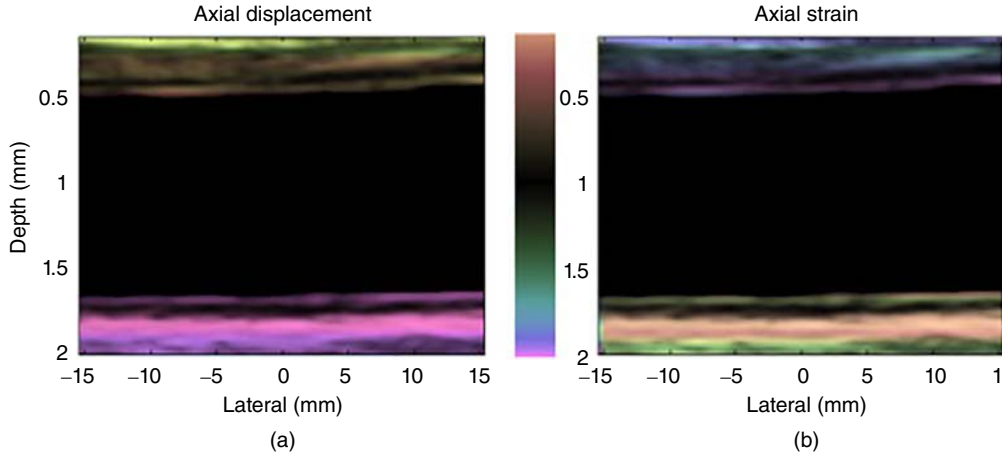

Figure 12.4 Elastograms obtained from the sagittal plane of the common carotid artery: (a) radial displacements and (b) radial strains overlaid on the sonograms.

the transducer to the vessel coordinate system (polar) as follows:

$$\{\varepsilon'\} = T_\varepsilon\{\varepsilon\} \tag{12.1}$$

The transformation matrix T_ε is given by [19]

$$T_\varepsilon = \frac{1}{x^2+z^2}\begin{bmatrix} x^2 & xz & xz & z^2 \\ -xz & x^2 & -z^2 & xz \\ -xz & -z^2 & x^2 & xz \\ z^2 & -xz & -xz & x^2 \end{bmatrix} \tag{12.2}$$

The radial (ε_{rr}) and circumferential ($\varepsilon_{\theta\theta}$) strain elastograms were computed from Eqs. (12.1) and (12.2)

$$\varepsilon_{rr} = \frac{1}{x^2+z^2}[x^2\varepsilon_{xx} + xz(\gamma_{xz}+\gamma_{zx}) + z^2\varepsilon_{zz}] \tag{12.3}$$

$$\varepsilon_{\theta\theta} = \frac{1}{x^2+z^2}[z^2\varepsilon_{xx} - xz(\gamma_{xz}+\gamma_{zx}) + x^2\varepsilon_{zz}] \tag{12.4}$$

This transformation requires reliable estimates of both axial and lateral displacements, which standard ultrasound imaging methods cannot provide. More specifically, the phase information in the direction of the propagating wave allows ultrasound to measure axial displacement precisely. However, the relatively broad lateral beam width and the lack of phase information in that lateral direction degrades the precision of lateral displacements [20, 21]; the precision of axial displacements is an order of magnitude better than that of lateral displacements [22–24]. Sparse array or plane wave imaging in combination with beam forming can reduce this problem. More specifically, they significantly reduce the lateral extent of the ultrasound point spread function to allow reliable estimates of axial and lateral displacements (Figure 12.5).

12.2.2 Model-based Imaging

Assuming that soft tissues exhibit isotropic, nearly incompressible ($\nu = 0.495$) linear elastic behavior, then the governing equation that describes the resulting deformation is given by [25]

$$-\nabla p + \nabla\cdot(\mu(\nabla\mathbf{u} + \nabla\mathbf{u}^T)) = 0, \text{ where } p = -\lambda\nabla\cdot\mathbf{u} \tag{12.5}$$

where $\mathbf{u}$ represents the tissue displacement vector field, μ and λ are the Lamé constants, and p represents the internal hydrostatic pressure. The shear modulus (μ) can be reconstructed from measured radial displacements using a direct or iterative inversion technique. Direct inversion methods are fast; however, they are more prone to errors. Consequently, we will limit the discussion to iterative techniques. The reconstruction process consists of minimizing the following cost function

$$\pi[\mu] = \frac{1}{2}\int_\Omega (u^{\mathrm{r}}(\mu) - u^{\mathrm{r}}_{\mathrm{meas}})^2 + \pi_{\mathrm{r}}[\mu, u_0]\mathrm{d}\Omega \tag{12.6}$$

where $u^{\mathrm{r}}_{\mathrm{meas}}$ is the measured radial component of displacement, u^{r} is the radial component of displacement computed from the shear modulus distribution μ using a finite-element representation of Eq. (12.5); π_{r} is a regularization function. Since the inverse reconstruction method is not unique, the solution is constrained by applying a constant regularization function to all pixels in the reconstruction field of view. For some tissues this constraint is not ideal, because the magnitude of the regularization is noticeably higher in a positive contrast problem (stiff tumor in a soft background) compared to a negative contrast problem (soft plaque embedded in a stiffer vessel wall). A logarithmic regularization function can remove the dependence

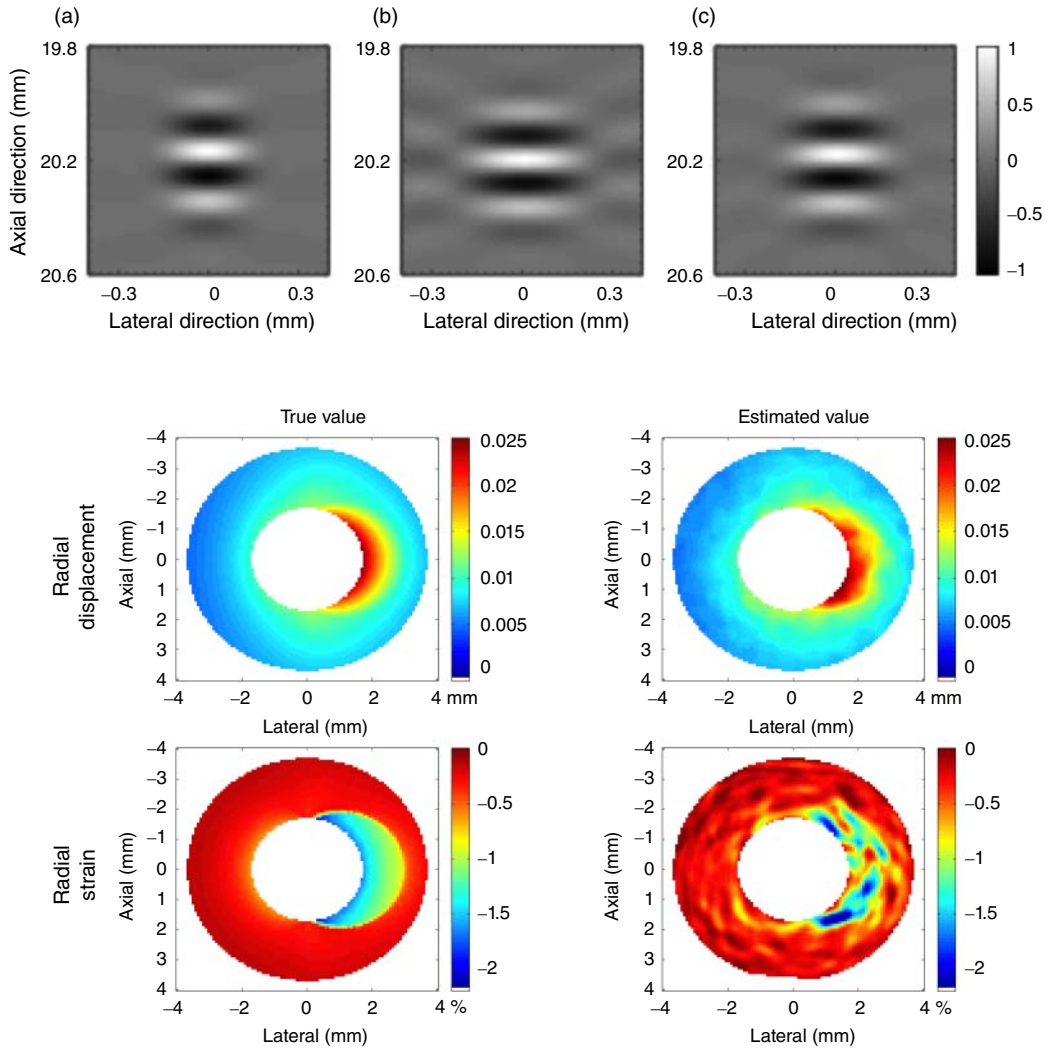

Figure 12.5 (i) Point spread function of (a) sparse array, (b) plane wave, and (c) compounded plane wave imaging system. (ii) Displacement and strain elastograms produced using compounded plane wave imaging.

of the regularization on modulus contrast. The logarithmic regularization function, $c(\mu, \mu_0)$ is given by [26]

$$c(\mu, \mu_0) = \ln\left(\frac{\mu}{\mu_0}\right) \tag{12.7}$$

where μ_0 is the baseline modulus for each region, which is analogous to a DC offset, which is computed as part of the reconstruction process. Since regularization methods may be problem-specific [27], several regularization approaches have been proposed in model-based elastography. The three most widely used regularization methods are Tikhonov, H1-seminorm, and the total-variation-diminishing (TVD) method, which are defined as follows [26]

- Tikhonov regularization:

$$\pi_{\mathrm{R}}[\mu, \mu_0] = \frac{\alpha}{2}\int_{\Omega} c(\mu, \mu_0)^2 \mathrm{d}\Omega \tag{12.8}$$

- H1-seminorm regularization:

$$\pi_R[\mu, \mu_0] = \frac{\alpha}{2}\int_\Omega (\nabla c(\mu, \mu_0) \cdot \nabla c(\mu, \mu_0))\mathrm{d}\Omega \tag{12.9}$$

- TVD regularization:

$$\pi_R[\mu, \mu_0] = \alpha \int_\Omega \sqrt{\nabla c(\mu, \mu_0) \cdot \nabla c(\mu, \mu_0) + \beta^2}\mathrm{d}\Omega \tag{12.10}$$

The regularization parameter α in Eqs. (12.8), (12.9), and (12.10) controls the weight given to the cost information. The variable β in Eq. (12.10) is a small scalar that is used to ensure the continuity of the regularization at $\nabla c = 0$, which was set to unity in all reconstructions. Minimizing Eq. (12.6) with respect to shear modulus variations is a nonlinear process, which is realized through an iterative solution using either a Gauss Newton iterative scheme [28] or the quasi-Newton BFGS (Broyden-Fletcher-Goldfarb-Shanno) algorithm and the adjoint method as described by Oberai [29]. For the adjoint method, the resulting shear modulus solution at the $(q + 1)$-th iteration has the general solution

$$\mu_{q+1} = \mu_q - \varphi_q B_q^{-1} g_q \tag{12.11}$$

where B_q is an approximation of the Hessian matrix that is computed using the BFGS algorithm [30] at the q-th iteration, φ_q represents the step size, and g_q is the functional gradient of πU evaluated at μ_q.

The inverse problem incurred in vascular elastography is highly ill-posed; consequently additional constraints (hard or soft priors) are used to stabilize the problem. The hard prior method can be viewed as parameter lumping [31–33] where all the nodes in a given region are assigned the same shear modulus. Structural information can be extracted by applying deformable curves to strain elastograms [32], manually segmenting sonograms or strain elastograms [34]. The hard prior reconstruction method used a similar objective function to that employed in the no prior reconstruction method; however, since this was a well-conditioned problem, no regularization is included in the objective function. To impose hard priors, first all the nodes within each segmented region are identified, and then reconstructed only a single μ within each region. To illustrate, let us assume that the reconstruction field of view was divided into M regions based on the structural information, and that the shear modulus within each region was computed by applying a matrix transformation to B (the approximate Hessian), such that

$$\widetilde{B} = KB \tag{12.12}$$

where K is an $M \times N$ sparse matrix, and N represents the number of nodal points. The prior matrix K then had the form

$$K = \begin{bmatrix} k_{1,1} & k_{1,2} & \cdots & k_{1,N} \\ k_{2,1} & k_{2,2} & \cdots & k_{2,N} \\ \vdots & \vdots & \ddots & \vdots \\ k_{M,1} & k_{M,2} & \cdots & k_{M,N} \end{bmatrix}, \text{ where } k_{m,n} = \begin{Bmatrix} 1 & n \in R_m \\ 0 & n \notin R_m \end{Bmatrix}, \; n = (1, N) \text{ and } m = (1, M) \tag{12.13}$$

A new gradient vector can be computed by summing all gradient components from each row that corresponded to the m-th region, and the shear modulus for each region was solved as follows

$$\widetilde{\mu}_{q+1} = \widetilde{\mu}_q - \varphi_q \widetilde{B}_q^{-1} \widetilde{g}_q \tag{12.14}$$

where the dimension of the update vector $\widetilde{\mu}_{q+1}$ was $\mathbf{M}$. Segmentation of congruent features always includes classification errors, which could degrade the performance of hard prior reconstruction methods. Soft priors can overcome this issue. Soft prior reconstruction methods use the same objective function (Eq. 12.6), but the regularization term was different, as given by Tikhonov

$$\pi_{\mathrm{R}}[\mu, \mu_0^m] = \frac{\alpha}{2}\int_{\Omega} \ln\left(\mu/\mu_0^m\right)^2 \mathrm{d}\Omega, \text{ where } m = 1, M \tag{12.15}$$

and M is the number of segmented regions.

The soft prior method has been employed in endovascular elastography. Geometric information can be included in the image reconstruction process by minimizing the following objective function

$$\Omega(\mu) = \|\mathbf{u_m} - \mathbf{u_c}(\mu)\|^2 + \alpha\|\mathbf{L}[\mu]\|^2 \tag{12.16}$$

where $\mathbf{L}$ is a penalty matrix that was defined as follows

$$L_{i,j} = \begin{cases} 1 & i = j \\ 0 & i, j \notin R \\ -\dfrac{1}{m} & i, j \in R \end{cases} \tag{12.17}$$

where m is the total number of nodes contained in a given region, R, and i and j are indices of $\mathbf{L}$. The $\mathbf{L}$ matrix (i.e. Laplacian) computes the average modulus in each region explicitly as follows

$$L_1 \cdot \mu = \mu_1 - \frac{\mu_2}{N} - \frac{\mu_3}{N} - \cdots - \frac{\mu_N}{N} \approx \mu_1 - \langle\mu\rangle \tag{12.18}$$

Figure 12.6 shows representative examples of modulus elastograms obtained with this method.

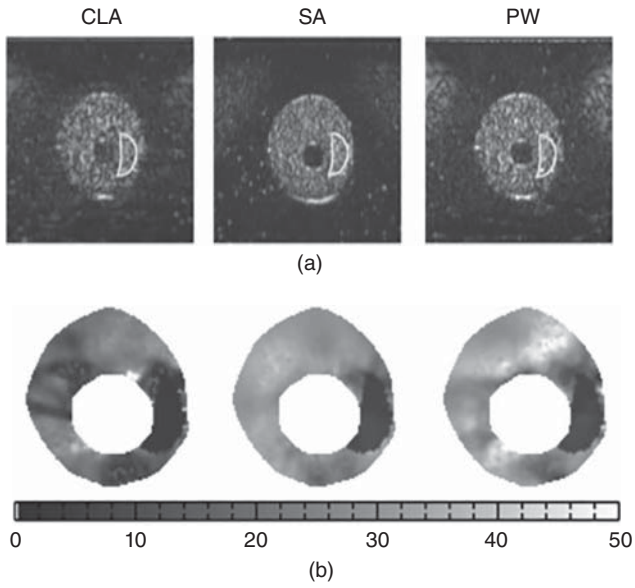

Figure 12.6 (a) Sonograms and (b) modulus elastograms obtained from a vessel phantom using a conventional linear array (CLA), sparse array (SA), and plane wave (PW) imaging. Source: reprinted from *Journal of Medical Imaging* [35], with permission from SPIE.

12.3 Conclusion

Vascular elastography has emerged as a useful imaging technique for visualizing the strain distribution within vascular tissues and characterizing the mechanical properties of different vessel components. The technique is now widely used to detect life-threatening plaques, and to understand how mechanical properties vary with age in diseases such as hypertension.

References

1 Rosamond, W., Flegal, K., Furie, K., et al. (2008). Heart disease and stroke statistics – 2008 update: a report from the American Heart Association Statistics Committee and Stroke Statistics Subcommittee. *Circulation* 117: e25–146.

2 de Korte, C.L., Cespedes, E.I., van der Steen, A.F., et al. (1998). Intravascular ultrasound elastography: assessment and imaging of elastic properties of diseased arteries and vulnerable plaque. *Eur. J. Ultrasound* 7: 219–224.

3 Naghavi, M., Madjid, M., Khan, M.R., et al. (2001). New developments in the detection of vulnerable plaque. *Curr. Atheroscler. Rep.* 3: 125–135.

4 Schroeder, A.P. and Falk, E. (1995). Vulnerable and dangerous coronary plaques. *Atherosclerosis* 118 (suppl.): S141–149.

5 Fayad, Z.A. and Fuster, V. (2001). Clinical imaging of the high-risk or vulnerable atherosclerotic plaque. *Circ. Res.* 89: 305–316.

6 Schaar, J.A., Mastik, F., Regar, E., et al. (2007). Current diagnostic modalities for vulnerable plaque detection. *Curr. Pharm. Des.* 13: 995–1001.

7 Kwee, R.M., Truijman, M.T., Mess, W.H., et al. (2011). Potential of integrated [^{18}F]fluorodeoxyglucose positron-emission tomography/CT in identifying vulnerable carotid plaques. *Am. J. Neuroradiol.* 32: 950–954.

8 Yuan, C., Beach, K.W., Smith, L.H., Jr., and Hatsukami, T.S. (1998). Measurement of atherosclerotic carotid plaque size in vivo using high resolution magnetic resonance imaging. *Circulation* 98: 2666–2671.

9 Bots, M.L., Hoes, A.W., Koudstaal, P.J., et al. (1997). Common carotid intima-media thickness and risk of stroke and myocardial infarction: the Rotterdam Study. *Circulation* 96: 1432–1437.

10 Lorenz, M.W., Markus, H.S., Bots, M.L., et al. (2007). Prediction of clinical cardiovascular events with carotid intima-media thickness: a systematic review and meta-analysis. *Circulation* 115: 459–467.

11 de Korte, C.L., Sierevogel, M.J., Mastik, F., et al. (2002). Identification of atherosclerotic plaque components with intravascular ultrasound elastography in vivo: a Yucatan pig study. *Circulation* 105: 1627–1630.

12 Doyley, M.M. (2012). Model-based elastography: a survey of approaches to the inverse elasticity problem. *Phys. Med. Biol.* 57: R35–73.

13 Cespedes, E.I., de Korte, C.L., van der Steen, A.F., et al. (1997). Intravascular elastography: principles and potentials. *Semin. Interv. Cardiol.* 2: 55–62.

14 de Korte, C.L., Cespedes, E.I., and Pasterkamp, G. (1997). Intravascular elastography of human femoral arteries: an in vitro study. *Ultrason. Symposium, 1997. Proceedings., 1997 IEEE* 2: 1075–1078.

15 Cespedes, E.I., de Korte, C.L., and van der Steen, A.F. (2000). Intraluminal ultrasonic palpation: assessment of local and cross-sectional tissue stiffness. *Ultrasound Med. Biol.* 26: 385–396.

16 Doyley, M.M., Mastik, F., de Korte, C.L., et al. (2001). Advancing intravascular ultrasonic palpation toward clinical applications. *Ultrasound Med. Biol.* 27: 1471–1480.

17 Schaar, J.A., de Korte, C.L., Mastik, F., et al. (2003). Intravascular palpography for high-risk vulnerable plaque assessment. *Herz* 28: 488–495.

18 Doyley, M.M., Bamber, J.C., Fuechsel, F., and Bush, N.L. (2001). A freehand elastographic imaging approach for clinical breast imaging: system development and performance evaluation. *Ultrasound Med. Biol.* 27: 1347–1357.

19 Korukonda, S., Nayak, R., Carson, N., et al. (2013). Noninvasive vascular elastography using plane-wave and sparse-array imaging. *IEEE Trans. Ultrason., Ferroelect., Freq. Control* 60: 332–342.

20 Korukonda, S. and Doyley, M.M. (2011). Estimating axial and lateral strain using a synthetic aperture elastographic imaging system. *Ultrasound Med. Biol.* 37: 1893–1908.

21 Korukonda, S. and Doyley, M.M. (2012). Visualizing the radial and circumferential strain distribution within vessel phantoms using synthetic-aperture ultrasound elastography. *IEEE Trans. Ultrason., Ferroelect., Freq. Control* 59: 1639–1653.

22 Konofagou, E. and Ophir, J. (1998). A new elastographic method for estimation and imaging of lateral displacements, lateral strains, corrected axial strains and Poisson's ratios in tissues. *Ultrasound Med. Biol.* 24: 1183–1199.

23 Sumi, C. (2007). Ultrasonic axial strain measurement for lateral tissue deformation. *Ultrasound Med. Biol.* 33: 1830–1837.

24 Sumi, C., Noro, T., and Tanuma, A. (2008). Effective lateral modulations with applications to shear modulus reconstruction using displacement vector measurement. *IEEE Trans. Ultrason., Ferroelect., Freq. Control* 55: 2607–2625.

25 Timoshenko, S.P. and Goodier, J.N. (1970). *Theory of Elasticity*. New York: McGraw-Hill.

26 Richards, M.S. and Doyley, M.M. (2011). Investigating the impact of spatial priors on the performance of model-based IVUS elastography. *Phys. Med. Biol.* 56: 7223–7246.

27 Meaney, P.M., Demidenko, E., Yagnamurthy, N.K., et al. (2001). A two-stage microwave image reconstruction procedure for improved internal feature extraction. *Med. Phys.* 28: 2358–2369.

28 Doyley, M.M., Meaney, P.M., and Bamber, J.C. (2000). Evaluation of an iterative reconstruction method for quantitative elastography. *Phys. Med. Biol.* 45: 1521–1540.

29 Oberai, A.A., Gokhale, N.H., Goenezen, S., et al. (2009). Linear and nonlinear elasticity imaging of soft tissue in vivo: demonstration of feasibility. *Phys. Med. Biol.* 54: 1191–1207.

30 Zhu, C., Byrd, R., Lu, P., and Nocedal, J. (1997). Algorithm 778: L-BFGS-B: Fortran subroutines for large-scale bound-constrained optimization. *ACM Trans. Math. Softw.* 23 (4): 550–560.

31 Baldewsing, R.A., Schaar, J.A., Mastik, F., et al. (2005). Assessment of vulnerable plaque composition by matching the deformation of a parametric plaque model to measured plaque deformation. *IEEE Trans. Med. Imaging* 24: 514–528.

32 Baldewsing, R.A., Mastik, F., Schaar, J.A., et al. (2006). Young's modulus reconstruction of vulnerable atherosclerotic plaque components using deformable curves. *Ultrasound Med. Biol.* 32: 201–210.

33 Baldewsing, R.A., Danilouchkine, M.G., and van der Steen, A.F.W. (2008). An inverse method for imaging the local elasticity of atherosclerotic coronary plaques. *IEEE Trans. Inf. Technol. Biomed.* 12: 277–289.

34 Le Floc'h, S., Ohayon, J., Tracqui, P., et al. (2009). Vulnerable atherosclerotic plaque elasticity reconstruction based on a segmentation-driven optimization procedure using strain measurements: theoretical framework. *IEEE Trans. Med. Imaging* 28: 1126–1137.

35 Huntzicker, S., Nayak, R., and Doyley, M.M. (2014). Quantitative sparse array vascular elastography: the impact of tissue attenuation and modulus contrast on performance. *J. Med. Imaging* 1: 027001-1-01-13.

13

Viscoelastic Creep Imaging

Carolina Amador Carrascal

Department of Physiology and Biomedical Engineering, Mayo Clinic, Rochester, MN, USA

13.1 Introduction

Elasticity imaging is an emerging imaging approach that uses the elasticity of tissue as the contrast mechanism in images. Elasticity or stiffness is a physical property of a material that returns to its original shape after the stress (e.g. external force) that made it deform is removed. The mathematical description of such property is known as elastic modulus or modulus of elasticity. It has been shown that the elastic modulus of tissues in the body can vary over 6 orders of magnitude, making the dynamic range of this contrast mechanism quite large [1]. Moreover, it is established that soft biological tissue exhibits viscoelastic behavior [2].

Viscoelastic materials exhibit both elastic and viscous behavior characterized by being time or frequency dependent. Measuring tissue viscoelasticity is important because:

(a) if the mechanical properties of a viscoelastic material are characterized only from its elasticity, the elasticity measurement can be biased higher than the actual value [3];
(b) besides the advantages of dynamic range in elastic modulus of tissue, measuring tissue viscosity complements the diagnostic capability of elasticity imaging; for instance a study has showed better discrimination between malignant and benign tumors when measuring the time-varying viscous response of breast to a small deforming force [4].

In a laboratory setting, viscoelastic behavior is usually studied either by transient or harmonic tests.

Transient tests are in the time domain and study viscoelastic properties such as creep and relaxation. Time-dependent creep and relaxation tests, with conventional mechanical test system, are not capable of completely evaluating the mechanical behavior of viscoelastic materials. There are situations where the response of materials to a loading for short times, usually below the resolving capability of the measurement device (approximately 0.01 s), is of practical importance [5]. Moreover, the majority of creep studies assume step-loading conditions, which are analytically convenient but experimentally impossible to implement. To overcome these challenges, dynamic or oscillatory tests are used to study viscoelastic material response from about 10^{-8} seconds [5].

Harmonic experiments are formulated in the frequency domain and study viscoelastic properties such as complex modulus and loss tangent. Viscoelastic properties can also be measured by studying shear wave propagation. Shear wave methods are usually non-invasive and are based on measuring vertical particle motion from shear strain (angular deformation) that is

Ultrasound Elastography for Biomedical Applications and Medicine, First Edition.
Edited by Ivan Nenadic, Matthew Urban, James Greenleaf, Jean-Luc Gennisson, Miguel Bernal, and Mickael Tanter.

involved in the passage of transverse waves [6, 7]. Although shear wave propagation methods can provide maps of shear modulus and viscosity, they are limited to fitting rheological models to shear wave velocity dispersion and the shear wave attenuation dispersion is usually unknown.

Viscoelastic creep imaging is an emerging field where the viscoelastic properties of soft tissues are measured by monitoring the soft tissue strain or displacement response to an applied constant stress. The constant stress can be applied externally or internally. External constant stress is usually applied to the surface of the tissue with the ultrasound transducer and ultrasound imaging is used to estimate the tissue creep response. While this method had shown success with tissue viscoelastic characterization, it is limited to applications where the tissue of interest is encapsulated in a hard shell or deep organs. Alternative techniques using acoustic radiation force can generate constant stress that is focused internally and localized. In this chapter, acoustic radiation force creep methods will be reviewed.

13.2 Overview of Governing Principles

13.2.1 Viscoelastic Behavior

Solid materials (e.g. elastic, plastic, viscoelastic) are characterized by their shear strain response $\gamma(t)$ to an applied shear stress $\tau(t)$, as illustrated in Figure 13.1 [5]. Although the former statement is valid for either shear or direct strain/stress, shear nomenclature will be used hereafter. An elastic material exhibits immediate strain upon loading, constant strain as long as the stress is fixed, and no strain once the load is removed (Figure 13.1). Materials that exhibit time-dependent strain as a response to an applied stress are called viscoelastic (Figure 13.1). If instead an oscillatory stress is applied to a viscoelastic material, the strain response will be an oscillation at the same frequency ω of the stress but lagging behind by a phase angle δ (Figure 13.1). As a result of the phase lag between stress and strain, the relation between these two variables is a complex number and it is called the complex shear modulus, $G^*(\omega)$. The real and imaginary parts of the complex modulus are called the storage modulus $G_s(\omega)$ and the loss modulus $G_l(\omega)$, respectively.

13.2.2 Creep

Most viscoelastic materials exhibit the following transient behavior: instantaneous elasticity upon loading, followed by a slow continuous deformation under constant stress, instantaneous recovery once the load is removed, and a slow continuous decrease in deformation once the load is removed [5]. Creep is the slow, progressive deformation of a material under constant stress. The constitutive equations of linear viscoelastic materials are based on connecting linear springs and linear viscous dashpots. The linear spring represents the pure elastic response,

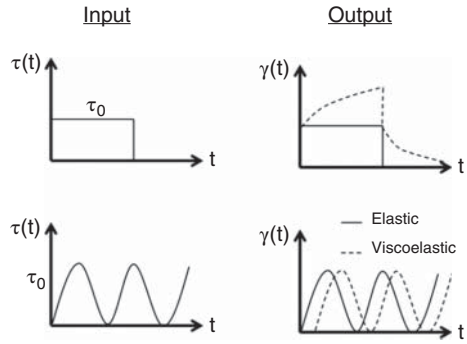

Figure 13.1 Strain response of elastic and viscoelastic materials to a constant and oscillatory stress.

Table 13.1 Viscoelastic models properties when a step-stress is applied.

Model	**Kelvin-Voigt**	**Standard linear solid**
	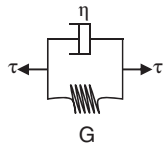	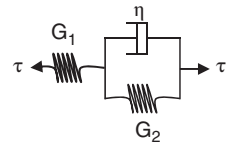
Constitutive equation	$\tau = G\gamma + \eta\frac{d\gamma}{dt}$	$\tau = G_1\left(\gamma + \left(\frac{\eta}{G_1} + \frac{\eta}{G_2}\right)\frac{d\gamma}{dt}\right)$
Creep strain	$\gamma(t) = \frac{\tau}{G}\left(1 - e^{-\frac{G}{\mu}t}\right)$	$\gamma(t) = \frac{\tau}{G_1} - \frac{\tau G_2}{G_1(G_1+G_2)}e^{-\frac{G_1G_2}{\eta(G_1+G_2)}t}$

therefore it exhibits instantaneous elasticity and instantaneous recovery. The linear spring constitutive equation is described as [5]

$$\tau(t) = G\gamma(t) \tag{13.1}$$

where $\tau(t)$ is the shear stress, $\gamma(t)$ is the shear strain and G is the shear modulus. On the other hand, the dashpot element represents the pure viscous response, a linear increase in strain under constant stress. The linear viscous dashpot element constitutive equation is described as [5]

$$\tau(t) = \eta\frac{d\gamma(t)}{dt} \tag{13.2}$$

where $\tau(t)$ is the shear stress, $\frac{d\gamma(t)}{dt}$ is the shear strain rate or the first derivative of the shear strain and η is the shear viscosity. Table 13.1 summarizes the properties of most common linear viscoelastic models that are used in viscoelastic creep imaging methods [5].

13.2.3 Acoustic Radiation Force

As an ultrasound beam propagates through an absorbing medium, the energy transfer results in a second-order effect that produces a force, which is termed radiation force [8]. Acoustic radiation force has been described as

$$F = \frac{2\alpha I}{c} \tag{13.3}$$

where F (N/m^3) is the acoustic radiation body force, c (m/s) is the speed of sound in the medium, α (Np/m) is the absorption coefficient of the medium and I (W/m^2) is the in situ temporal average intensity at a given spatial resolution [8]. In viscoelastic creep imaging, acoustic radiation force is used to apply a step-stress excitation and the creep response is monitored with traditional ultrasound imaging. A conventional acoustic radiation force beam pulse sequence to generate and monitor creep and recovery is shown in Figure 13.2. High intensity pushing beams are interspersed with conventional tracking beams during the creep period, while only tracking beams are used during the recovery period.

13.3 Imaging Techniques

13.3.1 Kinetic Acoustic Vitreoretinal Examination (KAVE)

Motivated by the medical evaluation of ocular disorders, Walker et al. developed a method to study the viscous and elastic components of tissue using acoustic radiation force called Kinetic acoustic vitreoretinal examination (KAVE) [10, 11]. The KAVE method consisted in translating

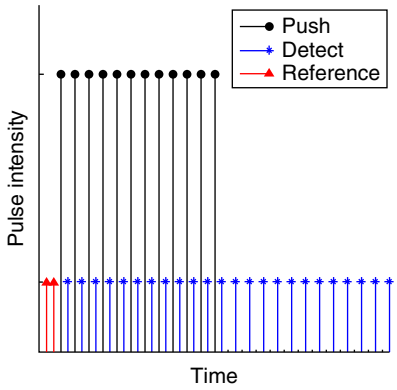

Figure 13.2 Illustration of a conventional acoustic radiation force pulse sequence to generate and monitor creep and recovery. Source: © Institute of Physics and Engineering in Medicine, reproduced by permission of IOP Publishing, all rights reserved [9].

a piston transducer that was used for ultrasonic transmission and detection. The transducer was translated through 150 lateral locations with a computer-controlled positioning system. At each location, 5000 pulses were transmitted at 5.0 kHz pulse repetition frequency. Ultrasound echoes were received every 100th pulse. Displacement due to the acoustic radiation force was estimated by performing a sum absolute difference search between the first and each consecutive ultrasound echo. The measured creep displacement was modeled with a Kelvin-Voigt model. In the proposed experimental set up, the initial location of the tissue and the applied force were unknown, therefore the measured displacement $u(t)$ was modeled as [10]

$$u(t) = \frac{1}{k_r}(e^{-k_r N\Delta t/\eta_r} - e^{-k_r t/\eta_r}) \tag{13.4}$$

where k_r is the relative measure of elasticity ($k_r = k/A$, k is the elastic constant, A is the force amplitude), η_r is the relative measure of viscosity ($\eta_r = \eta/A$, η is the viscous constant, A is the force amplitude), Δt is the pulse interval, and N is the total number of detecting pulses. Figure 13.3 illustrates the measured and modeled creep displacement response in four soft acrylamide gel phantoms [10].

Figure 13.4 illustrates experimental B-mode, maximum displacement, relative elasticity and relative viscosity images from four soft acrylamide gel phantoms [10]. The advantage of this technique is the increase in dynamic contract achieved from the relative elasticity and viscosity images that is limited with conventional the B-mode images.

Viola and Walker [11] developed the KAVE method further by proposing a Kelvin-Voigt model with added mass in series to account for inertial response. The Kelvin-Voigt model with mass component differential equation is [11]

$$F(t) = kx(t) + \mu\frac{\mathrm{d}}{\mathrm{d}t}x(t) + m\frac{\mathrm{d}^2}{\mathrm{d}t^2}x(t) \tag{13.5}$$

where $F(t)$ and $x(t)$ are the applied force and the induced displacement as a function of time, k is the elastic constant, μ is the viscous constant and m is the inertial component. Solving the differential equation to a step force $F(t) = AU(t)$, where $U(t)$ is the unit step function, the creep displacement equations is described as [11]

$$x(t) = -\frac{\xi + \sqrt{\xi^2 - 1}}{2\sqrt{\xi^2 - 1}} s \cdot e^{(-\xi + \sqrt{\xi^2 - 1})\omega t} + \frac{\xi - \sqrt{\xi^2 - 1}}{2\sqrt{\xi^2 - 1}} s \cdot e^{(-\xi - \sqrt{\xi^2 - 1})\omega t} + s \tag{13.6}$$

where ξ is the damping ratio, ω is the natural frequency, and s is the static sensitivity. The previous parameters can be defined in terms of the properties of the medium as follows [11]

$$\xi = \frac{\mu}{2\sqrt{k \cdot m}}, \omega = \sqrt{\frac{k}{m}}, s = \frac{A}{k} \tag{13.7}$$

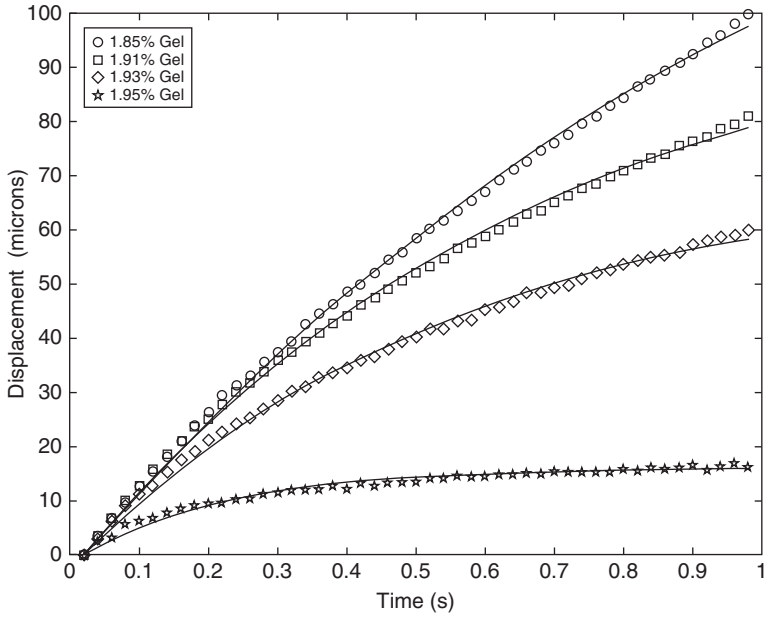

Figure 13.3 Experimental measured displacement (open symbols) and Kelvin-Voigt model fit (continuous line) in acrylamide gel phantoms. Source: © Institute of Physics and Engineering in Medicine, reproduced by permission of IOP Publishing, all rights reserved [10].

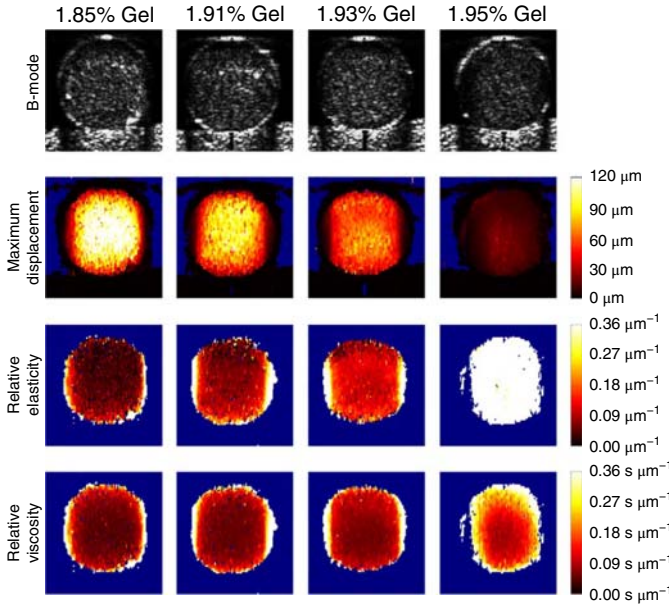

Figure 13.4 Experimental images in tissue-mimicking phantoms. The first row depicts B-mode images, the second row depicts maximum displacement, third row depicts relative viscosity, and the fourth row depicts relative viscosity. Source: © Institute of Physics and Engineering in Medicine, reproduced by permission of IOP Publishing, all rights reserved [10].

To address the limitation of unknown force, force-free parameters of natural frequency ω, damping ratio ξ, and time constant τ are proposed [11]

$$\xi = \frac{\mu_r}{2\sqrt{k_r \cdot m_r}}, \omega = \sqrt{\frac{k_r}{m_r}}, \tau = \frac{\mu_r}{k_r} \tag{13.8}$$

where $k_r = k/A$, $\mu_r = \mu/A$, and $m_r = m/A$. Images of the force-free parameters in gel mimicking phantoms have been reported [11].

13.3.2 Monitored Steady-state Excitation and Recovery (MSSER) Radiation Force Imaging

Mauldin et al. [12] developed a non-invasive acoustic radiation force based method with a commercial ultrasound scanner and a linear array transducer to monitor steady-state tissue response as in KAVE. In addition to the KAVE method, the monitored steady-state excitation and recovery (MSSER) radiation force imaging method also accounts for the response after the cessation of the step-stress (recovery). In the MSSER method, a Kelvin-Voigt model and a standard linear viscoelastic model are proposed during creep and recovery displacements.

Solving the Kelvin-Voigt (KV) model differential equation to a creep and recovery excitation gives creep $x_{\text{KV,creep}}(t)$ and recovery $x_{\text{KV,recovery}}(t)$ displacements as [12]

$$x_{\text{KV,creep}}(t) = \frac{A}{E_\mu}\left(1 - e^{-\frac{t}{\tau_\sigma}}\right); \quad for \quad 0 < t < t' \tag{13.9}$$

$$x_{\text{KV,recovery}}(t) = \frac{A}{E_\mu}\left(1 - e^{-\frac{t'}{\tau_\sigma}}\right) e^{-\frac{(t-t')}{\tau_\sigma}}; \quad for \quad t > t' \tag{13.10}$$

where A is the force magnitude (N), E_μ or μ is the relax elastic modulus (N/m), and τ_σ or $\frac{\eta}{\mu}$ is the relaxation time for constant stress (s). Similarly, solving the Standard linear solid (SLS) model differential equation for a creep and recovery excitation gives creep $x_{\text{SLS,creep}}(t)$ and recovery $x_{\text{SLS,recovery}}(t)$ displacements as [12]

$$x_{\text{SLS,creep}}(t) = \frac{A}{E_\mu} - \frac{A(\tau_\sigma - \tau_\varepsilon)}{E_\mu \tau_\sigma} e^{-\frac{t}{\tau_\sigma}}; \quad for \quad 0 < t < t' \tag{13.11}$$

$$x_{\text{SLS,recovery}}(t) = \frac{A(\tau_\sigma - \tau_\varepsilon)}{E_\mu \tau_\sigma}\left(e^{\frac{t'}{\tau_\sigma}} - 1\right) e^{-\frac{(t-t')}{\tau_\sigma}}; \quad for \quad t > t' \tag{13.12}$$

where A is the force magnitude (N), E_μ or μ_0 is the relax elastic modulus (N/m), τ_ε or $\frac{\eta_1}{\mu_1}$ is the relaxation time for constant stress (s), and τ_σ is $\eta_1\left(\frac{\mu_0+\mu_1}{\mu_0\mu_1}\right)$.

As in the KAVE method, the magnitude of the force A is unknown. However, Mauldin et al. proposed two approaches to estimate A. The force magnitude A is related to the magnitude of the radiation force per unit volume F by [12]

$$A = F \times \ell_{\text{Lat}} \times \ell_{\text{Elev}} \times \ell_{\text{Axial}} \tag{13.13}$$

where ℓ_{Lat} (m), ℓ_{Elev} (m), and ℓ_{Axial} (m) are the lateral, elevational, and axial span over which the acoustic radiation force F acts. The acoustic radiation force F (N/m^3) is defined in Eq. (13.3). The first approach to estimate A consisted in measuring the absorption coefficient of the medium α (Np/m), the speed of sound in the medium c (m/s), and the in situ temporal average intensity I (W/m^2) to directly estimate F. Because the first approach is not clinically relevant, the second

proposed approach was based in measuring the Young's modulus E (N/m^2) of tissue with shear wave elasticity imaging (SWEI). To do so, the Young's modulus E is defined as follows [12]

$$\tilde{E} = \frac{\Delta\tilde{\sigma}}{\Delta\tilde{\varepsilon}} = \frac{\Delta(F\ell_{\text{Axial}}\ell_0)}{\Delta x_{\text{ss}}} \times C \tag{13.14}$$

where ℓ_0 is the original axial length (m), x_{ss} is the steady-state displacement (m), and C is a correction factor implemented because of system-dependent factors that lead to underestimation of steady-state displacement as well as error in estimating the axial length. The axial length was estimated as the −6 dB width of the MSSER pushing pulse. The Young's modulus was estimated by [12]

$$E = 2(1+\nu)\rho c_{\text{s}}^2 \tag{13.15}$$

where ν is the Poisson's ratio, ρ is the density, and c_{s} is the shear wave speed.

Figure 13.5 illustrates the measured and modeled creep and recovery displacement response in four gel phantoms and an excised pig muscle [12]. It can be seen that for the same applied force in the gelatin phantoms, the stiffer phantoms (A and B) exhibited less displacement than the softer phantoms (C and D). On the other hand, the excised pig muscle was excited with different force amplitude and as expected the steady-state displacement increased as the applied force amplitude increased.

Parametric images of gelatin phantoms using the Kelvin-Voigt model fit of creep and recovery are shown in Figure 13.6 [12].

The excised pig muscle B-mode image, conventional acoustic radiation force impulse (ARFI) image and standard linear solid model parametric images are shown in Figure 13.7 [12].

13.3.3 Viscoelastic Response (VisR) Imaging

Selzo et al. [13] introduced a faster alternative to MSSER and KAVE which assesses the viscoelastic properties of tissue using two successive acoustic radiation force (ARF) impulses and observing three points along the viscoelastic creep profile predicted by the Kelvin-Voigt model. The method is called viscoelastic response (VisR) imaging.

Figure 13.8 illustrates the displacement response of the VisR excitation and the pulse sequence of VisR, MSSER, and ARFI [13].

The VisR method uses the solution of the Kelvin-Voigt model differential equation during recovery, as illustrated in Eq. (13.10), to describe the displacement D_1 measured at $t = t_1$ after a first ARF push applied at $t = t_{\text{ARF}}$ [13]

$$D_1 = \frac{A}{E}e^{-\frac{(t_1 - t_{\text{ARF}})}{\tau_\sigma}} - \frac{A}{E}e^{-\frac{t_1}{\tau_\sigma}} \tag{13.16}$$

After allowing partial recovery, the displacement remaining is called D_2. Then, a second ARF push of duration t_{ARF} is applied $t = t_2$. Finally, a displacement D_3 measured at t_4, $t_4 - t_2 = t_1$, is defined by solving the differential equation with the initial condition $x(0) = D_2$ [13]

$$D_3 = \frac{A}{E}e^{-\frac{(t_1 - t_{\text{ARF}})}{\tau_\sigma}} - \frac{A}{E}e^{-\frac{t_1}{\tau_\sigma}} + D_2 e^{-\frac{t_1}{\tau_\sigma}} \tag{13.17}$$

Substituting Eq. (13.16) from Eq. (13.17) and solving for τ_σ yields [13]

$$\tau_\sigma = \frac{-t_1}{\ln\left(\frac{D_3 - D_1}{D_2}\right)} = \frac{\eta}{E} \tag{13.18}$$

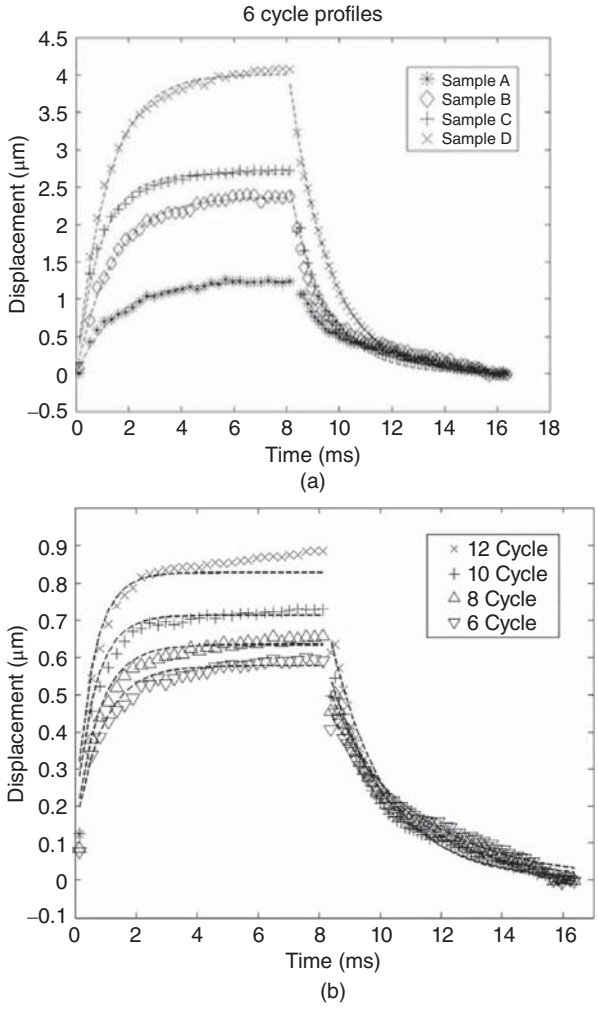

Figure 13.5 Representative displacement profiles with fitted model for (a) gelatin phantoms with 6 cycle applied force and (b) excised pig muscle with different pushing beam sequences. The Kelvin-Voigt model was fitted to the gelatin phantoms data and the standard linear solid was fitted to the excised pig muscle. Source: © 2008 IEEE, reprinted, with permission, from [12].

An alternative approach to assess τ_σ with only one ARF excitation and measuring displacements D_{1a} and D_{2a} at t_{1a} and t_{2a} can also be used [13]

$$\tau_\sigma = \frac{t_{1a} - t_{2a}}{\ln\left(\frac{D_{2a}}{D_{1a}}\right)} \tag{13.19}$$

It is important to note that τ_σ in Eqs. (13.18) and (13.19) is independent of the applied force magnitude A. Figure 13.9 shows a measured displacement from a double push VisR excitation in homogeneous tissue-mimicking phantom using a conventional ultrasound scanner equipped with a linear array transducer [13].

Two-dimensional images of structured (spherical inclusion) tissue-mimicking phantoms were achieved by administering the VisR and ARFI beam sequences in 40 lateral locations, as illustrated in Figure 13.10 [13].

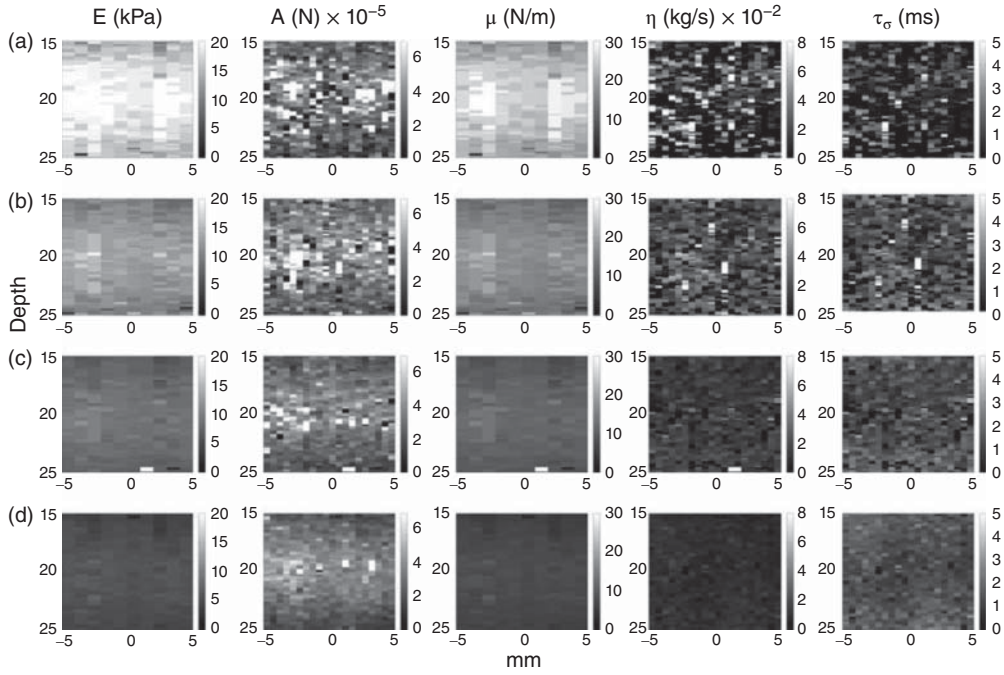

Figure 13.6 Kelvin-Voigt model parametric images from SWEI and MSSER. Gelatin phantom samples are indicated by row label. Source: © 2008 IEEE, reprinted, with permission, from [12].

The phantom studies demonstrated that the double push VisR method produced better contrast images than ARFI and single push VisR. The feasibility of the double push VisR imaging method was evaluated in vivo in a semitendinosus muscle of a golden retriever dog with an unknown musculoskeletal disorder. The double push VisR image was compared with microscopy images of the same region, as illustrated in Figure 13.11 [13]. As expected, the τ_σ estimates were lower in regions of highly collagenated connective tissue than in surrounding normal muscle.

13.3.4 Acoustic Radiation Force-induced Creep (RFIC)

Amador et. al. [9] introduced a method that quantifies viscoelastic properties in a model-independent way by estimating the complex elastic modulus from time-dependent creep response induced by acoustic radiation force. The method called acoustic radiation force induced creep (RFIC), uses the analytical solution of the Boltzmann integral (integral equation of the viscoelastic constitutive equations) to convert the time-dependent creep response to the frequency-dependent complex modulus. By definition, the ratio between the shear strain response, $\gamma(t)$, and the applied shear constant stress, τ_0, is called the creep compliance, $J(t)$. Under any given stress history, provided that the creep compliance is known, the creep strain is described by the Boltzmann integral representation [5]

$$\gamma(t) = \int_0^t J(t-\xi)\frac{\partial \tau(\xi)}{\partial \xi} d\xi \tag{13.20}$$

where $\frac{\partial[\cdot]}{\partial \xi}$ represents first derivative respect to the independent variable ξ. When Fourier transform convolution and derivative properties are applied to Eq. (13.20), it can be seen that the

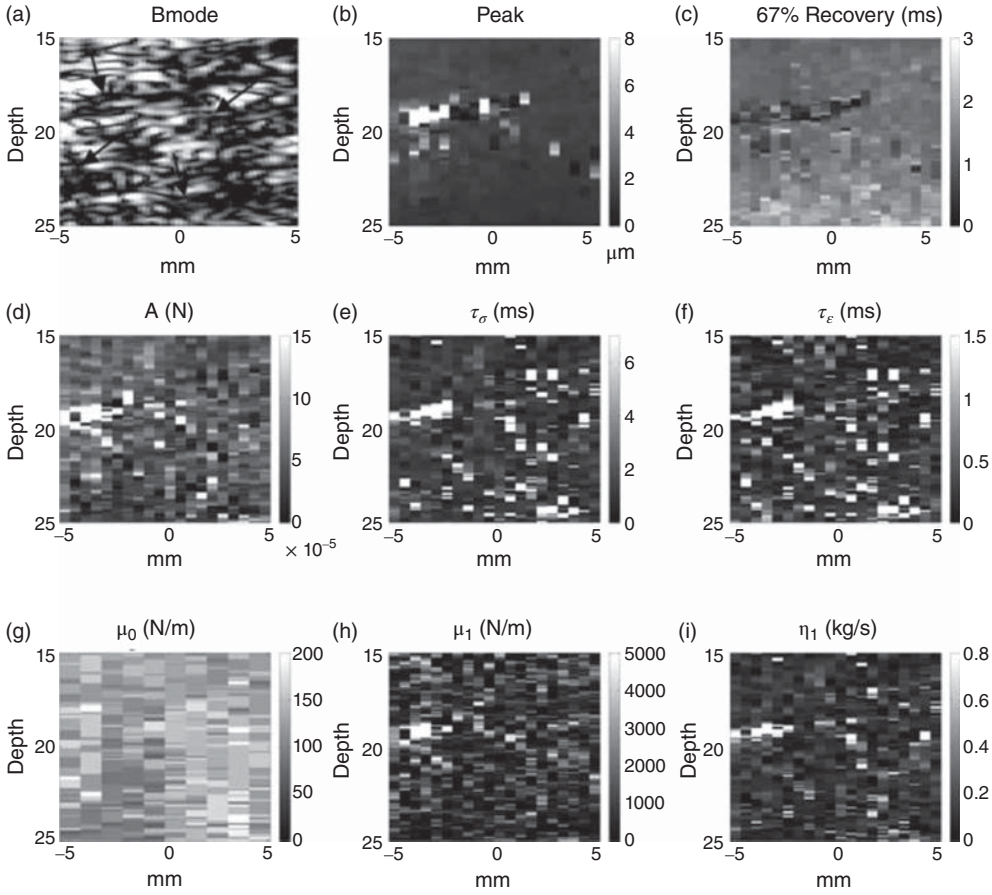

Figure 13.7 Standard linear solid model parametric images on excised pig muscle. (a) B-mode image; (b) peak displacement; (c) time to 67% recovery; (d) force magnitude; (e) time constant for constant stress; (f) time constant for constant strain; (g); (h) both spring constants; and (i) coefficient of viscosity. Source: © 2008 IEEE, reprinted, with permission, from [12].

frequency ω domain complex shear modulus, $G^*(\omega)$, is related to the time domain compliance $J(t)$ as follows

$$\mathrm{FT}[\gamma(t)] = \mathrm{FT}[J(t)]\mathrm{FT}\left[\frac{\partial \tau(t)}{\partial t}\right] \tag{13.21}$$

$$\mathrm{FT}[\gamma(t)] = \mathrm{FT}[J(t)]i\omega\mathrm{FT}[\tau(t)] \tag{13.22}$$

$$G^*(\omega) = \frac{\mathrm{FT}[\tau(t)]}{\mathrm{FT}[\gamma(t)]} = \frac{1}{i\omega\mathrm{FT}[J(t)]} \tag{13.23}$$

where $\mathrm{FT}[\cdot]$ represents the Fourier transform. Because $J(t)$ is a function that grows with increasing time, its Fourier transform is not convergent. Evans et. al. [14] reported the analytic solution of Eq. (13.23)

$$G^*(\omega) = \frac{i\omega}{\left[\begin{array}{c} i\omega J(0) + (1 - e^{-i\omega t(1)})\frac{(J(1)-J(0))}{t(1)} + \frac{e^{-i\omega t(N)}}{\eta} \cdots \\ +\sum_{n=2}^{N}\left(\frac{J(n)-J(n-1)}{t(n)-t(n-1)}\right)\left(e^{-i\omega t(n-1)} - e^{-i\omega t(n)}\right) \end{array}\right]}, n = 1 : N \tag{13.24}$$

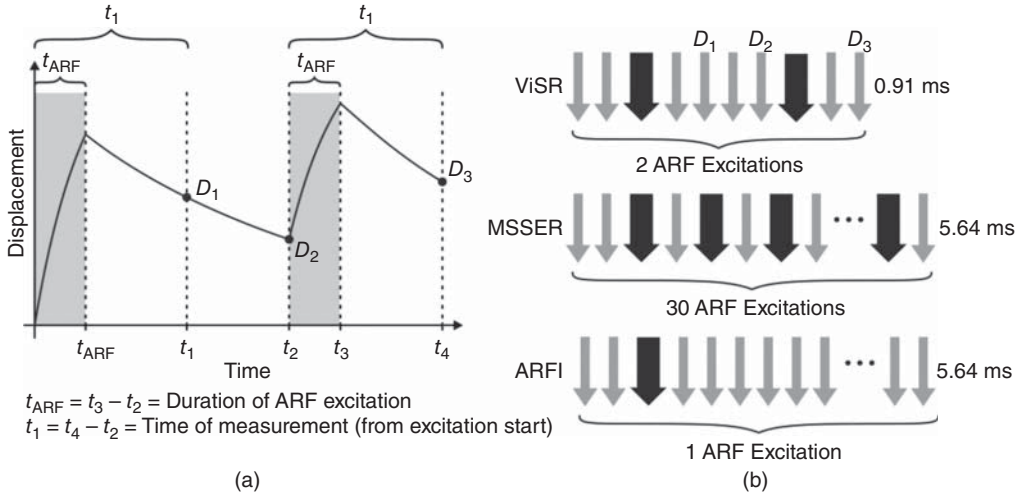

Figure 13.8 (a) VisR excitation displacement response, which involves measuring the displacement after the first ARF excitation, D_1, the level of displacement after allowing partial recovery time, D_2, and the displacement caused by a second ARF push, D_3. (b) Pulse sequence of VisR, MSSER, and ARFI, the black arrows represent the ARF pulses and the gray arrows represent the tracking pulses. Source: © 2013 IEEE, reprinted, with permission, from [13].

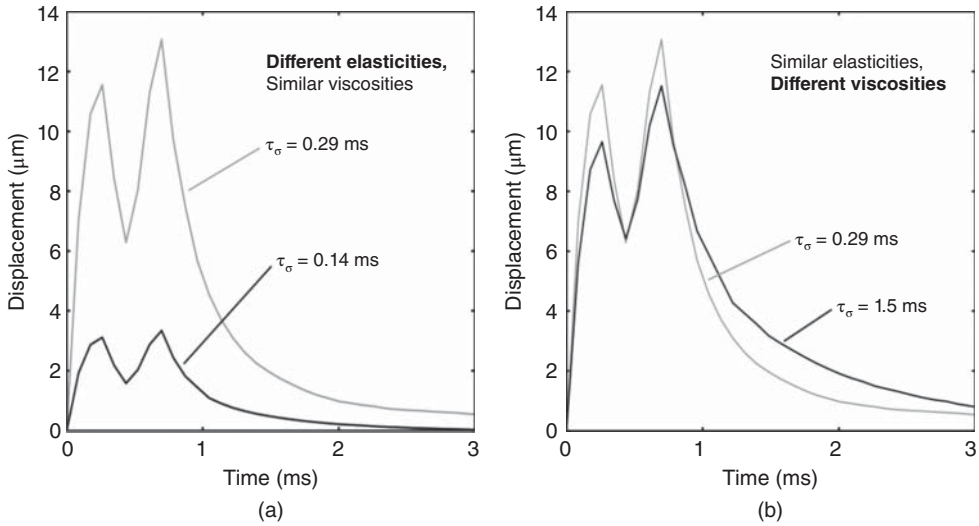

Figure 13.9 Measured displacement in homogenous viscoelastic phantoms after a double push VisR excitation. (a) Phantoms with different elasticities but similar viscosities; (b) phantoms with different viscosities but similar elasticities. Source: © 2013 IEEE, reprinted, with permission, from [13].

where $J(0)$ and η are the compliance at $n = 0$ and the steady-state viscosity. $J(0)$ is estimated by extrapolation of the compliance function to $t \to 0$. Similarly, η is estimated by extrapolation of compliance function to $t \to \infty$. The frequency range depends on the resolution (the time of the first data point, $t(1)$) and duration (the time of the last data point, $t(N)$) of the data set.

As in KAVE, MSSER, and VisR the actual applied force is generally unknown; therefore, the magnitude of the applied stress is also unknown. In addition, ultrasound motion detection

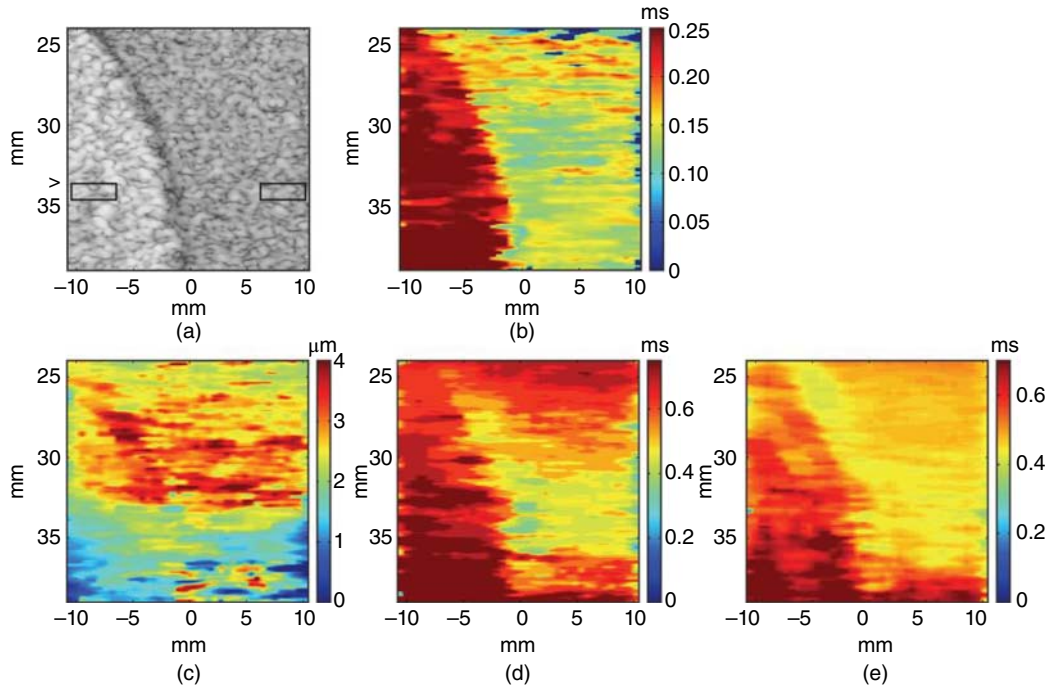

Figure 13.10 Structured (spherical inclusion) tissue-mimicking phantom (a) B-mode image; (b) double push VisR τ_σ image; (c) ARFI peak displacement image; (d) ARFI recovery time image; and (e) single push VisR τ_σ image. Source: © 2013 IEEE, reprinted, with permission, from [13].

applications usually estimate the displacement response instead of the strain response. Assuming that the material is linear, the creep compliance, $J(t)$, is linearly proportional to displacement $u(t)$ by a constant factor β, which relates to the magnitude of the applied step-stress and the length of the infinitesimal especial region of excitation. Equation (13.23) can be rewritten as [9]

$$G^*(\omega) = \frac{1}{i\omega\beta \mathrm{FT}[u(t)]} \tag{13.25}$$

The outcome of Eq. (13.25) will be $\beta G^*(\omega)$, which is referred to as the extracted complex modulus, $C^*(\omega)$, and will vary as a function of material absorption and acoustic beam intensity. To overcome this problem, a widely used property of viscoelastic materials called the loss tangent or $\tan(\delta)$, defined as the ratio of the imaginary part and real part of the storage modulus, is not dependent on material absorption and acoustic beam intensity [9]

$$\tan(\delta) = \frac{\mathrm{Im}[C^*(\omega)]}{\mathrm{Re}[C^*(\omega)]} = \frac{\mathrm{Im}[\beta G^*(\omega)]}{\mathrm{Re}[\beta G^*(\omega)]} = \frac{\mathrm{Im}[G^*(\omega)]}{\mathrm{Re}[G^*(\omega)]} \tag{13.26}$$

Representative creep displacement responses obtained in the same tissue-mimicking phantom with different acoustic beam intensities show a proportional increase in displacement and the extracted complex modulus, whereas the estimated loss tangent did not change as function of acoustic beam intensity, as shown in Figure 13.12 [9].

The estimated loss tangent of two tissue-mimicking phantoms that had different storage modulus and similar loss modulus, as reported by the manufacturer, is illustrated in Figure 13.13 [9].

The proportionality factor β can be found using shear wave velocity dispersion; this approach is described in Chapter 28 of this book.

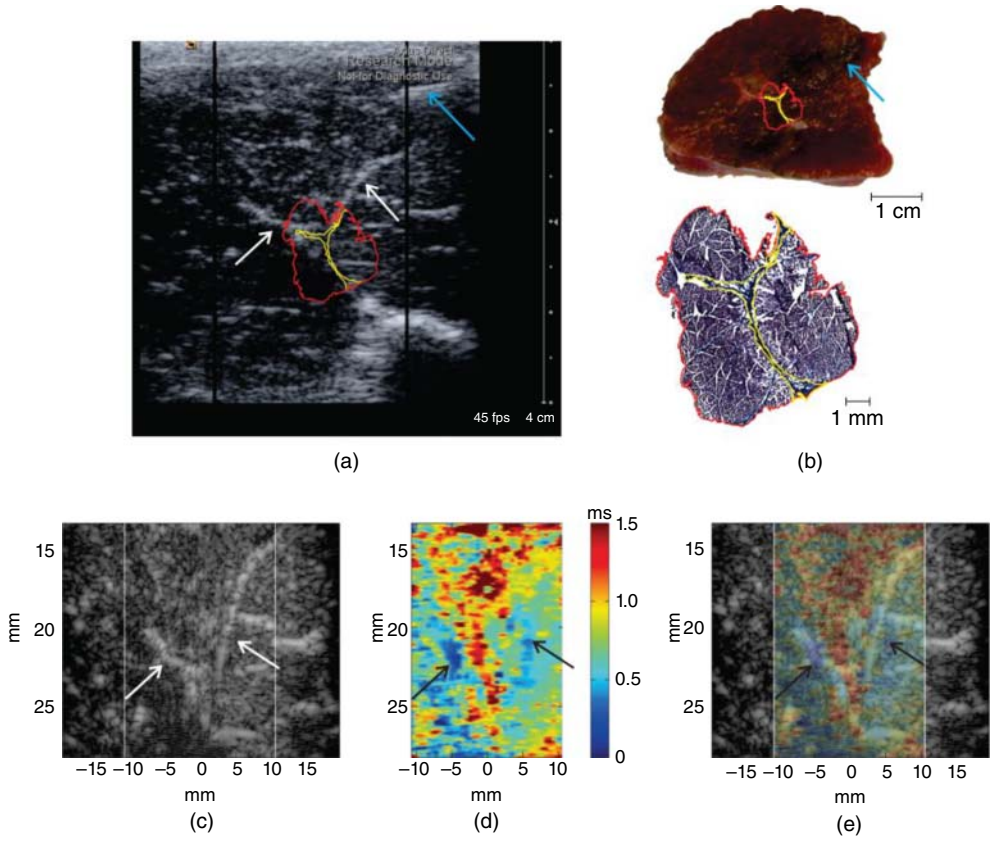

Figure 13.11 In vivo double push VisR imaging in normal canine muscle. (a) Conventional B-mode image; (b) gross image of the dissected muscle; (c) B-mode imaged reconstructed after VisR excitation; (d) single push VisR τ_σ image; and (e) overlaid τ_σ image in B-mode image. Source: © 2013 IEEE, reprinted, with permission, from [13].

13.3.5 Acoustic Radiation Force-induced Creep-recovery (RFICR)

In the RFIC method, both creep and recovery are induced but only the creep period is used. Moreover, to study a wide range of frequencies, the creep period needs to be maintained for long periods of time, for instance, 30 milliseconds of acoustic radiation force exposure. The acoustic radiation force-induced creep-recovery (RFICR) method, developed by Amador et. al. [15, 16], consisted of estimating the model-free complex shear modulus from the recovery response after acoustic radiation force creep excitation.

The RFIC method theory can be applied to the recovery period as follow. The recovery period or the response to the removal of the step-stress may be expressed as the application at $t = t'$ of another step equal in magnitude but of opposite sign to the step applied at $t = 0$. This excitation can be expressed in terms of the unit step function as [15]

$$\tau(t) = \tau_0 u(t) - \tau_0 u(t - t') \tag{13.27}$$

The first term in Eq. (13.27) represents the imposition of a step-stress of magnitude τ_0 at $t = 0$, while the second term represents the removal of the stress, expressed as the imposition of a step-stress of equal magnitude but opposite direction delayed by the amount t'. Such stimulus and its response are illustrated in Figure 13.14, where the creep or the response to

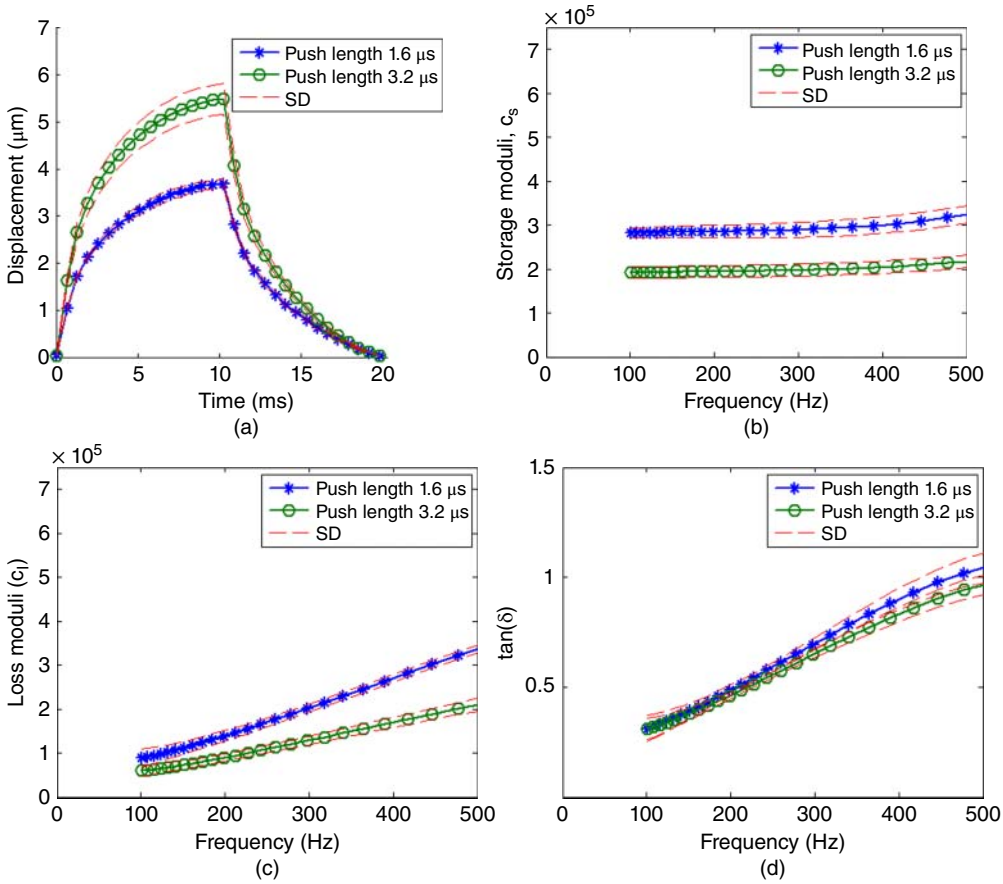

Figure 13.12 Tissue-mimicking phantom (a) mean creep displacement; (b) estimated storage moduli; (c) loss moduli; and (d) loss tangent of a 1.6 μs (o) and 3.2 μs (*) push duration. Average of five repeated measurements. The dashed lines represent the standard deviation of five repeated measurements. Source: © Institute of Physics and Engineering in Medicine, reproduced by permission of IOP Publishing, all rights reserved [9].

the step-stress (shear strain $\gamma(t)$) is shown with circles and the recovery or the response to an opposite step-force is shown with asterisks [16].

The creep and recovery curves can be brought into superposition by reflecting either one around the time axis and then shifting them along both axes. Then, creep and recovery contain the same information on the time-dependent behavior of a linear viscoelastic material. Moreover, in Eqs. (13.23) and (13.24), the compliance $J(t)$ for the recovery signal remains the same but with negative magnitude from the negative step-stress and it is defined from $t > t'$ [16]. To illustrate this, Figure 13.15a shows the numerical simulation of a normalized Kelvin-Voigt model creep strain and recovery for different recovery times and Figure 13.15b shows the estimated loss tangent on simulated creep strain and flipped-shifted recovery strain. It can be observed that the estimated loss tangent from the creep strain and the flipped-shifted recovery strain contains the same information on the time-dependent behavior of a linear viscoelastic Kelvin-Voigt material [15].

Another improvement presented in the RFICR method is the definition and estimation of the shear strain $\gamma(t)$ [16].

$$\gamma_{ZX}(t) = \gamma(t) = \frac{\partial u_z(t)}{\partial x} + \frac{\partial u_x(t)}{\partial z} \tag{13.28}$$

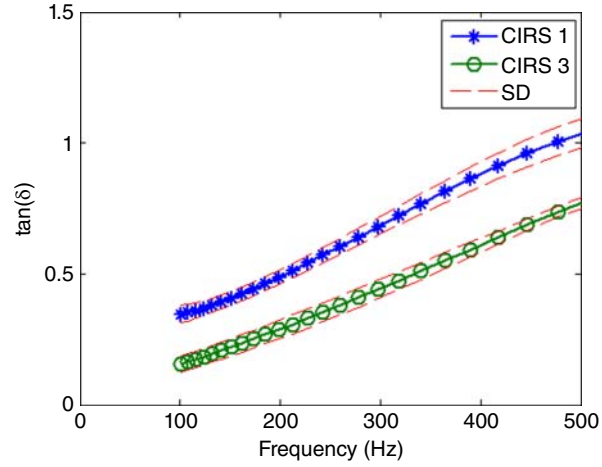

Figure 13.13 Loss tangent (average of five measured locations) as a function of frequency for CIRS 1 (*) and CIRS 3 (o) phantom. The dashed lines represent the standard deviation of five measured locations in each phantom. Source: © Institute of Physics and Engineering in Medicine, reproduced by permission of IOP Publishing, all rights reserved [9].

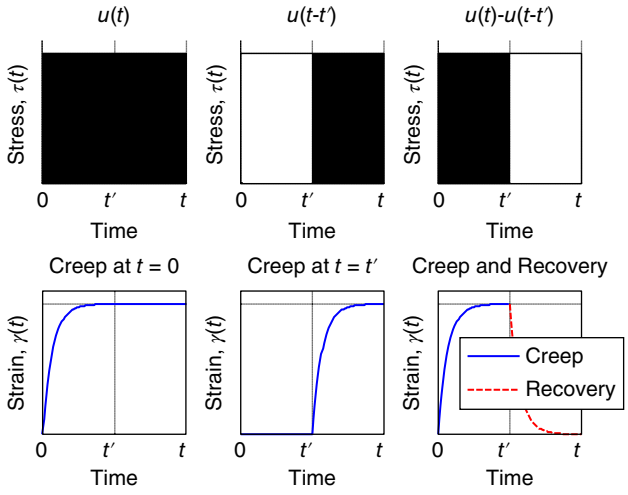

Figure 13.14 Illustration of creep and recovery applied stimulus and response. The upper row illustrates the different applied stimulus to excite creep and recovery response (shear strain) shown in the lower row.

where $u_z(t)$ and $u_x(t)$ are displacements along the ultrasound beam direction z, and lateral direction x, and $\frac{\partial}{\partial}[\cdot]$ represent a partial derivative [16]. As a result, Eq. (13.25) will be in terms of the shear strain $\gamma(t)$ instead of displacement $u(t)$, and the proportionality constant β will be only related to the magnitude applied stress. Although Eq. (13.28) defines the shear strain $\gamma(t)$ as a function of the partial derivative of lateral and axial displacements, in finite element modeling simulations Amador et al have shown that second term of Eq. (13.28) is considerably smaller than the first term, therefore the shear strain is dominated by the partial derivative of axial displacement with respect to the lateral distance [16].

The main advantage of the RFICR method is that a pulse sequence used for shear wave elasticity imaging (SWEI) will generate a shear wave that propagates outside the focal point and it will also inducer creep-recovery at the focal point. Figure 13.16 illustrates an excised swine kidney creep-recovery strain and loss tangent measured resulting from a continuous acoustic radiation force impulse.

The shear wave group velocity and center frequency from the induced shear wave using acoustic radiation force in the excised kidney is shown in Figure 13.17.

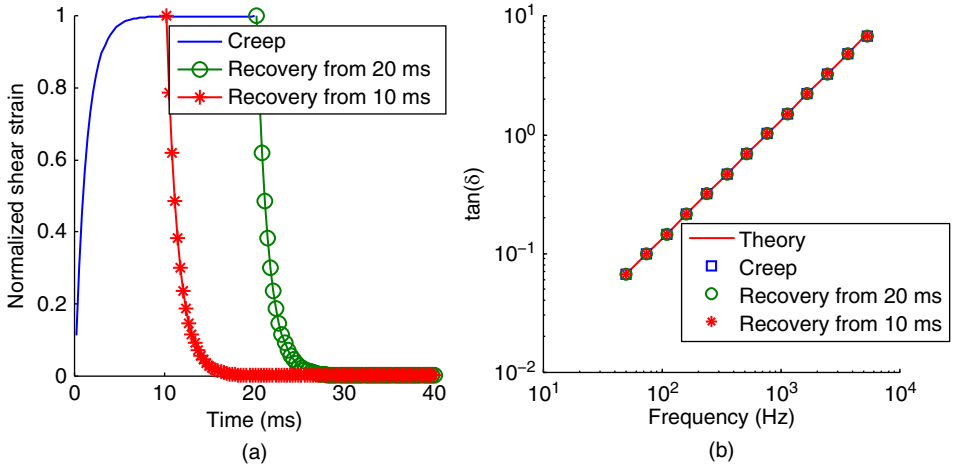

Figure 13.15 Kelvin-Voigt model (a) normalized simulated creep and recovery shear strain and (b) loss tangent from simulated data in (a).

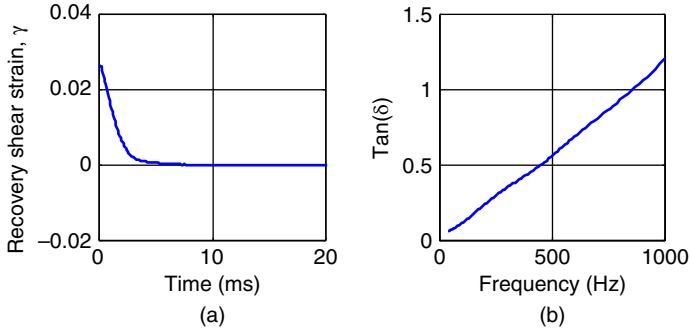

Figure 13.16 Excised swine kidney (a) creep-recovery shear strain and (b) estimated loss tangent from flipped-shifted creep-recovery shear strain.

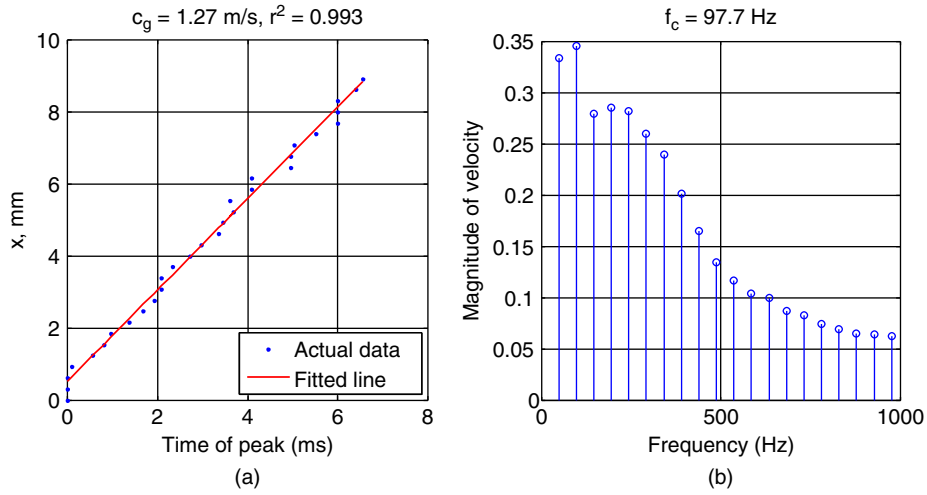

Figure 13.17 Excised swine kidney (a) time-to-peak calculation to estimate shear wave group velocity and (b) magnitude of Fourier spectrum to estimate shear wave center frequency.

The loss tangent, group velocity, and center frequency estimation can be used to reconstruct the complex modulus G^* of viscoelastic materials with a method that will be addressed in Chapter 28.

13.4 Conclusion

Quantitative characterization of viscoelastic properties (elasticity and viscosity) of human soft tissues has the potential to provide an independent indicator of soft tissue health. Viscoelastic creep imaging offers a more complete alternative to the conventional shear wave elasticity imaging method by characterizing both elasticity and viscosity properties. The kinetic acoustic vitreoretinal examination (KAVE), monitored steady-state excitation and recovery (MSSER) radiation force imaging and viscoelastic response (VisR) imaging methods are able to create color maps of viscoelastic parameters using rheological models. Although the acoustic radiation force creep (RFIC) and acoustic radiation force creep-recovery (RFICR) methods have not been implemented to create color maps of viscoelastic properties, they are able to estimate viscoelastic parameters without the need of a rheological model. Moreover, the techniques employed in KAVE, MSSER, and VisR to create viscoelastic maps can be implemented with RFIC and RFICR methods.

An important component of viscoelastic material characterization is to account for inertial effects that happen when the step-force is imposed and removed. The KAVE method proposed a modification of the Kelvin-Voigt model that accounts for inertial or mass effect. Since MSSER and VisR methods are also based on using rheological models, the modified Kelvin-Voigt model with the mass component proposed in the KAVE method could be easily implemented to MSSER and VisR. On the other hand, the RFIC and RFICR methods are based on the constitutive equations of viscoelasticity, which by definition allow any stress excitation, meaning that the analytic solutions of the constitutive equation used in RFIC and RFICR are only valid for a specific creep response. Therefore, the mass and inertial effects on the creep and creep-recovery responses need to be further studied.

References

1 Sarvazyan, A.P., Rudenko, O.V., Swanson, S.D., et al. (1998). Shear wave elasticity imaging: A new ultrasonic technology of medical diagnostics. *Ultrasound Med. Biol.* 24: 1419–1435.

2 Fung, Y. (1993). *Biomechanics: Mechanical Properties of Living Tissues*. Springer-Verlag.

3 Kruse, S.A., Smith, J.A., Lawrence, A.J., et al. (2000). Tissue characterization using magnetic resonance elastography: preliminary results. *Phys. Med. Biol.* 45: 1579–1590.

4 Qiu, Y.P., Sridhar, M., Tsou, J.K., et al. (2008). Ultrasonic viscoelasticity imaging of nonpalpable breast tumors: preliminary results. *Acad. Radiol.* 15: 1526–1533.

5 Findley, W.N., Lai, J.S., and Onaran, K. (1989). *Creep and Relaxation of Nonlinear Viscoelastic Materials: With an Introduction to Linear Viscoelasticity*. Dover.

6 Deffieux, T., Montaldo, G., Tanter, M., and Fink, M. (2009). Shear wave spectroscopy for in vivo quantification of human soft tissues visco-elasticity. *IEEE Trans. Med. Imaging* 28: 313–322.

7 Chen, S., Urban, M., Pislaru, C., et al. (2009). Shearwave dispersion ultrasound vibrometry (SDUV) for measuring tissue elasticity and viscosity. *IEEE Trans. Ultrason., Ferroelect., Freq. Control* 56: 55–62.

8 Torr, G.R. (1984). The acoustic radiation force. *Am. J. Phys.* 52: 402–408.

9 Amador, C., Urban, M.W., Chen, S.G., and Greenleaf, J.F. (2012). Loss tangent and complex modulus estimated by acoustic radiation force creep and shear wave dispersion. *Phys. Med. Biol.* 57: 1263–1282.
10 Walker, W.F., Fernandez, F.J., and Negron, L.A. (2000). A method of imaging viscoelastic parameters with acoustic radiation force. *Phys. Med. Biol.* 45: 1437–1447.
11 Viola, F. and Walker, W.F. (2003). Radiation force imaging of viscoelastic properties with reduced artifacts. *IEEE Trans. Ultrason., Ferroelect., Freq. Control* 50: 736–742.
12 Mauldin, F.W., Haider, M.A., Loboa, E.G., et al. (2008). Monitored steady-state excitation and recovery (MSSER) radiation force imaging using viscoelastic models. *IEEE Trans. Ultrason., Ferroelect., Freq. Control* 55: 1597–1610.
13 Selzo, M.R. and Gallippi, C.M. (2013). Viscoelastic response (VisR) imaging for assessment of viscoelasticity in Voigt materials. *IEEE Trans. Ultrason., Ferroelect., Freq. Control* 60: 2488–2500.
14 Evans, R.M.L., Tassieri, M., Auhl, D., and Waigh, T.A. (2009). Direct conversion of rheological compliance measurements into storage and loss moduli. *Phys. Rev. E* 80: 012501.
15 Amador, C., Urban, M.W., Chen, S., and Greenleaf, J.F. (2012). Complex shear modulus quantification from acoustic radiation force creep-recovery and shear wave propagation. *IEEE UFFC International Ultrasonic Symposium*, Dresden, Germany.
16 Amador, C., Bo, Q., Urban, M.W., et al. (2013). Acoustic radiation force creep-recovery: Theory and finite element modeling, *Ultrasonics Symposium (IUS), IEEE International*, 363–366.

14

Intrinsic Cardiovascular Wave and Strain Imaging

Elisa Konofagou

Department of Biomedical Engineering, Columbia University, New York, NY, USA

14.1 Introduction

Cardiovascular diseases remain America's primary killer by a large margin, claiming the lives of more Americans than the next two main causes of death combined (cancer and pulmonary complications). In particular, coronary artery disease (CAD) is by far the most lethal, causing 17% of all deaths every year (whether cardiac related or not). One of the main reasons for this high death toll is the severe lack of effective and accessible imaging tools upon anomaly detected on the electrocardiogram (ECG), especially at the early stages when CAD can be stabilized with appropriate pharmacological regimen. Arrhythmias refer to the disruption of the natural heart rhythm. Cardiac arrhythmias lead to a significant amount of cardiovascular morbidity and mortality. An irregular heart rhythm causes the heart to suddenly stop pumping blood. Atrial pathologies are the most common arrhythmias, with atrial fibrillation and atrial flutter being the most prevalent. Similarly, arterial stiffening has been linked to a variety of diseases – spanning from cardiovascular disease and dementia to Parkinson's, diabetes, and end-stage renal disease. Yet, in sharp contrast with the clear universality and significance of pulse waveform velocity (PWV) as a biomarker, is the lack of such measurements in the clinic. There is currently no technique that yields a regional PWV or maps the PWV along a detected pathology to evaluate risk. This is because current methodology assumes a single stiffness value over the entire circulation obtained through a carotid-to-femoral pressure measurement. Clearly, this single stiffness value is not sufficient to localize or characterize focal disease such as aneurysms or atherosclerotic plaques. In this chapter, we introduce ultrasound-based methodologies that are based on inferring the mechanical and electrical properties of the myocardium as well as mechanical properties of the vascular wall in order to better image the onset and progression of the aforementioned diseases.

14.2 Cardiac Imaging

14.2.1 Myocardial Elastography

14.2.1.1 Introduction

According to the latest report on Heart Disease and Stroke Statistics by the American Heart Association [1], more than 2150 Americans die of cardiovascular disease each day, an average of 1 death every 40 seconds. Cardiovascular disease currently claims more lives each year in both men and women than the next two most deadly diseases combined, i.e. cancer and chronic

Ultrasound Elastography for Biomedical Applications and Medicine, First Edition.
Edited by Ivan Nenadic, Matthew Urban, James Greenleaf, Jean-Luc Gennisson, Miguel Bernal, and Mickael Tanter.

lower respiratory disease. Among the cardiovascular diseases, coronary artery disease (CAD) is by far the most deadly, causing approximately 1 of every 6 deaths in the United States in 2010. Approximately every 34 seconds, one American has a coronary event, and approximately every 1 minute 23 seconds, an American will die of one. It is estimated that an additional 150 000 silent first myocardial infarctions occur each year [1]. However, there are currently no screening or early detection imaging techniques that can identify abnormalities prior to any symptoms or fatalities. Clinically available imaging techniques such as echocardiography or nuclear perfusion (radionuclide imaging) are typically used after a cardiac event has already occurred to determine the extent of damage. Despite the fact that over the past few years therapeutic techniques, such as angioplasty, heart valve surgery, and pacemakers, have experienced exponential growth in new procedures, the progress in the development of novel diagnostic techniques has stalled by comparison.

14.2.1.2 Mechanical Deformation of Normal and Ischemic or Infarcted Myocardium

Detection of cardiac dysfunction through assessment of the mechanical properties of the heart, and more specifically, the left-ventricular muscle, has been a long-term goal in diagnostic cardiology. This is because both ischemia [2], i.e. the reduced oxygenation of the muscle necessary for its contraction, and infarction [3], i.e. the complete loss of blood supply inducing myocyte death, alter the mechanical properties and contractility of the myocardium. In the ischemic heart, the diastolic left-ventricular pressure–volume or pressure–length curve slope is typically increased, suggesting increased chamber stiffness [4]. Regional myocardial stiffness has also been reported to increase as a result of ischemia [5–8]. The increased stiffness could be due to myocardial remodeling, including elevated collagen and desmin expression as well as the titin isoform switch [4]. Acute myocardial infarction caused by partial or total blockage of one or more coronary arteries can cause complex structural alterations of the left-ventricular muscle [9]. These alterations may lead to collagen synthesis and scar formation, which can cause the myocardium to irreversibly change its mechanical properties. Holmes et al. [10] reported that this myocardial stiffening can be measured within the first 5 minutes following ischemic onset. As reported by Gupta et al. [9], in vitro mechanical testing showed that the stiffness of the infarcted region increases within the first 4 hours, and continues to rise by up to 20 times, peaking 1–2 weeks following the infarct and decreasing 4 weeks later (down to 1–10 times the non-infarcted value). The fact that the mechanical properties induced by the ischemia change right at the onset, continue changing thereafter, and peak two weeks later, indicate the potential for a mechanically based imaging technique to detect the ischemia and infarct extent early. Regarding its conduction pattern, ischemia or infarction will alter the normal pattern and result in reduced and complete lack of conduction, respectively, at the region of abnormality since the myocytes no longer properly conduct the action potential.

14.2.1.3 Myocardial Elastography

Our group has pioneered the technique of myocardial elastography that we have been developing for more than a decade [11–18]. This technique encompasses imaging of mechanical (cumulative or systolic; Figure 14.1) or electromechanical (incremental or transient) strain or activation times to respectively highlight the mechanical or electrical function of the myocardium. Myocardial elastography benefits from the development of techniques used for high precision 2D time-shift-based strain estimation [19] and high frame rates available in echocardiography scanners [13] to obtain a detailed map of the transmural strain in normal [20–22], ischemic [21], and infarcted [23] cases in vivo. These strain-imaging techniques aim at achieving high precision estimates through recorrelation techniques [19] and customized cross-correlation methods [24] and are thus successful in mapping the full 2D and 3D strain tensors [18, 25, 26].

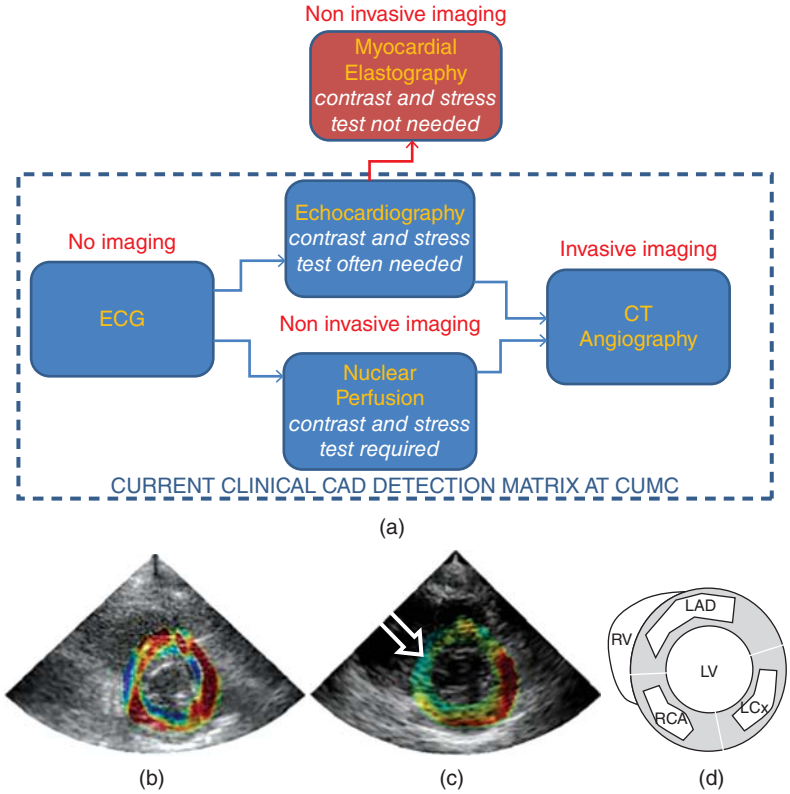

Figure 14.1 (a) Envisioned role and (b, c) initial findings of myocardial elastography in the current clinical routine to avoid false positives and/or thus unnecessary invasive procedures and false negatives by the currently used techniques. (b) Normal short-axis radial strain image, largely thickening myocardium, in an echocardiography false positive case where CT angiography was administered only to confirm normal function. (c) Abnormal short-axis radial strain image containing an ischemic region (thinning; arrow) in a nuclear perfusion. Subsequent CT angiography confirmed the myocardial elastography findings regarding two occluded territories (64-year-old female, 40% LAD and 30% RCA occlusion). (d) Coronary territories given for reference. CUMC: Columbia University Medical Center. LAD: left anterior descending artery, LCx: left circumflex artery, RCA: right coronary artery. Myocardial Elastography was capable of detecting normal function and identifying both compromised territories.

2D Strain Estimation and Imaging A fast, normalized cross-correlation function is first used on RF signals from consecutive frames to compute two-dimensional motion and deformation [19, 27]. The cross-correlation function uses a 1D kernel (length = 5.85 mm, overlap = 90%) in a 2D (or 3D) search to estimate both axial and lateral (and elevational) displacements (Eq. 14.1; Figures 14.1 and 14.2). The correlation kernel size is approximately 10 wavelengths, which has been found to be the optimal length using cross-correlation [28]. It should also be noted that the elastographic resolution has been shown to depend mainly on the kernel shift (not the kernel size) [29], which in our studies is 10%, or 0.6 mm. When searching in the lateral (or, elevational) direction, the RF signals are linearly interpolated by a factor of 10 in order to improve lateral (or, elevational) displacement [19, 21, 30]. Recorrelation techniques are applied in two iterations that aim at increasing the correlation coefficient of each strain component by correction or shifting the RF signals by the displacements estimated in the other (two) orthogonal direction(s) [19, 30]. A least-squares kernel [31] is finally applied to compute the axial and lateral strains in 2D-PBME (parallel beamforming myocardial elastography) and axial, lateral, and elevational strains in 3D-PBME. The estimated displacements use a reference

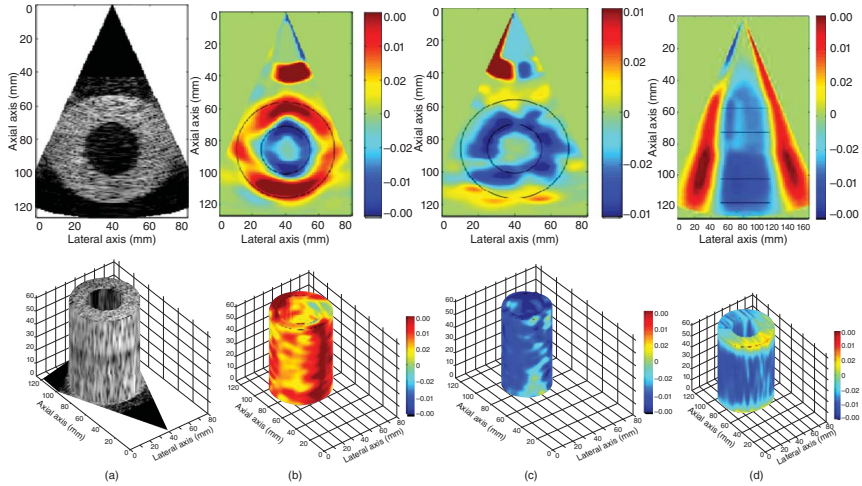

Figure 14.2 (a) B-mode, (b) radial, (c) circumferential, and (d) longitudinal strain images of a cylindrical model undergoing radial deformation using PBME in phased array configuration in FIELD II for 2D (top panel) and 3D (bottom panel) myocardial elastography. In the proposed study, the canine LV geometry and electromechanical simulation model (Figure 14.3) are used. The black boundaries in the top panel represent where the simulated myocardium. Strains outside the tissue are not taken into account.

point of the first frame in each estimation pair, yielding incremental (inter-frame) strains that are then accumulated over the entire systolic phase. Radial, circumferential, and longitudinal strains are then calculated. For 2D, radial and circumferential strains are estimated in a short-axis view (Figures 14.2b and 14.2c). In 2D-PBME, rotation matrices, **R**, for each material point within the myocardium in a 2D short axis view are written as

$$\mathbf{R} = \begin{bmatrix} \cos\theta & \sin\theta \\ -\sin\theta & \cos\theta \end{bmatrix} \tag{14.1}$$

where θ is the angle relative to the origin of the Cartesian coordinates in the FE models. Strains in cardiac coordinates are therefore obtained by

$$\hat{\mathbf{E}} = \mathbf{R}\mathbf{E}\mathbf{R}^{\mathrm{T}} \tag{14.2}$$

where $\hat{\mathbf{E}}$ is the 2D radial-circumferential strain tensor. The diagonal components of $\hat{\mathbf{E}}$ are radial ($\mathbf{E}_{\mathrm{rr}}$) and circumferential ($\mathbf{E}_{\mathrm{cc}}$) strains. Positive and negative radial strains indicate myocardial thickening and thinning, respectively, while myocardial stretching and shortening are represented by positive and negative circumferential strains, respectively. A standard B-mode image (Figure 14.2a) is reconstructed from the RF data, allowing for manually initialized segmentation of the myocardial border, which is subsequently automatically tracked throughout the cardiac cycle based on the estimated displacements – as previously developed by our group [27].

3D Strain Estimation and Imaging 3D includes the estimation of longitudinal strains. The MATLAB function interp3 is used to interpolate all three orthogonal components (axial, lateral, radial, and circumferential) between each of the 16 slices. The interpolated data set is depicted in 3D, on two surfaces: one located near the endocardium, the other located near the epicardium. The frame rate is lower by 16-fold compared to 2D, i.e. 344 frames/s in 3D (from 5500 frames/s in 2D) but is tested whether it can be sufficient to estimate strain at high signal to noise ratio (SNR) as predicted by preliminary findings (Figure 14.3).

PBME Performance Assessment A probabilistic framework has been developed by our group in order to compare the strain estimation quality between conventional and parallel beamforming [23, 32]. The elastographic signal-to-noise-ratios ($\mathrm{SNR_e}$) are calculated for each sequence over the phase of systole. $\mathrm{SNR_e}$ is computed for every point in an image using

$$\mathrm{SNR_e} = \frac{\mu(\varepsilon)}{\sigma(\varepsilon)} \tag{14.3}$$

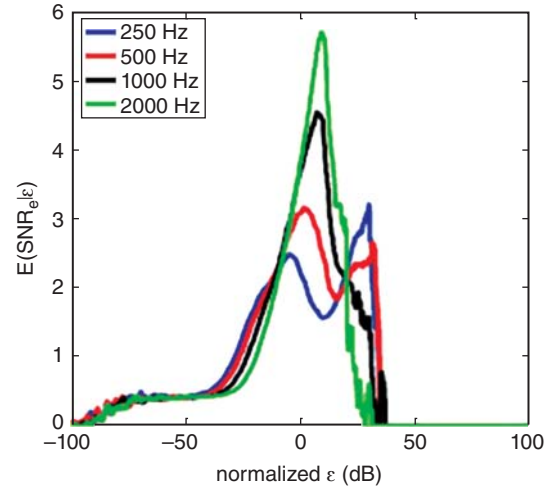

Figure 14.3 $E(\mathrm{SNR_e}|\varepsilon)$ transverse strain curves increase with frame rate.

where $\mu(\varepsilon)$ and $\sigma(\varepsilon)$ refer to the mean and standard deviation of the strain (ε) magnitude within a small 2D region of interest (ROI) (3.0×3.2 mm). Since both strain and SNR_e are computed for each point in the myocardium throughout systole, a large number (>600 000) of strain-SNR_e pairs are generated for each sequence [23]. The conditional expected values of SNR_e for each strain are calculated using [23, 32]

$$E(\mathrm{SNR_e}|\varepsilon) = \int_0^{+\infty} \mathrm{SNR_e} \frac{f(\mathrm{SNR_e}, \varepsilon)}{f(\varepsilon)} \mathrm{dSNR_e} \tag{14.4}$$

$E(SNR_e|\varepsilon)$ curves are generated for each sequence, which allows for a relatively easy comparison to be performed between different sequences for a wide range of strain values. Examples of $E(SNR_e|\varepsilon)$ curves for radial strain estimation are provided in Figure 14.3. The SNR_e of both 2D-PBME and 3D-PBME are computed with respect to the strain (equivalent to frame rate) and compared to focused (standard 2D and 3D myocardial elastography) to perform a quality comparison with parallel beamforming techniques. Both inter-frame (electromechanical) and cumulative (mechanical) strain SNR_e are quantified.

Compounding A compounding technique is applied to determine increase in SNR when parallel beamforming is applied. Plane waves are electronically steered and transmitted at three different angles separated by 20° (–20°, 0°, 20°) and the resulting RF frames are combined into a compounded image. The received radiofrequency (RF) frames are reconstructed by applying a delay-and-sum method on GPU-based parallel computing to accelerate reconstruction processing [32]. In preliminary studies, we have found that compounding in human hearts in vivo decreases the frame rate from 5500 fps to 1375 fps, which is sufficiently high for myocardial elastography (Figure 14.3) while SNR increases by 4-fold.

14.2.1.4 Simulations

A phased array simulation model was implemented for the quality assessment of PBME. Field II, an established and publicly available ultrasound field simulation program [33, 34] is used to simulate the RF signals of the myocardium. The simulated mesh, including the myocardium, cavity, and background are loaded into FIELD II [28, 35]. Instead of a focused wave, a diverging wave sequence is employed for transmit by placing the focus 6.75 mm (half the size of the aperture) behind the array surface to achieve a 90° angle insonification [32]. For 2D-PBME, the RF signals are obtained from 192 elements and 3.5 MHz center frequency with 60% bandwidth (at −6dB) phased array similar to those used in the canine study. Hanning apodization is applied both during transmit and receive to reduce grating lobes. The width and height of the phased array are 43 and 7 mm, respectively. The RF signals are reconstructed by coherent summation of the signals received by all the elements using a delay-and-sum algorithm. For 3D-PBME, RF signals are obtained from a 2D array with 16×16, 32×32, and 64×64 elements and 3 MHz center frequency, similar to those used in experiments.

14.2.1.5 Myocardial ischemia and infarction detection in canines in vivo

Ischemic Model In order to test myocardial elastography in the assessment of ischemia by depicting the change in both mechanical and electrical properties, twelve ($n = 12$) adult male dogs (20–25 kg) were used according to well-established anesthetized canine models. The flow in the coronary artery was continuously controlled via pressure-flow curves.

- Step 1 (control): Mongrel dogs with normal/healthy myocardium, as verified using standard echocardiography, are used for control measurements. Channel data with both 2D- and 3D-PBME are continuously acquired during 5 min in sets of three cardiac cycles each taken 20 s apart, i.e. approximately 15 sets in total. This established the strain baseline.

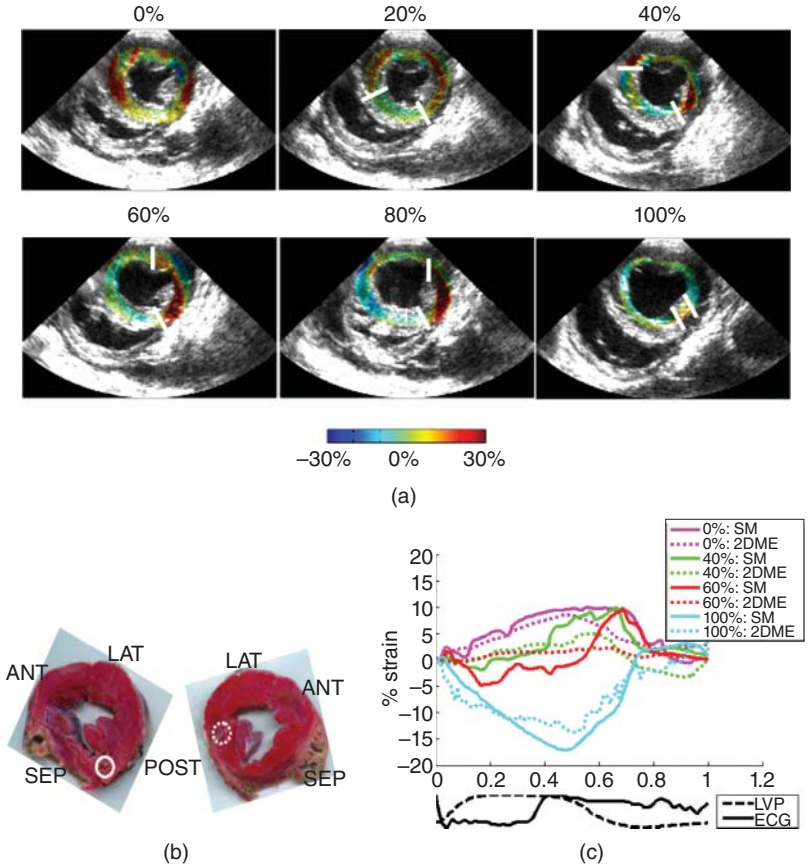

Figure 14.4 (a) Progression of ischemia, shown as thinning systolic strain as indicated compared to the surrounding non-ischemic (thickening) strain, from 0% to 100% occlusion in the same dog using 2D-PBME and identifying the region and extent of ischemia in each case (shown with the ROI). (b) TTC pathology showing pale (unstained by TTC; ischemic) vs. red (stained by TTC; normal) myocardium. (c) Temporal radial strain profiles in the anterior wall region of 3×3 mm^2 at 0%, 40%, 60%, and 100% occlusion levels with sonomicrometry (SM) and 2DME [21].

- Step 2 (mild to acute ischemia): The dogs undergo a left thoracotomy followed by gradual constriction of the mid-proximal left anterior descending coronary artery (LAD) using the Ameroid constrictor by 0–100% of baseline, at intervals of 20% for 15 min each. Strain images are shown in Figure 14.4a. The slope of the coronary pressure-flow curves (using Millar catheters and sonomicrometry) are used to monitor the ischemic onset at each occlusion step. RF data in the same views as in Step 1 were continuously acquired during the full 15 min in sets of three cardiac cycles (10 s apart), i.e. approx. 70 sets total.

Infarct Model Mongrel dogs underwent similar surgical procedure as in the ischemia model but survived for four days after complete ligation only in order to develop a fully developed infarct (Figure 14.5).

14.2.1.6 Validation of Myocardial Elastography against CT Angiography

CT angiography is an established technique used for reliable detection of a coronary occlusion and was used to confirm the occlusion and validate the location of the ischemia or infarct

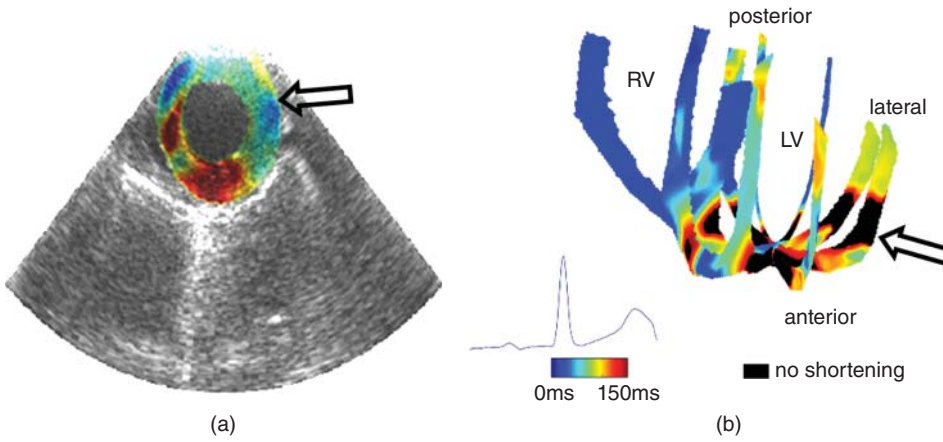

Figure 14.5 (a) Transthoracic systolic radial strain image of a canine left ventricle in vivo. Thinning strain region clearly indicates the extent of infarction. (b) Electromechanical isochrones in 3D identifying spatial extent of MI. Arrow denotes MI region.

as detected by myocardial elastography. The objectives of this study were to show that 2D myocardial strains can be imaged with diverging wave imaging and are different in average between healthy subjects and coronary artery disease (CAD) patients. In this study, 15 CAD patients and 8 healthy subjects were imaged with ME. Patients with more than 50% occlusion in one of the main coronary arteries were considered to have obstructive CAD. Incremental axial and lateral displacements were estimated using normalized 1D cross-correlation and then accumulated during systole. Axial and lateral cumulative strains were then estimated from the displacements and converted to radial cumulative strains (Figures 14.6 and 14.7). The end-systolic radial strain in the total cross-section of the myocardium in healthy subjects ($14.9 \pm 8.2\%$) was significantly higher than obstructive CAD patients ($-0.9 \pm 7.4\%$, $p < 0.001$) and in non-obstructive CAD patients ($3.7 \pm 5.7\%$, $p < 0.05$). End-systolic radial strain in the left anterior descending (LAD) territory was found to be significantly higher in healthy subjects ($16.9 \pm 12.9\%$) than in patients with obstructed LAD ($2.2 \pm 7.0\%$, $p < 0.05$) and patients with non-obstructed LAD ($1.7 \pm 10.3\%$, $p < 0.05$) (Figure 14.8). These findings indicate that end-systolic radial strain measured with myocardial elastography is higher on average in healthy subjects compared to CAD patients and indicates that myocardial elastography has the potential to be used for non-invasive, radiation-free early detection of CAD.

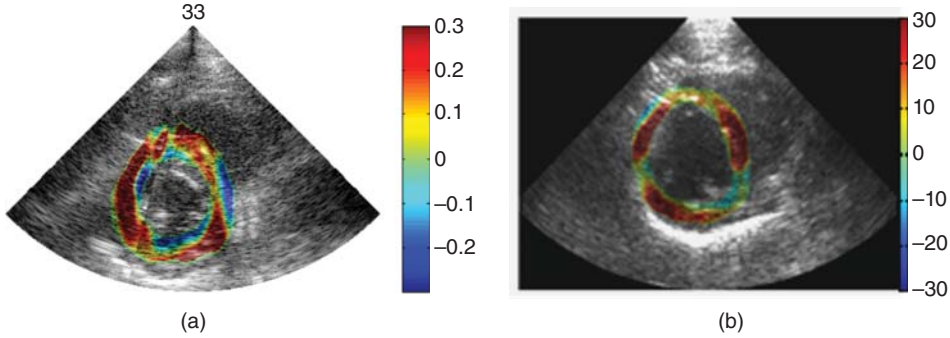

Figure 14.6 Comparison between (a) 2D-ME (conventional (focused) beamforming) using ECG gating and (b) 2D-PBME (parallel beamforming) systolic radial strain image in a normal patient. The quality is comparable without the artifacts from sector matching and ECG gating in part (a).

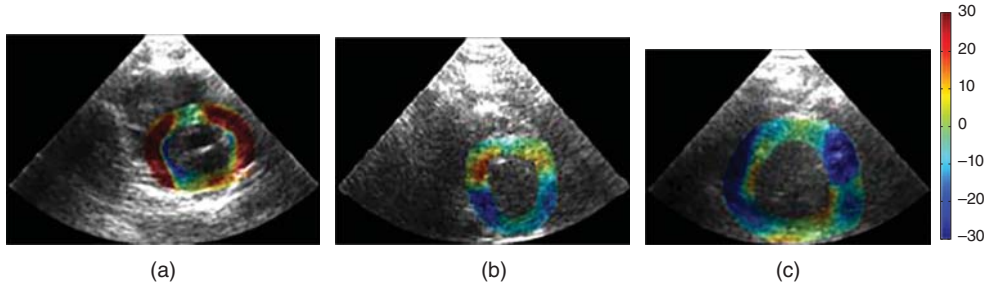

Figure 14.7 2D-PBME showing progression of coronary disease in three different patients: (a) Normal; (b) occlusions – RCA: 90%; LAD: 20%, LCX: 20%; and (c) occlusions – RCA: 99%; LAD: 100%, LCX: 100%. Figure 14.1d can be used for reference of the position of the coronary arteries.

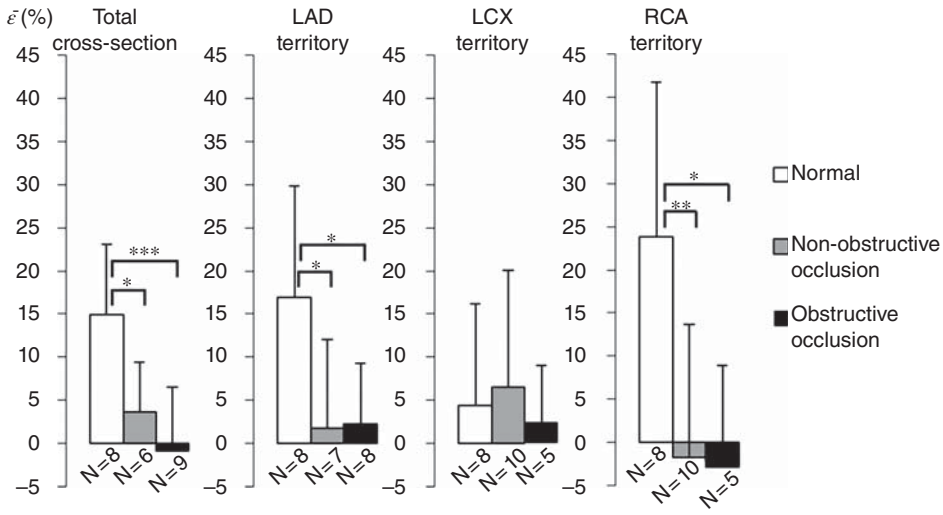

Figure 14.8 Preliminary findings in 25 human subjects (19 patients and 6 normals) using PBME. Non-severe CAD (stenosis <50%) and severe (>50% stenosis). LAD: left anterior descending artery; LCx: left-circumflex artery; RCA: right coronary artery; total: all territories. In all territories except LCx PBME was capable of differentiating normal from non-severe and from severe CAD.

14.2.2 Electromechanical Wave Imaging (EWI)

14.2.2.1 Cardiac Arrhythmias

Cardiac arrhythmias can be separated into atrial (or supraventricular) and ventricular. While ventricular arrhythmias, such as ventricular fibrillation (chaotic rhythm), ventricular tachycardia (rapid rhythm), and ventricular bradycardia (slow rhythm) incur the most episodes of sudden death, they are less common and easier to diagnose than atrial arrhythmias. Atrial arrhythmias, including atrial fibrillation (Afib or AF) and atrial flutter (AFL), are the most common. Similar to the ventricular definition, atrial fibrillation denotes the chaotic rhythm while atrial flutter denotes the regular but abnormal (rapid or slow) rhythm. The number of individuals with atrial fibrillation in the United States is expected to reach 12 million by 2050 [36] with atrial flutters, often a result of treatment, also expected to rise as more of these treatments are administered. The EWI methodology has the dual purpose of both enhancing the diagnosis and treatment planning and guidance of arrhythmias that are both the most common but also the most difficult to diagnose, i.e. the atrial arrhythmias. A short overview of the state-of-the-art diagnostic and treatment techniques is provided.

14.2.2.2 Clinical Diagnosis of Atrial Arrhythmias

ECG recordings and no imaging modality is typically used for the noninvasive identification of atrial arrhythmias. If ECG recordings indicate atrial flutter or fibrillation, Radio-frequency (RF) ablation (see Section 14.2.2.3) is warranted that allows for catheterized cardiac mapping during its procedure. Cardiac mapping involves the insertion of a catheter containing a small number of electrodes in the heart chamber to contact the endocardium and measure times of activation. The procedure is minimally invasive and ionizing since it uses computed tomography (CT) guidance, but it can be a lengthy procedure requiring topical or general anesthesia and is warranted only when the ECG recordings indicate that RF ablation is the appropriate course of treatment. Limitations include some inaccessible endocardial sites and the inability to map the mid-myocardium and epicardium. More importantly, as potentials in only one or a few locations in the atrium are measured per heartbeat it can be used only to study stable, repeatable arrhythmias.

14.2.2.3 Treatment of Atrial Arrhythmias

Radio-frequency ablation is a minimally invasive technique rapidly emerging as the most commonly used therapeutic modality for atrial flutter and atrial fibrillation. For this treatment, a catheter, whose tip carries an electrode, is inserted through the femoral vein and the tip of the electrode is positioned at the arrhythmic origin. The tip causes a frictional heat generated by intracellular ions moving in response to an alternating current. The electrode is connected to a function generator and the electrical current flows and raises the local temperature up to 95 °C, maintaining it for about 15 min, generating thermal lesions in the vicinity of the ablating catheter. The treatment consists thus in modifying or blocking the circuits of electrical conduction in the heart. Current surgical procedures are invasive and have a moderate efficiency in the persistent forms of atrial fibrillation. AF in some patients may be due to focal activity originating in the pulmonary veins and 70% of these patients can be successfully treated by RF ablation of the focus inside the pulmonary veins [37]. However, the treatment of AF using RF ablation can often lead to the development of other arrhythmias. For example, a sizeable increase of atypical flutter is due to catheter ablation of atrial fibrillation.

14.2.2.4 Electromechanical Wave Imaging (EWI)

Cardiac Electromechanics The heart will not adequately contract unless it is electrically activated via a very specific route (Figure 14.9; green arrows). In sinus rhythm (that is, natural contraction), the path of activation originates at the sinoatrial (SA) node (right before the ECG's P-wave), from which the electrical signal in the form of an action potential spreads to both right and left atria causing their contraction (during the P-wave). The wave then propagates to the atrioventricular (AV) node (right after the P-wave), through the bundle of His and along the left and right bundles on the interventricular septum (during the Q-R segment) to the Purkinje fibers (S-wave) finally causing both ventricles to synchronously contract, starting at the apex towards their lateral and posterior walls (Figure 14.9). The heart is thus an electromechanical pump that needs to first be electrically activated in order to contract. Propagating electrical waves of excitation result in localized contractions. Each electrical activation in Figure 14.9b is followed by an electromechanical one, i.e. the depolarization of a cardiac muscle cell, or, myocyte, is followed by an uptake of calcium, which triggers contraction after a certain electromechanical delay of a few milliseconds [38, 39]. In the presence of arrhythmia, electrical and electromechanical patterns are disrupted.

Electromechanical Wave Imaging (EWI) Our group has pioneered a unique noninvasive and direct (as opposed to inverse problem) imaging technique that could reliably map the conduction wave in the heart in all of its four cardiac chambers. Electromechanical wave imaging

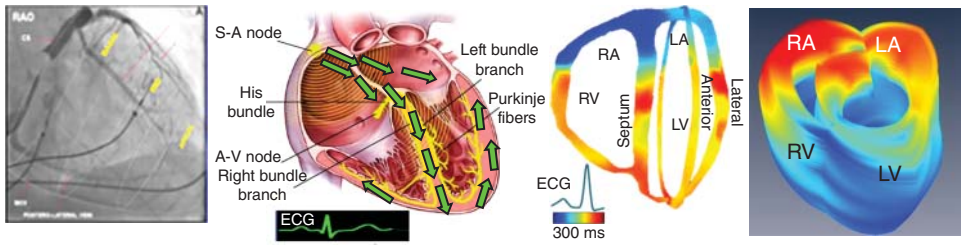

Figure 14.9 (a) State-of-the-art CT angiography of the CRT leads. The ablation catheters and coronary arteries are clearly visible but the heart and the myocardium are not visible. A similar system is used to guide electroanatomic mapping. (b) Illustration of the cardiac conduction system. The arrows indicate the path of activation as the action potential propagates from the sinoatrial node (SA node) in the right atrium along the Purkinje fiber network. (c) Current (2D) 4-chamber EWI activation map with conventional beamforming in a normal human heart obtained transthoracically. (d) 3D-rendered, 4-chamber EWI activation map (reversed color map used compared to part c) in vivo.

[15, 16, 20, 40–48] has been shown capable of noninvasively mapping the conduction wave during propagation. We identified that high frame rate (>500 frames/s, fps) and precise 2D imaging of the cardiac deformation is feasible so that the transient cardiac motion resulting from the fast electromechanical wave can be mapped in murine [15, 16, 40–43], canine [20, 46–48], and human [15, 32, 45] hearts in vivo. We were also capable of demonstrating that EWI is angle-independent [47], has excellent correlation with electrical activation measurements in canines in vivo [47] (slope of 0.99 and $r^2 = 0.88$; Figures 14.10 and 14.11) and is in excellent agreement with electromechanical simulations [32, 49]. More importantly, our group was capable of recently showing that EWI was feasible in the atria of human hearts in vivo undergoing sinus rhythm. [32]. There is simply no other modality that can directly map the conduction of the atria under sinus rhythm noninvasively in the clinic. An important additional advantage of this methodology is that it can be routinely applied in the clinic through straightforward integration with any echocardiography system. It could thus be used both at the diagnostic and at the treatment guidance levels, either off- or on-line. Despite the fact that EWI can map both the atria and the ventricles, we chose to focus on the atrial arrhythmias in this study given that they are far more common, more salvageable, and completely lacking of any noninvasive imaging modality that can map their conduction properties.

EWI can be useful in a number of diseases that can be treated with ablation therapy: e.g. atrial fibrillation, atrial flutter, ventricular tachycadia, Wolff-Parkinson-White (WPW) syndrome, etc. WPW is a heart condition where an additional electrical pathway links the atria to the ventricles. It is the most common heart rate disorder in infants and children and is preferably treated using catheter ablation. EWI could be used in predicting the location of the accessory pathway, thus reducing the overall time of the ablation procedure. Since a sizeable increase of atypical flutter is due to catheter ablation of atrial fibrillation, the prevalence of atrial flutter is also expected to rise. However, the relationship between AF and AFL is still not fully understood [50]. Atrial flutter, a type of atrial tachycardia, has historically been defined exclusively from the ECG recordings. More specifically, differentiation between flutter and other tachycardias was based on the atrial rate and the presence or absence of isoelectric baselines between atrial deflections. Since then, electrophysiological studies and RF ablation brought new understanding into the atrial tachycardia mechanisms, which did not correlate well with these ECG-based definitions [51]. In other words, ECG recordings offer only a limited value in the determination of specific atrial tachycardia mechanisms, and, ultimately, for the selection of the appropriate course of treatment. Cardiac mapping allowed different mechanisms of macroreentrant atrial tachycardia to be identified, such as typical flutter, reverse typical flutter, left atrial flutter, etc.,

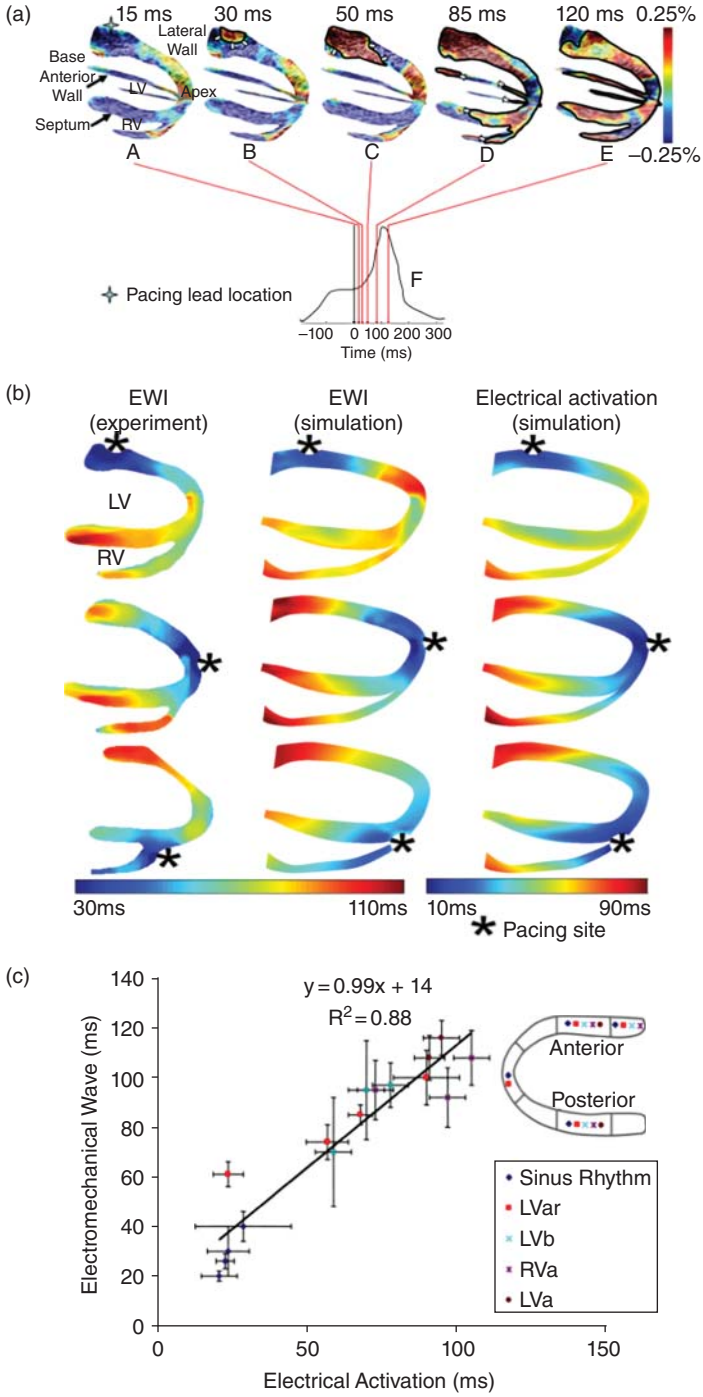

Figure 14.10 (a) Propagation of the electromechanical wave when paced from the lateral wall, near the base. Activation in this view corresponds to thickening of the tissue. Activated regions are traced at (A) 15 ms, (B) 30 ms, (C) 50 ms (D) 85 ms, and (E) 120 ms and indicated on the electrocardiogram (F). 0 ms corresponds to the pacing stimulus. A–C: The EW propagates from the basal part of the lateral wall towards the apex. D: Note that in the apical region, a transition from lengthening to shortening is observed rather than a transition from thinning to thickening. D, E: In the anterior wall, the EW propagates from both the base and apex. The scale shows inter-frame strains. (b) Correlation of EWI with simulation findings of electromechanical and electrical activation [46]. (c) Electrical and electromechanical activation times during the four pacing protocols and sinus rhythm in four different heart segments in the posterior and anterior walls [46].

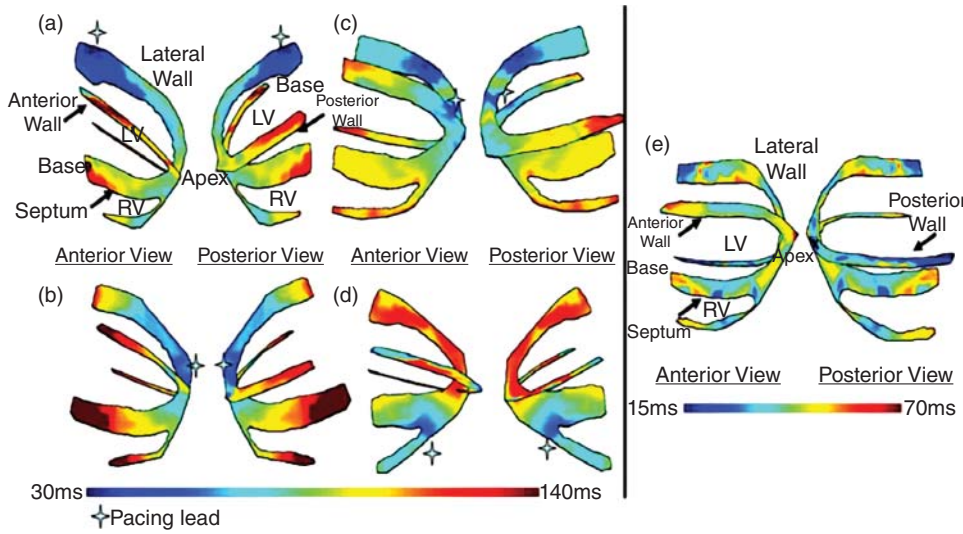

Figure 14.11 Isochrones showing the activation sequence under different pacing protocols as shown. Arrow indicates the pacing origin. (a) Pacing from the basal region of the lateral wall; (b) pacing from the apex; (c) pacing from the apical region of the lateral wall; (d) pacing from the apical region of the right-ventricular wall; and (e) Isochrones showing the EW activation sequence during sinus rhythm. The activation sequence exhibits early activation at the median level and late activation at the basal and apical levels. Activation of the right ventricular wall occurred after the activation of the septal and lateral walls. The cross indicates the pacing lead location.

although a significant number of atypical flutters are still poorly understood [51, 52]. While mapping the right atrium is routinely undertaken successfully using this procedure, mapping the left atrium is riskier since it requires a transseptal puncture. However, as it currently stands in the clinic, right atrium arrhythmia cannot be distinguished from left atrium arrhythmia prior to treatment and only the latter warrants transseptal puncture, which is a riskier procedure. In some cases, the left atrium arrhythmia is not diagnosed until the entire right atrium is ablated (which may involve several unproductive hours of intervention), posing further risk to the patient. Consequently, left atrial activation sequences are not well characterized in many atrial tachycardia cases [51]. Moreover, the surface ECG is insufficiently specific to distinguish left from right atrial flutters [50, 52]. EWI could thus offer an important step for the localization of the right vs. left atrial arrhythmia as well as localizing the origin(s) at the treatment planning stage, i.e. prior to the catheterization of the patient rendering the treatment to be more efficient, much shorter in duration, and with unnecessary ablations in the wrong chamber or avoiding unnecessary transseptal punctures.

Treatment Guidance Capability of EWI Currently, there is simply no noninvasive electrical conduction mapping techniques of the heart that can be used in the clinic. In addition, apart from the currently available clinical electrical mapping methods being all catheter-based and limited to mapping the endocardial or epicardial activation sequence, they are also time-consuming and costly. Even in a laboratory setting, mapping the 3D electrical activation sequence of the heart can be a daunting task [53]. Studies of transmural electrical activation usually require usage of a large number of plunge electrodes to attain sufficient resolution [54–56], or are applied to small regions of interest in vivo [38]. Non-contact methods to map the electrical activation sequence have also emerged but are not used in the clinic. Optical imaging techniques use voltage-sensitive dyes that bind to cardiac cell membranes and, following illumination, fluoresce if the cell undergoes electrical activation. Optical imaging methods can map the activation

sequence of ex vivo tissue on the endocardial and epicardial surfaces [57–62] but cannot be applied in the clinic since they require the use of an electromechanical decoupler that inhibits cardiac contraction during imaging. Other newly developed methods to map the local electrical activity of the heart based on inverse problems are available: electrocardiographic imaging (ECGI) [63–65] and non-contact mapping [66–68]. The former is based on body surface potentials and CT or MRI scans and provides reconstructed epicardial action potentials, including the atria [69]. The latter consists in reconstructing the transmural potentials from potentials measured in the heart chamber based on specific assumptions that may be susceptible to inverse problem errors [70–72].

14.2.2.5 Imaging the Electromechanics of the Heart

As of today, no imaging method currently used in the clinic has been capable of mapping the electromechanics of the heart. Initial measurements to determine the correlation between the electrical and electromechanical activities have been reported [73, 74]. These results suggest that the electrical activation sequence could be deduced from the electromechanics. Clinically available imaging modalities, such as standard echocardiography or MRI, cannot adequately detect the electromechanical wave (EW) since they are too slow, i.e. the time required to acquire a single image is similar to the duration of the entire ventricular depolarization. The electrical activation lasts approximately 60 to 100 ms and requires a resolution of a few milliseconds (e.g. 2–5 ms) to generate precise activation maps. Moreover, the regional inter-frame deformation to be measured at these frame rates is very small (~0.25% at a 2 ms temporal resolution) and requires a highly accurate strain estimator [20, 46–48]. We have shown that EWI is capable of reaching high frame rates (up to 2000 frames/s) as well attain the precision of the incurred strains (up to 0.25%) which result from an electromechanical activation and therefore fulfill the requirements of both high temporal and spatial resolution unique to our technology.

14.2.2.6 EWI Sequences

A block diagram of EWI is shown in Figure 14.12. Two imaging sequences, the automated composite technique (ACT) [45] and the temporally-unequispaced acquisition sequences (TUAS) [32, 75] have been developed and implemented [20, 32, 46–48, 75–77] as well as the single-heartbeat sequence [32, 75–79].

The ACT Sequence An Ultrasonix RP system with a 3.3 MHz phased array was used to acquire RF frames from 390 to 520 frames/s (fps) using an automated composite technique (ACT) [45]. Briefly, to increase the resulting frame rate, the image is divided into partially overlapping sectors corresponding to separate cardiac cycles (Figure 14.12a). The axial incremental displacements are obtained with a RF-based cross-correlation method (Figure 14.12b) (window size: 4.6 mm, 80% overlap). Briefly, this method consists in dividing every ultrasound beam in a large number of overlapping, one-dimensional, 4.6 mm-long windows. Then, the following process is applied to each window and each sampled time t. A reference window at time t_1 is compared with all the windows contained in the same beam at sampled time t_2. The axial location of the window providing the highest correlation determines the axial displacement between two consecutive sampled times. After repeating this process for every available window and every available sampled time, we obtain axial displacements at multiple locations along the ultrasound beam and for every sampled time. The full-view image is then reconstructed using the motion-matching technique (Figure 14.12c) [20]. Briefly, this method consists of comparing, through a cross-correlation method, the incremental displacements measured in the overlapping line of two sectors obtained at different heartbeats to synchronize the sectors. More specifically, the acquisition sequence is designed such that each sector contains at least one ultrasound beam that is also part of the following sector. Therefore, this

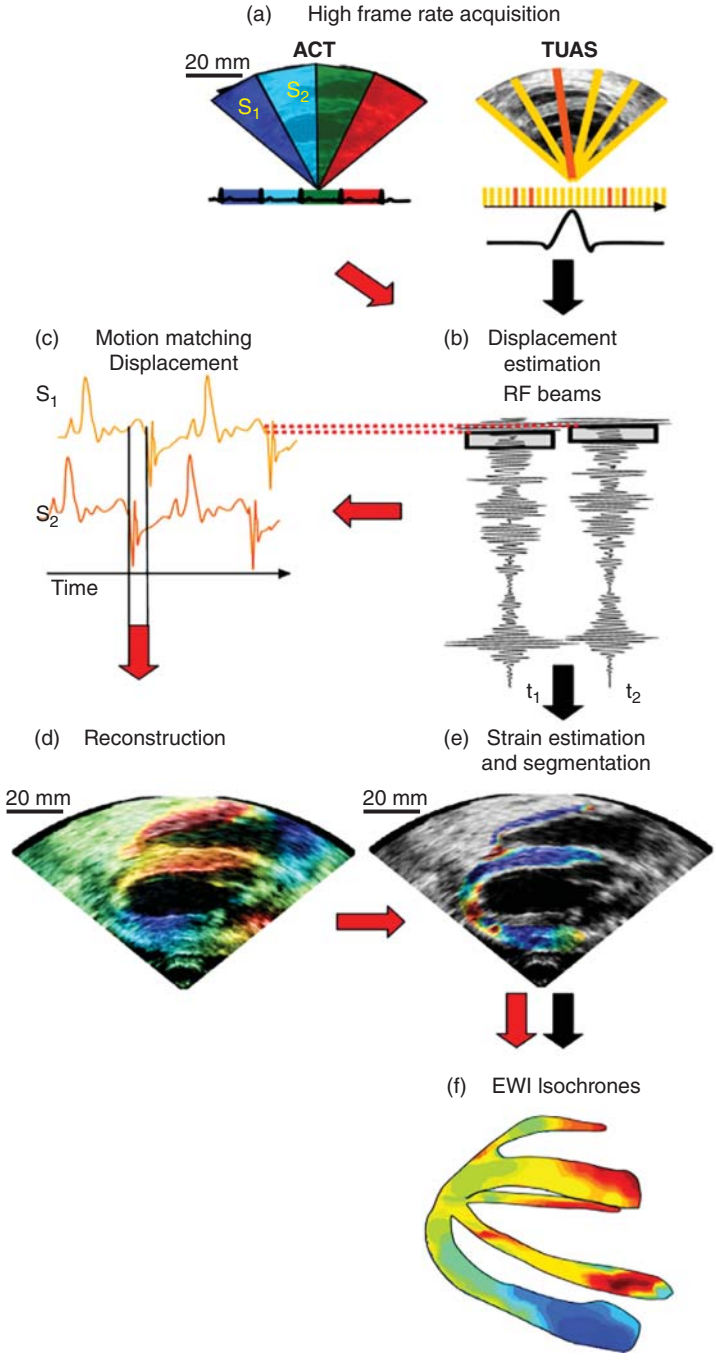

Figure 14.12 Block diagram of the EWI technique. (a) High frame-rate acquisition is first performed using either ACT (follow lighter arrows) or TUAS (black arrows). (b) High precision displacement estimation between two consecutively acquired RF beams (t_1, t_2) is then performed using very high frame rate RF speckle tracking. (c) In ACT only, a region of the heart muscle, common to two neighboring sectors, is then selected. By comparing the temporally varying displacements measured in neighboring sectors (s_1, s_2) via a cross-correlation technique, the delay between them is estimated. (d) In ACT only, a full-view ciné-loop of the displacement overlaid onto the B-mode can then be reconstructed with all the sectors in the composite image synchronized. (e) In ACT and TUAS, the heart walls are then segmented, and incremental strains are computed to depict the EW. (f) By tracking the onset of the EW, isochrones of the sequence of activation are generated.

overlapping beam is expected to result in identical (or highly similar) axial displacements whether they corresponds to heartbeat h that occurred when sector s was acquired or to heartbeat $h + 1$ that occurred when sector $s + 1$ was acquired. By comparing, over time, the displacements obtained in the overlapping beams, the time delay corresponding to the maximum cross-correlation coefficient are obtained to synchronize each set of neighboring sectors. The procedure is repeated for each pair of sectors, allowing the reconstruction of the full-view of the heart, hence ensuring the continuity of the transition incremental displacements across sectors. This method does not rely on the ECG. Therefore it is especially useful in cases where the ECG may be unavailable or too irregular to perform ECG gating [20]. The axial incremental strains were then obtained by taking the spatial derivative of incremental strains in the axial direction using a least-squares estimator [31] with a kernel equal to 6.75 mm (Figure 14.12d). The myocardium was segmented using an automated contour tracking technique [80] and displacement and strain maps were then overlaid onto the corresponding B-mode images (Figure 14.12e). Isochrones were generated by mapping the first time occurrence at which the incremental strains crossed zero following the Q-wave. More specifically, the absolute value of the incremental strains was minimized in a temporal window following the Q-wave in up to a hundred manually selected regions. Noisy data were excluded. Subsample resolution was obtained through spline interpolation and Delaunay interpolation was used to construct continuous isochronal maps. Two echocardiographic planes, identical to the planes imaged in the standard apical four- and two-chamber views, were imaged across the long axis of the heart. These two views were temporally co-registered using the ECG signals, spatially co-registered by an echocardiography expert, and displayed in a three-dimensional biplane view in Amira 4.1 (Visage Imaging, Chelmsford, MA) (Figure 14.12f).

The TUAS Sequence We have developed and implemented in an Ultrasonix MDP system a temporally unequispaced acquisition sequence (TUAS) (Figure 14.12) [32], which is a sector-based sequence [81], adapted to optimally estimate cardiac deformations. In TUAS, it is possible to simultaneously achieve a wide range of frame rates for motion estimation, large beam density, and a large field of view in a single heartbeat, thus avoiding the motion-matching and reconstruction steps in EWI, with little dependence on depth and beam density. Consequently, for a given set of imaging parameters, motion can be estimated at frame rates varying from a few Hz to kHz. The prior knowledge, in this case, is the minimum sampling rate, i.e. the Nyquist rate, of the motion over time at a given pixel. The conventional way to construct an ultrasound image using a phased array is to acquire a finite number of beams, typically 64 or 128, over a 90° angle. These beams are acquired sequentially, and the process is repeated for each frame. For example, a given beam, e.g. beam 3 (Figure 14.13), is acquired at a fixed rate (Figure 14.13, conventional sequence). In TUAS, the beam acquisition sequence is reordered to provide two distinct rates, defined as follows (Figure 14.13): the motion-estimation rate and the motion-sampling rate. The motion-estimation rate r_{me} is defined as the inverse of the time, i.e. T_{me}, lapsing between the two RF frames used to estimate motion. The motion-sampling rate $\mathrm{r_{ms}}$ is defined as the inverse of the time, i.e. T_{ms}, lapsing between two consecutive displacement maps. In conventional imaging sequences, these two rates are equal, because a given frame is typically used for two motion estimations (u_n and u_{n+1} in Figure 14.13). In TUAS, the operator can adjust the motion-estimation rate. As shown in Figure 14.13, a frame in the TUAS case is used only once for motion estimation, thus halving the motion-sampling rate relative to the conventional method. For example, an acquisition performed at a 12 cm depth with 64 beams with a conventional sequence corresponds to a frame rate of 100 Hz. However, while 100 Hz may suffice to satisfy the Nyquist sampling criterion of cardiac motion, it is usually insufficient for accurate motion tracking using RF cross-correlation. Therefore, to reach a higher frame rate of, e.g. 400 Hz typically used for EWI, the conventional sequence requires to divide the

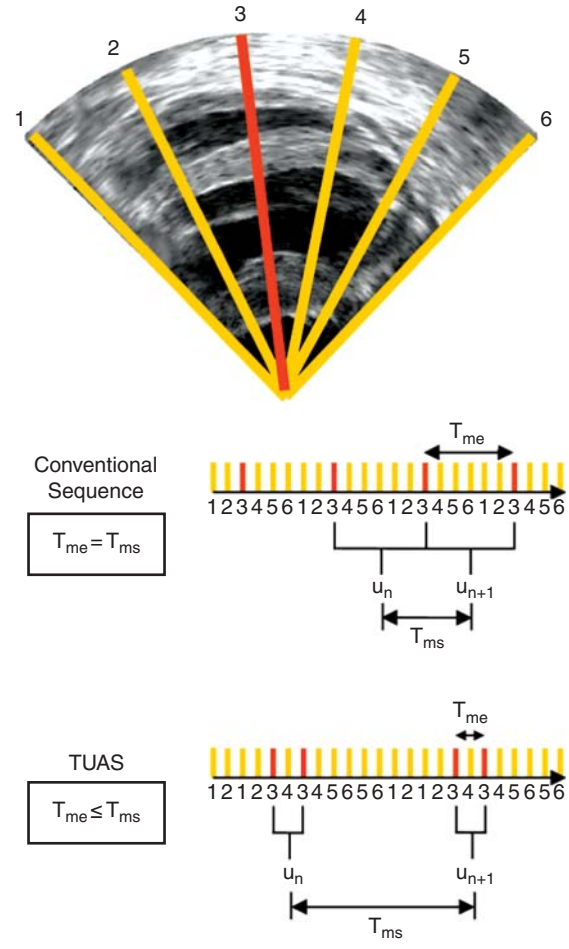

Figure 14.13 Illustration of an acquisition sequence in a simple case where only six lines form an image, with each sector using two lines. In a conventional acquisition sequence, the time separating two acquisitions of the same line is the same. In TUAS, the time separating two acquisitions of the same line is modulated to optimize motion estimation.

number of beams by four, and thus reduce either the beam density, the field of view, or both. At the same depth and beam density, TUAS provides a motion-sampling rate of 50 Hz and a motion-estimation rate that can be varied, as shown in the following section, within the following group: {6416, 3208, 1604, 802, 401, 201, 100} Hz. This has numerous advantages. For example, both the beam density and the field of view can be maintained while estimating the cardiac motion with an optimal frame rate, which could be, e.g. either 401 or 802 Hz, depending on the amplitude of the cardiac motion. This results into a halving of the motion-sampling rate; however, the motion-sampling rate has only little effect on the motion estimation accuracy. Theoretically, if this rate remains above the Nyquist rate of the estimated cardiac motion, it will have no effect. We estimated that at a motion-sampling rate above 120 Hz, the effect of the motion-sampling rate became negligible compared to the effect of the motion-estimation rate [32].

Single-heartbeat EWI and Optimal Strain Estimation In TUAS, a wide range of frame rates can be achieved, including very high frame rates, independently of other imaging parameters. Therefore, by maintaining a set of imaging parameters (e.g. field of view, imaging depth) and varying the frame rate, it is possible to identify an optimal frame rate by studying the link between the strain signal-to-noise ratio (SNR_e) and the EW. A previous report [82] on the strain filter indicates that the SNR_e depends mostly on the value of the strains to be measured when the

imaging parameters are fixed. This theoretical framework allows the construction of an upper limit on the SNR_e as a function of the strain amplitude (also known as the strain filter). The strain filter corresponds, in this case, to the Ziv-Zakai lower bound (ZZLB) on the variance. The ZZLB is a combination of the Cramér-Rao lower bound (CRLB) and the Barankin bound (BB). The ZZLB transitions from the CRLB to the BB when decorrelation becomes important to the point that only the envelope of the signal contains information on the motion [83]. In the correlation model used here [84], this transition occurs only at very large strains. Since the amplitude of strains to be measured is directly related to the motion-estimation rate (a large motion-estimation rate will result in small inter-frame strains), finding an optimal strain value is equivalent to finding an optimal motion-estimation rate. The strain filter was calculated with the imaging parameters used in this study as a reference; however, it was developed for the analysis of strains occurring in static elastography and is not adapted to the more complex motion of the heart. We have therefore developed a new probabilistic framework based on experimental data acquired in a paced canine in vivo to not only establish an upper bound on the SNR_e, but to estimate the probability of obtaining a given SNR_e for a given strain amplitude [32]. Since the motion-estimation rate can be used as a means to translate and narrow the strain distribution), the optimal motion-estimation rate can be found by studying the link between the strains and the SNR_e. More specifically, a conditional probability density function spanning a large range of strains values was constructed (Figure 14.14) and was found in agreement with the strain-filter theory, which provides a higher bound on the SNR_e. The ZZLB predicts a sharp transition between the CRLB and BB when decorrelation becomes important, to the point that the phase of the signal does not contain information about motion. Figure 14.14 shows that the conditional probability density function is comprised within the CRLB up to approximately 4% before it becomes comprised within the BB. A sharp decrease in the expected value of the SNR_e is also observed at 4% strain, underlining the importance of using the phase information of the RF signal for accurate strain measurements. A distortion in the strain distribution may indicate that while a high SNR_e can be maintained, the accuracy of the strain estimator is strongly impaired at low motion-estimation rates, i.e. less than 350 Hz in this case (Figure 14.14). Finally, we showed that TUAS is capable of accurately depicting non-periodic events at high temporal resolution. Therefore, the optimal frame rate will need to be between 389 and 3891 Hz according to the strains estimated (Figure 14.14). Strain patterns expected during such a phenomenon were depicted, such as a disorganized contraction, leading to little to no large scale motion of the heart. Regions of the myocardium were oscillating rapidly from thinning to thickening and thickening to thinning over time. Studying the frequencies of these oscillations could be useful in understanding the mechanisms of fibrillation [85] and we plan to use Fourier-based analysis and principal component analysis in order to identify those

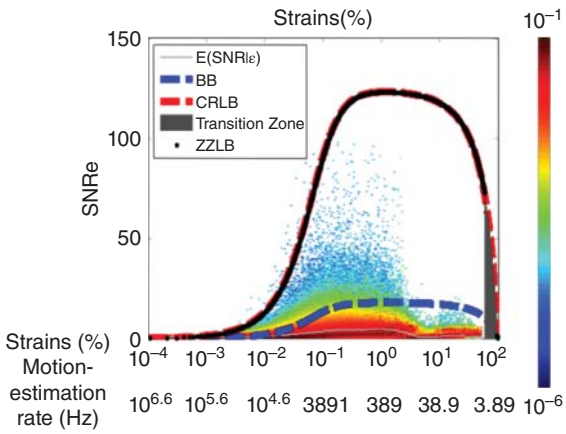

Figure 14.14 Distribution of strains during the EW for different motion-estimation rates. Conditional probability density function of the SNR_e knowing the strain value (and the corresponding motion-estimation rate). The conditional expectation values of SNR_e, the ZZLB, BB, and CRLB are also displayed.

components in fibrillation and better identify the arrhythmic origin(s). Ciaccio et al. [86] have developed such methods, including non-harmonic analysis for the analysis of electrical signals in the heart during fibrillation (and will assist in further development for EWI).

14.2.2.7 Characterization of Atrial Arrhythmias in Canines In Vivo

Electrical Mapping Data from the St. Jude EnSite system was exported to a workstation for co-registration with EWI isochrones. Comma separated value (CSV) files containing the coordinates of the 3D mesh as well as the data from each acquired point (activation time and spatial coordinates) were retrieved. The 3D mesh was recreated in Maya (Maya 2016, Autodesk, San Rafael, CA, USA) and the open-source software MeshLab (Visual Computing Lab – ISTI, CNR, meshlab.sourceforge.net). 3D co-registration was performed by aligning the isochrones with the 3D mesh using anatomical landmarks such as the location of the apex, the mitral valve annulus, the lateral wall, or the septum. Once both the isochrones and the mesh were aligned, positions of the acquired points on the EnSite system were projected onto the isochrones and times of activation were compared. This process provided pairs of electrical and electromechanical activation times which were then plotted against each other. Linear regression was then performed and slope, intercept, and R^2 values were obtained.

Validation The objective of this study was to validate EWI against electrical mapping using an electroanatomical mapping system, in all four chambers of the heart. Six ($n = 6$) normal adult canines were used in this study. The electrical activation sequence was mapped in all four chambers of the heart, both endocardially and epicardially using a St. Jude EnSite mapping system (St. Jude Medical, Secaucus, NJ). EWI acquisitions were performed during normal sinus rhythm and pacing and isochrones of the electromechanical activation were generated. Electromechanical and electrical activation times were plotted against each other and linear regression was performed for each pair of activation maps. Electromechanical and electrical activations were found to be highly correlated with slopes of the correlation ranging from 0.77 to 1.83, electromechanical delays between 9 and 58 ms and R^2 values from 0.71 to 0.92 (Figure 14.15). The excellent linear correlation between electromechanical and electrical activation and good agreement between the activation maps indicate that the electromechanical activation follows the pattern of propagation of the electrical activation. This suggests that EWI could be used to accurately characterize arrhythmias and localize their source.

14.2.2.8 EWI in Normal Human Subjects and with Arrhythmias

The objectives of the clinical studies [23, 32, 46–48, 77] were (i) to determine the potential for clinical role of EWI, by predicting activation patterns in normal subjects, (ii) to determine the feasibility of EWI to identify the site of origin in subjects with tachyarrhythmia, and (iii) to identify the myocardial activation sequence in patients undergoing CRT. In normal subjects (Figures 14.16 and 14.17), the EW propagated, in both the atria and the ventricles, in accordance with the expected electrical activation sequences based on reports in the literature. In subjects with CRT, EWI successfully characterized two different pacing schemes, i.e. LV epicardial pacing and RV endocardial pacing versus sinus rhythm with conducted complexes. In two subjects with AFL (Figure 14.18), the propagation patterns obtained with EWI were in agreement with results obtained from invasive intracardiac mapping studies, indicating that EWI may be capable of distinguishing LA from RA flutters transthoracically. Finally, we have shown the feasibility of EWI to describe the activation sequence during a single heartbeat in a patient with AFL and RBBB (Figure 14.18) [32]. The results presented demonstrate for the first time that mapping the transient strains occurring in response to the electrical activation, i.e. the electromechanical wave propagation, can be used to characterize both normal rhythm and arrhythmias in humans, in all four cardiac chambers transthoracically using multiple-

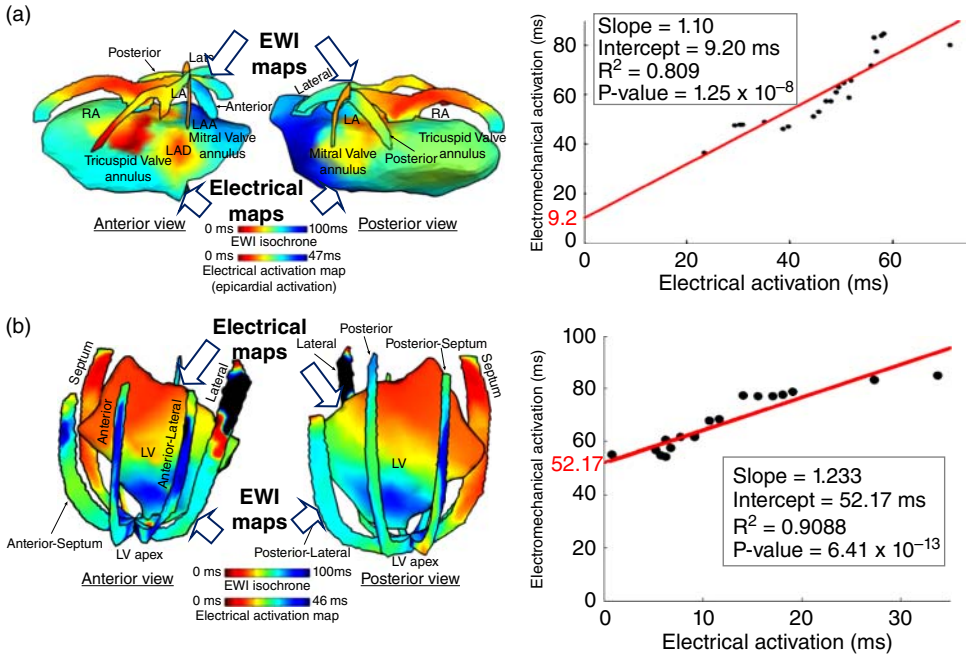

Figure 14.15 Comparison of EWI against electroanatomical mapping. Anterior and posterior views in the (a) right (RA) and left (LA) atria and (b) entire canine left ventricle (LV) using EWI noninvasively and electroanatomical mapping with the proposed clinical system (Ensite, St. Jude Medical). Linear regression analysis shows excellent correlation between the electromechanical and electrical activation with the intercept indicating the electromechanical delay [79].

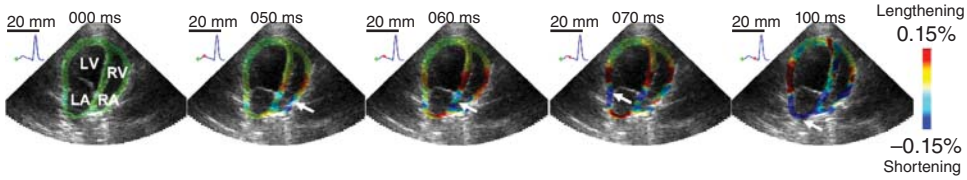

Figure 14.16 EWI using a flash sequence for motion estimation (motion sampling rate: 2000 Hz, motion estimation rate: 500 Hz) overlaid on a standard 128-beams, 30-fps B-mode. All four chambers are mapped but only atrial activation is shown here. Activation (shortening) was initiated in the right atrium (RA) (50 ms) and propagated towards the atrial septum (60 ms) and the left atrium (LA) (70 ms) until complete activation of both atria (100 ms). RV: right ventricle, LV: left ventricle.

and single-heartbeat methodologies. EWI has the potential to noninvasively assist in clinical decision making prior to invasive treatment, and to aid in optimizing and monitoring responses to CRT. Some more recent endeavors are using multi-2D rendering for reconstruction of the ventricular [87] and atrial surfaces.

14.3 Vascular Imaging

14.3.1 Stroke

Stroke is one of the leading causes of death often associated with severe, long-term disability [88]. One of the main reasons behind this large death toll is that characterization of plaque

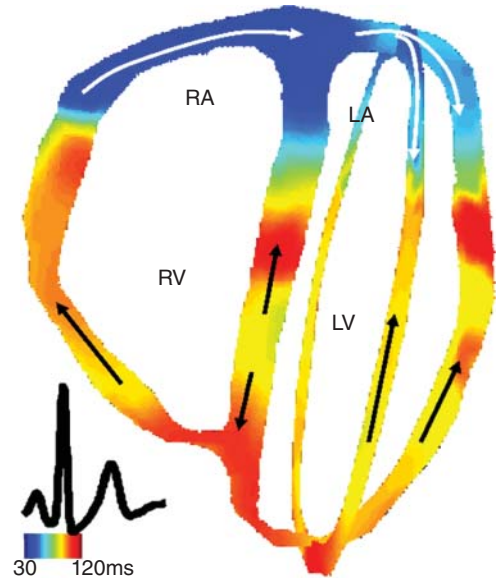

Figure 14.17 EWI isochrone in all four chambers in a healthy, 23-year-old male subject. Activation in this view corresponds to shortening of the tissue. Activation is initiated in the right atrium and propagates in the left atrium. After the atrio-ventricular delay, activation is initiated in the ventricles from multiple origins, which are possibly correlated with the Purkinje terminal locations. Arrows (both white and black) indicate the direction of propagation.

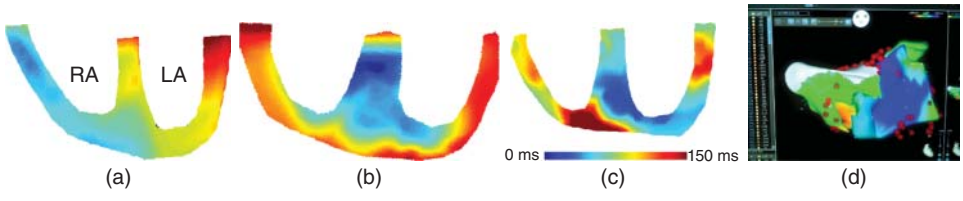

Figure 14.18 Noninvasively detecting and characterizing atrial flutter with EWI in three human subjects (RA: right atrium, LA: left atrium). (a) Normal subject: activation is initiated in the right atrium and propagates towards the left atrium. (b) Unknown atrial flutter in a flutter patient with a prosthetic mitral valve, which was believed to cause the atrial flutter from the left side. Since the patient could not sustain the long procedure needed to construct a full activation map using cardiac mapping, ablation was attempted without complete information in two locations in the left atrium, which did not lead to cardioversion, i.e. did not return to sinus rhythm. The patient was sent home and a second ablation is scheduled in the near future. This case exemplifies the need for a faster mapping method, which could have led to the proper identification of the ablation site and so potentially limit the number of ablation procedures needed to treat this patient. Indeed, the EWI isochrones shown here display the initial activation in the left atrium, close to the septum. (c) Atypical left atrial flutter patient confirmed by cardiac mapping. EWI isochrones also show early activation is initiated in the left atrium. (d) CARTO map of a left-sided flutter case.

composition in the clinic remains a remarkable challenge with no real consensus and no non-invasive modalities, as MRI, CT, and ultrasound currently fall short for different reasons [89]. In addition, approximately 795 000 people in the United States suffer new strokes every year [1]. About 20–30% of new strokes are attributed to atherosclerotic carotid artery disease, i.e. approximately 200 000 per year [90]. Atherosclerotic plaques are characterized by a focal accumulation of lipids, complex carbohydrates, blood cells, fibrous tissues, and calcified deposits [91]. Currently, despite major advances in the treatment of atherosclerosis, a large percentage of individuals with the disease die without any prior symptoms [92].

14.3.2 Stroke and Plaque Stiffness

The development of carotid plaques has been generally associated with local changes in the vascular mechanical properties [91]. However, none of the aforementioned modalities provide

any mechanical property information. Biomechanical studies have been conducted to assess lesion morphology while the tissue properties are related to the tissue stresses and the vulnerability of the plaque. For example, using 2D finite element analysis (FEA), the presence of a lipid pool has been shown to increase the tissue stress in the overlying fibrous cap compared to a fibrous core [93]. Based on the assumption that decreasing the cap thickness could increase the risk of rupture [94], the effect of the cap thickness was investigated experimentally. A criterion was thus proposed with caps smaller than 65 μm prone to rupture in coronaries [95, 96], while in carotids this critical cap thickness was found to be higher (200 μm) [97]. However, it has been observed that thicker caps can also rupture, the rupture can occur at stresses lower than the predicted threshold of 300 kPa, and the ruptures frequently do not coincide with the location of peak circumferential stress [98]. Therefore, additional parameters are warranted as determinants of plaque rupture in addition to the cap thickness [99]. A large histological study has evidenced that the composition of the plaque is correlated to the vulnerability [97]. Furthermore, Lee et al [100] demonstrated the radial Young's modulus of different types of plaques, non-fibrous (41.2 ± 18.8 kPa), fibrous (81.7 ± 33.2 kPa), and calcified (354.5 ± 245.4 kPa), showing thus that stable (mainly calcified) plaques can be differentiated from unstable (mainly lipid or fibro-fatty) plaques based on the plaque mechanical properties. Increased arterial stiffness has also been previously reported in stroke patients [101] and in patients with myocardial infarction [102, 103]. In addition, it has been widely accepted that atherosclerotic arterial segments are characterized by marked stiffening [104]. Clinical observations show that the formation, expansion, and rupture phases of a vessel are each associated with changes in arterial stiffness, mainly driven by elastin and collagen degradation [105]. However, there is currently no medical imaging technique in the clinic that can reliably map the stiffness in carotid walls [106].

14.3.3 Abdominal Aortic Aneurysms

Vascular stiffening happens naturally with aging. The elastin components of the blood vessel wall are gradually reduced and the collagen that remains leads to overall hardening of the arteries. One of the results of vascular aging is also a higher probability of developing an abdominal aortic aneurysm (AAA), which is a focal, balloon-like dilation of the terminal aortic segment that occurs gradually over a span of years. This condition is growing in prevalence in the elderly population, with approximately 150 000 new cases being diagnosed every year [107, 108]. An AAA may rupture if it is not treated, and this is ranked as the 13th most common cause of death in the US and the most common aneurysm type [109]. Current AAA repair procedures are expensive and carry significant morbidity and mortality risks [110–116]. Despite the advent of sophisticated imaging techniques over the last three decades, none of the available imaging techniques is entirely satisfactory for detection and monitoring of this often silent and deadly disease. The most standard diagnostic technique is abdominal ultrasound or CT imaging. In both cases, images of the abdominal aorta are obtained and the aneurysm is measured. If its transverse diameter is found to be higher than 5.5 cm, the chance of aneurysm rupture increases by 10–20% within a year [117] and the patient typically has to undergo surgery to remove the aneurysm. If left untreated, more than 30% of the aneurysms will rupture and the patient will die as a result. There are, therefore, two main emergent problems that the current clinical diagnostic practice cannot resolve. First, most AAAs are asymptomatic and, therefore, rupture can occur without a warning. This warrants an effective screening technique, especially since family history is such a strong risk factor. Second, despite the fact that since an AAA diameter increase beyond 5.5 cm correlates with only 10–20% chance of aneurysm rupture, it is the currently the only criterion used for AAA surgery. The obvious difficulty is that a large number of patients are exposed to the risks of surgery or endovascular intervention, but their AAAs might never

rupture. Autopsy studies have shown that small AAAs can rupture [118, 119], while some of those considered large will not rupture [120], given the life expectancy of the patient [121]. In the study by Darling et al. [121], they found 473 non-resected AAAs, of which 118 were ruptured. Nearly 13% of AAA 5 cm in diameter or smaller ruptured, and 60% of the aneurysms greater than 5 cm in diameter (including 54% of those within 7.1 and 10 cm) never ruptured.

14.3.4 Pulse Wave Velocity (PWV)

Several techniques have been proposed for non-invasive measurement of the global PWV [122–127].

Hoctor et al. [128] defined PWV as the speed at which the arterial pulse propagates throughout the entire circulation tree, and which is directly linked to stiffness or Young's modulus through the Moens-Korteweg (MK) equation. In fact, the global PWV is widely considered as a surrogate to arterial stiffness and as a reliable indicator of cardiovascular mortality and morbidity in the case of hypertension [129]. Given that the two sites of measurement between which the time delay in the foot or peak of the wave is estimated, are typically several centimeters apart, the accuracy of the PWV measurement suffers from poor specificity and large measurement errors [63]. Despite its shortcomings, PWV is considered the gold standard for hypertension management and has been adopted by the European Society of Hypertension and the European Society of Cardiology [129].

14.3.5 Pulse Wave Imaging

Pulse wave imaging (PWI) (Figure 14.19) is an ultrasound-based method of imaging the pulse wave induced displacement on the vascular wall during end-systole at very high frame rates (>500 fps). As a result, unlike in alternative techniques, the pulse wave propagation (>1 m/s) can be sufficiently sampled and depicted as well as characterized. This entails the steps of: (i) acquiring sequential RF frames at high frame rates; (ii) estimating the wall displacement using 1D cross-correlation on RF frames and qualitatively imaging the pulse wave induced displacement (e.g. in red along the anterior wall) propagation; (iii) segmenting the vascular wall and automatically tracking it [27] for diameter measurements over time along the entire vessel segment; (iv) generating a spatio-temporal plot that depicts the axial/radial wall velocity, equal to the displacement normalized by the frame rate (to standardize with respect to the latter) over time, identifying the 50% upstroke of the wall velocity and performing linear regression for regional pulse wave velocity (PWV) estimation of the entire vessel segment; (v) performing piecewise regression for detailed PWV mapping; and (vi) generating the PWV and stiffness maps overlaid onto the B-mode images. The wall stiffness, or Young's modulus (E), is calculated in each vessel segment based on the regional PWV value.

PWI is thus a localized PWV and stiffness mapping modality that is highly suitable in characterizing focal disease such as plaques before the onset of pathology (normal, thin wall) to its later stages. The parameters mapped with PWI are the PWV (Figure 14.19d), r^2 (coefficient of determination; Figure 14.19c), and compliance (Figure 14.19e), which indicate the magnitude of the velocity of the pulse wave, its uniformity of propagation, and the underlying stiffness, respectively, all of which can be mapped and used as biomarkers that are highly complementary to the ultrasound and CT scan clinical standards.

14.3.6 Methods

In order to accommodate both current clinical ultrasound practice but also ongoing methodologies developed by our group, a new PWI system was developed that optimized parameters

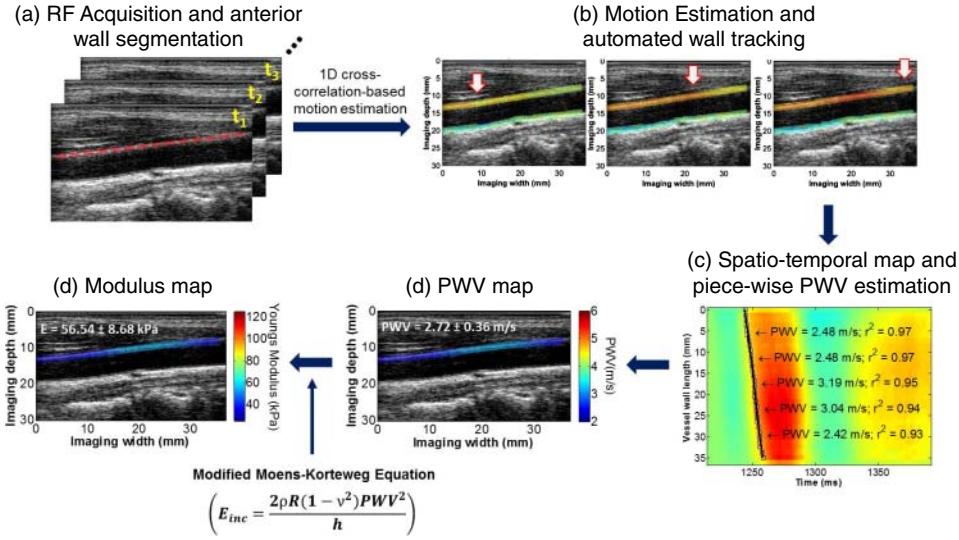

Figure 14.19 Block diagram of the pulse wave imaging (PWI) technique on a normal carotid artery in vivo. (a) RF frame sequence and ciné-loop of RF frames. (b) PWI ciné-loop and frames: Pulse waves induce upward wall displacement along the anterior wall. The white arrows indicate the propagation of the wavefront along the anterior wall. (c) Spatiotemporal map of the pulse wave induced displacement along the vessel length and time with a single PWV value given in the entire segment imaged. (e) PWV and (f) stiffness maps overlaid on the anterior wall of the B-mode.

such as beam density and frame rate. New PWI methodologies, such as those described below, are applied in phantom studies. The high frame rates facilitated by plane wave imaging allowed us to apply the following techniques that significantly enhance the quality and performance.

14.3.6.1 PWI System using Parallel Beamforming

An open-architecture system (Vantage, Verasonics, Redmond, WA) allows for software-based beamforming for simultaneous high frame rate and high beam density. Similar to others in the field, we have found that the performance of speckle tracking is not compromised when such systems are used, based on the advantages of differential, phase-based measurements (as opposed to amplitude-based approaches) [23, 32]. The acoustic exposure is on the same level as that of a standard ultrasound scanner. We have implemented such a sequence [32] that excites the transducer elements with specific delays, allowing a large field of view and then uses the delay-and-sum method to reconstruct the RF signals from the channel data. The associated frame rate is only limited by the depth and speed of sound. As a result, the system can obtain up to 8333 fps. Both conventional (with lower beam density to increase the frame rate) and parallel beamforming sequences are used with the same system for the purpose of this study. Because of the parallel beamforming used, the highest beam density (128 beams) and frame rate (up to 8333 fps) in PWI can simultaneously be achieved. The transducers to be used are the 128-element linear array at a center frequency of 5.5 MHz (L7-4 (4–7 MHz)) and the 128-element linear array at a center frequency of 17.5 MHz (L22-15 (15–22 MHz)) for higher spatial resolution allowing us to characterize composition and determine vulnerable plaques. We will determine the effect of lower spatial resolution and SNR associated with plane wave imaging on PWV and stiffness estimates with PWI.

- Automated diameter and wall thickness algorithms have also been implemented, similar to the segmentation and tracking methods our group has already developed [27].

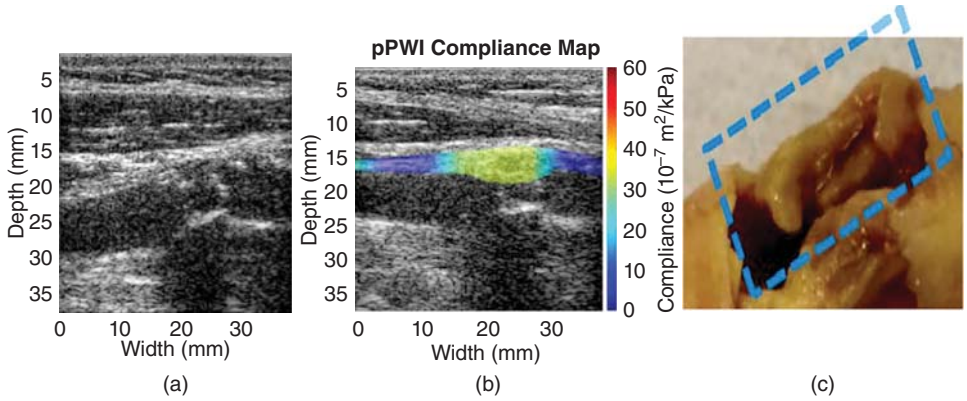

Figure 14.20 PWI in a vulnerable plaque with a fibrous cap (male, age 75). (a) Ultrasound B-mode image only of the detected plaque. (b) PWI: B-mode with overlaid PWI compliance map. (c) Gross pathology of the plaque with lipid core following endarterectomy. The B-mode in part (a) provides information on the level of stenosis but not the stiffness of the plaque, like PWI in part (b). PWI was capable of mapping plaque stiffness across its thickness to identify a mostly lipid plaque (low stiffness, i.e. high compliance) confirmed by (c) pathology [138].

- PWV mapping – our fast 1D normalized cross-correlation method is applied on the consecutively acquired RF signals to estimate the normalized wall displacement (Figure 14.19), as in our previously published studies [27, 28]. In order to obtain the regional PWV, all of the 50% upstroke points of the spatio-temporal plots are divided into overlapping segments. 50% upstroke was determined to yield highest SNR for PWV estimation in both human aortas and carotids [130]. Fixed regression windows have been used thus far to perform linear regression for PWV estimation, especially due to the low beam density afforded by conventional beamforming techniques. A piecewise, linear regression fit has thus been developed. Sub-regional PWVs are estimated within 2–4 mm segments along the length of the arterial wall and estimates the regional stiffness using the methodology described previously. Instead of single values for the entire vessel, this method provides maps of PWV along the entire wall imaged (Figure 14.19) but also within the plaque itself (Figure 14.20).
- Automated PWV estimation – a dynamic programming algorithm is implemented to automatically select the size, location, and number of windows according to a mean r^2 optimization routine with criteria based on the performance of the resulting linear regression. More specifically, the windows are appropriately selected to satisfy the maximization criterion:

$$\max_{\mathrm{NW},\mathrm{SW}_i,\mathrm{PW}_i} \frac{1}{\mathrm{NW}} \left(\sum_{i=1}^{\mathrm{NW}} {r_i}^2 \right) \max_{\mathrm{NW},\mathrm{SW}_i,\mathrm{PW}_i} \frac{1}{\mathrm{NW}} \cdot \left(\sum_{i=1}^{\mathrm{NW}} {r_i}^2 \right) \tag{14.5}$$

  where NW is the number of windows used to model the stiffness of the imaged arterial wall, SW_i is the size of the i-th window (namely the number of markers that it contains). and PW_i is its position (namely the number of the starting marker).
- Stiffness/compliance mapping – the 1D system of the coupled governing pulse wave propagation is

$$\frac{\mathrm{d}A}{\mathrm{d}t} + \frac{\mathrm{d}}{\mathrm{d}x}(uA) = 0 \tag{14.6}$$

  and

$$\frac{\mathrm{d}u}{\mathrm{d}t} + u\frac{\mathrm{d}u}{\mathrm{d}x} + \frac{1}{\rho}\frac{\mathrm{d}P}{\mathrm{d}x} + K_{\mathrm{R}}u = 0 \tag{14.7}$$

  where u is the fluid velocity, P is the pressure, A is the cross-sectional area, ρ the fluid density, and K_{R} is the resistance per unit length. The relationship between the PWV and vessel

stiffness is derived by assuming a pressure–area relationship. Commonly, a thin-walled cylindrical elastic vessel is assumed, so that the wall displacement

$$\Delta r = \frac{r^2(1-\nu^2)}{Eh}\Delta P \tag{14.8}$$

for a pressure increment ΔP in a vessel of Young's modulus E, Poisson's ratio ν, radius r, and thickness h, which gives the well-known Moens-Korteweg equation. In this study of carotid plaques, cylindrical geometry cannot be reasonably assumed, so we use a generalized linear pressure–area relationship, which is valid for non-circular cross-sections

$$\Delta A = k_p \Delta P \tag{14.9}$$

The compliance, k_p, is related to the PWV through the Bramwell-Hill equation [131, 132], i.e.

$$k_p = \frac{\pi r^2}{4\rho(\mathrm{PWV})^2}; \quad \mathrm{PWV} = \sqrt{\frac{A}{\rho k_p}} \tag{14.10}$$

and can be related to the effective Young's modulus as follows

$$E_{\mathrm{eff}} = \frac{2\pi r^3(1-\nu^2)}{k_p h} \tag{14.11}$$

that shows that compliance and stiffness are inversely proportional for a given geometry [133]. As a result, as a first approximation, the longitudinal distribution of k_p can be computed by a regional PWV estimation map without homogeneity or symmetry assumptions (Figure 14.19e).

14.3.6.2 Coherent Compounding

A coherent compounding technique can be applied to determine an increase in SNR when parallel beamforming is applied. Plane waves are electronically steered and transmitted 1-, 3-, 5-, 9- and 12-plane-waves and the resulting RF frames are combined into a compounded image [134]. The received radiofrequency (RF) frames are reconstructed by applying a delay-and-sum method on GPU-based parallel computing to accelerate reconstruction processing [32]. In preliminary studies, we have found that compounding in human carotids in vivo decreases the frame rate from 8333 fps to 2273 fps, which remains sufficiently high for PWI (Figure 14.21) while SNR increases by 5-fold using the framework described here (Figure 14.21a).

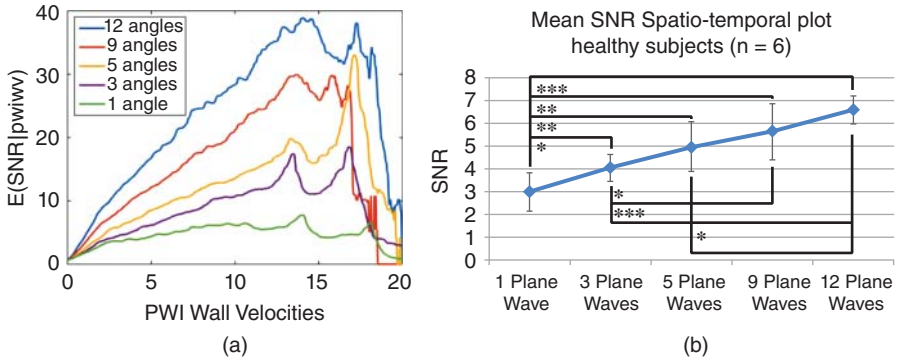

Figure 14.21 $E(\mathrm{SNR}_d|\delta)$ increase with number of angles in coherent compounding in (a) phantoms and (b) in vivo humans.

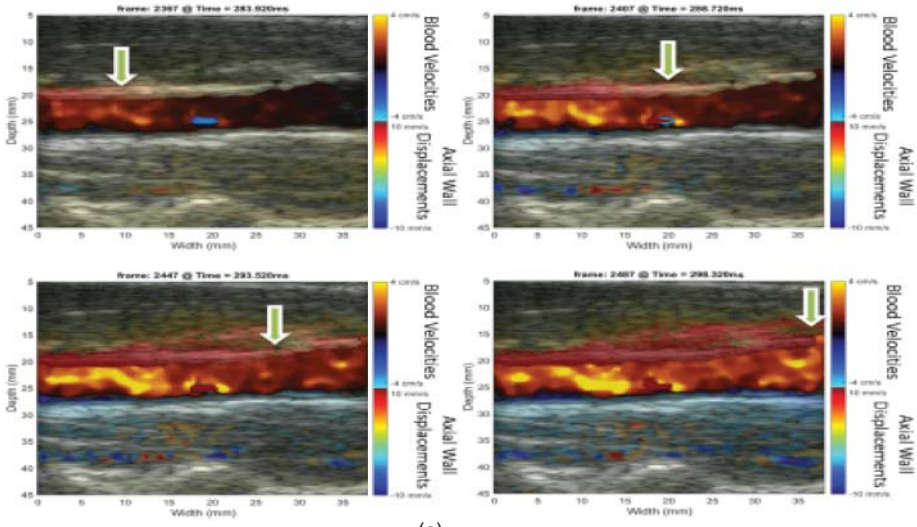

(a)

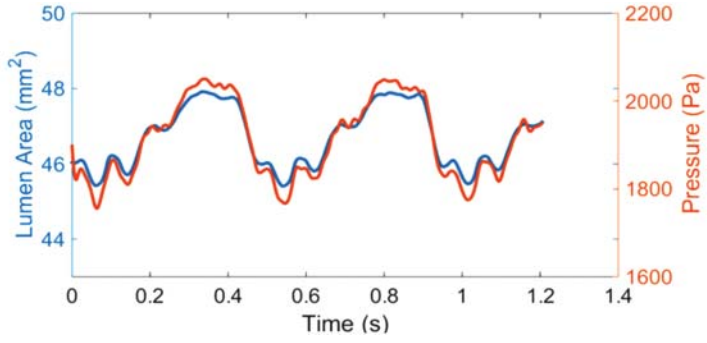

(b)

Figure 14.22 (a) PWI frames with Doppler flow; (b) pressure/displacement curves revealing the phase lag amount and thus viscoelasticity of the vessel (phantom). The dark curve denotes the pressure, the lighter the cumulative displacement, and the last curve shows these two overlaid.

14.3.6.3 Flow Measurement

A 2D autocorrelation method is utilized [135] to generate color Doppler images (Figure 14.22a). A wall filter consisting of an FIR high-pass filter is used to only retain the blood velocities that are fused with the corresponding PWI frames. This allows us to determine the effect of the blood pressure wave on the pulse wave propagation along the wall imaged on the PWI images as well as infer about the wall viscoelasticity (Figure 14.22b).

14.3.6.4 3D PWI

A 2D matrix array (Sonic Concepts, Inc., Bothell, WA) is used in this study with a total of 1024 elements (32 × 32) and a 4.5 MHz center frequency and will be used with the Verasonics Vantage system for the highest frame rate. A custom diverging beam sequence with a virtual focus placed behind the transducer face is implemented in order to interrogate the entire field of view in a single transmit sequence. Element data is acquired and reconstructed in a pixel-wise fashion. In sections of the common carotid prior to the bifurcation, inter-frame pulse wave induced axial displacements (not the full 3D vector) are mapped in 3D given the lower SNR

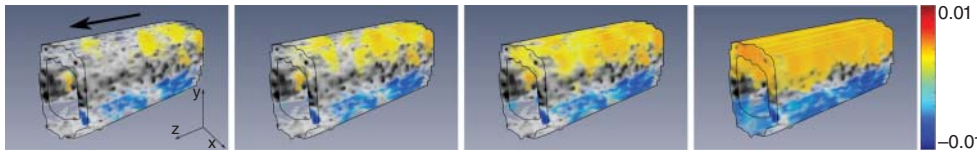

Figure 14.23 3D PWI frames with wave propagating from right to left in a human carotid in vivo on both the proximal (top) and distal (bottom) walls.

Table 14.1 Preliminary validation of PWV values in a PVA phantom and a silicone phantom (with soft and stiff layers). The static PWV is a mechanical testing method. PVA: poly-vinyl alcohol.

Material	Static PWV estimates (m/s)	PWI-derived PWV values (m/s)
Phantom 1, PVA	1.57	1.53
Phantom 2, soft	2.31	1.86
Phantom 2, stiff	2.87	2.86

in lateral and elevational displacement estimations. Bicubic Hermite interpolation is implemented to render the vessel in 3D, which provides better visualization of the complex anatomy and motion of non-axisymmetric plaques. The frame rate is expected to similar to 2D, i.e. up to 5500 fps, and sufficient to visualize the pulse wave and estimate the PWI parameters. 3D B-mode feasibility and strain imaging are shown in Figure 14.23 [136].

14.3.7 PWI Performance Assessment in Experimental Phantoms

In order to ensure highest quality PWI in vivo, its performance is optimized in phantoms prior to application in vivo. Parallel beamforming provides images with reduced sonographic SNR; however, this issue has been addressed with coherent compounding. This is at the cost, however, of frame rate. Thus, by varying the number of angled plane wave acquisitions this tradeoff between frame rate and image SNR can be fine tuned and adjusted to the requirements of the application. This is verified in PVA cryogel [130] and silicone [133] phantoms with preliminary results shown in Table 14.1. Carotid artery phantoms with a plaque-mimicking inclusion are constructed from a mixture (w/w) of 87% deionized water, 10% polyvinyl alcohol (PVA) with a molecular weight of 56.140 g/mol (Sigma-Aldrich, St. Louis, MO, USA), and 3% graphite powder with particle size < 50 μm (Merck KGaA) [137].

A peristaltic pump (Manostat Varistaltic, Barrington, IL) operating at 2 Hz is used. The parameters to be studied for optimizing the PWI performance are: (i) frame rate; (ii) number of transmitted plane waves (coherent compounding); (iii) motion estimation rate (MER); and (iv) size of kernel in piecewise PWI (pPWI) (PWV is estimated within these kernels). A probabilistic framework has been developed by our group in order to compare the strain estimation quality between conventional and parallel beamforming [23, 32]. The signal-to-noise-ratio of the displacement (SNR_d) is calculated for each sequence over the phase of systole. SNR_e is computed for every point in an image within a small 2D ROI (3.0 × 3.2 mm). Since both strain and SNR_d are computed for each point in the vessel, a large number (>600 000) of displacement–SNR_d pairs are generated for each sequence [23]. The conditional expected values of SNR_d for each strain are calculated using $E(SNR_d|\delta)$ curves generated for each sequence, which allows for a relatively easy comparison to be performed between different

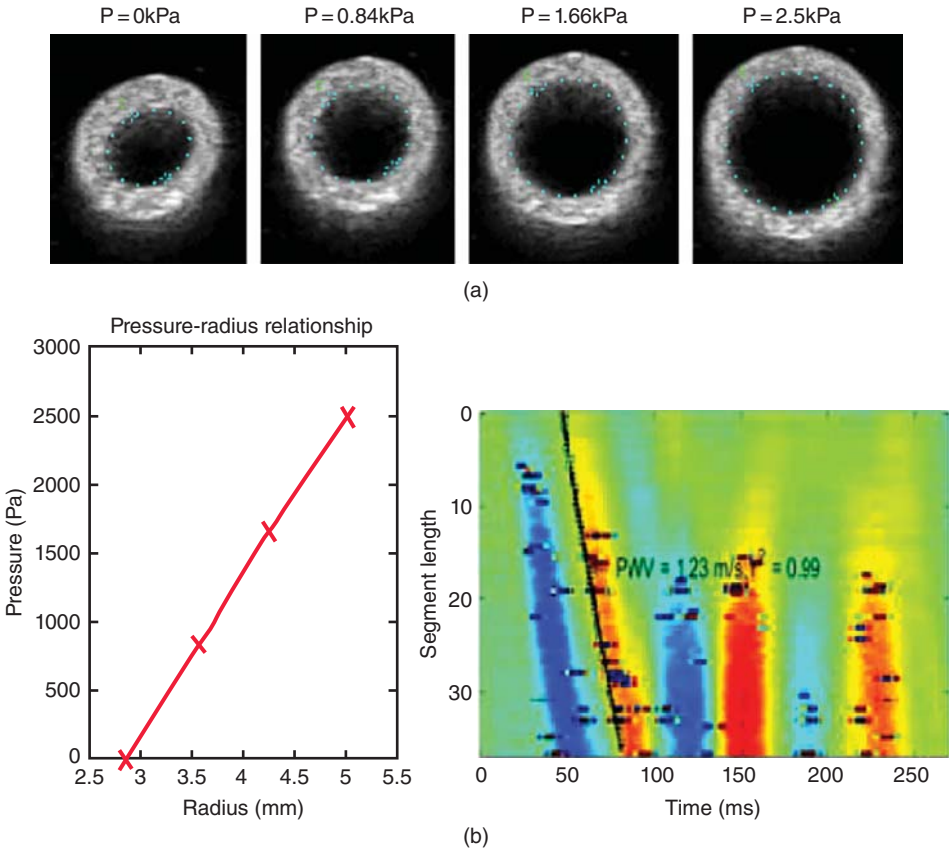

Figure 14.24 (a) Static estimation of the PWV (Eq. 14.13) from a vessel phantom compared with PWI showing the B-mode of a phantom at different static pressures. (b) Measurements in phantom with PWI and static expansion test, respectively.

sequences for a wide range of strain values. Examples of $E(SNR_d|\delta)$ curves for displacement estimation are provided in Figure 14.21a. The SNR_d of both 2D PWI and 3D PWI are computed.

14.3.8 Mechanical Testing

Three types of mechanical testing are performed to validate our in vivo PWI findings. First, in order to preserve the geometry of the sample and reproduce the in vivo pre-stretch, effect of surrounding tissue, and loading conditions, the entire sample is kept intact and inflated at static pressures (Figure 14.24). The compliance

$$k_p = \frac{dA}{dP} \tag{14.12}$$

can be measured experimentally by applying this static pressure and measuring the diameter change on the B-mode images. The PWV can then be estimated by

$$\text{PWV} = \sqrt{\frac{k_p r}{2\rho}} \tag{14.13}$$

A phantom example showing good agreement between the PWV estimated through static testing and PWI is shown in Table 14.1.

14.3.9 PWI in Aortic Aneurysms and Carotid Plaques in Human Subjects In Vivo

The clinical potential of PWI to provide complementary information on the mechanical properties of vessels in order to help stage disease and inform treatment are assessed. Therefore, the underlying hypothesis of this study is that imaging the regional pulse wave propagation at high temporal resolution is sufficient to determine regional elastic vessel wall properties and thus localize and characterize focal vascular disease at its very early stages, i.e. before changes in aortic diameter or other anatomical changes may occur or become detectable. It is also hypothesized that the regional stiffness changes will unveil the regions most susceptible to wall rupture.

14.3.9.1 Abdominal Aortic Aneurysms

The clinical feasibility of PWI was evaluated in normal and aneurysmal human aortas. PWI was performed in normal ($N = 15$, mean age 32.5 years ± 10.2), and aneurysmal ($N = 5$, mean age 71.6 years ± 11.8) human subjects (Figure 14.25) [138]. The PWV of the AAA aortas was significantly higher ($p < 0.001$) compared to that of the other two groups. The average r^2 in the AAA subjects was significantly lower ($p < 0.001$) than that in the normal subjects, very similar to what was shown in mice.

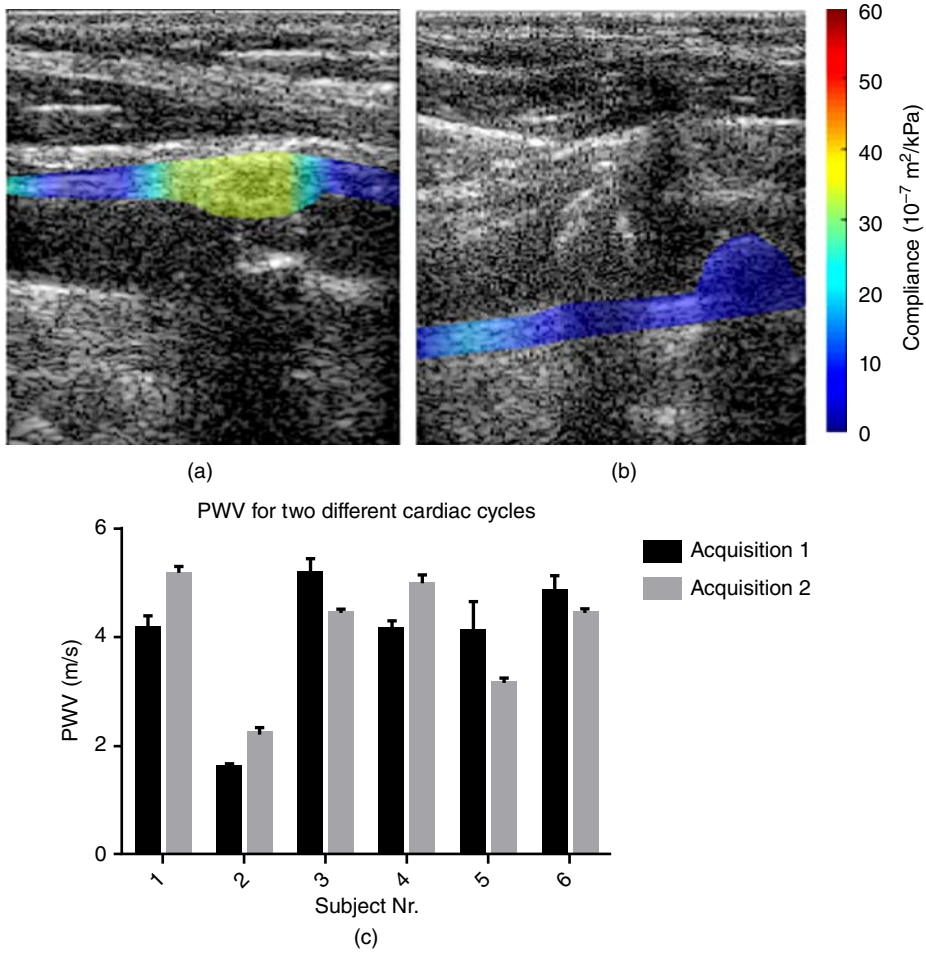

Figure 14.25 PWI compliance maps in human carotids in vivo: (a) lipid plaque (male, aged 75); (b) calcified plaque (female, aged 78); and (c) PWI reproducibility in 6 normal subjects and different acquisitions.

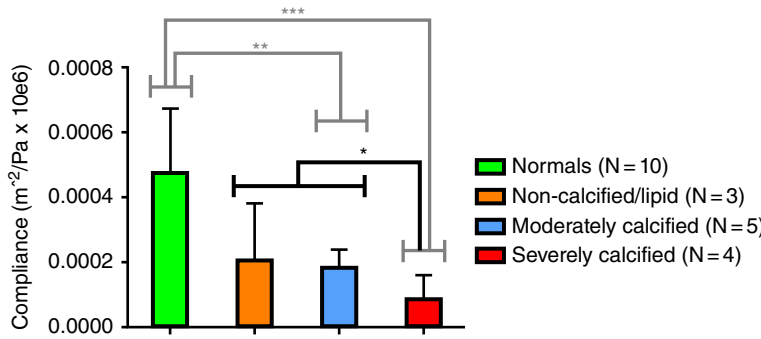

Figure 14.26 Preliminary compliance findings across 10 normal and 12 atherosclerotic carotids confirmed with endarterectomy and/or CT. * $p < 0.05$; ** $p < 0.01$; *** $p < 0.001$.

14.3.9.2 Carotid Plaques

The feasibility of PWI in normal [139] and atherosclerotic (Figure 14.20) common carotid arteries has been demonstrated in vivo. The pulse wave velocity (PWV) in eight ($N = 8$) normals varied between 4.0 and 5.2 m/s with high propagation uniformity ($r^2 > 0.90$) with excellent reproducibility (Figures 14.25 and 14.26).

Acknowledgements

The results presented here were produced by current and previous members of the Ultrasound and Elasticity Imaging Laboratory: Iason Apostolakis, PhD; Ethan Bunting, PhD; Alexandre Costet, PhD; Julien Grondin, PhD; Wei-Ning Lee, PhD; Ronny Li, PhD; Pierre Nauleau, PhD; and Jean Provost, PhD. The studies were in part supported by grants from the National Institutes of Health: R01 EB006042, R01 HL098830, and R01 HL 114358.

References

1 Go, A.S., Mozaffarian, D., Roger, V.L. et al. (2014). Heart disease and stroke statistics – 2014 Update: A report From the American Heart Association. *Circulation* 129: e28–e292.
2 Haga, J.H., Beaudoin, A.J., White, J.G., and Strony, J. (1998). Quantification of the passive mechanical properties of the resting platelet. *Ann. Biomed. Eng.* 26: 268–277.
3 Bertrand, M.E., Rousseau, M.F., Lefebvre, J.M., et al. (1978). Left-ventricular compliance in acute transmural myocardial-infarction in man. *Eur. J. Cardiol.* 7: 179–193.
4 Neagoe, C., Kulke, M., del Monte, F., et al. (2002). Titin isoform switch in ischemic human heart disease. *Circulation* 106 (11): 1333–1341.
5 Edwards, C.H., Rankin, J. S., Mchale, P.A., et al. (1981). Effects of ischemia on left-ventricular regional function in the conscious dog. *Am. J. Physiol.* 240 (3): H413–H420.
6 Amano, J., Thomas, J.X., Lavallee, M., et al. (1987). Effects of myocardial-ischemia on regional function and stiffness in conscious dogs. *Am. J. Physiol.* 252 (1): H110–H117.
7 Varma, N., Eberli, F.R., and Apstein, C.S. (2000). Increased diastolic chamber stiffness during demand ischemia – Response to quick length change differentiates rigor-activated from calcium-activated tension. *Circulation* 101 (18): 2185–2192.

8 Varma, N., Eberl, F.R. and Apstein, C.S. (2001). Left ventricular diastolic dysfunction during demand ischemia: Rigor underlies increased stiffness without calcium-mediated tension. Amelioration by glycolytic substrate. *J. Am. Coll. Cardiol.* 37 (8): 2144–2153.

9 Gupta, K.B., Ratcliffe, M.B., Fallert, M.A., et al. (1994). Changes in passive mechanical stiffness of myocardial tissue with aneurysm formation. *Circulation* 89: 2315–2326.

10 Holmes, J.W., Borg, T.K., and Covell, J.W. (2005). Structure and mechanics of healing myocardial infarcts. *Annu. Rev. Biomed. Eng.* 7: 223–253.

11 Konofagou, E., D'hooge, J., and Ophir, J. (2000). Cardiac elastography – A feasibility study. *Proc. IEEE Ultrason. Symp.* 1273–1276.

12 Konofagou, E.E., Harrigan, T., and Solomon, S. (2001). Assessment of regional myocardial strain using cardiac elastography: distinguishing infarcted from non-infarcted myocardium. *Proc. IEEE Ultrason. Symp.* 1589–1592.

13 Konofagou, E.E., D'Hooge, J., and Ophir, J. (2002). Myocardial elastography – A feasibility study in vivo. *Ultrasound Med. Biol.* 28: 475–482.

14 Konofagou, E.E., Manning, W., Kissinger, K., and Solomon, S.D. (2003). Myocardial elastography – Comparison to results using MR cardiac tagging. *Proc. IEEE Ultrason. Symp.* 130–133.

15 Konofagou, E.E., Fung-Kee-Fung, S., Luo, J., and Pernot, M. (2006). Imaging the mechanics and electromechanics of the heart. *Proc. IEEE EMBS Conf.* 6648–6651.

16 Konofagou, E.E., Luo, J., Fujikura, K., et al. (2006). Imaging the electromechanical wave activation of the left ventricle in vivo. *Proc. IEEE Ultrason. Symp.* 985–988.

17 Konofagou, E.E., Lee, W.-N., and Luo, J. (2008). Cardiovascular elasticity imaging. In: *Biomedical Applications of Vibration and Acoustics in Imaging and Characterizations* (ed. M. Fatemi, A. Al-Jumaily). Chapter 6: 93–117. New York, NY: ASME Press.

18 Konofagou, E.E. and Provost, J., (2012). Electromechanical wave imaging for noninvasive mapping of the 3D electrical activation sequence in canines and humans in vivo. *J. Biomech.* 45(5): 856–864.

19 Konofagou, E. and Ophir, J. (1998). A new elastographic method for estimation and imaging of lateral displacements, lateral strains, corrected axial strains and Poisson's ratios in tissues. *Ultrasound Med. Biol.* 24: 1183–1199.

20 Provost, J., Lee, W.N., Fujikura, K., Konofagou, E.E. (2010). Electromechanical wave imaging of normal and ischemic hearts in vivo. *IEEE Trans. Med. Imaging* 29 (3): 625–35.

21 Lee, W.N., Provost, J., Fujikura, K., et al. (2011). In vivo study of myocardial elastography under graded ischemia conditions. *Phys. Med. Biol.* 56 (4): 1155–72.

22 Konofagou, E.E. and Provost, J. (2012). Electromechanical wave imaging for noninvasive mapping of the 3D electrical activation sequence in canines and humans in vivo. *J. Biomech.* 45 (5): 856–864.

23 Bunting, E., Provost, J., and Konofagou, E.E. (2014). Performance analysis of two-dimensional cardiac strain estimation using novel sequences, different beamforming and temporal resolution in vivo. *Phys. Med. Biol.* 59 (22): 6841–6858.

24 Konofagou, E.E. (1999). *Estimation and Imaging of Three-dimensional Motion and Poisson's Ratio in Elastography*. Ph.D. dissertation, University of Houston, TX.

25 Zervantonakis, I.K., Fung-Kee-Fung, S.D., Lee, W.N., and Konofagou, E.E. (2007). A novel, view-independent method for strain mapping in myocardial elastography: eliminating angle and centroid dependence. *Phys. Med. Biol.* 52: 4063–4080.

26 Lee, W.N. and Konofagou, E.E. (2008). Angle-independent and multi-dimensional myocardial elastography – From theory to clinical validation. *Ultrasonics* 48: 563–567.

27 Luo, J. and Konofagou, E. (2010). A fast normalized cross-correlation calculation method for motion estimation. *IEEE Trans. Ultrason., Ferroelect., Freq. Control* 57 (6): 1347–1357.

28 Luo J., Lee, W.-N., and Konofagou, E.E. (2009). Fundamental performance assessment of 2-D myocardial elastography in a phased array configuration. *IEEE Trans. Ultrason., Ferroelect., Freq. Control* 56 (10): 2620–2627.

29 Righetti, R., Ophir, J., and Ktonas, P. (2002). Axial resolution in elastography. *Ultrasound Med. Biol.* 28 (1): 101–113.

30 Lee, W.N., Ingrassia, C.M., Fung-Kee-Fung, S.D., et al. (2007). Theoretical quality assessment of myocardial elastography with in vivo validation. *IEEE Trans. Ultrason., Ferroelect., Freq. Control* 54: 2233–2245.

31 Kallel, F. and Ophir, J. (1997). A least-squares strain estimator for elastography. *Ultrason. Imaging* 19: 195–208.

32 Provost, J. Thiebault, S., Luo, J. and Konofagou, E.E. (2012). Single-heartbeat electromechanical wave imaging with optimal strain estimation using temporally-unequispaced acquisition sequences. *Phys. Med. Biol.* 57 (4): 1095–1112.

33 Jensen, J.A. and Svendsen, N.B. (1992). Calculation of pressure fields from arbitrarily shaped, apodized, and excited ultrasound transducers. *IEEE Trans. Ultrason., Ferroelect., Freq. Control* 39: 262–267.

34 Jensen, J.A. (1996). Field: a program for simulating ultrasound systems. Paper presented at the 10th Nordic-Baltic Conference on Biomedical Imaging. *Med. Biol. Eng. Comput.* 34: 1351–1353.

35 Luo, J. and Konofagou, E.E. (2008). High-frame rate, full-view myocardial elastography with automated contour tracking in murine left ventricles in vivo. *IEEE Trans. Ultrason., Ferroelect., Freq. Control* 55: 240–248.

36 Lloyd-Jones, D., Adams, R., Carnethon, M. et al. (2009). Heart disease and stroke statistics – 2009 update: a report from the American Heart Association Statistics Committee and Stroke Statistics Subcommittee. *Circulation* 119 (3): e21–181.

37 Haïssaguerre, M., Jaïs, P., Shah, D.C., et al. (1998). Spontaneous initiation of atrial fibrillation by ectopic beats originating in the pulmonary veins. *N. Engl. J. Med.* 339: 659–666.

38 Ashikaga, H., Coppola, B.A., Hopenfeld, B., et al. (2007). Transmural dispersion of myofiber mechanics: implications for electrical heterogeneity in vivo. *J. Am. Coll. Cardiol.* 49: 909–916.

39 Cordeiro, J.M., Greene, L., Heilmann, C., et al. (2004). Transmural heterogeneity of calcium activity and mechanical function in the canine left ventricle. *Am. J. Physiol. Heart Circ. Physiol.* 286: H1471–1479.

40 Pernot, M. and Konofagou, E.E. (2005). Electromechanical imaging of the myocardium at normal and pathological states. *Proc. IEEE Ultrason. Symp.* 2005: 1091–1094.

41 Konofagou, E.E., Lee, W.-N., and Fung-Kee-Fung, S.D. (2007). Angle-independent myocardial elastography: Theoretical analysis and clinical validation. *Proc. SPIE*, 6513: 65130G-1–65130G-10.

42 Konofagou, E.E., Luo, J., Saluja, D., et al. (2007). Noninvasive electromechanical wave imaging and conduction velocity estimation in vivo. *Proc. IEEE Ultrason. Symp.* 2007: 969–972.

43 Konofagou, E.E., Luo, J., Saluja, D., et al. (2010). Noninvasive electromechanical wave imaging and conduction-relevant velocity estimation in vivo. *Ultrasonics* 50: 208–215.

44 Konofagou, E.E., Lee, W.-N., Luo, J., et al. (2011). Physiologic cardiovascular strain and intrinsic wave imaging, *Annu. Rev. Biomed. Eng.* 13: 477–505.

45 Wang, S.G., Lee, W.N., Provost, J. et al. (2008). A composite high-frame-rate system for clinical cardiovascular imaging. *IEEE Trans. Ultrason., Ferroelect., Freq. Control* 55: 2221–2233.

46 Provost, J., Gurev, V., Trayanova, N., and Konofagou, E.E. (2011). Mapping of cardiac electrical activation with electromechanical wave imaging: an in silico-in vivo reciprocity study. *Heart Rhythm* 8 (5): 752–759.

47 Provost, J., Nguyen, V.T., Legrand, D., et al. (2011). Electromechanical wave imaging for arrhythmias. *Phys. Med. Biol.* 56 (22): L1–11.

48 Provost, J., Lee, W.-N., Fujikura, K., and Konofagou E.E. (2011). Imaging the electromechanical activity of the heart in vivo, *Proc. Natl. Acad. Sci.* 108 (21): 8565–8570.

49 Gurev, V., Constantino, J., Rice, J.J., and Trayanova, N.A.. (2010). Distribution of electromechanical delay in the heart: Insights from a three-dimensional electromechanical model. *Biophys. J.* 99 (3): 745–754.

50 Garan, H. (2008). Atypical atrial flutter. *Heart Rhythm* 5: 618–621.

51 Saoudi, N., Cosío, F., Waldo, A., et al. (2001). A classification of atrial flutter and regular atrial tachycardia according to electrophysiological mechanisms and anatomical bases. A statement from a Joint Expert Group from The Working Group of Arrhythmias of the European Society of Cardiology and the North American Society of Pacing and Electrophysiology. *Eur. Heart J.* 22: 1162–1182.

52 Bochoeyer, A., Yang, Y., Cheng, J., et al. (2003). Surface electrocardiographic characteristics of right and left atrial flutter. *Circulation* 108: 60–66.

53 Nash, M.P. and Pullan, A.J. (2005). Challenges facing validation of noninvasive electrical imaging of the heart. *Ann. Noninvasive Electrocardiol.* 10: 73–82.

54 Chattipakorn, N. and Ideker, R.E. (2003). The vortex at the apex of the left ventricle: A new twist to the story of the electrical induction of rotors? *J. Cardiovasc. Electrophysiol.* 14: 303–305.

55 Durrer, D., Van Dam, R.T., Freud, G.E., et al. (1970). Total excitation of the isolated human heart. *Circulation* 41: 899–912.

56 Sutherland, D.R., Ni, Q., MacLeod, R.S., et al. (2008). Experimental measures of ventricular activation and synchrony. *Pacing Clin. Electrophysiol.* 31: 1560–1570.

57 Kay, M.W., Amison, P.M., and Rogers, J.M. (2004). Three-dimensional surface reconstruction and panoramic optical mapping of large hearts. *IEEE Trans. Biomed. Eng.* 51: 1219–1229.

58 Qu, F., Ripplinger, C.M., Nikolski, V.P., et al. (2007). Three-dimensional panoramic imaging of cardiac arrhythmias in rabbit heart. *J. Biomed. Opt.* 12: 044019.

59 Ripplinger, C.M., Lou, Q., Li, W., et al. (2009). Panoramic imaging reveals basic mechanisms of induction and termination of ventricular tachycardia in rabbit heart with chronic infarction: implications for low-voltage cardioversion. *Heart Rhythm* 6: 87–97.

60 Hooks, D.A., LeGrice, I.J., Harvey, J.D., and Smaill, B.H. (2001). Intramural multisite recording of transmembrane potential in the heart. *Biophys. J.* 81: 2671–2680.

61 Hillman, E.M.C., Bernus, O., Pease, E., et al. (2007). Depth-resolved optical imaging of transmural electrical propagation in perfused heart. *Opt. Express* 15: 17827–17841.

62 Kong, W., Ideker, R.E., and Fast, V.G. (2009). Transmural optical measurements of V_m dynamics during long-duration ventricular fibrillation in canine hearts. *Heart Rhythm* 6: 796–802.

63 Zhang, X., Ramachandra, I., Liu, Z., et al. (2005). Noninvasive three-dimensional electrocardiographic imaging of ventricular activation sequence. *Am. J. Physiol. Heart Circ. Physiol.* 289: H2724–32.

64 Ramanathan, C., Ghanem, R.N., Jia, P., et al. (2004). Noninvasive electrocardiographic imaging for cardiac electrophysiology and arrhythmia. *Nat. Med.* 10: 422–428.

65 Ramanathan, C., Jia, P., Ghanem, R., et al. (2006). Activation and repolarization of the normal human heart under complete physiological conditions. *Proc. Natl. Acad. Sci.* 103: 6309–6314.

66 Schilling, R.J., Peters, N.S., and Davies, W. (1998). Simultaneous endocardial mapping in the human left ventricle using a noncontact catheter – Comparison of contact and reconstructed electrograms during sinus rhythm. *Circulation* 98: 887–898.

67 Tai, C.-T., Liu, T.-Y., Lee, P.-C., et al. (2004). Non-contact mapping to guide radiofrequency ablation of atypical right atrial flutter. *J. Am. Coll. Cardiol.* 44: 1080–1086.

68 Taccardi, B., Arisi, G., Macchi, E., et al. (1987). A new intracavitary probe for detecting the site of origin of ectopic ventricular beats during one cardiac cycle. *Circulation* 75: 272–281.

69 Wang, Y., Schuessler, R.B., Damiano, R.J., et al. (2007). Noninvasive electrocardiographic imaging (ECGI) of scar-related atypical atrial flutter. *Heart Rhythm* 4: 1565–1567.

70 Belgacem, F.B. (2007). Why is the Cauchy problem severely ill-posed? *Inverse Probl.* 23: 823–836.

71 Lux, R.L. (2008). Noninvasive assessment of cardiac electrophysiology for predicting arrhythmogenic risk: are we getting closer? *Circulation* 118: 899–900.

72 Olshansky, B. (2011). Electrocardiographic imaging: Back to the drawing board? *Heart Rhythm* 8: 700–701.

73 Badke, F.R., Boinay, P., and Covell, J.W. (1980). Effects of ventricular pacing on regional left ventricular performance in the dog. *Am. J. Physiol. Heart Circ. Physiol.* 238: H858–867.

74 Wyman, B.T., Hunter, W.C., Prinzen, F.W., and McVeigh, E.R. (1999). Mapping propagation of mechanical activation in the paced heart with MRI tagging. *Am. J. Physiol. Heart Circ. Physiol.* 276: H881–891.

75 Provost, J., Gambhir, A., Vest, J., et al. (2013). A clinical feasibility study of atrial and ventricular electromechanical wave imaging. *Heart Rhythm* 10 (6): 856–862.

76 Provost, J., Papadacci, C., Arango, J., et al. (2014). 3D ultrafast ultrasound imaging. *Phys. Med. Biol.* 59 (19): L1–L13.

77 Provost, J., Costet, A., Wan, E., et al. (2015). Assessing the atrial electromechanical coupling during atrial focal tachycardia, flutter, and fibrillation using electromechanical wave imaging in humans, *Comput. Biol. Med.* 65: 161–167.

78 Costet, A., Provost, J., Gambhir, A., et al. (2014). Electromechanical wave imaging of biologically and electrically paced canine hearts in vivo. *Ultrasound Med. Biol.* 40 (1): 177–187.

79 Costet, A., Bunting, E., Grondin, J., et al. (2015). Atrial electromechanical cycle length mapping in paced canine hearts in vivo. *IEEE Trans. Ultrason., Ferroelect., Freq. Control* 62 (7): 1277–1287.

80 Luo, J. and Konofagou, E.E. (2008). High-frame rate, full-view myocardial elastography with automated contour tracking in murine left ventricles in vivo. *IEEE Trans. Ultrason., Ferroelect., Freq. Control* 55: 240–248.

81 Baghani, A., Brant, A., Salcudean, S., and Rohling, R. (2010). A high-frame-rate ultrasound system for the study of tissue motions. *IEEE Trans. Ultrason., Ferroelect., Freq. Control* 57: 1535–1547.

82 Varghese, T. and Ophir, J. (1997). A theoretical framework for performance characterization of elastography: the strain filter. *IEEE Trans. Ultrason., Ferroelect., Freq. Control* 44: 164–172.

83 Weinstein, E. and Weiss, A. (1984). Fundamental limitations in passive time-delay estimation – Part II: Wide-band systems. *IEEE Trans. Acoust., Speech, Signal Process.* 32: 1064–1078.

84 Meunier, J. and Bertrand, M. (1995). Ultrasonic texture motion analysis: theory and simulation. *IEEE Trans. Med. Imaging* 14: 293–300.

85 Chen, J., Mandapati, R., Berenfeld, O., et al. (2000). High-frequency periodic sources underlie ventricular fibrillation in the isolated rabbit heart. *Circ. Res.* 86: 86–93.

86 Ciaccio, E., Biviano, A.B., Whang, W., et al. (2011) A new transform for the analysis of complex fractionated atrial electrograms. *BioMed. Eng. OnLine* 10: 35.

87 Nauleau, P., Melki, L., Wan, E., Konofagou, E. (2017). A 3-D rendering algorithm for electromechanical wave imaging of a beating heart. *Med. Phys.* 44 (9): 4766–4772.

88 Rosamond, W., Flegal, K., Friday, G., et al. (2007). American Heart Association Statistics C, Stroke Statistics S. Heart disease and stroke statistics – 2007 update: a report from the American Heart Association Statistics Committee and Stroke Statistics Subcommittee. *Circulation* 115 (5): e69–171.

89 Makris, G.C., Nicolaides, A.N., Xu, X.Y., Geroulakos, G. (2010). Introduction to the biomechanics of carotid plaque pathogenesis and rupture: review of the clinical evidence. *Br. J. Radiol.* 83 (993): 729–35.

90 Timsit, S.G., Sacco, R.L., Mohr, J.P., et al. (1992). Early clinical differentiation of cerebral infarction from severe atherosclerotic stenosis and cardioembolism. *Stroke* 23 (4): 486–491.

91 Maurice, R.L., Fromageau, J., Brusseau, E., et al. (2007). On the potential of the Lagrangian estimator for endovascular ultrasound elastography: in vivo human coronary artery study. *Ultrasound Med. Biol.* 33(8): 1199–205.

92 Naghavi, M., Libby, P., Falk, E., et al. (2003). From vulnerable plaque to vulnerable patient: a call for new definitions and risk assessment strategies: Part I. *Circulation* 108 (14): 1664–72.

93 Huang, H., Virmani, R., Younis, H., et al. (2001). The impact of calcification on the biomechanical stability of atherosclerotic plaques. *Circulation* 103 (8): 1051–1056.

94 Loree, H.M., Kamm, R.D., Stringfellow, R.G., Lee, R.T. (1992). Effects of fibrous cap thickness on peak circumferential stress in model atherosclerotic vessels. *Circulation Res.* 71 (4): 850–858.

95 Burke, A.P., Farb, A., Malcom, G.T., et al. (1997). Coronary risk factors and plaque morphology in men with coronary disease who died suddenly. *N. Engl. J. Med.* 336 (18): 1276–1282.

96 Virmani, R., Burke, A.P., Kolodgie, F.D., Farb, A. (2003). Pathology of the thin-cap fibroatheroma: a type of vulnerable plaque. *J. Interv. Cardiol. Electrophysiol.* 16 (3): 267–272.

97 Redgrave, J.N., Gallagher, P., Lovett, J.K., Rothwell, P.M. (2008). Critical cap thickness and rupture in symptomatic carotid plaques: the Oxford plaque study. *Stroke* 39 (6): 1722–1729.

98 Cheng, G.C., Loree, H.M., Kamm, R.D., et al. (1993). Distribution of circumferential stress in ruptured and stable atherosclerotic lesions. A structural analysis with histopathological correlation. *Circulation* 87 (4): 1179–1187.

99 Cardoso, L. and Weinbaum, S. (2014). Changing views of the biomechanics of vulnerable plaque rupture: a review. *Ann. Biomed. Eng.* 42 (2): 415–431.

100 Lee, R.T., Richardson, S.G., Loree, H.M., et al. (1992). Prediction of mechanical properties of human atherosclerotic tissue by high-frequency intravascular ultrasound imaging. An in vitro study. *Arterioscler. Thromb.* 12 (1): 1–5.

101 Lehmann, E.D., Hopkins, K.D., Jones, R.L., et al. (1995). Aortic distensibility in patients with cerebrovascular disease. *Clin. Sci.* 89 (3): 247–253.

102 Hirai, T., Sasayama, S., Kawasaki, T., Yagi, S. (1989). Stiffness of systemic arteries in patients with myocardial infarction. A noninvasive method to predict severity of coronary atherosclerosis. *Circulation* 80 (1): 78–86.

103 Gatzka, C.D., Cameron, J.D., Kingwell, B.A., Dart, A.M. (1998). Relation between coronary artery disease, aortic stiffness, and left ventricular structure in a population sample. *Hypertension* 32 (3): 575–578.

104 Giannattasio, C., Failla, M., Emanuelli, G., et al. (2001). Local effects of atherosclerotic plaque on arterial distensibility. *Hypertension* 38 (5): 1177–1180.

105 Raghavan, M.L., Vorp, D.A., Federle, M.P., et al. (2000). Wall stress distribution on three-dimensionally reconstructed models of human abdominal aortic aneurysm. *J. Vasc. Surg.* 31 (4): 760–769.

106 Canton, G., Hippe, D.S., Sun, J., et al. (2012). Characterization of distensibility, plaque burden, and composition of the atherosclerotic carotid artery using magnetic resonance imaging. *Med. Phys.* 39 (10): 6247–6253.

107 Ouriel, K., Green, R.M., Donayre, C., et al. (1992). An evaluation of new methods of expressing aortic aneurysm size: relationship to rupture. *J. Vasc. Surg.* 15 (1): 12–18.

108 Bengtsson, H., Sonesson, B., Bergqvist, D. (1996). Incidence and prevalence of abdominal aortic aneurysms, estimated by necropsy studies and population screening by ultrasound. *Ann. NY Acad. Sci.* 800: 1–24.

109 Patel, M.I., Hardman, D.T., Fisher, C.M., Appleberg, M. (1995). Current views on the pathogenesis of abdominal aortic aneurysms. *J. Am. Coll. Surg.* 181 (4): 371–382.

110 Darling, R.C., Messina, C.R., Brewster, D.C., Ottinger, L.W. (1977). Autopsy study of unoperated abdominal aortic aneurysms. The case for early resection. *Circulation* 56 (3 Suppl): II161–164.

111 Wain, R.A., Marin, M.L., Ohki, T. et al. (1998). Endoleaks after endovascular graft treatment of aortic aneurysms: classification, risk factors, and outcome. *J. Vasc. Surg.* 27 (1): 69–78, discussion 78–80.

112 Turnipseed, W.D., Carr, S.C., Tefera, G., et al. (2001). Minimal incision aortic surgery. *J. Vasc. Surg.* 34 (1): 47–53.

113 Velazquez, O.C., Larson, R.A., Baum, R.A., et al. (2001). Gender-related differences in infrarenal aortic aneurysm morphologic features: issues relevant to Ancure and Talent endografts. *J. Vasc. Surg.* 33 (2 Suppl): S77–84.

114 Gabrielli, L., Baudo, A., Molinari, A., Domanin, M. (2004). Early complications in endovascular treatment of abdominal aortic aneurysm. *Acta Chirurgica Belgica* 104 (5): 519–526.

115 Ghansah, J.N. and Murphy, J.T. (2004). Complications of major aortic and lower extremity vascular surgery. *Semin. Cardiothorac. Vasc. Anesth.* 8 (4): 335–361.

116 Dillavou, E.D., Muluk, S.C., Makaroun, M.S. (2006). A decade of change in abdominal aortic aneurysm repair in the United States: Have we improved outcomes equally between men and women? *J. Vasc. Surg.* 43 (2): 230–238; discussion 238.

117 Brewster, D.C., Cronenwett, J.L., Hallett, J.W., Jr., et al. (2003). Joint Council of the American Association for Vascular Surgery and Society for Vascular Surgery. Guidelines for the treatment of abdominal aortic aneurysms. Report of a subcommittee of the Joint Council of the American Association for Vascular Surgery and Society for Vascular Surgery. *J. Vasc. Surg*. 37 (5): 1106–1117.

118 Choksy, S.A., Wilmink, A.B.M., and Quick, C.R. (1999). Ruptured abdominal aortic aneurysm in the Huntingdon district: a 10-year experience. *Ann. R. Coll. Surg. Engl.* 81: 27–31.

119 Hall, A.J., Busse, E.F.G., McCarville, D.J. and Burgess, J.J. (2000). Aortic wall tension as a predictive factor for abdominal aortic aneurysm rupture: Improving the selection of patients for abdominal aortic aneurysm repair. *Ann. Vasc. Surg.* 14: 152–157.

120 Vorp, D.A. (2007). Biomechanics of abdominal aortic aneurysm. *J. Biomech.* 40: 1887–1902.

121 Darling, R.C., Messina, C.R., Brewster, D.C. and Ottinger, L.W. (1977). Autopsy study of unoperated abdominal aortic-aneurysms – case for early resection. *Circulation* 56: 161–164.

122 Hartley, C.J., Taffet, G.E., Michael, L.H., et al. (1997). Noninvasive determination of pulse-wave velocity in mice. *Am. J. Physiol.* 42: H494–H500.

123 Brands, P.J., Hoeks, A.P.G., Ledoux, L.A.F., and Reneman, R.S. (1997). A radio frequency domain complex cross-correlation model to estimate blood flow velocity and tissue motion by means of ultrasound. *Ultrasound Med. Biol.* 23: 911–920.

124 Meinders, J.M., Kornet, L., Brands, P.J. and Hoeks, A.P.G. (2001). Assessment of local pulse wave velocity in arteries using 2D distension waveforms. *Ultrason. Imaging* 23: 199–215.

125 Eriksson, A., Greiff, E., Loupas, T., et al. (2002). Arterial pulse wave velocity with tissue Doppler imaging. *Ultrasound Med. Biol.* 28: 571–580.

126 Rabben, S.I., Stergiopulos, N., Hellevik, L.R., et al. (2002). An ultrasound-based method for determining pulse-wave velocity in the carotid artery. *Eur. Heart J.* 23: 611–611.

127 Hermeling, E., Reesink, K.D., Reneman, R.S., and Hoeks, A.P.G. (2007). Measurement of local pulse wave velocity: Effects of signal processing on precision. *Ultrasound Med. Biol.* 33: 774–781.

128 Hoctor, R.T., Dentinger, A.M., and Thomenius, K.E. (2007). Array signal processing for local arterial pulse wave velocity measurement using ultrasound. *IEEE Trans. Ultrason., Ferroelect., Freq. Control* 54: 1018–1027.

129 Mancia, G., de Backer G., Dominiczak A., et al. (2007). 2007 Guidelines for the management of arterial hypertension: The task force for the management of arterial hypertension of the European Society of Hypertension (ESH) and of the European Society of Cardiology (ESC). *J. Hypertens.* 25 (6): 1105–1187.

130 Li, R.X., Qaqish, W.W., and Konofagou, E.E. (2015). Performance assessment of pulse wave imaging using conventional ultrasound in canine aortas ex vivo and normal human arteries in vivo. *Artery Res.* 11: 19–28.

131 Westenberg, J.J., van Poelgeest, E.P., Steendijk, P, et al. (2012). Bramwell-Hill modeling for local aortic pulse wave velocity estimation: a validation study with velocity-encoded cardiovascular magnetic resonance and invasive pressure assessment. *J. Cardiovasc. Magn. Reson.* 14: 2.

132 Asmar, R., Benetos, A., Topouchian, J., et al. (1995). Assessment of arterial distensibility by automatic pulse wave velocity measurement. Validation and clinical application studies. *Hypertension* 26 (3): 485–490.

133 McGarry, M., Li, R., Apostolakis, I., et al. (2016). An inverse approach to determining spatially varying arterial compliance using ultrasound imaging. *Phys. Med. Biol.* 61 (15): 5486–5507.

134 Apostolakis, I.-Z., Nandlall, S.D., Konofagou, E.E. (2016). Adaptive stiffness mapping in murine atherosclerotic and aneurysmal aortas using pulse wave imaging (PWI) in vivo. *IEEE Trans. Med. Imaging* 35 (1): 13–28.

135 Waksman, R., Serruys, P.W., and Schaar, J. (2007). *Handbook of the Vulnerable Plaque*. CRC Press.

136 Apostolakis, I.Z., Nauleau, P., Papadacci, C., et al. (2017). Feasibility and validation of 4-D pulse wave imaging in phantoms and in vivo. *IEEE Trans. Ultrason., Ferroelect., Freq. Control* 64 (9): 1305–1317.

137 Widman, E., Maksuti, E., Larsson, D., et al. (2015). Shear wave elastography plaque characterization with mechanical testing validation: a phantom study. *Phys. Med. Biol.* 60 (8): 3151–3174.

138 Li, R.X., Luo, J., Balaram, S.K., et al. (2013). Pulse wave imaging in normal, hypertensive and aneurysmal human aortas in vivo: a feasibility study. *Phys. Med. Biol.* 58 (13): 4549–4562.

139 Luo, J., Li, R.X., Konofagou, E.E. (2012). Pulse wave imaging of the human carotid artery: an in vivo feasibility study. *IEEE Trans. Ultrason., Ferroelect., Freq. Control* 59 (1): 174–181.

Section V

Harmonic Elastography Methods

15

Dynamic Elasticity Imaging

Kevin J. Parker

Department of Electrical and Computer Engineering, University of Rochester, Rochester, NY, USA

15.1 Vibration Amplitude Sonoelastography: Early Results

Vibration amplitude sonoelastography entails the application of a continuous low-frequency vibration (40–1000 Hz) to excite internal shear waves within the tissue of interest [1, 2]. A disruption in the normal vibration patterns will result if a stiff inhomogeneity is present in soft tissue surroundings. A real-time vibration image can be created by Doppler detection algorithms. Modal patterns can be created in certain organs with regular boundaries. The shear wave speed of sound in the tissue of these organs can be ascertained with the information revealed by these patterns [3].

Figure 15.1 reproduces the first vibration-amplitude sonoelastography image [1, 2], which marked the emergence of elastography *imaging* from the previous studies of tissue motion. The vibration within a sponge and saline phantom containing a harder area (the dark region) is depicted by this low resolution image. Range-gated Doppler was used to calculate the vibration amplitude of the interior of the phantom as it was vibrated from below. By 1990, a modified color Doppler instrument was used by the University of Rochester group to create real-time vibration-amplitude sonoelastography images. In these images, vibration above a certain threshold (in the 2 μm range) produced a saturated color (Figure 15.2).

Measurements of tissue elastic constants, finite-element modeling results, and phantom and ex vivo tissue sonoelastography were later reported [5–7]. Thus, by the end of 1990, the working elements of vibration elastography (sonoelastography and sonoelasticity were other names used at the time) were in place, including real-time imaging techniques and stress-strain analysis of tissues such as prostate, with finite-element models and experimental images demonstrating conclusively that small regions of elevated Young's modulus could be imaged and detected using conventional Doppler-imaging scanners.

15.2 Sonoelastic Theory

Along with the useful finite-element approach of Lerner et al. [5] and Parker et al. [7], there were important theoretical questions to be answered by analytical or numerical techniques. How did vibration fields behave in the presence of elastic inhomogeneities? What is the image contrast of lesions in a vibration field, and how does the contrast depend on the choice of parameters? How do we optimally detect sinusoidal vibration patterns and image them using Doppler or related techniques? These important issues were addressed in a series of papers through the 1990s.

Ultrasound Elastography for Biomedical Applications and Medicine, First Edition.
Edited by Ivan Nenadic, Matthew Urban, James Greenleaf, Jean-Luc Gennisson, Miguel Bernal, and Mickael Tanter.

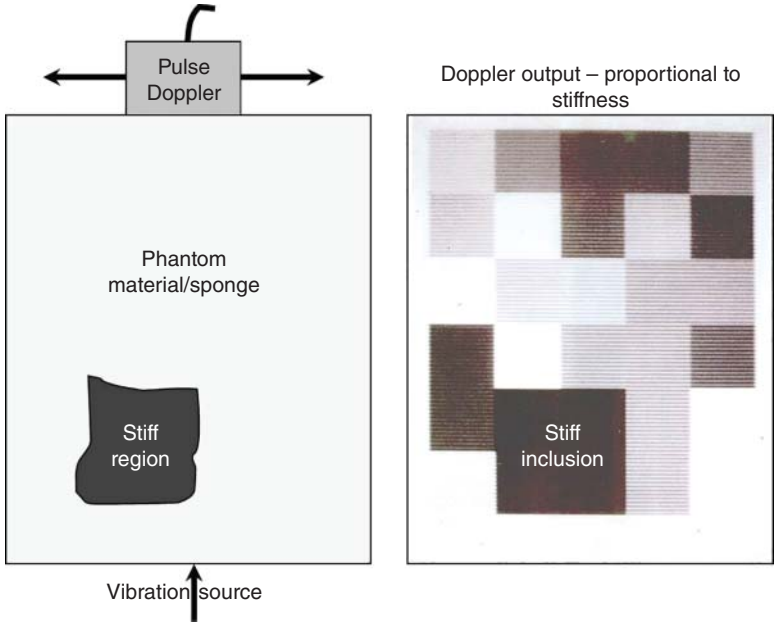

Figure 15.1 Original imaging data and schematic of the first known image of relative stiffness, derived from Doppler data in a phantom with applied vibration. The original image was published in 1987 and 1988 and marks the emergence of elastographic imaging.

One foundational result was published in 1992 under the title: "Sonoelasticity of Organs, Shear Waves Ring a Bell" [3]. This paper demonstrated experimental proofs that vibrational eigenmodes could in fact be created in whole organs, including the liver and kidneys, where extended surfaces create reflections of sinusoidal steady-state shear waves. Lesions would produce a localized perturbation of the eigenmode pattern, and the background Young's modulus could be calculated from the patterns at discrete eigenfrequencies. Thus, both quantitative and relative imaging contrast detection tasks could be completed with vibration elastography in a clinical setting, in vivo, by 1992. A later review of eigenmodes and a strategy for using multiple frequencies simultaneously (called "chords") was given in Taylor et al. [8].

Furthermore, a vibration-amplitude analytical model was created [9, 10]. This model used a sonoelastic Born approximation to solve the wave equations in an inhomogeneous, isotropic medium. The total shear wave field inside the medium can be expressed as

$$\Phi_{\text{total}} = \Phi_{\text{i}} + \Phi_{\text{s}} \tag{15.1}$$

where Φ_{i} is the homogeneous or incident field, and Φ_{s} is the field scattered by the inhomogeneity. They satisfy, respectively

$$(\nabla^2 + k^2)\Phi_{\text{i}} = 0 \tag{15.2}$$

$$(\nabla^2 + k^2)\Phi_{\text{s}} = \delta(x) \tag{15.3}$$

where $\delta(x)$ is a function of the properties of inhomogeneity and k is the wavenumber of shear wave propagation at a frequency ω_0. The theory accurately describes how a hard or soft lesion appear as disturbances in a vibration pattern. Figure 15.3 summarizes the theoretical and experimental trends.

Signal processing estimators were also developed in the study of vibration amplitude sonoelastography. Huang et al. suggested a method to estimate a quantity denoted β, which is proportional to the vibration amplitude of the target, from the spectral spread [11]. They found a

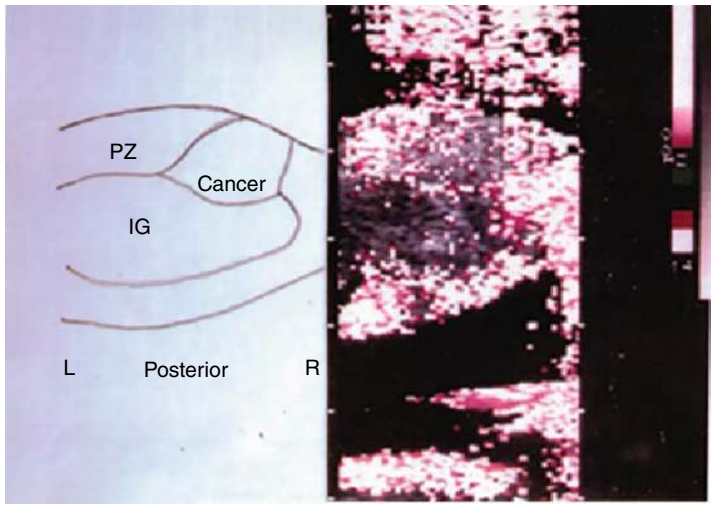

Figure 15.2 A representative first-generation image of vibration sonoelastography, circa 1990. Doppler spectral variance is employed as an estimator of vibration in the 1–10 μm range and displayed over the B-scan images. No color implies low vibrations below threshold. Shown is the fill-in of vibration within a whole prostate, with a growing cancerous region indicated by the deficit of color within the peripheral zone. Source: courtesy of Dr. R. M. Lerner; Anastasio and La Riviere [4], Figure 12.4, p. 186; reproduced with permission from Taylor and Francis Group.

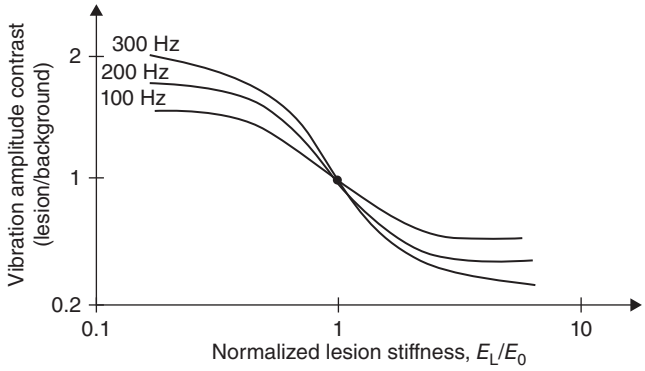

Figure 15.3 Theoretical results of the contrast of vibration sonoelastography for soft or hard lesions in a background medium. The image contrast increases with both increasing frequency and with increasing size of the lesion.

simple correlation between β and the Doppler spectral spread σ_ω

$$\beta = \sqrt{2}(\sigma_\omega/\omega_L) \tag{15.4}$$

where ω_L is the vibration frequency of the vibrating target. This is an uncomplicated and very useful property of the Bessel Doppler function. The effect of noise, sampling, and nonlinearity on the estimation was also considered. In their later work, they studied real-time estimators of vibration amplitude, phase, and frequency that could be used for a variety of vibration sonoelastography techniques [12].

Finally, an overall theoretical approach that places vibration sonoelastography on a biomechanical spectrum with other techniques including compression elastography, magnetic resonance elastography (MRE), and the use of impulsive radiation force excitations, is found

in "A Unified View of Imaging the Elastic Properties of Tissues" [13]. This perspective is highlighted in Chapter 3 of this book.

15.3 Vibration Phase Gradient Sonoelastography

In parallel to the early work at the University of Rochester, a vibration phase gradient approach to sonoelastography was developed by Sato and collaborators at the University of Tokyo [14]. They mapped the amplitude and the phase of low frequency wave propagation inside tissue. From this mapping, they were able to derive wave-propagation velocity and dispersion properties, which are directly linked to the elastic and viscous characteristics of tissue.

The phase-modulated (PM) Doppler spectrum of the signal returned from sinusoidally oscillating objects approximates that of a pure-tone frequency modulation (FM) process, as given in Eq. (15.2). This similarity indicates that the tissue vibration amplitude and phase of tissue motion may be estimated from the ratios of adjacent harmonics. The amplitude ratio between contiguous Bessel bands of the spectral signal is

$$A_{i+1}/A_i = |J_{i+1}(\beta)/J_i(\beta)| \tag{15.5}$$

where A_i is the amplitude at the i-th harmonic, β is the unknown amplitude of vibration in the tissue, and $J_i(\cdot)$ is an i-th order Bessel function. β can be estimated from the experimental data if A_{i+1}/A_i is calculated as a function of β beforehand. The phase of the vibration was calculated from the quadrature signals.

The display of wave propagation as a moving image is permitted by constructing phase and amplitude maps (Figure 15.4) as a function of time. The use of a minimum squared error algorithm to estimate the direction of wave propagation and to calculate phase and amplitude gradients in this direction allows images of amplitude and phase to be computed offline. By assuming that the shear viscosity effect is negligible at low frequencies, Sato's group obtained preliminary in vivo results [14].

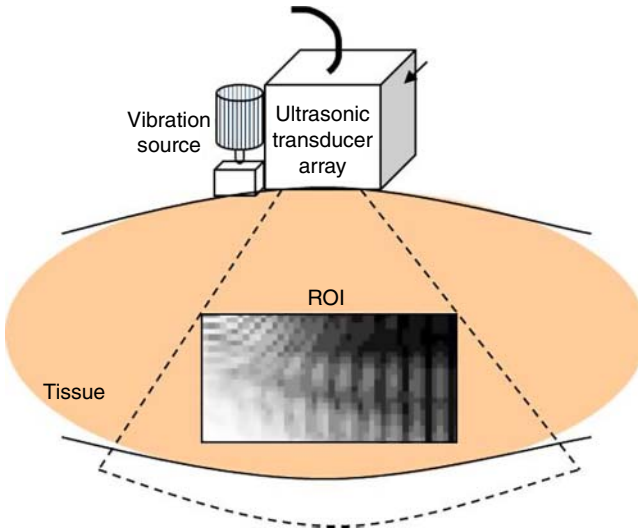

Figure 15.4 A depiction of the system developed by Prof. Sato and colleagues at the University of Tokyo, including external vibration and an imaging array with signal processing for estimating the phase of the vibration in tissue. The rate of change of phase can be estimated to yield tissue hardness.

Sato's technique was used and refined by Levinson [15], who developed a more general model of tissue viscoelasticity and a linear recursive filtering algorithm based on cubic B-spline functions. Levinson took the Fourier transform of the wave equation and derived the frequency-domain displacement equation for a linear, homogeneous, isotropic viscoelastic material. From this, equations that relate the shear modulus of elasticity and viscosity to the wave number and the attenuation coefficient of the wave can be derived.

Levinson et al. [15] conducted a series of experiments on the quadriceps muscle group in human thighs. It was assumed that shear waves predominate and that viscosity at low frequencies is negligible. Phase gradient images of the subjects' thighs under conditions of active muscle contraction enabled the calculation of Young's modulus of elasticity. The tension applied to the muscle was controlled using a pulley device. The measured vibration propagation speed and the calculated values of Young's modulus increased with the increasing degrees of contraction needed to counteract the applied load.

15.4 Crawling Waves

A fascinating extension of vibration sonoelastography is the use of an interference pattern formed by two parallel shear wave sources. The interference patterns reveal the underlying local elastic modulus of the tissue. The term "crawling waves" comes from the useful fact that by implementing a slight frequency difference, typically on the order of 0.1 Hz, between the two parallel sources, the interference pattern will move across the imaging plane at a speed controlled by the sources [16]. Thus, the crawling waves are readily visualized by conventional Doppler imaging scanners at typical Doppler frame rates; there is no need for ultrafast scanning. Other advantages of crawling waves include: (1) the region of interest excited between the two sources is large; (2) most of the energy in the crawling waves is aligned in the Doppler (axial) direction; and (3) a number of analysis or estimation schemes can be applied in a straightforward manner to derive the quantitative estimate of local shear wave velocity and Young's modulus. Crawling waves can also be implemented by a number of techniques including mechanical line sources, surface applicators, or radiation force excitations of parallel beams.

The use of crawling waves was first described in 2004 by Wu et al. at the University of Rochester [16]. It was shown that crawling waves could be used to accurately derive the Young's modulus of materials and to delineate stiff inclusions [17–20]. Estimators of shear wave speed and Young's modulus and the shear wave attenuation are derived by Hoyt et al. [21–23] and McLaughlin et al. [24].

Implementation into scanning probes can be accomplished by utilizing radiation force excitation along parallel beams [25–27], or by utilizing a pair of miniature vibration sources [28].

15.5 Clinical Results

The initial applications of amplitude sonoelastography were to characterize average tissue properties using eigenmode information [3, 29] and to identify stiff lesions by the amplitude contrast effect. In particular, the demonstration of improved detectability of prostate cancer was published in *Radiology* in 1995 [30]. This work was then adapted to in vivo and 3D studies of the prostate [8, 19, 31–34], and it was demonstrated that the sensitivity and specificity of prostate cancer detection could be markedly improved using sonoelasticity. Separately, it was shown that the definition and volumetric measurement of thermal lesions in tissue could be greatly improved by sonoelastography [35–38].

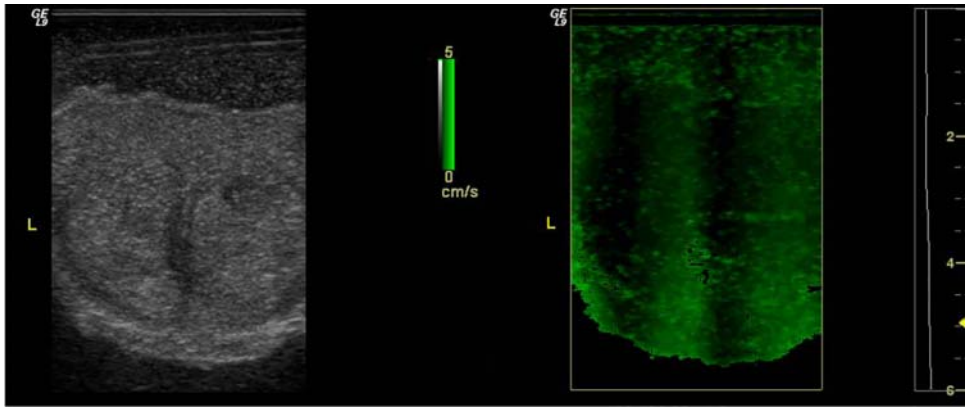

(a)

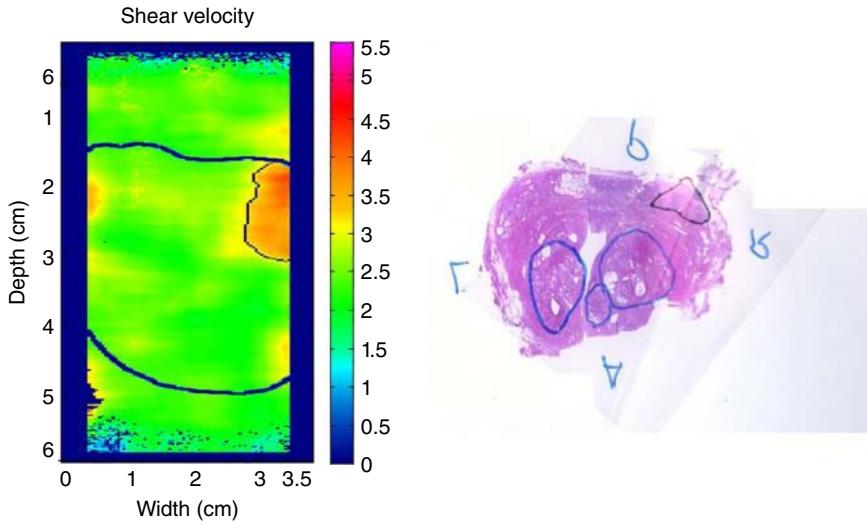

(b)

Figure 15.5 Crawling waves in the prostate. (a), left: B-scan of whole excised prostate; right: crawling waves frame; (b), right: pathology with labels: upper triangle = cancer and lower ovals = benign prostatic hyperplasis (BPH); left: quantitative estimates of shear velocity from crawling waves analysis, indicating the hard region as a upper right area (corresponding to the region with cancer). Estimates from an average of three frequencies are shown. All images are co-registered. Source: Anastasio and La Riviere [4], Figure 12.8, p. 190; reproduced with permission from Taylor and Francis Group.

Applications of crawling waves include the ex vivo prostate [39–41], in vivo muscle [42], and ex vivo liver [20]. An example from ex vivo prostate is given in Figures 15.5a and 15.5b.

Other applications of crawling waves include quantification of the elastic properties of muscle [42, 43], thyroid [44], and fatty livers [45–48].

15.6 Conclusion

There are a number of key advantages to "sonoelastography" imaging and crawling waves imaging. First, in sinusoidal steady-state shear wave excitation, the amplitude contrast effect (of stiff lesions) can be seen with any Doppler imaging platform; it is not necessary to have any

synchronization system or specialized platform [49]. Second, by proper choice of shear wave frequency, entire organs can be covered with shear waves, providing large ROIs for analysis [3]. This fact has been used to great advantage in MRE, as well. Finally, the crawling waves approach provides data that can be analyzed with a number of simple local estimators, while producing comparable resolution and accuracy to the very best shear wave tracking approaches using radiation force excitations [50]. In addition, the crawling waves patterns can be produced simply by external transducers [18, 28] or by an alternating pair of radiation force beams, one on the right and on the left of the ROI [51, 52]. Thus these techniques are widely applicable and efficacious for studies of tissue elastography in the breast, liver, thyroid, muscle, and other soft tissues.

Acknowledgments

This work was supported by the Hajim School of Engineering and Applied Sciences at the University of Rochester, and by National Institutes of Health grants R01 AG016317 and R01 AG029804.

References

1 Lerner, R.M. and Parker, K.J. (1987). *Sonoelasticity images derived from ultrasound signals in mechanically vibrated targets*. In Seventh European Communities Workshop (ed. J. Tjissen). Nijmegen, The Netherlands.
2 Lerner, R.M., Parker, K.J., Holen, J., et al. (1988). Sonoelasticity: medical elasticity images derived from ultrasound signals in mechanically vibrated targets. *Acoust. Imag.* 16: 317–327.
3 Parker, K. J. and Lerner, R.M. (1992). Sonoelasticity of organs: shear waves ring a bell. *J. Ultrasound Med.* 11: 387–392.
4 Anastasio, M.A. and La Riviere, P. (2013). *Emerging Imaging Technologies in Medicine*. Boca Raton: CRC Press.
5 Lerner, R.M., Huang, S.R., and Parker, K.J. (1990). "Sonoelasticity" images derived from ultrasound signals in mechanically vibrated tissues. *Ultrasound Med. Biol.* 16: 231–239.
6 Parker, K.J., Huang, S.R., Lerner, R.M., et al. (1993). Elastic and ultrasonic properties of the prostate. In: *Proceeding of the 1993 Ultrasonics Symposium*, 1032: 1035–1038.
7 Parker, K.J., Huang, S.R., Musulin, R.A., and Lerner, R.M. (1990). Tissue response to mechanical vibrations for "sonoelasticity imaging". *Ultrasound Med. Biol.* 16: 241–246.
8 Taylor, L.S., Porter, B.C., Rubens, D.J., and Parker, K.J. (2000). Three-dimensional sonoelastography: principles and practices. *Phys. Med. Biol.* 45: 1477–1494.
9 Gao, L., Parker, K.J., Alam, S.K., and Lernel, R.M. (1995). Sonoelasticity imaging: theory and experimental verification. *J. Acoust. Soc. Am.* 97: 3875–3886.
10 Parker, K.J., Fu, D., Graceswki, S.M., et al. (1998). Vibration sonoelastography and the detectability of lesions. *Ultrasound Med. Biol.* 24: 1437–1447.
11 Huang, S.R., Lerner, R.M., and Parker, K.J. (1990). On estimating the amplitude of harmonic vibration from the doppler spectrum of reflected signals. *J. Acoust. Soc. Am.* 88: 2702–2712.
12 Huang, S.R., Lerner, R.M., and Parker, K.J. (1992). Time domain Doppler estimators of the amplitude of vibrating targets. *J. Acoust. Soc. Am.* 91: 965–974.
13 Parker, K.J., Taylor, L.S., Gracewski, S., and Rubens, D.J. (2005). A unified view of imaging the elastic properties of tissue. *J. Acoust. Soc. Am.* 117: 2705–2712.
14 Yamakoshi, Y., Sato, J., and Sato, T. (1990). Ultrasonic imaging of internal vibration of soft tissue under forced vibration. *IEEE Trans. Ultrason., Ferroelect., Freq. Control* 37: 45–53.

15 Levinson, S.F., Shinagawa, M., and Sato, T. (1995). Sonoelastic determination of human skeletal-muscle elasticity. *J. Biomech.* 28: 1145–1154.

16 Wu, Z., Taylor, L.S., Rubens, D.J., and Parker, K.J. (2004). Sonoelastographic imaging of interference patterns for estimation of the shear velocity of homogeneous biomaterials. *Phys. Med. Biol.* 49: 911–922.

17 Wu, Z. (2005). Shear wave interferometry and holography, an application of sonoelastography. In: *Electrical & Computer Engineering*, 104. University of Rochester, Rochester, NY.

18 Wu, Z., Hoyt, K., Rubens, D.J., and Parker, K.J. (2006). Sonoelastographic imaging of interference patterns for estimation of shear velocity distribution in biomaterials. *J. Acoust. Soc. Am.* 120: 535–545.

19 Wu, Z., Taylor, L.S., Rubens, D.J., and Parker, K.J. (2002). Shear wave focusing for three-dimensional sonoelastography. *J. Acoust. Soc. Am.* 111: 439–446.

20 Zhang, M., Castaneda, B., Wu, Z., et al. (2007). Congruence of imaging estimators and mechanical measurements of viscoelastic properties of soft tissues. *Ultrasound Med. Biol.* 33: 1617–1631.

21 Hoyt, K., Castaneda, B., and Parker, K.J. (2007). Feasibility of two-dimensional quantitative sonoelastographic imaging. In: *Proceedings of the 2007 Ultrasonics Symposium*, 2032–2035.

22 Hoyt, K., Castaneda, B., and Parker, K.J. (2008). Two-dimensional sonoelastographic shear velocity imaging. *Ultrasound Med. Biol.* 34: 276–288.

23 Hoyt, K., Parker, K.J., and Rubens, D.J. (2007). Real-time shear velocity imaging using sonoelastographic techniques. *Ultrasound Med. Biol.* 33: 1086–1097.

24 McLaughlin, J., Renzi, D., Parker, K., and Wu, Z. (2007). Shear wave speed recovery using moving interference patterns obtained in sonoelastography experiments. *J. Acoust. Soc. Am.* 121: 2438–2446.

25 An, L., Rubens, D.J., and Strang, J. (2010). Evaluation of crawling wave estimator bias on elastic contrast quantification. In: *American Institute of Ultrasound in Medicine Annual Convention*, S1–14. San Diego, CA.

26 Cho, Y.T., Hah, Z., and An, L. (2010). Theoretical investigation of strategies for generating crawling waves using focused beams. In: *American Institue for Ultrasound in Medicine Annual Convention*, S1–14. San Diego, CA.

27 Hah, Z., Hazard, C., Cho, Y.T., et al. (2010). Crawling waves from radiation force excitation. *Ultrason. Imaging* 32: 177–189.

28 Partin, A., Hah, Z., Barry, C.T., et al. (2014). Elasticity estimates from images of crawling waves generated by miniature surface sources. *Ultrasound Med. Biol.* 40: 685–694.

29 Alam, S.K., Richards, D.W., and Parker, K.J. (1994). Detection of intraocular pressure change in the eye using sonoelastic Doppler ultrasound. *Ultrasound Med. Biol.* 20: 751–758.

30 Rubens, D.J., Hadley, M.A., Alam, S. K., et al. (1995). Sonoelasticity imaging of prostate cancer: in vitro results. *Radiology* 195: 379–383.

31 Castaneda, B., Hoyt, K., Zhang, M., et al. (2007). P1C-9 Prostate cancer detection based on three dimensional sonoelastography. In: *Proceedings of the 2007 Ultrasonics Symposium*, 1353–1356.

32 Taylor, L.S., Gaborski, T.R., Strang, J.G., et al. (2002). Detection and three-dimensional visualization of lesion models using sonoelastography. In: *SPIE Medical Imaging 2002: Ultrasonic Imaging and Signal Processing* (ed. M. F. Insana and W. F. Walker), 421–429.

33 Taylor, L.S., Rubens, D.J., Porter, B.C. et al. (2005). Prostate cancer: three-dimensional sonoelastography for in vitro detection. *Radiology* 237: 981–985.

34 Zhang, M., Nigwekar, P., Castaneda, B., et al. (2008). Quantitative characterization of viscoelastic properties of human prostate correlated with histology. *Ultrasound Med. Biol.* 34: 1033–1042.

35 Castaneda, B., Tamez-Pena, J.G., and Zhang, M., (2008). Measurement of thermally-ablated lesions in sonoelastographic images using level set methods. In *Proc SPIE 2008* (ed. S. A. McAleavey and J. D'hooge), 692018-692011-692018-692018.

36 Castaneda, B., Zhang, M., Hoyt, K., et al. (2007). P1C-4 real-time semi-automatic segmentation of hepatic radiofrequency ablated lesions in an in vivo porcine model using sonoelastography. In: *Proceedings of the 2007 Ultrasonics Symposium*, 1341–1344.

37 Taylor, L.S. and Zhang, M. (2002). In-vitro imaging of thermal lesions using three-dimensional vibration sonoelatography. In: *Second International Symposium on Therapeutic Ultrasound*, 176–184.

38 Zhang, M., Castaneda, B., Christensen, J., et al. (2008). Real-time sonoelastography of hepatic thermal lesions in a swine model. *Med. Phys.* 35: 4132–4141.

39 Castaneda, B., An, L., Wu, S., et al. (2009). *Prostate cancer detection using crawling wave sonoelastography* (ed. S. A. McAleavey and J. D'Hooge), 726513-726511-726513-726510. SPIE, Lake Buena Vista, FL, USA.

40 Hoyt, K., Castaneda, B., Zhang, M., et al. (2008). Tissue elasticity properties as biomarkers for prostate cancer. *Cancer Biomark.* 4: 213–225.

41 Hoyt, K., Parker, K.J., and Rubens, D.J. (2006). Sonoelastographic shear velocity imaging: experiments on tissue phantom and prostate. In: *Proceedings of the 2006 Ultrasonics Symposium*, 1686–1689.

42 Hoyt, K., Kneezel, T., Castaneda, B., and Parker, K.J. (2008). Quantitative sonoelastography for the in vivo assessment of skeletal muscle viscoelasticity. *Phys. Med. Biol.* 53: 4063–4080.

43 Hoyt, K., Castaneda, B., and Parker, K.J. (2007). Muscle tissue characterization using quantitative sonoelastography: preliminary results. In: *Proceedings of the 2007 Ultrasonics Symposium*, 365–368.

44 Walsh, J., An, L., Mills, B., et al. (2012). Quantitative crawling wave sonoelastography of benign and malignant thyroid nodules. *Otolaryngol. Head Neck Surg.* 147: 233–238.

45 Barry, C.T., Hah, Z., Partin, A., et al. (2014). Mouse liver dispersion for the diagnosis of early-stage fatty liver disease: a 70-sample study. *Ultrasound Med. Biol.* 40: 704–713.

46 Barry, C.T., Hazard, C., Hah, Z., et al. (2015). Shear wave dispersion in lean versus steatotic rat livers. *J. Ultrasound Med.* 34: 1123–1129.

47 Barry, C.T., Mills, B., Hah, Z., et al. (2012). Shear wave dispersion measures liver steatosis. *Ultrasound Med. Biol.* 38: 175–182.

48 Parker, K.J., Partin, A., and Rubens, D.J. (2015). What do we know about shear wave dispersion in normal and steatotic livers? *Ultrasound Med. Biol.* 41: 1481–1487.

49 Torres, G., Chau, G.R., Parker, K.J., et al. (2016). Temporal artifact minimization in sonoelastography through optimal selection of imaging parameters, *J. Acoust. Soc. Am.* 140: 714–717.

50 Ormachea, J., Lavarello, R.J., McAleavey, S.A., et al. (2016). Shear wave speed measurements using crawling wave sonoelastography and single tracking location shear wave elasticity imaging for tissue characterization. *IEEE Trans. Ultrason., Ferroelect., Freq. Control.* 63: 1351–1360.

51 Hah, Z., Hazard, C., Mills, B., et al. (2012). Integration of crawling waves in an ultrasound imaging system. part 2: signal processing and applications. *Ultrasound Med. Biol.* 38: 312–323.

52 Hazard, C., Hah, Z., Rubens, D., and Parker, K. (2012). Integration of crawling waves in an ultrasound imaging system. part 1: system and design considerations. *Ultrasound Med. Biol.* 38: 296–311.

16

Harmonic Shear Wave Elastography

Heng Zhao

Department of Physiology and Biomedical Engineering, Mayo Clinic, Rochester, MN, USA

16.1 Introduction

As introduced in Chapter 5 in this book, shear wave propagation speed can be used to noninvasively quantify tissue mechanical properties such as elasticity, which is an indicator of tissue health [1]. Unlike elastography/strain imaging using quasi-static compression, which shows the contrast among materials with different stiffness [2], absolute elasticity/viscosity can be derived from the shear wave speed [1].

We need to introduce shear waves to the tissue in order to measure the propagation speed, which can be done either externally or internally. Internal sources include physiological movement such as heart beat, respiration, vocal cords vibration, etc., which are safe and do not involve additional devices [3]. However, shear waves generated by such sources are generally weak and lack control. Alternatively, the shear waves can be introduced using external sources. Ultrasound radiation force has been widely used for its capability of producing localized waves and evaluating the mechanical properties of a specified region, i.e. virtual biopsy [4, 5]. However, the motion in tissue generated by such a force is typically weak (amplitude of several micrometers) and subject to attenuation, phase aberration, and diffraction. Some methods such as supersonic shear imaging (SSI) [6] and comb-push ultrasound shear elastography (CUSE) [7] have been applied to maximize the existence of shear waves and extend the field of view (FOV). However, weak shear waves become challenging issues for deeper organs and especially overweight/obese patients.

Mechanical vibration does not require a high voltage transmitter pulser that would be necessary for ultrasound radiation force. Therefore, it can be implemented on low-cost imaging systems [8, 9]. More importantly, shear waves generated by mechanical vibration are much stronger than those produced by radiation force and can be delivered through thicker tissues to deeper organs. Multiple shear waves can be generated such that the shear wave propagation speed can be measured in a large FOV. Such advantages have strong implications in diagnosing overweight or obese patients. However, because the waves are typically delivered from the skin surface into the tissue, it is difficult to control the location or direction of the waves, which is essential for measuring the shear wave speed based on conventional time-of-flight methods [4, 10].

Some adapters have been introduced to guide the shear waves from the vibrator into the tissue [11], but they are effective for superficial muscles or organs only. For deeper organs (some of which are inside the rib cage), the shear wave field would be more complicated due

Ultrasound Elastography for Biomedical Applications and Medicine, First Edition.
Edited by Ivan Nenadic, Matthew Urban, James Greenleaf, Jean-Luc Gennisson, Miguel Bernal, and Mickael Tanter.

to the diffractions and reflections. Direct inversion can be applied to calculate the model-free complex modulus based on a complicated wave field [12]. However, such a method requires three-dimensional displacement/velocity data, and taking the spatial gradient of the wave distribution is highly susceptible to noise [13]. A time-reversal approach also has been proposed to calculate shear wave speed or wave length based on cross-correlation of a diffuse wave field [14]. Yet a diffuse wave field is difficult to obtain in vivo.

Recently, time-harmonic elastography (THE) has been developed to measure the speed of shear waves generated by continuous external vibration [15]. Multiple measurements were taken at different angles to estimate the actual shear wave speed. However, THE only provides one-dimensional localized elasticity measurement, which does not meet the need of modern diagnostic modalities.

Harmonic shear wave elastography (HSWE) or external vibration multi-direction ultrasound shear wave elastography (EVMUSE) uses similar external vibration as THE to create a multi-direction shear wave field [16]. There is no restriction on the direction, location, or occurrence of the shear waves within the imaging plane. Directional filters are used to separate shear waves propagating in different directions. For each direction, a two-dimensional (2D) shear wave speed estimator is used to calculate a local 2D shear wave speed map. The final shear wave speed map is constructed by compounding the speed maps from all directions. In this chapter, we are going to introduce the basic principles of the harmonic shear wave elastography, followed by validation of the method ex vivo using phantoms. Finally, harmonic shear wave elastography is applied for in vivo liver fibrosis staging in patients with liver diseases.

16.2 Basic Principles

16.2.1 Vibration Source

Ultrasound imaging systems do not have magnetic compatibility issues that magnetic resonance imaging (MRI) systems do [17]. Therefore, a large variety of magnetic vibrators can be chosen for HSWE, which are generally cheaper and more powerful than the pneumatic devices used by magnetic resonance elastography (MRE). One or several vibrators can be positioned judiciously on the skin surface to deliver proper shear waves into the tissue, and at the same time leaving a window for the ultrasound probe to access. The vibrators are typically driven by single frequency sinusoidal waves to maximize the harmonic motion output. The frequency usually ranges from tens to several hundred Hertz. Special attention needs to be paid to avoid interference between the vibrators and the ultrasound probe, for the probe motion would introduce artifacts into shear wave motion detection. Alternatively, high frame rate motion detection can start shortly after the vibrator motion terminates, such that shear wave propagation is still present in the FOV, whereas the transducer motion is negligible [16].

16.2.2 Motion Detection

As mentioned above, a high frame rate plane wave imaging technique is used to detect the shear wave motion in the axial direction [18]. A short pulse (one or two cycles) at the transducer center frequency is transmitted by all the channels to form a plane beam, and the signals are received by all the channels for beamforming. Spatial compounding and/or coded excitation can be used to compensate for the signal-to-noise ratio (SNR) loss due to the unfocused beam [18, 19]. One dimensional (1D) [20]/two-dimensional (2D) autocorrelation [21] or cross-correlation [22] can be used to calculate the axial displacement/velocity at each pixel

within the image plane from the demodulated in-phase/quadrature (IQ) signals or beamformed radio-frequency (RF) signals, respectively.

16.2.3 Directional Filter

As mentioned above, vibrators typically create a multi-direction shear wave field in the region of interest (ROI), because of multiple contact locations between the vibrators and the skin. This means at any given time, multiple shear waves may occur at multiple locations and propagate in different directions. Such shear waves have to be separated in order to use conventional time-of-flight methods to calculate the shear wave speed [4, 10]. First, the spatiotemporal (x, z, t) motion signals are converted to the spatiotemporal frequency (k_x, k_z, f_t) domain, or k-f domain, using a three-dimensional (3D) Fourier transform. Tukey windows are applied to the spatiotemporal signals to create a smooth transition from the FOV to surrounding zeros, minimizing the edge effects due to the Fourier transform. Then the directional filters are applied by multiplying the directional filter response with the signals in the k-f domain [23]. Figure 16.1 shows the directional filter response in eight directions. For each direction, shear waves propagating within an angular range near the primary direction can pass through whereas shear waves moving in other directions are suppressed.

Both compressional waves [24] and out-of-plane shear waves [25] appear as high speed waves which are present as low spatial frequency components in the k-f domain. They need to be suppressed in order to measure the shear wave speed accurately. Given an upper speed limit c_h at a temporal frequency f_t, a spatial frequency limit $k_l = f_t/c_h$ can be imposed upon the directional filter to suppress waves with propagation speeds higher than c_h, by removing spatial frequency components lower than k_l as indicated by the regions inside the white circles at the center of the directional filter response in Figure 16.1. Such a speed limit is reasonable because the shear wave speed inside a certain tissue should be within a physiologically possible range. A Butterworth high-pass filter was designed to apply smooth transitions for k_l to avoid Gibbs ringing effects. Based on the relation between k_l and f_t, the radius of the removed region (cutoff frequency of the high-pass filter) increases with the temporal frequency f_t.

Besides the spatial high-pass filtering, another Butterworth band-pass filter can be applied in the temporal frequency direction to remove low frequency drift and high frequency noise

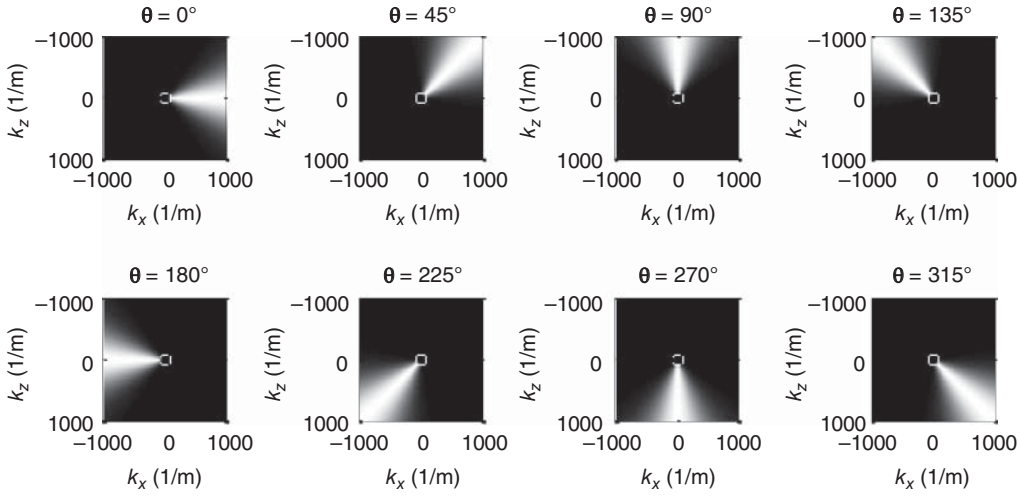

Figure 16.1 Eight directional filters from 0° to 315° with 45° steps. The white circle indicates the cutoff region where c_h is imposed at f_t. Source: © 2014 IEEE, reprinted, with permission, from [16].

in the temporal signals [16]. The cutoff frequencies are selected according to the vibration frequency to allow possible shear wave signals to pass through. For example, if the vibrators are driven at 50 Hz, the cutoff frequencies are set at 10 Hz and 100 Hz, respectively. After the directional filtering, the resulting shear wave signals in different directions are converted back to the spatiotemporal domain using an inverse 3D Fourier transform.

16.2.4 2D Shear Wave Speed Estimation

After directional filtering, the shear wave propagation speed in each direction is measured separately using a 2D shear wave speed estimation method. Data filtered by each directional filter mainly contain waves propagating in that direction, which can be at an oblique angle to the lateral and axial coordinates (x, z) of the ultrasound detection data grid. Similar to the methods introduced by Hoyt et al. [26] and Song et al. [27], cross-correlation is applied to calculate the time delays between the temporal signal at one pixel and the signals from two other pixels a certain distance away in the x and z directions, respectively. As illustrated in Figure 16.2, consider a plane shear wave (indicated by the long dashed lines) moving at a constant speed of c_s with an angle of θ with respect to the x axis. The time delays are measured between the origin o and two locations x and z, both with a distance of r from o. There is a tradeoff for the selection of r, since a shorter distance would result in higher resolution and lower signal decorrelation, but also a larger percentage error for time delay estimation [28]. The time for the shear wave to travel from o to x is Δt_x, and the time for the shear wave to propagate from o to z is Δt_z. Based on geometry, it follows that

$$r\cos\theta = c_s \cdot \Delta t_x$$

and

$$r\sin\theta = c_s \cdot \Delta t_z$$

Therefore,

$$c_s = \frac{r}{\sqrt{\Delta t_x^2 + \Delta t_z^2}}$$

To improve the estimation accuracy, the temporal signals are upsampled 10 times and parabolic interpolation was applied to locate the sub-pixel correlation peaks [29, 30]. Normalized correlation coefficients (CC) [31] are also calculated in both the x and z directions to

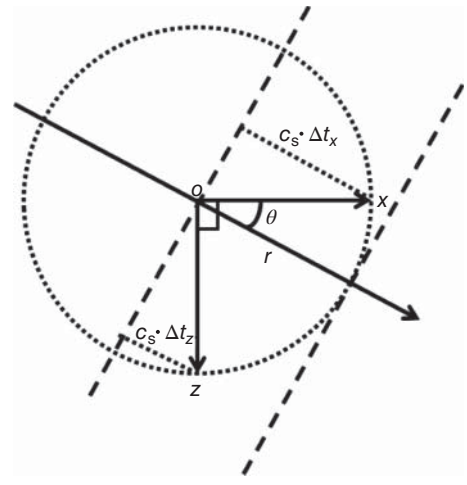

Figure 16.2 Illustration of the principle of the 2D c_s estimation. Source: © 2014 IEEE, reprinted, with permission, from [16].

control the quality of c_s estimation. Because there are two CCs for each pixel from shear wave estimation along x and z directions, respectively, the lower value of the two are selected to represent the CC for that pixel to be conservative.

16.2.5 Weighted Averaging

To further improve the robustness of the measurement, the value of c_s at one pixel ($\bar{c}_s$) was determined by averaging with estimates from the surrounding pixels. Both inverse distance weighting (IDW) [32] and correlation coefficient weighting (CCW) are applied to calculate the average speed as described in Eq. (16.1) [27]

$$\bar{c}_s(0,0) = \frac{\sum_{x=-N}^{N}\sum_{z=-N}^{N} c_s(x,z)\cdot \mathrm{cc}(x,z)^2 / r(x,z)}{\sum_{x=-N}^{N}\sum_{z=-N}^{N} \mathrm{cc}(x,z)^2 / r(x,z)}, \quad r(x,z) = \begin{cases} \sqrt{x^2+z^2} (x^2+z^2 \neq 0) \\ 0.1 (x^2+z^2 = 0) \end{cases} \tag{16.1}$$

where $c_s(x, z)$ is the speed measured at a location with a CC of $\mathrm{cc}(x, z)$ and a distance of $r(x, z)$ (unit: pixel) away from the center pixel (0, 0). N determines the range of the pixels involved in the averaging (also the spatial resolution of the c_s image). The above process is applied to each image pixel in the shear wave speed map, and forms a 2D c_s image in each direction.

16.2.6 Shear Wave Speed Image Compounding

After the 2D c_s maps from each of the directions are calculated, they can be compounded into a final image by averaging the measured c_s in each direction. In some cases, especially for in vivo measurement, the shear wave field may mostly propagate in one or two directions instead of in many directions. The c_s results should be more reliable in directions where there are strong shear waves. Therefore, the final c_s value at each pixel is calculated as a weighted average of the c_s results in different directions, using the shear wave energy for that direction as the weight. The shear wave energy at each pixel in each direction is calculated by summation of the corresponding squared temporal signal, and normalized by the aggregation of the shear wave energy over different directions, such that the weights in different directions from each pixel always add up to 1 [27].

16.3 Ex Vivo Validation

16.3.1 Experimental Setup

As mentioned above, one or several electromagnetic vibrators can be used to generate shear waves. For the particular application in this chapter, we use a single loudspeaker (Pioneer SW-8, Pioneer Electronics Inc., Japan) embedded as a part of the examination bed [33], with the diaphragm exposed and facing upward, as illustrated in Figure 16.3. For the phantom experiments, the phantoms are placed on the examination bed with the bottom coupled with the loudspeaker.

A Verasonics ultrasound system with a C5-2v curved array transducer (Verasonics Inc., Kirkland, WA) is programmed to have both B-mode imaging and shear wave motion detection capabilities. Under the guidance of the B-mode imaging, the transducer can be adjusted to locate the ROI. By hitting a button, the system immediately sends a trigger signal to a function generator (Agilent 33250A, Agilent Technologies, Inc., Santa Clara, CA), which sends

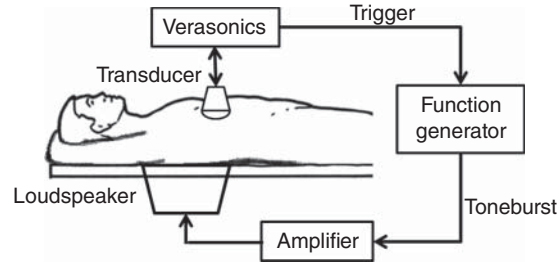

Figure 16.3 Illustration of the experimental setup. The embedded loudspeaker is driven by an amplifier controlled by a function generator. The Verasonics ultrasound system sends out a trigger signal to activate the vibration, and then acquires the B-mode image and records the motion. Source: © 2014 IEEE, reprinted, with permission, from [16].

out a 50 Hz tone burst with a duration of 100 ms and an amplitude of 1.2 V to activate the loudspeaker, after the signal is amplified (Crown XLS202, Crown Audio, Inc., Elkhart, IN) with a voltage gain of 30 dB. 10 ms after the vibration terminates the program switches to the high frame rate imaging mode for shear wave motion detection which lasts for 200 ms with 0.5 mm spatial resolution and 3-angle (−2°, 0°, and 2°) spatial compounding [18] at a frame rate of 1 kHz.

16.3.2 Phantom Experiments

First, two homogeneous elasticity phantoms (Phantom 1 and 2; CIRS Inc., Norfolk, VA) calibrated with SSI using the Aixplorer scanner (SuperSonic Imagine, Aix-en-Provence, France) were studied using HSWE. The C5-2v transducer was held by hand perpendicularly to the surface of the phantom with minimum pressure. Five measurements were taken for each phantom at five random locations on the phantom. For each measurement, eight directional filters, as shown in Figure 16.1, with 5 m/s speed limit and 10–100 Hz band-pass filter in the temporal direction were applied to the shear wave signals. 2D shear wave speed was calculated with 4 mm (8 pixels) estimation and averaging window, resulting in a 4 mm resolution. Then a 2D c_s image was constructed and a mean value was calculated from all the pixels of the image. For comparison, five SSI images were acquired at five random locations on the phantom using a curved array transducer SC6-1 and the Aixplorer [6]. The SSI images were analyzed offline, and a mean Young's modulus (E) was measured from a round ROI with 2 cm diameter centered at 3 cm depth in each of the SSI images, from which a mean c_s value was calculated based on $E \approx 3\mu = 3\rho c_s^2$ [6], where ρ is the mass density of the medium (assumed to be 1000 kg/m^3) and μ is the shear modulus.

Figure 16.4 shows representative 2D c_s images measured from the two phantoms superimposed over their B-mode images. The edges of the c_s images were 1 cm away from the edges of the FOV to avoid possible edge effects due to the Fourier transform in the directional filters. The measured c_s averaged over five measurements were 1.18 ± 0.04 m/s and 2.08 ± 0.05 m/s for phantom 1 and 2, respectively, compared to 1.18 ± 0.01 m/s and 2.04 ± 0.01 m/s, respectively using SSI. The penetration of HSWE in both phantoms was over 7 cm.

To further demonstrate the penetration of HSWE, a multi-purpose phantom (Model 040GSE; CIRS Inc., Norfolk, VA) was studied. The maximum depth of the measured phantom section is 16 cm with attenuation coefficient of 0.7 dB/cm/MHz. One HSWE measurement was taken with an ROI reaching the depth of 14 cm using the C5-2v transducer. For comparison, one SSI measurement was taken using the Aixplorer and SC6-1 with an ROI centered at 6.5 cm depth where measurements failed at the bottom half of the ROI due to the penetration limitations. Five more SSI measurements were taken using the Aixplorer and the SC6-1 with the ROI centered at 3 cm depth where elasticity of the phantom was reliably measured. Figure 16.5a shows the 2D HSWE c_s image superimposed over a B-mode image. The ROI of the image was centered at 12.5 cm depth (11–14 cm) with averaged c_s of 2.60 ± 0.15 m/s. For SSI image at 6.5 cm depth, no elasticity result could be acquired from the lower part of the ROI due to the attenuation. For

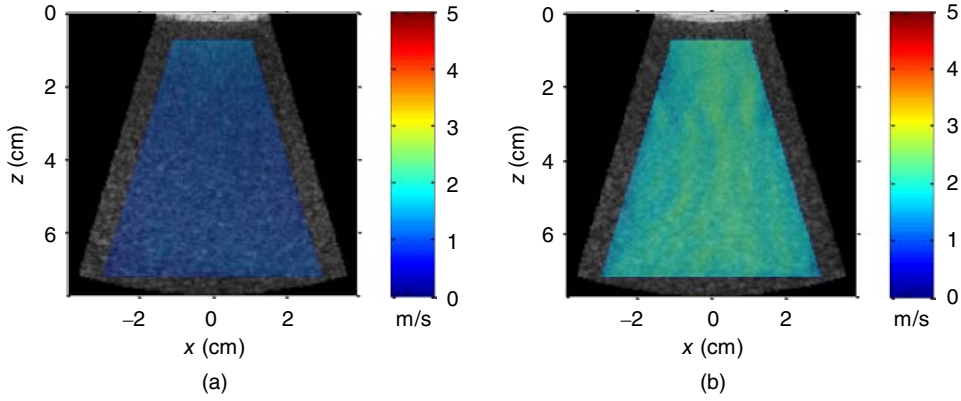

Figure 16.4 Representative c_s images of phantoms 1 (a) and 2 (b) superimposed over their corresponding B-mode images. Source: © 2014 IEEE, reprinted, with permission, from [16].

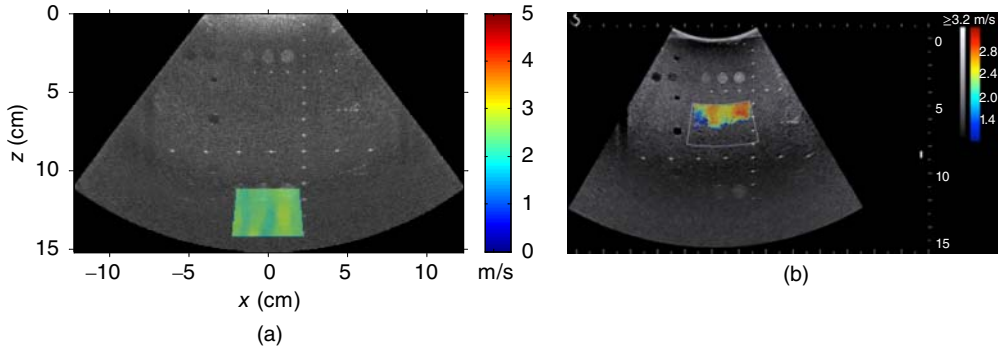

Figure 16.5 (a) 2D c_s image of the multi-purpose phantom superimposed over its B-mode image. The ROI of the image was centered at 12.5 cm with measured average c_s over the ROI of 2.60 ± 0.15 m/s; (b) SSI image of the same phantom with ROI centered at 6.5 cm depth. Source: © 2014 IEEE, reprinted, with permission, from [16].

the other five SSI measurements at 3 cm depth, the c_s averaged over different measurements was 2.60 ± 0.01 m/s, which was comparable to the single HSWE measurement result. Note that the standard deviation for HSWE was calculated from the c_s at different pixels within the ROI, whereas the standard deviation for SSI was from the mean c_s of different measurements.

16.4 In Vivo Application

Liver fibrosis and cirrhosis are the result of chronic liver injury, and affect hundreds of millions of patients worldwide [34]. A variety of methods has been applied for liver fibrosis staging [4, 35–37] as noninvasive alternatives to the gold standard of liver biopsy [38]. However, ultrasound radiation-based methods failed to obtain reliable measurement in overweight or obese patients [39, 40], whereas the prevalence of adult obesity (defined as body mass index or BMI ≥ 30) in the United States is over one third of the population and keeps increasing [41]. As demonstrated in the phantom experiments above, HSWE is capable of 2D elasticity imaging and has superior image penetration over other methods, which could be useful in liver fibrosis staging, especially for overweight or obese subjects.

Ten patients (8 women and 2 men; age range: 30–77 years; BMI: 19.4–34.0) undergoing clinically indicated liver MRE exams participated in the study. Five patients were overweight with BMI between 25 and 30, and two patients were obese with BMI over 30. The study was approved by the institutional review board (IRB) of the Mayo Clinic and written consent was obtained from each subject.

The MRE exams were performed using a 1.5T MRI scanner (GE Healthcare, Milwaukee, WI), with a pneumatic driver attached to the subject's abdomen to provide a harmonic mechanical vibration at 60 Hz. Standard MRE exam-acquired images of wave propagation in the liver were analyzed by physicians following the standardized clinical routine [42].

The experimental setup is the same as that of phantom studies as illustrated in Figure 16.3. During the experiment, the subject was laid supine with the back (lower rib cage) coupled with the loudspeaker and right arm abducted, giving the transducer access to the available intercostal acoustic windows. For each measurement, a sonographer positioned the transducer using B-mode imaging to locate a relatively large liver region free of major vessels through intercostal spaces. Then the subject was instructed to suspend breathing while the operator activated HSWE measurement. For each subject, 15 measurements were obtained through three intercostal spaces (between ribs 9 and 10, 8 and 9, 7 and 8) with five repetitions for each intercostal space.

For each HSWE measurement, a 2D c_s image was calculated. Figure 16.6a shows a representative c_s image superimposed over the B-mode image from one measurement of one patient (BMI: 26.4). The HSWE ROI of in vivo liver reached around 7 cm. Similar to the phantom study, a mean value was computed over a trapezoidal ROI, the edges of which were 1 cm away from the liver capsule, the left, right, and bottom edges of the FOV, respectively. Among the 10 patients, five patients were also examined by SSI following a similar protocol (15 measurements through three different intercostal spaces). A representative SSI image of the same patient is shown in Figure 16.6b.

For each patient, a median value was calculated from the 15 mean values from the HSWE measurements as that patient's result. The interquartile ratio, defined as the ratio between the interquartile range (from the first quartile to the third quartile) and the median value, was also calculated to evaluate the reliability of the results [40, 43]. The interquartile ratios for the HSWE results are listed in Table 16.1. All of the ratios using HSWE were below the 30% boundary, within which the results are regarded as reliable [43]. The ratios of the SSI measurements from

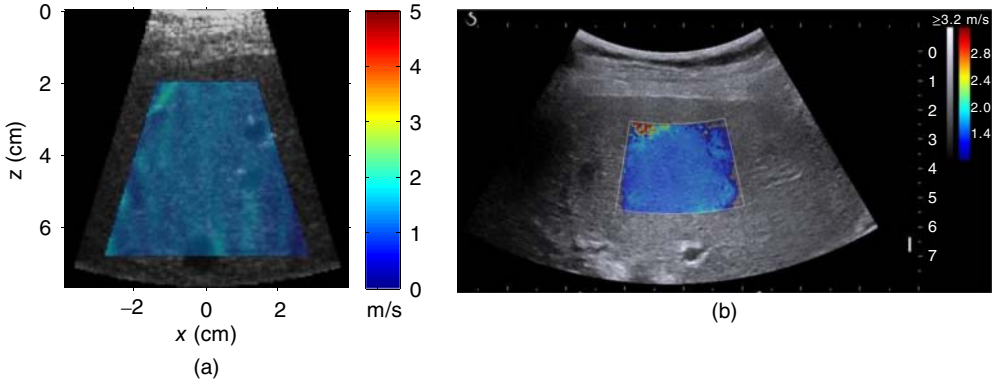

Figure 16.6 (a) Representative c_s image of the in vivo liver superimposed over its corresponding B-mode images from one patient (patient No. 6). The measured c_s within the colored region of the image was 1.48 ± 0.07 m/s. (b) Representative SSI image of the same patient. The measured c_s based on the offline analysis described in the phantom study was 1.46 m/s. The mean shear modulus of the patient measured by MRE was 2.3 kPa which corresponds to a c_s of 1.52 m/s. Source: © 2014 IEEE, reprinted, with permission, from [16].

Table 16.1 Interquartile ratios of EVMUSE and SSI results. © 2014 IEEE. Reprinted, with permission, from [16].

Patient No.	BMI	EVMUSE ratio (%)	SSI ratio (%)
1	26.9	8.0	
2	28.4	22.8	
3	27.4	9.8	
4	34.0	17.1	
5	22.7	8.0	5.0
6	26.4	10.1	10.8
7	19.4	13.5	
8	32.3	15.6	74.4
9	24.2	19.8	69.0
10	23.5	9.1	84.1

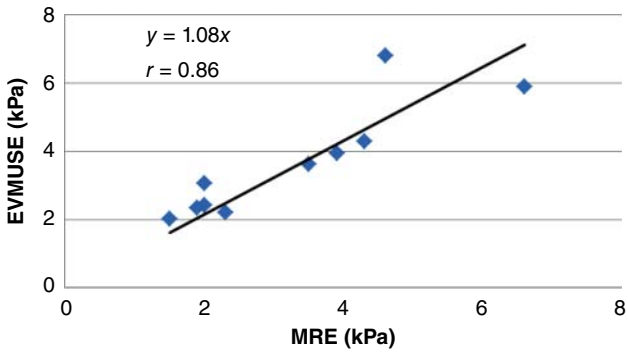

Figure 16.7 EVMUSE results from the 10 patients plotted against the MRE results. The Pearson product–moment correlation coefficient r was 0.86 with $p < 0.001$, indicating the correlation was significant. Source: © 2014 IEEE, reprinted, with permission, from [16].

the five patients are also listed in Table 16.1. The interquartile ratios of the HSWE and SSI measurements for the patient shown in Figure 16.6 were 10.1% and 10.8%, respectively, whereas the ratios for another patient with BMI of 32.3 were 15.6% and 74.4%, respectively, indicating HSWE may be able to give more consistent results within each patient, especially for overweight/obese patients.

HSWE results from the 10 patients were plotted against MRE results, as shown in Figure 16.7. The Pearson product–moment correlation coefficient between the MRE and ultrasound results was 0.86 (95% confidence interval: 0.71–0.98) with $p < 0.001$, indicating the correlation was significant.

16.5 Summary

In this chapter, we have introduced the harmonic shear wave elastography (HSWE) method for 2D elasticity imaging by measuring the c_s from a multi-directional shear wave field generated by harmonic mechanical vibration. Results showed HSWE is capable of measuring tissue elasticity accurately, as validated by SSI in in vitro phantom studies, and the in vivo measurements in patients with liver disease correlate well with MRE results. HSWE was demonstrated

to have better penetration than the radiation force-based method, and thus has potential for non-invasive staging of liver fibrosis in obese patients.

Acknowledgments

The authors would like to thank Dr. Stefan Catheline for the helpful discussions and Theresa Nielson for coordinating the patient study. This work was supported by NIH grants EB002167, DK092255, and DK082408. The content is solely the responsibility of the authors and does not necessarily represent the official views of NIH. The technology described here has been licensed, and Mayo Clinic and some of the authors may have conflicts of interest.

References

1 Sarvazyan, A.P., Rudenko, O.V., and Swanson, S.D., (1998). Shear wave elasticity imaging: A new ultrasonic technology of medical diagnostics. *Ultrasound Med. Biol.* 24: 1419–1435.
2 Ophir, J., Cespedes, I., Ponnekanti, H., et al. (1991). Elastography: a quantitative method for imaging the elasticity of biological tissues. *Ultrason. Imaging* 13: 111–134.
3 Gallot, T., Catheline, S., Roux, P., et al. (2011). Passive elastography: shear-wave tomography from physiological-noise correlation in soft tissues. *IEEE Trans. Ultrason., Ferroelect., Freq. Control* 58: 1122–1126.
4 Palmeri, M.L., Wang, M.H., Dahl, J.J., et al. (2008). Quantifying hepatic shear modulus in vivo using acoustic radiation force. *Ultrasound Med. Biol.* 34: 546–558.
5 Chen, S., Urban, M.W., Pislaru, C., et al. (2009). Shearwave dispersion ultrasound vibrometry (SDUV) for measuring tissue elasticity and viscosity. *IEEE Trans. Ultrason., Ferroelect., Freq. Control* 56: 55–62.
6 Bercoff, J., Tanter, M., and Fink, M. (2004). Supersonic shear imaging: A new technique for soft tissue elasticity mapping. *IEEE Trans. Ultrason., Ferroelect., Freq. Control* 51: 396–409.
7 Song, P., Zhao, H., Manduca, A., et al. (2012). Comb-push ultrasound shear elastography (CUSE): a novel method for two-dimensional shear elasticity imaging of soft tissues. *IEEE Trans. Med. Imaging* 31: 1821–1832.
8 Wu, Z., Taylor, L.S., Rubens, D.J., and Parker, K.J. (2004). Sonoelastographic imaging of interference patterns for estimation of the shear velocity of homogeneous biomaterials. *Phys. Med. Biol.* 49: 911–922.
9 Sandrin, L., Tanter, M., Gennisson, J.L., et al. (2002). Shear elasticity probe for soft tissues with 1-D transient elastography. *IEEE Trans. Ultrason., Ferroelect., Freq. Control* 49: 436–446.
10 McLaughlin, J. and Renzi, D. (2006). Shear wave speed recovery in transient elastography and supersonic imaging using propagating fronts. *Inverse Probl.* 22: 681–706.
11 Gennisson, J.L., Cornu, C., Catheline, S., et al. (2005). Human muscle hardness assessment during incremental isometric contraction using transient elastography. *J. Biomech.* 38: 1543–1550.
12 Oliphant, T.E., Manduca, A., Ehman, R.L., and Greenleaf, J.F. (2001). Complex-valued stiffness reconstruction for magnetic resonance elastography by algebraic inversion of the differential equation. *Magn. Reson. Med.* 45: 299–310.
13 McGee, K.P., Lake, D., Mariappan, Y., et al. (2011). Calculation of shear stiffness in noise dominated magnetic resonance elastography data based on principal frequency estimation. *Phys. Med. Biol.* 56: 4291–4309.

14 Catheline, S., Benech, N., Brum, J., and Negreira, C. (2008). Time reversal of elastic waves in soft solids. *Phys. Rev. Lett.* 100: 064301.

15 Tzschatzsch, H., Ipek-Ugay, S., Guo, J., et al. (2014). In vivo time-harmonic multifrequency elastography of the human liver. *Phys. Med. Biol.* 59: 1641–1654.

16 Zhao, H., Song, P., Meixner, D.D., et al. (2014) External vibration multi-directional ultrasound shearwave elastography (EVMUSE): application in liver fibrosis staging. *IEEE Trans. Med. Imaging* 33: 2140–2148.

17 Schenck, J.F. (1996). The role of magnetic susceptibility in magnetic resonance imaging: MRI magnetic compatibility of the first and second kinds. *Med. Phys.* 23: 815–850.

18 Tanter, M., Bercoff, J., Sandrin, L., and Fink, M. (2002). Ultrafast compound imaging for 2-D motion vector estimation: Application to transient elastography. *IEEE Trans. Ultrason., Ferroelect., Freq. Control* 49: 1363–1374.

19 Song, P., Urban, M.W., Manduca, A., et al. (2015). Coded excitation plane wave imaging for shear wave motion detection. *IEEE Trans. Ultrason., Ferroelect., Freq. Control* 62: 1356–1372.

20 Kasai, C., Namekawa, K., Koyano, A., and Omoto, R. (1985). Real-time two-dimensional blood flow imaging using an autocorrelation technique. *IEEE Trans. Sonics Ultrasonics* Su-32: 458–464.

21 Loupas, T., Powers, J.T., and Gill, R.W. (1995). An axial velocity estimator for ultrasound blood-flow imaging, based on a full evaluation of the Doppler equation by means of a 2-dimensional autocorrelation approach. *IEEE Trans. Ultrason., Ferroelect., Freq. Control* 42: 672–688.

22 Bonnefous, O. and Pesque, P. (1986). Time domain formulation of pulse-Doppler ultrasound and blood velocity estimation by cross correlation. *Ultrason. Imaging* 8: 73–85.

23 Manduca, A., Lake, D.S., Kruse, S.A., and Ehman, R.L. (2003). Spatio-temporal directional filtering for improved inversion of MR elastography images. *Med. Image Anal.* 7: 465–473.

24 Sarvazyan, A.P., Urban, M.W., and Greenleaf, J.F. (2013). Acoustic waves in medical imaging and diagnostics. *Ultrasound Med. Biol.* 39: 1133–1146.

25 Zhao, H., Song, P., Urban, M.W., et al. (2011). Bias observed in time-of-flight shear wave speed measurements using radiation force of a focused ultrasound beam. *Ultrasound Med. Biol.* 37: 1884–1892.

26 Hoyt, K., Castaneda, B., and Parker, K.J. (2008). Two-dimensional sonoelastographic shear velocity imaging. *Ultrasound Med. Biol.* 34: 276–288.

27 Song, P., Manduca, A., Zhao, H., et al. (2014). Fast shear compounding using robust 2-D shear wave speed calculation and multi-directional filtering. *Ultrasound Med. Biol.* 40: 1343–1355.

28 Wang, M., Byram, B., Palmeri, M., et al. (2013). On the precision of time-of-flight shear wave speed estimation in homogeneous soft solids: initial results using a matrix array transducer. *IEEE Trans. Ultrason., Ferroelect., Freq. Control* 60: 758–770.

29 Lai, X. and Torp, H. (1999). Interpolation methods for time-delay estimation using cross-correlation method for blood velocity measurement. *IEEE Trans. Ultrason., Ferroelect., Freq. Control* 46: 277–290.

30 Pinton, G.F., Dahl, J.J., and Trahey, G.E. (2006). Rapid tracking of small displacements with ultrasound. *IEEE Trans. Ultrason., Ferroelect., Freq. Control* 53: 1103–1117.

31 Viola, F. and Walker, W.F. (2003). A comparison of the performance of time-delay estimators in medical ultrasound. *IEEE Trans. Ultrason., Ferroelect., Freq. Control* 50: 392–401.

32 Shepard, D. (1968). A two-dimensional interpolation function for irregularly-spaced data. *Proceedings of the ACM Conf.* 517–524.

33 Tzschatzsch, H., Hattasch, R., Knebel, F., et al. (2013) Isovolumetric elasticity alteration in the human heart detected by in vivo time-harmonic elastography. *Ultrasound Med. Biol.* 39: 2272–2278.

34 Friedman, S.L. (2003). Liver fibrosis – from bench to bedside. *J. Hepatol.* 38 (Suppl 1): S38–53.

35 Bavu, E., Gennisson, J.L., Couade, M., et al. (2011). Noninvasive in vivo liver fibrosis evaluation using supersonic shear imaging: a clinical study on 113 hepatitis C virus patients. *Ultrasound Med. Biol.* 37: 1361–1373.

36 Chen, S., Sanchez, W., Callstrom, M.R., et al. (2013) Assessment of liver viscoelasticity by using shear waves induced by ultrasound radiation force. *Radiology* 266: 964–970.

37 Sandrin, L., Fourquet, B., Hasquenoph, J.M., et al. (2003). Transient elastography: a new noninvasive method for assessment of hepatic fibrosis. *Ultrasound Med. Biol.* 29: 1705–1713.

38 Bravo, A.A., Sheth, S.G., and Chopra, S. (2001). Liver biopsy. *New Engl. J. Med.* 344: 495–500.

39 Sirli, R., Bota, S., Sporea, I., et al. (2013). Liver stiffness measurements by means of supersonic shear imaging in patients without known liver pathology. *Ultrasound Med. Biol.* 39: 1362–1367.

40 Cassinotto, C., Lapuyade, B., Ait-Ali, A., et al. (2013). Liver fibrosis: noninvasive assessment with acoustic radiation force impulse elastography – comparison with Fibroscan M and XL probes and Fibrotest in patients with chronic liver disease. *Radiology* 269: 283–292.

41 Ogden, C.L., Carroll, M.D., Kit, B.K., and Flegal, K.M. (2012). Prevalence of obesity in the United States, 2009–2010. *NCHS Data Brief* 1–8.

42 Venkatesh, S.K., Yin, M., and Ehman, R.L. (2013). Magnetic resonance elastography of liver: technique, analysis, and clinical applications. *J. Magn. Reson. Imaging* 37: 544–555.

43 Ferraioli, G., Tinelli, C., Dal Bello, B., et al. (2012). Accuracy of real-time shear wave elastography for assessing liver fibrosis in chronic hepatitis C: a pilot study. *Hepatology* 56: 2125–2133.

17

Vibro-acoustography and its Medical Applications

Azra Alizad[1] *and Mostafa Fatemi*[2]

[1] *Department of Radiology, Mayo Clinic, Rochester, MN, USA*
[2] *Department of Physiology and Biomedical Engineering, Mayo Clinic, Rochester, MN, USA*

17.1 Introduction

Vibro-acoustography (VA), a new ultrasound-based imaging modality, has gained much interest in the medical field in recent years. This acoustic imaging modality uses the radiation force of ultrasound to induce low-frequency vibrations in the tissue and creates images of the acoustic response. This chapter focuses on potential biomedical applications of VA. The purpose is to bring together the results of various studies, ex vivo and in vivo, on breast, thyroid, human arteries, and prostate. Here, after a brief discussion about the general principle of VA, we describe the applications. Future developments and potential impact of VA in breast and thyroid imaging are also discussed.

17.2 Background

New imaging modalities based on radiation force of ultrasound have been developed for characterizing mechanical properties of soft tissues. All of these methods aim to differentiate normal tissue from diseased tissue by exploiting the elasticity as a contrast mechanism. Ultrasound radiation force vibrates and deforms soft tissues noninvasively, and the resulting mechanical response of tissues provides elasticity information useful in detection and differentiation.

17.2.1 General Principles of VA and Method

VA is a noninvasive imaging technique that produces palpation-like information by measuring the acoustic response of a tissue or object to a vibration induced by the radiation force of ultrasound [1, 2]. The VA technique can be summarized in three steps:

(1) applying a localized oscillating force on or inside the tissue to induce vibration,
(2) recording the resulting sound arising from the vibrating tissue, and
(3) creating an image from the recorded acoustic signal [3].

The basic concept of the VA technique is using the force of ultrasound. Numerous investigators have studied the theory of acoustic radiation force [4–7], and the biomedical applications of acoustic radiation force has been described by Sarvazyan et al. [8].

VA uses two ultrasound beams at slightly different frequencies, f_1 and f_2, and these beams focus at a common location to produce a modulated ultrasound radiation force at Δf and

Ultrasound Elastography for Biomedical Applications and Medicine, First Edition.
Edited by Ivan Nenadic, Matthew Urban, James Greenleaf, Jean-Luc Gennisson, Miguel Bernal, and Mickael Tanter.

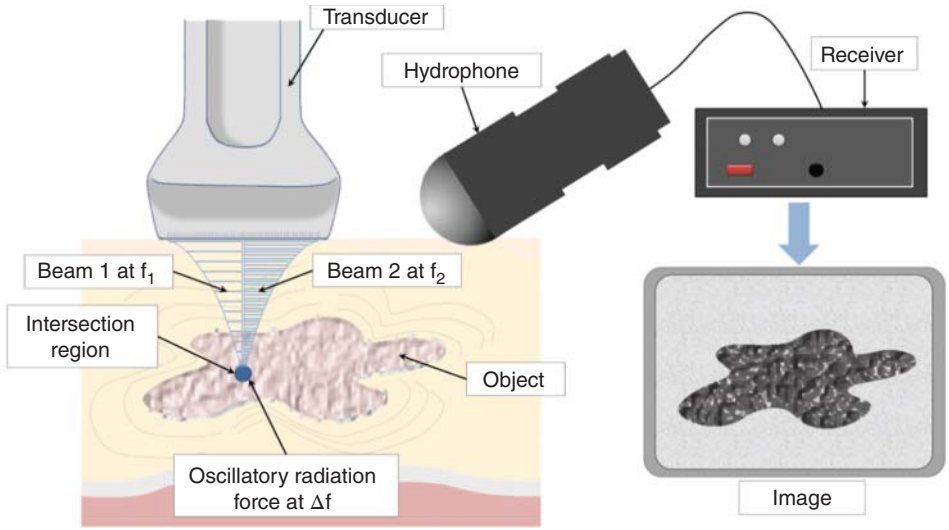

Figure 17.1 Generation of localized oscillatory radiation force using two ultrasound beams.

creates an acoustic field. The focused US beam is scanned across the tissue. A hydrophone placed nearby obtains acoustic emissions to form an image. The resulting VA images are speckle free. Figure 17.1 shows a simplified VA system [3, 9].

17.2.2 Features of a Vibro-acoustography Image

A VA image illustrates information about ultrasonic properties such as the scattering and power absorption characteristics, which are also seen in conventional ultrasonography. Most importantly, VA depicts the dynamic characteristics of the tissue at frequency Δf that represents how the tissue responds to a vibrating force, which are related to mechanical properties and tissue stiffness. Such information is not available from conventional ultrasonography [1, 2].

Furthermore, VA produces images free of speckle, the snowy pattern seen in conventional US images. Speckle reduces the contrast of ultrasound images and small structures such as microcalcifications. In addition, low-contrast lesions in tissue cannot be easily seen. The acoustic emission signal in VA, which is at a low frequency, creates speckle-free images with high contrast [3]. VA is still in the research stage. A number of experiments have been conducted to evaluate its effectiveness in various applications.

17.3 Application of Vibro-acoustography for Detection of Calcifications

Ex vivo VA has been used to characterize and image biological tissues [10–14]. VA is capable of detecting macro- and micro-calcifications and delineates these calcifications with high contrast. Microcalcifications are common findings in a wide spectrum of breast lesions, ranging from benign to malignant [15]. The clinical application of VA in detection of microcalcifications in radiologically dense breasts found in younger, pregnant, or lactating women has great potential. The ability of VA to detect calcification has been studied in vitro in a variety of human tissues including breast [16–20], prostate [21, 22], heart valve leaflets [23], and human arteries [24].

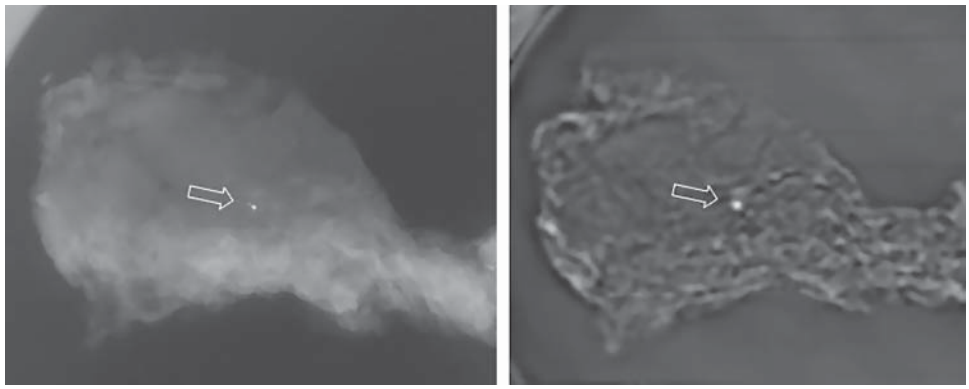

(a) (b)

Figure 17.2 Single microcalcification: (a) X-ray image of the breast tissue showing a microcalcification at the center of the sample; (b) VA of the same tissue shows the calcification as bright spot. Source: © 2004 IEEE, reprinted, with permission, from [17].

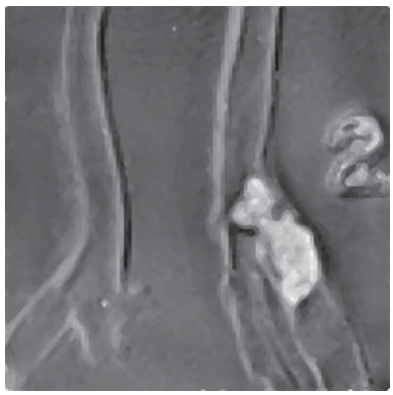

Figure 17.3 VA of excised human carotid arteries: vibro-acoustography of the normal and calcified arteries The calcification is seen as a bright region in vibro-acoustography images. Source: © Institute of Physics and Engineering in Medicine; reproduced by permission of IOP Publishing, all rights reserved [11].

We present an example of breast tissue microcalcification detected by VA. A bright spot at the center of X-ray represents the microcalcification. VA of this tissue clearly shows the microcalcification also as a bright spot. The shape and position of the microcalcification match well with the corresponding spot in the X-ray. VA also shows the structure of the soft tissue (Figure 17.2).

Figure 17.3 shows VA images of two carotid arteries. The left artery is from a young person and has no calcification. The right artery is from an older person. The arteries were immersed in a water tank for scanning. The Δf in this experiment is 7 kHz. The VA image shows no calcification on the left artery, while some calcium deposit near the bifurcation on the right artery is seen as a bright region.

Figure 17.4 shows VA images of an aortic valve and the corresponding radiography. The VA image resembles the radiography of this heart valve. The arrow in both images points to a small piece of calcification, about 1 mm in diameter, that is visible in both the radiograph and the vibro-acoustic scans. This image demonstrates that VA may be used to identify early calcification buildup on heart valves.

VA scanning has been conducted on a series of prostate tissues. Imaging results of ex vivo prostate tissues reveals the potency of VA as a promising tool to detect abnormalities, delineate tissue structures and anatomical zones, and locate calcifications. We present the X-ray, US, and VA images of a prostate tissue in Figure 17.5. Tissue X-ray shows a cluster of micro and macro-calcification, but the US image is not informative. The VA image of this prostate tissue

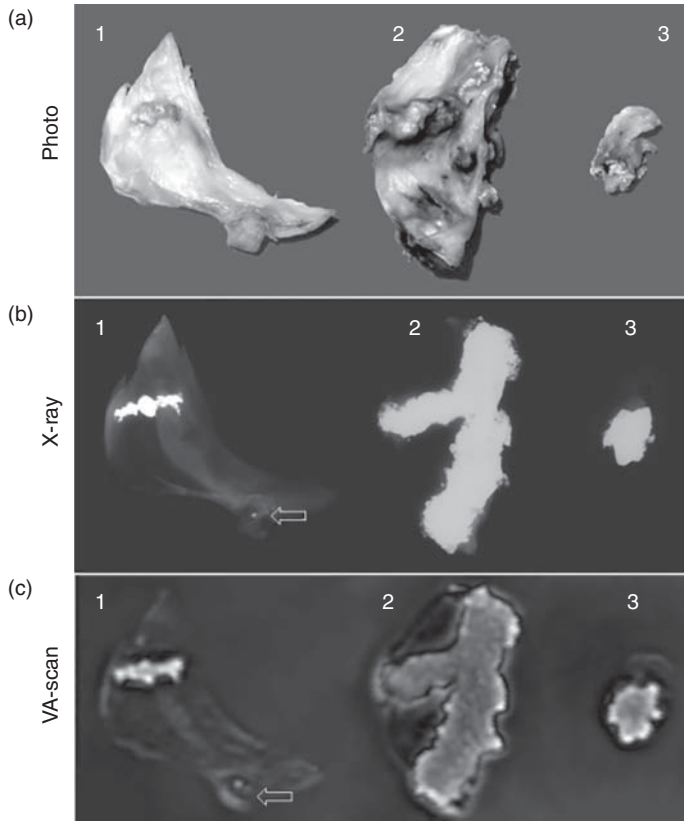

Figure 17.4 (a) Photograph of calcified aortic valve; (b) X-ray of aortic valve mounted on scanning bracket; and (c) VA image of calcified tissue valve. VA scan image resembles the corresponding radiography of heart valve tissue. Arrow points to small piece of calcification (1 mm in diameter), seen in both X-ray and VA scan images. Source: reprinted from [23], copyright 2002, with permission from Elsevier.

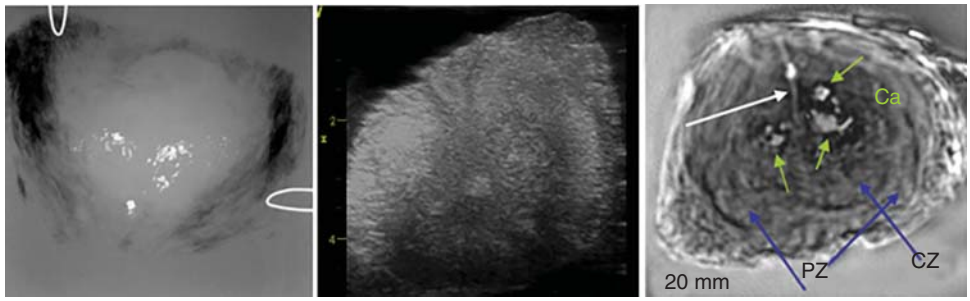

Figure 17.5 (a) X-ray of a prostate tissue (calcification is seen in the center); (b) US of the tissue; and (c) VA image of this prostate tissue shows calcification plus anatomical zones, peripheral zone (PZ) and central zone (CZ).

clearly demonstrates a group of large calcifications as well as the anatomical zones, peripheral zone (PZ) and central zone (CZ).

17.4 In Vivo Breast Vibro-acoustography

17.4.1 Background on Breast Imaging

Breast cancer is the most common non-skin cancer among women in the USA and the second leading cause of cancer death in US women, after lung cancer [25]. Depending on their application, many of the current imaging modalities have low specificity rates. The diagnostic performance of mammography is greatly reduced, especially in dense breasts. This is particularly important in the case of high- and moderate-risk women who need to be screened at younger age when they have dense breasts, obscured masses, or lesions with microcalcifications (MCs) and small lesions. Ultrasound imaging is not sensitive to MCs. Even as studies report high sensitivity with MRI, one of the major limitations of breast MRI is that false-positive enhancement can occur in benign breast lesions, resulting in relatively low specificity. The poor specificity results in unnecessary follow-ups and biopsies, extra cost, and great emotional distress. Breast MRI also relies on other tissue parameters that do not contrast mass lesions based on tissue stiffness [26, 27].

Tissue stiffness is known to be associated with pathology [28, 29]. Except for the emerging elastography methods, none of the current imaging modalities used in clinics today, such as conventional breast US, mammography, and MRI, is sensitive to stiffness. Manual detection of breast lumps (palpation) is the simplest, yet is effective for identifying and differentiation of breast masses. However, the diagnostic performance is poor in deep lesions and depends on the expertise of examiner.

Part of these problems, if not all, could be resolved with VA (as an imaging tool). VA is sensitive to stiffness and provides palpation-like information that is sensitive to tissue stiffness – thus it may be used to improve the diagnosis of breast cancer. VA, a low-cost and noninvasive imaging modality, is sensitive to mechanical properties of breast and can provide information not available in other imaging modalities. In particular, VA is sensitive to microcalcifications (MCs) [17], which are markers of some breast cancers. In addition, the performance of VA is not reduced in dense breast. MRI is not sensitive to MCs and it is hard to detect MCs with ultrasound. Breast imaging by VA has been reported before [3, 18, 19, 30, 31], where the images were mainly evaluated against X-ray mammography. The purpose of this section is to present the results of various studies on in vivo breast VA to demonstrate the potentials of this technology and the role it may play in the future as a breast-imaging tool.

17.4.2 Method of In Vivo VA and Results

A VA system was integrated into a stereotactic mammography machine (Fischer Imaging Inc., Mammotest^{TM} system) and has been tested for in vivo breast imaging [18]. This combined system enables the operator to obtain matching VA and mammography images of the human breast. The patient lies down in a prone position while her breast is passed through a hole in the bed. The breast is placed between the back panel, which includes the X-ray detector, and a sliding compression panel. The compression panel consists of a window covered with a thin latex membrane transparent to US beam. An annular confocal US transducer is located behind the window. VA images were acquired in the cranial-caudal view at different depths from the skin. The VA image area was 5×5 cm. A hydrophone is placed on the side of the breast to receive the acoustic emission generated by the radiation force of US. The simplified diagram of the VA system is shown in Figure 17.6.

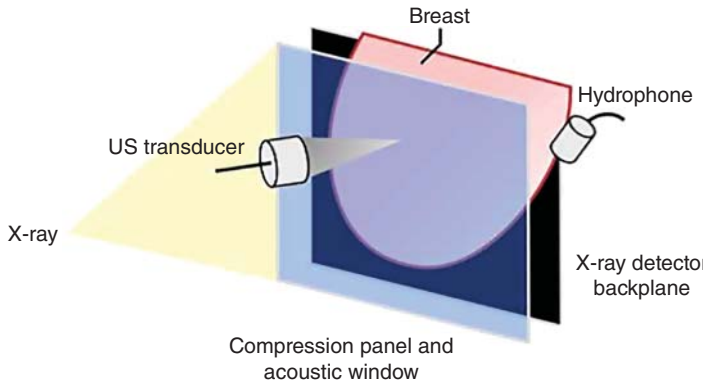

Figure 17.6 Diagram of the combined mammography and vibro-acoustic system. Breast positioning between panels is shown. Source: adapted from [31].

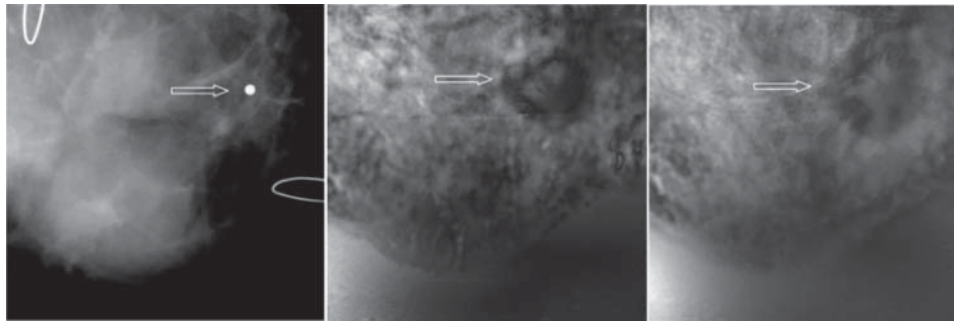

Figure 17.7 Fibroadenoma: (a) mammography shows the marker placed on the location of palpable mass; (b) and (c) VA images of the same breast at 2.0 cm depth (b) and 2.5 cm depth (c) show a lobulated well-defined mass (arrows). Source: adapted from [31].

In vivo breast VA using the integrated system has been studied on 60 female patients with breast lesions [31]. Benign and malignant breast cases will be discussed as follows.

A female patient in her 40s with a palpable mass in her right breast has been examined. Targeted US examination on palpable site revealed a 29 × 19 ×13 mm lobulated well-defined, mildly hypoechoic mass. Diagnostic mammography showed heterogeneous, dense parenchyma in both breasts, but did not show the palpable mass. A marker was placed on the skin to identify the location of the palpable mass (Figure 17.7). The result of pathology has proved the mass to be a fibroadenoma. The importance of this case is that VA can identify masses not seen on mammograms.

A case of fibroadenoma is shown in Figure 17.8. The patient is in her 70s. Scattered fibroglandular densities and two masses were identified on both breasts in mammography screening. The diagnostic mammography showed a 2 cm sharply marginated mass with coarse lobulation on the right breast (Figure 17.8a). The VA image of the right breast clearly showed the margins and mass with the gentle coarse lobulation that are classic findings in fibroadenoma. The calcification seen in mammogram is at a different depth and is not visible at the depth of this VA image.

Figure 17.9 shows another case, a woman in her 60s, whose screening and diagnostic mammography identified a small group of suspicious microcalcifications of different sizes and shapes along with minimal architectural distortion and increased soft-tissue density. Targeted

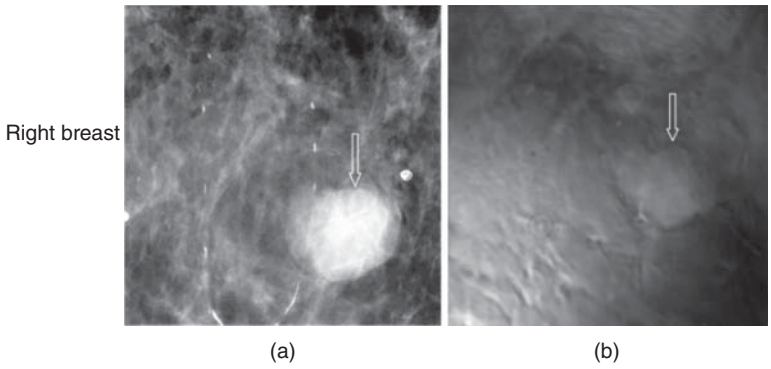

Figure 17.8 Fibroadenoma: (a) mammography of the right breast shows a round well defined mass (arrow); (b) VA at 2.5 cm depth shows a well-defined mass (arrow). Patient moved after mammography and during the examination, thus the mass slightly shifted upward. Source: reprinted from [31].

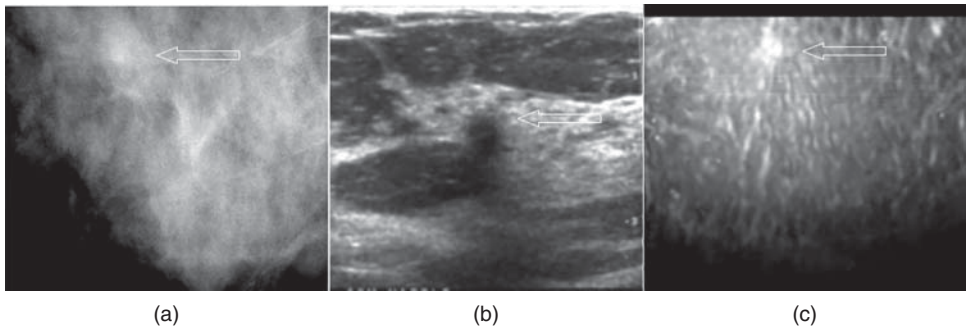

Figure 17.9 Invasive ductal carcinoma: (a) Mammography demonstrations increased soft-tissue density (arrow); (b) US image shows a hypoechoic lesion with shadowing; and (c) VA shows an irregular mass with spiculation (arrow). Source: reprinted from [31].

US confirmed a 5 × 7 cm hypoechoic lesion with an irregular border and posterior shadowing. The biopsy revealed an invasive ductal carcinoma, Nottingham grade II/III, in her right breast. The VA image was able to identify the lesion as a small irregular mass with fine spiculation that is characteristic of this type of malignant mass. The characteristic spiculation was difficult to see in the mammogram.

A patient in her 60s with mammographically dense breasts was examined. During mammography, a spiculated mass with no calcification was noted in her left breast (Figure 17.10a). Breast MRI identified a large, enhancing, irregular, spiculated mass measuring 8.5 × 3.3 × 5.4 cm in the left breast (Figure 17.10b). This was associated with left breast shrinkage and nipple inversion. VA of this breast also identified the lesion, which extended beyond the 5 × 5 cm of the imaging window, with remarkable spiculation that is suggestive of malignancy (Figure 17.10c). The pathology revealed the mass as grade I infiltrating lobular carcinoma. This case demonstrates that VA can detect breast cancer.

VA studies using a confocal VA system demonstrate the ability of VA in identifying various breast abnormalities, including microcalcifications as well as benign and malignant masses with relatively high specificity [3, 31]. This system was equipped with a water tank to accommodate acoustic coupling to tissue during scanning. A drawback of this system is limited access to parts of the breast near the chest wall and slower image acquisition.

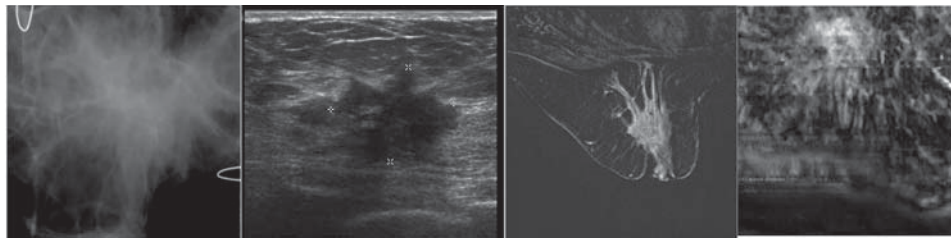

Figure 17.10 Infiltrating lobular carcinoma. (a) Mammogram identifies a large distorted area with spiculation. The U-shaped wires are used to present image orientation. (b) US images shows a large irregular hypoechoic mass with shadowing. (c) Magnetic resonance image shows a large, irregular region. (d) VA shows a large spiculated mass that almost covers the imaging window. Source: adapted and modified from [31].

To overcome the limitations of the annular confocal VA system, to shorten the scanning time, and to provide optimum coverage of the breast for imaging, we have advanced our imaging system by implementing VA on a clinical ultrasound scanner equipped with a "quasi-2D" array transducer. We call this technique "quasi-2D vibro-acoustography" (Q2-DVA). A clinical ultrasound scanner (GE Vivid 7, GE Healthcare Ultrasound Cardiology, Horten, Norway) was modified to perform both ultrasound imaging and VA. The Q2-D transducer array is in the form of a matrix with multiple rows and columns of ultrasound elements. This transducer is electronically constructed to generate an ultrasound beam resembling that of the confocal transducer. The newly designed VA system was tested on patients with breast lesions [32]. Our results indicate that our newly modified VA system can identify benign and malignant solid breast lesions and can easily detect microcalcification. Our results suggest that with further development, Q2-DVA can provide high-resolution images and has the potential to provide diagnostic information in the clinical setting and may be used as a complementary tool in support of other clinical imaging modalities. Here, we present the preliminary in vivo results of breast VA obtained by the new VA system equipped with the array Q2-D transducer [33].

First we present a case of invasive ductal carcinoma. The patient is a woman in her 50s with a palpable lump in her right breast. Her mammography demonstrated a heterogeneous dense breast with a central focal asymmetry (dashed yellow contour) and small microcalcifications (red arrows). Targeted clinical US showed a 21 mm × 14 mm irregular hypoechoic mass with an indistinct margin and posterior acoustic shadowing. VA images obtained with the handheld 1.75D probe show the mass and dimensions of the lesions are larger than those of the clinical US image (Figure 17.11). Similar findings have been seen and confirmed in our previous VA study [31] where malignant breast masses appeared lager in VA than in B-mode US. The pathology of this mass revealed it to be invasive ductal carcinoma, Nottingham grade II.

VA imaging of a benign fibroadenoma is presented here. A woman in her 40s with a palpable lump in her left breast was examined. Diagnostic mammography showed a heterogeneous dense breast with a 15 mm well-circumscribed solid mass at the anterior depth (yellow arrow), shown in Figure 17.12. Her targeted US demonstrated a corresponding solid round mass with circumscribed margins. VA images were obtained at a depth of 20 mm and revealed a well-defined mass (yellow arrows). US guided biopsy revealed a benign fibroadenoma.

A diagnostic mammogram in a patient discovered a partially obscured oval mass (yellow arrow in Figure 17.13a). A targeted transverse US image demonstrated an oval hypoechoic mass with posterior shadowing measuring 19 × 10 × 10 mm (Figure 17.13b). The VA image obtained at a depth of 30 mm showed an elongated mass with a well-defined border, suggesting a benign lesion. The biopsy result revealed the lesion as sclerosing fibroadenoma with densely hyalinized stroma. The sclerosing accounts for the shadowing posterior to the lesion. The mass

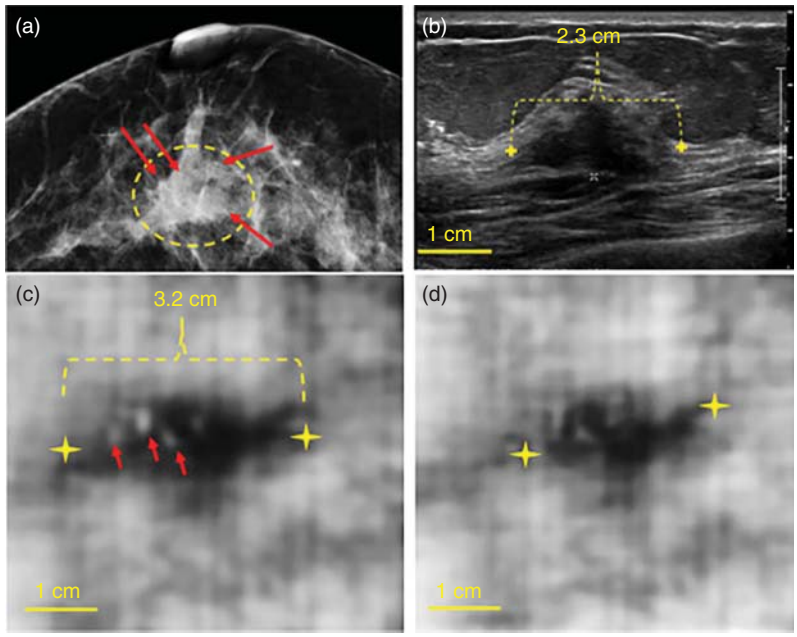

Figure 17.11 Invasive ductal carcinoma. (a) Mammogram of the right breast demonstrates a central focal asymmetry. Microcalcifications are marked with arrows. (b) B-mode US shows an irregular 23 mm hypoechoeic mass. (c, d) VA images obtained by array probe at depths of 25 mm and 27.5 mm, respectively. The lesion is marked with cross markers on panel (c). The presence of calcifications is also noted in the VA image at 25 mm (marked with red arrows). Source: reprinted from [33]; copyright 2014, with permission from Elsevier.

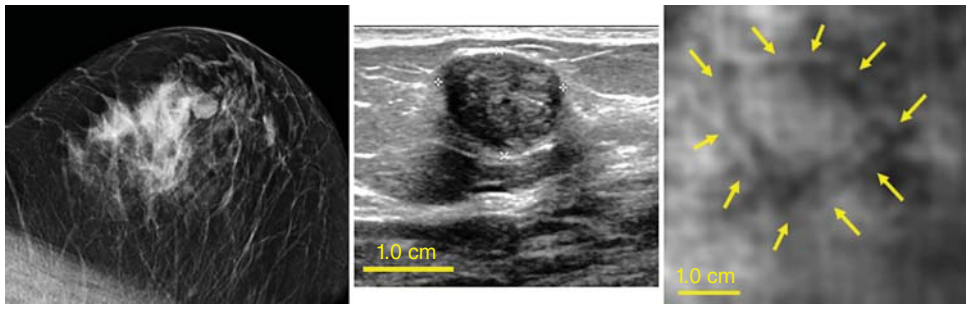

Figure 17.12 (a) Magnified mammography of the left breast shows a round mass with circumscribed margin. (b) US image demonstrates the round mass with mixed internal echogenicity and circumscribed margins. (c) 1.75D VA image of the breast outlines the corresponding mass (arrows). Source: reprinted from [33], copyright 2014, with permission from Elsevier.

is well-visualized (dark) in the VA image. The lesion shown to be at deeper depths by VA than shown in B-mode imaging, due to more compression applied during the clinical US imaging procedure.

The results of the study using VA implemented on a clinical ultrasound scanner equipped with a Q2-D US transducer indicate that this new VA has the potential to identify and differentiate breast lesions. The Q2-DVA system can also overcome the difficulties associated with using confocal VA, such as the inability to image lesions close to the chest wall or the discomfort associated with patient positioning and compression. Our results provide a foundation

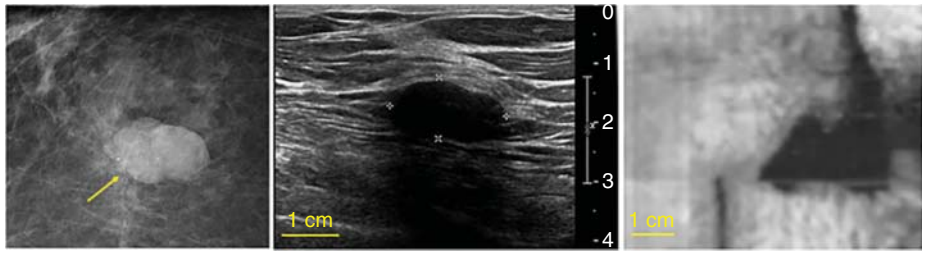

Figure 17.13 Sclerosing fibroadenoma: (a) magnified mammogram shows an oval mass in the posterior depth of the right breast; (b) clinical B-mode ultrasound documents the corresponding mass; (c) quasi-2D vibro-acoustography image of breast tissue with a sclerosing fibroadenoma at a depth of 30 mm. Source: reprinted from [33], copyright 2014, with permission from Elsevier.

for further development of clinical VA systems and further investigation in a larger group of patients.

17.5 In Vivo Thyroid Vibro-acoustography

Ultrasonography of thyroid does not always lead to conclusive results. Furthermore, current ultrasound imaging technology has a poor performance in detecting important microcalcifications and its role in diagnosis of malignant nodules is limited and carries poor specificity [34]. Uncertainties in ultrasound and other thyroid imaging methods lead to a large number of unnecessary biopsies. Fine needle aspiration biopsy (FNAB) is associated with false-negative rate of up to 11%, a false-positive rate of up to 8%, with a sensitivity of about 80%, and a specificity of 73% [35–38]. Vibro-acoustography is sensitive not only to the ultrasound properties of the tissue but also to the dynamic behavior at low frequencies; thus VA offers information that is not available with conventional ultrasound.

We have investigated the feasibility of using VA with a handheld array US transducer for detection and localization of thyroid nodules [39]. The results demonstrate that VA implemented on a clinical ultrasound scanner equipped with a handheld array US transducer can identify and has potential to differentiate thyroid nodules.

A 48-year-old female patient with a benign thyroid nodule was examined. B-mode ultrasound identifies large hypoechoic nodule with small cystic appearance measuring about 47 × 27 mm (x-z dimensions). The nodule appears on C-mode US, taken at 2 cm depth, measuring about 44.2 × 30.5 mm (x-z dimensions). The VA at 2.0 cm depth reveals the large nodule with distinct margin measuring about 30.5 mm in the y direction and more than 47 mm in the x direction, with its side margins extending out of VA image window. Its shape and location corresponds to the C-scan US at 2 cm depth (Figure 17.14).

US and VA images of the right side thyroid of a 37-year-old male with papillary thyroid carcinoma are shown in Figure 17.15. Targeted US shows a cystic nodule measuring about 1.0 × 1.3 × 1.4 cm with peripheral calcifications, one of the characteristics of papillary carcinoma. The VA scan at 2.5 cm depth identifies the nodule with a cystic appearance in slightly larger dimensions as well as some peripheral calcifications with greater clarity than shown in the US image, denoted by arrows.

These results suggest that VA may have a potential as a clinical tool in thyroid imaging; however, VA is not intended to replace B-mode US or FNAB. Larger studies are needed to determine sensitivity and specificity of this imaging tool in thyroid cancer detection and differentiation.

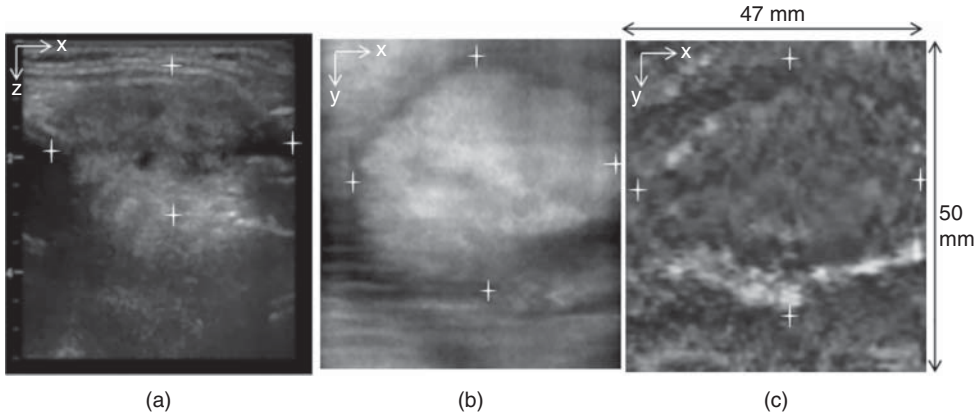

Figure 17.14 Benign nodule: (a) B-mode US of a patients thyroid shows a large solid nodule with small cystic component; (b) ultrasound C-scan at 2.0 cm depth measuring about 44.2 × 30.5 mm in the *x-y* dimensions; and (c) in vivo VA image of thyroid (with 7 L array probe) at 2.0 cm depth which corresponds to the C-scan plane, measuring more than 47 mm. The VA image is 47 × 50 mm. Source: reprinted from [39].

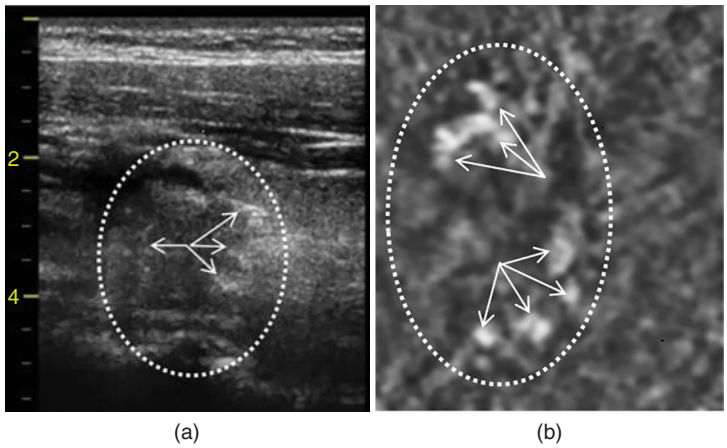

Figure 17.15 Papillary thyroid cancer: (a) B-mode US shows a cystic nodule measuring 1.0 × 1.3 × 1.4 cm with peripheral calcifications, as denoted by arrows; (b) VA scan at 2.5 cm depth shows the nodule with cystic appearance slightly in larger size with coarse peripheral calcifications. Source: reprinted from [39].

17.6 Limitations and Further Future Plans

This VA system can overcome the difficulties associated with using confocal VA, such as inability to image the lesions close to the chest wall, and the discomfort associated with patient positioning, breast compression, and longer scanning duration. There were a few problems that were encountered in the in vivo study. First, a system artifact that is associated with steering the VA beams across the aperture, which created streaks in the VA image. We have developed an algorithm to correct for these streaks [40], but this algorithm can diminish image details. Effort is continued to find alternatives to correct this artifact. In addition, motion artifacts are associated with patient breathing occurring during in vivo VA scanning and manifested as jagged image detail. Our results should provide a foundation for further development of clinical VA systems and further investigation in a larger group of patients.

One step in further development of a VA system is using a reconfigurable array (RCA) transducer that would provide another route for clinical implementation of VA imaging. VA using a RCA transducer has important advantages. Using a 2D RCA transducer eliminates the need for mechanical translation as is needed with a confocal transducer [2] or a linear array transducer [40]. The RCA electronic scanning is expected to take about 2 ms per pixel, which is 6-fold improvement over the confocal transducer [41]. The simulation study performed by our group provides a strong framework for optimization of VA imaging with RCA transducers for different medical applications. Further development and implantation with RCA transducer is in progress to achieve the optimum VA imaging.

Acknowledgments

The work described in this chapter was supported by grants from grant BCTR0504550 from the Susan G. Komen for the cure and National Institutes of Health (NIH) grants R21 CA121579, R01CA127235, R21 EB00535, R33 EB00535, R01EB017213, R01CA148994, R01CA148994-S1, R01CA168575, and R01CA174723 from the NIH-National Cancer Institute. The content of this chapter is solely the responsibility of the author and does not necessarily represent the official views of NIH. The authors are very grateful to Dr. James Greenleaf and Dr. Matthew Urban for their collaboration during the study and Ms. Adriana Gregory for providing a VA scheme figure for this chapter.

Disclosure: MF and AA disclose that MF and Mayo Clinic hold patents on VA technology (discussed in this chapter) as a potential financial conflict of interest. MF has received royalties from a company that has licensed the VA technology from Mayo Clinic.

References

1 Fatemi, M. and Greenleaf, J.F. (1998). Ultrasound-stimulated vibro-acoustic spectrography. *Science* 280 (5360): 82–85.
2 Fatemi, M. and Greenleaf, J.F. (1999). Vibro-acoustography: An imaging modality based on ultrasound-stimulated acoustic emission. *Proc. Natl. Acad. Sci.* 96 (12): 6603–6608.
3 Alizad, A. and Fatemi, M. (2005). Breast vibro-acoustography. In: *Emerging Technologies in Breast Imaging and Mamography* (ed. R.R. Suri and J.S. Laximinaryan), 1st edn., vol. 1, 9. Stevenson Ranch, CA: American Scientific Publishers.
4 Westervelt, P.J. (1951). The theory of steady forces caused by sound waves. *J. Acoust. Soc. Am.* 23 (3): 312–315.
5 Westervelt, P.J. (1957). Acoustic radiation pressure. *J. Acoust. Soc. Am.* 29 (1): 26–29.
6 Torr, G. (1984). The acoustic radiation force. *Am. J. Phys.* 52 (5): 402–408.
7 Jiang, Z.Y. and Greenleaf, J.F. (1996). Acoustic radiation pressure in a three-dimensional lossy medium. *J. Acoust. Soc. Am.* 100 (2): 741–747.
8 Sarvazyan, A.P., Rudenko, O.V., and Nyborg, W.L. (2010). Biomedical applications of radiation force of ultrasound: historical roots and physical basis. *Ultrasound Med. Biol.* 36 (9): 1379–1394.
9 Urban, M.W., Alizad, A., Aquino, W., et al. (2011). A review of vibro-acoustography and its applications in medicine. *Curr. Med. Imaging Rev.* 7 (4): 350–359.
10 Greenleaf, J., Ehman, R.L., Fatemi, M., et al. (1998). Imaging elastic properties of tissue. In: *Ultrasound in Medicine* (ed. F. A. Duck, A. C. Baker, and H. Z. Starritt), 263–277. Bristol, England: Institute of Physics Publishing.

11 Fatemi, M. and Greenleaf, J.F. (2000). Probing the dynamics of tissue at low frequencies with the radiation force of ultrasound. *Phys. Med. Biol.* 45 (6): 1449.

12 Fatemi, M., Manduca, A., and Greenleaf, J.F. (2003). Imaging elastic properties of biological tissues by low-frequency harmonic vibration. *Proc. IEEE* 91 (10): 1503–1519.

13 Fatemi, M. and Greenleaf, J.F. (2002). Imaging the viscoelastic properties of tissue. In: *Imaging of Complex Media with Acoustic and Seismic Waves*, 257–276. Springer.

14 Fatemi, M. and Greenleaf, J. (2000). Imaging and evaluating the elastic properties of biological tissues. *Ultrasound* 8 (4): 16–18.

15 Lester, S.C. and Cortan, R.S. (1999). The breast. In: *Robins Pathologic Basis of Diseases*, 6th edn. (ed. C.T. Kumar and T. Collins). Philadelphia: Saunders.

16 Fatemi, M., et al. (2002). Vibro-acoustic tissue mammography. *IEEE Trans. Med. Imaging* 21 (1): 1–8.

17 Alizad, A., et al. (2004). Performance of vibro-acoustography in detecting microcalcifications in excised human breast tissue: A study of 74 tissue samples. *IEEE Trans. Med. Imaging* 23 (3): 307–312.

18 Alizad, A., et al. (2005). Potential applications of vibro-acoustography in breast imaging. *Technol. Cancer Res. Treat.* 4 (2): 151–157.

19 Alizad, A., et al. (2006). Critical issues in breast imaging by vibro-acoustography. *Ultrasonics* 44: e217–e220.

20 Alizad, A., et al. (2004). Application of vibro-acoustography for detection of calcified arteries in breast tissue. *J. Ultrasound Med.* 23 (2): 267–273.

21 Mitri, F., et al. (2009). Vibro-acoustography imaging of permanent prostate brachytherapy seeds in an excised human prostate – preliminary results and technical feasibility. *Ultrasonics* 49 (3): 389–394.

22 Alizad, A., et al. (2013). Application of vibro-acoustography in prostate tissue imaging. *Med. Phys.* 40 (2): 022902.

23 Alizad, A., et al. (2002). Detection of calcium deposits on heart valve leaflets by vibro-acoustography: An in vitro study. *J. Am. Soc. Echocardiogr.* 15 (11): 1391–1395.

24 Pislaru, C., et al. (2008). In vivo vibroacoustography of large peripheral arteries. *Invest. Radiol.* 43 (4): 243.

25 Ferlay, J., et al. (2015). Cancer incidence and mortality worldwide: sources, methods and major patterns in GLOBOCAN 2012. *Int. J. Cancer* 136 (5): E359–E386.

26 Friedrich, M. (1998). MRI of the breast: state of the art. *Eur. Radiol.* 8 (5): 707–725.

27 Esserman, L., Wolverton, D., and Hylton, N. (2002). Magnetic resonance imaging for primary breast cancer management: current role and new applications. *Endocrine Rel. Cancer* 9 (2): 141–153.

28 Levy, M., Bass, H., and Stern, R. (2002). *Handbook of Elastic Properties of Solids, Liquids, and Gases*. Academic Press.

29 Krouskop, T.A., et al. (1998). Elastic moduli of breast and prostate tissues under compression. *Ultrason. Imaging* 20 (4): 260–274.

30 Alizad, A., et al. (2008). Image features in medical vibro-acoustography: In vitro and in vivo results. *Ultrasonics* 48 (6): 559–562.

31 Alizad, A., et al. (2012). Breast vibro-acoustography: initial results show promise. *Breast Cancer Res.* 14 (5): R128.

32 Urban, M., et al. (2013). A beamforming study for implementation of vibro-acoustography with a 1.75-D array transducer. *IEEE Trans. Ultrason., Ferroelect., Freq. Control* 60 (3): 535–551.

33 Mehrmohammadi, M., et al. (2014). Preliminary in vivo breast vibro-acoustography results with a quasi-2-D array transducer: a step forward toward clinical applications. *Ultrasound Med. Biol.* 40 (12): 2819–2829.

34 Papini, E., et al. (2002). Risk of malignancy in nonpalpable thyroid nodules: predictive value of ultrasound and color-Doppler features. *J. Clin. Endocrinol. Metabol.* 87 (5): 1941–1946.

35 Gharib, H. and Goellner, J.R. (1993). Fine-needle aspiration biopsy of the thyroid: an appraisal. *Ann. Intern. Med.* 118 (4): 282–289.

36 Burch, H.B., et al. (1996). Fine needle aspiration of thyroid nodules. *Acta Cytolog.* 40 (6): 1176–1183.

37 Alexander, E.K. (2008). Approach to the patient with a cytologically indeterminate thyroid nodule. *J. Clin. Endocrinol. Metabol.* 93 (11): 4175–4182.

38 Raab, S.S., et al. (2006). Errors in thyroid gland fine-needle aspiration. *Am. J. Clin. Pathol.* 125 (6): 873–882.

39 Alizad, A., et al. (2013). In vivo thyroid vibro-acoustography: a pilot study. *BMC Med. Imaging* 13 (1): 12.

40 Urban, M.W., et al. (2011). Implementation of vibro-acoustography on a clinical ultrasound system. *IEEE Trans. Ultrason., Ferroelect., Freq. Control* 58 (6): 1169–1181.

41 Kamimura, H.A., et al. (2012). Vibro-acoustography beam formation with reconfigurable arrays. *IEEE Trans. Ultrason., Ferroelect., Freq. Control* 59 (7): 1421–1431.

18

Harmonic Motion Imaging

Elisa Konofagou

Department of Biomedical Engineering, Columbia University, New York, NY, USA

18.1 Introduction

Harmonic motion imaging (HMI) uses a focused ultrasound (FUS) beam to generate an oscillatory acoustic radiation force for an internal, non-contact palpation to internally estimate relative tissue hardness. HMI estimates and maps the tissue dynamic motion in response to the oscillatory force at the same frequency, and has been shown to be feasible in simulations, phantoms, ex vivo human and bovine tissues, as well as animals in vivo. Using an FUS beam, HMI can also be used in an ideal integration setting with thermal ablation using high-intensity focused ultrasound (HIFU), which leads to an alteration in the tumor stiffness. In this chapter, the capability of HMI to localize and target the tumor as well as monitor its subsequent ablation is assessed. The findings presented here demonstrate that HMI is capable of both detecting and characterizing the tumor as well as efficiently detecting the onset of ablation. More importantly, HMI is shown to be capable of distinguishing the tumor margins from the margins of the thermal lesion in vivo in order to assess the treatment success. HMI may thus constitute an integrated, real-time method for efficient HIFU monitoring.

18.2 Background

18.2.1 Ultrasound-guided HIFU

In ultrasound-guided methods, the HIFU lesion can only be detected when cavitation or boiling occurs due to the high bubble concentration that causes high echo amplitudes [1]. However, bubble occurrence is usually unpredictable or random and therefore unreliable in HIFU treatment monitoring [2]. Given that tissue coagulation has been associated with changes in tissue stiffness [3–5], elastography has been applied in the detection and monitoring of laser, RF, and HIFU lesions [6–12]. Unlike the small and non-reproducible acoustic contrast between coagulated and surrounding tissue, the mechanical contrast was found to increase by up to one order of magnitude [5, 8, 10, 13–15]. As a result, over the past two decades, several ultrasound-based elasticity-imaging techniques have been developed for monitoring changes in tissue elasticity during HIFU treatment, including quasi-static elastography [6, 8], supersonic shear imaging (SSI) [16–18], acoustic radiation force imaging (ARFI) [19, 20], and HMI [21–32]. Quasi-static elastography that involves manual compression was initially proposed as a method for monitoring the ablation of tumors due to its sensitivity to stiffness changes, as has been shown in bovine liver in vitro [6, 8] and remains the only elasticity-imaging technique

Ultrasound Elastography for Biomedical Applications and Medicine, First Edition.
Edited by Ivan Nenadic, Matthew Urban, James Greenleaf, Jean-Luc Gennisson, Miguel Bernal, and Mickael Tanter.

applied in patients in a prostate cancer study [33]. However, the external compression of the organ adds significant challenges in registration for planning and guidance in vivo [33], thereby stalling elastography's clinical translation for HIFU monitoring over the past decade. The aforementioned radiation-force methodologies were developed to overcome the contact and manual compression requirements of quasi-static elastography. The first method to be applied to HIFU monitoring was HMI by our group followed by other methodologies.

18.2.2 MR-guided HIFU

For MRI guidance, T1-weighted images are consecutively acquired to monitor the temperature rise during HIFU by measuring the spectral shifts occurring as a result of temperature change. Reliable functional and anatomical information during HIFU treatment can currently be provided only by using MRI-based techniques, i.e. MR-guided FUS (MRgFUS) [34–37]. In one of the first breast cancer clinical trials, nine patients (eleven fibroadenomas) were treated over 2 hours for 2 cm lesions and 45 min for 1 cm lesions with an average temperature rise of up to 45.9 °C. Common side-effects, such as skin burn or swelling following the treatment, were not observed six months after treatment [34] and no sign of tumor re-growth in the same treated region was detected 3-4 years following treatment [34]. Gianfelice et al. [38] applied the MRI-monitoring method and demonstrated that 79% of 24 patients had negative biopsy results after 1 or 2 HIFU sessions. More recently, Khiat et al. [39] used dynamic contrast-enhanced MRI (DCE-MRI) in 25 patients (26 invasive ductal carcinomas) after HIFU and tumor resection. After correlation with histopathology, it was concluded that in most patients, the tumors were eliminated by more than 90%. Magnetic resonance elastography (MRE) [40] relies on the stiffness change to detect HIFU lesions [5]. Despite its exquisite imaging quality and accurate thermometry feedback, MRgFUS involves steep healthcare costs and low temporal resolution resulting in lengthy procedures (up to 6 hours for uterine fibroid HIFU ablation [41]), apart from the alignment challenges, restrictions in the patient pool, and large physical space requirements. Both MRgFUS and MRE are currently hindered by the same limitations of low framerates and high costs associated with MRI. HIFU therefore remains an effective and low-cost technology currently incurring steep costs in monitoring methodologies. As a result, despite the promise shown in studies over the past 15 years, breast HIFU remains unavailable to patients. This is in contrast to other ablative procedures in the clinic that are far more invasive and risky but have highly affordable, fast, and reliable monitoring. The current lack of low-cost and reliable monitoring methods may result in the confinement of this promising treatment and low-cost technique to large research centers worldwide – as proclaimed by Kennedy [1] more than a decade ago. In addition, MRgFUS provides only temperature elevation and not the coagulation onset, and it is coagulation onset that is most important for informing lesioning and has been reported to occur at distinct temperatures across organs or even within the same organ.

18.2.3 Harmonic Motion Imaging

Harmonic motion imaging (HMI) is a radiation-force-based technique of HMI that utilizes the ultrasound beam to induce local vibration of tissues and thus infer to their underlying mechanical properties. HMI is thus an elasticity-imaging technique, but, unlike quasi-static elastography, it does not require any direct contact, alignment, or external tissue deformation. The localized vibration is achieved using amplitude modulation on the probing beam that induces a vibration at the focus of the transducer in order to image the mechanical responses of the tissue being imaged. The mechanical property of the tissue changes as a result of pancreatic cancer and, thus, the displacement changes during tumor growth. The oscillatory motion can be monitored in real time using cross-correlation techniques on the acquired RF signals using an

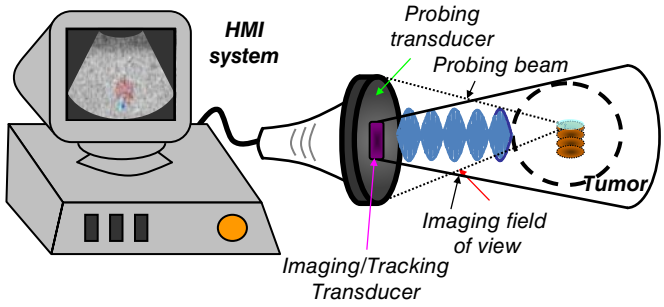

Figure 18.1 In vivo HMI showing the displacement image on the ultrasound system screen (left) with an example of displacement measurement at the tumor. The force is applied remotely and internally at the focus of the probing (or force) transducer (ellipsoids in focal area) through AM modulation of the FUS beam (as shown in path between the transducer and ellipsoids).

ultrasound imaging transducer, confocal with the probing transducer (Figure 18.1). The system can thus be used to localize the tumor and image its stiffness-based displacement amplitude at variable depths [25, 42–47] (Figure 18.1). Due to its use of pulse-echo methods, B-mode and HMI images can be seamlessly co-registered while sharing the advantages of portability, lack of ionizing radiation, low cost, and noninvasiveness. In summary, HMI combines the advantages of diagnostic ultrasound for high spatial and temporal resolution with the advantages of radiation-force-based elasticity imaging for sensitive, reliable, stiffness-based measurements at large depths.

18.2.4 Harmonic Motion Imaging for Focused Ultrasound (HMIFU)

The all-ultrasound-based (imaging and therapy) technique of HMIFU utilizes the same ultrasound beam for both HIFU and local vibration of tissues before, during, and after HIFU treatment (Figure 18.1). The same system can thus be used to localize [25, 42–47], monitor [21, 22, 24–26, 48], and ablate [27–31, 42–45, 49] the tumor. HMI is a radiation-force-based technique that induces oscillatory displacements in the focal zone of the HIFU transducer for the detection of localized stiffness changes. HMI is thus an elasticity-imaging technique, but, unlike quasi-static elastography, it does not require any direct contact, alignment, or external tissue deformation. HMIFU denotes the seamless application of HMI to HIFU monitoring (Figure 18.2a). The combination into a single device (Figure 18.1) has been shown successful in monitoring lesion formation in real time in tumors ex vivo and in vivo. Due to its use of pulse-echo methods, B-mode and HMI images can be seamlessly co-registered while sharing the advantages of portability, lack of ionizing radiation, low cost, and noninvasiveness. HMIFU entails the simultaneous integration of HMI into HIFU treatment by utilizing an amplitude modulation (vibration; low frequency) onto the therapeutic beam (ablation; high frequency) (Figure 18.2a). More importantly, the HMIFU system is easily integratable into ultrasound systems already in use in the clinic, ensuring thus its rapid translation by using standard arrays with an additional module for ablation (Figure 18.1). Therefore, in HMIFU (Figure 18.2a), monitoring and ablation methods are inherently fully co-registered. The localized vibration is achieved using amplitude modulation on the therapeutic beam, which will not affect the treatment duration or efficacy but only induce a vibration at the focus of the transducer in order to detect the mechanical property changes of the treated tissue. The mechanical property of the treated tissue changes before, during, and after ablation, and, thus, the displacement also changes during treatment (Figure 18.2b). The oscillatory motion can be monitored in real time using cross-correlation techniques on the acquired RF signals using an ultrasound imaging

transducer, confocal with the HIFU transducer (Figure 18.1). The slope reversal denotes the coagulation onset (Figure 18.2b) based on the associated rapid and irreversible stiffening [5]. In summary, the HMIFU method combines the advantages of diagnostic ultrasound for high spatial and temporal resolution with the advantages of therapeutic ultrasound for noninvasive, low-cost treatment, and the advantages of elasticity imaging for sensitive, reliable, stiffness-based measurements during ablation. This combination results in a technique that is fast, low-cost, reliable, and noninvasive, expanding thus the potential of HIFU for treatment of focal breast tumors and simultaneously setting the foundations for future HIFU applications in early-stage tumors in other organs such as liver and pancreatic cancer. Due to the inherent registration between the imaging and therapeutic components, prolonged co-registration, plaguing other modalities, is not required.

18.3 Methods

Our group has developed 1D (Figure 18.2b) and 2D (Figure 18.2c) methodologies as well as parallel beamforming that has allowed us to use the 2D methodology without the associated tradeoff in frame rate.

18.3.1 The HMIFU System

The HMIFU system (Figure 18.2a) utilizes a new 93-element HIFU phased array transducer. The individual element diameter = 10 mm, overall outer diameter = 110 mm, inner diameter = 44 mm (to fit the imaging probe, Figure 18.2c, center frequency = 1.1 MHz, and focal depth = 70 mm). This transducer by Sonic Concepts Inc. (Bothell, WA, USA), operates at the fundamental (1.1 MHz) for human specimens and at the third harmonic (3.3 MHz) for mice. The HIFU array was concentric with a 64-element imaging phased array (ATL, Bothell, WA, USA; Figure 18.2c) which will have different center frequencies for mice and humans. The 93-element HIFU transducer was driven in phase by an amplitude-modulated (AM frequency

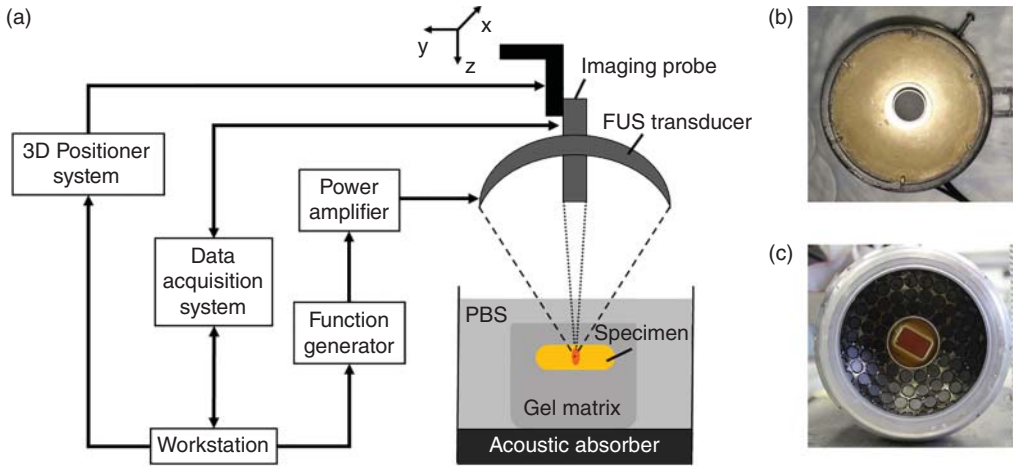

Figure 18.2 Schematic of harmonic motion imaging (HMI) system with experimental setup: (a) block diagram of HMI system. The small ellipsoid region indicates the focus of the FUS transducer; (b) the 1D HMI system comprises of a single-element FUS transducer (outer diameter = 80 mm, inner diameter = 16.5 mm) coaligned with a single-element pulse-echo transducer (diameter = 15 mm); (c) the 2D HMI system consists of a probing phased array transducer and a concentric phased array imaging probe.

ω_{AM} = 25 Hz) sinusoidal signal generated by a dual-channel arbitrary waveform generator (AT33522A, Agilent Technologies Inc. Santa Clara, CA, USA) and amplified by a nominal 50 dB gain power amplifier (325LA, E&I, Rochester, NY, USA). Each HIFU and imaging transducer was operated by a dedicated open-architecture system (Vantage, Verasonics, Redmond, WA, USA) with the HIFU array powered by the external HIFU supply option to induce sufficient power. The HIFU and imaging arrays are at different center frequencies, so as to effectively employ analog bandpass filters and remove the HIFU beam interference prior to HMIFU estimation [24, 29].

18.3.2 Parallel Beamforming

Similar to others in the field, we have found that the performance of motion estimation is not compromised [50, 51] when such systems are used, based on the advantages of differential, phase-based measurements (as opposed to amplitude-based approaches) [50]. We have implemented beamforming sequences [50] that excite the transducer elements with specific delays allowing a large field of view and then uses the delay-and-sum method to reconstruct the RF signals from the channel data. This mode is similar to plane wave imaging, but the diverging wave from a virtual point source behind the transducer allows imaging with a large field of view [50, 51]. The associated frame rate is only limited by the depth and speed of sound. As a result, the system can obtain up to 5000 fps for breast imaging. Parallel beamforming has thus recently allowed us to obtain similar frame rates in our 2D system (Figure 18.2c) as with our previously developed 1D system (Figure 18.2b) but with the added advantage of full 2D HMI.

18.3.3 HIFU Treatment Planning

Beam localization was performed prior to ablation, as recently developed by our group [52]. A burst of AM signal at 231 W/cm^2 was applied in order to localize the beam without significant temperature rise. Based on the maximum peak-to-peak HMI displacement, the −3 dB HIFU focal zone was calculated in order to quantitatively monitor the ablation [52].

18.3.4 HIFU Treatment Monitoring

After the planning phase, a continuous AM wave (Figure 18.1) was generated at 1086 W/cm^2 for 50 s for fast and efficient ablation [31, 47]. The temporal variation of the displacement amplitude was continuously imaged using HMI. The change in the slope of the HMI displacement variation over time (Figures 18.3a and 18.3b) indicates lesion formation [29, 45].

18.3.5 HIFU Treatment Assessment

After the ablation is completed, HMI was performed across the entire specimen to determine the extent of the HIFU lesion (Figure 18.3e).

18.3.6 Displacement Estimation

A fast, normalized 1D cross-correlation function implemented by our group [53] was used on the continuously acquired, reconstructed RF signals from the channel data acquired using the imaging array during the application of the radiation force by the HIFU array (see Figure 18.2). The cross-correlation function uses a 1D kernel (length = 5.85 mm, overlap = 90%) for search in the axial direction. The correlation kernel size is approximately 10 wavelengths, which was found to be the optimal length using cross-correlation [54].

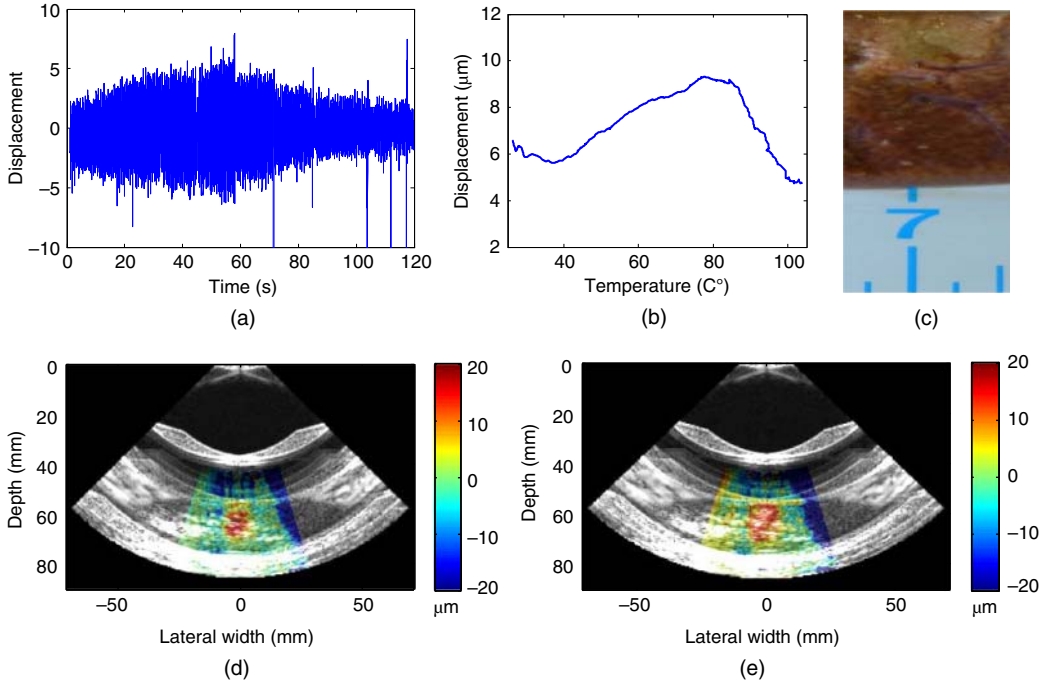

Figure 18.3 (a) Real-time HMI displacement. (b) Peak-to-peak HMI displacement against temperature showing coagulation at the slope change or ~80 °C or temperature elevation of ~60 °C. (c) Resulting HIFU lesion (arrow). 2D HMI monitoring of HIFU lesion (d) at the start and (e) at the end of the HIFU treatment. The lesion can be identified and its displacement drops due to stiffening while the extent of the region has increased.

18.3.7 Real-time Implementation

In order to implement HMIFU in real time, we apply our GPU-based, sparse-matrix reconstruction algorithm that will accelerate the delay-and-sum beamforming (Figure 18.4) as well as the scan conversion in matrix-vector products since these operations are linear [29, 56]. In order to obtain every beamformed RF frame, two sparse matrices were generated for reconstruction and scan conversion, respectively. More specifically, every RF frame was reconstructed by first multiplying the channel data matrix with the reconstruction sparse matrix, then multiplying the product matrix by another sparse matrix for scan conversion, each performed as a single

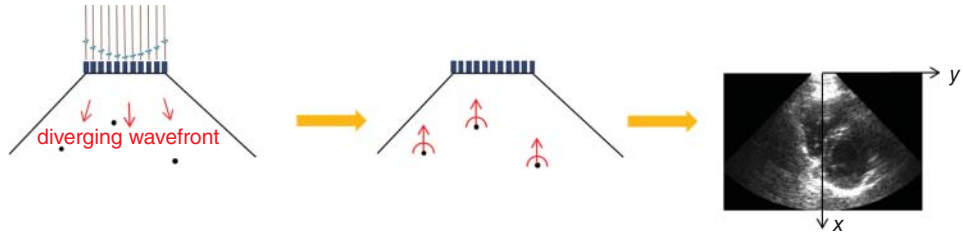

Figure 18.4 Parallel beamforming sequence to be used on the Verasonics system.

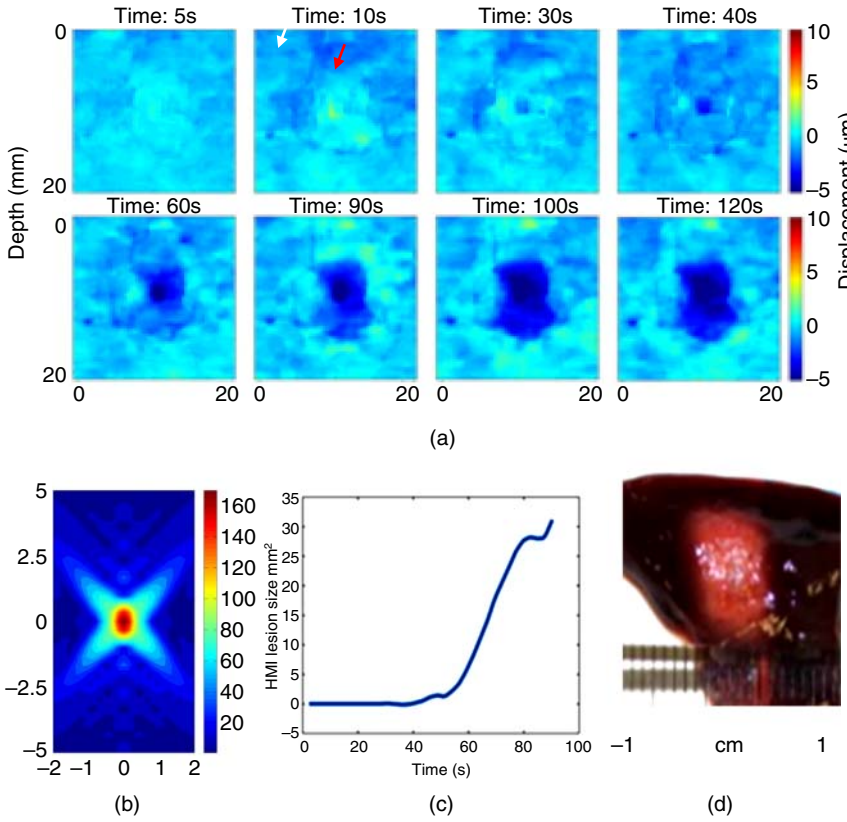

Figure 18.5 (a) 2D HMIFU real-time monitoring of HIFU lesion in ex vivo liver (showing eight HMIFU frames during treatment (0–120 s). The method localizes the focal spot of the HIFU beam (white arrow at 30 s) and follows the formation of the lesion based on the HMI displacement decrease until the end of the treatment with the final lesion (dark arrow). (b) Focal spot plot in water confirming the focal spot size in (a). (c) Automated lesion size monitoring in real time with HIFU showing lesion formation beyond 20 s. (d) Resulting HIFU lesion (discolored region). The lesion can be identified and its displacement drops due to stiffening [55]. The lesioning can be completed at 100 s instead of 120 s.

operation. The RF signals were upsampled to 80 MHz and reconstructed on a 90° field of view with 128 beam lines. Our group has pioneered this algorithm in another methodology [29] with resulting RF ultrasound frame rates of 1000 Hz and HMI frame rates of 10 Hz [56]. This methodology allows for real-time monitoring (Figure 18.5).

18.3.8 Beam Steering

To achieve an even shorter treatment monitoring time, one of the earliest challenges of clinical HIFU translation, electronically steered beams can provide up to 66% increased speed compared to mechanical scanning [57]. The HIFU array is operated through a four-board VDAS system and the imaging array by a separate four-board VDAS system. This has allowed us to develop real-time steering (Figure 18.6), which is essential in implementing a fast application of HMI without physically moving the transducer [58]. The HMI displacement can be imaged within the steering range up to 5 mm in the lateral and 27 mm in the axial through the proposed array. Using the steered HIFU beam across the tumor, HMI can be used to image and ablate a larger tissue volume with higher efficiency and without requiring physical movement

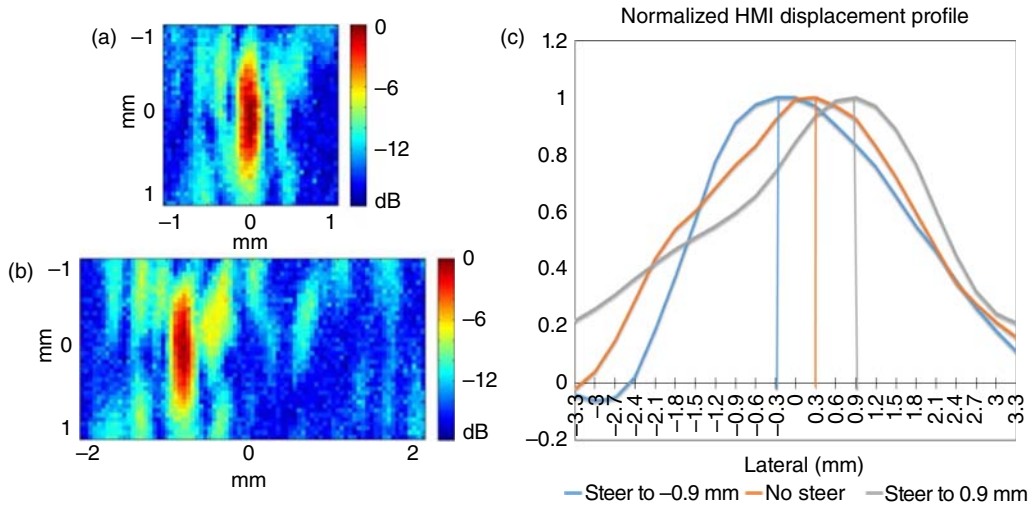

Figure 18.6 Example of beam steering capability by the HIFU array: (a) before and (b) after steering to the left. (c) Lateral HMI displacement profile at different steering angles.

of the transducer. This allows for faster treatment and treatment of larger lesions with the same transducer.

18.3.9 Modulus Estimation

Noninvasive measurement of mechanical properties of biological tissues in vivo could play a significant role in improving the current understanding of tissue biomechanics. In this study, we propose a method for measuring elastic properties noninvasively by using internal indentation as generated by harmonic motion imaging (HMI). In HMI, an oscillating acoustic radiation force is produced by a focused ultrasound transducer at the focal region, and the resulting displacements are estimated by tracking RF signals acquired by an imaging transducer. The focal spot region was modeled as a rigid cylindrical piston that exerts an oscillatory, uniform internal force to the underlying tissue. The HMI elastic modulus E_{HMI} was defined as the ratio of the applied force to the axial strain measured by 1D ultrasound imaging. The reliability and the quality of the E_{HMI} estimate were assessed numerically, in polyacrylamide tissue-mimicking phantoms and in biological liver specimens ex vivo. Very good correlation and agreement was found between the actual Young's modulus and the HMI modulus in the numerical study ($r^2 > 0.99$, relative error $< 10\%$) and on polyacrylamide gels ($r^2 = 0.95$, relative error $< 24\%$). The average HMI modulus on five liver samples was found to be $E_{\mathrm{HMI}} = 2.62 \pm 0.41$ kPa, compared to $E_{\mathrm{MechTesting}} = 4.2 \pm 2.58$ kPa measured by rheometry. This study has demonstrated for the first time the initial feasibility of a non-invasive, model-independent method to estimate local elastic properties of biological tissues at a submillimeter scale using an internal indentation-like approach. The method is based on the localized, internal acoustic radiation force, instead of an external mechanical indenter, as the source of stress. In HMI, a focused ultrasound (FUS) transducer is used to generate an oscillating force at the focal region. The force density can be measured experimentally as part of the transducer calibration, and its spatial profile can be therefore known. The resulting displacement is measured using the consecutive RF signals acquired during the application of the oscillatory force. In the proposed method, the focal region is modeled as a cylindrical region inside which the volumetric acoustic radiation force is uniform. This is an approximation since the actual radiation force has a well-defined spatial

distribution (see Figures 18.10a and 18.10b). This cylindrical region is therefore assumed to act as an oscillating rigid piston.

Under the assumption of linear elasticity, the balance of forces on the z-axis acting on this cylindrical region can be written as

$$\rho \frac{\partial^2 u_z}{\partial t^2} V = \iiint_V f_V \mathrm{d}V = F_{\text{shear}} - F_{\text{top}} - F_{\text{bottom}} \tag{18.1}$$

F_{shear}, F_{top}, and F_{bottom} correspond to the vertical forces acting on the lateral, superior, and inferior surfaces of the cylinder, respectively. V is the volume of the cylinder, u_z is the vertical displacement of the cylinder, ρ is the density of the tissue, and f_V is the local, volumic acoustic radiation force. The inertia term on the right-hand side of Eq. (18.1) is considered negligible, as its order of magnitude is approximately 0.1% of the one of the other terms within the typical HMI frequency range (10–50 Hz). Therefore, Eq. (18.1) can be rewritten as

$$\iiint_V f_V \mathrm{d}V = F_{\text{shear}} + F_{\text{top}} + F_{\text{bottom}} \tag{18.2}$$

which can be simply deemed as a static balance of forces, where the applied acoustic radiation force equals the sum of elastic forces related to the deformation of the tissue around the piston

$$\begin{cases} F_{\text{top}} = F_{\text{bottom}} = \pi R^2 * E \frac{\partial u_z}{dz} \\ F_{\text{shear}} = 2\pi Rh * G \frac{\partial u_z}{dr} \end{cases} \tag{18.3}$$

where R, h denote the radius and the height of piston, respectively, and E, G denote the Young's and shear modulus of the tissue, respectively. Under the assumption of quasi-incompressibility ($E = 3G$), Eq. (18.2) becomes

$$\iiint_V f_V \mathrm{d}V = E * \left(2\pi R^2 * \frac{\partial u_z}{dz} + \frac{1}{3} 2\pi Rh * \frac{\partial u_z}{dr} \right) \tag{18.4}$$

Equation (18.4) can be rewritten with tensorial strain components

$$\iiint_V f_V \mathrm{d}V = 2E\pi R * \left(R * \varepsilon_{zz} + \frac{2}{3} h * \varepsilon_{rz} \right) \tag{18.5}$$

which assumes that the displacement occurs along the z-axis only with $\varepsilon_{rz} = \frac{1}{2} \frac{\partial u_z}{dr}$.

Another major assumption in this study is that the compressive and shear strains are equal. As it will be demonstrated in the numerical study, they are indeed very close in a cylindrical geometry as the one used here. Consequently, Eq. (18.5) can be written as

$$\iiint_V f_V \mathrm{d}V = 2E\pi R \varepsilon_{zz} * \left(R + \frac{2}{3} h \right) \tag{18.6}$$

Finally, we define our HMI modulus as

$$E_{\text{HMI}} = \frac{\iiint_V f_V \mathrm{d}V}{2\pi R \varepsilon_{zz} * \left(R + \frac{2}{3} h \right)} \tag{18.7}$$

The HMI elastic modulus method requires knowledge of the acoustic radiation force. In this study, we used the experimental pressure profile obtained using a needle hydrophone in water, as described elsewhere [45]. The corresponding 3D acoustic radiation force distribution was used as the input in both simulations and experiments throughout the study. The acoustic radiation force f_{exp} was then calculated as

$$f_{\text{exp}} = \frac{2\alpha I}{c_s} \tag{18.8}$$

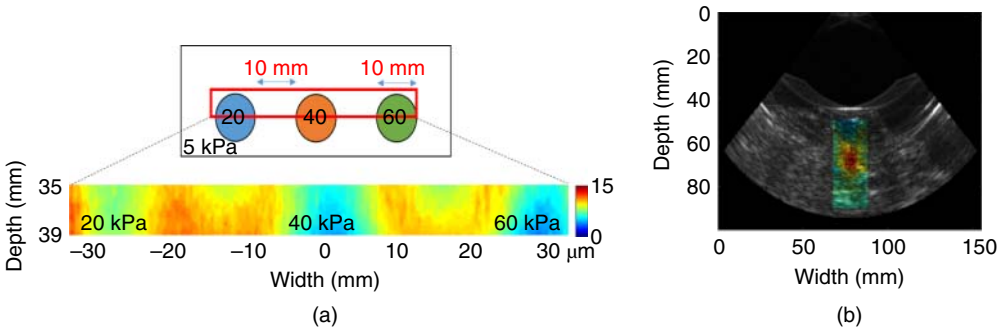

Figure 18.7 (a) CIRS phantom results with three inclusions of different stiffness (20–60 kPa). HMI successfully depicts all inclusions of different stiffness which is the expected range of variation during ablation. (b) HMI overlaid on a B-mode in a mastectomy specimen.

where I is the acoustic intensity, c_s the speed of sound ($c_s = 1530$ m/s), and α is the acoustic absorption of the medium. The attenuation of the tissue above the focus was taken into account in order to obtain realistic estimates of the acoustic intensity at the focus.

18.4 Preclinical Studies

18.4.1 Detection and Diagnosis of Breast Tumors

18.4.1.1 Phantom Studies

The elasticity phantoms from CIRS (Computerized Imaging Reference Systems, Inc., Norfolk, VA) are the only commercially available materials developed for elasticity-imaging quality assurance. We used a customized 049A phantom that is made of a patented solid elastic material called Zerdine®. The background has tissue-mimicking properties with the speed of sound equal to 1540 m/s, an attenuation of 0.5 dB/cm/MHz and a Young's modulus of 25 kPa. The inclusions are 8 stepped cylinders arranged in a 4 by 2 array, allowing two different depths (30 and 60 mm). Each inclusion consists of six diameters ranging from 1.58 mm to 16.67 mm. Feasibility in such a phantom is shown in Figure 18.7.

18.4.1.2 Ex Vivo Breast Specimens

Thirty postsurgical specimens (15 fibroadenomas, FA, i.e. benign tumors, and 15 invasive ductal carcinomas, IDC, i.e. malignant tumors) of stage I without systemic metastasis) were collected at the Breast Center in the Irving Pavilion of the Columbia University Medical Center from patients who have been imaged and diagnosed by our collaborator, Dr. Bret Taback, MD, Clinical Professor of Surgery at the Columbia Breast Center, and who performed the surgeries and identified the cases needed for the proposed study. Specimens were carried in a sealed container. Upon arrival in our laboratory, the specimens was carefully handled and embedded in a gel matrix (similar to that used for the phantoms) for protective purposes but also to contain them and simulate the surrounding breast, especially in the case of lumpectomy specimens. All specimens were scanned using the HMI technique and the findings were compared to mammography, sonography, and histopathology findings. Orientation of the specimen was provided by the surgeon. Baseline HMI was acquired immediately followed by HMIFU of the specimen (see Figure 18.9a). In our preliminary studies with the HMIFU system, in all successful ablation cases, the ablation onset was identified and lesioning was detected (Figures 18.8 and 18.9). Through the department of pathology, there has been an agreement in place to utilize for tumor ablation discarded tumor parts that are typically not useful in pathology or histological analysis

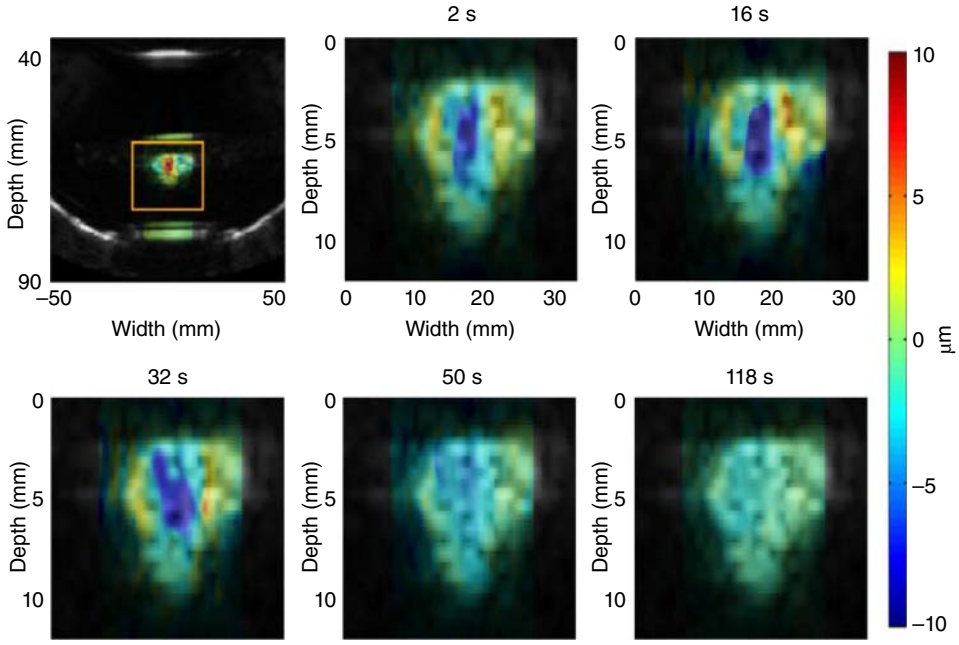

Figure 18.8 HMIFU ablation monitoring in 2D overlaying on B-mode images in an invasive ductal carcinoma (IDC) lumpectomy specimen. Peak negative HMI displacement frames at 50 Hz HMI at five representative time points during treatment are shown. The focal displacement decreases as the thermal lesion forms. At 50 s, the treatment is completed and can be stopped.

of the tumor. The mass to be obtained was ~1–2 cm in diameter, which is the tumor size that is intended to have HIFU used in its in vivo human application. HMIFU feasibility in normal, malignant, and benign human breast specimens after ablation is shown in Figure 18.9, demonstrating that human breast lesion detection due to the fact that the lesion is several times harder than the unablated breast tissue [15]. Those tissues were subsequently utilized in order to assess the imaging parameters, such as SNR and resolution, which can be achieved for displacement and viscoelastic property estimation before and after ablation. The same HIFU transducer that is used to generate the radiation force (Figure 18.1), but at higher intensities (1086 W/cm^2), was employed here to generate HIFU lesions of 2–12 mm in diameter.

18.4.2 Detection and Treatment Monitoring of Breast and Pancreatic Tumors In Vivo

18.4.2.1 Breast Mouse Tumor Model

Over the past few years, Dr. Thomas Ludwig's group has generated mice carrying conditional alleles for *Brca1*, *Brca2*, *Bard1*, and *p53*, which are human cancer mutations known to result in tumor growth in mice. To inactivate these conditional alleles in the mammary glands, animals were crossed with mice expressing *cre* under control of regulatory elements from the whey acidic protein (*Wap*) gene, expression of which is normally restricted to mammary epithelial cells during late pregnancy and lactation. Mammary gland-specific inactivation of *Brca2* [59], *Brca1*, and *Bard1* results in the development of mammary adenocarcinomas. The tumors typically grown using the aforementioned techniques reach a diameter of 1–2 cm before the mice are sacrificed. The tumor localization, temperature dependence, and coagulation-onset detection of the HMIFU technique were evaluated based on our preliminary feasibility studies (Figure 18.11) [45]. Small tumors (<1 cm) as shown in our preliminary results in both human and mouse tissues (Figure 18.11) can be detected at the frequencies used in our HMIFU system

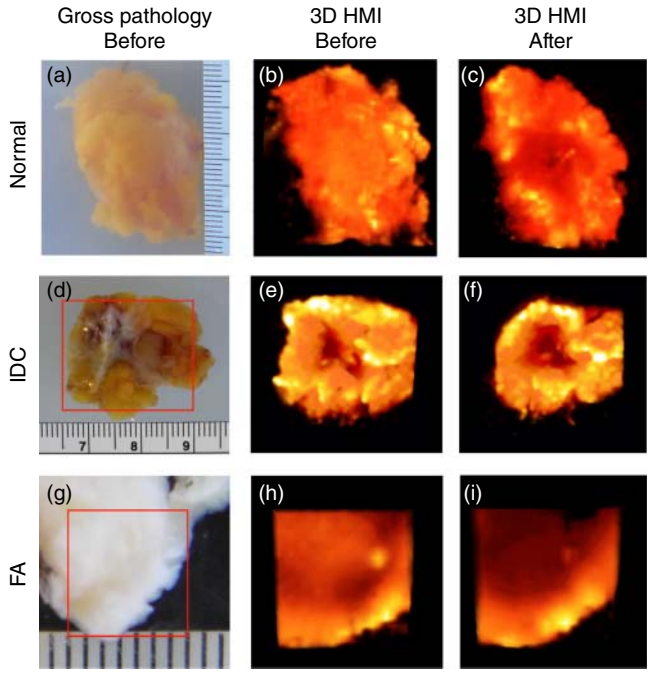

Figure 18.9 Multi-2D HMI displacement images of normal breast tissue (top panel), IDC (middle panel), and FA (bottom panel). (a) Gross pathology photograph of a normal breast specimen mounted on the gel matrix, and the 3D reconstructed HMI of the selected tissue (b) before and (c) after HMIFU ablation. (d) Gross pathology photograph of an IDC specimen mounted on the gel matrix, and the 3D reconstructed HMI of the selected tissue (e) before and (f) after HMIFU ablation. (g) Gross pathology photograph of a FA specimen mounted on the gel matrix, and the 3D reconstructed HMI of the selected tissue (h) before and (i) after ablation. The brighter (darker) colors indicate higher (lower) HMI displacement and lower (higher) relative stiffness.

due to the high mechanical contrast. The setup can easily accommodate animals in vivo due to the suspended waterbath, i.e. without incurring underwater submergence of the animals. The mammary glands in the transgenic tumor model mice were imaged. Each animal was placed on top of a platform (THM100, Indus Instruments, Houston, TX, USA) monitoring its temperature, ECG, and blood pressure, available in our laboratory during mouse imaging. A thermocouple manufactured out of 50 μm manganin and constantan wire was fed through a catheter that was implanted in the superficial tumor. The B-mode image was used in order to visualize the tumor and guide the catheter. The HIFU beam was thus properly aligned perfectly with the thermocouple tip. The catheter is then removed prior to the sonications. The signal was amplified and detected by an acquisition board (CS14200, Gage Applied Technologies, Lachine, Canada), which was used to capture band-pass filtered RF data at the sampling frequency of 80 MHz. For the raster-scanning process, the transducer was moved along a 3D grid using a computer-controlled positioner (Velmex Inc., Bloomfield, NY, USA) with a step size of 1 mm. The system also allows control of the amplitude and frequency of the therapy beam.

Based on our preliminary results ex vivo (Figures 18.8 and 18.9) and in vivo (Figure 18.11), sonication for 20–40 s was used and the tissue heating was monitored before, during, and after ablation. Both the temperature and HMI measurements was acquired and stored for further analysis. The HMI measurements were repeated in five locations in each tumor with target temperatures within 45–80 °C to ensure coagulation. Our preliminary in vivo results in ten ($n = 10$) mice enabled by our previous study indicated that the thermal lesion can be successfully mapped when generated in the tumor, since the lesion is significantly harder than the tumor

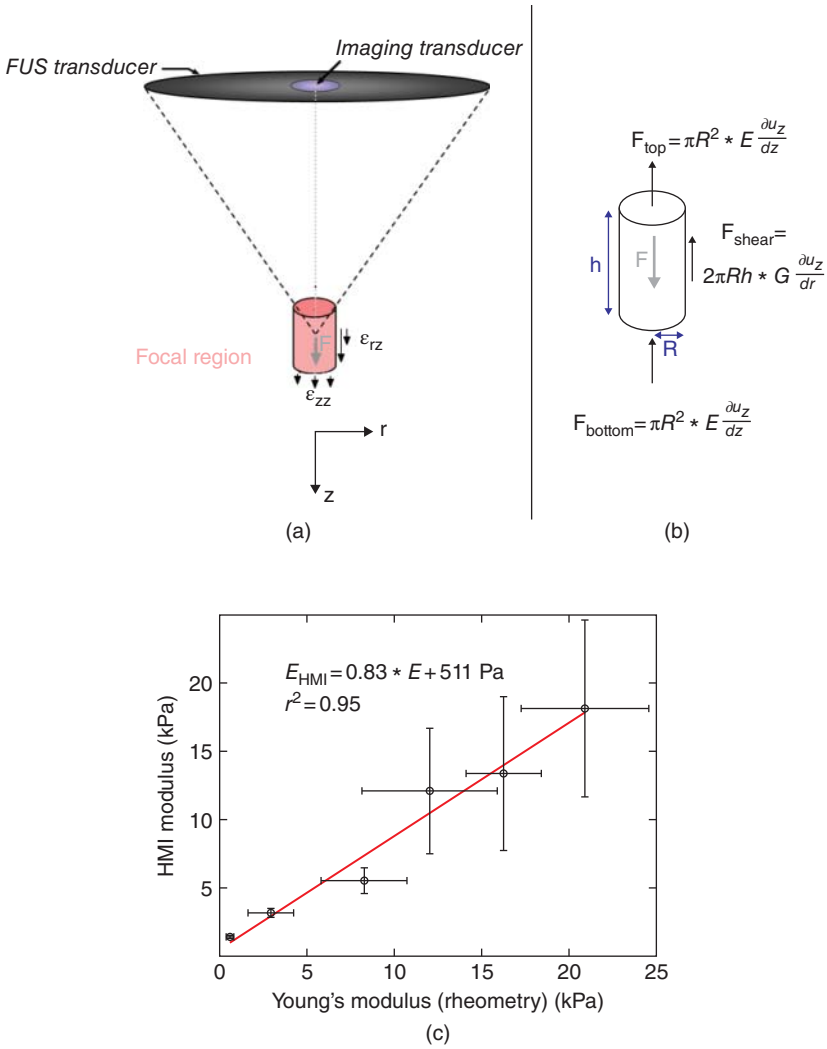

Figure 18.10 (a) Illustration of the focal region as a cylindrical piston exerting a vertical force, and corresponding deformations of the surrounding tissue, (b) illustration of the forces acting on this cylinder. (c) HMI modulus vs Young's modulus measured by rheometry on the six polyacrylamide phantoms. Vertical and horizontal errorbars denote standard deviations among the different samples tested by HMI and rheometry, respectively.

(Figure 18.11b) [45]. Twenty-five animals ($n = 25$) were used altogether after approximately 6 weeks, when the mammary tumor is expected to have reached 1 cm in diameter (Figure 18.11a). In each animal, the tumor was scanned before, during, and after ablation. In the first ten animals, the thermocouple was inserted and kept in place in the tumor during ablation to validate temperature resolution characteristics, temperature dependence, and coagulation onset detection of the HMIFU monitoring. In the remaining 15 animals, the same procedure was repeated without the thermocouple so as to ensure minimal interference in the thermal treatment duration. All animals were anesthetized during the entire procedure using an isofluorane system available in our laboratory. After HIFU treatment, the animals were sacrificed, and the HMI images was compared with histological examinations of the tumors. This was performed in both tumors in each mouse.

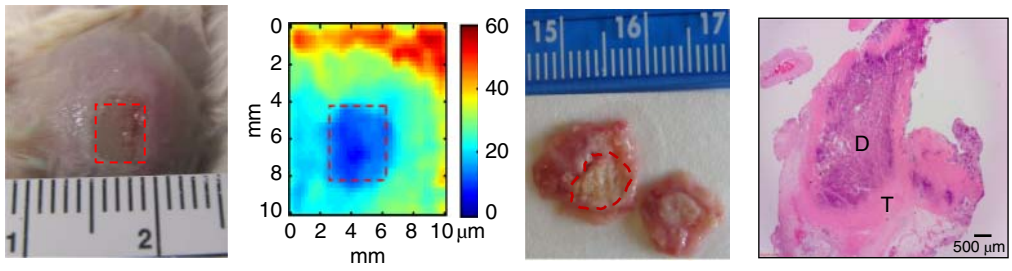

Figure 18.11 In vivo tumor ablation and imaging. (a) Visualization of the mouse mammary tumor surface after ablation with discoloration of the tumor in the ablated region (dashed contour). (b) HMI image of the same thermal lesion at a higher depth (dashed contour) with the unablated tumor around it. (c) Gross pathology of the transverse cross-section of the same tumor (dashed contour). (d) Gross pathology of the mammary tumor after excision. (d) H&E histology images with 12.5× magnification. Scale bar = 500 μm. Ablated regions are indicated as dark purple (D). Non-ablated regions (or, viable cells) are shown in pink (T).

18.4.2.2 Pancreatic Mouse Tumor Model

Dr. Kenneth Olive's group has extensive experience in the development of mouse tumor models. We have used mice carrying conditional alleles for *Brca1*, *Brca2*, *Bard1*, and *p53*, which are human cancer mutations known to result in mammary tumor growth in mice. However, the mammary tumor was superficial and hence was not providing the challenge of a deep-seated tumor. In accordance with the National Institutes of Health guidelines for animal research, all animal procedures were reviewed and approved by the Institutional Animal Care and Use Committee of the Columbia University. The animal model used was a transgenic mouse model of pancreatic ductal carcinoma PDA, K-rasLSL.G12D/+; p53R172H/+; PdxCre (KPC) mice [60, 61]. The KPC mice develop pancreatic tumors with pathophysiological and molecular features resembling those of human PDA [60]. Feasibility in both accurately detecting the tumor (Figure 18.12) and monitoring ablation (Figure 18.13) have been shown in those mice using HMI and MIFU, respectively [62, 63].

18.5 Future Prospects

As indicated previously, despite the successful implementation of our approach with conventional (focused) beamforming, our group has also developed parallel beamforming for HMI, which we have found to be extremely advantageous due to the high frame rates involved according to our initial feasibility. In this study, we used HMI and HMIFU (Figure 18.3) with parallel beamforming and tested its capability for reliable displacement and modulus mapping in phantoms and ex vivo human breast specimens.

In order to precisely locate the pancreas, a high-frequency ultrasound imaging system (Vevo 770, VisualSonics Inc. Toronto, Canada) coupled with a high-frequency ultrasound probe (RMV-707B) of a nominal center frequency of 30 MHz was used [64–66]. The mouse abdomen is first be scanned by the Vevo system to find the tumors in the KPC mice or normal pancreases in the wild-type mice. Under the guidance of the Vevo system, a grid is then placed in the water container above the mouse and adjusted so that the node on the grid will lie directly above the targeted tumor location. The Vevo is then replaced by the HMIFU system and the tumor was found by localizing a metallic grid [62]. Real-time 2D and/or 3D HMI was performed during ablation in each location. Ablation onset, and therefore completion of treatment in each lesion location, was detected based on the HMI displacement slope reversal (Figures 18.2b and 18.5b). Our in vivo results in ten (n = 10) mice [62] indicated that the

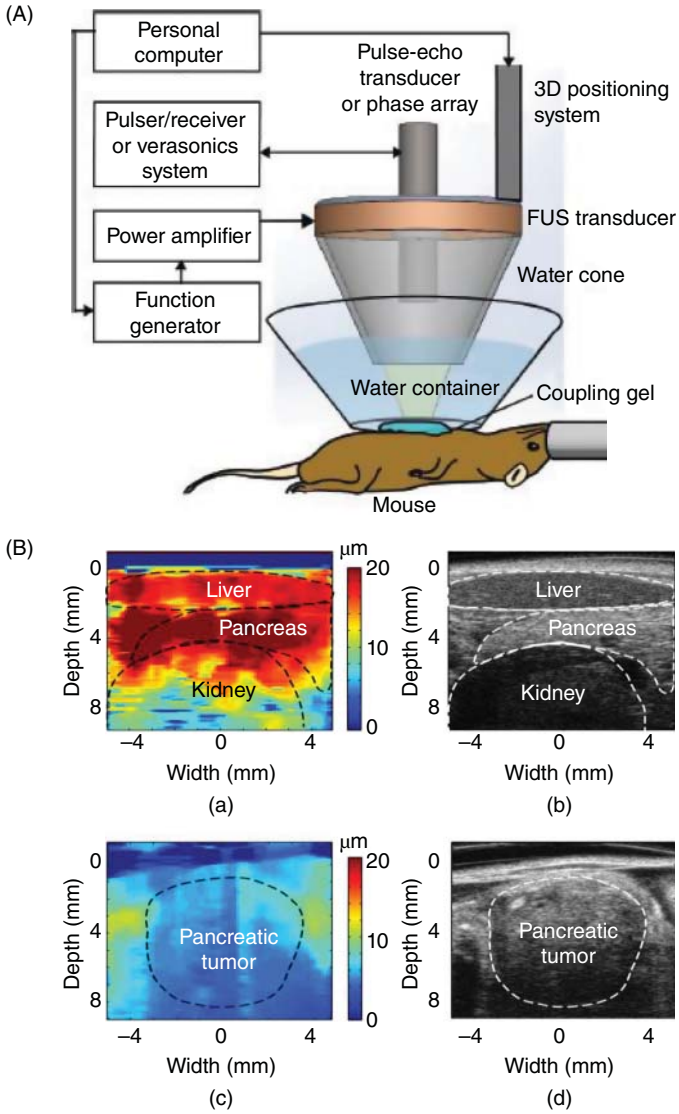

Figure 18.12 (A) Mouse HMIFU setup in vivo. (B) Abdominal imaging with HMI and B-mode before (a, b) and after (c, d) tumor development, respectively.

thermal lesion can be successfully mapped when generated in the tumor, since the lesion is significantly harder (Figure 18.13) [62]. The tumor localization, temperature dependence, and coagulation onset detection of the HMIFU technique was evaluated based on our preliminary feasibility studies [45, 62]. Small tumors (<1 cm) as shown in our preliminary results in both human and mouse tissues can be detected at the frequencies used in our HMIFU system due to the high mechanical contrast. The same HMIFU system developed and evaluated is used. The setup can easily accommodate animals in vivo due to the suspended water bath, i.e. without incurring underwater submergence of the animals. As in our prior studies, the duration of 120 s was used that ensured the largest lesion size (~1 cm) (Figure 18.13); therefore, for tumors of up to 1 cm in diameter, four sonications with real-time steering was performed in four 2D planes, i.e. 16 sonications for full tumor ablation, i.e. perilesional tissue of up to 1 cm is also

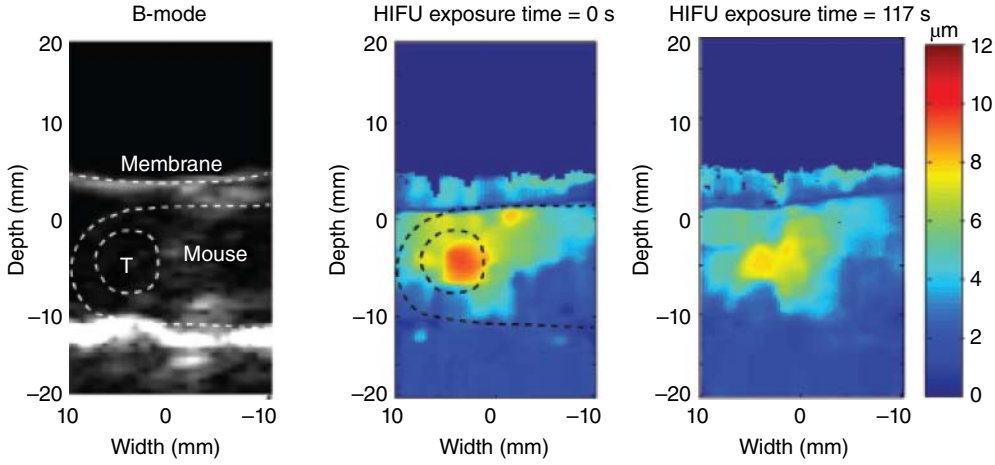

Figure 18.13 HMI sequence of during HIFU ablation in mouse tumor (T) in vivo. The displacement decrease indicates successful ablation in the tumor.

ablated. The transducer was moved 4 times since steering will not require physical movement. This results in a total treatment duration of ~30 min. Prior lesions did not affect monitoring in individual locations given the differential nature of the measurement (Figure 18.13) [62].

Acknowledgements

This work was supported by NIH R01EB014496. The author acknowledges the work performed by the following group members of the Ultrasound and Elasticity Imaging Laboratory at Columbia University: Yang Han, MS, Shutao Wang, PhD, Hong Chen, PhD, Thomas Payen, PhD, Jonathan Vappou, PhD. and Caroline Maleke, PhD.

References

1 Kennedy, J.E. (2005), High-intensity focused ultrasound in the treatment of solid tumours. *Nat. Rev. Cancer* 5 (4): 321–327.
2 Kovatcheva, R., Guglielmina, J.N., Abehsera, M., et al. (2015). Ultrasound-guided high-intensity focused ultrasound treatment of breast fibroadenoma – a multicenter experience. *J. Therap. Ultrasound* 3 (1): 1.
3 van Kleef, F.S., Boskamp, J.V., and van den Tempel, M. (1978). Determination of the number of cross-links in a protein gel from its mechanical and swelling properties. *Biopolymers* 17: 225–235.
4 Chen, S.S., Wright, N.T., and Humphrey, J.D. (1998). Heat-induced changes in the mechanics of a collagenous tissue: isothermal, isotonic shrinkage. *J. Biomech. Eng.* 120 (3): 382–388.
5 Wu, T., Felmlee, J.P., Greenleaf, J.F., et al. (2001). Assessment of thermal tissue ablation with MR elastography. *Magn. Reson. Med.* 45 (1): 80–87.
6 Stafford, R.J., Kallel, F., Price, R.E., et al. (1998). Elastographic imaging of thermal lesions in soft tissue: A preliminary study in vitro. *Ultrasound Med. Biol.* 24 (9): 1449–1458.
7 Kallel, F., Stafford, R.J., Price, R.E., et al. (1999). The feasibility of elastographic visualization of HIFU-induced thermal lesions in soft tissues. Image-guided high-intensity focused ultrasound. *Ultrasound Med. Biol.* 25 (4): 641–647.

8 Righetti, R., Kallel, F., Stafford, R.J., et al. (1999). Elastographic characterization of HIFU-induced lesions in canine livers. *Ultrasound Med. Biol.* 25 (7): 1099–1113.

9 Doyley, M.M., Bamber, J.C., Rivens, I., et al. (1999). Elastographic imaging of thermally ablated tissue in vitro. In: *Proc IEEE Ultrasonics Symp.* 1631–1634. Caesars Tahoe, NV, USA.

10 Shi, X.G., Martin, R.W., Rouseff, D., et al. (1999). Detection of high-intensity focused ultrasound liver lesions using dynamic elastometry. *Ultrason. Imaging* 21 (2): 107–126.

11 Fahey, B.J., Hsu, S.J., Wolf, P.D., et al. (2006). Liver ablation guidance with acoustic radiation force impulse imaging: challenges and opportunities. *Phys. Med. Biol.* 51 (15): 3785–3808.

12 Daniels, M.J., Varghese, T., Madsen, E.L., and Zagzebski, J.A. (2007). Non-invasive ultrasound-based temperature imaging for monitoring radiofrequency heating-phantom results. *Phys. Med. Biol.* 52 (16): 4827–4843.

13 Zhang, M., Castaneda, B., Christensen, J., et al. (2008). Real-time sonoelastography of hepatic thermal lesions in a swine model. *Med. Phys.* 35 (9): 4132–4141.

14 Vappou, J., Maleke, C., and Konofagou, E.E. (2009). Quantitative viscoelastic parameters measured by harmonic motion imaging. *Phys. Med. Biol.* 54 (11): 3579–3594.

15 Shahmirzadi, D., Hou, G.Y., Chen, J., and Konofagou, E.E. (2014). Ex vivo characterization of canine liver tissue viscoelasticity after high-intensity focused ultrasound ablation. *Ultrasound Med. Biol.* 40 (2): 341–350.

16 Bercoff, J., Pernot, M., Tanter, M., and Fink, M. (2004). Monitoring thermally-induced lesions with supersonic shear imaging. *Ultrason. Imaging* 26 (2): 71–84.

17 Arnal, B., Pernot, M., and Tanter, M. (2011). Monitoring of thermal therapy based on shear modulus changes: I. Shear wave thermometry. *IEEE Trans. Ultrason., Ferroelectr., Freq. Control* 58 (2): 369–378.

18 Arnal, B., Pernot, M., and Tanter, M. (2011). Monitoring of thermal therapy based on shear modulus changes: II. Shear wave imaging of thermal lesions. *IEEE Trans. Ultrason., Ferroelectr., Freq. Control* 58 (8): 1603–1611.

19 Lizzi, F.L., Muratore, R., Deng, C.X., et al. (2003). Radiation-force technique to monitor lesions during ultrasonic therapy. *Ultrasound Med. Biol.* 29 (11): 1593–1605.

20 Bing, K.F., Rouze, N.C., Palmeri, M.L., et al. (2011). Combined ultrasonic thermal ablation with interleaved ARFI image monitoring using a single diagnostic curvilinear array: a feasibility study. *Ultrason. Imaging* 33 (4): 217–232.

21 Konofagou, E., Thierman, J., and Hynynen, K. (2001). A focused ultrasound method for simultaneous diagnostic and therapeutic applications – a simulation study. *Phys. Med. Biol.* 46 (11): 2967–2984.

22 Konofagou, E.E., Thierman, J., Karjalainen, T., and Hynynen, K. (2002). The temperature dependence of ultrasound-stimulated acoustic emission. *Ultrasound Med. Biol.* 28 (3): 331–338.

23 Konofagou, E.E. and Hynynen, K. (2003). Localized harmonic motion imaging: theory, simulations and experiments. *Ultrasound Med. Biol.* 29 (10): 1405–1413.

24 Maleke, C. and Konofagou, E.E. (2008). Harmonic motion imaging for focused ultrasound (HMIFU): a fully integrated technique for sonication and monitoring of thermal ablation in tissues. *Phys. Med. Biol.* 53 (6): 1773–1793.

25 Maleke, C. and Konofagou, E.E. (2010). In vivo feasibility of real-time monitoring of focused ultrasound surgery (FUS) using harmonic motion imaging (HMI). *IEEE Trans. Biomed. Eng.* 57 (1): 7–11.

26 Konofagou, E.E., Maleke, C., and Vappou, J. (2012). Harmonic motion imaging (HMI) for tumor imaging and treatment monitoring. *Curr. Med. Imaging Rev.* 8 (1) :16–26.

27 Hou, G.Y., Luo, J., Marquet, F., et al. (2011). Performance assessment of HIFU lesion detection by harmonic motion imaging for focused ultrasound (HMIFU): A 3-D

finite-element-based framework with experimental validation. *Ultrasound Med. Biol.* 37 (12): 2013–2027.

28 Hou, G.Y., Marquet, F., Wang, S., and Konofagou, E.E. (2013). Optimization of real-time acoustical and mechanical monitoring of high intensity focused ultrasound (HIFU) treatment using harmonic motion imaging for high focused ultrasound (HMIFU). *Conf. Proc. IEEE Eng. Med. Biol. Soc.* 6281–6284.

29 Hou, G.Y., Marquet, F., Wang, S., and Konofagou, E.E. (2014). Multi-parametric monitoring and assessment of high-intensity focused ultrasound (HIFU) boiling by harmonic motion imaging for focused ultrasound (HMIFU): an ex vivo feasibility study. *Phys. Med. Biol.* 59 (5): 1121–1145.

30 Hou, G.Y., Provost, J., Grondin, J., et al. (2014). Sparse matrix beamforming and image reconstruction for 2-D HIFU monitoring using harmonic motion imaging for focused ultrasound (HMIFU) with in vitro validation. *IEEE Trans. Med. Imaging* 33 (11): 2107–2117.

31 Hou, G.Y., Marquet, F., Wang, S., et al. (2015). High-intensity focused ultrasound monitoring using harmonic motion imaging for focused ultrasound (HMIFU) under boiling or slow denaturation conditions. *IEEE Trans. Ultrason., Ferroelect., Freq. Control* 62 (7): 1308–1319.

32 Hou, G.Y. (2013). Biomechanical assessment and monitoring of thermal ablation using Harmonic Motion Imaging for Focused Ultrasound (HMIFU), PhD Dissertation, Columbia University.

33 Souchon, R., Rouviere, O., Gelet, A., et al. (2003). Visualisation of HIFU lesions using elastography of the human prostate in vivo: Preliminary results. *Ultrasound Med. Biol.* 29 (7): 1007–1015.

34 Hynynen, K., Pomeroy, O., Smith, D.N. (2001). MR imaging-guided focused ultrasound surgery of fibroadenomas in the breast: a feasibility study. *Radiology* 219 (1): 176–185.

35 Huber, P.E., Jenne, J.W., Rastert, R., et al. (2001). A new noninvasive approach in breast cancer therapy using magnetic resonance imaging-guided focused ultrasound surgery. *Cancer Res.* 61 (23): 8441–8447.

36 Furusawa, H., Namba, K., Thomsen, S., et al. (2006). Magnetic resonance-guided focused ultrasound surgery of breast cancer: reliability and effectiveness. *J. Am. Col. Surg.* 203 (1): 54–63.

37 Shen, S.H., Fennessy, F., McDannold, N., et al. (2009). Image-guided thermal therapy of uterine fibroids. *Semin. Ultrasound, CT MR* 30 (2): 91–104.

38 Gianfelice, D., Khiat, A., Boulanger, Y., et al. (2003). Feasibility of magnetic resonance imaging guided focused ultrasound surgery as an adjunct to tamoxifen therapy in high-risk surgical patients with breast carcinoma. *J. Vasc. Interv. Radiol.* 14: 1275–1282.

39 Khiat, A., Gianfelice, D., Amara, M., and Boulanger, Y. (2006). Influence of post-treatment delay on the evaluation of the response to focused ultrasound surgery of breast cancer by dynamic contrast enhanced MRI. *Br. J. Radiol.* 79 (940): 308–314.

40 Muthupillai, R., Lomas, D.J., Rossman, P.J., (1995). Magnetic resonance elastography by direct visualization of propagating acoustic strain waves. *Science* 269 (5232): 1854–1857.

41 Tempany, C.M., McDannold, N.J., Hynynen, K., and Jolesz, F.A. (2011). Focused ultrasound surgery in oncology: overview and principles. *Radiology* 259 (1): 39–56.

42 Maleke, C., Pernot, M., and Konofagou, E.E. (2005). A single-element focused transducer method for harmonic motion imaging. In: *Ultrasonics Symposium, 2005 IEEE,* Rotterdam, Netherlands.

43 Maleke, C., Pernot, M., and Konofagou, E.E. (2006). Single-element focused ultrasound transducer method for harmonic motion imaging. *Ultrason. Imaging* 28 (3): 144–158.

44 Maleke, C., Luo, J., Pelegri, M., and Konofagou, E.E. (2007). Mapping of regional tissue mechanical changes using harmonic motion imaging. In: *Proc. ASME International Mechanical Engineering Congress and Exposition*. Seattle, WA.

45 Maleke, C., Luo, J., Gamarnik, V., et al. (2010). Simulation study of amplitude-modulated (AM) harmonic motion imaging (HMI) for stiffness contrast quantification with experimental validation. *Ultrason. Imaging* 32 (3): 154–176.

46 Maleke, C. and Konofagou, E.E. (2006). An all-ultrasound-based system for real-time monitoring and sonication of temperature change and ablation. In: *Annual International Conference of the IEEE Engineering in Medicine and Biology Society* 1: 164–167.

47 Han, Y., Wang, S., and Konofagou, E.E. (2015). Harmonic motion imaging for detection and focused ultrasound ablation monitoring of ex vivo human breast tumors, In: *15th International Symposium on Therapeutic Ultrasound*. Utrecht, Netherlands.

48 Maleke, C. (2010). In vivo detection and thermal treatment monitoring of breast tumors using harmonic motion imaging (HMI). Ph.D. dissertation, Columbia University, New York.

49 Konofagou, E.E. and Maleke, C. (2008). Harmonic motion imaging in HIFU monitoring. In: *Vibrations and Acoustics and in Biomedical Applications: Therapy and Sports* (ed. A. Al-Jumaily and M. Fatemi), 115–135. New York: ASME Press.

50 Provost, J., Thiebault, S., Luo, J., and Konofagou, E.E. (2012). Single-heartbeat electromechanical wave imaging with optimal strain estimation using temporally unequispaced acquisition sequences. *Phys. Med. Biol.* 57 (4): 1095–1112.

51 Bunting, E.A., Provost, J., and Konofagou, E.E. (2014). Stochastic precision analysis of 2D cardiac strain estimation in vivo. *Phys. Med. Biol.* 59 (22): 6841–6858.

52 Han, Y., Hou, G.Y., Wang, S., and Konofagou, E. (2015). High intensity focused ultrasound (HIFU) focal spot localization using harmonic motion imaging (HMI). *Phys. Med. Biol.* 60 (15) :5911–5924.

53 Luo, J. and Konofagou, E. (2010). A fast normalized cross-correlation calculation method for motion estimation. *IEEE Trans. Ultrason., Ferroelect., Freq. Control* 57 (6): 1347–1357.

54 Luo, J., Lee, W.N., and Konofagou, E.E. (2009). Fundamental performance assessment of 2-D myocardial elastography in a phased-array configuration. *IEEE Trans. Ultrason., Ferroelect., Freq. Control* 56 (10): 2320–2327.

55 Han, Y., Payen, T., Wang, S., and Konofagou, E.E. (2016). Real-time monitoring of high-intensity focused ultrasound treatment using harmonic motion imaging for focused ultrasound. In: *16th International Symposium on Therapeutic Ultrasound*, Tel Aviv, Israel.

56 Grondin, J., Payen, T., Wang, S., and Konofagou, E. (2015). Real-time monitoring of HIFU ablation of in vitro canine livers using harmonic motion imaging for focused ultrasound (HMIFU). *J. Vis. Exp.* 105: 53050.

57 Mehrmohammadi, M., Fazzio, R.T., Whaley, D.H., et al. (2014). Preliminary in vivo breast vibro-acoustography results with a quasi-2-D array transducer: a step forward. *Ultrasound Med. Biol.* 40 (12): 2819–2829.

58 Han, Y., Payen, T., Wang, S., and Konofagou, E.E. (2015). Real-time steering for inducing and monitoring HIFU ablation using harmonic motion imaging. In: *IEEE International Ultrasonics Symposium*, Taipei, Taiwan.

59 Ludwig, T., Fisher, P., Murty, V., and Efstratiadis, A. (2001). Development of mammary adenocarcinomas by tissue-specific knockout of Brca2 in mice. *Oncogene* 20 (30): 3937–3948.

60 Olive, K.P. and Tuveson, D.A. (2006). The use of targeted mouse models for preclinical testing of novel cancer therapeutics. *Clin. Cancer Res.* 12 (18): 5277–5287.

61 Olive, K.P., Jacobetz, M.A., Davidson, C.J., et al. (2009). Inhibition of Hedgehog signaling enhances delivery of chemotherapy in a mouse model of pancreatic cancer. *Science* 324 (5933): 1457–1461.

62 Chen, H., Hou, G.Y., Han, Y., et al. (2015) Harmonic motion imaging for abdominal tumor detection and high-intensity focused ultrasound ablation monitoring: a feasibility study in a transgenic mouse model of pancreatic cancer. *IEEE Trans. Ultrason., Ferroelect., Freq. Control* 62 (9): 1662–1673.

63 Payen, T., Palermo, C.T., Sastra, S., et al. (2016). Elasticity mapping of murine abdominal organs in vivo using harmonic motion imaging (HMI). *Phys. Med. Biol.* 61 (15): 5741–5754.
64 Luo, J., Fujikura, K., Tyrie, L.S., et al. (2009). Pulse wave imaging of normal and aneurysmal abdominal aortas in vivo. *IEEE Trans. Med. Imaging* 28 (4) :477–486.
65 Nandlall, S.D., Goldklang, M.P., Kalashian, A., et al. (2014). Monitoring and staging abdominal aortic aneurysm disease with pulse wave imaging. *Ultrasound Med. Biol.* 40 (10): 2404–2414.
66 Apostolakis, I., Nandlall, S., and Konofagou, E. (2015). Piecewise pulse wave imaging (pPWI) for detection and monitoring of focal vascular disease in murine aortas and carotids in vivo. *IEEE Trans. Med. Imaging* 35 (1): 13–28.

19

Shear Wave Dispersion Ultrasound Vibrometry

Pengfei Song and Shigao Chen

Department of Radiology, Mayo Clinic, Rochester, MN, USA

19.1 Introduction

This chapter introduces an ultrasound imaging method called shear wave dispersion ultrasound vibrometry (SDUV) that can quantify both tissue elasticity and viscosity noninvasively. SDUV generates multi-frequency wide-band harmonic shear waves using both acoustic radiation force (ARF) and external mechanical vibration to obtain the shear wave speed dispersion curve, from which tissue viscoelasticity can be robustly estimated [1, 2]. SDUV has been used on a variety of ex vivo and in vivo tissues including liver, heart, artery, kidney, prostate, and muscle. In this chapter we will first provide reviews of the principles of the SDUV technique, followed by brief reviews of existing clinical applications of SDUV.

19.2 Principles of Shear Wave Dispersion Ultrasound Vibrometry (SDUV)

Shear wave speed (c_s) in a homogeneous Voigt medium depends on the frequency of the shear wave ω_s

$$c_s(\omega_s) = \sqrt{2\left(\mu_1^2 + \omega_s^2\mu_2^2\right) / \rho\left(\mu_1 + \sqrt{\mu_1^2 + \omega_s^2\mu_2^2}\right)} \tag{19.1}$$

where ρ, μ_1, and μ_2 are the density, shear elasticity, and shear viscosity of the medium, respectively [1]. The density of the soft tissue can be assumed to be 1000 kg/m^3. If shear wave speed at multiple frequencies can be measured (i.e. a shear wave dispersion curve can be obtained), one can calculate both μ_1 and μ_2 by fitting the dispersion curve with a Voigt model. To achieve such measurements, several SDUV setups have been proposed (Figure 19.1). The original setup used single-element transducers to push at different frequencies and detect shear waves at different spatial locations (Figure 19.1a) so that $c_s(\omega_s)$ can be obtained by

$$c_s(\omega_s) = \omega_s \Delta r / \Delta\phi_s \tag{19.2}$$

where $\Delta\phi_s = \phi_1 - \phi_2$ is the phase change over the traveled distance Δr [1]. An alternative approach is to use an array transducer and electronically move the push and detection beam locations to achieve measurement of phase difference at different locations (Figure 19.1b). Both these methods use ARF as the source for shear wave generation. SDUV can also be realized by using external mechanical vibration (Figure 19.1c), where harmonic shear waves are produced

Ultrasound Elastography for Biomedical Applications and Medicine, First Edition.
Edited by Ivan Nenadic, Matthew Urban, James Greenleaf, Jean-Luc Gennisson, Miguel Bernal, and Mickael Tanter.

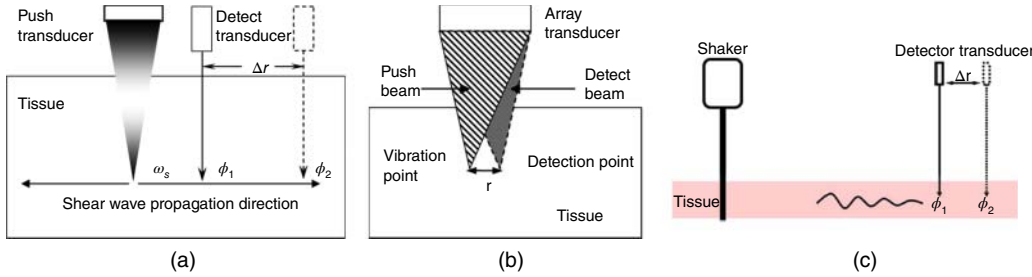

Figure 19.1 Different SDUV implementations. (a) Two transducers are used, with one transducer generating shear waves and the other transducer detecting shear waves at different locations. One can also fix the detection transducer and move the push transducer to different spatial locations. (b) An array transducer is used with electronically focused push and detection beams. (c) A external mechanical shaker-based setup where harmonic shear waves are produced by a shaker and shear waves at different spatial locations are being detected. Source: © 2009 IEEE, reprinted with permission from [1], and © Institute of Physics and Engineering in Medicine, reproduced by permission of IOP Publishing. All rights reserved [3].

by a mechanical shaker and shear wave motion is detected at different spatial locations [3]. To achieve multi-frequency broad-band shear wave excitation, the ARF-based SDUV approach uses repeated push sequences at a certain pulse-repetition frequency (e.g. 100 Hz) to produce shear waves at the fundamental frequency of the push pulse (e.g. 100 Hz) as well as shear waves at the harmonics (e.g. 200, 300, and 400 Hz). The detection pulses are interleaved between the push pulses to detect the wide-band shear wave signal.

Figure 19.2 shows a typical in vivo SDUV measurement in pig liver: one can see the harmonic shear wave motion from the repeated push pulses at different spatial locations (Figures 19.2a and 19.2b); the shear wave phase at different frequencies can be estimated at different positions (Figure 19.2c), from which a frequency-dependent shear wave dispersion curve can be obtained and fitted to a Voigt model to calculate elasticity and viscosity (Figure 19.2d). Another approach of implementing SDUV is to replace the push transducer with a mechanical shaker, which can vibrate at different frequencies to generate multi-frequency broad band shear waves (Figure 19.2c) [3–5]. More robust shear wave signals with higher amplitude can be produced by use of such methods. Also, mechanical vibration does not rely on generating shear wave harmonics from the fundamental frequency, which improves the shear wave signals especially at the harmonics and higher frequencies. However, the mechanical vibration approach needs certain mechanical coupling between the shaker and the tissue (ideally by direct contact), which limits its in vivo implementations in deep organs such as heart and kidney.

One practical challenge of the original SDUV technique is that the repeated push pulse may result in excessive transducer and tissue heating. Another challenge is that since multiple repeated push and detection cycles are needed, the total data acquisition time can be long, which makes the method vulnerable to tissue physiological motion. To resolve these issues, a single push pulse-version of SDUV was developed by Bernal et al., in which a short tone-burst of push pulse is used to produce a wide-band shear wave signal, and by use of k-space analysis (i.e. Fourier transform) of the shear wave spectrum one can obtain frequency-dependent shear wave speeds and calculate both elasticity and viscosity [6] (Figure 19.3). In the 2D k-space analysis, the dominant or highest energy points at each frequency are extracted and used to calculate the phase velocity of the shear wave (Figures 19.3b–19.3e). A similar approach using phase gradient analysis for shear wave dispersion named shear wave spectroscopy was proposed by Deffieux et al. [7], in which the supersonic shear imaging (SSI) push beam configuration was used to excite broadband transient shear wave signals. These transient shear wave-based dispersion analysis approaches only need a single push-detect data acquisition cycle, which is more practical for in vivo applications. However, these methods may not be

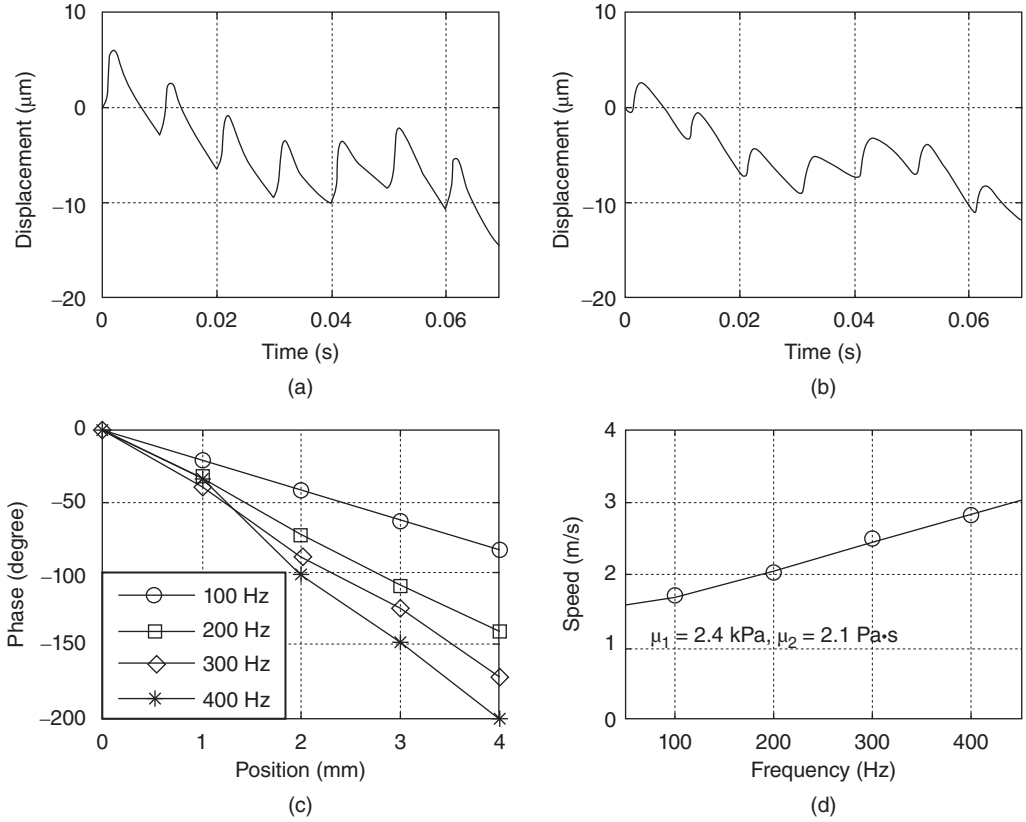

Figure 19.2 In vivo SDUV measurement in liver: (a) shear wave motion signal at location 0 mm; (b) shear wave motion signal at location 2 mm; (c) phase-position plot calculated from the shear wave motion signals; and (d) shear wave speed dispersion curve and the Voigt-model fitting results for elasticity and viscosity. Source: © 2009 IEEE, reprinted, with permission, from [1].

able to produce sufficiently wideband shear wave signals in vivo, which results in poor shear wave dispersion analysis.

19.3 Clinical Applications

19.3.1 Tissue-mimicking Phantoms

Early work on SDUV showed that in tissue-mimicking phantoms, the viscoelastic properties of a gelatin phantom could be well characterized by SDUV and were in good agreement to the properties found using another independent method involving an embedded sphere [8]. Zhang and Greenleaf also demonstrated using the SDUV principle to estimate surface wave dispersion over a range of 100–400 Hz on a tissue-mimicking phantom [9]. Nenadic et al. used SDUV to analyze Lamb and Rayleigh wave dispersion on plate gelatin phantoms and studied geometry-dependent tissue dispersion [3, 10, 11]. Bernal et al. used the single-push dispersion analysis to study the wave dispersion in an artery-mimicking urethane tube under different transmural pressures [6]. Recently, Zhu et al. used SDUV to quantify the viscoelasticity of oil-in-gelatin phantoms and reported significantly increased tissue viscosity with increased oil concentration [12].

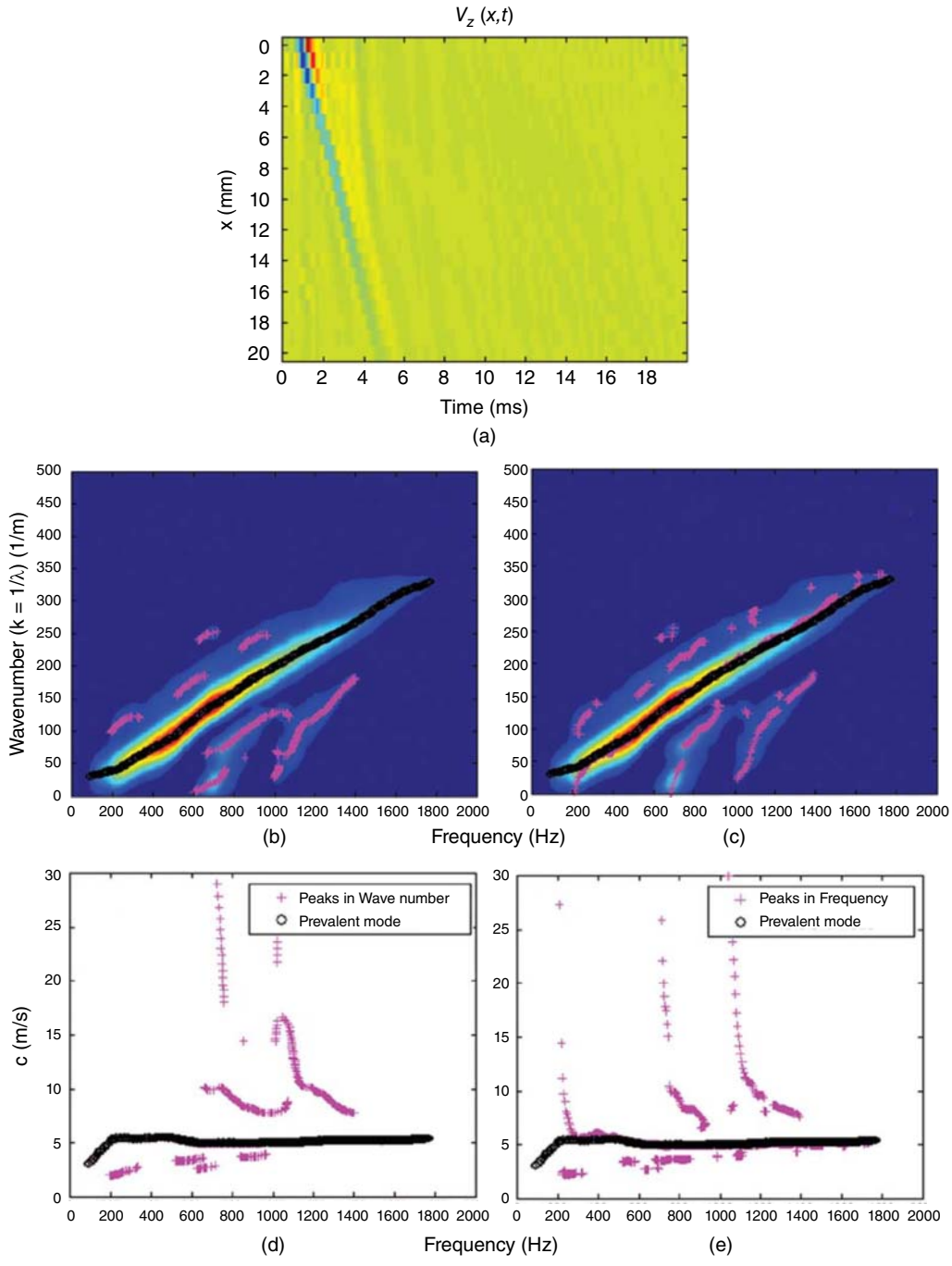

Figure 19.3 Dispersion analysis with a broadband shear wave signal generated by a single ultrasound push pulse. (a) Shear wave signal propagating in time and space in an arterial wall. (b) and (c) show the 2D Fourier transform of the shear wave signal and the dominant or highest energy mode for each frequency. (d) and (e) show the dispersion curves extracted from (b) and (c); the frequency-dependent phase velocity of the shear wave can be obtained and fitted to calculate elasticity and viscosity. Source: reprinted with permission from [6], copyright 2011, Acoustical Society of America.

19.3.2 Liver

SDUV was first demonstrated to be able to provide both elasticity (2.2 ± 0.63 kPa) and viscosity (1.96 ± 0.34 Pa·s) measurements from in vivo porcine liver that were in good agreement with MRE results [1]. Deffieux et al. used the shear wave spectroscopy method based on SSI and showed that human liver is very dispersive and ranges from 1.2 m/s to 3 m/s from 75 Hz to 459 Hz [7]. Chen et al. used the SDUV technique to investigate the value of viscosity in liver fibrosis staging and showed that elasticity and viscosity measured between 95 Hz and 380 Hz are correlated and both can be used to stage liver fibrosis, although elasticity had a better AUC than viscosity (0.98 vs. 0.86) [13]. A similar observation was reported from an in vitro rat liver study in which viscosity was found to be not as robust as elasticity for liver fibrosis staging [14]. The impact of tissue viscosity on liver fibrosis staging using shear wave speed was recently studied by Nightingale et al. and it was showed that the cutoff shear wave speed value for differentiating advanced fibrosis from mild-to-moderate fibrosis is frequency-dependent [15]. This is an important factor that needs to be accounted for when comparing shear wave speed measurements from different commercial machines or imaging modalities.

19.3.3 Skeletal Muscle

Skeletal muscle is a highly anisotropic material and exhibits different elasticity and viscosity along different fiber orientations. Chen et al. used SDUV on ex vivo bovine muscle and reported elasticity of 29 kPa, viscosity of 9.9 Pa·s when imaging along the fiber, versus elasticity of 12 kPa and viscosity of 5.7 Pa·s when imaging across the fiber [1]. Urban et al. measured shear viscoelasticity of ex vivo porcine muscle and also reported higher elasticity and viscosity along the fibers than across the fibers [16, 17]. Deffieux et al. [7] and Gennisson et al. [18] used a SSI-based shear wave spectroscopy technique and reported similar behavior of shear elasticity in in vivo human muscle under different loading conditions (Figure 19.4), but opposite viscosity behavior: shear viscosity is very small along the fiber than across the fiber, which suggests that muscle is more dispersive across the fiber and almost nondispersive along the fiber (Figures 19.4c and 19.4d). One possible reason contributing to the different results is that the muscle tissue in Chen et al. and Urban et al. was ex vivo and from the loin, while Deffieux et al. and Gennisson et al. conducted the study in vivo on human biceps muscle. The difference in the muscle materials and the muscle activities may have an influence on the elasticity and viscosity measurements from these studies [2]. To date, no studies have been reported using muscle viscosity as a clinical biomarker for musculoskeletal pathology.

19.3.4 Heart

The viscoelastic properties of the heart throughout a cardiac cycle have been investigated using the SDUV technique on in vivo porcine hearts [4, 5, 19–22]. Mechanical vibration was mainly used in these studies to obtain robust multi-frequency broadband shear wave signals (Figure 19.5). Nenadic et al. proposed to use a Lamb wave model instead of a shear wave model to fit the myocardial mechanical waves due to the plate-like geometry of the myocardial wall [10]. Pislaru et al. first investigated the feasibility of using SDUV in vivo using a pig model and reported $\mu_1 = 1.7$ kPa and $\mu_2 = 3.2$ Pa·s for diastole, and $\mu_1 = 31.0$ kPa and $\mu_2 = 5.0$ Pa·s for systole [19]. Urban et al. used a similar setup and studied eight pigs in an open-chest preparation, reporting $\mu_1 = 1.5$ kPa and $\mu_2 = 2.5$ Pa·s for diastole, and $\mu_1 = 28.3$ kPa and $\mu_2 = 2.1$ Pa·s for systole when using a shear wave frequency ranging from 50 to 400 Hz [4]. Recently Pislaru et al. studied the viscoelastic properties of normal and infarcted myocardium using the SDUV approach and found that both end-diastolic μ_1 and μ_2 and systolic μ_2

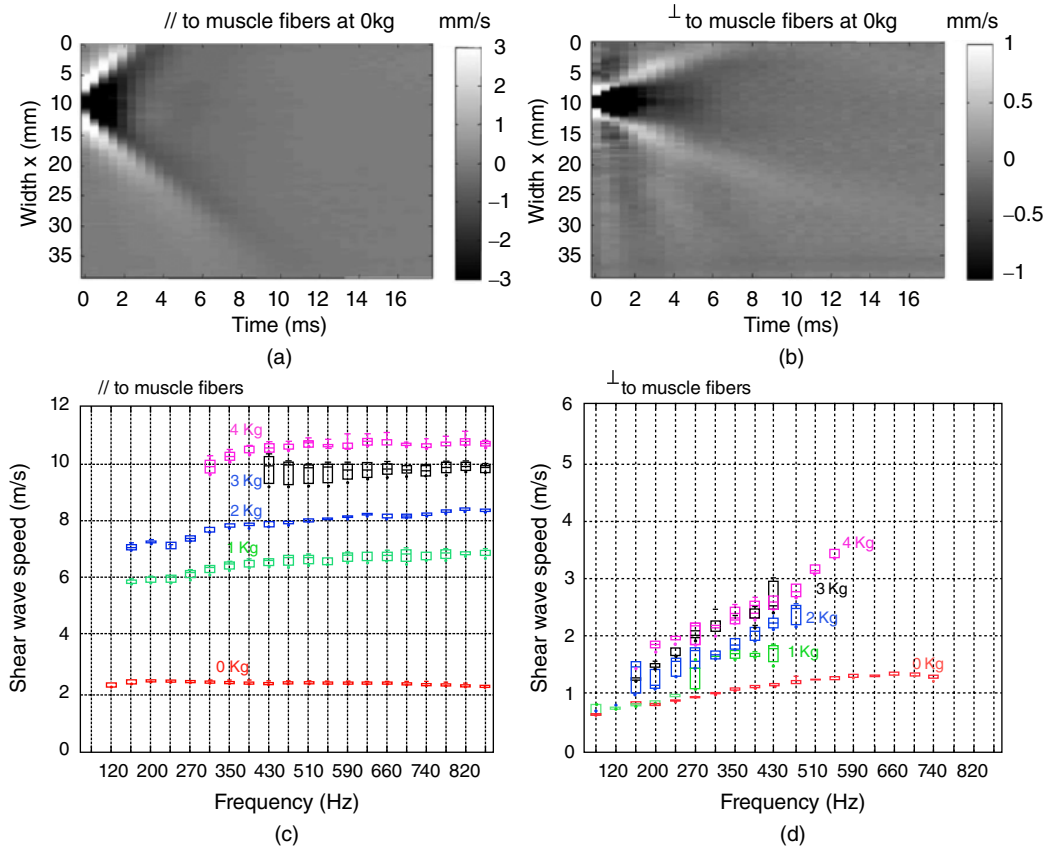

Figure 19.4 Shear wave signal (a) along the muscle fiber and (b) across the muscle fiber with 0 kg loading conditions. (c) Shear wave dispersion curves along the muscle fiber under different loading conditions. (d) Shear wave dispersion curves across the muscle fiber under different loading conditions. Source: reprinted from [18], copyright 2010, with permission from Elsevier.

increased after reperfusion of the infarcted myocardium, indicating that infarcted perfused myocardium was significantly stiffer and more viscous than normal myocardium [5]. For clinical applications, it is challenging to use such a mechanical vibration-based SDUV setup and open-chest procedure to evaluate myocardial viscoelasticity. Although acoustic radiation force-based shear wave methods can remotely generate shear waves trans-thoratically, it is challenging to obtain robust shear wave signals with wide bandwidth to support shear wave dispersion [23]. On the other hand, shear elasticity can be more robustly measured from transthoracic scans among non-obese patients with ideal acoustic windows [24]. However, so far only diastolic myocardial shear elasticity has been reported by use of transthoracic scan. Systolic measurements are very difficult to obtain because the myocardium is much stiffer in systole, and consequently shear wave motion can be very small and shear wave speed can be very high, both resulting in unreliable shear elasticity estimates. More robust technique needs to be developed to quantify myocardial viscoelasticity throughout the cardiac cycle.

19.3.5 Prostate

SDUV can quantify the shear elasticity and viscosity of the prostate tissue and potentially be used for diagnosis of prostate cancer. Mitri et al. used the SDUV to measure the viscoelasticity

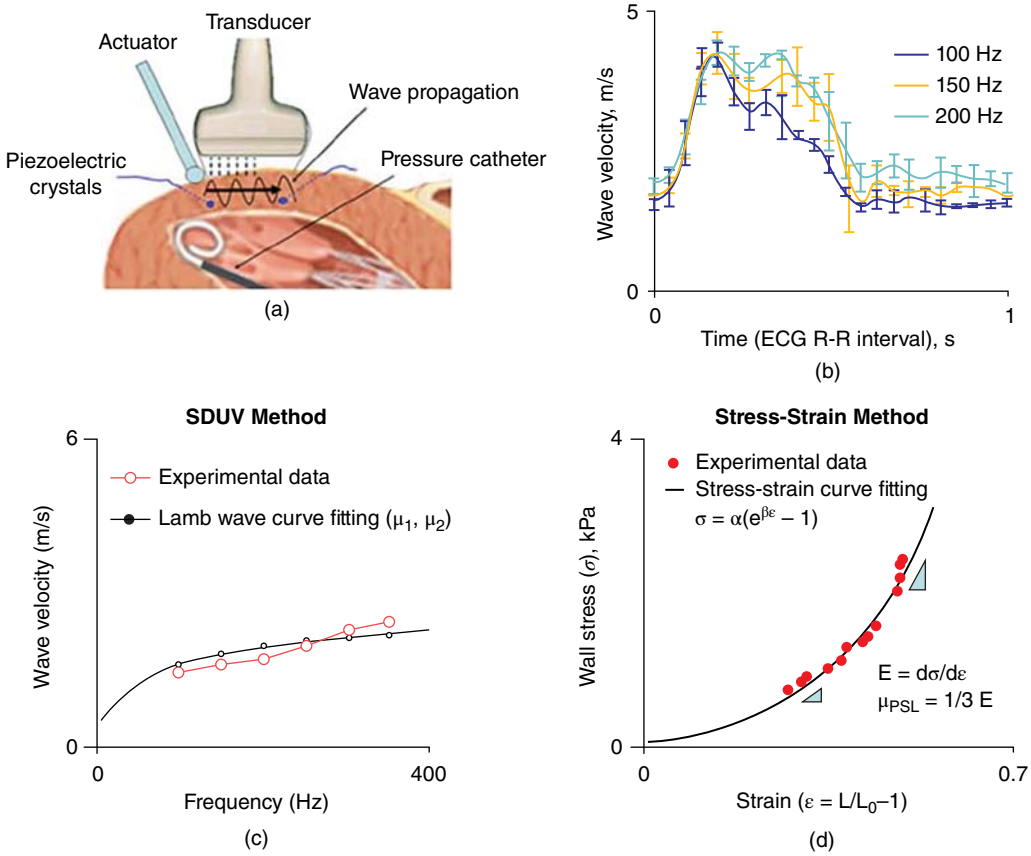

Figure 19.5 (a) Experiment setup for in vivo myocardial viscoelasticity measurements using SDUV; (b) shear wave speed measurements throughout the cardiac cycle for different frequencies; (c) estimation of elasticity μ_1 and viscosity μ_2 by curve fitting the experimental data with a Lamb wave model; (d) calculation of the shear elastic modulus from stress-strain data. Source: reprinted from [5], copyright 2014, with permission from Elsevier.

of excised human prostate (Figure 19.6) and reported μ_1 of 1.78 kPa and μ_2 of 1.11 Pa·s [25]. Although previous studies based on shear wave elasticity imaging (SWEI) have shown correlations between prostate pathology and shear elasticity (i.e. shear wave speed) [26–28], the role of viscosity in prostate cancer detection still remains unknown. However, like liver fibrosis staging, the frequency-dependent shear wave speed or shear elasticity needs to be accounted for when setting up cutoff values for diagnosis.

19.3.6 Kidney

Kidney viscoelasticity is related to various kidney diseases or dysfunction such as renal fibrosis, hypertension, and renal transplant rejection. SDUV has been implemented on kidney to quantify elasticity and viscosity in both in vitro and in vivo settings [29–33]. For normal kidney, Amador et al. reported average cortex elasticity of 1.81 ± 0.17 kPa and viscosity of 1.48 ± 0.49 Pa·s [32]. Both shear elasticity and shear viscosity were found to be correlated to kidney anisotropy [32]. By submerging kidney in formalin, both shear elasticity and shear viscosity significantly increased, resulting from the formation of methylene bridges induced by formaldehyde [32]. In vivo clinical application of SDUV on kidney faces the same penetration

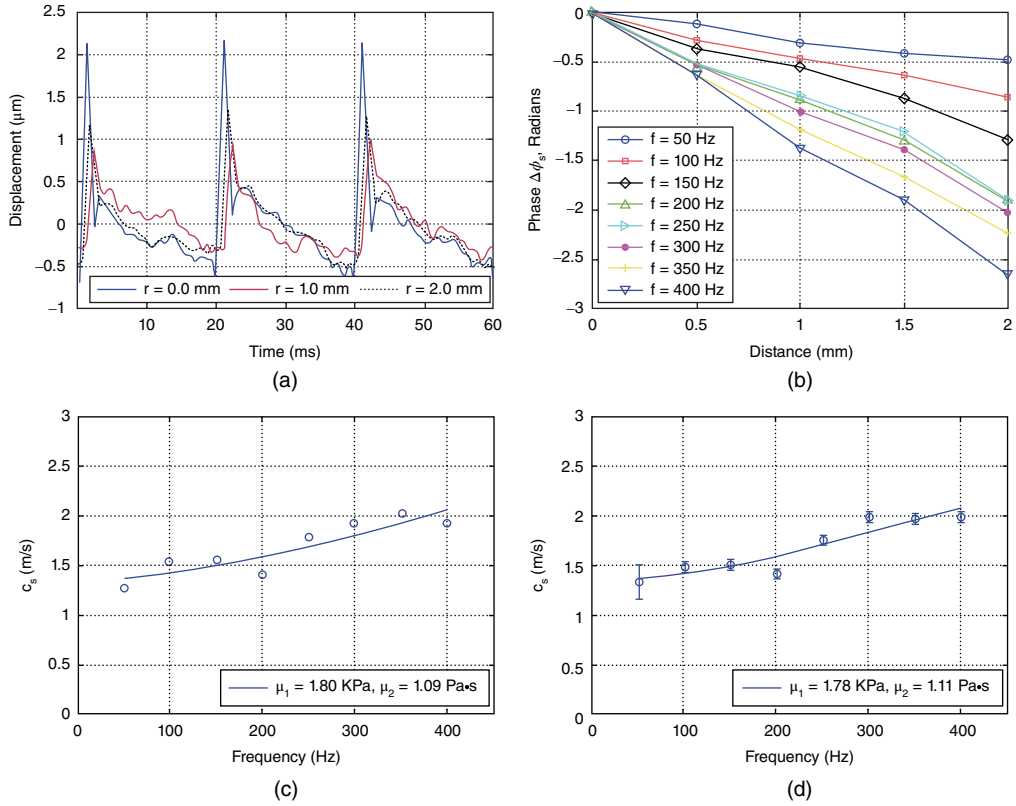

Figure 19.6 Examples of an SDUV viscoelasticity measurement of an excised human prostate: (a) shear wave motion signal from three different locations at different distance from the push origin; (b) shear wave phase as a function of propagation distance at different frequencies; (c) shear wave dispersion curve with Voigt model fitting; (d) repeated measurements from the same location with Voigt model fitting. Source: © 2011 IEEE, reprinted, with permission, from [25].

challenge as the heart application because the native kidney is typically deep from the body surface. This results in poor shear wave generation and detection and consequently suboptimal shear wave signal. For kidney transplants, however, the depth is typically very shallow and thus ideal for SDUV and other shear wave applications. In addition to the penetration issue, other challenges for kidney applications include the anisotropic nature of the kidney tissue, which results in different shear elasticity and viscosity measurements with shear waves propagating at different angles to the renal fiber. Another confounding factor in kidney application is that shear elasticity and viscosity may be pressure dependent and needs to be accounted for when interpreting results.

19.4 Summary

In this chapter we introduced the shear wave dispersion ultrasound vibrometry (SDUV) technique that first introduced the concept of using ultrasound to remotely quantify elasticity and viscosity of the soft tissue. Different configurations of SDUV have been developed using acoustic radiation force and external mechanical vibration. The concept of SDUV has been extended to using a transient shear wave signal and dispersion analysis to quantify tissue viscoelasticity.

SDUV has been performed in both ex vivo and in vivo tissues. Several clinical applications of SDUV and other similar techniques that provide viscoelasticity measurements have been briefly reviewed. Future directions include developing and exploring different physical models that take both the geometry and boundary conditions of the tissue into account for dispersion curve analysis; developing improved shear wave generation and detection methods to improve the shear wave signal quality, facilitating more robust and accurate estimates of both elasticity and viscosity; and continuing investigating the role of viscosity and exploring potential clinical applications that can use viscosity as a new biomarker.

References

1 Chen, S., Urban, M.W., Pislaru, C., et al. (2009). Shearwave dispersion ultrasound vibrometry (SDUV) for measuring tissue elasticity and viscosity. *IEEE Trans. Ultrason., Ferroelect., Freq. Control* 56: 55–62, Jan 2009.

2 Urban, M.W., Chen, S., and Fatemi, M. (2012). A review of shearwave dispersion ultrasound vibrometry (SDUV) and its applications. *Curr. Med. Imaging Rev.* 8: 27–36.

3 Nenadic, I.Z., Urban, M.W., Aristizabal, S., et al. (2011). On Lamb and Rayleigh wave convergence in viscoelastic tissues. *Phys. Med. Biol*. 56: 6723–6738.

4 Urban, M.W., Pislaru, C., Nenadic, I.Z., et al. (2013). Measurement of viscoelastic properties of in vivo swine myocardium using Lamb wave dispersion ultrasound vibrometry (LDUV). *IEEE Trans. Med. Imaging* 32: 247–261.

5 Pislaru, C., Urban, M.W., Pislaru, S.V., et al. (2014). Viscoelastic properties of normal and infarcted myocardium measured by a multifrequency shear wave method: comparison with pressure-segment length method. *Ultrasound Med. Biol.* 40: 1785–1795.

6 Bernal, M., Nenadic, I., Urban, M.W., and Greenleaf, J.F. (2011). Material property estimation for tubes and arteries using ultrasound radiation force and analysis of propagating modes. *J. Acoustic. Soc. Am.* 129: 1344–1354.

7 Deffieux, T., Montaldo, G., Tanter, M., and Fink, M. (2009). Shear wave spectroscopy for in vivo quantification of human soft tissues visco-elasticity. *IEEE Trans. Med. Imaging* 28: 313–322.

8 Chen, S., Fatemi, M., and Greenleaf, J.F. (2004). Quantifying elasticity and viscosity from measurement of shear wave speed dispersion. *J. Acoustic. Soc. Am.* 115: 2781–2785.

9 Zhang, X.M. and Greenleaf, J.F. (2007). Estimation of tissue's elasticity with surface wave speed. *J. Acoustic. Soc. Am.* 122: 2522–2525.

10 Nenadic, I.Z., Urban, M.W., Mitchell, S.A., and Greenleaf, J.F. (2011). Lamb wave dispersion ultrasound vibrometry (LDUV) method for quantifying mechanical properties of viscoelastic solids. *Phys. Med. Biol.* 56: 2245.

11 Nenadic, I.Z., Urban, M.W., Bernal, M., and Greenleaf, J.F. (2011). Phase velocities and attentuations of shear, Lamb, and Rayleigh waves in plate-like tissues submerged in a fluid. *J. Acoustic. Soc. Am.* 130: 3549–3552.

12 Zhu, Y., Dong, C., Yin, Y., et al. (2015). The role of viscosity estimation for oil-in-gelatin phantom in shear wave based ultrasound elastography. *Ultrasound Med. Biol.* 41: 601–609.

13 Chen, S., Sanchez, W., Callstrom, M.R., et al. (2013). Assessment of liver viscoelasticity by using shear waves induced by ultrasound radiation force. *Radiology* 266: 964–970.

14 Chen, X., Shen, Y., Zheng, Y., et al. (2013). Quantification of liver viscoelasticity with acoustic radiation force: a study of hepatic fibrosis in a rat model. *Ultrasound Med. Biol.* 39: 2091–2102.

15 Nightingale, K.R., Rouze, N.C., Rosenzweig, S.J., et al. (2015). Derivation and analysis of viscoelastic properties in human liver: impact of frequency on fibrosis and steatosis staging. *IEEE Trans. Ultrason., Ferroelect., Freq. Control* 62: 165–175.

16 Urban, M.W. and Greenleaf, J.F. (2009). A Kramers-Kronig-based quality factor for shear wave propagation in soft tissue. *Phys. Med. Biol.* 54: 5919–5933.

17 Urban, M.W., Chen, S., and Greenleaf, J.F. (2009). Error in estimates of tissue material properties from shear wave dispersion ultrasound vibrometry. *IEEE Trans. Ultrason., Ferroelect., Freq. Control* 56: 748–758.

18 Gennisson, J.-L., Deffieux, T., Macé, E., et al. (2010). Viscoelastic and anisotropic mechanical properties of in vivo muscle tissue assessed by supersonic shear imaging. *Ultrasound Med. Biol.* 36: 789–801.

19 Pislaru, C., Urban, M.W., Nenadic, I., and Greenleaf, J.F. (2009). Shearwave dispersion ultrasound vibrometry applied to in vivo myocardium. In: *2009 Annual International Conference of the IEEE Engineering in Medicine and Biology Society*, 2891–2894.

20 Pislaru, C., Urban, M.W., and Greenleaf, J.F. (2010). Increases in viscous and elastic moduli of infarcted myocardium measured in vivo by a new ultrasound method. *Eur. Heart J.* 31: 865–866.

21 Urban, M.W., Pislaru, C., Kinnick, R.R., and Greenleaf, J.F. (2010). In vivo measurements of viscoelasticity of the swine heart using Shearwave Dispersion Ultrasound Vibrometry (SDUV). In: *2010 IEEE Ultrasonics Symposium*, 686–689, San Diego, CA.

22 Nenadic, I.Z., Urban, M.W., Pislaru, C., et al. (2011). In vivo open and closed chest measurements of myocardial viscoelasticity through a heart cycle using Lamb wave Dispersion Ultrasound Vibrometry (LDUV). In: *2011 International IEEE Ultrasonics Symposium*, 17–20, Orlando, FL.

23 Song, P., Zhao, H., Urban, M.W., et al. (2013). Improved shear wave motion detection using pulse-inversion harmonic imaging with a phased array transducer. *IEEE Trans. Med. Imaging* 32: 2299–2310.

24 Song, P., Urban, M.W., Chen, S., et al. (2014). In vivo transthoracic measurement of end-diastolic left ventricular stiffness with ultrasound shear wave elastography. In: *IEEE International Ultrasonics Symposium*, 109–112, Chicago, IL.

25 Mitri, F.G., Urban, M.W., Fatemi, M., and Greenleaf, J.F. (2011). Shearwave Dispersion Ultrasonic Vibrometry (SDUV) for measuring prostate shear stiffness and viscosity – An in vitro pilot study. *IEEE Trans. Biomed. Eng.* 58: 235–242.

26 Zhai, L., Madden, J., Mouraviev, V., (2009). Correlation between SWEI and ARFI image findings in ex vivo human prostates. In: *2009 IEEE Ultrasonics Symposium*, 523–526, Rome, Italy.

27 Zhang, M., Nigwekar, P., Castaneda, B., et al. (2008). Quantitative characterization of viscoelastic properties of human prostate correlated with histology. *Ultrasound Med. Biol.* 34: 1033–1042.

28 Hoyt, K., Castaneda, B., Zhang, M., et al. (2008). Tissue elasticity properties as biomarkers for prostate cancer. *Cancer Biomarkers* 4: 213–225.

29 Amador, C., Urban, M.W., Greenleaf, J.F., and Warner, L.V. (2009). Measurements of swine renal cortex shear elasticity and viscosity with Shearwave Dispersion Ultrasound Vibrometry (SDUV). In: *2009 IEEE International Ultrasonics Symposium*, 491–494.

30 Amador, C., Urban, M.W., Warner, L.V., and Greenleaf, J.F. (2009). In vitro renal cortex elasticity and viscosity measurements with shearwave dispersion ultrasound vibrometry (SDUV) on swine kidney. In: *2009 Annual International Conference of the IEEE Engineering in Medicine and Biology Society*, 4428–4431.

31 Amador, C., Urban, M.W., Kinnick, R., et al. (2010). Viscoelastic measurements on perfused and non-perfused swine renal cortex in vivo. In: *2010 IEEE Ultrasonics Symposium*, San Diego.

32 Amador, C., Urban, M.W., Chen, S., and Greenleaf, J.F. (2011). Shearwave Dispersion Ultrasound Vibrometry (SDUV) on swine kidney. *IEEE Trans. Ultrason., Ferroelect., Freq. Control* 58: 2608–2619.

33 Amador, C. (2011). Measurements of kidney viscoelasticity with shearwave dispersion ultrasound vibrometry. Ph.D. Thesis, pp. 51–89. Department of Physiology and Biomedical Engineering, Mayo Graduate School, Rochester, MN, USA

Section VI

Transient Elastography Methods

20

Transient Elastography: From Research to Noninvasive Assessment of Liver Fibrosis Using Fibroscan®

Laurent Sandrin[1], Magali Sasso[1], Stéphane Audière[1], Cécile Bastard[1], Céline Fournier[1], Jennifer Oudry[1], Véronique Miette[1], and Stefan Catheline[2]

[1] *Echosens, Paris, France*
[2] *LabTAU, INSERM-University of Lyon, France*

20.1 Introduction

Initially developed with the critical aim of improving the management of deadly breast and prostate cancers, elastography eventually succeeded in the field of diffuse liver diseases. As a matter of fact, liver diseases are very common diseases which have long been known as affecting liver stiffness. In *Aphorisms* from more than two thousand years ago, Hippocrates noticed that it is a bad sign if the liver becomes hard during a jaundice. The breakthrough of quantitative elastography of the liver came with the development of Vibration-Controlled Transient Elastography based FibroScan® which is now considered as the noninvasive standard for the measurement of liver stiffness. Today liver stiffness is widely used as a surrogate marker of liver fibrosis, which is part of the structural and functional alterations in most chronic liver diseases. Among chronic liver diseases, hepatitis C and B lead to nearly 1.4 million deaths every year according to the World Health Organization. The principles of transient elastography are presented in this chapter. The FibroScan® device is detailed, along with a clinical review of its applications to liver diseases. Other applications of transient elastography are discussed in the last part of this chapter.

20.2 Principles of Transient Elastography

Though transient elasticity imaging refers to elastography techniques that rely on the use of transient shear waves, the term "transient elastography" specifically addresses transient elasticity imaging methods in which the transient shear waves are induced mechanically. Indeed, the methods developed for transient elastography were extended to radiation force based shear wave generation.

20.2.1 Elastic Wave Propagation in Soft Tissues

The human body has very long been considered by the ultrasound community as a fluid. In 1987, Krouspok et al [1] started to study the shear wave inherent to any solid. Harmonic vibrations were generated on the surface by mechanical vibrators and the induced shear waves were tracked using Doppler imaging; this is the so-called sonoelasticity. However, these early observations of elastic wave propagation in soft tissues were not clearly understood: for example,

Ultrasound Elastography for Biomedical Applications and Medicine, First Edition.
Edited by Ivan Nenadic, Matthew Urban, James Greenleaf, Jean-Luc Gennisson, Miguel Bernal, and Mickael Tanter.

the observed shear wave was longitudinally polarized and, its phase velocity was puzzlingly increasing at low frequency [2]. In 1999, together with a pulsed or transient generation of shear waves, a theoretical approach of elastic wave in soft solids was reported [3, 4]. It was based on the exact solution of the elastodynamic equation, namely the Green's function. This solution, mentioned in numerous textbooks [5, 6], was first given by Stockes in 1849 and was later adapted to semi-infinite solids [7]. It was shown that the shear wave field measured at a few wavelengths from the source in soft tissues using transient elastography was under the influence of the near field. This near field, usually neglected in the ultrasound community, is responsible for the strange polarization of the shear wave as well as for the phase velocity behavior. The theoretical approach of Oestreicher [8], based on an oscillating sphere embedded in a viscoelastic medium, is worth mentioning [9]. However, the computation treats separately the two shear and compression wave equations without a source. As a consequence, Oestreicher's solutions for an infinitely small sphere are incompatible with the Green's function, except in the far field. In elastography, the importance of the near field is such that the exact solution of the Green's functions are needed. For source size bigger than a shear wavelength (typically a few centimeters), the diffraction effect based on the Green's function decomposition was shown to nicely fit experimental data [10]. But some questions remained: the near-field term, sometimes called the coupling term, responsible for the longitudinally polarized shear wave on the axis of a piston source is neither curl-free nor divergence-free. Thus does this shear wave deserve its name? In a recent approach [11], the near-field term was split into a divergence-free term and a curl-free term. It does not change anything about the Green's function but allows us to clearly identify the compression wave and the shear wave. As shown in Figure 20.1, not only the shear wave can be longitudinally polarized but also a compression wave can be transversely polarized. The longitudinal shear wave and the transverse compression wave are located inside the dashed boxes called Zoom #1 and #2. The Zoom #1 box shows the transverse compression wave which propagates at the compression wave speed with a wave vector q. The transversal component of displacements along the vertical axis of symmetry is clearly apparent (arrows). The strain sequence illustrated in the upper right panel implies neither volume change nor particle velocity circulation: it is divergence- and curl-free. The Zoom #2 box shows the longitudinal shear wave which is subjected to a special strain field propagating at the shear speed with a wave vector k. It is represented as a semi-transparent rectangle. The longitudinal component of displacements along the horizontal axis of symmetry is clearly apparent (black and red arrows). The strain sequence illustrated in the upper right panel implies neither volume change nor particle velocity circulation: it is divergence- and curl-free.

20.2.2 Early Developments of Transient Elastography

Transient elastography emerged in the late 1990s [3, 4, 12]. At that time the objective was to overcome limitations of existing quantitative elastography techniques such as magnetic resonance elastography [13] or sonoelastography [1, 14]. As a matter of fact, in dynamic elastography techniques, the medium is stimulated with a continuous vibration which induces interference nodes due to reflections at boundaries. The sensitivity to boundary conditions is reduced in transient elastography by using a transient excitation which allows the separation of compression and shear waves and avoids the presence of interference nodes within the investigated medium. Indeed, the speed of compression waves is orders of magnitude superior to the shear wave speed. As transient shear waves travel through the tissues within tens of milliseconds (typical speed ranging from 1 to 10 m/s), the ultrasound-based imaging modality needs to be ultrafast to be able to track the shear wave propagation. Indeed the displacements induced by the shear wave propagation are obtained using cross-correlation algorithms applied to the raw ultrasound A-lines which are divided into segments as a function of depth.

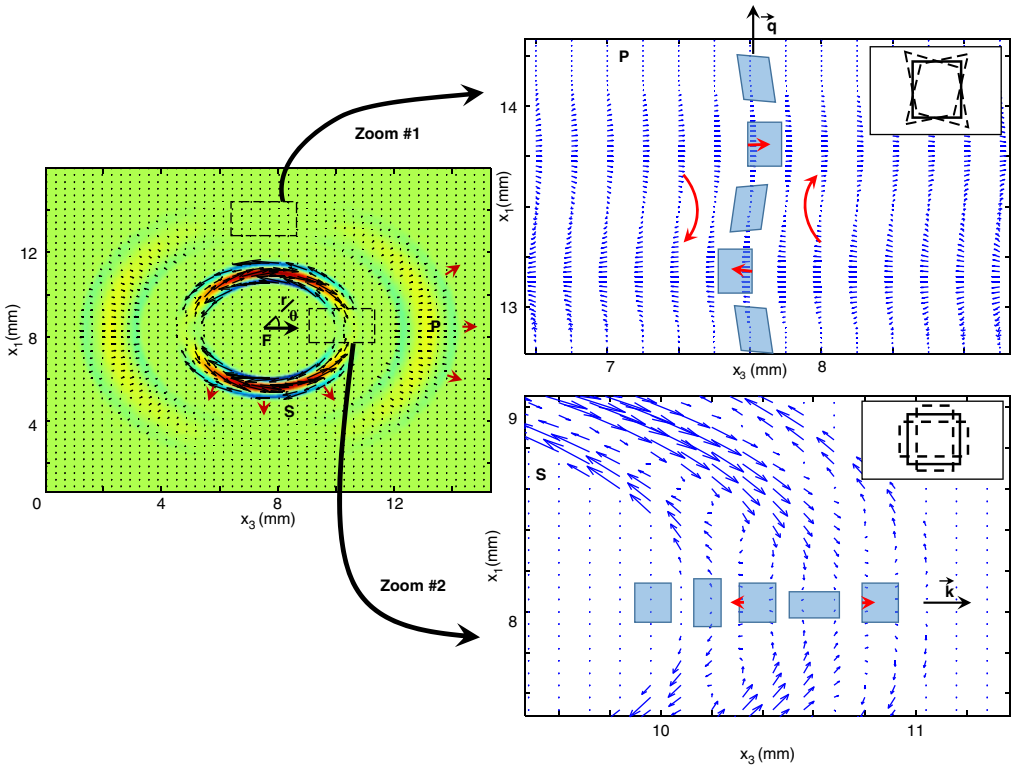

Figure 20.1 Elastic Green's function. The dilatational wave and the shear wave are clearly visible at angles $\Theta = 0$ and $\Theta = \pi/2$. Source: reprinted with permission from [11], copyright 2015, Acoustical Society of America.

Cross-correlation analysis is used to measure the similarity of two windows obtained at different times as a function of the lag of one relative to the other. Commonly used cross-correlation matching algorithms are normalized cross-correlation, sum of absolute differences, and sum of squared differences. Frame rates of several thousand per second are be obtained to measure the displacements induced by the shear wave propagation. Initially used to follow the propagation of mechanically induced shear waves [12, 15], ultrafast imaging was later used to follow the propagation of shear waves induced by radiation-force as proposed in the early 1990s by Sugimoto et al. [16] and later developed by other groups [17–19].

20.2.3 1D Transient Elastography: A Purely Longitudinal Shear Wave

Transient elastography yielded the development of an average stiffness measurement method referred as 1D transient elastography [20]. The technique relies on a single element ultrasound transducer and a mechanical actuator. The ultrasound transducer and the vibrator are located on the same axis. As shown in Figure 20.2, two modes have been described so far: the transmit mode, where the ultrasound transducer and the vibrator are located on opposite sides of the medium, and the reflection mode, in which the ultrasound transducer is mounted on the axis of the vibrator. The reflection mode is very favorable not only because it does not require access to two sides of the investigated object, but also because it ensures a perfect alignment of the ultrasound and shear wave axis of propagation. Interestingly, when the ultrasound transducer is mounted on the axis of the vibrator, the low-frequency shear wave and the ultrasound signals are generated by the same piston-like transducer. Indeed, the ultrasound beam coincides

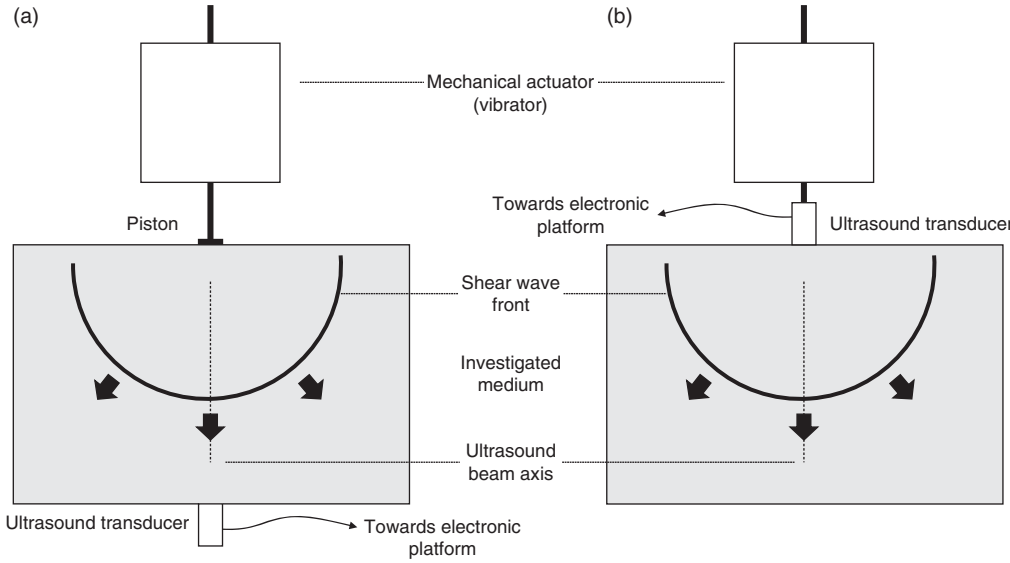

Figure 20.2 In 1D transient elastography, the ultrasound transducer and the vibrator are located on the same axis. They may be located (a) on opposite sides of the medium (transmit mode) or (b) on the same side (reflection mode).

with the vibrator axis, which means that only purely longitudinal displacements can be measured with this setup under the assumption of homogeneity. The observation of a longitudinally polarized shear wave on the axis of symmetry is a consequence of the diffraction effects from the piston-like transducer surface and the presence of the so-called coupling term [10]. A technique called maximum likelihood estimation (MLE) [21] was developed to compensate for the diffraction effects observed in transient elastography. MLE is based an analytical approximation of the displacements induced in the medium. Green's functions are being computed with the geometry of a semi-infinite medium hit by a circular piston. The MLE technique enables improvements of shear wave speed estimation by transient elastography in homogeneous semi-infinite media. 1D transient elastography was successfully applied to in vivo measurement of liver stiffness [22]. This technique was also applied to the assessment of viscoelastic properties of blood during clotting [23], to the assessment of arterial stiffness in vitro [24], to the monitoring of heat-induced changes in fresh bovine skeletal muscle samples [25], and to the assessment of thin-layered soft tissue stiffness [26].

20.2.4 Ultrafast Imaging for Transient Elastography

The development of ultrasound-based transient elastography for elasticity imaging was made possible through the use of programmable electronic platforms for ultrasound. These electronic platforms were originally designed by Jean-Michel Hasquenoph for time-reversal mirror experiments in nondestructive evaluation [27]. Dedicated programming of these platforms allowed the development of ultrafast imaging to track the displacements induced by transient shear waves in soft tissues using 2D transient elastography [12, 15, 28]. As a matter of fact, by using plane wave illumination instead of standard ultrasound beamforming, the frame rate of an ultrafast programmable electronic platform is only limited by the travel time of ultrasound and is therefore able to reach several thousands of frames per second. Depending on the attenuation of the medium and the ultrasound frequency being used, it can reach several thousands of frames per second. The limitations of high frame rate imaging are the image dynamic and the

sensitivity to heterogeneities which affect the ultrasound plane wave. Indeed focusing only in receive mode does allow a higher frame rate but it is not likely to be used as itself for standard ultrasound imaging where image quality is crucial.

20.2.5 Validation on Phantoms

Few manufacturers provide tissue-mimicking phantoms compatible with quantitative elastography techniques. Indeed such phantoms should not only mimic ultrasound properties of soft tissues but should also have similar viscoelastic properties. Therefore, Oudry et al. [29] proposed the use of copolymer in oil as a new material for testing shear wave-based ultrasound elastography devices. CIRS (CIRS Incorporated, USA) manufactures quantitative elastography phantoms using a patented elastic material (Zerdine®) that are compatible with transient elastography. The stiffness of manufactured phantoms is measured using ASTM standards D575-91 [30]. Since viscoelastic properties of phantoms are influenced by the applied force [31], it is important to apply minimal force on the phantom surface when measuring stiffness for performance evaluation. Oudry et al. [32] evaluated stiffness of phantoms using two common mechanical techniques, quasi-static compression (QSC) and dynamic mechanical analysis (DMA), and two techniques based on shear wave propagation, VCTE and hyper-frequency viscoelastic spectroscopy (HFVS). All measurements were performed at 50 Hz except for QSC.

20.3 Fibroscan

20.3.1 An Average Stiffness Measurement Device

FibroScan® was introduced by Echosens (Paris, France) which was founded in 2001 (co-founders: Laurent Sandrin, Jean-Michel Hasquenoph, Sylvain Yon, Bertrand Fourquet). Early research and development activities were performed between 2001 and 2002 during a pilot trial at the Institut Montsouris (Paris, France). The commercialization of FibroScan® started in December 2003. The most recent model is FibroScan 502 Touch (Figure 20.3). The background technology, vibration-controlled transient elastography (VCTE) [22, 33, 34], is covered by several US patents and their foreign counterparts. Though the algorithms it involves are complex, the basic principle of FibroScan® remains simple: a single element ultrasound transducer is mounted on the axis of a mechanical actuator (Figure 20.3b).

As shown in Figure 20.4, the ultrasound transducer emits and receives ultrasound to measure the displacements induced in the medium by the propagation of a low-frequency (50 Hz) transient shear wave induced by the displacement of the ultrasound transducer. The technique is taking advantage of two interesting effects: diffraction effects due to the piston-like vibrator surface and the existence of a coupling term. As the low frequency shear wave and the ultrasound signals are generated by the same piston-like transducer, longitudinal displacements due to the shear wave propagation through the liver can be measured using the ultrasound RF signals. Cross-correlation techniques are applied to the successive ultrasound RF lines acquired at high pulse repetition frequency (PRF) of 6 kHz. A spatial-temporal strain map is computed from the recorded displacements. The shear wave front can be observed in the strain map.

The average shear wave speed is calculated using proprietary algorithms and the average stiffness is deduced according to the well-known equation

$$E = 3\rho V_s^2 \tag{20.1}$$

where E is the Young's modulus, V_s is the shear wave speed, and ρ is the mass density. This also assumes an isotropic, homogeneous, and incompressible material. Three spatial-temporal strain maps measured in livers of increasing stiffness are shown in Figure 20.5.

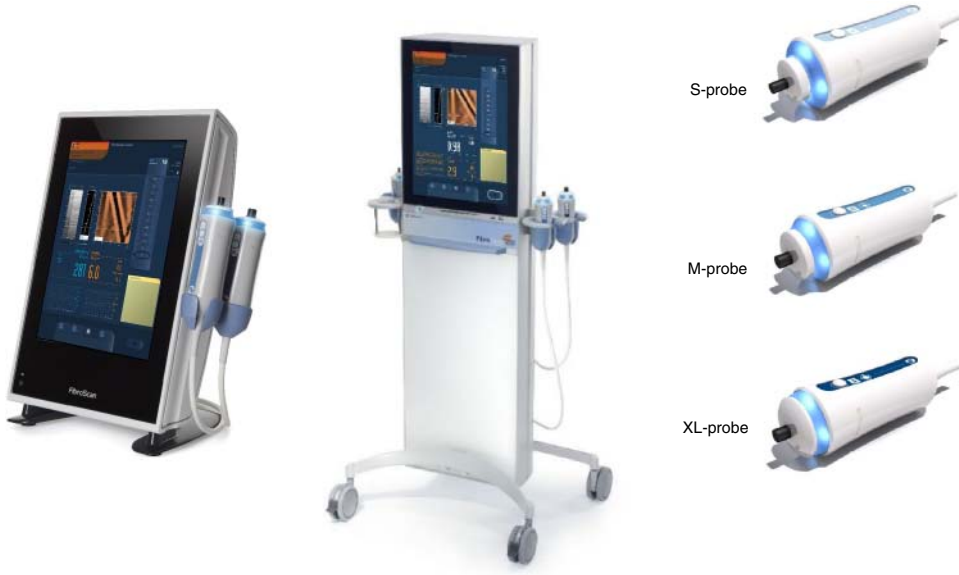

Figure 20.3 (a) FibroScan® 530 Compact and (b) FibroScan® 502 Touch with (c) M, S and XL probes.

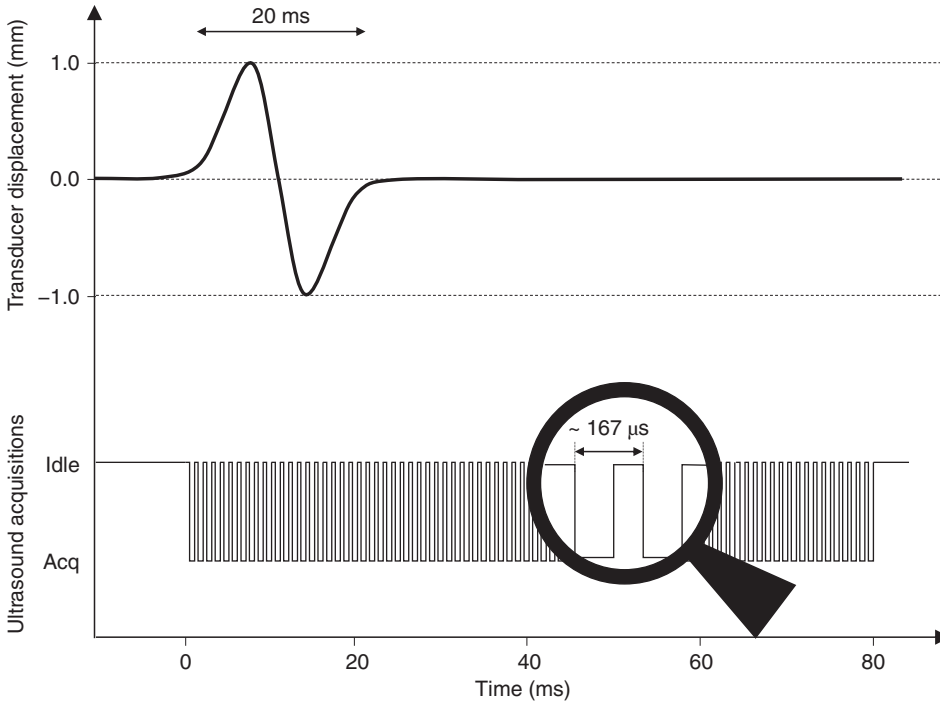

Figure 20.4 Typical VCTE acquisition. Ultrafast ultrasound acquisitions (PRF = 6 kHz) are performed during the propagation of a shear wave induced by a 50 Hz center frequency transient excitation.

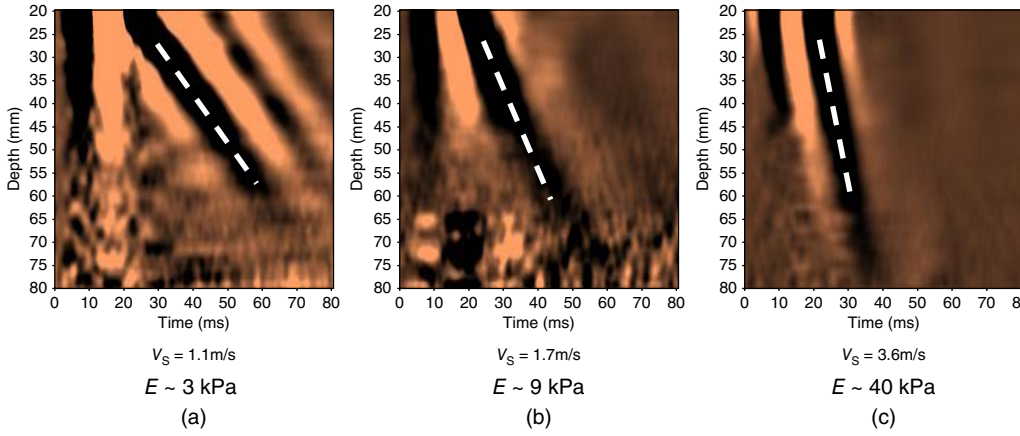

Figure 20.5 The shear wave slope (white dotted line) gets steeper as the stiffness of the medium increases: (a) normal liver; (b) medium stiff liver; and (c) cirrhotic liver. The shear wave speed is measured between 25 and 65 mm depth under the skin surface.

20.3.2 Probes Adapted to Patient Morphology

Several probes are being used with FibroScan® depending on the patient morphology. The M probe is the most common probe. It is based on a 3.5 MHz ultrasound transducer of 7 mm active diameter. Larger adults may be measured using the XL probe which signal penetrates deeper within the tissue as the center ultrasound frequency is decreased to 2.5 MHz and the active diameter increased to 10 mm. The S probe is used for measuring small adults or children, with a 5 mm active diameter transducer of 5.0 MHz. The amplitude of vibration for shear wave generation varies depending on the probe. The amplitude is 1 mm peak-to-peak with the S probe, 2 mm peak-to-peak with the M probe, and 3 mm peak-to-peak with the XL probe. Simulated acoustic fields in water of the three different ultrasound transducers are shown in Figure 20.6. Simulations were performed using Field II [35, 36].

20.3.3 Narrow Band and Controlled Shear Wave Frequency Content

The term "vibration-controlled" in VCTE was chosen to emphasize the importance of controlling the shape of the vibration to perform reproducible liver stiffness measurements. As shown in Figure 20.7, soft tissue viscoelastic properties vary as a function of frequency. The stiffness of a fresh liver sample can vary between 2 kPa at 50 Hz and 10 kPa at 400 Hz. It is therefore crucial to control the shear wave frequency. FibroScan® controls the shear wave frequency by two means. First FibroScan® generates a narrow band shear wave frequency content centered at 50 Hz which limits the influence of the dispersion of shear wave speed. Second it uses a servo-controlled motion actuator to precisely control the shape of the vibration: one period of a sinusoid at a center frequency of 50 Hz. The amplitude of the sinusoid varies as a function of exam type and therefore patient morphology. This control is important to ensure that the shape of the low-frequency excitation not be distorted. As a matter of fact, without a servo-controlled motion actuator, a frequency shift towards lower frequencies would be observed as the force applied on the tip of the probe increases.

The control of the shear wave frequency content is a significant advantage of VCTE compared to radiation-force based elastography techniques [16, 17, 37] which do not control the shear wave frequency content and therefore present depth-dependent and frequency-dependent bias [38–40]. Indeed, the frequency content of shear waves generated using radiation-force depends on several factors: the depth of measurement as the ultrasound frequency content changes with

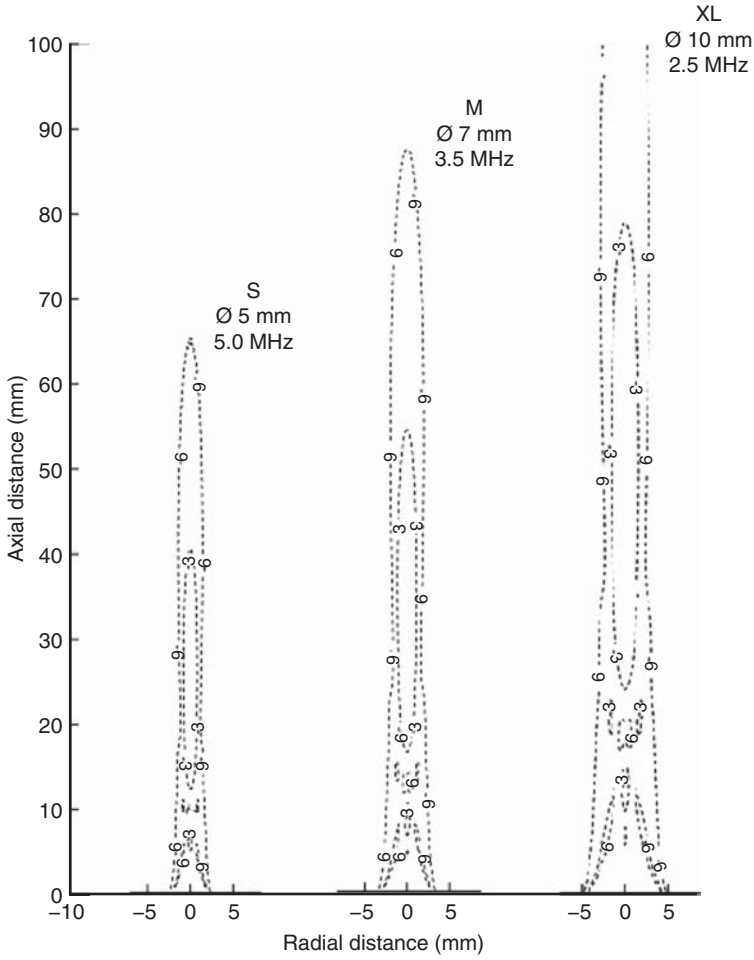

Figure 20.6 Simulated acoustic fields of S, M, and XL transducers.

depth due to the frequency dependence of attenuation at ultrasonic frequencies, the ultrasound transducer center frequency, the ultrasound transducer excitation duration. and the stiffness of the tissue at the location of the push due to radiation-force.

20.3.4 Low Acoustic Output Power

Using large acoustic output power is not recommended in some fragile patients or in the presence of disorders that may affect blood circulation and therefore the thermal convection in tissues. FibroScan® uses very limited acoustic output power since it only requires a single element ultrasound transducer. The peak ($I_{sppa.3} \approx 50$ W/cm^2) and average ($I_{spta.3} \approx 15$ mW/cm^2) acoustic output power are below the limits ($I_{sppa.3} < 190$ W/cm^2 and $I_{spta.3} < 94$ mW/cm^2) for abdominal imaging given by the relevant international standard (IEC60601-2-37) and therefore the thermal and mechanical indices do not even need to be displayed.

20.3.5 Standardized Examination Procedure

Depending on patient morphology and device (older devices include a slower CPU), the examination usually lasts between 1 and 5 minutes. The examination is highly standardized in order to

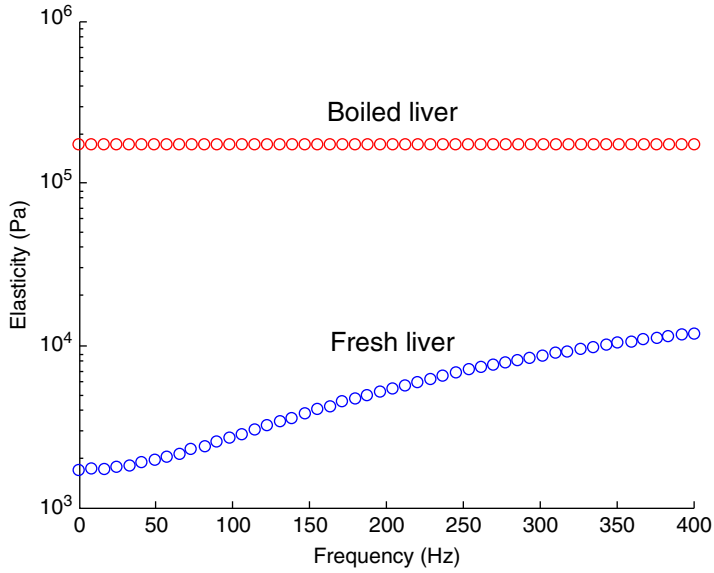

Figure 20.7 Elasticity of fresh and boiled pig liver samples as function of frequency. Measurements performed by viscoelastic spectroscopy. Source: courtesy of Rheolution Inc.

improve the overall performance. As shown in Figure 20.8, the probe is placed in the intercostal position in front of the right lobe of the liver at the level where a biopsy would be performed. The patient is lying in dorsal decubitus, with the right arm elevated to enlarge the intercostal spaces. The tip of the probe is contacted to the intercostal skin with coupling gel in the 9th to 11th intercostal space at the level where a liver biopsy would be performed.

The operator locates the measurement location using A-mode and TM-mode ultrasound images (Figures 20.9a and 20.9b). It is recommended that the measured liver portion be free of large vessels on A-mode and TM-mode ultrasound images and at least 6 cm deep. Interestingly, the measurement location is where a biopsy would be performed. The force applied on

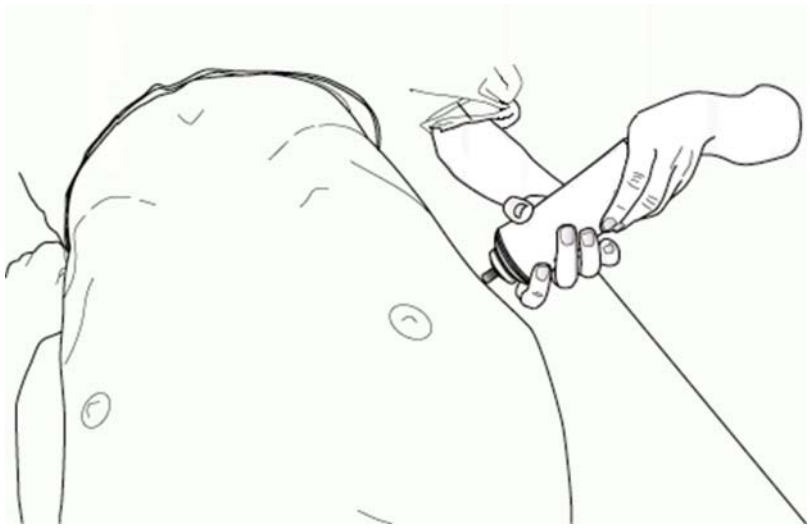

Figure 20.8 FibroScan® probe is placed in intercostal position in front of the right lobe of the liver. The patient is lying in dorsal decubitus and the right arm in maximal abduction in order to enlarge the intercostal space.

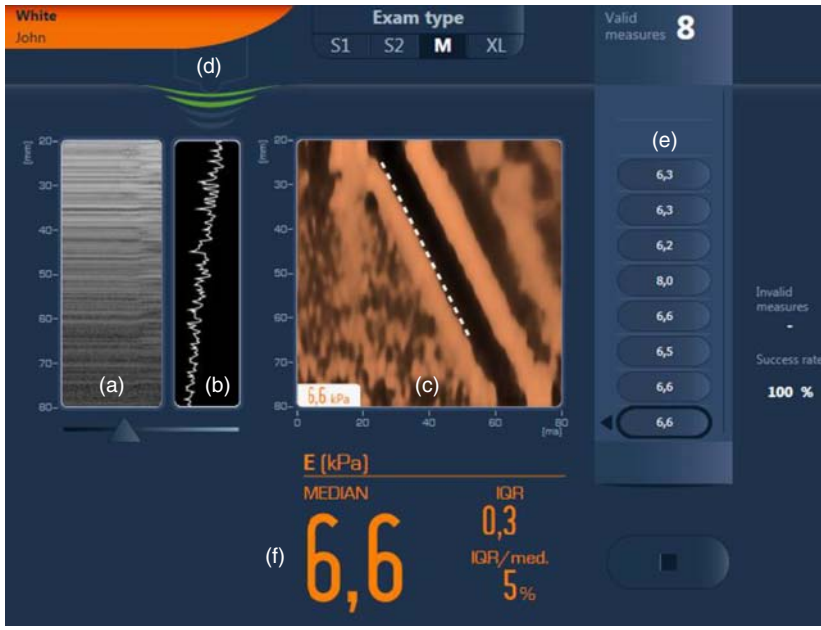

Figure 20.9 During the examination procedure, the operator locates the liver using TM-mode (a) and A-mode (b) ultrasound images. The applied force is displayed (d). The slope of the shear wave is represented by a white line on the shear wave propagation map (c) as a function of depth and time. The result (f) is the median of the individual valid measurements (e).

the patient skin at the tip of the probe is monitored during the exam. This monitoring does not aim to avoid direct compression of the liver as the ribs prevent direct compression of the liver. The force is monitored in order to ensure that the contact is sufficient to allow a correct shear wave transmission through the subcutaneous tissues while not being too high, which could distort the shear wave excitation shape. With M probe, the operator can trigger a measurement when the force lies within 4 to 8 N. A force indicator is used to assist the operator in getting a correct force value (Figure 20.9d). Data acquisition is almost instantaneous as data are acquired in only 80 ms and the processing time for each measurement ranges from 1 second to 3 seconds depending on FibroScan® model. The shear wave propagation map is displayed to the operator (Figure 20.9c). The average shear wave speed is measured within the 25 to 65 mm depths (M probe). A validity criteria is computed for each measurement. Invalid measurements are automatically rejected. A single valid measurement provides an estimate of the group shear wave speed around 50 Hz. Thereafter individual stiffness measurements are derived using Eq. (20.1). The median of valid measurements is kept as the final stiffness value (Figure 20.9f). The interquartile range (IQR = Q3 – Q1) value is provided as an indicator of the values dispersion (Figure 20.9e). Operators usually stop the examination after 10 valid measurements are obtained. FibroScan® can measure stiffness values in the range 1.5 kPa to 75.0 kPa.

20.4 Application of Vibration-controlled Transient Elastography to Liver Diseases

As of today there are more than 1000 publications in peer-reviewed journals and more than 30 guidelines issued by professional societies about liver stiffness measurement (LSM) by FibroScan® for the management of patients with chronic liver diseases, which together make transient elastography (TE) by FibroScan® the noninvasive standard for LSM [41].

20.4.1 A Questioned Gold Standard

Most of the studies on noninvasive liver fibrosis tests use liver biopsy as the gold standard. Actually, the gold standard positioning of liver biopsy is more and more a matter of debate. Indeed, sampling errors and inter-observer variations limit the performance of liver biopsy for fibrosis staging. By using the METAVIR scoring system and a digital approach to artificially create virtual liver biopsy specimens, Bedossa et al. [42] showed that only 75% of liver biopsies were correctly categorized with 25-mm long specimens which corresponds to large specimens. Obviously the 100 % area under the ROC curves is not a correct objective to define a good noninvasive liver fibrosis test.

20.4.2 Viral Hepatitis

The first chronic liver disease in which LSM has been studied is viral hepatitis including HCV mono-infection [33, 34, 43–47], HBV mono-infection [48–52], and HIV co-infected patients [53–55]. Based on this large body of evidence, TE with FibroScan® is now recommended for use in all HCV patients as a screening tool to exclude cirrhosis and also to prioritize patients for antiviral therapy based on disease stage, as a better predictor than serum biomarkers for the prediction of advanced liver fibrosis and cirrhosis in HBV patients, and as a first line tool to exclude severe fibrosis and cirrhosis in HBV inactive carriers [41].

20.4.3 Fatty Liver Disease

The second group of chronic liver diseases where the use of LSM is of growing interest is fatty liver disease, either related to alcohol abuse [56, 57] or to metabolic syndrome [58, 59]. Though the existing literature in this field is not as comprehensive as for viral hepatitis, TE is also recommended as a first line procedure for the identification of patients at low risk of severe fibrosis/cirrhosis in alcoholic liver disease and non-alcoholic fatty liver disease [41].

20.4.4 Other Diseases

To complete the range of chronic liver diseases, the benefits of LSM have also been shown in conditions such as primary biliary cirrhosis [60–65], biliary atresia [66–72], cystic fibrosis [73–77], auto-immune hepatitis [78], hemochromatosis [79], diabetes [80–82], and Wilson's disease [76, 83].

20.4.5 Cirrhosis

LSM has also been shown to have utility beyond the assessment of liver fibrosis stage. Indeed, liver cirrhosis is the most advanced stage of chronic liver disease as defined histologically. However, cirrhosis is further subdivided into compensated and decompensated cirrhosis, the latter being defined by the occurrence of complications such as portal hypertension and its consequences (ascites, esophageal varicose veins, and encephalopathy) or hepatocellular carcinoma. Several studies have therefore evaluated the relationship between LSM and the occurrence of complications of cirrhosis [56, 84–94]. Today, in settings where hepatic venous pressure gradient measurement procedure is not available, TE is proposed to stratify patients at risk of clinically significant portal hypertension [41].

20.4.6 Prognosis

At last, there is increasing evidence for the prognostic value of LSM in patients [41]. The first study evaluating prospectively and longitudinally the prognosis value of LSM was performed

in Japan for the assessment of the risk of developing hepatocellular carcinoma in patients with chronic hepatitis C [95]. In another cohort of patients with primary biliary cirrhosis, progression of LSM was associated with increased risk of liver decompensation, liver transplantation, or death [65]. Finally, overall survival, and survival without liver-related death, were shown to be significantly associated with LSM and LSM progression in HCV and HBV patients [96–98].

20.4.7 Confounding Factors

As previously mentioned, FibroScan® measures a physical parameter (LSM) directly from the liver parenchyma. Initially, the first publications established that LSM was closely correlated to liver fibrosis [34] but the following 10 years of feedback and publications now provide a clearer understanding of the different clinical parameters affecting LSM. Indeed, independent of fibrosis, many factors may also increase LSM. The most well-known and widely studied is inflammation (or hepatitis). LSM can dramatically increase during acute hepatitis or transaminase flares [99–102] independently of the degree of fibrosis. Other factors identified so far are extrahepatic cholestasis [103], liver congestion and venous pressure due to cardiac insufficiency [104], and amyloid deposit [105–107].

20.4.8 The Pressure–Matrix–Stiffness Sequence Hypothesis

Mueller et al. [101] have introduced the paradigm of pressure–matrix–stiffness sequence hypothesis, which basically explains that liver stiffness is not only a consequence of liver fibrosis. Actually, the accumulation of interstitial liquid and inflammatory infiltrate during the course of chronic liver diseases yields to an increase mechanical stress. This stress not only translates into a stiffness increase but also stimulates fibrotic tissue growth and therefore the production liver fibrosis which eventually results in a permanent stiffness increase. Thus even before liver fibrosis starts to expand in the liver parenchyma, transient liver stiffness increase can be measured.

20.4.9 Advanced Applications: CAP

In vivo liver stiffness measurement with FibroScan® has been successfully combined with the measure of ultrasound attenuation to provide another physical parameter independent to liver stiffness which is related to steatosis. This parameter named controlled attenuation parameter (CAP) and expressed in dB/m [108, 109] is an estimate of the total ultrasonic attenuation (forward-and-return paths) at 3.5 MHz. CAP is evaluated using the same ultrasound signals used to measure the liver stiffness and is only appraised if the stiffness is "valid" so as to ensure that the operator gets an estimate of liver ultrasound attenuation in the liver exclusively. Many studies have demonstrated the good to excellent diagnostic accuracy of CAP using the M probe of the FibroScan® taking liver biopsy as a gold standard (see for instance [110–112]). More recently CAP was developed on the XL probe of the FibroScan® showing a good diagnostic accuracy similar to the CAP on the M probe [113, 114].

20.4.10 Spleen Stiffness Measurements

Esophageal varices (EV) represent one of the most severe complications of cirrhosis. Their prevalence among cirrhotic patients is between 50% and 60%. The performances of spleen stiffness measurement (SSM) were assessed with a modified FibroScan® in order to detect the presence of significant EV (grade 2 and 3) in cirrhotic patients. 100 patients underwent upper GI-endoscopy for assessment of EV grade: G0 (no varice), G1 (small varices), G2 (medium

varices), and G3 (large varices). Results showed that SSM and EV size were significantly correlated and that SSM could be used to distinguish G0/G1 grades from G2/G3 grades. This first study using a spleen-dedicated FibroScan® shows that spleen stiffness and fibrosis blood markers are independent predictors of significant EV in cirrhotic patients.

20.4.11 Conclusion

Obviously the quest for the perfect noninvasive test for liver fibrosis is likely to be illusory. LSM measured by FibroScan® demonstrates good to excellent performances as a noninvasive test for liver fibrosis. Other pathological conditions such as liver inflammation or liver congestion may influence LSM but these conditions are easily discernible within the clinical context. Therefore LSM measured by FibroScan® is definitively a key biomarker for liver diseases given that it is interpreted in the full clinical context of the patient by a liver specialist.

20.5 Other Applications of Transient Elastography

20.5.1 Preclinical Applications of Transient Micro-elastography

In the area of small animal experimentation, the use of elastography techniques has been reported by several groups with magnetic resonance elastography (MRE) [115, 116] and static ultrasound elastography [117]. However, the techniques proposed remain expensive (MRE) and are sometimes invasive and unsuitable for in vivo applications.

A dedicated version of FibroScan® (Figure 20.10) has been developed to measure liver stiffness measurements (LSM) in small laboratory animals. FibroScan® Lab (Echosens, Paris, France) relies on a high-frequency implementation of transient elastography which is called transient micro-elastography (TME). It comprises a probe, a high frequency electronic platform, and an integrated computer to control the ultrasound system and analyze the data. The ultrasonic transducer typically exhibits a center frequency of 10 MHz and the mechanical actuator was improved to generate low frequency shear waves between 200 Hz and 500 Hz.

The novel system was validated in both a classical fibrosis model (CCl_4) and a transgenic murine model of systemic amyloidosis [118]. TME was successfully performed in control mice below the xiphoid cartilage, with a mean LSM of 4.4 ± 1.3 kPa, a mean success rate of 88%, and

Figure 20.10 Transient micro-elastography using FibroScan® LAB for measurements in small laboratory animals. Source: courtesy of Pr Sebastian Mueller, setup at the University of Heidelberg.

an excellent intra-observer agreement (0.98). Treatment with CCl_4 over seven weeks drastically increased LSM as compared to controls (18.2 ± 3.7 kPa vs. 3.6 ± 1.2 kPa). Moreover, fibrosis stage highly correlated with LSM (Spearman coefficient = 0.88, $p < 0.01$). In the amyloidosis model, much higher LSM values were obtained, reaching maximum values of >150 kPa. LSM significantly correlated with the amyloidosis index (0.93, $p < 0.0001$) and the plasma concentration of mutant hapoA-II (0.62, $p < 0.005$). Transient micro-elastography is a promising technique to measure the evolution of pathologies such as fibrosis in the same animal during longitudinal studies.

Recently, TME has been used as a noninvasive tool to investigate skin stiffness with potential applications in dermatology and cosmetology.

20.5.2 Adipose Tissue

Subcutaneous adipose tissue (scAT) undergoes severe alteration such as fibrosis during obesity. It has been shown that this fibrosis is related to metabolic alterations and results in poor efficiency in losing weight after bariatric surgery [119, 120]. As of today no noninvasive tool is able to assess scAT. To that purpose a novel device named AdipoScan™, based on transient elastography, has been specifically developed to measure shear wave speed (SWS) in scAT [120–122]. Briefly, the probe of AdipoScan™ is made up of a flat mechanical actuator (center frequency of 70 Hz) associated to a flat ultrasound transducer (center frequency of 3.5 MHz). It was developed to fulfill the main constraint of being light enough to minimize the effect of the applied static force to avoid compressing the tissues which would modify the viscoelastic properties of the scAT. SWS is assessed using a novel algorithm based on the maximum likelihood estimate (MLE) [123]. The scAT SWS measurement zone is defined on the right side of the patient belly at a few centimeters from it, so as to obtain the more clinically pertinent scAT SWS.

The relevance of SWS evaluation using AdipoScan™ was assessed in a first pilot study on morbidly obese patients candidate to bariatric surgery who were enrolled one month before surgery at the nutrition department of the Pitié Salpêtrière hospital (APHP, Paris, France). 73 patients were assessed (86.3 % female, mean age: 44.3 ± 10.4 years, BMI ranging from 35 up to 71 kg/m^2 with a median value of 45 kg/m^2). AdipoScan™ exam was successful in all patients. scAT SWS ranged from 0.50 up to 2.52 m/s with a median value of 0.80 m/s and an interquartile range of 0.36 m/s. scAT SWS was associated with scAT total and peri-cellular fibrosis assessed histologically (Spearman coefficient $\rho = 0.51$, $p = 0.003$ and $\rho = 0.38$, $p = 0.03$, respectively) but also to body composition assessed by DXA ($\rho = 0.40$, $p < 10^{-3}$ with total body fat in percent), and obesity-induced comorbidities such as diabetic status, hypertension, and lipid and liver dysfunctions. Those results are being confirmed in an ongoing prospective clinical study [124, 125] and suggest that the characterization of scAT before bariatric surgery using AdipoScan™ could be used in clinical practice to better stratify patient phenotypes.

20.6 Conclusion

Transient elastography pioneered the development of quantitative elastography with the introduction of FibroScan®, the first commercial quantitative ultrasound elastography device, in 2003. Supported by more than 1000 peer-reviewed publications, 30 guidelines issued by professional societies and 3500 FibroScan® devices used worldwide in 2015, vibration-controlled transient elastography is by far the most validated and clinically used liver elastography technique. Indeed, the FibroScan® average stiffness measurement device proved very successful in the measurement of liver stiffness in patients with chronic liver diseases. Unlike cancer applications, which require imaging capabilities, FibroScan® focuses on diffuse liver diseases and

helps in limiting the number of liver biopsies performed for liver fibrosis assessment. Initially introduced as a research tool, FibroScan® is now widely used in routine clinical practice and can be considered the noninvasive standard for the measurement of liver stiffness [41]. The rapid adoption of this disruptive technology may be attributed to several factors, including the importance of liver stiffness in the management of patients with chronic liver diseases, the good to excellent performance for liver fibrosis assessment, the control of the shear wave frequency, the standardized and simple operation procedure, and the fact that the operation of the device does not require special skills in ultrasound which makes it operable by nurses. Advanced applications such as CAP, controlled attenuation parameter, increase the importance of FibroScan® in the field of hepatology.

References

1 Krouskop, T. (1987). A pulsed Doppler ultrasonic system for making noninvasive measurements of the mechanical properties of soft tissues. *J. Rehabil. Res. Dev.* 24: 1–8.
2 Yamakoshi, Y., Sato, J., and Sato, T. (1990). Ultrasonic imaging of internal vibration of soft tissue under forced vibration. *IEEE Trans. Ultrason., Ferroelect., Freq. Control* 37: 45–53.
3 Catheline, S., Thomas, J.L., Wu, F., and Fink, M.A. (1999). Diffraction field of a low frequency vibrator in soft tissues using transient elastography. *IEEE Trans. Ultrason., Ferroelect., Freq. Control* 46: 1013–1019.
4 Catheline, S., Wu, F., and Fink, M. (1999). A solution to diffraction biases in sonoelasticity: the acoustic impulse technique. *J. Acoust. Soc. Am.* 105: 2941–2950.
5 Achenbach, J. (1974). *Wave Propagation in Elastic Solids* (ed. H. A. Lauwerier and W. T. Koiter). North Holland.
6 Aki, K. and Richards, P. (2002). *Quantitative Seismology*. San Francisco: W. H. Freeman.
7 Gakenheimer, D.C. and Miklowitz, J. (1969). Transient excitation of an elastic half space by a point load traveling on the surface. *J. Appl. Mech.* 36: 505–515.
8 Oestreicher, H.L. (1951). Field and impedance of an oscillating sphere in a viscoelastic medium with an application to biophysics. *J. Acoust. Soc. Am.* 23: 707–714.
9 Carstensen, E.L. and Parker, K.J. (2015). Oestreicher and elastography. *J. Acoust. Soc. Am.* 138: 2317–2325.
10 Sandrin, L., Cassereau, D., and Fink, M. (2004). The role of the coupling term in transient elastography. *J. Acoust. Soc. Am.* 115: 73–83.
11 Catheline, S. and Benech, N. (2015). Longitudinal shear wave and transverse dilatational wave in solids. *J. Acoust. Soc. Am.* 137: EL200–205.
12 Sandrin, L., Catheline, S., Tanter, M., et al. (1999). Time resolved pulsed elastography with ultrafast ultrasonic imaging. *Ultrason. Imaging* 21: 259–272.
13 Muthupillai, R., Lomas, D., Rossman, P., et al. (1995). Magnetic resonance elastography by direct visualization of propagating acoustic strain waves. *Science* 269: 1854–1857.
14 Parker, K.J., Huang, S., Musulin, R., and Lerner, R. (1990). Tissue response to mechanical vibrations for "sonoelasticity imaging". *Ultrasound Med. Biol.* 16: 241–246.
15 Sandrin, L., Tanter, M., Catheline, S., and Fink, M. (2002). Shear modulus imaging with 2D transient elastography. *IEEE Trans. Ultrason., Ferroelect., Freq. Control* 49: 426–435.
16 Sugimoto, T., Ueha, S., and Itoh, K. (1990). Tissue hardness measurement using the radiation force of focused ultrasound. *Ultrason. Symp.* 1377–1380.
17 Bercoff, J., Tanter, M., and Fink, M. (2004). Supersonic shear imaging: a new technique for soft tissues elasticity mapping. *IEEE Trans. Ultrason., Ferroelect., Freq. Control* 51: 374–409.

18 Sarvazyan, A.P., Rudenko, O.V., Swanson, S.D., et al. (1998). Shear wave elasticity imaging: a new ultrasonic technology of medical diagnostics. *Ultrasound Med. Biol.* 24: 1419–1435.

19 Nightingale, K., Palmeri, N., Nightingale, R., and Trahey, G. (2001). On the feasibility of remote palpation using acoustic radiation force. *J. Acoust. Soc. Am.* 110: 625–634.

20 Sandrin, L., Tanter, M., Gennisson, J.-L., et al. (2002). Shear elasticity probe for soft tissues with 1D transient elastography. *IEEE Trans. Ultrason., Ferroelect., Freq. Control* 49: 436–446.

21 Audière, S., Angelini, E.D., Sandrin, L., and Charbit, M. (2014). Maximum likelihood estimation of shear wave speed in transient elastography. *IEEE Trans. Med. Imaging* 33: 1338–1349.

22 Sandrin, L., Fourquet, B., Hasquenoph, J.-M., et al. (2003). Transient elastography: a new noninvasive method for assessment of hepatic fibrosis. *Ultrasound Med. Biol.* 29: 1705–1713.

23 Gennisson, J.L., Lerouge, S., and Cloutier, G. (2006). Assessment by transient elastography of the viscoelastic properties of blood during clotting. *Ultrasound Med. Biol.* 32: 1529–1537.

24 Brum, J., Balay, G., Bia, D., et al. (2010). Feasibility of a transient elastography technique for in vitro arterial elasticity assessment. *Conf. Proc. IEEE Eng. Med. Biol. Soc.* 37–40.

25 Benech, N. and Negreira, C.A. (2010). Monitoring heat-induced changes in soft tissues with 1D transient elastography. *Phys. Med. Biol.* 55: 1753–1765.

26 Brum, J., Gennisson, J.L., Nguyen, T.M., et al. (2012). Application of 1-D transient elastography for the shear modulus assessment of thin-layered soft tissue: comparison with supersonic shear imaging technique. *IEEE Trans. Ultrason., Ferroelect., Freq. Control* 59: 703–714.

27 Fink, M. (1992). Time reversal of ultrasonic fields. I. Basic principles. *IEEE Trans. Ultrason., Ferroelect., Freq. Control* 39: 555–566.

28 Bercoff, J., Chaffai, S., Tanter, M., et al. (2003). In vivo breast tumor detection using transient elastography. *Ultrasound Med. Biol.* 29: 1387–1396.

29 Oudry, J., Bastard, C., Miette, V., et al. (2009). Copolymer-in-oil phantom materials for elastography. *Ultrasound Med. Biol.* 35: 1185–1197.

30 ASTM (2012). Standard test methods for rubber properties in compression. ASTM D575–591. See http://www.astm.org/index.shtml

31 Catheline, S., Gennisson, J.L., and Fink, M. (2003). Measurement of elastic nonlinearity of soft solid with transient elastography. *J. Acoust. Soc. Am.* 114: 3087–3091.

32 Oudry, J., Lynch, T., Vappou, J., et al. (2014). Comparison of four different techniques to evaluate the elastic properties of phantom in elastography: is there a gold standard? *Phys. Med. Biol.* 59: 5775.

33 Castera, L., Vergniol, J., Foucher, J., et al. (2005). Prospective comparison of transient elastography, Fibrotest, APRI, and liver biopsy for the assessment of fibrosis in chronic hepatitis C. *Gastroenterology* 128: 343–350.

34 Ziol, M., Handra-Luca, A., Kettaneh, A., et al. (2005). Noninvasive assessment of liver fibrosis by measurement of stiffness in patients with chronic hepatitis C. *Hepatology* 41: 48–54.

35 Jensen, J.A. (1996). Field: A program for simulating ultrasound systems. *Med. Biol. Eng. Comput.* 34: 351–353.

36 Jensen, J.A. and Svendsen, N.B. (1992). Calculation of pressure fields from arbitrarily shaped, apodized, and excited ultrasound transducers. *IEEE Trans. Ultrason., Ferroelect., Freq. Control* 39: 262–267.

37 Nightingale, K., McAleavey, S., and Trahey, G. (2003). Shear-wave generation using acoustic radiation force: in vivo and ex vivo results. *Ultrasound Med. Biol.* 29: 1715–1723.

38 Chang, S., Kim, M.J., Kim, J., and Lee, M.J. (2013). Variability of shear wave velocity using different frequencies in acoustic radiation force impulse (ARFI) elastography: a phantom and normal liver study. *Ultraschall Med.,* 34: 260–265.

39 Potthoff, A., Attia, D., Pischke, S., et al. (2013). Influence of different frequencies and insertion depths on the diagnostic accuracy of liver elastography by acoustic radiation force impulse imaging (ARFI). *Eur. J. Radiol.* 82: 1207–1212.

40 Zhao, H., Song, P., Urban, M.W., et al. (2011). Bias observed in time-of-flight shear wave speed measurements using radiation force of a focused ultrasound beam. *Ultrasound Med. Biol.* 37: 1884–1892.

41 EASL-ALEH Clinical Practice Guidelines (2015). Non-invasive tests for evaluation of liver disease severity and prognosis. *J. Hepatol.* 63: 237–264.

42 Bedossa, P., Dargere, D., and Paradis, V. (2003). Sampling variability of liver fibrosis in chronic hepatitis C. *Hepatology* 38: 1449–1457.

43 Lupsor Platon, M., Stefanescu, H., Feier, D., et al. (2013). Performance of unidimensional transient elastography in staging chronic hepatitis C. Results from a cohort of 1,202 biopsied patients from one single center. *J. Gastrointestin. Liver Dis.* 22: 157–166.

44 Shaheen, A.A., Wan, A.F., and Myers, R.P. (2007). FibroTest and FibroScan for the prediction of hepatitis C-related fibrosis: a systematic review of diagnostic test accuracy. *Am. J. Gastroenterol.* 102: 2589–2600.

45 Talwalkar, J.A., Kurtz, D.M., Schoenleber, S.J., et al. (2007). Ultrasound-based transient elastography for the detection of hepatic fibrosis: systematic review and meta-analysis. *Clin. Gastroenterol. Hepatol.* 5: 1214–1220.

46 Hezode, C., Castera, L., Roudot-Thoraval, F., et al. (2011). Liver stiffness diminishes with antiviral response in chronic hepatitis C. *Aliment. Pharmacol. Ther.* 34: 656–663.

47 Martinez, S.M., Foucher, J., Combis, J.M., et al. (2012). Longitudinal liver stiffness assessment in patients with chronic hepatitis C undergoing antiviral therapy. *PLoS One* 7: e47715.

48 Castera, L., Bernard, P.H., Le Bail, B., et al. (2011). Transient elastography and biomarkers for liver fibrosis assessment and follow-up of inactive hepatitis B carriers. *Aliment. Pharmacol. Ther.* 33: 455–465.

49 Chan, H.L., Wong, G.L., Choi, P.C., et al. (2009). Alanine aminotransferase-based algorithms of liver stiffness measurement by transient elastography (Fibroscan) for liver fibrosis in chronic hepatitis B. *J. Viral Hepat.* 16: 36–44.

50 Chon, Y.E., Choi, E.H., Song, K.J., et al. (2012). Performance of transient elastography for the staging of liver fibrosis in patients with chronic hepatitis B: a meta-analysis. *PLoS One* 7: e44930.

51 Marcellin, P., Ziol, M., Bedossa, P., et al. (2009). Non-invasive assessment of liver fibrosis by stiffness measurement in patients with chronic hepatitis B. *Liver Int.* 29: 242–247.

52 Ogawa, E., Furusyo, N., Murata, M., et al. (2011). Longitudinal assessment of liver stiffness by transient elastography for chronic hepatitis B patients treated with nucleoside analog. *Hepatol. Res.* 41: 1178–1188.

53 Carton, J.A., Collazos, J., de la Fuente, B., and Asensi, V. (2013). Course of liver fibrosis in HIV-hepatitis C virus-coinfected patients depending on the response to hepatitis C therapy. *AIDS Res. Human Retroviruses* 29: 215–222.

54 de Ledinghen, V., Douvin, C., Kettaneh, A., et al. (2006). Diagnosis of hepatic fibrosis and cirrhosis by transient elastography in HIV/hepatitis C virus-coinfected patients. *J. Acquir. Immune Defic. Syndr.* 41: 175–179.

55 Miailhes, P., Pradat, P., Chevallier, M., et al. (2011). Proficiency of transient elastography compared to liver biopsy for the assessment of fibrosis in HIV/HBV-coinfected patients. *J. Viral Hepat.* 18: 61–69.

56 Lemoine, M., Katsahian, S., Ziol, M., et al. (2008). Liver stiffness measurement as a predictive tool of clinically significant portal hypertension in patients with compensated HCV or alcohol-related cirrhosis. *Aliment. Pharmacol. Ther.* 28: 1102–1110.

57 Nguyen-Khac, E., Chatelain, D., Tramier, B., et al. (2008). Assessment of asymptomatic liver fibrosis in alcoholic patients using fibroscan: prospective comparison with seven non-invasive laboratory tests. *Aliment. Pharmacol. Ther.* 28: 1188–1198.

58 Musso, G., Gambino, R., Cassader, M., and Pagano, G. (2011). Meta-analysis: natural history of non-alcoholic fatty liver disease (NAFLD) and diagnostic accuracy of non-invasive tests for liver disease severity. *Ann. Med.* 43: 617–649.

59 Wong, V.W., Vergniol, J., Wong, G.L., et al. (2010). Diagnosis of fibrosis and cirrhosis using liver stiffness measurement in nonalcoholic fatty liver disease. *Hepatology* 51: 454–462.

60 Corpechot, C., El Naggar, A., Poujol-Robert, A., et al. (2006). Assessment of biliary fibrosis by transient elastography in patients with PBC and PSC. *Hepatology* 43: 1118–1124.

61 Friedrich-Rust, M., Mueller, C., Winckler, A., et al. (2008). Evaluation of different non-invasive methods for assessment of liver fibrosis in primary biliary cirrhosis (PBC): a comparative study using FibroScan®, MRI, MR-spectroscopy and serum fibrosis markers. In *59th Annual Meeting the American Association for the Study Liver Disease*, San Francisco, CA, USA.

62 Gomez-Dominguez E., Mendoza, J., Garcia-Buey, L., et al. (2008). Transient elastography to assess hepatic fibrosis in primary biliary cirrhosis. *Aliment. Pharmacol. Ther.* 27: 441–447.

63 Friedrich-Rust, M., Muller, C., Winckler, A., et al. (2010). Assessment of liver fibrosis and steatosis in PBC with FibroScan, MRI, MR-spectroscopy, and serum markers. *J. Clin. Gastroenterol.* 44: 58–65.

64 Floreani, A., Cazzagon, N., Martines, D., et al. (2011). Performance and utility of transient elastography and noninvasive markers of liver fibrosis in primary biliary cirrhosis. *Digestive Liver Dis.* 43: 887–892.

65 Corpechot, C., Carrat, F., Poujol-Robert, A., et al. (2012). Noninvasive elastography-based assessment of liver fibrosis progression and prognosis in primary biliary cirrhosis. *Hepatology* 56: 198–208.

66 Chang, H.K., Park, Y.J., Koh, H., et al. (2009). Hepatic fibrosis scan for liver stiffness score measurement: a useful preendoscopic screening test for the detection of varices in postoperative patients with biliary atresia. *J. Pediatr. Gastroenterol. Nutrit.* 49: 323–328.

67 Honsawek, S., Chayanupatkul, M., Chongsrisawat, V., et al. (2010). Increased osteopontin and liver stiffness measurement by transient elastography in biliary atresia. *World J. Gastroenterol.* 16: 5467–5473.

68 Honsawek, S., Praianantathavorn, K., Chongsrisawat, V., et al. (2011). High serum matrix metalloproteinase-3 and liver stiffness in postoperative biliary atresia. *Pediatr. Surgery Int.* 27: 681–687.

69 Honsawek, S., Chayanupatkul, M., Chongsrisawat, V., et al. (2011). Serum adiponectin and transient elastography as non-invasive markers for postoperative biliary atresia. *BMC Gastroenterol.* 11: 16.

70 Chayanupatkul, M., Honsawek, S., Chongsrisawat, V., et al. (2011). Serum retinol binding protein 4 and clinical outcome in postoperative biliary atresia. *Hepatol. Int.* 5: 906–912.

71 Honsawek, S., Chongsrisawat, V., Praianantathavorn, K., et al. (2011). Elevation of serum galectin-3 and liver stiffness measured by transient elastography in biliary atresia. *Eur. J. Pediatr. Surg.* 21, 250–254.

72 Chongsrisawat, V., Vejapipat, P., Siripon, N., and Poovorawan, Y. (2011). Transient elastography for predicting esophageal/gastric varices in children with biliary atresia. *BMC Gastroenterol.* 11: 41.

73 Witters, P., De Boeck, K., Dupont, L., et al. (2009). Non-invasive liver elastography (FibroScan®) for detection of cystic fibrosis-associated liver disease. *J. Cystic Fibrosis* 8: 392–399.

74 Menten, R., Leonard, A., Clapuyt, P., et al. (2010). Transient elastography in patients with cystic fibrosis. *Pediatr. Radiol.* 40: 1231–1235.

75 Malbrunot-Wagner, A.C., Bridoux, L., Nousbaum, J.B., et al. (2011). Transient elastography and portal hypertension in pediatric patients with cystic fibrosis. *J. Cystic Fibrosis* 10: 338–342.

76 Karlas, T., Hempel, M., Troltzsch, M., et al. (2012). Noninvasive evaluation of hepatic manifestation in Wilson disease with transient elastography, ARFI, and different fibrosis scores. *Scand. J. Gastroenterol.* 47: 1353–1361.

77 Monti, L., Manco, M., Lo Zupone, C., et al. (2012). Acoustic radiation force impulse (ARFI) imaging with Virtual Touch Tissue Quantification in liver disease associated with cystic fibrosis in children. *Radiolog. Med.* 117: 1408–1418.

78 Romanque, P., Stickel, F., and Dufour, J.F. (2008). Disproportionally high results of transient elastography in patients with autoimmune hepatitis. *Liver Int.* 28: 1177–1178.

79 Adhoute, X., Foucher, J., Laharie, D., et al. (2008). Diagnosis of liver fibrosis using FibroScan and other noninvasive methods in patients with hemochromatosis: a prospective study. *Gastroentérol. Clin. Biol.* 32: 180–187.

80 Jacqueminet, S., Lebray, P., Morra, R., et al. (2008). Screening for liver fibrosis by using a noninvasive biomarker in patients with diabetes. *Clin. Gastroenterol. Hepatol.* 6: 828–831.

81 de Ledinghen, V., Vergniol, J., Gonzalez, C., et al. (2012). Screening for liver fibrosis by using FibroScan((R)) and FibroTest in patients with diabetes. *Digestive Liver Dis.* 44: 413–418.

82 Casey, S.P., Kemp W.W., McLean, C.A., et al. (2012). A prospective evaluation of the role of transient elastography for the detection of hepatic fibrosis in type 2 diabetes without overt liver disease. *Scand. J. Gastroenterol.* 47: 836–841.

83 Sini, M., Sorbello, O., Civolani, A., et al. (2012). Non-invasive assessment of hepatic fibrosis in a series of patients with Wilson's Disease. *Digestive Liver Dis.* 44: 487–491.

84 Foucher, J., Chanteloup, E., Castera, L., et al. (2006). Diagnosis of cirrhosis and its complications by transient elastography (FibroScan®) : a prospective study. *Gut* 55: 403–408.

85 Carrion, J.A., Navasa, M., Bosch, J., et al. (2006). Transient elastography for diagnosis of advanced fibrosis and portal hypertension in patients with hepatitis C recurrence after liver transplantation. *Liver Transplant.* 12: 1791–1798.

86 Vizzutti, F., Arena, U., Romanelli, R.G., et al. (2007). Liver stiffness measurement predicts severe portal hypertension in patients with HCV-related cirrhosis. *Hepatology* 45: 1290–1297.

87 Bureau, C., Metivier, S., Peron, J.M., et al. (2008). Clinical trial: transient elastography accurately predicts the presence of significant portal hypertension in patients with chronic liver disease. *Aliment. Pharmacol. Ther.* 27: 1261–1228.

88 Sanchez-Conde, M., Miralles, P., Maria Bellon, J., et al. (2011). Use of transient elastography (FibroScan®) for the noninvasive assessment of portal hypertension in HIV/HCV-coinfected patients. *J. Viral Hepat.* 18: 685–691.

89 Kazemi, F., Kettaneh, A., N'Kontchou, G., et al. (2006). Liver stiffness measurement selects patients with cirrhosis at risk of bearing large oesophageal varices. *J. Hepatol.* 45: 230–235.

90 Nguyen-Khac, E., Saint-Leger, P., Tramier, B., et al. (2009). Noninvasive diagnosis of large esophageal varices by FibroScan: strong influence of the cirrhosis etiology. *Alcoholism, Clin. Exp. Res.* 34: 1146–1153.

91 Castera, L., Bail, B.L., Roudot-Thoraval, F., et al. (2009). Early detection in routine clinical practice of cirrhosis and oesophageal varices in chronic hepatitis C: Comparison of transient elastography (FibroScan) with standard laboratory tests and non-invasive scores. *J. Hepatol.* 50: 59–68.

92 Pineda, J.A., Recio, E., Camacho, A., et al. (2009). Liver stiffness as a predictor of esophageal varices requiring therapy in HIV/hepatitis C virus-coinfected patients with cirrhosis. *J. Acquir. Immune Defic. Syndr.* 51: 445–449.

93 Pritchett, S., Cardenas, A., Manning, D., et al. (2010). The optimal cut-off for predicting large oesophageal varices using transient elastography is disease specific. *J. Viral Hepat.* 18: 75–80.

94 Malik, R., Lai, M., Sadiq, A., et al. (2010). Comparison of transient elastography, serum markers and clinical signs for the diagnosis of compensated cirrhosis. *J. Gastroenterol. Hepatol.* 25: 1562–1568.

95 Masuzaki, R., Tateishi, R., Yoshida, H., et al. (2008). Risk assessment of hepatocellular carcinoma in chronic hepatitis C patients by transient elastography. *J. Clin. Gastroenterol.* 42: 839–843.

96 Vergniol, J., Boursier, J., Coutzac, C., et al. (2014). The evolution of non-invasive tests of liver fibrosis is associated with prognosis in patients with chronic hepatitis C. *Hepatology* 60: 65–76.

97 de Ledinghen, V., Vergniol, J., Barthe, C., et al. (2013). Non-invasive tests for fibrosis and liver stiffness predict 5-year survival of patients chronically infected with hepatitis B virus. *Aliment. Pharmacol. Ther.* 37: 979–988.

98 Vergniol, J., Foucher, J., Terrebonne, E., et al. (2011). Noninvasive tests for fibrosis and liver stiffness predict 5-year outcomes of patients with chronic hepatitis C. *Gastroenterology* 140: 1970–1979, 1979 e1–3.

99 Arena, U., Vizzutti, F., Corti, G., et al. (2008). Acute viral hepatitis increases liver stiffness values measured by transient elastography. *Hepatology* 47: 380–384.

100 Coco, B., Oliveri, F., Maina, A.M., et al. (2007). Transient elastography: a new surrogate marker of liver fibrosis influenced by major changes of transaminases. *J. Viral Hepat.* 14: 360–369.

101 Mueller, S., Millonig, G., Sarovska, L., et al. (2010). Increased liver stiffness in alcoholic liver disease: differentiating fibrosis from steatohepatitis. *World J. Gastroenterol.* 16: 966–972.

102 Sagir, A., Erhardt, A., Schmitt, M., and Haussinger, D. (2008). Transient elastography is unreliable for detection of cirrhosis in patients with acute liver damage. *Hepatology* 47: 592–595.

103 Millonig, G., Reimann, F.M., Friedrich, S., et al. (2008). Extrahepatic cholestasis increases liver stiffness (FibroScan) irrespective of fibrosis. *Hepatology* 48: 1718–1723.

104 Lebray, P., Varnous, S., Charlotte, F., et al. (2008). Liver stiffness is an unreliable marker of liver fibrosis in patients with cardiac insufficiency. *Hepatology* 48: 2089.

105 Lanzi, A., Gianstefani, A., Mirarchi, M.G., et al. (2010). Liver AL amyloidosis as a possible cause of high liver stiffness values. *Eur. J. Gastroenterol. Hepatol.* 22: 895–897.

106 Janssens, E., Spahr, L., Rubbia-Brandt, L., et al. (2010). Hepatic amyloidosis increases liver stiffness measured by transient elastography. *Acta Gastroenterolog. Belg.* 73: 52–54.

107 Loustaud-Ratti, V.R., Cypierre, A., Rousseau, A., et al. (2011). Non-invasive detection of hepatic amyloidosis: FibroScan, a new tool. *Amyloid* 18: 19–24.

108 Sasso, M., Beaugrand, M., de Ledinghen, V., et al. (2010). Controlled attenuation parameter (CAP): a novel VCTE guided ultrasonic attenuation measurement for the evaluation of hepatic steatosis: preliminary study and validation in a cohort of patients with chronic liver disease from various causes. *Ultrasound Med. Biol.* 36: 1825–1835.

109 Sasso, M., Miette, V., Sandrin, L., and Beaugrand, M. (2012). The controlled attenuation parameter (CAP): a novel tool for the non-invasive evaluation of steatosis using Fibroscan. *Clin. Res. Hepatol. Gastroenterol.* 36: 13–20.

110 de Ledinghen, V., Vergniol, J., Capdepont, M., et al. (2013). Controlled attenuation parameter (CAP) for the diagnosis of steatosis: A prospective study of 5323 examinations. *J. Hepatol.* 60 (5): 1026–1031.

111 Sasso, M., Tengher-Barna, I., Ziol, M., et al. (2012). Novel controlled attenuation parameter for noninvasive assessment of steatosis using Fibroscan®: validation in chronic hepatitis C. *J. Viral Hepat.* 19: 244–253.

112 Shi, K.Q., Tang, J.Z., Zhu, X.L., et al. (2014). Controlled attenuation parameter for the detection of steatosis severity in chronic liver disease: A meta-analysis of diagnostic accuracy. *J. Gastroenterol. Hepatol.* 29 (6): 1149–1158.

113 Sasso, M., Audière, S., Kemgamg, A., et al. (2016). Liver steatosis assessed with Controlled Attenuation Parameter (CAP™) on the XL Probe of the FibroScan – A pilot study assessing diagnostic accuracy. *Ultrasound Med. Biol.* 42 (1): 92–103.

114 de Ledinghen, V., Corpechot, C., Vergniol, J., et al. (2015). Steatosis assessment by CAP using XL probe. In: *Annual Meeting of the American Association for the Study of Liver Diseases (AASLD),* Boston, MA, USA.

115 Salameh, N., Larrat, B., Abarca-Quinones, J., et al. (2009). Early detection of steatohepatitis in fatty rat liver by using MR elastography. *Radiology* 253: 90–97.

116 Yin, M., Woollard, J., Wang, X., et al. (2007). Quantitative assessment of hepatic fibrosis in an animal model with magnetic resonance elastography. *Magn. Reson. Med.* 58: 346–353.

117 Bilgen, M., Srinivasan, S., Lachman, L.B., and Ophir, J. (2003). Elastography imaging of small animal oncology models: a feasibility study. *Ultrasound Med. Biol.* 29: 1291–1296.

118 Bastard, C., Bosisio, M.R., Chabert, M., et al. (2011). Transient micro-elastography: A novel non-invasive approach to measure liver stiffness in mice. *World J. Gastroenterol.* 17: 968–975.

119 Divoux, A., Tordjman, J., Lacasa, D., et al. (2010). Fibrosis in human adipose tissue: composition, distribution, and link with lipid metabolism and fat mass loss. *Diabetes* 59: 2817–2825.

120 Abdennour, M., Reggio, S., Le Naour, G., et al. (2014). Association of adipose tissue and liver fibrosis with tissue stiffness in morbid obesity: links with diabetes and BMI loss after gastric bypass. *J. Clin. Endocrinol. Metab.* 99: 898–907.

121 Sasso, M., Abdennour, M., Yuejun, L., et al. (2014). AdipoScan – A novel transient elastography based tool to assess subcutaneous adipose tissue shear wave speed in morbidly obese patients. In: *IEEE International Ultrasonics Symposium (IUS)* 1124–1127.

122 Sasso, M., Abdennour, M., Liu, Y., et al. (2015). Relevance of adipose tissue stiffness evaluated by transient elastography (AdipoScan™) in morbidly obese patients before bariatric surgery. *Phys. Proc.* 70: 1264–1268.

123 Audiere, S., Angelini, E.D., Sandrin, L., and Charbit, M. (2014). Maximum likelihood estimation of shear wave speed in transient elastography. *IEEE Trans. Med. Imaging* 33: 1338–1349.

124 Liu, Y., Abdennour, M., Clet, M., et al. (2014). The stiffness of adipose tissue is associated with metabolic parameters in morbidly obese patients. In: *European Congress on Obesity (ECO),* Sofia, Bulgaria.

125 Liu, Y., Aron-Wisnewsky, J., Pelloux, V., et al. (2015). Adipose tissue stiffness evaluated by non-invasive elastometry (AdipoScan) associates with structural and molecular actors of extracellular matrix. In: *European Congress on Obesity (ECO),* Prague, Czech Republic.

21

From Time Reversal to Natural Shear Wave Imaging

Stefan Catheline

LabTAU, INSERM-University of Lyon, France

21.1 Introduction: Time Reversal Shear Wave in Soft Solids

The potential of time-reversal methods [1] includes different areas such as telecommunication [2, 3], nondestructive testing [4], interactivity [5], medical imaging, and therapy [6]. It is an elegant and robust adaptive focusing method. In practical situations, a source or a strong reflector embedded in the medium is required in order to observe a forward wave scene. Then, a time-reversal mirror is used to recreate the backward scene. The time-reversed wave finally collapses on its source location. The problem of the source in a time-reversal experiment is known in the medical field [7] as the "artificial ultrasonic stars", in reference to analogous laser-guided artificial stars used for optic adaptive focusing in astronomy [8]. In the time-reversal experiments presented in Figure 21.1a, a reverberant solid cavity has been used. The great advantage of such a configuration is that a perfect time-reversal cavity can be approached experimentally using a point source mounted on a vibrator: it is the so-called one-channel time-reversal mirror [9]. The elastic field was measured noninvasively from the solid surface using a single transducer and ultrasonic techniques developed in the field of transient elastography [10]. In this medical field, propagation media are soft solids such as soft tissues, muscles, organs [11], or tissue-mimicking phantoms. The low-frequency shear waves (a few hundred hertz) propagate at a speed of a few meters per second, which results in centimeter size wavelength (Figure 21.1b). Consequently, the original aspects of these time-reversal elastography experiments are (1) no "artificial stars" are needed, (2) the time-reversal collapse is directly observed inside a solid, and (3) for centimeter wavelength, near field-like effects are clearly apparent.

Contrary to the case of fluids, the elastic field before and after the collapse differs, and the focus spot at $t = 0$ s is no longer isotropic (Figure 21.1b). Its size remains, however, in the dimension of the wavelength in the absence of the high spatial frequencies of evanescent waves [12]. The non-isotropic shape of the focus spot emerging from a homogeneous reverberating field might appear surprising at first sight. However, this observation follows the symmetry of the Green's functions and the nature of their simplest associated point sources in liquids and solids or, more generally, in a scalar or an elastic field. As far as elasticity imaging is concerned, the experiment of Figure 21.1 demonstrates that it is in principle feasible to extract the local shear wavelength from the time reversal focus spot and to extract the local frequency from the time recompression. As a result, the local shear wave speed can be deduced. Nevertheless, no time reversal mirror is used in seismology. Instead, correlation algorithms are used for the whole approach. The process thus becomes passive in the sense that only a wave field observation is needed. The close link between time reversal and correlation is discussed in the next section.

Ultrasound Elastography for Biomedical Applications and Medicine, First Edition.
Edited by Ivan Nenadic, Matthew Urban, James Greenleaf, Jean-Luc Gennisson, Miguel Bernal, and Mickael Tanter.

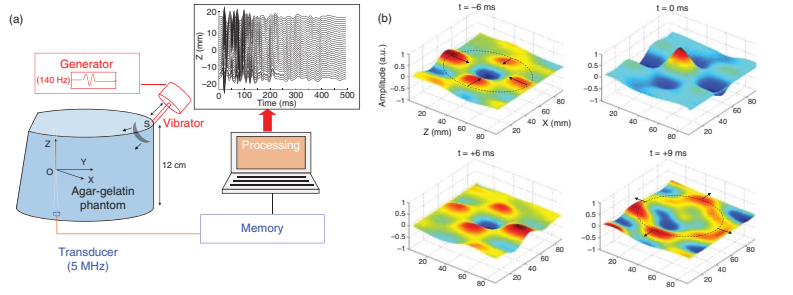

Figure 21.1 (a) The experimental setup. An acoustic pulse sent by a piston vibrator generates motion in a soft solid. An ultrasonic device developed for transient elastography allows the measurement of the displacement field, represented here as a seismogram. (b) Experimental results. Four pictures of a time-reversal field were selected around the refocusing time, $t = 0$ ms. The initial point body force was aligned in the z direction. The z component of the displacement field is represented here. Arrows indicate the propagation direction. The focus spot at time $t = 0$ ms reaches the diffraction limit of a half wavelength. Source: reprinted with permission from [25], copyright 2008 by the American Physical Society.

21.2 Shear Wave Elastography using Correlation: Principle and Simulation Results

Correlation of noise-like signals is a recent method for the extraction of information. The most important application to date relates to geophysics and crustal tomography [13, 14]. Earlier work relates to helioseismology [15], ultrasonics [16], and oceanography [17]. The general concept consists in retrieving the Green's function from the correlation of a complex noise-like wave field. The field nature depends on the context: it can be diffuse, reverberated, multiply scattered, or equipartitioned. Up to now, noise field measurement is correctly sampled in space and time, i.e. obeys the Shannon-Nyquist sampling theorem. With our approach, which combines correlation of the field, its gradient, and its time derivative, a tomography reconstruction is obtained even though measurements are well below the Shannon-Nyquist limit. From a wave physics point of view, we explored configurations for which each realization of time and space field measurement is independent. In other words, the spatiotemporal coherence of the field is a delta function. Practically speaking, tomography reconstruction in this situation allows the use of slow imaging devices working at a rate independent of any characteristic time period of the noise field. This general approach is valid for any wave nature, as is demonstrated in the specific field of shear wave imaging or elastography. The present technique thus offers the advantage of being compatible with both recent ultrafast ultrasonic scanners and the slower conventional ultrasonic scanners widely available in the market. In most recent applications of elastography, controlled shear wave sources are used [11, 18–21]. Nevertheless, some authors have chosen to work with natural motion induced by physiological activities such as the heart beating [22, 23] or MRI device vibrations [24]. Instead of synchronizing detection to natural sources, our approach consists in measuring natural shear wave noise, ideally a diffuse field. Retrieving elastic parameters is done through correlation techniques [13] or, using wave physics terminology, through time reversal [25–27]. Compared to time reversal, the correlation technique offers the great advantage of being fully passive, so no active re-emission of the time-reversal field is needed and thus no fancy time-reversal mirror. The first step of a time-reversal experiment only is conserved, which is the observation of a wave field. It is important to point out that using elastography as a tool for observing an elastic wave scene inside a soft solid still involves active ultrasound sources. This approach of elastography is passive in the sense that, in vivo experiments, no active shear wave source is used.

For the sake of clarity, the mathematics are conducted through scalar rather than elastic wave fields [28]. Besides, based on the previously presented background, the time-reversal interpretation of spatiotemporal correlations is extensively used. From a linear systems point of view, the field $\phi(\vec{r}_0, t)$ can be expressed as a time-convolution product between the excitation function $e(\vec{r}_s, t)$ of a source located on $\vec{r}_s$ and the impulse response h between the source and a receiver on point $\vec{r}_0$

$$\varphi(\vec{r}_0, t) = e(\vec{r}_s, t) \underset{t}{\otimes} h(\vec{r}_0, \vec{r}_s, t) \tag{21.1}$$

The time-reversal field is obtained when the emitted signal $e(t)$ is replaced by the time-reversed version of the impulse response

$$\Psi^{TR}(\vec{r}, t) = h(\vec{r}_0, \vec{r}_s, -t) \underset{t}{\otimes} h(\vec{r}, \vec{r}_s, t) \tag{21.2}$$

This approach of time reversal is known as the monopole time reversal [29]. It differs from the perfect time reversal in that it provides the impulse responses correlation. A perfect time reversal would be equivalent to the time derivative of the correlation [30]. Whether monopole or perfect, the time-reversal approach developed in this section is not impacted by this latter time derivative. Equation (21.2) is valid for point, pulsed sources $e(\vec{r}_s, t) = \delta(\vec{r}_s, t)$ and can be

generalized to sources with any spatial dimension and with any time dependence [31]. As a consequence, for any field that obeys the wave equation, one can associate the following generalized time-reversal field

$$\Psi^{\mathrm{TR}}(\vec{r},-t)=\varphi(\vec{r}_0,-t)\underset{t}{\otimes}\varphi(\vec{r},t) \tag{21.3}$$

This generalized time-reversal field happens to be the spatiotemporal correlation widely used in seismology and known as coda wave interferometry. However, the physical time-reversal interpretation of correlation is the following: Ψ^{TR} is the field that would be observed if the sources responsible for the noise field were able to be controlled and were acting as a time-reversal mirror. In this approach, correlation of broadband diffuse waves allows one to retrieve the Green's function between any pair of measuring points [32].

The strain $\varepsilon_z=\frac{\partial\Phi}{\partial z}$, i.e. the gradient of the displacement field ϕ, or the particle velocity $v=\frac{\partial\Phi}{\partial t}$, i.e. the time derivative of the displacement field ϕ, obeys the wave equation as well. As a consequence, different time-reversal fields are envisaged

$$\begin{cases}\Delta\varepsilon_z-\dfrac{1}{c^2}\dfrac{\partial^2\varepsilon_z}{\partial t^2}=0\\ \Delta v-\dfrac{1}{c^2}\dfrac{\partial^2 v}{\partial t^2}=0\end{cases}\Rightarrow\begin{cases}\xi^{\mathrm{TR}}(\vec{r}_0,\vec{r},t)=\varepsilon_z(\vec{r}_0,-t)\underset{t}{\otimes}\varepsilon_z(\vec{r},t)\\ V^{\mathrm{TR}}(\vec{r}_0,\vec{r},t)=v(\vec{r}_0,-t)\underset{t}{\otimes}v(\vec{r},t)\end{cases} \tag{21.4}$$

In Eq. (21.4), ξ^{TR} designates the time-reversal strain field whereas V^{TR} represents the time-reversal particle velocity field and Δ represents the Laplacian operator. It is worth pointing out that Ψ^{TR}, ξ^{TR}, and V^{TR} have the dimensions of the square of the displacement, of strain (dimensionless), and of velocity, respectively. We now focus our attention on one single spatiotemporal point, i.e. the source $\vec{r}_0$ at the focus time $t=0$ s. Notations with a subscript "0" account for this point

$$\Psi^{\mathrm{TR}}(\vec{r}_0,\vec{r}_0,t=0)\equiv\Psi_0^{\mathrm{TR}}.$$

In an ideal isotropic diffuse field, plane wave decomposition at a given central frequency allows one to use an approximation of the gradient $\varepsilon_z\approx k\phi$ and particle velocity $v\approx-\omega\phi$ in the right-hand side of Eq. (21.4). Thus the different aforementioned time-reversal fields are linked according to

$$\begin{cases}\xi_0^{\mathrm{TR}}\approx k^2\Psi_0^{\mathrm{TR}}\\ V_0^{\mathrm{TR}}\approx\omega^2\Psi_0^{\mathrm{TR}}\end{cases} \tag{21.5}$$

The coefficient of proportionality, the wave vector k, and the angular frequency ω in Eq. (21.5) allows one to estimate the local wave speed c according to the classical relationship

$$c=\frac{\omega}{k}=\sqrt{\frac{V_0^{\mathrm{TR}}}{\xi_0^{\mathrm{TR}}}} \tag{21.6}$$

Equivalently, the local wavelength k can be reconstructed

$$\lambda\approx 2\pi\sqrt{\frac{\Psi_0^{\mathrm{TR}}}{\xi_0^{\mathrm{TR}}}} \tag{21.7}$$

Depending on experimental situations that will be described later, Eqs. (21.3), (21.6), and (21.7) are used. A finite difference simulation of the 2D elastic wave equation was used to test this approach. The field ϕ now represents the vertical displacement. As shown in Figure 21.2a, a 400 by 400 grid meshes a solid cavity, a circle with one segment cut-off, surrounded by vacuum. The shear wave speed within the solid is $c_s=3$ m/s. The central frequency, $f_0=100$ Hz,

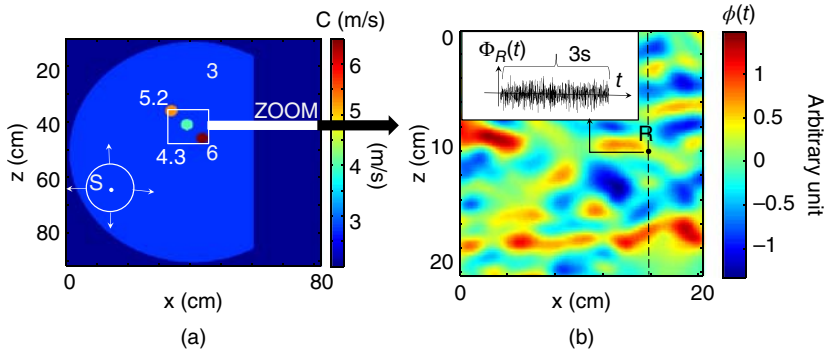

Figure 21.2 Finite difference simulation tests for the passive shear wave imaging. (a) A lossless reverberating cavity (a circle with one segment cut-off) contains three inclusions with different shear wave speeds. (b) Magnified image of the fluctuating field ϕ in the region of the three inclusions. A typical noise-like signal measured on R is represented in the top panel. Source: reprinted with permission from [28], copyright 2007 by the American Physical Society.

is chosen to give quantitative values of shear wavelength $\lambda_s \approx 3$ cm and the shear elasticity $\mu \approx 9$ kPa compatible with elastography experiments conducted in soft tissues. However, realism was not the objective of this 2D simulation, which explains its dimensions, 80 cm by 80 cm, and its unlikely Poisson's ratio of 0.4 (c_P =10 m/s). The aim of this simulation was rather to test the ability of new algorithms to extract the local wave speed from any diffuse field. Three circular inclusions of shear wave speed $c_s = 4.3$ m/s, $c_s = 5.2$ m/s, and $c_s = 6$ m/s are introduced within the solid (Figure 21.2a). The diffuse field is obtained using a pulsed source S set at coordinates $x = 20$ cm and $z = 60$ cm. The reverberation of the waves trapped in the 2D cavity rapidly give a homogeneous wave pattern, as represented in Figure 21.2b. Such a field of finite bandwidth in a finite media is considered as diffuse by definition [33]. This diffuse reverberated wave field is sampled at 1000 Hz and recorded during 3 s on each point of a 20 cm by 20 cm square in the area of the three inclusions. A typical noise-like signal $\phi_R(t)$ on a receiving point R is shown on the upper left panel. Using correlation through Eq. (21.6) is the key to reconstruct the input shear wave speed map of Figure 21.2a. Green's functions are retrieved along the vertical dotted line (Figure 21.2b), including R as a pseudo source.

On the spatiotemporal representation of the correlation field (Figure 21.3a), the retrieved Green's functions typically appear as a cross. The time recompression and the spatial focus spot are also represented on both sides. They are representative of the mean period and wavelength of the diffuse field or in other words its time and spatial coherence. The corresponding tomography reconstruction of Figure 21.3b is obtained by focusing on each point of the domain from the particle velocity and the strain field. The ratio, according to Eq. (21.6), gives the local shear wave speed. The speed of the three inclusions is nicely retrieved with a quantitative agreement better than 5%. It fully validates the assumption of plane wave decomposition used to obtain Eq. (21.5). In the previous ideal configuration, the whole spatiotemporal information is available in the data. Practically speaking, it means that diffuse fields should be sampled according to the Shannon-Nyquist theorem, with imaging systems faster than the highest wave period. As far as shear wave imaging is concerned, an ultrafast scanner working at typical frame rate of 1000 Hz is needed. Thus a second configuration is tested: a 25 Hz frame rate perfectly compatible with most modern ultrasonic scanners is used in a simulation to sample a 100 Hz central frequency diffuse field. As an inevitable consequence of this slow imaging frame rate, each field measurement can be considered to be the result of a random process. This is clearly apparent on the spatiotemporal correlation where the typical cross has disappeared. The time coherence on the bottom of Figure 21.3c is now a delta function which expresses the independence

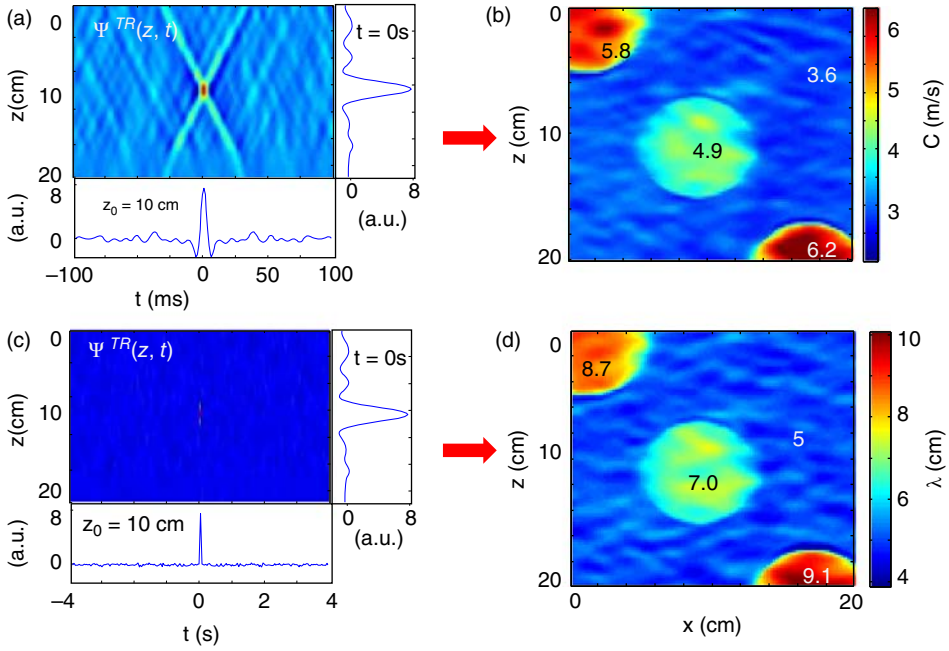

Figure 21.3 Left column: Spatiotemporal correlation field centered on point R along the dashed line of Figure 21.1b, time recompression (bottom panel) and spatial focusing (right panel). Right column: tomography reconstructions. (a) A 1000 Hz frame rate imaging is used for (b) wave speed tomography. (c) A 25 Hz frame rate imaging is used for (d) wavelength tomography. Source: reprinted with permission from [28], copyright 2007 by the American Physical Society.

of each realization of the field measurement. In contrast, the spatial coherence is unchanged. Thus the loss of time information avoids computing the time-reversal particle velocity V^{TR}, but the preservation of space information allows one to estimate Ψ^{TR} and ξ^{TR} and, as a consequence, construct a wavelength tomography from Eq. (21.7). The local wavelength tomography is represented in Figure 21.3d and clearly retrieves the three inclusions with the same contrast and resolution as in Figure 21.3b. The fluctuations of the reconstructions of Figures 21.3b and 21.3d are a consequence of an imperfectly isotropic diffuse field. Although this aspect would deserve a complete study, it was noticed that the longer the observation time is, the smaller the elasticity fluctuations are. This isotropic distribution of the field energy is crucial for the reconstruction and can be improved by using a passive inverse filter, as shown in [34].

21.3 Experimental Validation in Controlled Media

The feasibility of this correlation-based passive elastography is first presented in tissue-mimicking-phantoms. They can either be homemade, using poly(vinyl alcohol) (PVA), gelatin, or agar, or they are available in the market (e.g. CIRS®). Ultrasound scanners for elastography are widespread. The first experimental validation of passive elastography (Figure 21.4) used an ultrafast ultrasound system by Lecoeur Electronic. From radio-frequency backscattered signals acquired at a typical repetition frequency of 1 kHz, standard speckle tracking algorithms delivered the displacement ϕ generated by the shear wave field. As proof of concept for passive elastography, a 9 s long noise-like elastic field was created by finger impacts applied randomly all over the surface (Figure 21.4a). The displacement $\phi_z(0, t)$ along the first transducer at 3 cm

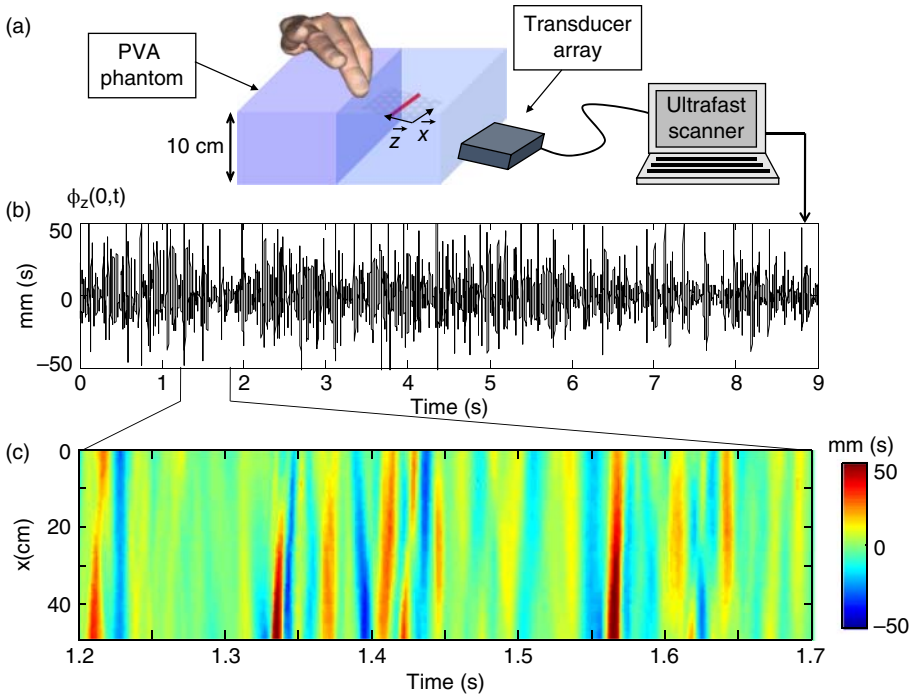

Figure 21.4 (a) Experimental setup for the in vitro correlation-based tomography. A complex shear wave field was created by random finger impacts applied to the surface of a tissue-mimicking phantom (PVA gel). Displacements were measured inside the volume using an ultrafast ultrasonic scanner and elastography algorithms. (b) The z-component of the particle velocity at $x = 0$, $z = 3$ cm. (c) The magnified image of 0.5 s of the particle velocity at $z = 3$ cm shows the wave propagation around 1.4 s. Source: © 2011 IEEE, reprinted, with permission, from [27].

inside the gel is shown in Figure 21.4b. The zoom of 0.5 s of the displacement field along one line parallel to the array (x-axis) is shown as a color-scale map (Figure 21.4c). The finger impacts generated a low-frequency random-like displacement field that was dominated by shear waves.

The noise-correlation function $C(x_0, x; t)$ or, equivalently, the time reversal field Ψ^{TR} is shown for six refocusing spots x_0 (Figure 21.5a). For each position, the amplitude was maximal at $x = x_0$ and $t = 0$, that is to say for the autocorrelation. The cross-shape correlation obtained from the simulation shown in Figure 21.3a is thus nicely retrieved from experiments; its physical interpretation is a 1D representation of a time-reversal field with a converging wave ($t < 0$ s), a spatiotemporal collapse ($t = 0$ s), and the diverging wave ($t > 0$ s). Then, different tomography strategies can be tested, as in Figures 21.5c, 21.5d, and 21.5e. The group velocity using Eq. (21.6) or the wavelength using Eq. (21.7) can be represented. The group velocity tomography, as in any shear wave elastography technique, is probably the closest to the elasticity palpation. However, the shear wavelength tomography presents a fantastic result: it is perfectly compatible with a slow imaging device. By slow, this means having a frame rate totally independent of the Shannon-Nyquist limit and possibly in the limit of 0 Hz. As an experimental demonstration, a 100 Hz shear wave field is detected by a conventional ultrasound scanner (Bruel et Kajer; Hoack System) working at 25 Hz and by a MRI system working at 0.7 Hz (i.e. one frame every 1.5 s).

In the ultrasound experiments, the field is again created using finger impacts randomly distributed at the surface of a calibrated CIRS phantom (Figure 21.6a). For a period of 18 s, 450

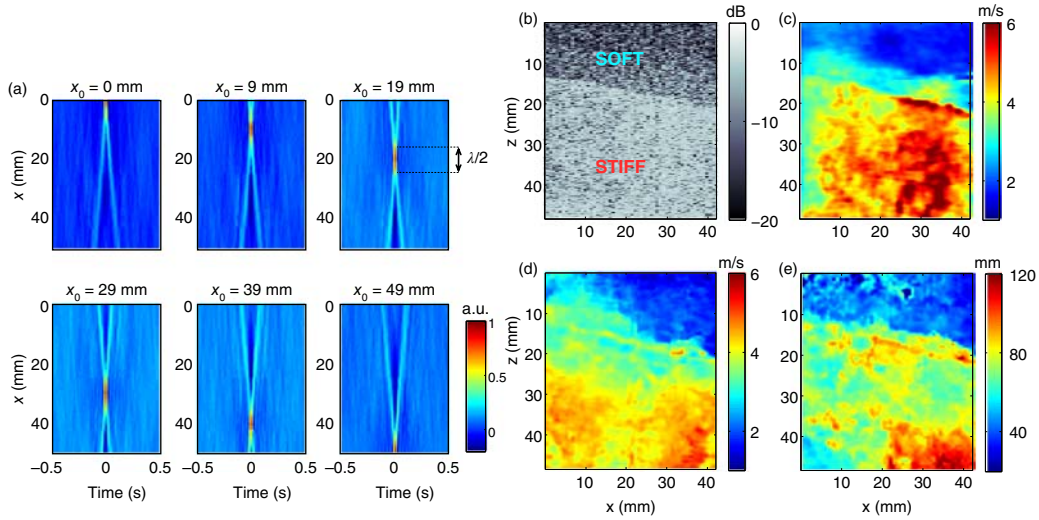

Figure 21.5 (a) Correlation maps measured at six refocusing spots x_0 in a homogeneous hydrogel. The converging and diverging waves are responsible for this typical cross-like shape of the TR field in this spatiotemporal representation. The group velocity of these waves can be estimated from the delay δt of the maximum of the field along δx (bottom right). Another approach estimates the −6 dB focal spot width close to the half wavelength $\lambda/2$ (top right). (b) Sonogram of the bilayer hydrogel, where the two layers with different scatterer concentrations are clearly apparent. (c) Shear wave speed tomography estimated from local group-speed estimation. (d) Shear wavelength tomography estimated from the refocusing width. (e) Slow shear wavelength tomography estimated from a displacement field sampled at 50 Hz. The interface between the two layers is in the same position in the four images, and good quantitative agreement was found for the shear speed values. Source: reprinted with permission from [28], copyright 2007 by the American Physical Society.

radio-frequency ultrasound frames are stored in memory and then converted into displacement field $\phi_s(x, z; t)$ using speckle tracking algorithms as usual. Then, correlation algorithms are applied to this latter diffuse elastic field and, using Eq. (21.7), the tomography reconstructions of Figure 21.6b are obtained in a calibrated CIRS elastography phantom. The four inclusions, from the hardest to the softest, are clearly apparent. The expected values given by the CIRS company are in reasonable agreement with the retreived Young modulus $\overline{E}$ based on the assumption of a constant frequency field of 50 Hz. This agreement thus fully validates the use of wavelength retreival from correlation in passive elastography using slow commercial utrasound scanners.

In the magnetic resonance elastography (MRE) experiment, the diffuse elastic field cannot be induced by random finger impacts for technical reasons. As shown in the experimental setup (Figure 21.7a), vibrations are generated synchronously from 12 contact points by a device mounted on a piezoelectric source and working with a 80.3 s modulated sinusoid excitation. The emitted frequencies range from 20 to 200 Hz. The acquisition of 320 frames for the out-of-plane component of the displacement field was carried out at ∼0.7 Hz on six slices that were equally spaced by 3 mm, with $3 \times 3 \times 3$ mm^3 isotropic voxels, over 8 min. According to the Shannon-Nyquist limit, the maximum shear wave frequency was ∼0.35 Hz, which is far below the central frequency of shear waves in the experiment. The first six consecutive snapshots of the displacement field of a total of 320 snapshots are shown in Figure 21.7b. These snapshots clearly show the rectangular phantom surrounded by the random-phase noise. The elastic field shows complex spatial patterns with characteristic dimensions driven by the wavelengths associated with the 20–200 Hz frequency content of the sweep source signal. Small wavelengths are visible at $t = 1.5$ s, whereas larger wavelengths dominate at

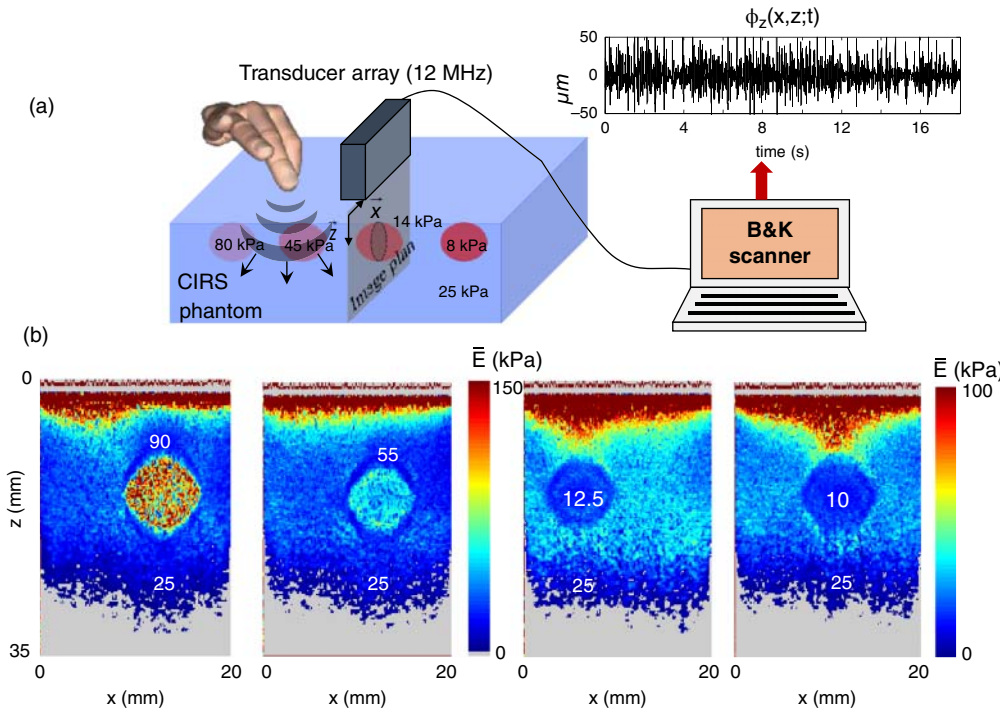

Figure 21.6 (a) Experimental setup in a CIRS phantom. Random finger impacts are used to create a diffuse elastic field measured using speckle tracking algorithms. (b) Normalised shear elasticity maps retreived from a diffuse shear wave field showing three spherical inclusions of a CIRS phantom using a 25 Hz frame rate ultrasound scanner. The characteristics given by the manufacturer are 80 kPa, 45 kPa, 14 kPa, and 8 kPa for the inclusions from the left to the right, and 25 kPa for the background. Source: reprinted with permission from [28], copyright 2007 by the American Physical Society.

$t = 3$ s. A correlation coefficient smaller than 5% between consecutive snapshots of the wave pattern confirms the random property of the diffuse elastic field. The extraction of the elastic parameters from 320 snapshots was then carried out using noise correlation, using Eq. (21.7).

The dimensions of the focal spot vary according to the local stiffness of the medium at the location $\vec{r}_0$ chosen for the virtual point source: a small focal spot in the soft inclusion, a medium one in the background, and a large one in the hard inclusion (Figure 21.8a). The same logic holds for the focal spots in the two remaining inclusions. As a consequence, by sequentially selecting each point of the field as a virtual source location $\vec{r}_0$, tomography of the wavelength is conducted in a processing time of 1 s. Compared with a T2-weighted sequence (Figure 21.8b), the wavelength tomography shows good agreement on the location and the size of the four inclusions (Figure 21.8c); a slight geometric distortion probably introduced by the effect of magnetic field inhomogeneity on the echo planar acquisition (EPI) is also visible. As expected, their growing stiffness is clearly apparent from left to right.

Snapshots are acquired at a sampling time longer than the mean wave period. Therefore, they show independent wave patterns, which prevents the determination of the exact time course of the wave. Nevertheless, the existence of wave patterns implies that motion in one region is correlated with motion in its vicinity at a distance of a mean wavelength. This spatial extension is the key parameter to estimate the shear wavelength. It is close to what is known as the spectral autocorrelation method in seismology. A second physical time-reversal interpretation of correlation states that Ψ^{TR} is the field that would be observed if the sources responsible for the noise waves were able to be controlled and act as a time-reversal mirror. The waves would, thus, back

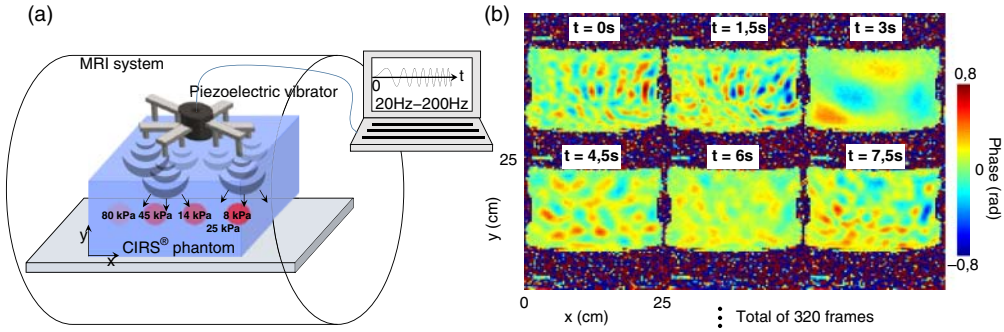

Figure 21.7 (a) Experimental setup. The complex shear wave field is generated from 12 point sources located at the surface and mounted on a MRI-compatible piezoelectric vibrator. The excitation signal is a 80.3 s modulated sinusoid, with the frequency range of 20 to 200 Hz. (b) Phase images that represent the out-of-plane displacement field u_y in the *zx*-plane of the inclusions. These first six snapshots were extracted from a movie of 320 images that was acquired using a gradient-echo MRE sequence every 1.5 s. Source: figure extracted from [42].

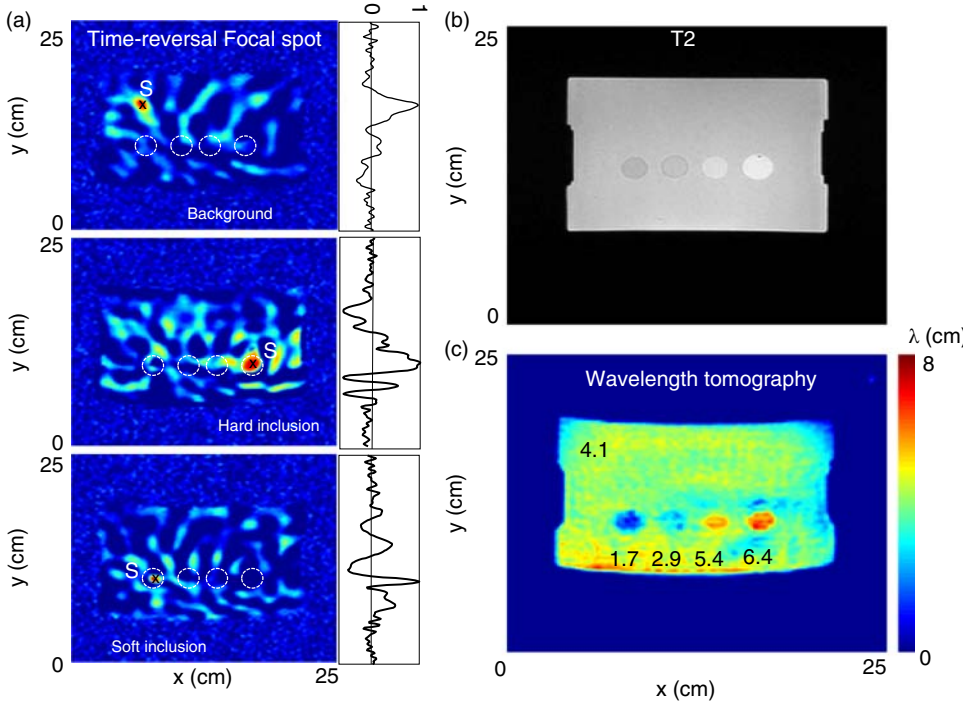

Figure 21.8 Phantom correlation results (a) Time-reversal focal spots for three different virtual source locations S in the phantom background (25 kPa; top), the hard inclusion (80 kPa; middle) and the soft inclusion (8 kPa; bottom). The virtual source S can be set arbitrarily to any location. (b) T2-weighted image of the phantom. (c) Shear wavelength tomography: the four inclusions are clearly apparent, and their local wavelength estimations are proportional to the square root of their local elasticity. Source: figure extracted from [42].

propagate and reach the location of the virtual point source $\vec{r}_0$ at a special spatiotemporal refocusing time t_0. The energy concentration at t_0 defines a region around the virtual source $\vec{r}_0$ called the focal spot. This approach offers a simple and robust way to estimate the mean wavelength (Figure 21.8a); indeed, the time-reversal focal spot reaches the diffraction limit that is known as the Rayleigh criterion [16, 17]. The sampling rate under the Shannon-Nyquist limit prevents

the computation of the time-reversal field as a function of time but leaves the spatiotemporal refocusing at time t_0 unaltered [18, 19]. The extraction of the shear wavelength as spatial information from this latter time-reversal field Ψ^{TR} does not contradict the Shannon-Nyquist sampling theorem that addresses time information.

21.4 Natural Shear Wave Elastography: First In Vivo Results in the Liver, the Thyroid, and the Brain

For the in vivo experiments, the physiological noise that is inherently present in the body creates a natural complex shear wave field. To start with, the liver was imaged at a 750 Hz repetition frequency, by placing the transducer array under the ribs of the subject (Figure 21.9a). The material and method is described in Section 21.3 and Figure 21.4. In Figure 21.9b, the particle displacements in the low-frequency bandwidth from 5 to 70 Hz are mainly caused by cardiac activity. The displacement field in the liver shows a cardiac pulse each 0.5 s, followed by reverberation

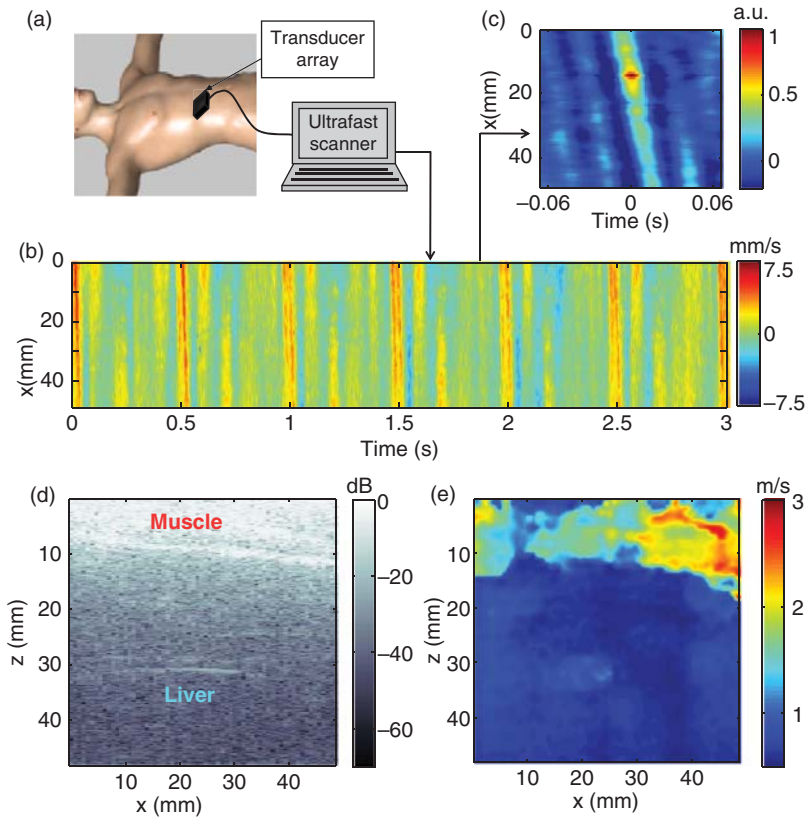

Figure 21.9 (a) Experimental setup for the in vivo correlation-based tomography: an ultrafast scanner was used to measure the natural displacement field in the liver region. (b) The particle velocity along an acquisition line at 4 cm, and parallel to the array, shows the physiological elastic field. (c) In the correlation map $C(x_0, x; t)$ with $x_0 = 14$ mm, only one direction of propagation emerged from the refocusing field. (d) Sonogram of the liver region. The interface between the abdominal muscles and the liver is visible around $z = 12$ mm. (e) The passive shear wave speed tomography from the correlation width clearly shows the two regions. The averaged shear speed estimations are in agreement with values in the literature. Source: © 2011 IEEE, reprinted, with permission, from [27].

and scattering. This complex field was used to compute the correlation function (Figure 21.9c). Compared with the refocusing field in Figure 21.5, only one branch of the cross shape was recovered, which can be explained by the strong directivity of the field. In other words, using a time-reversal analogy, we were not dealing with a perfect time-reversal cavity, in which the converging wave was coming from all directions of a closed surface, but rather with a time-reversal mirror that was located around the heart region and that was re-emitting waves in the direction of the liver. In addition to this problem of directivity, it should be noted that the particle velocity amplitudes were weak, at only 7.5 mm/s, which was quite close to the sensitivity limit of the elastography, at around 1 mm/s. For these two reasons, only the more robust technique, i.e. the wavelength approach, was used for in vivo passive tomography. In the sonogram data (Figure 21.9d), two zones were visible. Above $z = 12$ mm, the bright region corresponded to the abdominal muscles and the dark region was the liver. Good correspondence was seen with the shear wave speed tomography (Figure 21.9e), where the interface between these two regions was seen around $z = 12$ mm. In muscle and liver, the averaged shear wave speeds were in quantitative agreement with other studies [26, 27]. The variability of the reconstructed tomography results shown in Figure 21.9 is believed to be related to the directivity variance of the shear wave field. Indeed, it is well established in seismology that the flux resulting from a diffuse field [35, 36] can be responsible for bias in the tomography. Special efforts need to be made to compensate for this effect.

An in vivo experiment on the thyroid of a healthy volunteer with a signed consent was conducted using passive elastography and a commercial ultrasound scanner. The material shown in Figure 21.10 has previously been described for the CIRS phantom experiment in Section 21.3 (Figure 21.6). The medical array was hand-held during the acquisition of 800 ultrasound frames at 25 Hz. Breathing was prohibited and moving was avoided during these 32 s. The real-time acquisition movie includes the sonogram, speckle tracking correlation, displacement, and strain. Shear waves present in the entire thyroid are thought to be mainly generated by

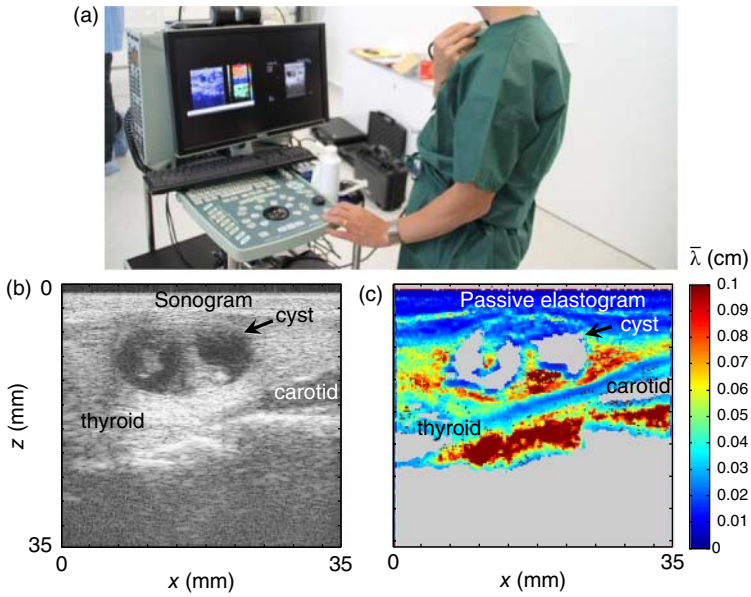

Figure 21.10 (a) A typical in vivo experiment in the thyroid. (b) On the sonogram, a benign cyst and the carotid artery responsible for shear waves is visible. (c) The passive shear wavelength imaging clearly shows the same structure. Source: Source: reprinted with permission from [28], copyright 2007 by the American Physical Society.

the pulsing of the neighboring carotid artery. As is clearly apparent on both the sonogram (Figure 21.10b) and the passive elastogram (Figure 21.10c), a benign cyst is present. Its structure is a mix of viscous fluid and solid parietal tissue. Some artifacts are visible in this image since the diffuse nature of the shear wave field is probably not verified. Despite this handicap, a good general agreement is found between the results of sonogram and the passive elastogram. As a conclusion, a standard ultrasound scanner together with natural shear waves can give relevant elastography images.

In the brain, the natural motion is caused by arterial pulsation and cerebrospinal fluid exchange [23, 24]. The MRE sequence presented in the brain of a healthy volunteer with a signed consent is the same as the one described for the phantom in Section 21.3 (Figure 21.7), except for the three following parameters: the voxel size of six slices is 4 mm × 4 mm × 4 mm to improve the signal-to-noise ratio (SNR), the total time of the in vivo experiments is 11 min, and three components of the displacements are acquired. The out-of-plane component only is investigated here. The first six 64 × 64 pixel snapshots shown in Figure 21.11 show that the MRE sequence can reveal the natural motion in the brain. The amplitudes are relatively small at only 5 μm, but the signal is clearly apparent. Because correlation computation is equivalent to an adaptive filter, the focal spot clearly emerges from the noise (Figure 21.11b). The existence of these time-reversal focus spots is a convincing clue that natural motions in the brain are transported by shear waves. They are responsible for correlation decreasing down to negative values. The black −6 dB isolevel boundary lines more clearly illustrate the different sizes of the focal spots. With a mean of 10 cm, the wavelength estimations are within the expected range. Indeed, assuming that the motion is proportional to the intracranial pressure [37] and given the frequency-dependent sensitivity of the 50 Hz motion-encoding gradient used in our in vivo experiment, the central frequency of displacement (as encoded in the phase images) is expected to be ∼1 Hz [38]; 10% of energy is nonetheless present at a frequency of 15 Hz. It is expected that the wavelength estimation is dominated by the higher frequencies. Therefore, the shear wave speed in the brain is around 1.5 m/s [39, 40]. Therefore, the expected smaller wavelength ranges from 8 to 15 cm. In addition, longer wavelengths are observed on the periphery of the frontal and parietal lobes than in the center of the brain (Figure 21.11b), which is clearly apparent on the shear wavelength tomography reconstructions (Figure 21.12). The anatomic details of T2 images are apparent on the shear wavelength tomography, especially along the

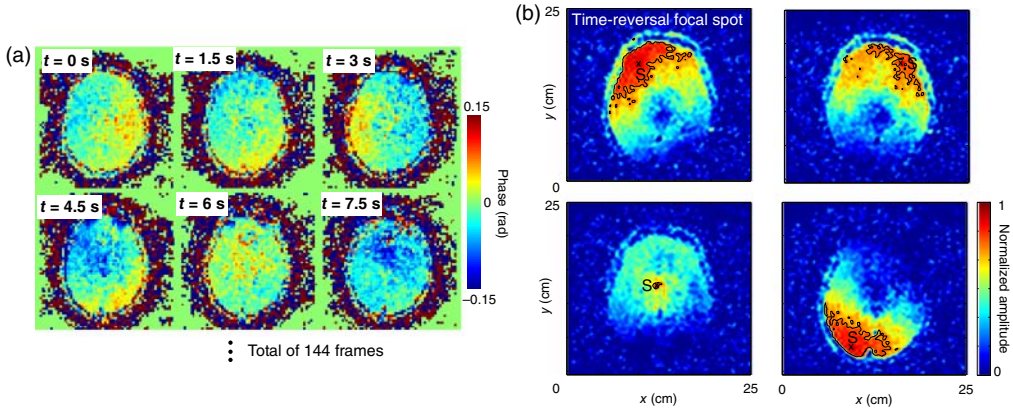

Figure 21.11 In vivo brain results. (a) Phase representation of the displacement field. Six snapshots were extracted from a movie of 144 images. These in vivo measurements of brain motion were acquired with a gradient-echo MRE sequence every 1.5 s. (b) Time-reversal focal spots in the brain for four different virtual-source locations S. The isolevel black boundary lines stress the shear wavelength variations. Source: figure extracted from [42].

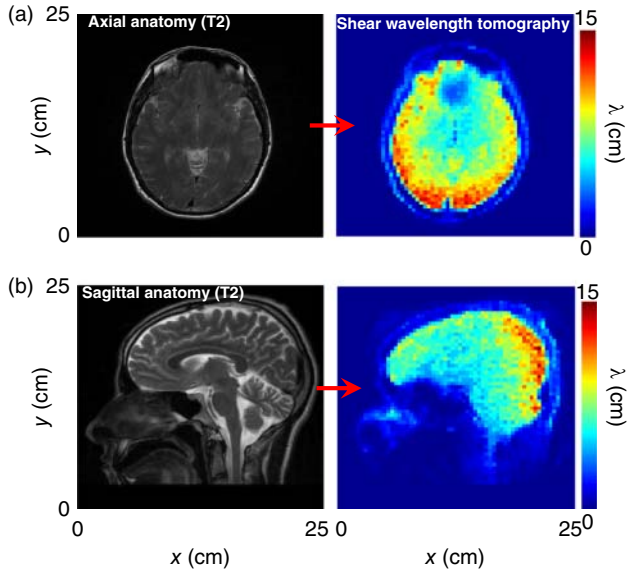

Figure 21.12 In vivo brain passive MRE. (a) Axial view of the T2-weighted image (left) and its corresponding shear wavelength tomography (right). (b) Sagittal view of the T2-weighted image (left) and its corresponding shear wavelength tomography (right). Source: figure extracted from [42].

longitudinal fissure in the axial view (Figure 21.11a). Finally, the longest wavelengths are visible in the posterior region of the brain, in the axial (Figure 21.12a) or sagittal reconstructions (Figure 21.12b).

21.5 Conclusion

From a general point of view, extracting information from complex reverberant fields and natural shear waves in the human body [41, 42] is thought to be potentially useful for medicine as it is for seismology [43]. Compared to active elastography, this passive approach might bring a solution in situations where shear wave generation is tricky. This is the case for deep organs such as the prostate, for protected organs such as the brain, and for fragile organs such as the retina. It is also the case for obese patients. Passive elastography is thus foreseen in the short term to be complementary to active methods. Our long-term vision would be to use tiny natural elastic vibrations due to thermal motion: any shear wave sources would no longer be required for elastography imaging.

References

1 Fink, M. (1997). Time reversed acoustics. *Phys. Today* 50: 34.
2 Lerosey, G., de Rosny, J., Tourin, A., and Fink, M. (2007). Focusing beyond the diffraction limit with far-field time reversal. *Science* 315: 1120.
3 Kuperman, W.A., Hodgkiss, W.S., Song, H.C., et al. (1998). A long-range and variable focus phase-conjugation experiment in shallow water. *J. Acoust. Soc. Am.* 103: 25.
4 Ulrich, T.J., Johnson, P.A., and Guyer, R.A. (2007). Interaction dynamics of elastic waves with a complex nonlinear scatterer through the use of a time reversal mirror. *Phys. Rev. Lett.* 98: 104301.

5 Ing, R.K., Quieffin, N., Catheline, S., and Fink, M. (2005). In solid localization of finger impacts using acoustic time-reversal process. *Appl. Phys. Lett.* 87: 204104.

6 Thomas, J.L., Wu, F., and Fink, M. (1996). Time reversal focusing applied to lithotripsy. *Ultrason. Imaging* 18: 106.

7 Pernot, M., Montaldo, G., Tanter, M., and Fink, M. (2006). "Ultrasonic stars" for time-reversal focusing using induced cavitation bubble. *Appl. Phys. Lett.* 88: 034102.

8 Thompson, L.A. and Gardner, C.S. (1987). Experiments on laser guide stars at Mauna Kea Observatory for adaptive imaging in astronomy. *Nature (London)* 328: 229.

9 Draeger, C. and Fink, M. (1997). One-channel time reversal of elastic waves in a chaotic 2D-silicon cavity. *Phys. Rev. Lett.* 79: 407.

10 Catheline, S., Wu, F., and Fink, M. (1999). A solution to diffraction biases in sonoelasticity: the acoustic impulse technique. *J. Acoust. Soc. Am.* 105: 2941.

11 Muthupillari, R., Lomas, D.J., Rossman, P.J., et al. (1995). Magnetic resonance elastography by direct visualization of propagating acoustic strain waves. *Science* 269: 1854.

12 deRosny, J. and Fink, M. (2002). Overcoming the diffraction limit in wave physics using a time-reversal mirror and a novel acoustic sink. *Phys. Rev. Lett.* 89: 124301.

13 Shapiro, N.M., Campillo, M., Stehly, L., and Ritzwoller, M.H. (2005). High-resolution surface-wave tomography from ambient seismic noise. *Science* 307: 1615.

14 Larose, E., Margerin, L., Derode, A., et al. (2006). Correlation of random wavefields: An interdisciplinary review. *Geophysics* 71: SI11.

15 Duvall, T.L. Jr., Jefferies, S.M., Harvey, J.W., and Pomerantz, M.A. (1993). Time-distance helioseismology. *Nature* 362 (6419): 430–432.

16 Lobkis, O.I. and Weaver, R.L. (2001). On the emergence of the Green's function in the correlations of a diffuse field. *J. Acoust. Soc. Am.*, 110 (1–8): 3011.

17 Roux, P. and Kuperman, W.A. (2004). Extracting coherent wave fronts from acoustic ambient noise in the ocean. *J. Acoust. Soc. Am.* 116 (4): 1995.

18 Sandrin, L., Catheline, S., Tanter, M., et al. (1999). Time-resolved pulsed elastography with ultrafast ultrasonic imaging. *Ultrason. Imaging* 21: 259.

19 Nightingale, K., Soo, M.S., Nightingale, R., and Trahey, G. (2002). Acoustic radiation force impulse imaging: in vivo demonstration of clinical feasibility. *Ultrasound Med. Biol.* 28: 227.

20 Bercoff, J., Tanter, M., and Fink, M. (2004). Supersonic shear imaging: a new technique for soft tissue elasticity mapping. *IEEE Trans. Ultrason., Ferroelect., Freq. Control* 51 (4): 396.

21 Parker, K.J. and Lerner, R.M. (1992). Sonoelasticity of organs: shear waves ring a bell. *J. Ultrasound Med.* 11: 387.

22 Sunagawa, K. and Kanai, H. (2005). Measurement of shear wave propagation and investigation of estimation of shear viscoelasticity for tissue characterization of the arterial wall. *J. Med. Ultrason.* 32: 39.

23 Luo, J., Li, R.X., and Konofagou, E.E. (2012). Pulse wave imaging of the human carotid artery: an in vivo feasibility study. *IEEE Trans. Ultrason., Ferroelect., Freq. Control* 59 (1): 174.

24 Gallichan, D., Robson, M.D., Bartsch, A., and Miller, K.L. (2009). TREMR: Table-resonance elastography with MR. *Magn. Res. Med.* 62: 815.

25 Catheline, S., Benech, N., Brum, J., and Negreira, C. (2008). Time reversal of elastic waves in soft solids. *Phys. Rev. Lett.* 100: 064301.

26 Benech, N., Catheline, S., Brum, J., et al. (2009), 1-D elasticity assessment in soft solids from shear wave correlation: the time-reversal approach. *IEEE Trans. Ultrason., Ferroelect., Freq. Control* 56: 2400.

27 Gallot, T., Catheline, S., Roux, P., et al. (2011). Passive elastography: shear-wave tomography from physiological-noise correlation in soft tissues. *IEEE Trans. Ultrason., Ferroelect., Freq. Control* 58: 1122.

28 Catheline, S., Souchon, R., Ruppin, M., et al. (2013). Tomography from diffuse waves: passive shear wave imaging using low frame rate scanners. *Appl. Phys. Lett.* 103: 014101.

29 de Rosny, J. and Fink, M. (2007). Focusing properties of near-field time reversal. *Phys. Rev. A* 76: 065801.

30 Roux, P., Sabra, K., Kuperman, W.A., and Roux, A. (2005). Ambient noise cross correlation in free space: Theoretical approach. *J. Acoust. Soc. Am.* 117 (1):79.

31 Derode, A., Larose, E., Tanter, M., et al. (2003). Recovering the Green's function from field-field correlations in an open scattering medium (L). *J. Acoust. Soc. Am.* 113 (6): 2973.

32 Gouedard, P., Stehly, L., Brenguier, F., et al. (2008). Cross-correlation of random fields: Mathematical approach and applications. *Geophys. Prospect* 56 (3): 375.

33 Weaver, R.L. (1982). On diffuse waves in solid media. *J. Acoust. Soc. Am.* 71: 1608–1609.

34 Gallot, T., Catheline, S., Roux, P., and Campillo, M. (2012). A passive inverse filter for Green's function retrieval. *J. Acoust. Soc. Am.* 131 (1): EL21.

35 Weaver, R., Froment, B., and Campillo, M. (2009). On the correlation of non-isotropically distributed ballistic scalar diffuse waves. *J. Acoust. Soc. Am.* 126: 1817.

36 Gouedard, P., Roux, P., Campillo, M., and Verdel, A. (2008), Convergence of the two-point correlation function toward the Green's function in the context of a seismic-prospecting data set. *Geophysics* 73: V47.

37 Wagshul, M.E., Eide, P.K., and Madsen, J.R. (2011). The pulsating brain: a review of experimental and clinical studies of intracranial pulsatility. *Fluids Barriers CNS* 8: 5.

38 Weaver, J.B., et al. (2012). Brain mechanical property measurement using MRE with intrinsic activation. *Phys. Med. Biol.* 57: 7275.

39 Kruse, S.A., et al. (2008). Magnetic resonance elastography of the brain. *Neuroimage* 39: 231.

40 Sack, I., Beierbach, B., Hamhaber, U., et al. (2008). Non-invasive measurement of brain viscoelasticity using magnetic resonance elastography. *NMR Biomed.* 21: 265.

41 Sabra, K.G., Conti, S., Roux, P., and Kuperman, W.A. (2007). Passive in vivo elastography from skeletal muscle noise. *Appl. Phys. Lett.* 90: 194101.

42 Zorgani, A., Souchon, R., Hoang-Dinh, A., et al. (2015). Brain palpation from physiological vibrations using MRI. *Proc. Natl. Acad. Sci.* 112 (42): 12917–12921.

43 Campillo, M. and Paul, A. (2003). Long-range correlations in the diffuse seismic coda. *Science* 299: 547.

22

Acoustic Radiation Force Impulse Ultrasound

Tomasz J. Czernuszewicz and Caterina M. Gallippi

The Joint Department of Biomedical Engineering, The University of North Carolina at Chapel Hill and North Carolina State University, Chapel Hill and Raleigh, NC, USA

22.1 Introduction

An approach to ultrasonically evaluating the mechanical properties of tissue is acoustic radiation force impulse (ARFI) imaging [1]. ARFI is distinguished from alternative elastographic imaging methods in that the mechanical excitation used to induce tissue motion is delivered with temporal and spatial precision via impulsive, focused acoustic radiation force (ARF). Relative to compression elastography, an advantage to ARFI imaging is that the force is applied directly to the tissue of interest, which obviates challenges associated with indirect force coupling and minimizes the stresses needed to achieve sufficient contrast of mechanical features. In this chapter, the fundamental physics of impulsive ARF are presented first, followed by detailed descriptions of both qualitative and quantitative ARFI imaging methods.

22.2 Impulsive Acoustic Radiation Force

A critical component of ARFI imaging is the impulsive ARF excitation force, which is delivered by a focused ultrasound pulse with longer length and/or higher acoustic power than conventional B-mode imaging pulses [2, 3]. The force magnitude, in a tissue medium in which absorption is the primary cause of attenuation, is directly proportional to tissue absorption (α) and sound-beam local average temporal intensity (I), and inversely proportional to the speed of sound (c)

$$F = \frac{2\alpha \boldsymbol{I}}{c} \tag{22.1}$$

Equation (22.1) reflects several important considerations in ARFI imaging. Examining $\boldsymbol{I}$, which represents the volumetric intensity field transmitted by the focused ultrasound pulse, it is apparent that the ARF is a body force that is delivered to the spatial location of the transmitted point spread function (PSF). As the PSF magnitude is spatially variable, so is the magnitude of the achieved ARF. Also, higher $\boldsymbol{I}$ achieves greater ARF magnitude and thus larger tissue displacements, with the possibility of improving contrast of mechanical features. Figure 22.1 shows the spatial and temporal characteristics of an impulsive ARF excitation.

Next, considering α in Eq. (22.1), it is clear that the amplitude of the ARF depends on the absorbing properties of tissue as well as the focal configuration of the beam. In low attenuating media, focal gains will dominate, and the ARF will be delivered with the greatest amplitude at

Ultrasound Elastography for Biomedical Applications and Medicine, First Edition.
Edited by Ivan Nenadic, Matthew Urban, James Greenleaf, Jean-Luc Gennisson, Miguel Bernal, and Mickael Tanter.

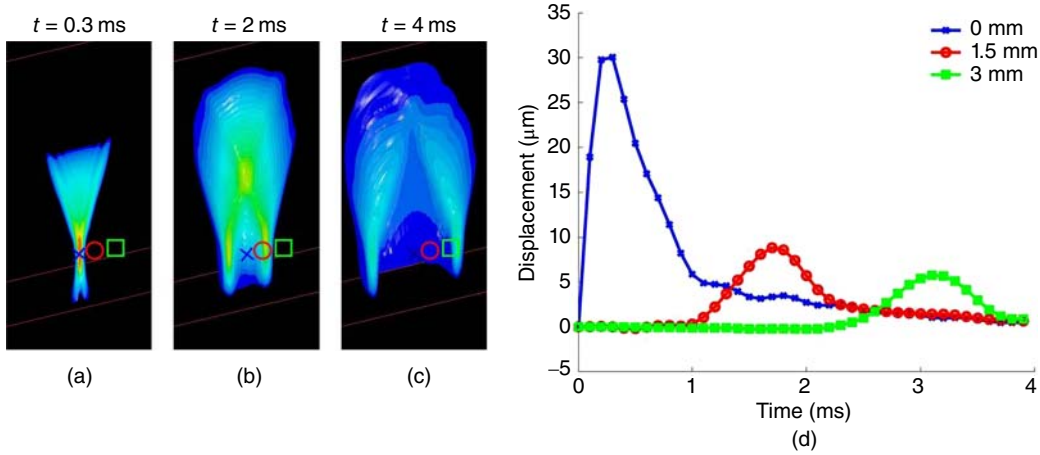

Figure 22.1 Spatial geometry and temporal dynamics of an impulse of acoustic radiation force. Images (a)–(c) show the simulated axial displacement response in three dimensions for a homogenous, isotropic, elastic material (Young's modulus = 4 kPa) at three time points following excitation (0.3 ms, 2 ms, and 4 ms). The transducer is located at the top of the image. The displacement versus time curves at each symbol (x, circle, square) are shown in (d), where the legend indicates lateral distance from the region of excitation. Within the region of excitation, displacement is highest and occurs immediately after excitation. As time progresses, a shear wave propagates away from the region of excitation, instigating time-lagged displacements at positions some distance away from the region of excitation. Source: reprinted with permission from [31].

the focal zone. In highly attenuating media, ARF will be more broadly distributed in the near field, equaling or even exceeding that experienced by the focal zone, and may result in a larger volume of tissue being set in motion. Furthermore, because attenuation is frequency dependent, the displacement fields from ARF excitations with higher frequencies may experience more near-field broadening compared to lower frequency excitations of the same tissue region [4]. Thus, the ideal center frequency for the ARF excitation is material and application dependent.

Peak acoustic radiation force magnitudes are typically on the order of dynes for in vivo applications, creating tissue displacements in the range of 1 to 10 μm. Such ARF magnitudes are achievable within the US Food and Drug Administration (FDA)-regulated diagnostic ultrasound limits for thermal index (TI), mechanical index (MI), and spatial peak temporal average intensity (I_{spta}). Palmeri and Nightingale demonstrated, using finite element method (FEM) models with experimental validation and neglecting cooling effects, that conventional ARFI imaging methods heat tissue less than 1 °C, which is below the 6 °C FDA limit [5, 6]. However, the existing FDA limits were established without specific regard to the methods of ARFI imaging, and the possibility of safely expanding these limits to support deeper penetration and improve contrast in ARFI is under investigation [7, 8].

22.3 Monitoring ARFI-induced Tissue Motion

22.3.1 Displacement Resolution

In ARFI imaging, one-dimensional axial displacements induced in the location of force application, or the "region of excitation" (ROE), is considered to reflect relative tissue stiffness, and thus a critical component to ARFI imaging is accurate displacement measurement. ARFI-induced displacements are small, typically less than 10 μm, and correlation-based time delay estimators are conventionally used to track them [9]. Error in correlation-based displacement estimates is due to large false peak errors, defined as displacement estimates that are greater than

one-quarter cycle larger than the true displacement, and small jitter errors, which are displacement errors too small to be classified as false peaks [10]. False peak errors may be mitigated using non-linear approaches [11], but jitter error cannot be removed and therefore places a fundamental limit on displacement resolution. The magnitude of this limit, which has been predicted using the Cramér-Rao lower bound (CRLB), is [10]

$$\widehat{\sigma} \geq \sqrt{\frac{3}{2f_0^3\pi^2 T(B^3+12B)}\left(\frac{1}{\rho^2}\left(1+\frac{1}{\mathrm{SNR}^2}\right)^2-1\right)} \tag{22.2}$$

where f_0 is the pulse center frequency, B is the pulse bandwidth, T is the kernel size, ρ is the normalized correlation between signals, and SNR is the signal-to-noise ratio.

This fundamental limit on displacement resolution as predicted by the CRLB pertains to unbiased estimators (such as normalized cross-correlation, Loupas [12], and Kasai [13] methods). However, by implementing a small amount of bias into the estimator, the Bayesian speckle tracking method achieves displacement resolution that surpassed the CRLB [14, 15]. Continued optimization of the biased estimator is in development, and this technique has potential for improving displacement resolution in ARFI as well as other imaging methods that rely on motion tracking.

22.3.2 Displacement Underestimation

Aside from jitter error, acoustic displacement estimation in ARFI imaging suffers another limitation. This limitation is caused by the focused nature of the acoustic radiation force that is used to excite tissue. In the lateral and elevational dimensions of this force, induced scatterer displacements are non-uniform because the force magnitude varies (i.e. as a sinc function) over space. More specifically, induced scatterer displacements are largest in the center of the pulse and decrease with distance away from the center. Such a distribution of scatterer displacements within the tracking pulse's PSF causes error, or "shearing" artifact. Shearing artifacts have two primary consequences. First, ARFI-measured peak displacement will tend to underestimate true tissue peak displacement due to averaging of scatterer motion under the tracking resolution cell. This can lead to a reduction in contrast in ARFI images because soft features may appear stiffer than they truly are. Second, due to the non-uniform displacement of scatterers, the correlation between the reference pulse and tracking pulses immediately following the ARFI excitation will decrease. This reduction in correlation will ultimately lead to an increase in jitter variance in the displacement estimate and, therefore, noisier ARFI images.

Shearing artifact in ARFI was first explored analytically by McAleavey et al. [16] under simplifying assumptions that modeled the displacement field and tracking beam pattern as Gaussians and ignored the effects of non-axial motion. In this work, expressions were derived for echo correlation, jitter, and mean ARFI displacement as functions of lateral and elevational beam widths for pushing and tracking pulses. A significant conclusion was that displacement underestimation in ARFI can be mitigated by adjusting the ratio of pushing and tracking beam widths; specifically, when the pushing beam width is much wider than the tracking beam width, the ARFI-derived displacement estimate matches the true tissue displacement much more closely than when the pushing and tracking beam widths are identical. In a common imaging scenario (1D linear array) where control over F/# can only be exerted in the lateral dimension, ARFI-derived peak displacement could, at most, be only $1/\sqrt{2}$ of the true tissue peak displacement. The expressions derived by McAleavey et al. were later improved by Dhanaliwala et al. [17] by adding additional terms to account for the effect of mechanical coupling of tissue in three dimensions. In the original derivation, McAleavey et al. assumed that the dimensionality of the tissue region displaced by ARFI was equal to the width of the two-way response of

the pushing beam. Dhanaliwala et al., using 3D finite element simulations, demonstrated that the displaced tissue region is actually wider than the pushing beam width due to mechanical coupling and adjusted McAleavey's expression accordingly. Using the Dhanaliwala modification, the expression for the jitter lower bound ($\hat{\sigma}$) in ARFI imaging can be written as the following [17]

$$\hat{\sigma} \geq \sqrt{\frac{3}{2f_0^3\pi^2 T(B^3+12B)}\left(\frac{1}{\left(1-\frac{1}{c^2}4A^2f_0^2\pi^2L_xL_y\left(\frac{1}{\sqrt{(1+L_x^2)(1+L_y^2)}}-\frac{4L_xL_y}{(1+2L_x^2)(1+2L_y^2)}\right)\right)^2}\left(1+\frac{1}{\mathrm{SNR}_E^2}\right)^2-1\right)} \tag{22.3}$$

$$L_x = \frac{D_x}{T_x},\ L_y = \frac{D_y}{T_y} \tag{22.4}$$

where A is the maximum scatterer displacement, c is the speed of sound, and D_x, T_x, D_y, T_y, are displacement and tracking beam widths in the lateral and elevational dimensions, respectively. Likewise, the expression for mean ARFI-derived displacement (μ) can be written as the following

$$\mu = \frac{2AL_xL_y}{\sqrt{(2L_x^2+1)(2L_y^2+1)}} \tag{22.5}$$

And finally, using Eqs. (22.3) and (22.5) and scaling by $c/2$ to maintain consistent units, an expression for the upper bound of $\mathrm{SNR}_{\mathrm{ARFI}}$ can be written as the following:

$$\widehat{\mathrm{SNR}}_{\mathrm{ARFI}} \leq \frac{\mu}{\sigma_{\frac{c}{2}}} \tag{22.6}$$

Figure 22.2 shows the predicted $\mathrm{SNR}_{\mathrm{ARFI}}$ for a 1D linear array as a function of peak displacement amplitude. This figure demonstrates that increasing ARFI displacement has diminishing returns in terms of improving $\mathrm{SNR}_{\mathrm{ARFI}}$ due to displacement underestimation and differential motion decorrelation.

Interestingly, underestimation bias in ARFI-derived displacements is not constant with time. Palmeri et al. [18, 19], using 3D finite element simulations, demonstrated that underestimation is worst in the early time points following the ARF excitation, but resolves over time at a rate corresponding to the shear wave speed of the material. Therefore, stiffer materials with faster shear wave speeds are less susceptible to underestimation bias compared to softer materials with slower shear wave speeds. Note that this phenomenon exacerbates the reduction in ARFI contrast as soft tissues experience more acoustic displacement underestimation than stiff tissues. The material dependence of displacement underestimation was validated experimentally by Czernuszewicz et al. [20] using a high-speed camera and a series of optically translucent ultrasound phantoms. Figure 22.3 shows underestimated ARFI displacement curves from FEM and phantom experiments.

To mitigate differential motion decorrelation in post-processing, Mauldin et al. proposed using principal component analysis (PCA) as either a filter prior to conventional time-delay estimation [21], or as a unique time-delay estimator itself [22]. In PCA, a linear transformation is used to convert a set of possibly correlated variables (e.g. scatterer displacements encoded as phase shifts in radio frequency, RF, data) into a set of uncorrelated variables or basis vectors, with the stipulation that the basis vectors are orthogonally distributed. While PCA-based

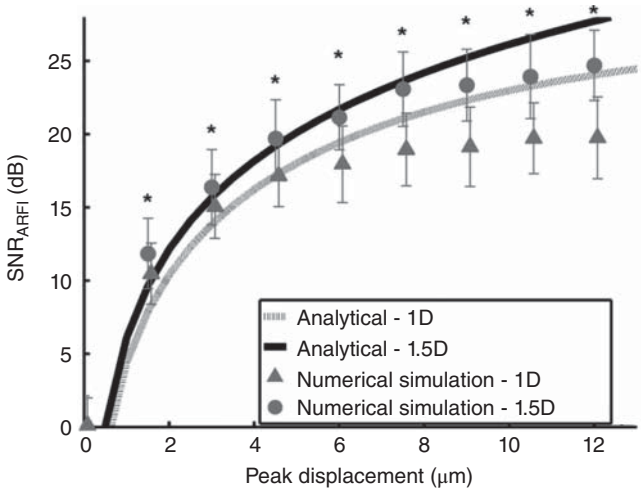

Figure 22.2 SNR$_{ARFI}$ as a function of peak displacement. The solid lines represent the derived analytical model for a 1D and 1.5D array respectively, while the symbols represent the finite element simulation results. Asterisks represent significant difference ($p < 0.05$) between 1D and 1.5D simulations. Source: © 2012 IEEE, reprinted, with permission, from [17].

approaches are not necessarily able to resolve underestimation bias completely, results suggest that they are more robust to decorrelation, and provide estimates with lower jitter compared to conventional estimation techniques such as the Loupas autocorrelation method.

Instead of rejecting differential motion decorrelation in post-processing, it is possible to minimize the occurrence of shearing artifact by increasing the uniformity of the ARFI excitation within the tracking PSF. This is achieved by employing an ARFI excitation pulse that is wider laterally and elevationally than the tracking pulse. While manipulating the lateral width of acoustic pulses is readily possible with conventional one-dimensional linear array transducers, expanding the width of the ARFI excitation in the elevational dimension relative to that of the tracking pulse requires multi-dimensional arrays capable of two-dimensional focusing.

22.3.3 Clutter Artifacts

Another source of error in ARFI displacement estimation is clutter. Clutter arises from sound reverberation in tissue layers, scattering from off-axis structures, ultrasound beam distortion, returning echoes from previously transmitted pulses, and random acoustic or electronic noise [23]. It is typically recognized as a coherent ring-down artifact or a diffuse haze in B-mode images that degrades feature contrast. In application to measuring tissue displacement for ARFI imaging, clutter signal from stationary or slowly moving tissue can bias the displacement estimate, while decorrelation from near-field reverberation clutter increases jitter magnitude. Therefore, the quality and diagnostic accuracy of ARFI imaging can be improved by reducing clutter [24]. Conventional frequency domain-based clutter filters [25] have limited relevance to ARFI imaging because the frequency spectra of the ARFI-induced motion and the clutter signals generally overlap. Adaptive time domain-based clutter filters may be pertinent, but these have not been specifically evaluated for clutter rejection in ARFI imaging [26]. Alternatively, clutter reduction may be achieved in ARFI, as it is in B-mode [27], by harmonic imaging [24].

Doherty et al. [24] proposed the use of harmonic sequences to track ARFI-induced displacements. In this study, the authors implemented two conventional tissue harmonic imaging (THI) methods (bandpass filtering and pulse inversion) in ARFI ensembles. In the bandpass approach,

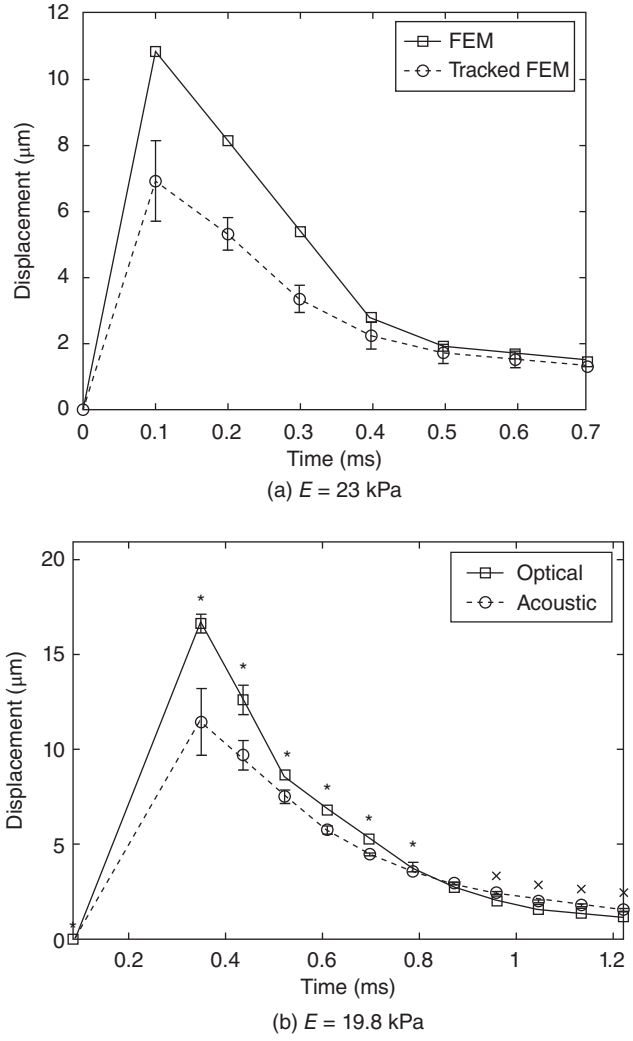

Figure 22.3 Acoustic tracking of ARFI displacements underestimate peak tissue displacement validated with (a) FEM simulation and (b) experimentally with optical tracking. Solid lines represent the true tissue displacement (from FEM or optical tracking, respectively), while dashed lines represent matched acoustic tracking. Substantial underestimation is observed in the early time points, and eventually resolves after approximately 0.6–0.8 ms. FEM simulation data reprinted with permission from [19]. Optical tracking data reprinted with permission from [20].

conventional ARFI ensembles are acquired with a broadband transducer, and a bandpass filter is used to isolate the harmonic component in each tracking line prior to motion estimation. In the pulse inversion approach, tracking pulses of opposite polarity are transmitted serially, and the echoes are summed to cancel out the fundamental signal. One of the disadvantages of the pulse inversion approach is that the pulse repetition frequency (PRF) of the ARFI ensemble is effectively cut in half. To mitigate this, the authors developed a fully sampled pulse inversion sequence to maintain PRF, which utilized a sliding window when summing pulses of opposite polarity (Figure 22.4). The results of this work demonstrated a marked improvement in both B-mode and ARFI image quality when using THI tracking pulses (particularly with a fully sampled pulse inversion sequence). As was the case in conventional B-mode imaging,

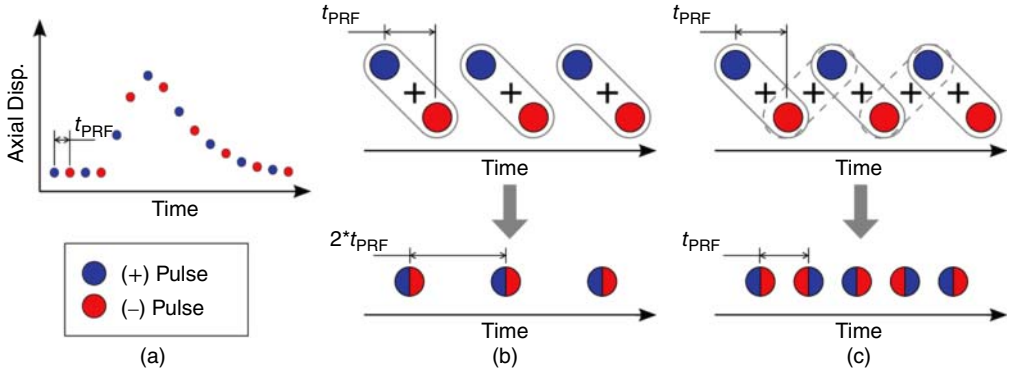

Figure 22.4 Implementation of pulse-inversion ARFI tracking sequence. (a) Arbitrary ARFI deformation response monitored with a pulse-inversion scheme that transmits pulses of alternating polarity (+ and –) at a pulse repetition time equal to t_{PRF}. (b) Conventional pulse inversion sums each (+) pulse with the subsequent (–) pulse, resulting in half the native temporal sampling frequency. (c) Fully sampled pulse-inversion method sums each (+) pulse with the subsequent (–) and also sums each (–) pulse with the subsequent (+) pulse to maintain native temporal sampling. Source: © 2013 IEEE, reprinted, with permission, from [24].

harmonic ARFI has the potential to replace fundamental ARFI in many clinical applications due to improvements in contrast and image quality.

In addition to accuracy, the speed of displacement estimation in ARFI imaging is an important consideration because it determines the real-time applicability of the method (see Section 22.6). Computation time is reduced relative to normalized cross-correlation using the Loupas [12] and Kasai [13] algorithms, but at the expense of performance [9]. While the Kasai displacement estimator is faster, the Loupas algorithm achieves lower displacement jitter and bias, with comparable performance to normalized cross-correlation except when the kernel size is small and the SNR is low or when the bandwidth is large. Therefore, the Loupas algorithm is useful for displacement estimation in ARFI imaging when fast calculations are required.

22.4 ARFI Data Acquisition

ARFI imaging is implemented using a single ultrasound transducer for both generating impulsive ARF and monitoring the induced displacements. The beam sequence used to acquire ARFI data in a single lateral location begins with two or more "reference" pulses, which serve to establish a baseline for the position of the tissue prior to the ARFI excitation. Following the reference pulses, an ARFI excitation, or "pushing", pulse is administered to generate the impulsive ARF that induces tissue deformation. Finally, multiple "tracking" pulses are collected in ensemble form, from which ARFI-induced displacements are measured. The ensemble length varies with application but is typically in the range of 5 ms to enable observation of tissue recovery from deformation. Both reference and tracking pulses are conventional, two-cycle B-mode style pulses, while the pushing pulse has longer duration and/or higher acoustic power than conventional ultrasound imaging pulses. Using such a pulse sequence, a two-dimensional matrix of RF data is collected through depth and time in a single lateral location. To achieve two-dimensional ARFI imaging, the pulse sequence is repeated in multiple lateral positions, generating a three-dimensional matrix of RF data through depth, time, and lateral position. The order of interrogating lateral positions is non-sequential in space. For example, data in a lateral position on the extreme left of the imaging field of view (FOV) will be acquired, following by data acquisition in the center of the FOV, then in one position to the right of the left-most,

then in one position to the right of center, etc. This non-sequential ordering reduces the potential for motion interference between adjacent lateral sampling positions and minimizes tissue heating.

22.5 ARFI Image Formation

One-dimensional axial displacement tracking, as described in Section 22.3, is applied to ARFI data sets to measure ARFI-induced displacements through time, or ARFI "displacement profiles", for each pixel in the two-dimensional imaging FOV. The displacement profiles may be corrupted by motion artifacts arising from physiological motion as well as shear and/or longitudinal wave reflections back into the ARFI ROE. Such motion artifacts are corruptive to ARFI imaging because they distort the relevant parameters of the displacement profiles, namely: the magnitude of displacement at a given time, the magnitude of the peak displacement, the time to peak displacement, and the time to recovery from peak displacement.

22.5.1 Physiological Motion Rejection

Because motion artifact is detrimental to ARFI imaging, a number of motion rejection methods have been developed [26, 28, 29]. The majority of these approaches fit a line or a polynomial to select displacement versus time samples, using only the first and last few displacement measurements. These methods assume that ARFI-induced displacement is resolved prior to the end of the observation period, such that only physiological motion remains in the late-time displacement samples. The fit line or polynomial is then subtracted from the measured displacement profile to reject physiological motion but retain ARFI-induced displacement [28, 29] (Figure 22.5). An alternative approach uses adaptive blind source separation (BSS)-based time-domain methods to statistically separate the disparate motion signatures of physiological and ARFI-induced motion, assuming that the more dynamic ARFI motion is statistically orthogonal to or independent from the physiological motion signature [26].

22.5.2 ARFI Image Resolution and Contrast

From the motion-filtered ARFI displacement profiles, parameters of interest are extracted and rendered into two-dimensional images. As with any imaging modality, the quality of parametric ARFI images is assessed by resolution and contrast metrics. It has been shown that the spatial resolution of ARFI images, which does not depend on the size of the ROE, is comparable to that of B-mode imaging, which follows logically from the fact that ARFI-induced displacements are tracked using conventional B-mode style pulses [30].

Contrast in ARFI images, however, is unlike that of B-mode. First, the mechanisms for contrast generation differ. While B-mode renders images displaying differences in the acoustic properties of tissue, ARFI details differences in the mechanical properties of tissue. For example, tissues that exhibit similar acoustic properties but very different mechanical properties are better contrasted by ARFI than B-mode imaging (Figure 22.6). Owing to the dynamic response of tissue to the impulsive ARF, contrast in ARFI images varies over time. It is shown byNightingale et al. [30] that contrast is highest shortly after the ARFI excitation ceases and then decreases over time. Under certain circumstances, contrast may reverse due to shear wave interactions with nearby boundaries, local differences in shear moduli, and inertial effects. Specialized finite element method (FEM) models show that, in regard to contrasting a spherical lesion embedded within a homogeneous background, contrast shortly after the ARFI force ceases is independent

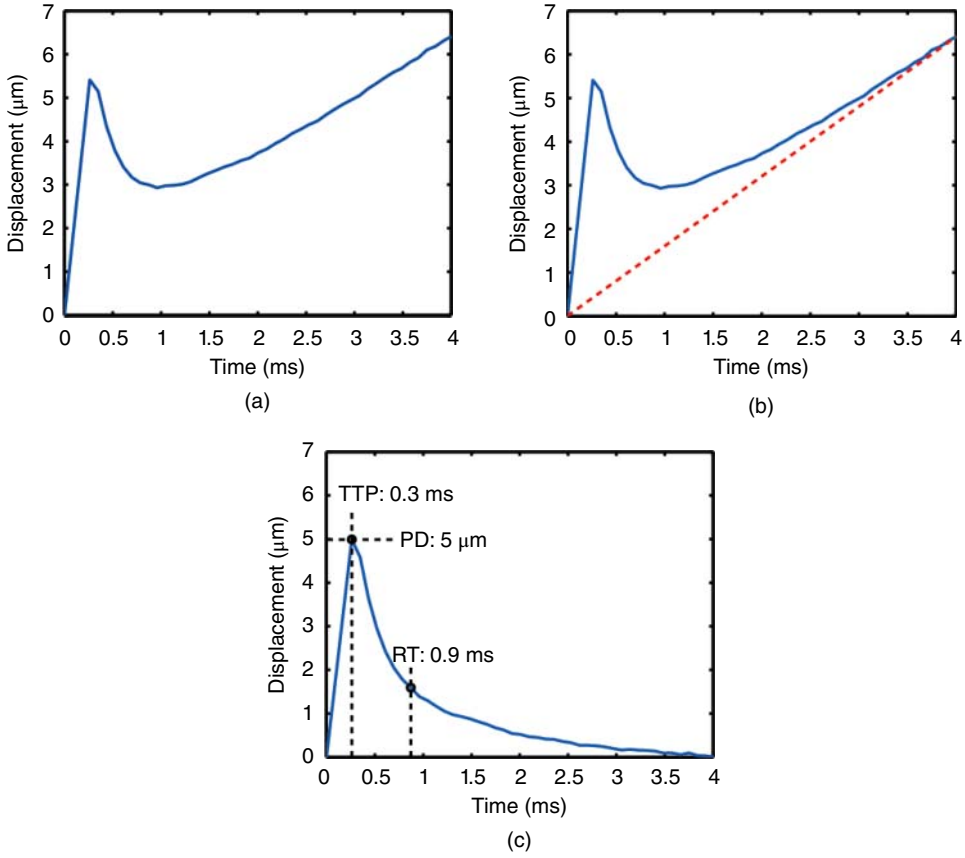

Figure 22.5 Motion filtering of ARFI displacement profiles. (a) ARFI displacement curve corrupted by a constant velocity, non-ARFI motion. (b) An idealized fit to the non-ARFI motion estimated from the first and last data points (i.e. time points where ARFI-induced motion is assumed to be zero). (c) Motion-filtered ARFI displacement curve with linear motion profile subtracted from raw ARFI data. Common parameters measured from ARFI displacement curves to produce 2D images include peak displacement (PD), time-to-peak (TTP), and recovery time (RT) to two-thirds of peak displacement.

of the applied ARF magnitude, directly proportional to lesion stiffness, and inversely proportional to the size of the ROE [30].

In regard to the relationship between contrast and lesion stiffness, it is important to understand that because contrast in ARFI images is dynamic and dependent on the ROE size, the ratio of ARFI-induced displacements inside and outside a stiff lesion does not directly reflect the corresponding ratio of elastic moduli [31].

Relative to the relationship between contrast and ROE size, higher contrast ARFI imaging is achieved using excitation pulses that are tightly focused in the lateral-elevational plane. However, more tightly focused pushing pulses excite a smaller volume of tissue per push and thus require more pushes, tracking ensembles, and time to acquire ARFI data. To achieve high-contrast ARFI imaging while minimizing the impact on frame rate, rapid multi-focal-zone ARFI imaging was developed [32, 33]. Rosenzweig et al. [33] demonstrated that using rapid multi-focal-zone ARFI acquisitions substantially improves ARFI depth-of-field, increases the contrast-to-noise ratio (CNR) by up to 40% compared to conventional single-focal zone ARFI, and incurs less than 20% loss in contrast compared to sequential multi-focal-zone ARFI. Figure 22.7 shows an example of single-focal-zone and rapid multi-focal-zone images

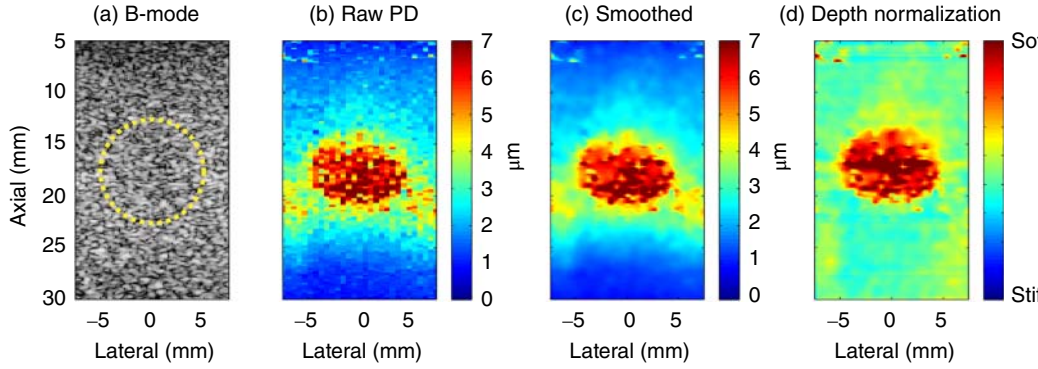

Figure 22.6 B-mode and qualitative ARFI imaging of a phantom with a soft spherical inclusion (8 kPa) embedded in a stiffer background (25 kPa). (a) The spherical inclusion (outlined in dashed line) is nearly invisible on B-mode imaging, but (b) is obvious as an area of increased peak displacement (PD) in the ARFI image. (c) The quality of ARFI imaging can be improved by applying lateral interpolation and a smoothing filter, such as a two-dimensional (1 mm^2) Wiener filter. (d) Finally, depth-dependent gain (DDG) normalization can be applied, in a manner similar to time-gain compensation, to improve the uniformity of the ARFI image through depth.

taken in a stiff, 4 mm cylindrical target. Comparable image quality is achieved in all three rapid multi-focal-zone acquisitions, whereas in the single-focal-zone acquisitions, only the image that is focused on the lesion achieves good image quality. A drawback to using rapid multi-focal-zone ARFI is the acoustic energy output. A two-dimensional multi-focal-zone ARFI image may require more than 100 ARFI excitations. Therefore, the benefits in image quality have to be weighed against the potential for bioeffects when using rapid multi-focal zone ARFI.

Improving ARFI contrast through depth can also be achieved by applying depth-dependent gain (DDG) normalization in a manner similar to time-gain compensation (TGC) that is done in conventional B-mode (see Figure 22.6). During ARFI excitation, a non-uniform force is deposited through depth in the tissue due to focusing and tissue-dependent attenuation, which can lead to spatial gradients in otherwise homogeneous tissue. To account for this, the ARFI displacement response can be normalized by the applied force field [30], which can either be measured experimentally in a phantom or predicted with FEM simulation. While this technique works well in tissue with largely homogeneous attenuation coefficients, it can be challenging in heterogeneous tissues where the applied force field is not so easily predicted.

22.6 Real-time ARFI Imaging

Conventional ARFI pulse sequences require approximately 5 ms of data acquisition per lateral position and, for 40 or more lateral positions spanning the imaging FOV, 200 ms or more to acquire a full ARFI data set. Displacement estimation is also time consuming, but efficient ARFI beam sequencing approaches, combined with graphical processing unit (GPU)-based processing approaches, make real-time ARFI image generation realizable.

22.6.1 Efficient Beam Sequencing

Several beam sequencing schemes have been designed to reduce acquisition time and, because fewer ARFI excitations are needed, reduce heating [34]. One approach exploits parallel-receive acquisition, in which multiple, adjacent A-lines are receive beamformed

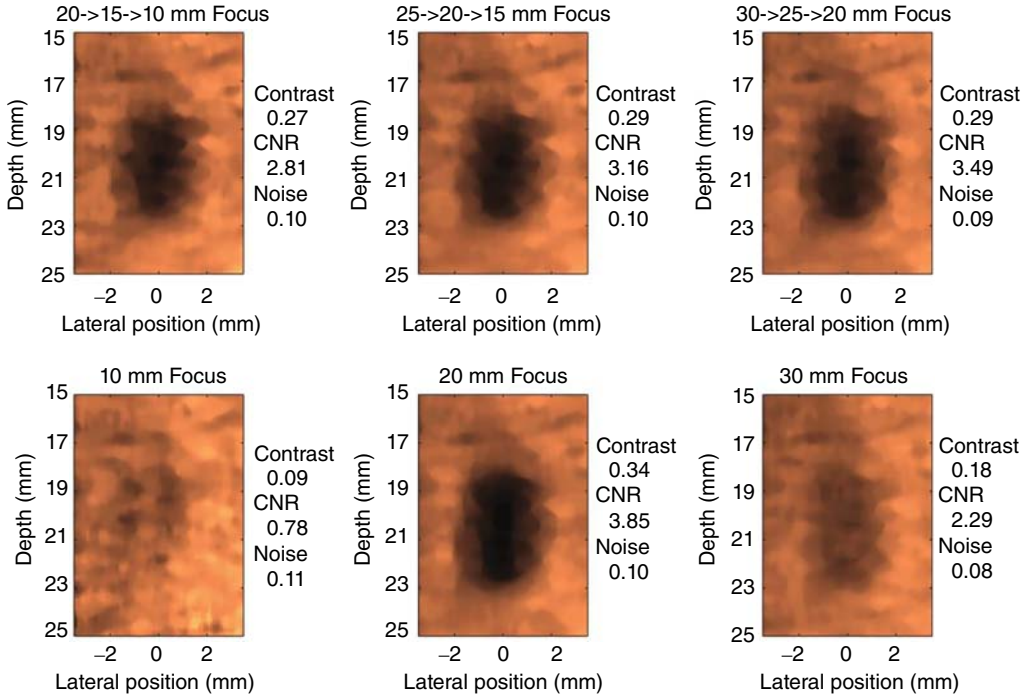

Figure 22.7 ARFI displacement images of a 4 mm cylindrical target, displayed 0.6 ms after force cessation. The top row shows three different multi-focal-zone sequences and the bottom row shows three different triple-push, single-focal-zone sequences. Comparable image quality is achieved in all of the multi-focal-zone images, while in the single-focal-zone cases, the 10 mm and 30 mm sequence show very poor contrast. Source: © 2015 IEEE, reprinted, with permission, from [33].

from a single, wide-transmit pulse [35, 36]. For implementation, the ARFI pushing pulse and the tracking transmit pulse are positioned in the center of the beamformed parallel-receive tracking lines, with displacements in the tracking positions outside the ARF ROE resulting from ARFI-induced shear wave propagation. For systems capable of highly parallelized receive, or "plane wave imaging" [37], shear wave attenuation is the primary limitation to the lateral extent of the observation region.

Another beam sequencing approach to reducing ARFI data acquisition time involves multiplexed displacement tracking. The rationale for multiplexing considers that the majority of relevant information in an ARFI displacement profile resides at the beginning (which encodes the peak induced displacement and thus reflects tissue elasticity) and the end (which is assumed to encode full recovery and is used for rejecting motion artifacts, as described in Section 22.5.1). Therefore, rather than observing the dispensable displacement information in the center of the profile, the tracking position is toggled between two different lateral positions; both experience deformation from different ARFI excitations. Combined with parallel-receive tracking in each of the two tracking locations, this approach may yield a $2N$-fold improvement in ARFI data acquisition time, where N is the number of parallel-receive lines per tracking location. For additional reduction in the number of required ARFI excitations, the two tracking locations may be centered about a common ROE. As in the case of parallel tracking alone, displacements in the tracking locations outside the ARF ROE are induced by propagating shear waves, so shear wave attenuation remains a limitation on the lateral extent of the observation window. Note that plane wave imaging methods may be implemented on relevant systems without multiplexing to observe *full* displacement profiles along the same or larger observation regions, but at the

potential expense of spatial resolution and SNR. The reader is referred to Bouchard et al. [34] for illustrations of the described ARFI beam sequencing methods.

An additional benefit to designing efficient ARFI beam sequencing techniques is the potential for combination-mode imaging [38]. Specifically, ARFI imaging pulse sequences can be designed to simultaneously acquire B-mode, ARFI, and spectral Doppler (to capture anatomical, mechanical, and hemodynamic information, respectively) using the parallelization and multiplexing techniques mentioned above. These combination-mode imaging techniques have specific relevance to vascular and cardiac applications, where combined B-mode and Doppler imaging are currently the clinical gold standard.

22.6.2 GPU-based Processing

These efficient beam-sequencing schemes have been demonstrated to substantially decrease ARFI frame rates and tissue heating with little sacrifice in image quality, which is critical for real-time ARFI applications, but another critical component is computational efficiency. To address the computation time requirements for ARFI processing, ultrasound researchers have turned to using GPUs. GPUs are specialized computer circuits that include hundreds of processing cores for highly parallelized computation. Rosenzweig et al. [39] demonstrated that a GPU-based implementation of the ARFI processing chain can substantially improve computation performance (by approximately 40-fold) and enable ARFI frame rates of less than a second. To achieve this, the authors developed custom implementations of cubic spline interpolation and Loupas' autocorrelation estimator written in Compute Unified Device Architecture (CUDA), a programming interface developed by Nvidia Corporation to facilitate using GPUs for general purpose processing. Using the GPU processing chain, the authors showed that displacement estimate computation was no longer the rate-limiting step; instead, displaying the image to the monitor took the most time due to an additional RAM copy.

The greatest challenge with implementing ARFI on the GPU is the significant development time that is needed to efficiently port algorithms into a parallelized environment. Cubic spline interpolation, for example, is not well suited for parallel execution because the solution is dependent upon all data points. Nevertheless, once a parallel version of a given algorithm is developed, the GPU can serve as a powerful tool to speed up lengthy computations and make real-time implementations feasible.

22.7 Quantitative ARFI Imaging

Because the applied ARF amplitude is tissue-dependent and generally unknown, ARFI imaging methods that monitor induced displacements in the ROE are limited to qualitative analysis of tissue stiffness. However, quantitative assessment of tissue elasticity is possible by exploiting ARFI-induced shear wave propagation [40–42], as in shear wave elasticity imaging (SWEI) [40]. This approach takes advantage of the fact that the shear wave velocity (SWV) is proportional to the stiffness of the propagating tissue medium. Specifically, for a homogeneous, isotropic, linear elastic material with Poisson's ratio of 0.5, the Young's modulus, E, is related to the SWV according to $E = 3 \times {c_T}^2 \rho$, where c_T is the SWV and ρ is the material density [43].

Originally, SWV was measured by inversion of the wave equation [44], but large jitter error and associated variability in shear wave speed estimates are problematic. Therefore, SWV is now generally estimated using time-of-flight algorithms [45–49], which measure the shear wave arrival time (time of peak displacement) in multiple lateral positions outside of the ARFI ROE. A linear regression is then performed to determine the slope of the relationship between arrival time and distance from the ROE, and from the inverse slope, shear wave velocity is estimated

(Figure 22.8). The size of the linear regression kernel is relevant to SWV estimation performance [50]. The larger the kernel, the more precise the SWV estimate, provided that the tissue medium is homogeneous. However, applied to inhomogeneous media, large linear regression kernels result in averaging. Therefore, there is a tradeoff between spatial resolution and SWV estimation precision. To improve the robustness of shear wave speed measurement in the case of noisy data, and enable smaller linear regression kernel sizes, algorithms such as RANSAC [49] or the Radon sum transform [51] have been employed to reject outliers.

The data sets acquired to measure shear wave velocity are similar to those obtained for qualitative ARFI imaging. The beam sequencing methods for SWV measurement can use the same reference, pushing, and tracking pulses as used for qualitative ARFI imaging. The primary difference is that the tracking pulses are positioned lateral to, rather than centered on, the ROE (Figure 22.9). For systems only capable of single A-line receive beamforming, multiple ARFI excitations are needed in each ROE so that shear wave-induced displacements may be observed in multiple lateral positions for time-of-flight calculation. For systems capable of highly parallelized receive beamforming, the induced shear wave propagation is observed across multiple lateral tracking locations simultaneously, so only one ARFI excitation may be needed to measure SWV across a region of interest spanning as much as 2 cm × 2 cm. Limiting this range is shear wave attenuation, which is material dependent, and the requirement for high displacement SNR for elastic reconstruction algorithms. Beam sequencing methods that exploit plane wave imaging capabilities to combine qualitative ARFI with shear wave velocity information are anticipated [31].

22.8 ARFI Imaging in Clinical Applications

The clinical utilities of both qualitative ARFI and quantitative SWV estimation have been demonstrated in numerous applications. Generally speaking, qualitative ARFI achieves finer spatial resolution and is therefore relevant for applications in which structural information is important, as in delineating the structure and composition of atherosclerotic plaques [52–54]. However, quantitative imaging is advantageous for longitudinal and cross-sectional analyses of tissue elastic properties, where variations in the magnitude and distribution of ARF from time point to time point or from subject to subject can confound comparisons. Also, quantitative metrics may have diagnostic meaning, as in staging advanced liver fibrosis [55]. Other clinical applications of qualitative and quantitative ARFI imaging include: liver and kidney [56, 57], breast [58], prostate [59], cardiac [60] and skeletal [61] muscle, nerves [32], skin [62], ablation monitoring [63–65], and vasculature [52–54]. We herein provide an in-depth overview of the challenges and opportunities unique to clinical ARFI imaging in the context of one of the first proposed ARFI applications, atherosclerosis imaging. For brevity, we do not provide a similar review of other clinical ARFI applications, but the reader is encouraged to pursue the above-referenced sources for more information.

Cardio- and cerebro-vascular diseases (CVD) are among the leading causes of death and disability around the world. It has been shown that plaques composed of large, mechanically soft necrotic cores covered by thin fibrous caps have a propensity to rupture and induce cardiovascular accidents such as heart attack or stroke. Because the mechanical properties of atherosclerotic plaques are inherently tied to their rupture potential, many groups have proposed using elasticity-based imaging techniques to improve plaque vulnerability staging.

Indeed, one of the first clinical applications for ARFI, proposed by Trahey et al. [66], was arterial plaque characterization. The initial studies were performed ex vivo in femoral and popliteal arteries acquired from amputated human legs, and showed that regions of higher displacement (i.e. qualitatively soft) correlated with areas of lipid/necrotic core from matched histological

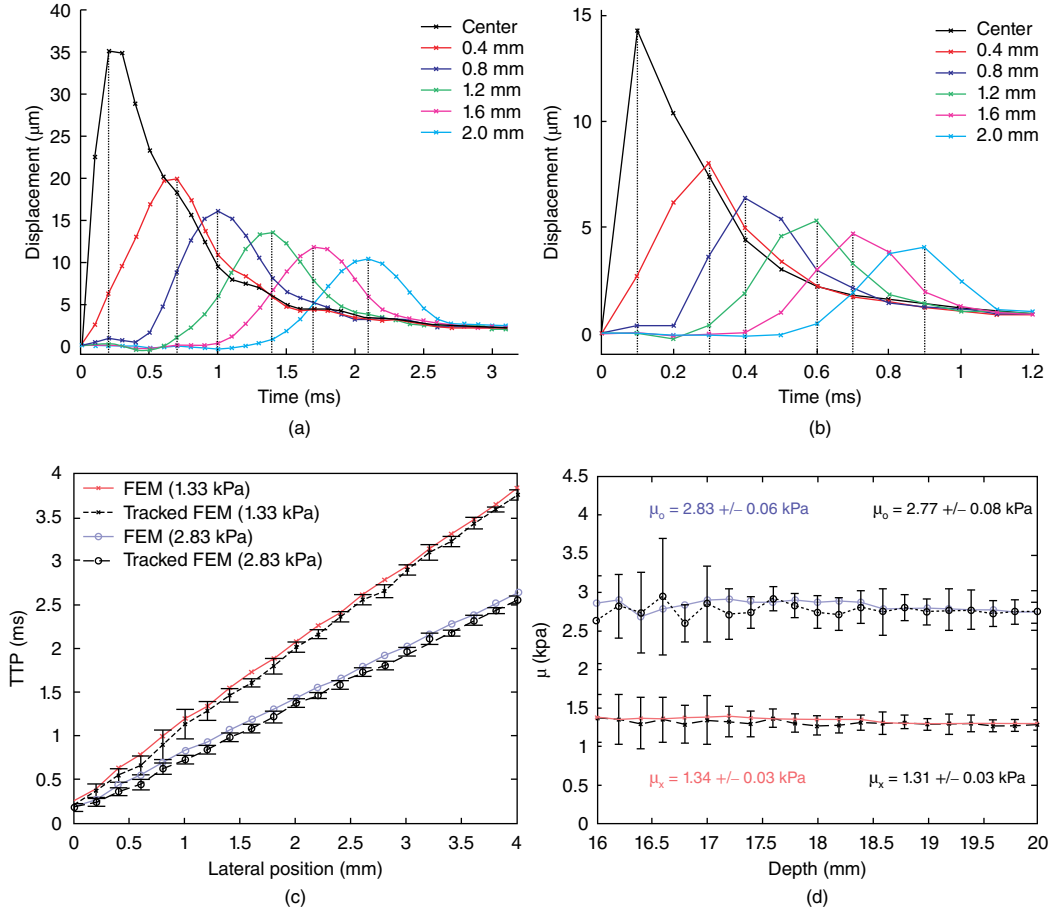

Figure 22.8 Top row: simulated displacement through time profiles, without ultrasonic tracking, at lateral positions offset from the excitation location for elastic media with shear moduli of (a) 1.33 kPa and (b) 8 kPa. Notice that the curve appears more finely sampled in the more compliant medium (1.33 kPa) because of its slower propagation speed and the fixed 10 kHz temporal sampling (simulating a fixed PRF in the experimental system). The vertical dotted lines indicate the TTP values that would be estimated from this data, although experimentally the data would be upsampled using a low-pass interpolation from the acquired PRF to 50 kHz. Notice that the two plots are on different time scales. Bottom row: (c) time of peak displacement at the focal depth (20 mm) as a function of lateral position in simulation data for elastic materials, with shear moduli of 1.33 kPa and 2.83 kPa. The inverse slopes of these lines represent the shear wave speeds in these materials. (d) Reconstructed shear moduli over depths from 16 to 20 mm using the time to peak displacement data at lateral ranges from 2 to 8 mm outside of the ROE to estimate the shear wave speed for elastic materials with 1.33 (x) and 2.83 (o) kPa shear moduli. The raw FEM data are represented by the (x) and (o) lines, with the mean ± one standard deviation shear modulus estimates over the range of depths represented in each colored text box. The corresponding ultrasonic displacement-tracked data, using 20 independent speckle realizations, is shown in the black lines. Source: figure reproduced with permission from [31].

sections, while regions of lower displacement (i.e. qualitatively stiff) correlated with areas of fibrosis and calcification. Subsequent studies done both ex vivo and in vivo in a porcine model of atherosclerosis corroborated the initial findings [67, 68]. To quantify sensitivity and specificity of ARFI to various plaque features, Behler et al. [69] performed a study in which trained, blinded readers scored ex vivo ARFI images for various plaque components. The results showed that ARFI was most sensitive to calcification (sens: 96%, spec: 85%), slightly less sensitive to lipid core (80%, 86%) and fibrous cap (86%, 82%), and least sensitive to general fibrosis (78%, 77%).

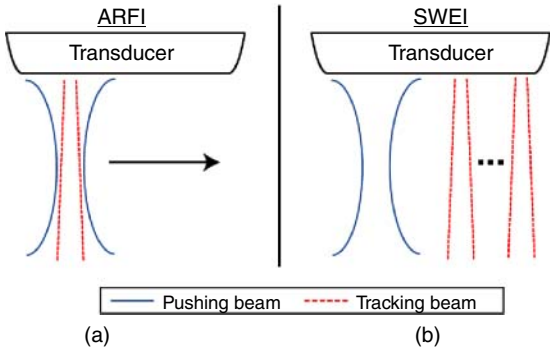

Figure 22.9 Illustration depicting two beam sequencing approaches for (a) qualitative and (b) quantitative ARFI imaging. (a) Qualitative ARFI imaging involves tracking ARF-induced displacement within the region of excitation, and translating both the pushing and tracking location to build a 2D image. (b) Quantitative ARFI imaging, also referred to as shear wave elasticity imaging (SWEI), involves tracking shear wave induced displacement outside of the region of the excitation. Displacements from at least two lateral positions are used to measure shear wave velocity. Source: image adapted from [85].

Interestingly, ARFI was also reported to be sensitive to detecting degraded internal elastic lamina (IEL, 92%, 75%). The IEL is a thin layer of elastin that separates the intima and media and, when disrupted, is associated with increased plaque rupture risk [70].

The first in vivo ARFI images of human atherosclerotic plaque were reported by Dahl et al. [71] in the carotids and Dumont et al. [72] in the popliteals. Neither of these studies were done with matched histology, but subsequent in vivo clinical studies performed in patients undergoing carotid endarterectomy (CEA) [53] and carotid magnetic resonance imaging (MRI) [54] independently demonstrated that ARFI displacements correlate with underlying plaque compositional elements. Figure 22.10 shows the imaging results from the right internal carotid artery (ICA) of a symptomatic 57-year-old male. B-mode imaging shows a generally echolucent plaque, with two bright echogenic foci located 9.8 mm apart. ARFI imaging shows that the plaque exhibits generally low PD throughout (mean PD: 1.25 ± 0.7 μm), with the exception of a higher displacing region above the left-most echogenic foci (mean PD: 3.11 ± 3.6 μm). Histology confirms the presence of two sizable calcium deposits that correlate with the two echogenic foci in the B-mode image. Directly above the left-most calcification there is a necrotic core that extends around the right side of the plaque and spatially corresponds to the area of higher PD in the ARFI image. The leftmost part of the plaque consists mostly of collagen fibers corroborating the small displacements seen in the ARFI image.

While these preliminary efforts have shown promising results for using ARFI for plaque characterization, there are substantial challenges. First, heavy arterial calcification and shadowing may prevent ARFI from accurately characterizing plaque. Calcification is known to have high ultrasonic attenuation, which, when performing ARFI, can hamper delivery of radiation force to areas behind the calcification, potentially reducing ARFI's ability to fully characterize the plaque. Thus, the position of calcium deposits, which are usually apparent as hyperechoic regions in conventional B-mode imaging, should be considered carefully when performing ARFI imaging. Second, the proximal wall can often be obscured with clutter from overlying tissues and make the lumen/plaque border difficult to identify. Implementing harmonic ARFI imaging, as described in Section 22.3.3, has been shown to achieve substantial clutter reduction and improve delineation of the lumen in ARFI atherosclerosis imaging [24]. Third, due to the heterogeneous nature of plaques, shear wave reflections may influence the temporal response measured in a given ARFI ensemble. Improved motion rejection methods, including methods that implement directional filters, such as those that have been developed for shear wave-based imaging methods [73], may be relevant to improving assessment of the dynamic response of tissue. Finally, due to physiological pulsation of the arterial wall, motion artifact may be present in ARFI displacement profiles. To minimize physiological motion and improve reproducibility, vascular ARFI images can be gated to diastole.

A common question regarding the application of ARFI to atherosclerosis imaging relates to the potential for the ARFI excitation to induce rupture. The question was evaluated by

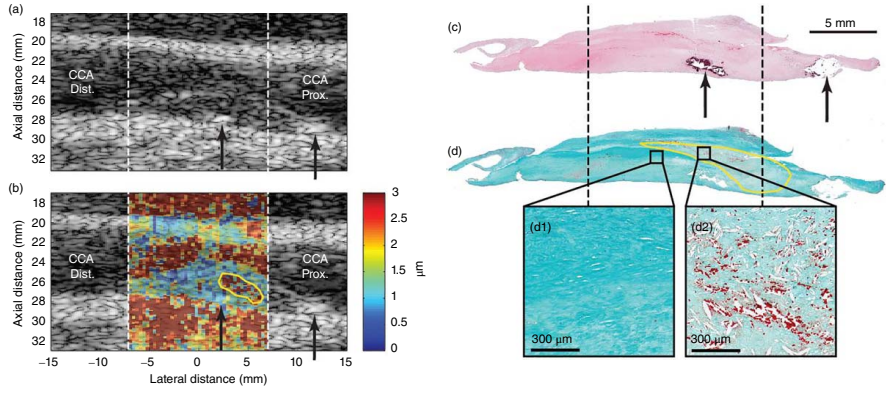

Figure 22.10 ARFI image of carotid plaque from the common carotid artery (CCA) of a 57-year-old symptomatic male. (a) B-mode imaging shows an echolucent plaque with two echogenic foci located ~10 mm apart (black arrows) suggesting calcification. (b) Hybrid B-mode/ARFI peak displacement images show a plaque with generally low displacement except for an area of higher displacement located on the right (outline) suggesting a lipid/necrotic core covered with a stiffer fibrous cap. (c) H&E staining confirms the presence of two calcifications (black arrows), while (d) combined Masson's staining shows a necrotic region (outline) located above the leftmost calcification underneath a fibrous cap. Inset panels show a magnification of fibrotic (d1) and necrotic regions (d2). The necrotic region is characterized by cholesterol clefts and free erythrocytes suggesting intra-plaque hemorrhage (d2). Source: image adapted from [53].

Doherty et al. [74]. In this study, the authors segmented a number of plaque geometries taken from the MRI literature and implemented them in the ARFI FEM framework developed by Palmeri et al. [4] to determine the maximum stress imparted on the fibrous cap by ARFI. The results demonstrated that the maximum von Mises stress imparted by an ARFI excitation on fibrous caps was <1.2 kPa, which, compared to the circumferential stress from blood pulsation, was much smaller. In the biomechanics literature, a value of 300 kPa is typically cited as the critical stress necessary to cause plaque rupture [75]. While ARFI plaque imaging has not had any adverse events reported to date, the ALARA principle ("as low as reasonably achievable") should always be implemented to minimize patient risk [76].

22.9 Commercial Implementation

ARFI imaging has been translated to commercial ultrasound systems in the form of the Virtual Touch™ and Virtual Touch IQ™ tissue imaging and quantification tools that are available on the Siemens S2000 and S3000 scanner models (Siemens Medical Solutions, USA Inc. Ultrasound Division). Using Virtual Touch™, a qualitative grayscale map of relative stiffness for a user-defined region of interest is produced. With Virtual Touch IQ™, the velocities of shear waves induced by ARFI within a user-defined region of interest are displayed as a color-coded velocity map, enabling subjective assessment of stiffness. Virtual Touch™ was cleared by the US Food and Drug Administration (FDA) in 2013 for use in abdominal, breast, thyroid, small parts, and musculoskeletal exams, but the technology has been commercially available in Europe and Asia since 2008. In addition to Siemens, Philips Ultrasound has developed a radiation force-based shear wave elastography product, ElastPQ™, which is available on the iU22 system (Philips Ultrasound, Inc., Bothell Washington). Using ElastPQ™, the average and standard deviation shear wave velocity or Young's modulus are measured in a region of interest, with application to assessing liver fibrosis. The commercial availability of ARFI imaging tools has enabled greater breadth of clinical investigation into relevant ARFI applications, conducted by research groups worldwide.

22.10 Related Technologies

Several related ultrasound imaging methods exploit ROE displacements induced by impulsive acoustic radiation force to assess tissue mechanical property.

In ARFI Surveillance of Subcutaneous Hemorrhage (ASSH) [77–80], elevated jitter variance in ARFI-induced displacement profiles detects the presence of subcutaneous hemorrhage. By mapping the detected hemorrhagic cross-sectional area versus time, bleeding dynamics (rate of bleeding and time to hemostasis) are measured.

In Kinetic Acoustic Vitroretinal Examination (KAVE) [81, 82], several successive acoustic pulses per lateral location are used to induce a steady-state tissue displacement. Assuming that the ARFI forces approximated a temporal step function and that tissue could be described discretely by the Voigt model, images were generated of force-free parameters depicting the time constant, damping ratio, and natural frequency of homogeneous tissue mimicking material.

Similarly, in Monitored Steady-State Excitation Recovery (MSSER) ultrasound [83], a material creep test is mimicked using multiple successive ARF excitations. In concert with Young's modulus data provided through shear wave velocity measurement, mechanical properties, including time constants, elasticity, and viscosity, were estimated in calibrated tissue-mimicking materials and in excised muscle.

Using fewer ARF excitations than MSSER, Viscoelastic Response (VISR) ultrasound [84] also approximates a creep response to assess the viscoelastic properties of tissue. In the VisR

approach, the dynamic response of tissue to two successive ARF excitations, separated in time by less than 1 ms and delivered to the same ROE, is fitted to the mass-spring-damper model to estimate viscoelastic properties.

These methods and their applications are in continued development. Methods related to quantitative shear wave velocity imaging are presented in Chapters 15, 16, 19–21, and 23–25.

22.11 Conclusions

ARFI ultrasound exploits impulsive, focused acoustic radiation force excitations to induce, with temporal and spatial precision, micrometer-scale tissue displacements that are tracked, conventionally by correlation-based time delay estimators. The estimated displacements in and near the ROE qualitatively reflect tissue stiffness, and displacement estimates outside the ROE support quantitative measures of SWV. Factors impacting ARFI performance include displacement resolution and underestimation, clutter artifact, and physiological motion; however, potential detrimental effects have been minimized by biased displacement estimators, large excitation relative to tracking beam focal configurations, harmonic tracking, and motion rejection algorithms, respectively. ARFI achieves higher image contrast using excitation pulses that are tightly focused in the lateral-elevational plane, although with a tradeoff in frame rate unless rapid multi-focal zone imaging is implemented. Efficient beam sequencing combined with GPU processing make ARFI real-time realizable, and the imaging method has been implemented on commercial ultrasound scanners. ARFI imaging has been demonstrated in numerous clinical applications, and progress in the field is rapidly advancing.

References

1 Nightingale, K., Soo, M.S., Nightingale, R., and Trahey, G. (2002). Acoustic radiation force impulse imaging: in vivo demonstration of clinical feasibility. *Ultrasound Med. Biol.* 28 (2): 227–235.

2 Nyborg, W. (1965). Acoustic streaming. In: *Physcial Acoustics* IIB (ed. W. Mason), 265–311. New York: Academic Press.

3 Sarvazyan, A.P., Rudenko, O.V., and Nyborg, W.L. (2010). Biomedical applications of radiation force of ultrasound: historical roots and physical basis. *Ultrasound Med. Biol.* 36 (9): 1379–1394.

4 Palmeri, M.L., Sharma, A.C., Bouchard, R.R., et al. (2005). A finite-element method model of soft tissue response to impulsive acoustic radiation force. *IEEE Trans. Ultrason., Ferroelect., Freq. Control* 52 (10): 1699–1712.

5 Palmeri, M.L., and Nightingale, K.R. (2004). On the thermal effects associated with radiation force imaging of soft tissue. *IEEE Trans. Ultrason., Ferroelect., Freq. Control* 51 (5): 551–565.

6 Palmeri, M.L., Frinkley, K.D., and Nightingale K.R. (2004). Experimental studies of the thermal effects associated with radiation force imaging of soft tissue. *Ultrason. Imaging* 26 (2): 100–114.

7 Church, C.C., Labuda, C., and Nightingale, K. (2012). Should the mechanical index be revised for ARFI imaging? In: *IEEE International Ultrasonics Symposium, IUS*, 17–20.

8 Deng, Y., Palmeri, M.L., Rouze, N.C., et al. (2015). Analyzing the impact of increasing mechanical index and energy deposition on shear wave speed reconstruction in human liver. *Ultrasound Med. Biol.* 41 (7): 1948–1957.

9 Pinton, G.F., Dahl, J.J., and Trahey G.E. (2006). Rapid tracking of small displacements with ultrasound. *IEEE Trans. Ultrason., Ferroelect., Freq. Control* 53 (6): 1103–1117.

10 Walker W.F. and Trahey G.E. (1995). A fundamental limit on delay estimation using partially correlated speckle signals. *IEEE Trans. Ultrason., Ferroelect., Freq. Control* 42 (2): 301–308.

11 Jensen, J.A. (1993). Range velocity limitations for time-domain blood velocity estimation. *Ultrasound Med. Biol.* 19 (9): 741–749.

12 Loupas T., Peterson, R.B., and Gill R.W. (2000). Experimental evaluation of velocity and power estimation for ultrasound blood flow imaging, by means of a two-dimensional autocorrelation approach. *IEEE Trans. Ultrason., Ferroelect., Freq. Control* 42 (4): 689–699.

13 Kasai, C., Namekawa, K., Koyano, A., and Omoto, R. (1985). Real-time two-dimensional blood-flow imaging using an auto-correlation technique. *IEEE Trans. Sonics Ultrason.* 32 (3): 458–464.

14 Byram, B., Trahey, G., and Palmeri, M. (2013). Bayesian speckle tracking. Part I: An implementable perturbation to the likelihood function for ultrasound displacement estimation. *IEEE Trans. Ultrason. Ferroelect. Freq. Control* 60 (1): 132–143.

15 Byram, B., Trahey, G., and Palmeri, M. (2013). Bayesian speckle tracking. Part II: Biased ultrasound displacement estimation. *IEEE Trans. Ultrason., Ferroelect., Freq. Control* 60 (1): 144–157.

16 McAleavey, S.A., Nightingale, K.R., and Trahey, G.E. (2003). Estimates of echo correlation and measurement bias in acoustic radiation force impulse imaging. *IEEE Trans. Ultrason., Ferroelect., Freq. Control* 50 (6): 631–641.

17 Dhanaliwala, A., Hossack, J., and Mauldin, F. (2012). Assessing and improving acoustic radiation force image quality using a 1.5-D transducer design. *IEEE Trans. Ultrason., Ferroelect., Freq. Control* 59 (7): 1602–1608.

18 Palmeri, M.L., McAleavey, S.A., Fong, K.L., et al. (2006). Dynamic mechanical response of elastic spherical inclusions to impulsive acoustic radiation force excitation. *IEEE Trans. Ultrason., Ferroelect., Freq. Control* 53 (11): 2065–2079.

19 Palmeri, M.L., McAleavey, S.A., Trahey, G.E., and Nightingale, K.R. (2006). Ultrasonic tracking of acoustic radiation force-induced displacements in homogeneous media. *IEEE Trans. Ultrason., Ferroelect., Freq. Control* 53 (7): 1300–1313.

20 Czernuszewicz, T.J., Streeter, J.E., Dayton, P.A., and Gallippi, C.M. (2013). Experimental validation of displacement underestimation in ARFI ultrasound. *Ultrason. Imaging* 35 (3): 196–213.

21 Mauldin, F.W., Viola, F., and Walker, W.F. (2009). Reduction of echo decorrelation via complex principal component filtering. *Ultrasound Med. Biol.* 35 (8): 1325–1343.

22 Mauldin, F.W., Viola, F., and Walker, W.F. (2010). Complex principal components for robust motion estimation. *IEEE Trans. Ultrason., Ferroelect., Freq. Control* 57 (11): 2437–2449.

23 Lediju, M.A., Pihl, M.J., Dahl, J.J., and Trahey, G.E. (2008). Quantitative assessment of the magnitude, impact and spatial extent of ultrasonic clutter. *Ultrason. Imaging* 30 (3): 151–168.

24 Doherty, J.R., Dahl, J.J., and Trahey, G.E. (2013). Harmonic tracking of acoustic radiation force-induced displacements. *IEEE Trans. Ultrason., Ferroelect., Freq. Control* 60 (11): 2347–2358.

25 Jensen, J.A. (1996). *Estimation of Blood Velocities Using Ultrasound*. New York, NY: Cambridge University Press.

26 Gallippi, C.M., Nightingale, K.R., and Trahey, G.E. (2003). Adaptive filtering of physiological and ARFI-induced tissue and blood motion in vivo. *Ultrasound Med. Biol.* 29 (11): 1583–1592.

27 Tranquart, F., Grenier, N., Eder, V., and Pourcelot, L. (1999). Clinical use of ultrasound tissue harmonic imaging. *Ultrasound Med. Biol.* 25 (6): 889–894.

28 Giannantonio, D.M., Dumont, D.M., Trahey, G.E., and Byram, B.C. (2011). Comparison of physiological motion filters for in vivo cardiac ARFI. *Ultrason. Imaging* 33: 89–108.

29 Fahey, B.J., Palmeri, M.L., and Trahey, G.E. (2007). The impact of physiological motion on tissue tracking during radiation force imaging. *Ultrasound Med. Biol.* 33 (7): 1149–1166.

30 Nightingale, K., Palmeri, M., and Trahey, G. (2006). Analysis of contrast in images generated with transient acoustic radiation force. *Ultrasound Med. Biol.* 32 (1): 61–72.

31 Nightingale, K. (2011). Acoustic radiation force impulse (ARFI) imaging: a review. *Curr. Med. Imaging Rev.* 7 (4): 328–339.

32 Palmeri, M.L., Dahl, J.J., MacLeod, D.B., et al. (2009). On the feasibility of imaging peripheral nerves using acoustic radiation force impulse imaging. *Ultrason. Imaging* 31 (3): 172–182.

33 Rosenzweig, S., Palmeri, M.L., and Nightingale, K.R. (2015). Analysis of rapid multi-focal-zone ARFI imaging. *IEEE Trans. Ultrason., Ferroelect., Freq. Control* 62 (2): 280–289.

34 Bouchard, R.R., Dahl, J., Hsu, S., et al. (2009). Image quality, tissue heating, and frame rate trade-offs in acoustic radiation force impulse imaging. *IEEE Trans. Ultrason., Ferroelect., Freq. Control* 56: 63–76.

35 Shattuck, D.P., Weinshenker, M.D., Smith, S.W., and von Ramm, O.T. (1984). Explososcan: a parallel processing technique for high speed ultrasound imaging with linear phased arrays. *J. Acoust. Soc. Am.* 75 (4): 1273–1282.

36 Dahl, J.J., Pinton, G.F., Palmeri, M.L., et al. (2007). A parallel tracking method for acoustic radiation force impulse imaging. *IEEE Trans. Ultrason., Ferroelect., Freq. Control* 54 (2): 301–311.

37 Tanter, M. and Fink, M. (2014). Ultrafast imaging in biomedical ultrasound. *IEEE Trans. Ultrason., Ferroelect., Freq. Control* 61 (1): 102–119.

38 Dumont, D.M., Doherty, J.R., and Trahey, G.E. (2011). Noninvasive assessment of wall-shear rate and vascular elasticity using combined ARFI/SWEI/spectral Doppler imaging system. *Ultrason. Imaging* 33 (3): 165–188.

39 Rosenzweig, S., Palmeri, M., and Nightingale, K. (2011). GPU-based real-time small displacement estimation with ultrasound. *IEEE Trans. Ultrason., Ferroelect., Freq. Control* 58 (2): 399–405.

40 Sarvazyan, A.P., Rudenko, O.V., Swanson, S.D., et al. (1998). Shear wave elasticity imaging: a new ultrasonic technology of medical diagnostics. *Ultrasound Med. Biol.* 24 (9): 1419–1435.

41 Nightingale, K., McAleavey, S., and Trahey, G. (2003). Shear-wave generation using acoustic radiation force: in vivo and ex vivo results. *Ultrasound Med. Biol.* 29 (12): 1715–1723.

42 Bercoff, J., Tanter, M., and Fink, M. (2004). Supersonic shear imaging: a new technique for soft tissue elasticity mapping. *IEEE Trans. Ultrason., Ferroelect., Freq. Control* 51 (4): 396–409.

43 Lai, W., Rubin, D., and Krempel, E. (1999). *Introduction to Continuum Mechanics*. Burlington, MA: Butterworth-Heinmann.

44 Oliphant, T.E., Manduca, A., Ehman, R.L., and Greenleaf, J.F. (2001). Complex-valued stiffness reconstruction for magnetic resonance elastography by algebraic inversion of the differential equation. *Magn. Reson. Med.* 45 (2): 299–310.

45 McLaughlin, J. and Renzi, D. (2006). Shear wave speed recovery in transient elastography and supersonic imaging using propagating fronts. *Inverse Probl.* 22 (2): 681–706.

46 McLaughlin, J. and Renzi, D. (2006). Using level set based inversion of arrival times to recover shear wave speed in transient elastography and supersonic imaging. *Inverse Probl.* 22 (2): 707–725.

47 Palmeri, M.L., Wang, M.H., Dahl, J.J., et al. (2008). Quantifying hepatic shear modulus in vivo using acoustic radiation force. *Ultrasound Med. Biol.* 34 (4): 546–558.

48 Tanter, M., Bercoff, J., Athanasiou, A., et al. (2008). Quantitative assessment of breast lesion viscoelasticity: initial clinical results using supersonic shear imaging. *Ultrasound Med. Biol.* 34 (9): 1373–1386.

49 Wang, M.H., Palmeri, M.L., Rotemberg, V.M., et al. (2010). Improving the robustness of time-of-flight based shear wave speed reconstruction methods using RANSAC in human liver in vivo. *Ultrasound Med. Biol.* 36 (5): 802–813.

50 Rouze, N.C., Wang, M.H., Palmeri, M.L., and Nightingale, K.R. (2012). Parameters affecting the resolution and accuracy of 2-D quantitative shear wave images. *IEEE Trans. Ultrason., Ferroelect., Freq. Control* 59 (8): 1729–1740.

51 Rouze, N.C., Wang, M.H., Palmeri, M.L., and Nightingale, K.R. (2010). Robust estimation of time-of-flight shear wave speed using a Radon sum transformation. *IEEE Trans. Ultrason., Ferroelect., Freq. Control* 57 (12): 2662–2670.

52 Allen, J.D., Ham, K.L., Dumont, D.M., et al. (2011). The development and potential of acoustic radiation force impulse (ARFI) imaging for carotid artery plaque characterization. *Vasc. Med.* 16 (4): 302–311.

53 Czernuszewicz, T.J., Homeister, J.W., Caughey, M.C., et al. (2015). Non-invasive in vivo characterization of human carotid plaques with acoustic radiation force impulse ultrasound: comparison with histology after endarterectomy. *Ultrasound Med. Biol.* 41 (3): 685–697.

54 Doherty, J.R., Dahl, J.J., Kranz, P.G., et al. (2015). Comparison of acoustic radiation force impulse imaging derived carotid plaque stiffness with spatially registered MRI determined composition. *IEEE Trans. Med. Imaging* 34 (11): 2354–2365.

55 Palmeri, M.L., Wang, M.H., Rouze, N.C., et al. (2011). Noninvasive evaluation of hepatic fibrosis using acoustic radiation force-based shear stiffness in patients with nonalcoholic fatty liver disease. *J. Hepatol.* 55 (3): 666–672.

56 Fahey, B.J., Nightingale, K.R., Nelson, R.C., et al.(2005). Acoustic radiation force impulse imaging of the abdomen: demonstration of feasibility and utility. *Ultrasound Med. Biol.* 31 (9): 1185–1198.

57 Fahey, B.J., Nelson, R.C., Bradway, D.P., et al. (2008). In vivo visualization of abdominal malignancies with acoustic radiation force elastography. *Phys. Med. Biol.* 53 (1): 279–293.

58 Sharma, A., Soo, M., Trahey, G., and Nightingale, K. (2004). Acoustic radiation force impulse imaging of in vivo breast masses. *IEEE Ultrason., Ferroelect., Freq. Control: Joint Symposium* 1: 728–731.

59 Zhai, L., Polascik, T.J., Foo, W.-C., et al. (2012). Acoustic radiation force impulse imaging of human prostates: initial in vivo demonstration. *Ultrasound Med. Biol.* 38 (1): 50–61.

60 Hsu, S.J., Bouchard, R.R., Dumont, D.M., et al. (2007). In vivo assessment of myocardial stiffness with acoustic radiation force impulse imaging. *Ultrasound Med. Biol.* 33 (11): 1706–1719.

61 Nightingale, K., Nightingale, R., Stutz, D., and Trahey, G. (2002). Acoustic radiation force impulse imaging of in vivo vastus medialis muscle under varying isometric load. *Ultrason. Imaging* 24 (2): 100–108.

62 Lee, S.Y., Cardones, A.R., Doherty, J., et al. (2015). Preliminary results on the feasibility of using ARFI/SWEI to assess cutaneous sclerotic diseases. *Ultrasound Med. Biol.* 41 (11): 2806–2819.

63 Fahey, B.J., Nelson, R.C., Hsu, S.J., et al. (2008). In vivo guidance and assessment of liver radio-frequency ablation with acoustic radiation force elastography. *Ultrasound Med. Biol.* 34 (10): 1590–1603.

64 Bing, K.F., Rouze, N.C., Palmeri, M.L., et al. (2011). Combined ultrasonic thermal ablation with interleaved ARFI image monitoring using a single diagnostic curvilinear array: a feasibility study. *Ultrason. Imaging* 33 (4): 217–232.

65 Eyerly, S.A., Bahnson, T.D., Koontz, J.I., et al. (2014). Contrast in intracardiac acoustic radiation force impulse images of radiofrequency ablation lesions. *Ultrason. Imaging* 36 (2): 133–148.

66 Trahey, G.E., Palmeri, M.L., Bentley, R.C., and Nightingale, K.R. (2004). Acoustic radiation force impulse imaging of the mechanical properties of arteries: in vivo and ex vivo results. *Ultrasound Med. Biol.* 30 (9): 1163–1171.

67 Dumont, D., Behler, R.H., Nichols, T.C., et al. (2006). ARFI imaging for noninvasive material characterization of atherosclerosis. *Ultrasound Med. Biol.* 32 (11): 1703–1711.

68 Behler, R.H., Nichols, T.C., Zhu, H., et al. (2009). ARFI imaging for noninvasive material characterization of atherosclerosis. Part II: toward in vivo characterization. *Ultrasound Med. Biol.* 35 (2): 278–295.

69 Behler, R.H., Czernuszewicz, T.J., Wu, C.-D., et al. (2013). Acoustic radiation force beam sequence performance for detection and material characterization of atherosclerotic plaques: preclinical, ex vivo results. *IEEE Trans. Ultrason., Ferroelect., Freq. Control* 60 (12): 2471–2487.

70 Moreno, P.R., Purushothaman, K.R., Fuster, V., and O'Connor, W.N. (2002). Intimomedial interface damage and adventitial inflammation is increased beneath disrupted atherosclerosis in the aorta: implications for plaque vulnerability. *Circulation* 105 (21): 2504–2511.

71 Dahl, J.J., Dumont, D.M., Allen, J.D., et al. (2009). Acoustic radiation force impulse imaging for noninvasive characterization of carotid artery atherosclerotic plaques: a feasibility study. *Ultrasound Med. Biol.* 35 (5): 707–716.

72 Dumont, D., Dahl, J., Miller, E., et al. (2009). Lower-limb vascular imaging with acoustic radiation force elastography: demonstration of in vivo feasibility. *IEEE Trans. Ultrason., Ferroelect., Freq. Control* 56 (5): 931–944.

73 Deffieux, T., Gennisson, J.L., Bercoff, J., and Tanter, M. (2011). On the effects of reflected waves in transient shear wave elastography. *IEEE Trans. Ultrason., Ferroelect., Freq. Control* 58 (10): 2032–2035.

74 Doherty, J.R., Dumont, D.M., Trahey, G.E., and Palmeri M.L. (2013). Acoustic radiation force impulse imaging of vulnerable plaques: a finite element method parametric analysis. *J. Biomech.* 46 (1): 83–90.

75 Cardoso, L. and Weinbaum, S. (2014). Changing views of the biomechanics of vulnerable plaque rupture: A review. *Ann. Biomed. Eng.* 42 (2): 415–431.

76 Nelson, T.R., Fowlkes, J.B., Abramowicz, J.S., and Church, C.C. (2009). Ultrasound biosafety considerations for the practicing sonographer and sonologist. *J. Ultrasound Med.* 28 (2): 139–150.

77 Behler, R.H., Scola, M.R., Nichols, T.C., et al. (2009). ARFI ultrasound for in vivo hemostasis assessment postcardiac catheterization, part II: pilot clinical results. *Ultrason. Imaging* 31 (3): 159–171.

78 Behler, R.H., Scola, M.R., Nichols, T.C., et al. (2009). ARFI ultrasound for in vivo hemostasis assessment postcardiac catheterization, part I: preclinical studies. *Ultrason. Imaging* 31 (3): 153–158.

79 Scola, M.R., Nichols, T.C., Zhu, H., et al. (2011). ARFI ultrasound monitoring of hemorrhage and hemostasis in vivo in canine von Willebrand disease and hemophilia. *Ultrasound Med. Biol.* 37 (12): 2126–2132.

80 Scola, M.R., Baggesen, L.M., Nichols, T.C., et al. (2012). A review of current methods for assessing hemostasis in vivo and introduction to a potential alternative approach. *Thromb. Res.* 129 (Suppl.): S57–61.

81 Viola, F. and Walker, W.F. (2003). Radiation force imaging of viscoelastic properties with reduced artifacts. *IEEE Trans. Ultrason., Ferroelect., Freq. Control* 50 (6): 736–742.

82 Walker, W.F., Fernandez, F.J., and Negron, L.A. (2000). A method of imaging viscoelastic parameters with acoustic radiation force. *Phys. Med. Biol.* 45 (6): 1437–1447.

83 Mauldin, F.W., Haider, M.A., Loboa, E.G., et al. (2008). Monitored steady-state excitation and recovery (MSSER) radiation force imaging using viscoelastic models. *IEEE Trans. Ultrason., Ferroelect., Freq. Control* 55 (7): 1597–1610.

84 Selzo, M.R. and Gallippi, C.M. (2013). Viscoelastic response (VisR) imaging for assessment of viscoelasticity in Voigt materials. *IEEE Trans. Ultrason., Ferroelect., Freq. Control* 60): 2488–2500.

85 Doherty, J.R., Trahey, G.E., Nightingale, K.R., and Palmeri, M.L. (2013). Acoustic radiation force elasticity imaging in diagnostic ultrasound. *IEEE Trans. Ultrason., Ferroelect., Freq. Control* 60 (4): 685–701.

23

Supersonic Shear Imaging

Jean-Luc Gennisson[1] *and Mickael Tanter*[2]

[1] *Imagerie par Résonance Magnétique Médicale et Multi-Modalités, Université Paris-Saclay, Orsay, France*
[2] *Institut Langevin–Waves and Images, Ecole Superieure de Physique et de Chimie Industrielle (ESPCI), Paris, France*

23.1 Introduction

The physical principle of the supersonic shear imaging (SSI) technique was described for the first time in Bercoff et al. [1]. It can be decomposed in three main stages: excitation by acoustic radiation force, acquisition by ultrafast imaging and calculation of speed maps. It is the combination of an excitation by acoustic radiation force and an ultrafast ultrasound imaging of the resulting shear waves which characterize the specificity of this elastography mode.

23.2 Radiation Force Excitation

The basis of the SSI technique is to use radiation force to excite the medium. It is this slight displacement of the medium which will then propagate in the form of a mechanical wave if the medium is solid, or create a flux if the medium is liquid. It is therefore the essential component of the SSI that allows the generation of the shear wave and replaces the techniques based on external vibrators.

23.2.1 Radiation Force

The radiation pressure is a volumetric or surface force which results from a transfer of momentum between a wave and its propagation medium. Originally discovered in acoustics by Rayleigh, it could only be reliably observed with piezoelectric transducers of sufficient power [2–4]. According to the equations of motion and continuity applied to a fluid particle (in implicit summation)

$$\rho\left(\frac{\partial v_i}{\partial t} + v_k \frac{\partial v_i}{\partial x_k}\right) = -\frac{\partial p}{\partial x_i} \tag{23.1}$$

and

$$\frac{\partial p}{\partial t} + \frac{\partial \rho v_j}{\partial x_j} = 0 \tag{23.2}$$

where ρ is the density, v is the compressional wave speed, and p is the pressure.

Ultrasound Elastography for Biomedical Applications and Medicine, First Edition.
Edited by Ivan Nenadic, Matthew Urban, James Greenleaf, Jean-Luc Gennisson, Miguel Bernal, and Mickael Tanter.

We find the expression of the quantity of motion at a point in the middle

$$\frac{\partial \rho_0 v_i}{\partial t} = -\frac{\partial (p\delta_{ik} + \rho_0 v_i v_k)}{\partial x_k} = -\frac{\partial M_{ik}}{\partial x_k} \tag{23.3}$$

where M_{ik} is the defined momentum flux tensor.

The radiation force is then defined as the mean force resulting from the passage of the wave in the medium and is therefore equal to the mean variation of the linear momentum undergone by the medium at this point

$$\vec{f}_i = -\frac{\partial \overline{M_{ik}}}{\partial x_k}\vec{u}_i \tag{23.4}$$

where $\overline{M_{ik}}$ is the Brillouin tensor which corresponds to the mean value over a period.

The linear momentum variation along the propagation axis is then related to several effects [5] – wave dissipation, wave reflections, and non-linearity.

When the wave is not confined to the medium [6], which means that its extension is much smaller than the medium size, the overpressure p has a mean of zero [7] and the average of the linear momentum flux is written $M_{ik} = \overline{\rho_0 v_i v_k}$; this is called the Langevin radiation force.

- For a plane wave in a non-attenuating medium $v(x,t) = e^{j\omega t - kx}$, the linear momentum is constant during wave propagation and there is therefore no transfer to the medium: the radiation force is null.
- For a plane wave in an attenuating medium $v(x,t) = e^{j\omega t - kx + j\alpha x}$, we have a variation of the linear momentum. From Eq. (23.4), we deduce the expression of the associated radiation force f

$$\vec{f}_i = -\frac{\partial \overline{M_{ik}}}{\partial x_k}\vec{u}_i = -2\rho_0 \overline{\left(v_i \frac{\partial v_k}{\partial x_k}\right)}\vec{u}_i = 2\rho_0 \alpha \overline{v_i^2}\vec{u}_i = 2\alpha \frac{p_0^2}{\rho_0 c^2}\vec{u}_i \tag{23.5}$$

  where u is the displacement, α is the attenuation, c the ultrasound speed, and p_0 the pressure field within the focal zone.
- For a plane wave reflecting perfectly on a surface, the radiation force is written

$$\vec{f}_i = 2\frac{p_0^2}{\rho_0 c^2}\vec{u}_i \tag{23.6}$$

- For a plane wave partially reflecting on a surface with a coefficient R, the radiation force is written

$$\vec{f}_i = \left(1 + R - (1-R)\frac{c_1}{c_2}\right)\frac{p_0^2}{\rho_0 c}\vec{u}_i \tag{23.7}$$

In general, in vivo radiation force is mainly related to the attenuation in soft tissues (about 0.3–1.0 dB/cm/MHz) as well as to the reflections by the interfaces of the organs.

23.2.2 Focus Duration

The acoustic radiation force generates a distant mechanical force F. Being proportional to the square of the amplitude of the ultrasound, a focusing law is used to locally raise the amplitude of the ultrasound waves and thus to generate a peak of force at a precise point.

The duration of the focusing does not change the amplitude of the radiation force, but only its temporal duration. The typical focusing times used are of the order of a few hundred microseconds. The radiation force can then be modeled by

$$F(\vec{r},t) = 2\alpha \frac{p_0(\vec{r})^2}{\rho_0 c^2}\mathrm{rect}_\mathrm{T}(t) \tag{23.8}$$

23.2.3 Impulse Response

The impulse response of the induced mechanical force can be calculated through the elastic Green's function. This impulse response was developed by Aki and Richards [8] in a purely elastic medium. It is written for the *j* component of the displacement field generated by a radiation force along the axis u_i

$$G_{ij}(\vec{r},t) = (g_{ij}^{\mathrm{P}}(\vec{r},t) + g_{ij}^{\mathrm{S}}(\vec{r},t) + g_{ij}^{\mathrm{PS}}(\vec{r},t)) \tag{23.9}$$

where

- g_{ij}^{P} is a compressional wave propagating longitudinally with a speed $c_{\mathrm{P}} = \sqrt{\frac{\lambda+2\mu}{\rho}}$

$$g_{ij}^{\mathrm{P}}(\vec{r},t) = \frac{1}{4\pi\rho c_{\mathrm{P}}^2}\gamma_i\gamma_j\frac{1}{r}\delta\left(t-\frac{r}{c_{\mathrm{P}}}\right) \tag{23.10}$$

  where γ_j is the cosine director of unit vector $\vec{r}$ and $r = ||\vec{r}||$, λ and μ are the Lamé coefficients, and *i,j* are the direction index numbers of the displacement and the source respectively
- g_{ij}^{S} is a shear wave propagating transversally with a speed $c_{\mathrm{S}} = \sqrt{\frac{\mu}{\rho}}$

$$g_{ij}^{\mathrm{S}}(\vec{r},t) = \frac{1}{4\pi\rho c_{\mathrm{S}}^2}\frac{\delta_{ij}-\gamma_i\gamma_j}{r}\delta\left(t-\frac{r}{c_{\mathrm{S}}}\right) \tag{23.11}$$

- g_{ij}^{PS} is a coupling term between shear and compression

$$g_{ij}^{\mathrm{PS}}(\vec{r},t) = \frac{1}{4\pi\rho}(3\gamma_i\gamma_j-\delta_{ij})\frac{1}{r^3}\int_{\frac{r}{c_{\mathrm{P}}}}^{\frac{r}{c_{\mathrm{S}}}}\tau\delta(t-\tau)\mathrm{d}\tau \tag{23.12}$$

An analytical formulation of the Green's function taking into account the viscosity has been proposed by Bercoff et al. [9] and allows one to simulate experimental observations. For a compressive α_{P} and shear α_{S} viscosity, the viscous Green's function is then written

- For g_{ij}^{P}

$$g_{ij}^{\mathrm{P}}(\vec{r},t) = \frac{1}{4\pi\rho c_{\mathrm{P}}^2}\frac{1}{\sqrt{2\pi\upsilon_{\mathrm{P}}t}}\gamma_i\gamma_j\frac{1}{r}e^{-\frac{(t-\tau)^2c_{\mathrm{P}}^2}{2\upsilon_{\mathrm{P}}t}} \tag{23.13}$$

  where γ_j cosine director of unit vector $\vec{r}$ and $r = ||\vec{r}||$, $\upsilon_{\mathrm{P}} = \frac{\eta_{\mathrm{P}}+2\eta_{\mathrm{S}}}{\rho}$.
- For g_{ij}^{S}

$$g_{ij}^{\mathrm{S}}(\vec{r},t) = \frac{1}{4\pi\rho c_{\mathrm{S}}^2}\frac{1}{\sqrt{2\pi\upsilon_{\mathrm{S}}t}}\frac{\delta_{ij}-\gamma_i\gamma_j}{r}e^{-\frac{(t-\tau)^2c_{\mathrm{S}}^2}{2\upsilon_{\mathrm{S}}t}} \tag{23.14}$$

  where $\upsilon_{\mathrm{S}} = \frac{\eta_{\mathrm{S}}}{\rho}$
- For g_{ij}^{PS}

$$g_{ij}^{\mathrm{PS}}(\vec{r},t) = \frac{1}{4\pi\rho}(3\gamma_i\gamma_j-\delta_{ij})\frac{1}{r^3}[I_{\mathrm{P}}(\vec{r},t)+I_{\mathrm{S}}(\vec{r},t)] \tag{23.15}$$

  with

$$I_{\mathrm{P}}(\vec{r},t) = \frac{\sqrt{\upsilon_{\mathrm{P}}t}}{\sqrt{2\pi}c_{\mathrm{P}}}\left[e^{-\frac{t^2c_{\mathrm{P}}^2}{2\upsilon_{\mathrm{P}}t}} - e^{-\frac{\left(t-\frac{r}{c_{\mathrm{P}}}\right)^2c_{\mathrm{P}}^2}{2\upsilon_{\mathrm{P}}t}}\right] + \frac{t}{2}\left[\mathrm{Erf}\left(\frac{c_{\mathrm{P}}t}{\sqrt{2\upsilon_{\mathrm{P}}t}}\right) - \mathrm{Erf}\left(\frac{c_{\mathrm{P}}\left(t-\frac{r}{c_{\mathrm{P}}}\right)}{\sqrt{2\upsilon_{\mathrm{P}}t}}\right)\right]$$

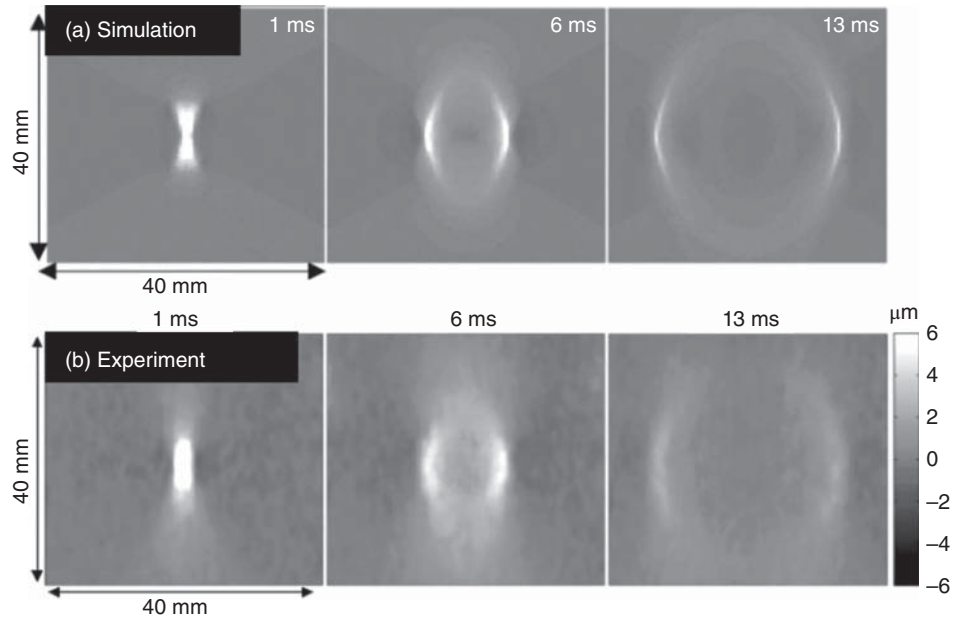

Figure 23.1 Impulse response after 100 μs of ultrasound focalization. (a) Simulation calculated from the viscous Green's function. (b) Experimental validation in an agar–gelatin phantom [10].

$$I_S(\vec{r},t) = \frac{\sqrt{\upsilon_S t}}{\sqrt{2\pi}c_S}\left[e^{-\frac{t^2 c_S^2}{2\upsilon_S t}} - e^{-\frac{\left(t-\frac{r}{c_S}\right)^2 c_S^2}{2\upsilon_S t}}\right] + \frac{t}{2}\left[\mathrm{Erf}\left(\frac{c_S t}{\sqrt{2\upsilon_S t}}\right) - \mathrm{Erf}\left(\frac{c_S\left(t-\frac{r}{c_S}\right)}{\sqrt{2\upsilon_S t}}\right)\right]$$

and Erf being the error function.

Then the Green's function is convolved with the radiation force impulse in order to compute the displacement field resulting from it with the impact of the focalization duration and the size of the focal spot. Figure 23.1 presents simulation results and experimental results in an agar–gelatin phantom.

23.2.4 Mach Cone and Quasi Plane Shear Wave

The radiation force allows one to generate a mechanical wave (including a shear term) at a precise location within the medium. Unfortunately, the amplitude of this wave is quite low and, in addition, decreases sharply during propagation due to strong diffraction in the imaging plane (Figure 23.1). To remedy this, the idea of SSI is to focus the ultrasound successively at different depths; the interference of the shear waves generated by each focusing makes it possible to construct a quasi-plane shear wave [11].

As the speed at which the shear wave source is moved in depth is higher than the shear wave rate of the medium, it will create a supersonic regime and a Mach cone [12]. From this analogy was born the name of "supersonic shear imaging". The interference of the "pushes" makes possible the generation of a quasi-plane shear wave whose angle depends on the ratio of the velocities of the source and of the shear wave, that is to say the Mach number (Figure 23.2). The

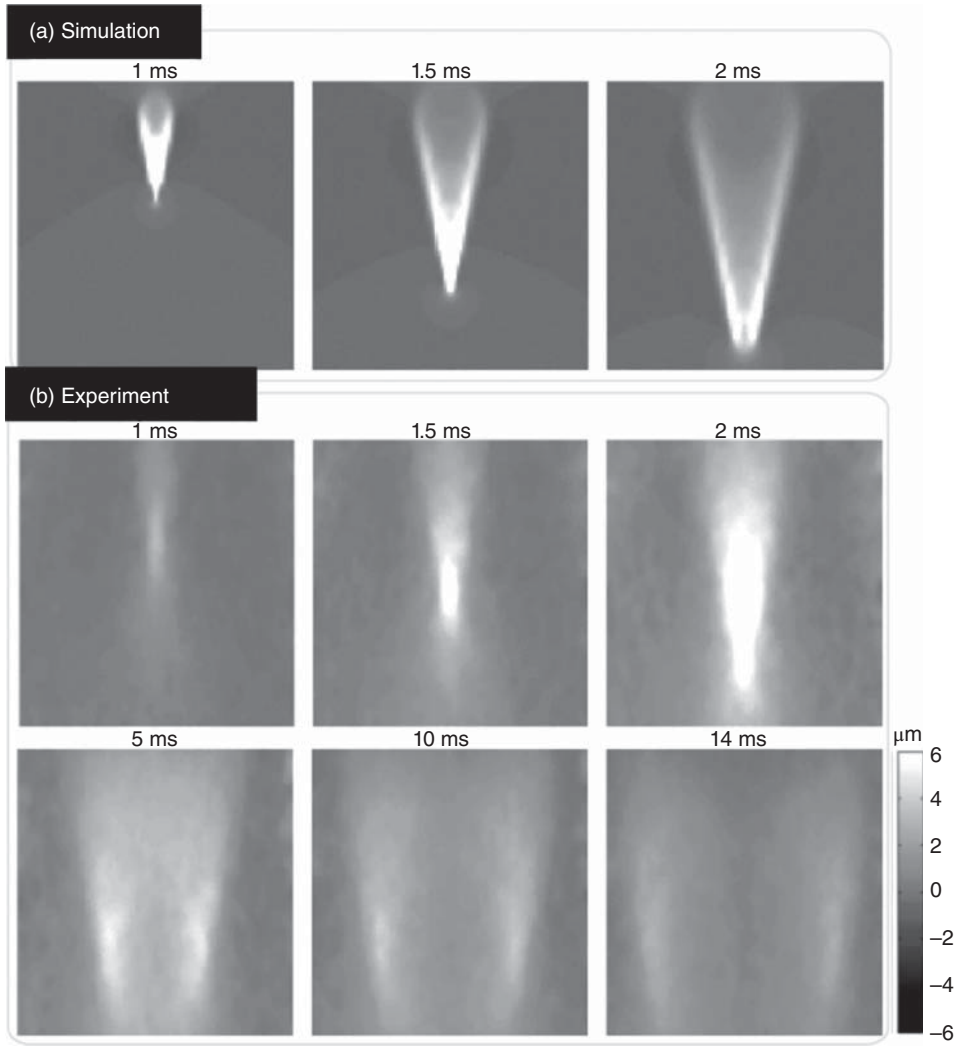

Figure 23.2 (a) Mach cone simulation by using the Green's function defined above. (b) Experimental validation in an agar–gelatin phantom. The shear wave speed in the gel is 2 m/s and the speed of the shear source is 6 m/s resulting in a Mach number of 3 [10].

plane wave thus generated is inclined by an angle $\theta = \tan^{-1}(M)$, where M is the Mach number. Such phenomenon can be simulated with the previous Green's function described above.

23.2.5 Norms and Safety

Focusing large amplitude ultrasound in biological tissue can lead to tissue damage [13]. It is thus necessary to study the effects of the radiation pressure on the tissues in order to ensure its safety for short application times.

Ultrasound has two physical properties that can damage the integrity of living cells.

- Heating: the absorption of the wave by the viscous forces leads to a rise in temperature locally which can cause tissue necrosis.
- Cavitation: high negative pressures can induce cavitation that tears and destroys cells.

It is therefore important to control these two effects. For this reason, the Food and Drug Administration (FDA) has put in place several standards to insure that these two physical quantities (pressure and temperature) remain below damaging thresholds [14].

- Intensity spatial peak temporal average (ISPTA) evaluates the mean energy deposited in the focus using the formula

$$\mathrm{ISPTA} = \frac{p_0^2}{\rho_0 c} \frac{\Delta t_{\mathrm{US}}}{\Delta t_{\mathrm{pause}} + \Delta t_{\mathrm{US}}} \tag{23.16}$$

  where p_0 is the pressure corrected by tissue absorption (~0.3 dB/cm/MHz), t_{US} is the ultrasound duration, and t_{pause} is the time without focalization. This value must be lower than 720 mW/cm^2 for almost all the organs of the body.
- Mechanical index (MI) evaluates the cavitation risk using the formula

$$\mathrm{MI} = \frac{p_0}{\sqrt{f_0}} \tag{23.17}$$

  where f_0 is the ultrasound frequency. This value must be lower than 1.9 for almost all the organs of the body.

The SSI technique, by generating a quasi-plane shear wave in the imaging plane (which goes through the whole medium and is imaged at once) greatly reduces the total ultrasound focusing time in the medium. By this way, norm values are respected in the SSI sequence and this allows one to conduct multiple clinical protocols in vivo [15, 16].

23.3 Ultrafast Imaging

After generation of the shear wave in situ, it must be observed in order to deduce the mechanical properties of the medium from its propagation. Since the propagation speed of the shear wave generally varies between 1 and 20 m/s in biological tissues, this implies, for an imaging zone of the order of 40 mm, that the shear wave goes through the imaging plane in less than 40 ms. It is therefore a very fast phenomenon that must be imaged with an excellent temporal resolution, which is not possible for conventional ultrasound scanners since they usually produce an image every 20 ms.

It has therefore been necessary to develop an imaging mode capable of making several thousand images per second to follow this wave. For this reason the idea of the SSI technique is to use ultrafast imaging by illuminating the medium with ultrasonic plane wave, a method already used in the 2D transient elastography technique [17].

23.3.1 Ultrasonic Plane Wave Imaging

In classical ultrasound imaging, the medium is illuminated by several ultrasonic transmissions successively focused in different areas of the image (usually line by line). This makes it possible to concentrate the energy in a precise zone, which has two effects: a better signal-to-noise ratio and a better discrimination of the imaged area at emission, which improves resolution and contrast since all echoes come from the focal zone alone. Unfortunately this technique involves repeating the focusing step a lot of times in order to reconstruct a complete image.

Plane wave imaging is performed with a single emission [18]. The entire field-of-view is illuminated at once, and as soon as the ultrasound is transmitted, the ultrasound device can switch into a receive mode to record the first echoes, thus saving a lot of time [19].

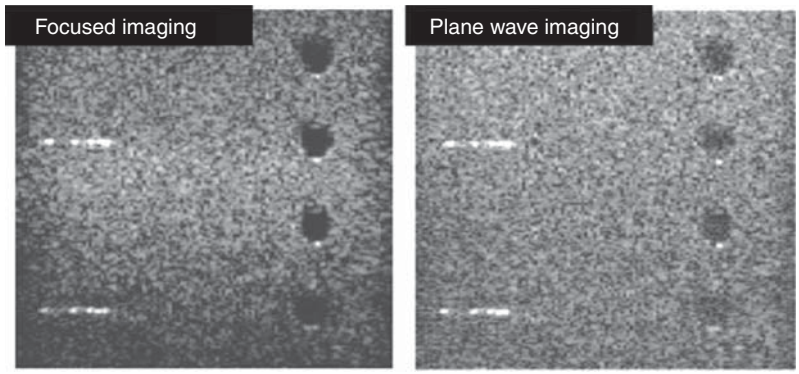

Figure 23.3 Comparison between focused imaging and plane wave imaging. Focused imaging has better contrast and lateral resolution but does not achieve the plane wave frame rate [10]. Experiment performed on a Philips ATS550 phantom with a 4.3 MHz ultrasonic probe.

Unsurprisingly, the plane wave mode is less effective for contrast and lateral resolution [10] (Figure 23.3). With only focusing on reception, a diffraction impulse response corresponding laterally to a cardinal sine instead of a cardinal sinus squared (obtained with focalization on transmit and reception) is obtained. The lateral resolution is thus slightly degraded (the width of the focal spot is slightly diminished) and the contrast decreased by a factor almost equal to two (lobes at about −35 dB instead of −70 dB). Nevertheless, in most cases, since the generated shear wavelengths are much greater than the resolution of the ultrasound image obtained, the loss of resolution does not significantly influence the quality of the motion estimation. However, resolution and contrast can be enhanced by using ultrasonic compound imaging described in Montaldo et al. [20]. This technique consists in coherently summing different ultrasound images obtained with different angles of plane wave insonification. Such a technique reduces the frame rate by the number of angles but remains fast enough to follow transient motions due to the shear wave propagation. Finally, a tradeoff between frame rate and image resolution is chosen depending on the purpose of the SSI technique.

23.3.2 Shear Wave Detection

The last step to be able to follow the shear wave is to measure the displacement of the tissue from the ultrafast movie. For this purpose, each image is cut into axial windows which are compared from one image to the next to measure the temporal offset [21]. This technique, called ultrasonic speckle interferometry [22], makes it possible to estimate the speckle speed at each point of the image and so to calculate a movie of the axial displacement $u_z(z,x,t)$. Since the displacement generated by the radiation pressure is low (some μm), the correlation of the non-demodulated ultrasonic signals $s(z,x,t)$ is used. This allows one to measure displacements smaller than the ultrasonic wavelength, which can be improved by parabolic interpolation of the correlation functions.

As in most of the ultrasonic devices, signals are directly demodulated in IQ (in phase and quadrature demodulation), then a phase measurement between the IQ samples is directly used with ω being the pulsation frequency

$$s(z,x,t) = I(z,x,t)\cos(\omega z/c) + Q(z,x,t)\sin(\omega z/c) \tag{23.18}$$

$$\tau(z,x,t) = \frac{1}{\omega} a\tan^{-1}\left(\frac{Q(t)I(t+1) + Q(t+1)I(t)}{I(t+1)I(t) + Q(t+1)Q(t)}\right) \tag{23.19}$$

$$u_z(z,x,t) = \frac{\tau(z,x,t) * c}{2} * \text{frame rate} \tag{23.20}$$

23.4 Shear Wave Speed Mapping

One possible way to map the shear wave speed in tissues is to use a time-of-flight algorithm. Time-of-flight is a simple and intuitive way to find the time that the shear wave travels between two spatial points. Although this approach is less general than the wave equation inversion (since it requires a flat shear wave), it offers better stability to noise. The time-of-flight is calculated by cross-correlating the axial displacements u_z of two points spaced a distance dx (called the correlation distance) and located on the same horizontal line (the direction of propagation of the plane wave). The maximum of the cross-correlation function makes it possible to obtain the time shift dt and the speed of propagation of the shear wave is then simply estimated by $v_s = \mathrm{d}x/\mathrm{d}t$.

In order to express the link between the time-of-flight measurement and the shear modulus, we can study the cross-correlation function of two waves separated by a distance dr in the case of a purely elastic model. Under a purely elastic model, the link between time-of-flight and shear modulus is simple because there is no shear wave dispersion. One can write the wave displacement u_z of amplitude A_0 in x and $x + \mathrm{d}r$ by

$$u_z(x,t) = A_0(t) \text{ and } u_z(x+dr,t) = A_0(t) * \delta\left(t - \sqrt{\frac{\rho}{\mu}}\mathrm{d}r\right) \tag{23.21}$$

Correlation of $u_z(x, t)$ and $u_z(x + \mathrm{d}r, t)$ is then maximal for $\tau = \sqrt{\frac{\rho}{\mu}}\mathrm{d}r$, which gives the shear wave speed by time-of-flight as $v_s = \sqrt{\frac{\rho}{\mu}}$.

23.4.1 Building an Image

Time-of-flight is used to reconstruct a shear wave speed map wherever the shear wave has propagated. Thus, in the push zone, no shear wave propagates and it is therefore impossible to find the values of the elasticity in this zone. In order to reconstruct a complete image of the medium, it is therefore necessary to generate another Mach cone, or even a third cone to completely "explore" the imaging zone. Conventionally, three Mach cones are used and are sufficient to reconstruct the entire image. In practice, each pushing beam is followed by an ultrafast imaging sequence and all the pushes are chained automatically in a few milliseconds. This "multizone" sequence is thus as straightforward to use as a simple sequence. Instead of acquiring a single film of the shear wave propagation, three films are obtained. On each film, the time-of-flight algorithm is used to reconstruct a piece of the shear wave speed map, as illustrated in Figure 23.4. Finally, in order to obtain the full map shear wave speed map, the "push zone" is masked by using a dedicated algorithm. Then the three maps are combined with a quality criterion such as a local weighting [24].

The whole technique was firstly implemented on an ATL HDI 1000 ultrasound device and initially showed its potential in breast cancer detection (Figure 23.5) [16]. After this technique was implemented on an ultrasound diagnostic imaging device called the Aixplorer® (Supersonic Imagine, Aix-en-Provence, France), its diagnosis performance as well as its reproducibility were demonstrated in several organs, and more particularly in the breast [25]. In particular, a multicentric study in 939 patients with breast cancer showed an important increase in specificity for breast lesion characterization (+17.4%) with the addition of the elasticity parameters to the classical BIRADs criteria [26].

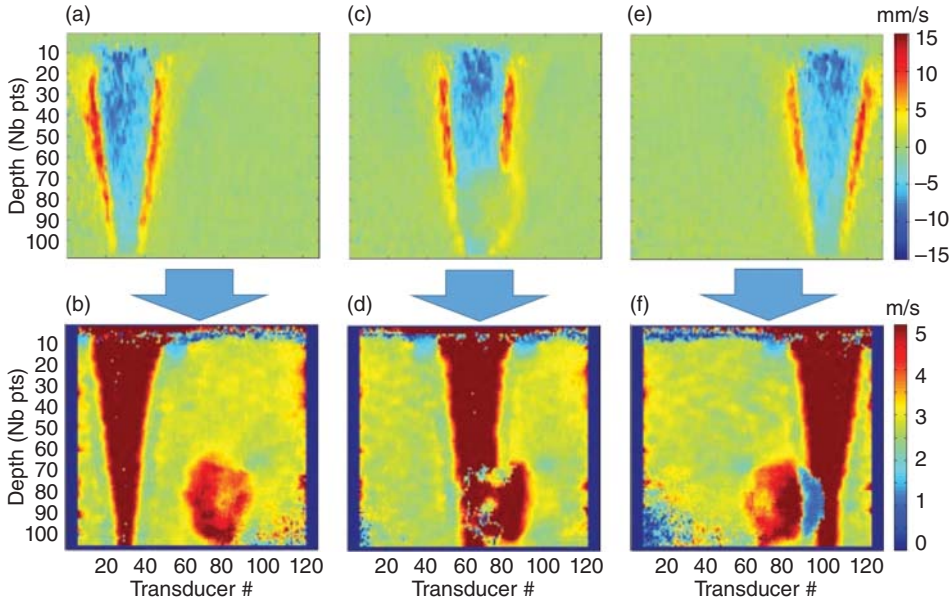

Figure 23.4 (a), (c), (e): Shear wave displacements at one time of the acquired shear wave movie for three different Mach cone genrerated consecutively. (b), (d), (f): Corresponding shear wave speed map for each Mach cone [23].

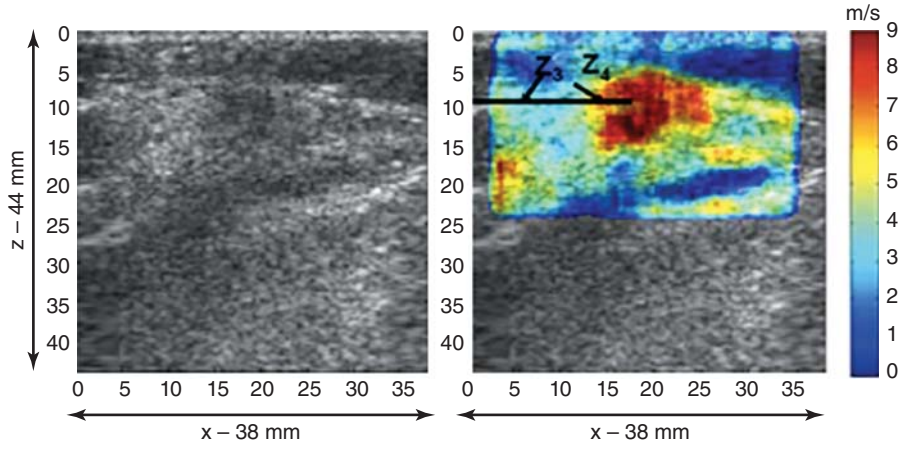

Figure 23.5 Ductal infiltrating carcinoma. The B-mode image brings out a hypo-echogenic mass with blurry borders with a shadow posterior to the lesion. The lesion is classified as ACR5. The elasticity imaging clearly brings out a very stiff mass at more than 150 kPa (7.1 m/s). Source: reprinted from [16] with permission from Elsevier.

23.5 Conclusion

The supersonic shear imaging technique allows quantitative and real-time imaging of elasticity by judiciously using radiation pressure to generate a shear wave and ultrafast imaging for acquisition. The use of a time-of-flight algorithm makes it possible to determine the shear wave propagation speed and thus to find shear modulus maps of the medium. This method makes it possible to produce maps in vivo with a good spatial resolution. Beyond the production of

stiffness maps, it is possible to construct different estimation strategies to obtain, for example, an average value of stiffness that is as precise as possible. This elastography method, improved here for in vivo acquisition, has already been tested on several clinical applications, from breast cancer diagnosis to liver stiffness staging or muscle characterization.

References

1 Bercoff, J., Tanter, M., and Fink, M. (2004). Supersonic shear imaging : a new technique for soft tissue elasticity mapping. *IEEE Trans. Ultrason., Ferroelect., Freq. Control* 51 (4): 396–409.

2 Beyer, R. (1950). Radiation pressure in a sound wave. *Am. J. Phys.* 18 (1): 25–29.

3 Westervelt, P. (1957). Acoustic radiation pressure. *J. Acoust. Soc. Am.* 29 (1): 26–29.

4 Rooney, J. and Nyborg, W. (1972). Acoustic radiation pressure in a traveling plane wave. *Am. J. Phys.* 40 (12): 1825–1830.

5 Torr, G. (1984). The acoustic radiation force. *Am. J. Phys.* 52 (5): 402–408.

6 Chu, B. and Apfel, R. (1982). Acoustic radiation pressure produced by a beam of sound. *J. Acoust. Soc. Am.* 72 (6): 1673–1687.

7 Shutilov, V. and Alferieff, M.A. (1988). *Fundamental Physics of Ultrasound*. CRC Press.

8 Aki, K. and Richards, P. (1980). *Quantitative Seismology: Theory and Methods*, vol. 2. Freeman.

9 Bercoff, J., Tanter, M., Muller, M., and Fink, M. (2004). The role of viscosity in the impulse diffraction field of elastic waves induced by the acoustic radiation force. *Ultrasonics* 51 (11): 1523–1536.

10 Bercoff, J. (2004). L'imagerie échographique ultrarapide et son application à l'étude de la viscoelasticité du corps humain. Ph.D. Thesis in French, from Denis Diderot University, Paris VII, France.

11 Bercoff, J., Tanter, M., Chaffai, S., and Fink, M. (2002). Ultrafast imaging of beamformed shear waves induced by the acoustic radiation force, application to transient elastography. In: *IEEE Ultrasonics Symposium Proceedings* 1899–1902.

12 Bercoff, J., Tanter, M., and Fink, M. (2004). Sonic boom in soft materials: The elastic Cerenkov effect. *Appl. Phys. Lett.* 84 (12): 2202–2204.

13 Stratmeyer, M.E., and Lizzi, F.L. (1986). Special issue on the biological effects of ultrasound. *IEEE Trans. Ultrason., Ferroelect., Freq. Control* 33 (2): 137–138.

14 Barnett, S. and Kossoff, G. (1998). *Safety of Diagnostic Ultrasound*. Informa Health Care.

15 Muller, M., Gennisson, J.L., Deffieux, T., et al. (2009). Quantitative viscoelasticity mapping of human liver using supersonic shear imaging: preliminary in vivo feasibility study. *Ultrasound Med. Bio.* 35 (2): 219–229.

16 Tanter, M., Bercoff, J., Athanasiou, A., et al. (2008). Quantitative assessment of breast lesions viscoelasticity using supersonic shear imaging technique: Initial clinical investigation. *Ultrasound Med. Biol.* 34 (9): 1373–1386.

17 Sandrin, L., Tanter, M., Catheline, S., and Fink, M. (2002). Shear modulus imaging with 2-D transient elastography. *Ultrasonics* 49 (4): 426–435.

18 Shattuck, D.P., Weinshenker, M.D., Smith, S.W., and von Ramm, O.T. (1984). Explososcan: a parallel processing technique for high speed ultrasound imaging with linear phased arrays. *J. Acoust. Soc. Am.* 75 (4): 1273–1282.

19 Lu, J. (1997). 2D and 3D high frame rate imaging with limited diffraction beams. *IEEE Trans. Ultrason., Ferroelect., Freq. Control* 44 (4): 839–856.

20 Montaldo, G., Tanter, M., Bercoff, J., et al. (2009). Coherent plane-wave compounding for very high frame rate ultrasonography and transient elastography. *IEEE Trans. Ultrason., Ferroelect., Freq. Control* 56 (3): 489–506.

21 Loupas, T., Powers, J., and Gill, R. (1995). An axial velocity estimator for ultrasound blood flow imaging, based on a full evaluation of the two-dimensional autocorrelation approach. *IEEE Trans. Ultrason., Ferroelect., Freq. Control* 42 (4): 672–688.

22 Walker, W., Friemel, B., Bohs, L., and Trahey, G. (1993). Real-time imaging of tissue vibration using a two-dimensional speckle tracking system. *Ultrason. Symp.* 2: 873–877.

23 Deffieux, T. (2008). Palpation par force de radiation ultrasonore et échographie ultrarapide: Applications à la caractérisation tissulaire in vivo. Ph.D. Thesis in French, from Denis Diderot University, Paris VII, France.

24 Deffieux, T., Gennisson, J.L., Larrat, B., et al. (2012). The variance of quantitative estimates in shear wave imaging: theory and experiments. *IEEE Trans. Ultrason., Ferroelect., Freq. Control* 59 (11): 2390–2410.

25 Cosgrove, D.O., Berg, W.A., Doré, C.J., et al. (BE1 Study Group) (2012). Shear wave elastography for breast masses is highly reproducible. *Eur. Radiol.* 22 (5): 1023–1032.

26 Berg, W.A., Cosgrove, D.O., Doré, C.J., et al. (BE1 Investigators) (2012). Shear-wave elastography improves the specificity of breast. The BE1 multinational study of 939 masses. *Radiology* 262 (2): 435–449.

24

Single Tracking Location Shear Wave Elastography

Stephen A. McAleavey

Biomedical Engineering Department, University of Rochester, Rochester, NY, USA

24.1 Introduction

Shear wave elastography (SWE) infers tissue mechanical properties by observing the propagation of shear waves in the tissue [1–3]. Conventional methods for estimating tissue mechanical properties (e.g. indentation, uniaxial loading [4]) are invasive and require direct contact with tissue samples. Compared with these methods, SWE has the advantages of being noninvasive and nondestructive, and allows in vivo quantification of tissue mechanical properties. The speed, attenuation, and distortion of a shear wave as it propagates are determined by the mechanical properties of the tissue. By measuring these wave characteristics we can in principle estimate the properties of the tissue that supports the wave.

For instance, in an elastic medium the speed c of a shear wave is related to the shear modulus G by $G = \rho c^2$, where ρ is the density of the medium. Thus, by measuring the speed of propagation of a shear wave in a medium of known density, we can determine its modulus. Within the human body shear modulus varies over many orders of magnitude between tissues, while soft tissue density is equivalent to water within an error of a few percent. The relative uniformity of density compared to shear modulus makes shear wave speed measurements in tissue effective surrogates of shear modulus.

Implementation of this measurement requires that we first generate a shear wave and then measure its propagation speed. Several shear wave sources have been used for SWE, including electromechanical actuators – voice coils mechanically coupled to the tissue. These have the advantage of being able to generate large forces over a wide range of frequencies, from DC up to a kilohertz. A disadvantage is that, in noninvasive applications, the shear waves must propagate from the skin surface to the region of interest, which may be subject to shadowing. The mechanical shaker is an additional device that must be positioned along with the ultrasound transducer, which can be cumbersome.

Another method of generating shear waves relies on the phenomenon of acoustic radiation force [5]. This is a body force associated with the propagation of an acoustic wave in an absorptive medium. The direction of the force is in the direction flow of acoustic energy. For a weakly focused ultrasound beam of intensity I, the associated acoustic radiation force F is given by $F = \frac{2\alpha I}{c_u}$, where α is the ultrasound attenuation coefficient of tissue and c_u is the ultrasound wave speed. In soft tissues the variations in c_u and α are small compared to the variations in I that can be achieved by focusing. We can thus generate force distributions in tissue in equal proportion to our ability to shape the intensity of an ultrasound beam. The same electronic beamforming that allows transmit beams for B-mode image formation to be tightly focused

Ultrasound Elastography for Biomedical Applications and Medicine, First Edition.
Edited by Ivan Nenadic, Matthew Urban, James Greenleaf, Jean-Luc Gennisson, Miguel Bernal, and Mickael Tanter.

and rapidly steered from point to point allows equally fine localization and rapid translation of radiation force. High-intensity ultrasound tonebursts with durations of 10^{-5} to 10^{-3} s are thus able to be used to generate localized body forces that act as shear wave sources, a method called acoustic radiation force impulse (ARFI) [5, 6]. Here the term "impulse" is used to imply that the duration of force application is short compared with the timescale of the mechanical response of the tissue. To illustrate this notion in a typical case, the ultrasound toneburst and associated radiation force may be a few hundred microseconds long, while the time to peak tissue displacement at the ultrasound focus is on the order of milliseconds. The amplitudes associated with the resulting waves are small, less than 100 μm, but sufficient to be measured ultrasonically in vivo.

ARFI may be used to generate a shear wave at a point of interest distal to an ultrasound transducer. The speed of the shear wave as it propagates away from the source can be measured by timing its arrival at two or more "gates" a known distance apart. This approach is illustrated in Figure 24.1a. The arrival time of the shear wave at each tracking location may be determined by a particular metric, e.g. the time of peak displacement. Using two tracking locations a known distance Δx apart, the shear wave speed can be calculated from the arrival time difference Δt as $c = \Delta x/\Delta t$. Tracking at more than two locations provides redundancy and can be used to reduce error in the shear wave speed measurement due to noise in the arrival time estimates. We will refer to this approach, involving timing of shear arrival at several locations, as the multiple tracking location (MTL) method. Examples of MTL methods include shear dispersion ultrasound vibrometry (SDUV [7, 8]), supersonic shear wave imaging (SSI [9]), and ARFI shear wave elastography (ARFI-SWE [10]).

The great flexibility in the position and form of the shear wave source afforded by electronic beamforming and the acoustic radiation force phenomenon allows a complementary approach to be implemented, which we call single tracking location (STL). In this approach, illustrated in Figure 24.1b, tissue motion due to shear wave propagation is tracked at one point. An ARFI shear wave source with multiple peaks with known spacing Δx is applied to the tissue. The difference in the arrival time of the shear wave peaks Δt at the single tracking location is used to estimate the shear wave speed $c = \Delta x/\Delta t$.

The two approaches, STL and MTL, are complementary, with the location of push beams and track beams reversed between each. In STL the spatial information, Δx, is encoded in the push beam spacing, while MTL prescribes it in the spacing of the tracking beams. The estimation of shear wave speed relies on the same ratio of beam spacing to arrival time difference.

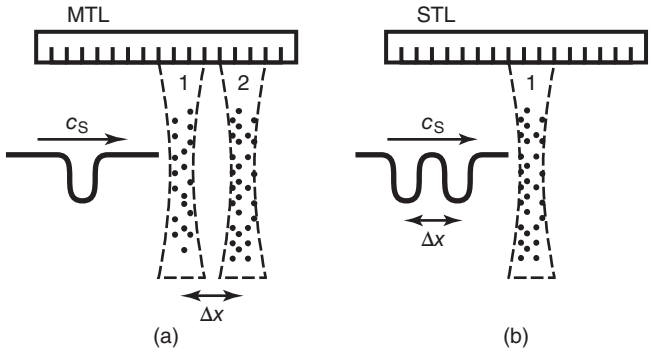

Figure 24.1 Schematic illustrations of (a) MTL SWEI and (b) STL SWEI. The measurement of wave speed requires both a spatial and a temporal component. In MTL, the value of Δx is set by the distance between the two tracking beams. In STL methods, Δx is determined by a spatial property of the shear wave excitation. In SMURF, this is the spacing between simultaneously applied ARFI intensity peaks, while in STL-SWEI, Δx is the distance between sequentially applied ARFI pushing beams.

We shall see that asymmetries in the uncertainty of push and tracking locations, however, leads to significant differences in the noise associated with each method. STL approaches, and their associated advantages and disadvantages compared with MTL methods, are the focus of this chapter.

First, we shall examine implementation details of the STL method in more detail. Next we demonstrate the effect of ultrasound speckle on shear wave speed estimates, and describe how STL methods are immune to speckle noise. Finally, we will consider the extension of STL methods to the estimation of tissue viscoelastic parameters.

24.2 SMURF

The first STL SWEI method developed is called spatially modulated ultrasound radiation force (SMURF) [11, 12]. The core idea in SMURF is to use a spatially varying acoustic radiation force to generate a shear wave with a known wavelength λ. Once created, the speed of this wave can be estimated by measuring its frequency f, using the relationship $c = \lambda f$. This approach is the complement of sonoelastography, SDUV, and similar MTL methods that generate a shear wave of known frequency and measure its wavelength.

To understand how an acoustic radiation force impulse applied to an elastic medium can give rise to a shear wave of a desired wavelength, we can consider an analogous 1D model, that of the "struck string" illustrated in Figure 24.2 [13]. Let us define u as the displacement of the string, $\dot{u}$ its speed (particle velocity), and x a point along the string. Initially the string is at rest, so that $u = \dot{u} = 0$. At time zero a hammer strikes the string. The transverse force F applied by the hammer can be separated into a spatial component and an impulsive temporal component, so that

$$F(x,t) = f(x)\delta(t) \tag{24.1}$$

This force results in a step change in the velocity of the string proportional to the force, so that at time $t = 0^+$, just after the application of the impulse force

$$\dot{u} = \frac{1}{\rho} f(x) \tag{24.2}$$

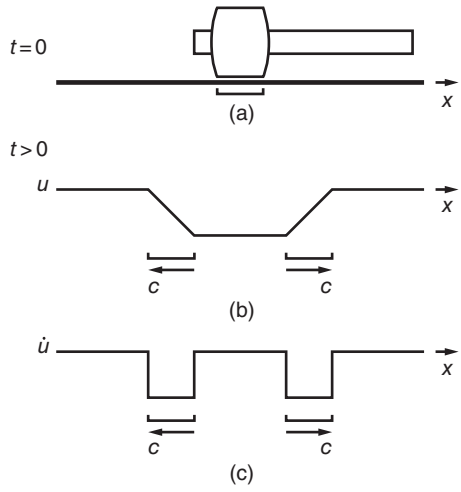

Figure 24.2 "Struck string" model of SMURF imaging. (a) A hammer strikes a taut string at time zero. The hammer face is in contact with the string for just an instant, and applies a uniform force over the region indicated by the bracket. (b) D'Alembert derived the solution for the wave resulting from the hammer blow. (c) The displacement velocity $\dot{u}(x,t)$ is a scaled replica of applied force propagating at a speed c, so that $\dot{u}(x,t) \propto f(x-ct) + f(x+ct)$. The displacement $u(x,t)$ is the running integral of the velocity, $u(x,t) = \int_{-\infty}^{t} \dot{u}(x,\tau)\mathrm{d}\tau$ (center).

and $u = 0$. The solution for $t > 0$ of the one-dimensional wave equation

$$\frac{\mathrm{d}^2 u}{\mathrm{d}t^2} - c^2 \frac{\mathrm{d}^2 u}{\mathrm{d}x^2} = 0 \tag{24.3}$$

with these initial conditions is

$$\dot{u}(x,t) = \frac{1}{2\rho}\{f(x-ct) + f(x+ct)\} \tag{24.4}$$

An impulsive force with spatial dependence $f(x)$ thus gives rise to a particle velocity described by forward and backward propagating replicas of $f(x)$, i.e. $f(x-ct)$ and $f(x+ct)$.

In this example let us choose $f(x)$ to have a sinusoidal variation with a particular spatial frequency k, e.g. let

$$f(x) = \cos(kx) \tag{24.5}$$

In response to this forcing function, the particle velocity of the wave that develops is proportional to $\cos(k(x-ct)) + \cos(k(x+ct))$. Using the relationship $kc = \omega$ this can be written as $\cos(\omega t - kx) + \cos(\omega t + kx)$. Thus, an impulsively applied force with a known, controlled spatial frequency k gives rise to a shear wave with temporal frequency ω. By measuring the frequency ω and using the known spatial frequency k, we find the wave speed by taking the ratio ω/k.

In three dimensions, the relationship between the spatial distribution of an impulsive body force and the resulting shear wave field is more complicated. We can, however, create an approximately 1D situation by confining rapid variation F to a single direction, so that close to the shear wave source the force is well approximated by a 1D function. For instance, consider a forcing function that acts in the z direction of the form

$$F(x,y,z,t) = e^{-\frac{x^2}{\sigma_x^2} - \frac{y^2}{\sigma_y^2} - \frac{z^2}{\sigma_z^2}} \cos(kx)\delta(t)\hat{Z} \tag{24.6}$$

with $\sigma_x \ll \sigma_y, \sigma_z$, as illustrated in Figure 24.3. This pulse is concentrated near $x = 0$, but decays much more slowly in the y and z directions. For points along the x axis near the origin, this forcing function will give rise to shear wave packets of the form

$$e^{-(x\pm ct)^2/\sigma_x^2} \cos(\omega t \pm kx)\hat{Z} \tag{24.7}$$

with frequency $\omega = kc$. As illustrated, the induced particle motion is in the $\pm z$ direction, and the wave packet propagates principally in the $\pm x$ direction. With increasing distance from the origin diffraction effects distort the wave so that it is not a perfect replica of F. Nonetheless, in an elastic medium spatially modulated ARFI can generate a shear wave with a defined wavelength.

With the shear wave thus generated, the wave speed c may be estimated by measuring the frequency ω associated with the particle velocity of the medium, that is, the time derivative of displacement. Many methods for estimating tissue velocity are known [14, 15], including Doppler methods, time-domain cross correlation methods, and speckle tracking. In all cases, a succession of ultrasound pulses is transmitted and echoes collected. Because it is the velocity of the tissue induced by the shear wave, and not the absolute displacement, that is of interest, the tracking operation may be performed on successive echoes. This is an inherently high-pass operation that has the salutary effect of suppressing the low frequency associated with the envelope of the shear wave and passing the high frequency component that carries the information about shear modulus.

The frequency of the induced shear wave is determined by the shear wave speed in the region of excitation. Assuming linear propagation of the shear wave, its frequency does not change as it propagates. Redundant measurements of the shear wave frequency at multiple spatial locations can thus be used to reduce estimate noise. Note that while the frequency may be measured at multiple spatial positions, the frequency is determined at each location individually, so that this is still essentially an STL measurement.

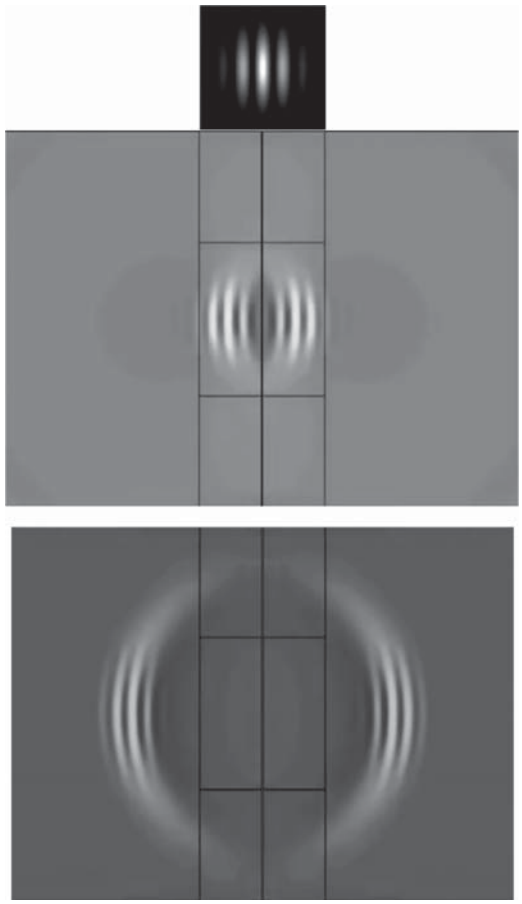

Figure 24.3 Idealized SMURF push pulse and resulting shear wave. A localized, impulsive force in the axial (z) direction, with a sinusoidal amplitude modulation in the lateral (x) direction (top) gives rise to a shear wave packet propagating in the $\pm x$ direction. The form of the particle velocity associated with the shear wave packet is approximately a replica of the spatially modulated forcing function. The temporal frequency of the shear wave is determined by the spatial frequency of the forcing function and the shear modulus of the region of excitation. As the wave propagates, the frequency remains constant, even as the wavelength may vary when the wave propagates to regions of differing shear modulus.

Elegbe evaluated several approaches for generation of the spatially modulated push beam [16]. The first is an application of the Fraunhofer approximation, wherein the pressure amplitude in the focal region of a transducer is the Fourier transform of the velocity amplitude of the aperture. Thus, for instance, a Gaussian-enveloped sinusoidal lateral variation in pressure is achieved with an apodization function consisting of Gaussians on either side of the beam axis, as illustrated in Figure 24.4. A second approach is to interfere a pair of plane waves propagating at angles $\pm\theta$ to the beam axis, producing a lateral modulation with spatial frequency $2k_l \sin\theta$. The analysis presented models limited aperture size and includes a metric for selection between the two methods based on imaging depth and ROI size.

Rather than simultaneously generate multiple shear wave peaks, one may generate two or more peaks sequentially in time [11]. If these peaks are generated rapidly enough, the effect is the same as that of the simultaneously generated peaks described above (SMURF). "Rapidly" in this case means that the entire set of peaks is generated before any appreciable shear wave propagation takes place. This is satisfied if the time required is much less than the peak spacing divided by the shear wave speed. When the time required to generate the peaks is not negligible, the frequency estimate can be corrected using the known push-beam spacing and time between push pulses [11].

The spatial resolution associated with SMURF is determined by the size of the region of excitation. Increasing the spatial resolution of the shear wave speed estimate requires reducing the

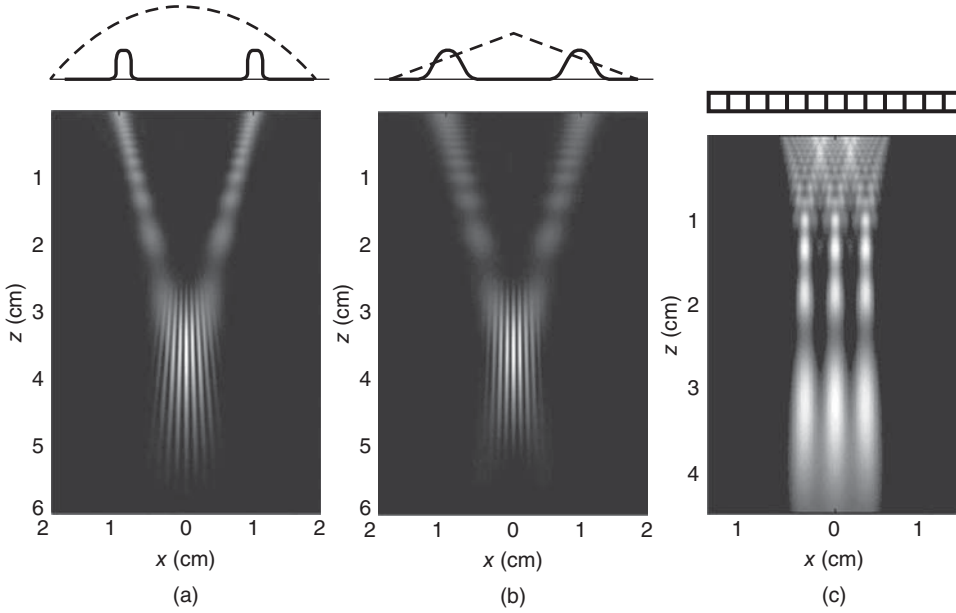

Figure 24.4 Simulated practical SMURF push beams. (a) A desired spatial modulation may be generated using the focal Fraunhofer approximation – that the lateral pressure amplitude profile is the Fourier transform of the velocity amplitude in the transducer plane. (b) A spatial modulation of the ultrasound intensity can also be generated by intersecting Gaussian beams. (c) Conventionally focused push beams may be transmitted in rapid succession to sequentially generate a series of shear wave peaks of controlled spacing. All simulations were performed in Field II and modeled a 3 MHz, λ-sampled array at the top of the field (centered at (0,0)) radiating in the $+z$ direction (downwards). Tissue attenuation was modeled as 0.7 dB/cm/MHz attenuation. Source: © 2007 Sage Publishing, reprinted with permission from [12].

size of the region of excitation, with a consequent reduction in the space between peaks. This in turn leads to an increase in the induced shear wave frequency.

A limitation of the SMURF approach is the assumption of a purely elastic model. Under this assumption the speed of propagation of a wave is independent of its frequency. All components of the induced shear wave propagate at the same speed c, so that the propagating wave retains the shape of $f(x)$. Biological tissues, however, are viscoelastic [4]. Shear wave speed exhibits significant frequency dependence at frequencies greater than 100 Hz. The attenuation of shear waves increases with frequency in viscoelastic media. As a consequence of these effects, SMURF push beams containing high spatial frequencies do not result in propagating shear waves. High frequency components are rapidly attenuated. As a result, attempting to generate a shear wave with a short wavelength in viscoelastic material results in the rapid attenuation of the high frequency component. The low frequency envelope portion continues to propagate a measureable distance, but without the spatial modulation, without a wavelength defined by the push beam, there is no measurable frequency from which to calculate the wave speed.

24.3 STL-SWEI

The applicability of SMURF is limited to cases where the viscoelasticity of the medium does not inhibit generation of shear waves of the desired spatial frequency. As a consequence, high spatial resolution SMURF imaging, which requires high spatial frequencies, is possible only in a relatively elastic medium.

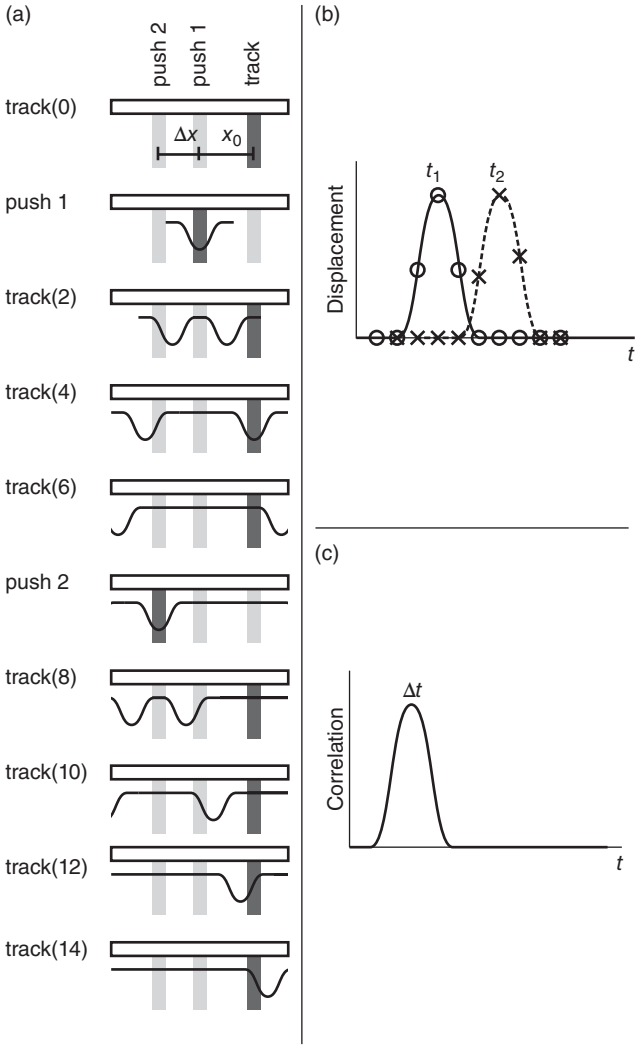

Figure 24.5 STL-SWEI beam sequence for a single ensemble. (a) Schematic illustration of push and track beam locations and sequence. Tissue motion in response to ARFI push pulses is tracked along a common A-line (track). A reference echo is collected prior to the application of ARFI (top row). A first pushing pulse is applied along an A-line (push 1) a distance x_0 from the tracking A-line. A series of tracking echoes is collected to measure tissue motion in response to the shear wave induced by the push pulse. After the shear wave has propagated through the tracking beam, a second push pulse is fired (push 2), offset by Δx from the first. Tracking echoes are collected and the motion in response to this second push tracked at the tracking A-line. (b) Tracked displacement in response to "push 1" (solid) and "push 2" (dashed). The difference in the arrival time of the shear waves Δt relative to the transmission of push beams "push 1" and "push 2" is determined by cross-correlation of the shear wave signals (c).

Relaxing the requirement that the shear wave be generated with a specific spatial frequency allows the development of an STL approach for viscoelastic tissue. We will denote this method, illustrated in Figure 24.5, as STL-SWEI [17, 18]. In this approach, a shear wave is generated using the acoustic radiation force of a focused ultrasound beam. The beam intensity is localized, but no sinusoidal modulation is applied as in SMURF. Tissue motion is tracked at a location offset laterally to the push beam, and the time of arrival t_1 of the shear wave is measured, for instance, by time to peak velocity. Here the arrival time is determined with reference to the time of ARFI

excitation. A second shear wave is then generated, from a push beam focal point translated by Δx relative to the first focus, and its arrival time t_2 at the same tracking location calculated. The shear wave speed is determined

$$c = \frac{\Delta x}{t_2 - t_1} = \frac{\Delta x}{\Delta t} \tag{24.8}$$

In contrast to the SMURF approach, there is no requirement that Δx be greater than some minimum value to allow shear wave propagation; Δx plays no role in determining the temporal frequency of the shear wave. Inserting an adequate time delay between the generation of the first and second shear waves avoids their overlap spatially. The STL-SWEI approach eliminates the tight coupling between shear wave frequency and spatial resolution inherent in SMURF and allows a single tracking location approach to be pursued in viscoelastic media with high spatial resolution. In contrast to the MTL implementation that determines the shear wave speed between two tracking beams, STL-SWEI determines the shear wave speed between the two push beams.

MTL imaging sequences, such as SSI [9], can use parallel receive beamforming or high frame rate imaging to obtain shear wave speed estimates throughout a tissue region in response to a single push beam. STL-SWEI sequences, in contrast, require that the pulse sequences ensembles described above be "walked" across the region of interest. Each lateral pixel in the final shear wave speed image requires a push beam on either side. As shown in Figure 24.6, an STL-SWEI image M pixels wide thus requires at least $M + 1$ push beams to be transmitted. If two-to-one parallel receive beamforming is not available, the number of required push beams increases

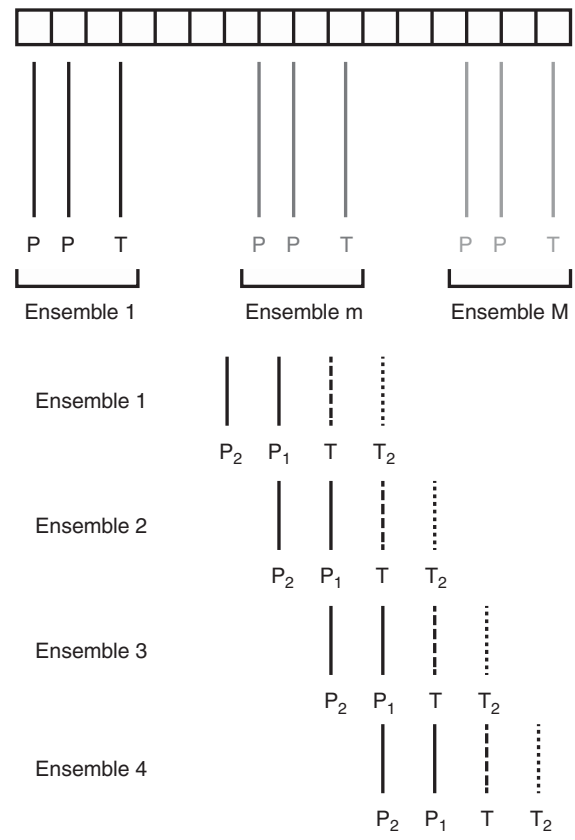

Figure 24.6 STL imaging beam sequences. MTL SWEI implemented with planewave imaging (e.g. SSI) can generate a shear wave speed image over a region of interest with a single ARFI push pulse. In contrast, each line of an STL-SWEI requires push pulses on either side of it. STL images are formed by walking an ensemble across the region of interest (top). In a single receive beam implementation, each ensemble consists of two push pulses and a tracking beam T (bottom). A total of 2M push pulse transmissions is required to form an M-line image. If two-to-one parallel receive beamforming is implemented, the number of push pulses can be reduced. Note that P_1 and T_2 for the n-th ensemble correspond to P_2 and T for the $(n + 1)$-th ensemble. An implementation with parallel receive beamforming can thus generate an M-line image with $M + 1$ push pulses.

to $2M$. The acquisition time of STL-SWEI and SMURF are thus inherently greater than that of MTL-SWEI.

24.4 Noise in SWE/Speckle Bias

Shear wave elastography is dependent on estimates of tissue displacement u at one or more points within the tissue $\vec{x}$. Ultrasonic tracking of shear wave propagation is subject to measurement error, which produces noise in shear wave speed images [19]. This noise arises from a variety of sources, including uncorrelated thermal noise, as well as correlated noise sources associated with the coherent nature of ultrasound backscatter imaging, e.g. speckle. Compared to MTL-SWEI, a characteristic of STL-SWEI imaging is that, for a given spatial resolution, it is comparatively insensitive to correlated noise in the shear wave arrival time estimate [20, 21]. As an illustration, Figure 24.7 presents two shear wave speed images of the same phantom, one obtained by STL, the other by MTL. While the spatial resolution of the images is similar – the push beam spacing Δx for the STL image is the same as the track beam spacing for the MTL image – the STL image exhibits less noise. This section describes the effect of correlated noise sources in shear wave tracking and arrival time estimation, and the relative immunity of STL to these sources.

Ultrasound tracking of tissue motion and measurement of $u(\vec{x})$ can be achieved by a variety of methods [22, 23], including windowed normalized cross correlation [24, 25] and phase shift estimation [26, 27]. The echoes used to track tissue motion exhibit limited signal-to-noise ratio (SNR), due to thermal noise in the transducer and receiver electronics, and other sources. The finite SNR results in a "jitter" in the displacement estimate [28, 29]. As an uncorrelated noise source, this jitter tends to zero on average. Repeated measurements at the same location $\vec{x}$ can be combined to reduce the error in u.

Shearing of the tissue is another source of echo distortion and tracking error [28, 30, 31]. Changes in the relative positions of scattering sites within the tissue, as caused by a shear wave or other deformation of the tissue, results in echoes that are imperfectly correlated [30]. In contrast to thermal noise, the error in displacement estimate resulting from shearing is repeatable and correlated with the echo. If the tissue undergoes the same shearing in two successive

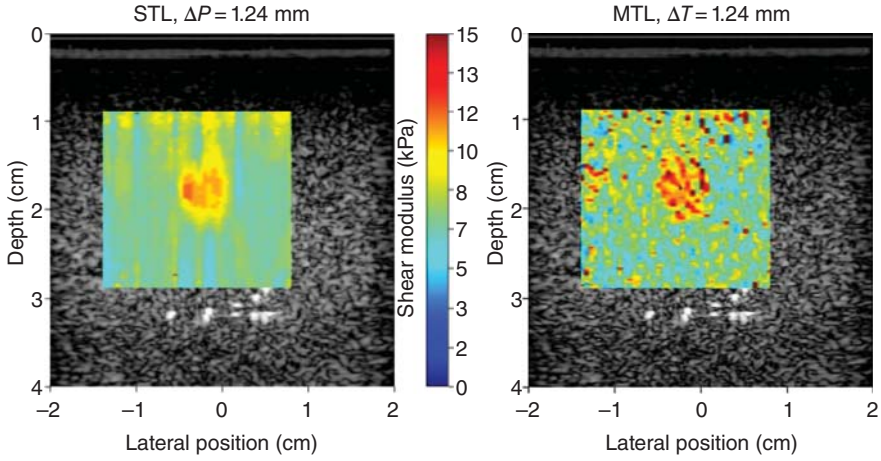

Figure 24.7 Matched STL and MTL images of a stiff inclusion. Both the STL and MTL images are obtained with a beam spacing of 1.24 mm. The increased spatial noise in the STL image is evident.

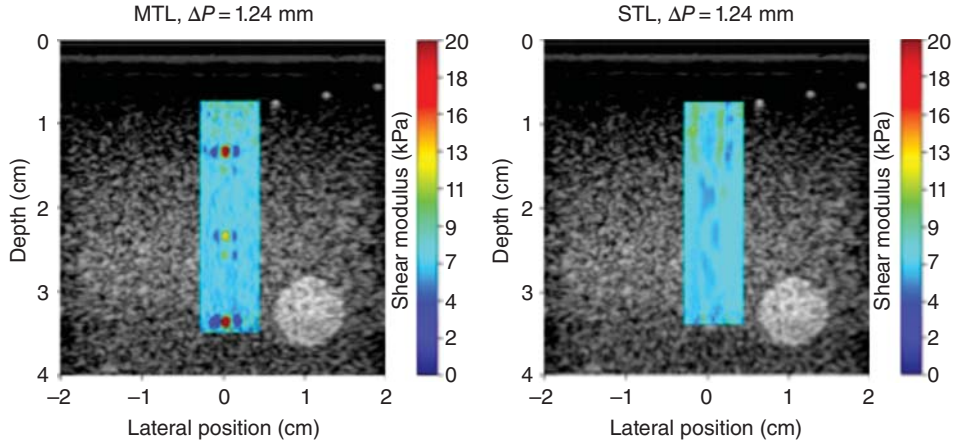

Figure 24.8 STL and MTL modulus images of a nylon monofilament target. MTL imaging shows a distinct artifact associated with the presence of a bright scatterer, realized here by subresolvable nylon filaments. Tracking beams in the vicinity of the bright scatterer track its motion preferentially to that of the background medium. As a result, arrival time estimates correspond to the arrival time of the shear wave at the bright scatterer, rather than at the tracking beam axis. The STL image does not exhibit this artifact, as the arrival time of the shear wave from each push location exhibits the same arrival time bias.

measurements, the same error in displacement estimate will be observed [32]. Thus, averaging of repeated measurements of a given speckle realization will not diminish the error in u at a given $\vec{x}$ due to this source.

In addition to error in the displacement amplitude [31, 33], ultrasound tracking of tissue motion is subject to uncertainty and error in the position $\vec{x}$ that is tracked. The motion measured by ultrasound may not correspond precisely to the assumed beam axis for a variety of reasons. For instance, refraction of the acoustic beam due to variations in the speed of sound of tissue can displace the beam from the desired alignment. Deflection of the tracking beam will result in a biased estimate of the shear wave speed.

Variation in the strength of the echo generated at different points within the tracking beam can induce a similar bias in the shear wave speed measurement. A simple example is illustrated in Figure 24.8, wherein a dominant scatterer (a nylon filament) is embedded in a comparatively weakly scattering matrix. The strong echo from the filament dominates the total echo over a range of tracking beam positions. As a result, the tracked motion corresponds to that of the wire, rather than that of the matrix on the tracking beam axis. The estimated arrival time likewise corresponds to the arrival time of the shear wave at the filament, rather than the tracking beam axis.

This bias in arrival time estimates is not limited to isolated bright scatterers, but can be observed in uniformly echogenic media with fully developed speckle [32]. Ultrasound backscatter images are dominated by speckle due to coherent insonification and detection of echoes. Echoes from the scattering sites within the tissue constructively and destructively interfere, producing the speckle characteristic of B-mode images. From a tracking standpoint, speckle results in non-uniform sensitivity to tissue motion with the tracking beam. This is illustrated schematically in Figure 24.9. On one side of the tracking beam axis, echoes from scatterers destructively interfere. The tracked signal is thus insensitive to the motion of these scatterers. Areas exhibiting constructive interference produce a detectable echo and are tracked. Thus, areas of constructive interference are tracked, while areas of destructive interference are effectively hidden. The resulting coherent error in the shear wave arrival time estimate is called speckle bias [20, 32, 34, 35].

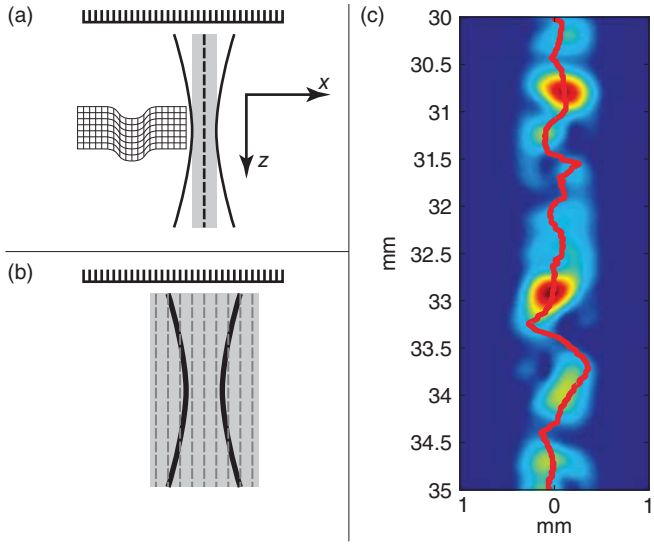

Figure 24.9 Speckle bias in a diffuse scattering medium. (a, b) Constructive and destructive interference of echoes from randomly distributed scatterers results in speckle. Regions of constructive interference contribute strongly to the echo signal, and are tracked preferentially to regions of destructive interference. This leads to arrival time biases associated with the speckle pattern, similar to that observed with a single bright scatterer. This is illustrated in (c). An image of the local speckle pattern may be generated by holding the transmit beam position fixed, and sweeping the receive beam pattern over the region of interest. This in effect creates an image of the transmit beam in the medium. Overlaid on this image is the measured shear wave arrival time, by time to peak displacement, scaled by the shear wave speed. Note the correlation between the shear wave arrival time bias and the speckle patter. Source: © 2015 IEEE, reprinted, with permission, from [32].

A simulation study [32] demonstrated a significant correlation between the error in the shear wave arrival time estimate and the lateral position of the local speckle pattern in a fully developed speckle model. Arrival time estimates were scaled by the shear wave speed (known in the simulation, estimated from the overall average in a homogeneous phantom) and plotted on an image of the local speckle pattern. A qualitative agreement between the arrival time bias and the speckle position was seen. The speckle bias effect was demonstrated in three dimensions by Hollender and Trahey [35]. MTL arrival times were shown to have a spatially varying error due to tracking of different speckle realizations, while STL showed a fixed offset error.

Strictly speaking, the arrival time estimate error will be the same only if the experiment is repeated precisely; that is, the shape and amplitude of the shear waves must be identical, and the same scatterers must be tracked, to avoid introducing decorrelation-based tracking errors. However, in both the phantom measurements and simulation [32], the arrival time error was seen to be relatively insensitive to the amplitude of the shear wave, which varied from −20 μm to +20 μm, as shown in Figure 24.10. That is, the mean squared error of the arrival time at any given pixel was ∼10 × larger than the change in the error as the shear wave amplitude was varied. This suggests that the speckle bias, rather than decorrelation, is the dominant source of error in the simulation. A matched phantom experiment yielded similar results.

Correlated errors in shear wave arrival time estimates manifest differently between MTL and STL SWEI. This difference explains the relatively greater noise in MTL images produced at the same spatial resolution as STL images. In the MTL case, motion is tracked at two separate locations. Since the scatterers tracked at the two locations are distinct, the arrival time estimates at each location will include independent errors. While some of this noise is uncorrelated due to finite SNR, repeating and averaging the measurement will not reduce the error in the arrival

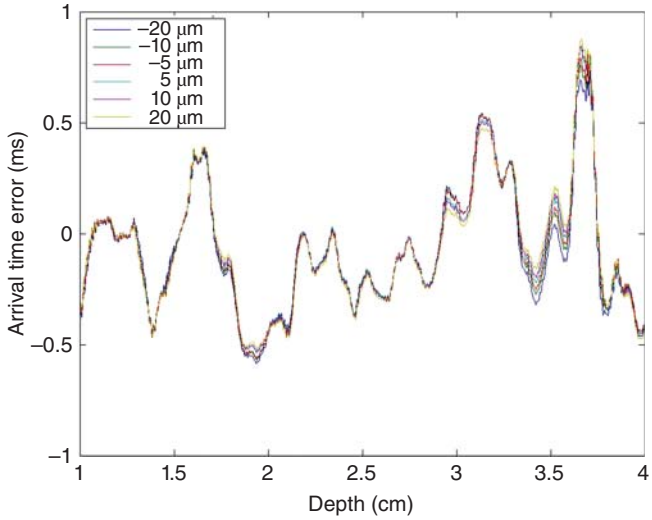

Figure 24.10 Representative arrival time graph. Simulated shear waves of several amplitudes were applied to a uniform speckle target mode. Arrival time errors showed little change with peak shear wave amplitude compared with the variation at different axial locations, corresponding to different speckle realizations. This result suggests that the underlying speckle pattern, rather than echo decorrelation, is responsible for the observed arrival time errors.

time estimate due to echo decorrelation. The shear wave speed estimate will contain a term due to the arrival time estimate errors

$$c_{\mathrm{MTL}} = \frac{\Delta x}{(\tau_2 + \epsilon_2) - (\tau_1 + \epsilon_1)} = \frac{\Delta x}{\Delta t + \Delta \epsilon} \tag{24.9}$$

If the arrival time errors $\Delta\epsilon$ are comparable to the true difference in arrival time $\Delta t = \Delta x/c$, the shear wave speed estimate will exhibit large errors. To improve spatial resolution, the spacing between tracking beams is decreased. As the true arrival time decreases with decreasing beam spacing, the error in the MTL shear wave speed estimate increases. In STL-SWEI, because the measurement is repeated at the same location, the error in arrival time estimate ϵ is the same for both shear waves. When the shear wave speed is calculated, the common error is suppressed

$$c_{\mathrm{MTL}} = \frac{\Delta x}{(\tau_2 + \epsilon) - (\tau_1 + \epsilon)} = \frac{\Delta x}{\Delta t} \tag{24.10}$$

Figure 24.11 presents matched STL and MTL images of a uniform phantom with $\Delta x = 1.24$ mm. The tracking window length is $\sim 2\lambda$. The relatively lower noise of the STL image is evident. Also shown is the measured standard deviation of shear wave speed estimates in the phantom using both approaches for a range of Δx. These results suggest that, when echo SNR and tissue motion are not limiting factors, the suppression of speckle bias by STL allows for lower noise images for a given spatial resolution. This benefit comes at the cost of increased acquisition time compared to an MTL sequence.

The reduction in noise and the improvement in image quality due to suppression of correlated noise has been reported by several authors. Elegbe et al. demonstrated a marked reduction in STL measurement variance compared to MTL in liver tissue [20]. Hollender et al. quantified the improved contrast-to-noise ratio (CNR) of STL vs. MTL and conventional ARFI in imaging inclusions of 1.5 to 6 mm diameter [21]. STL-SWEI exhibited the highest CNR of the three methods. The authors describe the close beam spacing and high resolution allowed by STL-SWEI as enabling micro-elastography, µE [18].

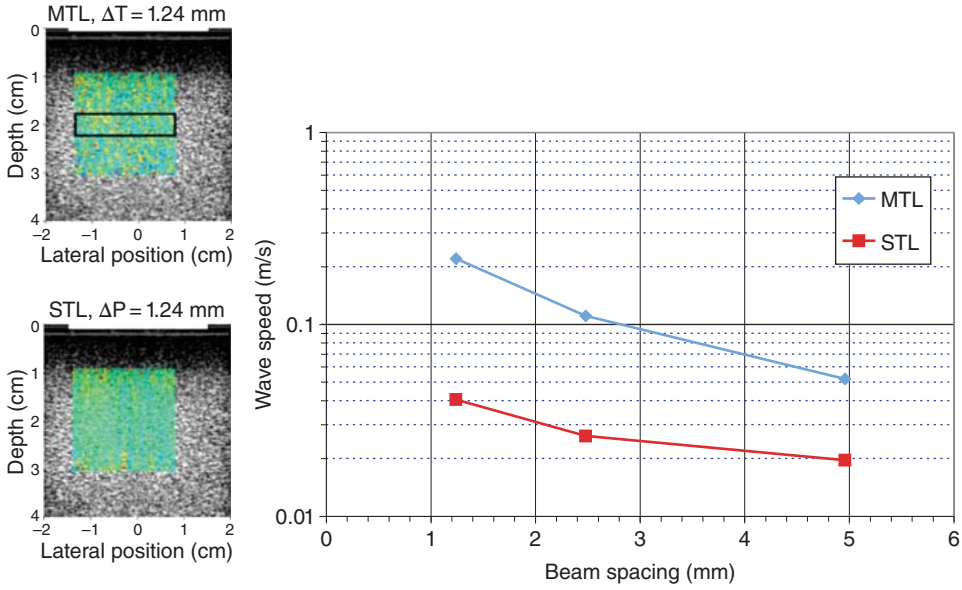

Figure 24.11 Comparison of standard deviations of STL and MTL shear wave speed estimates in a uniform phantom as a function of beam spacing. A uniform phantom scanned with MTL exhibits greater shear wave speed estimate variance than an STL sequence of identical spatial resolution (left). Repeated scans of the phantom yielded identical noise patterns, indicating that the noise was due to a correlated source, e.g. speckle bias, rather than inadequate SNR. The greater image uniformity of the STL imaging for a given spatial resolution is quantified by the correspondingly lower standard deviations (right).

24.5 Estimation of viscoelastic parameters (STL-VE)

Biological tissues are viscoelastic and exhibit frequency-dependent shear wave speed and attenuation. The methods described so far in this chapter estimate the group speed of shear waves, but do not model or directly measure the frequency dependence of shear wave speed or attenuation. Measurement of viscoelastic parameters is more challenging than group wave speed estimation but offers some potential benefits.

One advantage of methods that incorporate a viscoelastic model is reduced sensitivity to system parameters. The speed and attenuation of shear waves in tissue varies with frequency. As a result, the frequency content and group speed of transient shear waves varies with propagation distance. As the wave propagates, faster-moving high-frequency components are rapidly attenuated, leaving the slower-moving low-frequency component of the wave. The frequency content of the shear wave is itself a function of the push beam shape and duration. Thus, measured shear wave speed in a viscoelastic medium will vary significantly with changes in push beam focusing and duration, and with push and track beam separation. When a naïve elastic model is applied to measurements made in a viscoelastic medium, these system-dependent variations can be mistaken for variations in tissue mechanical properties. Different measurement systems, exciting shear waves at differing frequencies in the same viscoelastic material, will register differences in shear wave speed and apparent elastic modulus. For example, the confounding role of viscoelasticity in quantitative shear wave elastography of the liver has been recognized as a challenge by the RSNA Quantitative Imaging Biomarker Alliance (QIBA) Ultrasound Shear Wave Speed (SWS) committee [36, 37].

A second benefit of methods that quantify viscoelasticity is that that such parameters of tissue can themselves be diagnostic. Several studies have demonstrated a strong correlation between

measured viscosity parameters and liver fibrosis stage [38–46]. Shear wave dispersion may provide information about the microscopic structure of tissue [41, 47], and may provide a marker of disease progression prior to the onset of fibrosis [40]. Changes in viscoelastic parameters are associated with tissue damage and inflammatory response. For example, Wuerfel showed early stage multiple sclerosis results in a lowering of the viscoelastic parameter of brain tissue, prior to any morphological change [48]. Aubrey et al. observed that tendonopathy results in a reduction of the viscoelastic parameter compared with healthy tendon [49]. While measurement of viscoelastic parameters is potentially useful as a diagnostic tool, viscosity estimates are challenged by larger measurement variance relative to elasticity or shear wave group speed. The omission of viscosity measurement is largely due to the inability to obtain stable, reproducible measurements [44].

In a viscoelastic material, the wave number k is a complex-valued function of ω. A plane wave can be modeled as $e^{j(\omega t - k(\omega)x)} = e^{j(\omega t - k_r(\omega)x)} e^{-k_i(\omega)x}$, with the real part of the wavenumber k_r denoting the change in phase with position, and the imaginary part k_i generating the loss in amplitude due to viscoelastic attenuation. The relationship between k and ω is material dependent. Numerous models exist for viscoelastic solids [50], including the Kelvin-Voigt (KV), Zener, fractional-derivative Kelvin-Voigt, and microchannel [51] models. While a given viscoelastic model may fit over a limited range of frequencies, e.g. less than a decade, there is not yet an established model that accurately models tissue over a wide frequency range. The KV model is perhaps the simplest model that captures viscoelastic behavior of a solid. In this model, the storage μ and loss η moduli are related to the wave number by

$$k_r = \omega \sqrt{\frac{\rho(\mu + \sqrt{\mu^2 + \omega^2\eta^2})}{2(\mu^2 + \omega^2\eta^2)}} \tag{24.11}$$

and

$$k_i = \sqrt{\frac{\rho(-\mu + \sqrt{\mu^2 + \omega^2\eta^2})}{2(\mu^2 + \omega^2\eta^2)}} \tag{24.12}$$

Viscoelastic measurement methods may be model based, wherein the goal is to estimate the parameters of the viscoelastic model. Alternatively, a model-free approach can be taken, wherein the goal is to estimate a spectrum $k(\omega)$, from which the shear wave speed as a function of frequency is determined $c(\omega) = \frac{\omega}{k(\omega)}$ [47]. We will first consider a model-free approach, spectroscopy, in the context of STL vs. MTL, before developing a model-based STL technique, STL-VE.

Let us denote the spectrum of the first shear wave signal as

$$S_1(\omega) = F\{s_1(t)\} = A_0(\omega)e^{j(k(\omega)x_1 + \phi_0(\omega))} = A_0(\omega)e^{j(k_r(\omega)x_1 + \phi_0(\omega))}\, e^{-k_i(\omega)x_1} \tag{24.13}$$

The second shear wave signal has spectrum

$$S_2(\omega) = F\{s_2(t)\} = A_0(\omega)e^{j(k(\omega)x_2 + \phi_0(\omega))} \tag{24.14}$$

Both waves contain a priori unknown phase components $\phi_0(\omega)$ and spectral amplitude $A(\omega)$. The locations x_1 and x_2 are also subject to speckle-bias errors. In the STL implementation, x_1 and x_2 share a common tracking position error ϵ, while in the MTL realization each location has independent errors ϵ_1 and ϵ_2.

The phase shift associated with the shear wave propagation over the distance $\Delta x = x_2 - x_1$ can be obtained by forming the cross spectrum $H(\omega) = S_2(\omega)S_1^*(\omega)$. The phase of $H(\omega)$ is the difference between the phase of $S_2(\omega)$ and that of $S_1(\omega)$. Using the expression $x_1 + \Delta x = x_2$ the STL cross spectrum can be written

$$H(\omega) = S_2(\omega)S_1^*(\omega) = A_0^2(\omega)e^{-k_i(\omega)2(x_1+\epsilon)}e^{jk(\omega)\Delta x} \tag{24.15}$$

The STL spectrogram, formed by dividing the cross spectrum by the power spectrum of S_1, i.e.

$$P(\omega) = \frac{H(\omega)}{S_1(\omega)S_1^*(\omega)} = e^{jk_r(\omega)\Delta x}e^{-k_i(\omega)\Delta x} \tag{24.16}$$

which provides the real and imaginary part of the wave number without speckle bias. In contrast, the MTL cross spectrum

$$H(\omega) = A_0^2(\omega)e^{-k_i(\omega)2x_1+\epsilon_1+\epsilon_2}e^{jk(\omega)(\Delta x+\epsilon_2-\epsilon_1)} \tag{24.17}$$

and spectrogram retain speckle bias errors. Langdon demonstrated that speckle bias noise in the spectrogram can mimic tissue viscoelasticity [52, 53].

The spectrogram is not constrained to a particular model and represents a challenging estimation problem with high noise sensitivity [54]. A model-based approach attempts to estimate a small number (2 or 3) of viscoelastic parameters that can be more robust in the face of noise. One potential approach to viscoelastic parameter estimation is to fit a particular viscoelastic model to the spectrogram data. While intuitive, this approach has shortcomings. The spectrogram is subject to truncation artifacts due to the finite spatial and temporal support of the data acquired; this introduces "ringing" artifacts and spectral blurring. Multiple model parameter combinations may be found to fit the data over the measured frequency range, and the spectrogram does not itself provide data to distinguish among the possibilities.

A maximum-likelihood approach was proposed by Langdon, called STL viscosity estimation (STL-VE) [55]. The method is illustrated conceptually in Figure 24.12. The propagation of a shear wave through a region of tissue Δx can be modeled as the action of a filter K on the shear wave, transforming shear wave s_1 into shear wave s_2. The filter models both geometrical properties of the wave (e.g. plane, cylindrical, or other form) as well as the viscoelastic properties of the tissue according to the selected model. A KV model was used in the initial development but other models are equally applicable. In the absence of noise, when the correct geometric and viscoelastic parameters are selected the filter output matches the observed shear wave and $s_2 = \mathcal{F}^{-1}\{K\mathcal{F}\{s_1\}\}$. In the case of a plane wave geometry in a Kelvin-Voigt material, the filter takes the form

$$K(\omega) = \exp\left(\frac{j\omega\Delta x}{c(\omega)}\right) \tag{24.18}$$

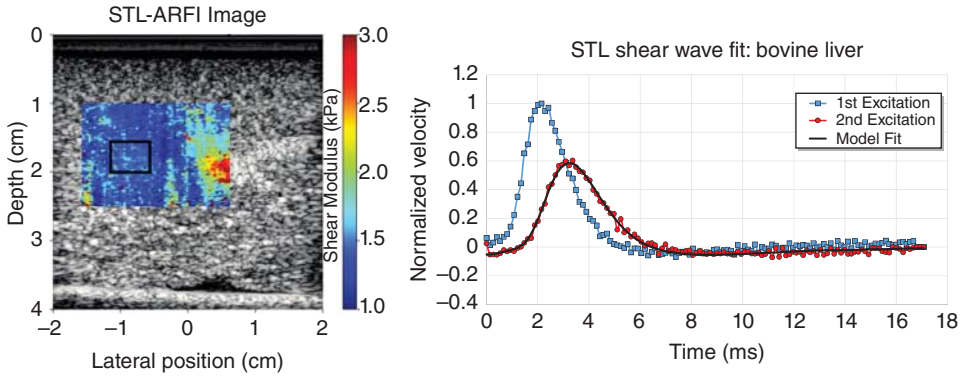

Figure 24.12 Representative STL-VE model fits in viscoelastic tissue. STL-SWEI shear wave data collected in bovine liver (left) was fitted to a KV model using the STL-VE approach (right). Shear wave traces s_1 and s_2 in VE material. The "model fit" trace (solid black line) is obtained by passing the shear wave trace from the first excitation through the propagation filter. A high degree of correspondence results between the observed s_2 shear wave trace and the model fit. Source: © 2015 IEEE, reprinted, with permission, from [53].

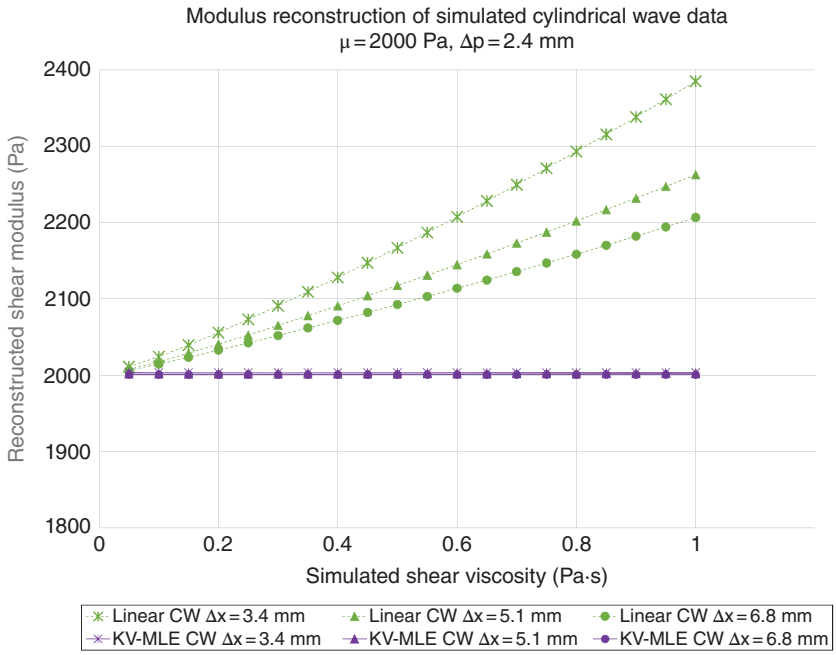

Figure 24.13 STL-VE yields a consistent estimate of storage modulus over a wide range of simulated loss modulus values. In contrast, a naïve linear elastic STL-SWEI model shows increasing estimated shear modulus as the viscoelastic parameter is increased. Source: © 2015 IEEE, reprinted, with permission, from [53].

with

$$c(\omega) = \sqrt{\frac{2\left(\mu^2 + \omega^2\eta^2\right)}{\rho\left(\sqrt{\mu^2 + \omega^2\eta^2} + \mu\right)}} \tag{24.19}$$

given in terms of the viscoelastic parameters μ and η.

With each measured signal shear wave signal corrupted by noise, Langdon et al. [53] demonstrated that the maximum likelihood estimator is that which minimizes the residual between the observed noisy signal $y_2 = s_2 + n_2$ and the observed input shear wave filtered by the wave filter $\mathcal{F}^{-1}\{K\mathcal{F}\{y_1\}\}$, where $y_1 = s_1 + n_1$. In other words, the STL-VE approach estimates the viscoelatic parameters of the tissue by finding the parameters of the filter K that minimize

$$|y_2 - \mathcal{F}^{-1}\{K\mathcal{F}\{y_1\}\}|^2 = |n_2 - \mathcal{F}^{-1}\{K\mathcal{F}\{n_1\}\}|^2 \tag{24.20}$$

A benefit of this approach is that the fitting and comparison of signals is performed in the time domain, rather than the frequency domain, avoiding truncation issues associated with frequency domain approaches [53].

Figure 24.13 compares the output of STL-SWEI with a naïve $G = \rho c^2$ estimator to the STL-VE estimate of shear modulus μ as shear viscosity is varied from 0 Pa·s to 1 Pa·s [52]. The precise dependence of the STL-SWEI overestimation of the shear modulus in practice will depend on the spectral content of the shear wave [56]. STL-VE yields the correct shear modulus estimate independent of viscosity. The accuracy of the shear modulus estimate is dependent on the correct geometrical model for the shear wave. In the example shown, a plane wave was modeled and assumed for the estimator. Langdon quantified biases due to the assumption of an incorrect shear wave geometry [52, 53]. Figure 24.14 compares the variance of shear modulus and shear viscosity estimates obtained with STL and MTL implementations of STL-VE,

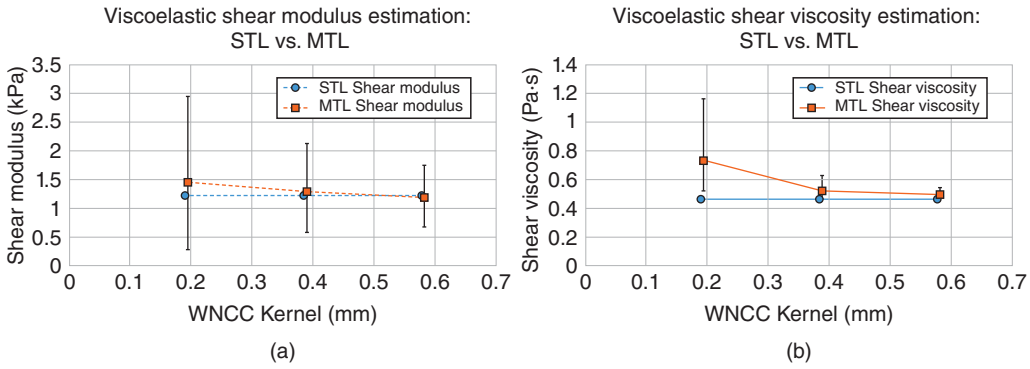

Figure 24.14 STL-VE using STL vs. MTL data. Speckle bias increases the variance in the estimate of (a) storage modulus μ and (b) loss modulus η when MTL-SWEI data are applied to the STL-VE estimator. STL-SWEI suppresses the speckle bias, resulting in correct storage and loss modulus estimates for a range of tracking kernel lengths. When the speckle bias is particularly pronounced (low kernel length) a bias in the MTL estimate, in addition to the increased variance, is also observed. Source: © 2015 IEEE, reprinted, with permission, from [53].

demonstrating that speckle bias not only increases the variance of the parameter estimates, but can also increase the apparent viscosity.

24.6 Conclusion

STL-SWEI methods for shear wave elastography are characterized by the use of a common ultrasound tracking location to measure tissue motion in response to shear waves generated with a known characteristic spatial dimension. The common tracking location inherently suppresses speckle noise, which can be a limiting factor in generating shear wave speed estimates with closely spaced beams. STL-SWEI is a complement to other acoustic radiation force methods, with its principle advantage being reduced estimate variance and improved contrast-to-noise ratio compared to an MTL implementation with similar spatial resolution. The use of STL-SWEI is potentially advantageous for high spatial resolution shear wave speed imaging. STL-VE, a method of processing STL-SWEI echo data, allows the estimation of viscoelastic parameters, with potential benefits to reducing system-dependent measurement results and diagnostic viscoelastic images.

References

1 Sarvazyan, A.P., Rudenko, O.V., Swanson, S.D., et al. (1998). Shear wave elasticity imaging: a new ultrasonic technology of medical diagnostics. *Ultrasound Med. Biol.* 24: 1419–1435.
2 Parker, K.J., Doyley, M.M., and Rubens, D.J. (2011). Imaging the elastic properties of tissue: the 20 year perspective. *Phys. Med. Biol.* 56: R1–R29.
3 Greenleaf, J.F., Fatemi, M., and M. Insana (2003). Selected methods for imaging elastic properties of biological tissues. *Annu. Rev. Biomed. Eng.* 5: 57–78.
4 Fung, Y.C. (1993). *Biomechanics: Mechanical Properties of Living Tissues*, 2nd edn. New York: Springer-Verlag.
5 Nightingale, K.R., Palmeri, M.L., Nightingale, R.W., and Trahey, G.E. (2001). On the feasibility of remote palpation using acoustic radiation force. *J. Acoust. Soc. Am.* 110: 625–634.

6 Nightingale, K., Soo, M.S., Nightingale. R., and Trahey, G. (2002). Acoustic radiation force impulse imaging: In vivo demonstration of clinical feasibility. *Ultrasound Med. Biol.* 28: 227–235.

7 Chen, S., Urban, M.W., Pislaru, C., et al. (2009). Shearwave dispersion ultrasound vibrometry (SDUV) for measuring tissue elasticity and viscosity. *IEEE Trans. Ultrason., Ferroelect., Freq. Control* 56: 55–62.

8 Chen, S., Fatemi, M., and Greenleaf, J.F. (2004). Quantifying elasticity and viscosity from measurement of shear wave speed dispersion. *J. Acoust. Soc. Am.* 115: 2781–2785.

9 Bercoff, J., Tanter, M., and Fink, M. (2004). Supersonic shear imaging: a new technique for soft tissue elasticity mapping. *IEEE Trans. Ultrason., Ferroelect., Freq. Control* 51: 396–409.

10 Palmeri, M.L., Wang, M.H., Dahl, J.J., et al. (2008). Quantifying hepatic shear modulus in vivo using acoustic radiation force. *Ultrasound Med. Biol.* 34: 546–558.

11 McAleavey, S., Collins, E., Kelly, J., et al. (2009). Validation of SMURF estimation of shear modulus in hydrogels. *Ultrason. Imaging* 31: 131–150.

12 McAleavey, S.A., Menon, M., and Orszulak, J. (2007). Shear-modulus estimation by application of spatially-modulated impulsive acoustic radiation force. *Ultrason. Imaging* 29: 87–104.

13 Blackstock, D.T. (2000). *Fundamentals of Physical Acoustics*. New York: Wiley.

14 Jensen, J.A. (1996). *Estimation of Blood Velocities Using Ultrasound: A Signal Processing Approach*. New York: Cambridge University Press.

15 Routh, H. (1996). Doppler ultrasound – The ability to measure and image blood flow. *IEEE Eng. Med. Biol.* 15: 31–40.

16 Elegbe, E.C., Menon, M.G., and McAleavey, S.A. (2011). Comparison of two methods for the generation of spatially modulated ultrasound radiation force. *IEEE Trans. Ultrason., Ferroelect., Freq. Control* 58: 1344–1354.

17 McAleavey, S., Menon, M., and Elegbe, E. (2009). Shear modulus imaging with spatially-modulated ultrasound radiation force. *Ultrason. Imaging* 31: 217–234.

18 Hollender, P., Rosenzweig, S., Nightingale, K., and Trahey, G. (2014). Micro-elasticity (μ-E): CNR and resolution of acoustic radiation force impulse imaging and single- and multiple track location shear wave elasticity imaging for visualizing small targets. In: *IEEE International Ultrasonics Symposium (IUS),* 2014, 703–706.

19 Deng, Y., Rouze, N.C., Palmeri, M.L., and Nightingale, K.R. (2016). On system dependent sources of uncertainty and bias in ultrasonic quantitative shear wave imaging. *IEEE Trans. Ultrason., Ferroelect., Freq. Control* 63 (3): 381–393.

20 Elegbe, E.C. and McAleavey, S.A. (2013). Single tracking location methods suppress speckle noise in shear wave velocity estimation. *Ultrason. Imaging* 35: 109–125.

21 Hollender, P.J., Rosenzweig, S.J., Nightingale, K.R., and Trahey, G.E. (2015). Single- and multiple-track-location shear wave and acoustic radiation force impulse imaging: matched comparison of contrast, contrast-to-noise ratio and resolution. *Ultrasound Med. Biol.* 41: 1043–1057.

22 Viola, F. and Walker, W.F. (2003). A comparison of the performance of time-delay estimators in medical ultrasound. *IEEE Trans. Ultrason., Ferroelect., Freq. Control* 50: 392–401.

23 Hein, I.A. and Obrien, W.D. (1993). Current time-domain methods for assessing tissue motion by analysis from reflected ultrasound echoes – a review. *IEEE Trans. Ultrason., Ferroelect., Freq. Control* 40: 84–102.

24 Bonnefous, O and Pesque, P. (1986). Time domain formulation of pulse-Doppler ultrasound and blood velocity estimation by cross-correlation. *Ultrason. Imaging* 8: 73–85.

25 deKorte, C.L., vanderSteen, W.A.F., and Dijkman, B.H.J. (1997). Performance of time delay estimation methods for small time shifts ultrasonic signals. *Ultrasonics* 35: 263–274.

26 Loupas, T., Powers, J.T., and Gill, R.W. (1995). An axial velocity estimator for ultrasound blood-flow imaging, based on a full evaluation of the Doppler equation by means of a 2-dimensional autocorrelation approach. *IEEE Trans. Ultrason., Ferroelect., Freq. Control* 42: 672–688.

27 Pinton, G.F., Dahl, J.J., and Trahey, G.E. (2006). Rapid tracking of small displacements with ultrasound. *IEEE Trans. Ultrason., Ferroelect., Freq. Control* 53: 1103–1117.

28 Walker, W.F. and Trahey, G.E. (1995). A fundamental limit on delay estimation using partially correlated speckle signals. *IEEE Trans. Ultrason., Ferroelect., Freq. Control* 42: 301–308.

29 Bilgen, M. and Insana, M.F. (1997). Error analysis in acoustic elastography .1. Displacement estimation. *J. Acoust. Soc. Am.* 101: 1139–1146.

30 McAleavey, S.A., Nightingale, K.R., and Trahey, G.E. (2003). Estimates of echo correlation and measurement bias in acoustic radiation force impulse imaging. *IEEE Trans. Ultrason., Ferroelect., Freq. Control* 50: 631–641.

31 Palmeri, M.L., McAleavey, S.A., Trahey, G.E., and Nightingale, K.R. (2006). Ultrasonic tracking of acoustic radiation force-induced displacements in homogeneous media. *IEEE Trans. Ultrason., Ferroelect., Freq. Control* 53: 1300–1313.

32 McAleavey, S.A., Osapoetra, L.O., and Langdon, J. (2015). Shear wave arrival time estimates correlate with local speckle pattern. *IEEE Trans. Ultrason., Ferroelect., Freq. Control* 62: 2054–2067.

33 McAleavey, S.A., Nightingale, K.R., and Trahey, G.E. (2003). Estimates of echo correlation and measurement bias in acoustic radiation force impulse imaging. *IEEE Trans. Ultrason., Ferroelect., Freq. Control* 50: 631–641.

34 McAleavey, S., Langdon, J., and Osapoetra, L. (2014). Shear wave arrival time estimates correlate with local speckle pattern. In: *IEEE International Ultrasonics Symposium (IUS),* 2014, 643–646.

35 Hollender, P. and Trahey, G. (2015). Speckle bias as a 3-D offset for the tracking location of shear wave imaging. In: *IEEE International Ultrasonics Symposium (IUS),* 2015, 1–4.

36 Hall, T.J., Milkowski, A., Garra, B., et al. (2013). RSNA/QIBA: shear wave speed as a biomarker for liver fibrosis staging. In: *IEEE International Ultrasonics Symposium (IUS), 2013*, 397–400.

37 Palmeri, M., Nightingale, K., Fielding, S., et al. (2015). RSNA QIBA ultrasound shear wave speed Phase II phantom study in viscoelastic media. In: *IEEE International Ultrasonics Symposium (IUS), 2015*, 1–4.

38 Huwart, L., Sempoux, C., Salameh, N., et al. (2007). Liver fibrosis: noninvasive assessment with MR elastography versus aspartate aminotransferase-to-platelet ratio index. *Radiology* 245: 458–466.

39 Muller, M., Gennisson, J.L., Deffieux, T., et al. (2009). Quantitative viscoelasticity mapping of human liver using supersonic shear imaging: preliminary in vivo feasibility study. *Ultrasound Med. Biol.* 35: 219–229.

40 Salameh, N., Larrat, B., Abarca-Quinones, J., et al. (2009). Early detection of steatohepatitis in fatty rat liver by using MR elastography. *Radiology* 253: 90–97.

41 Bavu, E., Gennisson, J.L., Couade, M., et al. (2011). Noninvasive in vivo liver fibrosis evaluation using supersonic shear imaging: a clinical study on 113 hepatitis C virus patients. *Ultrasound Med. Biol.* 37: 1361–1373.

42 Chen, S., Sanchez, W., Callstrom, M.R., et al. (2013). Assessment of liver viscoelasticity by using shear waves induced by ultrasound radiation force. *Radiology* 266: 964–970.

43 Zhu, Y., Zhang, X., Zheng, Y., et al. (2014). Quantitative analysis of liver fibrosis in rats with shearwave dispersion ultrasound vibrometry: comparison with dynamic mechanical analysis. *Med. Eng. Phys.* 36: 1401–1407.

44 Nenadic, I.Z., Urban, M.W., Zhao, H., et al. (2014). Application of attenuation measuring ultrasound shearwave elastography in 8 post-transplant liver patients. In: *IEEE International Ultrasonics Symposium (IUS), 2014*, 987–990.

45 Reiter, R., Freise, C., Johrens, K., et al. (2014). Wideband MRE and static mechanical indentation of human liver specimen: sensitivity of viscoelastic constants to the alteration of tissue structure in hepatic fibrosis. *J. Biomech.* 47: 1665–1674.

46 Asbach, P., Klatt, D., Schlosser, B., et al. (2010). Viscoelasticity-based staging of hepatic fibrosis with multifrequency MR elastography. *Radiology* 257: 80–86.

47 Deffieux, T., Montaldo, G., Tanter, M., and Fink, M. (2009). Shear wave spectroscopy for in vivo quantification of human soft tissues visco-elasticity. *IEEE Trans. Med. Imaging* 28: 313–322.

48 Wuerfel, J., Paul, F., Beierbach, B., et al. (2010). MR-elastography reveals degradation of tissue integrity in multiple sclerosis. *Neuroimage* 49: 2520–2525.

49 Aubry, S., Nueffer, J.P., Tanter, M., et al. (2015). Viscoelasticity in Achilles tendonopathy: quantitative assessment by using real-time shear-wave elastography. *Radiology* 274: 821–829.

50 Lakes, R.S. (2009). *Viscoelastic Materials*. New York: Cambridge University Press.

51 Parker, K.J. (2014). A microchannel flow model for soft tissue elasticity. *Phys. Med. Biol.* 59: 4443–4457.

52 Langdon, J. (2015). Development of single track location shearwave viscoelasticity imaging for real-time characterization of biological tissues. Ph.D. Thesis, Department of Biomedical Engineering, University of Rochester, Rochester, NY, USA.

53 Langdon, J.H., Elegbe, E., and McAleavey, S.A. (2015). Single tracking location acoustic radiation force impulse viscoelasticity estimation (STL-VE): A method for measuring tissue viscoelastic parameters. *IEEE Trans. Ultrason., Ferroelect., Freq. Control* 62 (7): 1225–1244.

54 Rouze, N.C., Palmeri, M.L., and Nightingale, K.R. (2014). Estimation of model parameters characterizing dispersion in ARFI induced shear waves in in vivo human liver. In: *IEEE International Ultrasonics Symposium (IUS), 2014*, 983–986.

55 Langdon J.H. and McAleavey, S.S. (2014). Single track location viscosity estimation by maximum likelihood estimation. In: *IEEE International Ultrasonics Symposium (IUS),* 2014, 991–996.

56 Palmeri, M.L., Deng, Y., Rouze, N.C., and Nightingale, K.R. (2014). Dependence of shear wave spectral content on acoustic radiation force excitation duration and spatial beamwidth. In: *IEEE International Ultrasonics Symposium (IUS), 2014*, 1105–1108.

25

Comb-push Ultrasound Shear Elastography

Pengfei Song and Shigao Chen

Department of Radiology, Mayo Clinic, Rochester, MN, USA

25.1 Introduction

Comb-push ultrasound shear elastography (CUSE) is one of the acoustic radiation force-based ultrasound shear wave elastography methods that first introduced the concept of simultaneous generation of multiple shear wave sources, which allows reconstruction of a full field-of-view (FOV) shear elasticity map with a single shear wave push-and-detection cycle. In conventional ultrasound shear wave elastography, a single shear wave source at a fixed lateral location is typically used for shear wave generation (Figure 25.1a). As a result, the shear wave speed under the shear wave source region cannot be recovered because of the absence of shear waves (Figure 25.1b) [1]. A second challenge in conventional ultrasound shear wave elastography is that as shear waves propagate in tissue, significant shear wave attenuation will occur in areas that are far away from the push beam region (Figure 25.1c), which results in poor shear wave signal-to-noise ratio (SNR).

One typical solution for these limitations is to transmit multiple push beams at different spatial locations and detect the resulting shear waves in multiple push-detect data acquisitions, so that the push beam artifacts can be removed and the shear wave SNR can be improved by concatenating multiple shear elasticity maps from these acquisitions [2]. This solution, however, requires multiple push-detection data acquisitions that increase the total data acquisition time. This may introduce artifacts caused by physiologic motion and also make it challenging to study tissue dynamic mechanical properties during fast physiological event such as muscle contraction.

CUSE was recently proposed by Song et al. [3–5] to address these challenges by using multiple laterally distributed shear wave sources to simultaneously generate multiple shear waves inside the FOV. By using a directional filter to remove the wave interference and separate the left-to-right and right-to-left shear waves, CUSE can reconstruct a full FOV 2D shear elasticity map without push beam artifacts with a single push-detection data acquisition. Also in CUSE, each imaging pixel always has a shear wave source close by, which effectively alleviates the shear wave attenuation and increases shear wave SNR. In this chapter, we will introduce the principles of CUSE, different configurations of CUSE with various ultrasound push beams, and several clinical applications using the CUSE technique.

Ultrasound Elastography for Biomedical Applications and Medicine, First Edition.
Edited by Ivan Nenadic, Matthew Urban, James Greenleaf, Jean-Luc Gennisson, Miguel Bernal, and Mickael Tanter.

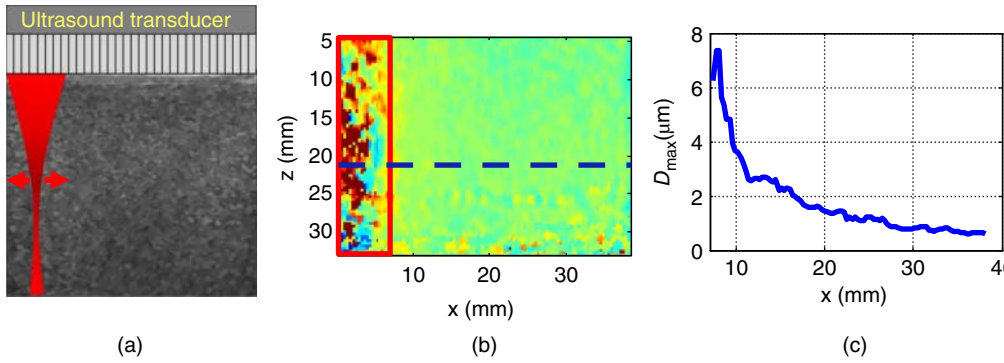

Figure 25.1 (a) A schematic plot of an ultrasound push beam and the resulting shear wave propagation direction. The focused ultrasound push beam (indicated by the red shape) produces two shear wave fronts propagating away from the push beam (indicated by the two red arrows pointing at opposite directions) in a homogeneous phantom. (b) A shear elasticity map of this phantom was reconstructed by calculating the shear wave propagation speed at each imaging pixel location. The area marked by the rectangle indicates the artifact caused by absence of shear waves at the push beam region. The dashed line indicates the path of shear wave propagation. (c) The maximum shear wave amplitude along the blue dashed line in (b). Source: reprinted from [1].

25.2 Principles of Comb-push Ultrasound Shear Elastography (CUSE)

The basic concept of CUSE is to distribute multiple shear wave sources inside the tissue *simultaneously*. Multiple configurations of the push beam have been developed (Figure 25.2): simultaneous transmission of multiple unfocused ultrasound push beams (unfocused-CUSE, U-CUSE), simultaneous transmission of multiple focused ultrasound push beams (focused-CUSE, F-CUSE), and sequentially marching the focused push beams in lateral

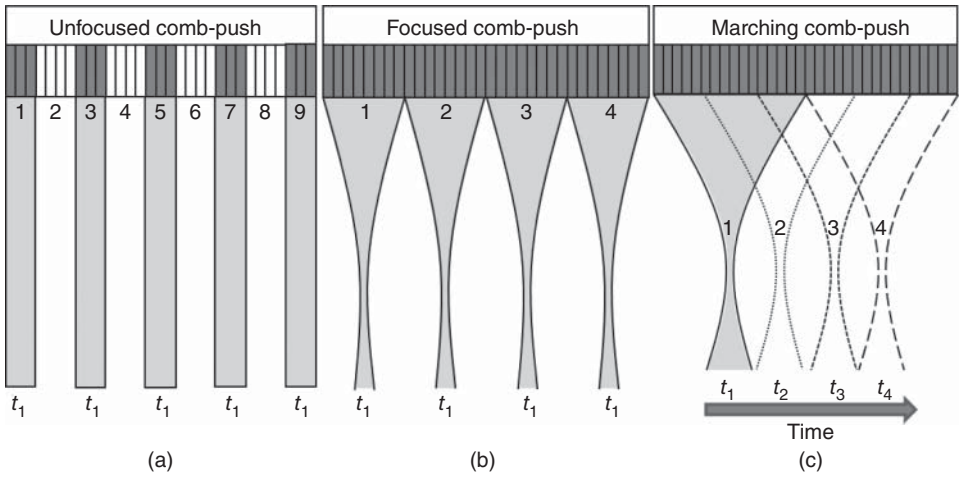

Figure 25.2 Schematic plots of different CUSE imaging sequences. (a) U-CUSE: transmits multiple unfocused ultrasound push beams simultaneously at time t_1. (b) F-CUSE: transmits multiple focused ultrasound beams simultaneously at time t_1. (c) M-CUSE: transmits single focused ultrasound beam using element subgroup 1 at time t_1, then marches laterally to push with subgroup 2 at time t_2, subgroup 3 at time t_3, and subgroup 4 at time t_4. The time interval between the end and start of consecutive push beams was 15 μs. Source: reprinted from [1].

direction (marching-CUSE, M-CUSE). Each push beam produces two shear waves propagating at opposite directions away from the push beam. The shear waves from different push beams interfere with each other and eventually fill the entire FOV, so that the push beam artifact can be removed because each imaging pixel always has at least one shear wave propagating through (Figure 25.3). This allows a reconstruction of full FOV 2D shear elasticity map with a single push-detection data acquisition, which improves the theoretical frame rate of shear wave imaging. Figure 25.3 shows examples of the shear wave motion signal from the three different kinds of CUSE. One can clearly observe the shear wave interferences during propagation. The number of push beams and the configuration of each push beam (e.g. F/#, center frequency, etc.) can be variable and typically optimized for different applications.

Before one can use the comb-push shear wave field to reconstruct shear elasticity maps, there is a key challenge that needs to be addressed. As shown in Figure 25.4, due to the shear wave interference, shear wave signals from adjacent spatial pixels are severely decorrelated (Figure 25.4b). As a result, it is difficult to accurately estimate the shear wave speed using such shear wave signals. The shear wave interference has to be removed in order to obtain robust local shear wave speed calculations. One way of removing the interference is to use directional filters [6]. As shown in Figure 25.5, one can convert the shear wave signal to the Fourier domain and selectively preserve or discard the spectra that are corresponding to waves traveling in a certain direction. By application of an inverse Fourier transform of the filtered spectrum, one can recover shear waves that are purely propagating from left to right or from right to left. We can now revisit the two shear wave waveforms that are severely decorrelated in Figure 25.4b. After directional filtering (Figure 25.4c), one can clearly see that the interference is removed and the shear wave signals resemble each other. One can easily calculate the time delay between the two signals using techniques such as time-of-flight and cross-correlation, and accurately estimate the local shear wave speed.

Using the left-to-right (LR) and right-to-left (RL) propagating shear waves, one can reconstruct two shear wave speed maps. Figure 25.6 shows an example of the U-CUSE shear wave speed map reconstruction. The push beam artifacts appear under the subgroup 1 region in the LR map, and subgroup 9 region in the RL map, both due to absence of shear waves. However, by blending the two maps, one can get a full FOV shear wave speed map without the push beam artifact (Figure 25.6c). The two shear wave speed maps can be blended by averaging or can be weighted some by certain metrics such as the cross-correlation coefficient generated in local shear wave speed calculation. Figure 25.7 shows the schematic plot of the F-CUSE shear wave speed map reconstruction and an example of the reconstruction in an inclusion phantom.

It was shown by Song et al. [5] that U-CUSE is suited for shallow shear wave imaging, F-CUSE is suited for mid to deep range imaging, and M-CUSE is suited for deep shear imaging. Because multiple shear waves are being generated into the tissue, multiple shear wave signals can be observed at each imaging pixel, which improves the robustness of the local shear wave speed calculation [5].

The multi-source shear wave imaging concept can be extended to other configurations of shear wave generation. A method of "rain-push" CUSE was proposed by Song [1] which not only distributes multiple shear wave sources at different lateral locations simultaneously, but multiple sources at different axial locations as well. Figure 25.8 shows an example of the rain-push CUSE shear wave field. Similar post-processing methods as conventional CUSE can be used to reconstruct the rain-push shear wave field. Another multi-source shear wave imaging approach is to randomize the push aperture apodization to produce randomly located shear wave sources inside the tissue [7]. This approach maximizes the quantity of shear wave sources and shows excellent performance in inclusion phantoms. A common limitation of these multi-source shear wave imaging methods is that, because the total amount of acoustic energy that can be transmitted inside the tissue is limited (i.e. power limited, transducer and tissue heating limited, etc.),

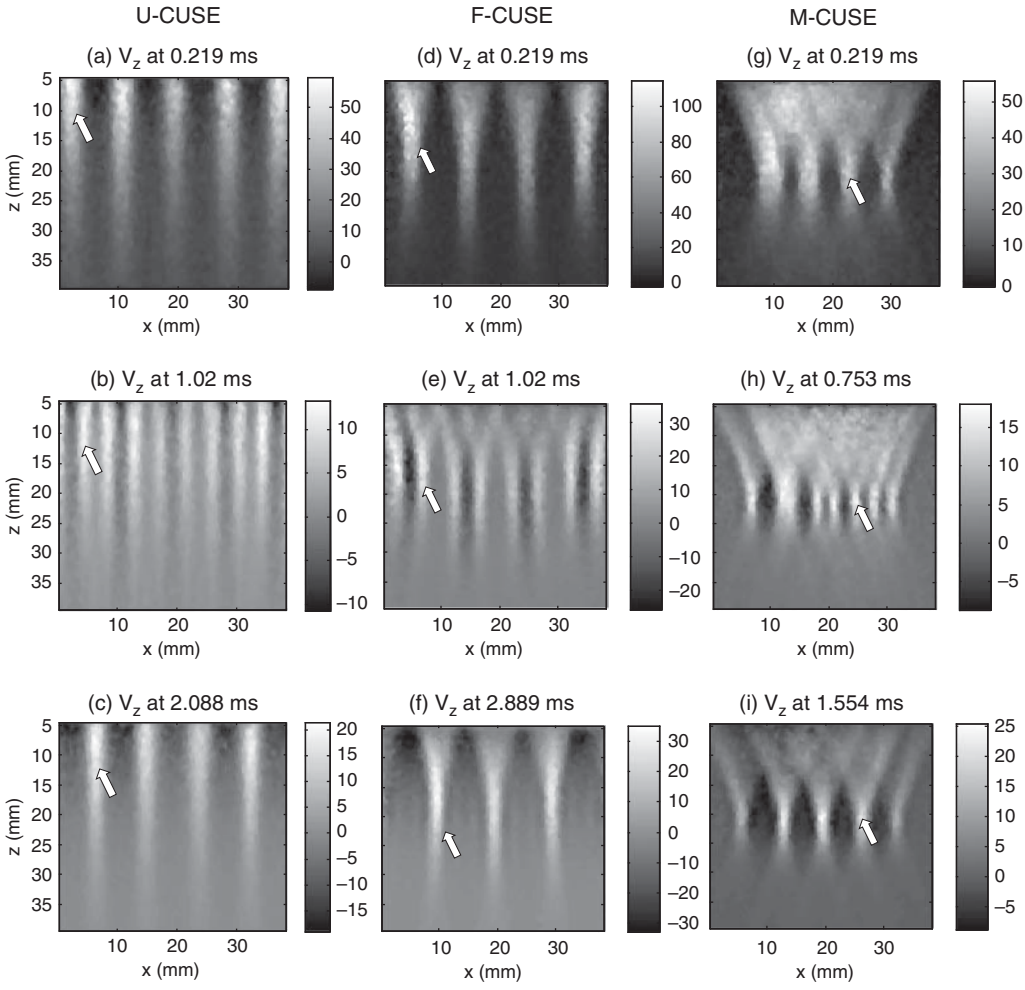

Figure 25.3 Plots of particle axial velocity at different time steps for U-CUSE, F-CUSE, and M-CUSE in a homogeneous elastic phantom with shear wave speed of about 1.5 m/s. Shear waves from different push beams interfere with each other and eventually fill the entire FOV. Left column: U-CUSE: The white arrows indicate the left-to-right propagating shear wave front from the leftmost tooth (subgroup 1) of the comb-push. (a) Initial positions of shear waves produced by 5 teeth, white arrow is at the shear wave front from subgroup 1 of the comb-push. (b) Shear waves from each push beam begin to propagate away from the push beam on opposite directions, the right-propagating shear wave from subgroup 1 is shown by the white arrow. (c) The right-propagating shear wave from subgroup 1 merged with the left-propagating shear wave from subgroup 3. Middle column: F-CUSE: (d), (e), and (f) show that four shear wave sources were generated by the four focused push beams. Each push beam generates two shear wave fronts that propagate away from the push beam. As indicated by the white arrows, the left-to-right shear wave from subgroup 1 appears in (e) and merges with the right-to-left shear wave from subgroup 2 in (f). Right column: M-CUSE. (g), (h), and (i) show that four shear waves were generated by the four focused push beams. As indicated by the white arrows, the right-to-left shear wave from subgroup 4 appears in (h) and merges with the left-to-right wave from subgroup 3 in (i). The color bar is in units of mm/s and the scale is different for each time step. "*x*" represents the lateral dimension, "*z*" represents the axial dimension. Source: reprinted from [1].

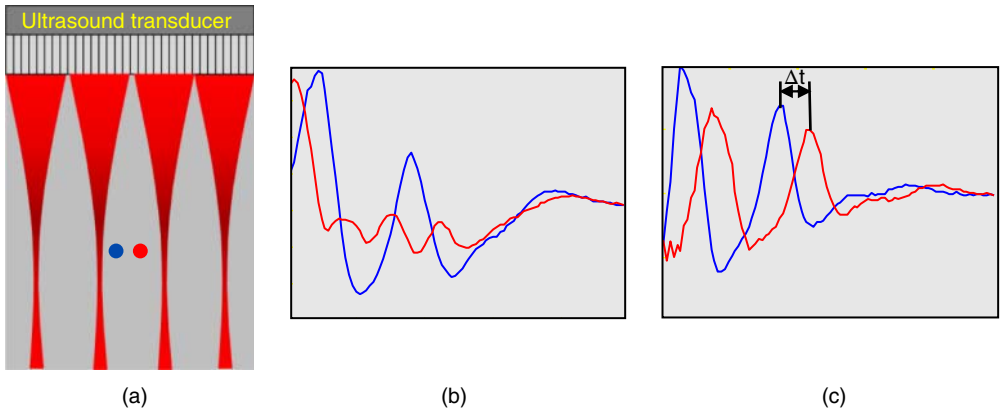

Figure 25.4 (a) Relative positioning between the targeting pixels and the comb-push beam. (b) Shear wave signals from the two pixels indicated in (a). The dark curve corresponds to the dark dot and the light curve corresponds to the light dot. Due to shear wave interferences, the two shear waveforms have large discrepancies. (c) After directional filtering, the shear wave interference is removed and one can easily estimate the time delay between the two signals. Source: reprinted from Song [1], courtesy of Pengfei Song.

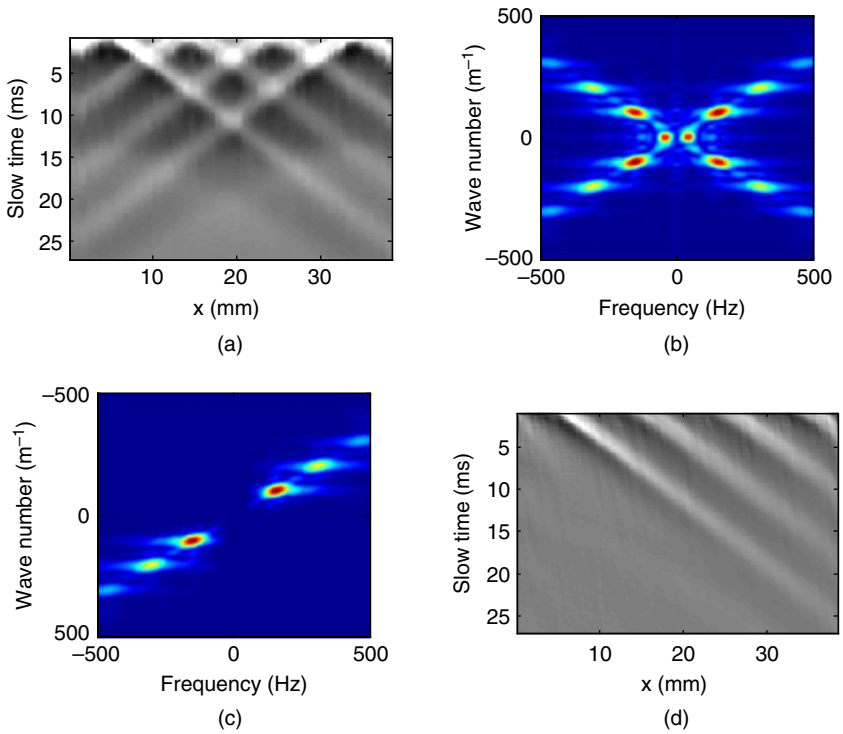

Figure 25.5 Directional filtering. (a) The original shear wave field created by F-CUSE before directional filtering. (b) The 2D Fourier transform of (a). (c) The directional filter masked out the 2nd and 4th quadrants (corresponding to RL shear waves) and preserved the 1st and 3rd quadrants (corresponding to LR shear waves). (d) Extracted LR shear waves by a 2D inverse Fourier transform of (c). Source: reprinted from [1].

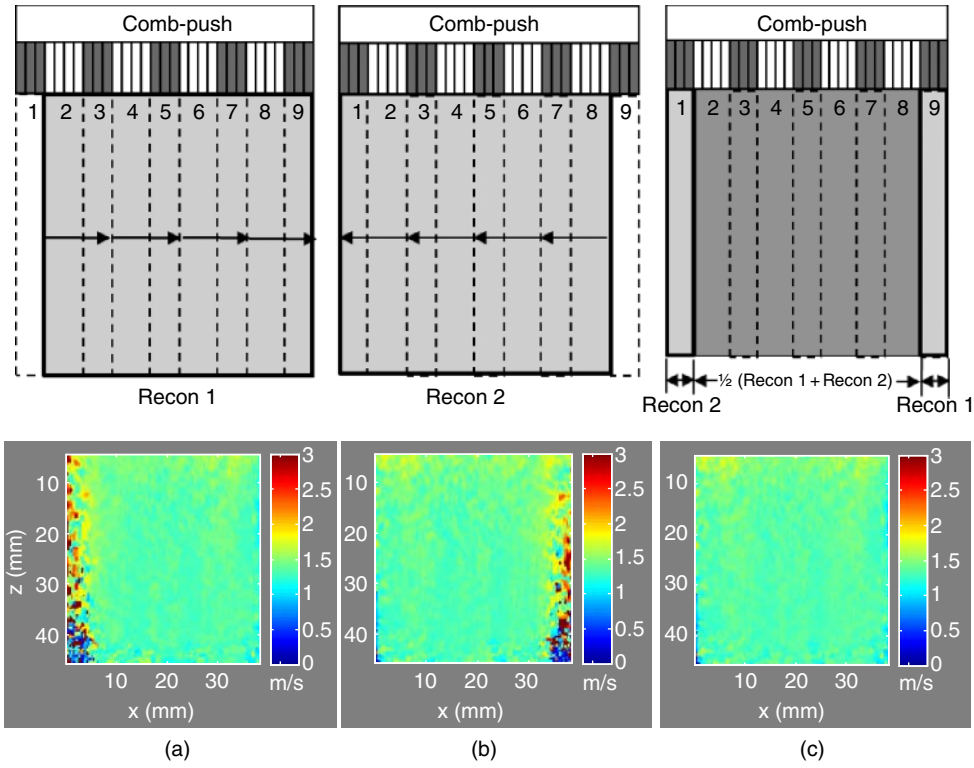

Figure 25.6 Schematic plots of 2D shear wave speed map reconstruction and the reconstructed 2D shear wave speed maps. Column (a): shear wave speed map reconstructed using LR waves. Column (b): shear wave speed map reconstructed using RL waves. Column (c): final shear wave speed map combined by Recon1 and Recon2. Source: reprinted from [1].

the shear wave energy from each individual source is inversely proportional to the number of sources being generated. Therefore, it is important to balance the number of shear wave sources and the shear wave energy from each source to achieve robust shear wave speed estimation at each imaging pixel.

CUSE can be implemented on different types of ultrasound transducers. Figure 25.9a shows an F-CUSE implementation on a curved array transducer with four focused ultrasound push beams transmitted simultaneously into the tissue. Because of the curvature of the transducer, the ultrasound push beams are tilted at a certain angle. As a result, the shear waves do not propagate horizontally (i.e. along the x-axis of the azimuthal plane). Conventional local shear wave speed calculation methods assume a lateral shear wave propagation direction, which will introduce overestimate bias when the shear wave propagates at a tilted angle. To address this issue, a 2D shear wave speed calculation method was proposed which can accurately calculate the speed of tilted shear waves without a priori knowledge of the propagation angle [8]. The 2D shear wave speed calculation method performs local cross-correlation both along the lateral and the axial directions to obtain the correct shear wave speed. To avoid angled shear wave propagation, one can also steer each push beam to the vertical direction so that shear waves only propagate along the horizontal direction. Figure 25.9b shows an M-CUSE implementation on a cardiac phased array transducer with two focused ultrasound push beams transmitted at different steering angles. Due to the limited aperture size of a phased array, M-CUSE is a preferred comb-push setup which uses a large portion of the aperture for each push beam. 2D shear wave speed calculation is necessary for accurate shear wave speed estimation from the steered push beams.

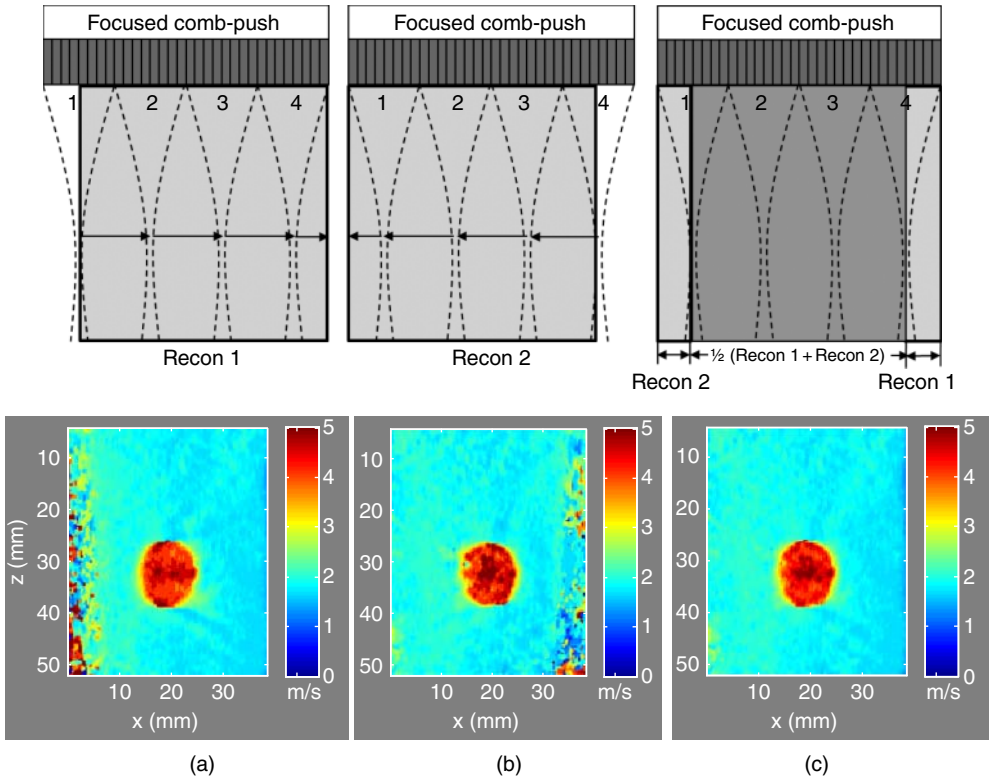

Figure 25.7 Schematic plots of 2D shear wave speed map reconstruction in F-CUSE and the reconstructed 2D shear wave speed maps. Column (a): shear wave speed map reconstructed using LR waves (indicated by black arrows). Column (b): shear wave speed map reconstructed using RL waves. Column (c): final shear wave speed map combined by Recon1 and Recon2. Source: reprinted from [1].

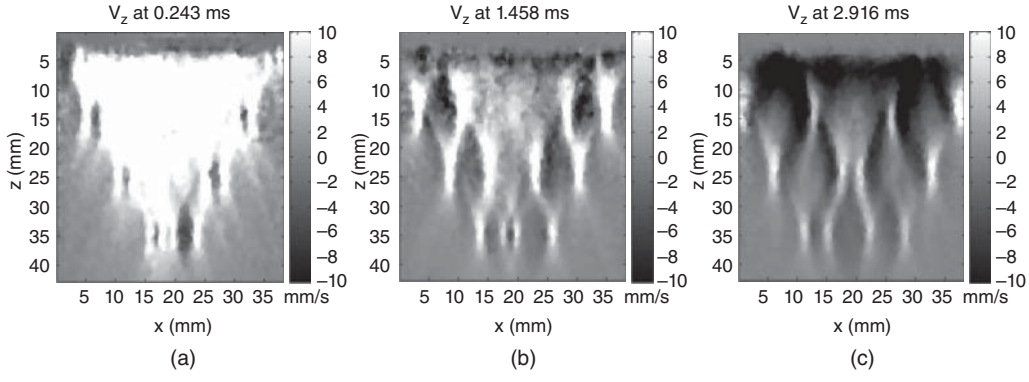

Figure 25.8 Rain-push CUSE example: a total of 8 push beams were excited to produce 8 shear wave sources. (a)–(c): snapshots of the shear wave propagation movie from a homogeneous phantom of rain-push CUSE. Source: reprinted from [1].

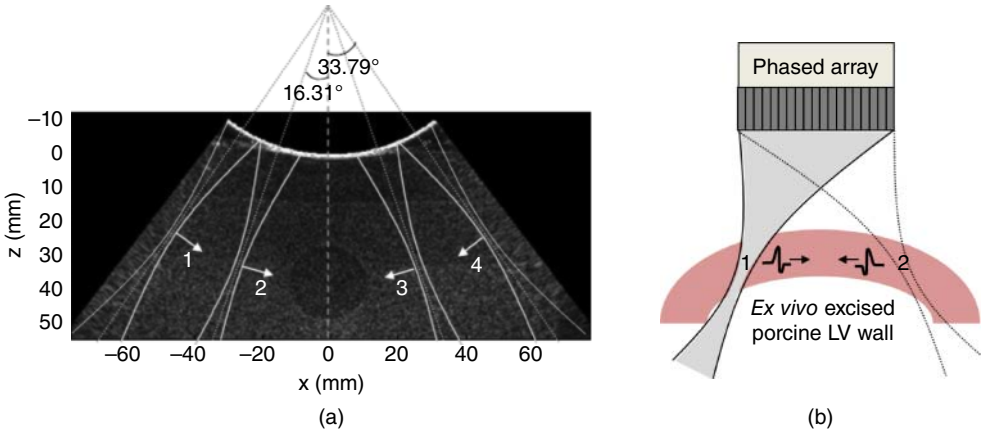

Figure 25.9 Schematic plots of CUSE implementations on a curved array with F-CUSE (a) and on a phased array with M-CUSE (b). Figure (a) reprinted from [8]. Source: copyright 2014, with permission from Elsevier; part (b) reprinted from [1].

CUSE can be implemented on both software beamforming-based ultrasound systems with plane wave imaging capability [3, 5] and hardware beamforming-based systems with conventional a line-by-line scanning scheme [9]. With conventional ultrasound systems that cannot support massive parallel beamforming for plane wave imaging, a time-aligned sequential tracking (TAST) technique was proposed to enable 2D shear wave elastography on these systems [9]. Figure 25.10 shows a realization of CUSE on a conventional ultrasound system GE LOGIQ E9.

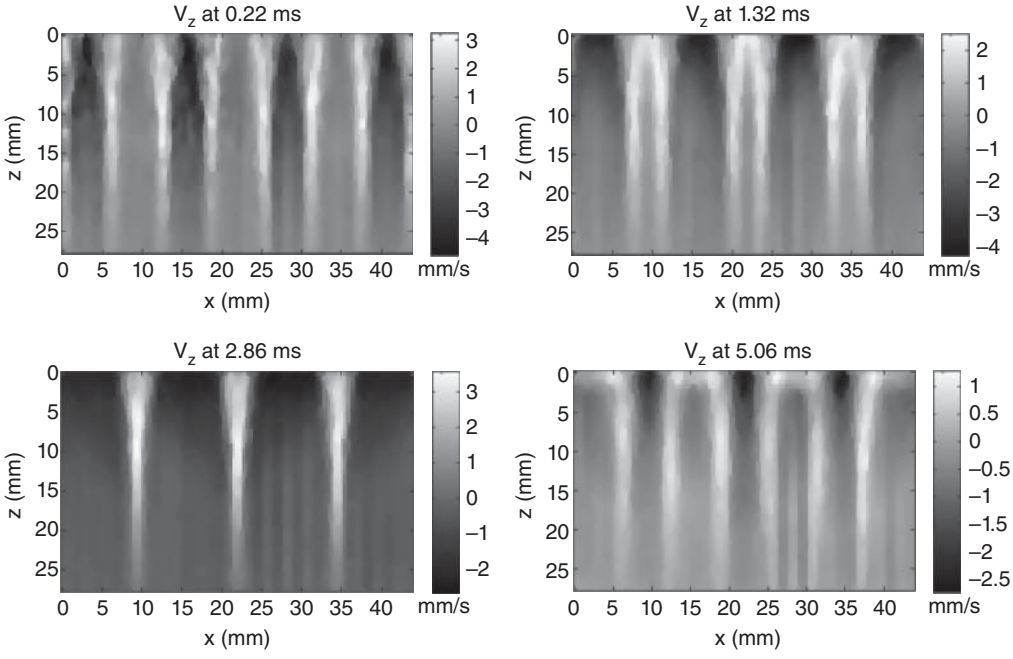

Figure 25.10 Snapshots of the CUSE shear wave propagation movie at different time instants obtained from the LOGIQ E9. A 4-tooth focused comb-push was transmitted and the resulting shear waves were tracked by TAST. Source: © 2015 IEEE, reprinted, with permission, from [9].

25.3 Clinical Applications of CUSE

Initial clinical applications of CUSE are being conducted in breast cancer detection [10, 11], thyroid nodule evaluation [12], and liver fibrosis staging [13]. Figure 25.11a shows an example case of the 2D shear elasticity map of a mass that was diagnosed as an invasive mammary carcinoma Nottingham grade III of III. Figure 25.11b shows that tissue stiffness varies significantly among normal, benign, and malignant thyroid nodules. Figures 25.11c and 25.11d show example cases of a 2D shear elasticity maps of healthy liver and fibrotic liver, respectively. In the breast cancer detection pilot study, CUSE showed 89.19% sensitivity, 88.69% specificity, and 0.911 for the area under the curve (AUC) with a cutoff Young's modulus value of 83 kPa [10, 11]. For liver fibrosis detection, preliminary results showed 0.83 sensitivity, 0.88 specificity, and 0.9 AUC with a cutoff shear wave speed of 1.43 m/s [13].

25.4 Summary

In this chapter we introduced a new multi-source shear wave imaging technique named comb-push ultrasound shear elastography (CUSE). The flexible distribution of shear wave sources by simultaneous or rapid-sequential firing of sub-apertures of elements allows versatile imaging configurations that can be fine tuned to meet the needs of different imaging applications. When combined with plane wave detection, CUSE only needs one shear wave push-detect data acquisition to generate a full FOV 2D shear wave speed map, which offers the highest theoretical shear wave imaging (acoustic radiation force-based) frame rate. The

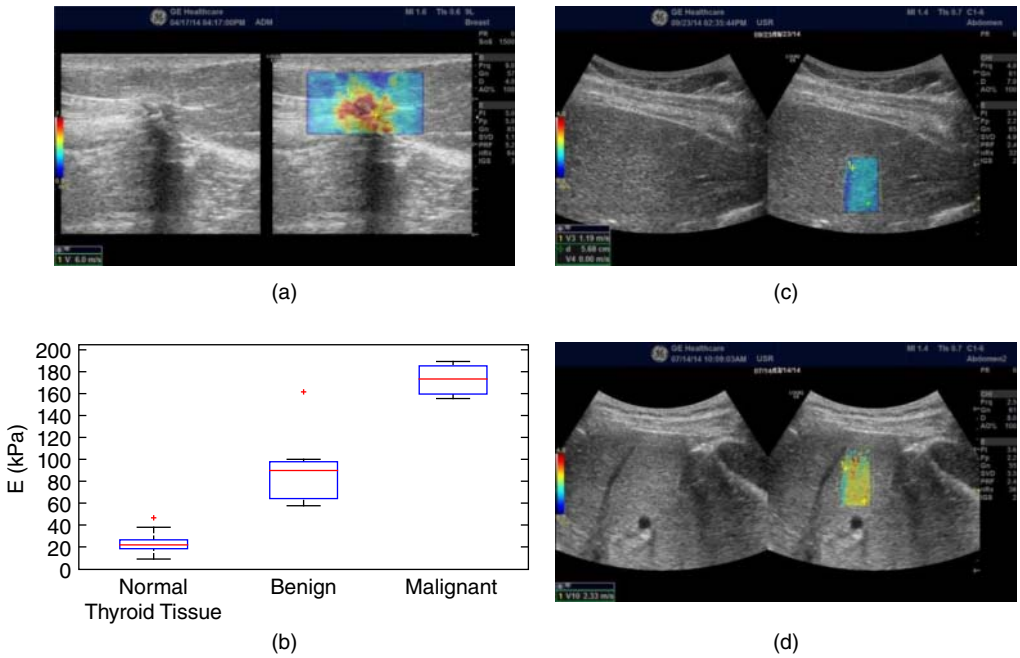

Figure 25.11 (a) 2D shear elasticity map of a malignant breast lesion. © 2015 IEEE. Reprinted, with permission, from [9]. (b) Box plots of Young's modulus of normal, benign, and malignant thyroid nodules. © 2015 IEEE. Reprinted, with permission, from [12]. (c) 2D shear elasticity map of a healthy liver. (d) 2D shear elasticity map of a fibrotic liver. Source: republished with permission of American Institute of Medicine from [13]; permission conveyed through Copyright Clearance Center, Inc.

directional filter is the key to resolve the complicated comb-push shear wave field which enables robust shear elastogram reconstruction. CUSE has been implemented on different types of ultrasound transducers and has been successfully translated to different ultrasound imaging platforms with conventional hardware beamformers (i.e. a line-by-line scan system) as well as emerging software beamformers (i.e. a plane wave imager). Preliminary in vivo results of CUSE showed promise in a variety of clinical applications such as breast cancer and liver fibrosis.

References

1 Song, P. (2014). *Innovations in ultrasound shear wave elastography. PhD Thesis, Department of Physiology and Biomedical Engineering, Mayo Clinic College of Medicine*, Rochester, USA.

2 Tanter, M., Bercoff, J., Athanasiou, A., et al. (2008). Quantitative assessment of breast lesion viscoelasticity: Initial clinical results using supersonic shear imaging. *Ultrasound Med. Biol.* 34: 1373–1386.

3 Song, P., Zhao, H., Manduca, A., et al. (2012). Comb-push ultrasound shear elastography (CUSE): a novel method for two-dimensional shear elasticity imaging of soft tissues. *IEEE Trans. Med. Imaging* 31: 1821–1832.

4 Song, P., Urban, M.W., Manduca, A., et al. (2012). *Comb-push ultrasound shear elastography (CUSE): A novel and fast technique for shear elasticity imaging. Presented at the IEEE International Ultrasonics Symposium*, Dresden, Germany.

5 Song, P., Urban, M.W., Manduca, A., et al. (2013). Comb-push ultrasound shear elastography (CUSE) with various ultrasound push beams. *IEEE Trans. Med. Imaging* 32: 1435–1447.

6 Manduca, A., Lake, D.S., Kruse, S.A., and Ehman, R.L. (2003). Spatio-temporal directional filtering for improved inversion of MR elastography images. *Med. Image Anal.* 7: 465–473.

7 Nabavizadeh, A., Song, P., Chen, S., et al. (2015). Multi-source and multi-directional shear wave generation with intersecting steered ultrasound push beams. *IEEE Trans. Ultrason., Ferroelect., Freq. Control* 62: 647–662.

8 Song, P., Manduca, A., Zhao, H., et al. (2014). Fast shear compounding using robust 2-D shear wave speed calculation and multi-directional filtering. *Ultrasound Med. Biol.* 40: 1343–1355.

9 Song, P., Macdonald, M., Behler, R., et al. (2015). Two-dimensional shear-wave elastography on conventional ultrasound scanners with time-aligned sequential tracking (TAST) and comb-push ultrasound shear elastography (CUSE). *IEEE Trans. Ultrason., Ferroelect., Freq. Control* 62: 290–302.

10 Denis, M., Mehrmohammadi, M., Song, P., et al. (2015). Comb-push ultrasound shear elastography of breast masses: initial results show promise. *PLoS One* 10: e0119398.

11 Denis, M., Bayat, M., Mehrmohammadi, M., et al. (2015). Update on breast cancer detection using comb-push ultrasound shear elastography. *IEEE Trans. Ultrason., Ferroelect., Freq. Control* 62: 1644–1650.

12 Mehrmohammadi, M., Song, P., Meixner, D.D., et al. (2015). Comb-push ultrasound shear elastography (CUSE) for evaluation of thyroid nodules: Preliminary in vivo results. *IEEE Trans. Med. Imaging* 34: 97–106.

13 Song, P., Mellema, D.C., Sheedy, S.P., et al. (2016). Performance of 2-dimensional ultrasound shear wave elastography in liver fibrosis detection using magnetic resonance elastography as the reference standard: A pilot study. *J. Ultrasound Med.* 35: 401–412.

Section VII

Emerging Research Areas in Ultrasound Elastography

26

Anisotropic Shear Wave Elastography

Sara Aristizabal

Well Living Lab, Rochester, MN, USA

26.1 Introduction

Shear wave elastography constitutes the principle behind a large range of techniques developed in the last two decades for noninvasive assessment of the mechanical properties of soft tissues such as the breast, skeletal muscle, liver, myocardium, prostate, and kidney, under normal and abnormal conditions [1–4]. The basic principle of most shear wave elastography techniques relies on the use of focused ultrasound to generate acoustic radiation force to vibrate the tissue and generate shear waves. The shear wave group velocity (c_g) is then tracked as a function of time (Δt) and distance (Δx). Under the assumption that the tissue is purely elastic, locally homogenous, and isotropic, the shear wave group velocity (c_g) can then be related to the shear modulus (μ) and the underlying tissue stiffness can be estimated. Based on these principles, several acoustic radiation force-based shear wave methods have been developed. Acoustic radiation force impulse (ARFI) [1] uses impulsive radiation force to generate shear waves outside of the excitation region. Supersonic shear imaging (SSI) [3] creates shear waves inside the tissues by applying focused ultrasound beams at different depths. Shear wave dispersion ultrasound vibrometry (SDUV) [4] creates shear waves with harmonic components applying repeated tonebursts of a focused ultrasonic beam. The abovementioned methods provide the ability of accurately quantifying the tissue mechanical properties when dealing with isotropic media or tissues whose mechanical properties are independent of the relative orientation of the transducer with respect to the tissue volume. However, the diagnostic potential of these techniques is challenged when the tissues under evaluation have properties that are directionally dependent, a phenomenon known as anisotropy. The importance of anisotropy has long been stated in the field of seismology [5], where it has been shown that the wave motion in anisotropic solids is fundamentally different from motion in isotropic solids, where the most distinctive feature of the propagation in uniform anisotropic solids seems to be the variation of properties with direction [6]. The human body is not exempt of this behavior, as tissues such as the kidney [7], myocardium [8], and skeletal muscle [9] have directionally dependent properties. Anisotropic effects occur when the direction of shear wave propagation is perpendicular to main axis of the tissue structure that is being evaluated. As a result of this, differences in shear wave speed with respect to tissue fiber orientation arise, leading to incorrect interpretation of the shear wave speed values which, consequently, affects the quantification of tissue elasticity. To facilitate the estimation of the elastic parameters of these types of tissues, it is common to assume that these anisotropic biological media can be modeled as being transversely isotropic (TI). TI tissues can be considered as tissues with physical properties which are symmetric about one plane, normal to the plane of isotropy; in this plane of symmetry the

Ultrasound Elastography for Biomedical Applications and Medicine, First Edition.
Edited by Ivan Nenadic, Matthew Urban, James Greenleaf, Jean-Luc Gennisson, Miguel Bernal, and Mickael Tanter.

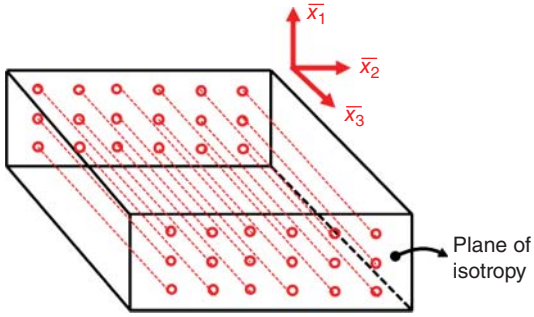

Figure 26.1 Representation of a transversely isotropic material, with two orthogonal planes of symmetry and an additional plane of material isotropy ($\overline{x_2}$, $\overline{x_3}$), where properties are the same in all directions.

material properties of the media are the same in all directions [10]. This behavior is illustrated on Figure 26.1. This chapter summarizes some of the work that has been done in the field to demonstrate why elastography techniques must take into account the property of anisotropy in the measurement of the viscoelastic properties of tissues. In particular, the chapter concentrates on summarizing the findings from previous studies that have investigated the feasibility of estimating the mechanical properties of various tissues with an anisotropic behavior under this transversely isotropic assumption.

26.2 Shear Wave Propagation in Anisotropic Media

The wave propagation in anisotropic media is governed by the strain-stress relations or constitutive equations governing the dynamic and static deformation of a material. In order to estimate these relations, it is necessary to first define the strain-energy volume density, which can be expressed using Cartesian components in the form of a 4th order elasticity tensor (C_{ijkl}) [11], as

$$2V = C_{ijkl}\varepsilon_{ij}\varepsilon_{kl} \tag{26.1}$$

where $\varepsilon_{ij}\varepsilon_{kl}$ corresponds to the strain tensors and V corresponds to strain energy. Using the symmetries between the strain and stress tensors, and the independence of the second partial derivatives of V with respect to the strain components, the number of independent elastic constants can be reduced from 81 to 21 [11]. Furthermore, assuming the following form of the strain tensor $\varepsilon = \sum \varepsilon_{ij}\hat{e_i} \otimes \hat{e_j}$, which corresponds to the sum of the tensor product of the vectors $\hat{e_i}$ and $\hat{e_j}$ multiplied by the strain tensor ε_{ij}, if the material is transversely isotropic and therefore it possesses an axis of symmetry (x_3), perpendicular to a plane of isotropy (x_1, x_2), the strain energy volume density will not be modified by rotations around that axis of symmetry and it can be defined [11] as

$$\begin{aligned} 2V = {} & C_{11}({e_{11}}^2 + {e_{22}}^2) + C_{33}{e_{33}}^2 + 2(C_{11} - 2C_{66})e_{11}e_{22} + 2C_{13}(e_{11} + e_{22})e_{33} \\ & + C_{44}({e_{23}}^2 + {e_{13}}^2) + C_{66}{e_{12}}^2 \end{aligned} \tag{26.2}$$

After determining the strain-energy volume density expression, it is necessary to consider the stress, which in its more general form can be defined as

$$\sigma_{ij} = \frac{\partial V}{\partial \varepsilon_{ij}} \tag{26.3}$$

Again, using the Cartesian components, the stress for a linear elastic solid (Hooke's law) can be expressed as

$$\sigma_{ij} = C_{ijkl}\varepsilon_{kl} \tag{26.4}$$

where C_{ijkl} and σ_{ij} represent the elasticity tensor and stress tensor, respectively [11].

The strain-stress relations described above represent the basis to determine the wave propagation in reference to the displacement in a transversely isotropic material, for which the elasticity tensor contains only five independent elastic constants based on the axial symmetry of TI materials and can be expressed using a matrix notation [10] as:

$$\begin{bmatrix}\sigma_{11}\\ \sigma_{22}\\ \sigma_{33}\\ \sigma_{23}\\ \sigma_{31}\\ \sigma_{12}\end{bmatrix} = \begin{pmatrix} C_{11} & C_{12} & C_{13} & & & \\ C_{12} & C_{11} & C_{13} & & & \\ C_{13} & C_{13} & C_{33} & & & \\ & & & C_{44} & & \\ & & & & C_{44} & \\ & & & & & C_{66}\end{pmatrix} = \begin{bmatrix}\varepsilon_{11}\\ \varepsilon_{22}\\ \varepsilon_{33}\\ 2\varepsilon_{23}\\ 2\varepsilon_{31}\\ 2\varepsilon_{12}\end{bmatrix} \tag{26.5}$$

where the conditions of existence are

$$C_{12} = C_{11} - 2C_{66} \text{and} C_{11} > 0,\ C_{33} > 0,\ C_{44} > 0,\ C_{66} > 0.$$

Wang et al. [10] has described the mathematical derivations necessary to find the shear wave group velocity in a transversely isotropic material, where the wave equation determined from the relationship between the stress-strain constitutive equations and the equation of motion can be solved assuming plane wave solutions and the symmetry relations that exist for a TI material. The solution of the wave equation becomes a Christoffel equation with the form of an eigenvector eigenvalue problem; from which the shear wave group velocity for a TI material can be calculated as

$$\rho {c_g}^2 = \frac{C_{44}C_{66}}{C_{44}\sin^2\Theta + C_{66}\cos^2\Theta} \tag{26.6}$$

where Θ is the angle of wave propagation with respect to the fibers in the propagation plane, c_g is the shear wave group velocity, ρ is density, C_{44} is the longitudinal shear modulus, and C_{66} is the transverse shear modulus [10].

26.3 Anisotropic Shear Wave Elastography Applications

26.3.1 Influence of Tissue Anisotropy on the SWE Evaluation of Kidneys

The presence of anisotropy can be identified in tissues such as the kidneys, where the effect of anisotropy commonly occurs as its two basic layers, the cortex and the medulla, contain structures such as the renal tubules, capillaries, and small blood vessels that are radially oriented [12]. It has been shown that the shear wave speed and material properties vary with the direction of the shear wave interrogation with respect to the renal structures [13–15]. The most relevant findings [13] are summarized below.

26.3.1.1 Experimental Setup

Gennisson et al. [13] used three adult female pigs (CIRHYO origin) for the study. The pigs were anaesthetized and intubated. After laparotomy, each kidney with its renal pedicle was exposed. Renal artery, renal vein, and the lumbar ureter were isolated for subsequent ligation. The ureter was cannulated for retrograde filling and for intrapelvic pressure measurement. Renal elasticity was measured before and after total occlusion of the renal artery and after occlusion of the renal vein.

Shear waves were generated and measured using an ultrafast scanner (Aixplorer; SuperSonic Imagine, Aix-en-Provence, France) equipped with an 8 MHz transducer. The principles of SSI are described in Chapter 23 of this book. To evaluate the influence of anisotropy at each

stage of the experiment, measurements were performed in a renal segment with a pyramid axis parallel to the US beam, then in a renal segment with a pyramid axis perpendicular to the US beam. As the medium is considered to be anisotropic and therefore the relationship $E = 3\mu$ is no longer valid, the findings shown in this section of the chapter are presented in terms of μ_{parallel}, which corresponds to the case where pyramid axis is perpendicular to the US beam and $\mu_{\text{perpendicular}}$, which corresponds to the case where pyramid axis is parallel to the US beam.

26.3.1.2 Experimental Results

The impact of anisotropy was evaluated by measuring μ_{parallel} and $\mu_{\text{perpendicular}}$ in three different renal compartments, outer cortex, inner cortex, and the medulla for the six different pig kidneys. Measurements were performed under baseline conditions (no perfusion), during the occlusion of the renal artery, and during occlusion of the renal vein, as illustrated in Figures 26.2a, 26.2b, and 26.2c, respectively. In all three studies, the estimates for μ_{parallel} were higher than those obtained for $\mu_{\text{perpendicular}}$ for the three different compartments. This described behavior was showed to be more significant at the renal medulla.

The reason behind the shear modulus behavior in Figure 26.2 has to do with the internal organization of the kidney and the direction of shear wave propagation with respect to the tissue structures. The medulla is composed of tubules oriented perpendicular to the capsule, while the cortex is composed of spherical glomeruli and convoluted tubes. In the case where the US beam is sent parallel to the structures, the shear waves will propagate perpendicular to them, therefore decreasing the speed of propagation and the value of μ obtained. On the contrary, when the US beam is sent perpendicular to the structures, the shear waves will propagate parallel to them, resulting in a higher μ value. As the medulla is more linearly organized than the cortex, the velocity of wave propagation is higher as there is less resistance in the path of propagation.

26.3.2 Influence of Tissue Anisotropy on the SWE Evaluation of the Achilles Tendon

The Achilles tendon is a strong unidirectional arrangement of collagen fibers within a supporting matrix that connects the calf muscles to the heel bone (calcaneus) [15]. It serves as a mechanical buffer to optimize muscle work, making it more efficient. Unfortunately, it is a commonly injured tendon; it can tear completely or partially due to overstretch affecting the ability to walk properly. Due to its complex TI nature, it has been difficult to develop noninvasive tools to assess the stiffness of the tendon. Brum et al. [16] showed the possibility of estimating the elastic properties of the in vivo transverse isotropic Achilles tendon using shear wave dispersion analysis with the goal of underlying a new technique to diagnose tendon injury. The most relevant findings by Brum et al. [16] are summarized below.

26.3.2.1 Experimental Setup

Brum et al. [16] evaluated the left and right tendons of five healthy volunteers in the study. For each experiment, the volunteer was in a sitting position with a 90° angle between the foot and the tibia, and between the tibia and the femur. The foot and the ultrasonic transducer were submerged in a water tank to avoid pre-compression of the tendon. Shear waves were generated and measured using an ultrafast scanner (Aixplorer; SuperSonic Imagine, Aix-en-Provence, France) equipped with an 8 MHz linear array transducer (SL15-4, Supersonic Imagine). The principles of SSI are described in Chapter 23 of this book. To evaluate the influence of anisotropy, measurements were taken along and across to the tendon fiber orientation by first placing the transducer parallel to the tendon and then by tilting it by a 90° angle to study wave propagation perpendicular to the fibers.

The phase velocity determination was done using the dispersion curves (phase velocity as a function of frequency) [17]. This method consists of taking a spatiotemporal matrix of particle displacement or velocity signals from different locations along the propagation direction for a

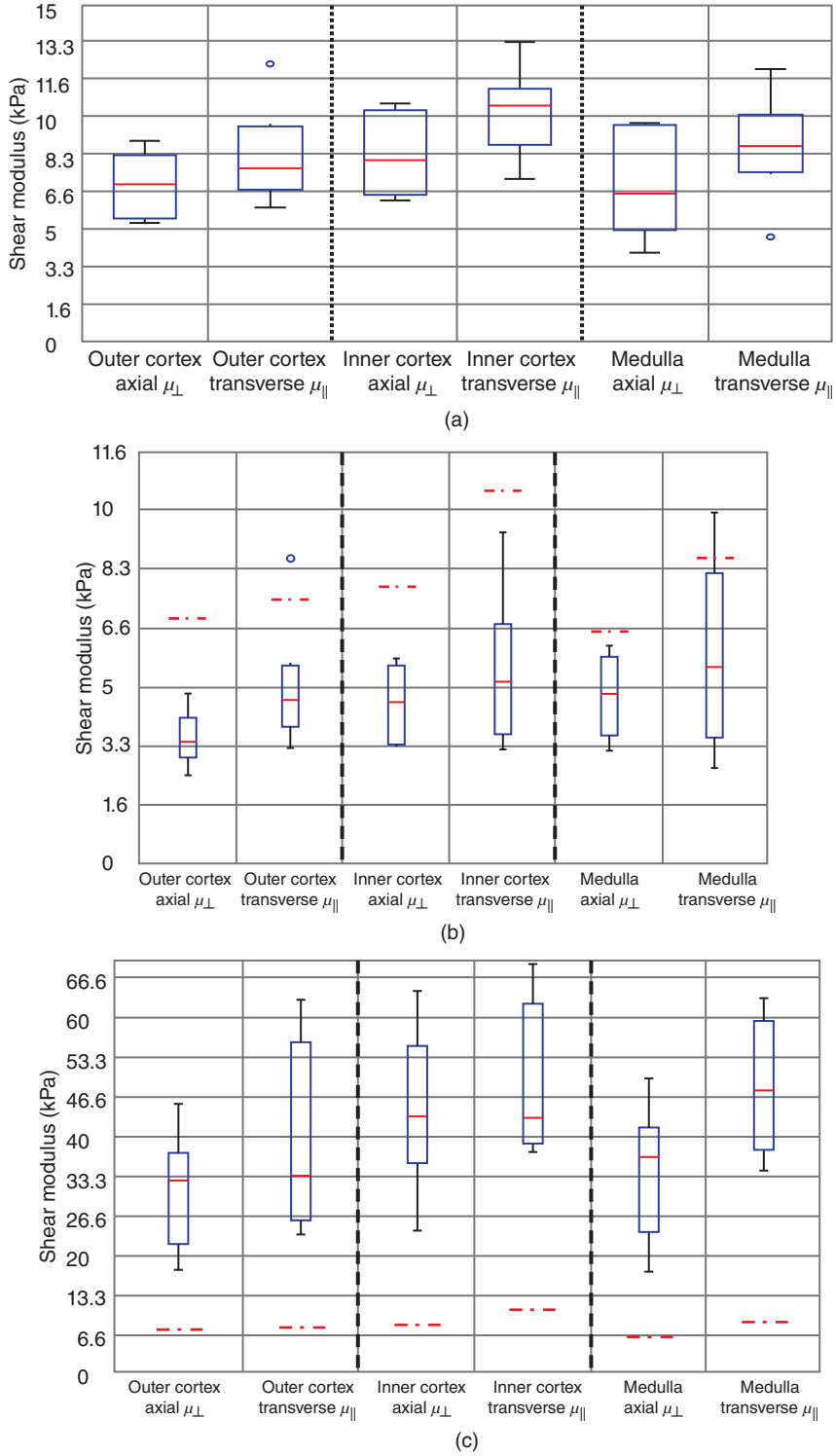

Figure 26.2 Boxplot of the shear modulus calculation over the six pig kidneys in the outer cortex, inner cortex, and the medulla during **(a)** Baseline condition (no perfusion), **(b)** occlusion of the renal artery, and **(c)** occlusion of the renal vein with the US beam along (||) and perpendicular (⊥) to the main pyramid axis. Source: reprinted from [13], copyright 2012, with permission from Elsevier.

given region of interest (ROI) and then the k-space is calculated by taking 2D Fourier transform (FT) of the matrix. From the magnitude distribution of this Fourier representation of the wave motion data, the global peak is found for each temporal frequency. Then, the wavenumber, k_s, corresponding to the peak in frequency, f, in k-space is used to calculate shear wave phase velocity, c_s

$$c_s = \frac{f}{k_s} \tag{26.7}$$

For the final dispersion curve, an average over the ROI width is performed. The method is illustrated on Figure 26.3. Due to its dispersive nature, produced by guided wave propagation (shear wavelengths in the parallel and perpendicular direction are bigger than the mean tendon thickness); a model has to be fitted to the curve, in order to recover the elasticity values. To model the observed velocity dispersive behavior, the wave propagation in the Achilles tendon is assumed to take place in an infinite transverse isotropic viscoelastic plate (waves attenuate before they arrive at the tendon's end) of constant thickness, surrounded by liquid (leaky Lamb waves). The guided wave propagation equation along and perpendicular to the fiber direction for a transverse isotropic viscoelastic plate submerged in nonviscous fluid was derived by Brum et al. [16] using the global matrix technique developed by Lowe [18]. The complete mathematical derivation can be found in Brum et al. [16].

26.3.2.2 Experimental Results

The experimental velocity dispersion curves and the corresponding model fit for left and right tendon of one subject for the parallel and perpendicular direction of wave propagation are shown on Figures 26.4a, 26.4b, 26.4c, and 26.4d. By fitting the model to the experimental data, the mechanical properties of the tissue represented by three elasticity constants and a viscous component were estimated. There is a good agreement between the model and the experimental data; the mean correlation coefficient and mean relative deviation along the fibers is 0.995 $\pm$ 0.004 and 1.2%, respectively. The mean correlation coefficient and mean relative deviation across the fibers is 0.993 $\pm$ 0.004 and 1.4%, respectively.

It is then possible to appreciate that the direction of shear wave propagation with respect to the fibers primary orientation has an effect in the estimation of the elastic properties of the Achilles tendon. Brum et al. [16] have demonstrated that the use of a dispersion model can aid on the correct estimation of the tendon elasticity when its behavior is assumed to be that of a TI media.

26.3.3 Influence of Tissue Anisotropy on the SWE Evaluation of Skeletal Muscle

Anisotropy constitutes one of the primary challenges in musculoskeletal ultrasound imaging. Muscle consists of cylindrical fibers organized parallel to each other in clusters called fasciculi. Anisotropy artifacts occur when these clusters of muscle fibers are oblique with respect to the main axis of the muscle or when the orientation of the muscle fibers with respect to the axis of tendons (muscle insertion) occurs in different patterns [9]. Previous work has demonstrated the feasibility of estimating the mechanical properties of the skeletal muscle under the assumption that it can be modelled as being transversely isotropic. Wang et al. [10] and Gennisson et al. [19] have provided quantitative speed measurements of shear waves generated by ARFI on ex vivo muscle and by low-frequency vibrations on beef muscle and the human biceps, respectively. The most relevant findings by Gennisson et al. [19] and by Wang et al. [10] are summarized below.

26.3.3.1 Experimental Setup

Gennisson et al. [19] evaluated the feasibility of transient elastography for the estimation of the mechanical properties of anisotropic media such as muscle. For the evaluation of the elastic

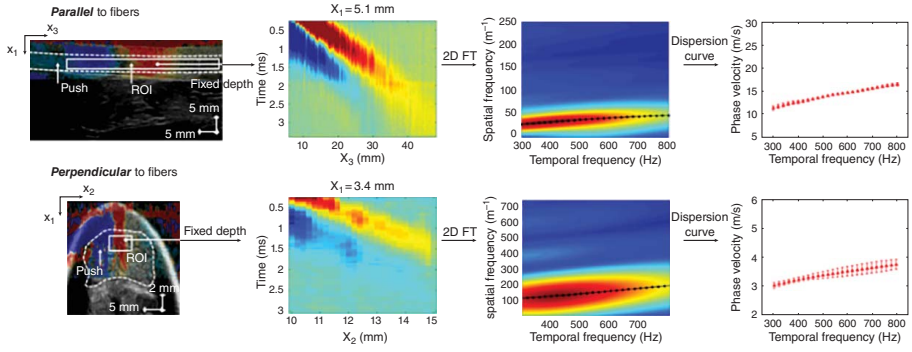

Figure 26.3 Shear wave dispersion method used for the analysis of the wave propagation parallel and perpendicular to the fibers of the Achilles tendon. © Institute of Physics and Engineering in Medicine. Source: reproduced by permission of IOP Publishing, all rights reserved [16].

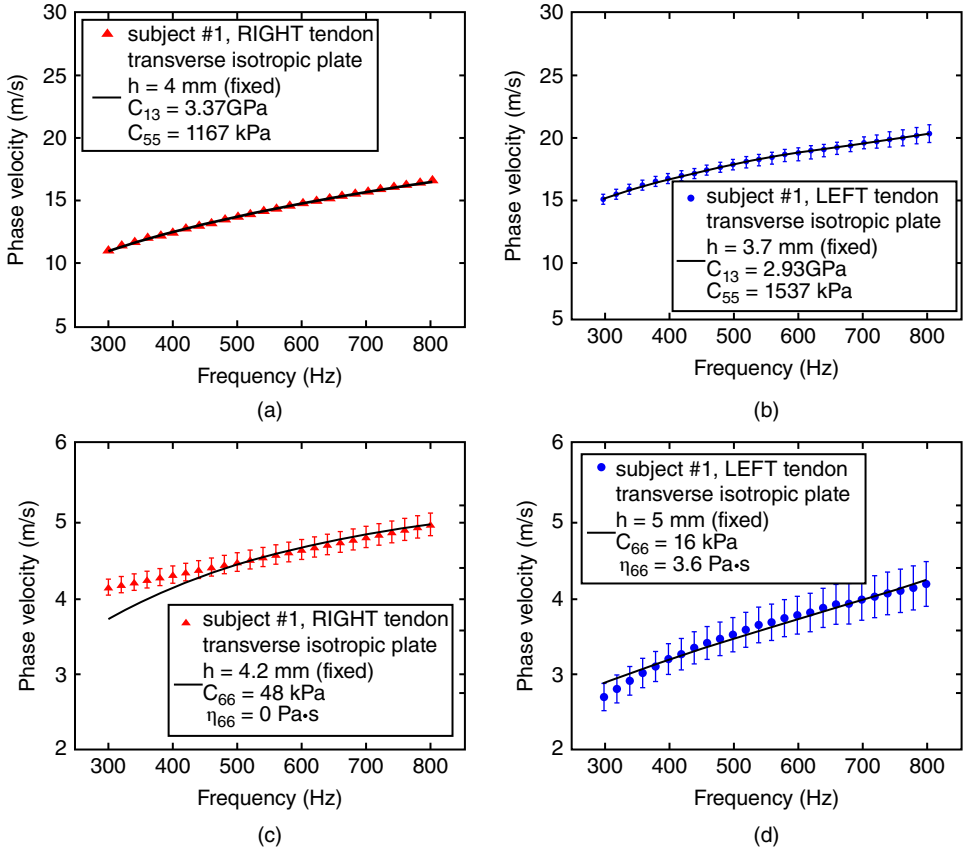

Figure 26.4 Phase velocity dispersion curves and the corresponding fit for one subject (a, b) in the direction parallel to the fibers and (c, d) in the direction perpendicular to the fibers. Source: © Institute of Physics and Engineering in Medicine, reproduced by permission of IOP Publishing, all rights reserved [16].

properties of isotropic media, a 5 MHz ultrasound transducer is set up on a vibrator (Bruel & Kjaer, type 4810) and an acoustic impulse (100 Hz) is generated by the transducer while it works as a pulse echo system. When the pulse is applied, both compressional and shear waves are generated by the transducer (piston source). The determination of the Young's modulus of the media depends on the estimation of the low frequency (50–150 Hz) shear wave speed. By estimating the displacement field with a cross-correlation technique on successive A-lines, and linearly fitting the phase as a function of depth, the speed can be evaluated. The Young's modulus of the simplest isotropic media can then be calculated as

$$E = 3\rho V_s^2 \tag{26.8}$$

In the case of a transverse isotropic media such as muscle, which possesses an axis of symmetry in the principal direction of the muscle fibers, it is necessary to determine the speed of two different waves, a shear wave with polarization perpendicular to the fibers and a shear wave with a polarization parallel to the fibers, to characterize the media. The use of a rod source instead of a piston source allows the shear wave to induce a strain field in a preferential direction. When the rod is positioned parallel to the fibers, it is possible to obtain the speed of the shear wave with a polarization perpendicular to the fibers; when the rod is set perpendicular to the fibers, it is possible to obtain the speed of the shear wave with a polarization parallel to the fibers. To obtain the complete TI behavior, the rod is rotated with respect to the fibers from 0° to 180°, in

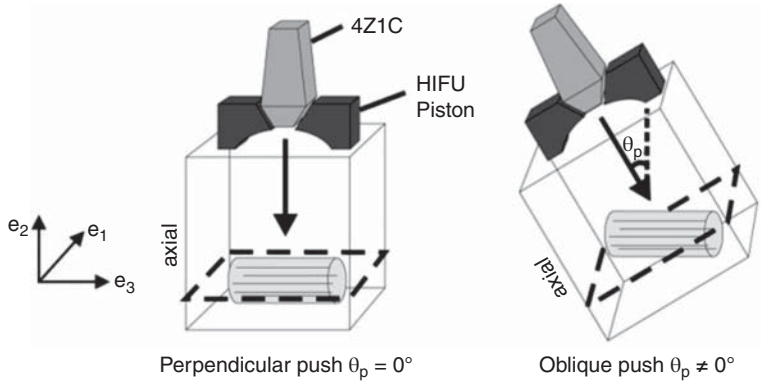

Figure 26.5 Transducer–muscle sample configurations for the shear wave imaging. First, the push configuration (black arrow) is set perpendicular to the fibers and therefore wave propagation is observed in the coronal plane of the imaging coordinate system (dashed plane). Second, the push configuration is set oblique to the fibers. Source: © 2013 IEEE, reprinted, with permission, from [10].

10° steps, and the shear wave speed is estimated at each angle. In order to test this hypothesis, Gennisson et al. [19] evaluated the mechanical properties of an in vitro beef muscle and an in vivo human biceps.

Wang et al. [10] evaluated the feasibility of imaging the transverse isotropic properties of muscle by tracking the shear wave propagation induced by ARFI using a 2D matrix array in an ex vivo canine muscle. Six canine ex vivo muscle samples embedded in agar gel and immersed in a water bath were evaluated in the study. Shear waves were generated and measured using an annular focused HIFU piston transducer (H-101, Sonic Concepts, Bothell, WA). First, shear waves were acquired, with the push axis perpendicular to the fiber orientation. In this configuration, the wave propagation in a plane of symmetry can be observed in the coronal plane of the imaging coordinate system. With the purpose of evaluating whether it was possible to estimate the fiber orientation when the push was not oriented perpendicular to the fibers, shear waves were also acquired with the push oblique to the fibers by tilting the ultrasound probe. In this configuration, the plane where wave propagation occurs and the fiber orientation have to be found by assessing the dominant spatial orientation of the wave displacement amplitude using an iterative system. The two different configurations are shown on Figure 26.5. The evaluation of the shear wave propagation in 3D allows access to the shear wave group velocity (c_g) and phase velocity (c_s) in all directions; c_g and c_s were measured for ray angles from 0° to 360° in 1° steps by finding the TTP of the displacement time profile and by calculating the local spatial derivative of the shear wave arrival time, respectively.

26.3.3.2 Experimental Results

The results from the Gennisson et al. [19] study show the shear wave speed as a function of the angle of rotation of the rod with respect to the fibers for the ex vivo muscle sample and the in vivo human biceps (Figures 26.6a and 26.6b respectively). The speed increases gradually as the rod is rotated to an angle perpendicular to the fibers, and it decreases gradually as the rod is rotated to an angle parallel to the fibers. In other words, the speed is maximum when the shear wave propagates parallel to the fibers and a minimum when the shear wave propagates perpendicular to them. This behavior is characteristic of a TI material.

The findings by Wang et al. [10] are shown in Figure 26.7, where the behavior of the phase and group velocities when the shear wave propagates in the coronal plane are illustrated in a polar coordinate system. The group velocity behavior approximates the profile of an ellipse, where

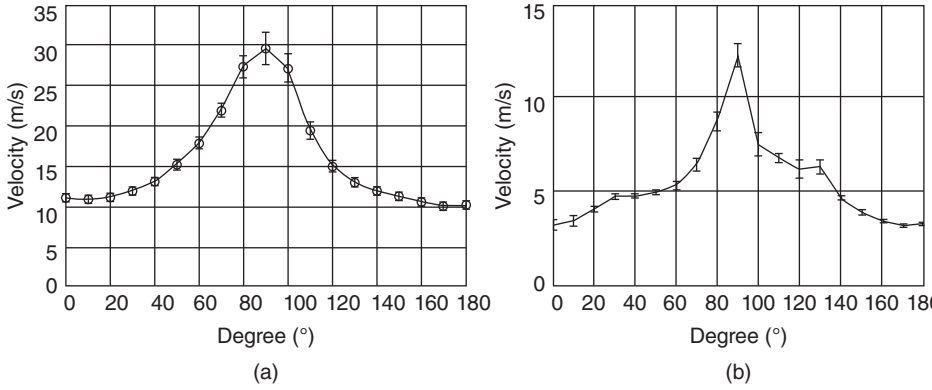

Figure 26.6 Shear wave speed as a function rotation angle of the rod with respect to the fibers for (a) the ex vivo muscle sample and (b) the in vivo human biceps. Source: reprinted with permission from [19], copyright 2003, Acoustical Society of America.

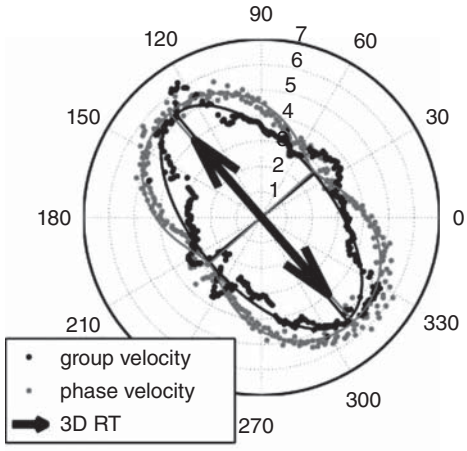

Figure 26.7 Group and phase velocity when the shear wave propagates in the coronal plane is shown in a polar coordinate system. The true fiber orientation estimated using a 3D Radon Transform method is represented by the black arrow. Source: © 2013 IEEE, reprinted, with permission, from [10].

speed is higher parallel to the fibers than perpendicular to them. The phase velocity behavior approximates the profile of a hippopede.

The predominant fiber orientation, estimated by applying a 3D Radon Transform method to the B-mode ultrasound volumes of the muscle samples for all possible 3D orientations is also shown as a projection in Figure 26.7.

The results from Gennisson et al. [19] and Wang et al. [10] indicate that the property of anisotropy has to be taken into account when assessing the mechanical properties of skeletal muscle using shear wave elastography. By using the methods described in this section, it is possible to estimate the shear wave group and phase velocity as a function of the angle between the transducer and the fibers in addition to the fibers' main orientation axis.

26.3.4 Influence of Tissue Anisotropy on the SWE Evaluation of the Myocardium

Anisotropy issues are also present in the myocardium as cardiomyocytes enclosed by endomysial sheaths of collagen are grouped together in fascicles by a sheath of connective tissue (perimysium) organized in a honeycomb-like arrangement. This network gives rise to directionally dependent mechanical properties [8], as demonstrated by Lee et al. [20]. Elastic tensor imaging [20] has emerged as a noninvasive ultrasound elastography-based

technique capable of accurately assessing the tissue fiber orientation and therefore the stiffness anisotropy. The principle of this technique is described below.

26.3.4.1 Experimental Setup

Lee et al. [21] introduced in 2012 a technique capable of estimating the tissue fibers' orientation through a tensor-based approach for ultrasound-based shear wave imaging (SWI). This technique was called elastic tensor imaging (ETI). To evaluate the feasibility of the technique, ETI was compared to magnetic resonance diffusion tensor imaging (DTI), which has been extensively investigated and its ability in mapping 2D and 3D myocardial fiber architecture has been previously demonstrated by multiple studies [22–25]. The principles of DTI can be found in Le Bihan et al. [26].

The ETI technique is based on the SWI technique [21]; SWI relies on the above mentioned principle, where shear waves propagate faster along the fibers than across the fibers and therefore the shear wave speed of propagation is dependent on the local fiber orientation and stiffness to estimate the fiber direction. Due to the myocardium's complex architecture, the SWI technique presented several limitations, including limited angular step resolution and complications when estimating the shear wave speed. ETI aims at overcoming these limitations by utilizing a tensor-based approach to improve the robustness and accuracy of the fiber angle estimation.

The ETI procedure can be summarized in three steps. First, shear waves are generated using ARF [27] on a programmable prototype ultrasound system (Supersonic Imagine, Aix-en-Provence, France) and a phased array transducer. Special care is taken in generating intense planar shear waves that can cover a large wall thickness of the myocardial sample. Shear waves are imaged using an ultrafast frame rate, higher than that of conventional echocardiography scanners and coherent-compounded images are obtained by averaging three different angled plane waves transmitted from the ultrasonic array at angles of −2°, 0°, and 2°.

Second, to evaluate the anisotropic characteristics of the in vitro porcine myocardial samples shear waves are generated and measured from −90° to 90° in 5° steps, as shown in Figure 26.8a. The transducer was rotated with respect to the samples, where 0° was defined along the fibers, and 90° and −90° were defined across the fibers. 2D images were taken to visualize the shear wave propagation across different time points, as illustrated in Figure 26.8b. The shear wave group velocity across the different rotation angles was estimated using spatiotemporal images of the shear wave propagation at different myocardial wall depths, as shown in Figures 26.8c and 26.8d.

Lastly, in order to map the fiber orientation independent of the rotation angle resolution (5° increments of the probe rotation), the elastic wave equation was solved in a tensor form using a least-square approximation and an eigendecomposition to estimate both the elasticity tensor and the high-precision fiber angle estimates.

26.3.4.2 Experimental Results: ETI Method

The comparison between the estimated myocardial fiber orientation according to the estimated angles and wall depths using the ETI and DTI methods for one of the myocardium samples are shown in Figure 26.9. The fiber distribution across the three different regions of the wall ventricle (anterior, lateral, and posterior) are shown in Figures 26.9a, 26.9b, and 26.9c. It is possible to observe on the corresponding scatter plots (Figures 26.9d, 26.9e, and 26.9f) that there is a very good correlation between the ETI and DTI estimations ($r^2 = 0.95$, 0.77 and 0.94) and therefore this ultrasound technique can help in the estimation of the shear wave speed along and across the fibers and in the determination of the myofiber orientation.

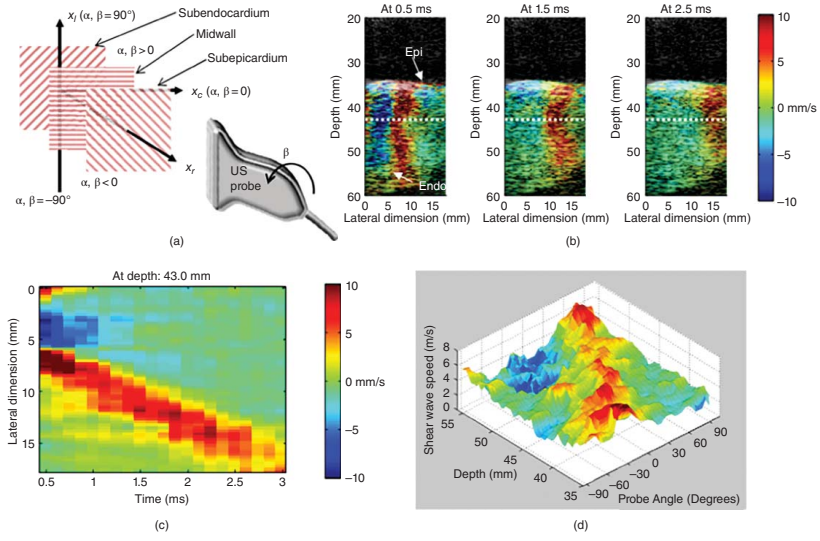

Figure 26.8 (a) Imaging system set-up and coordinate system. The ultrasound transducer is rotated from −90° to 90° in 5° steps. The rotation range is represented by α and β. (b) 2D images of shear wave propagation at different time points since the beginning of the shear wave acquisition. (c) and (d) Spatiotemporal images of shear wave propagation at different myocardial depths and rotation angles are used for shear wave speed estimation. Source: © Institute of Physics and Engineering in Medicine, reproduced by permission of IOP Publishing, All rights reserved [21].

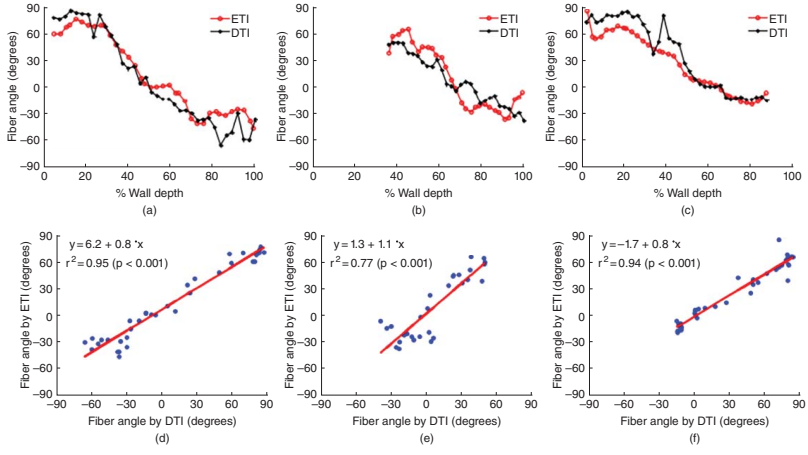

Figure 26.9 (a)–(c) Fiber orientation as a function of wall depth estimated using ETI and DTI of one sample of left ventricular anterior region. 0% to 33% wall depths indicate sub-endocardium, 33% and 67% wall depths indicate midwall and 67% to 100% wall depths indicate sub-epicardium, respectively. (d) to (f) Scatterplot of the estimated fiber orientation using the ETI method vs. the fiber orientation estimated using DTI. Source: © Institute of Physics and Engineering in Medicine, reproduced by permission of IOP Publishing, all rights reserved [21].

26.3.5 Design and Evaluation of Tissue-mimicking Phantoms to Characterize the Anisotropy Phenomenon in a Laboratory Setting

As can be seen, anisotropy is present in most of the soft tissues of the human body and therefore the consideration and study of this phenomenon when using ultrasound-based shear wave elastography methods [1–4] is a rule rather than an exception. Aristizabal et al. [28] and Chatelin et al. [29] have developed tissue-mimicking phantoms that have characteristics that mimic the shear moduli and shear wave speed variation found in TI materials. Phantoms with TI characteristics that can take into consideration different parameters related to anisotropy can help in the accurate interpretation of the shear wave speed measurements and the characterization of this phenomenon in a laboratory setting.

26.3.5.1 Experimental Setup

In order to characterize TI materials in a laboratory setting, Aristizabal et al. [30] created two different phantom designs using fibrous material and fishing line material with directionally dependent properties. The two phantom designs consisted of cube-shaped phantoms using multiple parallel layers of fibrous material (polyester) and using a parallel arrangement of monofilament fishing line material (20 lb, Test R6, transparent nylon, 0.50 mm diameter,

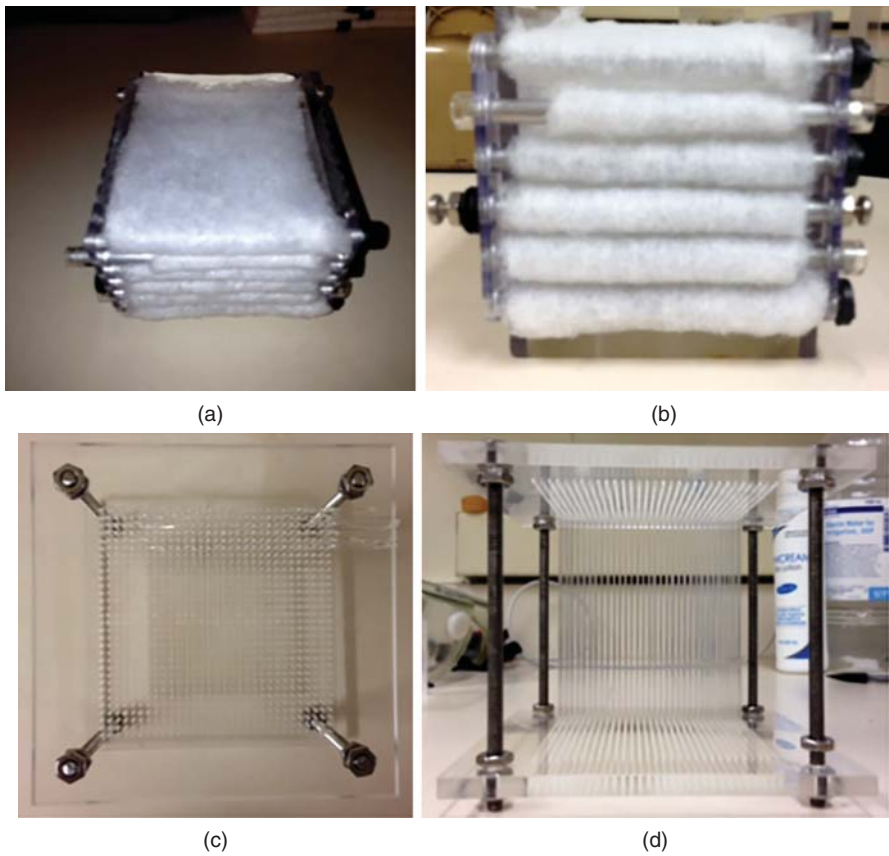

Figure 26.10 Phantom designs incorporating fibrous material (a), (b) fishing line material (c), (d) that have preferential orientations. Both set of phantoms were embedded in porcine 300 Bloom gelatin using two different concentrations of the gelatin (8%, 14%). Source: © Institute of Physics and Engineering in Medicine, reproduced by permission of IOP Publishing, all rights reserved [30].

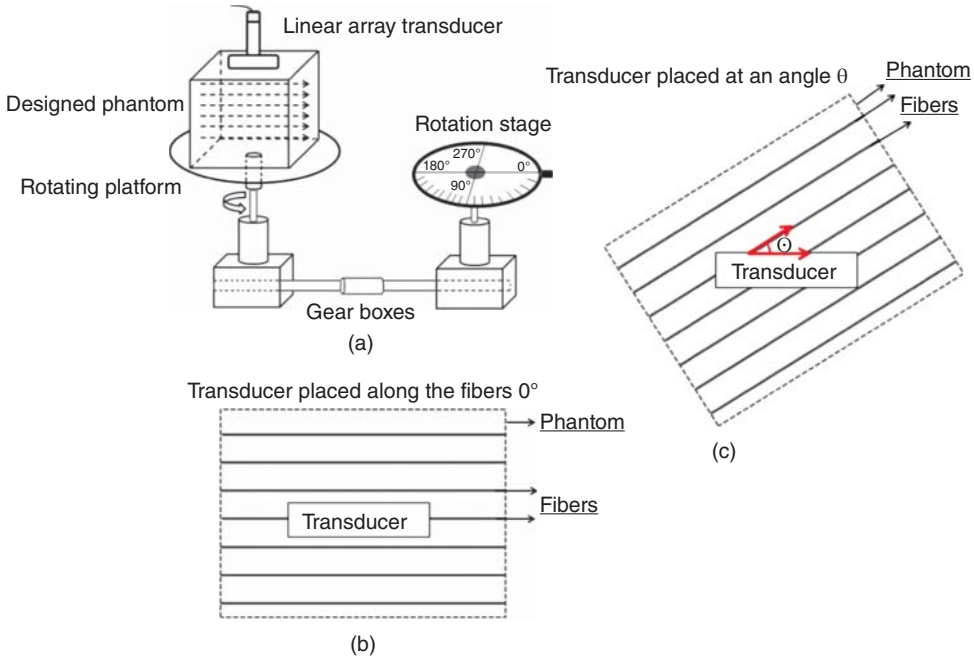

Figure 26.11 (a) Experimental setup with the designed phantom and pork muscle placed on a rotating platform with a rotation range oscillating between 0° and 360° in 10° steps. (b) Top view of the designed phantom, when the ultrasound transducer is placed along the axis of the fibers (0°). (c) Top view of the designed phantom after rotation when the ultrasound transducer is placed at an angle Θ with respect to the axis of the fibers. Source: © Institute of Physics and Engineering in Medicine, reproduced by permission of IOP Publishing, all rights reserved [30].

Eagle Claw, Denver, CO) with a spacing of 3 mm between them. Both phantom designs were embedded in porcine 300 Bloom gelatin (Sigma-Aldrich, St. Louis, MO) using two different concentrations of the gelatin (8%, 14%) (Figures 26.10a, 26.10b, 26.10c, and 26.10d, respectively). Moreover, in order to evaluate the ability of the phantom designs to effectively mimic TI tissues, they evaluated the anisotropic characteristics of an ex vivo sample of pork tenderloin in a saline bath at 30 °C for comparison.

To evaluate the TI characteristics of the four phantoms and the excised pork muscle, each individual phantom and the muscle sample were placed on a rotating platform with the rotation ranging between 0° to 360° in 10° steps, as shown in Figure 26.11a. The phantoms and muscle were rotated with respect to the transducer, where 0° and 180° were defined along the fibers, and 90° and 270° were defined across the fibers, as shown in Figures 26.11b and 26.11c. Three shear wave acquisitions were performed at each angle. They also evaluated two different locations for each phantom. To characterize the shear wave speed variation in TI materials, the shear wave group velocity was estimated as a function of the angle between the transducer and the fibers of the two phantom designs and the ex vivo muscle sample.

Chatelin et al. ([29]) designed a PVA hydrogel phantom capable of mimicking fibrous tissue such as cardiac, muscular or tendon. The phantom was created using 5wt% PVA solution and 1wt% cellulose was added as scattering particles. The mechanical TI of the phantoms was achieved by stretching the physical crosslinks of the polymeric chains along a preferential direction while undergoing freeze/thaw cycles using a customized static tensile-test setup. The characterization of the mechanical anisotropy of this phantom using shear wave elastography was done using an ultrafast scanner (Aixplorer; SuperSonic Imagine, Aix-en-Provence,

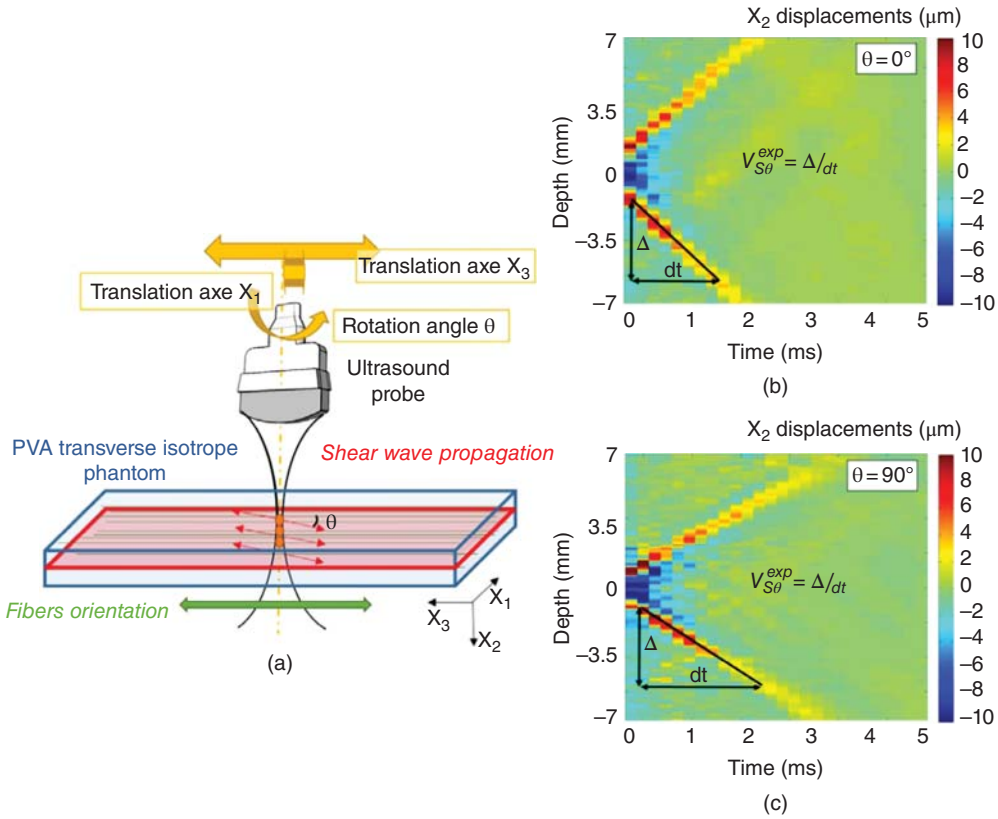

Figure 26.12 (a) Shear wave imaging setup. Ultrasound generated the focused acoustic beam (orange dots) source of cylindrical shear waves. To estimate the shear wave speed, spatiotemporal images are taken of the wave propagation as a function of the rotation angles (b) and (c). Source: © Institute of Physics and Engineering in Medicine, reproduced by permission of IOP Publishing, all rights reserved [29].

France) equipped with a 6 MHz transducer in supersonic shear imaging mode (SSI). The principles of SSI are described in Chapter 23 of this book. To characterize the shear wave speed variation in the phantom, the shear wave group velocity was measured from −90° to 90° in 10° steps throughout the sample by taking a spatiotemporal image at the depth of interest and fitting its profile, as shown in Figures 26.12a, 26.12b, and 26.12c. Additionally, the anisotropic characteristics of the phantom were characterized using linear transverse shearing dynamical mechanical analysis (DMA), BTI, and optical coherence tomography (FFOCT).

26.3.5.2 Experimental Results

The B-mode images of the two transversely isotropic phantom designs at a gelatin concentration of 14% and the pork muscle sample when the transducer was set parallel ($\Theta = 0°$) and perpendicular ($\Theta = 90°$) to the fibers are illustrated in Figures 26.13a, 26.13b, and 26.13c. Here, it is possible to appreciate the changes in the pattern of fiber organization when the angle between the transducer and the fibers goes from $\Theta = 0°$ (along the fibers) to $\Theta = 90°$ (across the fibers).

The shear wave group velocity measurements obtained at different angles between the transducer and the fibers demonstrate that the shear wave group velocity increases gradually as the pork muscle sample and both phantoms designs are rotated to an angle parallel to the fibers (Figure 26.14). The shear wave group velocity decreases gradually as the phantoms and pork muscle are rotated to an angle perpendicular to the fibers. Similar characteristics for the group

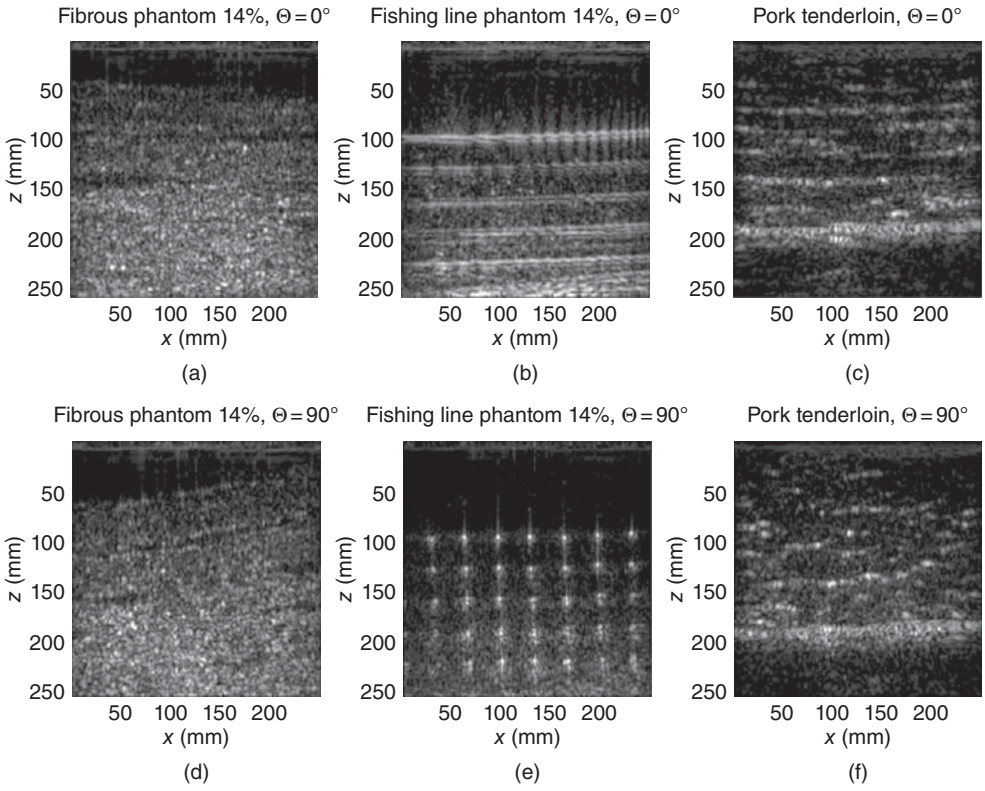

Figure 26.13 B-mode Images for (a) fibrous phantom, (b) fishing line phantom, and (c) pork tenderloin, when the ultrasound transducer is placed along the axis of the fibers (0°). B-mode Images for (d) fibrous phantom, (e) fishing line phantom, and (f) pork tenderloin, when the ultrasound transducer is placed across the axis of the fibers (90°). Source: © Institute of Physics and Engineering in Medicine, reproduced by permission of IOP Publishing, all rights reserved [30].

velocity in an anisotropic media have been reported in this chapter. Transversely isotropic phantoms represent an alternative when it is desired to characterize the properties of transversely isotropic body organs such as the kidney, skeletal muscle, myocardium, and tendons in a laboratory setting.

As mentioned above, Chatelin et al. [29] performed a multimodality characterization of the PVA hydrogel phantom. The shear wave speed variation from the SSI measurements in shown in Figure 26.15a. It can be observed that there is a good correlation between the results obtained experimentally and the TI model. The spatial coherence of the ultrasonic speckle was also characterized in the constructed phantom using backscatter tensor imaging (BTI) [31], where, by means of a spatially averaged coherence factor (SACF), it was possible to observe that the spatial coherence varied as a function of the rotation angle, where the scatterers were more coherent in the direction of the fibers than in the direction perpendicular to them. Lastly, the volumetric mechanical anisotropy characteristics (main anisotropy axis and fiber orientation) of the designed phantom were evaluated using FFOCT combined with elastography (Figures 26.15b, 26.15c, and 26.15d). The PVA hydrogel phantom proved to be a potential tool to evaluate the mechanical and optical anisotropy of biological fibrous tissues such as SSI and FFOCT.

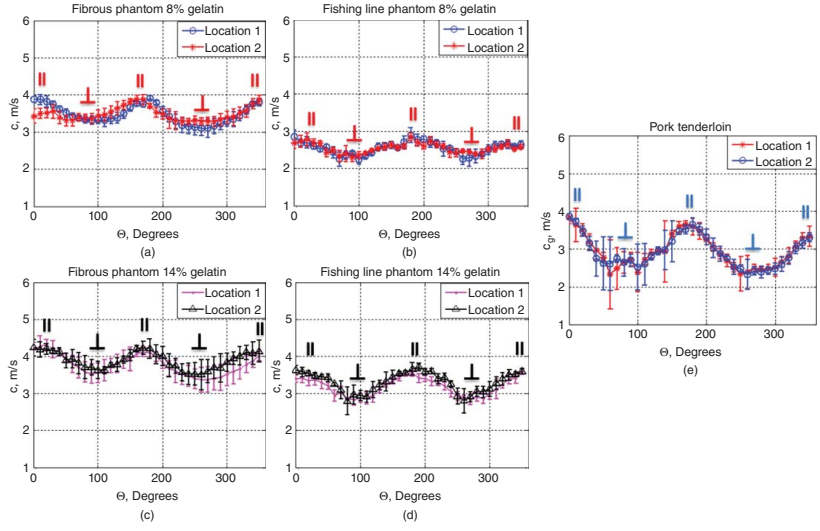

Figure 26.14 Shear wave group velocity, c_g, as a function of the angle of rotation (Θ from 0° to 360°) for (a) the fibrous phantom at 8% gelatin concentrations and two different locations within the same phantom; (b) the fishing line phantom at 8% gelatin concentrations and two different locations within the same phantom; (c) the fibrous phantom at 14% gelatin concentrations and two different locations within the same phantom; (d) the fishing line phantom at 14% gelatin concentrations and two different locations within the same phantom; and (e) the pork tenderloin. Source: © Institute of Physics and Engineering in Medicine, reproduced by permission of IOP Publishing, all rights reserved [30].

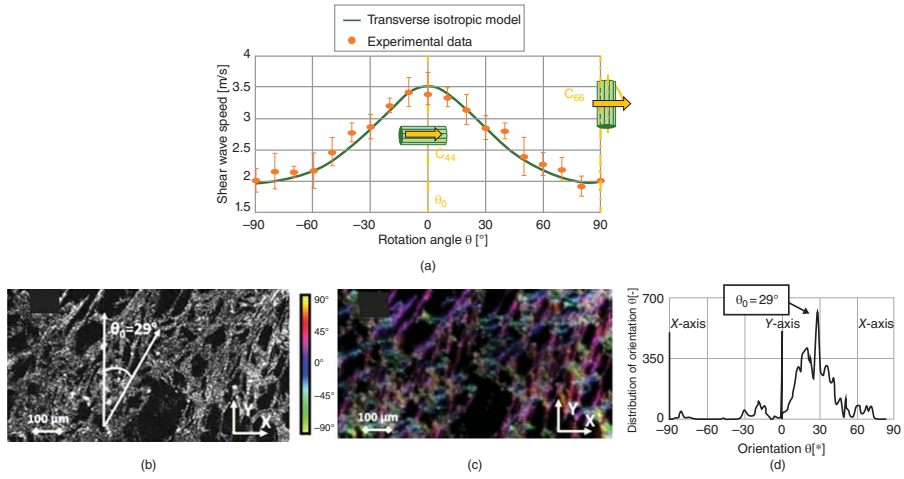

Figure 26.15 Multimodality characterization of the polyvinyl alcohol hydrogel phantom. (a) Shear wave speed variation as a function of the angle between the probe and the fibers. The experimental data is fitted by a TI model to obtain the main TI parameters. (b) to (d) FFOCT-obtained images for the PVA phantom. Source: © Institute of Physics and Engineering in Medicine, reproduced by permission of IOP Publishing, all rights reserved [29].

26.4 Conclusion

Consideration of the phenomenon of anisotropy in tissues such as the kidney, tendons, myocardium, and skeletal muscle is a necessity rather than an exception when assessing the mechanical properties of this type of tissue using shear wave based elastography techniques. Methods that can provide complementary information about the tissue fiber orientation, thereby helping in the accurate interpretation of the shear wave speed measurements and the characterization of this phenomenon in a clinical and laboratory setting, have been described. The evaluation of the medium anisotropy has emerged as a potential tool to study other mechanical factors that can help improve the accuracy and robustness of current elastography methods for the assessment of the viscoelastic properties of biological soft tissues.

References

1 Nightingale, K.R., Palmeri, M.L., Nightingale, R.W., and Trahey, G.E. (2001). On the feasibility of remote palpation using acoustic radiation force. *J. Acoust. Soc. Am.* 110: 625–634.

2 Sarvazyan, A.P., Rudenko, O.V., Swanson, S.D., et al. (1998). Shear wave elasticity imaging: A new ultrasonic technology of medical diagnostics. *Ultrasound Med. Biol.* 24: 1419–1435.

3 Bercoff, J., Tanter, M., and Fink, M. (2004). Supersonic shear imaging: A new technique for soft tissue elasticity mapping. *IEEE Trans. Ultrason., Ferroelect., Freq. Control* 51: 396–409.

4 Chen, S., Urban, M.W., Pislaru, C., et al. (2009). Shearwave dispersion ultrasound vibrometry (SDUV) for measuring tissue elasticity and viscosity. *IEEE Trans. Ultrason., Ferroelect., Freq. Control* 56: 55–62.

5 Crampin, S. and Yedlin, M. (1981). Shear-wave singularities of wave-propagation in anisotropic media. *J. Geophys. Zeitschrift Fur Geophysik* 49: 43–46.

6 Crampin, S. (1984). An introduction to wave-propagation in anisotropic media. *Geophys. J. Roy. Astronom. Soc.* 76: 17–28.

7 Giebisch, G. and Windhage, E. (2009). Organization of the urinary system. In: *Medical Physiology*, 2nd edn., 749–796. Saunders, Elsevier.

8 Engelmayr, G.C., Cheng, M.Y., Bettinger, C.J., et al. (2008). Accordion-like honeycombs for tissue engineering of cardiac anisotropy. *Nature Mat.* 7: 1003–1010.

9 Neill, J.O. (ed.) (2008). *Musculoskeletal Ultrasound: Anatomy and Technique*. New York: Springer Science and Business Media.

10 Wang, M., Byram, B., Palmeri, M., et al. (2013). Imaging transverse isotropic properties of muscle by monitoring acoustic radiation force induced shear waves using a 2-D matrix ultrasound array. *IEEE Trans. Med. Imaging* 32: 1671–1684.

11 Carcione, J.M. (2007). Anisotropic elastic media. In: *Wave Fields in Real Media: Wave Propagation in Anisotropic, Anelastic, Porous and Electromagnetic Media* (ed. J.M. Carcione), 1st edn., vol. 38, 1–24. Amsterdam: Elsevier.

12 Giebisch, E.G.W. (2009). Organization of the urinary system. In: *Medical Physiology* (ed. W.F.B. Boron and L. Emile), 1352. Philadelphia: Elsevier Health Sciences.

13 Gennisson, J.-L., Grenier, N., Combe, C., and Tanter, M. (2012). Supersonic shear wave elastography of in vivo pig kidney: influence of blood pressure, urinary pressure and tissue anisotropy. *Ultrasound Med. Biol.* 38: 1559–1567.

14 Amador, C., Urban, M.W., Chen, S., and Greenleaf, J.F. (2011). Shearwave dispersion ultrasound vibrometry (SDUV) on swine kidney. *IEEE Trans. Ultrason., Ferroelect., Freq. Control* 58: 2608–2619.

15 Staff, M.C. (2014). *Achilles tendon rupture*. Available: http://www.mayoclinic.org/diseases-conditions/achilles-tendon-rupture/basics/definition/con-20020370

16 Brum, J.B., Bernal, M., Gennisson, J.L., and Tanter, M. (2014). In vivo evaluation of the elastic anisotropy of the human Achilles tendon using shear wave dispersion analysis. *Phys. Med. Biol.* 59: 505–523.

17 Bernal, M., Nenadic, I., Urban, M.W., and Greenleaf, J.F. (2011). Material property estimation for tubes and arteries using ultrasound radiation force and analysis of propagating modes. *J. Acoust. Soc. Am.* 129: 1344–1354.

18 Lowe, M.J.S. (1995). Matrix techniques for modeling ultrasonic waves in multilayered media. *IEEE Trans. Ultrason., Ferroelect., Freq. Control* 42: 525–542.

19 Gennisson, J.L., Catheline, S., Chaffai, S., and Fink, M. (2003). Transient elastography in anisotropic medium: Application to the measurement of slow and fast shear wave speeds in muscles. *J. Acoust. Soc. Am.* 114: 536–541.

20 Lee, W.N., Pernot, M., Couade, M., et al. (2012). Mapping myocardial fiber orientation using echocardiography-based shear wave imaging. *IEEE Trans. Med. Imaging* 31: 554–562.

21 Lee, W.N., Larrat, B., Pernot, M., and Tanter, M. (2012). Ultrasound elastic tensor imaging: comparison with MR diffusion tensor imaging in the myocardium. *Phys. Med. Biol.* 57: 5075–5095.

22 Hsu, E.W., Muzikant, A.L., Matulevicius, S.A., et al. (1998). Magnetic resonance myocardial fiber-orientation mapping with direct histological correlation. *Am. J. Physiol. Heart Circ. Physiol.* 274: H1627–H1634.

23 Reese, T.G., Weisskoff, R.M., Smith, R.N., et al. (1995). Imaging myocardial fiber architecture in-vivo with magnetic-resonance. *Magn. Reson. Med.* 34: 786–791.

24 Scollan, D.F., Holmes, A., Winslow, R., and Forder, J. (1998). Histological validation of myocardial microstructure obtained from diffusion tensor magnetic resonance imaging. *Am. J. Physiol. Heart Circ. Physiol.* 275: H2308–H2318.

25 Tseng, W.Y.I., Dou, J., Reese, T.G., Wedeen V.J. (2006). Imaging myocardial fiber disarray and intramural strain hypokinesis in hypertrophic cardiomyopathy with MRI. *J. Magn. Reson. Imaging* 23: 1–8.

26 Le Bihan, D., Mangin, J.F., Poupon, C., et al. (2001). Diffusion tensor imaging: concepts and applications. *J. Magn. Reson. Imaging* 13: 534–546.

27 Nightingale, K. (2011). Acoustic radiation force impulse (ARFI) imaging: a review. *Curr. Med. Imaging Rev.* 7: 328–339.

28 Aristizabal, S., Amador, C., Qiang, B., et al. (2014). Shear wave vibrometry evaluation in transverse isotropic tissue mimicking phantoms and skeletal muscle. *Phys. Med. Biol.* 59: 7735–7752.

29 Chatelin, S., Bernal, M., Deffieux, T., et al. (2014). Anisotropic polyvinyl alcohol hydrogel phantom for shear wave elastography in fibrous biological soft tissue: a multimodality characterization. *Phys. Med. Biol.* 59: 6923–6940.

30 Aristizabal, S., Amador, C., Qiang, B., et al. (2014). Shear wave vibrometry evaluation in transverse isotropic tissue mimicking phantoms and skeletal muscle. *Phys. Med. Biol.* 59: 7735–7752.

31 Papadacci, C., Tanter, M., Pernot, M., and Fink, M. (2014). Ultrasound backscatter tensor imaging (BTI): analysis of the spatial coherence of ultrasonic speckle in anisotropic soft tissues. *IEEE Trans. Ultrason., Ferroelect., Freq. Control* 61: 986–996.

27

Application of Guided Waves for Quantifying Elasticity and Viscoelasticity of Boundary Sensitive Organs

Sara Aristizabal[1], Matthew Urban[2], Luiz Vasconcelos[3], Benjamin Wood[3], Miguel Bernal[4], Javier Brum[5], and Ivan Nenadic[3]

[1] *Well Living Lab, Rochester, MN, USA*
[2] *Department of Radiology, Mayo Clinic, Rochester, MN, USA*
[3] *Department of Physiology and Biomedical Engineering, Mayo Clinic, Rochester, MN, USA*
[4] *Universidad Pontificia Bolivariana, Medellín, Colombia*
[5] *Laboratorio deAcustica Ultrasonora, Instituto de Fisica, Facultad de Ciencias, Universidad de la Republica, Montevideo, Uruguay*

27.1 Introduction

The field of shear wave elastography has offered numerous techniques to quantify the viscoelastic properties of various biological tissues such as kidneys, myocardium, breast, liver, prostate, and others [1–3]. The majority of these methods assume the presence of a "pure" shear wave and relate the observed shear wave velocity (c) to the shear modulus of elasticity (μ) via $\mu = c^2\rho$, where ρ is tissue density (around 1000 kg/m^3). The pure shear wave assumption is appropriate for tissues such as the liver, kidneys, and breast tissue (often referred to as bulky organs) when the shear waves propagate in the middle of the organ and do not reflect from the organ boundaries. In bulky organs, the focused radiation force excites shear waves and compressional waves that attenuate before they reach the edges of the medium, and therefore do not form an interference pattern. In organs such as the arteries, myocardial free wall, bladder, cornea, and tendons, this assumption is not appropriate [4] because the compressional and shear waves create an interference pattern resulting in types of shear waves that are traditionally modeled as Lamb and Rayleigh waves [5–7]. These organs are referred to as boundary sensitive media and the application of shear wave elastography methods in these organs requires additional theoretical consideration. The theoretical basis of guided waves in boundary sensitive media has been described in greater detail in Chapter 7 of this textbook (Transverse Wave Propagation in Bounded Media). Here, we briefly revisit the theory and summarize experimental results of in vivo application of guided waves in the viscoelastic assessment of the myocardium, large arteries, bladder, cornea, and tendons.

27.2 Myocardium

The general theory of wave propagation in boundary sensitive media has been laid out in Chapter 7 of this textbook (Transverse Wave Propagation in Bounded Media). Here, we briefly summarize the basic concepts and build on the previously presented work. Most techniques mentioned in this chapter rely on the anti-symmetric Lamb wave theory [8, 9].

Ultrasound Elastography for Biomedical Applications and Medicine, First Edition.
Edited by Ivan Nenadic, Matthew Urban, James Greenleaf, Jean-Luc Gennisson, Miguel Bernal, and Mickael Tanter.

Kanai [10] originally presented an anti-symmetric Lamb wave model used to represent the motion of the septal myocardium due to aortic-valve closure. The myocardium was modeled as a homogenous viscoelastic plate composed of a Voigt material so that the shear modulus $\mu = \mu_1 + i\omega\mu_2$, where μ_1 and μ_2 are the shear elasticity and viscosity, respectively. Additionally, this plate is considered to be surrounded by fluid on both edges. Assuming that the bulk modulus is much larger than the shear modulus, the anti-symmetric Lamb wave model requires the following equation to hold

$$4k_{\mathrm{L}}^3\beta\cosh(k_{\mathrm{L}}h)\sinh(\beta h) = (k_{\mathrm{s}}^2 - 2k_{\mathrm{L}}^2)^2\sinh(k_{\mathrm{L}}h)\cosh(\beta h) + k_{\mathrm{s}}^4\cosh(k_{\mathrm{L}}h)\cosh(\beta h) \tag{27.1}$$

where $k_{\mathrm{L}} = \omega/c_{\mathrm{L}}$ is the Lamb wave number, ω is the angular frequency, c_{L} is the frequency-dependent Lamb wave velocity, $\beta = \sqrt{k_{\mathrm{L}}^2 - k_{\mathrm{s}}^2}$, $k_{\mathrm{s}} = \omega\sqrt{\rho_{\mathrm{m}}/\mu}$ is the shear wave number, ρ_{m} is the density of the sample, and h is the half-thickness of the sample. In order to obtain the elasticity and viscosity coefficients μ_1 and μ_2 Eq. (27.1) is fitted to the Lamb wave dispersion curves (velocity versus frequency).

The myocardium is a soft tissue subject to the propagation of guided waves along its length. The thickness of the heart wall with respect to the shear wavelength can affect the velocity of propagation of shear waves, giving rise to guided waves which depend on both the geometry and the properties of the tissue. Alterations in the normal structure of the myocardium can change the tissue properties and function, hence the importance of developing a method that can assess the mechanical properties of the myocardial tissue noninvasively.

The left ventricular (LV) free myocardium is 10–20 mm thick and it can be considered in the same order of the magnitude of the focal length of the acoustic radiation force for many applications. The myocardium is characterized by being surrounded by blood and pericardial fluid on either side of it and can therefore be modelled as a solid plate submerged in fluid. Kanai [10] used a high sensitivity ultrasound method to detect shear wave propagation in the myocardial septum due to closure of the aortic valve. The motion of the septum was modeled by an antisymmetric plane Lamb wave in an infinite isotropic plate with incompressible fluid on both sides. This method was used to measure shear wave dispersion in the frequency range 10–90 Hz and fit the Lamb wave model to estimate elasticity and viscosity. Nenadic et al. proposed a similar method to measure the dispersion of anti-symmetric Lamb waves in the myocardium, called the Lamb wave dispersion ultrasound vibrometry method (LDUV) [8]. LDUV measures the velocity dispersion as a function of frequency of anti-symmetric Lamb waves in the tissue of interest. The principle of LDUV is shown in Figure 27.1.

A cross-spectral analysis or other type of analysis can be performed to calculate the motion as a function of time and the velocity is measured by calculating the phase shift over the distance of wave propagation [11, 12]. An antisymmetric Lamb wave model is then fitted to velocity dispersion data to estimate the elasticity and viscosity. An example in a rubber plate phantom is shown in Figure 27.2.

The LDUV method was used in ex vivo myocardial samples and the ranges of the viscoelastic parameters were $\mu_1 = 15$–18 kPa and $\mu_2 = 5$–7 Pa·s [8]. Nenadic et al. performed in vivo experiments of Lamb wave propagation in pig hearts using a transthoracic approach [13]. For these studies, the wave excitation was triggered by electrocardiographic (ECG) R-wave and the data was acquired during an entire heart cycle. The elasticity and viscosity of the myocardium were estimated by fitting Eq. (27.1) to the dispersion curves throughout the heart cycle. In these transthoracic measurements, the average group velocity, elasticity, and viscosity showed a similar pattern of increase in systole and decrease in diastole, consistent with the ECG signal, as shown in Figures. 27.3c, 27.3d, and 27.3e respectively.

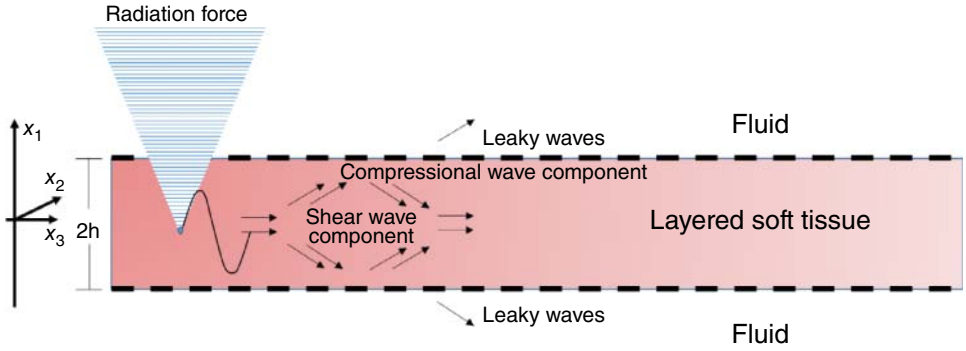

Figure 27.1 Acoustic radiation force is applied to a plate surround by fluid to make both shear and compressional waves which give rise to the Lamb waves. The same transducer used to generate the acoustic radiation force can then be switched to pulse-echo mode for motion detection or another transducer can be used. The pulse-echo interrogation is used to measure the resulting wave motion.

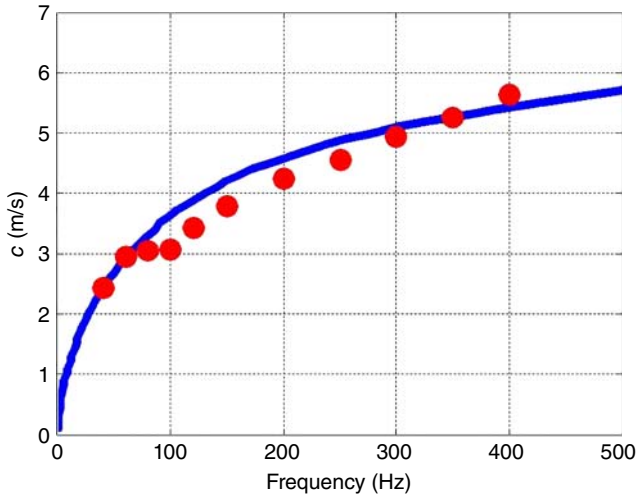

Figure 27.2 Lamb wave dispersion in a urethane rubber plate: experimentally obtained shear wave dispersion curves are shown as circles. Lamb wave model (solid line) was fitted to the data to obtain the values of elasticity and viscosity $\mu_1 = 45.1$ kPa and $\mu_2 = 6.5$ Pa·s.

Group velocity changed from around 1.5 m/s in diastole to around 5 m/s in systole (Figure 27.3c). Leftward and rightward propagating waves follow the same general pattern and are fairly similar. The values of elasticity (μ_1) increased from ~ 2 to 8 kPa, while the values of viscosity (μ_2) increased from ~2 to 12 Pa·s from diastole to systole.

Urban et al. used the LDUV method with mechanical excitation in eight pigs in an open-chest preparation [14]. Using a mechanical actuator, harmonic waves were generated to propagate in the myocardial wall and the velocities of wave propagation were measured in the range of 50–400 Hz over several cardiac cycles. The results of this study demonstrated that the dispersive phase velocity of the waves is consistent with an antisymmetric Lamb wave model. Additional work was done with the same method on pigs with myocardial infarction with reperfusion which demonstrated that the viscosity increased after reperfusion in diastole and systole and the shear elasticity increased in diastole after reperfusion [15]. Additionally, the LDUV method

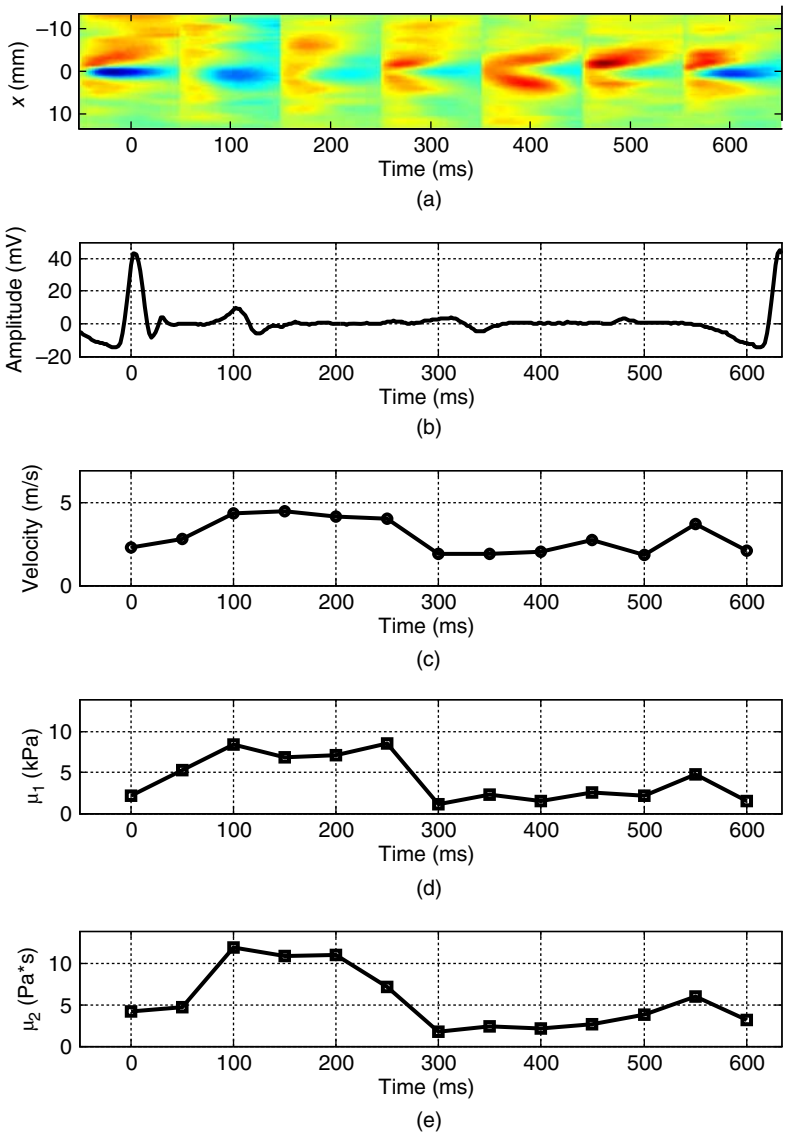

Figure 27.3 R-wave ECG-gated transthoracic measurements of Lamb wave group velocity, elasticity, and viscosity in a beating porcine left ventricular free wall averaged over 5–10 acquisitions. Average group velocity (c), elasticity (d), and viscosity (e) show a similar pattern of increase in systole and decrease in diastole, consistent with the ECG signal. Source: © Institute of Physics and Engineering in Medicine, reproduced by permission of IOP Publishing, all rights reserved [32].

allows for the estimation of elasticity and viscosity of the myocardial wall throughout the course of the cardiac cycle.

Similar open-chest studies have been performed by Couade et al. for the in vivo assessment of myocardial mechanical properties during the cardiac cycle. [16]. To estimate the shear modulus, μ, of the myocardium, the speed of propagation of the shear wave, c_T is measured and the following relationship is used to estimate μ

$$c_T = \sqrt{\frac{\mu}{\rho}} \tag{27.2}$$

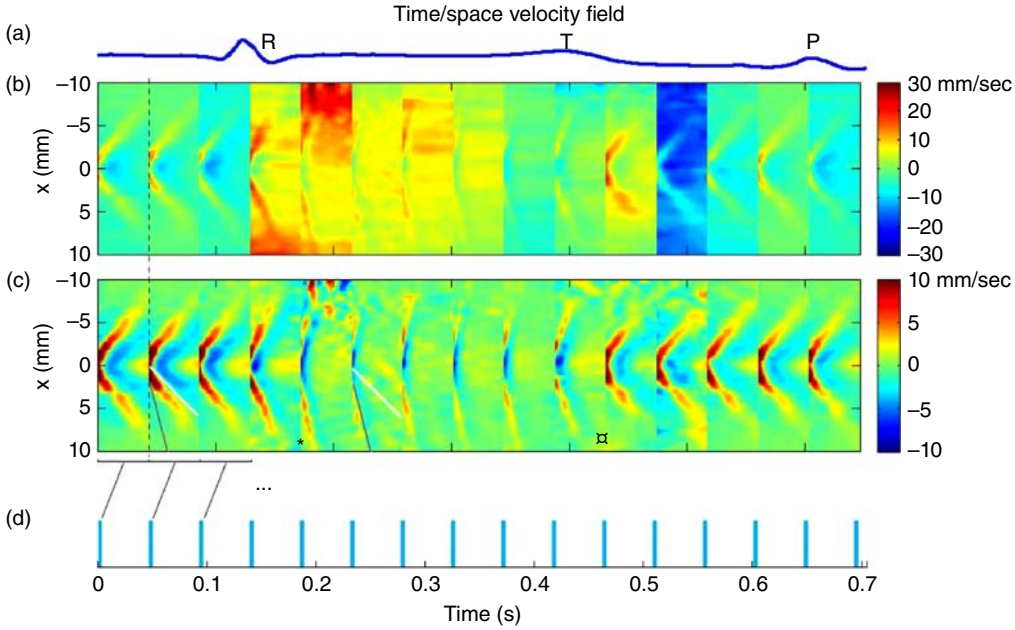

Figure 27.4 (a) ECG trace registered to the acquisition (including R-wave, T-wave, and then P-wave). (b) 2D spatiotemporal representation of the total particular velocity due to heart motion and shear wave induced 15 times by radiation force every 45 ms. (c) Particular velocity due to shear wave only: the heart motion is rejected by removing at each location the time average over the 4 ms length of the acquisition. (d) Time axis representing the global acquisition sequence: each blue rectangle is 4 ms wide and represents the combination of a pushing beam and an ultrafast sequence (as shown in Figure 27.2). Because the ultrafast imaging is used only every 45 ms for only 4 ms, the motion is not estimated continuously [16].

where ρ is the density of the myocardium, which is assumed to be equal to that of water (1000 kg/m^3). Couade et al. assumed that the shear waves induced using the SSI method have millimetric wavelengths and propagate only over a few millimeters, hence they are not subject to the condition of guided wave propagation since the propagation distance is not comparable to the thickness of the myocardial wall. Nevertheless, they are subjected to myocardial anisotropy.

To explore this phenomenon experiments were conducted on ten sheep. Shear waves were generated and measured at an ultrafast frame rate during an entire cardiac cycle using the supersonic shear imaging method whose principles have been described in Chapter 23. The measurement of elasticity was performed in a 2 cm wide region and the myocardium was imaged over its whole thickness. The speed of propagation of the shear wave was then calculated from backscattered ultrasonic echoes obtained at an ultrafast frame rate (up to 12 000 frames per second).

Figure 27.4 shows 15 wave acquisitions of 4 ms each where it is possible to appreciate the change of shear wave speed several times during the cardiac cycle. Additionally, the variation of the shear modulus of the myocardium as a function of time is shown in Figure 27.5, where it is possible to appreciate the temporal variation of μ for acquisitions within the same region.

27.3 Arteries

Estimating the mechanical properties of arteries has become a central role in the cardiovascular field as it has been shown to be a predictor of heart-related diseases such as type II diabetes,

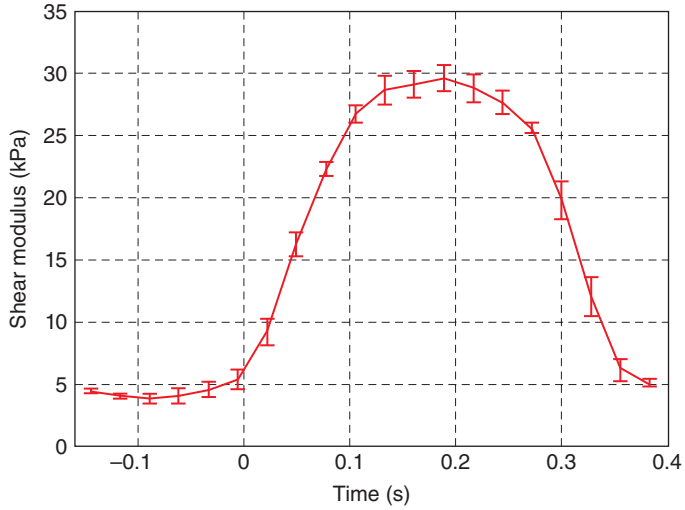

Figure 27.5 Time variation of shear modulus: four consecutive acquisitions were performed by removing/replacing the probe on the left ventricle in long axis view (mean SD). Based on coregistered ECG signal (not represented here), the time axis has been shifted for each acquisition in order to put the R-wave peak at $t = 0$ [16].

hypertension, and end-stage renal disease [17–19]. The viscoelastic properties of arteries have been widely studied over the last two decades but more recently arterial stiffness has become the subject of serious investigations to assess the progression of conditions that affect the arterial tree [20, 21]. In this chapter, we introduce the work performed by Bernal et al. and Couade et al., who have investigated the material properties of arteries using acoustic radiation force and shear wave imaging [9, 22].

Bernal et al. studied arterial elasticity by identifying the modes of wave propagation in tubes made out of urethane rubber and excised pig carotid arteries using the two-dimensional (2D) fast Fourier transform (2D FFT) [22]. From the magnitude distribution of the k-space of the propagating wave, the global peak is found by identifying the maximum magnitude for each temporal frequency and then determining the wavenumber, k_s, associated with it. Using the values of frequency, f, and wavenumber, $k_{s,}$ we can calculate the dispersion curves using $c = \lambda f$, where c is the velocity of the guided wave and λ is the wavelength $1/k_s$. The dispersion curves are then derived by finding the phase velocity for the maximum magnitude of the 2D Fourier transform at each individual frequency after filtering the interference of the arterial pulse wave from the cardiac cycle by removing the time-averaged particle velocity of each line. The dispersion curves are then used to estimate the shear modulus of the arterial wall using a leaky zero-order antisymmetric (A_0) Lamb wave model of propagation described elsewhere in this textbook (Chapter 7, Transverse Wave Propagation in Bounded Media). Urethane tubes and excised arteries were mounted in a metallic frame and embedded in tissue-mimicking gelatin. Arteries and tubes were pressurized over a range of 10–100 mmHg. Mechanical waves were generated and measured using a focused ultrasound and measured with a pulse-echo transducer, respectively.

To generate mechanical waves, Bernal et al. used acoustic radiation force, consisting of five tone bursts lasting 200 μs each, transmitted using a confocal transducer with center frequency of 3 MHz. Vibration of the arterial wall was measured using pulse-echo at 21 points along the length of the artery/phantom. A cross-spectral method was used to estimate the phase shifts between pulse-echo measurements [11]. The dispersion curves were obtained from the k-space representation using the 2D FFT method. The shear modulus of elasticity, μ_1, of the excised

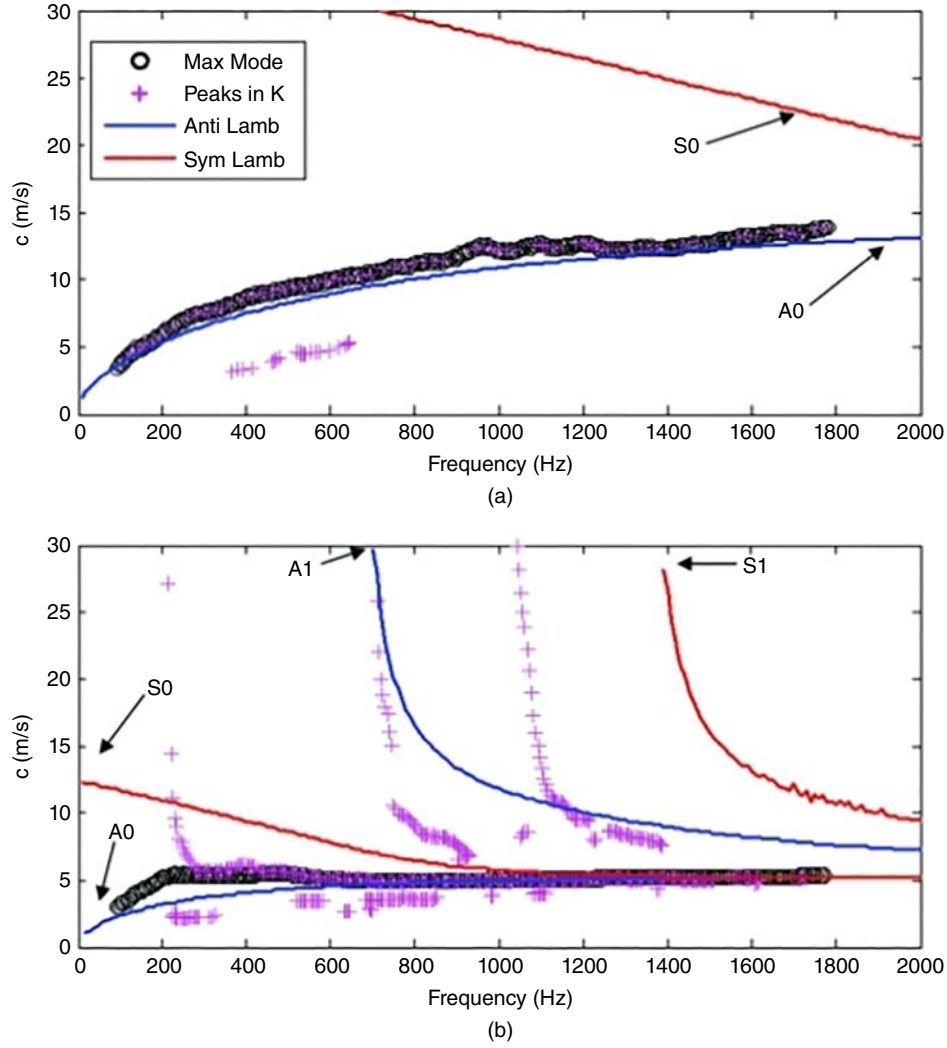

Figure 27.6 Experimental dispersion curves and fitting of a Lamb wave model. Panel A shows the dispersion curve for the urethane tube at 50 mmHg. The black circles represent the highest energy mode while the light circles represent the peaks in the wave number direction. The dark and the light lines represent the antisymmetric (A) and symmetric (S) modes for the Lamb wave model. Similarly, panel B shows the dispersion curves and Lamb wave fitting for the artery at 50 mmHg. The legend from panel A also applies to panel B [22].

arteries and urethane tubes were estimated by fitting the first antisymmetric Lamb wave mode, A_0 in Eq. (27.2), to the dispersion curves as shown in Figure 27.6. The lower order of longitudinal guided wave propagation in tubes can be approximated by the antisymmetric Lamb wave mode in plates.

Couade et al. proposed an ultrasound method based on supersonic shear imaging (SSI) [23] to assess the arterial wall stiffness. This technique generates a broadband guided shear wave (100–1500 Hz) in the arterial wall and tracks the wave propagation using ultrafast imaging. The studied was performed using a Aixplorer (SSI) scanner programmed to perform conventional B-mode imaging, acoustic radiation force for the generation of shear waves, and ultrafast imaging to image the propagation of shear waves at a frame rate higher than 2000 images per second.

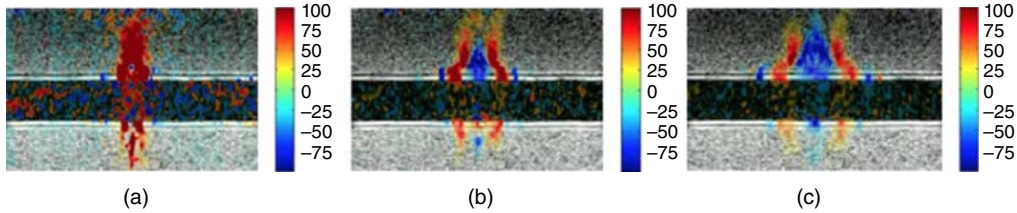

Figure 27.7 Shear wave propagation along the superior wall of an arterial phantom (agar gel) embedded into softer gelatin gel. The axial velocity field (tissue Doppler imaging) is superimposed to the anatomic grayscale image in color (mm/s) at different time steps: (a) $t = 0.5$ ms, (b) $t = 2$ ms, and (c) $t = 4$ ms. The ultrasonic probe is located on the top of the images. The elastic wave propagating along the wall is faster than in the surrounding softer gel [9].

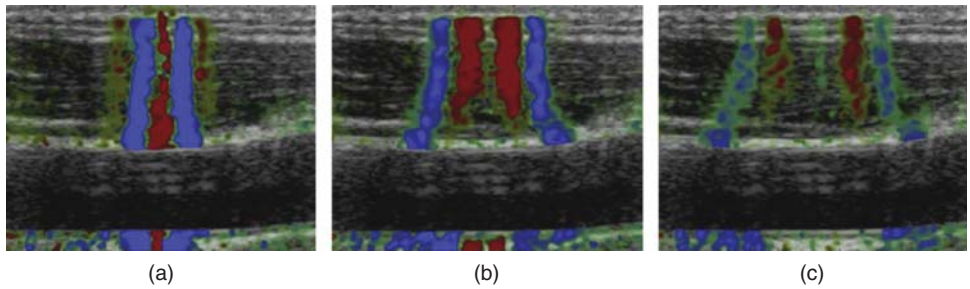

Figure 27.8 In vivo experiment in the carotid artery: propagation of a shear wave generated by acoustic remote palpation and acquired by ultrafast imaging: Color-coded axial displacements are superimposed to grayscale anatomic B-mode and represented at (a) $t = 0.5$ ms, (b) $t = 2$ ms, and (c) $t = 4$ ms after the generation of the acoustic radiation force [9].

To image the shear wave propagation in the arterial walls, the setup similar to that shown in Figure 27.1 is used, where the acoustic radiation force push and pulse-echo detection are performed with the same transducer. The transducer is aligned with the artery during the entire process. The generated push beam is transmitted at three specific locations in depth, spaced 1 mm apart. The average focal depth is set in the center of the arterial wall. This is done to compensate for any movement due to the cardiac cycle. Each push beam has duration of 100 μs, inducing a mean wall displacement of 10 μm along the plane of the probe. After the transmission of the shear wave was complete, the probe is switched to the ultrafast mode in order to scan and acquire data of the shear wave propagation. Beamforming is performed to create the 2D images of the entire motion of the shear wave propagation using the ultrasonic backscattered echoes (RF data). The wave's axial velocity is estimated via an in-phase/quadrature (IQ) auto-correlation of frame-by-frame motion detection [12]. Images are then stitched to create a "movie" of the axial velocity at a frame rate of 8000 images/second similar in appearance to Figures 27.7 and 27.8. The velocity of the shear wave in the arterial wall could then be extracted using Eq. (27.3), where x is the line number, t is the frame number, and $r_{\text{wall}}(x, t)$ is the detected position of the arterial wall at a specific line and frame number. Data from an experiment in a phantom is shown in Figure 27.7. In vivo measurements in the carotid artery are shown in Figure 27.8.

$$v_{\text{r}}(x, t) = v_{\text{r}}(r_{\text{wall}}(x, t), x; t) \tag{27.3}$$

As the mechanical properties of the arterial wall can vary across the cardiac cycle, Couade et al. also showed the feasibility of generating and measuring shear waves several times per second during the cardiac cycle in order to track these changes, as shown in Figure 27.9 [9].

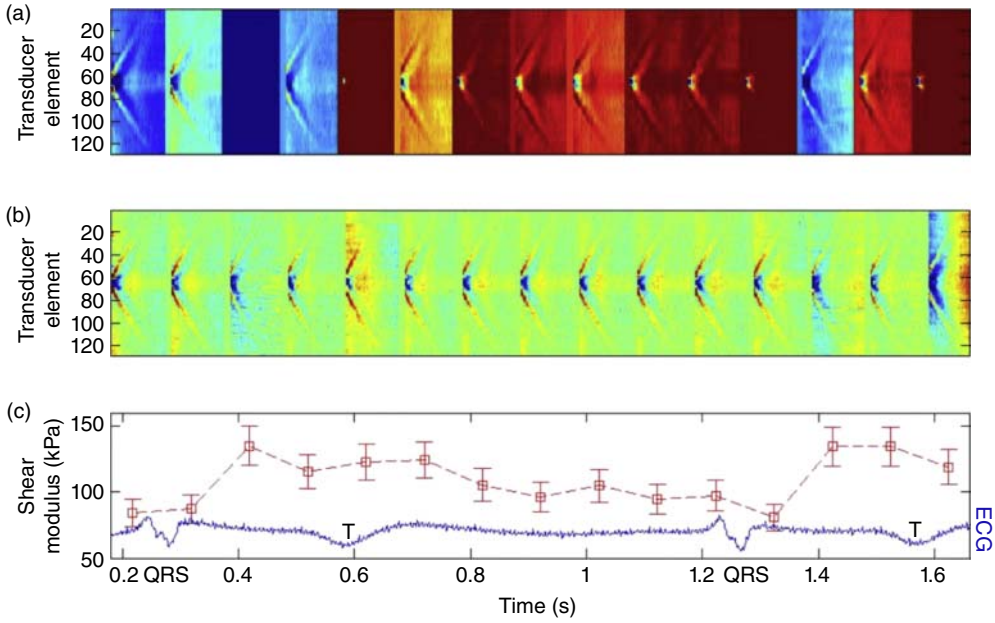

Figure 27.9 Real-time in vivo measurement of carotid arterial wall shear modulus variation during a single heart cycle (13 values/cycle) with time-registered ECG. (a) 15 successive space-time representations of tissue particle velocity in the arterial wall. One clearly notices on each successive set of data the presence of a propagating wave caused by the radiation force generation. (b) The same dataset after filtering of the homogeneous velocity offset as a result of the arterial pulse wave propagation for each ultrafast acquisition. One can clearly notice that this filtering enables discriminating both waves (arterial pulse wave and radiation force-induced wave). (c) Shear modulus deduced from each ultrafast acquisition owing to the estimation of the wave speed of the radiation force-induced wave [9].

Additional research has been carried out to estimate the elastic properties of the arterial wall and other thin layered organs. Nguyen et al. proposed a method called shear wave spectroscopy to estimate the viscoelastic properties of organs with thickness smaller than that of the shear wavelength [24]. These types of organs behave as soft plates and therefore the shear wave propagation in these types of tissues is guided and subjected to dispersive effects. Hence, by experimentally measuring the dispersion curves in these organs, the shear modulus can be approximated in viscoelastic plates using an analytic dispersion equation derived from the Lamb wave theory for the zero-order antisymmetric mode A_0

$$v_{\mathrm{ph}}(\omega) = \sqrt{\frac{hc_{\mathrm{T}}\omega}{2\sqrt{3}}} \tag{27.4}$$

where h is the plate thickness, c_{T} is the transverse velocity, and ω is the angular frequency. This formula provides a reasonable approximation of the shear modulus in the frequency range from 500 to 2000 Hz.

To investigate the influence of viscosity on dispersion curves, Nguyen et al. performed shear wave spectroscopy experiments using two phantoms with viscoelastic characteristics made using 5% gelatin/agar. Xanthan gum (0.5%) was added to one of the phantoms to increase the viscosity of the sample. Nguyen et al. showed that the non-viscous plate exhibited a dispersive effect because of the guided propagation of the shear waves and no significant differences were observed in the dispersive curves for the two phantoms, indicating that wave guides tend to affect the shear wave propagation significantly and therefore it is necessary to use shear wave spectroscopy to recover the shear modulus.

27.4 Urinary Bladder

Ultrasound bladder vibrometry (UBV) is a noninvasive technique developed by Nenadic et al. that uses Lamb waves to investigate the viscoelastic properties of the bladder wall [25]. An increase in the stiffness of bladder can be associated with pathogenic processes; hence there is a need for methods to monitor the rigidity of the bladder wall to ensure the adequate functioning of the urinary system. UBV allows monitoring the properties of the bladder wall as a function of filling volumes which is analogous to urodynamic studies. Urodynamic studies are the clinical gold standard in assessing bladder function; however, this method is invasive, costly, and can cause infection due to urinary catheterization.

UBV uses an ultrasonic array transducer to generate acoustic radiation force to excite anti-symmetric Lamb waves in the bladder wall and tracks the motion of the wave using pulse-echo techniques. To estimate the elastic properties of the bladder using the anti-symmetric Lamb wave theory described earlier, the bladder is modelled as an isotropic solid plate submerged in an incompressible non-viscous fluid. Nenadic, et al. performed experiments on formalin treated ex vivo porcine bladders to induce tissue stiffness and untreated excised porcine bladders. An example of a measurement is shown in Figure 27.10. The ex vivo experiments showed that UBV

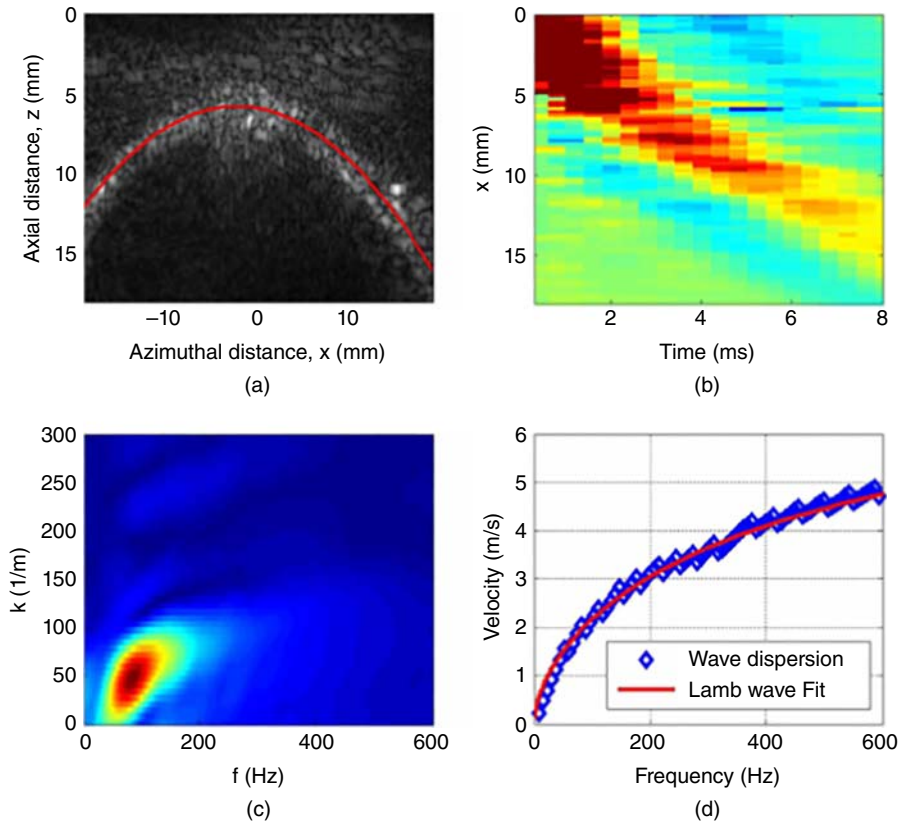

Figure 27.10 Ex vivo measurements of porcine bladder elasticity and viscosity. (a) B-mode of bladder wall outlined in solid line. (b) Wave propagation as a function of time and distance. (c) A 2D FFT of the time and spatial signals is used to calculate the guided wave propagation dispersion. (d) The resulting phase velocity as a function of frequency is fitted with an antisymmetric wave model (Eq. 27.1) to estimate the bladder elasticity and viscosity. Source: © Institute of Physics and Engineering in Medicine, reproduced by permission of IOP Publishing, all rights reserved [25].

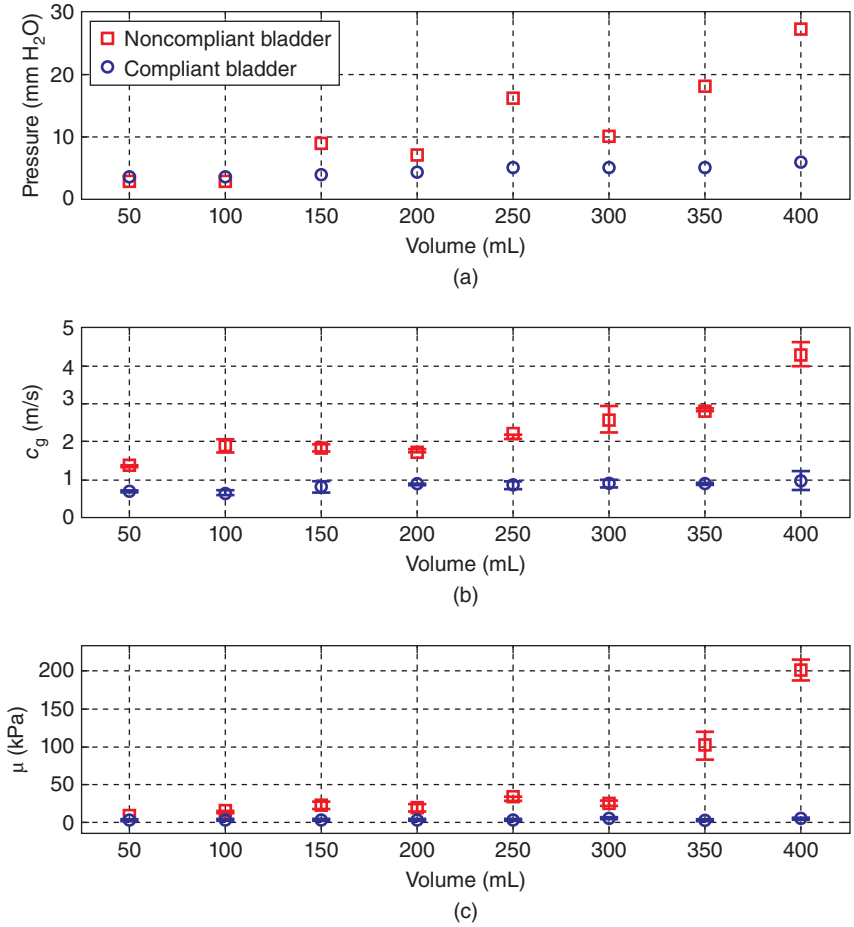

Figure 27.11 Summary of UDS and UBV comparative measurements obtained using the study design shown in Figure 27.4 in patients with a compliant (circles) and incompliant (squares) bladders. (a) UDS measurements of the detrusor pressure versus volume. (b) UBV measurements of the group velocity (c_g) versus volume. (c) UBV measurements of elasticity (μ) versus volume. Source: © reproduced by permission of PLOS, all rights reserved [26].

can track changes of the bladder wall's elastic properties, moreover there was a high correlation between the pressure measurements and the shear modulus estimated using UBV [25].

Nenadic et al. also evaluated the feasibility of the UBV method for the assessment of the viscoelastic properties of the human bladder. The UBV method was performed in two patients with at least one of the following conditions: neurogenic bladder, stress incontinence, or benign prostatic hyperplasia and scheduled to undergo UDS and UBV. One of the patients was known to have a noncompliant bladder through clinical documentation while the other had a normal compliant bladder [26]. Figure 27.11 shows the mean and standard deviation of the velocity of Lamb wave propagation along the bladder wall as well as the shear modulus as a function of filling volume. The shear modulus of the noncompliant bladder was higher than that of the normal compliant bladder. The results of the clinical studies performed in in vivo bladder demonstrated that the elastic parameters estimated using UBV closely correlate with the UDS estimated data. UBV could become a potential alternative to the invasive methods for bladder compliance evaluation.

27.5 Cornea

The assessment of the viscoelastic properties of the cornea is important for monitoring the progression of diseases such as the keratoconus, as well as a follow up strategy to evaluate the corneal biomechanical properties after patients undergo vision treatment.

Tanter et al. evaluated the feasibility of dynamic elastography to provide a map of corneal viscoelasticity using SSI. The cornea's boundary conditions can significantly affect the shear wave propagation since it can be characterized by a thin plate compared to the shear wavelength. The fact that the cornea is surrounded by a viscous fluid (aqueous humor) induces partially guided wave propagation due to reflections as the shear wave travels along the length of the cornea.

To estimate the viscoelastic properties of the corneal tissue, Tanter et al. modelled the cornea as a thin elastic plate surrounded by liquid. In this approximation, as the wave propagates along the plate it leaks energy at the wall interfaces on what is known as a "leaky" Lamb wave. Couade et al. derived an approximation for the phase velocity of this type of wave propagating in tissues (Eq. 27.4). This approximation is then used to estimate the viscoelastic properties of the tissue from the dispersion curves, $c(\omega)$.

Tanter et al. evaluated fresh excised porcine eyes, placed in a positioning cap and immersed in a water bath similar to the setup in Figure 27.1 [27]. The ultrasound probe is driven by an Aixplorer system. Three pushing sequences were performed, which allowed elasticity imaging in the center and edges of the imaged area for a complete mapping of the cornea elasticity. To meet the Food and Drug Administration (FDA) requirements for ophthalmological applications, the acoustic intensity was decreased in comparison to the intensities used for organs such as the breast or muscle. Local tissue particle velocity was estimated using a 1D cross-correlation of the successive ultrafast echographic images. The shear wave speed was subsequently estimated using a time-of-flight method between two points during the shear wave propagation and the shear wave group velocity was estimated over the whole shear wave bandwidth. To estimate the shear wave velocity, Tanter et al. used a shear wave spectroscopy algorithm, a Fourier transform of these signals was computed, and the ratio between wave number and frequency at each frequency peak was calculated to obtain the phase velocity. The Young's modulus is then estimated by reformulating Eq. (27.4) into the form

$$E = 36\frac{\rho c(\omega)^4}{h^2\omega^2} \tag{27.5}$$

The 2D spatial distribution of the excised corneas' relative displacements along the z-axis as the central push is being applied is shown in Figure 27.12.

An estimate of the shear wave speed at point A outside of the pushing zone (Figure 27.13) is obtained by estimating the time delay between time profiles at points B and C surrounding point A. The choice of the distance between B and C is optimized based on the data quality (i.e. the signal-to-noise level of tissue displacements estimates) at A. The complete 2D mapping of the cornea using the time-of-flight algorithm is shown in Figure 27.13 [27].

Using the time profiles of the z-displacement computed at each location, as shown in Figure 27.13, the Fourier transform is applied to each of them to estimate the phase of each spectral component. Finally, the dispersion curves were deduced from each pushing mode. The data was fitted to obtain the value of the Young's modulus (Figure 27.14).

This study by Tanter et al. demonstrated the ability to provide a quantitative mapping of corneal elasticity [27]. More recently, Nguyen et al. investigated the potential of corneal elasticity as a biomarker of the effectiveness of the UV-A/riboflavin-induced corneal collagen cross-linking treatment (CXL) for keratoconus, a vision disorder where the round cornea undergoes a progressive thinning resulting in an irregular cone-like shaped cornea [28]. One of the treatments available for this condition is CXL, which is a minimally invasive method

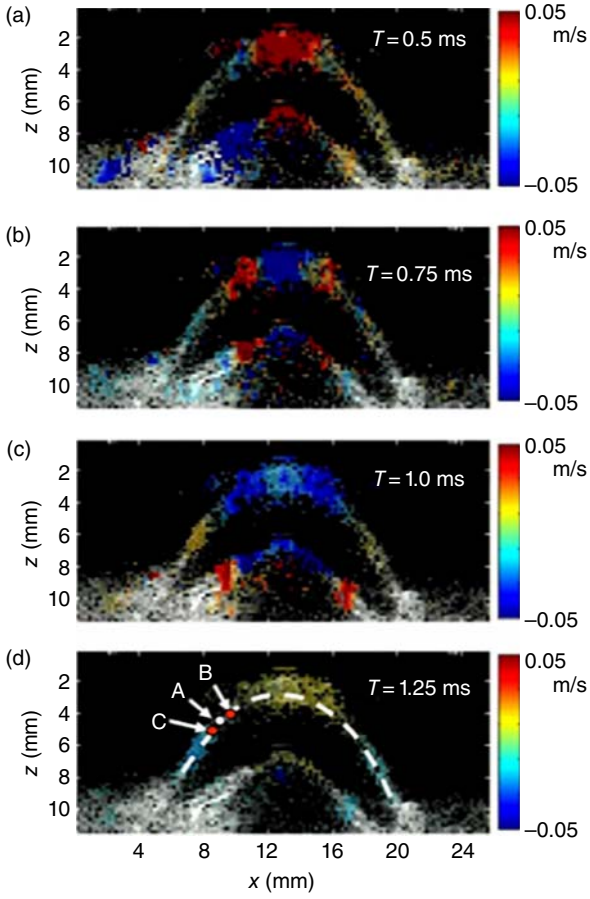

Figure 27.12 Cornea relative displacements between successive echographic images (i.e. particle velocity) at different time steps just after the ultrasonic radiation force generated at the center of the cornea. These color relative displacement images depict the shear wave propagation in the cornea and are superimposed on the echographic gray scale image. The resolution of the displacement map is 150 μm [27].

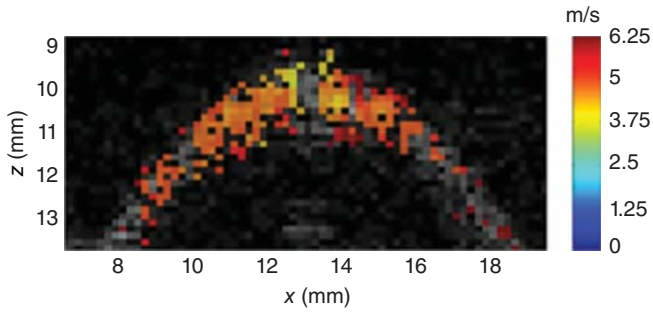

Figure 27.13 2D map of the shear wave speed superimposed on the gray scale ultrasound image of the cornea. From the knowledge of the corneal thickness (mm) and central frequency of the mechanical excitation (1500 Hz), this map can be converted into a quantitative Young's modulus map using Eq. (27.5) [27].

to stop the progression of the keratoconus disorder and it consists of photo-reticulating the collagen fibers of the cornea to stiffen its structure. Because there is no way to quantify the efficacy of the treatment, Nguyen et al. evaluated the biomechanical effects of CXL using corneal elasticity measured with SSI [28]. Nguyen et al. used the method previously laid out by Tanter et al. to study the biomechanical properties of ex vivo and in vivo porcine eyes using CXL experiments together with SSI. The shear wave imaging sequence consisted of four

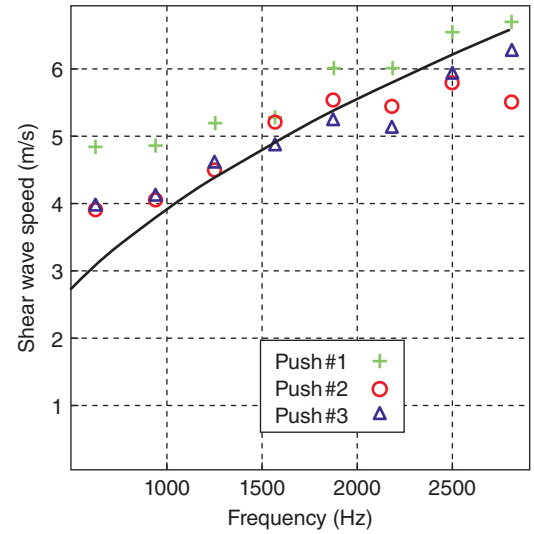

Figure 27.14 Shear wave dispersion curves estimated experimentally for the three successive mechanical waves generated by pushing modes no. 1, 2, and 3 into the porcine cornea. The solid line corresponds to Eq. (27.5) [27].

pushing beams applied along the cornea surface followed by an ultrafast imaging sequence after each push to map the entire cornea. A rubber ring was placed around the eye to enable the cornea immersion during elastography acquisition. Riboflavin 0.1% is dropped on the cornea for 20 minutes, and then the cornea was exposed to UV-A light for 30 minutes. Anesthetized pigs were used for the in vivo studies. Elastography acquisitions were performed before and after CXL treatment with the probe placed above the cornea, as shown in Figure 27.16. The elastography measurements were triggered with the respiratory and cardiac cycle to avoid physiological displacements. The wave speed maps obtained in two corneas are shown in Figure 27.15.

A map of the shear wave speed of the corneal tissue obtained after the application of the CXL treatment unilaterally on the cornea can be observed in Figure 27.16. The map was obtained from the wave acquisitions in different imaging planes. The superior half of the map was stiffer than the inferior half which matches well the areas of the cornea that were treated and untreated, respectively. The work done by Nguyen et al. demonstrated the feasibility of using SSI to monitor the biomechanical changes during the CXL treatment, and it has the potential to be used immediately after CXL treatment is applied [28].

27.6 Tendons

Tendons are structures that attach the muscle to a bone and other structures in the human body. Tendon ruptures are associated with significant morbidity in sports and daily life and therefore it is essential to find a noninvasive technique to evaluate the elastic properties of tendons in order to predict tendon rupture and monitor the recovery.

Tendons can be described as an arrangement of collagen fibers oriented in one main direction, hence they exhibit transverse isotropic characteristics. In other words the mechanical properties of tendons are directionally dependent and the value of elasticity is different along and across the fibers. Moreover, the thickness of tendons (4 mm) is smaller than the wavelength of the shear wave, which can give rise to the propagation of guided shear waves along the tissue in the form of Lamb waves.

Brum et al. evaluated the elastic properties of tendons by studying the wave propagation along and across the fibers as a function of frequency using shear wave spectroscopy.

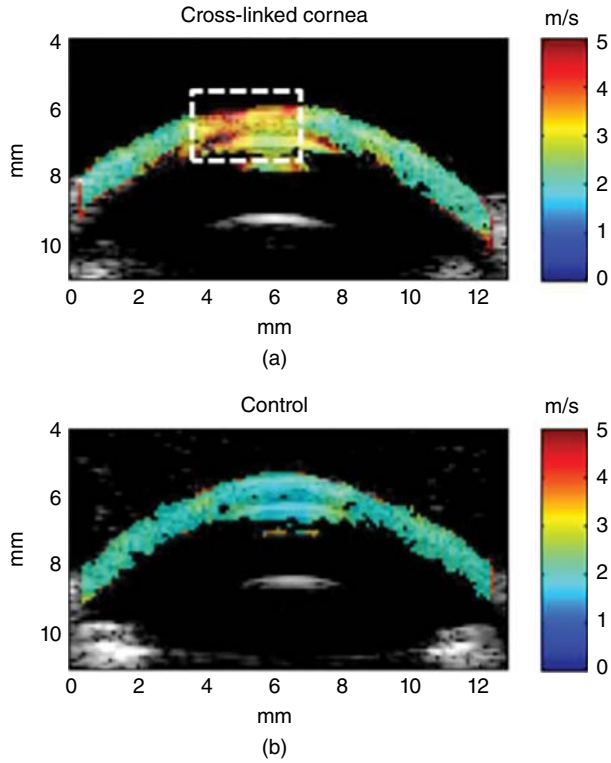

Figure 27.15 Ex vivo elastic maps acquired on porcine corneas superimposed on the echographic image. The color scale corresponds to the shear wave group velocity (m/s). A CXL was performed in vivo on the central part (delineated by the white dashed line) of the left cornea (a), while the right eye (b) of the same animal remained untreated. The color scale corresponds to the shear wave group velocity (m/s) [28].

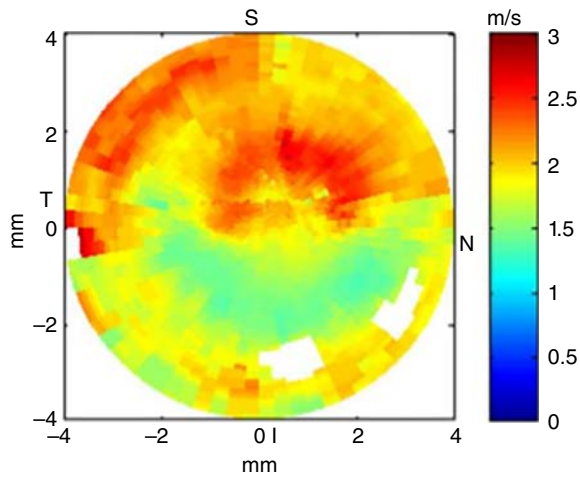

Figure 27.16 Ex vivo elastic map of the surface of the cornea after a CXL had been performed in vivo on the superior half on the cornea. The color scale corresponds to the shear group velocity (m/s). For each point, the shear wave speed has been averaged on the whole cornea thickness [28].

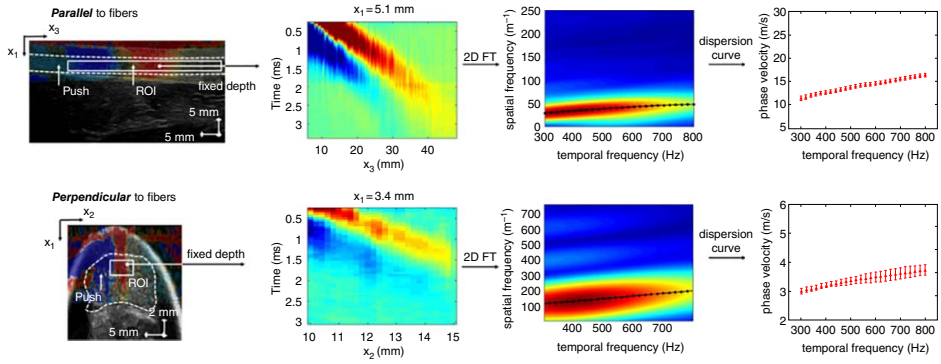

Figure 27.17 Shear wave spectroscopy in the Achilles tendon for the shear wave propagation direction parallel and perpendicular to the fibers. Source: © Institute of Physics and Engineering in Medicine, reproduced by permission of IOP Publishing, all rights reserved [29].

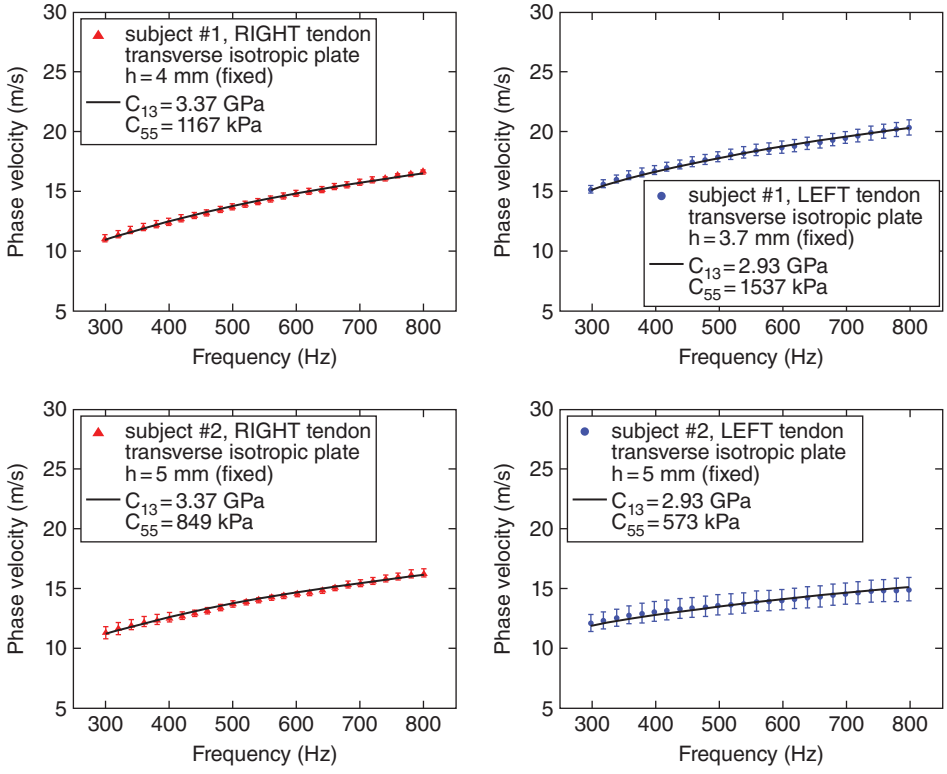

Figure 27.18 Shear wave dispersion curves for the propagation direction parallel to the fibers. The black solid line shows the least mean square fit of the transverse isotropic plate model. Source: © Institute of Physics and Engineering in Medicine, reproduced and adapted by permission of IOP Publishing, all rights reserved [29].

During this study, they evaluated the right and left Achilles tendon of five healthy volunteers. Volunteers were seated with a 90° angle between the foot and the tibia and also between the tibia and the femur. The feet of the volunteers were submerged in water to facilitate the positioning of the ultrasound array. The SSI technique was applied to the tendon in the direction parallel and perpendicular to the fibers. Shear waves were generated and measured using an ultrafast ultrasound scanner. From the measured displacement shear wave, spectroscopy was applied to obtain the dispersion [29]. The results for the measurements performed along and across the fibers are shown in Figure 27.17.

To obtain the elastic properties of the Achilles tendon, Brum, et al. assumed the wave propagation to take place in a transverse isotropic plate surrounded by liquid (leaky Lamb wave). Moreover, Brum et al. demonstrated that guided wave propagation along the tendon fibers can be described as a superposition of anti-symmetric and symmetric models of a transverse isotropic material. Meanwhile the propagation perpendicular to the fibers is governed by the leaky Lamb wave equation for an isotropic plate. It was found that it is essential to account for the viscosity in the direction perpendicular to the fibers, but in the parallel direction, the elasticity and viscosity are uncoupled due to strong guided wave effects. The dispersion curves obtained for two of the subjects of this study along and across the fibers are shown in Figures 27.18 and 27.19, respectively. It is possible to observe that the elastic plate behavior explains well the wave propagation along the fibers. However, this is not the case for the propagation across the fiber, where it is necessary to account for the tendons' viscosity in order

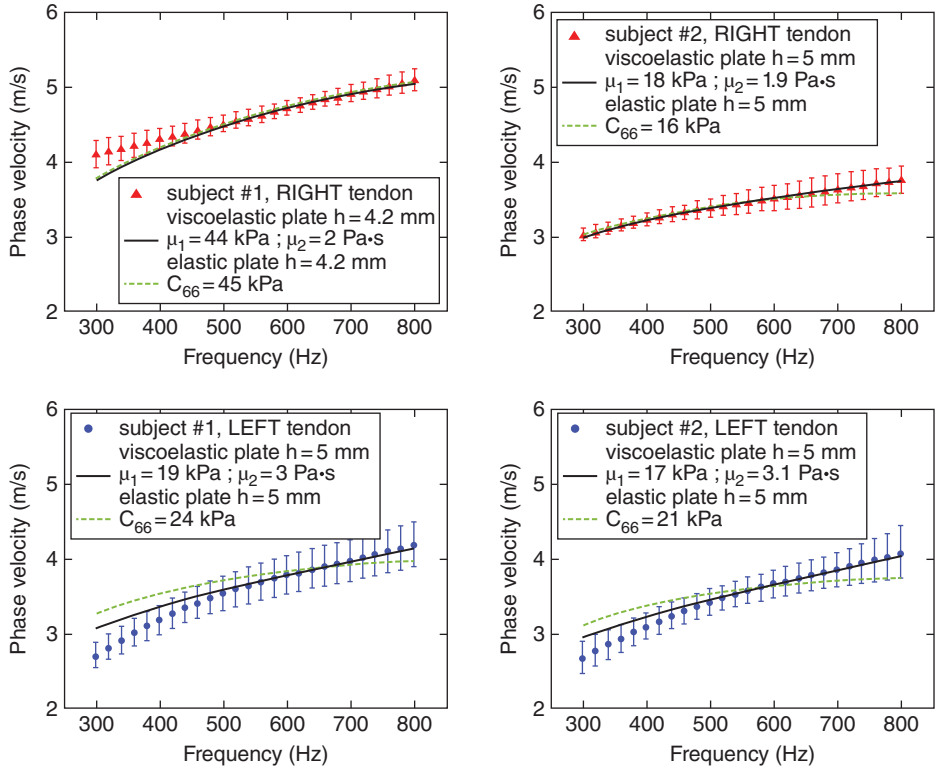

Figure 27.19 Shear wave dispersion curves for the propagation direction perpendicular to the fibers. The black solid line and the dashed line show the fit corresponding to the viscoelastic and elastic transverse isotropic plates, respectively. Source: © Institute of Physics and Engineering in Medicine, reproduced and adapted by permission of IOP Publishing, all rights reserved [29].

to have a good estimation. Additional work on this topic has been reported by Yeh et al. and Helfenstein-Didier et al. [30, 31].

27.7 Conclusions

Certain organs, because of their finite thickness with respect to the shear wavelength, produce guided wave behavior. Taking into account the geometry of these organs, myocardium, arteries, bladder, cornea, and tendons, allow for quantitative estimation of the elastic and viscoelastic properties. It is important to note that the wave speed alone may not be sufficient for this full characterization, but may serve to provide some differentiation among different patients. These methods still have yet to be added to clinical machines, but the applied uses of guided waves is growing for clinical evaluation.

References

1 Sarvazyan, A., Hall, T.J., Urban, M.W., et al. (2011). Elasticity imaging – an emerging branch of medical imaging. *An overview. Curr. Med. Imaging Rev.* 7: 255–282.

2 Sarvazyan, A.P., Urban, M.W., and Greenleaf, J.F. (2013). Acoustic waves in medical imaging and diagnostics. *Ultrasound Med. Biol.* 39: 1133–1146.

3 Gennisson, J.L., Deffieux, T., Fink, M., and Tanter, M. (2013). Ultrasound elastography: Principles and techniques. *Diagn. Interv. Imaging* 94: 487–495.

4 Urban, M.W., Nenadic, I.Z., Chen, S., and Greenleaf, J.F. (2013). Discrepancies in reporting tissue material properties. *J Ultrasound Med.* 32: 886–888.

5 Nenadic, I.Z., Urban, M.W., Aristizabal, S., et al. (2011). On Lamb and Rayleigh wave convergence in viscoelastic tissues. *Phys. Med. Biol.* 56: 6723–6738.

6 Nenadic, I.Z., Urban, M.W., Mitchell, S.A., and Greenleaf, J.F. (2010). Inversion of Lamb waves in shearwave dispersion ultrasound vibrometry (SDUV). In: *2010 IEEE Ultrasonics Symposium*, 1632–1635, San Diego, CA.

7 Brum, J., Gennisson, J.L., Nguyen, T.M., et al. (2012). Application of 1-D transient elastography for the shear modulus assessment of thin-layered soft tissue: comparison with supersonic shear imaging technique. *IEEE Trans. Ultrason., Ferroelectr., Freq. Control* 59: 703–714.

8 Nenadic, I.Z., Urban, M.W., Mitchell, S.A., and Greenleaf, J.F., (2011). Lamb wave dispersion ultrasound vibrometry (LDUV) method for quantifying mechanical properties of viscoelastic solids. *Phys. Med. Biol.* 56, 2245.

9 Couade, M., Pernot, M., Prada, C., et al. (2010). Quantitative assessment of arterial wall biomechanical properties using shear wave imaging. *Ultrasound Med. Biol.* 36: 1662–1676.

10 Kanai, H. (2005). Propagation of spontaneously actuated pulsive vibration in human heart wall and in vivo viscoelasticity estimation. *IEEE Trans. Ultrason., Ferroelectr., Freq. Control* 52: 1931–1942.

11 Hasegawa, H. and Kanai, H. (2006). Improving accuracy in estimation of artery-wall displacement by referring to center frequency of RF echo. *IEEE Trans. Ultrason., Ferroelectr., Freq. Control* 53: 52–63.

12 Kasai, C., Namekawa, K., Koyano, A., and Omoto, R. (1985). Real-time two-dimensional blood flow imaging using an autocorrelation technique. *IEEE Trans. Son. Ultrason.* SU-32: 458–464.

13 Nenadic, I.Z., Urban, M.W., Pislaru, C., et al. (2011). In vivo open and closed chest measurements of myocardial viscoelasticity through a heart cycle using Lamb wave dispersion ultrasound vibrometry (LDUV). In: *2011 International IEEE Ultrasonics Symposium*, 17–20, Orlando, FL.

14 Urban, M.W., Pislaru, C., Nenadic, I.Z., et al. (2013). Measurement of viscoelastic properties of in vivo swine myocardium using Lamb wave dispersion ultrasound vibrometry (LDUV). *IEEE Trans. Med. Imaging* 32: 247–261.

15 Pislaru, C., Urban, M.W., Pislaru, S.V., et al. (2014). Viscoelastic properties of normal and infarcted myocardium measured by a multifrequency shear wave method: comparison with pressure-segment length method. *Ultrasound Med. Biol.* 40: 1785–1795.

16 Couade, M., Pernot, M., Messas, E., et al. (2011). In vivo quantitative mapping of myocardial stiffening and transmural anisotropy during the cardiac cycle. *IEEE Trans. Med. Imaging* 30: 295–305.

17 Dolan, E., Thijs, L., Li, Y., et al. (2006). Ambulatory arterial stiffness index as a predictor of cardiovascular mortality in the Dublin outcome study. *Hypertension* 47: 365–370.

18 Laurent, S., Boutouyrie, P., Asmar, R., et al. (2001). Aortic stiffness is an independent predictor of all-cause and cardiovascular mortality in hypertensive patients. *Hypertension* 37: 1236.

19 Kingwell, B.A. and Gatzka, C.D. (2002). Arterial stiffness and prediction of cardiovascular risk. *J. Hypertension* 20: 2337–2340.

20 Cameron, J.D., Bulpitt, C.J., Pinto, E.S., and Rajkumar, C. (2003). The aging of elastic and muscular arteries. *Diabetes Care* 26: 2133.

21 Duprez, D.A. and Cohn, J.N. (2007). Arterial stiffness as a risk factor for coronary atherosclerosis. *Curr. Atherosclerosis Rep.* 9: 139–144.

22 Bernal, M., Nenadic, I., Urban, M.W., and Greenleaf, J.F. (2011). Material property estimation for tubes and arteries using ultrasound radiation force and analysis of propagating modes. *J. Acoust. Soc. Am.* 129: 1344–1354.

23 Bercoff, J., Tanter, M., and Fink, M. (2004). Supersonic shear imaging: a new technique for soft tissue elasticity mapping. *IEEE Trans. Ultrason., Ferroelectr., Freq. Control* 51: 396–409.

24 Nguyen, T.-M., Couade, M., Bercoff, J., and Tanter, M. (2011). Assessment of viscous and elastic properties of sub-wavelength layered soft tissues using shear wave spectroscopy: Theoretical framework and in vitro experimental validation. *IEEE Trans. Ultrason., Ferroelectr., Freq. Control* 58: 2305–2315.

25 Nenadic, I.Z., Qiang, B., Urban, M.W., et al. (2013). Ultrasound bladder vibrometry method for measuring viscoelasticity of the bladder wall. *Phys. Med. Biol.* 58: 2675–2695.

26 Nenadic, I., Mynderse, L., Husmann, D., et al. (2016). Noninvasive evaluation of bladder wall mechanical properties as a function of filling volume: potential application in bladder compliance assessment. *PLoS ONE* 11, e0157818.

27 Tanter, M., Touboul, D., Gennisson, J.L., et al. (2009). High-resolution quantitative imaging of cornea elasticity using supersonic shear imaging. *IEEE Trans. Med. Imaging* 28: 1881–1893.

28 Nguyen, T.-M., Aubry, J.-F., Touboul, D., et al. (2012). Monitoring of cornea elastic properties changes during UV-A/Riboflavin-induced corneal collagen cross-linking using supersonic shear wave imaging: a pilot study. *Invest. Ophthalmol. Vis. Sci.* 53: 5948–5954.

29 Brum, J., Bernal, M., Gennisson, J.L., and Tanter, M. (2014). In vivo evaluation of the elastic anisotropy of the human Achilles tendon using shear wave dispersion analysis. *Phys. Med. Biol.* 59, 505.

30 Yeh, C.L., Kuo, P.L., Gennisson, J.L., et al. (2016). Shear wave measurements for evaluation of tendon diseases. *IEEE Trans. Ultrason., Ferroelectr., Freq. Control* 63: 1906–1921.

31 Helfenstein-Didier, C., Andrade, R.J., Brum, J., et al. (2016). In vivo quantification of the shear modulus of the human Achilles tendon during passive loading using shear wave dispersion analysis. *Phys. Med. Biol.* 61: 2485–2496.

32 Nenadic, I.Z., Urban, M.W., Pislaru, C., Escobar, D., Vasconcelos, L., and Greenleaf, J.F. (2018). In vivo open- and closed-chest measurements of left-ventricular myocardial viscoelasticity using lamb wave dispersion ultrasound vibrometry (LDUV): a feasibility study, *Biomed. Phys. & Eng. Express* 4: 047001.

28

Model-free Techniques for Estimating Tissue Viscoelasticity

Daniel Escobar, Luiz Vasconcelos, Carolina Amador Carrascal, and Ivan Nenadic

Department of Physiology and Biomedical Engineering, Mayo Clinic, Rochester, MN, USA

28.1 Introduction

Current shear wave imaging techniques are useful to identify tissue linear viscoelastic properties; however, to quantify these properties a rheological model must be used. This chapter reviews current methods that have been proposed to quantify viscoelastic properties in a model-independent way. Two methods, called acoustic radiation force-induced creep (RFIC) and acoustic radiation force-induced creep–recovery (RFICR), estimate complex elastic modulus from time-dependent creep response or creep–recovery response induced by acoustic radiation force in combination with acoustic radiation force shear wave propagation [1–3]. A third model-free method named AMUSE (attenuation measuring ultrasound shearwave elastography), estimates shear wave velocity and attenuation independently. AMUSE measures the location and shape of the k-space magnitude maxima that is directly related to the speed and attenuation of the shear wave propagating in the tissue [4]. Measuring both the shear wave velocity and attenuation at given frequencies characterizes tissue mechanical properties and allows a true measurement of tissue viscoelasticity. It is important to note that all the models here described consider a source-free, harmonic shear wave propagating in a linear, homogeneous, isotropic, viscoelastic medium.

28.2 Overview of Governing Principles

28.2.1 Wave Propagation

Viscoelastic properties can be measured by studying shear wave propagation. Shear wave methods are usually noninvasive and are based on measured particle motion from shear strain (angular deformation) that is involved in the passage of transverse waves. The one-dimensional plane shear wave propagation in soft tissue is described by [5]

$$\frac{\partial^2 u(x,t)}{\partial x^2} + k^2 u(x,t) = 0 \tag{28.1}$$

where $u(x,t)$ is the displacement resulting from a shear wave propagating unidirectionally along the x-axis and k is the wave number. A solution for Eq. (28.1) in a linear viscoelastic medium is [5]

$$u(x,t) = u_0 e^{i\omega t} e^{ik_0 x} \tag{28.2}$$

Ultrasound Elastography for Biomedical Applications and Medicine, First Edition.
Edited by Ivan Nenadic, Matthew Urban, James Greenleaf, Jean-Luc Gennisson, Miguel Bernal, and Mickael Tanter.

where $\omega = 2\pi f$ is the angular frequency and f is the frequency of the wave, u_0 is the initial amplitude of the wave, and x and t are the spatial and temporal dimensions, respectively. Additionally, in the case of linear viscoelastic medium, the wave number k is complex, written as $k_0 = k_\mathrm{r} - ik_\mathrm{i}$ [5], and thus

$$u(x,t) = u_0 e^{i(\omega t + k_r x)} e^{(k_i x)} \tag{28.3}$$

where k_r and k_i are the real and imaginary parts of the wave number respectively. Shear wave phase velocity, c_s, is defined as the ratio between ω and k_r. On the other hand, the shear wave attenuation coefficient, α_s, is the imaginary wave number, k_i. The complex wave number, $k_0 = k_\mathrm{r} - ik_\mathrm{i}$, and complex shear modulus, $G^*(\omega) = G_\mathrm{s}(\omega) + iG_\mathrm{l}(\omega)$, are related by [6]

$$G_\mathrm{s}(\omega) = \rho\omega^2 \frac{k_\mathrm{r}^2 - k_\mathrm{i}^2}{(k_\mathrm{r}^2 + k_\mathrm{i}^2)} \tag{28.4}$$

$$G_\mathrm{l}(\omega) = -2\rho\omega^2 \frac{k_\mathrm{r} k_\mathrm{i}}{(k_\mathrm{r}^2 + k_\mathrm{i}^2)} \tag{28.5}$$

where ρ is the mass density. Shear wave phase velocity, c_s, and shear wave attenuation, α_s, written as a function of shear complex modulus yield [7]

$$c_\mathrm{s}(\omega) = \sqrt{\frac{2(G_\mathrm{s}^2 + G_\mathrm{l}^2)}{\rho(G_\mathrm{s} + \sqrt{G_\mathrm{s}^2 + G_\mathrm{l}^2})}} \tag{28.6}$$

$$\alpha_\mathrm{s}(\omega) = \sqrt{\frac{\rho\omega^2\left(\sqrt{G_\mathrm{s}^2 + G_\mathrm{l}^2} - G_\mathrm{s}\right)}{2(G_\mathrm{s}^2 + G_\mathrm{l}^2)}} \tag{28.7}$$

The wave velocity in a given medium is defined by the velocity of a single frequency component (phase velocity) or the velocity of the wave packet (group velocity). The change in the phase velocity of a propagated wave with frequency is known as dispersion; therefore, phase velocity is not the same as group velocity in a dispersive medium. On the other hand, in a nondispersive medium, phase velocity is the same as group velocity. Dispersion can be caused by both tissue geometry and material properties. Equation (28.3) assumes an infinite medium; therefore, geometric dispersion is negligible.

28.3 Imaging Techniques

28.3.1 Acoustic Radiation Force-induced Creep (RFIC) and Acoustic Radiation Force-induced Creep–Recovery (RFICR)

As described in Chapter 13 of this book, the acoustic radiation force-induced creep (RFIC) and acoustic radiation force-induced creep–recovery (RFCR) methods use the analytical solution of the Boltzmann integral (integral equation of the viscoelastic constitutive equations) to convert the time-dependent creep response to the frequency-dependent complex modulus [1–3]. Recalling the constitutive equation of linear viscoelastic materials, under any given stress history, the creep strain is described by the Boltzmann integral representation [8]

$$\gamma(t) = \int_0^t J(t-\xi)\frac{\partial\tau(\xi)}{\partial\xi}\mathrm{d}\xi \tag{28.8}$$

where $\gamma(t)$ is the shear strain, τ is shear stress, $J(t)$ is the creep compliance, and $\frac{\partial[\cdot]}{\partial\xi}$ represents first derivative respect to the independent variable ξ. Equation (28.7) represents the

time-dependent response of a linear viscoelastic material and by using Fourier transforms, it can be converted to the frequency domain to obtain the complex shear modulus $G^*(\omega)$

$$G^*(\omega) = \frac{\mathrm{FT}[\tau(t)]}{\mathrm{FT}[\gamma(t)]} = \frac{1}{i\omega \mathrm{FT}[J(t)]} \tag{28.9}$$

where FT[·] represents the Fourier transform. Because $J(t)$ is a function that grows with increasing time, its Fourier transform is not convergent. Evans et al. [9] reported the analytic solution of Eq. (28.9).

In RFIC and RFICR, Eq. (28.9) is used to estimate $\beta G^*(\omega)$, which is referred to as the extracted complex modulus, $C^*(\omega)$, and it will vary as a function of material absorption and acoustic beam intensity. To overcome this problem, a widely used property of viscoelastic materials called loss tangent or $\tan(\delta)$, defined as the ratio of the imaginary part and real part of the storage modulus, is not dependent on material absorption and acoustic beam intensity [2]

$$\tan(\delta) = \frac{\mathrm{Im}[C^*(\omega)]}{\mathrm{Re}[C^*(\omega)]} = \frac{\mathrm{Im}[\beta G^*(\omega)]}{\mathrm{Re}[\beta G^*(\omega)]} = \frac{\mathrm{Im}[G^*(\omega)]}{\mathrm{Re}[G^*(\omega)]} \tag{28.10}$$

The loss tangent or $\tan(\delta)$ written in terms of the complex wave number is [6]

$$\tan(\delta) = \frac{2k_\mathrm{r}k_\mathrm{i}}{k_\mathrm{r}^2 - k_\mathrm{i}^2} \tag{28.11}$$

If both $\tan(\delta)$ and k_r are known, the negative solution for k_i in Eq. (28.11) is [6]

$$k_\mathrm{i} = k_\mathrm{r}\left[\left(\frac{1}{\tan(\delta)}\right) - \sqrt{\left(1 - \left(\frac{1}{\tan(\delta)}\right)^2\right)}\right] \tag{28.12}$$

Finally, by knowing k_r and k_i, the shear storage and loss moduli are obtained from Eq. (28.4) and Eq. (28.5).

Figures 28.1a and 28.1b show the mean creep displacement response and loss tangent ($\tan(\delta)$) from five locations in an excised swine kidney, respectively. The solid line represents the mean and the dashed lines represent the standard deviation from the mean. Figures 28.1c and 28.1d illustrates the shear wave phase velocity dispersion and estimated shear wave attenuation dispersion.

Figure 28.2 shows the estimated model-free shear complex modulus in an excised kidney that was reconstructed by the shear wave velocity and shear wave attenuation.

28.3.2 Attenuation Measuring Ultrasound Shear Wave Elastography (AMUSE)

AMUSE is a method that measures shear wave velocity and attenuation independently to provide a model-free characterization of the mechanical properties of tissue. Together with RFIC and RFCR, these are the only known methods of their kind.

The most basic implementation of AMUSE requires a shear wave propagating in the medium (tissue) and the ability to track tissue motion in the spatiotemporal domain; such requirement is fulfilled using, for example, ultrasound technology.

Performing a two-dimensional Fourier transform (2D FT) of the tissue motion as a function of time (t) and distance (x), results in the frequency (f) versus wave number (k) domain, also known as the k-space. Shear wave velocity and attenuation are directly related to the location and shape of the k-space magnitude maxima [4].

Taking into account that the displacement (u) of a one-dimensional, harmonic plane shear wave propagating in an infinite viscoelastic medium in respect to the complex wave number k_0

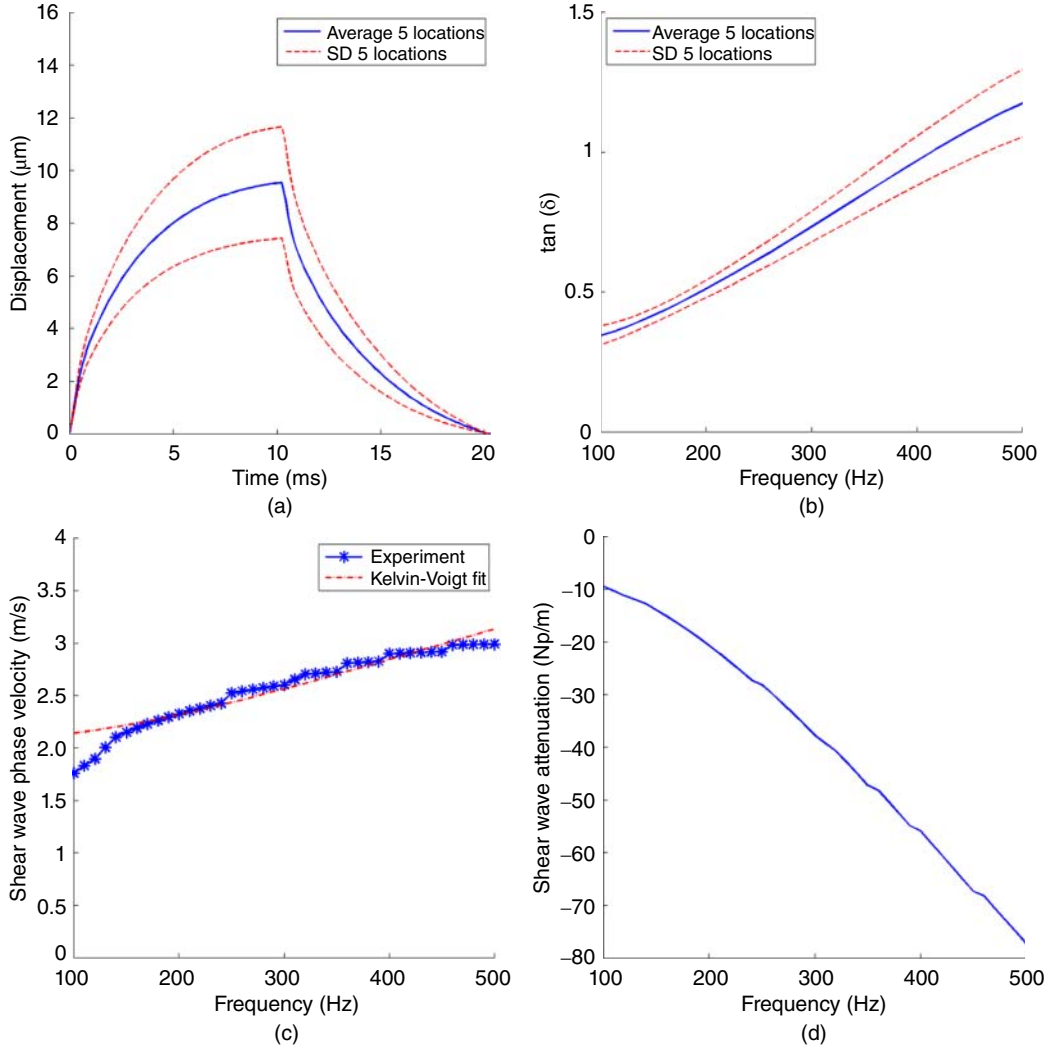

Figure 28.1 Excised swine kidney: (a) acoustic radiation force-induced creep; (b) estimated loss tangent; (c) shear wave phase velocity; and (d) shear wave attenuation. Source: © Institute of Physics and Engineering in Medicine, reproduced by permission of IOP Publishing, all rights reserved [2].

is defined by Eq. (28.2), we can then also define k_0 as

$$k_0 = \frac{\omega_0}{c} + i\alpha \tag{28.13}$$

where $\omega_0 = 2\pi f_0$ is the angular frequency and f_0 is the frequency of the wave, c is the shear wave velocity, and α is the shear wave attenuation. With this said, we can rewrite Eq. (28.2) as

$$u(x,t) = u_0 e^{i\omega_0 t} e^{i(\omega_0/c)x} e^{-\alpha x} \tag{28.14}$$

Taking the absolute value of the 2D FT of this equation of motion results in

$$|U(k,f)| = \frac{u_0 \delta(f - f_0)}{\sqrt{\alpha^2 + 4\pi^2\left(k - \frac{f_0}{c}\right)^2}} \tag{28.15}$$

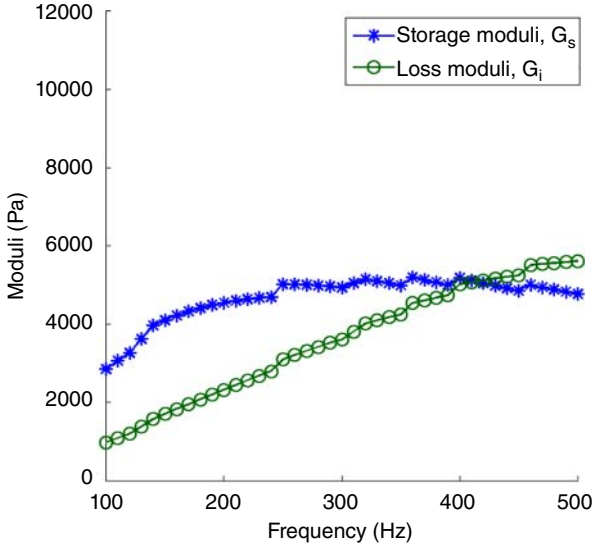

Figure 28.2 Excised swine kidney model-free shear complex modulus. Source: © Institute of Physics and Engineering in Medicine, reproduced by permission of IOP Publishing, all rights reserved [2].

where k is the wave number, f is the frequency, $\delta(\cdot)$ is the Dirac delta function, and $|U(k,f)|$ is the magnitude of the 2D FT of $U(k,f)$.

Equation (28.15) shows that for a wave with frequency f_0, the magnitude of its 2D FT distribution, or the k-space, has a corresponding peak at $(k,f) = (f_0/c, f_0)$. Thus, the k-space analysis can be used to calculate wave velocity. Upon further visual inspection of Eq. (28.15), one can notice that the equation is similar to the Lorentzian distribution, which has a convenient relationship between the width of the peak and one of the parameters, in this case, α. In practice, the Dirac delta function $\delta(\cdot)$ has a finite amplitude, and in this case its maximum amplitude A lies at $k = f_0/c$. The maximum amplitude of the k-space is thus equal to $|U(k,f)|_{\max} = u_0 A/\alpha$, and the relationship between the maximum and half-maximum is

$$\frac{u_0 A}{2\alpha} = \frac{u_0 A}{\sqrt{\alpha^2 + 4\pi^2\left(k_{1/2} - \frac{f_0}{c}\right)^2}} \tag{28.16}$$

where $k_{1/2}$ is the wave-number at half-maximum amplitude of the peak. Solving Eq. (28.16) for $k_{1/2}$ yields

$$k_{1/2} = \pm\frac{\sqrt{3}}{2\pi}\alpha + \frac{f_0}{c} \tag{28.17}$$

Considering that the full-width at the half-maximum (FWHM) is the distance between the two half-maxima along the k-axis then we can cite that $\text{FWHM} = \alpha\sqrt{3}/\pi$, consequently the shear wave attenuation α is

$$\alpha = \frac{\pi \times \text{FWHM}}{\sqrt{3}} \tag{28.18}$$

In conclusion, both shear wave velocity and attenuation can be calculated based on the 2D FT of the tissue displacement as a function of time and distance, and we can find, with no need of rheological models, the complex shear wave number. For some ultrasound elastography methods, the particle velocity instead of displacement is the raw measurement. Because the particle velocity is the time derivative of the displacement, the differentiation property of the Fourier transform can still be applied, and Eq. (28.18) still holds [4].

The impulsive focused radiation force produced by a linear array transducer approximately generates a cylindrical wave whose energy dissipates via cylindrically shaped wave fronts of increasing radius as the wave propagates away from the source. These cylindrical wave fronts are different than the plane wave fronts, so the equation that defines displacement of the particle in the tissue in the direction of wave propagation (x) would be

$$u_z(x,t) = \frac{i}{4} H_0^{(1)}(k_0^* x) e^{i\omega_0 t} \tag{28.19}$$

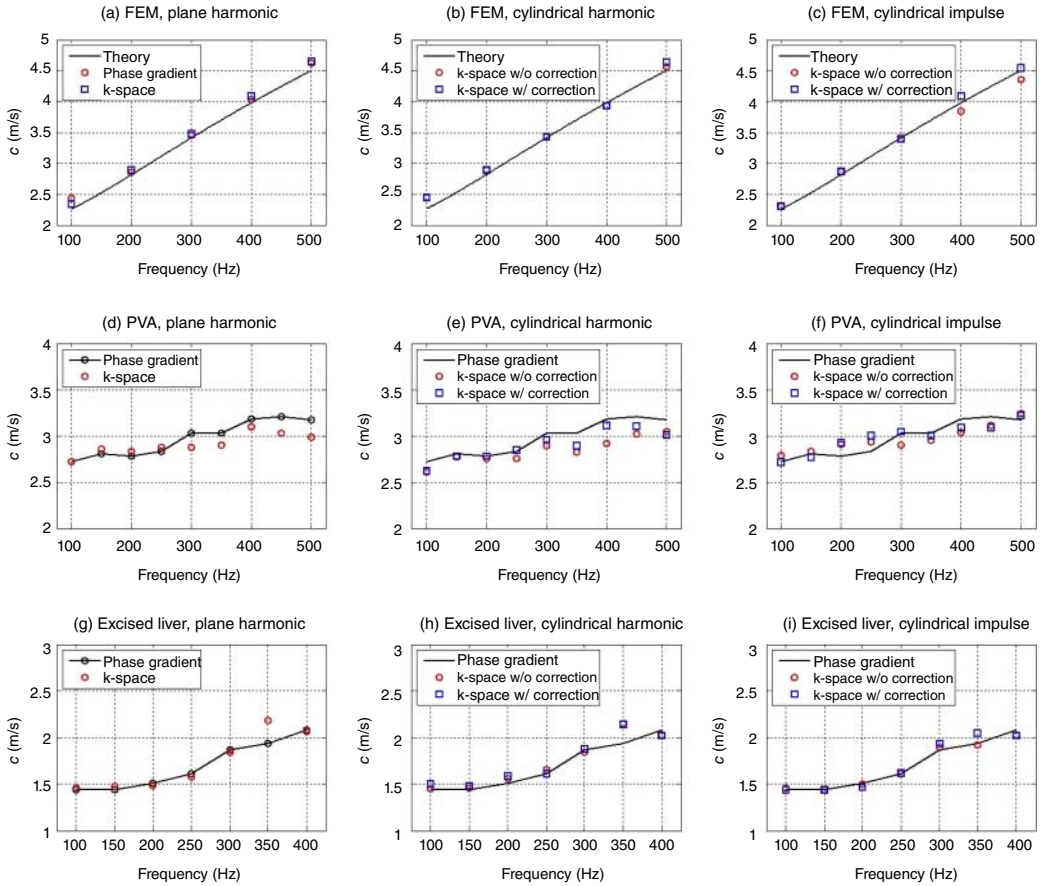

Figure 28.3 FEM simulation, PVA phantoms, and excised pig liver were used to measure the shear wave velocity. In each medium, plane harmonic, cylindrical harmonic, and cylindrical impulse sources were used to excite shear waves. In the FEM, the theoretical prediction curve is plotted as a solid line for comparison. For the PVA and excised liver phantoms, the phase gradient was considered as the gold standard for the velocity estimates plotted for comparison. During FEM studies: (a) the velocity calculations using the phase gradient and the *k*-space method in plane harmonic waves are in good agreement with the theoretical curve; (b) the *k*-space-based velocities with and without the $\sqrt{x}$ correction for cylindrical harmonic waves are close to the theoretical values; (c) similar results are observed in case of cylindrical impulse propagation. For PVA phantom: (d) the phase gradient and the *k*-space methods are in good agreement for the harmonic plane wave propagation; (e) the *k*-space-based velocities with and without the correction in case of cylindrical harmonic waves are similar to the plane wave phase gradient measurements; (f) the *k*-space velocities due to impulse are also in good agreement. (g), (h), (i): The pattern is similar in the excised pig liver. Source: [4].

where $H_0^{(1)}$ is the zeroth-order Hankel function, and $k_0 = \omega_0/c + i\alpha$ is the complex wave number. In the limit of $(k_0 x) \gg 0$, Eq. (28.19) converges to

$$u_z(x,t) = \frac{i}{4}\sqrt{\frac{2}{\pi k_0 x}} e^{i(\omega_0/c)x} e^{-\alpha x} e^{i\omega_0 t} \tag{28.20}$$

By multiplying both sides of the equation by $\sqrt{x}$, and taking into account that $A = \frac{i}{4}\sqrt{\frac{2}{\pi k_0}}$ is a constant, one obtains

$$\left(\sqrt{x}\right) u_z(x,t) = A e^{i(\omega_0/c)x} e^{-\alpha x} e^{i\omega_0 t} \tag{28.21}$$

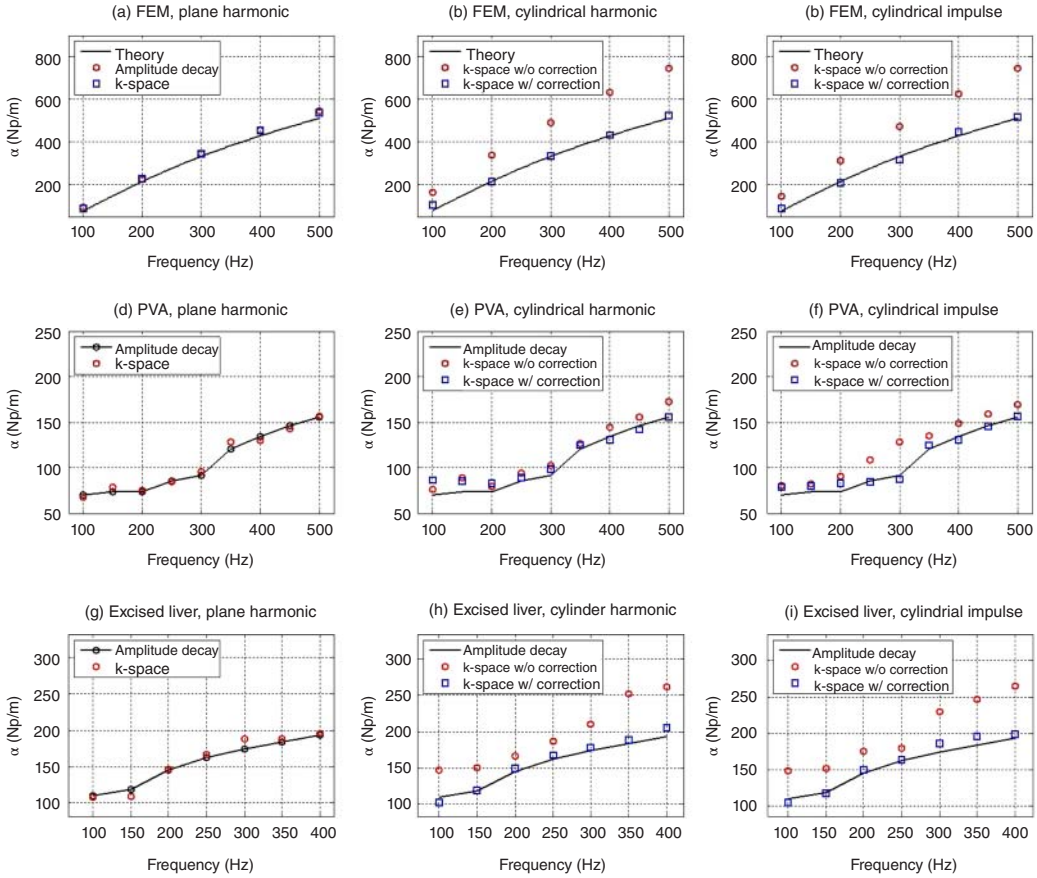

Figure 28.4 FEM simulation, PVA phantoms, and excised pig liver were used to measure the shear wave attenuation. To excite shear waves, plane harmonic, cylindrical harmonic, and cylindrical impulse sources were used. In the FEM, the theoretical prediction curve is plotted as a solid line for comparison. The attenuation estimates using the amplitude decay were considered the gold standard and are plotted for comparison to PVA and excised liver measurements. During FEM studies: (a) the attenuations calculated from the amplitude decay and the *k*-space for plane harmonic waves are in good agreement with the theory; (b) the *k*-space estimates with the $\sqrt{x}$ correction for cylindrical harmonic waves are close to the theoretical values, but the estimates without the correction are not; (c) similar behavior is observed for cylindrical impulse propagation. In PVA: (d) the amplitude decay and the *k*-space method is in good agreement for the harmonic plane wave propagation; (e) the *k*-space attenuations with the correction in case of cylindrical harmonic waves are close to the gold standard proposed, while the estimates without the correction are not as close; (f) this behavior persists in case of the cylindrical impulse. (g), (h), (i): The results are similar in the excised pig liver. Source: © Institute of Physics and Engineering in Medicine, reproduced by permission of IOP Publishing, all rights reserved [4].

If one compares the right hand sides of Eqs. (28.14) and (28.21), it is noticeable that both equations only differ in the amplitude of the wave, and so the relationship between the attenuation equation (α) and FWHM still holds if one is analyzing a cylindrical wave field multiplied by the square root of the propagation distance vector. Throughout the chapter, this multiplication will be simply called the correction. Figures 28.3 and 28.4 demonstrate, in a brief manner, the importance of using this correction when estimating shear wave speed and attenuation for a cylindrical shear wave. The results shown in these figures validate the shear wave velocity and attenuation measurements obtained with AMUSE against laboratory gold standard measurements, using FEM simulation, PVA phantoms, and excised pig liver. The shear wave velocity measurements were in good agreement with the gold standard for all excitation scenarios, while the evaluation of shear wave attenuation due to cylindrical excitation requires the correction factor. In conclusion, the results in Figures 28.3 and 28.4 validate the AMUSE method from a numerical and experimental perspective.

28.4 Conclusion

In this chapter, methods to fully quantify regional viscoelastic properties in a manner independent of models are described. Previous work in this area involved the use of rheological models, but the need for such models affects the viscoelastic parameter estimation as well as the fitting process. The acoustic radiation force-induced creep and creep–recovery use a conversion formula that is the analytic solution of a constitutive equation of linear viscoelastic material to estimate the loss tangent, then shear wave propagation is used in combination with the loss tangent to calculate the model-free complex modulus. The AMUSE method estimates shear wave speed by calculating directly from the k-space the peak at a given frequency and dividing the f-coordinate by the k_x-coordinate. Shear wave attenuation is calculated by measuring the full-width-at-half-maximum (FWHM) in the f-coordinate and using an equation to determine the attenuation. These methods can be used noninvasively for viscoelastic characterization of different tissues for increased understanding of how disease processes change mechanical properties.

References

1 Amador, C., Qiang, B., Urban, M.W., et al. (2013). Acoustic radiation force creep-recovery: Theory and finite element modeling. In: *2013 IEEE International Ultrasonics Symposium (IUS)*.

2 Amador, C., Urban, M.W., Chen, S, and Greenleaf, J.F. (2012). Loss tangent and complex modulus estimated by acoustic radiation force creep and shear wave dispersion. *Phys. Med. Biol.* 57 (5): 1263–1282.

3 Amador, C., Urban, M.W., Chen, S., and Greenleaf, J.F. (2012). Complex shear modulus quantification from acoustic radiation force creep-recovery and shear wave propagation. In: *2012 IEEE International Ultrasonics Symposium (IUS)*.

4 Nenadic, I.Z., Qiang, B., Urban, M.W., et al. (2017). Attenuation measuring ultrasound shearwave elastography and in vivo application in post-transplant liver patients. *Phys. Med. Biol.* 62 (2): 484–500.

5 Blackstock, D.T. (2000). *Fundamentals of Physical Acoustics*. Wiley.

6 Vappou, J., Maleke, C., and Konofagou, E.E. (2009). Quantitative viscoelastic parameters measured by harmonic motion imaging. *Phys. Med. Biol.* 54 (11): 3579–3594.

7 Oliphant, T.E., Manduca, A., Ehman, R.L., and Greenleaf, J.F. (2001) Complex-valued stiffness reconstruction for magnetic resonance elastography by algebraic inversion of the differential equation. *Magn. Reson. Med.* 45 (2): 299–310.
8 Findley, W.N., Lai, J.S., and Onaran, K. (1989). *Creep and Relaxation of Nonlinear Viscoelastic Materials: With an Introduction to Linear Viscoelasticity*. Dover.
9 Evans, R.M.L., Tassieri, M., Auhl, D., and Waigh, T.A. (2009). Direct conversion of rheological compliance measurements into storage and loss moduli. *Phys. Rev. E 80* (1): 012501.

29

Nonlinear Shear Elasticity

Jean-Luc Gennisson[1] *and Sara Aristizabal*[2]

[1] *Imagerie par Résonance Magnétique Médicale et Multi-Modalités, Université Paris-Saclay, Orsay, France*
[2] *Well Living Lab, Rochester, MN, USA*

29.1 Introduction

The characterization of mechanical properties of soft matter is of interest for medical applications. For example, shear elasticity is a pertinent indicator for a diagnosis of tissue degradation. Linear and nonlinear elastic moduli of soft materials can be obtained (i) by dynamic experiments imaging low-frequency shear wave propagation or (ii) by acoustoelastic measurements of speed variations under static strains. The first part goes through solving an inverse problem in the linear case or fitting experimental and theoretical results in the nonlinear one. The second part describes the measurement of linear shear wave in a material under uniaxial stress. Quantifying shear nonlinearity may be important for medical applications. For example, it could be used to tell malignancies apart from benign tumors. In this chapter, nonlinearity is defined from the expression of the strain energy density at higher orders and specifically expressed in the case of soft media [1]. Three different methods to assess third-order shear coefficients are presented (Sections 29.2, 29.3, and 29.4). Finally, an estimation of the fourth-order parameter is presented (Section 29.5).

29.2 Shocked Plane Shear Waves

Although the nonlinear behavior of transverse waves is common to optics (an electromagnetic field in a nonlinear isotropic dielectric), seismology, and acoustics, the experimental observation of a shocked transverse wave is very rarely observed. In comparison, the nonlinear behavior of longitudinal waves in fluids or solids is well established from both a theoretical and an experimental point of view [2], and the sawtooth shape of a shock longitudinal wave is a well-known result. Now, the shape of a shock transverse wave is very unknown, though it has been theoretically predicted [3–5]. The main reason for this lack of experiment is that the nonlinear effects of transverse waves are very small. For example, in acoustics, they are one order of magnitude smaller than the nonlinear effects of longitudinal waves. Moreover, the high stiffness of crystals or metals does not allow any source to impose a high particle velocity compared to the speed of the wave itself, and a typical Mach number in such media is 10^{-4}. In the field of soft solids, such as biological tissues (muscle, fat, and breast) or agar/gelatin-based phantoms (a soft tissue model), the very low value of the shear elasticity (typically 2.5 kPa) allows the propagation of a low-frequency transverse wave (some hundreds of Hz) with a very high particle velocity

Ultrasound Elastography for Biomedical Applications and Medicine, First Edition.
Edited by Ivan Nenadic, Matthew Urban, James Greenleaf, Jean-Luc Gennisson, Miguel Bernal, and Mickael Tanter.

compared to its speed. Thus Mach numbers as large as unity are obtained. Consequently, in this peculiar configuration, third-order nonlinear effects become very high and clearly modify the transverse wave shape [6].

29.2.1 Theoretical Developments

The detailed development of elastic nonlinear theory can be found in numerous textbooks [7]. Here we summarize the general equations in the case of cubic approximation in quasi-incompressible soft media.

In the isotropic case, the energy (W_S) can be expressed as a function of the three scalar invariants of the strain S (the invariants defined by Landau, usually denoted I_1, I_2, and I_3, are the respective traces of S, S^2, and S^3) [4].

$$W_S = \mu I_2 + \frac{\lambda}{2} I_1^2 + \frac{A}{3} I_3 + B I_2 I_3 + \frac{C}{3} I_1^3 + E I_1 I_3 + F I_2 I_1^2 + G I_2^2 + H I_1^4 \tag{29.1}$$

The form of Eq. (29.1) takes into account both compression and shear strains, with a complete set of elastic constants or moduli: two at the second order (linear elastic approximation expressed with the Lamé coefficients μ and λ), three at the third order (A, B, C), and four at the fourth order (E, F, G, H).

It has been pointed out in previous papers, from theoretical [1, 8] and experimental [9] points of view, that soft solids can be considered as quasi-incompressible. The physical interpretation of shear moduli can be attributed to μ and A, because both are zero for a perfect fluid. This physical interpretation can be obtained by comparing the energy development, valid for a perfect fluid and written with strain tensor invariants (and solid-like Landau moduli), to the development Eq. (29.1) of the isotropic solid.

In fluids and solids, incompressibility can be commonly expressed by: $\left(\frac{\rho}{\rho_0}\right)^2 = 1 = \mathrm{Det}(F_{ij})^2$, where $F_{ij} = \partial x_i / \partial a_j$ is the transformation tensor. The dilatation tensor C_{ij} respects a similar constraint: $III_C = \mathrm{Det}(C_{ij}) = 1$, but cannot be used to develop the energy because it is not an infinitesimal quantity. This tensor is commonly used in hyperelasticity theory [10]. Starting from the general form given by Eq. (29.1), the energy has been written in a simplified form as

$$W = W_0(\rho) + \mu(\rho) I_2 \frac{A(\rho)}{3} I_3 + D(\rho) I_2^2 \tag{29.2}$$

To obtain this form, we start with the following relations

$$III_c = 1 + 2I_1 - 2I_2 + 2I_1^2 + \frac{4}{3} I_1^3 - 4 I_1 I_2 + \frac{8}{3} I_3 \tag{29.3}$$

Since only I_2 and I_3 seem to be involved in shear energy, we can first express the invariant I_1 as a combination of the other ones, assuming $III_C = 1$ in the previous relation,

$$I_1 = I_2 - I_1^2 - \frac{2}{3} I_1^3 + 2 I_1 I_2 - \frac{A}{3} I_3 \tag{29.4}$$

which becomes by recursion (substituting I_1 in Eq. 29.4 until terms involving I_1 are insignificant)

$$I_1 = I_2 - \frac{A}{3} I_3 + I_2^2 \tag{29.5}$$

Then, by substituting this expression of I_1 in the development Eq. (29.1), we obtain Eq. (29.2) with

$$D = \frac{\lambda}{2} + B + G \tag{29.6}$$

With this method the reference value $W(\rho_0)$ is zero, and the three elastic moduli are those of the equilibrium state: $\mu(\rho_0)$, $A(\rho_0)$, and $D(\rho_0)$. In the course of calculation, supposing we know the order of magnitude of each term, the fourth-order terms involving moduli C, E, F, H and higher-order term combination of invariants have been neglected.

29.2.2 Numerical Simulation with Modified Burgers Equation

By numerically simulating this theoretical approach and by comparison with experiments it is possible to deduce the nonlinear coefficients. Here the detail of the modified Burgers equation governing the numerical simulation is given. We consider a plane transverse wave of wave number k propagating in the z direction in an isotropic medium (the displacement, denoted u, is polarized along directions x or y; axis are defined on Figure 29.1). In this simpler case, the viscous stress can be added and is assumed to be

$$\tau_{ik} = 2\eta \left[\frac{\mathrm{d}S_{ik}}{\mathrm{d}t} - \frac{1}{3}\partial_{ik}\frac{\mathrm{d}S_{ll}}{\mathrm{d}t} \right] + \xi \partial_{ik}\frac{\mathrm{d}S_{ll}}{\mathrm{d}t} \tag{29.7}$$

where η and ξ are the shear and volumetric viscosity coefficients. This corresponds to a viscoelastic Voigt's model. Equation (29.7) and the energy development equation (Eq. 29.2) simplify assuming a pure shear wave polarized along the z axis. The wave equation can then be rewritten in its nondimensional form ($\tilde{u} = u/u_0$, $\tilde{z} = kz$, and $\tilde{t} = \omega t$)

$$\frac{\partial^2 \tilde{u}}{\partial \tilde{z}^2} - \frac{\partial^2 \tilde{u}}{\partial \tilde{t}^2} = -\beta M^2 \frac{\partial^2 \tilde{u}}{\partial \tilde{z}^2}\left(\frac{\partial \tilde{u}}{\partial \tilde{z}}\right)^2 - \frac{\eta\omega}{\mu}\frac{\partial^3 \tilde{u}}{\partial \tilde{z}^2 \partial \tilde{t}} \tag{29.8}$$

With

$$\beta = 3\left(1 + \frac{\frac{A}{2} + D}{\mu}\right) \tag{29.9}$$

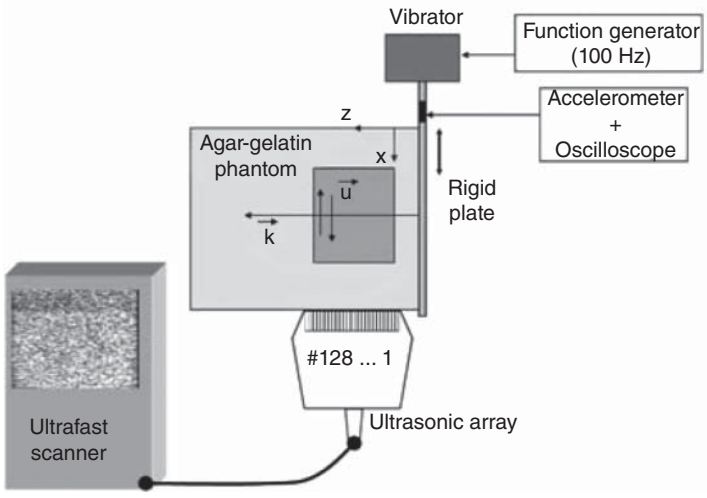

Figure 29.1 Experimental setup. Transient elastography technique: a medical transducer array connected to an ultrafast scanner insonifies a tissue-mimicking phantom. A 100 Hz shear wave strain is generated by a vibrator from a rigid plate applied on one side of the phantom. Simultaneously, frames (at a 3000 Hz repetition rate) are stored in memory. With cross-correlation algorithms between frames, the transverse displacement field (along the z axis) of the shear wave is measured along the central axis of the plate (parallel to the x axis). Source: reprinted with permission from [6], copyright 2003, Acoustical Society of America.

Table 29.1 Parameters corresponding to experimental conditions for longitudinal and transverse waves in gels. Reprinted with permission from [14]. Copyright 2007, Acoustical Society of America.

Polarization	transverse	longitudinal
Elastic moduli (Pa)	$\mu = 5 \times 10^3$	$\lambda = 2.5 \times 10^9$
Velocity (m/s)	2	1500
Viscosity (Pa·s)	$\eta = 0.6$	0.005
Frequency (Hz)	100	4.3×10^6
Attenuation (Np/m)	13.4	0.025
Nonlinear parameter	20	3.5
Wavelength (mm)	20	1.5

This equation is simplified by first introducing the (dimensionless) retarded time $\tilde{\tau} = \omega\tau = \tilde{t} - \tilde{z}$, and then substituting to $\tilde{z}$ the slow coordinate $M^2\tilde{z}$:

$$\frac{\partial^2 \tilde{u}}{\partial \tilde{\tau} \partial \tilde{z}} = \frac{\beta M^2}{2} \frac{\partial^2 \tilde{u}}{\partial \tilde{\tau}^2} \left(\frac{\partial \tilde{u}}{\partial \tilde{\tau}} \right)^2 + \frac{\eta \omega}{2\mu} \frac{\partial^3 \tilde{u}}{\partial \tau^3} \tag{29.10}$$

This cubic nonlinear equation is valid if $\beta M^2 \ll 1$, i.e. by neglecting the fourth-order terms compared with both cubic nonlinearity and viscosity terms on the right-hand side of Eq. (29.10). The characteristic values, in experimental conditions, are presented in Table 29.2. The previous approximation is not always well verified, since βM^2 can reach a value equal to 0.5, but remains conceivable in most cases. Finally, the so-called modified Burgers equation [11] is expressed with the particle velocity $v = \partial u/\partial \tau$ and can be compared to the longitudinal case of quadratic nonlinearity [12]

$$\frac{\partial v}{\partial z} = \frac{\beta}{2V_T^3} v^2 \frac{\partial v}{\partial \tau} + \frac{\eta}{\rho_0 V_T^3} \frac{\partial^2}{\partial \tau^2} \tag{29.11}$$

Neglecting the dissipation term allows one to solve this equation with classical methods (implicit solution for simple boundary conditions [3, 11, 12] or successive approximations for weak nonlinearity). The shock distance is given by

$$z_c = \frac{2V_T^3}{\beta \omega_0 v_0^2} \tag{29.12}$$

and the attenuation coefficient is given by

$$\alpha = \frac{\eta \omega_0^2}{2\rho_0 V_T^3} \tag{29.13}$$

Nevertheless, as in gels, the attenuation length $L_\alpha = 1/\alpha$ is significant, and such a simplification is no longer relevant. A numerical model, transposed from the quadratic (longitudinal) case [13] has thus been developed for this cubic nonlinear equation.

29.2.3 Experimental Study

Here we present an experimental study of a shock transverse wave using an ultrafast ultrasonic scanner. Such a scanner provides images of the tissues similar to a standard ultrasound device but with a rate of more than 5000 frames per second (Figure 29.1). It includes a medical ultrasonic array (5 MHz) with 128 channels [15]. In a typical experiment, 250 ultrasound images

(at a 3000 Hz frame rate) are recorded in memory. A displacement movie is obtained using cross-correlation algorithms between successive speckle images [16]. Indeed, agar powder (3%) in suspension in a solid gelatin solution (3%) gives birth to backscattered ultrasonic signals. Tracking methods such as cross-correlation algorithms allow one to interpret the speckle modifications induced by low-frequency shear waves in terms of tissue motion within the medium. The whole technique is known as transient elastography. As shown in Figure 29.1, the low frequency (100 Hz) shear wave is generated by shaking a rigid aluminum plate (11 cm × 17 cm) transversally, which is applied on one side of the phantom, with a vibrator (Bruel&Kjaer 4809 type). The transverse displacement field of the shear wave is measured in one dimension along the axis of the rigid plate at a distance of 40 mm, which represents a few shear wavelengths. An accelerometer is set on the vibrator to control the possible harmonics of the source itself.

From the particle velocity movie $v_x(z,t)$, averaged over x, we measure the speed of the shear wave ($V_T = 2.1$ m/s) and the attenuation coefficient ($\alpha = 8.6$ Np/m) using, respectively, the phase and amplitude evolutions versus propagation distance. The viscosity coefficient is deduced from attenuation assuming a viscoelastic Voigt's model. Since nonlinear effects affect the amplitude of the fundamental component (100 Hz), the measurement of attenuation has to be done at a low excitation level.

At a higher excitation level ($v_0 = 0.5$ m/ s and $M = 0.24$), the sensor placed between the vibrator and the plate allows one to check that no harmonic is present at the source, as shown in Figure 29.2 by the wave form and its spectrum. The wave form distortion, presented in Figure 29.2, differs significantly from a nonlinearity distorted longitudinal wave. Here, only odd harmonics at 300 and 500 Hz are present in the spectrum in Figure 29.2, which is a characteristic of cubic nonlinear effects affecting transverse waves. It may be pointed out that coupling effects [4, 17, 18] are too small to give rise to a longitudinal component centered at the double frequency. The measured field $v_x(z,t)$, obtained by placing the transducer array in front of the plate, does not contain any 200 Hz component. This effect should be greater in "hard solids" because of the favorable ratio of velocities, but remains relative to the incident shear wave amplitude.

The nonlinear coefficient β, relative to shear waves, has been estimated by fitting experimental and numerical results. The waveform and spectrum of the particle velocity, represented in Figure 29.2, are fitted near the source. Then the parameter is corrected to fit the evolutions of the fundamental 100 Hz and harmonic 300 and 500 Hz amplitudes as a function of propagation distance (Figure 29.3). Using the value of $\beta = 17$, the parameters entered in the model are listed in Table 29.2 are obtained with an uncertainty of the order of ±10%.

29.3 Nonlinear Interaction of Plane Shear Waves

Similar comparisons, between experiment and simulation, can be performed using the more general case of two-wave interactions at frequencies f_1 and f_2, which are reduced to the harmonic generation when $f_1 = f_2$. Such an interaction, involving cubic nonlinearity, will give rise to numerous odd-frequency components.

The vibrator was excited by a superposition of two sinusoidal components. Different frequency ratios have been tested. The more significant results have been obtained for two frequencies close to each other because of the strong attenuation of agar/gelatin phantoms. Choosing frequencies of the excitation signal in the lower part of the bandwidth allows one to observe harmonic components at sum and difference frequencies. In fact, higher frequencies are too quickly distorted and attenuated and the use of lower frequencies is limited by the burst duration.

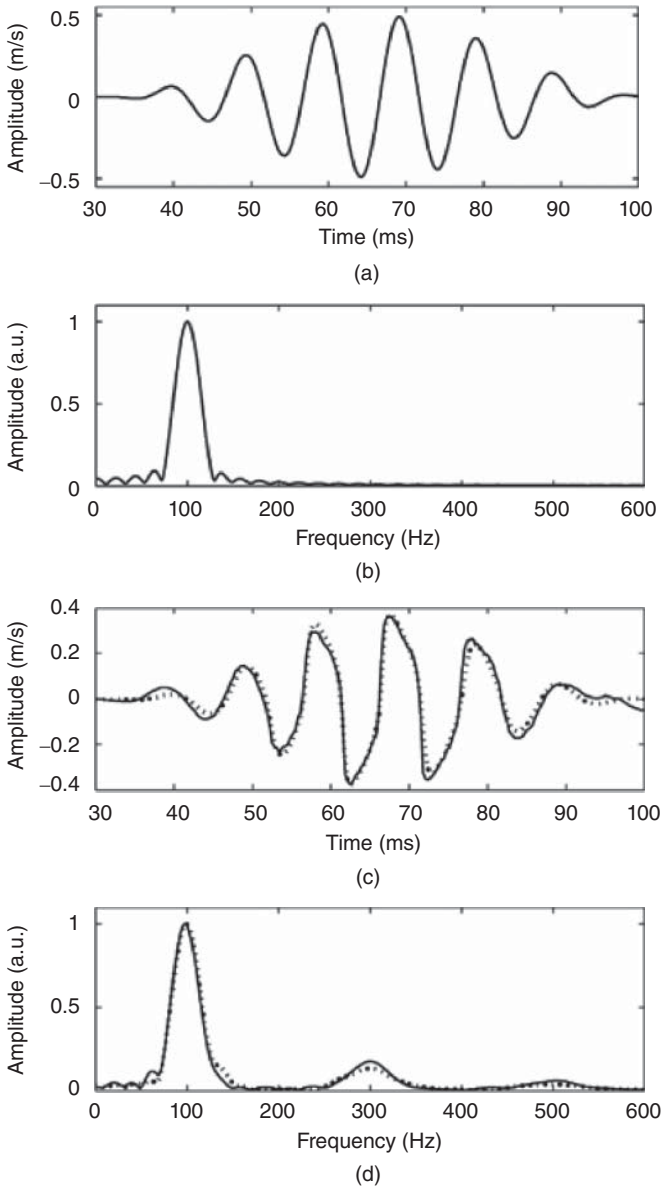

Figure 29.2 Comparison between experiment and simulation in the case of harmonic generation. The temporal profile of the shear wave propagation (a, c) and the corresponding Fourier transform (b, d) in linear and nonlinear cases, respectively, are shown. The input parameters of the simulation are listed in Table 29.2. Source: reprinted with permission from [14], copyright 2007, Acoustical Society of America.

The signal applied to the vibrator is composed of a superposition of sinusoidal components at frequencies f_1 =100 Hz and f_2 = 140 Hz. The signal measured by the force sensor and its spectrum are represented in Figures 29.4a and 29.4c. This wave form, as for the shocked plane shear wave, is used as an input in the simulation while its amplitude is estimated from the particle velocity measured in front of the first element of the array.

In the spectrum, the fundamental frequencies at 100 and 140 Hz are clearly observed. The comparison between experiment and simulation is shown in Figures 29.4b and 29.4d.

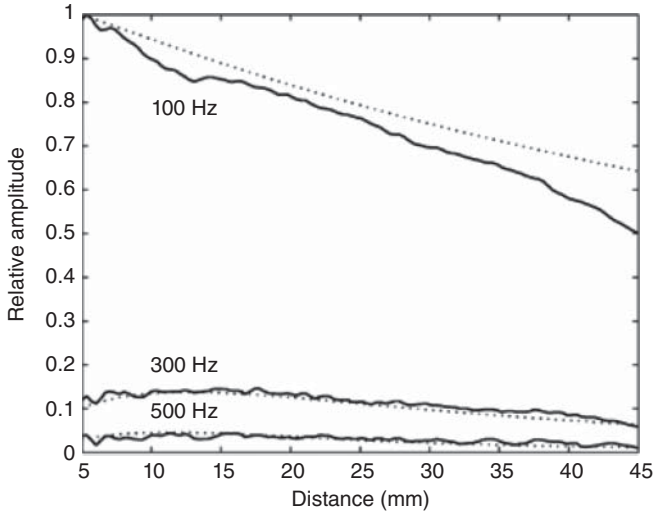

Figure 29.3 Evolution of fundamental component and third and fifth harmonics versus propagation distance, showing experiment (dotted lines) and simulation (solid lines). Source: reprinted with permission from [14], copyright 2007, Acoustical Society of America.

Table 29.2 Input parameters of the numerical model of the modified Burgers equation corresponding to both the harmonic generation experiment presented and to the nonlinear interaction case. Reprinted with permission from [14]. Copyright 2007, Acoustical Society of America.

Experiment	harmonic generation	two-wave interaction
Shear modulus (Pa)	4400	6300
Speed (m/s)	2.1	2.4
Particle velocity (m/s)	0.5	0.62
Mach number	0.24	0.26
Viscosity (Pa·s)	0.45	0.7
Frequency (Hz)	100	100, 140
Attenuation (Np/m)	8.6	9.1, 17.8
Nonlinear parameter	17	20
Wavelength (mm)	21	24, 17
Shock distance (mm)	7	5.7, 4.1

A closer look at the spectra as a function of depth represented on a gray scale image in Figure 29.5 is necessary to compare the results and to highlight the created harmonics. The sum ($2f_1 + f_2$, $2f_2 + f_1$) and odd frequencies ($3f_1$, $3f_2$) are clearly observed in experiments and in simulations. Unfortunately, difference frequencies ($2f_1 - f_2$, $2f_2 - f_1$), although present in the spectrum, have the same level as side lobes of the emitted signal. These side lobes are due to the finite duration of the emitted signal. The emitted signal is imposed by the size of the sample: For a longer emission signal, the echo coming from the side opposite to the plate interferes with the direct traveling wave.

Another way of testing the model is to change the amplitude of one of the two primary components. At a given depth $z = 10$ mm, relative amplitudes of the most significant harmonics are plotted in Figure 29.5 versus increasing amplitudes of the component centered at f_2.

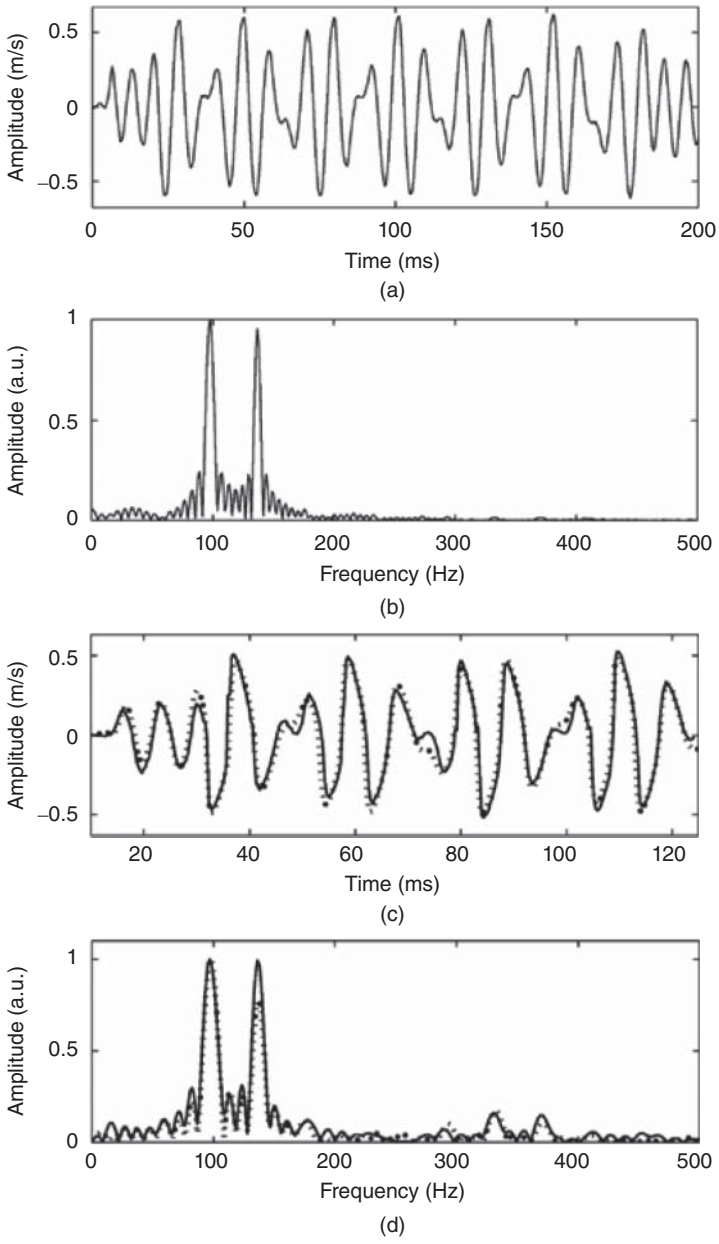

Figure 29.4 Comparison between experiment and simulations. The signal shown in the first line, obtained from the force sensor, is used as source signal for the calculation. The input parameters for the simulation are listed in Table 29.2. Source: reprinted with permission from [14], copyright 2007, Acoustical Society of America.

The component at $(2f_2 + f_1)$ involving two times this frequency varies faster than the other one $(2f_1 + f_2)$. This follows qualitatively the results of a perturbation method. This method, also called successive approximation and equivalent to series development, could be applied to the lossless wave equation. This consists in considering the nonlinear contribution as a correction of the linear solution [12], which gives the $(2f_2 + f_1)$ and $(2f_1 + f_2)$ component amplitudes,

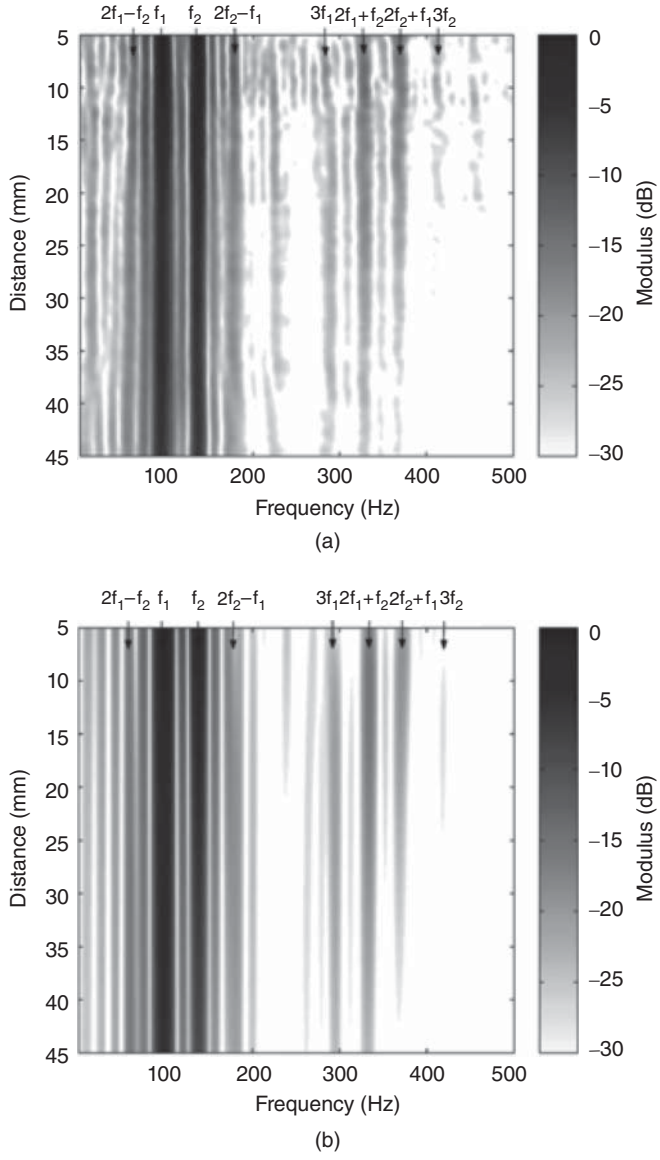

Figure 29.5 Fourier spectra of the υx component vs. propagation distance z: (a) experiment and (b) simulation. Source: reprinted with permission from [14], copyright 2007, Acoustical Society of America.

respectively, proportional to $k_1 k_2 U_1 {U_2}^2$ and $k_1 k_2 {U_1}^2 U_2$. U_1 and U_2 are the amplitudes and k_1 and k_2 are the wave numbers of the components f_1 and f_2 at the source. The quadratic dependence on U_2 is not checked in the experiment, which confirms that in gels the attenuation cannot be neglected and the level of nonlinearity is too high to use such solutions.

The numerical model, which takes into account attenuation, is in good agreement with these experiments. The input parameters for the model are recalled in Table 29.3. The adjustment of the experimental and theoretical data has been done using the wave form and spectrum and the evolution of the most significant harmonics versus distance. The use of wave interaction allows one to take full advantage of the large bandwidth of ultrafast imaging. An accurate measurement

Table 29.3 Elastic moduli measured in two different soft solids. Reprinted with permission from [19]. Copyright 2007, Acoustical Society of America.

Materials	Linear shear modulus (Lamé coefficient μ (kPa) mean value at 0 stress)	Nonlinear shear modulus [Landau coefficient A (kPa)]			
		Indice of propagation 12	Indice of propagation 21	Shear wave indices 13	Mean value
Agar/gelatin phantom 1	6.6 ± 0.6	−35.0	−48.6	−29.4	−37.7 ± 9.8
Agar/gelatin phantom 2	8.5 ± 0.8	−21.5	−25.6	−21.0	−22.7 ± 2.5
Agar/gelatin phantom 5	9.9 ± 0.5	−7.1	−5.9	−4.8	−5.9 ± 1.2
Agar/gelatin phantom 3	16.6 ± 0.1	109.8	91.8	102.8	101.4 ± 9.0
Agar/gelatin phantom 4	19.2 ± 0.1	466.4	404.1	312.8	394.4 ± 77.2
PVA phantom 1	4.1 ± 0.1	−25.8	−15.4	−11.2	−17.5 ± 7.5
PVA phantom 2	8.1 ± 0.1	10.7	9.7	12.6	11.0 ± 1.4
PVA phantom 3	20.4 ± 0.1	31.8	56.3	42.8	43.6 ± 12.2

of the source amplitude would lead to a better agreement with all spectral components and an accurate estimation of the nonlinearity coefficient.

The possibility of having nonlinear behavior that depends on the attenuation amplitude is omitted in the theoretical approach. The quadratic dependence of the attenuation coefficient versus frequency comes from the hypothesis of a viscous stress tensor being proportional to the deformation rate. Such comparison between experiments and simulations could be used to test nonlinear viscoelastic models and improve the measurement accuracy.

29.4 Acoustoelasticity Theory

Another way to measure the shear nonlinearity of a medium is to perform acoustoelasticity (AE) experiments, i.e. assessing the shear wave speed in a uniaxially stressed media. Acoustoelasticity can be defined as the phenomenon of change of wave speed when uniaxial stress is applied. Experimentally, it consists of determining the third-order nonlinear coefficient, in other words the nonlinear parameter A, by measuring the speed of an acoustic wave along different directions in a medium submitted to uniaxial stress. Recently, AE has attracted a special interest in the field of ultrasound for two reasons. First, AE has the potential of becoming a new mechanical parameter in addition to the second-order elastic modulus (μ) and anisotropy, that will help to improve the characterization of the properties of the tissues in the field of shear wave elastography [19]. Second, Urban et al. [20] have recently shown that AE can be also used as an alternative method to create phantoms with a TI behavior.

The theory behind AE is based on the speed of elastic waves in a uniaxially stressed loss-less solid [19]. The equation of motion in Lagrangian coordinates (a, t) can be expressed as

$$\rho_0 \ddot{\mu}_i = \frac{\partial P_{ik}}{\partial a_k} \text{ for } 1 \leq i,\ k \leq 3 \tag{29.14}$$

where ρ_0, ρ_{ik}, and $\ddot{\vec{\mu}} = \frac{\partial^2 \vec{\mu}}{\partial t^2}$ represent the density, the Piola-Kirchhoff stress tensor, and the particle acceleration, respectively. The Piola-Kirchhoff stress tensor is given by

$$P_{ik} = \frac{\partial e}{\partial \left(\frac{\partial \mu_i}{\partial a_k} \right)} \tag{29.15}$$

e, the strain energy density, can be expressed as a third-order relationship

$$e = \mu I_2 + \frac{\lambda}{2} I_1^2 + \frac{A}{3} I_3 + B I_1 I_2 + C I_1^3 \tag{29.16}$$

where λ and μ represent the Lamé first- and second-order parameters that describe the linear behavior of a solid. A, B, and C represent the third-order elastic coefficients of Landau, which describe the nonlinear response of the deformed solid. I_1, I_2, and I_3 are invariants of the Lagrangian stress tensor. In the case of an incompressible media, the strain energy density (e) can be expressed in terms of a set of independent parameters (III_c, I_2, I_3), with $III_c = 1$ due to the assumption of incompressibility.

$$e = \mu I_2 + \frac{A}{3} I_3 + D I_2^2 \tag{29.17}$$

The parameter D is the fourth-order elastic constant but as only the propagation of plane waves of small amplitude is considered, fourth-order terms are ignored for the rest of the theoretical derivation. The strain tensor can now be defined as

$$S_{ik} = \frac{1}{2}\left(\frac{\partial \mu_i}{\partial a_k} + \frac{\partial \mu_k}{\partial a_i} + \frac{\partial \mu_l}{\partial a_i}\frac{\partial \mu_l}{\partial a_k}\right) \tag{29.18}$$

and, based on Eq. (29.15), the equation of motion becomes

$$\begin{aligned}\rho_0 \frac{\partial^2 \mu_i}{\partial t^2} = \frac{\partial P_{ik}}{\partial a_k} &= \mu\left(\frac{\partial^2 \mu_i}{\partial a_k^2} + \frac{\partial^2 \mu_k}{\partial a_i \partial a_k}\right) + \left(\mu + \frac{A}{4}\right) \\ &\times\left(\frac{\partial^2 \mu_l}{\partial a_i \partial a_k}\frac{\partial \mu_l}{\partial a_k} + \frac{\partial \mu_l}{\partial a_i}\frac{\partial^2 \mu_l}{\partial a_k^2} + \frac{\partial^2 \mu_k}{\partial a_l \partial a_k}\frac{\partial \mu_i}{\partial a_l} + \frac{\partial^2 \mu_l}{\partial a_k^2}\frac{\partial \mu_i}{\partial a_l} + 2\frac{\partial \mu_k}{\partial a_l}\frac{\partial^2 \mu_l}{\partial a_k \partial a_i}\right) \\ &+ \frac{A}{4}\left(\frac{\partial^2 \mu_k}{\partial a_k \partial a_l}\frac{\partial \mu_l}{\partial a_i} + \frac{\partial \mu_k}{\partial a_l}\frac{\partial^2 \mu_l}{\partial a_k \partial a_i}\right)\end{aligned} \tag{29.19}$$

As the AE experiment consists on measuring the speed of an acoustic wave along different directions in a medium submitted to uniaxial stress, two main displacements are considered in the theory, a static displacement and a dynamic displacement. The static displacement is a result of the uniaxial stress applied and the dynamic displacement corresponds to the propagation of shear waves induced by ARF. The displacement can then be expressed as the sum of the static displacement ($\overrightarrow{\mu^{\mathrm{S}}}$) and the dynamic displacement ($\overrightarrow{\mu^{\mathrm{D}}}$)

$$\overrightarrow{\mu^{\mathrm{TOT}}} = \overrightarrow{\mu^{\mathrm{D}}} + \overrightarrow{\mu^{\mathrm{S}}} \tag{29.20}$$

If the nonlinear dynamic and static deformations of higher order are ignored, the wave equation becomes

$$\begin{aligned}\rho_0 \frac{\partial^2 {\mu_i}^{\mathrm{D}}}{\partial t^2} &= \mu\left(\frac{\partial^2 {\mu_i}^{\mathrm{D}}}{\partial a_k^2} + \frac{\partial^2 {\mu_k}^{\mathrm{D}}}{\partial a_i \partial a_k}\right) + \left(\mu + \frac{A}{4}\right) \\ &\times\left(\frac{\partial^2 {\mu_l}^{\mathrm{D}}}{\partial a_i \partial a_k}\frac{\partial {\mu_l}^{\mathrm{S}}}{\partial a_k} + \frac{\partial {\mu_l}^{\mathrm{S}}}{\partial a_i}\frac{\partial^2 {\mu_l}^{\mathrm{D}}}{\partial a_k^2} + \frac{\partial^2 {\mu_k}^{\mathrm{D}}}{\partial a_l \partial a_k}\frac{\partial {\mu_i}^{\mathrm{S}}}{\partial a_l} + \frac{\partial^2 {\mu_l}^{\mathrm{D}}}{\partial a_k^2}\frac{\partial {\mu_i}^{\mathrm{S}}}{\partial a_l} + 2\frac{\partial {\mu_k}^{\mathrm{S}}}{\partial a_l}\frac{\partial^2 {\mu_i}^{\mathrm{D}}}{\partial a_k \partial a_l}\right) \\ &+ \frac{A}{4}\left(\frac{\partial^2 {\mu_k}^{\mathrm{D}}}{\partial a_k \partial a_l}\frac{\partial {\mu_l}^{\mathrm{S}}}{\partial a_i} + \frac{\partial {\mu_k}^{\mathrm{S}}}{\partial a_l}\frac{\partial^2 {\mu_l}^{\mathrm{D}}}{\partial a_k \partial a_i}\right)\end{aligned} \tag{29.21}$$

To simplify the calculations, it is possible to consider linearly polarized plane shear waves, as shown in Figure 29.6.

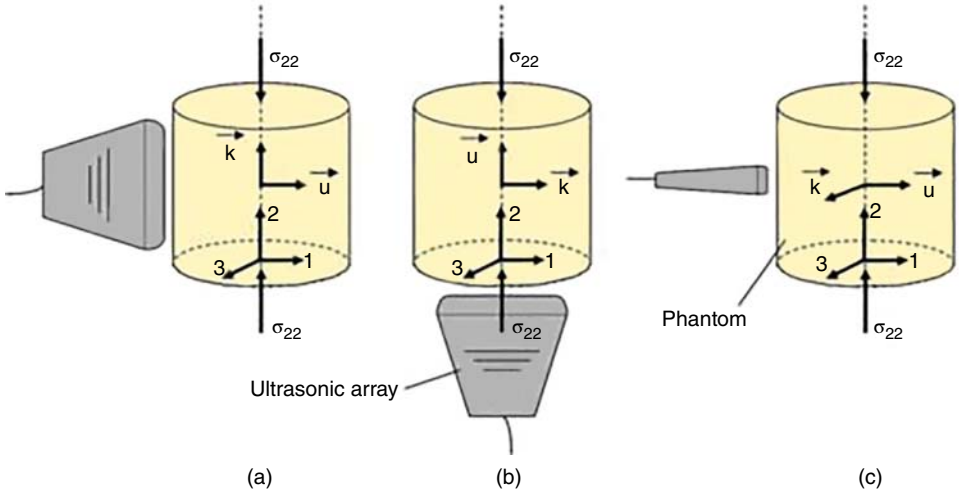

Figure 29.6 Three different experimental configurations for generating and detecting the shear wave propagation during compression (application of uniaxial stress σ_{22}). Source: reprinted with permission from [19], copyright 2007, Acoustical Society of America.

The particle displacement in the wave is characterized by two indices in the following convention (12): the first index indicates the direction of the shear wave displacement induced by ARF and the second corresponds to the axis of propagation of the shear wave. In the case where the wave propagates along the a_2 the wave equation can be expressed as

$$\rho_0 \frac{\partial^2 {\mu_1}^D}{\partial t^2} = \mu \frac{\partial^2 {\mu_1}^D}{\partial a_2^2} + \left(2\mu + \frac{A}{2}\right)\left(\frac{\partial^2 {\mu_1}^D}{\partial a_2^2}\right)\left(\frac{\partial {\mu_1}^S}{\partial a_1} + \frac{\partial {\mu_2}^S}{\partial a_2}\right) \tag{29.22}$$

Now, to define the nonlinear elastodynamic equations it is important to first express the wave equation in terms of the initial coordinates. For simplicity, the initial strain and stress are defined as uniform and they are described by the static displacement as $x = a + \mu^s$. The dynamic displacement is defined by $y = x + \mu^D$, where a, x, and y denote the natural, initial, and current state of the shear wave propagation respectively. Using the change of variable $a \to x$,

$$\frac{\partial^2 {\mu_i}^D}{\partial a_k^2} \cong \frac{\partial^2 {\mu_i}^D}{\partial x_k^2}\left(1 + 2\frac{\partial {\mu_k}^S}{\partial x_k}\right), \quad \frac{\partial^2 {\mu_k}^D}{\partial a_i \partial a_k} \cong \frac{\partial^2 {\mu_k}^D}{\partial x_i \partial x_k} \tag{29.23}$$

and the wave equation becomes

$$\rho_0 \frac{\partial^2 {\mu_1}^D}{\partial t^2} = \frac{\partial^2 {\mu_1}^D}{\partial x_2^2}\left[\mu + 2\mu\left(\frac{\partial {\mu_1}^S}{\partial x_1} + 2\frac{\partial {\mu_2}^S}{\partial x_2}\right) + \frac{A}{2}\left(\frac{\partial {\mu_1}^S}{\partial x_1} + \frac{\partial {\mu_2}^S}{\partial x_2}\right)\right] \tag{29.24}$$

Assuming incompressibility and by using Hooke's law, the spatial derivatives of μ^s are

$$\frac{\partial {\mu_2}^S}{\partial x_2} = \frac{-\sigma_{22}}{E} \approx \frac{-\sigma_{22}}{3\mu}, \quad \frac{\partial {\mu_1}^S}{\partial x_1} = \frac{\partial {\mu_3}^S}{\partial x_3} = \frac{\nu\sigma_{22}}{E} \approx \frac{\sigma_{22}}{6\mu} \tag{29.25}$$

and based on these derivatives the elastodynamic equations are written as follows:

- For the first configuration (Figure 29.6a) where the shear waves are designated as 12 or 32

$$\rho_0 V_{S12}^2 = \mu - \sigma_{22}\left(1 + \frac{A}{12\mu}\right) \tag{29.26}$$

where V_s denotes the shear wave velocity.

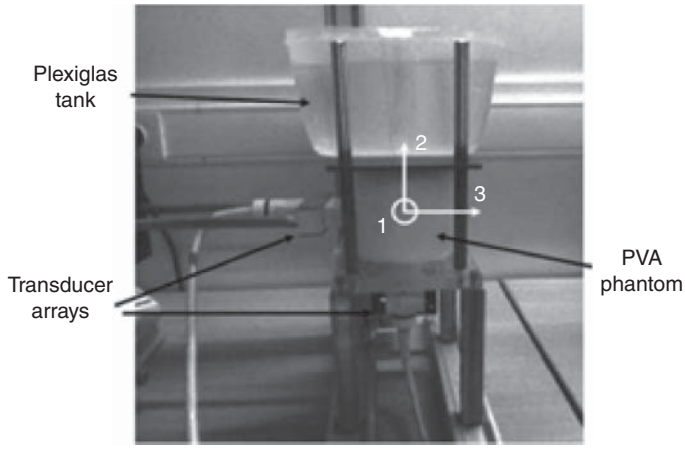

Figure 29.7 Experimental setup. A Plexiglas tank gradually filled up with water is placed on the top of the PVA phantom. Two transducer arrays are placed along the vertical axis in contact with the side and bottom of the homogeneous phantom. Source: reprinted with permission from [19], copyright 2007, Acoustical Society of America.

- For the second configuration (Figure 29.6b) where the shear waves are designated as 21 or 23

$$\rho_0 V_{S21}^2 = \mu - \sigma_{22}\left(\frac{A}{12\mu}\right) \tag{29.27}$$

- For the third configuration (Figure 29.6c) where the shear waves are designated as 13 or 31

$$\rho_0 V_{S13}^2 = \mu + \sigma_{22}\left(1 + \frac{A}{6\mu}\right) \tag{29.28}$$

For the elastodynamic equations (Eqs. 29.26–29.28), in the case where the medium is unstressed $\sigma_{22} = 0$. On the contrary, when the stress is varying μ will change according to a linear dependence with a linear slope defined by μ and the nonlinear parameter (A).

Therefore, by estimating experimentally V_s, and the stress applied to the soft solid σ_{22}, it is possible to obtain the linear (μ) and nonlinear (A) elastic moduli in AE.

To evaluate the AE method, Gennisson et al. [19] estimated the third-order elastic modulus (A) in phantoms made out agar/gelatin and polyvinyl alcohol. For the experimental setup, a Plexiglas tank was placed on the top of the phantoms, the tank was filled with different amounts of water to simulate the uniaxial stress. Two transducers were placed along the vertical axis of the phantom and on the bottom of the phantoms to measure the shear wave propagation, as shown in Figure 29.7.

Shear wave propagation was investigated in each of the three configurations described above, the ultrasonic beam was therefore two times parallel and one time perpendicular to the uniaxial applied stress. Shear waves were generated using ARF and the shear wave propagation was imaged with an ultrafast echography scanner and an ultrafast imaging sequence by sending plane wave insonifications at a really high frame rate (2 kHz). The shear wave speed was estimated from displacement fields induced by the shear wave at successive times after the push. The values for the linear (μ) and nonlinear (A) elastic moduli calculated at each configuration are shown in Table 29.3. As can be seen in Table 29.1, the set-up used for the experiment allows us to obtain (A) in three different manners. The agreement on the estimation of the nonlinear parameter across all the three configurations was very good for the agar/gelatin phantoms and fairly good for the PVA phantoms, which can be explained by difficulties in the setup when

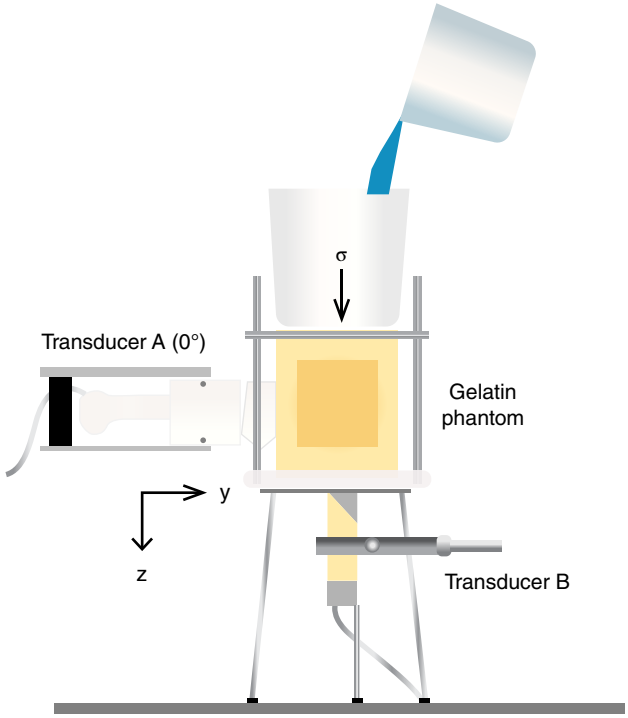

Figure 29.8 Experimental setup; a plastic tank gradually filled up with water is placed on the top of the cylindrical phantom. Transducer A is placed on the side of the phantom and it is rotated from 0° to 180° in 10° steps. Transducer B is placed in contact with the bottom of the phantom. Source: © 2015 IEEE, reprinted, with permission, from [20].

testing a very soft phantom. These experiments have shown that it is possible to use AE to characterize the nonlinear shear behavior of soft solids.

Gennisson et al. [19] and Urban et al. [20] have also shown that the application of an uniaxial stress creates a situation where a homogeneous material presents an anisotropic behavior due to the nonlinear effects producing a change in shear wave speed. Urban et al. [20] have shown that this behavior can be characterized using a TI model and therefore it could be used to create elasticity phantoms that can mimic the behavior of anisotropic materials. To evaluate this hypothesis, Urban et al. [20] evaluated the properties of six cylindrical shape phantoms made with different concentrations of gelatin (7%, 8.25%, 8.5%, and 10% by volume). The phantoms were placed on a Plexiglas platform and two transducers were put in contact with the phantom. Transducer A was attached to a stepper motor, which was rotated from 0° to 180° in 10° steps. To induce a uniaxial stress, a Plexiglas plate was placed on the top of the phantom as well as a large container, which was filled up with water in increments of either 400 or 600 ml. The experimental setup is shown in Figure 29.8.

For the AE measurements, the stress was calculated from the added volumes of water and the surface area of the phantom. The strain was calculated by measuring the distance between the plates at each water increment and calculating the change in distance with respect to the original distance when no stress other than that produced by the weight of the Plexiglas plate was applied. The shear wave speed was calculated using a Radon transform method [20] and the speeds estimated at each rotation angle were used to fit a TI model to the data. Figure 29.9 shows the mean and standard deviation from shear wave velocity with different applied values of stress

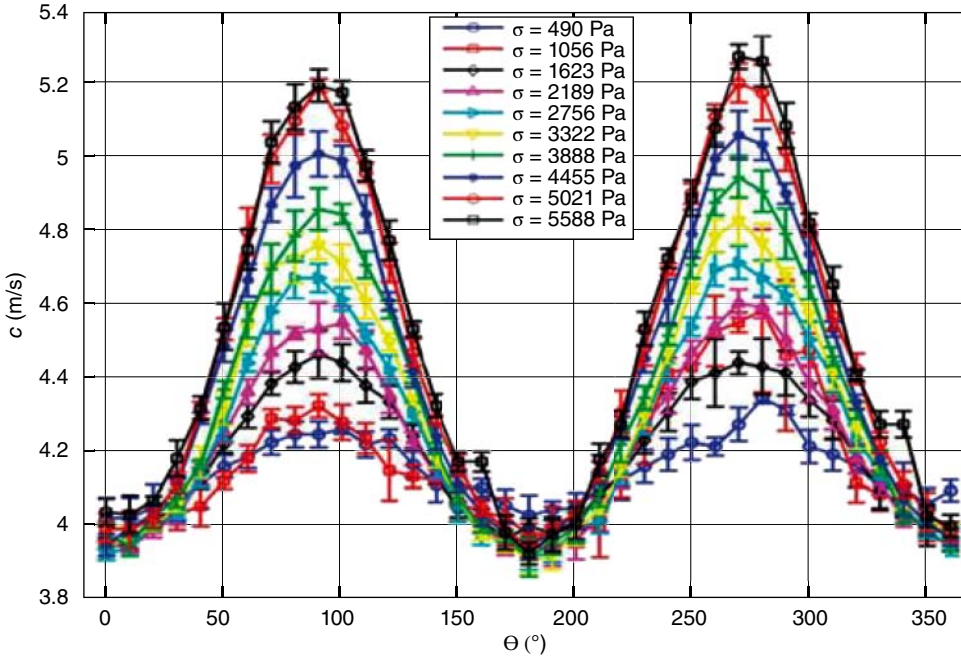

Figure 29.9 Shear wave velocity as a function of the angle of rotation of transducer A at different applied values of uniaxial stress for the 10% gelatin phantom. Source: © 2015 IEEE, reprinted, with permission, from [20].

for the 10% gelatin phantom. It is possible to appreciate that the compression of homogeneous phantoms generates a TI behavior that can be assessed using shear wave based methods.

Recently the feasibility of the technique was demonstrated in vivo which opens a new way to characterize lesions in breast cancer. Figure 29.10 presents in vivo results on healthy breast (Subject 1: $\mu = 1.0 \pm 0.5$ kPa, $\mu_{\mathrm{NL}} = 52 \pm 10$ kPa), benign lesion (Patient 1: $\mu = 7.8 \pm 2.4$ kPa, $\mu_{\mathrm{NL}} = -698 \pm 1014$ kPa), and malignant lesion (Patient 6: $\mu = 3.5 \pm 1.4$ kPa, $\mu_{\mathrm{NL}} = -1203 \pm 2675$ kPa) [21]. However, clinical studies on a large scale would be needed to show the usefulness of this new technique for in vivo diagnosis.

29.5 Assessment of 4th Order Nonlinear Shear Parameter

In this last part of the chapter we present ways to recover fourth-order nonlinear shear coefficients by combining high amplitude shear wave propagation and acoustoelasticity experiments.

The experimental setup is presented in Figure 29.1. In order to generate plane shear waves with an amplitude large enough to observe cubic nonlinear effects, a tone burst of central frequency $f_0 = \omega_0/2\pi = 100$ Hz is emitted by a vibrator connected to a rigid large plate applied on one side of the phantom (an agar/gelatin phantom). The chosen frequency represents a compromise between a maximal nonlinear cumulative effect and a prohibitive absorption. In order to check that nonlinear components are not emitted by the source, an accelerometer is connected to the vibrator.

The transverse particle velocity field along the x axis of the shear wave is measured along the central axis of the plate parallel to the z axis. Then, using a numerical band-pass filter, the third harmonic component is extracted from the total particle velocity. Finally, the evolution of the amplitude of this component with respect to the propagation distance z is measured for various amplitudes v_0 of the vibration transmitted by the source.

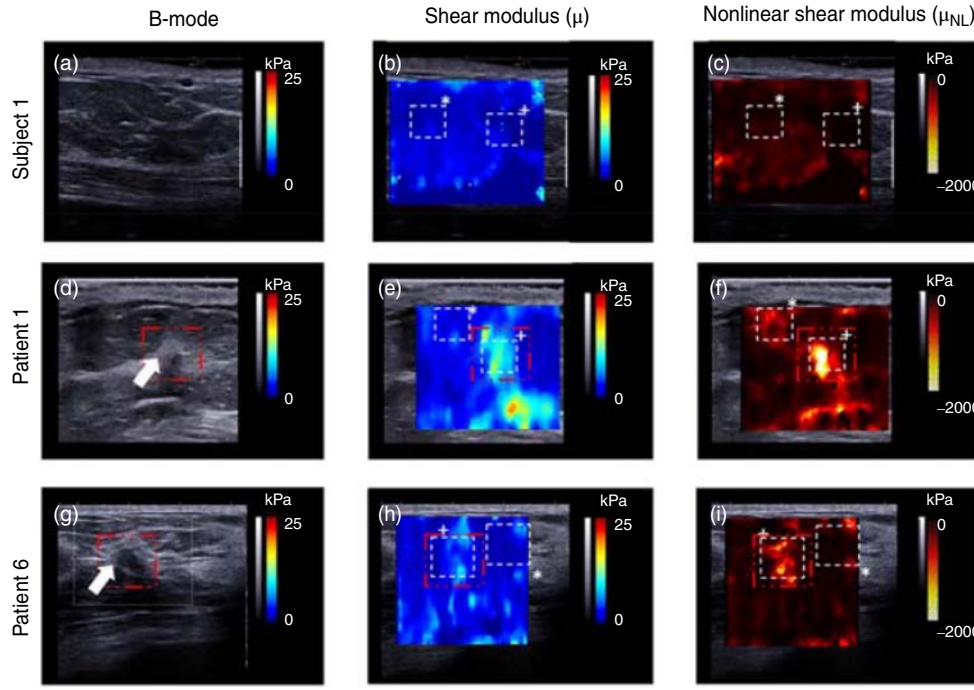

Figure 29.10 Results of the nonlinear shear modulus (NLSM) on three patients, a healthy volunteer, a patient presenting with a tumor, and a patient with a benign lesion. The left column shows the ultrasound images, where the mass is enclosed in dashed squares. The center and the right columns show the corresponding images for the shear and the NLSM, respectively. The dotted squares are the ROIs used in the mean and standard deviation values. Source: © 2016 IEEE, reprinted, with permission, from [21].

In order to measure the nonlinearity parameter β, two methods have been used. In the first method, experimental results of the third harmonic amplitude as a function of the propagation distance are compared to a numerical simulation of the shear wave propagation based on a finite difference scheme of Eq. (29.11). The second method results from the comparison with an analytical formulation of the third harmonic amplitude given by Zabolotskaya et al. [11]. This formulation is obtained under the well-known assumption of weak nonlinearity, which assumes that the Goldberg number, defined as the ratio of the shear shock formation distance (Eq. 29.12, characteristic length of nonlinear effects) and the absorption characteristic length $L_\alpha = 1/\alpha_0$ is small. In that case, Eq. (29.11) is solved analytically using a perturbation method. Assuming that α_0 varies as the square of the frequency, the third harmonic component expresses as

$$v^{II}(z,t) = -\frac{\beta\omega_0 v_0^3}{24\alpha_0 V_T^3}(e^{-3\alpha_0 z} - e^{-9\alpha_0 z})\sin(3\omega_0\tau) \tag{29.29}$$

In order to deduce the nonlinearity parameter from the third harmonic evolution, it is necessary to know accurately three parameters: the attenuation coefficient α_0, the shear wave speed V_T, and the amplitude of the source v_0. Indeed, these three parameters are involved in Eq. (29.29) and are also used as input parameters in the numerical simulation. First, we have checked the assumption of a quadratic dependence of the shear attenuation coefficient with frequency.

Measurements of α_0 were performed for different values of the tone burst central frequency from 50 to 600 Hz, emitted in a linear regime small amplitude of the source, in an agar/gelatin phantom with 5% of gelatin. The measured attenuation coefficients were obtained by measuring

Table 29.4 Results for the linear shear modulus μ, the Landau nonlinear modulus A [19], the attenuation coefficient α_0, the shear nonlinearity parameter β, and the fourth-order elastic constant D in the two agar/gelatin phantoms [22].

% of gelatin	μ (kPa)	A (kPa)	α_0 (Np/m)	β	D (kPa)
5	6.6 ± 0.6	-37.7 ± 9.8	17	4.0 ± 0.5	30 ± 10
7	8.5 ± 0.8	-22.7 ± 2.5	12	2.5 ± 1	17 ± 9

the amplitude of the central frequency for each frequency. The shear wave speed, deduced from the phase delay between the signals measured at different distances, is found to be 2.56 m/s. It corresponds to the shear modulus given in Table 29.4. The amplitude of the source is measured at the closest distance separating the source and the transducer array $z = 3$ mm and corrected of the absorption effect. Results for the linear shear modulus, the attenuation coefficient α_0, and the nonlinear Landau modulus A are reported in Table 29.4 for the two tested agar/gelatin phantoms. The dots represent experimental results; the solid lines correspond to the analytical formulation Eq. (29.29) and the dashed lines to the simulation output.

As predicted by Eq. (29.29), the third harmonic amplitude increases linearly with the distance (nonlinear cumulative effect) near the source. At larger distances, this growth is limited by absorption effects affecting both the fundamental and third harmonic components. The results provided by the analytical and numerical methods are in good agreement. Thus, for the source amplitude range tested (Figure 29.11 was obtained for the largest emission amplitude, leading to a Goldberg number of 0.97 for the 5% gelatin gel), the quasilinear approximation, necessary

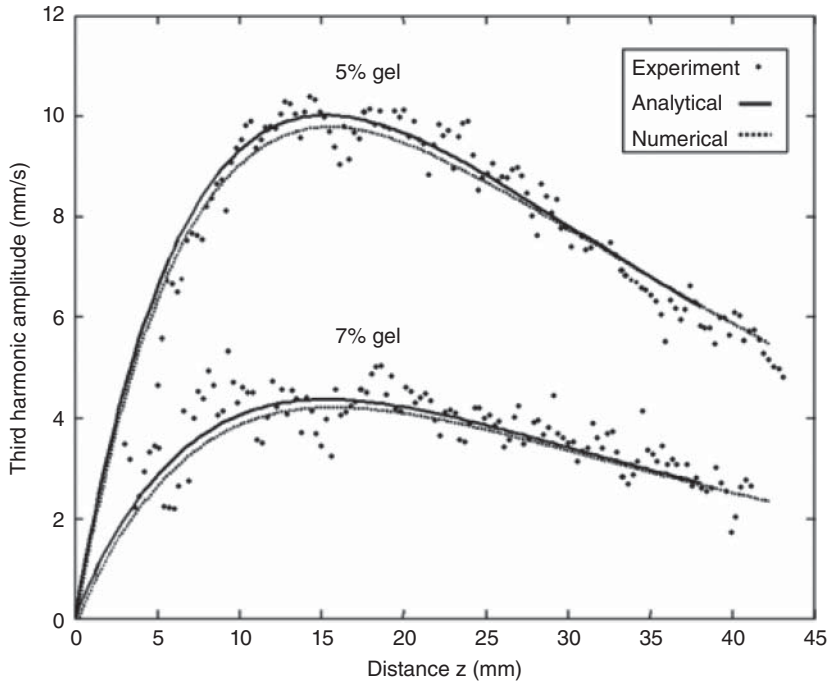

Figure 29.11 Third harmonic amplitude as a function of the propagation distance z. The dots represent experiments, the solid lines correspond to the analytical expression Eq. (29.29), and the dashed lines are numerical outputs. Reprinted with permission from [22]. Copyright 2008 by the American Physical Society.

to derive Eq. (29.29), remains valid. Shear nonlinearity parameters β were measured in the two samples for five emission amplitudes v_0. Mean values and corresponding standard deviations are listed in Table 29.4. For the 7% gelatin sample, the standard deviation is larger: since the inverse of the square of the Mach number increases, the signal-to-noise ratio was smaller in this case. However, it seems that the nonlinearity parameter becomes smaller when the gelatin concentration increases.

Finally, taking into account the previous measurements of the Landau nonlinear modulus A and using Eq. (29.9), an estimation of the fourth-order shear elastic constant D is then obtained (Table 29.4). For both samples, this constant is found to be positive and of the order of 10 kPa. It seems that while the linear shear modulus and the Landau modulus A increase with the gelatin concentration [19], both the nonlinearity parameter β and the fourth-order elastic constant D are decreasing. This tendency needs to be confirmed.

29.6 Conclusion

Finding new parameters to improve diagnosis for physicians is challenging. So, the evaluation of quantified nonlinear shear parameters could help to answer this need. Different methods allow one to estimate nonlinear parameters, acoustoelasticity theory, high amplitude shear waves propagation, or nonlinear interaction of shear wave. So far, only acoustoelasticity theory has showed some in vivo results and seems to be the easiest one to implement. However, assessment of nonlinear shear parameters is still quite young in soft tissues in vivo and ex vivo and needs to prove its usefulness for clinical practice.

References

1 Hamilton, M.F., Ilinskii, Y.A., and Zabolotskaya, E.A. (2004). Separation of compressibility and shear deformation in the elastic energy density. *J. Acoust. Soc. Am.* 116: 41–44.
2 Mendousse, J.S. (1953). *J. Acoust. Soc. Am.* 25: 51.
3 Lardner, R.W. (1985). Nonlinear effects on transverse shear waves in an elastic medium. *J. Elast.* 15: 53–57.
4 Zabolotskaya, E.A. (1986). Sound beams in a nonlinear isotropic solid. *Sov. Phys. Acoust.* 32: 296.
5 Lee-Bapty, I.P. and Crighton, D.G. (1987). Nonlinear wave motion governed by the modified Burgers equation. *Philos. Trans. R. Soc. London A* 323: 173.
6 Catheline, S., Gennisson, J.L., and Fink, M. (2003). Measurement of elastic nonlinearity of soft solid with transient elastography. *J. Acoust. Soc. Am.* 114 (6): 3087–3091.
7 Naugolnykh, K. and Ostrovsky, L. (1998). *Nonlinear Wave Processes in Acoustics*, 74. New York: Cambridge University Press.
8 Hamilton, M.F., Ilinskii, Y.A., and Zabolotskaya, E.A. (2003). New formulation of the elastic energy density for soft tissue. *J. Acoust. Soc. Am.* 114: 2436.
9 Jacob, X., Gennisson, J.L., Catheline, S., et al. (2003). Study of elastic nonlinearity of soft solids with transient elastography. *Proc. IEEE Ultrason. Symp.* 660–663.
10 Mase, G.T. and Mase, G.E. (eds.) (1999). *Continuum Mechanics for Engineers*, 2nd edn. Boca Raton: CRC Press.
11 Zabolotskaya, E.A., Hamilton, M.F., Ilinskii, Y.A., and Meegan, G.D. (2004). Modeling of nonlinear shear waves in soft solids. *J. Acoust. Soc. Am.* 116: 2807–2813.
12 Hamilton, M.F. and Blackstock, D.T. (eds.) (1998). *Nonlinear Acoustics*. San Diego: Academic.

13 McDonald, B. and Ambrosiano, J. (1984). High-order upwind flux correction methods for hyperbolic conservation laws. *J. Comput. Phys.* 56: 449–460.
14 Jacob, X., Catheline, S., Gennisson, J.L., et al. (2007). Nonlinear shear wave interaction in soft solids. *J. Acoust. Soc. Am.* 122 (4): 1917–1926.
15 L. Sandrin, M. Tanter, Catheline, S., and Fink, M., (2002). *IEEE Trans. Ultrason., Ferroelect., Freq. Control* 49: 425.
16 Ophir, J., Céspedes, I., Ponnekanti, H., et al. (1991). *Ultrason. Imaging* 13: 111.
17 Zarembo, L. and Krasil'nikov, V. (1971). A nonlinear phenomena in the propagation of elastic waves in solids. *Sov. Phys. Usp.* 13: 778–797.
18 Jones, G.L. and Kobett, D.R. (1962). Interaction of elastic waves in an isotropic solid. *J. Acoust. Soc. Am.* 35: 5–10.
19 Gennisson, J.L., Renier, M., Catheline, S., et al. (2007). Acoustoelasticity in soft solids: assessment of the nonlinear shear modulus with the acoustic radiation force. *J. Acoust. Soc. Am.* 122 (6): 3211–3219.
20 Urban, M.W., Lopera, M., Aristizabal, S., et al. (2015). Characterization of transverse isotropy in compressed tissue-mimicking phantoms. *IEEE Trans. Ultrason., Ferroelect., Freq. Control* 62 (6): 1036–1046.
21 Bernal, M., Chamming's, F., Couade, M., et al. (2016). In vivo quantification of the nonlinear shear modulus in breast lesions: feasibility study. *IEEE Trans. Ultrason., Ferroelect., Freq. Control* 63 (1): 101–109.
22 Rénier, M., Gennisson, J.-L., Barriere, C., et al. (2008). Fourth-order shear elastic constant assessment in quasi-incompressible soft solids. *Appl. Phys. Lett.* 93: 101912.

Section VIII

Clinical Elastography Applications

30

Current and Future Clinical Applications of Elasticity Imaging Techniques

Matthew Urban

Department of Radiology, Mayo Clinic, Rochester, MN, USA

30.1 Introduction

Elastography or elasticity imaging is a field of medical imaging that is aimed at quantifying the mechanical properties of living tissues [1]. Palpation has been used for centuries by physicians to examine patients because it is well known that diseased tissue "feels" stiffer than normal tissue in many pathologies. Disease changes structure, which alters function, and manifests as symptoms. However, change in structure and composition also changes the mechanical properties of the tissue. For example, fibrosis is the result of an inflammatory response that destroys working functional units in an organ. Fibrosis results from an increase in collagen replacing the normal tissue, which makes the organ stiffer than when the healthy functional units are present [2]. Additionally, blood flow and environmental changes due to tumor presence can also alter the local stiffness of organs. However, palpation has several disadvantages, including its subjectivity, dependence on the proficiency of the examiner, reproducibility, and insensitivity to deep structures.

Elastography offers an approach for noninvasive, reproducible, objective, and high resolution characterization of the mechanical properties of tissues [1]. Any form of elastography depends on deforming the tissue with some sort of stress and the measurement of the resulting deformation – typically with ultrasound or magnetic resonance imaging techniques. The role of magnetic resonance elastography (MRE) has been significant in establishing this elasticity imaging field and has efficacious applications, particularly in the case of liver fibrosis staging. While this chapter will primarily focus on ultrasound-based methods, MRE results will also be highlighted in certain application areas.

There are many different parameters that have been used to characterize tissues. Most elastography methods assume that the tissues are elastic, homogeneous, incompressible, and isotropic. In this case the diagnostic parameters that are used are related to the displacement, strain, shear wave speed, shear, or Young's modulus [1]. However, some tissues are not homogenous, such as a breast with a tumor. In this case there is normal tissue and the lesion to evaluate. Some tissues have directionally dependent material properties, such as a skeletal muscle which has muscle fibers oriented in a certain direction. It is well known that the shear modulus along the fibers is higher than that across the fibers [3]. Lastly, most, if not all, tissues are inherently viscoelastic [4]. This adds a new dimension to a number of parameters that can be used to characterize the tissues.

The field of elastography has been populated with a multitude of methods for measuring the mechanical properties of different tissues, which have been detailed in chapters in this book

Ultrasound Elastography for Biomedical Applications and Medicine, First Edition.
Edited by Ivan Nenadic, Matthew Urban, James Greenleaf, Jean-Luc Gennisson, Miguel Bernal, and Mickael Tanter.

(see Chapters 10–25). Some of the methods that have been discussed are naturally point-based measurement techniques and others are imaging techniques. The ultimate aim of the development of these methods is to evaluate whether they can be used for clinical diagnosis and monitoring of therapeutic interventions.

Many different tissues have been evaluated using different technologies. These applications can broadly be separated into two categories: (i) evaluating a systemic disease that affects the whole organ in a homogeneous manner or (ii) evaluating a localized disease such as a cancerous lesion. In the case of the systemic diseases, such as liver fibrosis, it is assumed that the entire liver is affected and changes are global. Therefore, a point-based or imaging method would be suitable for this type of evaluation. Alternatively, for a localized disease, such as a breast tumor, information about both the normal surrounding tissue and the tumor itself are often desired, in particular to use the contrast between the two regions as diagnostic indicators. Therefore, an imaging method would be desired to acquire data in both the normal and abnormal regions.

30.2 Clinical Implementation and Use of Elastography

To be useful in the clinic, the elastography methods must be available on clinical ultrasound machines. Strain elastography has been implemented on machines produced by Siemens, Toshiba, Hitachi, General Electric, Philips, Ultrasonix, Zonare, and Samsung Medison. Shear wave elastography (SWE) methods have been implemented on systems made by Siemens, Supersonic Imagine, Philips, Echosens, Toshiba, Samsung Medison, and General Electric. Shear wave point-based measurement techniques are available on Siemens, Philips, Echosens, and Samsung Medison machines. Shear wave speed imaging has been implemented on Siemens, Supersonic Imagine, Toshiba, and General Electric instruments. The Supersonic Imagine Aixplorer can also perform three-dimensional shear wave elastography with a linear array transducer on a mechanical wobbler to obtain multiple planes of elastographic data. Different array transducers are being used and developed for specific clinical applications.

As these methods are introduced into clinical practice, guidelines for their use are of critical importance so that consistency is maintained in practice and so that measurements that are reported in the biomedical literature are comparable from study to study. Sets of guidelines for liver, breast, and thyroid applications have been introduced by the World Federation for Ultrasound in Medicine and Biology (WFUMB) and the European Federation of Societies for Ultrasound in Medicine and Biology (EFSUMB) [2, 5–8].

These guidelines are important for describing and understanding the physics related to the measurement of material properties and parameters related to these properties. It was found that in some early literature that misreporting of elastographic parameters was occurring [9], which is why these guidelines are so important for clinicians and day-to-day users of these technologies. Additionally, the procedures for using the techniques are also detailed in these guidelines. The ultrasound scanner manufacturers provide best practices for their respective equipment and those practices should be considered. Approaches to avoid known artifacts should also be respected.

Additional efforts have been put forth by the Radiological Society of North America's Quantitative Imaging Biomarker Alliance (RSNA's QIBA), which has undertaken a standardization of shear wave velocity measurement for particular application in liver fibrosis staging [10]. Studies involving phantom measurements, simulations, measurements in patients, and creation of a measurement profile have been done or are in progress to study the effects of viscoelasticity and the differences between different machines to obtain consistent shear wave velocity measurements [11].

All of these methods that have been implemented on clinical machines have been approved by regulatory agencies. Vibration levels imposed in the body needed to be assessed for safety in patients [12]. Additionally, methods based on acoustic radiation force also need to meet regulatory limits for the acoustic output, particularly the mechanical index ($MI_{0.3}$), thermal index (TI), and spatial peak temporal average intensity ($I_{spta,0.3}$) after derating by 0.3 dB/cm/MHz [13]. Typically, the MI is the limiting factor for most methods, though the thermal stress on the transducer also needs to be addressed, usually through executing the measurements at low repetition rates of 0.5–1 Hz.

30.3 Clinical Applications

The organs that have been explored substantially include the liver, breast, and thyroid. Liver fibrosis and steatosis have been the target diseases for many shear wave elastography studies. Breast and thyroid cancer diagnosis and differentiation have been the application areas for strain-based and, more recently, shear wave elastography methods. Many other organs or diseases have also been investigated with various elastographic techniques and are emerging as potential clinical applications. Previously reported work in other organs (such as prostate), in lymph nodes, in thrombosis, and for tumors in organs other than breast, thyroid, and liver have been reviewed by Sarvazyan et al. [1]. In this chapter, the use of ultrasound-based elastography will also be reviewed for the emerging areas of musculoskeletal, renal, cardiac, and vascular applications.

30.3.1 Liver

Liver fibrosis is a systemic disease resulting from inflammation and other insults [2]. Liver fibrosis is a progressive disease that ends in cirrhosis, which results in total destruction of the functional units of the liver. Cirrhosis can lead to portal hypertension and hepatocellular carcinoma. Nonalcoholic fatty liver disease (NAFLD) covers a spectrum of disease which involves steatosis (the build-up of lipids within the liver), and which can ultimately lead to fibrosis, cirrhosis, and hepatocellular carcinoma [14].

Multiple methods have been employed to characterize fibrosis in the liver. Shear wave speed measurements have shown great promise through the transient elastography (TE) technique and through shear wave point-based or imaging methods. Due to the depth of the liver, strain elastography methods have not been applied with nearly the same success as the shear wave-based methods. There have been numerous TE studies to evaluate staging of hepatic fibrosis in large populations with different disease etiologies [15–18]. Magnetic resonance elastography has also been used extensively to examine hepatic fibrosis [19–21]. MRE has been so successful that at the Mayo Clinic MRE scans are the standard of care for staging of liver fibrosis in many cases. ARF-based methods implemented on Siemens, Supersonic Imagine, and Philips devices have also been used and compared against TE [22–28]. Among these methods, they are generally very accurate for diagnosing advanced fibrosis or cirrhosis, but the intermediate fibrosis stages are more difficult to separate.

A few complications remain for these shear wave-based methods, including distinguishing between intermediate fibrosis stages and grading steatosis or dealing with the effects posed by the presence of steatosis [2]. Measuring the ultrasound attenuation of the liver and the shear phase velocity dispersion have been proposed as alternatives to addressing the problems of steatosis characterization [14, 29–33]. Some additional work has been done in the area of characterizing hepatic tumors with SWE techniques [2].

30.3.2 Breast

Ultrasound has long been an adjuvant imaging modality for breast cancer detection in addition to screening mammography. Ultrasound becomes very useful, particularly in patients with radiographically dense breast tissue. Early work in the study of breast cancer detection and characterization was performed with strain elastography because the breast is easily accessible and compressible. Numerous studies and grading approaches have been developed for characterizing breast lesions and their classification as benign or malignant based on the strain distribution [1, 6]. The Tsukuba score has been developed to evaluate breast lesions [6]. Different features related to the geometry and strain ratios have also been investigated. Some studies have reported good sensitivities and specificities for differentiating malignant from benign lesions [34, 35]. However, without substantial knowledge of the boundary conditions and stress, absolute quantitative evaluations cannot be done. SWE has also been applied to breast imaging as it can provide quantitative shear modulus measurements.

In general, malignant lesions have been shown to have larger shear moduli than benign lesions [36–38]. The parameters that are used to characterize the lesions and have the most clinical efficacy are somewhat controversial. The analyses are ultimately based on selecting a region-of-interest (ROI) in the image. Some groups have reported the use of the maximum, mean, or median modulus. It still remains for the community to determine what may be most appropriate for proper diagnosis and characterization of breast lesions. Measurement accuracy of the shear modulus is dependent on the size of the lesion, as larger inclusions which incorporate more shear wavelengths will be characterized accurately. This is a common issue with all SWE methods because of the physics related to the shear wave propagation.

There are also some artifacts that are associated with imaging of breast lesions, including imaging of calcifications [39] and the effects of compression. Calcified lesions can produce characteristic artifacts on SWE images that may be a useful indicator of calcified tissue. Additionally, it is known that compression of soft tissues can yield changes in the measured shear modulus [40, 41]. This occurs because of a phenomenon known as nonlinear elasticity. Typically, the clinical guidelines advocate that minimal to no compression be applied so as to not incur these effects. However, some research groups are using compression in addition to shear wave elastography to get additional information on the mechanical properties in the breast and the tumors under investigation [41].

30.3.3 Thyroid

The thyroid is another shallow organ that has been the subject of many elastography studies. Ultrasound is the first-line imaging modality used for thyroid imaging. One aspect of B-mode ultrasound in the thyroid is that thyroid nodules are very common, so sensitivity is very high, but specificity is not.

Strain elastography has been applied extensively for the characterization of thyroid nodules [42–45]. Scoring systems are variable among many different studies. Additionally, many different parameters related to geometry, contrast, and ultrasound echogenicity have been evaluated for their diagnostic effectiveness. In recent years, SWE has also been applied for thyroid nodule evaluation [46–49]. The sensitivity and specificity is slightly lower than for strain elastography, but this area of application is still relatively naïve to make solid conclusions.

30.3.4 Musculoskeletal

Ultrasound of the musculoskeletal (MSK) system has been growing progressively. The use of SWE in MSK applications has also been increasing [50–52]. Some preliminary studies to characterize muscles in relaxed and loaded states have been reported. The applicability of SWE in

skeletal muscle may be useful for longitudinal studies of muscle disorders or rehabilitation from injuries. In a similar vein, SWE has been applied in tendons, specifically the Achilles tendon, for the application of evaluating Achilles tendon tear or rupture recovery [53–55].

There are a few challenges with MSK applications in that skeletal muscle and tendons are composed of sets of fibers that are preferentially oriented. Because of this structural organization, the material properties of these tissues are spatially dependent or anisotropic. The orientation of the shear wave propagation needs to be carefully controlled in these tissues to obtain consistent results among different individuals and within the same individual.

Additionally, these tissues can become quite stiff, particularly in loaded or stretched states, so some devices may not be able to measure the material properties at the full range of loading or stretch. This is because most devices have a defined upper limit for reliable measurements.

Magnetic resonance elastography has been used in the investigation of muscle in previously reported studies [56–59]. Quantitative shear modulus changes were found in normal subjects compared with patients with diseased muscle. Additionally, the anisotropic nature of skeletal muscle [60–62] as well as its viscoelastic properties [63, 64] have been investigated.

Transient elastography was one of the first methods used for investigation of skeletal muscle [3, 65, 66]. Sonoelastography is a method that uses external actuators to create propagating shear waves in tissue and the motion is measured by pulse-echo ultrasound techniques [67]. Application of different harmonic frequencies to the actuators can yield data for dispersive velocity analysis. Viscoelastic measurements in muscle have been made in human subjects, but the need for external hardware is a limiting factor for widespread clinical implementation [68].

Acoustic radiation force impulse (ARFI) imaging was used to explore stiffness in skeletal muscle [69]. Supersonic shear imaging (SSI) is an ARF-based method to perform SWE imaging has been used for multiple studies in various skeletal muscle applications [50, 51, 70–75]. These studies have demonstrated that the shear modulus can be related to muscle activity or contractile state [50, 51, 75]. Additionally, changes in muscle stiffness are associated with pathology [72, 73]. SWE has been used to quantify the shear wave velocity (SWV) in the neck muscles in subjects with chronic neck pain [76]. A 2D matrix array was used to measure shear wave propagation in a plane orthogonal to the radiation force to quantify the anisotropic properties of ex vivo skeletal muscle [77].

Skeletal muscle, like many other soft tissues, is a viscoelastic material, that is, muscle has both elastic and viscous properties. Viscoelastic materials exhibit time-dependent deformation when a stress is applied, whereas elastic materials exhibit immediate deformation. Many mechanical testing studies have demonstrated these effects [78–83], but most of these studies examine very low frequency characteristics (<10 Hz) of the skeletal muscle, while most clinically relevant information is contained in a higher bandwidth (50–1000 Hz).

The shear wave-based methods mentioned above for applications in skeletal muscle using either MR or ultrasound have explored viscoelastic properties from 50–500 Hz [63, 68, 70, 84, 85]. Shear wave measurement techniques have emerged over the last decade as a prominent way to assess the viscoelastic properties of tissue. To fully characterize skeletal muscle, measurements of the elastic and viscous components of the tissue and their anisotropic distribution need to be measured [86]. This is a topic of ongoing research for multiple groups.

30.3.5 Kidney

Chronic kidney disease (CKD) encompasses a long-term decrease in function of the kidneys. The prevalence of CKD in stages 1–5, where the stage is determined by albuminuria and estimated glomerular filtration rate (eGFR) based on serum creatinine concentration, increased in the years 1999–2004 compared to that during the period of 1988–1994 from 10.0% to 11.5% in adults aged 20 and over [87]; more than 20 million people. Another stark reality concerning

CKD is that patients with this affliction carry 2–5 times the disease burden of non-CKD patients because large numbers of CKD patients also have diabetes, hypertension, cardiovascular disease, and chronic obstructive pulmonary disease [88].

CKD can progress to kidney failure or end-stage renal disease (ESRD) and the treatment options for these patients include hemodialysis or kidney transplant [89]. Hemodialysis treatment is not a long-term solution. Patient and graft survival rates have increased over the past two decades [88], but long-term survival of grafts is still an issue. The patient survival probabilities for patients receiving deceased- or living-donor transplants are higher than the graft survival rates, indicating that the patient will often outlive the graft and have to be retransplanted or undergo dialysis treatment.

The kidney has been studied using several elasticity imaging techniques. Strain elastography has been used in several ex vivo studies in kidneys [90–92] and some in vivo human studies of kidney transplant patients [93, 94]. Areas of lower strain correlated with fibrotic or scarred tissue, implying that this tissue is stiffer than normal tissue.

MRE has been applied to quantitatively evaluate the stiffness of renal cortex and medulla in ex vivo porcine kidneys, in in vivo rat and swine models, and in healthy human adults [95–98]. In the study in rats, comparisons were made between normal animals and animals that developed nephrocalcinosis due to exposure to ethylene glycol. The shear stiffness in the renal cortex increased after 2- and 4-week exposures [96] In studies in swine, the renal artery was occluded in progressive steps, and the cortical and medullary shear stiffness decreased as a result of decreased perfusion [97, 99].

SWE measurements in patients with CKD and renal transplants have been reported. It has been shown that SWV changes in patients with CKD compared to healthy individuals [100–103]. Results using TE showed that stiffness in renal allografts correlated significantly with the degree of fibrosis and eGFR [104]. Several studies using SWE compared shear wave speed and renal transplant Banff biopsy scores for measurements made in transplanted kidneys [105, 106]. The study by Syversveen et al. examined 30 patients and did not find a significant correlation of shear wave speed with fibrosis [105]. Stock et al. studied 18 patients and found positive correlations between shear wave speed and level of fibrosis [106]. The kidney, like many other soft tissues, can be modeled as a viscoelastic material, that is, the kidney has both elastic and viscous characteristics [107–111].

30.3.6 Heart

Many conditions in the heart alter the structure of the heart and typically lead to an increase in tissue stiffness. Strain and strain rate measurements are part of the cadre of tools that are used routinely in echocardiography as they can be used to detect abnormalities in the motion of the heart due to systemic stiffening related to systolic or diastolic dysfunction or localized dysfunction related to myocardial infarctions [112–115]. Additional recent work has been targeted towards examining the electromechanical waves in the heart [116–122].

Multiple ultrasound-based methods that measure propagating waves have been used for evaluating myocardial mechanical properties. Kanai observed that the aortic valve closure generated a measurable wave in the ventricular septum [123]. A Lamb wave model was used to estimate the viscoelastic properties of the myocardial tissue. Shear waves propagating in a bounded medium reflect at the surfaces and cause mode conversion at the boundaries, which creates shear and longitudinal waves and which influences the observed wave velocities. Nenadic et al. built upon Kanai's observations to develop the Lamb wave dispersion ultrasound vibrometry (LDUV) method that used external vibration to create harmonic anti-symmetric Lamb waves [124–126]. Phase velocities at frequencies with a bandwidth of 50–500 Hz were fit to the same anti-symmetric Lamb wave model proposed by Kanai [123]. The LDUV technique was utilized

for studies in normal pigs and pigs with myocardial infarctions to quantify the viscoelastic mechanical properties of the left ventricular heart wall in an open heart preparation [127, 128].

Acoustic radiation force has been used to generate shear waves in the myocardium for studies involving wave propagation. Couade et al. used the SSI technique in the left ventricle of in vivo sheep in an open chest preparation [129]. Measurements of dynamic variation through the cardiac cycle were performed in different scanning orientations, revealing anisotropic wave propagation. In addition, changes in the wave velocities through the thickness of the myocardium at different angles in an explanted heart sample was also studied. Additional ARF-based studies have been performed in open chest dogs [130] and Langendorff perfused isolated rat and rabbit hearts [131, 132]. The used of intracardiac transducers has been reported in normal pigs and pigs with infarcted regions [133, 134]. Most of the previously described work with ultrasound-based SWE has been done with invasive preparations or procedures. Transthoracic measurements in humans have recently been performed and are an initial step towards translating SWE methods into clinical applications in humans [135].

Some studies have explored the spatial variation of the wave velocity through the thickness of the myocardium. The intrinsic anisotropic architecture of the myocardial tissue and the rotation of the muscle fiber directions through the thickness of the ventricular wall is the explanation for these observations [136]. Two important studies have investigated the anisotropy of the heart wall using waves generated using ARF in ex vivo and in vivo hearts [137, 138]. The elastic tensor imaging (ETI) technique that was developed for analysis of myocardial anisotropy adopted the approach of modeling the heart as a series of transversely isotropic layers [138]. In a transverse isotropic medium, such as skeletal muscle which has muscle fibers running in a preferred direction, the wave will travel faster when propagating along the fibers and will travel slower when propagating perpendicular to the fiber direction [3, 77, 139]. The fiber direction at each depth was estimated using ETI by rotating the transducer and acquiring data at multiple angles and estimating the angle which provides the fastest wave velocity. This was performed in numerous heart samples and the results were validated against histology of the samples or measurements made using magnetic resonance diffusion tensor imaging [137, 138].

30.3.7 Arteries and Atherosclerotic Plaques

Many groups have worked on various ultrasound-based approaches for evaluating the carotid artery and atherosclerotic plaques, including transcutaneous strain imaging, intravascular ultrasound (IVUS) strain imaging, ARFI imaging, and SWE. MRE has been used for ex vivo and in vivo applications of the porcine and human aorta and human femoral artery [140–143].

Pulse wave imaging (PWI) is a method that measures the motion of the arterial wall due to the pressure pulse to quantify the local pulse wave velocity (PWV), and has been utilized in the aortas of mice with and without aneurysms [144], and in human aortas and carotid arteries [117, 145–147]. This method has the advantage of assessing the PWV over a short segment (1–9 cm) compared to the longer segment used clinically in carotid-femoral pulse wave velocity (cfPWV) measurements. One limitation of PWI is that only one measurement can be made for each cardiac cycle, so the spatial resolution is higher than traditional cfPWV methods, but the temporal resolution is no better.

Acoustic radiation force has been utilized for perturbing arterial vessels for material characterization. Acoustic radiation force has also been used to create high frequency propagating waves in human carotid arteries to measure the material properties through the cardiac cycle [148]. One method, called vibro-acoustography, was used to image arteries with calcifications in ex vivo tissues and in in vivo porcine arteries [149–151]. Another method, called shearwave dispersion ultrasound vibrometry (SDUV), uses ARF to generate and measure shear waves in soft tissues and analyze the shear wave velocity dispersion, or velocity variation with frequency, to

extract viscoelastic material properties [84, 152]. We have used ARF in tubes and ex vivo arteries to produce high frequency waves (100–500 Hz) in the wall of the tube or vessel to investigate the material properties [153–161].

Noninvasive strain imaging has been under investigation for the last decade, with the goal of using the motion of the artery from the pressure pulse variation to examine the stiffness of the arterial wall and plaques [162–175]. In addition to strain imaging performed using transcutaneous ultrasound, strain-based elastography using IVUS has been proposed and developed to image vulnerable plaques to ascertain their likelihood of rupture and formation of emboli [176–187]. ARFI imaging has been used to explore localized plaque formation in arterial vessels [188–197]. Analysis of the displacement amplitude and time course was used in swine models to investigate the ability to localize and classify atherosclerotic plaques [190, 193]. SWE has been used to measure the material properties in arterial phantoms and atherosclerotic plaques in humans [159, 198–200].

30.4 Future Work in Clinical Applications of Elastography

Future work by several academic and industrial research groups is directed towards refinement of elastographic techniques to improve accuracy and precision so that values reported by clinical machines meet similar standards of performance. New techniques are constantly being developed and time will tell if they are integrated into clinical devices.

Artifact identification and avoidance is also an area that will expand as these methods, particularly SWE, is used more in clinical settings. The importance of adherence to the initial guidelines will aid in normalizing data reported in the biomedical literature.

As the SWE methods are used more consistently, data reported could be assembled to build databases of normal and abnormal values for the benefit of making clinical decisions. Within these endeavors variations with sex, age, and other factors need to be identified. However, one aspect of this is that results may be dependent on the device and its settings so that information needs to be taken into account for proper interpretation of the assembled data.

It is inevitable that new clinical applications will arise or that nascent ones will be developed further. Additionally, the expansion of investigation into additional mechanical properties, such as nonlinearity, anisotropy, and viscoelasticity, provide a landscape that could be used for improved diagnosis or techniques for monitoring of patients undergoing therapeutic interventions.

30.5 Conclusions

This chapter has provided a brief overview of clinical applications for elastographic imaging using ultrasound-based methods. There are many active application areas in which strain elastography and shear wave elastography have been used. Due to the translation of these methods from academic laboratories to clinical instruments, patients have benefited and continue to benefit from the development with these largely noninvasive methods. The future is bright as other clinical areas expand their use of these methods for diagnosis, prognosis, and treatment monitoring.

Acknowledgments

This work was supported by grant R01DK092255 from the National Institute of Diabetes and Digestive and Kidney Diseases (NIDDK) and National Institutes of Health (NIH). The content

is solely the responsibility of the authors and does not necessarily represent the official views of the NIDDK and NIH.

References

1 Sarvazyan, A., Hall, T.J., Urban, M.W., et al. (2011). Elasticity imaging – an emerging branch of medical imaging. *An overview. Curr. Med. Imaging Rev.* 7: 255–282.

2 Ferraioli, G., Filice, C., Castera, L., et al. (2015). WFUMB guidelines and recommendations for clinical use of ultrasound elastography: Part 3: Liver. *Ultrasound Med. Biol.* 41: 1161–1179.

3 Gennisson, J.L., Catheline, S., Chaffai, S., and Fink, M. (2003). Transient elastography in anisotropic medium: application to the measurement of slow and fast shear wave speeds in muscles. *J. Acoust. Soc. Am.* 114: 536–541.

4 Fung, Y.C. (1993). *Biomechanics : Mechanical Properties of Living Tissues*, 2nd edn. New York: Springer-Verlag.

5 Shiina, T., Nightingale, K.R., Palmeri, M.L., et al. (2015). WFUMB guidelines and recommendations for clinical use of ultrasound elastography: Part 1: Basic principles and terminology. *Ultrasound Med. Biol.* 41: 1126–1147.

6 Barr, R.G., Nakashima, K., Amy, D., et al. (2015). WFUMB guidelines and recommendations for clinical use of ultrasound elastography: Part 2: Breast. *Ultrasound Med. Biol.* 41: 1148–1160.

7 Bamber, J., Cosgrove, D., Dietrich, C.F., et al. (2013). EFSUMB guidelines and recommendations on the clinical use of ultrasound elastography. part 1: basic principles and technology. *Ultraschall. Med.* 34: 169–184.

8 Cosgrove, D., Piscaglia, F., Bamber, J., et al. (2013). EFSUMB guidelines and recommendations on the clinical use of ultrasound elastography. part 2: clinical applications. *Ultraschall. Med.* 34: 238–253.

9 Urban, M.W., Nenadic, I.Z., Chen, S., and Greenleaf, J.F. (2013). Discrepancies in reporting tissue material properties. *J. Ultrasound Med.* 32: 886–888.

10 Radiological Society of North America Quantitative Imaging Biomarker Alliance (RSNA QIBA) (2012). Ultrasound Shear Wave Speed Technical Commitee.

11 Hall, T.J., Milkowski, A., Garra, B., et al. (2013). RSNA/QIBA: Shear wave speed as a biomarker for liver fibrosis staging. In: *2013 IEEE International Ultrasonics Symposium (IUS)* 397–400.

12 Ehman, E.C., Rossman, P.J., Kruse, S.A., et al. (2008). Vibration safety limits for magnetic resonance elastography. *Phys. Med. Biol.* 53: 925–935.

13 Herman, B.A. and Harris, G.R. (2002). Models and regulatory considerations for transient temperature rise during diagnostic ultrasound pulses. *Ultrasound Med. Biol.* 28: 1217–1224.

14 Lin, S.C., Heba, E., Wolfson, T., et al. (2015). Noninvasive diagnosis of nonalcoholic fatty liver disease and quantification of liver fat using a new quantitative ultrasound technique. *Clin. Gastroenterol. Hepatol.* 13: 1337–1345, e6.

15 Friedrich-Rust, M., Ong, M.-F., Martens, S., et al. (2008). Performance of transient elastography for the staging of liver fibrosis: a meta-analysis. *Gastroenterology* 134: 960–974, e8.

16 Tsochatzis, E.A., Gurusamy, K.S., Ntaoula, S., et al. (2011). Elastography for the diagnosis of severity of fibrosis in chronic liver disease: A meta-analysis of diagnostic accuracy. *J. Hepatol.* 54: 650–659.

17 Talwalkar, J.A., Kurtz, D.M., Schoenleber, S.J., et al. (2007). Ultrasound-based transient elastography for the detection of hepatic fibrosis: systematic review and meta-analysis. *Clin. Gastroenterol. Hepatol.* 5: 1214–1220.

18 Stebbing, J., Farouk, L., Panos, G., et al. (2010). A meta-analysis of transient elastography for the detection of hepatic fibrosis. *J. Clin. Gastroenterol.* 44: 214–219.

19 Singh, S., Venkatesh, S.K., Wang, Z., et al. (2015). Diagnostic performance of magnetic resonance elastography in staging liver fibrosis: a systematic review and meta-analysis of individual participant data. *Clin. Gastroenterol. Hepatol.* 13: 440–451, e6.

20 Venkatesh, S.K., Yin, M., and Ehman, R.L. (2013). Magnetic resonance elastography of liver: Technique, analysis, and clinical applications. *J. Magn. Reson. Imaging* 37: 544–555.

21 Su, L.N., Guo, S.L., Li, B.X., and Yang, P. (2014). Diagnostic value of magnetic resonance elastography for detecting and staging of hepatic fibrosis: A meta-analysis. *Clin. Radiol.* 69: e545–e552.

22 Sporea, I., Sirli, R., Bota, S., et al. (2012). Comparative study concerning the value of acoustic radiation force impulse elastography (ARFI) in comparison with transient elastography (TE) for the assessment of liver fibrosis in patients with chronic hepatitis B and C. *Ultrasound Med. Biol.* 38: 1310–1316.

23 Sporea, I., Bota, S., Jurchis, A., et al. (2013). Acoustic radiation force impulse and supersonic shear imaging versus transient elastography for liver fibrosis assessment. *Ultrasound Med. Biol.* 39: 1933–1941.

24 Bota, S., Herkner, H., Sporea, I., et al. (2013). Meta-analysis: ARFI elastography versus transient elastography for the evaluation of liver fibrosis. *Liver Int.* 33: 1138–1147.

25 Bota, S., Paternostro, R., Etschmaier, A., et al. (2015). Performance of 2-D shear wave elastography in liver fibrosis assessment compared with serologic tests and transient elastography in clinical routine. *Ultrasound Med. Biol.* 41: 2340–2349.

26 Ferraioli, G., Parekh, P., Levitov, A.B., and Filice, C. (2014). Shear wave elastography for evaluation of liver fibrosis. *J. Ultrasound Med.* 33: 197–203.

27 Bavu, É., Gennisson, J.-L., Couade, M., et al. (2011). Noninvasive in vivo liver fibrosis evaluation using Supersonic Shear Imaging: a clinical study on 113 hepatitis C virus patients. *Ultrasound Med. Biol.* 37: 1361–1373.

28 Chen, S., Sanchez, W., Callstrom, M.R., et al. (2013). Assessment of liver viscoelasticity by using shear waves induced by ultrasound radiation force. *Radiology* 266: 964–970.

29 Sasso, M., Beaugrand, M., de Ledinghen, V., et al. (2010). Controlled attenuation parameter (CAP): A novel VCTE guided ultrasonic attenuation measurement for the evaluation of hepatic steatosis: preliminary study and validation in a cohort of patients with chronic liver disease from various causes. *Ultrasound Med. Biol.* 36: 1825–1835.

30 Sasso, M., Miette, V., Sandrin, L., and Beaugrand, M. (2012). The controlled attenuation parameter (CAP): A novel tool for the non-invasive evaluation of steatosis using Fibroscan®. *Clin. Res. Hepatol. Gastroenterol.* 36: 13–20.

31 Sasso, M., Audière, S., Kemgang, A., et al. (2016). Liver steatosis assessed by controlled attenuation parameter (CAP) measured with the XL probe of the FibroScan: a pilot study assessing diagnostic accuracy. *Ultrasound Med. Biol.* 42: 92–103.

32 Barry, C.T., Mills, B., Hah, Z., et al. (2012). Shear wave dispersion measures liver steatosis. *Ultrasound Med. Biol.* 38: 175–182.

33 Barry, C.T., Hah, Z., Partin, A., et al. (2014). Mouse liver dispersion for the diagnosis of early-stage fatty liver disease: a 70-sample study. *Ultrasound Med. Biol.* 40: 704–713.

34 Barr, R.G., Destounis, S., Lackey, L.B., et al. (2012). Evaluation of breast lesions using sonographic elasticity imaging: a multicenter trial. *J. Ultrasound Med.* 31: 281–287.

35 Raza, S., Odulate, A., Ong, E.M.W., et al. (2010). Using real-time tissue elastography for breast lesion evaluation: our initial experience. *J. Ultrasound Med.* 29: 551–563.

36 Denis, M., Mehrmohammadi, M., Song, P., et al. (2015). Comb-push ultrasound shear elastography of breast masses: initial results show promise. *PLoS One* 10: e0119398.

37 Chen, L., He, J., Liu, G., et al. (2014). Diagnostic performances of shear-wave elastography for identification of malignant breast lesions: a meta-analysis. *Jpn. J. Radiol.* 32: 592–599.

38 Li, G., Li, D.-W., Fang, Y.-X., et al. (2013). Performance of shear wave elastography for differentiation of benign and malignant solid breast masses. *PLoS One* 8: e76322.

39 Gregory, A., Mehrmohammadi, M., Denis, M., et al. (2015). Effect of calcifications on breast ultrasound shear wave elastography: an investigational study. *PLoS One* 10: e0137898.

40 Gennisson, J.L., Renier, M., Catheline, S., et al. (2007). Acoustoelasticity in soft solids: Assessment of the nonlinear shear modulus with the acoustic radiation force. *J. Acoust. Soc. Am.* 122: 3211–3219.

41 Latorre-Ossa, H., Gennisson, J.L., De Brosses, E., and Tanter, M. (2012). Quantitative imaging of nonlinear shear modulus by combining static elastography and shear wave elastography. *IEEE Trans. Ultrason., Ferroelectr., Freq. Control* 59: 833–839.

42 Wolinski, K., Szkudlarek, M., Szczepanek-Parulska, E., and Ruchala, M. (2014). Usefulness of different ultrasound features of malignancy in predicting the type of thyroid lesions: a meta-analysis of prospective studies. *Pol. Arch. Med. Wewn.* 124: 97–104.

43 Remonti, L.R., Kramer, C.K., Leitao, C.B., et al. (2015). Thyroid ultrasound features and risk of carcinoma: a systematic review and meta-analysis of observational studies. *Thyroid* 25: 538–550.

44 Veer, V. and Puttagunta, S. (2015). The role of elastography in evaluating thyroid nodules: a literature review and meta-analysis. *Eur. Arch. Otorhinolaryngol.* 272: 1845–1855.

45 Ghajarzadeh, M., Sodagari, F., and Shakiba, M. (2014). Diagnostic accuracy of sonoelastography in detecting malignant thyroid nodules: a systematic review and meta-analysis. *Am. J. Roentgenol.* 202: W379–W389.

46 Lin, P., Chen, M., Liu, B., et al. (2014). Diagnostic performance of shear wave elastography in the identification of malignant thyroid nodules: a meta-analysis. *Eur. Radiol.* 24: 2729–2738.

47 Zhang, B., Ma, X., Wu, N., et al. (2013). Shear wave elastography for differentiation of benign and malignant thyroid nodules: a meta-analysis. *J. Ultrasound Med.* 32: 2163–2169.

48 Liu, B.-J., Li, D.-D., Xu, H.-X., et al. (2015). Quantitative shear wave velocity measurement on acoustic radiation force impulse elastography for differential diagnosis between benign and malignant thyroid nodules: a meta-analysis. *Ultrasound Med. Biol.* 41: 3035–3043.

49 Sebag, F., Vaillant-Lombard, J., Berbis, J., et al. (2010). Shear wave elastography: A new ultrasound imaging mode for the differential diagnosis of benign and malignant thyroid nodules. *J. Clin. Endocrinol. Metab.* 95: 5281–5288.

50 Nordez, A. and Hug, F. (2010). Muscle shear elastic modulus measured using supersonic shear imaging is highly related to muscle activity level. *J. Appl. Physiol.* 108: 1389–1394.

51 Bouillard, K., Hug, F., Guével, A., and Nordez, A. (2012). Shear elastic modulus can be used to estimate an index of individual muscle force during a submaximal isometric fatiguing contraction. *J. Appl. Physiol.* 113: 1353–1361.

52 Lapole, T., Tindel, J., Galy, R., and Nordez, A. (2015). Contracting biceps brachii elastic properties can be reliably characterized using supersonic shear imaging. *Eur. J. Appl. Physiol.* 115: 497–505.

53 Chen, X.-M., Cui, L.-G., He, P., et al. (2013). Shear wave elastographic characterization of normal and torn Achilles tendons: a pilot study. *J. Ultrasound Med.* 32: 449–455.

54 Aubry, S., Risson, J.-R., Kastler, A., et al. (2013). Biomechanical properties of the calcaneal tendon in vivo assessed by transient shear wave elastography. *Skeletal Radiol.* 42: 1143–1150.

55 Brum, J., Bernal, M., Gennisson, J.L., and Tanter, M. (2014). In vivo evaluation of the elastic anisotropy of the human Achilles tendon using shear wave dispersion analysis. *Phys. Med. Biol.* 59: 505.

56 Basford, J.R., Jenkyn, T.R., An, K.N., et al. (2002). Evaluation of healthy and diseased muscle with magnetic resonance elastography. *Arch. Phys. Med. Rehabil.* 83: 1530–1536.

57 Ringleb, S.I., Bensamoun, S.F., Chen, Q., et al. (2007). Applications of magnetic resonance elastography to healthy and pathologic skeletal muscle. *J. Magn. Reson. Imaging* 25: 301–309.

58 Chen, Q., Bensamoun, S., Basford, J.R., et al. (2007). Identification and quantification of myofascial taut bands with magnetic resonance elastography. *Arch. Phys. Med. Rehabil.* 88: 1658–1661.

59 Dresner, M.A., Rose, G.H., Rossman, P.J., et al. (2001). Magnetic resonance elastography of skeletal muscle. *J. Magn. Reson. Imaging* 13: 269–276.

60 Papazoglou, S., Braun, J., Hamhaber, U., and Sack, I. (2005). Two-dimensional waveform analysis in MR elastography of skeletal muscles. *Phys. Med. Biol.* 50: 1313–1325.

61 Papazoglou, S., Rump, J., Braun, J., and Sack, I. (2006). Shear wave group velocity inversion in MR elastography of human skeletal muscle. *Magn. Reson. Med.* 56: 489–497.

62 Qin, E.C., Juge, L., Lambert, S.A., et al. (2014). In vivo anisotropic mechanical properties of dystrophic skeletal muscles measured by anisotropic MR elastographic imaging: the mdx mouse model of muscular dystrophy. *Radiology* 273: 726–735.

63 Klatt, D., Papazoglou, S., Braun, J., and Sack, I. (2010). Viscoelasticity-based MR elastography of skeletal muscle. *Phys. Med. Biol.* 55: 6445.

64 Debernard, L., Leclerc, G.E., Robert, L., et al. (2013). In vivo characterization of the muscle viscoelasticity in passive and active conditions using multifrequency MR elastography. *J. Musculoskeletal Res.* 16: 1350008.

65 Gennisson, J.L., Cornu, C., Catheline, S., et al. (2005). Human muscle hardness assessment during incremental isometric contraction using transient elastography. *J. Biomech.* 38: 1543–1550.

66 Nordez, A., Gennisson, J.L., Casari, P., et al. (2008). Characterization of muscle belly elastic properties during passive stretching using transient elastography. *J. Biomech.* 41: 2305–2311.

67 Krouskop, T.A., Dougherty, D.R., and Vinson, F.S. (1987). A pulsed Doppler ultrasonic system for making noninvasive measurements of the mechanical properties of soft tissue. *J. Rehabil. Res. Dev.* 24: 1–8.

68 Hoyt, K., Kneezel, T., Castaneda, B., and Parker, K.J. (2008). Quantitative sonoelastography for the in vivo assessment of skeletal muscle viscoelasticity. *Phys. Med. Biol.* 53: 4063–4080.

69 Nightingale, K., Nightingale, R., Stutz, D., and Trahey, G. (2002). Acoustic radiation force impulse imaging of in vivo vastus medialis muscle under varying isometric load. *Ultrason. Imaging* 24: 100–108.

70 Gennisson, J.-L., Deffieux, T., Macé, E., et al. (2010). Viscoelastic and anisotropic mechanical properties of in vivo muscle tissue assessed by supersonic shear imaging. *Ultrasound Med. Biol.* 36: 789–801.

71 Akagai, R. and Takahashi, H. (2013). Acute effect of static stretching on hardness of the gastrocnemius muscle. *Med. Sci. Sports Exercise* 45: 1348–1354.

72 Botanlioglu, H., Kantarci, F., Kaynak, G., et al. (2013). Shear wave elastography properties of vastus lateralis and vastus medialis obliquus muscles in normal subjects and female patients with patellofemoral pain syndrome. *Skeletal Radiol.* 42: 659–666.

73 Lv, F., Tang, J., Luo, Y., et al. (2012). Muscle crush injury of extremity: quantitative elastography with supersonic shear imaging. *Ultrasound Med. Biol.* 38: 795–802.

74 Shinohara, M., Sabra, K., Gennisson, J.-L., et al. (2010). Real-time visualization of muscle stiffness distribution with ultrasound shear wave imaging during muscle contraction. *Muscle Nerve* 42: 438–441.

75 Maïsetti, O., Hug, F., Bouillard, K., and Nordez, A. (2012). Characterization of passive elastic properties of the human medial gastrocnemius muscle belly using supersonic shear imaging. *J. Biomech.* 45: 978–984.

76 Kuo, W.-H., Jian, D.-W., Wang, T.-G., and Wang, Y.-C. (2013). Neck muscle stiffness quantified by sonoelastography is correlated with body mass index and chronic neck pain symptoms. *Ultrasound Med. Biol.* 39: 1356–1361.

77 Wang, M., Byram. B., Palmeri, M., et al. (2013). Imaging transverse isotropic properties of muscle by monitoring acoustic radiation force induced shear saves using a 2-D matrix ultrasound array. *IEEE Trans. Med. Imaging* 32: 1671–1684.

78 Palmer, B.M., Tanner, B.C., Toth, M.J., and Miller, M.S. (2013). An inverse power-law distribution of molecular bond lifetimes predicts fractional derivative viscoelasticity in biological tissue. *Biophys. J.* 104: 2540–2552.

79 Meyer, G.A., McCulloch, A.D., and Lieber, R.L. (2011). A nonlinear model of passive muscle viscosity. *J. Biomech. Eng.* 133: 091007.

80 Then, C., Vogl, T.J., and Silber, G. (2012). Method for characterizing viscoelasticity of human gluteal tissue. *J. Biomech.* 45: 1252–1258.

81 Van Loocke, M., Lyons, C.G., and Simms, C.K. (2008). Viscoelastic properties of passive skeletal muscle in compression: Stress-relaxation behaviour and constitutive modelling. *J. Biomech.* 41: 1555–1566.

82 Van Loocke, M., Simms, C.K., and Lyons, C.G. (2009). Viscoelastic properties of passive skeletal muscle in compression – Cyclic behaviour. *J. Biomech.* 42: 1038–1048.

83 Gras, L.-L., Mitton, D., Viot, P., and Laporte, S. (2013). Viscoelastic properties of the human sternocleidomastoideus muscle of aged women in relaxation. *J. Mech. Behav. Biomed. Mat.* 27: 77–83.

84 Chen, S., Urban, M.W., Pislaru, C., et al. (2009). Shearwave dispersion ultrasound vibrometry (SDUV) for measuring tissue elasticity and viscosity. *IEEE Trans. Ultrason., Ferroelectr., Freq. Control* 56: 55–62.

85 Urban, M.W. and Greenleaf, J.F. (2009). A Kramers-Kronig-based quality factor for shear wave propagation in soft tissue. *Phys. Med. Biol.* 54: 5919–5933.

86 Rudenko, O.V. and Sarvazyan, A.P. (2014). Wave anisotropy of shear viscosity and elasticity. *Acoust. Phys.* 60: 710–718.

87 Levey, A.S., Stevens, L.A., Schmid, C.H., et al. (2009). A new equation to estimate glomerular filtration rate. *Ann. Intern. Med.* 150: 604–612.

88 USRDS (2009). U.S. Renal Disease System 2009 *Annual Data Report: Atlas of End-Stage Renal Disease in the United States*. Bethsada, MD.

89 USRDS (2010). U.S. Renal Disease System 2010 *Annual Data Report: Atlas of End-Stage Renal Disease in the United States*. Bethsada, MD.

90 Emelianov, S.Y., Lubinski, M.A., Weitzel, W.F., et al. (1995). Elasticity imaging for early detection of renal pathology. *Ultrasound Med. Biol.* 21: 871–883.

91 Chaturvedi, P., Insana, M.F., and Hall, T.J. (1998). Ultrasonic and elasticity imaging to model disease-induced changes in soft-tissue structure. *Med. Imaging Anal.* 2: 325–338.

92 Emelianov, S.Y., Lubinski, M.A., Skovoroda, A.R., et al. (2000). Reconstructive ultrasound elasticity imaging for renal transplant diagnosis: kidney ex vivo results. *Ultrason. Imaging* 22: 178–194.

93 Weitzel, W.F., Kim, K., Rubin, J.M., et al. (2004). Feasibility of applying ultrasound strain imaging to detect renal transplant chronic allograft nephropathy. *Kidney Int.* 65: 733–736.

94 Weitzel, W.F., Kim, K., Rubin, J.M., et al. (2005). Renal advances in ultrasound elasticity imaging: measuring the compliance of arteries and kidneys in end-stage renal disease. *Blood Purif.* 23: 10–17.

95 Kruse, S.A., Smith, J.A., Lawrence, A.J., et al. (2000). Tissue characterization using magnetic resonance elastography: preliminary results. *Phys. Med. Biol.* 45: 1579–1590.

96 Shah, N.S., Kruse, S.A., Lager, D.J., et al. (2004). Evaluation of renal parenchymal disease in a rat model with magnetic resonance elastography. *Magn. Reson. Med.* 52: 56–64.

97 Yin, M., Chen, J., Glaser, K.J., et al. (2009). Abdominal magnetic resonance elastography. *Top. Magn. Reson. Imaging* 20: 79–87.

98 Rouvière, O., Souchon, R., Pagnoux, G., et al. (2011). Magnetic resonance elastography of the kidneys: Feasibility and reproducibility in young healthy adults. *J. Magn. Res. Imaging* 34: 880–886.

99 Warner, L., Yin, M., Glaser, K.J., et al. (2011). Noninvasive in vivo assessment of renal tissue elasticity during graded renal ischemia using MR elastography. *Invest. Radiol.* 46: 509–514.

100 Samir, A.E., Allegretti, A.S., Zhu, Q.L., et al. (2015). Shear wave elastography in chronic kidney disease: a pilot experience in native kidneys. *BMC Nephrol.* 16: 119.

101 Asano, K., Ogata, A., Tanaka, K., et al. (2014). Acoustic radiation force impulse elastography of the kidneys: is shear wave velocity affected by tissue fibrosis or renal blood flow? *J. Ultrasound Med.* 33: 793–801.

102 Guo, L.-H., Xu, H.-X., Fu, H.-J., et al. (2013). Acoustic radiation force impulse imaging for noninvasive evaluation of renal parenchyma elasticity: preliminary findings. *PLoS One* 8: e68925.

103 Hu, Q., Wang, X.-Y., He, H.-G., et al. (2014). Acoustic radiation force impulse imaging for non-invasive assessment of renal histopathology in chronic kidney disease. *PLoS One* 9: e115051.

104 Arndt, R., Schmidt, S., Loddenkemper, C., et al. (2010). Noninvasive evaluation of renal allograft fibrosis by transient elastography – a pilot study. *Transplant Int.* 23: 871–877.

105 Syversveen, T., Brabrand. K., Midtvedt, K., et al. (2011). Assessment of renal allograft fibrosis by acoustic radiation force impulse quantification – a pilot study. *Transplant Int.* 24: 100–105.

106 Stock, K.F., Klein, B.S., Vo Cong, M.T., et al. (2010). ARFI-based tissue elasticity quantification in comparison to histology for the diagnosis of renal transplant fibrosis. *Clin. Hemorheol. Microcirc.* 46: 139–148.

107 Farshad, M., Barbezat, M., Flüeler, P., et al. (1999). Material characterization of the pig kidney in relation with the biomechanical analysis of renal trauma. *J. Biomech.* 32: 417–425.

108 Miller, K. (2000). Constitutive modelling of abdominal organs. *J. Biomech.* 33: 367–373.

109 Nasseri, S., Bilston, L.E., and Phan-Thien, N. (2002). Viscoelastic properties of pig kidney in shear, experimental results and modelling. *Rheolog. Acta* 41: 180–192.

110 Bschleipfer, T., Kallieris, D., Hauck, E.W., et al. (2002). Blunt renal trauma: biomechanics and origination of renal lesions. *Eur. Urol.* 42: 614–621.

111 Snedeker, J.G., Barbezat, M., Niederer, P., et al. (2005). Strain energy density as a rupture criterion for the kidney: impact tests on porcine organs, finite element simulation, and a baseline comparison between human and porcine tissues. *J. Biomech.* 38: 993–1001.

112 Pislaru, C., Abraham, T.P., and Belohlavek, M. (2002). Strain and strain rate echocardiography. *Curr. Opin. Cardiol.* 17: 443–454.

113 Pislaru, C., Bruce, C.J., Anagnostopoulos, P.C., et al. (2004). Ultrasound strain imaging of altered myocardial stiffness: stunned versus infarcted reperfused myocardium. *Circulation* 109: 2905–2910.

114 D'Hooge, J., Konofagou, E., Jamal, F., et al. (2002). Two-dimensional ultrasonic strain rate measurement of the human heart in vivo. *IEEE Trans. Ultrason., Ferroelectr., Freq. Control* 49: 281–286.

115 Sutherland, G.R., Di Salvo, G., Claus, P., et al. (2004). Strain and strain rate imaging: a new clinical approach to quantifying regional myocardial function. *J. Am. Soc. Echocardiogr.* 17: 788–802.

116 Konofagou, E.E., D'Hooge, J., and Ophir, J. (2002). Myocardial elastography – a feasibility study in vivo. *Ultrasound Med. Biol.* 28: 475–482.

117 Pernot, M., Fujikura, K., Fung-Kee-Fung, S.D., and Konofagou, E.E. (2007). ECG-gated, mechanical and electromechanical wave imaging of cardiovascular tissues in vivo. *Ultrasound Med. Biol.* 33: 1075–1085.

118 Luo, J.W., Fujikura, K., Homma, S., and Konofagou, E.E. (2007). Myocardial elastography at both high temporal and spatial resolution for the detection of infarcts. *Ultrasound Med. Biol.* 33: 1206–1223.

119 Qian, Z., Lee, W.-N., Konofagou, E.E., et al. (2007). Ultrasound myocardial elastography and registered 3D tagged MRI: quantitative strain comparison. *In* 10th International Conference on Medical Image Computing and Computer-assisted Intervention, Brisbane, Australia.

120 Provost, J., Lee, W.N., Fujikura, K., and Konofagou, E.E. (2010). Electromechanical wave imaging of normal and ischemic hearts in vivo. *IEEE Trans. Med. Imaging* 29: 625–635.

121 Provost, J., Nguyen, V.T.-H., Legrand, D., et al. (2011). Electromechanical wave imaging for arrhythmias. *Phys. Med. Biol.* 56: L1.

122 Provost, J., Lee, W.-N., Fujikura, K., and Konofagou, E.E. (2011). Imaging the electromechanical activity of the heart in vivo. *Proc. Natl. Acad. Sci. USA* 108: 8565–8570.

123 Kanai, H. (2005). Propagation of spontaneously actuated pulsive vibration in human heart wall and in vivo viscoelasticity estimation. *IEEE Trans. Ultrason., Ferroelectr., Freq. Control* 52: 1931–1942.

124 Nenadic, I.Z., Urban, M.W., Mitchell, S.A., and Greenleaf, J.F. (2011). Lamb wave dispersion ultrasound vibrometry (LDUV) method for quantifying mechanical properties of viscoelastic solids. *Phys. Med. Biol.* 56: 2245.

125 Nenadic, I.Z., Urban, M.W., Aristizabal, S., et al. (2011). On Lamb and Rayleigh wave convergence in viscoelastic tissues. *Phys. Med. Biol.* 56: 6723–6738.

126 Nenadic, I.Z., Urban, M.W., Bernal, M., and Greenleaf, J.F. (2011). Phase velocities and attentuations of shear, Lamb, and Rayleigh waves in plate-like tissues submerged in a fluid. *J. Acoust. Soc. Am.* 130: 3549–3552.

127 Urban, M.W., Pislaru, C., Nenadic, I.Z., et al. (2013). Measurement of viscoelastic properties of in vivo swine myocardium using Lamb wave dispersion ultrasound vibrometry (LDUV). *IEEE Trans. Med. Imaging* 32: 247–261.

128 Pislaru, C., Urban, M.W., Pislaru, S.V., et al. (2014). Viscoelastic properties of normal and infarcted myocardium measured by a multifrequency shear wave method: comparison with pressure-segment length method. *Ultrasound Med. Biol.* 40: 1785–1795.

129 Couade, M., Pernot, M., Messas, E., et al. (2011). In vivo quantitative mapping of myocardial stiffening and transmural anisotropy during the cardiac cycle. *IEEE Trans. Med. Imaging* 30: 295–305.

130 Bouchard, R.R., Hsu, S.J., Wolf, P.D., and Trahey, G.E. (2009). In vivo cardiac, acoustic-radiation-force-driven, shear wave velocimetry. *Ultrason. Imaging* 31: 201–213.

131 Pernot, M., Couade, M., Mateo, P., et al. (2011). Real-time assessment of myocardial contractility using shear wave imaging. *J. Am. Coll. Cardiol.* 58: 65–72.

132 Vejdani-Jahromi, M., Nagle, M., Trahey, G.E., and Wolf, P.D. (2015). Ultrasound shear wave elasticity imaging quantifies coronary perfusion pressure effect on cardiac compliance. *IEEE Trans. Med. Imaging* 34: 465–473.

133 Hollender, P.J., Wolf, P.D., Goswami, R., and Trahey, G.E. (2012). Intracardiac echocardiography measurement of dynamic myocardial stiffness with shear wave velocimetry. *Ultrasound Med. Biol.* 38: 1271–1283.

134 Hollender, P., Bradway, D., Wolf, P., et al. (2013). Intracardiac acoustic radiation force impulse (ARFI) and shear wave imaging in pigs with focal infarctions. *IEEE Trans. Ultrason., Ferroelectr., Freq. Control* 60: 1669–1682.

135 Song, P., Zhao, H., Urban, M.W., et al. (2013). Improved shear wave motion detection using pulse-inversion harmonic imaging with a phased array transducer. *IEEE Trans. Med. Imaging* 32: 2299–2310.

136 Streeter, D.D., Spotnitz, H.M., Patel, D.P., et al. (1969). Fiber orientation in the canine left ventricle during diastole and systole. *Circ. Res.* 24: 339–347.

137 Lee, W.N., Pernot, M., Couade, M., et al. (2012). Mapping myocardial fiber orientation using echocardiography-based shear wave imaging. *IEEE Trans. Med. Imaging* 31: 554–562.

138 Lee, W.-N., Larrat, B., Pernot, M., and Tanter, M. (2012). Ultrasound elastic tensor imaging: comparison with MR diffusion tensor imaging in the myocardium. *Phys. Med. Biol.* 57: 5075–5095.

139 Aristizabal, S., Amador, C., Qiang, B., et al. (2014). Shear wave vibrometry evaluation in transverse isotropic tissue mimicking phantoms and skeletal muscle. *Phys. Med. Biol.* 59: 7735–7752.

140 Woodrum, D.A., Romano, A.J., Lerman, A., et al. (2006). Vascular wall elasticity measurement by magnetic resonance imaging. *Magn. Reson. Med.* 56: 593–600.

141 Woodrum, D.A., Herrmann, J., Lerman, A., et al. (2009). Phase-contrast MRI-based elastography technique detects early hypertensive changes in ex vivo porcine aortic wall. *J. Magn. Reson. Imaging* 29: 583–587.

142 Kolipaka, A., Woodrum, D., Araoz, P.A., and Ehman, R.L. (2012). MR elastography of the in vivo abdominal aorta: A feasibility study for comparing aortic stiffness between hypertensives and normotensives. *J. Magn. Reson. Imaging* 35: 582–586.

143 Xu, L., Chen, J., Yin, M., et al. (2012). Assessment of stiffness changes in the ex vivo porcine aortic wall using magnetic resonance elastography. *Magn. Reson. Imaging* 30: 122–127.

144 Luo, J.W., Fujikura, K., Tyrie, L.S., et al. (2009). Pulse wave imaging of normal and aneurysmal abdominal aortas in vivo. *IEEE Trans. Med. Imaging* 28: 477–486.

145 Vappou, J., Luo, J.W., and Konofagou, E.E. (2010). Pulse wave imaging for noninvasive and quantitative measurement of arterial stiffness in vivo. *Am. J. Hypertension* 23: 393–398.

146 Luo, J., Li, R.X., and Konofagou, E.E. (2012). Pulse wave imaging of the human carotid artery: an in vivo feasibility study. *IEEE Trans. Ultrason., Ferroelectr., Freq. Control* 59: 174–181.

147 Konofagou, E., Lee, W.-N., Luo, J., et al. (2011). Physiologic cardiovascular strain and intrinsic wave imaging. *Annu. Rev. Biomed. Eng.* 13: 477–505.

148 Couade, M., Pernot, M., Prada, C., et al. (2010). Quantitative assessment of arterial wall biomechanical properties using shear wave imaging. *Ultrasound Med. Biol.* 36: 1662–1676.

149 Fatemi, M. and Greenleaf, J.F. (1998). Ultrasound-stimulated vibro-acoustic spectrography. *Science* 280: 82–85.

150 Alizad, A., Fatemi, M., Whaley, D.H., and Greenleaf, J.F. (2004). Application of vibro-acoustography for detection of calcified arteries in breast tissue. *J. Ultrasound Med.* 23: 267–273.

151 Pislaru, C., Kantor, B., Kinnick, R.R., et al. (2008). In vivo vibroacoustography of large peripheral arteries. *Invest. Radiol.* 43: 243–252.

152 Chen, S., Fatemi, M., and Greenleaf, J.F. (2004). Quantifying elasticity and viscosity from measurement of shear wave speed dispersion. *J. Acoust. Soc. Am.* 115: 2781–2785.

153 Zhang, X., Fatemi, M., Kinnick, R.R., and Greenleaf, J.F. (2003). Noncontact ultrasound stimulated optical vibrometry study of coupled vibration of arterial tubes in fluids. *J. Acoust. Soc. Am.* 113: 1249–1257.

154 Zhang, X., Kinnick, R.R., Fatemi, M., and Greenleaf, J.F. (2005). Noninvasive method for estimation of complex elastic modulus of arterial vessels. *IEEE Trans. Ultrason., Ferroelectr., Freq. Control* 52: 642–652.

155 Zhang, X. and Greenleaf, J.F. (2006). Estimation of complex arterial elastic modulus from ring resonance excited by ultrasound radiation force. *Ultrasonics* 44: e169–e172.

156 Zhang, X. and Greenleaf, J.F. (2006). Generation of a torsion wave and measuring its propagation velocity in the circumferential direction of arterial wall. *Ultrasonics* 44: e165–e168.

157 Zhang, X. and Greenleaf, J.F. (2006). Noninvasive generation and measurement of propagating waves in arterial walls. *J. Acoust. Soc. Am.* 119: 1238–1243.

158 Zhang, X. and Greenleaf, J.F. (2006). Measurement of wave velocity in arterial walls with ultrasound transducers. *Ultrasound Med. Biol.* 32: 1655–1660.

159 Bernal, M., Nenadic, I., Urban, M.W., and Greenleaf, J.F. (2011). Material property estimation for tubes and arteries using ultrasound radiation force and analysis of propagating modes. *J. Acoust. Soc. Am.* 129: 1344–1354.

160 Dutta, P., Urban, M.W., Le Maitre, O.P., et al. (2015). Simultaneous identification of elastic properties, thickness, and diameter of arteries excited with ultrasound radiation force. *Phys. Med. Biol.* 60: 5279–5296.

161 Maksuti, E., Widman, E., Larsson, D., et al. (2016). Arterial stiffness estimation by shear wave elastography: validation in phantoms with mechanical testing. *Ultrasound Med. Biol.* 42: 308–321.

162 Maurice, R.L., Ohayon, J., Fretigny, Y., et al. (2004). Noninvasive vascular elastography: theoretical framework. *IEEE Trans. Med. Imaging* 23: 164–180.

163 Schmitt, C., Soulez, G., Maurice, R.L., et al. (2007). Noninvasive vascular elastography: toward a complementary characterization tool of atherosclerosis in carotid arteries. *Ultrasound Med. Biol.* 33: 1841–1858.

164 Fromageau, J., Lerouge, S., Maurice, R.L., et al. (2008). Noninvasive vascular ultrasound elastography applied to the characterization of experimental aneurysms and follow-up after endovascular repair. *Phys. Med. Biol.* 53: 6475–6490.

165 Mercure, E., Deprez, J.-F., Fromageau, J., et al. (2011). A compensative model for the angle-dependence of motion estimates in noninvasive vascular elastography. *Med. Phys.* 38: 727–735.

166 Korukonda, S. and Doyley, M.M. (2011). Estimating axial and lateral strain using a synthetic aperture elastographic imaging system. *Ultrasound Med. Biol.* 37: 1893–1908.

167 Korukonda, S. and Doyley, M.M. (2012). Visualizing the radial and circumferential strain distribution within vessel phantoms using synthetic-aperture ultrasound elastography. *IEEE Trans. Ultrason., Ferroelectr., Freq. Control* 59: 1639–1653.

168 Korukonda, S., Nayak, R., Carson, N., et al. (2013). Noninvasive vascular elastography using plane–wave and sparse-array imaging. *IEEE Trans. Ultrason., Ferroelectr., Freq. Control* 60: 332–342.

169 Hansen, H., Richards, M., Doyley, M., and Korte, C. (2013). Noninvasive vascular displacement estimation for relative elastic modulus reconstruction in transversal imaging planes. *Sensors* 13: 3341–3357.

170 Hansen, H.H.G., Saris, A.E.C.M., Vaka, N.R., et al. (2014). Ultrafast vascular strain compounding using plane wave transmission. *J. Biomech.* 47: 815–823.

171 Wan, J., He, F., Zhao, Y., et al. (2014). Non-invasive vascular radial/circumferential strain imaging and wall shear rate estimation using video images of diagnostic ultrasound. *Ultrasound Med. Biol.* 40: 622–636.

172 Larsson, M., Verbrugghe, P., Smoljkić, M., et al. (2015). Strain assessment in the carotid artery wall using ultrasound speckle tracking: validation in a sheep model. *Phys. Med. Biol.* 60: 1107.

173 Larsson, M., Kremer, F., Claus, P., et al. (2011). Ultrasound-based radial and longitudinal strain estimation of the carotid artery: a feasibility study. *IEEE Trans. Ultrason., Ferroelectr., Freq. Control* 58: 2244–2251.

174 Larsson, M., Heyde, B., Kremer, F., et al. (2015). Ultrasound speckle tracking for radial, longitudinal and circumferential strain estimation of the carotid artery – An in vitro validation via sonomicrometry using clinical and high-frequency ultrasound. *Ultrasonics* 56: 399–408.

175 Widman, E., Caidahl, K., Heyde, B., et al. (2015). Ultrasound speckle tracking strain estimation of in vivo carotid artery plaque with in vitro sonomicrometry validation. *Ultrasound Med. Biol.* 41: 77–88.

176 De Korte, C.L., Cespedes, E.I., van der Steen, A.F.W., et al. (1998). Intravascular ultrasound elastography: assessment and imaging of elastic properties of diseased arteries and vulnerable plaque. *Eur. J. Ultrasound* 7: 219–224.

177 Schaar, J.A., De Korte, C.L., Mastik, F., et al. (2003). Intravascular palpography for high-risk vulnerable plaque assessment. *Herz* 28: 488–495.

178 Schaar, J.A., De Korte, C.L., Mastik, F., et al. (2005). Three-dimensional palpography of human coronary arteries. *Ex vivo validation and in-patient evaluation. Herz* 30: 125–133.

179 Majdouline, Y., Ohayon, J., Keshavarz-Motamed, Z., et al. (2014). Endovascular shear strain elastography for the detection and characterization of the severity of atherosclerotic plaques: in vitro validation and in vivo evaluation. *Ultrasound Med. Biol.* 40: 890–903.

180 Richards, M.S., Jing, S., and Doyley, M.M. (2010). Visualization of atherosclerotic plaque mechanical properties using model based intravascular ultrasound elastography. *J. Acoust. Soc. Am.* 127: 1730–1730.

181 Richards, M.S. and Doyley, M.M. (2011). Investigating the impact of spatial priors on the performance of model-based IVUS elastography. *Phys. Med. Biol.* 56: 7223–7246.

182 Richards, M.S. and Doyley, M.M. (2013). Non-rigid image registration based strain estimator for intravascular ultrasound elastography. *Ultrasound Med. Biol.* 39: 515–533.

183 Liang, Y., Zhu, H., and Friedman, M.H. (2008). Estimation of the transverse strain tensor in the arterial wall using IVUS image registration. *Ultrasound Med. Biol.* 34: 1832–1845.

184 Maurice, R.L., Brusseau, É., Finet, G., and Cloutier, G. (2005). On the potential of the Lagrangian speckle model estimator to characterize atherosclerotic plaques in endovascular elastography: In vitro experiments using an excised human carotid artery. *Ultrasound Med. Biol.* 31: 85–91.

185 Maurice, R.L., Fromageau, J., Cardinal, M.H., et al. (2008). Characterization of atherosclerotic plaques and mural thrombi with intravascular ultrasound elastography: a potential method evaluated in an aortic rabbit model and a human coronary artery. *IEEE Trans Inf. Tech Biomed.* 12: 290–298.

186 Doyley, M.M., Mastik, F., De Korte, C.L., et al. (2001). Advancing intravascular ultrasonic palpation toward clinical applications. *Ultrasound Med. Biol.* 27: 1471–1480.

187 Baldewsing, R.A., Schaar, J.A., Mastik, F., et al. (2005). Assessment of vulnerable plaque composition by matching the deformation of a parametric plaque model to measured plaque deformation. *IEEE Trans. Med. Imaging* 24: 514–528.

188 Trahey, G.E., Palmeri, M.L., Bentley, R.C., and Nightingale, K.R. (2004). Acoustic radiation force impulse imaging of the mechanical properties of arteries: in vivo and ex vivo results. *Ultrasound Med. Biol.* 30: 1163–1171.

189 Dahl, J.J., Dumont, D.M., Allen, J.D., et al. (2009). Acoustic radiation force impulse imaging for noninvasive characterization of carotid artery atherosclerotic plaques: a feasibility study. *Ultrasound Med. Biol.* 35: 707–716.

190 Dumont, D., Behler, R.H., Nichols, T.C., et al. (2006). ARFI imaging for noninvasive material characterization of atherosclerosis. *Ultrasound Med. Biol.* 32: 1703–1711.

191 Behler, R.H., Nichols, T.C., Merricks, E.R., and Gallippi, C.M. (2007). ARFI ultrasound for enhanced delineation of atherosclerosis in women. *J. Womens Health* 16: 1112–1113.

192 Behler, R., Nichols, T., Merricks, E., and Gallippi, C. (2008). ARFI ultrasound for discrimination of calcification in arterial plaques: additional progress toward improved atherosclerosis imaging in women. *J. Womens Health* 17: 1243–1243.

193 Behler, R.H., Nichols, T.C., Zhu, H.T., et al. (2009). ARFI imaging for noninvasive material characterization of atherosclerosis part II: toward in vivo characterization. *Ultrasound Med. Biol.* 35: 278–295.

194 Allen, J.D., Ham, K.L., Dumont, D.M., et al. (2011). The development and potential of acoustic radiation force impulse (ARFI) imaging for carotid artery plaque characterization. *Vasc. Med.* 16: 302–311.

195 Doherty, J.R., Dumont, D.M., Trahey, G.E., and Palmeri, M.L. (2013). Acoustic radiation force impulse imaging of vulnerable plaques: a finite element method parametric analysis. *J. Biomech.* 46: 83–90.

196 Patel, V., Dahl, J.J., Bradway, D.P., et al. (2014). Acoustic radiation force impulse imaging (ARFI) on an IVUS circular array. *Ultrason. Imaging* 36: 98–111.

197 Doherty, J.R., Dahl, J.J., and Trahey, G.E. (2013). Harmonic tracking of acoustic radiation force-induced displacements. *IEEE Trans. Ultrason., Ferroelectr., Freq. Control* 60: 2347–2358.

198 Ramnarine, K.V., Garrard, J.W., Dexter, K., et al. (2014). Shear wave elastography assessment of carotid plaque stiffness: in vitro reproducibility study. *Ultrasound Med. Biol.* 40: 200–209.

199 Ramnarine, K.V., Garrard, J.W., Kanber, B., et al. (2014). Shear wave elastography imaging of carotid plaques: feasible, reproducible and of clinical potential. *Cardiovasc. Ultrasound* 12: 49.

200 Widman, E., Maksuti, E., Larrsson, D., et al. (2015). Shear wave elastography plaque characterization with mechanical testing validation – a phantom study. *Phys. Med. Biol.* 60: 3151–3174.

31

Abdominal Applications of Shear Wave Ultrasound Vibrometry and Supersonic Shear Imaging

Pengfei Song and Shigao Chen

Department of Radiology, Mayo Clinic, Rochester, MN, USA

31.1 Introduction

Abdominal applications have been one of the major research and clinical interests of shear wave elastography since the birth of the technology. Many abdominal pathological conditions present abnormal tissue mechanical properties such as elevated stiffness, which can be quantitatively and noninvasively characterized by ultrasound shear wave imaging. To date, abdominal application of shear wave imaging has been investigated and reported in liver, prostate, kidney, intestine, uterine cervix, spleen, pancreas, and bladder, with active ongoing explorations of other abdominal applications. In this chapter, we provide brief technical and clinical reviews of each of the above-mentioned abdominal applications.

31.2 Liver Application

At present, liver application is the most significant and well-established field of ultrasound shear wave imaging research, owing to the longer period of time that shear wave elastography has been investigated in liver. Several seminal reviews of liver shear wave elastography and clinical guidelines by different organizations have been published [1–7]. Readers can refer to these reviews and guidelines for in-depth technical and clinical details. In parallel to liver ultrasound shear wave research, a large body of liver shear wave elastography research based on magnetic resonance elastography (MRE) is also under active development and investigation [8–11].

One key application of liver shear wave imaging is fibrosis staging of chronic liver disease [3]. Liver fibrosis is represented by deposition of collagen and other components of the extracellular matrix in response to chronic injury [3], which results in increased liver stiffness. Currently the clinical gold standard for fibrosis staging is biopsy, which is invasive and suffers from sampling variability. On the other hand, liver shear wave elastography provides noninvasive and quantitative measurement of liver stiffness. It has been shown that shear wave measurements are strongly correlated to the biopsy staging results (Figure 31.1) and can potentially be used to stage liver fibrosis with high sensitivity and specificity [9, 12–18].

Various ultrasound shear wave imaging techniques have been developed and implemented in liver application, including transient elastography [19, 20] (Figure 31.2a), acoustic radiation force (ARF)-based point shear wave elastography (pSWE) [3, 21–24] (Figure 31.2b),

Ultrasound Elastography for Biomedical Applications and Medicine, First Edition.
Edited by Ivan Nenadic, Matthew Urban, James Greenleaf, Jean-Luc Gennisson, Miguel Bernal, and Mickael Tanter.

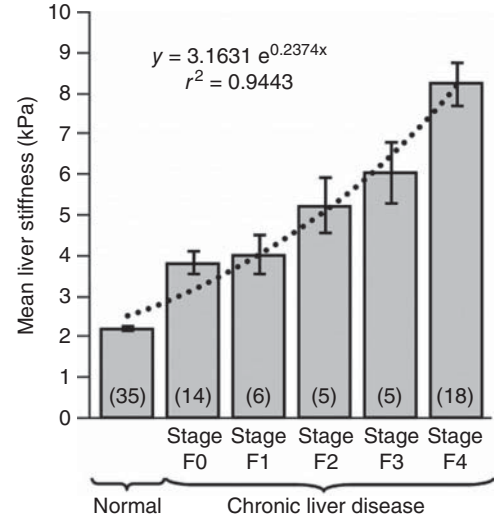

Figure 31.1 Mean liver stiffness with increased fibrosis stage in patients. Source: reprinted from [9], copyright 2007, with permission from Elsevier.

two-dimensional ultrasound shear wave elastography based on ARF [12, 25–27] (Figures 31.2c and 31.2d), and external mechanical vibration [28, 29]. Among these techniques, transient elastography and mechanical vibration-based methods produce shear waves externally and use ultrasound to track the shear wave motion. These methods have superior penetration performance compared to ARF-based techniques. The advantage of the ARF-based techniques is that no external wave source is needed: the same transducer can be used to both generate and track shear waves. However, these techniques may suffer from low success rate among obese patients. For both transient elastography and pSWE, a single shear elasticity value is reported per data acquisition (Figures 31.2a and 31.2b). For 2D shear wave elastography methods, a 2D shear elasticity map can be produced (Figures 31.2c and 31.2d). While both point and 2D measurements are suitable for diffuse liver diseases such as fibrosis, the 2D methods may be more beneficial for focal liver diseases such as hepatocellular carcinoma (HCC).

Among these different imaging techniques, different quantities are being reported, including shear wave speed (c_s), shear modulus or shear elasticity or shear stiffness (μ), and Young's modulus (E). It is commonly assumed that soft tissues including liver are pure elastic, isotropic, and incompressible, and therefore

$$E = 3\mu = 3\rho c_s^2 \tag{31.1}$$

where ρ is the density of the tissue and can be assumed to be 1000 kg/m^3. One can use Eq. (31.1) to conveniently convert from one stiffness quantity to another.

In addition to shear elasticity measurement using shear waves, shear waves can also be used quantify tissue viscosity from the shear wave dispersion curve [24, 30, 31]. Like other soft tissues, liver is viscoelastic and shear wave speed of the liver is frequency dependent [30] (Figure 31.3). The frequency-dependent shear wave dispersion can potentially be used to diagnose early-stage fatty liver disease [32, 33]. Viscosity has also been reported to be used for fibrosis staging, but with poorer diagnosing performance than elasticity [24, 34]. One possible reason of the poor performance of using viscosity in vivo is the suboptimal shear wave signal quality obtained from in vivo tissue, which makes accurate estimate of tissue viscosity challenging. Nevertheless, because shear wave speed is frequency dependent in liver (Figure 31.3), one should account for the difference of the frequency of the shear waves when reporting shear wave speed measurements using different techniques and determining cutoff values for fibrosis staging.

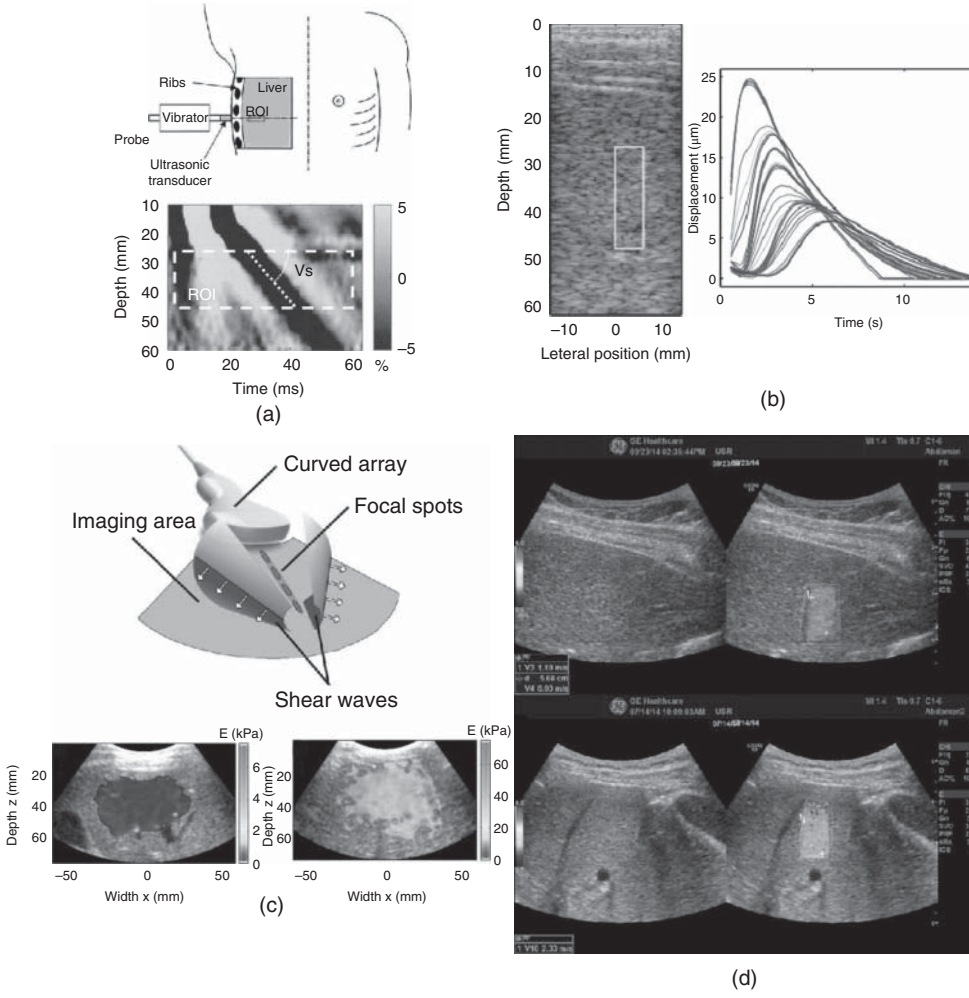

Figure 31.2 (a) Upper panel: schematic plot of probe positioning for liver elasticity measurements using transient elastography; lower panel: the resulting shear wave signal and ROI selection for shear wave speed (V_s) measurement. Reprinted from [20]. Copyright 2003, with permission from Elsevier. (b) pSWE (a.k.a. acoustic radiation force impulse (ARFI) shear wave imaging) data acquisition (left panel) from the ROI positioned inside the liver; right panel: shear wave signals recorded inside the ROI from which shear wave speed is calculated based on time-to-peak. Reprinted from [21]. Copyright 2008, with permission from Elsevier. (c) 2D shear wave elastography with the supersonic imaging (SSI) technique (upper panel) and examples of 2D liver shear modulus maps (lower panel) from a healthy liver (left) and fibrotic liver (right). Reprinted from [12]. Copyright 2011, with permission from Elsevier. (d) 2D shear wave elastography with the comb-push ultrasound shear elastography (CUSE) technique and shear wave speed maps of a normal liver (above) and a fibrotic liver with advanced fibrosis (below). Source: republished with permission from [27]; permission conveyed through Copyright Clearance Center, Inc.

31.3 Prostate Application

Prostate cancer is a common disease in men worldwide. Serum prostate-specific antigen (PSA) tests and ultrasound-guided biopsy are clinical standards for diagnosing prostate cancer but suffer from poor diagnosis accuracy and are invasive [35]. Ultrasound shear wave elastography can provide quantitative measurement of the tissue stiffness and potentially differentiate benign and malignant tumors [36–38]. The majority of the current prostate cancer shear wave studies

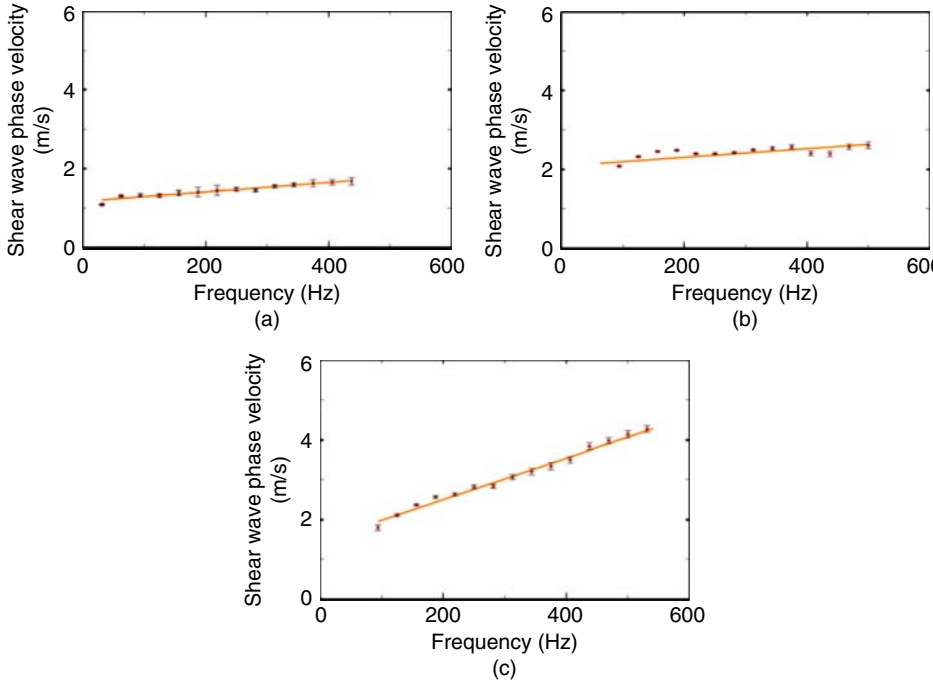

Figure 31.3 Shear wave dispersion curves for (a) a stage F1 patient liver and (b), (c) two stage F3 patient livers. The slope of the dispersion curve is 1.21 mm for (a), 1.09 mm for (b), and 5.17 mm for (c). Source: reprinted from [12], copyright 2011, with permission from Elsevier.

used the transrectal ultrasound transducer equipped with real-time 2D shear wave elastography function based on supersonic shear imaging [25]. Barr et al. reported a prostate cancer diagnosing sensitivity of 96.2%, specificity of 96.2%, positive predictive value (PPV) of 69.4%, and negative predictive value (NPV) of 99.6% when using a cutoff value of 37 kPa from 53 patients [36]. Woo et al. used a mean stiffness cutoff value of 43.9 kPa and reported 60.8% sensitivity and 66.4% specificity, with an AUC of 0.599 from 87 patients [35]. Ahmad et al. studied 50 patients and reported a sensitivity of 90% and a specificity of 88% for patients with PSA < 20 μg/L; and a sensitivity of 93% and specificity of 93% for patients with PSA > 20 μg/L. Recently, Correas et al. reported a large scale study in 184 men and reported 96% sensitivity, 85% specificity, 48% PPV, 99% NPV, and 95% AUC when using a stiffness cutoff value of 35 kPa [38]. Woo et al. also demonstrated excellent intra-observer reproducibility of the shear wave elastography technique in prostate with an interclass correlation coefficient (ICC) of 0.876 [39]. Overall, shear wave elastography is a very promising tool for the detection and biopsy of prostate cancer. The high NPV has been reported by multiple studies, which is particularly useful to reduce the biopsy rate clinically [36].

31.4 Kidney Application

Kidney viscoelasticity is an important biomarker for renal dysfunction and renal fibrosis. To date many studies of implementing shear wave imaging on kidney have been reported both in vivo and in vitro, and both in animal models and in humans [40–50]. Kidney is a particularly challenging tissue for ultrasound shear wave elastography because of the anisotropic nature of the kidney tissue and the various vascular and urinary pressure levels, both of which can change

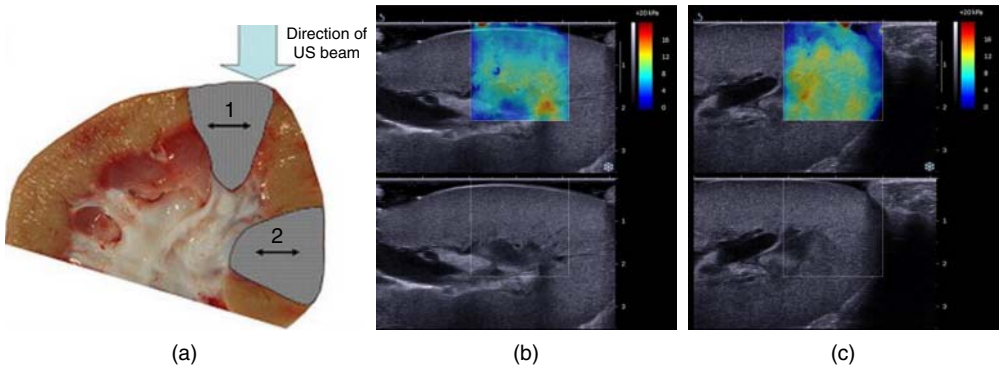

Figure 31.4 (a) Image of a lower half of a pig kidney. In region 1 shear waves propagate across the renal fibers and in region 2 shear waves propagate along the renal fibers. (b) Shear elasticity map of region 1 in part (a). (c) Shear elasticity map of region 2 in part (a). Shear wave speed is higher along the fiber orientation than across the fiber orientation. Source: reprinted from [40], copyright 2012, with permission from Elsevier.

the shear wave speed measurement significantly [40, 42] (Figure 31.4). Gennisson et al. showed that both cortical and medullary elasticity values were higher when shear waves propagate along the renal fiber than across the fiber (7.7 ± 2.3 kPa vs. 6.9 ± 1.4 kPa for cortex; 8.7 ± 2.5 kPa vs. 6.6 ±2.3 kPa for medulla) [40]. They also showed that inner cortex was stiffer than outer cortex, and parenchymal elasticity changed significantly with vascular and urinary pressure levels. These factors need to be accounted for when using shear wave elastography for kidney disease diagnosis. Another significant challenge for kidney shear wave application is that native human kidneys are typically deep from the body surface, which makes robust shear wave generation and detection challenging. This is one main reason why the majority of the studies reported to date were from kidney transplants [44–47, 49]. Among these studies, Syversveen et al. used pSWE techniques (ARFI quantification) to quantify kidney transplant stiffness and found no correlation between shear wave speed and kidney fibrosis [44, 45]; Grenier et al. used 2D SWE techniques based on supersonic shear imaging (SSI) and also reported no significant correlation between renal cortical stiffness and fibrosis [46]. On the other hand, Arndt et al. used the transient elastography technique to evaluate renal allograft fibrosis and found significant correlation between stiffness and the extent of interstitial fibrosis [47]; Gennisson et al. used 2D SWE based on SSI and found moderate correlation between correlation between kidney stiffness and fibrosis [49]. In addition to the technical challenges mentioned above that may have resulted in these controversial results, it was noted that kidney pathology leading to transplant failures may impact the outcome of the kidney stiffness [49]. Also, the relatively low intra- and inter-observer agreement still remains as a critical challenge for robust estimate of transplant kidney stiffness [44–46].

31.5 Intestine Application

Crohn's disease (or inflammatory bowel disease, IBD) is the major clinical application for ultrasound shear wave elastography. The use is to differentiate intestinal inflammation from fibrosis; this is a clinically significant yet challenging task that lacks robust biomarkers [51]. Early ultrasound elastography studies using strain elastography (qualitative approach) revealed the feasibility of differentiating between inflammatory from fibrotic intestine in rat models but not in human with Crohn's disease [51]. Recently, Dillman et al. used 2D shear wave elastography based on ARFI shear wave imaging techniques to distinguish inflammation from fibrosis in a

Crohn's disease animal model [52]. The study showed elevated tissue stiffness with both acute inflammation and fibrosis and by using the ratio of shear wave speed to applied strain, one can well differentiate inflammation from fibrosis with an AUC of 0.971. Another study by Dillman et al. on ex vivo human intestinal specimens revealed that point pSWE and 2D SWE methods can distinguish low- from high-fibrosis score bowel segments [53]. At present, no in vivo human studies on Crohn's disease with shear wave elastography have been reported.

31.6 Uterine Cervix Application

Quantification of cervical stiffness using ultrasound shear wave elastography can be a promising tool for screening and treatment for preterm birth prevention [54]. The cervix softens in preparation for delivery. Shear wave elastography has been used to assess cervical stiffness on ex vivo human samples [55, 56]. These studies found that cervical tissues were highly anisotropic and unripened cervical tissue was significantly stiffer than the ripened cervical tissue. Gennisson et al. studied 21 women using the 2D shear wave elastography technique based on SSI and found that normal cervix is stiffer than pathological cervix (19.0 ± 18.6 kPa vs. 7.0 ± 3.0 kPa) [57]. It was also shown by Gennisson et al. [57] that uterus contraction could be imaged in real time using the 2D SWE technique. Meanwhile, better shear wave imaging methods for uterine cervix application are also being developed [58].

31.7 Spleen Application

Spleen stiffness can be used to predict the presence of liver cirrhosis and the severity of esophageal varices [59–61]. A MRE study also showed that splenic stiffness was correlated with portal hypertension [62]. Among the ultrasound shear wave studies, Bota et al. showed that cirrhotic patients' spleens are significantly stiffer than those of the healthy patients (3.10 ± 0.55 m/s vs. 2.04 ± 0.28 m/s) and with a cutoff value of > 2.51 m/s, pSWE based on ARFI had 85.2% sensitivity, 91.7% specificity, 95.8% PPV, 73.3% NPV, 87.1% accuracy, and AUC of 0.91 [59]. Grgurevic et al. also used pSWE based on ARFI and showed that with a cutoff of 2.73 m/s, spleen stiffness could be used differentiate patients with liver cirrhosis and non-cirrhotic chronic viral hepatitis with AUC of 0.82 [63]. Ye et al. used ARFI-based pSWE techniques on spleen and found that spleen stiffness can be used to differentiate stage 4 liver fibrosis with a cutoff of 2.72 m/s (AUC = 0.96), and that the spleen stiffness correlated linearly with the varix grade [60]. Leung et al. used SSI-based 2D SWE techniques and transient elastography to evaluate both liver and spleen stiffness among 226 liver patients and 171 healthy subjects, and found that combining spleen stiffness with liver stiffness did not further improve the diagnostic accuracy of fibrosis staging [64]. Cassinotto et al. also used SSI-based 2D SWE approachs to evaluate cirrhosis and oesophageal varices and found relatively high failure rate of measuring spleen stiffness although spleen stiffness showed promising results for the detection of esophageal varices [61]. Further studies are necessary to develop more robust techniques for measuring spleen stiffness.

31.8 Pancreas Application

To date, most of the pancreas elastography studies used strain-based elastography techniques with endoscopic ultrasound transducers [65–67]. These studies support the use of shear wave

elastography to quantify the stiffness of the pancreas for various disease diagnoses. Pancreas shear wave speed from healthy subjects was measured by 2D SSI-based shear wave elastography and reported as 4.8 ± 3 kPa [68]. D'Onofrio et al. used pSWE to quantify pancreatic cystic lesions and found that shear wave speed can be used to differentiate more complex (mucinous) from simple (serous) content in the cystic lesions [69].

31.9 Bladder Application

Ultrasound shear wave elastography can be used to quantify both the elasticity and the viscosity of the bladder wall, which can be used to evaluate variations of bladder stiffness and understand various diseases. Nenadic et al. reported the use of ultrasound bladder vibrometry (UBV) to measure both the elasticity and viscosity of the bladder wall and showed good correlations between elasticity and bladder volume and pressure [70]. An in vivo pig study demonstrated the feasibility of translating this technique to the clinic (Figure 31.5).

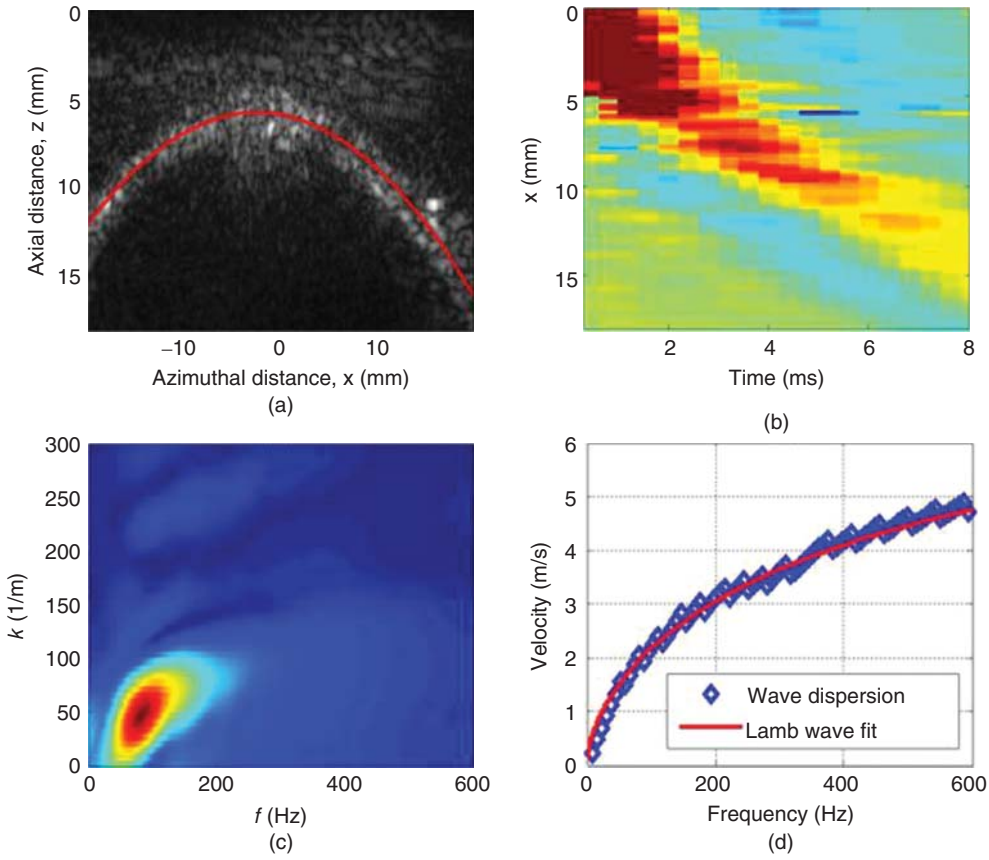

Figure 31.5 Ex vivo measurement of porcine bladder elasticity and viscosity: (a) B-mode image of the bladder wall. (b) Shear wave signal extracted from the bladder wall. (c) 2D Fourier transform of the shear wave signal in part (b). (d) Dispersion analysis of the Fourier-domain signal yields viscoelastic measurements of the bladder wall. Source: © Institute of Physics and Engineering in Medicine, reproduced by permission of IOP Publishing, all rights reserved [70].

31.10 Summary

Abdominal applications are one of the most important and attractive fields of research for ultrasound shear wave elastography. In this chapter we have briefly reviewed several applications in different abdominal organs including liver, prostate, kidney, intestine, uterine cervix, spleen, pancreas, and bladder. Some of these applications, such as liver, have been developed for over a decade and are moving towards clinical practice with maturing guidelines and clinical protocols. Some new applications, such as bladder, are still under active investigation. Newer techniques are still being developed to further improve the performance of abdominal shear wave elastography in the context of better penetration, higher frame rate, and more robust algorithms to estimate both elasticity and viscosity. Shear wave elastography is also being translated to different ultrasound transducers such as transvaginal and catheter transducers for specialized ultrasound applications.

References

1 Ferraioli, G., Filice, C., Castera, L., et al. (2015). WFUMB guidelines and recommendations for clinical use of ultrasound elastography: Part 3: liver. *Ultrasound Med. Biol.* 41: 1161–1179.

2 Cosgrove, D., Piscaglia, F., Bamber, J., et al. (2013). EFSUMB guidelines and recommendations on the clinical use of ultrasound elastography: Part 2: clinical applications. *Ultraschall. Med.* 34: 238–253.

3 Barr, R.G., Ferraioli, G., Palmeri, M.L., et al. (2015). Elastography assessment of liver fibrosis: Society of Radiologists in Ultrasound consensus conference statement. *Radiology* 276: 845–861.

4 EASL Clinical Practice Guidelines (2012). Management of chronic hepatitis B virus infection. *J. Hepatol.* 57: 167–185.

5 EASL Clinical Practice Guidelines (2014). Management of hepatitis C virus infection. *J. Hepatol.* 60: 392–420.

6 Myers, R.P., Ramji, A., Bilodeau, M., et al. (2012). An update on the management of hepatitis C: consensus guidelines from the Canadian Association for the Study of the Liver. *Can. J. Gastroenterol.* 26: 359–375.

7 Sarri, G., Westby, M., Bermingham, S., et al. (2013). Diagnosis and management of chronic hepatitis B in children, young people, and adults: summary of NICE guidance. *BMJ* 346, 3893.

8 Huwart, L., Sempoux, C., Vicaut, E., et al. (2008). Magnetic resonance elastography for the noninvasive staging of liver fibrosis. *Gastroenterology* 135: 32–40.

9 Yin, M., Talwalkar, J.A., Glaser, K.J., et al. (2007). Assessment of hepatic fibrosis with magnetic resonance elastography. *Clin. Gastroenterol. Hepatol.* 5: 1207–1213 e2.

10 Venkatesh, S.K. and Ehman, R.L. (2014). Magnetic resonance elastography of liver. *Magn. Reson. Imaging Clin. N. Am.* 22: 433–446.

11 Yin, M., Glaser, K.J., Talwalkar, J.A., et al. (2015). Hepatic MR elastography: clinical performance in a series of 1377 consecutive examinations. *Radiology* 278: 114–124.

12 Bavu, É., Gennisson, J.-L., Couade, M., et al. (2011). Noninvasive in vivo liver fibrosis evaluation using Supersonic Shear Imaging: a clinical study on 113 hepatitis C virus patients. *Ultrasound Med. Biol.* 37: 1361–1373.

13 Friedrich-Rust, M., Ong, M.-F., Martens, S. (2008). Performance of transient elastography for the staging of liver fibrosis: a meta-analysis. *Gastroenterology* 134: 960–974, e8.

14 Tsochatzis, E.A., Gurusamy, K.S., Ntaoula, S., et al. (2011). Elastography for the diagnosis of severity of fibrosis in chronic liver disease: a meta-analysis of diagnostic accuracy. *J. Hepatol.* 54: 650–659.

15 Singh, S., Venkatesh, S.K., Wang, Z., et al. (2014). Diagnostic performance of magnetic resonance elastography in staging liver fibrosis: a systematic review and meta-analysis of individual participant data. *Clin. Gastroenterol. Hepatol.* 13: 440–451.

16 Bota, S., Herkner, H., Sporea, I., et al. (2013). Meta-analysis: ARFI elastography versus transient elastography for the evaluation of liver fibrosis. *Liver Int.* 33: 1138–1147.

17 Wang, Q.B., Zhu, H., Liu, H.L., and Zhang, B. (2012). Performance of magnetic resonance elastography and diffusion-weighted imaging for the staging of hepatic fibrosis: A meta-analysis. *Hepatology* 56: 239–247.

18 Friedrich-Rust, M., Nierhoff, J., Lupsor, M., et al. (2012). Performance of acoustic radiation force impulse imaging for the staging of liver fibrosis: a pooled meta-analysis. *J. Viral Hepat.* 19: e212–e219.

19 Sandrin, L., Tanter, M., Gennisson, J.L., et al. (2002). Shear elasticity probe for soft tissues with 1-D transient elastography. *IEEE Trans. Ultrason., Ferroelect., Freq. Control* 49: 436–446.

20 Sandrin, L., Fourquet, B., Hasquenoph J.M., et al. (2003). Transient elastography: a new noninvasive method for assessment of hepatic fibrosis. *Ultrasound Med. Biol.* 29: 1705–1713.

21 Palmeri, M.L., Wang, M.H., Dahl, J.J., et al. (2008). Quantifying hepatic shear modulus in vivo using acoustic radiation force. *Ultrasound Med. Biol.* 34: 546–558.

22 Palmeri, M.L., Wang, M.H., Rouze, N.C., et al. (2011). Noninvasive evaluation of hepatic fibrosis using acoustic radiation force-based shear stiffness in patients with nonalcoholic fatty liver disease. *J. Hepatol.* 55: 666–672.

23 Zhao, H., Chen, J., Meixner, D.D., et al. (2014). Noninvasive assessment of liver fibrosis using ultrasound-based shear wave measurement and comparison to magnetic resonance elastography. *J. Ultrasound Med.* 33: 1597–1604.

24 Chen, S., Sanchez, W., Callstrom, M.R., et al. (2013). Assessment of liver viscoelasticity by using shear waves induced by ultrasound radiation force. *Radiology* 266: 964–970.

25 Bercoff, J., Tanter, M., and Fink, M. (2004). Supersonic shear imaging: a new technique for soft tissue elasticity mapping. *IEEE Trans. Ultrason., Ferroelect., Freq. Control* 51: 396–409.

26 Ferraioli, G., Tinelli, C., Dal Bello, B., et al. (2012). Accuracy of real-time shear wave elastography for assessing liver fibrosis in chronic hepatitis C: a pilot study. *Hepatology* 56: 2125–2133.

27 Song, P., Mellema, D.C., Sheedy, S.P., et al. (2016). Performance of 2-dimensional ultrasound shear wave elastography in liver fibrosis detection using magnetic resonance elastography as the reference standard: a pilot study. *J. Ultrasound Med.* 35: 401–412.

28 Zhao, H., Song, P., Meixner, D.D., et al. (2014). External vibration multi-directional ultrasound shearwave elastography (EVMUSE): application in liver fibrosis staging. *IEEE Trans. Med. Imaging* 33: 2140–2148.

29 Wu, Z., Taylor, L.S., Rubens, D.J., and Parker, K.J. (2004). Sonoelastographic imaging of interference patterns for estimation of the shear velocity of homogeneous biomaterials. *Phys. Med. Biol.* 49: 911–922.

30 Chen, S., Urban, M.W., Pislaru, C., et al. (2009). Shearwave dispersion ultrasound vibrometry (SDUV) for measuring tissue elasticity and viscosity. *IEEE Trans. Ultrason., Ferroelect., Freq. Control* 56: 55–62.

31 Deffieux, T., Montaldo, G., Tanter, M., and Fink, M. (2009). Shear wave spectroscopy for in vivo quantification of human soft tissues visco-elasticity. *IEEE Trans. Med. Imaging* 28: 313–322.

32 Barry, C.T., Mills, B., Hah, Z., et al. (2012). Shear wave dispersion measures liver steatosis. *Ultrasound Med. Biol.* 38: 175–182.

33 Barry, C.T., Hah, Z., Partin, A., et al. (2014). Mouse liver dispersion for the diagnosis of early-stage fatty liver disease: a 70-sample study. *Ultrasound Med. Biol.* 40: 704–713.

34 Deffieux, T., Gennisson, J.L., Bousquet, L., et al. (2015). Investigating liver stiffness and viscosity for fibrosis, steatosis and activity staging using shear wave elastography. *J. Hepatol.* 62: 317–324.

35 Woo, S., Kim, S.Y., Cho, J.Y., and Kim, S.H. (2014). Shear wave elastography for detection of prostate cancer: a preliminary study. *Korean J. Radiol.* 15: 346–355.

36 Barr, R.G., Memo, R., and Schaub, C.R. (2012). Shear wave ultrasound elastography of the prostate: initial results. *Ultrasound Quarterly* 28: 13–20.

37 Ahmad, S., Cao, R., Varghese, T., et al. (2013). Transrectal quantitative shear wave elastography in the detection and characterisation of prostate cancer. *Surgical Endoscopy* 27: 3280–3287.

38 Correas, J.M., Tissier, A.M., Khairoune, A., et al. (2015). Prostate cancer: diagnostic performance of real-time shear-wave elastography. *Radiology* 275: 280–289.

39 Woo, S., Kim, S.Y., Lee, M.S., et al. (2015). Shear wave elastography assessment in the prostate: an intraobserver reproducibility study. *Clin. Imaging* 39: 484–487.

40 Gennisson, J.-L., Grenier, N., Combe, C., and Tanter, M. (2012). Supersonic shear wave elastography of in vivo pig kidney: influence of blood pressure, urinary pressure and tissue anisotropy. *Ultrasound Med. Biol.* 38: 1559–1567.

41 Gallotti, A., D'Onofrio, M., and Pozzi Mucelli, R. (2010). Acoustic radiation force impulse (ARFI) technique in ultrasound with Virtual Touch tissue quantification of the upper abdomen. *La Radiol. Med.* 115: 889–897.

42 Amador, C., Urban, M.W., Chen, S., and Greenleaf, J.F. (2011). Shearwave dispersion ultrasound vibrometry (SDUV) on swine kidney. *IEEE Trans. Ultrason., Ferroelect., Freq. Control* 58: 2608–2619.

43 Wang, T.Y., Hall, T.L., Xu, Z., et al. (2012). Imaging feedback of histotripsy treatments using ultrasound shear wave elastography. *IEEE Trans. Ultrason., Ferroelect., Freq. Control* 59: 1167–1181.

44 Syversveen, T., Brabrand, K., Midtvedt, K., et al. (2011). Assessment of renal allograft fibrosis by acoustic radiation force impulse quantification – a pilot study. *Transplant Int.* 24: 100–105.

45 Syversveen, T., Midtvedt, K., Berstad, A., et al. (2012). Tissue elasticity estimated by acoustic radiation force impulse quantification depends on the applied transducer force: an experimental study in kidney transplant patients. *Eur. Radiol.* 22: 2130–2137.

46 Grenier, N., Poulain, S., Lepreux, S., et al. (2012). Quantitative elastography of renal transplants using supersonic shear imaging: a pilot study. *Eur. Radiol.* 22: 2138–2146.

47 Arndt, R., Schmidt, S., Loddenkemper, C., et al. (2010). Noninvasive evaluation of renal allograft fibrosis by transient elastography – a pilot study. *Transplant Int.* 23: 871–877.

48 Derieppe, M., Delmas, Y., Gennisson, J.-L., et al. (2012). Detection of intrarenal microstructural changes with supersonic shear wave elastography in rats. *Eur. Radiol.* 22: 243–250.

49 Gennisson, J.L., Grenier, N., Hubrecht, R., et al. (2010). Multiwave technology introducing shear wave elastography of the kidney: Pre-clinical study on a kidney fibrosis model and clinical feasibility study on 49 human renal transplants. In: *IEEE Ultrasonics Symposium* 2010 1356–1359.

50 Asano, K., Ogata, A., Tanaka, K., et al. (2014). Acoustic radiation force impulse elastography of the kidneys: is shear wave velocity affected by tissue fibrosis or renal blood flow? *J. Ultrasound Med.* 33: 793–801.

51 Stidham, R.W., Xu, J., Johnson, L.A., et al. (2011). Ultrasound elasticity imaging for detecting intestinal fibrosis and inflammation in rats and humans with Crohn's disease. *Gastroenterology* 141: 819–826 e1.

52 Dillman, J.R., Stidham, R.W., Higgins, P.D.R., et al. (2013). US Elastography-derived shear wave velocity helps distinguish acutely inflamed from fibrotic bowel in a Crohn disease animal model. *Radiology* 267: 757–766.

53 Dillman, J.R., Stidham, R.W., Higgins, P.D., et al. (2014). Ultrasound shear wave elastography helps discriminate low-grade from high-grade bowel wall fibrosis in ex vivo human intestinal specimens. *J. Ultrasound Med.* 33: 2115–2123.

54 Feltovich, H. and Hall, T.J. (2013). Quantitative imaging of the cervix: setting the bar. *Ultrasound Obstet. Gynecol.* 41: 121–128.

55 L. C. Carlson, Feltovich, H., Palmeri, M.L., et al. (2014). Statistical analysis of shear wave speed in the uterine cervix. *IEEE Trans. Ultrason., Ferroelect., Freq. Control* 61: 1651–1660, Oct.

56 L. C. Carlson, Feltovich, H., Palmeri, M.L., et al. (2014). Estimation of shear wave speed in the human uterine cervix. *Ultrasound Obstet. Gynecol.* 43: 452–458.

57 Gennisson, J.L., Muller, M., Ami, O., et al. (2011). Shear wave elastography in obstetrics: quantification of cervix elasticity and uterine contraction. In: *IEEE International Ultrasonics Symposium* 2011 2094–2097.

58 Palmeri, M.L., Feltovich, H., Homyk, A.D., et al. (2013). Evaluating the feasibility of acoustic radiation force impulse shear wave elasticity imaging of the uterine cervix with an intracavity array: a simulation study. *IEEE Trans. Ultrason., Ferroelect., Freq. Control* 60: 2053–2064.

59 Bota, S., Sporea, I., Sirli, R., et al. (2010). Spleen assessment by acoustic radiation force impulse elastography (ARFI) for prediction of liver cirrhosis and portal hypertension. *Med. Ultrason.* 12: 213–217.

60 Ye, X.-P., Ran, H.-T., Cheng, J., et al. (2012). Liver and spleen stiffness measured by acoustic radiation force impulse elastography for noninvasive assessment of liver fibrosis and esophageal varices in patients with chronic hepatitis B. *J. Ultrasound Med.* 31: 1245–1253.

61 Cassinotto, C., Charrie, A., Mouries, A., et al. (2015). Liver and spleen elastography using supersonic shear imaging for the non-invasive diagnosis of cirrhosis severity and oesophageal varices. *Dig. Liver Dis.* 47: 695–701.

62 Nedredal, G.I., Yin, M., McKenzie, T., et al. (2011). Portal hypertension correlates with splenic stiffness as measured with MR elastography. *J. Magn. Reson. Imaging* 34: 79–87.

63 Grgurevic, I., Cikara, I., Horvat, J., et al. (2011). Noninvasive assessment of liver fibrosis with acoustic radiation force impulse imaging: increased liver and splenic stiffness in patients with liver fibrosis and cirrhosis. *Ultraschall Med.* 32: 160–166.

64 Leung, V.Y., Shen, J., Wong, V.W., et al. (2013). Quantitative elastography of liver fibrosis and spleen stiffness in chronic hepatitis B carriers: comparison of shear-wave elastography and transient elastography with liver biopsy correlation. *Radiology* 269: 910–918.

65 Giovannini, M., Thomas, B., Erwan, B., et al. (2009). Endoscopic ultrasound elastography for evaluation of lymph nodes and pancreatic masses: A multicenter study. *World J. Gastroenterol.* 15: 1587–1593.

66 Hirche, T.O., Ignee, A., Barreiros, A.P., et al. (2008). Indications and limitations of endoscopic ultrasound elastography for evaluation of focal pancreatic lesions. *Endoscopy* 40: 910–917.

67 Janssen, J., Schlorer, E., and Greiner, L. (2007). EUS elastography of the pancreas: feasibility and pattern description of the normal pancreas, chronic pancreatitis, and focal pancreatic lesions. *Gastrointest. Endosc.* 65: 971–978.

68 Arda, K., Ciledag, N., Aktas, E., et al. (2011). Quantitative assessment of normal soft-tissue elasticity using shear-wave ultrasound elastography. *Am. J. Roentgenol.* 197: 532–536.

69 D'Onofrio, M., Gallotti, A., Salvia, R., et al. (2011). Acoustic radiation force impulse (ARFI) ultrasound imaging of pancreatic cystic lesions. *Eur. J. Radiol.* 80: 241–244.

70 Nenadic, I.Z., Qiang, B., Urban, M.W., et al. (2013). Ultrasound bladder vibrometry method for measuring viscoelasticity of the bladder wall. *Phys. Med. Biol.* 58: 2675–2695.

32

Acoustic Radiation Force-based Ultrasound Elastography for Cardiac Imaging Applications

Stephanie A. Eyerly-Webb[1], Maryam Vejdani-Jahromi[1], Vaibhav Kakkad[1], Peter Hollender[1], David Bradway[1], and Gregg Trahey[1,2]

[1] *Department of Biomedical Engineering, Duke University, Durham, NC, USA*
[2] *Department of Radiology, Duke University Medical Center, Durham, NC*

32.1 Introduction

Heart diseases are the leading cause of death for both men and women in developed countries, accounting for approximately 1 out of every 4 deaths in the United States each year [1]. Virtually every form of heart disease involves modifications to myocardial elasticity, and the past several decades have seen significant developments in elastography-based imaging techniques to clinically evaluate myocardial stiffness for diagnosis and monitoring of cardiac diseases. In addition to being a powerful diagnostic tool for cardiac function, elasticity imaging techniques are also showing promise for guiding clinical cardiac ablation treatment for heart rhythm disorders.

This chapter reviews the current research and applications for acoustic radiation force (ARF)-based methods, namely acoustic radiation force impulse (ARFI) imaging and shear wave elasticity imaging (SWEI) methods, in the diagnosis and treatment of cardiac diseases.

32.2 Acoustic Radiation Force-based Elastography Techniques

ARFI imaging is an ultrasound-based elastography method that provides information about the local mechanical properties of tissue. ARFI imaging uses short duration (0.03–1 ms) acoustic radiation force excitations to generate localized displacements in tissue, and these displacements are tracked using ultrasonic correlation-based methods [2–5]. Soft tissues typically displace 2–10 μm in response to an ARFI excitation and exhibit an overdamped response with a recovery time of 3–4 ms to the pre-excitation position. The tissue response to these forces is monitored both spatially and temporally using conventional ultrasound methods [5]. Local physiological motion is typically measured before the push pulse and after tissue recovery, interpolated within the period during ARFI-induced motion, and removed or "filtered" from the tissue response signal [6, 7]. The ARFI-induced tissue displacement is inversely related to tissue stiffness, and tissue recovery response is related to tissue viscoelastic properties [8, 9]. It is important to note that the measured ARFI-induced displacements are qualitative surrogates for relative tissue stiffness, and do not directly quantify an absolute material property [10]. ARFI imaging is optimally suited to discrete targets of differing stiffness, such as ablation lesions.

SWEI imaging is another ARF-based elastography technique that uses acoustic impulses to displace tissue, but rather than tracking the displacement in the region of ARF excitation,

Ultrasound Elastography for Biomedical Applications and Medicine, First Edition.
Edited by Ivan Nenadic, Matthew Urban, James Greenleaf, Jean-Luc Gennisson, Miguel Bernal, and Mickael Tanter.

the SWEI method monitors the region laterally off-axis for the propagation of the radiation force-induced transverse shear wave [11–13]. The velocity of propagation, or shear wave speed (SWS), is a function of the tissue material properties and is proportional to the tissue stiffness (shear and Young's modulus). Traditional SWS calculations require a spatial kernel that can result in lower resolution than ARFI imaging, and SWEI imaging is best used for quantifying a global elasticity metric than for differentiating discrete targets [10]; more sophisticated sequencing methods are under investigation to improve the resolution [13].

SWEI and ARFI imaging are currently implemented on software-modified diagnostic ultrasound scanners and use conventional and prototype ultrasound transducers for the generation of radiation force and the tracking of the tissue response [14]. The use of conventional diagnostic equipment provides the ability to acquire spatially and temporally co-registered traditional B-mode images and facilitates fast translation to the clinic.

32.3 ARF-based Elasticity Assessment of Cardiac Function

Cardiovascular disorders are among the leading causes of morbidity and mortality in the world and cardiovascular researchers have been trying to develop tools for clinical assessment of cardiac function for decades. Ideally, a clinician could diagnose and monitor a treatment course for common cardiac diseases with a noninvasive evaluation of cardiac function. The gold standard technique for cardiac mechanical assessment is the pressure-volume loop measurements [15], a highly invasive test that requires catheter-based measurements of intra-ventricular pressure and volume and therefore it has not been adopted widely in the clinic. To develop a noninvasive technique, measures of cardiac function have been developed based on imaging techniques such as ultrasound strain imaging and tissue Doppler imaging [16, 17]. While promising, these measurements are usually indirect and load dependent. Therefore, there is currently no noninvasive and dependable technique to provide direct measurement of systolic and diastolic functions such as contractility, compliance, or relaxation time constant in clinical practice.

32.3.1 ARF-based Measurement of Cardiac Elasticity and Function

Ultrasound elastography can provide direct tissue stiffness measurements throughout the cardiac cycle, and cardiac functional indices can be extracted from these mechanical measurements. As a qualitative elastography technique, ARFI imaging can provide relative measurements of cardiac function such as a systolic/diastolic stiffness ratio or indices that are time dependent such as relaxation time constants. In addition to these indices, SWEI can provide a quantitative measurement of myocardial stiffness during systole and diastole that represent contractility and compliance measurements respectively. Figure 32.1 shows the myocardial stiffness through the cardiac cycle measured by ARFI imaging and SWEI. This figure displays data acquired using M-mode ARFI imaging and SWEI in an isolated rabbit heart setup. This figure illustrates that cardiac stiffness increases during systole as the heart contracts and decreases in diastole when the heart is relaxed. A number of significant cardiac functional indices that can be derived from these stiffness measurements are identified.

In 2007, Hsu et al. first used M-mode and 2D ARFI imaging to evaluate the changes in myocardial stiffness through the cardiac cycle in an open chest canine heart model [7, 18]. Couade et al. measured the diastolic shear modulus at ~2 kPa and the systolic shear modulus as ~30 kPa using quantitative shear wave imaging methods [19].

Pernot et al. have studied contractility assessment using SWEI stiffness measurements in isolated rat hearts by recording systolic stiffness before and after administration of

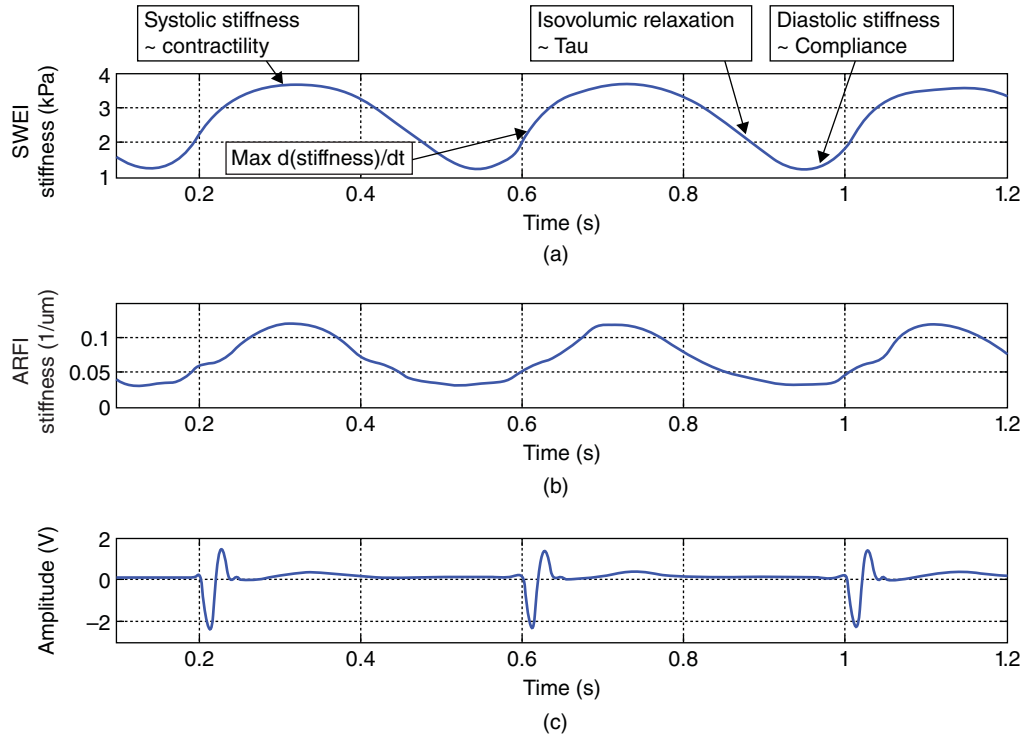

Figure 32.1 (a) SWEI and (b) ARFI stiffness measurements through the cardiac cycle respectively. SWEI measurements are shear modulus of stiffness and ARFI measurement are inverse displacement values (a measure of stiffness). (c) Simultaneous ECG signal. Note that cardiac stiffness increases during systole as the heart contracts and decreases during diastole when the heart is relaxed. The potential cardiac functional indices are marked on the SWEI measurements curve.

isoproterenol, an inotropic agent [20]. The myocardial stiffness and change in stiffness over time (d(stiffness)/dt_{max}) increased significantly during systole and represented contractility. The measured myocardial stiffness also correlated strongly with isovolumic systolic pressure. In addition, the study reports significantly higher diastolic stiffness in hypertrophic rat hearts compared to a control group, suggesting shear wave imaging can quantify cardiac compliance. In another study in an in vivo large animal model, Pislaru et al. showed that measurements of passive myocardial elasticity quantified by a shear wave imaging method were correlated with elastic modulus and pressure-segment length, an invasive measure of compliance [21].

In order to investigate the ability of SWEI to detect changes in compliance and contractility, Vejdani-Jahromi et al. conducted experiments that used the known phenomena of the "Garden Hose effect" and "Gregg effect" respectively on isolated rabbit hearts [22]. It was shown that SWEI could detect the change in compliance due to the Garden Hose effect, the passive effect of coronary perfusion on cardiac compliance. The Gregg effect is the active effect of coronary perfusion on cardiac contractility. It was shown that SWEI could detect the increase in contractility corresponding to the increase in coronary perfusion shown by other methods in the literature. In addition, the Gregg effect was blocked by inhibiting Ca channels which resulted in a decrease in the contractility changes by coronary perfusion [23]. Figure 32.2 shows the effect of coronary perfusion pressure on cardiac contractility and compliance recorded by SWEI at different coronary perfusion pressure steps [23]. The potential of deriving relaxation time constant and systolic/diastolic ratio using ARFI imaging and SWEI techniques is also under investigation [24].

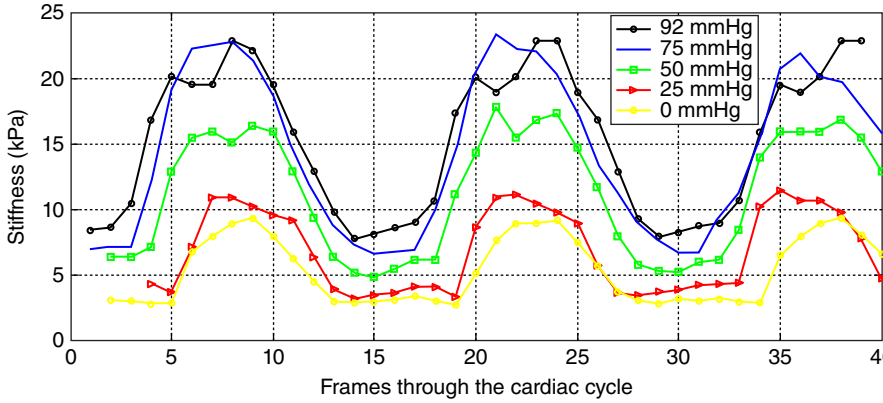

Figure 32.2 SWEI measurements of stiffness through cardiac cycle in an isolated rabbit heart. Myocardial stiffness increases in systole and diastole as the coronary perfusion is increased, corresponding to the known Gregg and Garden Hose effects. Systolic change is more prominent and is an active contractility change and diastolic change is less significant with a passive effect on compliance, as shown in the literature by pressure-volume loop measurement. This is consistent with the SWEI stiffness recordings [23].

Considering the complicated nature of cardiac tissue, one can anticipate several factors that could affect elastography measurements of cardiac function. First of all, a linear, elastic, isotropic medium is assumed in the calculation of shear modulus of stiffness from the shear wave velocity or SWS [12]. However, it has been shown that cardiac tissue is a nonlinear, viscoelastic, and anisotropic medium. The previously mentioned work by Vejdani-Jahromi et al. could imply the nonlinearity of cardiac tissue [22]. Researchers have utilized viscoelastic models to isolate elastic and viscous moduli of the cardiac tissue from each other [21, 25]. Therefore, it might be more practical if shear velocity is reported as the measure of stiffness rather than converting it to shear modulus using the above-mentioned assumptions.

The quantitative measurements for ARFI imaging (displacement) and SWEI (SWS) are largely affected by anisotropy, particularly regarding the dependency of the shear wave propagation velocity on fiber orientation and the presence of heterogeneities [26, 27]. Myocardium is known to be highly anisotropic [28, 29] and shear waves propagate faster along fibers; without knowledge of local fiber orientation any quantitative measurements are of suspect value. A number of studies have examined the effect of anisotropy on SWEI measurements in the cardiac tissue and found significant effects of fiber orientation on SWEI shear wave velocity [19, 30, 31]. In addition, in an in vitro experiment Lee et al. showed that fiber angle could be mapped by rotating the transducer and finding the maximum SWS at each myocardial layer. Further developments using matrix probes could acquire and incorporate fiber orientation information into the elastic parameter calculations, thus improving the accuracy of the myocardial stiffness measurement.

Another issue to consider when calculating ARF-induced SWS is the presence of Lamb-Rayleigh waves, mechanical waves that propagate along the surface of a tissue. Lamb-Rayleigh waves have different propagation properties than shear waves, and in ARF-based imaging methods they are indistinguishable from shear waves and can affect the SWS calculation. Nonetheless, Nenadic et al. found that the velocity of Lamb-Rayleigh waves is related to the shear wave velocity [32, 33].

Further studies are needed to characterize the relationship between ARFI imaging, SWEI-derived local elasticity measurements, and global measurements of cardiac function, such as the pressure-volume loop and relaxation time constants. Furthermore, the relationship between ARFI-derived indices compared to SWEI should be studied in detail. Cardiac functional indices, including relaxation time constants measured by other techniques, need to be

investigated and compared to the ones measured using ARF-based methods. In summary, this is the first time in the history of cardiovascular research that a technique is able to detect the stiffness of cardiac tissue directly in vivo, and these methods have great potential for research and clinical applications in the field of cardiovascular research.

32.3.2 Clinical Translation of Transthoracic ARF-based Methods for Cardiac Stiffness Assessment

As described in the previous section, imaging the stiffness of the heart with ultrasound has yielded highly encouraging results in ex vivo isolated heart preparations as well as open chest settings. While the above-mentioned studies demonstrate the ability of cardiac elastography to provide novel information about myocardial function, its clinical applicability is contingent upon the ability to extract these functional indices through noninvasive means such as transthoracic imaging.

Transthoracic translation of ARFI and SWEI has been the topic of significant research by several groups over the last decade. Bradway et al. first demonstrated the ability of M-mode ARFI to generate and track displacements in the interventricular septum through intercostal and subcostal imaging windows on porcine subjects [34]. They observed cyclic variations in displacement magnitude that corresponded to expected myocardial stiffness trends through the cardiac cycle based on the simultaneous ECG signal. In 2012, they also reported on the safety and feasibility of M-mode ARFI in human subjects at varying levels of mechanical index (MI) at and above the FDA limit of 1.9 [35]. Their findings suggested that high MI sequences were thermally and mechanically safe for human use. While the use of higher MI resulted in larger tissue displacements in both cardiac phases, the ratio of diastolic to systolic displacements was relatively steady, suggesting that this ratio could be used as a radiation force-independent metric of cardiac function. Most recently, Kakkad et al. reported on implementing M-mode ARFI with harmonic tracking on a clinical ultrasound system to interrogate the stiffness of the interventricular septum through the cardiac cycle in parasternal long and short axis views within the FDA limits [36]. They measured diastolic to systolic displacement ratios in the range of 1.32 to 2.27 on human subjects. Figure 32.3 shows a transthoracic M-mode ARFI acquisition.

Studies using transthoracic SWEI have primarily been limited to measuring stiffness of the myocardium at end diastole. Song et al. demonstrated improvements in the ability to track shear waves in vivo in the left ventricle through a short axis view with the use of pulse inversion harmonic tracking [37]. They measured mean end diastolic shear wave speeds of 1.56 m/s and saw successful shear wave propagation in 80% of acquisitions. They have further shown that improvements in success rates and shear wave signal quality can be made by tracking at higher frequencies using pediatric phased array transducers [38].

Even though transient elastography has shown promise for transthoracic applications, the results to date tend to have a large amount of variability associated with the derived indices of cardiac function. The cause of this variability has largely been attributed to three main challenges: (i) the difficulty in generating substantial displacements at depth, ii) the difficulty in accurately tracking induced displacements amidst ultrasonic clutter, and (iii) the difficulty in separating radiation force-induced displacements from complex, multi-dimensional intrinsic cardiac motion.

The first challenge can be addressed using high MI and/or longer push pulses. However the FDA currently limits the MI of all ultrasound applications to 1.9, and the use of longer pulses raises concerns about transducer and tissue heating. Stationary ultrasonic clutter is a routine issue in transthoracic imaging [39]. It not only degrades border detection and image quality but also adversely affects the accuracy of displacement tracking algorithms that are at the heart of ultrasound elastography [5]. The use of pulse inversion harmonic on tracking has been shown to

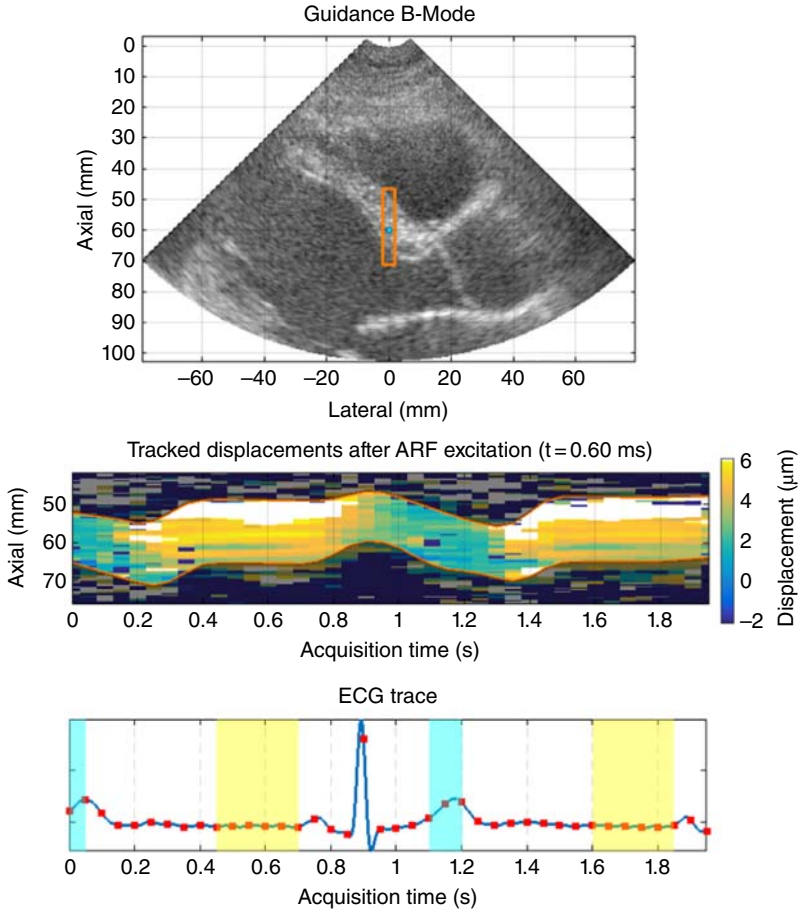

Figure 32.3 Transthoracic M-mode ARFI displacements in the interventricular septum measured through a parasternal long axis view. When compared with simultaneous ECG, the ARFI displacements show the expected cyclic pattern with high displacements in diastole (prior to P-wave) and low displacements in systole (following the QRS complex).

improve the quality of displacement estimates for ARFI imaging [40] and SWEI [37]. Plane wave coherent compounding has also been shown to suppress clutter and improve displacement estimation [41]. Motion filtering has traditionally been performed after displacement estimation to remove axial components of tissue motion using linear or quadratic polynomial fit algorithms [6, 18]. However, the heart goes through complex motions, such as stretch, shear, and torsion, which need to be accounted for in order to better characterize its mechanical response to spatially confined impulsive excitations.

Given the inherent challenges posed by transthoracic imaging windows, transesophageal echocardiography (TEE) could provide a more viable alternative for the interrogation of cardiac elasticity. Transesophageal imaging would allow for lower clutter levels, better image quality, and shorter depths of penetration to the cardiac walls of interest at the expense of being a more intrusive procedure compared to transthoracic imaging. This avenue, while theoretically feasible, has yet to be explored in practice due to the limited availability of TEE probes capable of generating ARF excitation pulses.

Noninvasive measurement of cardiac stiffness through transthoracic imaging has great prognostic potential to diagnose a myriad of cardiomyopathies. Indices of cardiac function derived

from transient elastography could be used to differentiate between systolic and diastolic heart failure, identify hypertrophy, assess transplant rejection, etc. Overcoming the challenges for these techniques could lead to a robust, real-time tool with wide applications in general and interventional cardiology.

32.3.3 ARFI Imaging of Myocardial Ischemia and Infarct

ARFI and SWEI techniques have been explored as a means of characterizing damaged myocardium following an ischemic event. Couade et al. noted a reversible decrease in systolic shear wave speeds in response to temporary local ischemia induced by ligation in open-chested sheep [19]. Hollender et al. used intracardiac ARFI and SWEI (M-mode and 2D × time) to image pigs that had focal infarctions induced by coronary occlusion, finding local decreases in contractility months after the event and increased diastolic stiffness within the infarcted septum [42]. The same study noted the spatial heterogeneity of stiffness and contractility measurements, corresponding to the scattered locations of infarct confirmed with ex vivo MRI. The complexity of ischemic heart disease presents an opportunity for an ARFI-based imaging system to have diagnostic impact, but requires a solution for reliably imaging the elasticity of large sections of myocardium with high spatial and temporal resolution throughout the cardiac cycle that is yet to be demonstrated.

32.4 ARF-based Image Guidance for Cardiac Radiofrequency Ablation Procedures

Cardiac arrhythmias, heart rhythm disorders caused by fast, slow, or irregular heartbeats, affect millions patients each year. The most commonly diagnosed arrhythmia in clinical practice is atrial fibrillation (AF), which affects between 3 and 6 million people in the United States annually [1, 43]. Arrhythmias such as AF can arise due to a variety of factors (abnormal tissue, random firing), but most can be diagnosed with a comprehensive electrocardiography exam [43]. Nearly all cardiac arrhythmias can be managed with pharmaceutical intervention or palliatively treated with transcatheter ablation (TCA) [44]. Tens of thousands of TCA procedures are performed in the US annually, and diagnoses of AF are expected to more than double in the coming decades [1].

TCA aims to restore the normal rhythm of the heart by directly destroying or electrically isolating abnormally conducting myocardium with thermal radiofrequency ablation (RFA) lesions. To permanently stop the arrhythmia, the RFA lesions must extend the full depth of the myocardium (be transmural) and lesion lines must not have conductive gaps in between discrete lesions [45–47]. TCA procedures can be curative, but there is currently no clinically available method to directly visualize RFA lesions in the tissue; without a reliable way to assess lesion presence, size, and transmurality, post-TCA arrhythmia recurrence is common and a significant number of patients (10–30%) require additional ablation procedures [48]. Ideally, direct visualization of the ablated region following RF delivery would provide feedback of RFA lesion presence and transmurality as well as lesion line continuity.

RF-induced tissue heating creates a localized necrotic lesion that is stiffer than the surrounding myocardium. This change in viscoelasticity is due to the thermocoagulation and denaturation of the myocardium structural proteins (collagen [49], elastin) and myofilaments (myosin, actin [49–53]). Myocyte injury and tissue necrosis during thermal ablation are considered permanent and irreversible once protein thermocoagulation has occurred [50, 54], making relative tissue stiffness a useful measure for acutely differentiating a permanent lesion from healthy myocardium.

Eyerly et al. demonstrated that ARFI imaging could visualize the active stiffening process of the myocardium during thermal lesion formation in vitro [55]. It was found that the mean ARF-induced displacements measured outside the lesion remained consistently high, but displacements decreased inside the pathological lesion during RF delivery. This finding confirmed that RF-induced thermocoagulation actively stiffened the lesion site and that ARFI imaging could detect the change in relative tissue stiffness. It is important to note that in this case the stiffening was not due to immune-fluid swelling or edema [56] as the preparation was in vitro.

In another in vitro experiment, Pernot et al. measured the increase in absolute tissue stiffness at RFA sites to be roughly twice that of the unablated tissue (unablated Young's modulus ~27 kPa vs. ablated ~54 kPa) using shear wave imaging methods [57]. Kwiecinski et al. similarly measured the increase in shear modulus at two- to five-fold (22 ± 5 kPa unablated vs. 99 ± 17 kPa ablated) after ablation in vitro using shear wave elastography methods [58]. The accuracy of using ARFI imaging to determine RFA lesion size was investigated in vitro by Eyerly et al. [59]. This study determined that lesion dimensions from ARFI and pathology images were statistically similar, exhibiting borders within 1–2 mm.

32.4.1 Clinical Translation of ARFI Imaging for Acute Ablation Lesion Assessment

Translation of ARF-based imaging methods for intraprocedure visualization of RFA lesions in an in vivo heart introduces five primary considerations: (1) the stiffness contrast of the lesion during the cardiac cycle, (2) the effects of bulk tissue motion on the displacement estimations, (3) transient physiological tissue stiffening processes, such as edema, that can affect the accuracy of the stiffness-based lesion visualization, (4) imaging access, and (5) correlation of the elastography-defined lesion with electrical block.

Acquiring ARFI images in diastole resolves considerations (1) and (2). As described in the cardiac function section, the myocardium is most compliant during diastole, and diastole-gated ARFI imaging maximizes lesion contrast [57, 58, 60–62]. Figure 32.4 illustrates the relative stiffness difference between systole and diastole around a ventricular epicardial RFA lesion [60]. The lesion is visible as a semicircular region of relatively low ARFI-induced displacement (dark blue). Using shear wave imaging, Kwiecinski et al. found absolute atrial stiffness was lowest during diastole (R-wave) for both unablated and ablated myocardium [58]. Also, late diastole is the time of least intrinsic motion during the cardiac cycle and reduces the effects of bulk cardiac motion on the tissue displacement measurements. It has been shown that bulk cardiac motion can be effectively managed with post-processing "motion-filter" techniques [6]. Overall, diastole gated ARFI imaging provides the highest contrast between any stiff lesions and the surrounding myocardium, but this approach limits the acquisition frame rate to one image per heartbeat.

While in vitro work demonstrated the ability of ARFI imaging to visualize thermocoagulated lesions, the myocardium surrounding the pathological lesion in vivo can be temporarily affected by the diffusive hyperthermia immediately following ablation [63–65]. This "border" zone is characterized by injured or "stunned" myocytes that suffer a temporary loss of cellular excitability and immune-fluid infiltration or edema [56, 63–65]. A study by Grondin et al. measured an increase in tissue stiffness (decrease in strain) at RFA sites in human patients using strain-imaging methods [66]. In three patients, they reported that the average of the absolute strain measurements decreased from 16.2 ± 17.7% to 10.0 ± 10.7% when re-measuring the strain of the ablation site at a later time step (5 to 20 minutes). These results suggested there was a stiffening of the tissue at the ablation site in the peri-ablation period; the stiffening could have been due to a hydrostatic pressure increase from acute transient edema at the thermal injury site that was large enough to increase the local tissue stiffness. Therefore to address consideration (3), Eyerly et al. characterized the spatial and temporal stability of the lesion, or

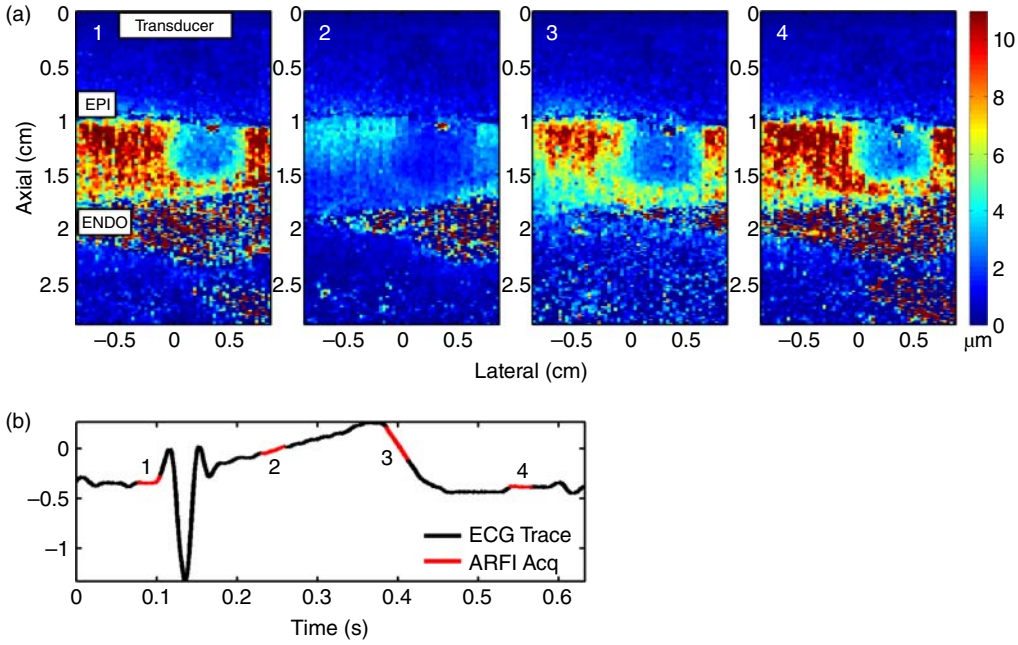

Figure 32.4 ARFI images of a right ventricular epicardial RFA lesion through the cardiac cycle. A nonirrigated electrode tip ablated the epicardial surface (EPI = epicardium, ENDO = endocardium) for 7 s at 20 W. (a) ARFI images acquired at different times during the cardiac cycle: (1) and (4) during diastole, (2) during systole, and (3) during end-systole. ARFI images were acquired with a linear transthoracic probe vacuum suctioned to the RV epicardium. Color bar units are maximum displacement away from the transducer in microns. Within the lesion, the ARFI-induced displacement is low throughout the cycle. The normal myocardium cycles between high displacement during diastole and low displacement during systole. (b) ARFI acquisition times corresponding to the ECG. Source: reprinted from [60], Copyright 2012, with permission from Elsevier.

region of stiffness increase (RoSI), in the peri-ablation period in vivo [48]. In six canine subjects, SWEI measurements and 2D ARFI images were acquired at six ventricular endocardial RFA sites before, during, and for 30 minutes post ablation. The imaging transducer was placed on the epicardial surface and the imaging plane penetrated inward while the ablation catheter and RFA was applied inside on the endocardial surface; the ablation catheter blocks the ARF excitation and this way the catheter was below the tissue being evaluated with ARFI imaging. In this setup, an immediate increase in tissue stiffness was detected during RFA, and the area of the RoSI as well as the relative stiffness at the RoSI center were stable approximately 2 minutes after ablation. Of note is the observation that relative stiffness in the region adjacent to the RoSI increased slightly in the first 15 minutes after ablation, consistent with local fluid displacement or edema. The magnitude of this increase, ~0.5-fold from baseline, was significantly less than the magnitude of the stiffness increase directly inside the RoSI, which was greater than 3-fold from baseline.

To translate ARF-based imaging techniques for clinical use in the hearts of human patients during TCA procedures, ARFI imaging and shear wave imaging methods were developed on intracardiac echocardiography (ICE) platforms [42, 58, 61, 62, 67]. ICE is clinically performed with a phased-array ultrasound transducer on an 8-10 French catheter, and during TCA provides real-time visualization of the cardiac anatomy and function from within the cardiac chambers [68–71]. ICE is an indispensable tool for guiding safe and accurate trans-septal punctures for left atrial (LA) access [68, 71–73] during ablation procedures and is often used for visualizing catheter placement and tissue contact for effective RF delivery.

Fahey et al. in 2005 and Hsu et al. in 2007 [61, 62] conducted preliminary in vivo feasibility studies of ICE-ARFI imaging in a canine model; they observed an increase in tissue stiffness at three endocardial RFA sites, evident by a decrease in the measured ARFI-induced displacement [62]. This work also described the challenges encountered when implementing ARFI imaging from an ICE catheter in vivo [62]. For example, it was discovered that the flexible transducer tip experienced a small rebound force, or "kick-back" from the generation of the ARFI excitations that is then measured along with the tissue-displacement response. Kwiecinski et al. reported a similar phenomenon when using ICE-based shear wave elastography [58]. Methods to minimize the effect of this kick-back on the data, such as adding "priming-pulses" to pre-load the imaging catheter before the tissue-excitation sequence [62], are being used and more sophisticated methods are under investigation. Additional challenges related to maximizing the energy delivery and the uniformity of the energy across the field of view were also described by Hsu et al. [62]. Their investigation suggested the ICE catheter be positioned at an imaging focal depth within 2 cm of the endocardium and as parallel to the transducer face as possible; this maximizes the induced displacement (contrast) and minimizes depth-dependent energy delivery to the tissue [9, 62, 74].

Eyerly et al. integrated the ICE-ARFI imaging techniques developed by Fahey et al. and Hsu et al. with an electroanatomical mapping (EAM) system, and used the combined system to precisely gather ARFI images of RFA lesions during TCA procedures in canine subjects [60, 75]. Readers of the ARFI images identified stiff lesion locations with high specificity and sensitivity and found that average measured displacements were lower in ablated myocardium (6.06 ± 0.94 μm) than unablated (11.23 ± 1.71 μm) myocardium; average lesion contrast was 0.29 ± 0.33 and the contrast to noise was 1.83 ± 1.75 [75]. Similarly, Kwiecinski et al. found a SWS increase ratio of 1.8 ± 0.3 from unablated to ablated with ICE-based shear wave imaging in a preclinical study in sheep [58].

To be a clinically relevant method for lesion evaluation during TCA, the stiffness-identified lesions in the ARFI images must also correlate with the electrical substrate modification or electrical block at the ablation site. Eyerly et al. conducted an experiment that showed ICE-ARFI imaging was able to identify lesions that correlated with the electrical destruction of the tissue [60]. Using the integrated ICE-ARFI imaging and EAM system, in eight canine subjects reviewers of the ARFI images identified conduction-disturbing RFA-treated sites with high sensitivity (95.7%) and specificity (91.5%). Identification of contiguous lesion sets or complete electrical block based on the ARFI images had 75.3% specificity and 47.1% sensitivity. An example from this study is shown in Figure 32.5. Before RFA the myocardial elasticity is homogeneous with relatively high ARFI-induced displacements (Figure 32.5, part 1C) and electrical propagation, represented by the color gradient, is smooth and uninhibited (Figure 32.5, part 1A). When a conductive unablated gap was left in the lesion line (Figure 32.5, part 2A), this is visible as the area of high tissue displacement (>7.5 μm) surrounded by areas of relatively low tissue displacements (<4.5 μm) in the ARFI image (Figure 32.5, part 2C). The final ARFI image shows a homogeneous region of low displacement (Figure 32.5, part 3C) correlating with the line of conduction block (Figure 32.5, part 3A), confirming complete ablation of the gap. This study also highlighted the necessity of the EAM system to guide the 2D ARFI imaging plane for efficient imaging of the RFA targets. Further development of 3D ARFI imaging methods[76] would be necessary to make ARFI a standalone tool for lesion assessment.

32.4.2 Preliminary Clinical Investigations of ARFI Imaging of Ablation Lesions

The preclinical work presented in the previous section demonstrated ARF imaging methods could visualize the relative stiffness difference between untreated myocardium and RFA lesions in vivo and that the stiff lesions created electrical propagation modifications. Based on these

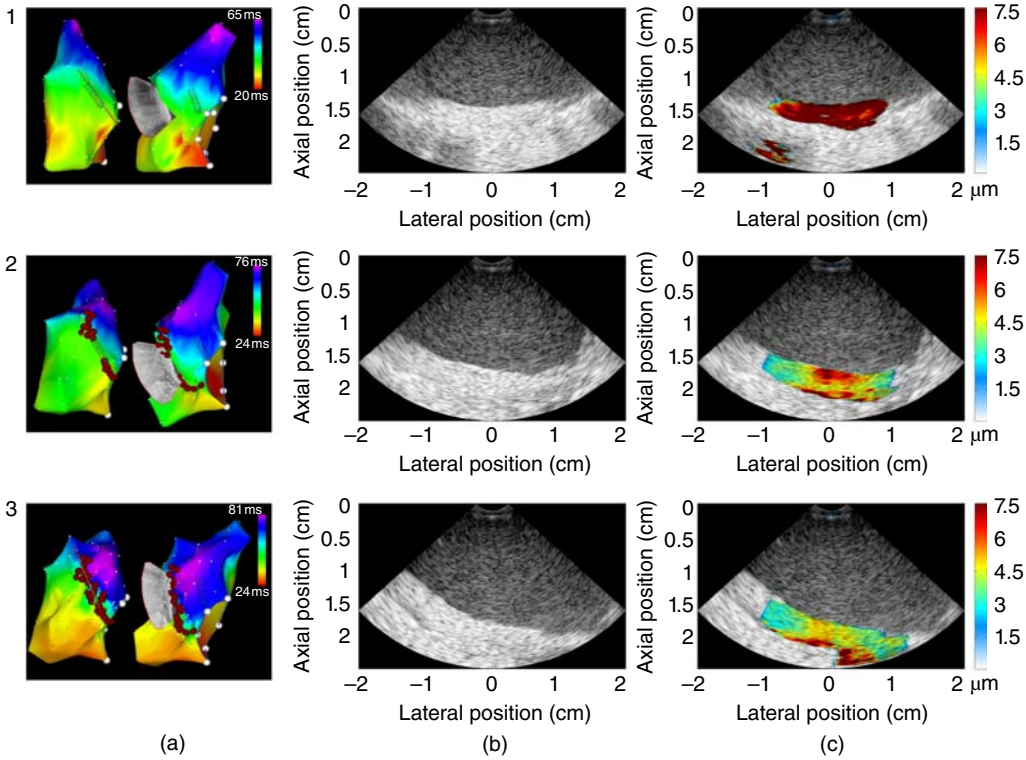

Figure 32.5 An example of three ARFI image-EAM map pairs. Row 1: acquired before RFA. Row 2: acquired after intentionally creating a 1 cm conductive gap. Row 3: acquired after closure of the 1 cm gap. Column A: electrical maps showing the imaging fan position in the canine right atrium and the location of delivered RFA lesions (red spherical markers). Column B: conventional B-mode images acquired at the location indicated on the LAT maps. There is no lesion visible in the B-mode images. Column C: maximum ARFI-induced displacement images. The color bar units are microns of tissue displacement away from the transducer. RFA lesion sites are visible as regions of lower relative displacement (stiffer tissue). Source: reprinted from [60], copyright 2012, with permission from Elsevier.

findings, a pilot clinical study by Bahnson et al. was undertaken to investigate the feasibility of intraprocedure RFA lesion evaluation with ARFI imaging in human patients [77]. In this study, intraprocedure ICE-ARFI images successfully identified acute RFA lesions in common ablation targets in the human heart, and ARFI imaging identified a ~47% reduction in the relative stiffness at RFA sites. This finding is similar to the difference between the increases in stiffness seen in the previously mentioned studies. An example image from this study is shown in Figure 32.6; the figure depicts ARFI imaging of sequential RFA sites at the LA roof of a patient undergoing TCA for AF. Tissue stiffening, relative to adjacent unablated tissue in the field of view, is produced by the sequential application of RF energy. The initial ablation near the left of each panel produced tissue stiffening that was reproducibly imaged over a period of the several minutes.

Based on the success of preclinical results and preliminary clinical trials, further investigation of ARFI imaging for intraprocedure ablation lesion assessment is underway. Improvements in imaging technology, image sequencing, and scanner and catheter hardware would greatly increase the chances of this technology being successfully integrated into clinical TCA procedures. Opportunities also exist for elastography-based assessment of chronic lesions and endogenous atrial scar tissue characterization for improving TCA treatment strategies [78]. If successfully translated for clinical use, elastography-based lesion assessment could improve

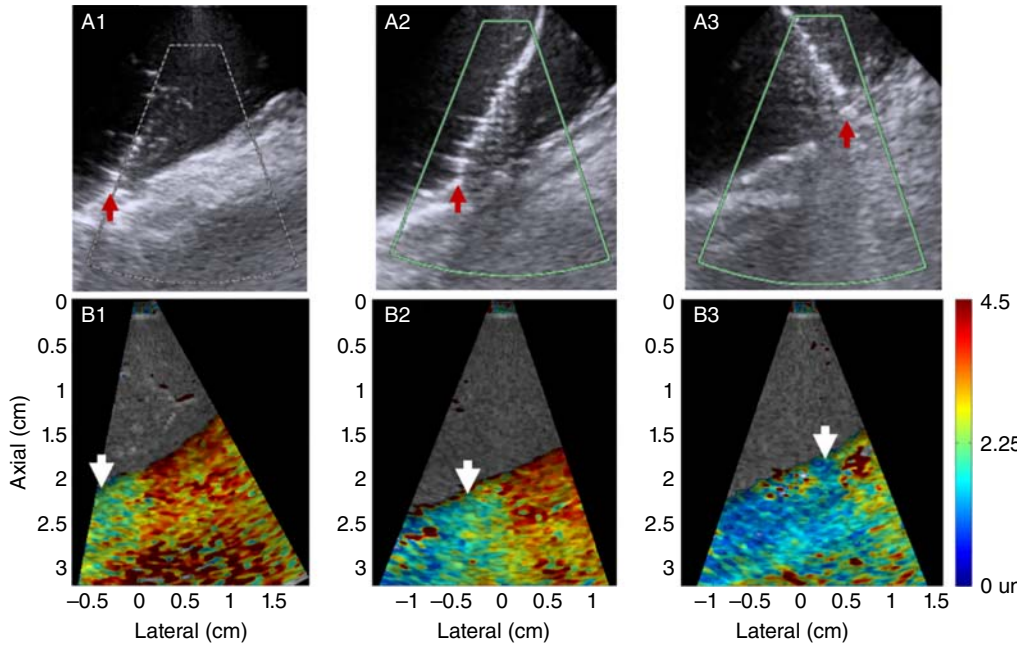

Figure 32.6 ICE and ARFI images of the ablation catheter contact location (red arrows, row A) for three consecutive RF applications (irrigated, 35 W power-controlled, 60 s each) at the LA roof. White arrows indicate the newly formed regions of increased tissue stiffness after RFA. The position and orientation of the ICE catheter was maintained between acquisitions, but note that the ARFI imaging plane in B1 was steered (an operator capability included on the clinical software platform) slightly to the right compared to panels B2 and B3 to keep the ablation catheter out of the field of view during ARFI imaging of B1. The color bar units are microns of tissue displacement away from the transducer. Source: reprinted from [77], copyright 2012, with permission from John Wiley and Sons.

the accuracy and safety of TCA procedures with minimal modifications to current procedure methods and equipment.

32.5 Conclusions

ARF-based elastography techniques have recently been under investigation for cardiac imaging applications. ARF-based imaging methods offer a myriad of opportunities for the diagnosis and treatment of various cardiac diseases as it provides previously unavailable information on the local dynamic stiffness characteristics of tissue. The content in this chapter presents the encouraging results encountered in our research into cardiac ARF-based elastography. Also, both ARFI imaging and SWEI techniques can be implemented on conventional ultrasound scanners and probes, thus providing a portable and cost-efficient imaging modality for cardiac imaging. These promising results highlight the many opportunities to improve and refine ARFI imaging and SWEI techniques for cardiac applications.

Funding Acknowledgements

NIH grant numbers R01-EB-012484 and R37-HL-096023.

References

1 Mozaffarian, D., et al. (2015). Heart disease and stroke statistics – 2015 update: a report from the American Heart Association. *Circulation* 131 (4): e29–322.
2 Doherty, J.R., et al. (2013). Acoustic radiation force elasticity imaging in diagnostic ultrasound. *IEEE Trans. Ultrason., Ferroelectr., Freq. Control* 60 (4): 685–701.
3 Nightingale, K. (2011). Acoustic radiation force impulse (ARFI) imaging: a review. *Curr. Med. Imaging Rev.* 7 (4): 328–339.
4 Palmeri, M.L. and Nightingale, K.R. (2011). Acoustic radiation force-based elasticity imaging methods. *Interface Focus* 1 (4): 553–564.
5 Pinton, G.F., Dahl, J.J., and Trahey, G.E. (2006). Rapid tracking of small displacements with ultrasound. *IEEE Trans. Ultrason., Ferroelect., Freq. Control* 53 (6): 1103–1117.
6 Giannantonio, D.M., Dumont, D.M., Trahey, G.E., and Byram, B.C. (2011). Comparison of physiological motion filters for cardiac ARFI. *Ultrason. Imaging* 33 (2): 89–108.
7 Hsu, S.J., et al. (2009). Novel acoustic radiation force impulse imaging methods for visualization of rapidly moving tissue. *Ultrason. Imaging* 31 (3): 183–200.
8 Nightingale, K., et al. (2005). Ultrasonic imaging of the mechanical properties of tissues using localized, transient acoustic radiation force. In: *2005 IEEE International Conference on Acoustics, Speech, and Signal Processing*, Vols 1–5, 981–984.
9 Palmeri, M.L., et al. (2005). A finite-element method model of soft tissue response to impulsive acoustic radiation force. *IEEE Trans. Ultrason., Ferroelect., Freq. Control* 52 (10): 1699–1712.
10 Nightingale, K.R., et al. (2011). Comparison of qualitative and quantitative acoustic radiation force based elasticity imaging methods. In: *2011 8th IEEE International Symposium on Biomedical Imaging: From Nano to Macro*, 1606–1609.
11 Nightingale, K., McAleavey, S., and Trahey, G. (2003). Shear-wave generation using acoustic radiation force: in vivo and ex vivo results. *Ultrasound Med. Biol.* 29 (12): 1715–1723.
12 Sarvazyan, A.P., et al. (1998). Shear wave elasticity imaging: a new ultrasonic technology of medical diagnostics. *Ultrasound Med. Biol.* 24 (9): 1419–1435.
13 Hollender, P.J., et al. (2015). Single- and multiple-track-location shear wave and acoustic radiation force impulse imaging: matched comparison of contrast, contrast-to-noise ratio and resolution. *Ultrasound Med. Biol.* 41 (4): 1043–1057.
14 Palmeri, M.L. and Nightingale, K.R. (2011). What challenges must be overcome before ultrasound elasticity imaging is ready for the clinic? *Imaging Med.* 3 (4): 433–444.
15 Burkhoff, D., Mirsky, I., and Suga, H. (2005). Assessment of systolic and diastolic ventricular properties via pressure-volume analysis: a guide for clinical, translational, and basic researchers. *Am. J. Physiol. Heart Circ. Physiol.* 289 (2): H501–512.
16 D'Hooge, J., Herbots, L., and Sutherland, G.R. (2003). Quantitative assessment of intrinsic regional myocardial deformation by Doppler strain rate echocardiography in humans. *Circulation* 107 (7): e49; author reply e49.
17 Urheim, S., et al. (2000). Myocardial strain by Doppler echocardiography. Validation of a new method to quantify regional myocardial function. *Circulation* 102 (10): 1158–1164.
18 Hsu, S.J., et al. (2007). In vivo assessment of myocardial stiffness with acoustic radiation force impulse imaging. *Ultrasound Med. Biol.* 33 (11): 1706–1719.
19 Couade, M., et al. (2011). In vivo quantitative mapping of myocardial stiffening and transmural anisotropy during the cardiac cycle. *IEEE Trans. Med. Imaging* 30 (2): 295–305.
20 Pernot, M., et al. (2011). Real-time assessment of myocardial contractility using shear wave imaging. *J. Am. Coll. Cardiol.* 58 (1): 65–72.

21 Pislaru, C., et al. (2014). Viscoelastic properties of normal and infarcted myocardium measured by a multifrequency shear wave method: comparison with pressure-segment length method. *Ultrasound Med. Biol.* 40 (8): 1785–1795.

22 Vejdani-Jahromi, M., et al. (2015). Ultrasound shear wave elasticity imaging quantifies coronary perfusion pressure effect on cardiac compliance. *IEEE Trans. Med. Imaging* 34 (2): 465–473.

23 Vejdani-Jahromi, M., Freedman, J., Nagle, M., et al. (2016). Quantifying myocardial contractility changes using ultrasound-based shear wave elastography. *J. Am. Soc. Echocardiogr.* 30 (1): 90–96.

24 Vejdani-Jahromi, M., Nagle, M., Jiang, Y., et al. (2016). A comparison of acoustic radiation force derived indices of cardiac function in the Langendorff perfused rabbit heart. *IEEE Trans. Ultrason., Ferroelectr., Freq. Control, March 2016*. 63 (9): 1288–1295.

25 Amador, C., et al. (2012). Loss tangent and complex modulus estimated by acoustic radiation force creep and shear wave dispersion. *Phys. Med. Biol.* 57 (5): 1263–1282.

26 Wang, M., et al. (2013). Imaging transverse isotropic properties of muscle by monitoring acoustic radiation force induced shear waves using a 2-D matrix ultrasound array. *IEEE Trans. Med. Imaging* 32 (9): 1671–1684.

27 Rouze, N.C., et al. (2012). Parameters affecting the resolution and accuracy of 2-D quantitative shear wave images. *IEEE Trans. Ultrason., Ferroelectr., Freq. Control* 59 (8): 1729–1740.

28 Helm, P.A., et al. (2005). Ex vivo 3D diffusion tensor imaging and quantification of cardiac laminar structure. *Magn. Reson. Med.* 54 (4): 850–859.

29 Streeter, D.D., Jr., et al. (1969). Fiber orientation in the canine left ventricle during diastole and systole. *Circ. Res.* 24 (3): 339–347.

30 Bouchard, R.R. (2010). Acoustic radiation force impulse-driven shear wave velocimetry in cardiac tissue. Ph.D. Thesis from Department of Biomedical Engineering, Duke University, Durham, NC, USA.

31 Lee, W.N., et al. (2012). Mapping myocardial fiber orientation using echocardiography-based shear wave imaging. *IEEE Trans. Med. Imaging* 31 (3): 554–562.

32 Nenadic, I.Z., et al. (2011). Lamb wave dispersion ultrasound vibrometry (LDUV) method for quantifying mechanical properties of viscoelastic solids. *Phys. Med. Biol.* 56 (7): 2245–2264.

33 Nenadic, I.Z., et al. (2011). Phase velocities and attenuations of shear, Lamb, and Rayleigh waves in plate-like tissues submerged in a fluid (L). *J. Acoust. Soc. Am.* 130 (6): 3549–3552.

34 Bradway, D.P., et al. (2007). 6B-6 Transthoracic cardiac acoustic radiation force impulse imaging: a feasibility study. In: *IEEE Ultrasonics Symposium, 2007*.

35 Bradway, D.P., et al. (2012). Feasibility and safety of transthoracic cardiac acoustic radiation force impulse imaging methods. In: *IEEE International Ultrasonics Symposium (IUS), 2012*.

36 Kakkad, V., et al. (2015). In vivo transthoracic measurements of acoustic radiation force induced displacements in the heart over the cardiac cycle. In: *IEEE International Ultrasonics Symposium (IUS), 2015*.

37 Song, P., et al. (2013). Improved shear wave motion detection using pulse-inversion harmonic imaging with a phased array transducer. *IEEE Trans. Med. Imaging* 32 (12): 2299–2310.

38 Pengfei, S., et al. (2015). Implementation of shear wave elastography on pediatric cardiac transducers with pulse-inversion harmonic imaging and time-aligned sequential tracking. In: *IEEE International Ultrasonics Symposium (IUS), 2015*.

39 Zwirn, G. and Akselrod, S. (2006). Stationary clutter rejection in echocardiography. *Ultrasound Med. Biol.* 32 (1): 43–52.

40 Doherty, J.R., Dahl, J.J., and Trahey, G.E. (2013). Harmonic tracking of acoustic radiation force-induced displacements. *IEEE Trans. Ultrason., Ferroelectr., Freq. Control* 60 (11): 2347–2358.

41 Papadacci, C., et al. (2014). High-contrast ultrafast imaging of the heart. *IEEE Trans. Ultrason., Ferroelectr., Freq. Control* 61 (2): 288–301.

42 Hollender, P.J., et al. (2012). Intracardiac echocardiography measurement of dynamic myocardial stiffness with shear wave velocimetry. *Ultrasound Med. Biol.* 38 (7): 1271–1283.

43 Calkins, H., et al. (2012). 2012 HRS/EHRA/ECAS expert consensus statement on catheter and surgical ablation of atrial fibrillation: recommendations for patient selection, procedural techniques, patient management and follow-up, definitions, endpoints, and research trial design. *Heart Rhythm* 9 (4): 632–696 e21.

44 Cappato, R., et al. (2010). Updated worldwide survey on the methods, efficacy, and safety of catheter ablation for human atrial fibrillation. *Circ. Arrhythm. Electrophysiol.* 3 (1): 32–38.

45 Kowalski, M., et al. (2012). Histopathologic characterization of chronic radiofrequency ablation lesions for pulmonary vein isolation. *J. Am. Coll. Cardiol.* 59 (10): 930–938.

46 Ranjan, R., et al. (2011). Gaps in the ablation line as a potential cause of recovery from electrical isolation and their visualization using MRI. *Circ. Arrhythm. Electrophysiol.* 4 (3): 279–286.

47 Miller, M.A., et al. (2012). Acute electrical isolation is a necessary but insufficient endpoint for achieving durable PV isolation: the importance of closing the visual gap. *Europace* 14 (5): 653–660.

48 Eyerly, S.A., Vejdani-Jahromi, M., Dumont, D.M., et al. (2015). The evolution of tissue stiffness at radiofrequency ablation sites during lesion formation and in the peri-ablation period. *J. Cardiovasc. Electrophysiol.* 26 (9): 1009–1018.

49 Wright, N.T. and Humphrey, J.D. (2002). Denaturation of collagen via heating: an irreversible rate process. *Annu. Rev. Biomed. Eng.* 4 : 109–128.

50 Bischof, J.C. and He, X. (2005). Thermal stability of proteins. *Ann. NY Acad. Sci.* 1066: 12–33.

51 Chen, S.S. and Humphrey, J.D. (1998). Heat-induced changes in the mechanics of a collagenous tissue: pseudoelastic behavior at 37 degrees C. *J. Biomech.* 31 (3): 211–216.

52 Wu, T., et al. (2001). Assessment of thermal tissue ablation with MR elastography. *Magn. Reson. Med.* 45 (1): 80–87.

53 Pearce, J.A. (2010). Models for thermal damage in tissues: processes and applications. *Crit. Rev. Biomed. Eng.* 38 (1): 1–20.

54 Lepock, J.R. (2003). Cellular effects of hyperthermia: relevance to the minimum dose for thermal damage. *Int. J. Hyperthermia* 19 (3): 252–266.

55 Eyerly, S.A., et al. (2013). In vitro monitoring of the dynamic elasticity changes during radiofrequency ablation with acoustic radiation force impulse imaging. *J. Cardiovasc. Electrophysiol.* 24 (4): 472–473.

56 Schwartzman, D., et al. (2001). Cardiac swelling associated with linear radiofrequency ablation in the atrium. *J. Interv. Card. Electrophysiol.* 5 (2): 159–166.

57 Pernot, M., et al. (2009). Mapping myocardial elasticity changes after RF-ablation using supersonic shear imaging. *Comput. Cardiol.* 793–796.

58 Kwiecinski, W., et al. (2014). Quantitative evaluation of atrial radio frequency ablation using intracardiac shear-wave elastography. *Med. Phys.* 41 (11): 112901.

59 Eyerly, S.A., et al. (2010). An in vitro assessment of acoustic radiation force impulse imaging for visualizing cardiac radiofrequency ablation lesions. *J. Cardiovasc. Electrophysiol.* 21 (5): 557–563.

60 Eyerly, S.A., et al. (2012). Intracardiac acoustic radiation force impulse imaging: a novel imaging method for intraprocedural evaluation of radiofrequency ablation lesions. *Heart Rhythm* 9 (11): 1855–1862.

61 Fahey, B.J., et al. (2005). Acoustic radiation force impulse imaging of myocardial radiofrequency ablation: initial in vivo results. *IEEE Trans. Ultrason., Ferroelect., Freq. Control* 52 (4): 631–641.

62 Hsu, S.J., et al. (2007). Challenges and implementation of radiation-force imaging with an intracardiac ultrasound transducer. *IEEE Trans. Ultrason., Ferroelect., Freq. Control* 54 (5): 996–1009.

63 Nath, S., et al. (1993). Cellular electrophysiological effects of hyperthermia on isolated guinea pig papillary muscle. Implications for catheter ablation. *Circulation* 88 (4, part 1): 1826–1831.

64 Wilber, D.J., Packer, D., and Stevenson, W.G. (2008). *Catheter Ablation of Cardiac Arrhythmias : Basic Concepts and Clinical Applications*, 3rd edn., Malden, Mass.: Blackwell Futura.

65 Ge, Y.Z., et al. (1995). Cellular electrophysiological changes induced in vitro by radiofrequency current: comparison with electrical ablation. *Pacing Clin. Electrophysiol.* 18 (2): 323–333.

66 Grondin, J., et al. (2015). Intracardiac myocardial elastography in canines and humans in vivo. *IEEE Trans. Ultrason., Ferroelectr., Freq. Control* 62 (2): 337–349.

67 Hsu, S.J., et al. (2008). Intracardiac echocardiography and acoustic radiation force impulse imaging of a dynamic ex vivo ovine heart model. *Ultrason. Imaging* 30 (2): 63–77.

68 Ruisi, C.P., Brysiewicz, N., Asnes, J.D., et al. (2013). Use of intracardiac echocardiography during atrial fibrillation ablation. *Pacing Clin. Electrophysiol.* 36: 781–788.

69 Proulx, T.L., Tasker, D., and Bartlett-Roberto, J. (2005). Advances in catheter-based ultrasound imaging: Intracardiac Echocardiography and the ACUSON AcuNav^{TM}. *Ultrasound Catheter* 1: 669–678.

70 Natale, A. (2006). *Intracardiac Echocardiography in Interventional Electrophysiology*. Abingdon UK: Informa Healthcare.

71 Robinson, M.R. and Hutchinson, M.D. (2010). Use of imaging techniques to guide catheter ablation procedures. *Curr. Cardiol. Rep.* 12 (5): 374–381.

72 Earley, M.J. (2009). How to perform a transseptal puncture. *Heart* 95 (1): 85–92.

73 Yamada, T., et al. (2007). One-puncture, double-transseptal catheterization manoeuvre in the catheter ablation of atrial fibrillation. *Europace* 9 (7): 487–489.

74 Nightingale, K., Palmeri, M., and Trahey, G. (2006). Analysis of contrast in images generated with transient acoustic radiation force. *Ultrasound Med. Biol.* 32 (1): 61–72.

75 Eyerly, S.A., et al. (2014). Contrast in intracardiac acoustic radiation force impulse images of radiofrequency ablation lesions. *Ultrason. Imaging* 36 (2): 133–148.

76 Hollender, P., et al. (2013). Three-dimensional fusion of shear wave imaging and electro-anatomical mapping for intracardiac radiofrequency ablation monitoring. In: *IEEE International Ultrasonics Symposium (IUS),* 2013 108–111.

77 Bahnson, T.D., et al. (2014). Feasibility of near real-time lesion assessment during radiofrequency catheter ablation in humans using acoustic radiation force impulse imaging. *J. Cardiovasc. Electrophysiol.* 25 (12): 1275–1283.

33

Cardiovascular Application of Shear Wave Elastography

Pengfei Song and Shigao Chen

Department of Radiology, Mayo Clinic, Rochester, MN, USA

33.1 Introduction

Cardiovascular diseases cause 17.3 million deaths a year worldwide, according to the World Heart Federation, and are the leading causes of death in the United States, claiming more lives than all forms of cancer combined [1]. Echocardiography has been playing a significant role in diagnosis and prognosis of cardiovascular diseases, thanks to its high imaging frame rate, low cost, and powerful imaging tools such as Doppler blood flow imaging and strain imaging. As evidenced by the success of strain imaging in cardiovascular applications, biomechanical properties of the myocardium and vessels are strong biomarkers for the state of the cardiovascular health [2]. Strain imaging directly measures the dynamic deformation of the tissue, and provides semi-quantitative assessment of myocardial and vascular stiffness in terms of strain or strain rate [3]. For instance, the ischemic infarcted myocardium contracts less than the normal myocardium and thus exhibits lower strain in strain maps [4]; fatty plaque tissue is softer than fibrous plaque tissue and therefore is represented as regions with higher strain. The main drawback of strain imaging, however, is the unknown stress field within cardiac or vascular walls, which makes quantitative assessment of cardiovascular stiffness challenging.

In the last decade, significant amounts of effort have been made to pursue quantitative assessment of cardiovascular viscoelasticity using shear wave-based techniques. Similar to the implementation of shear wave elastography in other soft tissues, one can quantify both shear elasticity and shear viscosity of the cardiovascular tissue by inducing shear waves and solving the shear wave equation. Thanks to the fast imaging speed, shear wave elastography can be used to measure dynamic cardiovascular stiffness throughout the cardiac cycle with high temporal and spatial resolutions [5–7], which is similar to strain imaging. However, different from strain imaging, shear wave imaging provides direct and quantitative measurements of the myocardial and vascular wall stiffness in the units of shear modulus, which is usually not available with strain imaging. The quantitative nature of shear wave enables measurement of local contractility of the heart and diastolic myocardial stiffness [5, 8–12], which have significant clinical values for many cardiovascular diseases. At present, many different shear wave imaging techniques have been developed for cardiovascular applications, including various shear wave generation methods [13–16], shear wave detection methods [10, 17], and inversion methods [18–21]. Cardiovascular application of shear wave imaging includes myocardial infarction [14, 22, 23], real-time assessment of myocardial contractility [8], myocardial architecture imaging with myocardial fiber orientation mapping [24, 25], quantitative evaluation of atrial radio frequency ablation [26], coronary perfusion pressure quantification [27], and carotid artery plaque characterization [28, 29], with new clinical applications being actively explored. In this chapter, we will first

Ultrasound Elastography for Biomedical Applications and Medicine, First Edition.
Edited by Ivan Nenadic, Matthew Urban, James Greenleaf, Jean-Luc Gennisson, Miguel Bernal, and Mickael Tanter.

review the different cardiovascular shear wave imaging techniques, followed by a brief review of the aforementioned different cardiovascular applications of shear wave elastography.

33.2 Cardiovascular Shear Wave Imaging Techniques

33.2.1 Cardiovascular Shear Wave Generation Methods

Three main shear wave generation methods have been developed for cardiovascular applications: external mechanical vibration, acoustic radiation force, and intrinsic physiological motion. Figure 33.1 shows an example of the external mechanical vibration setup used by Urban et al. [13]. A similar setup has been used by others [20, 23, 30]. In this category of methods, a mechanical coupling (e.g. shaker rod) is established between the tissue and the external shaker device to induce shear waves into the myocardial or vascular wall. The shaker rod can be placed on the surface of the plate-like tissue, such as myocardial wall, to produce Rayleigh waves, or be inserted throughout the thickness of the myocardial wall to produce Lamb waves [19]. Here we use shear waves to represent different types of waves for succinctness. We will explain the differences in the next section. For shear wave detection, an ultrasound transducer is positioned close to the shear wave source and tracks the shear wave motion. The advantage of using external mechanical vibration is that high-amplitude and multi-frequency (40–500 Hz) shear waves can be produced, which is ideal for assessing viscoelastic properties of the myocardium and vessel wall. However, because the shaker needs to be mechanically coupled to the tissue, for cardiac applications this setup is best suited for open-chest in vivo experiments or excised in vitro studies. For closed-chest transthoracic cardiac imaging, an external acoustic driver can be placed on the surface of the chest wall to generate shear waves into the myocardium, which is commonly used in cardiac magnetic resonance elastography (MRE) [31–37]. This method is currently under investigation for

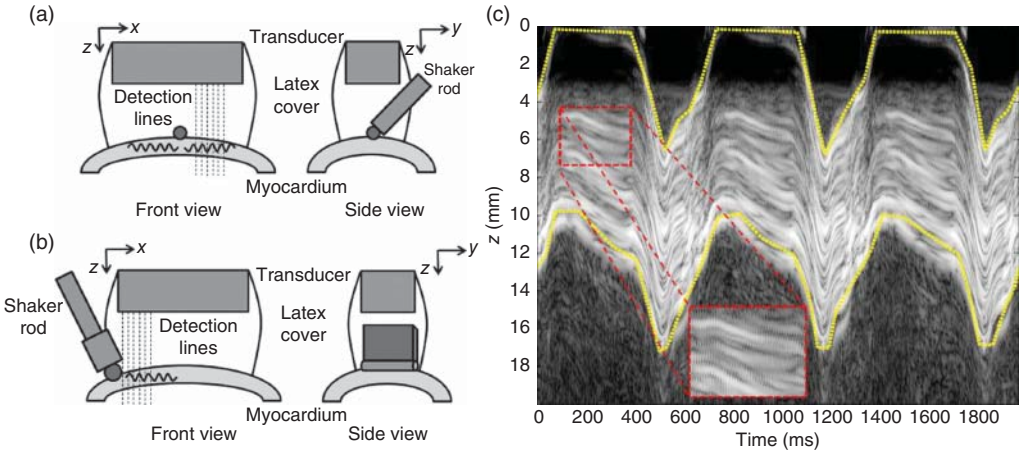

Figure 33.1 Shear wave generation with external mechanical vibration. (a) Rod with a ball bearing attached to the mechanical shaker is placed onto the surface of the myocardial wall. A linear array transducer was suspended above the heart wall and coupled with water-filled latex cover for shear wave detection. (b) Rod with a plate and steel cylinder bearing attached to the mechanical shaker is placed onto the surface of the myocardial wall. (c) M-mode recording of the wave motion generated by the mechanical shaker. Small oscillations can be observed from the 150 Hz vibration in the magnified inset. Source: © 2013 IEEE, reprinted, with permission, from [13].

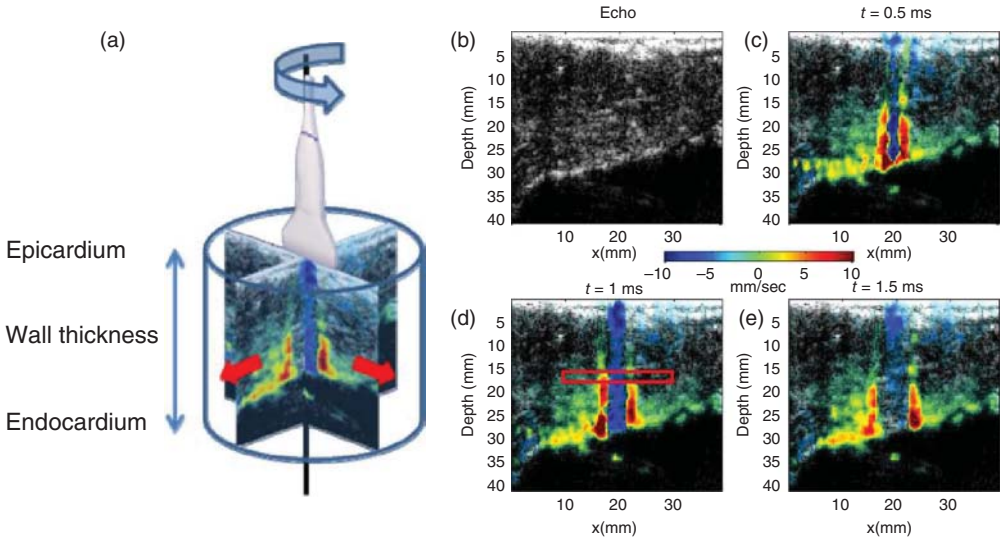

Figure 33.2 (a) The same ultrasound transducer was used for both shear wave generation using acoustic radiation force and for shear wave detection. The transducer is rotated around the pushing beam axis to investigate myocardial anisotropy. (b) B-mode image of the myocardium; (c)–(e) Color-coded shear wave motion signal superimposed to the B-mode image at different time instants after the push beam. Source: © 2011 IEEE, reprinted, with permission, from [5].

cardiac ultrasound implementations [38]. For vascular applications, one may be able to attach the shaker to the surface of the body to generate shear waves in superficial vessels such as the carotid artery, with the compromise of shear wave attenuation by surrounding tissues and the complicated wave field. MRE has shown the potential of using the acoustic driver to generate shear waves to deep vessels such as the abdominal aorta and assess the arterial stiffness [39]. One can use a similar vibration setup and use an ultrasound transducer to detect the shear wave motion.

The second method for cardiovascular shear wave generation is the use of acoustic radiation force (ARF) to remotely produce shear waves inside the tissue [40]. Figure 33.2 shows a supersonic shear imaging (SSI) implementation of this method [5]. A push beam is first transmitted to exert acoustic radiation force onto the tissue, which generates two shear wave fronts propagating in opposite directions away from the push beam (Figure 33.2, right panel). The same transducer is then used to track the shear wave motion with the ultrafast compound plane wave imaging technique [5]. ARF-based shear wave elastography can be implemented both on transthoracic phased arrays or intracardiac echocardiography catheter arrays [14, 15]. ARF-induced shear waves are transient and broadband, and can also be used for assessing viscoelasticity of the myocardial and vessel wall [5, 6, 21, 41]. The advantage of the ARF method is that the shear wave is being generated and detected by the same transducer, which can be used for both open-chest epicardial imaging and closed-chest transthoracic imaging [9, 10]. Meanwhile, as compared to the mechanical vibration method, the propagation direction of the shear wave is better controlled for the ARF method in closed-chest transthoracic imaging, which significantly simplifies the inversion process. However, ARF-induced shear waves suffer from the low wave motion amplitude caused by acoustic attenuation to the push beam, and consequently suffers from poorer signal-to-noise ratio (SNR) for closed-chest transthoracic imaging. Also, the ARF method requires a quasi-orthogonal relationship between the push beam and the tissue to ensure effective shear wave generation. For scan views where the myocardial wall

is vertical (e.g. the left ventricular walls under apical 4-chamber view) and parallel to the push beam, shear waves cannot be effectively generated.

The final shear wave generation method is based on intrinsic physiological motion. It has been shown that during a cardiac cycle, multiple spontaneously actuated pulsive vibration motions propagate in the heart wall, which can be utilized to measure both elasticity and viscosity of the myocardium [16, 42–44]. Among these waves, the diastolic myocardial stretch (Figure 33.3, left panel) induced by atrial systole or atrial kick enables robust shear wave measurements and has been validated by sonomicrometry [16]. This wave can be used to quantify diastolic ventricular myocardial stiffness. For vascular applications, pulse waves generated at the ejection phase of the left ventricle have been widely used to measure arterial stiffness (Figure 33.3, right panel), which has shown significant clinical value [45–48]. The advantage of using intrinsic physiological motion is that no additional shear wave sources are required. However, the wave source can be ambiguous and the wave propagation can be complicated. Advanced tracking techniques such as high frame-rate 3D imaging may be necessary to capture the full propagation pattern in cardiac tissue and obtain the correct wave speed. Also, intrinsic shear wave generation can be unstable and variable among different subjects. For instance, the atrial-kick induced diastolic wave does not work in patients without atrial systole.

33.2.2 Cardiovascular Viscoelasticity Calculation Methods

Both the myocardial and vascular walls are viscoelastic tissues and show significant frequency-dependent wave speed dispersion [6, 19–21]. It has been suggested that because the thickness of the cardiovascular wall is comparable to the wavelength of the shear wave, it is more appropriate to term these waves as Lamb waves instead of shear waves [6, 20, 42]. Differentiating Lamb waves from shear waves is important in wave dispersion analysis where the correct wave model is needed to calculate elasticity and viscosity. If only the group velocity is measured, the two terms can be used interchangeably because Lamb waves are one type of shear wave. For waves generated directly inside the cardiovascular tissue (e.g. the embedded shaker rod or ARF-induced shear waves), the waves can be treated as Lamb waves. For waves generated from the surface of the tissue (e.g. a shaker rod attached to the tissue surface), the resulting wave can be a Rayleigh wave if the excitation frequency is high and a Lamb wave if the excitation frequency is low. It has been shown that Raleigh waves converge to Lamb waves at high frequencies and, therefore, it is possible to use the Lamb wave dispersion model for viscoelasticity measurements [19].

The detailed derivation of the Lamb wave equations can be found in Couade et al. [6] and Nenadic et al. [20]. For post-processing, the wave motion signal is typically converted to Fourier domain for frequency-dependent analysis [6, 20, 21]. Phase velocities of the wave as a function of frequency can be obtained in Fourier domain, from which model fitting can then be performed to calculate elasticity (μ_1) and viscosity (μ_2). Figure 33.4 shows examples of myocardial Lamb wave dispersion analysis and carotid artery dispersion curves.

Dispersion analysis provides comprehensive details of elasticity and viscosity of the tissue. However, it is sensitive to noise and needs a relatively wide band shear wave signal to achieve robust model fitting. For in vivo applications, group velocity of the shear wave is more robust to noise and more commonly used to quantify the stiffness of the cardiovascular tissue. Neglecting dispersion and viscosity, shear wave speed (c_s) is related to the shear modulus (μ) of the tissue by: $\mu = \rho c_s^2$, where ρ is the density of the tissue and can be assumed to be 1000 kg/m^3. Shear wave group velocity can be measured by a variety of methods such as time-to-peak and time-of-flight [5, 49], cross-correlation [50, 51], and Radon-transform [9, 10]. The final results can be 2D shear wave speed or shear modulus maps (Figure 33.5a), or 1D point measurements from a local region of the tissue (Figure 33.5b).

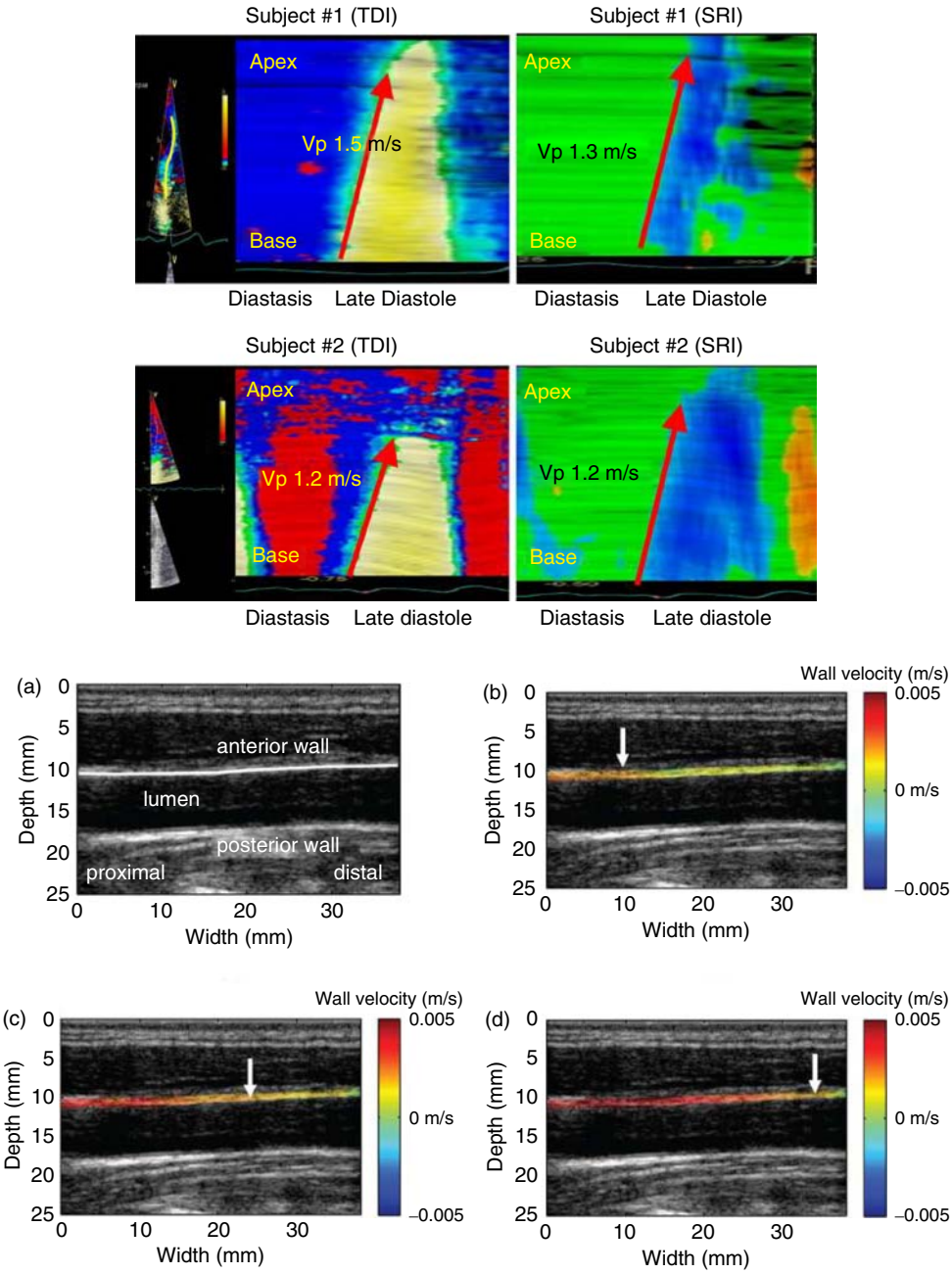

Figure 33.3 Cardiovascular shear waves induced by intrinsic physiological motion. Left panel: reconstructed maps of longitudinal tissue velocities from the left ventricle during late diastole measured by tissue Doppler imaging (TDI) in two normal subjects. Arrows indicate the direction of wave propagation. The slope of this wave represents wave speed (V_p). Comparable results were obtained by strain rate imaging (SRI). Source: with permission of Springer [16]. Right panel: (a) A B-mode image and (b)–(d) the sequence of the wall velocity images in the left common carotid artery of a healthy volunteer. In (b)–(d), the wall velocities are color coded and overlaid onto the B-mode image. Positive velocities represent upward motion, whereas negative velocities represent downward motion. Images in (b)–(d) are 3.5 ms apart. The solid arrows indicate the propagation of the pulse wave from the proximal (left) to the distal (right) sites. Source: © 2012 IEEE, reprinted, with permission, from [47].

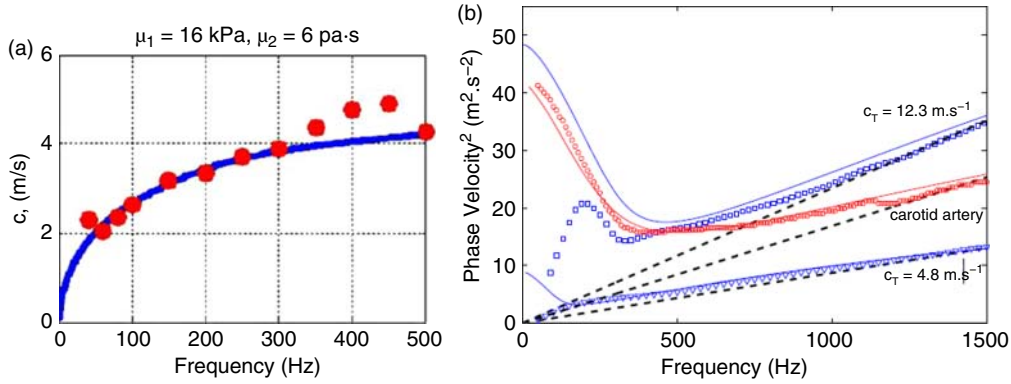

Figure 33.4 Viscoelasticity measurements of myocardium (left panel) and carotid artery (right panel). (a) Lamb wave dispersion in the excised porcine LV free-wall myocardium: experimentally obtained shear wave dispersion curves are shown as circles. Lamb wave model (solid line) was fitted to the data to obtain the values of elasticity (μ_1) and viscosity (μ_2). Source: © Institute of Physics and Engineering in Medicine, reproduced by permission of IOP Publishing, all rights reserved [18]. (b) Experimental dispersion curves obtained in arterial phantoms with different shear modulus (square) compared with numerical solutions (solid line); in vivo in the common carotid arterial wall of a healthy volunteer (square curve) compared with numerical simulation (solid line curve). Source: reprinted from [6], copyright 2010, with permission from Elsevier.

33.2.3 Cardiovascular Shear Wave Detection Methods

Shear wave speed in cardiovascular tissues ranges from ~1 m/s to over 10 m/s, which demands high frame-rate ultrasound imaging to robustly track the shear wave propagation. If a conventional line-by-line scanning scheme is used, one needs to substantially reduce the number of the imaging lines to satisfy frame rate [16, 42]. Ultrafast compound plane wave imaging can reach very high imaging frame rates with high spatial and temporal resolutions, which is ideal for cardiovascular shear wave detection [5–8]. To increase the dimension of the tracking region, one can use coherent compounding diverging wave imaging with very high frame rate [52, 53]. In cardiovascular imaging, ultrasound clutter noise can be severe, which significantly deteriorates the shear wave signal quality. Recently Song et al. proposed to use pulse-inversion harmonic imaging for shear wave detection and showed substantial improvement of shear wave signal quality under in vivo transthoracic scans compared to detection using fundamental imaging [10]. Pulse-inversion harmonic imaging has also been implemented in detecting ARF-induced tissue motion for carotid artery [17].

33.3 Clinical Applications of Cardiovascular Shear Wave Elastography

Like other tissues, stiffness is a strong biomarker for diagnosis and prognosis of numerous cardiovascular diseases. The quantitative shear elasticity measurements obtained with ultrasound shear wave elastography offers great potential for many clinical applications. Here we briefly review some of these clinical applications, including ischemic myocardial infarction, assessment of myocardial contractility, myocardial architecture imaging, evaluation of atrial radio frequency ablation, coronary perfusion pressure quantification, and carotid artery plaque characterization.

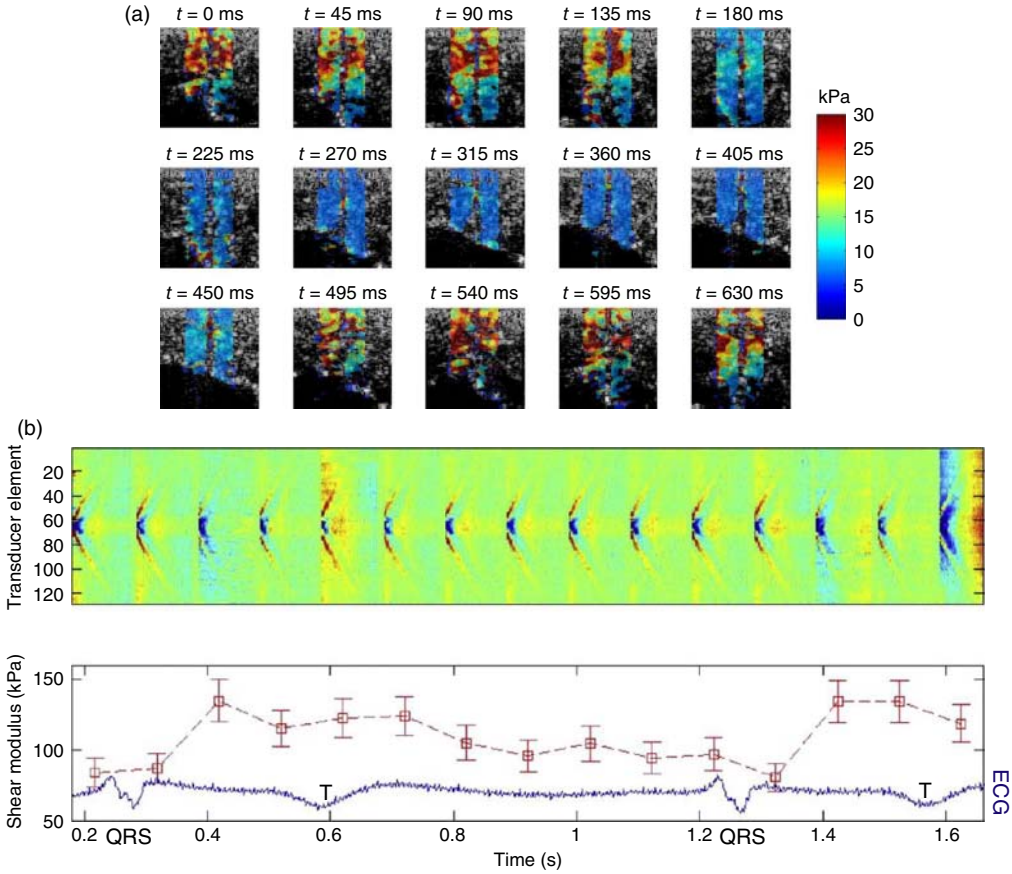

Figure 33.5 (a) 2D shear elasticity maps obtained at different stages of a same cardiac cycle superimposed on the B-mode images. Source: © 2011 IEEE, reprinted, with permission, from [5]. (b) Real-time in vivo measurement of carotid arterial wall shear modulus variation during a single heart cycle (13 values/cycle) with time-registered ECG. Upper panel: 15 successive space-time representations of the shear wave motion signal in the arterial wall. Lower panel: shear modulus measurements of the arterial wall throughout the cardiac cycle. Source: reprinted from [6], copyright 2010, with permission from Elsevier.

33.3.1 Ischemic Myocardial Infarction

Several animal studies have investigated the feasibility of using shear wave elastography to quantitatively measure myocardial stiffness changes induced by ischemic myocardial infarction and reperfusion [14, 23, 54]. It was found that for reversible ischemia (stunned), systolic myocardial shear elasticity first decreased with ischemia, and then gradually increased back to the baseline level after reperfusion; diastolic myocardial shear elasticity did not change significantly [54]. For irreversible ischemia (infarction), Pernot et al. reported decreased myocardial shear elasticity during ischemia and finally increased myocardial shear elasticity after reperfusion, while diastolic myocardial stiffness gradually increased during ischemia and reperfusion [54]. Pislaru et al. reported both increased diastolic shear elasticity and shear viscosity after reperfusion, while less consistent changes were found during systole [23]. Using an intracardiac catheter transducer, Hollender et al. reported increased shear wave speeds in infarcted left ventricular free wall, but no significant stiffness change in the intraventricular septum and no significant myocardial remodeling was observed [14]. It was noted in these studies that myocardial anisotropy can significantly vary the measured shear wave speed; therefore, the myocardial fiber orientation

needs to be accounted for when comparing shear wave speed measurements. Also, shear elasticity measurement is preload dependent. Shear wave speed measurements are more variable in systole than in diastole due to cardiac motion and high systolic shear wave speed. Meanwhile, because of the short propagation distance of shear waves due to significant shear wave attenuation in myocardium, only a small region of the myocardium can be imaged. Therefore, this method only works for pre-identified localized infarctions.

33.3.2 Assessment of Myocardial Contractility

Myocardial contractility is conventionally measured invasively by catheterization. A noninvasive technique that can monitor myocardial contractility in real time is of great interest. Pernot et al. investigated the use of shear wave elastography for myocardial contractility assessment and showed a strong correlation between the systolic myocardial stiffness and the systolic pressure, which indicates that peak systolic myocardial stiffness has the potential to be used as an index of myocardial contractility [8]. It was found that end-systolic myocardial stiffness was relatively load independent. Although the study was performed ex vivo on a Langendorff setup, it should be applicable for noninvasive imaging of the human heart.

33.3.3 Myocardial Architecture Imaging

Myocardium is a highly anisotropic tissue with organized myofibers oriented from approximately −60° near the epicardium to +60° near the endocardium [24]. It is known in physics that a shear wave propagates faster along the fiber than across the fiber. Therefore, by using shear wave elastography, one can map the myocardial fiber orientation to detect abnormal myocardial fiber orientation for hypertrophic or ischemic myocardium. In an in vivo open-chest animal model, Lee et al. showed strong correlation between shear wave mapped myofiber orientation and histology findings (Figure 33.6). They further demonstrated successful mapping of transmural fiber orientation in three beating ovine hearts [24]. In another study by Lee et al., good correlation of myofiber orientation mapping was found between shear wave elastography and magnetic resonance diffusing tensor imaging [25]. Noninvasive in vivo imaging of human myocardial fiber orientation is under investigation. Recently Song et al. reported that in in vivo human (both adults and pediatrics) transthoracic shear wave imaging, the myocardial shear wave speed measurements obtained from a parasternal short-axis view are significantly higher than those obtained from a parasternal long-axis view [11, 12]. These results corroborate with the animal study results by Lee et al. However, for in vivo human imaging, the available transducer rotation angles may be limited in transthoracic scans [11, 12]. Also, the accuracy of the method may be compromised by the low shear wave signal quality in vivo [11, 12].

33.3.4 Evaluation of Atrial Radio Frequency Ablation

Radio frequency catheter ablation (RFCA) is a well-established procedure for atrial fibrillation. However, precise ablation monitoring still remains challenging in the clinic. Kwiecinski et al. recently demonstrated the feasibility of using shear wave elastography on an intracardiac catheter transducer to quantitatively evaluate RFCA [26]. An approximately 4.5-fold increase in stiffness was observed in ablated ex vivo tissue, and a 3-fold increase in shear modulus was observed in vivo in three sheep (Figure 33.7) [26]. It was noted that the lack of navigation system was very challenging for the alignment of the ultrasound and the RFA catheters. Fluoroscopy was used in this study for the alignment. However, this major limitation can be addressed by a dual mode approach that uses a single catheter system which can both image and ablate with ultrasound.

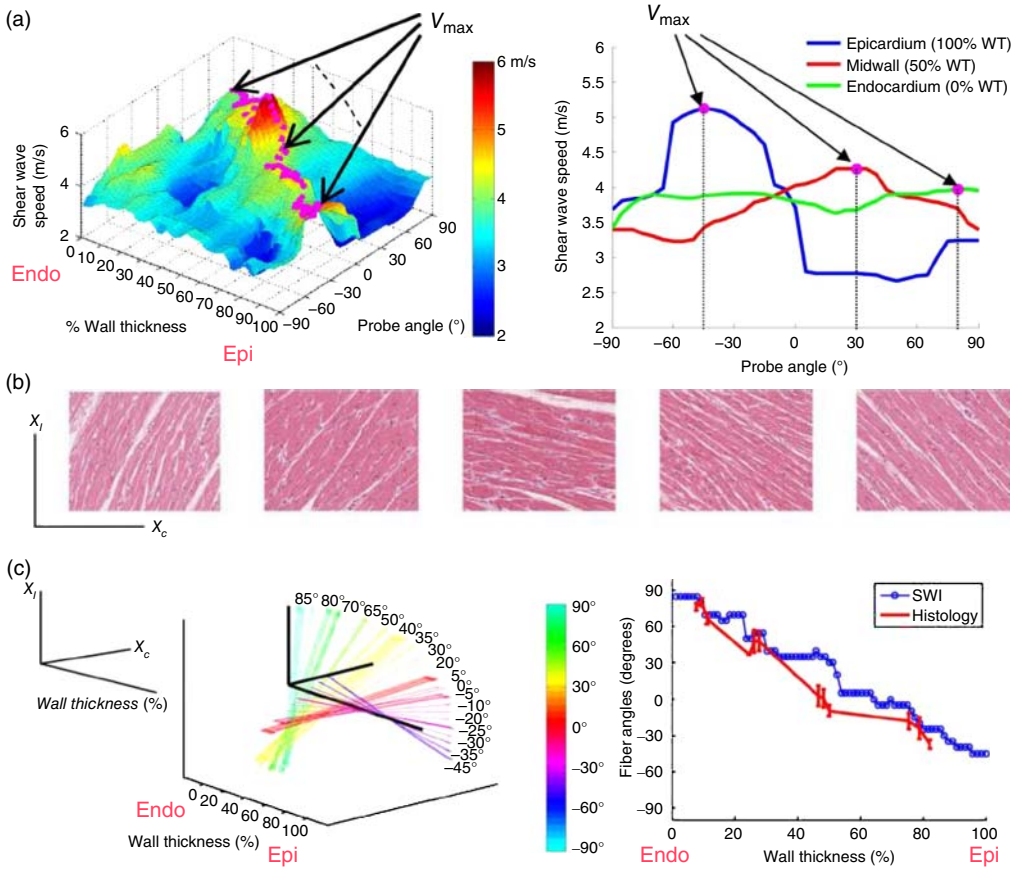

Figure 33.6 (a) Left panel: the surface plot of the shear wave speed across the myocardial wall (from epicardium (Epi, 100% wall thickness) to endocardium (Endo, 9% wall thickness)) for all the probe angles (−90° to 90°) performed. Right panel: paradigm extracted from the left panel, where the shear wave speed profiles are plotted as a function of probe angles at three distinct depths: epicardium, midwall, and endocardium. (b) Five histology slides of the myocardial specimen, depicting the fiber structure in the subendocardial (left) toward that in the subepicardial (right) circumferential-longitudinal slices. (c) Shear wave imaging fiber orientation plot and the comparison of transmural fiber angles between shear wave imaging and histology measurements from the same sample shown in (b). Source: © 2012 IEEE, reprinted, with permission, from [24].

33.3.5 Coronary Perfusion Pressure Quantification

A recent study by Vejdani-Jahromi et al. reported a good correlation between diastolic shear modulus measured by shear wave elastography and the coronary perfusion pressure on a Langendorff perfused rabbit heart setup [27]. Shear wave speed was found to be linearly correlated with the randomly varying coronary artery pressure. The study suggests SWEI might be used to evaluate the compliance of the heart when it is damaged by various cardiac disorders – including coronary artery diseases, diastolic heart failure, transplant rejection, or chemo-induced cardiotoxicity [27].

33.3.6 Carotid Artery Plaque Characterization

Carotid artery plaque characterization has been extensively investigated by non-shear wave-based techniques such as strain imaging [55–58] and acoustic radiation force impulse

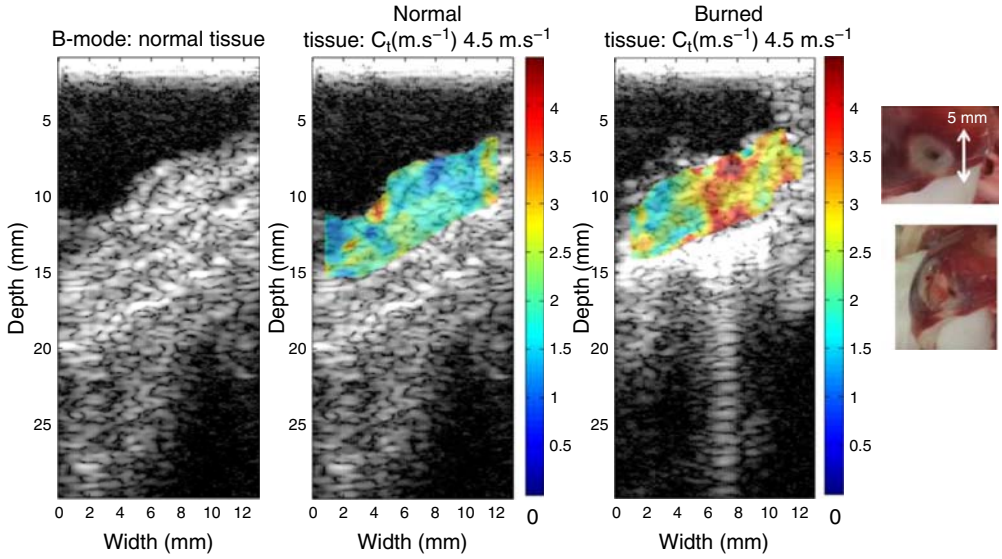

Figure 33.7 Shear wave speed maps in normal (middle), ablated (right) right atrial tissue, with B-mode images taken before ablation (left). The mean shear wave speed value varied in the central region of the sample from 1.6 ± 0.3 m/s in normal tissue to 3.3 ± 0.4 m/s in the ablated zone. Source: reprinted with permission from AAPM [24].

(ARFI) imaging [59–64]. Shear wave elastography applications were recently investigated by Ramnarine et al. [28, 29] and Widman et al. [65]. Both Ramnarine et al. and Widman et al. reported good repeatability and low sensitivity to pulsatile flow when using shear waves to quantify plaque stiffness [28, 65]. Widman showed good agreement of plaque stiffness measurement between shear wave imaging and mechanical tensile testing [65]. A patient study by Ramnarine et al. showed that shear wave elastography is able to quantify carotid plaque elasticity and an improved performance for assessing carotid plaques could be achieved when combining shear modulus measurement with gray scale ultrasound [29]. Currently, it is still challenging to correctly model the wave propagation in the plaque and accurately calculate the stiffness of small plaques. Further technical development and large-scale clinical studies are being conducted.

33.4 Summary

Similar to other shear wave applications, cardiac shear wave elastography offers direct and quantitative myocardial viscoelasticity measurements, which cannot be readily obtained from existing clinical tools. These measurements are vital to numerous critical clinical cardiovascular applications, with great potential to benefit hundreds of millions of patients worldwide. To date, the majority of the cardiac shear wave studies have been conducted under preclinical settings on animals. Clinical translation is undermined by the poor shear wave signal quality transthoracically in vivo. Current research topics include improving shear wave generation and detection, exploring alternative shear wave sources such as external vibration or intrinsic myocardial shear waves, and implementing shear wave elastography on intracardiac and transesophageal echocardiography (TEE) transducers to gain better imaging quality. Other potential clinical applications are also being actively investigated.

References

1 Center for Disease Control and Prevention. *Underlying Cause of Death 1999–2013*, on CDC WONDER Online Database, released 2015. Data are from the Multiple Cause of Death Files, 1999–2013, as compiled from data provided by the 57 vital statistics jurisdictions through the Vital Statistics Cooperative Program. [Online].

2 D'Hooge, J., Heimdal, A., Jamal, F., *et al.* (2000). Regional strain and strain rate measurements by cardiac ultrasound: principles, implementation and limitations. *Eur. J. Echocardiogr.* 1: 154–170.

3 Langeland, S., D'Hooge, J., Wouters, P.F., et al. (2005). Experimental validation of a new ultrasound method for the simultaneous assessment of radial and longitudinal myocardial deformation independent of insonation angle. *Circulation* 112: 2157–2162.

4 Serri, K., Reant, P., Lafitte, M., et al. (2006). Global and regional myocardial function quantification by two-dimensional strain: application in hypertrophic cardiomyopathy. *J. Am. Coll. Cardiol.* 47: 1175–1181.

5 Couade, M., Pernot, M., Messas, E., et al. (2011). In vivo quantitative mapping of myocardial stiffening and transmural anisotropy during the cardiac cycle. *IEEE Trans. Med. Imaging* 30: 295–305.

6 Couade, M., Pernot, M., Prada, C., et al. (2010). Quantitative assessment of arterial wall biomechanical properties using shear wave imaging. *Ultrasound Med. Biol.* 36: 1662–1676.

7 Couade, M., Pernot, M., Tanter, M., et al. (2008). Real time non-invasive quantitative imaging of arterial wall elasticity using Supersonic Shear Imaging. *Circulation* 118: S1008–S1008.

8 Pernot, M., Couade, M., Mateo, P., et al. (2011). Real-time assessment of myocardial contractility using shear wave imaging. *J. Am. Coll. Cardiol.* 58: 65–72.

9 Song, P., Urban, M.W., Chen, S., et al. (2014). In vivo transthoracic measurement of end-diastolic left ventricular stiffness with ultrasound shear wave elastography. In: *IEEE International Ultrasonics Symposium*, Chicago, IL, 109–112.

10 Song, P., Zhao, H., Urban, M.W., et al. (2013). Improved shear wave motion detection using pulse-inversion harmonic imaging with a phased array transducer. *IEEE Trans. Med. Imaging* 32: 2299–2310.

11 Song, P., Bi, X., Mellema, D.C., et al. (2016). Pediatric cardiac shear wave elastography for quantitative assessment of myocardial stiffness: a pilot study in healthy controls. *Ultrasound Med. Biol.* 42: 1719–1729.

12 Song, P., Bi, X., Mellema, D.C., et al. (2016). Quantitative assessment of left ventricular diastolic stiffness using cardiac shear wave elastography: a pilot study. *J. Ultrasound Med.* 35: 1419–1427.

13 Urban, M.W., Pislaru, C., Nenadic, I.Z., et al. (2013). Measurement of viscoelastic properties of in vivo swine myocardium using Lamb wave dispersion ultrasound vibrometry (LDUV). *IEEE Trans. Med. Imaging* 32: 247–261.

14 Hollender, P., Bradway, D., Wolf, P., et al. (2013). Intracardiac acoustic radiation force impulse (ARFI) and shear wave imaging in pigs with focal infarctions. *IEEE Trans. Ultrason., Ferroelect., Freq. Control* 60: 1669–1682.

15 Hollender, P.J., Wolf, P.D., Goswami, R., and Trahey, G.E. (2012). Intracardiac echocardiography measurement of dynamic myocardial stiffness with shear wave velocimetry. *Ultrasound Med. Biol.* 38: 1271–1283.

16 Pislaru, C., Pellikka, P.A., and Pislaru, S.V. (2014). Wave propagation of myocardial stretch: correlation with myocardial stiffness. *Basic Res. Cardiol.* 109: 438.

17 Doherty, J.R., Dahl, J.J., and Trahey, G.E. (2013). Harmonic tracking of acoustic radiation force-induced displacements. *IEEE Trans. Ultrason., Ferroelect., Freq. Control* 60: 2347–2358.

18 Nenadic, I., Urban, M.W., and Greenleaf, J.F. (2009). Ex vivo measurements of mechanical properties of myocardium using Lamb and Rayleigh wave dispersion velocities. In: *2009 IEEE International Ultrasonics Symposium* 2785–2788.

19 Nenadic, I.Z., Urban, M.W., Aristizabal, S., et al. (2011). On Lamb and Rayleigh wave convergence in viscoelastic tissues. *Phys. Med. Biol.* 56: 6723–6738.

20 Nenadic, I.Z., Urban, M.W., Mitchell, S.A., and Greenleaf, J.F. (2011). Lamb wave dispersion ultrasound vibrometry (LDUV) method for quantifying mechanical properties of viscoelastic solids. *Phys. Med. Biol.* 56: 2245.

21 Bernal, M., Nenadic, I., Urban, M.W., and Greenleaf, J.F. (2011). Material property estimation for tubes and arteries using ultrasound radiation force and analysis of propagating modes. *J. Acoust. Soc. Am.* 129: 1344–1354.

22 Pislaru, C., Urban, M.W., and Greenleaf, J.F. (2010). Increases in viscous and elastic moduli of infarcted myocardium measured in vivo by a new ultrasound method. *Eur. Heart J.* 31: 865–866.

23 Pislaru, C., Urban, M.W., Pislaru, S.V., et al. (2014). Viscoelastic properties of normal and infarcted myocardium measured by a multifrequency shear wave method: comparison with pressure-segment length method. *Ultrasound Med. Biol.* 40: 1785–1795.

24 Lee, W.N., Pernot, M., Couade, M., et al. (2012). Mapping myocardial fiber orientation using echocardiography-based shear wave imaging. *IEEE Trans. Med. Imaging* 31: 554–562.

25 Lee, W.N., Larrat, B., Pernot, M., and Tanter, M. (2012). Ultrasound elastic tensor imaging: comparison with MR diffusion tensor imaging in the myocardium. *Phys. Med. Biol.* 57: 5075–5095.

26 Kwiecinski, W., Provost, J., Dubois, R., et al. (2014). Quantitative evaluation of atrial radio frequency ablation using intracardiac shear-wave elastography. *Med. Phys.* 41: 112901.

27 Vejdani-Jahromi, M., Nagle, M., Trahey, G.E., and Wolf, P.D. (2015). Ultrasound shear wave elasticity imaging quantifies coronary perfusion pressure effect on cardiac compliance. *IEEE Trans. Med. Imaging* 34: 465–473.

28 Ramnarine, K.V., Garrard, J.W., Dexter, K., et al. (2014). Shear wave elastography assessment of carotid plaque stiffness: in vitro reproducibility study. *Ultrasound Med. Biol.* 40: 200–209.

29 Ramnarine, K.V., Garrard, J.W., Kanber, B., et al. (2014). Shear wave elastography imaging of carotid plaques: feasible, reproducible and of clinical potential. *Cardiovasc. Ultrasound* 12: 49.

30 Pislaru, C., Urban, M.W., Nenadic, I., and Greenleaf, J.F. (2009). Shearwave dispersion ultrasound vibrometry applied to in vivo myocardium. In: *2009 Annual International Conference of the IEEE Engineering in Medicine and Biology Society* 2891–2894.

31 Kolipaka, A., McGee, K.P., Araoz, P.A., et al. (2009). MR elastography as a method for the assessment of myocardial stiffness: comparison with an established pressure-volume model in a left ventricular model of the heart. *Magn. Reson. Med.* 62: 135–140.

32 Kolipaka, A., Araoz, P.A., McGee, K.P., et al. (2010). Magnetic resonance elastography as a method for the assessment of effective myocardial stiffness throughout the cardiac cycle. *Magn. Reson. Med.* 64: 862–870.

33 Kolipaka, A., McGee, K.P., Manduca, A., et al. (2011). In vivo assessment of MR elastography-derived effective end-diastolic myocardial stiffness under different loading conditions. *J. Magn. Reson. Imaging* 33: 1224–1228.

34 Kolipaka, A., Aggarwal, S.R., McGee, K.P., et al. (2012). Magnetic resonance elastography as a method to estimate myocardial contractility. *J. Magn. Reson. Imaging* 36: 120–127.

35 Elgeti, T., Rump, J., Hamhaber, U., et al. (2008). Cardiac magnetic resonance elastography initial results. *Invest. Radiol.* 43: 762–772.

36 Sack, I., Rump, J., Elgeti, T., et al. (2009). MR elastography of the human heart: noninvasive assessment of myocardial elasticity changes by shear wave amplitude variations. *Magn. Reson. Med.* 61: 668–677.

37 Elgeti, T., Laule, M., Kaufels, N., et al. (2009). Cardiac MR elastography: comparison with left ventricular pressure measurement. *J. Cardiovasc. Magn. Reson.* 11: 10.

38 Tzschätzsch, H., Elgeti, T., Rettig, K., et al. (2012). In vivo time harmonic elastography of the human heart. *Ultrasound Med. Biol.* 38: 214–222.

39 Kolipaka, A., Woodrum, D., Araoz, P.A., and Ehman, R.L. (2012). MR elastography of the in vivo abdominal aorta: A feasibility study for comparing aortic stiffness between hypertensives and normotensives. *J. Magn. Reson. Imaging* 35: 582–586.

40 Sarvazyan, A.P., Rudenko, O.V., Swanson, S.D., et al. (1998). Shear wave elasticity imaging: a new ultrasonic technology of medical diagnostics. *Ultrasound Med. Biol.* 24: 1419–1435.

41 Nenadic, I.Z., Urban, M.W., Pislaru, C., et al. (2011). In vivo open and closed chest measurements of myocardial viscoelasticity through a heart cycle using Lamb wave dispersion ultrasound vibrometry (LDUV). In: *2011 International IEEE Ultrasonics Symposium*, Orlando, FL, 17–20.

42 Kanai, H. (2005). Propagation of spontaneously actuated pulsive vibration in human heart wall and in vivo viscoelasticity estimation. *IEEE Trans. Ultrason., Ferroelect., Freq. Control* 52: 1931–1942.

43 Kanai, H. (2009). Propagation of vibration caused by electrical excitation in the normal human heart. *Ultrasound Med. Biol.* 35: 936–948.

44 Pernot, M., Fujikura, K., Fung-Kee-Fung, S.D., and Konofagou, E.E. (2007). ECG-gated, mechanical and electromechanical wave imaging of cardiovascular tissues in vivo. *Ultrasound Med. Biol.* 33: 1075–1085.

45 Luo, J.W., Fujikura, K., Tyrie, L.S., et al. (2009). Pulse wave imaging of normal and aneurysmal abdominal aortas in vivo. *IEEE Trans. Med. Imaging* 28: 477–486.

46 Vappou, J., Luo, J.W., and Konofagou, E.E. (2010). Pulse wave imaging for noninvasive and quantitative measurement of arterial stiffness in vivo. *Am. J. Hypertension* 23: 393–398.

47 Luo, J., Li, R.X., and Konofagou, E.E. (2012). Pulse wave imaging of the human carotid artery: an in vivo feasibility study. *IEEE Trans. Ultrason., Ferroelect., Freq. Control* 59: 174–181.

48 Ronny, X.L., Jianwen, L., Sandhya, K.B., et al. (2013). Pulse wave imaging in normal, hypertensive and aneurysmal human aortas in vivo : a feasibility study. *Phys. Med. Biol.* 58: 4549.

49 Palmeri, M.L., Wang, M.H., Dahl, J.J., et al. (2008). Quantifying hepatic shear modulus in vivo using acoustic radiation force. *Ultrasound Med. Biol.* 34: 546–558.

50 Tanter, M., Bercoff, J., Athanasiou, A., et al. (2008). Quantitative assessment of breast lesion viscoelasticity: Initial clinical results using supersonic shear imaging. *Ultrasound Med. Biol.* 34: 1373–1386.

51 Song, P., Manduca, A., Zhao, H., et al. (2013). *Fast shear compounding using directional filtering and two-dimensional shear wave speed calculation. Presented at the* IEEE International Ultrasonics Symposium, Prague, Czech Republic.

52 Hasegawa, H. and Kanai, H. (2011). High-frame-rate echocardiography using diverging transmit beams and parallel receive beamforming. *J. Med. Ultrason.* 38: 129–140.

53 Papadacci, C., Pernot, M., Couade, M., et al. (2014). High-contrast ultrafast imaging of the heart. *IEEE Trans. Ultrason., Ferroelect., Freq. Control* 61: 288–301.

54 Pernot, M., Lee, W.-N., Mateo, P., et al. (2012). Quantitative assessment of systolic and diastolic myocardial stiffness using shear wave imaging: in vivo validation in a large animal model. Presented at the American Heart Association.

55 de Korte, C.L., Cespedes, E.I., van der Steen, A.F.W., et al. (1998). Intravascular ultrasound elastography: assessment and imaging of elastic properties of diseased arteries and vulnerable plaque. *Eur. J. Ultrasound* 7: 219–224.

56 Baldewsing, R.A., Schaar, J.A., Mastik, F., et al. (2005). Assessment of vulnerable plaque composition by matching the deformation of a parametric plaque model to measured plaque deformation. *IEEE Trans. Med. Imaging* 24: 514–528.

57 Widman, E., Caidahl, K., Heyde, B., et al. (2015). Ultrasound speckle tracking strain estimation of in vivo carotid artery plaque with in vitro sonomicrometry validation. *Ultrasound Med. Biol.* 41: 77–88.

58 Majdouline, Y., Ohayon, J., Keshavarz-Motamed, Z., et al. (2014). Endovascular shear strain elastography for the detection and characterization of the severity of atherosclerotic plaques: in vitro validation and in vivo evaluation. *Ultrasound Med. Biol.* 40: 890–903.

59 Dahl, J.J., Dumont, D.M., Allen, J.D., et al. (2009). Acoustic radiation force impulse imaging for noninvasive characterization of carotid artery atherosclerotic plaques: a feasibility study. *Ultrasound Med. Biol.* 35: 707–716.

60 Dumont, D., Behler, R.H., Nichols, T.C., et al. (2006). ARFI imaging for noninvasive material characterization of atherosclerosis. *Ultrasound Med. Biol.* 32: 1703–1711.

61 Behler, R.H., Nichols, T.C., Merricks, E.R., and Gallippi, C.M. (2007). ARFI ultrasound for enhanced delineation of atherosclerosis in women. *J. Wom. Health* 16: 1112–1113.

62 Behler, R., Nichols, T., Merricks, E., and Gallippi, C. (2008). ARFI ultrasound for discrimination of calcification in arterial plaques: additional progress toward improved atherosclerosis imaging in women. *J. Wom. Health* 17: 1243–1243.

63 Behler, R.H., Nichols, T.C., Zhu, H.T., et al. (2009). ARFI imaging for noninvasive material characterization of atherosclerosis part II: toward in vivo characterization. *Ultrasound Med. Biol.* 35: 278–295.

64 Allen, J.D., Ham, K.L., Dumont, D.M., et al. (2011). The development and potential of acoustic radiation force impulse (ARFI) imaging for carotid artery plaque characterization. *Vasc. Med.* 16: 302–311.

65 Widman, E., Maksuti, E., Larsson, D., et al. (2015). Shear wave elastography plaque characterization with mechanical testing validation: a phantom study. *Phys. Med. Biol.* 60: 3151–3174.

34

Musculoskeletal Applications of Supersonic Shear Imaging

Jean-Luc Gennisson

Imagerie par Résonance Magnétique Médicale et Multi-Modalités, Université Paris-Saclay, Orsay, France

34.1 Introduction

In vivo muscle biomechanical properties have been classically inferred from inverse dynamics or measurements of joint torque performed using ergometers. However, these measures provide information about the combined behavior of several structures, such as muscles, tendons, nerves, and skin, all acting around a given joint. To isolate the behavior of an individual muscle is highly complicated. Since the introduction of elastography in the 1990s, many techniques have been developed with the aim to noninvasively assess localized muscle stiffness. In this chapter we focus on the supersonic shear imaging technique in musculoskeletal applications. As described in Chapter 23 of this book, this technique allows one to recover locally the stiffness of an organ by looking at the propagation of shear waves. Since propagation velocity is directly linked to the shear elastic modulus of the tissue, the stiffer the tissue, the faster the shear wave propagation (Eq. 34.1).

$$\mu = \rho V_s^{\,2} \tag{34.1}$$

where μ is the shear elastic modulus of the tissue, ρ is the density of muscle (1000 kg/m^3), and V_s is the shear wave velocity.

However, for the study of muscle biomechanics the relevance of the shear elastic modulus measurement requires some consideration. The Young's modulus (E) is the most relevant measure of stiffness of a given material. In the case of isotropic, locally homogeneous and quasi-incompressible biological tissues, for example liver, the shear elastic modulus is directly linked to the Young's modulus

$$E \approx 3\mu \tag{34.2}$$

However, because of its anisotropy (i.e. the muscle mechanical properties are not the same in all directions), this equation cannot be theoretically applied to skeletal muscles [1]. Eby et al. [2] demonstrated on an in vitro muscle that when the ultrasound probe is parallel to muscle fibers, muscle shear elastic modulus is strongly linearly related to the Young's modulus measured using classical ergometers. This demonstrates that in spite of the anisotropy of skeletal muscle the measurement of muscle shear elastic modulus provides an accurate characterization of muscle stiffness.

In this chapter we focus on the use of the supersonic shearwave imaging (SSI) technique that provides a quantitative imaging of tissue stiffness in real time. This technique uses an ultrafast

Ultrasound Elastography for Biomedical Applications and Medicine, First Edition.
Edited by Ivan Nenadic, Matthew Urban, James Greenleaf, Jean-Luc Gennisson, Miguel Bernal, and Mickael Tanter.

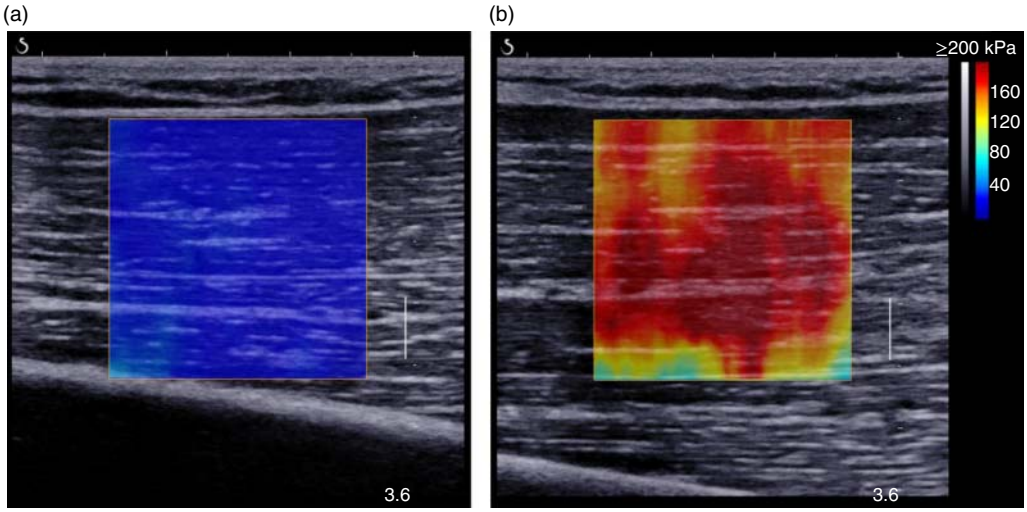

Figure 34.1 Examples of Young's modulus maps obtained in biceps brachialis (a) at rest and (b) during a moderate contraction. The quantitative stiffness maps coded in color are superposed onto the B-mode image. To obtain a representative value, the modulus is classically average over the whole map.

imaging modality combined with a transient and remote mechanical vibration, generated by radiation force induced by a focused ultrasonic beam (see Chapter 23). Each pushing beam generates a remote vibration in the target tissue that results in the propagation of a transient shear wave. Then, an ultrafast ultrasound imaging sequence is performed to acquire successive raw radio-frequency data at a very high frame rate (up to 20 kHz). A one-dimensional cross correlation of successive radio-frequency signals is used to calculate the shear wave velocity along the principal axis of the probe using a time-of-flight estimation, giving access to two-dimensional maps of the shear elastic modulus in quasi real time (1 frame/s; Figure 34.1) using Eq. (34.1).

Thanks to the accuracy of the SSI technique to quantify the shear elastic modulus with moderate stiffness, up to some hundreds of kPa [3], this technique seems to be really adapted to characterize muscles in different configurations: rest, passive stretching, passive contraction, dynamic contractions.

34.2 Muscle Stiffness at Rest and During Passive Stretching

Development of supersonic shear imaging gives access to noninvasive muscle stiffness assessment in vivo. In different studies this technique shows its reliability and its ease of use to make it a potentially interesting technique that would be of benefit to fundamental, applied, and clinical research projects that need an accurate assessment of muscle mechanical properties at rest. As an example, Dubois et al. [4] define a measurement protocol to be used in clinical routine for quantifying the shear modulus of lower limb muscles. Four positions were defined to evaluate shear modulus in 10 healthy subjects: parallel to the fibers, in the anterior and posterior aspects of the lower limb, at rest, and during passive stretching. Reliability was first evaluated on two muscles by three operators; these measurements were repeated six times. Then, measurement reliability was compared in 11 muscles by two operators; these measurements were repeated three times. Reproducibility of shear modulus was 0.48 kPa and repeatability was 0.41 kPa, with all muscles pooled. Position did not significantly influence reliability. Shear wave elastography appeared to be an appropriate and reliable tool to evaluate the shear modulus of lower limb muscles with the proposed protocol.

Reliability of shear elastic modulus measurements performed using supersonic shear imaging was also verified in muscles of different architectures and typologies [5]. Thirty healthy subjects were randomly assigned to the intra-session reliability ($n = 20$), inter-day reliability ($n = 21$), and the inter-observer reliability ($n = 16$) experiments. Muscle shear elastic modulus ranged from 2.99 kPa (gastrocnemius medialis) to 4.50 kPa (adductor digiti minimi and tibialis anterior). On the whole, very good reliability was observed, with a coefficient of variation (CV) ranging from 4.6% to 8%, except for the inter-operator reliability of adductor pollicis obliquus (CV = 11.5%). The intraclass correlation coefficients were good (0.871 ± 0.045 for the intra-session reliability, 0.815 ± 0.065 for the inter-day reliability, and 0.709 ± 0.141 for the inter-observer reliability).

Regarding passive stretching, muscle shear elastic modulus has been measured in humans (dorsiflexion [6] and plantarflexion [7]). Maïsetti et al. [6] showed that the relationship between muscle shear elastic modulus and muscle length is similar to that predicted by musculoskeletal modeling [8]. This suggested that muscle shear elastic modulus measured using elastography could be used to estimate the passive tension. This result has now been confirmed in vitro on chicken muscles [9], where a strong linear relationship (R^2 values ranging from 0.971 to 0.999) between shear elastic modulus and passive muscle force was reported.

Based on the Hoang's model, the slack length of the gastrocnemius muscle-tendon unit can be estimated. The slack length of the muscle-tendon unit is defined as the length beyond which the muscle-tendon unit begins to develop passive force. Although sensitivity analyses have shown that the slack length is the most important parameter for musculoskeletal modeling, until recently the experimental methods used to estimate the slack length were limited. Traditionally, slack length was determined as the muscle-tendon length at which the passive joint torque (measured using an ergometer) first exceeds zero. However, passive torque is influenced by all structures crossing the joint (e.g. all the agonist/antagonist muscles, skin, and tendons). Therefore the first increase in passive joint torque cannot be definitively associated to the true slack length of an individual muscle-tendon unit.

However, this model can only be used for this specific muscle, and it remains to be validated. Taking advantage of the strong linear relationship between muscle stiffness and passive muscle force [9], the slack length of individual muscles (e.g. gastrocnemius medialis [6], long and short head of biceps brachii [10]) has recently been determined using SSI. The slack length of gastrocnemius medialis was determined to be more plantarflexed (~20° of plantarflexion; knee extended) than when using the Hoang's model (~29° of plantarflexion; knee extended) [6]. Using shear wave elastography to determine the slack length of individual muscle-tendon units provides a unique opportunity to improve both the accuracy of musculoskeletal models and our understanding of passive muscle-tendon biomechanics.

Overall, the shear elastic modulus measurement provides a unique opportunity to measure localized muscle stiffness and thus to estimate the passive tension of individual muscles when being stretched. It can provide a deeper understanding of individual muscle mechanical behavior than more global measurements (such as maximal range of motion or joint torque during passive stretching). For example, Le Sant et al. [11] measured the shear elastic modulus of each hamstring muscle during passive knee extension at different hip angles. They found that the long head of the biceps femoris is stiffer than the semimembranosus, and the semimembranosus is stiffer than the semitendinosus. This is in accordance with the prevalence of strain injuries that occur in the biceps femoris. This example shows that SSI may be useful to determine which is the stiffer muscle, such that stretching interventions may target it using an optimal joint configuration.

34.3 Active and Dynamic Muscle Stiffness

Looking at contracting muscles, stiffness maps can provide useful insight for a better understanding of muscle behavior during isometric contractions and unvoluntary or voluntary contractions. The major questions associated with contraction are: what is the force developed by a muscle? Can it be linked to the shear elastic modulus quantified with the SSI technique? Does fatigue alter stiffness quantification? Recent studies have tried to explore these questions.

34.3.1 Isometric Contraction

Regarding the force during isometric contraction, this is the principal parameter quantified in musculoskeletal applications but it remains challenging to measure in complex structures. Bouillard et al. [12] investigated the relationship between muscle shear elastic modulus and force during isometric contractions of human finger muscles. In this study, two tasks were used: (i) isometric index finger abduction, which mainly involves the first dorsal interosseous, and (ii) isometric little finger abduction, which mainly involves the abductor digiti minimi. Assuming a negligible change in moment arm during the isometric contractions, the torque measured during these tasks was assumed to be directly related to force produced by the investigated muscle. During contractions with ramped torque (up to 30% of maximal voluntary contraction (MVC) for abductor digiti minimi and 60% of MVC for first dorsal interosseous), muscle shear elastic modulus measured using SSI was strongly linearly related to muscle force (R^2 values ranged from 0.951 to 0.997). Note that although the relationship between electromyogram (EMG) amplitude and torque was also linear, R^2 values were lower. Further, participants then performed isometric contractions where they were asked to freely vary the torque produced. Using the previously determined linear relationship between muscle shear elastic modulus and torque, Bouillard et al. [12] demonstrated the ability to accurately estimate the torque (RMS error < 6% of MVC) from the muscle shear elastic modulus measured. Further to this, Sasaki et al. [13] reported a linear relationship between force and shear elastic modulus of tibialis anterior during maximal isometric dorsiflexion performed at different ankle joint angles. This work provides solid evidence that an individual muscle force-length relationship can be estimated by measuring muscle shear elastic modulus.

Regarding the influence of fatigue during effort, force sharing during non-fatiguing contractions was investigated by Bouillard et al. [14], who measured the shear elastic modulus of elbow flexor muscles (brachialis, biceps brachii, brachioradialis) and extensor muscles (triceps brachii) during isometric elbow flexion with ramped torque (from rest to 40% of MVC). Each muscle exhibited a unique relationship between shear elastic modulus and elbow flexion torque, which provided evidence of torque-dependent changes in the force sharing strategy. More precisely, the characteristic shape of the change in shear elastic modulus of both heads of biceps brachii with increasing torque demonstrated little change initially, but showed increasingly large increments in modulus at higher torques. In contrast, the shear elastic modulus of the brachioradialis and brachialis increased rapidly at low torques and then plateaued for brachialis. These data provide an alternative explanation for the nonlinear relationship reported between surface EMG and torque in large muscles such as biceps brachii and contrasts with the long-held hypothesis of altered motor unit recruitment strategies [15]. Interestingly, the shear elastic modulus of the antagonist muscle (triceps brachii) did not simultaneously increase, and indeed remained very low throughout the ramp contraction. It provides evidence that the frequent reports of a systematic increase in surface EMG amplitude of antagonist muscles (i.e. increased co-activation) at high force levels may relate more to cross talk than increased drive to the antagonist muscles. Overall, these observations suggest that elastography might provide a unique opportunity to reconsider our current understanding of muscle co-contraction.

During fatiguing contraction, a change in force sharing between agonist muscles during a prolonged task is thought to limit the occurrence of neuromuscular fatigue and enhance the ability to sustain a contraction. A complete understanding of this adaptation is therefore crucial for sports scientists who aim to optimize human performance. Evidence of altered force-sharing strategies mainly comes from surface EMG studies. However, because fatigue alters the relationship between EMG amplitude and force [16], it is difficult to dissociate the effects of neuromuscular fatigue from putative compensations of force between muscles. Subsequently, these results cannot be directly interpreted as changes in muscle force and thus changes in force-sharing strategies. As the relationship between muscle shear elastic modulus and force is not altered by neuromuscular fatigue [17], elastography can be used to assess relative changes in force of individual muscles during isometric fatiguing contractions. In this way, some evidence for altered force sharing among the heads of the quadriceps muscle has been reported during a force-matched isometric knee extension task [17]. Interestingly, a change in force sharing was not observed in all participants, and when it was observed participants did not exhibit the same strategies, i.e. compensations did not systematically occur between the same muscles.

In order to investigate the origin of this variability in force sharing, Bouillard et al. [18] used electrical stimulation to selectively fatigue the vastus lateralis muscle. They observed a systematic decrease in the force produced by this muscle during a subsequent submaximal isometric force-matched task. However, the compensation strategy (i.e. the muscle(s) which produced more force to compensate for the reduction in force of vastus lateralis) varied between individuals. This data further confirmed the absence of a consistent redistribution of force sharing among the heads of the quadriceps muscles between individuals during force-matched fatiguing contractions.

Moreover, as neuromuscular fatigue dramatically alters the relationship between EMG amplitude and force, there is a paucity of data that describes changes in muscle force during fatiguing contractions. In contrast to EMG measurements that are influenced by several electrophysiological parameters, the shear elastic modulus is a mechanical property. As such, it is less likely to be influenced by neuromuscular fatigue. To test this hypothesis, Bouillard et al. [17] asked participants to perform linear isometric torque ramps (little finger abduction) before and after a fatiguing protocol. They demonstrated that the relationship between muscle shear elastic modulus and force is not affected by fatigue. Then, by using the linear regression of the relationship obtained before fatigue, they estimated with a good accuracy the change in little finger abduction torque during a submaximal isomeric fatiguing task performed until task failure. This experiment provides evidence that fatigue does not influence the ability to estimate the changes in muscle force using the shear elastic modulus measurement.

Taken together, the results presented above support the hypothesis that muscle stiffness is linearly related to both active and passive muscle force during isometric contractions. Although measurement of muscle shear elastic modulus alone cannot be used to estimate muscle force (in N) or torque (in N m), it can be used to estimate relative changes in muscle force. Concurrent measurements of shear elastic modulus of multiple agonist muscles will provide information about force-sharing strategies, and thus provide valuable insight into how the neural system choses to generate force in different muscles that cross the same joint. It is important to note that in the absence of normalization of the elastic modulus to that recorded during MVC, a change in force-sharing strategies could only be determined when different muscles demonstrate an opposite, or a different, profile of change in the shear elastic modulus. In contrast, if the changes in shear elastic modulus of two muscles both increased or decreased, a change in force sharing between these muscles could not be determined, even if different amplitudes of absolute change were noted. This is because the slope of the relationship between the elastic

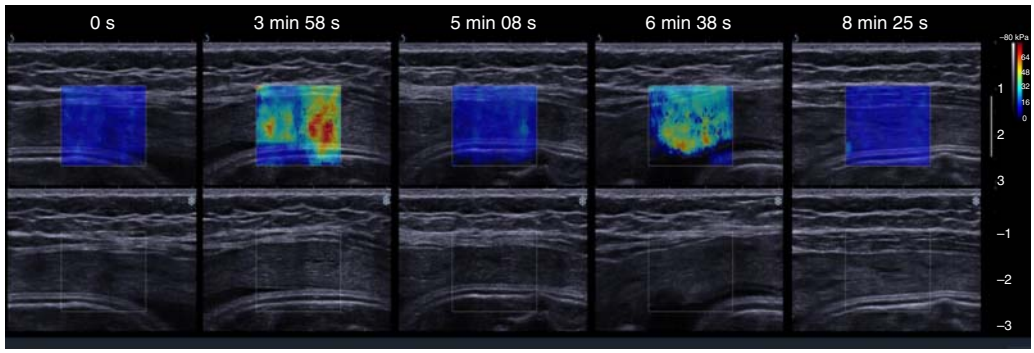

Figure 34.2 Elasticity of the myometrial wall over time during multiple contractions in the same region of interest. Source: reprinted from [19], copyright 2015, with permission from Elsevier.

modulus and force may differ between muscles, so the same absolute change in shear elastic modulus could relate to very different changes in force between muscles.

34.3.2 Involuntary and Voluntary Contraction

Thanks to the frame rate of the SSI technique (1 frame/s in shear wave elastography mode or more in research mode), involuntary contraction can be followed in quasi-real time. This is of a great importance for heart applications, as described in Chapter 33 of this book. As an example on another organ, Gennisson et al. [19] showed that SSI can help to better understand myometrium's physiology in terms of its shear modulus. This could considerably help the prevention of difficult births, the consequences of which are tremendous for neonate morbidity and pathologies. It shows the feasibility of the in vivo monitoring of myometrial stiffness changes in contraction and relaxation during pregnancy (Figure 34.2). In this study, SSI proved to be efficient for the monitoring of tissue elasticity during involuntary contraction. Changes in shear wave speed were tracked in real time during the uterine contraction and were well correlated with the uterine pressure, which is currently considered to be a gold standard. These results open a new way to better understand the myometrium contraction during labor.

In the case of voluntary contraction, the technique is still limited in commercial mode since it currently provides for only 1 frame/s. Actually in research applications it has been shown that SSI is able to follow fast muscle contraction in the heart [20, 21] or fast changes in elasticity, as in the carotid due to the pulse wave [22]. Nevertheless, slow voluntary contraction can be followed in real time. Shinohara et al. [23] reported the first data that detected the distribution of local muscle stiffness within and between contracting muscles at different muscle lengths. Tibialis anterior, medial gastrocnemius, and soleus were investigated during plantarflexion.

34.4 Tendon Applications

Mechanical properties of tendons play an important role in regulating physiological functions of muscles. The SSI technique was developed to characterize such hard organs under condition of contractions. Such a development was performed noninvasively in vivo on human Achilles tendon (AT) [24]. Clinically, the quantification of the Achilles tendon elastic properties may enhance diagnosis of tendon injury and the assessment of recovery treatments. Shear wave elastography has shown to be a powerful tool to estimate tissue mechanical properties. However, its applicability to quantitatively evaluate tendon stiffness is limited by the understanding

of the physics of the shear wave propagation in such a complex medium. First, tendon tissue is transverse isotropic. Second, tendons are very hard (i.e. they will conduct shear waves quickly). Hence, the shear wavelengths are greater than the tendon thickness, leading to guided wave propagation. Thus, to better understand shear wave propagation in tendons and consequently to properly estimate their mechanical properties, a dispersion analysis is required (presented in Chapter 5 of this book). In this study [24], shear wave dispersion was measured in vivo in ten Achilles tendons by applying the concept of shear wave spectroscopy parallel and perpendicular to the tendon fiber orientation. By modeling the tendon as a transverse isotropic viscoelastic plate immersed in fluid it was possible to fully describe the experimental data (deviation <1.4%). We show that parallel to fibers the dispersion curve is not influenced by viscosity, while it is so influenced perpendicularly to fibers. Elasticity and viscosity values were retrieved from the model in good agreement with reported results.

More recently, Helfenstein-Didier et al. [25] used this previous development to analyze the dispersion of shear wave propagation in the AT during passive dorsiflexion using the phase velocity method in order to obtain the tendon shear elastic modulus (C_{55}) [24]. Additional aims were: (i) to assess the reproducibility of the shear modulus for different ankle angles, (ii) to assess the effect of the probe locations, and (iii) to compare results with elasticity values obtained with the SSI technique. The AT shear modulus (C_{55}) consistently increased with the ankle angle ($n = 10$, main effect of angle: $p < 0.05$). Furthermore, the technique showed a very good reproducibility (all SEM values < 10.7 kPa and all CV values ≤ 0.05%). In addition, independently from the ankle angle, the shear modulus was significantly higher in the proximal location compared to the more distal one. The shear modulus μ provided by SSI was always lower than C_{55} and the difference increased with the ankle angles. However, shear modulus values provided by both methods were highly correlated ($R = 0.84$), indicating that the conventional SSI technique can be used to compare tendon mechanical properties across populations.

These previous studies showed that the SSI technique allows noninvasive quantification of tendon mechanical properties, and there is a need for that in clinical practice. Thus Yeh et al. [26] investigated the feasibility of using SSI to quantitatively differentiate normal and damaged tendons based on their mechanical properties in order to answer clinical questions. Five freshly harvested porcine tendons were used for an ex vivo experiment. Tendon damage was induced by incubating the tendons with a collagenase solution and degeneration of collagen fiber was observed. SSI and tensile stiffness measurement of the tendons in various loading conditions were conducted before and after collagenase treatment. Values of shear modulus were derived both by directly estimating from shear group velocity using an isotropic model and by fitting phase-velocity dispersion to a transverse isotropic model. Values of Young's modulus in different loading conditions were estimated using an incremental approach. Results show that the collagenase treatment successfully induced tendon damage. As the preload applied to the tendon increased from 0 to 3 N, the mean shear modulus from SSI and Young's modulus estimated from mechanical testing increased from 14.6 to 89.9 kPa and from 1.45 to 10.36 MPa, respectively, in untreated tendons, and from 8.4 to 67 kPa and from 0.93 to 7.2 MPa in collagenase-treated tendons. Both shear moduli correlated well with the changes in Young's moduli. These data indicate that shear modulus can be used to assess tendon stiffness dynamics and characterize normal and collagenase-damaged tendons, and holds the promise to improve the diagnostic accuracy of tendon dysfunctions.

Additionally, Zhang and Fu [27] showed on patellar tendon that SSI can be used to assess elastic properties without any physical model for guided waves. This gives access to a relative modulus which is in agreement with classic mechanical testing. Tests on the reliability of the technique was done on 22 patellar tendons. Spearman correlation coefficients for shear elastic modulus and tangent traction modulus ranged from 0.82 to 1.00 ($p < 0.05$). The intra- and

inter-operator reliabilities were 0.98 (95% CI: 0.93–0.99) and 0.97 (95% CI: 0.93–0.98) respectively. The SSI shows good intra- and inter-operator repeatability.

34.5 Clinical Applications

Estimation of individual muscle force and, more generally, quantification of stiffness of a localized area of muscle, provides the opportunity for new insights into changes in muscle mechanical properties with musculoskeletal and neurological disease progression and rehabilitation. Although elastography is widely used for diagnosis of breast cancer, liver fibrosis, and thyroid nodules, the musculoskeletal applications are just beginning to be realized. The main advantages of the SSI technique for clinical assessment and rehabilitation purposes are that it provides noninvasive, quantitative, reliable, and fast measurements. In addition, localized areas of several muscles, rather than global stiffness of a given joint, can be independently assessed.

Moreover, SSI was revealed to be accurate in terms of feasibility and reliability for passive muscle stiffness measurements in children as young as two years, which is of great interest for monitoring myopathies. Brandenburg et al. [28] conducted a prospective cross-sectional study quantifying the passive stiffness of bilateral lateral gastrocnemius muscles during passive stretching in 20 typically developing children (age range, 2.0–12.6 years). Four positions of progressive passive foot dorsiflexion, the demographic characteristics of the participants, and comparison of demographic characteristics were compared with shear modulus. Results show that passive stiffness increased with increasing stretching and that for all four foot positions, no significant difference was found between right and left legs or between the sexes. No correlation of passive muscle stiffness with age, body mass index, or ankle range of motion was found. The reliability of measurements was good to excellent (mean [95% confidence interval] range of reliability, 0.67 [0.44–0.83] to 0.80 [0.63–0.90]). Defining normal passive muscle stiffness in children is critical for identifying and understanding the implications of abnormal passive muscle stiffness in children with neuromuscular disorders.

As an example, Duchenne muscular dystrophy (DMD) is associated with increased muscle stiffness, leading to high degree of joint contractures. Lacourpaille et al. [29] have recently quantified this increased muscle stiffness in a cross-sectional study that compared people with DMD and healthy controls. As the disease severity evolves mainly in a proximal–distal manner, not all muscles are affected similarly. This work demonstrated that SSI could be used to provide a localized and sensitive measure of early changes in stiffness of targeted muscles. Such information may in the future be used to direct physical interventions and thus slow joint deformities and prolong autonomy. Assessment of muscle stiffness might also be helpful to quantify the efficacy of new therapies. Although longitudinal studies with large sample sizes are needed to determine the sensitivity of SSI to detect changes in muscle stiffness throughout the course of the disease, it opens interesting perspectives for many neurological conditions associated with increased muscle stiffness.

SSI may also be useful to quantify changes in muscle mechanical properties associated with musculoskeletal conditions. For example, in rabbits, a model of muscle crush injury, Lv et al. [30] demonstrated that it is possible to detect an increase in muscle stiffness subsequent to the injury. Similarly in exercise-induced muscle damage in humans, Lacourpaille et al. [31] reported increased muscle stiffness associated with more subtle muscle damage. This ability to accurately quantify the increase in passive stiffness associated with muscle injury and to objectively isolate this to the muscle that is damaged, might help the clinician to target interventions to the most affected muscle or muscle region.

Finally, quantification of muscle stiffness also provides crucial insight into the mechanisms that may underlie treatments and rehabilitation programs and, ultimately, to assess their

efficacy. Interventions that aim to alter muscle stiffness are common in physiotherapy/physical therapy practice (e.g. massage, taping, dry needling, stretching). Because of the lack of techniques to assess stiffness of a localized area of muscle tissue, their mechanical effect has not been verified. Therefore, controversies exist regarding their mechanical and thus clinical efficacy. Taking advantage of SSI, Hug et al. [32] demonstrated that de-loading tape applied to the skin directly over the rectus femoris muscle reduced tension in the underlying muscle region for the muscle conditions where the muscle was loaded (during moderate and high muscle stretch and contraction). These data provided a biomechanical explanation for the effect of de-loading tape observed in clinical practice (reduce pain, restore function, and aid recovery). Massage is another controversial technique that may be used to reduce muscle stiffness.

34.6 Future Directions

To date, the commercialized version of the SSI ultrasound device provides maps of shear elastic modulus at one sample per second, which limits the study of isometric contractions and slow passive stretching tasks (1 to 4 per second). Because the measure of shear wave propagation velocity is performed in less than 15 ms, this limitation can be overcome by improving hardware and software capabilities. In this way, a beta version of the SSI technique with a higher temporal resolution in terms of stiffness map frame rate of up to four samples per second has been recently used for measurements during ramped isometric muscle contraction [33].

Beyond the measurement of muscle stiffness, measurements of tendon stiffness may provide important insights into musculoskeletal biomechanics. However, the application of SSI technique for tendons requires some consideration. Because tendons are both very stiff and thin, shear wavelengths are greater than the tendon thickness, leading to guided wave propagation [24]. As a consequence, measurements are biased if no correction is applied. For instance, two tendons with the same stiffness but with different thickness will exhibit different shear elastic modulus values. But by analyzing shear wave dispersion (as presented in Chapter 5 of this book) this problem can be resolved and this technique has been shown to provide accurate tendon elasticity and viscosity values [24, 25]. This technique is therefore recommended for future elastography studies on the tendon. Alternatively, a method that takes into account tendon thickness to correct measurements performed using conventional shear wave elastography should be developed in the future.

Currently the SSI technique measures the shear wave velocity in 2D; however, the wave propagation occurs in 3D. New developments in ultrasound devices enables the measurements to be performed in 3D, in real time [34]. This pilot study demonstrated that it is possible to perform ultrafast ultrasound acquisition and SSI measurements in 3D using a 2D matrix array probe. This technique will provide a unique opportunity to assess spatial variability of muscle stiffness. In addition to information on muscle stiffness, 3D elastography will provide crucial information on muscle anisotropy and shear viscosity, which are thought to be related to the structural organization of the muscle. 3D elastography is promising for the evaluation of muscle neuromuscular conditions where muscle structure is affected.

References

1 Royer, D., Gennisson, J.L., Deffieux, T., and Tanter, M. (2011). On the elasticity of transverse isotropic soft tissues. *J. Acoust. Soc. Am.* 129 (5): 2757–2760.

2 Eby, S.F., Song, P., Chen, S., et al. (2013). Validation of shear wave elastography in skeletal muscle. *J. Biomech.* 46 (14): 2381–2387.

3 Yoshitake, Y., Takai, Y., Kanehisa, H., and Shinohara, M. (2014). Muscle shear modulus measured with ultrasound shear-wave elastography across a wide range of contraction intensity. *Muscle Nerve* 50: 103–113.

4 Dubois, G., Kheireddine, W., Vergari, C., et al. (2015). A reliable protocol for shear wave elastography of lower limb muscles at rest and during passive stretching. *Ultrasound Med. Biol.* 41 (9): 2284–2291.

5 Lacourpaille, L., Hug, F., Bouillard, K., et al. (2012). Supersonic shear imaging provides a reliable measurement of resting muscle shear elastic modulus. *Physiol. Meas.* 33 (3): N19–28.

6 Maïsetti, O., Hug, F., Bouillard, K., and Nordez, A. (2012). Characterization of passive elastic properties of the human medial gastrocnemius muscle belly using supersonic shear imaging. *J. Biomech.* 45 (6): 978–984.

7 Koo, T.K., Guo, J.Y., Cohen, J.H., and Parker K.J. (2014). Quantifying the passive stretching response of human tibialis anterior muscle using shear wave elastography. *Clin. Biomech.* 29 (1): 33–39.

8 Hoang, P.D., Gorman, R.B., Todd, G., et al. (2005). A new method for measuring passive length-tension properties of human gastrocnemius muscle in vivo. *J. Biomech.* 38 (6): 1333–1341.

9 Koo, T.K., Guo, J., Cohen, J.H., and Parker J.P. (2013). Relationship between shear elastic modulus and passive muscle force: an ex-vivo study. *J. Biomech.* 46 (14): 2534–2538.

10 Lacourpaille, L., Hug, F., and Nordez, A. (2013). Influence of the passive muscle tension on electromechanical delay in humans. *PLoS One* 8 (1): e53159.

11 Le Sant, G., Ates, F., Brasseur, J.L., and Nordez, A. (2015). Individual behaviors of hamstrings during passive knee extensions performed in various hip positions. In: *Proceedings of JFK2015*, Paris, France.

12 Bouillard, K., Nordez, A., and Hug, F. (2011). Estimation of individual muscle force using elastography. *PLoS One* 6 (12): e29261.

13 Sasaki, K., Toyama, S., and Ishii, N. (2014). Length-force characteristics of in vivo human muscle reflected by supersonic shear imaging. *J. Appl. Physiol.* 117 (2): 153–162.

14 Bouillard, K., Nordez, A., Hodges, P.W., et al. (2012). Evidence of changes in load sharing during isometric elbow flexion with ramped torque. *J. Biomech.* 45 (8): 1424–1429.

15 Lawrence, J.H. and De Luca, C.J. (1983). Myoelectric signal versus force relationship in different human muscles. *J. Appl. Phys.* 54 (6): 1653–1659.

16 Edwards, R.G. and Lippold, O.C. (1956). The relation between force and integrated electrical activity in fatigued muscle. *J. Physiol.* 132 (3): 677–681.

17 Bouillard, K., Hug, F., Guevel, A., and Nordez, A. (2012). Shear elastic modulus can be used to estimate an index of individual muscle force during a submaximal isometric fatiguing contraction. *J. Appl. Physiol.* 113 (9): 1353–1361.

18 Bouillard, K., Jubeau, M., Nordez, A., and Hug, F. (2014). Effect of vastus lateralis fatigue on load sharing between quadriceps femoris muscles during isometric knee extensions. *J. Neurophysiol.* 111 (4): 768–776.

19 Gennisson, J.L., Muller, M., Gabor, P., et al. (2015). Quantification of elasticity changes in the myometrium during labour using Shear Wave Elastography: a feasibility study. *Ultrasonics* 56: 183–188.

20 Couade, M., Pernot, M., Messas, E., et al. (2011). In vivo quantitative mapping of myocardium stiffening and transmural anisotropy during the cardiac cycle. *IEEE Trans. Med. Imaging* 30: 295–305.

21 Pernot, M., Couade, M., Mateo, P., et al. (2011). Real-time assessment of myocardial contractility using shear wave imaging. *J. Am. Col. Cardiol.* 58: 65–72.

22 Couade, M., Pernot, M., Prada, C., et al. (2010). Quantitative assessment of arterial wall biomechanical properties using shear wave imaging. *Ultrasound Med. Biol.* 36: 1662–1676.
23 Shinohara, M., Sabra, K., Gennisson, J.L., et al. (2010). Real-time visualization of muscle stiffness distribution with ultrasound shear wave imaging during muscle contraction. *Muscle Nerve* 42: 438–441.
24 Brum, J., Bernal, M., Gennisson, J.L., and Tanter, M. (2014). In vivo evaluation of the elastic anisotropy of human Achilles tendon using shear wave spectroscopy. *Phys. Med. Biol.* 59 (3): 505–523.
25 Helfenstein-Didier, C., Andrade, R.J., Brum, J., et al. (2016). In vivo quantification of the shear modulus of the human Achilles tendon during passive loading using shear wave dispersion analysis. *Phys. Med. Biol.* 61 (6): 2485–2496.
26 Yeh, C.L., Kuo, P.L., Gennisson, J.L., et al. (2016). Shear-wave imaging for evaluation of tendon diseases. *IEEE Trans. Ultrason., Ferroelect., Freq. Control* 63 (11): 1906–1921.
27 Zhang, Z.J. and Fu, S.N. (2013). Shear elastic modulus on patellar tendon captured from supersonic shear imaging: correlation with tangent traction modulus computed from material testing system and test–retest reliability. *PLoS One* 8 (6): e68216.
28 Brandenburg, J.E., Eby, S.F., Song, P., et al. (2015). Feasibility and reliability of quantifying passive muscle stiffness in young children by using shear wave ultrasound elastography. *J. Ultrasound Med.* 34 (4): 663–670.
29 Lacourpaille, L., Hug, F., Guevel, A., et al. (2014). Non-invasive assessment of muscle stiffness in patients with Duchenne muscular dystrophy. *Muscle Nerve* 51 (2): 284–286.
30 Lv, F., Tang, J., Luo, Y., et al. (2012). Muscle crush injury of extremity: quantitative elastography with supersonic shear imaging. *Ultrasound Med. Biol.* 38 (5): 795–802.
31 Lacourpaille, L., Nordez, A., Hug, F., et al. (2014). Time-course effect of exercise-induced muscle damage on localized muscle mechanical properties assessed using elastography. *Acta Physiol.* 211 (1): 135–146.
32 Hug, F., Ouellette, A., Vicenzino, B., et al. (2014). Deloading tape reduces muscle stress at rest and during contraction. *Med. Sci. Sports Exerc.* 46 (12): 2317–2325.
33 Ates, F., Hug, F., Bouillard, K., et al. (2015). Muscle shear elastic modulus is linearly related to muscle torque over the entire range of isometric contraction intensity. *J. Electromyogr. Kinesiol.* 25 (4): 703–708.
34 Gennisson, J.L., Provost, J., Deffieux, T., et al. (2015). 4D Ultrafast shear wave imaging. *IEEE Trans. Ultrason., Ferroelect., Freq. Control* 62 (6): 1059–1065.

35

Breast Shear Wave Elastography

Azra Alizad

Department of Radiology, Mayo Clinic, Rochester, MN, USA

35.1 Introduction

Emerging ultrasound elasticity imaging techniques have been of great interest as an adjunct to breast sonography to improve its sensitivity and specificity for diagnosis of breast cancer. Among elasticity imaging methods, shear wave elastography has gained much attention in recent years as a new imaging modality for differentiation of breast masses. This chapter focuses on applications of shear wave elastography techniques, more specifically comb-push ultrasound shear elastography (CUSE) in breast imaging. In addition, we will present the results of in vivo results of breast CUSE. Future developments and potential impact of CUSE in breast imaging are also discussed.

35.2 Background

Today, breast cancer remains a major health problem among women around the world. Breast cancer is the leading cause of cancer death in women aged 20 to 59 years and second to lung cancer in women 60 and older. According to the American Cancer Society in 2015, over 231 000 new cases of invasive breast cancer are expected to occur in one year alone, accounting for 29% of all new cancer cases among American women. There is a probability that 1 in 8 women are at risk of developing invasive breast cancer in their lifetime [1]. This data is shown in Table 35.1.

Manual breast examination is the oldest, simplest, yet effective, method for detection of breast masses, because the stiffness of breast tumors is significantly different from surrounding tissue. However, it has limited value in detecting deep and small masses.

Current imaging methods, e.g., mammography and ultrasound, carry low specificity rates that lead to a great number of unnecessary (i.e. benign) biopsies. According to the American College of Radiology Imaging Network (ACRIN), in women with dense breasts, using combined whole-breast screening, ultrasound (US), and mammography yielded a sensitivity of 77.5% versus 50% for mammography or ultrasound alone. However, the increased sensitivity in combined use of US and mammography is associated with a substantial increase in the number of false-positive cases [2]. Thus, due to low specificity of current imaging modalities, women encounter a high number of unnecessary follow-up examinations and procedures. Only 20% to 40% of breast biopsies are cancerous [3, 4]. Thus, the rate of false-positive cases seems to be common with current imaging tools. Consequently, the number of unnecessary benign breast biopsies that are performed annually in the US approaches 1 million cases,

Ultrasound Elastography for Biomedical Applications and Medicine, First Edition.
Edited by Ivan Nenadic, Matthew Urban, James Greenleaf, Jean-Luc Gennisson, Miguel Bernal, and Mickael Tanter.

Table 35.1 Estimated new cases and deaths in American women.

Estimated new cases in 2015	231 670
% of all new cancers among American women	29%
Estimated deaths in 2015	40 290
% of all cancer deaths among American women	15%

with an associated cost of an excision breast biopsy of $2400 per case [5]. Thus, the cost of potentially unwarranted biopsies is around $2 billion annually, which contributes substantially to US healthcare spending [5, 6]. Furthermore, women who undergo biopsy for benign disease experience great emotional distress and morbidity [7].

The efficacy of mammography is also greatly reduced in dense breasts [8, 9]. This is particularly important in the case of high- and moderate-risk women who need to be screened at a younger age [8, 9]. Even though magnetic resonance imaging (MRI) has high sensitivity, the poor specificity results in unnecessary follow-ups and biopsies that are associated with high extra cost and great emotional distress. Moreover, the limited availability and substantial cost of MRI limit the use of MRI in breast cancer detection [10–12].

To overcome the limitations of current breast imaging modalities, new noninvasive tools for breast imaging with high sensitivity and specificity are being developed. In the last 25 years or so, various ultrasound-based techniques [13–19] or MRI-based methodologies [20–25] have been developed to characterize the mechanical response of tissues under external stress.

More research is in progress in the development of ultrasound- or MRI-based elasticity technologies, especially those that provide palpation-like information, for example, information about tissue stiffness. In palpation, breast masses differ from surrounding tissue [26]. In fact, breast tumors are often stiffer than normal tissue [27] and malignant breast lesions are harder than benign lesions [28, 29]. Hence, new techniques are being developed to noninvasively evaluate the pathology of a tissue based on its mechanical properties [30].

35.3 Breast Elastography Techniques

Elasticity imaging is an emerging field that can noninvasively evaluate the tissue elasticity. From this group, magnetic resonance elastography (MRE) was introduced to differentiate pathological breast tissues from normal and increase diagnostic specificity [23, 31–34]. However, MRE, a MRI-based technology, is expensive and less likely to be available for a wide range of the patient population.

Ultrasound-based elasticity imaging is an emerging field and has been of great interest as an adjunct to breast sonography to improve its sensitivity and specificity for the diagnosis of breast cancer. Various elastography methods are available on many ultrasound systems, with most of them based on some form of tissue deformation (i.e. strain). This can be done either by manual pressure and release, or by taking advantage of normal cardiac or respiratory motion. Conventional quasi-static elastography is one such technique, which calculates the relative deformation of the tissue or strain. Studies have showed it can increase the specificity of conventional B-mode US in the detection of breast cancer [30]. Quasi-static elastography utilizes compression and US-based strain imaging to obtain maps of relative stiffness [35–39]. However, in most cases, it is a qualitative imaging technology so the results differ with users' experience in data acquisition and interpretation, and their operator dependency may hinder their clinical effectiveness [40]. The newly emerging shear wave elastography (SWE) techniques are the alternative, which use acoustic radiation force to induce shear waves and estimate tissue elasticity

from measured shear wave speed. Shear waves travel faster in stiffer tissues and slower in softer tissues; therefore, shear wave elastography could be an optimal technique to be used for differentiation of breast masses [41].

35.3.1 Shear Wave Elasticity Imaging (SWEI)

Shear wave elasticity imaging (SWEI) is the first shear wave elastography method, and was introduced by Sarvazyan et al. [42]. The 1D or 2D transient elastography technique was first performed by using an external vibrator. This technique uses an ultrafast ultrasound acquisition imaging system (5000 frames/s) that allows a real-time in vivo imaging of transient shear waves propagating in human tissues. The transient elastography technique has been tested to differentiate breast masses [19]. The use of large external vibrators has limited the clinical application of transient elastography. To overcome this limitation, efforts have been made to advance shear wave elastography techniques.

35.3.2 Supersonic Shear Imaging (SSI)

The ultrafast SWE system from Supersonic Imagine performs supersonic shear imaging (SSI), uses an acoustic radiation force, and through a focused ultrasound beam, remotely induces mechanical vibrations in breast tissue. SSI uses a conventional transducer and produces a supersonic regime of moving sources to generate shear waves, and by using ultrafast plane wave imaging captures the propagation of resulting shear waves and quantifies tissue elasticity from measured shear wave speed [41, 43, 44]. Promising results in studies with SSI for differentiation of breast masses have been reported [45–52]. Here, we present a SSI shear wave map and US image of a woman in her 80s who had abnormal screening mammography. Targeted ultrasound of the right breast demonstrates a $0.9 \times 0.9 \times 0.6$ cm hypoechoic mass, which corresponds to the mammographic abnormality as shown in Figure 35.1. A shear wave map using SSI showed a high value of mean elasticity, E_{mean} of 111.8 kPa. The result of pathology confirmed the malignant breast lesion as an invasive mammary carcinoma with mixed ductal and lobular features, grade I.

35.3.3 Virtual Touch Tissue Quantification using Acoustic Radiation Force Impulse

Shear wave elastography using acoustic radiation force impulse (ARFI) has also been used for differentiation of breast masses [53–55]. The ARFI shear wave elastography technique is based on generating an impulse-focused radiation force to induce shear waves in tissue and then use pulse-echo ultrasound to detect such waves. Then, the speed of shear waves estimated at each location is used to calculate the stiffness of the tissue [56].

35.3.4 Comb-push Ultrasound Shear Elastography (CUSE)

Recently, Song et al. [57, 58] have developed an US shear wave elastography technique called Comb-push ultrasound shear elastography (CUSE) that uses multiple simultaneous acoustic radiation force (ARF) beams. CUSE is a fast quantitative US shear wave elasticity imaging methodology that provides a two-dimensional map of shear wave speed. CUSE uses acoustic radiation force beams that are laterally distributed and simultaneously excite the tissue and generate shear waves [58]. CUSE uses four focused push beams that are spaced laterally for shear wave production and shear waves traveling in both lateral directions fill the entire field of view (FOV). A directional filter is used to separate the shear waves traveling in opposing directions and estimates the elasticity map of the FOV in one single comb-push acquisition [37, 59].

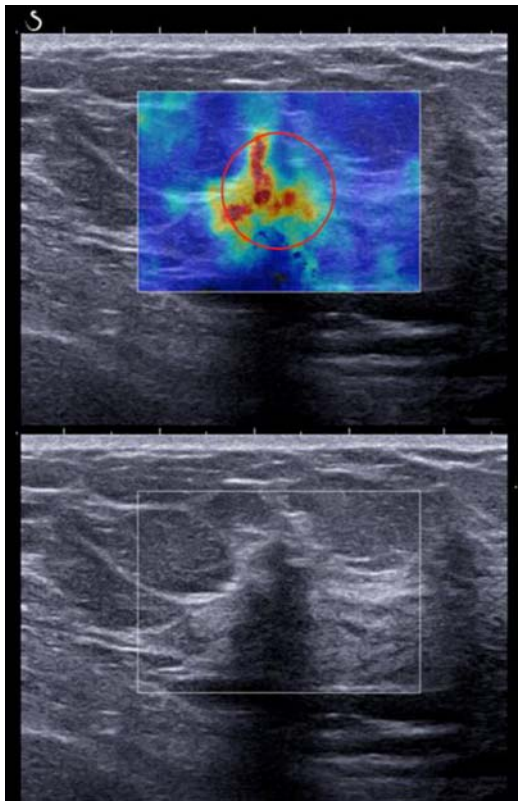

Figure 35.1 SSI and ultrasound images of a patient with invasive mammary carcinoma. The shear wave speed is significantly higher in the lesion.

35.4 Application of CUSE for Breast Cancer Detection

CUSE was conducted on patients with suspicious masses using a fully programmable ultrasound platform, Verasonics V-1 system (Verasonics Inc., Redmond, WA), using a linear array transducer L7-4 (Philips Healthcare, Andover, MA).

In the CUSE technique using Verasonics, after excitation of the tissue, the system instantly shifts to plane wave imaging mode in order to track the propagated shear wave. A graphical user interface was developed using Matlab (MathWorks Inc., MA) to process the obtained CUSE data and then reconstruct the shear wave speed map. As a quality control factor, a normalized cross-correlation coefficient of the shear wave speed map was used [60]. The performance of CUSE using a research ultrasound scanner has been reported with promising results [61, 62].

An example of breast CUSE, as such is presented in Figure 35.2. This case is a patient in her 70s. The targeted ultrasound of her right breast demonstrates an irregular mass measuring 1.4 cm in the longest dimension. The measured mean shear wave speed within the ROI was 2.63 ± 1.59 m/s with a Young's modulus of 20.75 kPa. Breast biopsy results were a benign fibroadenoma.

CUSE imaging using a Verasonics research US system was conducted for a patient in her 70s with a concerned lump in her right breast. Targeted ultrasound of her right breast shows a hypoechoic mass measuring 2.3 cm in the longest dimension, as shown in Figure 35.3. The measured mean shear wave speed of the ROI was 7.07 ± 1.18 m/s, with a Young's modulus 149.9 kPa. The result of a breast biopsy was malignant grade II invasive ductal carcinoma with ductal carcinoma and calcifications in situ adjacent to it.

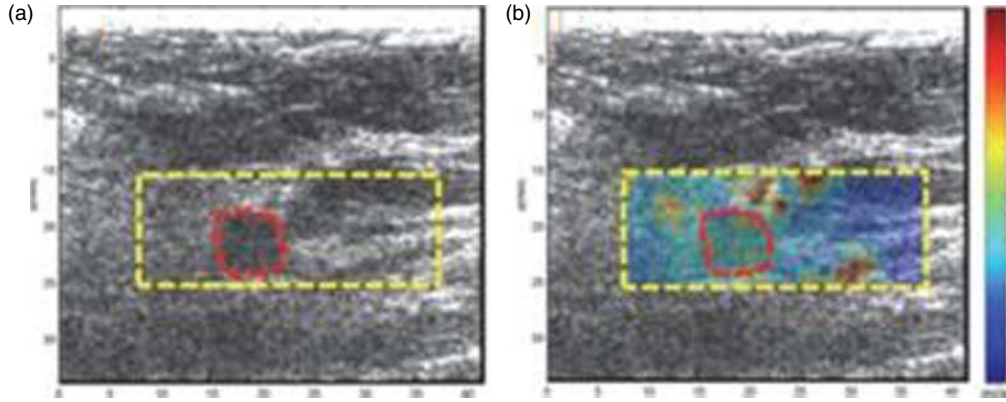

Figure 35.2 US image and CUSE shear wave speed map of breast tissue (dashed rectangle) including the breast mass ROI (dashed circular contour). (a) B-mode US image, (b) CUSE shear wave speed map. Source: adapted from [61].

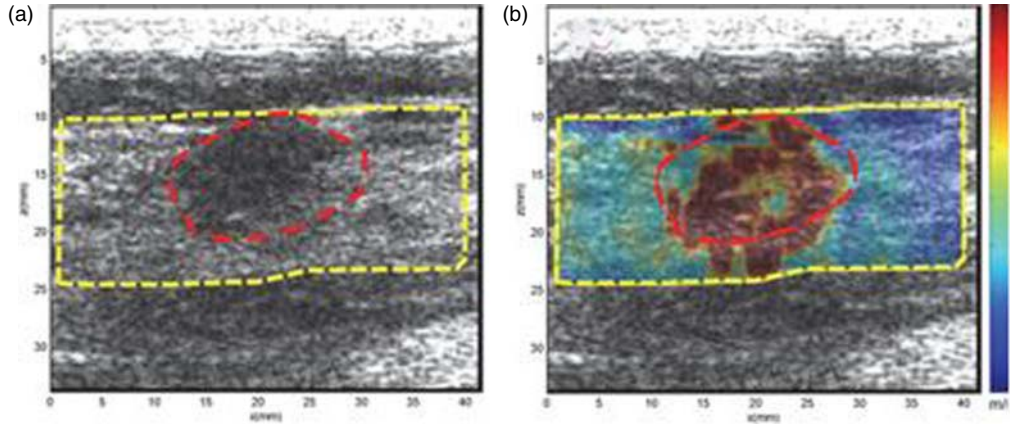

Figure 35.3 B-mode US and CUSE shear wave speed map of a patient's breast (dashed rectangular contour) including the breast mass ROI (red circular contour). (a) B-mode US image, (b) CUSE shear wave speed map. Source: adapted from [61].

35.5 CUSE on a Clinical Ultrasound Scanner

Recently, CUSE has been implemented in a GE LOGIQ E9 (LE9) (General Electric Healthcare, Wauwatosa, WI) ultrasound scanner [63]. We have studied more than 100 patients with breast masses detectable on ultrasound. Here, we present examples of breast CUSE images using a clinical ultrasound scanner. Figure 35.4 presents US and CUSE images of a patient using a clinical ultrasound scanner. The patient is a woman in her 60s with abnormal mammography screening. Targeted ultrasound of her right breast demonstrated a $1.0 \times 0.7 \times 0.8$ cm hypoechoic mass with a hyperechoic rim and angular margins in the right breast. SWE results showed a high elasticity value, $E_{\text{mean}} = 114.3$ kPa. Pathology results demonstrated invasive lobular carcinoma with alveolar variant features (grade II).

CUSE using a clinical US scanner has been performed on a patient in her 40s with an abnormal mammography screening. Targeted US of her right breast showed a hypoechoic complex cystic mass measuring $1.5 \times 0.4 \times 1.1$ cm, as shown in Figure 35.5. SWE showed low elasticity value, $E_{\text{mean}} = 14.5$ kPa. Pathology results of the mass showed clustered apocrine cysts.

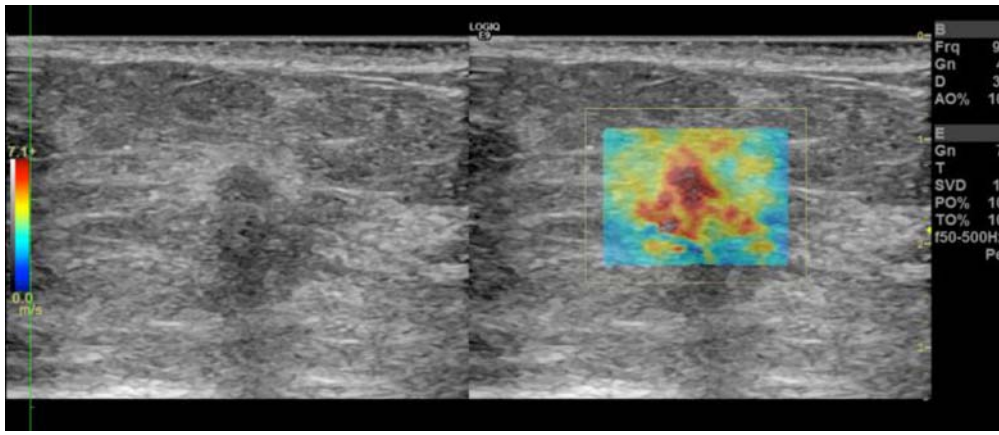

Figure 35.4 B-mode US and CUSE shear wave speed map of a patient's breast; invasive lobular carcinoma.

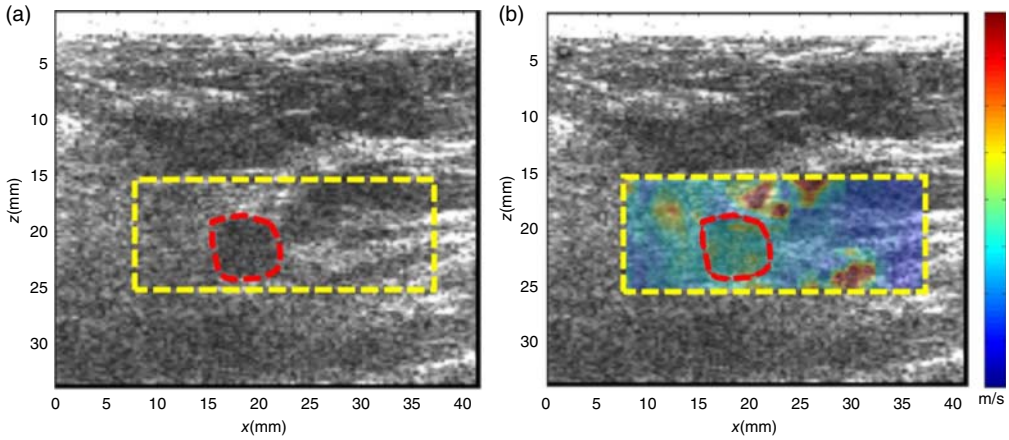

Figure 35.5 (a) B-mode US and (b) CUSE shear wave speed map of a patient's breast; benign clustered apocrine cysts.

An example of breast carcinoma examined by CUSE using a clinical US scanner is shown in Figure 35.6. The patient is a woman in her 70s with a palpable abnormality in her left breast. Targeted US confirmed a 12 × 9 mm oval circumscribed mass, as shown in Figure 35.6. SWE results showed a high elasticity value, with $E_{\text{mean}} = 132.7$ kPa. This mass was later diagnosed by pathology as mucinous carcinoma (grade I).

Another example of breast cancer evaluated by CUSE imaging using a clinical US scanner is shown in Figure 35.7. The patient is a woman in her 70s with a 1.3 cm asymmetry seen in her screening mammography. Targeted US demonstrated a 1.3 cm irregular region with posterior shadowing, as shown in Figure 35.7. SWE showed a high elasticity value, with $E_{\text{mean}} =$ 97.7 kPa. Pathology results classified the mass as invasive mammary carcinoma with mixed ductal and lobular features (grade I), and calcifications present in benign ducts and invasive carcinoma.

Figure 35.8 presents ultrasound and CUSE imaging of a patient in her 50s with an asymmetry presented as a 0.7 cm round mass during mammography screening. Targeted ultrasound showed a 0.7 cm round circumscribed mostly anechoic mass. SWE map is $E_{\text{mean}} = 6.8$ kPa. The mass was revealed as a cyst after biopsy.

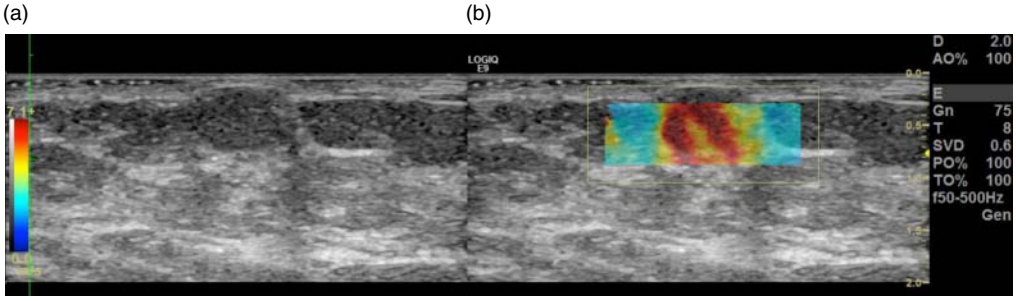

Figure 35.6 (a) B-mode US and (b) CUSE shear wave speed map of a patient's breast with a malignant breast mass; mucinous carcinoma (grade I).

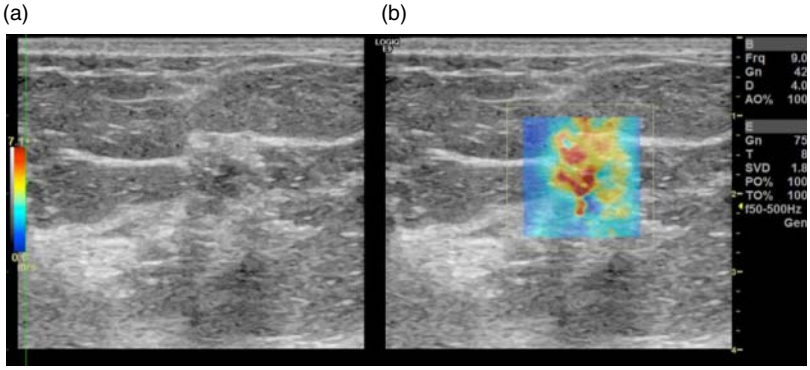

Figure 35.7 (a) B-mode US and (b) CUSE shear wave speed map of a patient's breast with a malignant breast mass; invasive mammary carcinoma.

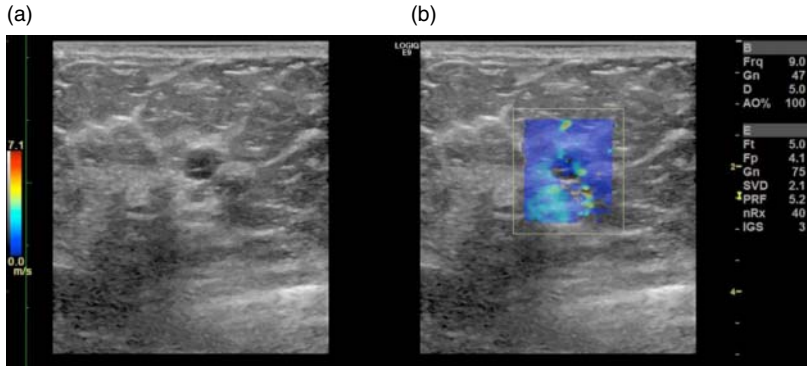

Figure 35.8 (a) B-mode US and (b) CUSE shear wave speed map of a patient's breast; benign cyst.

35.6 Limitations of Breast Shear Wave Elastography

There are some limitations in shear wave elastography. Technical factors, such as the amount of precompression used, can negatively alter the shear wave elastography results. However, that can be controlled by minimizing the compression [67].

Despite the promising results on breast shear wave elastography, significant overlap in elasticity between benign and malignant breast masses has been reported [50, 65, 67–72], which limits

the discriminating power of elasticity imaging regardless of the accuracy of the measurement method. Usually false-positive rates are higher than false-negative rates. Smaller lesion size and increased breast thickness and depth are associated with false-negative results. Conversely, large lesion size is associated with false-positive results [73]. Also, the presence of calcifications in benign lesions can induce the apparent high stiffness regions when they are evaluated by SWE methods, and that may lead to false-positive results [74, 75].

Future developments in shear wave elastography techniques would help to overcome the current limitations.

35.7 Conclusion

Shear wave elastography is a quantitative elasticity imaging technique that has the potential to help in the better differentiation of breast lesions and can be used complementary to conventional ultrasound to improve our certainty in the final assessment of solid breast masses. Studies on using SSI, the most well-known shear wave elastography, have shown that the addition of SWE to B-mode US increased the specificity of breast US mass assessment without the cost of decreasing the sensitivity [45, 64]. It has been shown that adding the elasticity ratio (E_{ratio}) improves the diagnostic performance of shear wave in differentiating benign and malignant breast lesions [49, 65].

Gray scale ultrasound may underestimate the size of cancerous tumor when compared to actual size at histology. Shear wave elastography of such tumors shows peritumoural stiffness 3 mm beyond the tumor border seen in an ultrasound image; as such, tumor size estimation is closer to the actual histological size. Therefore, shear wave elastography may have the potential to accurately estimate cancerous tumor size and help with breast-conserving surgery planning [66]. However, further studies are required to assess the relationship of the extent of SWE stiffness to grayscale US and final histological size of breast cancer.

Acknowledgments

The work described in this chapter was supported by the National Institutes of Health (NIH) grants R01CA148994, R01CA148994-S1, R01CA168575, R01EB017213, and R01CA174723 from the NIH-National Cancer Institute. The content is solely the responsibility of the author and does not necessarily represent the official views of NIH. The author is very grateful to the following individuals for their valuable work during the course of the study that presented in as this chapter: Dr. Max Denis, Dr. Mahdi Bayat, Dr. Mohammad Mehrmohammadi, Ms. Adriana Gregory, and Ms. Cynthia Andrist.

The author, AA, discloses that Mayo Clinic holds patents on the CUSE technology, and Mayo Clinic has also received royalties from companies that have licensed the CUSE technology. The author does not have any financial interest in the technology described in this chapter.

References

1 Siegel, R.L., Miller, K.D., and Jemal, A. (2015). Cancer statistics, 2015. *CA Cancer J. Clin.* 65 (1): 5–29.

2 Berg, W.A., et al. (2008). Combined screening with ultrasound and mammography vs mammography alone in women at elevated risk of breast cancer. *J. Am. Med. Assoc.* 299 (18): 2151–2163.

3 Saslow, D., et al. (2007). American Cancer Society guidelines for breast screening with MRI as an adjunct to mammography. *CA Cancer J. Clin.* 57 (2): 75–89.
4 Leach, M.O., et al. (2005). Screening with magnetic resonance imaging and mammography of a UK population at high familial risk of breast cancer: a prospective multicentre cohort study (MARIBS). *Lancet* 365 (9473): 1769–1778.
5 Burkhardt, J.H. and Sunshine, J.H. (1999). Core-needle and surgical breast biopsy: comparison of three methods of assessing cost 1. *Radiology* 212 (1): 181–188.
6 Chubak, J., et al. (2010). Cost of breast-related care in the year following false positive screening mammograms. *Med. Care* 48 (9): 815.
7 Rahbar, G., et al. (1999). Benign versus malignant solid breast masses: US differentiation 1. *Radiology* 213 (3): 889–894.
8 Corsetti, V., et al. (2011). Evidence of the effect of adjunct ultrasound screening in women with mammography-negative dense breasts: Interval breast cancers at 1 year follow-up. *Eur. J. Cancer* 47 (7): 1021–1026.
9 Zonderland, H.M., et al. (1999). Diagnosis of breast cancer: contribution of US as an adjunct to mammography 1. *Radiology* 213 (2): 413–422.
10 Berg, W.A., et al. (2012). Detection of breast cancer with addition of annual screening ultrasound or a single screening MRI to mammography in women with elevated breast cancer risk. *J. Am. Med. Assoc.* 307 (13): 1394–1404.
11 Orel, S.G. (2000). MR imaging of the breast. *Radiol. Clin. N. Am.* 38 (4): 899–913.
12 Heywang-Köbrunner, S., et al. (2001). International investigation of breast MRI: results of a multicentre study (11 sites) concerning diagnostic parameters for contrast-enhanced MRI based on 519 histopathologically correlated lesions. *Eur. Radiol.* 11 (4): 531–546.
13 Ophir, J., et al. (1991). Elastography: a quantitative method for imaging the elasticity of biological tissues. *Ultrason. Imaging* 13 (2): 111–134.
14 Parker, K.J. and Lerner, R. (1992). Sonoelasticity of organs: shear waves ring a bell. *J. Ultrasound Med.* 11 (8): 387–392.
15 Skovoroda, A., Emelianov, S., and O'Donnell, M. (1995). Tissue elasticity reconstruction based on ultrasonic displacement and strain images. *IEEE Trans. Ultrason., Ferroelect., Freq. Control* 42 (4): 747–765.
16 Levinson, S.F., Shinagawa, M., and Sato, T. (1995). Sonoelastic determination of human skeletal muscle elasticity. *J. Biomech.* 28 (10): 1145–1154.
17 Fatemi, M. and Greenleaf, J.F. (1998). Ultrasound-stimulated vibro-acoustic spectrography. *Science* 280 (5360): 82–85.
18 Nightingale, K.R., et al. (2001). On the feasibility of remote palpation using acoustic radiation force. *J. Acoust. Soc. Am.* 110 (1): 625–634.
19 Bercoff, J., et al. (2003). In vivo breast tumor detection using transient elastography. *Ultrasound Med. Biol.* 29 (10): 1387–1396.
20 Muthupillai, R., et al. (1995). Magnetic resonance elastography by direct visualization of propagating acoustic strain waves. *Science* 269 (5232): 1854–1857.
21 Chenevert, T.L., Skovoroda, A.R., and Emelianov, S.Y. (1998). Elasticity reconstructive imaging by means of stimulated echo MRI. *Magn. Reson. Med.* 39 (3): 482–490.
22 Kruse, S., et al. (2000). Tissue characterization using magnetic resonance elastography: preliminary results. *Phys. Med. Biol.* 45 (6): 1579.
23 Sinkus, R., et al. (2000). High-resolution tensor MR elastography for breast tumour detection. *Phys. Med. Biol.* 45 (6): 1649.
24 Sinkus, R., et al. (2005). Imaging anisotropic and viscous properties of breast tissue by magnetic resonance-elastography. *Magn. Reson. Med.* 53 (2): 372–387.
25 Plewes, D.B., et al. (2000). Visualization and quantification of breast cancer biomechanical properties with magnetic resonance elastography. *Phys. Med. Biol.* 45 (6): 1591.

26 McDonald, S., Saslow, D., and Alciati, M.H. (2004). Performance and reporting of clinical breast examination: a review of the literature. *CA Cancer J. Clin.* 54 (6): 345–361.

27 Sarvazyan, A. (2001). Elastic properties of soft tissues. In: *Handbook of Elastic Properties of Solids, Liquids and Gases* (ed. M. Levy, H.E. Bass, R.R. Stern, A.G. Every, and V. Keppens), vol. 3, 107–127. Academic Press.

28 Krouskop, T.A., et al. (1998). Elastic moduli of breast and prostate tissues under compression. *Ultrason. Imaging* 20 (4): 260–274.

29 Sewell, C.W. (1995). Pathology of benign and malignant breast disorders. *Radiol. Clin. N. Am.* 33 (6): 1067–1080.

30 Schaefer, F., et al. (2011). Breast ultrasound elastography – results of 193 breast lesions in a prospective study with histopathologic correlation. *Eur. J. Radiol.* 77 (3): 450–456.

31 Mariappan, Y.K., Glaser, K.J., and Ehman, R.L. (2010). Magnetic resonance elastography: a review. *Clin. Anat.* 23 (5): 497–511.

32 McKnight, A.L., et al. (2002). MR elastography of breast cancer: preliminary results. *Am. J. Roentgenol.* 178 (6): 1411–1417.

33 Lorenzen, J., Sinkus, R., and Adam, G. (2003). [Elastography: Quantitative imaging modality of the elastic tissue properties]. RoFo: *Fortschritte auf dem Gebiete der Rontgenstrahlen und der Nuklearmedizin* 175 (5): 623–630.

34 Sinkus, R., et al. (2007). MR elastography of breast lesions: understanding the solid/liquid duality can improve the specificity of contrast-enhanced MR mammography. *Magn. Reson. Med.* 58 (6): 1135–1144.

35 Ginat, D.T., et al. (2009). US elastography of breast and prostate lesions 1. *Radiographics* 29 (7): 2007–2016.

36 Garra, B.S., et al. (1997). Elastography of breast lesions: initial clinical results. *Radiology* 202 (1): 79–86.

37 Yoon, J.H., et al. (2011). Interobserver variability of ultrasound elastography: how it affects the diagnosis of breast lesions. *Am. J. Roentgenol.* 196 (3): 730–736.

38 Barr, R.G. (2010). Real-time ultrasound elasticity of the breast: initial clinical results. *Ultrasound Q.* 26 (2): 61–66.

39 Cho, N., et al. (2010). Sonoelastographic strain index for differentiation of benign and malignant nonpalpable breast masses. *J. Ultrasound Med.* 29 (1): 1–7.

40 Chang, J.M., et al. (2011). Breast mass evaluation: factors influencing the quality of US elastography. *Radiology* 259 (1): 59–64.

41 Bercoff, J., Tanter, M., and Fink, M. (2004). Supersonic shear imaging: a new technique for soft tissue elasticity mapping. *IEEE Trans. Ultrason., Ferroelect., Freq. Control* 51 (4): 396–409.

42 Sarvazyan, A.P., et al. (1998). Shear wave elasticity imaging: a new ultrasonic technology of medical diagnostics. *Ultrasound Med. Biol.* 24 (9): 1419–1435.

43 Fink, M. and Tanter, M. (2010). Multiwave imaging and super resolution. *Phys. Today* 63 (2): 28–33.

44 Montaldo, G., et al. (2009). Coherent plane-wave compounding for very high frame rate ultrasonography and transient elastography. *IEEE Trans. Ultrason., Ferroelect., Freq. Control* 56 (3): 489–506.

45 Chang, J.M., et al. (2011). Clinical application of shear wave elastography (SWE) in the diagnosis of benign and malignant breast diseases. *Breast Cancer Res. Treat.* 129 (1): 89–97.

46 Athanasiou, A., et al. (2010). Breast lesions: quantitative elastography with supersonic shear imaging – preliminary results 1. *Radiology* 256 (1): 297–303.

47 Cosgrove, D.O., et al. (2012). Shear wave elastography for breast masses is highly reproducible. *Eur. Radiol.* 22 (5): 1023–1032.

48 Li, G., et al. (2013). Performance of shear wave elastography for differentiation of benign and malignant solid breast masses. *PloS One* 8 (10).

49 Evans, A., et al. (2012). Differentiating benign from malignant solid breast masses: value of shear wave elastography according to lesion stiffness combined with greyscale ultrasound according to BI-RADS classification. *Br. J. Cancer* 107 (2): 224–229.

50 Evans, A., et al. (2010). Quantitative shear wave ultrasound elastography: initial experience in solid breast masses. *Breast Cancer Res.* 12 (6): R104.

51 Plecha, D.M., et al. (2014). Addition of shear-wave elastography during second-look MR imaging–directed breast US: effect on lesion detection and biopsy targeting. *Radiology* 272 (3): 657–664.

52 Lee, S.H., et al. (2014). Two-view versus single-view shear-wave elastography: comparison of observer performance in differentiating benign from malignant breast masses. *Radiology* 270 (2): 344–353.

53 Yao, M., et al. (2014). Diagnostic value of virtual touch tissue quantification for breast lesions with different size. *Biomed. Res. Int.* 142504.

54 Bai, M., et al. (2012). Virtual touch tissue quantification using acoustic radiation force impulse technology initial clinical experience with solid breast masses. *J. Ultrasound Med.* 31 (2): 289–294.

55 Ianculescu, V., et al. (2014). Added value of Virtual Touch IQ shear wave elastography in the ultrasound assessment of breast lesions. *Eur. J. Radiol.* 83 (5): 773–777.

56 Nightingale, K., et al. (2002). Acoustic radiation force impulse imaging: ex vivo and in vivo demonstration of transient shear wave propagation. In: *Proceedings. 2002 IEEE International Symposium on Biomedical Imaging*.

57 Song, P., et al. (2013). Comb-push ultrasound shear elastography (CUSE) with various ultrasound push beams. *IEEE Trans. Med. Imaging* 32 (8): 1435–1447.

58 Song, P., et al. (2012). Comb-push ultrasound shear elastography (CUSE): a novel method for two-dimensional shear elasticity imaging of soft tissues. *IEEE Trans. Med. Imaging* 31 (9): 1821–1832.

59 Song, P., et al. (2014). Fast shear compounding using robust 2-D shear wave speed calculation and multi-directional filtering. *Ultrasound Med. Biol.* 40 (6): 1343–1355.

60 Cohn, N.A., et al. (1997). An elasticity microscope. Part I: methods. *IEEE Trans. Ultrason., Ferroelect., Freq. Control* 44 (6): 1304–1319.

61 Denis, M., et al. (2015). Comb-push ultrasound shear elastography of breast masses: initial results show promise. *PLoS One* 10 (3): e0119398.

62 Denis, M., et al. (2015). Update on breast cancer detection using comb-push ultrasound shear elastography. *IEEE Trans. Ultrason., Ferroelect., Freq. Control* 62 (9): 1644–1650.

63 Song, P., et al. (2015). Two-dimensional shear-wave elastography on conventional ultrasound scanners with time-aligned sequential tracking (TAST) and comb-push ultrasound shear elastography (CUSE). *IEEE Trans. Ultrason., Ferroelect., Freq. Control* 62 (2): 290–302.

64 Berg, W.A., et al. (2012). Shear-wave elastography improves the specificity of breast US: the BE1 multinational study of 939 masses. *Radiology* 262 (2): 435–449.

65 Youk, J.H., et al. (2013). Diagnostic value of commercially available shear-wave elastography for breast cancers: integration into BI-RADS classification with subcategories of category 4. *Eur. Radiol.* 23 (10): 2695–2704.

66 Mullen, R., et al. (2014). Shear-wave elastography contributes to accurate tumour size estimation when assessing small breast cancers. *Clin. Radiol.* 69 (12): 1259–1263.

67 Barr, R.G. and Zhang, Z. (2012). Effects of precompression on elasticity imaging of the breast development of a clinically useful semiquantitative method of precompression assessment. *J. Ultrasound Med.* 31 (6): 895–902.

68 Tanter, M., et al. (2008). Quantitative assessment of breast lesion viscoelasticity: initial clinical results using supersonic shear imaging. *Ultrasound Med. Biol.* 34 (9): 1373–1386.

69 Barr, R.G. (2012). Shear wave imaging of the breast still on the learning curve. *J. Ultrasound Med.* 31 (3): 347–350.

70 Tozaki, M. and E. Fukuma (2011). Pattern classification of ShearWaveTM Elastography images for differential diagnosis between benign and malignant solid breast masses. *Acta Radiol.* 52 (10): 1069–1075.

71 Lee, S.H., et al. (2013). Differentiation of benign from malignant solid breast masses: comparison of two-dimensional and three-dimensional shear-wave elastography. *Eur. Radiol.* 23 (4): 1015–1026.

72 Lee, E.J., et al. (2013). Diagnostic performances of shear wave elastography: which parameter to use in differential diagnosis of solid breast masses? *Eur. Radiol.* 23 (7): 1803–1811.

73 Yoon, J.H., et al. (2013). Shear-wave elastography in the diagnosis of solid breast masses: what leads to false-negative or false-positive results? *Eur. Radiol.* 23 (9): 2432–2440.

74 Gregory, A., et al. (2015). Effect of calcifications on breast ultrasound shear wave elastography: an investigational study. *PloS One* 10 (9): e0137898.

75 Gregory, A., et al. (2015). An experimental phantom study on the effect of calcifications on ultrasound shear wave elastography. In: *Engineering in Medicine and Biology Society (EMBC), 37th Annual International Conference of the IEEE.*

36

Thyroid Shear Wave Elastography

Azra Alizad

Department of Radiology, Mayo Clinic, Rochester, MN, USA

36.1 Introduction

Shear wave elastography is a quantitative elasticity-based imaging method that has been of great research interest for thyroid nodule differentiation. This chapter focuses on application of shear wave elastography techniques, more specifically comb-push ultrasound shear elastography (CUSE), in thyroid imaging.

In addition, we will present the in vivo results of shear wave elastography (SuperSonic Imagine and CUSE) on thyroid. Future developments and potential impact of CUSE in thyroid imaging are also discussed.

36.2 Background

Four to seven percent of the adult population in the United States has a palpable thyroid nodule and only 5% of those identified nodules are malignant [1]. The high prevalence of thyroid nodules is associated with increased imaging examinations for cancerous lesions. Furthermore, incidental thyroid cancers are often identified after diagnostic examinations for non-thyroidal primary diseases. In recent years, the incidence of differentiated thyroid cancers of all sizes has increased drastically, with a 3-fold higher rate rise in women, and the numbers of new cases of thyroid cancer are rising faster than that of any other malignancy in recent years [2–5]. Currently, thyroid cancer is the 4th most common cancer in American women (Table 36.1).

The worldwide growth in thyroid cancer incidence is mostly due to the more frequent use of ultrasound or other sensitive diagnostic tools and of a true rise in the number of cancers, possibly as result of frequent radiation exposure and to other unknown carcinogens [4]. Furthermore, increasing numbers of small, asymptomatic incidental thyroid cancers are frequently being identified by ultrasound and cytology examinations.

36.3 Role of Ultrasound and its Limitation in Thyroid Cancer Detection

Real-time ultrasound (US) has revolutionized the clinical practice of thyroidology. Ultrasonography can identify thyroid nodules with high accuracy in determining the number and size of nodules. However, the vast majority of nodules discovered by ultrasound are

Ultrasound Elastography for Biomedical Applications and Medicine, First Edition.
Edited by Ivan Nenadic, Matthew Urban, James Greenleaf, Jean-Luc Gennisson, Miguel Bernal, and Mickael Tanter.

Table 36.1 Key statistics for thyroid cancer, 2015.

	Total	Women	Men
Estimated new cases in 2015	62 450	47 230	15 220
Estimated deaths in 2015	1950	1080	870

Data from http://www.cancer.org/cancer/thyroidcancer/detailedguide/thyroid-cancer-key-statistics.

small (less than a centimeter in diameter) and are benign. The prevalence for small thyroid nodules is remarkably high and more than 50% of individuals older than age 50 may harbor one or more nodules [5]. Only a small number of US identified thyroid nodules (5%) are malignant [5]. Ultrasound features associated with malignancy, such as microcalcifications, hypoechogenicity, intranodular vascularity, irregular margins, and absent halo sign, alone are suggestive of malignancy, but not sufficient for diagnosis [6]. With a low specificity of US in detecting malignant nodules, the ability of US to accurately distinguish them from the sea of benign nodules is limited [7]. As a result, ultrasound-guided fine needle aspiration biopsy (FNAB) is performed on many of these nodules for further characterization.

36.4 Fine Needle Aspiration Biopsy (FNAB)

While FNAB has a major role in differentiating benign thyroid nodule from malignant ones, it is also an imperfect technique. First, the results are non-diagnostic in approximately 15–20% of cases [8–10]. Second, there is a false-negative rate of approximately 3–5% [11]. Third, there is wide variability in interpretation of cytopathology of the FNAB samples; most commonly, sampling problems associated with insufficient FNA collected specimens as well as overlap in morphological markers between benignity and malignancy. Currently, most patients with FNAB cytological indicated "follicular neoplasm" or suggested as "suspicious for follicular neoplasm" undergo thyroidectomy, to make a definitive diagnosis [9], and only 15 to 32% of these patients have cancer [8, 12]. It appears that as the sensitivity of FNAB increases, its specificity decreases [13]. A report of a multi-institutional study indicates that inadequate FNAB specimens can cause diagnostic errors with false-negative and false-positive results up to 25% and 9.9%, respectively [14]. Furthermore, performing FNAB on such a large patient population with benign nodules is associated with a significant cost and psychological stress and may incorrectly select patients for an unnecessary surgery for true benign thyroid nodules.

36.5 The Role of Elasticity Imaging

The stiffness of thyroid nodules usually differs significantly from surrounding tissues. In fact, thyroid nodules are often stiffer than normal thyroid tissue [15] and malignant nodules are stiffer than benign nodules [16]. However, the use of palpation through the skin as a diagnostic tool has limited value in quantifying the nodule stiffness. The examiner's assessment of a nodule stiffness changes with the various characteristics of surrounding tissues. Also, the degree of stiffness estimation differs between multiple examiners.

Elasticity imaging is an emerging imaging modality that can noninvasively provide tissue viscoelasticity information. Magnetic resonance elastography (MRE) has been used by our group to distinguish normal and diseased thyroid [17]. However, this MRI-based technology is costly and is not widely available.

36.5.1 Thyroid Ultrasound Elastography

US-based elastography for thyroid nodule differentiation has been of great interest because of its advantages, including being nonionizing, real-time, low cost, easily transferrable, and widely available [18]. Amongst US-based elastography methodologies, strain or quasi-static elastography applies compression to obtain maps of relative stiffness, and has shown promise in thyroid nodule screening [19–22]. However, it is a *qualitative* imaging technology and is operator dependent; the results of data acquisition and interpretation vary with user experience. Static elastography has limited value in screening thyroid nodules with indeterminate cytology in FNAB. As a result, quantitative stiffness evaluation may help nodule differentiation become accurate [23].

36.5.2 Thyroid Shear Wave Elastography

Shear wave elastography (SWE) techniques use radiation force of ultrasound to induce shear waves within the tissue, and by measuring the generated shear wave speed one can make a quantitative estimation of tissue stiffness.

Supersonic shear imaging (SSI) and acoustic radiation force impulse (ARFI) imaging are pioneers in this SWE group. Both SSI and ARFI shear wave imaging provide 2D maps of shear elasticity.

36.5.3 Virtual Touch Tissue Imaging using Acoustic Radiation Force Impulse (ARFI)

Virtual Touch imaging (VTI), sometimes also referred to as Virtual Touch tissue imaging (VTTI), is available on the ACUSON S2000™ and ACUSON S3000™ ultrasound systems. Virtual Touch tissue imaging and quantification (VTIQ; Siemens Medical Solutions, Mountain View, CA, USA) is a two-dimensional quantitative SWS imaging and an ARFI-based method that uses an acquisition sequence consisting of reference, excitation, and tracking sonic pulse types.

Virtual Touch tissue imaging provides the relative stiffness in the selected region of interest (ROI). A short-duration high-intensity acoustic "pushing pulse" in Virtual Touch tissue imaging and quantification (VITQ) generates a localized tissue displacement. The displacement induces lateral shear wave propagation. By measuring the time peak of displacement at each lateral location, the shear wave velocity can be measured and its map can be reconstructed [24]. Studies on ARFI elasticity imaging (Virtual Touch imaging and tissue quantification) have shown good diagnostic value for thyroid nodules [24–26].

36.5.4 Supersonic Imagine (SSI)

SuperSonic Imagine introduced the Aixplorer in 2006 which uses transient pulses to generate propagating shear waves in tissue, and by measuring the speed of wave propagation, the elasticity will be estimated [27]. Studies reported promising results of the effectiveness of this technique in distinguishing malignancy from benignity in thyroid nodules [28–34].

Here we present two examples of SSI imaging conducted in an IRB approved study on a group of patients with thyroid nodules who were scheduled for FNAB.

The first case is a man in his 40s who had a nodule in his chest CT and was further evaluated with thyroid US. His US showed a 14 × 9 × 16 mm hypoechoic, predominantly solid nodule in the right side of the thyroid isthmus with indeterminate appearance. SWE of the nodule showed $E_{\text{mean}} = 81.8$ kPa. FNA of the thyroid isthmus revealed cytologic features consistent with papillary thyroid carcinoma (Figure 36.1).

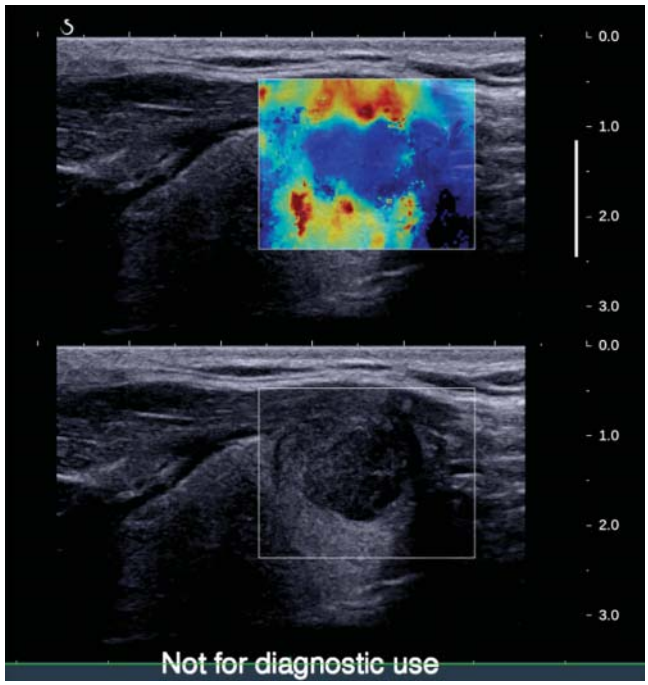

Figure 36.1 Ultrasound and SWE speed maps of a papillary thyroid carcinoma.

The second case is a woman in her 60s with a nodule in her right lobe. Ultrasound of thyroid showed a mixed cystic and solid nodule in the mid to lower pole of the right thyroid lobe measuring 36 × 13 × 18 mm. The superior portion of this nodule is predominantly cystic, as shown in Figure 36.2. The inferior portion is more solid, with scattered small cystic spaces, and also contains a focal cluster of small calcifications. SWE estimation using SSI resulted in $E_{\text{mean}} =$ 6.9 kPa. FNA of the nodule revealed cytologic features consistent with benign thyroid nodule with degenerative changes.

36.5.5 Comb-push Ultrasound Shear Elastography (CUSE)

Recently, Song et al. [35, 36] have developed an ultrasound shear elastography technique called comb-push ultrasound shear elastography (CUSE), which uses multiple simultaneous acoustic radiation force (ARF) beams. CUSE is a fast quantitative US shear wave elasticity imaging methodology that provides a two-dimensional map of shear wave speed. CUSE uses acoustic radiation force beams that are laterally distributed and simultaneously excite the tissue and generate shear waves [36]. CUSE uses four focused push beams that are spaced laterally for shear wave production and shear waves travelling in both lateral directions fill the entire field of view (FOV). A directional filter is used to separate the shear waves traveling in opposing directions and estimates the elasticity map of the FOV in one single comb-push acquisition [37, 38].

One major challenge in shear wave measurements using ultrasound radiation force is that the induced shear waves are very weak and can only propagate a short distance due to high attenuation in tissue. Therefore, shear wave speeds typically can only be reliably estimated in a small region close to the focus of the push beam.

In CUSE, the entire area under the transducer is filled with shear waves produced by multiple teeth of the comb-push. Therefore, every pixel always has a shear wave source nearby to provide shear waves of sufficient amplitude for high SNR (signal-to-noise ratio) measurement.

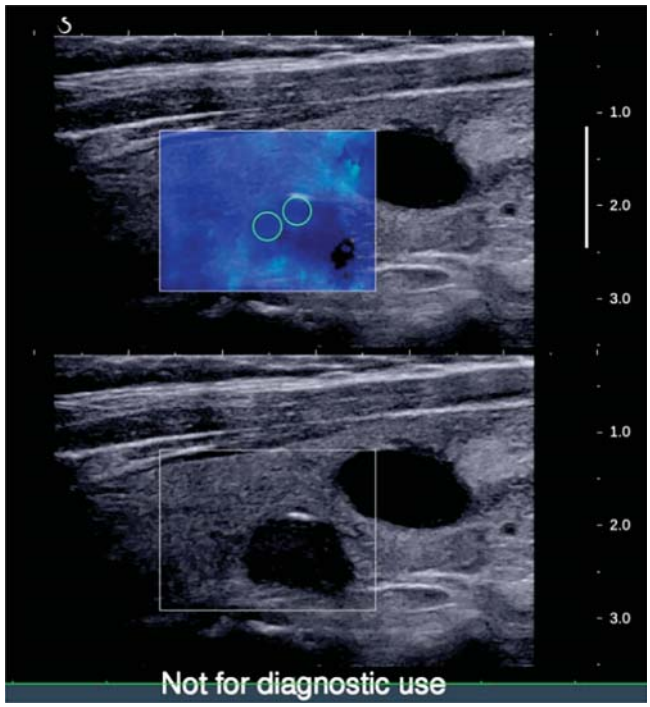

Figure 36.2 B-mode US and SWE speed maps of a benign thyroid nodule using SSI.

As a result, the full field of view (FOV) under the transducer can be obtained in one single comb-push acquisition, which only takes about 20 ms [39].

36.6 Application of CUSE on Thyroid

Here, we present examples of CUSE imaging using a Verasonics research ultrasound scanner on suspicious thyroid nodules under an IRB approved protocol.

A patient in his 60s was investigated for a suspicious thyroid nodule. Ultrasound of right thyroid lobe shows a round hypoechoic nodule, as shown in Figure 36.3. The CUSE image indicates higher shear wave speed within the nodule compared to the surrounding normal background, but lower than the cutoff for a malignant nodule. FNA of the thyroid nodule revealed cytologic features consistent with benign thyroid nodule.

Figure 36.4 shows a CUSE estimation of a patient in her 40s with a suspicious nodule in her left thyroid lobe. Her US image shows a suspicious 12 mm hypoechoic nodule in ultrasound. The shear wave speed measured by CUSE within the nodule was 7.60 ± 0.84 m/s, significantly faster than the normal thyroid background (2.76 ± 0.50 m/s). FNA of the nodule revealed cytologic features consistent with papillary thyroid carcinoma.

36.7 CUSE on Clinical Ultrasound Scanner

Recently, CUSE has been implemented in a GE LOGIQ E9 (LE9) (General Electric Healthcare, Wauwatosa, WI) ultrasound scanner [40]. We have processed more than 35 patients with ultrasound-identifiable thyroid nodules. Here, we present examples of thyroid CUSE images using a clinical ultrasound scanner.

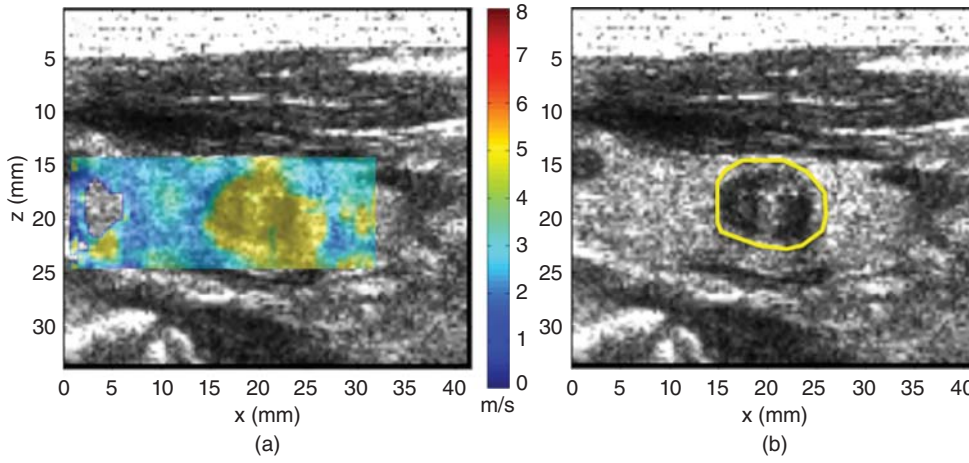

Figure 36.3 US image and CUSE shear wave speed maps of patient's thyroid with a benign nodule. (a) CUSE shear wave speed map; (b) B-mode US with a nodule (solid contour). The nodule is clearly visualized with a slightly higher speed map compared to background but much less than cut off. Both B-mode US and CUSE images were acquired in longitudinal planes. Shear wave speed: SWV (nodule): 4.96 ± 0.28 m/s, SWV (normal or background): 2.25 ± 0.89 m/s. Source: © 2015 IEEE, adapted, with permission, from [39].

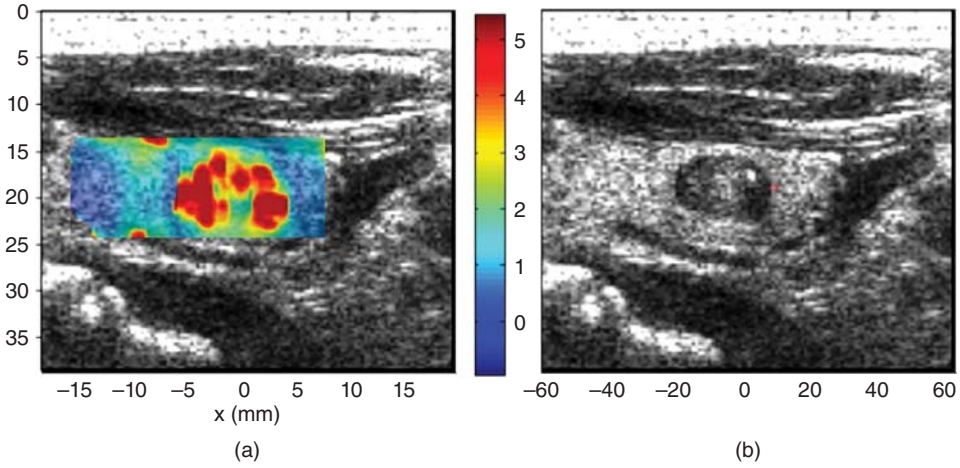

Figure 36.4 US image and CUSE shear wave speed map of a patient's thyroid tissue with a malignant nodule. (a) CUSE shear wave speed map; (b) B-mode US image shows a nodule. The nodule is clearly visualized with significantly higher shear wave speed. Both B-mode US and CUSE images were acquired in longitudinal planes. Shear wave speed: $SWV_{(nodule)} = 7.60 \pm 0.84$ m/s, $SWV_{(normal)} = 2.76 \pm 0.50$ m/s.

Figure 36.5 shows a woman in her 40s with a suspicious thyroid nodule. Ultrasound of her left thyroid shows a 7 × 7 × 8 mm hypoechoic nodule with moderate vascularity by color. Doppler imaging was present in the left thyroid bed. The nodule was concerning for recurrent neoplasm. SWE results showed $E_{mean} = 72.9$ kPa (Figure 36.5). FNA of the nodule revealed recurrent Hurthle cell carcinoma.

Figure 36.6 shows CUSE estimation of a thyroid nodule in a man in his 60s. Ultrasound shows a 36 × 13 × 18 mm mixed cystic and a solid nodule which was observed in the mid to lower pole of the right thyroid lobe. The superior portion of this nodule was predominantly cystic. The inferior portion was more solid with scattered small cystic spaces and also contained a focal

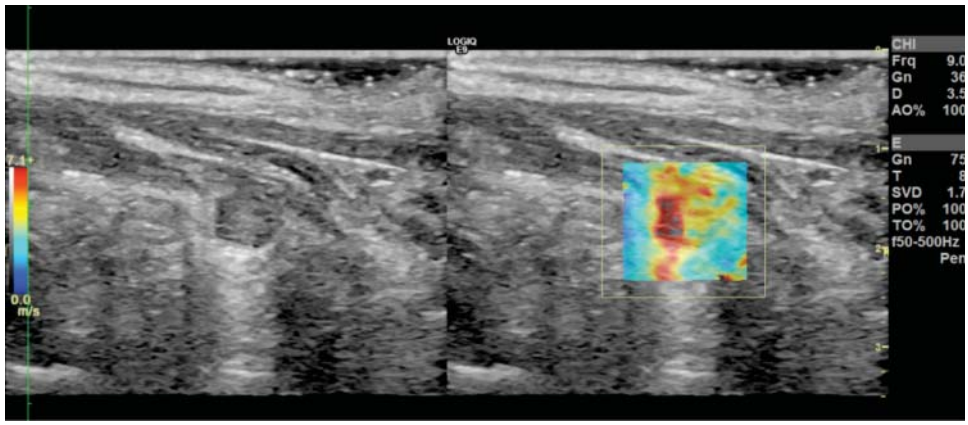

Figure 36.5 Ultrasound and shear wave speed map of a malignant thyroid nodule, using CUSE on a clinical ultrasound scanner.

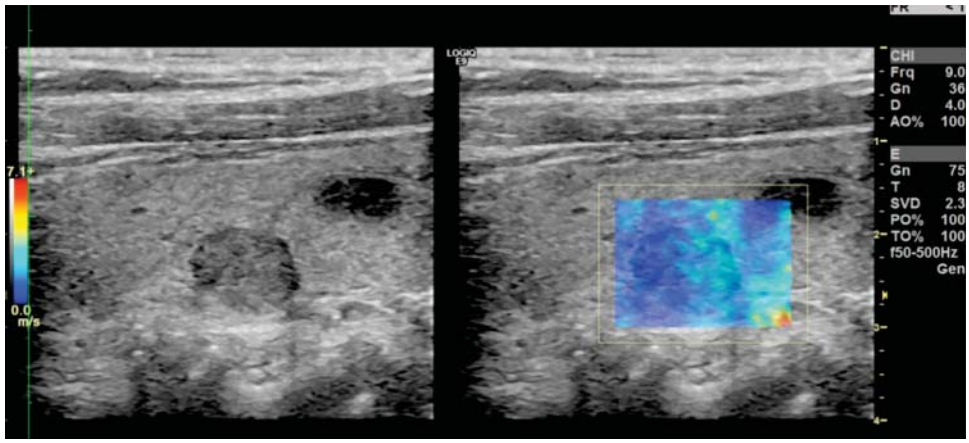

Figure 36.6 Ultrasound and shear wave speed map of a benign nodule, using CUSE on a clinical ultrasound scanner.

cluster of small calcifications. SWE resulted in $E_{\text{mean}} = 6.9$ kPa. FNA of the nodule resulted in cytologic features consistent with benign thyroid nodule with degenerative changes.

36.8 Conclusion

The prevalence of thyroid nodules detected by ultrasound is as high as 60%, and there are no single or combined sonographic criteria sensitive enough to accurately differentiate the nodules. As a result, the specificity of US in detection of malignant nodules is low. Shear wave elastography is a quantitative elasticity imaging technique that has the potential to help in better differentiation of thyroid nodules and can be used complementary to conventional ultrasound to improve our confidence in the final assessment of thyroid nodules [33]. Adding quantitative SWE to B-mode ultrasound will add the specificity for thyroid cancer [41]. Studies showed that a 66 kPa threshold in shear wave elastography is best for the differentiation of malignant and benign thyroid nodules [31]. Furthermore, quantitative SWE may have the potential to help accurately select thyroid nodules with indeterminate cytology for surgical intervention.

There is a significant effect of pre-compression on SWE estimation in normal thyroid tissue, benign nodules, and papillary carcinomas. These findings may explain some of the discrepancies that have been observed in the results of preliminary thyroid SWE studies for diagnostic performance of SWE for thyroid malignancy [42].

Another limitation is the diagnosis of calcified nodules. Presence of calcifications in benign lesions can induce the appearance of a high stiffness region when they are evaluated by SWE methods, and that may lead to false-positive results [43, 44]. Although SWE is simple, quantitative, and reproducible, more advances are still needed in order to differentiate calcified nodules and follicular tumors.

Acknowledgments

The work described in this chapter was supported by National Institutes of Health (NIH) grants R01CA148994, R01CA148994-S1, R01CA168575, R01EB017213, and R01CA174723 from the NIH-National Cancer Institute. The content is solely the responsibility of the author and does not necessarily represent the official views of NIH. The author is very grateful to the following individuals for their valuable work during the course of the study that presented in as this chapter: Dr. Max Denis, Dr. Mahdi Bayat, Dr. Mohammad Mehrmohammadi, Ms. Adriana Gregory, and Ms. Cynthia Andrist.

Disclosure: the author, AA, discloses that Mayo Clinic hold patents on the CUSE technology; and Mayo Clinic has also received royalties from companies that have licensed the CUSE technology. The author does not have any financial interest on the described technology in this chapter.

References

1 Hegedüs, L. (2004). The thyroid nodule. *N. Engl. J. Med.* 351 (17): 1764–1771.
2 Brito, J.P., Morris, J.C., and Montori, V.M. (2013). Thyroid cancer: zealous imaging has increased detection and treatment of low risk tumours. *Br. Med. J.* 347: f4706.
3 Chen, A.Y., Jemal, A., and Ward, E.M. (2009). Increasing incidence of differentiated thyroid cancer in the United States, 1988–2005. *Cancer* 115 (16): 3801–3807.
4 Pellegriti, G., et al. (2013). Worldwide increasing incidence of thyroid cancer: update on epidemiology and risk factors. *J. Cancer Epidemiol.* 2013: 965212.
5 Davies, L. and Welch, H.G. (2006). Increasing incidence of thyroid cancer in the United States, 1973–2002. *J. Am. Med. Assoc.* 295 (18): 2164–2167.
6 Reading, C.C., et al. (2005). Sonography of thyroid nodules: a "classic pattern" diagnostic approach. *Ultrasound Q.* 21 (3): 157–165.
7 Deandrea, M., et al. (2002). Fine-needle aspiration biopsy of the thyroid: comparison between thyroid palpation and ultrasonography. *Endocr. Pract.* 8 (4): 282–286.
8 Gharib, H. and Goellner, J.R. (1993). Fine-needle aspiration biopsy of the thyroid: an appraisal. *Ann. Int. Med.* 118 (4): 282–289.
9 Burch, H.B., et al. (1996). Fine needle aspiration of thyroid nodules. *Acta Cytolog.* 40 (6): 1176–1183.
10 Alexander, E.K. (2008). Approach to the patient with a cytologically indeterminate thyroid nodule. *J. Clin. Endocrinol. Metab.* 93 (11): 4175–4182.
11 Goellner, J.R. (1996). Fine needle aspiration of the thyroid gland. In: *Fine Needle Aspiration of Subcutaneous Organs and Masses* (ed. Y.S. Erozan), 1st edn. Philadelphia: Lippincott-Raven.

12 Haas, S., Trujillo, A., and Kunstle, J. (1993). Fine needle aspiration of thyroid nodules in a rural setting. *Am. J. Med.* 94 (4): 357–361.

13 Cap, J., et al. (1999). Sensitivity and specificity of the fine needle aspiration biopsy of the thyroid: clinical point of view. *Clin. Endocrinol. (Oxf.)* 51 (4): 509–515.

14 Raab, S.S., et al. (2006). Errors in thyroid gland fine-needle aspiration. *Am. J. Clin. Pathol.* 125 (6): 873–882.

15 Sarvazyan, A. (2001). Elastic properties of soft tissues. In: *Handbook of Elastic Properties of Solids, Liquids and Gases* (ed. M. Levy, H.E. Bass, R.R. Stern, A.G. Every, and V. Keppens), vol. 3, 107–127. Academic Press.

16 Krouskop, T.A., et al. (1998). Elastic moduli of breast and prostate tissues under compression. *Ultrason. Imaging* 20 (4): 260–274.

17 Bahn, M.M., et al. (2009). Development and application of magnetic resonance elastography of the normal and pathological thyroid gland in vivo. *J. Magn. Reson. Imaging* 30 (5): 1151–1154.

18 Szabo, T.L. (2004). *Diagnostic Ultrasound Imaging: Inside Out*. Academic Press.

19 Lyshchik, A., et al. (2005). Elastic moduli of thyroid tissues under compression. *Ultrason. Imaging* 27 (2): 101–110.

20 Rago, T., et al. (2007). Elastography: new developments in ultrasound for predicting malignancy in thyroid nodules. *J. Clin. Endocrinol. Metab.* 92 (8): 2917–2922.

21 Lyshchik, A., et al. (2005). Thyroid gland tumor diagnosis at US elastography 1. *Radiology* 237 (1): 202–211.

22 Dighe, M., et al. (2008). Differential diagnosis of thyroid nodules with US elastography using carotid artery pulsation 1. *Radiology* 248 (2): 662–669.

23 Bae, U., et al. (2007). Ultrasound thyroid elastography using carotid artery pulsation – preliminary study. *J. Ultrasound Med.* 26 (6): 797–805.

24 Gu, J., et al. (2012). Preliminary study on the diagnostic value of acoustic radiation force impulse technology for differentiating between benign and malignant thyroid nodules. *J. Ultrasound Med.* 31 (5): 763–771.

25 Bojunga, J., et al. (2012). Acoustic radiation force impulse imaging for differentiation of thyroid nodules. *PloS One* 7 (8): e42735.

26 Friedrich-Rust, M., et al. (2012). Acoustic radiation force impulse-imaging for the evaluation of the thyroid gland: a limited patient feasibility study. *Ultrasonics* 52 (1): 69–74.

27 Tanter, M., et al. (2008). Quantitative assessment of breast lesion viscoelasticity: initial clinical results using supersonic shear imaging. *Ultrasound Med. Biol.* 34 (9): 1373–1386.

28 Sebag, F., et al. (2010). Shear wave elastography: a new ultrasound imaging mode for the differential diagnosis of benign and malignant thyroid nodules. *J. Clin. Endocrinol. Metab.* 95 (12): 5281–5288.

29 Slapa, R.Z., et al. (2012). Shear wave elastography may add a new dimension to ultrasound evaluation of thyroid nodules: case series with comparative evaluation. *J. Thyroid Res.* 2012: 657147.

30 Magri, F., et al. (2012). Shear wave elastography in the diagnosis of thyroid nodules: feasibility in the case of coexistent chronic autoimmune Hashimoto's thyroiditis. *Clin. Endocrinol.* 76 (1): 137–141.

31 Veyrieres, J.-B., et al. (2012). A threshold value in Shear Wave elastography to rule out malignant thyroid nodules: a reality? *Eur. J. Radiol.* 81 (12): 3965–3972.

32 Szczepanek-Parulska, E., et al. (2013). Comparison of diagnostic value of conventional ultrasonography and shear wave elastography in the prediction of thyroid lesions malignancy. *PloS One* 8 (11): e81532.

33 Zhang, B., et al. (2013). Shear wave elastography for differentiation of benign and malignant thyroid nodules: a meta-analysis. *J. Ultrasound Med.* 32 (12): 2163–2169.

34 Cantisani, V., et al. (2014). Ultrasound elastography in the evaluation of thyroid pathology. Current status. *Eur. J. Radiol.* 83 (3): 420–428.

35 Song, P., et al. (2013). Comb-push ultrasound shear elastography (CUSE) with various ultrasound push beams. *IEEE Trans. Med. Imaging* 32 (8): 1435–1447.

36 Song, P., et al. (2012). Comb-push ultrasound shear elastography (CUSE): a novel method for two-dimensional shear elasticity imaging of soft tissues. *IEEE Trans. Med. Imaging* 31 (9): 1821–1832.

37 Song, P., et al. (2014). Fast shear compounding using robust 2-D shear wave speed calculation and multi-directional filtering. *Ultrasound Med. Biol.* 40 (6): 1343–1355.

38 Yoon, J.H., et al. (2011). Interobserver variability of ultrasound elastography: how it affects the diagnosis of breast lesions. *Am. J. Roentgenol.* 196 (3): 730–736.

39 Mehrmohammadi, M., et al. (2015). Comb-push ultrasound shear elastography (CUSE) for evaluation of thyoid nodules: preliminary in vivo results. *IEEE Trans. Med. Imaging* 34 (1): 97–106.

40 Song, P., et al. (2015). Two-dimensional shear-wave elastography on conventional ultrasound scanners with time-aligned sequential tracking (TAST) and comb-push ultrasound shear elastography (CUSE). *IEEE Trans. Ultrason., Ferroelect., Freq. Control* 62 (2): 290–302.

41 Kim, H., et al. (2013). Quantitative assessment of shear-wave ultrasound elastography in thyroid nodules: diagnostic performance for predicting malignancy. *Eur. Radiol.* 23 (9): 2532–2537.

42 Lam, A., et al. (2015). The influence of precompression on elasticity of thyroid nodules estimated by ultrasound shear wave elastography. *Eur. Radiol.* 26 (8): 2845–2852.

43 Gregory, A., et al. (2015). Effect of calcifications on breast ultrasound shear wave elastography: an investigational study. *PloS One* 10 (9): e0137898.

44 Gregory, A., et al. (2015). An experimental phantom study on the effect of calcifications on ultrasound shear wave elastography. In: *Engineering in Medicine and Biology Society (EMBC), 2015 37th Annual International Conference of the IEEE*.

Section IX

Perspective on Ultrasound Elastography

37

Historical Growth of Ultrasound Elastography and Directions for the Future

Armen Sarvazyan[1] *and Matthew W. Urban*[2]

[1] *Artann Laboratories, West Trenton, NJ, USA*
[2] *Department of Radiology, Mayo Clinic, Rochester, MN, USA*

37.1 Introduction

The field of elastography or elasticity imaging has grown from in its infancy more than two decades ago to become an emerging medical imaging modality. It has found utility among physicians for many different applications. The field and the level of clinical applications are projected to grow.

The purpose of this chapter is to examine how the field of ultrasound elastography has grown over time. To measure this impact we analyzed the publication record using PubMed for the field and looked at different distinctions and trends. Additionally, we offer a perspective on future investigations that could be pursued for the use of acoustic radiation force (ARF) for ultrasound elastographic applications.

There are numerous methods that fall under the umbrella of the field of "ultrasound elastography" that have been detailed in previous chapters of this book. Figure 37.1 demonstrates the various techniques employed in the field of elastography and elasticity imaging as a whole [1–22]. This figure lists the various means of excitation. The methods use mechanical, endogenous, or acoustic radiation force as the deformation source.

37.2 Elastography Publication Analysis

In order to evaluate the development of this field we will provide an overview of the growth of this field using the metric of published reports in the biomedical literature. We used PubMed to perform targeted searches in the biomedical literature and looked at the number of publications from 1995 to 2015. The histograms that follow provide insight into the publication dynamics which can be an efficient tool for exploring history and milestones of a branch of science or technology and for making projections on future applications in particular areas.

To make these analyses a limited set of keywords were used that would encompass the main aspects of the subject at hand, which is the measurement of tissue elasticity with ultrasound. The list consisted of the terms: ultrasound elastography, elastography, elasticity imaging, shear wave, and acoustic radiation force. The first search that was performed was on "ultrasound elastography" and is shown in Figure 37.2.

In the 1990s, few research groups (less than a dozen) in the United States, Europe, Japan, and Russia started working in this field and basic principles and various modalities of the technology were developed. The great surge in the publications in 2007/2008 seen in the histogram

Ultrasound Elastography for Biomedical Applications and Medicine, First Edition.
Edited by Ivan Nenadic, Matthew Urban, James Greenleaf, Jean-Luc Gennisson, Miguel Bernal, and Mickael Tanter.

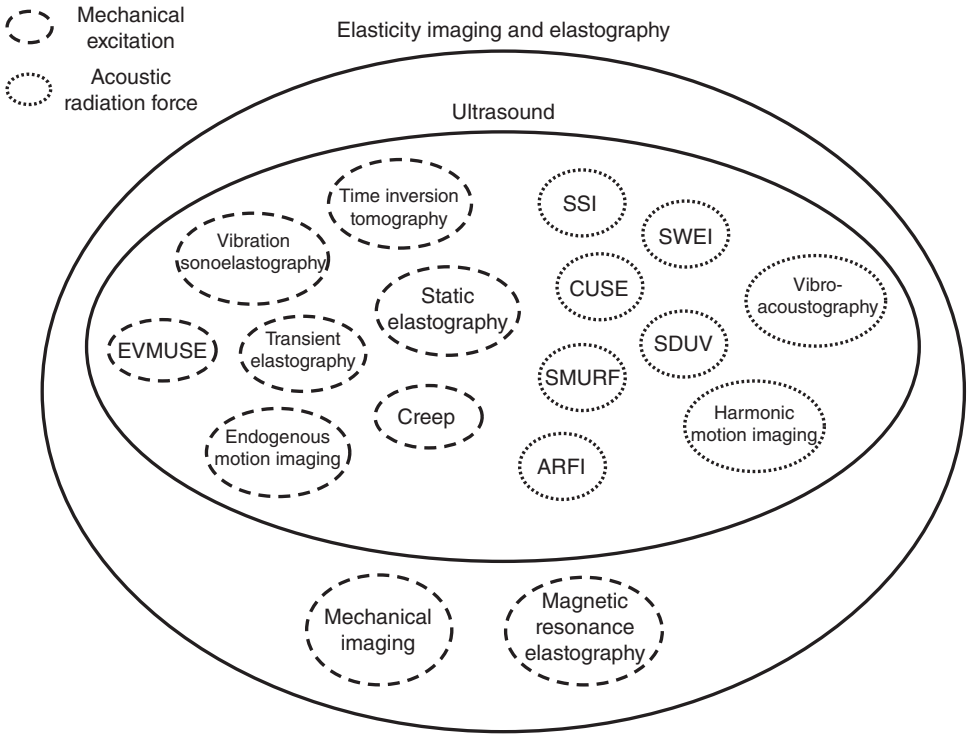

Figure 37.1 Diagram of elastography and elasticity imaging methods with excitation mode depicted by different line types. Mechanical excitation is denoted with dashed lines and acoustic radiation force is denoted with dotted lines.

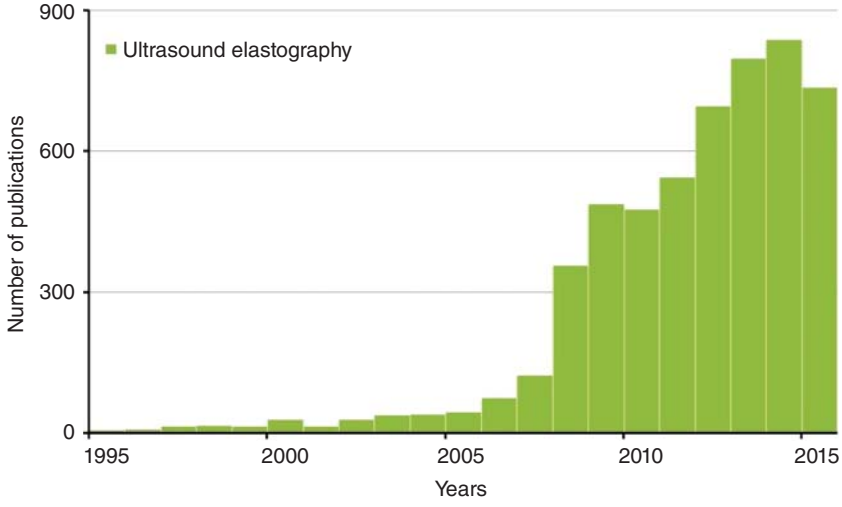

Figure 37.2 Dynamics of publications on "ultrasound elastography" according to the PubMed database from 1995 to 2015.

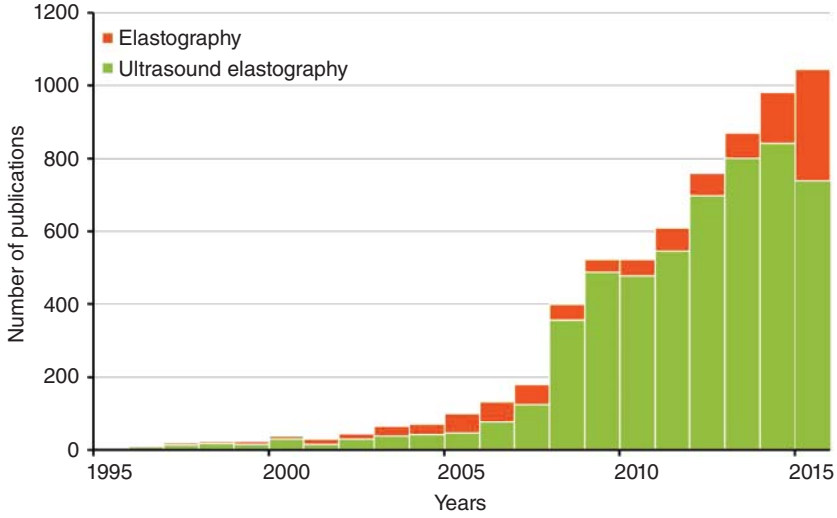

Figure 37.3 Comparison of histograms for "elastography" and "ultrasound elastography" from 1995 to 2015.

of Figure 37.2 shows the start of wide clinical use of ultrasound elastography. After that steep rise in the number of publications in 2008, we see a steady increase of activities in the field, demonstrating successful application of the technology in various areas of medical diagnostics and treatment monitoring. This shift coincided with the implementation of elastography methods in clinical ultrasound machines so that methods could be used in many different patient populations throughout the world.

It should be noted that ultrasound elastography is part of a larger field of elastography that encompasses other imaging techniques, including magnetic resonance imaging and mechanical or tactile imaging [21, 22]. However, because ultrasound is a relatively inexpensive and widely available modality, methods developed using ultrasound can be disseminated widely for access to patients. Figure 37.3 shows the proportion of ultrasound elastography reports with respect to all "elastography" reports. This figure clearly shows a significant increase in the number of the contributions in the last 2 or 3 years from elastography modalities other than ultrasound elastography, mainly owing to increased activities in the fields of MR elastography and tactile imaging.

Terminology and choice of key words are an important issue in science. In the literature related to the subject of this review two synonyms are commonly used: "elasticity imaging" or "elastography". Each of these terms has certain advantages. The term "elasticity imaging" marks the technology alongside the other diagnostic medical imaging tools such as MR imaging, X-ray imaging, acoustic imaging, tactile imaging, optoacoustic imaging, etc. At the same time, "elastography" is shorter and at the present, after elasticity imaging became a proven and widely accepted modality in the last couple of years, "elastography" is used more and more often, as illustrated in Figure 37.4. For example, "shear wave elasticity imaging" (SWEI), the first ultrasonic elastography technology using shear acoustic waves, is currently more often called "shear wave elastography" (SWE), not SWEI, which appears to rename the original technology. There is a disadvantage with splintering of terms, particularly in the case of literature searches, because relevant references may be missed. Also, as these methods have become commercialized, general names have been replaced by the names of marketed products.

Analysis of the underlying fine structure of the "ultrasound elastography" histogram allows one to see the dynamics of relative contributions of various modalities. For example, we found

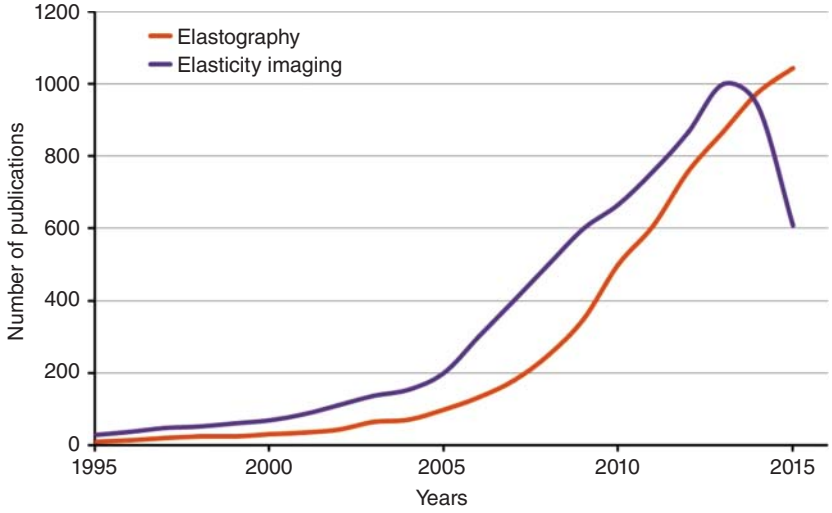

Figure 37.4 Comparison of trends for usage for "elasticity imaging" versus "elastography". The curves suggest a transition from using "elasticity imaging" to using "elastography".

a steady decline of the publications on "static elastography". We found out that the area of the fastest growth of ultrasonic elastography is related to the modalities based on the use of shear waves, as see in Figures 37.5 and 37.6. Before 2010, shear wave techniques contributed less than a quarter of ultrasound elastography publications; in 2015 they contribute more than 70%.

There are several advantages of using shear waves as opposed to compression-based strain elastography. First, the shear wave speed can be evaluated locally and can be used for calculating the absolute values of the shear modulus. Also, to obtain these quantitative values of the shear modulus it is not necessary to know the stress distribution as it is in strain elastography. Acoustic radiation force excitations typically generate shear waves with a broad frequency range which can be exploited for viscoelastic material characterization through analyzing shear wave velocity dispersion [13, 23–25]. The shear wave frequency can be modulated based on the application to obtain proper levels of propagation in order to estimate the shear wave speed with confidence. Amplitude modulation can also be used to generate ARF with specific frequency content [4, 5, 26–28]. Lastly, shear waves can be used not only to evaluate the isotropic, elastic material properties, but also the anisotropic and viscoelastic properties of tissues.

Most shear wave-based modalities use the acoustic radiation force of focused ultrasound and the fraction of the ARF-related modes of ultrasound elasticity imaging is constantly increasing. Therefore there is a strong correlation between the histograms of the "shear wave" and "acoustic radiation force", as illustrated in Figure 37.6. Although the biomedical applications of ARF are very diverse (they include targeted drug and gene delivery, manipulating of cells in suspension, acoustical tweezers, etc.), the widest new area of its applications is elasticity imaging and ARF-based methods are the largest part of the ultrasound elastography techniques. ARF currently demonstrates the steepest increase the publications histograms (see Figure 37.6).

ARF is one of the most important physical phenomena in ultrasound elastography and there are several more unexplored aspects of ARF which might further increase its role in ultrasound elastography. Among those three will be considered here:

- the presence of a push-pull ARF
- nonlinear enhancement of ARF
- design of radiation force beams for shear wave elastography.

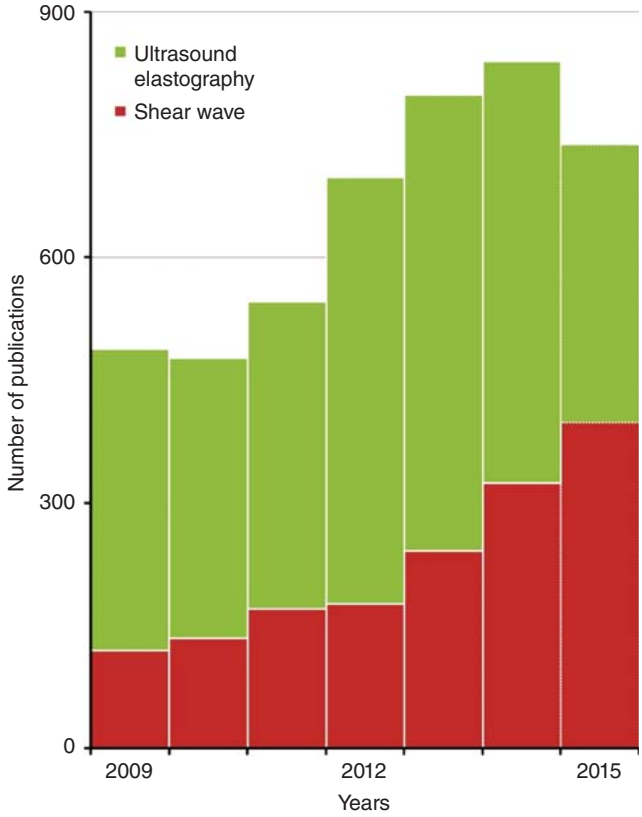

Figure 37.5 Comparison of publications on "ultrasound elastography" and "shear waves". The shear wave-based modalities have the steepest rise among other modalities of ultrasound elastography.

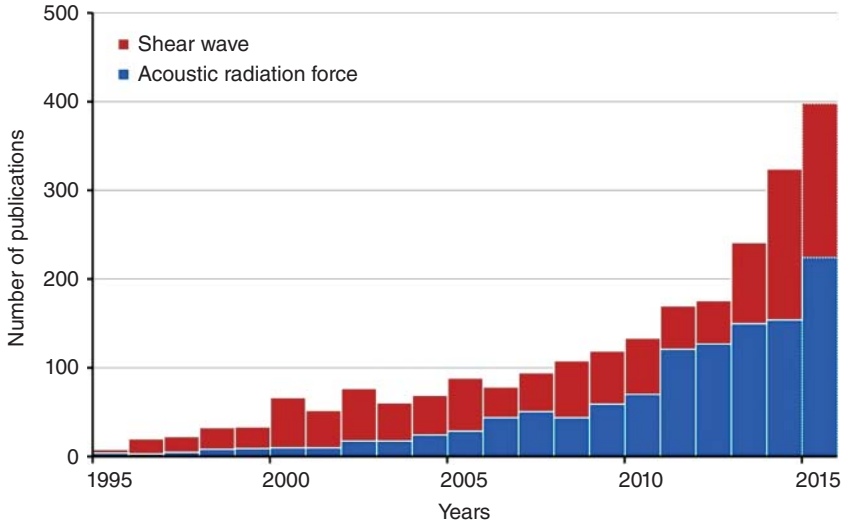

Figure 37.6 Comparison of publications on shear waves and ARF. Strong correlation between dynamics of publications on shear waves and on ARF.

37.3 Future Investigations of Acoustic Radiation Force for Elastography

37.3.1 Nondissipative Acoustic Radiation Force

In most of the ARF-based imaging modalities, the ARF is dependent on an absorbing or attenuating tissue. The simplified equation for the ARF, F, is given as

$$F = \frac{2\alpha I}{c} \tag{37.1}$$

where α is the ultrasound attenuation coefficient, I is the ultrasound intensity, and c is the longitudinal wave speed in the medium. However, ARF can be generated in media without attenuation or acoustic wave reflection. Gradients of acoustic properties of a medium, such as variations of sound velocity, cause gradients of the energy density in the propagating acoustic wave. As a result, radiation force is generated [29, 30]. Displacement produced by non-dissipative radiation force in inhomogeneous media can be in both directions (outward and inward toward the transducer).

Non-dissipative radiation force can be used to generate a differential force or pressure on an object. Figure 37.7 schematically illustrates the difference in the ARF effect on an inclusion in the tissue with the upper drawing corresponding to a solid tumor and in the bottom drawing corresponding to a liquid-filled cyst. We assume that the arrows represent an acoustic beam traveling through the inclusion, the solid lines represent the unperturbed shape, and the dashed lines represent the shape of the inclusion after the ARF stimulation.

Beyer showed the net pressure at the interface of two media is related to the difference in longitudinal wave speeds in a medium and the corresponding gradient of the energy density of an acoustic beam [30]

$$P_{\text{net}} = E\left[1 - \frac{c_1}{c_2} + m^2\left(1 + \frac{c_1}{c_2}\right)\right] \tag{37.2}$$

where E is the energy density of the acoustic beam, c_1 and c_2 are the longitudinal wave speeds in mediums 1 and 2, respectively, and m is the reflection coefficient defined as

$$m = \frac{\rho_2 c_2 - \rho_1 c_1}{\rho_2 c_2 + \rho_1 c_1} \tag{37.3}$$

and ρ_1 and ρ_2 are the mass densities in mediums 1 and 2. So in the case that the surrounding tissue has $\rho_1 = 1000\ \text{kg/m}^3$ and $c_1 = 1540\ \text{m/s}$ and the tumor has $\rho_2 = 1035\ \text{kg/m}^3$ and $c_2 =$

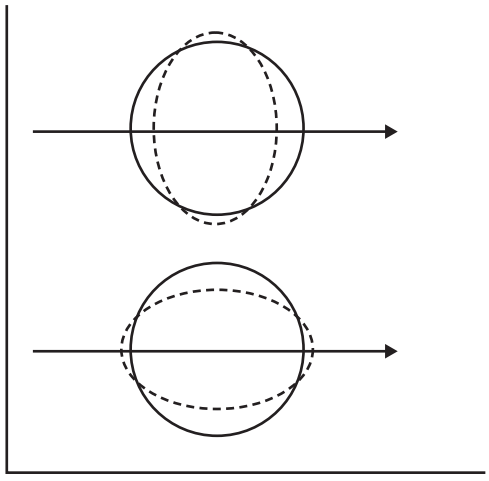

Figure 37.7 Comparison of deformation on a solid tumor (top) and cyst (bottom) due to an ARF beam applied to the inclusion. The arrow represents an acoustic beam traveling through the inclusion, the solid lines represent the unperturbed shape, and the dashed lines represent the shape of the inclusion after the ARF stimulation.

1573 m/s then $P_{net} = +0.0225E$ and then on the other side going from tumor to normal tissue, the subscripts 1 and 2 are exchanged and $P_{net} = -0.0199E$ [31]. In the second case, the surrounding tissue is used as defined above and the cyst has $\rho_2 = 1000$ kg/m^3 and $c_2 = 1500$ m/s, then $P_{net} = -0.0263E$ and then on the other side $P_{net} = +0.0263E$. The change in the signs of the force at the edges generates a squeezing or stretching of the inclusion. Investigations would have to be performed to evaluate the magnitude of these deformations to be used as metrics for diagnosis. It should be noted that non-dissipative force, in contrast to the dissipative radiation force, can be generated in tissue at low sub-megahertz frequencies despite the low attenuation coefficient of the media.

37.3.2 Nonlinear Enhancement of Acoustic Radiation Force

To improve the induced motion using ARF for various applications, it is desired to use any method to enhance the intensity of an acoustic beam to generate more ARF. Properly accounting for the ultrasonic properties of tissue, the nonlinear effects can enhance the amplitude and localization of the radiation force in the focal region. Focusing a transducer generates a harmonic wave which steepens due to nonlinearity and then, due to diffraction, transforms into a short impulse. Along the acoustic path, the content of higher frequencies in the emitted harmonic wave gradually increases, which results in an increased attenuation of the acoustic wave and a corresponding increase of the radiation force. This effect is most pronounced close to the focal area of the beam.

Figure 37.8 shows the relative power and radiation force for a focused beam from the linear case and nonlinear cases where N is the ratio of the focal length of the transducer and the nonlinear shock length.

If the shock length is constant, then the focal length could be adjusted to use the nonlinear enhancement advantageously to increase the radiation force. The amplitude and phase shift for each harmonic can be chosen so that the nonlinearity, diffraction, and dissipation will transform the initial wave into a shock wave near the focal region, as depicted in Figure 37.9. In addition, only linear and therefore not significant, losses will take place along the pre-focal distance, and the maximum transfer of ultrasonic energy into radiation force will occur at the focus.

37.3.3 Spatial Modulation of Acoustic Radiation Force Push Beams

For ARF-based elastography applications it is necessary to produce a strong shear wave because the shear waves attenuate in very short distances. As a result there has been significant work to use different focusing or beamforming strategies to optimize the force delivered. Conventional electronic focusing techniques have been used for many methods [3, 11]. Bercoff et al. proposed focusing at several different depths in a fast, successive fashion to create a strong shear wave through constructive interference in the supersonic shear imaging method [12]. Vibro-acoustography used linear array transducers with different sub-apertures to focus beams at different ultrasound frequencies to generate an oscillatory force [32, 33].

McAleavey et al. used unique apodization schemes to generate ARF push beams to generate shear waves with known spatial frequencies for estimation of the shear wave velocity in a medium [16]. Unfocused push beams were introduced by Zhao et al. to create shear waves near to the transducer [34]. Another advantageous aspect of this approach was to generate a shear wave with a large depth-of-field (DOF). Radiation force-based crawling waves were generated with traditional focusing and axicon focusing [35]. Additional work was performed to combine traditional and axicon focusing in a hybrid fashion to make beams with a large DOF [36].

Unfocused beams and focused beams were used in subsequent implementations of a method called comb-push ultrasound shear elastography (CUSE), which uses the simultaneous production of many shear waves and then uses directional filtering and correlation-based techniques

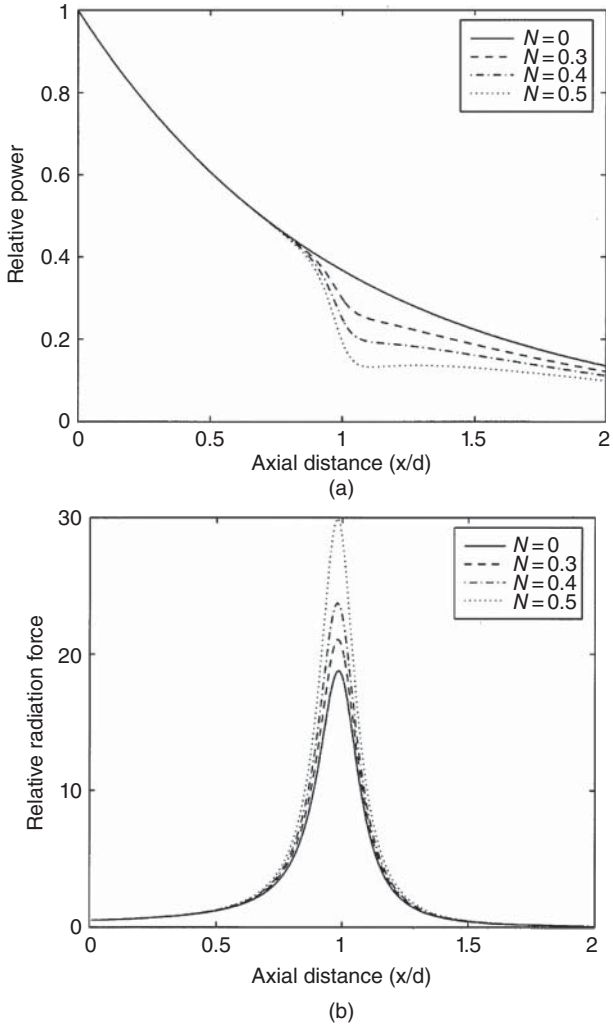

Figure 37.8 Nonlinear enhancements of the radiation force contrasted with a linear consideration. The ultrasound field characteristics (a) power and (b) radiation force are plotted as functions of axial distance for linear ($N = 0$) and nonlinear ($N = 0.3$, 0.4, and 0.5) regimes. Source: reprinted from [11], copyright 1998, with permission from Elsevier.

to measure shear wave velocity [14, 37]. Steered unfocused beams were also used to generate a collection of high density ARF push beams [38].

The spatial distribution of ARF push beams can be optimized based on the application. There are numerous ways to generate strong displacements with these methods for the purposes of perturbing soft tissues.

37.4 Conclusions

This chapter provides a unique analysis of the publication history in the field of elastography. It paints a picture that shows an incredible impact due to clinical acceptance. Shear wave-based applications are growing and a majority of those applications are using methods based on

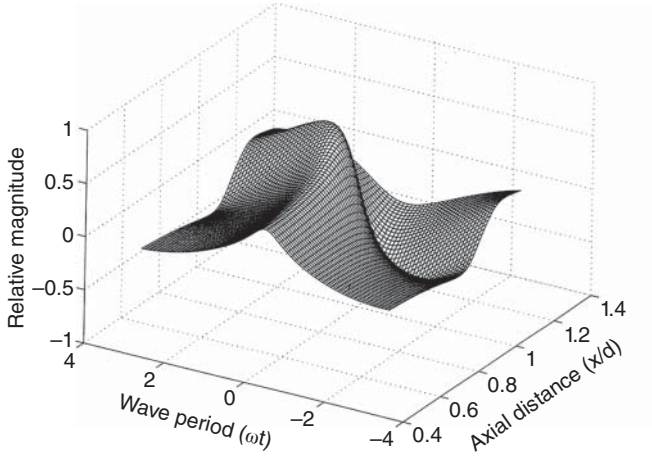

Figure 37.9 Transformation of the waveform for a focused ultrasonic field. Source: reprinted from [11], copyright 1998, with permission from Elsevier.

acoustic radiation force. We provide a few ideas for investigation to optimize and use acoustic radiation force for future elastographic applications. The field of elastography has grown from a few research laboratories into a very useful imaging modality that is making clinical impact in a number of different areas of study.

Acknowledgments

This work was supported by grant R01DK092255 from the National Institute of Diabetes and Digestive and Kidney Diseases (NIDDK) and grant R21AR065024 from the National Institute of Arthritis and Musculoskeletal and Skin Diseases (NIAMS) and National Institutes of Health (NIH). The content is solely the responsibility of the authors and does not necessarily represent the official views of the NIDDK, NIAMS, and NIH.

References

1 Sarvazyan, A., Hall, T.J., Urban, M.W., et al. (2011). Elasticity imaging – an emerging branch of medical imaging. *An overview. Curr. Med. Imaging Rev.* 7: 255–282.
2 Ophir, J., Cespedes, I., Ponnekanti, H., et al. (1991). Elastography: a quantitative method for imaging the elasticity of biological tissues. *Ultrason. Imaging* 13: 111–134.
3 Nightingale, K.R., Palmeri, M.L., Nightingale, R.W., and Trahey, G.E. (2001). On the feasibility of remote palpation using acoustic radiation force. *J. Acoust. Soc. Am.* 110: 625–634.
4 Konofagou, E.E. and Hynynen, K. (2003). Localized harmonic motion imaging: theory, simulations and experiments. *Ultrasound Med. Biol.* 29: 1405–1413.
5 Fatemi, M. and Greenleaf, J.F. (1998). Ultrasound-stimulated vibro-acoustic spectrography. *Science* 280: 82–85.
6 Pernot, M., Fujikura, K., Fung-Kee-Fung, S.D., and Konofagou, E.E. (2007). ECG-gated, mechanical and electromechanical wave imaging of cardiovascular tissues in vivo. *Ultrasound Med. Biol.* 33: 1075–1085.

7 Kanai, H. (2005). Propagation of spontaneously actuated pulsive vibration in human heart wall and in vivo viscoelasticity estimation. *IEEE Trans. Ultrason., Ferroelectr., Freq. Control* 52: 1931–1942.

8 Sandrin, L., Fourquet, B., Hasquenoph, J.M., et al. (2003). Transient elastography: a new noninvasive method for assessment of hepatic fibrosis. *Ultrasound Med. Biol.* 29: 1705–1713.

9 Lerner, R.M., Parker, K.J., Holen, J., et al. (1988). Sono-elasticity: Medical elasticity images derived from ultrasound signals in mechanically vibrated targets. In: *Acoustical Imaging*, vol. 16, 317–327. New York: Plenum Press.

10 Hoyt, K., Parker, K.J., and Rubens, D.J. (2007). Real-time shear velocity imaging using sonoelastographic techniques. *Ultrasound Med. Biol.* 33: 1086–1097.

11 Sarvazyan, A.P., Rudenko, O.V., Swanson, S.D., et al. (1998). Shear wave elasticity imaging: a new ultrasonic technology of medical diagnostics. *Ultrasound Med. Biol.* 24: 1419–1435.

12 Bercoff, J., Tanter, M., and Fink, M. (2004). Supersonic shear imaging: a new technique for soft tissue elasticity mapping. *IEEE Trans. Ultrason., Ferroelectr., Freq. Control* 51: 396–409.

13 Chen, S., Urban, M.W., Pislaru, C., et al. (2009). Shearwave dispersion ultrasound vibrometry (SDUV) for measuring tissue elasticity and viscosity. *IEEE Trans. Ultrason., Ferroelectr., Freq. Control* 56: 55–62.

14 Song, P., Zhao, H., Manduca, A., et al. (2012). Comb-push ultrasound shear elastography (CUSE): a novel method for two-dimensional shear elasticity imaging of soft tissues. *IEEE Trans. Med. Imaging* 31: 1821–1832.

15 Zhao, H., Song, P., Meixner, D.D., et al. (2014). External vibration multi-directional ultrasound shearwave elastography (EVMUSE): application in liver fibrosis staging. *IEEE Trans. Med. Imaging* 33: 2140–2148.

16 McAleavey, S.A., Menon, M., and Orszulak, J. (2007). Shear-modulus estimation by application of spatially-modulated impulsive acoustic radiation force. *Ultrason. Imaging* 29: 87–104.

17 Catheline, S., Souchon, R., Rupin, M., et al. (2013). Tomography from diffuse waves: Passive shear wave imaging using low frame rate scanners. *Appl. Phys. Lett.* 103: 014101–014105.

18 Sridhar, M. and Insana, M.F. (2007). Ultrasonic measurements of breast viscoelasticity. *Med. Phys.* 34: 4757–4767.

19 Amador, C., Urban, M.W., Chen, S., and Greenleaf, J.F. (2012). Loss tangent and complex modulus estimated by acoustic radiation force creep and shear wave dispersion. *Phys. Med. Biol.* 57: 1263–1282.

20 Mauldin, F.W., Haider. M.A., Loboa, E.G., et al. (2008). Monitored steady-state excitation and recovery (MSSER) radiation force imaging using viscoelastic models. *IEEE Trans. Ultrason., Ferroelectr., Freq. Control* 55: 1597–1610.

21 Muthupillai, R., Lomas, D.J., Rossman, P.J., et al. (1995). Magnetic resonance elastography by direct visualization of propagating acoustic strain waves. *Science* 269: 1854–1857.

22 Sarvazyan, A. and Egorov, V. (2011). Mechanical imaging – a technology for 3-D visualization and characterization of soft tissue abnormalities. A review.. *Curr. Med. Imaging Rev.* 8: 64–73.

23 Urban, M.W., Chen, S., and Fatemi, M. (2012). A review of shearwave dispersion ultrasound vibrometry (SDUV) and its applications. *Curr. Med. Imaging Rev.* 8: 27–36.

24 Deffieux, T., Montaldo, G., Tanter, M., and Fink, M. (2009). Shear wave spectroscopy for in vivo quantification of human soft tissues visco-elasticity. *IEEE Trans. Med. Imaging* 28: 313–322.

25 Nightingale, K.R., Rouze, N.C., Rosenzweig, S.J., et al. (2015). Derivation and analysis of viscoelastic properties in human liver: impact of frequency on fibrosis and steatosis staging. *IEEE Trans. Ultrason., Ferroelectr., Freq. Control* 62: 165–175.

26 Urban, M.W., Silva, G.T., Fatemi, M., and Greenleaf, J.F. (2006). Multifrequency vibro-acoustography. *IEEE Trans. Med. Imaging* 25: 1284–1295.

27 Urban, M.W., Fatemi, M., and Greenleaf, J.F. (2010). Modulation of ultrasound to produce multifrequency radiation force. *J. Acoust. Soc. Am.* 127: 1228–1238.

28 Zheng, Y., Yao, A., Chen, S., et al. (2013). Ultrasound vibrometry using orthogonal-frequency-based vibration pulses. *IEEE Trans. Ultrason., Ferroelectr., Freq. Control* 60: 2359–2370.

29 Ostrovsky, L., Sutin, A., Il'inskii, Y., et al. (2007). Radiation force and shear motions in inhomogeneous media. *J. Acoust. Soc. Am.* 121: 1324–1331.

30 Beyer, R.T. (1997). *Nonlinear Acoustics*. Woodbury, NY: Acoustical Society of America.

31 Duck, F.A. (1990). *Physical Properties of Tissue*. London: Academic Press.

32 Silva, G.T., Greenleaf, J.F., and Fatemi, M. (2004). Linear arrays for vibro-acoustography: a numerical simulation study. *Ultrason. Imaging* 26: 1–17.

33 Urban, M.W., Chalek, C., Kinnick, R.R., et al. (2011). Implementation of vibro-acoustography on a clinical ultrasound system. *IEEE Trans. Ultrason., Ferrorelect., Freq. Control* 58: 1169–1181.

34 Zhao, H., Song, P., Urban, M.W., et al. (2012). Shear wave speed measurement using an unfocused ultrasound beam. *Ultrasound Med. Biol.* 38: 1646–1655.

35 Hoyt, K., Hah, Z., Hazard, C., and Parker, K.J. (2012). Experimental validation of acoustic radiation force induced shear wave interference patterns. *Phys. Med. Biol.* 57: 21.

36 Nabavizadeh, A., Greenleaf, J.F., Fatemi, M., and Urban, M.W. (2014). Optimized shear wave generation using hybrid beamforming methods. *Ultrasound Med. Biol.* 40: 188–199.

37 Song, P., Urban, M.W., Manduca, A., et al. (2013). Comb-push ultrasound shear elastography (CUSE) with various ultrasound push beams. *IEEE Trans. Med. Imaging* 32: 1435–1447.

38 Nabavizadeh, A., Song, P., Chen, S.,et al. (2015). Multi-source and multi-directional shear wave generation with intersecting steered ultrasound push beams. *IEEE Trans. Ultrason., Ferroelectr., Freq. Control* 62: 647–662.

Index

Ultrasound Elastography for Biomedical Applications and Medicine, First Edition.
Edited by Ivan Nenadic, Matthew Urban, James Greenleaf, Jean-Luc Gennisson, Miguel Bernal, and Mickael Tanter.

d

e

WILEY END USER LICENSE AGREEMENT

Go to www.wiley.com/go/eula to access Wiley’s ebook EULA.